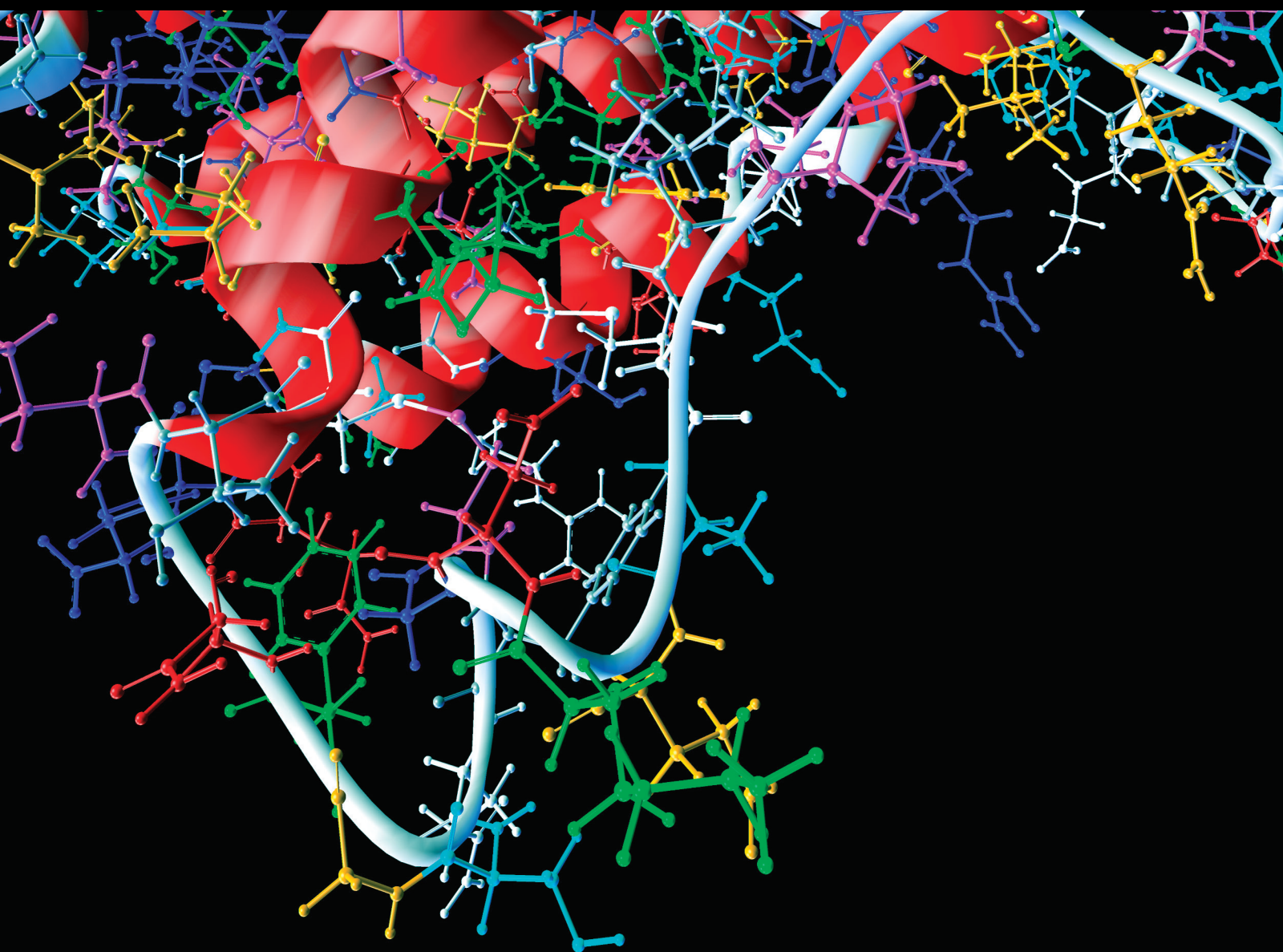


Computational and Mathematical Methods in Medicine

Machine Learning and AI Methods in Computer Vision and Visualisation for Healthcare 2022

Lead Guest Editor: Pan Zheng

Guest Editors: Xun Wang and Dennis Wong





**Machine Learning and AI Methods in
Computer Vision and Visualisation for
Healthcare 2022**

Computational and Mathematical Methods in Medicine

**Machine Learning and AI Methods in
Computer Vision and Visualisation for
Healthcare 2022**

Lead Guest Editor: Pan Zheng




Guest Editors: Xun Wang and Dennis Wong



Copyright © 2023 Hindawi Limited. All rights reserved.

This is a special issue published in “Computational and Mathematical Methods in Medicine.” All articles are open access articles distributed under the Creative Commons Attribution License, which permits unrestricted use, distribution, and reproduction in any medium, provided the original work is properly cited.

Associate Editors

Ahmed Albahri, Iraq
Konstantin Blyuss , United Kingdom
Chuangyin Dang, Hong Kong
Farai Nyabadza , South Africa
Kathiravan Srinivasan , India

Academic Editors

Laith Abualigah , Jordan
Yaser Ahangari Nanekaran , China
Mubashir Ahmad, Pakistan
Sultan Ahmad , Saudi Arabia
Akif Akgul , Turkey
Karthick Alagar, India
Shadab Alam, Saudi Arabia
Raul Alcaraz , Spain
Emil Alexov, USA
Enrique Baca-Garcia , Spain
Sweta Bhattacharya , India
Junguo Bian, USA
Elia Biganzoli , Italy
Antonio Boccaccio, Italy
Hans A. Braun , Germany
Zhicheng Cao, China
Guy Carrault, France
Sadaruddin Chachar , Pakistan
Prem Chapagain , USA
Huiling Chen , China
Mengxin Chen , China
Haruna Chiroma, Saudi Arabia
Watcharaporn Cholamjiak , Thailand
Maria N. D.S. Cordeiro , Portugal
Cristiana Corsi , Italy
Qi Dai , China
Nagarajan Deivanayagam Pillai, India
Didier Delignières , France
Thomas Desaive , Belgium
David Diller , USA
Qamar Din, Pakistan
Irina Doytchinova, Bulgaria
Sheng Du , China
D. Easwaramoorthy , India

Esmaeil Ebrahimie , Australia
Issam El Naqa , USA
Ilias Elmouki , Morocco
Angelo Facchiano , Italy
Luca Faes , Italy
Maria E. Fantacci , Italy
Giancarlo Ferrigno , Italy
Marc Thilo Figge , Germany
Giulia Fiscon , Italy
Bapan Ghosh , India
Igor I. Goryanin, Japan
Marko Gosak , Slovenia
Damien Hall, Australia
Abdulsattar Hamad, Iraq
Khalid Hattaf , Morocco
Tingjun Hou , China
Seiya Imoto , Japan
Martti Juhola , Finland
Rajesh Kaluri , India
Karthick Kanagarathinam, India
Rafik Karaman , Palestinian Authority
Chandan Karmakar , Australia
Kwang Gi Kim , Republic of Korea
Andrzej Kloczkowski, USA
Andrei Korobeinikov , China
Sakthidasan Sankaran Krishnan, India
Rajesh Kumar, India
Kuruva Lakshmana , India
Peng Li , USA
Chung-Min Liao , Taiwan
Pinyi Lu , USA
Reinoud Maex, United Kingdom
Valeri Makarov , Spain
Juan Pablo Martínez , Spain
Richard J. Maude, Thailand
Zahid Mehmood , Pakistan
John Mitchell , United Kingdom
Fazal Ijaz Muhammad , Republic of Korea
Vishal Nayak , USA
Tongguang Ni, China
Michele Nichelatti, Italy
Kazuhisa Nishizawa , Japan
Bing Niu , China

Hyuntae Park , Japan
Jovana Paunovic , Serbia
Manuel F. G. Penedo , Spain
Riccardo Pernice , Italy
Kemal Polat , Turkey
Alberto Policriti, Italy
Giuseppe Pontrelli , Italy
Jesús Poza , Spain
Maciej Przybyłek , Poland
Bhanwar Lal Puniya , USA
Mihai V. Putz , Romania
Suresh Rasappan, Oman
Jose Joaquin Rieta , Spain
Fathalla Rihan , United Arab Emirates
Sidheswar Routray, India
Sudipta Roy , India
Jan Rychtar , USA
Mario Sansone , Italy
Murat Sari , Turkey
Shahzad Sarwar, Saudi Arabia
Kamal Shah, Saudi Arabia
Bhisham Sharma , India
Simon A. Sherman, USA
Mingsong Shi, China
Mohammed Shuaib , Malaysia
Prabhishek Singh , India
Neelakandan Subramani, India
Junwei Sun, China
Yung-Shin Sun , Taiwan
Min Tang , China
Hongxun Tao, China
Alireza Tavakkoli , USA
João M. Tavares , Portugal
Jlenia Toppi , Italy
Anna Tsantili-Kakoulidou , Greece
Markos G. Tsipouras, North Macedonia
Po-Hsiang Tsui , Taiwan
Sathishkumar V E , Republic of Korea
Durai Raj Vincent P M , India
Gajendra Kumar Vishwakarma, India
Liangjiang Wang, USA
Ruisheng Wang , USA
Zhouchao Wei, China
Gabriel Wittum, Germany
Xiang Wu, China

KI Yanover , Israel
Xiaojun Yao , China
Kaan Yetilmezsoy, Turkey
Hiro Yoshida, USA
Yuhai Zhao , China

Contents

Retracted: Research on the Effect of Nursing Methods for Gestational Diabetes Mellitus Based on Comprehensive Nursing Intervention

Computational and Mathematical Methods in Medicine
Retraction (1 page), Article ID 9897201, Volume 2023 (2023)

Retracted: Risk Factors of Acute Radiation-Induced Lung Injury Induced by Radiotherapy for Esophageal Cancer

Computational and Mathematical Methods in Medicine
Retraction (1 page), Article ID 9895053, Volume 2023 (2023)

Retracted: Application of Digital Orthopedic Technology in Orthopedic Trauma

Computational and Mathematical Methods in Medicine
Retraction (1 page), Article ID 9765125, Volume 2023 (2023)

Retracted: The Development Relationship between Cross-Border e-Commerce and Internet of Things Technology Coupling in Digital Economy Based on Neural Network Model

Computational and Mathematical Methods in Medicine
Retraction (1 page), Article ID 9823297, Volume 2023 (2023)

Retracted: CX3CL1 Derived from Bone Marrow Mesenchymal Stem Cells Inhibits $A\beta_{1-42}$ -Induced SH-SY5Y Cell Pathological Damage through TXNIP/NLRP3 Signaling Pathway

Computational and Mathematical Methods in Medicine
Retraction (1 page), Article ID 9817614, Volume 2023 (2023)

Retracted: Clinical Study of Anti-PD-1 Immunotherapy Combined with Gemcitabine Chemotherapy in Multiline Treatment of Advanced Pancreatic Cancer

Computational and Mathematical Methods in Medicine
Retraction (1 page), Article ID 9814782, Volume 2023 (2023)

Retracted: Application of Mathematical Modeling in Cost Control of Medical Equipment Procurement in Public Hospitals

Computational and Mathematical Methods in Medicine
Retraction (1 page), Article ID 9808407, Volume 2023 (2023)

Retracted: Exploration of Landscape Lighting Design Based on Interactive Genetic Algorithm

Computational and Mathematical Methods in Medicine
Retraction (1 page), Article ID 9803673, Volume 2023 (2023)

Retracted: Efficacy of Cetuximab in Nasopharyngeal Carcinoma Patients Receiving Concurrent Cisplatin-Radiotherapy: A Meta-Analysis

Computational and Mathematical Methods in Medicine
Retraction (1 page), Article ID 9798503, Volume 2023 (2023)

Retracted: Analysis of Obstetric Clinical Nursing Integrating Situational Teaching Simulation

Computational and Mathematical Methods in Medicine
Retraction (1 page), Article ID 9798171, Volume 2023 (2023)

Retracted: The Application of Focused Care Model in the Management of Hepatitis B Patients in a Tertiary Care Hospital and the Impact on Patients' Quality of Life

Computational and Mathematical Methods in Medicine
Retraction (1 page), Article ID 9783918, Volume 2023 (2023)

Retracted: Analysis the Innovation Path on Psychological Ideological with Political Teaching in Universities by Big Data in New Era

Computational and Mathematical Methods in Medicine
Retraction (1 page), Article ID 9765891, Volume 2023 (2023)

Retracted: Efficacy of Gamma Globulin Combined with Azithromycin Sequential Therapy in the Treatment of RMPP and Its Effect on Th1/Th2 Cytokine Levels

Computational and Mathematical Methods in Medicine
Retraction (1 page), Article ID 9758016, Volume 2023 (2023)

Retracted: The Diagnosis of Early Gastric Cancer Based on Medical Imaging Technology and Mathematical Modeling

Computational and Mathematical Methods in Medicine
Retraction (1 page), Article ID 9867187, Volume 2023 (2023)

Retracted: Induction of Resistance of Antagonistic Bacterium Burkholderia contaminans to Postharvest Botrytis cinerea in Rosa vinifera

Computational and Mathematical Methods in Medicine
Retraction (1 page), Article ID 9865391, Volume 2023 (2023)

Retracted: Research on Land Utilization Spatial Classification Planning Method Based on Multiocular Vision

Computational and Mathematical Methods in Medicine
Retraction (1 page), Article ID 9864198, Volume 2023 (2023)

Retracted: Effect of Propofol Intravenous Anesthesia Combined with Press-Needle Therapy on Analgesic Effect during Painless Abortion

Computational and Mathematical Methods in Medicine
Retraction (1 page), Article ID 9858364, Volume 2023 (2023)

Retracted: Safety and Efficacy of Tirofiban Combined with Statins in the Perioperative Period of Intracranial Aneurysms: Systematic Review and Meta-Analysis

Computational and Mathematical Methods in Medicine
Retraction (1 page), Article ID 9854683, Volume 2023 (2023)

Retracted: Design and Application of Artificial Intelligence Technology-Driven Education and Teaching System in Universities

Computational and Mathematical Methods in Medicine
Retraction (1 page), Article ID 9848704, Volume 2023 (2023)

Contents

Retracted: Clinical Study of Different Treatment Methods for Tuberculous Pleuritis Complicated with Pleural Tuberculoma

Computational and Mathematical Methods in Medicine
Retraction (1 page), Article ID 9847416, Volume 2023 (2023)

Retracted: Deep Image Watermarking to JPEG Compression Based on Mixed-Frequency Channel Attention

Computational and Mathematical Methods in Medicine
Retraction (1 page), Article ID 9847397, Volume 2023 (2023)

Retracted: Serum Adiponectin Level in Different Stages of Type 2 Diabetic Kidney Disease: A Meta-Analysis

Computational and Mathematical Methods in Medicine
Retraction (1 page), Article ID 9846897, Volume 2023 (2023)

Retracted: Analysis of Efficacy, Complications, and Inflammatory Reactions of Bridge Combined Internal Fixation System for Periarticular Fractures of the Shoulder

Computational and Mathematical Methods in Medicine
Retraction (1 page), Article ID 9846594, Volume 2023 (2023)

Retracted: Epidural Anesthesia versus General Anesthesia for Total Knee Arthroplasty: Influences on Perioperative Cognitive Function and Deep Vein Thrombosis

Computational and Mathematical Methods in Medicine
Retraction (1 page), Article ID 9842421, Volume 2023 (2023)

Retracted: Impacts of Low-Dose Total Glycosides of Tripterygium wilfordii plus Methotrexate on Immunological Function and Inflammation Level in Patients with Rheumatoid Arthritis

Computational and Mathematical Methods in Medicine
Retraction (1 page), Article ID 9842325, Volume 2023 (2023)

Retracted: Effects of Dapagliflozin in Combination with Metoprolol Sustained-Release Tablets on Prognosis and Cardiac Function in Patients with Acute Myocardial Infarction after PCI

Computational and Mathematical Methods in Medicine
Retraction (1 page), Article ID 9838713, Volume 2023 (2023)


Retracted: A Method for Evaluating the Quality of Mathematics Education Based on Artificial Neural Network

Computational and Mathematical Methods in Medicine
Retraction (1 page), Article ID 9830191, Volume 2023 (2023)

Influence of Prehospital Emergency Care on Rescue Success Rate and Complication Rate of Senile Patients with Acute Myocardial Infarction






Yingchao Zhang, Lili Huang, and Xuehong Zhou 
Research Article (6 pages), Article ID 7557288, Volume 2022 (2022)

Analysis of Characteristic Factors of Nursing Safety Incidents in ENT Surgery by Deep Learning-Based Medical Data Association Rules Method

Ju Chen , Jie Zhou, and Fanglan Yang


Research Article (6 pages), Article ID 8491411, Volume 2022 (2022)

Alzheimer's Disease Prediction Algorithm Based on Group Convolution and a Joint Loss Function

Jiayuan Cheng , Huabin Wang , Shicheng Wei , Fei Liu , and Yonglin Chen 




Research Article (11 pages), Article ID 1854718, Volume 2022 (2022)

Influence of "Hospital-Community-Family" Integrated Management on Blood Pressure, Quality of Life, Anxiety and Depression in Hypertensive Patients

Wanzhe Shi, Lei Cheng, and Yang Li 


Research Article (9 pages), Article ID 1962475, Volume 2022 (2022)

[Retracted] The Diagnosis of Early Gastric Cancer Based on Medical Imaging Technology and Mathematical Modeling

Jingying Xiu, Lie Ma, Yanping Ding, Yang Li, Lili Kan, Shi Feng, Fei Wu, Shanshan Xu, Xinan Lu , Ting He , and Zhihai Han 


Research Article (7 pages), Article ID 8721654, Volume 2022 (2022)

Effect of Mirena Intrauterine Device on Endometrial Thickness, Quality of Life Score, and Curative Effect in Patients with Perimenopausal Abnormal Uterine Bleeding

Ying Yu, Zhi Zhou, Liping Wang, and Jie Liu 


Research Article (8 pages), Article ID 5648918, Volume 2022 (2022)

[Retracted] Safety and Efficacy of Tirofiban Combined with Statins in the Perioperative Period of Intracranial Aneurysms: Systematic Review and Meta-Analysis

Ming Hao, Rui Liu, Feiping Yan, and Youcai Luo 






Research Article (7 pages), Article ID 8264261, Volume 2022 (2022)

Deep Learning-Based Medical Data Association Rules to Explore the Connectivity and Regulation Mechanism of miRNA-mRNA Network in Myocarditis

Fang Li, Jingzhe Li, Jie Hao, Jinming Liu, XiuGuang Zu, and Bin Wang 


Research Article (8 pages), Article ID 9272709, Volume 2022 (2022)

Weighted Gene Coexpression Network Analysis Identified IL2/STAT5 Signaling Pathway as an Important Determinant of Peri-Implantitis

Li Tang , Hailun Zhou , Donghui Chen , Rong Xiang , and Jianjia Tang 

Research Article (15 pages), Article ID 4202823, Volume 2022 (2022)


TAOK1 Promotes Proliferation and Invasion of Non-Small-Cell Lung Cancer Cells by Inhibition of WWC1

Lian Chen 


Research Article (9 pages), Article ID 3157448, Volume 2022 (2022)

Contents


[Retracted] The Application of Focused Care Model in the Management of Hepatitis B Patients in a Tertiary Care Hospital and the Impact on Patients' Quality of Life

Jian-Wei Zhang, Yan Wang, Hai-Hong Shan, Jia-Yu Duan, and Juan Yu 
Research Article (11 pages), Article ID 7770955, Volume 2022 (2022)


[Retracted] Design and Application of Artificial Intelligence Technology-Driven Education and Teaching System in Universities

Fan Zhang 
Research Article (10 pages), Article ID 8503239, Volume 2022 (2022)

[Retracted] Epidural Anesthesia versus General Anesthesia for Total Knee Arthroplasty: Influences on Perioperative Cognitive Function and Deep Vein Thrombosis

Tao Ma, Guanhua Li, Hao Zhang, Yingxin Zhang, Lei Wang, Hailong Wu, Yang Chu, Xiaoli Zhao, and Wei Wang 
Research Article (6 pages), Article ID 4259499, Volume 2022 (2022)


Analysis of the Preventive Action of Rivaroxaban against Lower Extremity Deep Venous Thrombosis in Patients after Laparoscopic Radical Gastrectomy

Qinhui Dong, Xiayin Zhu, Yafen Gao, Zhengrong Wang, Dexing Zheng, and Jian Zhu 
Research Article (6 pages), Article ID 7140066, Volume 2022 (2022)



[Retracted] The Development Relationship between Cross-Border e-Commerce and Internet of Things Technology Coupling in Digital Economy Based on Neural Network Model

Qi Liu 
Research Article (10 pages), Article ID 8981618, Volume 2022 (2022)


[Retracted] CX3CL1 Derived from Bone Marrow Mesenchymal Stem Cells Inhibits $A\beta_{1-42}$ -Induced SH-SY5Y Cell Pathological Damage through TXNIP/NLRP3 Signaling Pathway

Chuan Guo, Qinxuan Li, Jiujiu Xiao, Xuhui Zhou, Meichen Tian, Lei Xie, and Xun Xia 
Research Article (12 pages), Article ID 1949344, Volume 2022 (2022)


The Effect of PD-1 Inhibitor Combined with Chemotherapy on the Level of Peripheral Blood T Lymphocytes among Patients with Non-Small-Cell Lung Cancer and Its Relationship with Prognosis

Yun Zhao, Jianbo He, Shaozhang Zhou, Ruiling Ning, Wenhua Zhao, Huilin Wang, Cuiyun Su, Wei Jiang, Xiaoning Zhong , and Qitao Yu 
Research Article (7 pages), Article ID 1679191, Volume 2022 (2022)


[Retracted] Clinical Study of Anti-PD-1 Immunotherapy Combined with Gemcitabine Chemotherapy in Multiline Treatment of Advanced Pancreatic Cancer

Yanfeng Liu, Yanchuan Li, Shan Du, Li Fan, and Junyan Wang 
Research Article (6 pages), Article ID 4070060, Volume 2022 (2022)

[Retracted] Analysis the Innovation Path on Psychological Ideological with Political Teaching in Universities by Big Data in New Era


Xiufen Luo 
Research Article (9 pages), Article ID 4305886, Volume 2022 (2022)

Influences of Ultrasonic Image-Guided Erector Spinae Plane Block on Postoperative Pulmonary Air Content of Lung Carcinoma Patients Undergoing Thoracoscopic Surgery

Xiuqing Xu, Shengrong Yang, and Pei Gao 


Research Article (11 pages), Article ID 1301361, Volume 2022 (2022)

Clinical Efficacy of Glucosamine plus Sodium Hyaluronate for Osteoporosis Complicated by Knee Osteoarthritis and Its Influence on Joint Function and Bone Metabolic Markers

Jing-Jin Yang and Xiu-Mei Zhang 

Research Article (6 pages), Article ID 6078254, Volume 2022 (2022)

Effects of Propofol Intravenous Anesthesia on Serum NGF, S100B Protein, and Immune Function in Patients with Bladder Cancer after Resection

Xiaohong Guan, Qingxiang Peng, Yongping Liu, and Jiansong Wang 


Research Article (5 pages), Article ID 5409323, Volume 2022 (2022)

[Retracted] Research on Land Utilization Spatial Classification Planning Method Based on Multiocular Vision

Zhifei Zhang and Shenmin Wang 



Research Article (13 pages), Article ID 9300278, Volume 2022 (2022)

[Retracted] Clinical Study of Different Treatment Methods for Tuberculous Pleuritis Complicated with Pleural Tuberculoma

Xiaoling Zhang and Jingyu Chi 

Research Article (9 pages), Article ID 5666067, Volume 2022 (2022)

Efficacy and Safety Analysis of Multislice Spiral CT-Guided Transthoracic Lung Biopsy in the Diagnosis of Pulmonary Nodules of Different Sizes

Huitong Liu , Xiao Yao, Bingqiang Xu, Wei Zhang, Yu Lei, and Xiaolong Chen 


Research Article (8 pages), Article ID 8192832, Volume 2022 (2022)

[Retracted] Efficacy of Cetuximab in Nasopharyngeal Carcinoma Patients Receiving Concurrent Cisplatin-Radiotherapy: A Meta-Analysis

Lin Wang, Dianjun Liu, and Deyou Wei 


Research Article (16 pages), Article ID 5145549, Volume 2022 (2022)

Effect of Ultrasound Image-Guided Nerve Block on the Postoperative Recovery Quality of Patients with Tibial Fractures Using the Concept of Enhanced Recovery after Surgery

Xiaohong Zhang, Lu He, Xiangqing Mo, Ling Jiang, and Chenhui Deng 

Research Article (8 pages), Article ID 4428883, Volume 2022 (2022)


[Retracted] Exploration of Landscape Lighting Design Based on Interactive Genetic Algorithm

Haixiao Shi and Jie Zheng 

Research Article (11 pages), Article ID 1771617, Volume 2022 (2022)

Contents

[Retracted] Analysis of Efficacy, Complications, and Inflammatory Reactions of Bridge Combined Internal Fixation System for Periarticular Fractures of the Shoulder

Haiyun Xu, Youliang Fan, Jiajun Lu, Yixiong Wu, and Xiaoguang Feng 


Research Article (6 pages), Article ID 5048172, Volume 2022 (2022)

Discussion on Repolarization Reserve between Patients with Coronary Heart Disease and Normal Controls

Rubing Kang, Yitong Li, Chunmei Gao, Jianhui Li, Cheng Zhang, and Junli Wang 


Research Article (8 pages), Article ID 7944969, Volume 2022 (2022)

[Retracted] Application of Digital Orthopedic Technology in Orthopedic Trauma

Jiangtao Lin, Junbo Ge, Jinpeng Gong, Huanyu Hong, and Chuanqiang Jiang 


Research Article (11 pages), Article ID 3157107, Volume 2022 (2022)

The Effect on Quality of Life after Three-Dimensional Intensity-Modulated Radiation Therapy in Patients with Low-Grade Glioma

Huili Chen, He Rao, and Yong Huang 


Research Article (6 pages), Article ID 5854013, Volume 2022 (2022)

[Retracted] A Method for Evaluating the Quality of Mathematics Education Based on Artificial Neural Network

Fuli Bao  and Chong Wang


Research Article (11 pages), Article ID 6976654, Volume 2022 (2022)

Efficacy of Postoperative Analgesia by Erector Spinal Plane Block after Lumbar Surgery: A Systematic Review and Meta-analysis of Randomized Controlled Trials

Xiao Xiao, Tingting Zhu, Lin Wang, Hongmei Zhou, and Yanli Zhang 


Review Article (9 pages), Article ID 3264142, Volume 2022 (2022)

Ultrasound Evaluation of Pelvic Floor Function after Transumbilical Laparoscopic Single-Site Total Hysterectomy Using Deep Learning Algorithm

Yan Zhu, Jiamiao Zhang, Zhonglei Ji, Wen Liu, Mingyue Li, Enhui Xia, Jing Zhang, and Jianqing Wang 


Research Article (10 pages), Article ID 1116332, Volume 2022 (2022)

Anatomical and Imaging Study on the Optimum Entry Point and Trajectory for Anterior Transpedicular Root Screw Placement into the Lower Cervical Spine

Jihui Zhang, LiuJun Zhao , Jingfei Xu, Yongjie Gu, and Liang Yu


Research Article (7 pages), Article ID 8159570, Volume 2022 (2022)

Early Diagnosis and Treatment of Coronary Heart Disease with Image Features of Optical Coherence Tomography under Adaptive Segmentation Algorithm


Chaozhang Lin 

Research Article (13 pages), Article ID 1261259, Volume 2022 (2022)


[Retracted] Effect of Propofol Intravenous Anesthesia Combined with Press-Needle Therapy on Analgesic Effect during Painless Abortion

Xia Zhu , Xueming He, Baojun Fan, Jing Liu, Shuqing Wu, Hongli Wang, and Chunwei Chen
Research Article (10 pages), Article ID 6543211, Volume 2022 (2022)


[Retracted] Effects of Dapagliflozin in Combination with Metoprolol Sustained-Release Tablets on Prognosis and Cardiac Function in Patients with Acute Myocardial Infarction after PCI

Hao Zhang  and Zeyan Liu
Research Article (8 pages), Article ID 5734876, Volume 2022 (2022)



[Retracted] Impacts of Low-Dose Total Glycosides of Tripterygium wilfordii plus Methotrexate on Immunological Function and Inflammation Level in Patients with Rheumatoid Arthritis

Yong Han , Jingri Jin, Fushun Wu, and Zhiwei Wang
Research Article (7 pages), Article ID 7523673, Volume 2022 (2022)


Therapeutic Effect of Ultrasound-Guided Peripherally Inserted Central Catheter Combined with Predictive Nursing in Patients with Large-Area Severe Burns

Baiyan He, Aiqiong Zhang, and Shuting He 
Research Article (11 pages), Article ID 1019829, Volume 2022 (2022)


Construction and Validation of Prediction Model of Severe Abdominal Pain Post-Transarterial Chemoembolization in Patients with HBV-Associated Primary Liver Cancer

Yaobo Yang, Sipan Chen , Zhaoyong Yan , Yang Jiao, Xiang Yan, and Yulong Li
Research Article (6 pages), Article ID 5203166, Volume 2022 (2022)


Efficacy of Gamma Globulins in Children with Kawasaki Disease and Factors Influencing Children's Short-Term Prognosis

Hao Sun , Huimin Lu, and Yunhong Wu
Research Article (6 pages), Article ID 5137874, Volume 2022 (2022)


Application Value of Evidence-Based Care in Patients with Lung Cancer Chemotherapy

Ying Chen, Hong Xu, Yun Cheng, and Yuan Qian 
Research Article (8 pages), Article ID 5747712, Volume 2022 (2022)

Tandem Mass Tag Analysis of the Effect of the Anterior Cingulate Cortex in Nonerosive Reflux Disease Rats with Shugan Jiangni Hewei Granules Treatment


Tianzuo Wang, Jing Li, Yuebo Jia, Jiaqi Zhao, Meijun He, and Guang Bai 
Research Article (19 pages), Article ID 8104337, Volume 2022 (2022)

A Nomogram Model for Individualized Prediction of the Risk of Respiratory Tract Infection within Six Months after Diagnosis in Patients with Primary Immune Thrombocytopenia

Jinhua Wei, Weiwei Pan, Feng Luo, Fengnian Tang, Jiashi Wei, Siwen Fang, and Honglian Huang 
Research Article (7 pages), Article ID 5002681, Volume 2022 (2022)


Contents

Correlation Analysis of Computed Tomography Features and Pathological Types of Multifocal Ground-Glass Nodular Lung Adenocarcinoma

Jieli Kou, Xiaofei Gu, and Liqing Kang 

Research Article (10 pages), Article ID 7267036, Volume 2022 (2022)

Efficacy Analysis of Endovascular Therapy for Nonthrombotic Iliac Vein Compression Syndrome Combined with Chronic Venous Insufficiency

Renda Zhu , Xiaodong Jin, and Jiayi Shen


Research Article (5 pages), Article ID 2718314, Volume 2022 (2022)

Intelligent Three-Dimensional Reconstruction Algorithm-Based Ultrasound-Guided Nerve Block in Intraoperative Anesthesia and Postoperative Analgesia of Orthopedic Surgery

Cuijie Liu, Lin Li, Xuan Zhou, and Xiuyan Wang 


Research Article (9 pages), Article ID 9447649, Volume 2022 (2022)

The Value of 320-Slice Spiral Computed Tomography Perfusion Imaging in Staging and Long-Term Dynamic Evaluation of Breast Cancer

Hequn Geng , Zhilin Zhang, Xiaochen Zhang, Zhandong Liang, Yong Li, and Shujun Cui

Research Article (8 pages), Article ID 7442123, Volume 2022 (2022)

[Retracted] Efficacy of Gamma Globulin Combined with Azithromycin Sequential Therapy in the Treatment of RMPP and Its Effect on Th1/Th2 Cytokine Levels

Jie Qi, Fang Jia, Hui Tian, and Shengmei Yang 


Research Article (5 pages), Article ID 5162768, Volume 2022 (2022)

[Retracted] Serum Adiponectin Level in Different Stages of Type 2 Diabetic Kidney Disease: A Meta-Analysis

Li Li , Jilai Shi , and Guoliang Wu




Research Article (11 pages), Article ID 1863243, Volume 2022 (2022)

[Retracted] Research on the Effect of Nursing Methods for Gestational Diabetes Mellitus Based on Comprehensive Nursing Intervention

Xueqiong Ren , Jianing Jin, Yaer Chen, and Jing Jin



Research Article (10 pages), Article ID 2396658, Volume 2022 (2022)

[Retracted] Deep Image Watermarking to JPEG Compression Based on Mixed-Frequency Channel Attention

Jun Tan , Yanan Hu, Ziming Shi , and Bin Wang 


Research Article (12 pages), Article ID 9880038, Volume 2022 (2022)

Prognostic Evaluation of CT Imaging Big Data-Assisted Arterial Chemoembolization Combined with ¹²⁵I Seed Implantation for Non-Small-Cell Lung Cancer

Peng Xie , Yan Zhang , and Lidong He


Research Article (8 pages), Article ID 3472982, Volume 2022 (2022)

[Retracted] Risk Factors of Acute Radiation-Induced Lung Injury Induced by Radiotherapy for Esophageal Cancer

Faen Zhang , Lihua Liao, Song Wei, and Yuqing Lu


Research Article (6 pages), Article ID 2416196, Volume 2022 (2022)

Diagnostic Value and High-Risk Factors of Two-Dimensional Ultrasonography Combined with Four-Dimensional Ultrasonography in Prenatal Ultrasound Screening of Fetal Congenital Malformations

Xinyou Yu, Fang Liu, Wei Gao, Xiangrong Shi, Ruiping Lu, and Lihua Pan 



Research Article (7 pages), Article ID 7082832, Volume 2022 (2022)

[Retracted] Application of Mathematical Modeling in Cost Control of Medical Equipment Procurement in Public Hospitals

Lihong Chen 

Research Article (12 pages), Article ID 3425873, Volume 2022 (2022)


Diagnosis of Brain Tumor Using Light Weight Deep Learning Model with Fine-Tuning Approach

Tejas Shelatkar, Dr. Urvashi, Mohammad Shorfuzzaman , Abdulmajeed Alsufyani , and Kuruva

Lakshmana 


Research Article (9 pages), Article ID 2858845, Volume 2022 (2022)

Observation of Visual Quality after Femtosecond Laser-Assisted Cataract Surgery Combined with Trifocal Intraocular Lens Implantation

Jianli Ma, Xuequan Sun, Yang Liu, and Yumei Liu 


Research Article (8 pages), Article ID 1519416, Volume 2022 (2022)

[Retracted] Induction of Resistance of Antagonistic Bacterium *Burkholderia contaminans* to Postharvest *Botrytis cinerea* in *Rosa vinifera*

Fengying Shen, Zigang Liu, Chenyang Du, Junhai Yuan, Weigang Wu , and Dong Wei




Research Article (12 pages), Article ID 7134161, Volume 2022 (2022)

Effects of Body Posture and Different Exercise Intensity on Athletes' Limb Injury

Di Jin  and Qian Ma






Research Article (7 pages), Article ID 5103017, Volume 2022 (2022)

Early Diagnosis of Retinal Blood Vessel Damage via Deep Learning-Powered Collective Intelligence Models

Pranjal Bhardwaj, Prajjwal Gupta , Thejineaswar Guhan , and Kathiravan Srinivasan 

Research Article (13 pages), Article ID 3571364, Volume 2022 (2022)


Boosted Sine Cosine Algorithm with Application to Medical Diagnosis

Xiaojia Ye , Zhenna Cai , Chenglang Lu , Huiling Chen , and Zhifang Pan 

Research Article (21 pages), Article ID 6215574, Volume 2022 (2022)


Contents

[Retracted] Analysis of Obstetric Clinical Nursing Integrating Situational Teaching Simulation

Shanshan Xiao, Jing Fang, Xiaoxiao Zhao, Liqin Yang, Hongyan Tang, and Yuanping Wang 

Research Article (12 pages), Article ID 6843196, Volume 2022 (2022)

Body Weight Is a Valid Predictor of the Long-Term Prognosis of Cervical Cancer

Li Lu , Shuqi Ji, Jing Jiang, and Yu Yan

Research Article (7 pages), Article ID 5613350, Volume 2022 (2022)

Retraction

Retracted: Research on the Effect of Nursing Methods for Gestational Diabetes Mellitus Based on Comprehensive Nursing Intervention

Computational and Mathematical Methods in Medicine

Received 26 September 2023; Accepted 26 September 2023; Published 27 September 2023

Copyright © 2023 Computational and Mathematical Methods in Medicine. This is an open access article distributed under the Creative Commons Attribution License, which permits unrestricted use, distribution, and reproduction in any medium, provided the original work is properly cited.

This article has been retracted by Hindawi following an investigation undertaken by the publisher [1]. This investigation has uncovered evidence of one or more of the following indicators of systematic manipulation of the publication process:

- (1) Discrepancies in scope
- (2) Discrepancies in the description of the research reported
- (3) Discrepancies between the availability of data and the research described
- (4) Inappropriate citations
- (5) Incoherent, meaningless and/or irrelevant content included in the article
- (6) Peer-review manipulation

The presence of these indicators undermines our confidence in the integrity of the article's content and we cannot, therefore, vouch for its reliability. Please note that this notice is intended solely to alert readers that the content of this article is unreliable. We have not investigated whether authors were aware of or involved in the systematic manipulation of the publication process.

In addition, our investigation has also shown that one or more of the following human-subject reporting requirements has not been met in this article: ethical approval by an Institutional Review Board (IRB) committee or equivalent, patient/participant consent to participate, and/or agreement to publish patient/participant details (where relevant).

Wiley and Hindawi regrets that the usual quality checks did not identify these issues before publication and have since put additional measures in place to safeguard research integrity.

We wish to credit our own Research Integrity and Research Publishing teams and anonymous and named external researchers and research integrity experts for contributing to this investigation.

The corresponding author, as the representative of all authors, has been given the opportunity to register their agreement or disagreement to this retraction. We have kept a record of any response received.

References

- [1] X. Ren, J. Jin, Y. Chen, and J. Jin, "Research on the Effect of Nursing Methods for Gestational Diabetes Mellitus Based on Comprehensive Nursing Intervention," *Computational and Mathematical Methods in Medicine*, vol. 2022, Article ID 2396658, 10 pages, 2022.

Retraction

Retracted: Risk Factors of Acute Radiation-Induced Lung Injury Induced by Radiotherapy for Esophageal Cancer

Computational and Mathematical Methods in Medicine

Received 26 September 2023; Accepted 26 September 2023; Published 27 September 2023

Copyright © 2023 Computational and Mathematical Methods in Medicine. This is an open access article distributed under the Creative Commons Attribution License, which permits unrestricted use, distribution, and reproduction in any medium, provided the original work is properly cited.

This article has been retracted by Hindawi following an investigation undertaken by the publisher [1]. This investigation has uncovered evidence of one or more of the following indicators of systematic manipulation of the publication process:

- (1) Discrepancies in scope
- (2) Discrepancies in the description of the research reported
- (3) Discrepancies between the availability of data and the research described
- (4) Inappropriate citations
- (5) Incoherent, meaningless and/or irrelevant content included in the article
- (6) Peer-review manipulation

The presence of these indicators undermines our confidence in the integrity of the article's content and we cannot, therefore, vouch for its reliability. Please note that this notice is intended solely to alert readers that the content of this article is unreliable. We have not investigated whether authors were aware of or involved in the systematic manipulation of the publication process.

In addition, our investigation has also shown that one or more of the following human-subject reporting requirements has not been met in this article: ethical approval by an Institutional Review Board (IRB) committee or equivalent, patient/participant consent to participate, and/or agreement to publish patient/participant details (where relevant).

Wiley and Hindawi regrets that the usual quality checks did not identify these issues before publication and have since put additional measures in place to safeguard research integrity.

We wish to credit our own Research Integrity and Research Publishing teams and anonymous and named external researchers and research integrity experts for contributing to this investigation.

The corresponding author, as the representative of all authors, has been given the opportunity to register their agreement or disagreement to this retraction. We have kept a record of any response received.

References

- [1] F. Zhang, L. Liao, S. Wei, and Y. Lu, "Risk Factors of Acute Radiation-Induced Lung Injury Induced by Radiotherapy for Esophageal Cancer," *Computational and Mathematical Methods in Medicine*, vol. 2022, Article ID 2416196, 6 pages, 2022.

Retraction

Retracted: Application of Digital Orthopedic Technology in Orthopedic Trauma

Computational and Mathematical Methods in Medicine

Received 26 September 2023; Accepted 26 September 2023; Published 27 September 2023

Copyright © 2023 Computational and Mathematical Methods in Medicine. This is an open access article distributed under the Creative Commons Attribution License, which permits unrestricted use, distribution, and reproduction in any medium, provided the original work is properly cited.

This article has been retracted by Hindawi following an investigation undertaken by the publisher [1]. This investigation has uncovered evidence of one or more of the following indicators of systematic manipulation of the publication process:

- (1) Discrepancies in scope
- (2) Discrepancies in the description of the research reported
- (3) Discrepancies between the availability of data and the research described
- (4) Inappropriate citations
- (5) Incoherent, meaningless and/or irrelevant content included in the article
- (6) Peer-review manipulation

The presence of these indicators undermines our confidence in the integrity of the article's content and we cannot, therefore, vouch for its reliability. Please note that this notice is intended solely to alert readers that the content of this article is unreliable. We have not investigated whether authors were aware of or involved in the systematic manipulation of the publication process.

In addition, our investigation has also shown that one or more of the following human-subject reporting requirements has not been met in this article: ethical approval by an Institutional Review Board (IRB) committee or equivalent, patient/participant consent to participate, and/or agreement to publish patient/participant details (where relevant).

Wiley and Hindawi regrets that the usual quality checks did not identify these issues before publication and have since put additional measures in place to safeguard research integrity.

We wish to credit our own Research Integrity and Research Publishing teams and anonymous and named external researchers and research integrity experts for contributing to this investigation.

The corresponding author, as the representative of all authors, has been given the opportunity to register their agreement or disagreement to this retraction. We have kept a record of any response received.

References

- [1] J. Lin, J. Ge, J. Gong, H. Hong, and C. Jiang, "Application of Digital Orthopedic Technology in Orthopedic Trauma," *Computational and Mathematical Methods in Medicine*, vol. 2022, Article ID 3157107, 11 pages, 2022.

Retraction

Retracted: The Development Relationship between Cross-Border e-Commerce and Internet of Things Technology Coupling in Digital Economy Based on Neural Network Model

Computational and Mathematical Methods in Medicine

Received 27 June 2023; Accepted 27 June 2023; Published 28 June 2023

Copyright © 2023 Computational and Mathematical Methods in Medicine. This is an open access article distributed under the Creative Commons Attribution License, which permits unrestricted use, distribution, and reproduction in any medium, provided the original work is properly cited.

This article has been retracted by Hindawi following an investigation undertaken by the publisher [1]. This investigation has uncovered evidence of one or more of the following indicators of systematic manipulation of the publication process:

- (1) Discrepancies in scope
- (2) Discrepancies in the description of the research reported
- (3) Discrepancies between the availability of data and the research described
- (4) Inappropriate citations
- (5) Incoherent, meaningless and/or irrelevant content included in the article
- (6) Peer-review manipulation

The presence of these indicators undermines our confidence in the integrity of the article's content and we cannot, therefore, vouch for its reliability. Please note that this notice is intended solely to alert readers that the content of this article is unreliable. We have not investigated whether authors were aware of or involved in the systematic manipulation of the publication process.

Wiley and Hindawi regrets that the usual quality checks did not identify these issues before publication and have since put additional measures in place to safeguard research integrity.

We wish to credit our own Research Integrity and Research Publishing teams and anonymous and named external researchers and research integrity experts for contributing to this investigation.

The corresponding author, as the representative of all authors, has been given the opportunity to register their agreement or disagreement to this retraction. We have kept a record of any response received.

References

- [1] Q. Liu, "The Development Relationship between Cross-Border e-Commerce and Internet of Things Technology Coupling in Digital Economy Based on Neural Network Model," *Computational and Mathematical Methods in Medicine*, vol. 2022, Article ID 8981618, 10 pages, 2022.

Retraction

Retracted: CX3CL1 Derived from Bone Marrow Mesenchymal Stem Cells Inhibits $A\beta_{1-42}$ -Induced SH-SY5Y Cell Pathological Damage through TXNIP/NLRP3 Signaling Pathway

Computational and Mathematical Methods in Medicine

Received 27 June 2023; Accepted 27 June 2023; Published 28 June 2023

Copyright © 2023 Computational and Mathematical Methods in Medicine. This is an open access article distributed under the Creative Commons Attribution License, which permits unrestricted use, distribution, and reproduction in any medium, provided the original work is properly cited.

This article has been retracted by Hindawi following an investigation undertaken by the publisher [1]. This investigation has uncovered evidence of one or more of the following indicators of systematic manipulation of the publication process:

- (1) Discrepancies in scope
- (2) Discrepancies in the description of the research reported
- (3) Discrepancies between the availability of data and the research described
- (4) Inappropriate citations
- (5) Incoherent, meaningless and/or irrelevant content included in the article
- (6) Peer-review manipulation

The presence of these indicators undermines our confidence in the integrity of the article's content and we cannot, therefore, vouch for its reliability. Please note that this notice is intended solely to alert readers that the content of this article is unreliable. We have not investigated whether authors were aware of or involved in the systematic manipulation of the publication process.

Wiley and Hindawi regrets that the usual quality checks did not identify these issues before publication and have since put additional measures in place to safeguard research integrity.

We wish to credit our own Research Integrity and Research Publishing teams and anonymous and named external researchers and research integrity experts for contributing to this investigation.

The corresponding author, as the representative of all authors, has been given the opportunity to register their agreement or disagreement to this retraction. We have kept a record of any response received.

References

- [1] C. Guo, Q. Li, J. Xiao et al., "CX3CL1 Derived from Bone Marrow Mesenchymal Stem Cells Inhibits $A\beta_{1-42}$ -Induced SH-SY5Y Cell Pathological Damage through TXNIP/NLRP3 Signaling Pathway," *Computational and Mathematical Methods in Medicine*, vol. 2022, Article ID 1949344, 12 pages, 2022.

Retraction

Retracted: Clinical Study of Anti-PD-1 Immunotherapy Combined with Gemcitabine Chemotherapy in Multiline Treatment of Advanced Pancreatic Cancer

Computational and Mathematical Methods in Medicine

Received 27 June 2023; Accepted 27 June 2023; Published 28 June 2023

Copyright © 2023 Computational and Mathematical Methods in Medicine. This is an open access article distributed under the Creative Commons Attribution License, which permits unrestricted use, distribution, and reproduction in any medium, provided the original work is properly cited.

This article has been retracted by Hindawi following an investigation undertaken by the publisher [1]. This investigation has uncovered evidence of one or more of the following indicators of systematic manipulation of the publication process:

- (1) Discrepancies in scope
- (2) Discrepancies in the description of the research reported
- (3) Discrepancies between the availability of data and the research described
- (4) Inappropriate citations
- (5) Incoherent, meaningless and/or irrelevant content included in the article
- (6) Peer-review manipulation

The presence of these indicators undermines our confidence in the integrity of the article's content and we cannot, therefore, vouch for its reliability. Please note that this notice is intended solely to alert readers that the content of this article is unreliable. We have not investigated whether authors were aware of or involved in the systematic manipulation of the publication process.

In addition, our investigation has also shown that one or more of the following human-subject reporting requirements has not been met in this article: ethical approval by an Institutional Review Board (IRB) committee or equivalent, patient/participant consent to participate, and/or agreement to publish patient/participant details (where relevant).

Wiley and Hindawi regrets that the usual quality checks did not identify these issues before publication and have since put additional measures in place to safeguard research integrity.

We wish to credit our own Research Integrity and Research Publishing teams and anonymous and named external researchers and research integrity experts for contributing to this investigation.

The corresponding author, as the representative of all authors, has been given the opportunity to register their agreement or disagreement to this retraction. We have kept a record of any response received.

References

- [1] Y. Liu, Y. Li, S. Du, L. Fan, and J. Wang, "Clinical Study of Anti-PD-1 Immunotherapy Combined with Gemcitabine Chemotherapy in Multiline Treatment of Advanced Pancreatic Cancer," *Computational and Mathematical Methods in Medicine*, vol. 2022, Article ID 4070060, 6 pages, 2022.

Retraction

Retracted: Application of Mathematical Modeling in Cost Control of Medical Equipment Procurement in Public Hospitals

Computational and Mathematical Methods in Medicine

Received 27 June 2023; Accepted 27 June 2023; Published 28 June 2023

Copyright © 2023 Computational and Mathematical Methods in Medicine. This is an open access article distributed under the Creative Commons Attribution License, which permits unrestricted use, distribution, and reproduction in any medium, provided the original work is properly cited.

This article has been retracted by Hindawi following an investigation undertaken by the publisher [1]. This investigation has uncovered evidence of one or more of the following indicators of systematic manipulation of the publication process:

- (1) Discrepancies in scope
- (2) Discrepancies in the description of the research reported
- (3) Discrepancies between the availability of data and the research described
- (4) Inappropriate citations
- (5) Incoherent, meaningless and/or irrelevant content included in the article
- (6) Peer-review manipulation

The presence of these indicators undermines our confidence in the integrity of the article's content and we cannot, therefore, vouch for its reliability. Please note that this notice is intended solely to alert readers that the content of this article is unreliable. We have not investigated whether authors were aware of or involved in the systematic manipulation of the publication process.

Wiley and Hindawi regrets that the usual quality checks did not identify these issues before publication and have since put additional measures in place to safeguard research integrity.

We wish to credit our own Research Integrity and Research Publishing teams and anonymous and named external researchers and research integrity experts for contributing to this investigation.

The corresponding author, as the representative of all authors, has been given the opportunity to register their agreement or disagreement to this retraction. We have kept a record of any response received.

References

- [1] L. Chen, "Application of Mathematical Modeling in Cost Control of Medical Equipment Procurement in Public Hospitals," *Computational and Mathematical Methods in Medicine*, vol. 2022, Article ID 3425873, 12 pages, 2022.

Retraction

Retracted: Exploration of Landscape Lighting Design Based on Interactive Genetic Algorithm

Computational and Mathematical Methods in Medicine

Received 27 June 2023; Accepted 27 June 2023; Published 28 June 2023

Copyright © 2023 Computational and Mathematical Methods in Medicine. This is an open access article distributed under the Creative Commons Attribution License, which permits unrestricted use, distribution, and reproduction in any medium, provided the original work is properly cited.

This article has been retracted by Hindawi following an investigation undertaken by the publisher [1]. This investigation has uncovered evidence of one or more of the following indicators of systematic manipulation of the publication process:

- (1) Discrepancies in scope
- (2) Discrepancies in the description of the research reported
- (3) Discrepancies between the availability of data and the research described
- (4) Inappropriate citations
- (5) Incoherent, meaningless and/or irrelevant content included in the article
- (6) Peer-review manipulation

The presence of these indicators undermines our confidence in the integrity of the article's content and we cannot, therefore, vouch for its reliability. Please note that this notice is intended solely to alert readers that the content of this article is unreliable. We have not investigated whether authors were aware of or involved in the systematic manipulation of the publication process.

Wiley and Hindawi regrets that the usual quality checks did not identify these issues before publication and have since put additional measures in place to safeguard research integrity.

We wish to credit our own Research Integrity and Research Publishing teams and anonymous and named external researchers and research integrity experts for contributing to this investigation.

The corresponding author, as the representative of all authors, has been given the opportunity to register their agreement or disagreement to this retraction. We have kept a record of any response received.

References

- [1] H. Shi and J. Zheng, "Exploration of Landscape Lighting Design Based on Interactive Genetic Algorithm," *Computational and Mathematical Methods in Medicine*, vol. 2022, Article ID 1771617, 11 pages, 2022.

Retraction

Retracted: Efficacy of Cetuximab in Nasopharyngeal Carcinoma Patients Receiving Concurrent Cisplatin-Radiotherapy: A Meta-Analysis

Computational and Mathematical Methods in Medicine

Received 27 June 2023; Accepted 27 June 2023; Published 28 June 2023

Copyright © 2023 Computational and Mathematical Methods in Medicine. This is an open access article distributed under the Creative Commons Attribution License, which permits unrestricted use, distribution, and reproduction in any medium, provided the original work is properly cited.

This article has been retracted by Hindawi following an investigation undertaken by the publisher [1]. This investigation has uncovered evidence of one or more of the following indicators of systematic manipulation of the publication process:

- (1) Discrepancies in scope
- (2) Discrepancies in the description of the research reported
- (3) Discrepancies between the availability of data and the research described
- (4) Inappropriate citations
- (5) Incoherent, meaningless and/or irrelevant content included in the article
- (6) Peer-review manipulation

The presence of these indicators undermines our confidence in the integrity of the article's content and we cannot, therefore, vouch for its reliability. Please note that this notice is intended solely to alert readers that the content of this article is unreliable. We have not investigated whether authors were aware of or involved in the systematic manipulation of the publication process.

Wiley and Hindawi regrets that the usual quality checks did not identify these issues before publication and have since put additional measures in place to safeguard research integrity.

We wish to credit our own Research Integrity and Research Publishing teams and anonymous and named

external researchers and research integrity experts for contributing to this investigation.

The corresponding author, as the representative of all authors, has been given the opportunity to register their agreement or disagreement to this retraction. We have kept a record of any response received.

References

- [1] L. Wang, D. Liu, and D. Wei, "Efficacy of Cetuximab in Nasopharyngeal Carcinoma Patients Receiving Concurrent Cisplatin-Radiotherapy: A Meta-Analysis," *Computational and Mathematical Methods in Medicine*, vol. 2022, Article ID 5145549, 16 pages, 2022.

Retraction

Retracted: Analysis of Obstetric Clinical Nursing Integrating Situational Teaching Simulation

Computational and Mathematical Methods in Medicine

Received 27 June 2023; Accepted 27 June 2023; Published 28 June 2023

Copyright © 2023 Computational and Mathematical Methods in Medicine. This is an open access article distributed under the Creative Commons Attribution License, which permits unrestricted use, distribution, and reproduction in any medium, provided the original work is properly cited.

This article has been retracted by Hindawi following an investigation undertaken by the publisher [1]. This investigation has uncovered evidence of one or more of the following indicators of systematic manipulation of the publication process:

- (1) Discrepancies in scope
- (2) Discrepancies in the description of the research reported
- (3) Discrepancies between the availability of data and the research described
- (4) Inappropriate citations
- (5) Incoherent, meaningless and/or irrelevant content included in the article
- (6) Peer-review manipulation

The presence of these indicators undermines our confidence in the integrity of the article's content and we cannot, therefore, vouch for its reliability. Please note that this notice is intended solely to alert readers that the content of this article is unreliable. We have not investigated whether authors were aware of or involved in the systematic manipulation of the publication process.

In addition, our investigation has also shown that one or more of the following human-subject reporting requirements has not been met in this article: ethical approval by an Institutional Review Board (IRB) committee or equivalent, patient/participant consent to participate, and/or agreement to publish patient/participant details (where relevant).

Wiley and Hindawi regrets that the usual quality checks did not identify these issues before publication and have since put additional measures in place to safeguard research integrity.

We wish to credit our own Research Integrity and Research Publishing teams and anonymous and named external researchers and research integrity experts for contributing to this investigation.

The corresponding author, as the representative of all authors, has been given the opportunity to register their agreement or disagreement to this retraction. We have kept a record of any response received.

References

- [1] S. Xiao, J. Fang, X. Zhao, L. Yang, H. Tang, and Y. Wang, "Analysis of Obstetric Clinical Nursing Integrating Situational Teaching Simulation," *Computational and Mathematical Methods in Medicine*, vol. 2022, Article ID 6843196, 12 pages, 2022.

Retraction

Retracted: The Application of Focused Care Model in the Management of Hepatitis B Patients in a Tertiary Care Hospital and the Impact on Patients' Quality of Life

Computational and Mathematical Methods in Medicine

Received 27 June 2023; Accepted 27 June 2023; Published 28 June 2023

Copyright © 2023 Computational and Mathematical Methods in Medicine. This is an open access article distributed under the Creative Commons Attribution License, which permits unrestricted use, distribution, and reproduction in any medium, provided the original work is properly cited.

This article has been retracted by Hindawi following an investigation undertaken by the publisher [1]. This investigation has uncovered evidence of one or more of the following indicators of systematic manipulation of the publication process:

- (1) Discrepancies in scope
- (2) Discrepancies in the description of the research reported
- (3) Discrepancies between the availability of data and the research described
- (4) Inappropriate citations
- (5) Incoherent, meaningless and/or irrelevant content included in the article
- (6) Peer-review manipulation

The presence of these indicators undermines our confidence in the integrity of the article's content and we cannot, therefore, vouch for its reliability. Please note that this notice is intended solely to alert readers that the content of this article is unreliable. We have not investigated whether authors were aware of or involved in the systematic manipulation of the publication process.

In addition, our investigation has also shown that one or more of the following human-subject reporting requirements has not been met in this article: ethical approval by an Institutional Review Board (IRB) committee or equivalent, patient/participant consent to participate, and/or agreement to publish patient/participant details (where relevant).

Wiley and Hindawi regrets that the usual quality checks did not identify these issues before publication and have since put additional measures in place to safeguard research integrity.

We wish to credit our own Research Integrity and Research Publishing teams and anonymous and named external researchers and research integrity experts for contributing to this investigation.

The corresponding author, as the representative of all authors, has been given the opportunity to register their agreement or disagreement to this retraction. We have kept a record of any response received.

References

- [1] J. Zhang, Y. Wang, H. Shan, J. Duan, and J. Yu, "The Application of Focused Care Model in the Management of Hepatitis B Patients in a Tertiary Care Hospital and the Impact on Patients' Quality of Life," *Computational and Mathematical Methods in Medicine*, vol. 2022, Article ID 7770955, 11 pages, 2022.

Retraction

Retracted: Analysis the Innovation Path on Psychological Ideological with Political Teaching in Universities by Big Data in New Era

Computational and Mathematical Methods in Medicine

Received 27 June 2023; Accepted 27 June 2023; Published 28 June 2023

Copyright © 2023 Computational and Mathematical Methods in Medicine. This is an open access article distributed under the Creative Commons Attribution License, which permits unrestricted use, distribution, and reproduction in any medium, provided the original work is properly cited.

This article has been retracted by Hindawi following an investigation undertaken by the publisher [1]. This investigation has uncovered evidence of one or more of the following indicators of systematic manipulation of the publication process:

- (1) Discrepancies in scope
- (2) Discrepancies in the description of the research reported
- (3) Discrepancies between the availability of data and the research described
- (4) Inappropriate citations
- (5) Incoherent, meaningless and/or irrelevant content included in the article
- (6) Peer-review manipulation

The presence of these indicators undermines our confidence in the integrity of the article's content and we cannot, therefore, vouch for its reliability. Please note that this notice is intended solely to alert readers that the content of this article is unreliable. We have not investigated whether authors were aware of or involved in the systematic manipulation of the publication process.

Wiley and Hindawi regrets that the usual quality checks did not identify these issues before publication and have since put additional measures in place to safeguard research integrity.

We wish to credit our own Research Integrity and Research Publishing teams and anonymous and named external researchers and research integrity experts for contributing to this investigation.

The corresponding author, as the representative of all authors, has been given the opportunity to register their agreement or disagreement to this retraction. We have kept a record of any response received.

References

- [1] X. Luo, "Analysis the Innovation Path on Psychological Ideological with Political Teaching in Universities by Big Data in New Era," *Computational and Mathematical Methods in Medicine*, vol. 2022, Article ID 4305886, 9 pages, 2022.

Retraction

Retracted: Efficacy of Gamma Globulin Combined with Azithromycin Sequential Therapy in the Treatment of RMPP and Its Effect on Th1/Th2 Cytokine Levels

Computational and Mathematical Methods in Medicine

Received 27 June 2023; Accepted 27 June 2023; Published 28 June 2023

Copyright © 2023 Computational and Mathematical Methods in Medicine. This is an open access article distributed under the Creative Commons Attribution License, which permits unrestricted use, distribution, and reproduction in any medium, provided the original work is properly cited.

This article has been retracted by Hindawi following an investigation undertaken by the publisher [1]. This investigation has uncovered evidence of one or more of the following indicators of systematic manipulation of the publication process:

- (1) Discrepancies in scope
- (2) Discrepancies in the description of the research reported
- (3) Discrepancies between the availability of data and the research described
- (4) Inappropriate citations
- (5) Incoherent, meaningless and/or irrelevant content included in the article
- (6) Peer-review manipulation

The presence of these indicators undermines our confidence in the integrity of the article's content and we cannot, therefore, vouch for its reliability. Please note that this notice is intended solely to alert readers that the content of this article is unreliable. We have not investigated whether authors were aware of or involved in the systematic manipulation of the publication process.

In addition, our investigation has also shown that one or more of the following human-subject reporting requirements has not been met in this article: ethical approval by an Institutional Review Board (IRB) committee or equivalent, patient/participant consent to participate, and/or agreement to publish patient/participant details (where relevant).

Wiley and Hindawi regrets that the usual quality checks did not identify these issues before publication and have since put additional measures in place to safeguard research integrity.

We wish to credit our own Research Integrity and Research Publishing teams and anonymous and named external researchers and research integrity experts for contributing to this investigation.

The corresponding author, as the representative of all authors, has been given the opportunity to register their agreement or disagreement to this retraction. We have kept a record of any response received.

References

- [1] J. Qi, F. Jia, H. Tian, and S. Yang, "Efficacy of Gamma Globulin Combined with Azithromycin Sequential Therapy in the Treatment of RMPP and Its Effect on Th1/Th2 Cytokine Levels," *Computational and Mathematical Methods in Medicine*, vol. 2022, Article ID 5162768, 5 pages, 2022.

Retraction

Retracted: The Diagnosis of Early Gastric Cancer Based on Medical Imaging Technology and Mathematical Modeling

Computational and Mathematical Methods in Medicine

Received 27 June 2023; Accepted 27 June 2023; Published 28 June 2023

Copyright © 2023 Computational and Mathematical Methods in Medicine. This is an open access article distributed under the Creative Commons Attribution License, which permits unrestricted use, distribution, and reproduction in any medium, provided the original work is properly cited.

This article has been retracted by Hindawi following an investigation undertaken by the publisher [1]. This investigation has uncovered evidence of one or more of the following indicators of systematic manipulation of the publication process:

- (1) Discrepancies in scope
- (2) Discrepancies in the description of the research reported
- (3) Discrepancies between the availability of data and the research described
- (4) Inappropriate citations
- (5) Incoherent, meaningless and/or irrelevant content included in the article
- (6) Peer-review manipulation

The presence of these indicators undermines our confidence in the integrity of the article's content and we cannot, therefore, vouch for its reliability. Please note that this notice is intended solely to alert readers that the content of this article is unreliable. We have not investigated whether authors were aware of or involved in the systematic manipulation of the publication process.

In addition, our investigation has also shown that one or more of the following human-subject reporting requirements has not been met in this article: ethical approval by an Institutional Review Board (IRB) committee or equivalent, patient/participant consent to participate, and/or agreement to publish patient/participant details (where relevant).

Wiley and Hindawi regrets that the usual quality checks did not identify these issues before publication and have since put additional measures in place to safeguard research integrity.

We wish to credit our own Research Integrity and Research Publishing teams and anonymous and named external researchers and research integrity experts for contributing to this investigation.

The corresponding author, as the representative of all authors, has been given the opportunity to register their agreement or disagreement to this retraction. We have kept a record of any response received.

References

- [1] J. Xiu, L. Ma, Y. Ding et al., "The Diagnosis of Early Gastric Cancer Based on Medical Imaging Technology and Mathematical Modeling," *Computational and Mathematical Methods in Medicine*, vol. 2022, Article ID 8721654, 7 pages, 2022.

Retraction

Retracted: Induction of Resistance of Antagonistic Bacterium *Burkholderia contaminans* to Postharvest *Botrytis cinerea* in *Rosa vinifera*

Computational and Mathematical Methods in Medicine

Received 27 June 2023; Accepted 27 June 2023; Published 28 June 2023

Copyright © 2023 Computational and Mathematical Methods in Medicine. This is an open access article distributed under the Creative Commons Attribution License, which permits unrestricted use, distribution, and reproduction in any medium, provided the original work is properly cited.

This article has been retracted by Hindawi following an investigation undertaken by the publisher [1]. This investigation has uncovered evidence of one or more of the following indicators of systematic manipulation of the publication process:

- (1) Discrepancies in scope
- (2) Discrepancies in the description of the research reported
- (3) Discrepancies between the availability of data and the research described
- (4) Inappropriate citations
- (5) Incoherent, meaningless and/or irrelevant content included in the article
- (6) Peer-review manipulation

The presence of these indicators undermines our confidence in the integrity of the article's content and we cannot, therefore, vouch for its reliability. Please note that this notice is intended solely to alert readers that the content of this article is unreliable. We have not investigated whether authors were aware of or involved in the systematic manipulation of the publication process.

Wiley and Hindawi regrets that the usual quality checks did not identify these issues before publication and have since put additional measures in place to safeguard research integrity.

We wish to credit our own Research Integrity and Research Publishing teams and anonymous and named external researchers and research integrity experts for contributing to this investigation.

The corresponding author, as the representative of all authors, has been given the opportunity to register their agreement or disagreement to this retraction. We have kept a record of any response received.

References

- [1] F. Shen, Z. Liu, C. Du, J. Yuan, W. Wu, and D. Wei, "Induction of Resistance of Antagonistic Bacterium *Burkholderia contaminans* to Postharvest *Botrytis cinerea* in *Rosa vinifera*," *Computational and Mathematical Methods in Medicine*, vol. 2022, Article ID 7134161, 12 pages, 2022.

Retraction

Retracted: Research on Land Utilization Spatial Classification Planning Method Based on Multiocular Vision

Computational and Mathematical Methods in Medicine

Received 27 June 2023; Accepted 27 June 2023; Published 28 June 2023

Copyright © 2023 Computational and Mathematical Methods in Medicine. This is an open access article distributed under the Creative Commons Attribution License, which permits unrestricted use, distribution, and reproduction in any medium, provided the original work is properly cited.

This article has been retracted by Hindawi following an investigation undertaken by the publisher [1]. This investigation has uncovered evidence of one or more of the following indicators of systematic manipulation of the publication process:

- (1) Discrepancies in scope
- (2) Discrepancies in the description of the research reported
- (3) Discrepancies between the availability of data and the research described
- (4) Inappropriate citations
- (5) Incoherent, meaningless and/or irrelevant content included in the article
- (6) Peer-review manipulation

The presence of these indicators undermines our confidence in the integrity of the article's content and we cannot, therefore, vouch for its reliability. Please note that this notice is intended solely to alert readers that the content of this article is unreliable. We have not investigated whether authors were aware of or involved in the systematic manipulation of the publication process.

Wiley and Hindawi regrets that the usual quality checks did not identify these issues before publication and have since put additional measures in place to safeguard research integrity.

We wish to credit our own Research Integrity and Research Publishing teams and anonymous and named external researchers and research integrity experts for contributing to this investigation.

The corresponding author, as the representative of all authors, has been given the opportunity to register their agreement or disagreement to this retraction. We have kept a record of any response received.

References

- [1] Z. Zhang and S. Wang, "Research on Land Utilization Spatial Classification Planning Method Based on Multiocular Vision," *Computational and Mathematical Methods in Medicine*, vol. 2022, Article ID 9300278, 13 pages, 2022.

Retraction

Retracted: Effect of Propofol Intravenous Anesthesia Combined with Press-Needle Therapy on Analgesic Effect during Painless Abortion

Computational and Mathematical Methods in Medicine

Received 27 June 2023; Accepted 27 June 2023; Published 28 June 2023

Copyright © 2023 Computational and Mathematical Methods in Medicine. This is an open access article distributed under the Creative Commons Attribution License, which permits unrestricted use, distribution, and reproduction in any medium, provided the original work is properly cited.

This article has been retracted by Hindawi following an investigation undertaken by the publisher [1]. This investigation has uncovered evidence of one or more of the following indicators of systematic manipulation of the publication process:

- (1) Discrepancies in scope
- (2) Discrepancies in the description of the research reported
- (3) Discrepancies between the availability of data and the research described
- (4) Inappropriate citations
- (5) Incoherent, meaningless and/or irrelevant content included in the article
- (6) Peer-review manipulation

The presence of these indicators undermines our confidence in the integrity of the article's content and we cannot, therefore, vouch for its reliability. Please note that this notice is intended solely to alert readers that the content of this article is unreliable. We have not investigated whether authors were aware of or involved in the systematic manipulation of the publication process.

Wiley and Hindawi regrets that the usual quality checks did not identify these issues before publication and have since put additional measures in place to safeguard research integrity.

We wish to credit our own Research Integrity and Research Publishing teams and anonymous and named external researchers and research integrity experts for contributing to this investigation.

The corresponding author, as the representative of all authors, has been given the opportunity to register their agreement or disagreement to this retraction. We have kept a record of any response received.

References

- [1] X. Zhu, X. He, B. Fan et al., "Effect of Propofol Intravenous Anesthesia Combined with Press-Needle Therapy on Analgesic Effect during Painless Abortion," *Computational and Mathematical Methods in Medicine*, vol. 2022, Article ID 6543211, 10 pages, 2022.

Retraction

Retracted: Safety and Efficacy of Tirofiban Combined with Statins in the Perioperative Period of Intracranial Aneurysms: Systematic Review and Meta-Analysis

Computational and Mathematical Methods in Medicine

Received 27 June 2023; Accepted 27 June 2023; Published 28 June 2023

Copyright © 2023 Computational and Mathematical Methods in Medicine. This is an open access article distributed under the Creative Commons Attribution License, which permits unrestricted use, distribution, and reproduction in any medium, provided the original work is properly cited.

This article has been retracted by Hindawi following an investigation undertaken by the publisher [1]. This investigation has uncovered evidence of one or more of the following indicators of systematic manipulation of the publication process:

- (1) Discrepancies in scope
- (2) Discrepancies in the description of the research reported
- (3) Discrepancies between the availability of data and the research described
- (4) Inappropriate citations
- (5) Incoherent, meaningless and/or irrelevant content included in the article
- (6) Peer-review manipulation

The presence of these indicators undermines our confidence in the integrity of the article's content and we cannot, therefore, vouch for its reliability. Please note that this notice is intended solely to alert readers that the content of this article is unreliable. We have not investigated whether authors were aware of or involved in the systematic manipulation of the publication process.

In addition, our investigation has also shown that one or more of the following human-subject reporting requirements has not been met in this article: ethical approval by an Institutional Review Board (IRB) committee or equivalent, patient/participant consent to participate, and/or agreement to publish patient/participant details (where relevant).

Wiley and Hindawi regrets that the usual quality checks did not identify these issues before publication and have since put additional measures in place to safeguard research integrity.

We wish to credit our own Research Integrity and Research Publishing teams and anonymous and named external researchers and research integrity experts for contributing to this investigation.

The corresponding author, as the representative of all authors, has been given the opportunity to register their agreement or disagreement to this retraction. We have kept a record of any response received.

References

- [1] M. Hao, R. Liu, F. Yan, and Y. Luo, "Safety and Efficacy of Tirofiban Combined with Statins in the Perioperative Period of Intracranial Aneurysms: Systematic Review and Meta-Analysis," *Computational and Mathematical Methods in Medicine*, vol. 2022, Article ID 8264261, 7 pages, 2022.

Retraction

Retracted: Design and Application of Artificial Intelligence Technology-Driven Education and Teaching System in Universities

Computational and Mathematical Methods in Medicine

Received 27 June 2023; Accepted 27 June 2023; Published 28 June 2023

Copyright © 2023 Computational and Mathematical Methods in Medicine. This is an open access article distributed under the Creative Commons Attribution License, which permits unrestricted use, distribution, and reproduction in any medium, provided the original work is properly cited.

This article has been retracted by Hindawi following an investigation undertaken by the publisher [1]. This investigation has uncovered evidence of one or more of the following indicators of systematic manipulation of the publication process:

- (1) Discrepancies in scope
- (2) Discrepancies in the description of the research reported
- (3) Discrepancies between the availability of data and the research described
- (4) Inappropriate citations
- (5) Incoherent, meaningless and/or irrelevant content included in the article
- (6) Peer-review manipulation

The presence of these indicators undermines our confidence in the integrity of the article's content and we cannot, therefore, vouch for its reliability. Please note that this notice is intended solely to alert readers that the content of this article is unreliable. We have not investigated whether authors were aware of or involved in the systematic manipulation of the publication process.

In addition, our investigation has also shown that one or more of the following human-subject reporting requirements has not been met in this article: ethical approval by an Institutional Review Board (IRB) committee or equivalent, patient/participant consent to participate, and/or agreement to publish patient/participant details (where relevant).

Wiley and Hindawi regrets that the usual quality checks did not identify these issues before publication and have since put additional measures in place to safeguard research integrity.

We wish to credit our own Research Integrity and Research Publishing teams and anonymous and named external researchers and research integrity experts for contributing to this investigation.

The corresponding author, as the representative of all authors, has been given the opportunity to register their agreement or disagreement to this retraction. We have kept a record of any response received.

References

- [1] F. Zhang, "Design and Application of Artificial Intelligence Technology-Driven Education and Teaching System in Universities," *Computational and Mathematical Methods in Medicine*, vol. 2022, Article ID 8503239, 10 pages, 2022.

Retraction

Retracted: Clinical Study of Different Treatment Methods for Tuberculous Pleuritis Complicated with Pleural Tuberculoma

Computational and Mathematical Methods in Medicine

Received 27 June 2023; Accepted 27 June 2023; Published 28 June 2023

Copyright © 2023 Computational and Mathematical Methods in Medicine. This is an open access article distributed under the Creative Commons Attribution License, which permits unrestricted use, distribution, and reproduction in any medium, provided the original work is properly cited.

This article has been retracted by Hindawi following an investigation undertaken by the publisher [1]. This investigation has uncovered evidence of one or more of the following indicators of systematic manipulation of the publication process:

- (1) Discrepancies in scope
- (2) Discrepancies in the description of the research reported
- (3) Discrepancies between the availability of data and the research described
- (4) Inappropriate citations
- (5) Incoherent, meaningless and/or irrelevant content included in the article
- (6) Peer-review manipulation

The presence of these indicators undermines our confidence in the integrity of the article's content and we cannot, therefore, vouch for its reliability. Please note that this notice is intended solely to alert readers that the content of this article is unreliable. We have not investigated whether authors were aware of or involved in the systematic manipulation of the publication process.

In addition, our investigation has also shown that one or more of the following human-subject reporting requirements has not been met in this article: ethical approval by an Institutional Review Board (IRB) committee or equivalent, patient/participant consent to participate, and/or agreement to publish patient/participant details (where relevant).

Wiley and Hindawi regrets that the usual quality checks did not identify these issues before publication and have since put additional measures in place to safeguard research integrity.

We wish to credit our own Research Integrity and Research Publishing teams and anonymous and named external researchers and research integrity experts for contributing to this investigation.

The corresponding author, as the representative of all authors, has been given the opportunity to register their agreement or disagreement to this retraction. We have kept a record of any response received.

References

- [1] X. Zhang and J. Chi, "Clinical Study of Different Treatment Methods for Tuberculous Pleuritis Complicated with Pleural Tuberculoma," *Computational and Mathematical Methods in Medicine*, vol. 2022, Article ID 5666067, 9 pages, 2022.

Retraction

Retracted: Deep Image Watermarking to JPEG Compression Based on Mixed-Frequency Channel Attention

Computational and Mathematical Methods in Medicine

Received 27 June 2023; Accepted 27 June 2023; Published 28 June 2023

Copyright © 2023 Computational and Mathematical Methods in Medicine. This is an open access article distributed under the Creative Commons Attribution License, which permits unrestricted use, distribution, and reproduction in any medium, provided the original work is properly cited.

This article has been retracted by Hindawi following an investigation undertaken by the publisher [1]. This investigation has uncovered evidence of one or more of the following indicators of systematic manipulation of the publication process:

- (1) Discrepancies in scope
- (2) Discrepancies in the description of the research reported
- (3) Discrepancies between the availability of data and the research described
- (4) Inappropriate citations
- (5) Incoherent, meaningless and/or irrelevant content included in the article
- (6) Peer-review manipulation

The presence of these indicators undermines our confidence in the integrity of the article's content and we cannot, therefore, vouch for its reliability. Please note that this notice is intended solely to alert readers that the content of this article is unreliable. We have not investigated whether authors were aware of or involved in the systematic manipulation of the publication process.

Wiley and Hindawi regrets that the usual quality checks did not identify these issues before publication and have since put additional measures in place to safeguard research integrity.

We wish to credit our own Research Integrity and Research Publishing teams and anonymous and named external researchers and research integrity experts for contributing to this investigation.

The corresponding author, as the representative of all authors, has been given the opportunity to register their agreement or disagreement to this retraction. We have kept a record of any response received.

References

- [1] J. Tan, Y. Hu, Z. Shi, and B. Wang, "Deep Image Watermarking to JPEG Compression Based on Mixed-Frequency Channel Attention," *Computational and Mathematical Methods in Medicine*, vol. 2022, Article ID 9880038, 12 pages, 2022.

Retraction

Retracted: Serum Adiponectin Level in Different Stages of Type 2 Diabetic Kidney Disease: A Meta-Analysis

Computational and Mathematical Methods in Medicine

Received 27 June 2023; Accepted 27 June 2023; Published 28 June 2023

Copyright © 2023 Computational and Mathematical Methods in Medicine. This is an open access article distributed under the Creative Commons Attribution License, which permits unrestricted use, distribution, and reproduction in any medium, provided the original work is properly cited.

This article has been retracted by Hindawi following an investigation undertaken by the publisher [1]. This investigation has uncovered evidence of one or more of the following indicators of systematic manipulation of the publication process:

- (1) Discrepancies in scope
- (2) Discrepancies in the description of the research reported
- (3) Discrepancies between the availability of data and the research described
- (4) Inappropriate citations
- (5) Incoherent, meaningless and/or irrelevant content included in the article
- (6) Peer-review manipulation

The presence of these indicators undermines our confidence in the integrity of the article's content and we cannot, therefore, vouch for its reliability. Please note that this notice is intended solely to alert readers that the content of this article is unreliable. We have not investigated whether authors were aware of or involved in the systematic manipulation of the publication process.

Wiley and Hindawi regrets that the usual quality checks did not identify these issues before publication and have since put additional measures in place to safeguard research integrity.

We wish to credit our own Research Integrity and Research Publishing teams and anonymous and named external researchers and research integrity experts for contributing to this investigation.

The corresponding author, as the representative of all authors, has been given the opportunity to register their agreement or disagreement to this retraction. We have kept a record of any response received.

References

- [1] L. Li, J. Shi, and G. Wu, "Serum Adiponectin Level in Different Stages of Type 2 Diabetic Kidney Disease: A Meta-Analysis," *Computational and Mathematical Methods in Medicine*, vol. 2022, Article ID 1863243, 11 pages, 2022.

Retraction

Retracted: Analysis of Efficacy, Complications, and Inflammatory Reactions of Bridge Combined Internal Fixation System for Periarticular Fractures of the Shoulder

Computational and Mathematical Methods in Medicine

Received 27 June 2023; Accepted 27 June 2023; Published 28 June 2023

Copyright © 2023 Computational and Mathematical Methods in Medicine. This is an open access article distributed under the Creative Commons Attribution License, which permits unrestricted use, distribution, and reproduction in any medium, provided the original work is properly cited.

This article has been retracted by Hindawi following an investigation undertaken by the publisher [1]. This investigation has uncovered evidence of one or more of the following indicators of systematic manipulation of the publication process:

- (1) Discrepancies in scope
- (2) Discrepancies in the description of the research reported
- (3) Discrepancies between the availability of data and the research described
- (4) Inappropriate citations
- (5) Incoherent, meaningless and/or irrelevant content included in the article
- (6) Peer-review manipulation

The presence of these indicators undermines our confidence in the integrity of the article's content and we cannot, therefore, vouch for its reliability. Please note that this notice is intended solely to alert readers that the content of this article is unreliable. We have not investigated whether authors were aware of or involved in the systematic manipulation of the publication process.

Wiley and Hindawi regrets that the usual quality checks did not identify these issues before publication and have since put additional measures in place to safeguard research integrity.

We wish to credit our own Research Integrity and Research Publishing teams and anonymous and named external researchers and research integrity experts for contributing to this investigation.

The corresponding author, as the representative of all authors, has been given the opportunity to register their agreement or disagreement to this retraction. We have kept a record of any response received.

References

- [1] H. Xu, Y. Fan, J. Lu, Y. Wu, and X. Feng, "Analysis of Efficacy, Complications, and Inflammatory Reactions of Bridge Combined Internal Fixation System for Periarticular Fractures of the Shoulder," *Computational and Mathematical Methods in Medicine*, vol. 2022, Article ID 5048172, 6 pages, 2022.

Retraction

Retracted: Epidural Anesthesia versus General Anesthesia for Total Knee Arthroplasty: Influences on Perioperative Cognitive Function and Deep Vein Thrombosis

Computational and Mathematical Methods in Medicine

Received 27 June 2023; Accepted 27 June 2023; Published 28 June 2023

Copyright © 2023 Computational and Mathematical Methods in Medicine. This is an open access article distributed under the Creative Commons Attribution License, which permits unrestricted use, distribution, and reproduction in any medium, provided the original work is properly cited.

This article has been retracted by Hindawi following an investigation undertaken by the publisher [1]. This investigation has uncovered evidence of one or more of the following indicators of systematic manipulation of the publication process:

- (1) Discrepancies in scope
- (2) Discrepancies in the description of the research reported
- (3) Discrepancies between the availability of data and the research described
- (4) Inappropriate citations
- (5) Incoherent, meaningless and/or irrelevant content included in the article
- (6) Peer-review manipulation

The presence of these indicators undermines our confidence in the integrity of the article's content and we cannot, therefore, vouch for its reliability. Please note that this notice is intended solely to alert readers that the content of this article is unreliable. We have not investigated whether authors were aware of or involved in the systematic manipulation of the publication process.

Wiley and Hindawi regrets that the usual quality checks did not identify these issues before publication and have since put additional measures in place to safeguard research integrity.

We wish to credit our own Research Integrity and Research Publishing teams and anonymous and named external researchers and research integrity experts for contributing to this investigation.

The corresponding author, as the representative of all authors, has been given the opportunity to register their agreement or disagreement to this retraction. We have kept a record of any response received.

References

- [1] T. Ma, G. Li, H. Zhang et al., "Epidural Anesthesia versus General Anesthesia for Total Knee Arthroplasty: Influences on Perioperative Cognitive Function and Deep Vein Thrombosis," *Computational and Mathematical Methods in Medicine*, vol. 2022, Article ID 4259499, 6 pages, 2022.

Retraction

Retracted: Impacts of Low-Dose Total Glycosides of *Tripterygium wilfordii* plus Methotrexate on Immunological Function and Inflammation Level in Patients with Rheumatoid Arthritis

Computational and Mathematical Methods in Medicine

Received 27 June 2023; Accepted 27 June 2023; Published 28 June 2023

Copyright © 2023 Computational and Mathematical Methods in Medicine. This is an open access article distributed under the Creative Commons Attribution License, which permits unrestricted use, distribution, and reproduction in any medium, provided the original work is properly cited.

This article has been retracted by Hindawi following an investigation undertaken by the publisher [1]. This investigation has uncovered evidence of one or more of the following indicators of systematic manipulation of the publication process:

- (1) Discrepancies in scope
- (2) Discrepancies in the description of the research reported
- (3) Discrepancies between the availability of data and the research described
- (4) Inappropriate citations
- (5) Incoherent, meaningless and/or irrelevant content included in the article
- (6) Peer-review manipulation

The presence of these indicators undermines our confidence in the integrity of the article's content and we cannot, therefore, vouch for its reliability. Please note that this notice is intended solely to alert readers that the content of this article is unreliable. We have not investigated whether authors were aware of or involved in the systematic manipulation of the publication process.

Wiley and Hindawi regrets that the usual quality checks did not identify these issues before publication and have since put additional measures in place to safeguard research integrity.

We wish to credit our own Research Integrity and Research Publishing teams and anonymous and named external researchers and research integrity experts for contributing to this investigation.

The corresponding author, as the representative of all authors, has been given the opportunity to register their agreement or disagreement to this retraction. We have kept a record of any response received.

References

- [1] Y. Han, J. Jin, F. Wu, and Z. Wang, "Impacts of Low-Dose Total Glycosides of *Tripterygium wilfordii* plus Methotrexate on Immunological Function and Inflammation Level in Patients with Rheumatoid Arthritis," *Computational and Mathematical Methods in Medicine*, vol. 2022, Article ID 7523673, 7 pages, 2022.

Retraction

Retracted: Effects of Dapagliflozin in Combination with Metoprolol Sustained-Release Tablets on Prognosis and Cardiac Function in Patients with Acute Myocardial Infarction after PCI

Computational and Mathematical Methods in Medicine

Received 27 June 2023; Accepted 27 June 2023; Published 28 June 2023

Copyright © 2023 Computational and Mathematical Methods in Medicine. This is an open access article distributed under the Creative Commons Attribution License, which permits unrestricted use, distribution, and reproduction in any medium, provided the original work is properly cited.

This article has been retracted by Hindawi following an investigation undertaken by the publisher [1]. This investigation has uncovered evidence of one or more of the following indicators of systematic manipulation of the publication process:

- (1) Discrepancies in scope
- (2) Discrepancies in the description of the research reported
- (3) Discrepancies between the availability of data and the research described
- (4) Inappropriate citations
- (5) Incoherent, meaningless and/or irrelevant content included in the article
- (6) Peer-review manipulation

The presence of these indicators undermines our confidence in the integrity of the article's content and we cannot, therefore, vouch for its reliability. Please note that this notice is intended solely to alert readers that the content of this article is unreliable. We have not investigated whether authors were aware of or involved in the systematic manipulation of the publication process.

In addition, our investigation has also shown that one or more of the following human-subject reporting requirements has not been met in this article: ethical approval by an Institutional Review Board (IRB) committee or equivalent, patient/participant consent to participate, and/or agreement to publish patient/participant details (where relevant).

Wiley and Hindawi regrets that the usual quality checks did not identify these issues before publication and have since put additional measures in place to safeguard research integrity.

We wish to credit our own Research Integrity and Research Publishing teams and anonymous and named external researchers and research integrity experts for contributing to this investigation.

The corresponding author, as the representative of all authors, has been given the opportunity to register their agreement or disagreement to this retraction. We have kept a record of any response received.

References

- [1] H. Zhang and Z. Liu, "Effects of Dapagliflozin in Combination with Metoprolol Sustained-Release Tablets on Prognosis and Cardiac Function in Patients with Acute Myocardial Infarction after PCI," *Computational and Mathematical Methods in Medicine*, vol. 2022, Article ID 5734876, 8 pages, 2022.

Retraction

Retracted: A Method for Evaluating the Quality of Mathematics Education Based on Artificial Neural Network

Computational and Mathematical Methods in Medicine

Received 27 June 2023; Accepted 27 June 2023; Published 28 June 2023

Copyright © 2023 Computational and Mathematical Methods in Medicine. This is an open access article distributed under the Creative Commons Attribution License, which permits unrestricted use, distribution, and reproduction in any medium, provided the original work is properly cited.

This article has been retracted by Hindawi following an investigation undertaken by the publisher [1]. This investigation has uncovered evidence of one or more of the following indicators of systematic manipulation of the publication process:

- (1) Discrepancies in scope
- (2) Discrepancies in the description of the research reported
- (3) Discrepancies between the availability of data and the research described
- (4) Inappropriate citations
- (5) Incoherent, meaningless and/or irrelevant content included in the article
- (6) Peer-review manipulation

The presence of these indicators undermines our confidence in the integrity of the article's content and we cannot, therefore, vouch for its reliability. Please note that this notice is intended solely to alert readers that the content of this article is unreliable. We have not investigated whether authors were aware of or involved in the systematic manipulation of the publication process.

Wiley and Hindawi regrets that the usual quality checks did not identify these issues before publication and have since put additional measures in place to safeguard research integrity.

We wish to credit our own Research Integrity and Research Publishing teams and anonymous and named external researchers and research integrity experts for contributing to this investigation.

The corresponding author, as the representative of all authors, has been given the opportunity to register their

agreement or disagreement to this retraction. We have kept a record of any response received.

References

- [1] F. Bao and C. Wang, "A Method for Evaluating the Quality of Mathematics Education Based on Artificial Neural Network," *Computational and Mathematical Methods in Medicine*, vol. 2022, Article ID 6976654, 11 pages, 2022.

Research Article

Influence of Prehospital Emergency Care on Rescue Success Rate and Complication Rate of Senile Patients with Acute Myocardial Infarction

Yingchao Zhang, Lili Huang, and Xuehong Zhou 

Department of Emergency, Taizhou First People's Hospital, Taizhou, 318020 Zhejiang, China

Correspondence should be addressed to Xuehong Zhou; zxh778119@163.com

Received 25 May 2022; Revised 11 July 2022; Accepted 16 September 2022; Published 12 October 2022

Academic Editor: Pan Zheng

Copyright © 2022 Yingchao Zhang et al. This is an open access article distributed under the Creative Commons Attribution License, which permits unrestricted use, distribution, and reproduction in any medium, provided the original work is properly cited.

Objective. This research mainly discusses the influence of prehospital emergency care (PHEC) on the rescue success rate and complication rate of senile patients with acute myocardial infarction (AMI). **Methods.** We selected 200 senile AMI patients who visited between January 2019 and January 2021, and retrospectively analyzed their clinical data. According to the differences in nursing methods, the patients were assigned to control group ($n = 90$) and observation group ($n = 110$), which were treated with routine nursing and PHEC, respectively. Intergroup comparisons were made in terms of rescue success rate, nursing efficacy, clinical parameters and complication rate. **Results.** After investigation, the nursing efficacy was higher in the observation group compared with the control group. Additionally, the observation group was observed with statistically shorter time to thrombolysis and hospital stay, as well as evidently lower mortality and complication rates. **Conclusion.** The above demonstrates that PHEC can effectively improve the rescue success rate and rescue efficacy, and facilitate the recovery of senile AMI patients, with a low complication rate compared with the routine care, which plays an important role in ensuring patients' life safety and is worth popularizing clinically.

1. Introduction

As a serious type of coronary heart disease, acute myocardial infarction (AMI) is an important cause of cardiovascular death with an incidence that continued to rise in recent years [1]. Against the background of accelerated population aging, AMI in the elderly has become a common multiple disease in clinical cardiovascular medicine [2]. Characterized by rapid onset and fast progression, the disease is a serious threat to senile patients who are accompanied by varying degrees of decline in physical function [3]. According to the results of the World Health Organization (WHO) epidemiological study on senile AMI, the morbidity and mortality of males in all age groups (except those over 80 years old) exceeded those of females [4]. The mortality rate of AMI remains very high, despite the standardization of its diagnosis and treatment [5]. Cardiogenic shock (CGS), one of the complications of AMI, is one of the prime reasons for death

in AMI patients [6]. However, at present, the clinical effect of AMI complicated with CGS leaves much to be desired, urgently demanding effective measures that can be taken to lower the incidence of complications to extend patient survival [7]. This study aims at finding a more suitable nursing method for senile AMI patients from the perspective of nursing care.

In the face of complex and rapidly developing diseases, delayed and ineffective first aid will often lead to serious adverse consequences for follow-up treatment [8]. While prehospital emergency care (PHEC) plays a vital role in providing timely and effective treatment for such patients [9]. The more accurate the judgment of the patient's condition and the faster the care given, the lower the patient's death rate between receiving the emergency task and the patient's admission [10]. At present, the PHEC model has been widely used in clinical emergency treatment of diseases such as acute cerebral infarction and acute craniocerebral trauma

[11]. The report of Pendyal et al. [12] on AMI nursing process in the United States suggested that PHEC was also applicable to the first aid of AMI. Based on the conclusions of previous studies and the clinical features of senile AMI, this study attempted to introduce PHEC into the clinical treatment of elderly AMI patients.

Although there are currently many related studies on the application of PHEC in AMI, fewer of them focus on senile AMI patients. Consequently, this study mainly makes a retrospective analysis of the rescue success rate, nursing efficacy, and complications of PHEC for senile AMI patients, hoping to provide a new clinical reference for the care of senile AMI.

2. Data and Methods

2.1. Baseline Data. In this study, 200 senile patients with AMI admitted between January 2019 and January 2021 were selected and divided into an observation group ($n = 110$) and a control group ($n = 90$) according to different nursing methods. Patients in the control group received routine nursing, while those in the observation group received PHEC intervention. The control group was comprised of 51 males and 39 females who were aged 79.02 ± 10.70 years, with 26 cases presenting with inferior wall myocardial infarction, 23 cases with anterior wall myocardial infarction, 20 cases with anteroseptal myocardial infarction, and 21 cases with high lateral wall infarction. In the observation group, the male to female ratio and age range were 60:50 and 79.75 ± 10.11 years old, respectively, with the number of cases with inferior wall, anterior wall, anteroseptal, and high lateral wall infarction of 29, 24, 30, and 27, respectively. The two groups showed clinical comparability with similar baseline data such as sex, age, and infarction type ($P > 0.05$). This study has been approved by the hospital Ethics Committee, and all subjects and their families were aware of the study purpose and provided informed consent.

2.2. Eligibility Criteria. The inclusion criteria were as follows: those with a definite diagnosis of AMI; those whose age conformed to the general standard of old age division; those with no serious organ function injury; those who signed the informed consent form and actively cooperate with the treatment, with high compliance.

Patients were excluded if they met any of the following criteria: vital organ diseases, coagulation disorders, and low tolerance; severe mental diseases; treatment interruption due to various reasons; tissue infection, necrosis, etc.; patients who did not meet the inclusion criteria, were unwilling to cooperate with the study, or whose incomplete data affected the research judgment.

2.3. Nursing Measures. Control Group (Routine Nursing Group). Patients in this group were closely monitored by medical staff for vital signs. In addition, they were given corresponding nursing care based on their actual situation and needs, as well as medication according to the doctor's advice

Observation Group (PHEC Group). This group of patients received PHEC, which was conducted by a tempo-

rary first-aid team composed of experienced medical staff. After receiving the first-aid task, the first-aid team quickly understood and made a general assessment of the patient's condition. Upon arrival at the scene, the first-aid team promptly instructed the patient to lie flat to administer oxygen using a mask or nasal catheter. Furthermore, the patient's blood pressure, pulse, and other signs were detected. If the patient was found to be at risk of shock, corresponding treatment was carried out in time. On the way to the hospital, the medical staff contacted the hospital to prepare for the treatment

2.4. Nursing Effect Evaluation. Marked Effectiveness. The patient's clinical symptoms and features were significantly improved or the patient was cured without complications after nursing

Effectiveness: patients' clinical symptoms and features were obviously relieved, and the condition was basically cured after nursing, with complications in individual patients

Ineffectiveness. The patient died or the clinical symptoms and characteristics were not significantly improved or even worsened with complications after nursing

2.5. Endpoints. Nursing Efficacy. The nursing effect evaluation standard is described as above, and the total effective rate is the percentage of the number of (marked effectiveness + effectiveness) cases in all patients

Rescue Success Rate. The number of deaths and successful rescues in the two groups during care were recorded and analyzed. The percentage of successful cases in all cases was the success rate of rescue

Clinical Parameters. The clinical parameters such as the start time of thrombolysis and hospitalization time were recorded

Incidence of Complications. Complications, including arrhythmia, heart failure (HF), and CGS were observed in both groups during recovery

2.6. Statistical Processing. All the medical records of 200 senile AMI patients were analyzed and visualized by SPSS 21.0 (SPSS, Inc., Chicago, IL, USA) and GraphPad Prism 6 (GraphPad Software, San Diego, USA), respectively. The analysis results with $P < 0.05$ were considered statistically significant. Enumeration data (sex, age, etc.) and measurement data (average age, time from onset to rescue, etc.) were expressed by number of cases/percentage ($n/\%$) and mean \pm SEM, respectively. As for their statistical methods, χ^2 test was used for intergroup comparisons of enumeration data, while independent samples had t test and paired t test for intergroup and intragroup comparisons of measurement data, respectively.

3. Results

3.1. Baseline Data of Senile AMI Patients. By analyzing the baseline data of 200 senile AMI patients, we found no obvious difference between the control group and the observation group in terms of sex, age, average age, time from onset to rescue, infarction type, education level, drinking

TABLE 1: Baseline data of senile patients with acute myocardial infarction [n (%), mean \pm SEM].

Factor	n	Control group ($n = 90$)	Observation group ($n = 110$)	χ^2/t	P
Sex				0.090	0.764
Male	111	51 (56.67)	60 (54.55)		
Female	89	39 (43.33)	50 (45.45)		
Age (years old)				0.098	0.755
<80	102	47 (52.22)	55 (50.00)		
≥ 80	98	43 (47.78)	55 (50.00)		
Average age (years old)	200	79.02 \pm 10.70	79.75 \pm 10.11	0.495	0.621
Time from onset to rescue (min)	200	20.17 \pm 6.62	20.90 \pm 7.28	0.735	0.463
Type of infarction				0.944	0.815
Inferior wall	55	26 (28.89)	29 (26.36)		
Anterior wall	47	23 (25.56)	24 (21.82)		
Anteroseptal wall	50	20 (22.22)	30 (27.27)		
High lateral wall	48	21 (23.33)	27 (24.55)		
Education level				0.119	0.730
Technical secondary school or above	84	39 (43.33)	45 (40.91)		
Technical secondary school below	116	51 (56.67)	65 (59.09)		
Drinking history				0.232	0.630
No	77	33 (36.67)	44 (40.00)		
Yes	123	57 (63.33)	66 (60.00)		
Overweight				0.170	0.680
Yes	101	44 (48.89)	57 (51.82)		
No	99	46 (51.11)	53 (48.18)		

TABLE 2: Rescue success rate of senile patients with acute myocardial infarction [n (%)].

Groups	n	Mortality rate (%)	Rescue success rate (%)
Control group	90	14 (15.56)	76 (84.44)
Observation group	110	7 (6.36)	103 (93.64)
χ^2 value	—	—	4.450
P value	—	—	0.035

history, overweight, etc., suggesting comparability ($P > 0.05$). See Table 1 for details.

3.2. Rescue Success Rate of Senile AMI Patients. The analysis and intergroup comparison (Table 2) of rescue success and mortality rates revealed a statistically higher rescue success rate in the observation group as compared to the control group (93.64% vs. 84.44%, $P < 0.05$).

3.3. Clinical Parameters of Senile AMI Patients. We recorded the time to start thrombolytic therapy and hospitalization time of the two groups to compare the effects of the two nursing methods on clinical parameters of senile AMI patients. The start time of thrombolysis and hospitalization time were found to be statistically shorter in the observation group as compared to the control group ($P < 0.05$). See Figure 1 for details.

3.4. Nursing Effect of Senile AMI Patients. The impacts of the two nursing methods on senile AMI patients were assessed by analyzing the nursing effects. The data identified a higher total effective rate of nursing in the observation group (92.73%) compared with the control group (80.00%), with statistical significance ($P < 0.05$, Table 3).

3.5. Complication Rate in Senile AMI Patients. We made an intergroup comparison regarding the incidence of complications such as arrhythmia, HF, and CGS and found that the total complication rate was statistically lower in the observation group compared with the control group (9.09% vs. 25.56%, $P < 0.05$, Table 4).

4. Discussion

AMI is a life-threatening condition when blood flow to the heart is suddenly blocked, causing myocardial damage or death [13]. Even though the treatment of AMI has been improved, the post-discharge mortality of patients is still very high. This is particularly true for those with complications after myocardial infarction, whose follow-up situation is even more dismal [14]. Gasior et al. [15] reported that only half of newly diagnosed HF patients managed to survive for four years, and the situation for senile patients is even less optimistic. Therefore, this study focuses on senile AMI patients and mainly analyzes the rescue success rate and complications, hoping to contribute to improving the management of senile AMI.

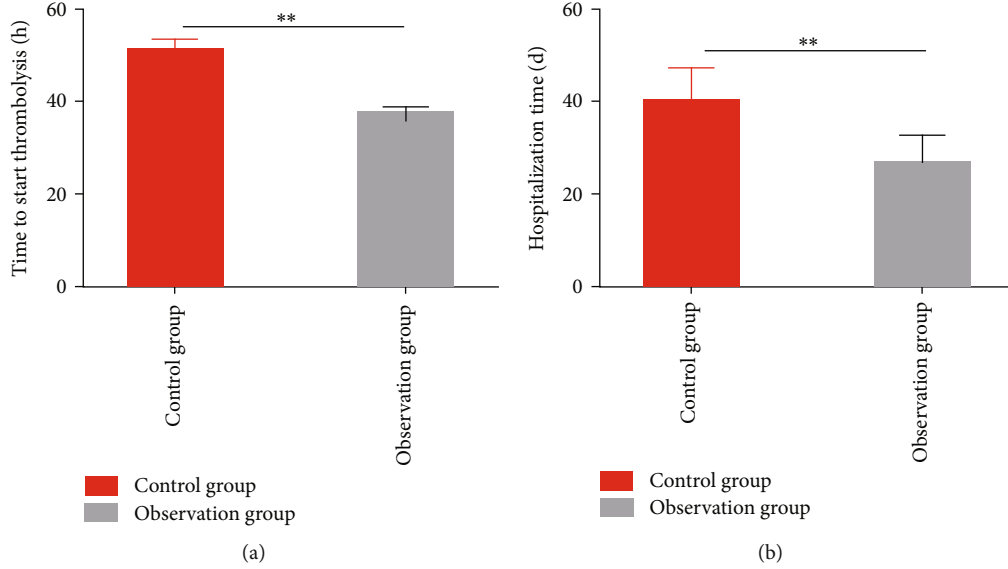


FIGURE 1: Clinical parameters of senile patients with acute myocardial infarction. (a) Time to start thrombolysis after nursing in the two groups. (b) Hospitalization time after nursing in the two groups. Note: $**P < 0.01$.

TABLE 3: Nursing effect of senile patients with acute myocardial infarction [n (%)].

Groups	n	Marked effectiveness	Effectiveness	Ineffectiveness	Total effective rate (%)
Control group	90	42 (46.67)	30 (33.33)	18 (20.00)	72 (80.00)
Observation group	110	74 (67.27)	28 (25.46)	8 (7.27)	102 (92.73)
χ^2 value	—	—	—	—	7.089
P value	—	—	—	—	0.008

TABLE 4: Complication rate in senile patients with acute myocardial infarction [n (%)].

Categories	Control group ($n = 90$)	Observation group ($n = 110$)	χ^2 value	P value
Arrhythmia	12 (13.33)	5 (4.55)	—	—
Heart failure	6 (6.67)	3 (2.72)	—	—
Cardiogenic shock	5 (5.56)	2 (1.82)	—	—
Total incidence	23 (25.56)	10 (9.09)	9.740	0.002

PHEC can provide emergency medical care for endogenous emergencies such as AMI and exogenous emergencies like burns and poisoning [16]. A previous clinical analysis shows that quite a number of AMI patients died before they arrived at the hospital [17]. On the contrary, if patients can get effective and timely prehospital first aid and are quickly transported to the hospital, the risk of death and complications will be greatly reduced [18]. This study included 200 elderly AMI patients who were divided into the control group receiving routine care and the observation group receiving PHEC according to the difference in nursing methods. The number of successfully rescued patients in the observation group was found to be significantly higher than that in the control group (93.64% vs. 84.44%), indicat-

ing that receiving PHEC can significantly improve the rescue success rate of senile AMI patients. Then, we recorded the clinical parameters of our case series. Through analysis, we found statistically shorter time to start thrombolysis and hospitalization time in the observation group compared with the control group, which suggested that the use of PHEC, an effective care model that provides timely interventions, has a positive impact on the rehabilitation process of patients. Our findings are consistent with the view that appropriate first aid, as reported by Mai et al. [19], will significantly improve patient survival chances and later treatment outcomes. In terms of nursing efficacy, a statistically higher total effective rate of nursing was determined in the observation group when compared to the control group (92.73% vs. 80.00%), demonstrating better nursing efficacy of PHEC that contributes to better nursing effects in senile AMI patients than conventional nursing. Wu et al. [20] pointed out in their report on acute stroke that the PHEC model significantly outperformed conventional emergency care in terms of nursing effect and nursing satisfaction, similar to our results.

With regard to complications, arrhythmia, HF, and CGS are the three common complications of AMI [21]. Volle et al. [22] indicated in their study that HF bore the main responsibility for morbidity and mortality in more than 10% of people over 70 years old, in addition to 10% of cases experiencing CGS immediately after the onset of AMI [23]. In our research, a statistically lower complication rate was

found in the observation group as compared to the control group (9.09% vs. 25.56%), suggesting that PHEC for senile AMI patients is safer than conventional care, which is consistent with the report of Lihui and Qing [24] on the application of PHEC.

Although this paper has confirmed the beneficial effects of PHEC for senile AMI patients in increasing the rescue success rate, improving clinical indicators and nursing effects, and reducing the incidence of complications, there is still room for improvement. First of all, there is no follow-up in this study, while in fact, AMI patients have a high recurrence rate after discharge. Hence, increasing the 12-month follow-up after discharge can more intuitively determine the recovery or recurrence of patients. Second, this study is a single-center study, which is prone to information deviation. We will continue to improve the research based on the above two points in the future.

5. Conclusion

Collectively, PHEC for senile AMI patients is worthy of clinical promotion as it has a remarkable effect, which can not only improve the survival rate of patients but also effectively shorten their rehabilitation process and reduce complications, providing an effective nursing method for the rehabilitation of senile AMI patients.

Data Availability

The labeled dataset used to support the findings of this study are available from the corresponding author upon request.

Conflicts of Interest

The authors declare no competing interests.

References

- [1] C. Y. Cui, M. G. Zhou, L. C. Cheng et al., "Admission hyperglycemia as an independent predictor of long-term prognosis in acute myocardial infarction patients without diabetes: a retrospective study," *Journal of Diabetes Investigation*, vol. 12, no. 7, pp. 1244–1251, 2021.
- [2] F. Van de Werf, "Reperfusion treatment in acute myocardial infarction in elderly patients," *Kardiologia Polska*, vol. 76, no. 5, pp. 830–837, 2018.
- [3] N. K. Kapur, K. L. Thayer, and E. Zweck, "Cardiogenic shock in the setting of acute myocardial infarction," *Methodist DeBakey Cardiovascular Journal*, vol. 16, pp. 16–21, 2020.
- [4] O. V. Tukish, S. A. Okrugin, E. Y. Yunusova, E. V. Efimova, and A. A. Garganeeva, "Acute myocardial infarction in elderly and senile patients: epidemiology study according to the who program "registry of acute myocardial infarction"," *Advances in Gerontology*, vol. 29, no. 1, pp. 123–127, 2016.
- [5] J. Li, X. Li, Q. Wang et al., "ST-segment elevation myocardial infarction in china from 2001 to 2011 (the China peace-retrospective acute myocardial infarction study): a retrospective analysis of hospital data," *Lancet*, vol. 385, no. 2015, pp. 441–451, 2015.
- [6] C. Tokunaga, A. Iguchi, H. Nakajima et al., "Surgical outcomes of bridge-to-bridge therapy with extracorporeal left ventricular assist device for acute myocardial infarction in cardiogenic shock," *BMC Cardiovascular Disorders*, vol. 22, no. 1, p. 54, 2022.
- [7] T. Nishi, M. Ishii, K. Tsujita et al., "Outcomes of venoarterial extracorporeal membrane oxygenation plus intra-aortic balloon pumping for treatment of acute myocardial infarction complicated by cardiogenic shock," *Journal of the American Heart Association*, vol. 11, no. 7, article e023713, 2022.
- [8] L. Wang and R. Wu, "Clinical effectiveness of pre-hospital and in-hospital optimized emergency care procedures for patients with acute craniocerebral trauma," *Frontiers in Surgery*, vol. 8, article 830571, 2021.
- [9] R. Y. Hsia, D. Huang, N. C. Mann et al., "A US national study of the association between income and ambulance response time in cardiac arrest," *JAMA Network Open*, vol. 1, no. 7, article e185202, 2018.
- [10] N. Dehghan-Nayeri, H. Nouri-Sari, F. Bahramnezhad, F. Hajibabae, and M. Senmar, "Barriers and facilitators to cardiopulmonary resuscitation within pre-hospital emergency medical services: a qualitative study," *BMC Emergency Medicine*, vol. 21, no. 1, p. 120, 2021.
- [11] A. Moreno-Carrillo, L. M. A. Arenas, J. A. Fonseca, C. A. Cacedo, S. V. Tovar, and O. M. Munoz-Velandia, "Application of queuing theory to optimize the triage process in a tertiary emergency care ("ER") department," *Journal of Emergencies, Trauma, and Shock*, vol. 12, no. 4, pp. 268–273, 2019.
- [12] A. Pendyal, C. Rothenberg, J. E. Scofi et al., "National trends in emergency department care processes for acute myocardial infarction in the United States, 2005 to 2015," *Journal of the American Heart Association*, vol. 9, no. 20, article e017208, 2020.
- [13] J. Lee, S. Lee, W. N. Street, and L. A. Polgreen, "Machine learning approaches to predict the 1-year-after-initial-AMI survival of elderly patients," *BMC Medical Informatics and Decision Making*, vol. 22, no. 1, p. 115, 2022.
- [14] D. Y. Chen, C. Y. Li, M. J. Hsieh et al., "Predictors of subsequent myocardial infarction, stroke, and death in stable post-myocardial infarction patients: a nationwide cohort study," *European Heart Journal Acute Cardiovascular Care*, vol. 8, no. 7, pp. 634–642, 2019.
- [15] M. Gasior, K. Wita, P. Buszman et al., "Managed care after acute myocardial infarction (MC-AMI) improves prognosis in AMI survivors with pre-existing heart failure: a propensity score matching analysis of Polish nationwide program of comprehensive post-MI care," *Kardiologia Polska (Polish Heart Journal)*, vol. 80, pp. 293–301, 2022.
- [16] K. Wake, T. Noguchi, H. Hishinuma et al., "Characteristics of patients who received helicopter emergency medical services in Japan from 2012 to 2019: a retrospective analysis of data from Tochigi prefecture," *Scandinavian Journal of Trauma, Resuscitation and Emergency Medicine*, vol. 30, no. 1, p. 25, 2022.
- [17] F. Rosell-Ortiz, F. J. Mellado-Vergel, P. Fernandez-Valle et al., "Initial complications and factors related to prehospital mortality in acute myocardial infarction with ST segment elevation," *Emergency Medicine Journal*, vol. 32, no. 7, pp. 559–563, 2015.
- [18] H. Najafi, E. Bahramali, M. Bijani, A. Dehghan, M. Amirkhani, and M. Balaghi Inaloo, "Comparison of the outcomes of ems vs. non-EMS transport of patients with ST-segment elevation

- myocardial infarction (STEMI) in southern Iran: a population-based study,” *BMC Emergency Medicine*, vol. 22, p. 46, 2022.
- [19] H. T. Mai, H. M. Vu, T. T. Ngo et al., “The status of first aid and its associations with health outcomes among patients with traffic accidents in urban areas of Vietnam,” *International Journal of Environmental Research and Public Health*, vol. 17, no. 12, p. 4600, 2020.
- [20] Y. Wu, Y. Yang, X. Guo et al., “Effect of pre-hospital early intervention combined with an in-hospital emergency model in the emergency care of patients with acute stroke,” *American Journal of Translational Research*, vol. 14, no. 1, pp. 672–678, 2022.
- [21] L. T. Petersen, S. Riddersholm, D. C. Andersen et al., “Temporal trends in patient characteristics, presumed causes, and outcomes following cardiogenic shock between 2005 and 2017: a Danish registry-based cohort study,” *European Heart Journal Acute Cardiovascular Care*, vol. 10, no. 9, pp. 1074–1083, 2021.
- [22] K. Volle, C. Delmas, A. Rollin et al., “Successful reversal of severe tachycardia-induced cardiomyopathy with cardiogenic shock by urgent rhythm or rate control: only rhythm and rate matter,” *Journal of Clinical Medicine*, vol. 10, no. 19, p. 4504, 2021.
- [23] M. D. Samsky, D. A. Morrow, A. G. Proudfoot, J. S. Hochman, H. Thiele, and S. V. Rao, “Cardiogenic shock after acute myocardial infarction: a review,” *JAMA*, vol. 326, no. 18, pp. 1840–1850, 2021.
- [24] L. Lihui and Y. Qing, “Optimizing the prehospital-hospital emergency care path application value in emergency treatment of patients with cerebral hemorrhage,” *Journal of Healthcare Engineering*, vol. 2021, Article ID 2352208, 5 pages, 2021.

Research Article

Analysis of Characteristic Factors of Nursing Safety Incidents in ENT Surgery by Deep Learning-Based Medical Data Association Rules Method

Ju Chen , Jie Zhou, and Fanglan Yang

Anesthesia Operation Center, 363 Hospital, Chengdu, Sichuan 610041, China

Correspondence should be addressed to Ju Chen; chenju5@gt.cn

Received 18 August 2022; Revised 13 September 2022; Accepted 19 September 2022; Published 12 October 2022

Academic Editor: Pan Zheng

Copyright © 2022 Ju Chen et al. This is an open access article distributed under the Creative Commons Attribution License, which permits unrestricted use, distribution, and reproduction in any medium, provided the original work is properly cited.

It is of great significance to explore the characteristic factors of postoperative nursing safety events in patients with otolaryngology surgery and to understand the characteristics of postoperative nursing safety events in otolaryngology surgery patients. This paper carried out preoperative safety protection for 385 inpatients, and the results showed that there were 52 cases of postoperative safety nursing events. This experiment found that the coinfectious lesions ($P = 0.001$, HR = 14.283, 95.0% CI: 9.365~21.038), the treatment period ($P = 0.001$, HR = 13.716, 95.0% CI: 7.147~20.275), during hospital treatment ($P = 0.002$, HR = 15.208, 95.0% CI: 8.918-24.237), antibiotic use ($P = 0.001$, HR = 14.054, 95.0% CI: 8.163-21.739), and hypertension ($P = 0.001$, HR = 13.976, 95.0% CI: 7.926-22.385) are the important factors affecting postoperative care; using the association rule method to control and analyze the main risk factors of postoperative infection and bleeding in ENT patients can significantly improve the prognosis.

1. Introduction

Since the discussion of data mining and knowledge discovery first appeared in the world, the current data mining technology has been quite perfect [1]. Data analysis technology is the continuous improvement of data processing and analysis capabilities, which can quickly discover valuable knowledge. Data mining technology and software have been widely used in all walks of life and have produced significant economic and social benefits in medical and health care. However, the application in healthcare is still in its initial stage. Compared with other industries, the healthcare industry needs data mining technology for data processing, and this industry can perform auxiliary examinations, experience summaries and data analysis after using this technology. Therefore, medical data mining has more practical significance. Development prospects [2] in medical research, the extensive application of data mining technology in medicine will be recognized by more medical institutions and personnel. The particularity, timeliness, complexity, instability, and incompleteness of medical data. At present, the urgent problem to be solved in the processing of medical data is how to

mine useful information from the data. These research results can play an important role in the diagnosis and treatment of diseases, the scientific decision-making of medical and health management departments, the epidemic of diseases, the prevention and treatment of infectious diseases, and health examinations [3–5]. Through research on the application of clinical and medical drugs, common clinical methods can be found to rationally use drugs for clinicians and reduce the physical and psychological burden of patients. If the means and means of data processing can be used to discover hidden, in-depth and diagnostically valuable data and rules from the massive data, and transform these massive data into valuable wisdom, it will greatly improve the hospital and the ability of medical workers to diagnose and treat, reduce the rate of misdiagnosis, and reduce the physical, mental, and financial pressure of patients. Due to the increasing popularity of computer science and technology, the amount of data required by various disciplines has increased dramatically. Therefore, how to find useful information from a large amount of data needs to be analyzed through data mining technology. During the development of association law, this new method was

used to conduct in-depth discussions on clinical disease monitoring, drug treatment effect evaluation, and disease prevention and treatment.

The safety of nursing is generally the absence of any mental, structural or functional impairment, handicap, defect, or lethality throughout the duration of medical care [6]. The work of nurses is complex, involves a wide range of areas, and has many reasons for instability, which will not only have a great negative impact on the quality of nurses' work but also have a negative impact on the hospital's society and economy. In recent years, nursing workers have been accumulating and accumulating experience in their work to improve the level of nursing safety, prevent the occurrence of medical safety incidents, enable patients to receive appropriate, timely and safe nursing care, and maintain and restore the patient's body.

Otolaryngology is a relatively common disease, and complications such as infection and massive bleeding often occur during surgery, which pose a great threat to the survival of patients [7]. There are several main reasons that affect the safety of nursing care of surgical patients [8]. This therapy not only brings more pain to the patient but also brings greater financial pressure to the patient. Taking appropriate nursing measures can prevent and reduce post-operative complications as soon as possible [9].

In this paper, 385 otorhinolaryngology surgical patients from October 2019 to December 2021 were selected as the survey subjects, using the deep learning-based medical data correlation rule method and using the single factor analysis and logistic variance regression methods to carry out the statistics of risk factors. The purpose is to provide a certain reference for the nursing safety of patients undergoing ENT surgery in clinical practice.

2. Introduction to Related Theories

2.1. Data Mining Based on Deep Learning. Data mining (DM), also known as KDD, is a new information processing technology emerging in recent years [10]. DM is to extract implicit, regular, unknown, but potential and understandable information or models from massive data in databases, data warehouses, or other databases [11]. DM is based on database technology, which organically integrates artificial intelligence, parallel computing, statistics, and neural networks. Data mining is a process that uses a variety of analytical methods to discover patterns and connections between data from a large amount of data, and use this to make predictions and help decision makers find possible connections between data and find possible overlooked connections. Therefore, it has become an effective means to deal with the current explosion of data and the lack of information.

DM can discover potential, novel, effective, easy-to-understand, and easy-to-store, and apply knowledge techniques and approaches from massive data [12]. DM does not need to establish accurate retrieval requirements when dealing with massive data and converts massive data into meaningful information to describe the trend of historical development, respond to future development directions, obtain effective query performance, and provide support

for decision-making news. Data mining is to unearth some hidden, unknown in advance but potential, and unearthed into rules, patterns, and other forms from the data warehouse.

The modes of data collection are as follows: classification model, regression model, and time series model are all model-based. The model consists of clustering model, association model, and sequential model.

The method first describes a predetermined set of data or concepts, and then models the database unit, assuming that the unit is a predetermined category, the unit is called a "class"; the units are called "class sets" and are "sampled" for said "training" selection;

The continuity of the regression model was simulated using multiple regression statistics. Many problems can be solved by linear regression, and nonlinear problems can be transformed into linearization to solve.

The time series model is to use the time series trend of the existing data to predict it. This is very similar to the linear regression model. However, timing analysis must take into account the time domain characteristics, especially the impact on the time domain. On this basis, in order to accurately predict the future values, the influence of time must be fully considered, and a dynamic analysis of a set of values must be carried out according to the existing data.

The cluster mode is to divide a population into several categories, so that the populations of the same population are as close as possible, while the number of populations between various groups is minimized. Combining a group of entities or a group of abstract objects into multiple categories of similar objects is called cluster mode, which is decomposed and merged according to specific cluster parameters. Once the purpose is achieved, the category parameters can be obtained by this method.

2.2. Association Rules. The data mining method of association law is divided into two stages: looking for the shortest number of occurrences (testing of the degree of support); based on the strong correlation criterion (CI) generated by the collection of current items, it needs to meet the least degree of support and the least credibility.

The first step is the most important, and its effectiveness is directly related to the overall effect of data mining. For better understanding, the algorithm for data collection should be as simple as possible. In order to test the correctness of the relevant criteria, this paper uses the support degree and credibility of the association criterion to measure its weight, and its promotion degree to measure its importance. Indicators such as support, confidence, and improvement of association criteria cannot only measure the quality of relevant criteria but also a key factor to measure the formulation of association criteria.

2.3. Association Rules Apriori Mining Algorithm. On this basis, Hongli et al. implemented a new data mining method using the Apriori algorithm [13]. The method can reduce the storage capacity of the database, increase the utilization rate of the system, and can find frequent items and discover the deeper rules.

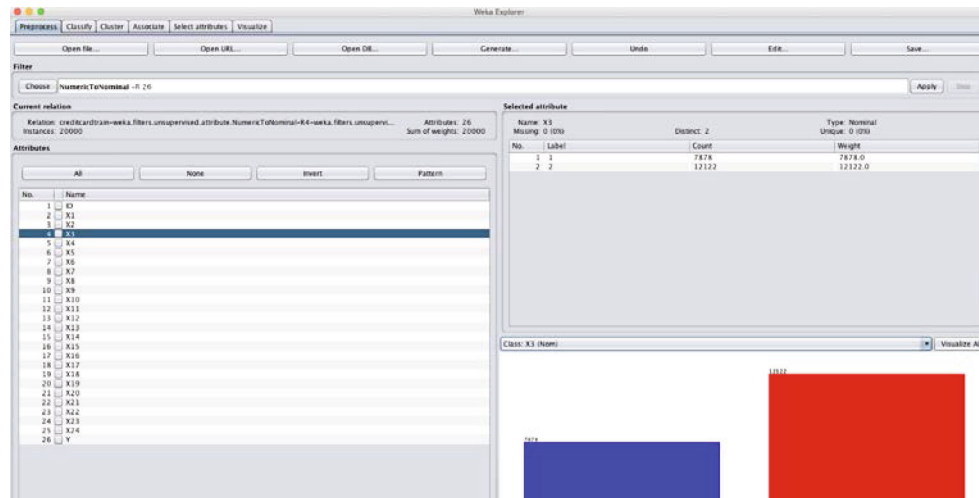


FIGURE 1: Weka software interface.

If the item set l is a regular item set, then all its nonempty item sets must also be a regular item set. If a $(k + 1)$ -item set is a frequent item set, then all its k -item sets must also be a frequent item set. On the contrary, if the k -item set is not a frequent item set, then all the k -item sets in the item set must be frequent itemsets. The $(k + 1)$ -item set is not a frequent itemset, so during the step-by-step retrieval, the generation of the frequency $(k + 1)$ -item can be realized by methods such as connection, pruning, and auxiliary statistics.

3. Application Method Design

3.1. Research Objects. From October 2019 to December 2021, a total of 385 otolaryngology patients aged 17-73 in a hospital were selected, with an average of $(47.8 + 13.2)$. Of these patients, 190 were men, and 195 were women. All patients underwent ENT surgery and were excluded. 264 patients also had hypertension. Postoperative care was given to 52 patients who had undergone otolaryngology surgery.

3.2. Methods. Risk factors such as gender, age, infection site, pathogen type, operation time, hospital stay, antibiotic use, and hypertension were collected in this experiment. All cases were followed for one year to determine the presence of comorbidities and recurrence.

3.3. Association Rules Method. Weka mining software was selected for this study. Weka, fully named Waikato Intelligent Analysis Environment, is a java-based open-source product for data mining and knowledge discovery.

Weka is one of the most complete data mining tools available today and is recognized as the most famous open source product for data mining. It provides a unified user interface and integrates a large number of machine learning algorithms that can undertake data mining tasks, including preprocessing of data, association rule mining, classification, clustering, etc., and provides rich visualization capabilities. At the same time, due to the openness of its source code,

Weka cannot only be used to complete the regular data mining tasks but also can be used for secondary development of data mining. As shown in Figure 1.

Data processing and transformation: web mining data comes in the form of arff files. First, save the marriage inspection data in the form of an Excel file, save the worksheet into a.csv file, then go to the Weka exploration program Explore, open the csv file, and then save it as an arff file, as shown in Figure 1 for the transformation of the file. Input the data into the data mining software Weka, convert it into the Associate label, click the "Choose" button, select Apriori, set minsupport = 30%, minconfidence = 80%, establish the relevant relationship, and click the "Start" button to start mining.

3.4. Statistical Processing. Used to conduct statistics on all data, and the measured values were expressed as $(\bar{x} + s)$. The count data were tested by using t -test for comparison, and multifactor logistic regression was carried out for the variables with important influence, $P < 0.05$ shows a significant difference.

4. Analysis of Applied Practice Experiments

4.1. Univariate Regression Analysis. Statistics show that operative time, intraoperative bleeding and length of hospital stay are the main factors affecting postoperative complications. In the statistical data, the use of antibiotics, the combination of hypertension, the site of infection, and whether there is blood transfusion during the operation are the main reasons that affect the complications of surgery. The above risk factors were significantly different among the risk factors in ear, nose, and throat surgery ($P < 0.05$). (see Tables 1 and 2).

4.2. Multivariate Logistic Regression Analysis of Risk Factors. Risk factors for each factor were analyzed, and it was found that the intraoperative OR was 2.537, $P = 0.023$; the hospitalization time was 5.208, $P = 0.003$; the antibiotic use OR

TABLE 1: Statistical *t*-test analysis of postoperative safety nursing factors for ENT patients.

Risk factors	(Age)	Operation time (time)	Length of hospital stay (d)	Intraoperative blood loss (mL)
Uncomplicated group ($n = 326$)	57.36 ± 5.67	28.73 ± 2.25	4.67 ± 0.56	46.52 ± 13.17
Complication group ($n = 59$)	58.77 ± 5.61	35.46 ± 2.31	5.69 ± 0.61	756.23 ± 20.65
<i>t</i> value	1.7605	21.0556	12.6960	53.4361
<i>P</i> value	0.0791	0.001	0.001	0.001

TABLE 2: Test and analysis of count data of nursing safety factors after ENT surgery χ^2 .

Risk factors		Number of cases	Complications (cases)	χ^2 value	<i>P</i> value
Infection concurrent site	Respiratory tract	179	43	18.184	0.001
	Urinary system	69	5		
	Digestive tract	83	6		
	Other	51	6		
Gender	Male	191	29	0.004	0.948
	Female	194	30		
Types of germs	Gram positive	203	31	0.012	0.912
	Gram negative	182	28		
Intraoperative blood transfusion	Have	73	48	171.775	0.001
	None	312	11		
Antibiotic use	Have	337	56	4.067	0.044
	None	52	3		
Hypertension	Have	271	53	11.557	0.001
	None	114	6		

TABLE 3: Multivariate logistic regression analysis of nursing safety factors after ENT surgery.

Risk factors	Partial regression coefficient	Standard deviation	OR	<i>P</i> value	Wald	95% confidence interval
Infection concurrent site	0.995	0.402	2.711	0.013	6.1174	1.229~5.867
Operation time	0.936	0.425	2.537	0.023	.736	1.103~5.931
Hospital stay	0.985	0.763	5.208	0.003	5.208	1.172~3.830
Intraoperative blood loss	0.004	0.001	1.005	0.001	16.608	1.002~1.006
Antibiotic use	0.833	0.372	2.234	0.028	4.271	1.079~3.267
Hypertension	0.702	0.284	2.013	0.015	6.017	1.149~3.521
Constant	0.506	1.136	1.662	0.661	0.192	

was 2.234, $P = 0.028$, and the intraoperative bleeding OR = 1.005, $P = 0.001$. Complicated with hypertension (OR = 2.013, $P = 0.015$), infection at the combined place (OR = 2.711, $P = 0.013$). See Table 3.

5. Conclusion

The three major types of ENT diseases include chronic otitis media, chronic tonsillitis, chronic sinusitis, nasal polyps, deviated nasal septum, acute and chronic laryngeal obstruction, ear, nasal cavity, sinus, and throat and neck tumors. Some ENT diseases require surgery, and nursing safety issues such as bleeding, infection, etc. are very common and can have a great negative impact on patient survival and survival. Lihua et al. [14] conducted a survey on 164 patients who had received ENT surgery, and the results showed that, on this basis, 14.02%

of the patients had nursing safety problems. A total of 59 of 385 patients in this paper, of which 59 patients had nursing safety accidents after surgery, the incidence rate was 15.3%, which was in line with the above reported situation.

Nursing safety accidents that occurred after surgery not only aggravated the patient's condition but also caused the patient and their families to bear unnecessary economic pressure. Therefore, the analysis of the safety risk of postoperative nursing of stroke patients has an important guiding role in the treatment and prognosis of the disease. Multivariate logistic regression was used to analyze the effect of nursing safety after otolaryngology surgery, and the public analysis of 5 j was preliminarily discussed.

5.1. Operation Time. The duration of the operation is one of the main causes of postoperative infection, and as the

operation progresses, the exposure time of the wound increases as the operation time goes on, and at the same time, as the operation continues, the postoperative bleeds. The amount and duration of anesthesia will also be greatly reduced, resulting in reduced patient tolerance, thereby increasing the infection rate of the wound surface, thereby greatly improving the safety of nurses. The survey results of Aghamohammadi et al. [15] showed that in ENT surgery, the incidence of nurse safety accidents within 30 minutes before the operation was 6%, and among patients with more than 30 minutes, 17.1% of the patients appeared nursing. On this basis, the postoperative treatment period ($35.46 + 2.31$) minutes of postoperative combined and noncombined patients had a significant effect on the treatment effect of $28.73 + 2.25$ minutes ($P < 0.05$); the multiple linear regression results showed that the OR was 2.537, $P = 0.023$. Therefore, in ear, nose, and throat surgery patients, the duration of surgery is an important reason for the safety of nurses.

5.2. Length of Hospital Stay. With the development of hospitals, patients have more and more contact with hospital patients, more and more pathogenic bacteria on their bodies, and more and more close contact with patients and medical staff, making them more susceptible to pathogens, and these viruses are emitted from the air [16]. In this test, the days of admission for the combined and noncombined ($5.69 + 0.61$) were significantly compared with $4.67 + 0.56$ d ($P < 0.05$); the multiple linear regression results showed that the difference between the two was significant OR was 5.208, $P = 0.003$. In conclusion, the length of hospital stay has a certain influence on the safety of nurses after surgery. However, if early intervention can reduce the recurrence after surgery, it remains to be further explored, and this trial is a single-point trial, involving a small number of patients, and has some limitations.

5.3. Intraoperative Blood Loss. Massive bleeding during surgery is unavoidable, but because blood will inhibit the body's immune system to a certain extent, this effect will cause strong resistance to cytokines, significantly increase the number and function of T lymphocytes, and also the response and response of lymphocytes to soluble antigens and mitogens, thereby inhibiting the normal killing of cells and increasing the safety of postoperative care. The results of multivariate regression showed that intraoperative blood loss was significantly associated with postoperative complications (OR = 1.005, $P = 0.001$). However, if you pay attention to enhancing the patient's immunity during blood transfusion, because intraoperative bleeding cannot be an important reason for affecting the safety of postoperative care in otolaryngology surgery, it is necessary to strengthen immunity during otolaryngology surgery to achieve purpose of prevention. At the same time, it is necessary to strengthen the technique of the surgeon, shorten the operation process as much as possible, reduce the postoperative blood loss rate, and ensure the standardization of the operation [17].

5.4. Antibiotic Use and Comorbid Hypertension. The application of various antibiotics will cause damage to the patient's

body, which means that the living environment of microorganisms has been greatly affected, and at the same time, the bacteria will develop resistance, thus greatly increasing the infection rate of bacteria [17]. Hypertension is a relatively common complication in chronic rhinitis patients, especially in the elderly, and with age, the patient's physical functions are also affected. After logistic regression analysis, it was found that the OR of antibiotics was 2.234, $P = 0.028$, and the combined hypertension OR was 2.013, $P = 0.015$; the difference between the two was significant, suggesting that the use of antibiotics and hypertension during surgery is the main cause of nurses' safety incidents.

5.5. Infection Complicated Site. Patients in ear, nose, and throat surgery are mainly due to respiratory infections. These bacteria will invade the human body from the mouth and nasal passages. When the human body is weak, it is easy to cause some respiratory system problems, and some viruses will suddenly enter the digestive tract. Therefore, in this trial, the probability of safety events in patients with postoperative respiratory care was 24%, which was significantly different from other wards.

The independent risk factors of postoperative nursing safety of ENT patients can guide doctors to control the risk factors of various nursing safety events during surgery. Clinical data of patients in the department of ENT, using deep learning-based medical data association rules method, univariate analysis and logistic regression to analyze the risk factors of postoperative nursing safety events in patients with ENT surgery, and the research results on postoperative infection and bleeding in ENT patients. The main risk factors can significantly improve the prognosis. Effectively reduce the occurrence of nursing safety incidents and improve patient prognosis. Of course, there are some problems in the research process. The sample size of this study is still small, and the collection and comparison of clinical data is not comprehensive.

Data Availability

The dataset used in this paper are available from the corresponding author upon request.

Conflicts of Interest

The authors declared that they have no conflicts of interest regarding this work.

References

- [1] Z. Cunhua, "Analysis of the influencing factors of infection after ENT surgery," *China Practical Medicine*, vol. 7, no. 2, pp. 74–76, 2012.
- [2] P. Xiaoling, Z. Hongmei, and D. Jie, "Common critical safety hazards and nursing care in ENT nursing work," *General Nursing*, vol. 8, no. 10, pp. 2694–2695, 2010.
- [3] L. Jiayi, L. Xingru, S. Gao, and X. Zhao, "Surgical resection and repair of laryngopharyngeal carcinoma with preservation of laryngeal function," *Chinese Journal of Otolaryngology Head and Neck Surgery*, vol. 44, no. 6, pp. 469–474, 2009.

- [4] Y. Junping and L. Guiquan, "Analysis of clinical risk factors for respiratory complications after gastric cancer surgery in the elderly," *Oncology*, vol. 17, no. 4, pp. 260–262, 2011.
- [5] Y. Jie, "Analysis of risk factors for postoperative complications in patients with ENT surgery," *China Practical Medicine*, vol. 8, no. 25, pp. 62–63, 2013.
- [6] H. Bing and H. Bei, "Analysis of the effectiveness of nosocomial infection management in ENT," *China Medical Innovation*, vol. 6, no. 8, pp. 38–39, 2009.
- [7] T. Yarong, S. Yumei, and L. Faxiang, "Analysis of risk factors for postoperative complications in patients with ENT surgery," *Journal of Chinese Contemporary Medicine*, vol. 20, no. 2, p. 182, 2013.
- [8] A. Géron, *Hands-on Machine Learning with Scikit-Learn, Keras, and TensorFlow: Concepts, Tools, and Techniques to Build Intelligent Systems*, O'Reilly Media, 2019.
- [9] Y. LeCun, Y. Bengio, and G. Hinton, "A logical calculus of the ideas immanent in nervous activity," *The Bulletin of Mathematical Biophysics*, vol. 5, no. 4, pp. 115–133, 1943.
- [10] B. Norgeot, B. S. Glicksberg, L. Trupin et al., "Assessment of a deep learning model based on electronic health record data to forecast clinical outcomes in patients with rheumatoid arthritis," *JAMA Network Open*, vol. 2, no. 3, article e190606, 2019.
- [11] R. Miotto, F. Wang, S. Wang, X. Jiang, and J. T. Dudley, "Deep learning for healthcare: review, opportunities and challenges," *Briefings in Bioinformatics*, vol. 19, no. 6, pp. 1236–1246, 2018.
- [12] Z. Yuying, "Hidden dangers and management countermeasures of nosocomial infection in the ENT department of primary hospitals," *Journal of China Practical Medicine*, vol. 6, no. 20, pp. 267–268, 2011.
- [13] L. Hongli, Y. Yun, and W. Shurong, "Analysis of the perioperative preventive use of antibiotics in a vascular surgery department in a hospital before and after special antibacterial treatment," *Chongqing Medicine*, vol. 41, no. 32, pp. 3448–3450, 2012.
- [14] L. Lihua, W. Quanzhen, Z. Huizhen, and J. Li, "Investigation and countermeasures of postoperative infection after ENT surgery," *Zhonghua Journal of Infectious Diseases*, vol. 20, no. 8, pp. 1091–1092, 2009.
- [15] A. Aghamohammadi, M. Moin, A. Karimi et al., "Immunologic evaluation of patients with recurrent ear, nose, and throat infections," *American Journal of Otolaryngology*, vol. 29, no. 6, pp. 385–392, 2008.
- [16] N. Vora, P. D. Eunson, K. K. Tallur et al., "P250 central nervous system (CNS) complications of ear nose throat (ENT) infections - case series," *European Journal of Paediatric Neurology*, vol. 13, article s99, 2009.
- [17] S. Permendra and W. Simon, "Anaesthesia for elective ear, nose and throat surgery in children," *Anaesthesia & Intensive Care Medicine*, vol. 10, no. 4, pp. 186–190, 2009.

Research Article

Alzheimer's Disease Prediction Algorithm Based on Group Convolution and a Joint Loss Function

Jiayuan Cheng ¹, Huabin Wang ¹, Shicheng Wei ², Fei Liu ¹ and Yonglin Chen ¹

¹International Brain Science and Engineering Center, School of Computer Science and Technology, Anhui University, Hefei 230039, China

²School of Electrical and Information Engineering, University of Sydney, Sydney 2006, Australia

Correspondence should be addressed to Huabin Wang; wanghuabin@ahu.edu.cn

Received 12 August 2022; Accepted 7 September 2022; Published 12 October 2022

Academic Editor: Pan Zheng

Copyright © 2022 Jiayuan Cheng et al. This is an open access article distributed under the Creative Commons Attribution License, which permits unrestricted use, distribution, and reproduction in any medium, provided the original work is properly cited.

Alzheimer's disease (AD) can effectively predict by 18F-fluorodeoxyglucose positron emission tomography (18F-FDG PET) of the brain, but current PET images still suffer from indistinct lesion features, low signal-to-noise ratios, and severe artefacts, resulting in poor prediction accuracy for patients with mild cognitive impairment (MCI) and unclear lesion features. In this paper, an AD prediction algorithm based on group convolution and a joint loss function is proposed. First, a group convolutional backbone network based on ResNet18 is designed to extract lesion features from multiple channels, which makes the expression ability of the network improved to a great extent. Then, a hybrid attention mechanism is presented, which enables the network to focus on target regions and learn feature weights, so as to enhance the network's learning ability of the lesion regions that are relevant to disease diagnosis. Finally, a joint loss function, that avoids the overfitting phenomenon, increases the generalization of the model, and improves prediction accuracy by adding a regularization loss function to the conventional cross-entropy function, is proposed. Experiments conducted on the public Alzheimer's Disease Neuroimaging Initiative (ADNI) dataset show that the algorithm we proposed gives a prediction accuracy improvement of 2.4% over that of the current AD prediction algorithm, thus proving the effectiveness and availability of the new algorithm.

1. Introduction

Alzheimer's disease (AD) is a kind of clinical neurodegenerative disease. Short-term memory loss is an early symptom of the condition, as the disease progresses, patients may develop language impairment, disorientation, and many behavioural problems. Eventually, the patient loses physical function, which leads to death. There is still no effective treatment to stop or reverse the progression of the disease [1].

To assist in the diagnosis of AD, clinicians utilize positron emission tomography (PET), magnetic resonance imaging (MRI), medical imaging techniques such as computed tomography (CT), and other techniques. Among them, PET can image the metabolic and functional statuses of brain lesion regions. Due to this property, PET-based neuroimaging diagnosis is an important method for the diagnosis of AD in the early stage. If patients with mild cognitive

impairment (MCI), a state between AD and normal control (NC), can be screened early and treated, further deterioration of the disease can be delayed.

Recently, the achievements of Convolutional Neural Network (CNN) in the diagnosis of brain diseases are increasingly recognized [2]. Syaifullah et al. [3] combined a voxel-based morphometry (VBM) with support vector machine (SVM) to construct a classification algorithm for differentiating patients with MCI from AD patients. The algorithm first uses VBM to normalize the input brain image data and then uses the SVM for the classification process, which tends to ignore potential lesion features due to its overreliance on image preprocessing. Pan et al. [4] designed a multiview and a separable pyramid network, based on deep learning. The network uses depthwise-separable convolution, in order to extract corresponding features from various PET images' slices, thereby preserves as much spatial information as possible and reducing the number of required

parameters. This network achieved 83.05% classification accuracy when used to predict patients with MCI. Yee et al. [5] proposed a three dimensional CNN with a residual structure for the AD prediction from 3D PET images; this approach uses batch normalization to normalize the features of each channel and adds instance normalization with a leaky rectified linear unit (ReLU) before each convolutional layer to enhance the generalization and robustness of this model. The AD classification accuracy of the model reaches 81.1%.

The classification accuracy of most AD classification networks is improved by simply adding the layers in the neural network. This practice tends to lose global image information, resulting in poor MCI classification accuracy. At the same time, due to the redundant information, high noise, and severe artefacts in PET images, the lesion features of MCI images cannot be accurately extracted, which further increases the difficulty of accurately distinguishing patients with MCI.

Aiming at the above problems, an AD prediction algorithm based on group convolution and a joint loss function is proposed. The algorithm uses a residual group convolution network as the backbone network, incorporates a hybrid attention mechanism into the backbone network to improve the learning of informative features, and then adds a joint loss function to increase the generalization of this model. We summarize below the new contributions of the paper.

- (1) ResNet18, based on the group convolutional network, is used as a basic network to complete the action of feature extraction; it uses the same topology to extract lesion features from multiple channels, in order to have an improvement of the network's expression ability
- (2) A hybrid attention mechanism is introduced after the network's convolutional layer to fully extract the features of the lesion region that makes the network have the function of adaptively learning the feature weights of lesion regions and thus, identify focal regions that are related to disease diagnosis
- (3) A joint loss function is designed to add a regularization loss function to the traditional cross-entropy loss function to prevent overfitting and increase the generalization of the model

The rest of the paper is organized as follows: in the related work section, the development achievements and some existing problems in the field of Alzheimer's disease prediction in recent years are introduced, and the innovation points of this paper are demonstrated according to these problems. In the material part, the source of the data set used in this paper and the specific method of preprocessing are introduced. In the method section, we introduce the group convolution, hybrid attention mechanism, and joint loss function in turn in detail. In section "experimental results and analysis", the experimental settings, evaluation criteria, model visualization, parameter experiment, ablation

experiment, and comparison experiment in this paper are elaborated in detail, and the experimental results are analyzed. In the conclusion section, the content of this paper is summarized.

2. Related Work

Recently, the great success of CNNs' application in medical image classification has been closely related to the high-speed progress of neural network models. Yang and Liu [6] used AlexNet-5 based on the convolution capable of fast feature embedding for the prediction of the risk of AD prevalence. Jo et al. [7] combined the multilayer basic neural networks with CNNs to extract features from the neuroimaging data. Ding et al. [8] used the neural network based on Inception v3 structure for AD prediction from PET images; this approach uses 11 Inception modules, each consisting of convolutional and pooling layers. However, the practice of simply adding the number of layers can result in the loss of lesion features during convolution, which prevents the accurate identification of patients with MCI. We conceive a neural network structure that can effectively solve this problem, using the same topology for group convolution.

It is generally believed that the study of human vision is the origin of attention mechanism. The brain's information processing capacity is limited, so when facing too much information, humans will selectively give attention to some of it. The rest of the information is ignored. Woo et al. [9] conceived the convolutional block attention module for generating channel and spatial attention feature maps to increase the expressiveness of CNNs. Han et al.'s [10] attention model can extract the features of different regions according to the attributes, so the model is capable to effectively discriminate the content in images, which is considered as an attribute-aware model. Suk and Shen [11] used a variety of SVM to complete the classification. Based on these complex SVM, they built a network prediction model with an automatic encoder to predict advertisements. The attention mechanism has a perfect result in medical image analysis, so we propose adding a hybrid attention model to our neural network to achieve the prediction network focus on more image areas, reduce the attention paid by the network to image redundant information, and enhance network capabilities of learning informative features.

Mikolov et al. [12] proposed the softmax function. For a multiclassification problem, assuming the category label $y \in \{1, 2, \dots, C\}$ and given a sample x , the softmax function returns the conditional probability that x is belonging to category c . The softmax function, which uses the cross-entropy loss function to learn the optimal parameter matrix, which may result in overfitting in cases with small samples. Therefore, a regularization operation is required to constrain its parameters to prevent overfitting. Robert [13] and Krogh and Hertz [14] stated L_1 and L_2 regularization, respectively, to limit the growth of weights, reduce the complexity of networks, and thus effectively alleviate the overfitting problem through the L_1 and L_2 paradigms. The dropout operation trains different networks by randomly dropping connections

between neurons in each training epoch, eventually fusing all models to predict the output. However, the current mainstream regularization operations constrain the weights of neural networks and do not regularize the output distribution. For PET image classification, the interclass distances between NC patients, patients with MCI, and AD patients are small, and the intraclass distances are not large. The use of mainstream regularization operations has limited the achievable in classification accuracy improvement. We conceive that a joint loss function is added to a regularization loss function to the traditional cross-entropy function, in order to prevent overfitting phenomenon, increase the generalization of the model, and have an improvement on its prediction accuracy.

3. Material

3.1. Dataset. Data used in preparation of this paper were obtained from the Alzheimer’s Disease Neuroimaging Initiative (ADNI) database (<http://adni.loni.usc.edu>). The ADNI was launched in 2003 as a public-private partnership, led by the Principal Investigator, Michael W. Weiner, M.D.. The primary goal of ADNI has been to test whether serial magnetic resonance imaging (MRI), positron emission tomography (PET), other biological markers, and clinical and neuropsychological assessment can be combined to measure the progression of mild cognitive impairment (MCI) and early Alzheimer’s disease (AD). As such, the investigators within the ADNI contributed to the design and implementation of ADNI but did not participate in analysis or writing of this paper.

ADNI-1 and ADNI-2 are two different research phases in the ADNI database. We use 190 AD cases, 350 MCI cases, and 200 NC cases among PET images as the training data from ADNI-1. Four hundred PET images are selected as the test data from ADNI-2. The detailed distributions of the dataset samples are displayed in Table 1.

3.2. Data Preprocessing. The PET image data downloaded from the ADNI database are in 3D format. Although the current 3D neural networks have achieved good results in terms of extracting neural image features [15], far more parameters are needed to build a 3D neural network than a 2D network, so more data are required for training to prevent accuracy degradation caused by overfitting. Unlike when addressing natural image datasets, it is still a challenge to collect sufficient medical neuroimaging data, and shape and size differences are present among the different individuals in PET images, so it is difficult to build a high-precision 3D prediction network.

To reduce the data volume of PET images and save computing costs, this paper decomposes the 3D brain PET images into 2D slices for model training. This operation requires a series of preprocessing steps to be conducted on the PET images. The specific process is as follows. First, the 3D PET image data are normalized to an International Brain Mapping Consortium template by the SPM tool [16]. Then, we performed special processing on the images, including averaging, alignment, and interpolation to achieve

TABLE 1: Detailed distributions of samples.

Datasets	Label	Case (n, M/F)	Age (year, mean \pm SD)
Train	AD	100/90	75.3 \pm 7.5
	MCI	150/100	74.9 \pm 7.6
	NC	100/100	75.8 \pm 5.0
Test	AD	70/54	74.2 \pm 8.0
	MCI	100/92	71.7 \pm 7.6
	NC	50/34	74.8 \pm 6.8

standard voxels, and their intensities are normalized; the other parameters are set to their default values to obtain images of size $79 \times 95 \times 79$. Finally, each 3D PET image is sliced and tiled into a 2D image sequence using the Python image data preprocessing library. The final image size is 95×79 . To filter out regions that are not related to classification, such as skulls, the first 10 and last 10 slices images are discarded, and the remaining images slices are used as the dataset in this paper.

4. Methods

This chapter elaborates the structures of the network model we conceived and its advantages, including the group convolution module, hybrid attention mechanism, and joint loss function. Figure 1 presents the AD prediction network structure used in the paper. This network is an improved version of ResNet18. First, the single branch convolution is adjusted to a group convolution of 32 branches, and each convolution branch performs three convolutions. There are two convolution kernels of 1×1 size and one convolution kernel of 3×3 size. Group convolution increases the width of the network and improves the expressiveness of the model. Then, the feature maps obtained by group convolution are summed up and sequentially went through the channel attention module and spatial attention module, so that the network adaptively learns the importance levels of different features, achieves an enhanced ability to learn informative features from PET images, and suppresses the redundant features. Finally, when all the convolution operations are completed, the obtained feature maps are input in the global average pooling layer, in order to enhance the relationships between features and categories. While preventing model overfitting, it can also improve the robustness and generalization performance of the model because no parameters are required in this layer.

4.1. Group Convolution. The current mainstream view is that, adding the depth and width of the network can effectively help us getting a good performance of a CNN. As a classic network, the Visual Geometry Group (VGG) network utilizes stacking blocks to add the depth of the network model, and the deep CNN models proposed afterwards use this strategy as well [17]. However, as the network size increases, the parameters of the network also increase dramatically, which inevitably leads to overfitting when the

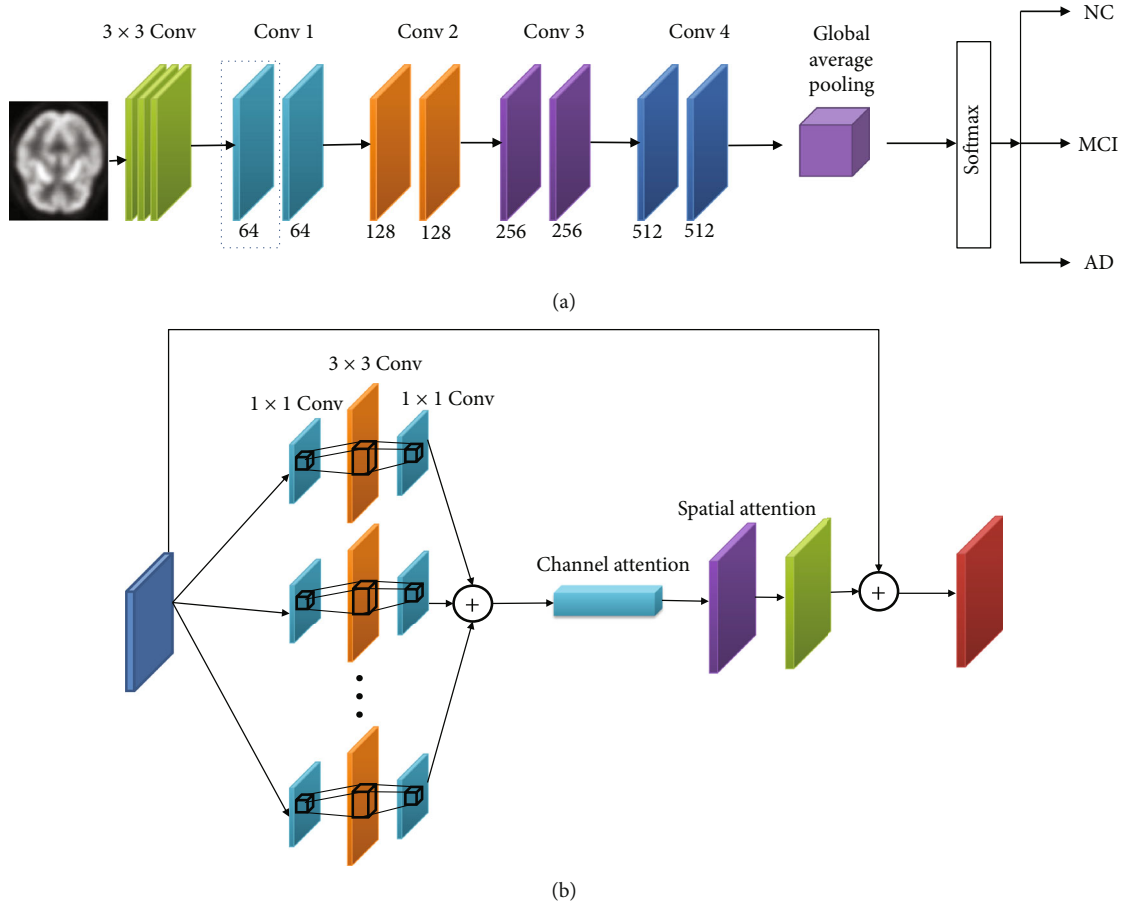


FIGURE 1: (a) is the AD prediction network structure used in this paper; and (b) is the detailed structure of Conv 1.

training data are insufficient, and the large number of parameters leads to a reduced training speed. Therefore, it is difficult to apply the above method to practical engineering problems. Szegedy et al. [18] designed the Inception structure, which extracts features simultaneously and decomposes the sparse matrices into dense matrices, in using various convolution kernels with unequal sizes. Richer features lead to higher accuracy in the final classification results, and areas with more 0 values can no longer be computed, thus greatly reducing the number of required calculations and speeding up the convergence process. Figure 2 shows a simple split-transform-merge structure. Given D -dimensional input data $x = [x_1, x_2, \dots, x_d]$ with input weights $w = [w_1, w_2, \dots, w_d]$, a linear activation neuron with no bias is $\sum_{i=1}^D w_i x_i$.

However, the different topologies of different branches in the Inception structure require a large number of hyper-parameters to be adjusted during the training process and the computational cost will increase significantly [19]. In this research, we conceive an improved Inception structure, group convolution, using the same topology in different branches, as shown in Figure 3. The given PET image is input into a group convolution with 32 branches, and each convolution branch performs three convolutions with one 3×3 convolution kernel and two 1×1 convolution kernel.

Then, the obtained feature maps are additively fused. The use of the same topology increases the network width, enhances the model's generalization, and makes the features learned by the model more diverse.

We combine the group convolution utilizing the same topology with the ResNet18 network to propose the G_ResNet18 network. For PET images, the features in lesion regions are often lost during the convolutional process of a deep convolutional network because of its large amount of redundant information, which makes discriminative lesion features' extraction more difficult. The G_ResNet18 network can extract lesion features from multiple channels to avoid the loss of image features during convolution and improve the accuracy of classification.

4.2. Hybrid Attention Mechanism. Taking Conv 1 as a sample, in Figure 4 the feature map $X \in R^{112 \times 112 \times 64}$ obtained by group convolution is used as input. First, both global max pooling (GMP) and global average pooling (GAP) are performed on the input by channel, and the two generated one-dimensional vectors are input in the fully connected layer operation to generate a one-dimensional channel attention $M_C \in R^{112 \times 1 \times 1}$. Then, multiply the feature map X with the channel attention to obtain the channel attention feature map X' . Next, GMP and GAP are performed

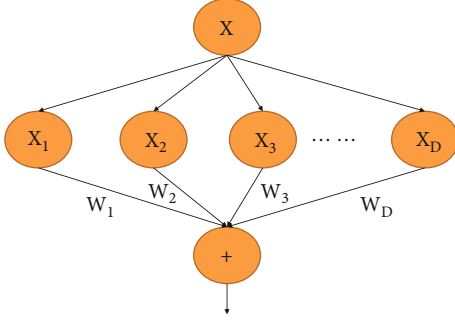


FIGURE 2: Schematic diagram of the split-transform-merge structure.

according to the space, and the two two-dimensional vectors generated after pooling are subjected to convolution to obtain a two-dimensional spatial attention $M_S \in R^{1 \times 112 \times 64}$. Finally, the spatial attention multiplied X' , and we can get the attention feature map.

The channel attention mechanism adds attention modules in different channels of the convolutional network. Through self-learning, two fully connected layers are used to acquire the loss of every channel in the feature map. Subsequently, the feature map weights that favour the decreasing loss function according to this loss are made larger. Finally, the feature map is weighted and fused with the original one, in order that the neural network can give more attention on the important feature channels [20]. Figure 5 presents the channel attention module. Firstly, for the feature maps $X \in R^{112 \times 112 \times 64}$, we separately perform a GMP and a GAP on them to acquire two $1 \times 1 \times 64$ feature maps. Then, the obtained feature maps are input into a multilayer perceptron (MLP) consisting of two fully connected layers. After that, the feature maps obtained in the MLP are summed and went through the sigmoid function, so as to obtain weight coefficients between 0 and 1. Finally, the weight coefficients are multiplied by the feature map X , and we can acquire the channel attention feature map. The formula for the channel attention mechanism is shown below:

$$\begin{aligned} M_c(X) &= \delta(\text{MLP}(\text{AvgPool}(X)) + \text{MLP}(\text{MaxPool}(X))) \\ &= \delta(\omega_1(\omega_0(X_{\text{avg}})) + \omega_1(\omega_0(X_{\text{max}}))), \end{aligned} \quad (1)$$

where MLP is a multilayer perceptron, AvgPool denotes GAP, MaxPool represents the GMP, X is the feature map, and δ is the sigmoid function.

Spatial attention mechanism adds attention modules in the spatial domain of the convolutional network, assigns corresponding importance levels to different positions of the feature map, enhances important regions, and suppresses unimportant regions [21]. Figure 6 reveals the spatial attention module. First, each feature map in $X \in R^{112 \times 112 \times 64}$ is subjected to GMP and also GAP, and then the multichannel features are compressed into a single channel through a 7×7 convolution kernel to eliminate the influence of the information distribution between channels. After that, the spatial weight is normalized through a sigmoid function.

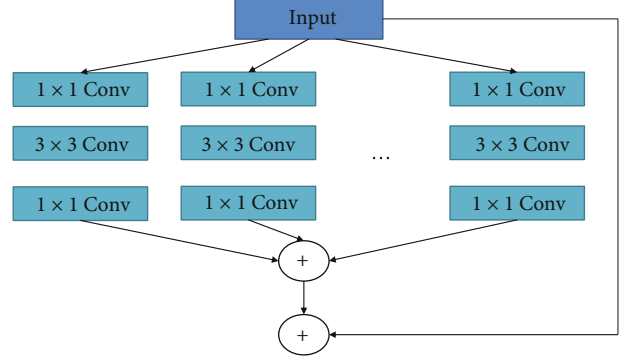


FIGURE 3: Group convolution with the same topology.

Finally, the feature map X multiply with the weights, so that we can acquire the spatial attention feature map. The formula for the spatial attention mechanism is shown below:

$$M_s(X) = \delta(f^{7 \times 7}[\text{AvgPool}(X); \text{MaxPool}(X)]), \quad (2)$$

where AvgPool is the GAP and MLP is the multilayer perceptron, MaxPool is the GMP, X is the feature map, and δ is the sigmoid function.

In clinical practice, different individuals have different absorption capacities with respect to the imaging agents, which makes their PET images have certain differences. At the same time, the features of PET images are not obvious, which makes it difficult for a general convolutional network to extract valid features. Therefore, many researchers have chosen to embed modules that have fewer parameters and focus on disease lesion regions into their algorithms when performing disease prediction tasks. To enhance the valid features of PET images and suppress redundant and invalid information, we use a hybrid attention mechanism. The features of the lesion region of PET images are fully extracted using two different attention modules, which strengthen the deep semantic nature of the features, enable the network to adaptively reduce the attention paid to redundant information, and further improve the network's learning ability of informative features.

4.3. Joint Loss Function. Cross-entropy loss function is considered to be the most common loss function in the task of image classification, which utilizes the softmax function to obtain the confidence of each category, and then calculates the cross-entropy loss. We defined here the cross-entropy loss function as following:

$$L_{\text{cross-entropy}} = -\frac{1}{N} \sum_{i=1}^N \sum_{j=1}^3 [y_i \ln p_{i,k}], \quad (3)$$

where N is the samples' total number; y_i denotes the labels, which correspond to AD patients, patients with MCI, and NC patients in this paper; and $p_{i,k}$ is the softmax function's output, which indicates the probability that the i th sample is one of the k th category.

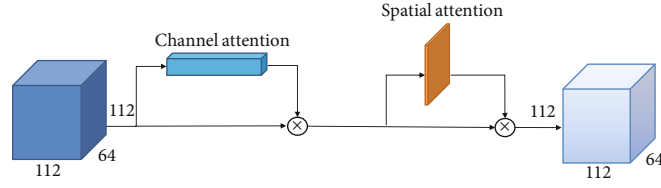


FIGURE 4: Schematic diagram of the hybrid attention mechanism.

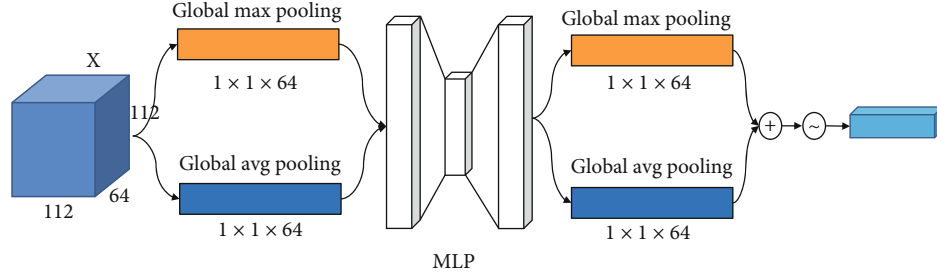


FIGURE 5: Schematic diagram of the channel attention mechanism.

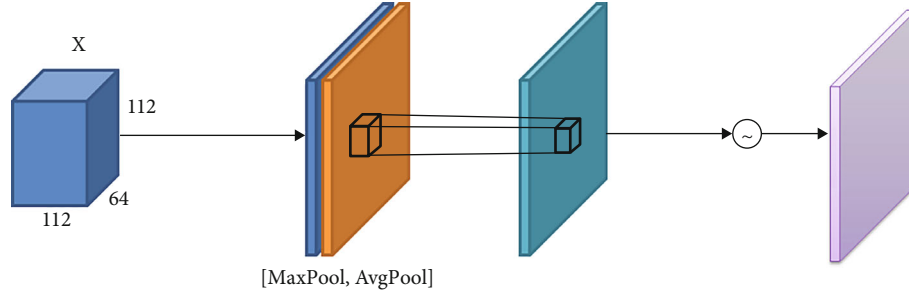


FIGURE 6: Schematic diagram of the spatial attention mechanism.

We defined the regularization loss function as following:

$$L_{\text{reg}} = \frac{1}{2} \sum_{i=1}^N \|f_i - C_{y_i}\|^2, \quad (4)$$

where f_i is the i th sample's feature vector. The center of the feature class of y_i is C_{y_i} , which is updated during each epoch by Equation (5), where α is the learning rate and φ is the delta function.

$$C_j = C_j - \alpha \Delta C_j = C_j - \alpha \frac{\partial L_{\text{reg}}}{\partial C_j} = C_j - \alpha \frac{\sum_{i=1}^N \varphi(y_i == j) (C_j - f_i)}{1 + \sum_{i=1}^N \varphi(y_i == j)}. \quad (5)$$

Thus, the joint loss function L proposed in this paper is defined as

$$L = L_{\text{cross-entropy}} + \beta L_{\text{reg}}, \quad (6)$$

where β is a hyperparameter that regulates the balance between the interclass and intraclass losses. When $\beta = 0$, it is said that the joint loss function degenerates into the cross-entropy loss function. In this paper, β is set to 0.01,

and the argumentation process is described in Section 5.4 (Parameter Experiments).

5. Experimental Results and Analysis

5.1. Experimental Setup. In this paper, experiments are performed in Windows 10, and the algorithm is implemented based on the Python 3.9 and the PyTorch-GPU. The main hardware configurations are introduced in Table 2, and all experimental parameters involved are shown in the next table (Table 3).

5.2. Evaluation Indicators. Sensitivity (SEN) is considered to be the probability of correctly diagnosing patients with AD or MCI, and specificity (SPE) refers to the probability of NC patients being correctly diagnosed. We use the following equations to compute the accuracy, sensitivity, and specificity:

$$\text{Accuracy} = \frac{\text{TP} + \text{TN}}{\text{TP} + \text{TN} + \text{FP} + \text{FN}}, \quad (7)$$

$$\text{Sensitivity} = \frac{\text{TP}}{\text{TP} + \text{FN}}, \quad (8)$$

$$\text{Specificity} = \frac{\text{TN}}{\text{TN} + \text{FP}}, \quad (9)$$

where TP means the true positives’ number, indicating AD and MCI samples’ number that are predicted correctly; FN represents false negatives, which means AD and MCI samples’ number are incorrectly predicted as NC; FP signs false positives, indicating the NC samples’ number that are wrongly predicted as AD or MCI samples; and TN refers to true negatives, indicating the NC samples’ number that are classified correctly.

In practice, the receiver operating characteristic (ROC) curve are often used to compare the predictive performance of various models. The false-positive rate (FPR) is placed on the horizontal coordinate, and the true-positive rates (TPRs) are placed on the vertical coordinates. The formulas of the FPR and TPR are presented as following:

$$\text{TPR} = \frac{\text{TP}}{\text{TP} + \text{FN}}, \quad (10)$$

$$\text{FPR} = \frac{\text{FP}}{\text{TN} + \text{FP}}. \quad (11)$$

One of the better performances of model B than model A is that the ROC curve of B can completely “wrap” the curve of A. Meanwhile, if that two curves cross, it is difficult to generally conclude which is better. In this case, their areas under the ROC curves (AUCs) should be compared [22]. We make the following assumption that the coordinate connection points together from the ROC curve: $\{(x_1, y_1), (x_2, y_2), \dots, (x_m, y_m)\} (x_1 = 0, x_m = 1)$. The AUC formula is as follows:

$$\text{AUC} = \frac{1}{2} \sum_{i=1}^{m-1} (x_{i+1} - x_i) \cdot (y_i + y_{i+1}). \quad (12)$$

5.3. Model Visualization. To investigate the feature learning process of the proposed AD prediction model, we design a model visualization experiment. The heat map produced during the model training process is shown in Figure 7; that is, the features obtained from the convolution layer through the deconv operation are presented [23]. As seen in Figure 7(a), the model gradually strengthens its focus on the frontal cortex, internal olfactory cortex, hippocampus, and occipital region of each AD sample during the training process. These areas are lesions found in clinical research [24]. As shown in Figure 7(b), the model pays more attention to the superior parietal lobe, middle frontal gyrus and postcentral gyrus of the MCI samples than those of the AD samples. This is in line with clinical studies on MCI [25], indicating that the model we conceived has the capacity of identifying the lesion regions of patients with MCI. As seen in Figure 7(c), the model is more sensitive to the occipital and temporal lobes of the NC samples. Therefore, the regions of interest of the proposed model are consistent with the findings in clinical research and are interpretable.

TABLE 2: Hardware configuration.

Name	Configuration
CPU	Intel i7-12700K@3.6 GHz
GPU	NVIDIA GeForce RTX 3060 12GB
RAM	64GB
Hard drive	1 TB

TABLE 3: Parameter settings.

Parameter	Value
Batch size	32
Number of epochs	100
K_fold	10
Learning rate	0.001
Optimizer	SGD

5.4. Parameter Experiments. To evaluate the contribution of the parameter β , we design a parametric experiments in which the other conditions are the same and only parameter β is different. Table 4 below introduces the experimental results.

As seen in Table 4, when $\beta = 0$, the joint loss function degenerates into a cross-entropy loss function, and compared to the best results the prediction accuracy and AUC decrease by 2.1% and 2.3%, respectively. When $\beta < 0.01$, the prediction accuracy and AUC increase with increasing β . When $\beta > 0.01$, the prediction accuracy and AUC decrease with increasing β . At present, it is still difficult to collect enough PET images. When the amount of data is small, the joint loss function regularizes the output distribution, thereby preventing overfitting, increasing the generalization of the model, and improving its prediction accuracy.

5.5. Ablation Experiments. To evaluate the contributions of the group convolution and hybrid attention mechanism, we design several control groups for ablation experiments. Table 5 gives the experimental results, and Figure 8 presents the ROC curves. The control groups are set up as follows.

- (1) ResNet18 is a CNN model with ResNet18 as the backbone network
- (2) G_ResNet18 is a CNN model with G_ResNet18 as the backbone network
- (3) G_ResNet18+CAM is a CNN model that adds a channel attention mechanism to G_ResNet18
- (4) G_ResNet18+SAM is a CNN model that adds a spatial attention mechanism to G_ResNet18
- (5) G_ResNet18+HAM is a CNN model that adds a hybrid attention mechanism to G_ResNet18

As seen in Table 5 and Figure 8, compared with those of ResNet18, the classification accuracy of G_ResNet18 using group convolution improves by 13.5%, and the AUC improves by 9.4%. This demonstrates the effectiveness of

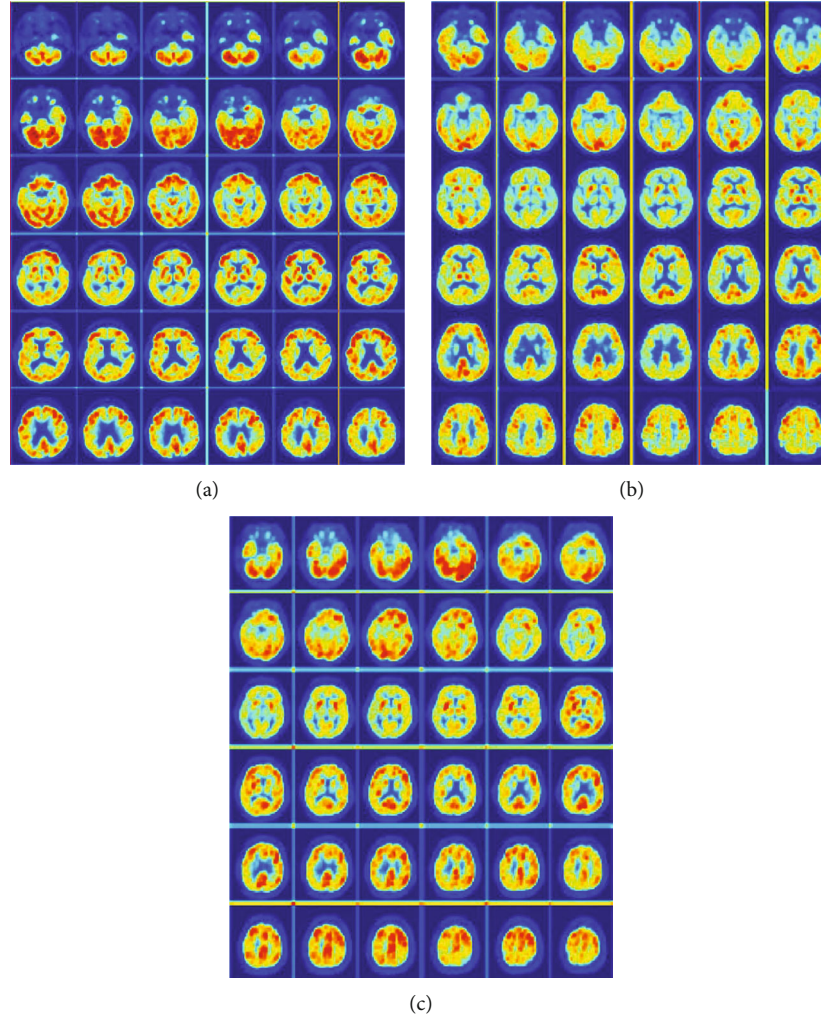


FIGURE 7: Regions of interest yielded by the proposed model: (a) AD samples, (b) MCI samples, and (c) NC samples.

TABLE 4: Parameter experiment.

Parameter value	ACC (%)	AUC (%)
0	87.5	90.2
0.005	88.9	91.8
0.01	89.4	92.3
0.015	88.6	91.7
0.02	87.9	91.4

TABLE 5: Ablation experiment.

Method	ACC (%)	AUC (%)
ResNet18	75.3	80.1
G_ResNet18	85.5	87.6
G_ResNet18+CAM	87.1	88.9
G_ResNet18+SAM	87.5	90.2
G_ResNet18+HAM	89.4	92.3

the group convolutional network for the three classification tasks. G_ResNet18 uses group convolution to prevent the loss of image features during convolution and to raise the diversity of the observed features. Compared with Resnet18, G_ResNet18 can extract more features that are distinguishable and potential lesion information, so it can learn more detailed features from PET images and achieve improved classification accuracy.

As seen in Table 5 and Figure 9, both the addition of the channel attention mechanism and spatial attention mechanism in G_ResNet18 increases the classification accuracy by 1.8% and 2.3%, respectively, and the AUC improves by 1.4% and 2.9%, respectively. The addition of the hybrid attention mechanism in G_ResNet18 improves the classification accuracy by 4.5% and the AUC by 5.3%. The attempt to use the channel attention module and the spatial attention module alone proves that this is not an improvement, but the addition of the hybrid attention mechanism has a greatly improvements on the network's classification results. It is shown that the use of two different attention mechanisms can fully extract the features of lesion regions in PET images, strengthen the deep semantics of these features, enable the

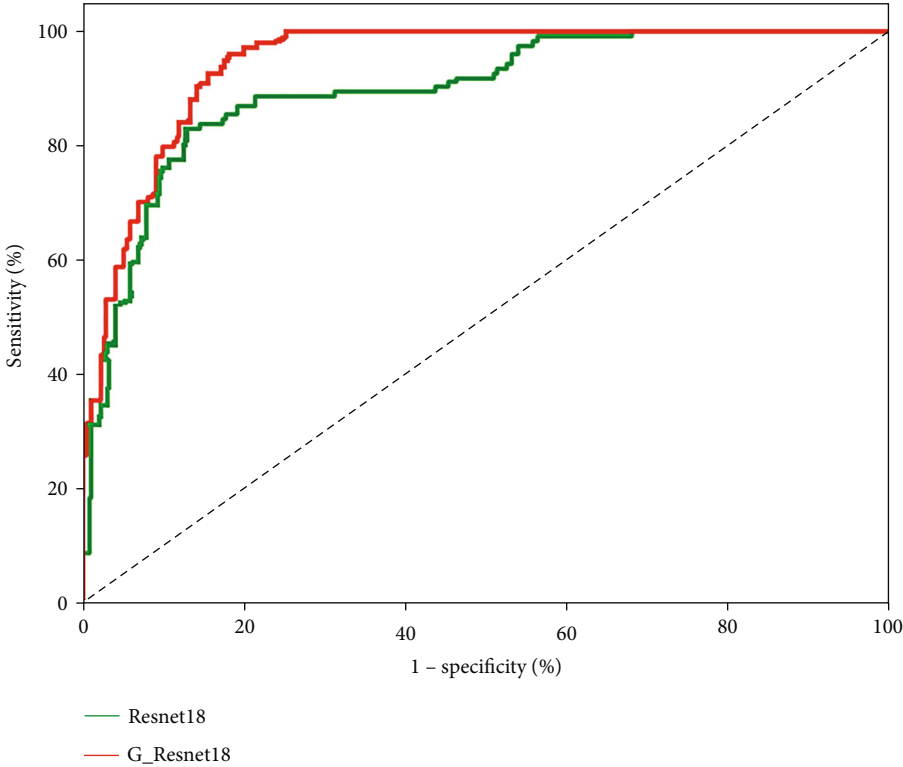


FIGURE 8: ROC curves produced in the group convolution ablation experiments.

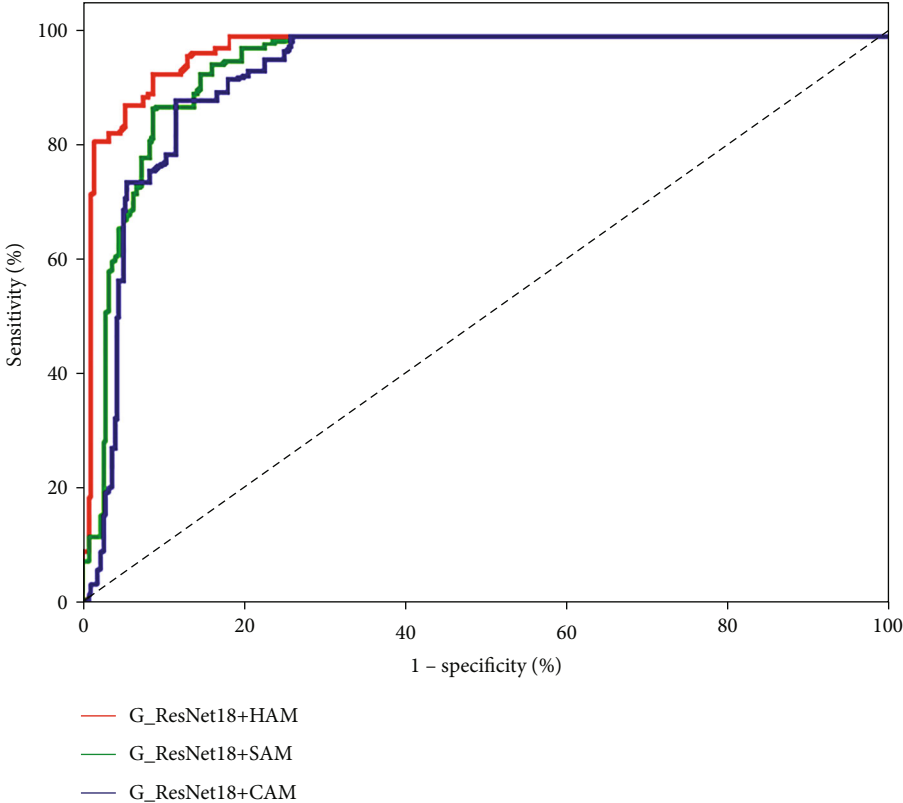


FIGURE 9: ROC curves produced in the hybrid attention mechanism ablation experiments.

TABLE 6: Comparison of the proposed method’s results and those of others.

Study	Subjects			Modality	Data			Classification result (%)			
	AD	MCI	NC		Type	Base	SEN	SPE	ACC	AUC	
Liu et al., 2017 [28]	121	126	120	2D	PET	ADNI	76.19	70.37	73.82	73.64	
Ding et al., 2018 [8]	36	79	73	2D	PET	ADNI	64.67	79	63.67	76.0	
Solano-Rojas and Villalón-Fonseca 2021 [29]	95	160	126	2D	PET	ADNI	87.3	83.5	86	—	
Sajjad et al., 2021 [26]	30	64	42	2D	PET	ADNI	73	72	72	—	
Lu et al., 2020 [27]	238	217	360	2D	PET	ADNI	79.69	83.84	82.93	—	
The proposed method	124	192	84	2D	PET	ADNI	87.43	88.26	89.4	92.3	

network to adaptively reduce the attention paid to redundant information, enhance the network’s capacity to learn informative features, and improve the prediction accuracy.

5.6. Comparative Experiment. This section compares it with current AD prediction algorithms, and the datasets are all derived from the ADNI database in order to verify whether the algorithm is really effective. The results of the comparative experiments are given in Table 6.

As shown in Table 6, compared with the AD prediction algorithms based on the Inception v3 structure proposed by Ding et al. [8], Sajjad et al. [26], and Lu et al. [27], the algorithm conceived improves the classification accuracy by up to 24%. This shows that the group convolution utilizing the same topology can improve the algorithmic performance, reduce the global information loss, enrich the lesion information extracted by the network, and avoid the errors caused by the singularity of feature extraction. Compared with the AD prediction algorithms based on DensNet proposed by Liu et al. [28] and Solano-Rojas and Villalón-Fonseca [29], the algorithm proposed improves the classification accuracy by up to 21%. This indicates that the hybrid attention mechanism can capture the correlations between features, suppress redundant features, enhance the correlations between features and lesion regions, and perform adaptive feature extraction for regions with more information in PET images, thus further enhancing the recognition capability of the model.

In summary, the algorithm proposed has an effectively improvement in prediction accuracy of patients with MCI.

6. Conclusion

It is difficult to accurately predict patients with MCI due to the difficulty of lesion feature extraction and the large amount of redundant information contained in PET images. To address the above problems, an AD prediction algorithm based on group convolution and a joint loss function is proposed. First, a group convolutional backbone network based on ResNet18 is designed to extract lesion features from multiple channels for enhancing the network’s expression ability. Then, a hybrid attention mechanism is displayed to fully extract the features of the lesion regions in PET images in order that the network can adaptively give attention to the target regions of learning the feature weights and have enhancement on the network’s ability to learn the lesion regions that are relevant to disease diagnosis. Finally, a joint

loss function, which puts a regularization loss function into the traditional cross-entropy loss function to prevent overfitting and increase the generalization of the model, is proposed. The research results show that the classification accuracy of the conceived algorithm has a better performance than that of the current mainstream algorithm, which is beneficial to the screening of patients with MCI and thus can achieve AD prediction.

Data Availability

In this research, the data we used are from ADNI public database, which can be openly downloaded on the website.

Conflicts of Interest

The authors declare that there is no conflict of interest in the publication of this paper.

Acknowledgments

This work was supported in part by the National Natural Science Foundation of China under grant number 61372137, in part by the National Science Foundation of Anhui Province under grant number 1908085MF209. Hua-bin Wang is the corresponding author. E-mail address: wanghuabin@ahu.edu.cn. Data collection and sharing for this project was funded by the Alzheimer’s Disease Neuroimaging Initiative (ADNI) (National Institutes of Health grant number U01 AG024904) and DOD ADNI (Department of Defense award number W81XWH-12-2-0012). ADNI is funded by the National Institute on Aging, the National Institute of Biomedical Imaging and Bioengineering, and through generous contributions from the following: AbbVie, Alzheimer’s Association; Alzheimer’s Drug Discovery Foundation; Araclon Biotech; BioClinica, Inc; Biogen; Bristol-Myers Squibb Company; CereSpir, Inc; Cogstate; Eisai Inc; Elan Pharmaceuticals, Inc; Eli Lilly and Company; EuroImmun; F. Hoffmann-La Roche Ltd and its affiliated company Genentech, Inc; Fujirebio; GE Healthcare; IXICO Ltd; Janssen Alzheimer Immunotherapy Research & Development, LLC; Johnson & Johnson Pharmaceutical Research & Development LLC; Lumosity; Lundbeck; Merck & Co., Inc; Meso Scale Diagnostics, LLC; NeuroRx Research; Neurotrack Technologies; Novartis Pharmaceuticals Corporation; Pfizer Inc; Piramal Imaging; Servier; Takeda Pharmaceutical Company; and Transition Therapeutics. The Canadian Institutes

of Health Research is providing funds to support ADNI clinical sites in Canada. Private sector contributions are facilitated by the Foundation for the National Institutes of Health (<http://www.fnih.org>). The grantee organization is the Northern California Institute for Research and Education, and the study is coordinated by the Alzheimer's Therapeutic Research Institute at the University of Southern California. ADNI data are disseminated by the Laboratory for Neuro Imaging at the University of Southern California.

References

- [1] S. Todd, S. Barr, M. Roberts, and A. P. Passmore, "Survival in dementia and predictors of mortality: a review," *International Journal of Geriatric Psychiatry*, vol. 28, no. 11, pp. 1109–1124, 2013.
- [2] A. S. Lundervold and A. Lundervold, "An overview of deep learning in medical imaging focusing on MRI," *Zeitschrift für Medizinische Physik*, vol. 29, no. 2, pp. 102–127, 2019.
- [3] A. H. Syaifullah, A. Shiino, H. Kitahara, R. Ito, M. Ishida, and K. Tanigaki, "Machine learning for diagnosis of AD and prediction of MCI progression from brain MRI using brain anatomical analysis using diffeomorphic deformation," *Frontiers in Neurology*, vol. 11, pp. 1894–1906, 2021.
- [4] X. Pan, T. L. Phan, M. Adel et al., "Multi-view separable pyramid network for AD prediction at MCI stage by 18F-FDG brain PET imaging," *IEEE Transactions on Medical Imaging*, vol. 40, no. 1, pp. 81–92, 2021.
- [5] E. Yee, K. Popuri, M. F. Beg, and the Alzheimer's Disease Neuroimaging Initiative, "Quantifying brain metabolism from FDG-PET images into a probability of Alzheimer's dementia score," *Human Brain Mapping*, vol. 41, no. 1, pp. 5–16, 2020.
- [6] Z. Yang and Z. Liu, "The risk prediction of Alzheimer's disease based on the deep learning model of brain 18F-FDG positron emission tomography," *Saudi Journal of Biological Sciences*, vol. 27, no. 2, pp. 659–665, 2020.
- [7] T. Jo, K. Nho, and A. J. Saykin, "Deep learning in Alzheimer's disease: diagnostic classification and prognostic prediction using neuroimaging data," *Frontiers in Aging Neuroscience*, vol. 11, p. 220, 2019.
- [8] Y. Ding, J. H. Sohn, M. G. Kawczynski et al., "A deep learning model to predict a diagnosis of Alzheimer disease by using 18F-FDG PET of the brain," *Radiology*, vol. 290, no. 2, pp. 456–464, 2019.
- [9] S. Woo, J. Park, J. Y. Lee, and I. S. Kweon, "CBAM: convolutional block attention module," *Proceedings of the European conference on computer vision (ECCV)*, pp. 3–19, 2018.
- [10] K. Han, J. Guo, C. Zhang, and M. Zhu, "Attribute-aware attention model for fine-grained representation learning," in *Proceedings of the 26th ACM International Conference on Multimedia (MM '18)*, pp. 2040–2048, New York, NY, USA, 2018.
- [11] H. I. Suk and D. Shen, "Deep learning in diagnosis of brain disorders," *Recent Progress in Brain and Cognitive Engineering*, vol. 5, pp. 203–213, 2015.
- [12] T. Mikolov, S. Kombrink, L. Burget, J. Černocký, and S. Khudanpur, "Extensions of recurrent neural network language model [C]," *IEEE International Conference on Acoustics Speech and Signal Processing (ICASSP)*, pp. 5528–5531, 2011.
- [13] T. Robert, "Regression shrinkage and selection via the lasso: a retrospective," *Journal of the Royal Statistical Society*, vol. 73, no. 3, pp. 273–282, 2011.
- [14] A. Krogh and J. A. Hertz, "A simple weight decay can improve generalization [C]. Neural information processing systems," *Morgan Kaufmann Publishers Inc*, vol. 4, pp. 950–957, 1992.
- [15] M. Tanveer, A. H. Rashid, M. A. Ganaie, M. Reza, I. Razzak, and K. L. Hua, "Classification of Alzheimer's disease using ensemble of deep neural networks trained through transfer learning," *IEEE Journal of Biomedical and Health Informatics*, vol. 26, no. 4, pp. 1453–1463, 2022.
- [16] W. D. Penny, K. J. Friston, J. T. Ashburner, S. J. Kiebel, and T. E. Nichols, "Statistical parametric mapping: the analysis of functional brain images [J]," *Neurosurgery*, vol. 61, no. 1, pp. 194–222, 2007.
- [17] K. Simonyan and A. Zisserman, "Very deep convolutional networks for large-scale image recognition [C]," *International Conference on Learning Representations (ICLR)*, pp. 1–14, 2015.
- [18] C. Szegedy, W. Liu, Y. Jia et al., "Going deeper with convolutions [C]," *Proceedings of the IEEE Conference on Computer Vision and Pattern Recognition*, pp. 1–9, 2015.
- [19] S. Xie, R. Girshick, P. Dollár, Z. Tu, and K. He, "Aggregated residual transformations for deep neural networks [C]," *Proceedings of the IEEE Conference on Computer Vision and Pattern Recognition*, pp. 5987–5995, 2017.
- [20] J. Hu, L. Shen, and G. Sun, "Squeeze-and-excitation networks," *IEEE Transactions on Pattern Analysis and Machine Intelligence*, vol. 42, no. 8, pp. 2011–2023, 2020.
- [21] X. Zhu, D. Cheng, Z. Zhang, S. Lin, and J. Dai, "An empirical study of spatial attention mechanisms in deep networks," in *Proceedings of the IEEE/CVF International Conference on Computer Vision*, pp. 6687–6696, Seoul, South Korea, 2019.
- [22] T. Fawcett, "An introduction to ROC analysis," *Pattern Recognition Letters*, vol. 27, no. 8, pp. 861–874, 2006.
- [23] M. D. Zeiler and R. Fergus, "Visualizing and understanding convolutional networks," *European conference on computer vision*, pp. 818–833, 2014.
- [24] X. Pan, M. Adel, C. Fossati, T. Gaidon, and E. Guedj, "Multi-level feature representation of FDG-PET brain images for diagnosing Alzheimer's disease," *IEEE Journal of Biomedical and Health Informatics*, vol. 23, no. 4, pp. 1499–1506, 2019.
- [25] H. I. Suk, S. W. Lee, and D. Shen, "Latent feature representation with stacked auto-encoder for AD/MCI diagnosis," *Brain Structure and Function*, vol. 220, no. 2, pp. 841–859, 2015.
- [26] M. Sajjad, F. Ramzan, M. U. G. Khan et al., "Deep convolutional generative adversarial network for Alzheimer's disease classification using positron emission tomography (PET) and synthetic data augmentation," *Microscopy Research and Technique*, vol. 84, no. 12, pp. 3023–3034, 2021.
- [27] D. Lu, K. Popuri, G. W. Ding, R. Balachandar, and M. F. Beg, "Multimodal and multiscale deep neural networks for the early diagnosis of Alzheimer's disease using structural MR and FDG-PET images," *Scientific Reports*, vol. 8, no. 1, p. 5697, 2018.
- [28] K. Liu, K. Chen, L. Yao, and X. Guo, "Prediction of mild cognitive impairment conversion using a combination of independent component analysis and the cox model," *Frontiers in Human Neuroscience*, vol. 11, p. 33, 2017.
- [29] B. Solano-Rojas and R. Villalón-Fonseca, "A low-cost three-dimensional DenseNet neural network for Alzheimer's disease early discovery," *Sensors*, vol. 21, no. 4, p. 1302, 2021.

Research Article

Influence of “Hospital-Community-Family” Integrated Management on Blood Pressure, Quality of Life, Anxiety and Depression in Hypertensive Patients

Wanzhe Shi, Lei Cheng, and Yang Li 

Department of Cardiovascular Medicine, First Affiliated Hospital of Baotou Medical College, Baotou, Inner Mongolia 014010, China

Correspondence should be addressed to Yang Li; 631406010203@mails.cqjtu.edu.cn

Received 5 August 2022; Revised 15 September 2022; Accepted 19 September 2022; Published 4 October 2022

Academic Editor: Pan Zheng

Copyright © 2022 Wanzhe Shi et al. This is an open access article distributed under the Creative Commons Attribution License, which permits unrestricted use, distribution, and reproduction in any medium, provided the original work is properly cited.

Objective. To explore the Influence of “hospital-community-family” integrated management on blood pressure, quality of life, anxiety and depression in hypertensive patients. **Methods.** A total of 60 patients with hypertension were treated in our hospital from July 2019 to July 2021. The patients were randomly divided into control group (n=30) and study group (n=30). The former accepts routine management, while the latter accepts “hospital-community-family” integrated management. Nursing satisfaction, blood pressure, disease awareness rate, anxiety and depression scores, disease control ability and quality of life scores were compared. **Results.** First of all, we compared the nursing satisfaction: the study group was very satisfied in 25 cases, satisfactory in 4 cases, general in 1 case, the satisfaction rate was 100.00%, while in the control group, 10 cases were very satisfied, 8 cases were satisfied, 7 cases were general, and 5 cases were dissatisfied, the satisfaction rate was 83.33%; The nursing satisfaction of the study group was higher than that of the control group ($P < 0.05$). Secondly, we compared the level of blood pressure. There was no significant difference before management ($P > 0.05$) but the blood pressure decreased after treatment. In the control group, the level of blood pressure in the study group was lower than that in the control group ($P < 0.05$). In terms of disease awareness rate the scores of hypertension related knowledge hypertension harmfulness community management methods regular reexamination and blood pressure monitoring in the study group were significantly higher than those in the control group ($P < 0.05$). There was no significant difference in anxiety and depression scores before treatment ($P > 0.05$), but decreased after treatment. Compared with the control group, the anxiety and depression scores of the study group were lower ($P < 0.05$). In terms of disease control ability, the total scores of diet management, medication management, behavior management and information management in the study group were higher compared to the control group ($P < 0.05$). Finally, we compared the scores of qualities of life. Before management, there exhibited no significant difference ($P > 0.05$). After management, the scores of quality of life decreased. Compared to the control group, the scores of physiological function, psychological function, social function and health self-cognition in the study group were lower than those in control group ($P < 0.05$). **Conclusion.** The application of integrated “hospital, community and family” management can vertically integrate medical resources and establish a truly effective hierarchical treatment model. Integrated “hospital-community-family” management can improve patient compliance with treatment, enhance patients’ self-management ability and confidence, and improve the management efficiency of medical staff.

1. Introduction

Hypertension is a common and frequently occurring disease among Chinese residents [1]. The results of epidemiological investigation indicate that the number of people suffering from hypertension in the world is more than 1 billion, and it is expected that the number of cases will reach 1.55 billion

in 10 years’ time. According to the latest hypertension guidelines in China, the prevalence of hypertension among adult residents in China is 27.9%, that is, one-third of adults suffer from hypertension, and the prevalence of hypertension in large and medium-sized cities is relatively high [2]. Cardiovascular and cerebrovascular diseases are caused, and the resulting medical expenses are also increasing year by year

[3]. How to control blood pressure within the standard range to reduce complications, reduce medical costs, and improve quality of life has always been the focus of our research [4]. The data indicate that the control rate of blood pressure in adult patients with hypertension is only 16.8%. An effective model of hypertension management is needed to improve patient adherence, control blood pressure and reduce complications [5]. At present, the management of hypertension in community include health education, family intervention, community intervention, self-management and individual intervention. The above management model will make patients aware of the importance of regular medication and knowledge about hypertension, which will help to lower their blood pressure levels and thus improve their blood pressure control rate. However, due to differences in each patient's cultural and educational background, personality and family conditions, there is also variability in patient acceptance, making it difficult to effectively control the blood pressure levels of all patients [6]. Previous studies have indicated that the etiology of patients with hypertension is complex, there are significant differences in the severity of the disease, the pertinence of traditional education is not strong, not combined with behavioral intervention, so that routine management is of little significance to effectively enhance patient compliance [7]. Therefore, it is particularly important to promote the understanding of hypertension, explore scientific, effective and standardized management models, and control the development of hypertension.

At present, the existing hypertension management in China mainly includes continuous nursing, home follow-up nursing, path-based comprehensive nursing, and file management intervention mode [8]. The management mode is relatively simple, mainly in tertiary hospitals. Medical staff lack time and energy, and the continuous care provided is limited. Hospital and community management are out of touch, patients are not within the jurisdiction of hospitals or community health institutions after discharge, lack of continuous and comprehensive education and supervision, and the management compliance of patients with hypertension is far lower compared to other chronic diseases [9]. In 2009, the opinions of the CPC Central Committee and the State Council on deepening the Reform of the Medical and Health system pointed out that it is necessary to speed up the construction of a health service system based on community health services, guide general diagnosis and treatment at the grass-roots level, and gradually achieve community first treatment, two-way referrals, emergency and slow triage, and linkage between upper and lower levels. The 2015 outline of the national health service system (2015-2020) puts forward the concept of "serious illness in hospital, minor illness in the community, rehabilitation back to the community", emphasizing the need to expand the field of nursing to the family, community and society [10]. With the promotion of graded diagnosis and treatment system, under the background of high incidence of chronic diseases and heavy burden, more scholars have proposed to establish a hospital-community-family integrated management model. That is, a management system that brings chronic patients into the cooperation between the hospital and the community. Hos-

pitals, communities and families are based on their own functions and positioning, with patients as the center. Information sharing and two-way referrals between tertiary hospitals and communities provide a comprehensive prevention and treatment model with full and continuous management services for patients in different courses of disease. At present, this model is mainly employed in the management of diabetes, stroke and other chronic diseases, and has achieved remarkable results [11]. Therefore, there is an urgent need to learn from some research experience, to explore a more scientific and effective management model of hypertension, to extend the management services of patients with hypertension from tertiary hospitals to communities and families, in order to achieve homogeneous management effect.

2. Patients and Methods

2.1. General Information. Sixty patients with hypertension treated in our hospital from July 2019 to July 2021 were enrolled. The patients were randomly divided into control group and study group. The former accepts routine management, while the latter accepts "hospital-community-family" integrated management. The age of the control group was 34-87 years, with an average of (65.78 ± 3.12) years, including 13 males and 17 females, while the study group was 34-88 years old, with an average age of (65.64 ± 3.55) years, including 15 males and 15 females. The general data have no statistical significance. With the permission of the Medical Ethics Association of our hospital, all patients signed the informed consent form.

Inclusion criteria: 1) all patients met the diagnostic criteria of the 2018 version of Chinese guidelines for Prevention and treatment of Hypertension [12]. The latest guidelines: systolic blood pressure (SBP) ≥ 140 mmHg and/or diastolic blood pressure (DBP) ≥ 90 mm Hg; 2) voluntarily participated in this study; 2) the age of the patients was more than 18 years old.

Exclusion criteria: 1) complicated with mental disorders or senile dementia; 2) complicated with liver and kidney diseases, malignant tumors or; 3) complicated with pregnancy or lactation; 4) complicated with congenital cerebrovascular diseases; 5) secondary hypertension; 6) patients with hypertension who refused to participate in this study after communication with members of the research team.

2.2. Treatment Methods. The control group carried out routine management: hypertension system health education, diet guidance, drug guidance, self-test, etc., and said that they had accepted relevant knowledge points at discharge and paid attention to patients' diet. In daily life, we should ensure adequate sleep time, dress loosely and comfortably, keep warm, and increase a certain amount of aerobic exercise.

The research group implemented the "hospital-community-family" trinity integrated management: 1) centralized visit: promote the relevant data, determine the patient's condition, confirm their lifestyle and eating habits,

and establish personal health management files according to the patient's condition. Grasp the patient's condition, actively evaluate, explain the knowledge of hypertension-related diseases, and formulate a health management plan. The patients in the community were organized to teach centrally, imparted the knowledge related to hypertension, and made into a publicity manual, including the etiology and prognosis of hypertension, the role of antihypertensive drugs and matters needing attention, and the importance of taking medicine regularly. And instruct the patients how to use the sphygmomanometer, and tell them to measure the time and frequency correctly, and give demonstration education to the community staff, consult the relevant guidance measures to ensure that the patients can master the knowledge of hypertension. 2) telephone follow-up: a special telephone follow-up team was set up to regularly follow up the patients with hypertension in the community. The main purpose is to control the patients' blood pressure, their physical condition during the medication period, care about the patients' mental state, and guide the patients to develop good living habits. And praise the patients with good behavior in strict accordance with the doctor's advice, correct and understand the patients with poor medication, and help patients standardize the use of drugs; 3) door-to-door follow-up: door-to-door follow-up needs to accurately understand the situation of patients, check patients' physique and blood pressure, understand the changes of patients' blood pressure, encourage patients to ask questions, and build confidence for patients. Communicate with patients' families, assist patients with standardized medication, appropriate training, guide diet and rest, promote healthy diet, and ensure adequate sleep. At the same time, for patients with poor mood, timely psychological counseling, guide patients to actively face treatment, encourage patients to say the causes of bad mood, nurses actively carry out psychological counseling.

2.3. Observation Index

2.3.1. Satisfaction. After consulting the literature and expert discussion, we designed patients' follow-up satisfaction, a total of 10 items, and recorded patients' satisfaction with follow-up management mode, health education, medical and nursing service, appointment registration process [13]. It is assigned into four dimensions: very satisfied, satisfied, general and dissatisfied. Satisfaction rate = very satisfaction rate + satisfaction rate + general rate.

2.3.2. Blood Pressure Level. Blood pressure levels (diastolic blood pressure, systolic blood pressure) were measured with a sphygmomanometer before and 6 months after management.

2.3.3. Disease Awareness Rate. A general questionnaire was adopted to investigate the awareness rate of hypertension related knowledge in the two groups 6 months after management, including hypertension related knowledge, hypertension harmfulness, community management methods, regular reexamination and blood pressure monitoring, etc., with a total score of 100, >90 as knowing, 70-90 as general awareness, <70 as not knowing [14].

2.3.4. Anxiety and Depression Score. Evaluated by SDS and SAS scale [15]. The SDS scale included 20 items, each of which was evaluated by a 4-grade scale of 1-4 points, with 50 points as the boundary, <50 points for no depression, 50-60 points for mild depression, 60-70 points for moderate depression and >70 points for severe depression. The SAS scale also takes 50 points as the limit, less than 50 points as normal, 50-60 points as mild, 61-70 points as moderate, and >70 points as severe.

2.3.5. Disease Control Ability. Based on the theory of self-management, combined with expert advice and actual situation, we developed a self-management questionnaire for patients with hypertension to understand the status of self-management in patients' daily diet and medication. Life. The questionnaire consists of 24 items, including diet management, medication management, behavior management and information management [16]. The questionnaire was evaluated by Likert 5 scale, with a score of 1-5 corresponding to "never, rarely, sometimes, often, always", that is, "never = 1, rarely = 2, sometimes = 3, often = 4, always = 5". Nine of the entries (T4 ~ T8, T11, T19 ~ T21) are reverse scores, that is, "never = 5 points, rarely = 4 points, sometimes = 3 points, often = 2 points, always = 1 points". The lowest score of the questionnaire is 24, and the highest score is 120. The higher the score, the better the patient's self-management. The Cronbach α coefficient was 0.80, and each Cronbach α coefficient was more than 0.77. After two rounds of expert consultation, the content validity (I-CVI) of all items was more than 0.85. The overall content validity index (S-CVI) was 0.90. The reliability and validity of the questionnaire are good.

2.3.6. Quality of Life Scale. The quality-of-life scale consists of four subscales, including physical, psychological, social and health self-awareness, with a total of 29 items [17]. The Cronbach's α coefficient of the scale is 0.79 to 0.91. The scale uses a 1-5 rating scale, and the lower the score, the higher the satisfaction.

2.4. Statistical Analysis. All the questionnaire data and score data were entered for the second time, and the data were statistically analyzed by SPSS 21.0 statistical software (Chinese version). All the data are in accordance with the normal distribution, and the measurement data are expressed by mean \pm standard deviation (\pm s), using t-test; for repeated data measurement, the analysis of variance of repeated measurement data is adopted; the counting data rate n (%) is expressed by χ^2 test. $P < 0.05$ indicates that the difference is statistically significant.

3. Results

3.1. Comparison of Nursing Satisfaction. First of all, we compared the nursing satisfaction: the study group was very satisfied in 25 cases, satisfactory in 4 cases, general in 1 case, and the satisfaction rate was 100.00%; in the control group, 10 cases were very satisfied, 8 cases were satisfied, 7 cases were general, and 5 cases were dissatisfied. The satisfaction rate was 83.33%. Compared to the control group, the

nursing satisfaction of the study group was higher than that in control group ($P < 0.05$). All the data results are indicated in figure 1.

3.2. Blood Pressure Level Comparison. Secondly, we compared blood pressure levels. There was no significant difference before management ($P > 0.05$). Blood pressure decreased after treatment, and the level of blood pressure in the study group was lower than that in the control group ($P < 0.05$). All the data results are indicated in figure 2.

3.3. Comparison of Disease Awareness Rate. Thirdly, we compared the rate of disease awareness. The scores of hypertension related knowledge, hypertension harmfulness, community management methods, regular reexamination and blood pressure monitoring in the study group were higher than those in the control group ($P < 0.05$). All the data results are indicated in Table 1.

3.4. Comparison of Anxiety and Depression Scores. Next, compare anxiety and depression scores. There was no significant difference before management ($P > 0.05$). The score of anxiety and depression in the study group was lower than that in the control group ($P < 0.05$). All the data results are indicated in Table 2.

3.5. Comparison of Disease Control Ability. Then, we compared the ability of disease control. The total scores of diet management, drug management, behavior management and information management in the study group were higher than those in the control group ($P < 0.05$). All the data results are indicated in Table 3.

3.6. Comparison of Quality of Life Scores. Finally, we compared the scores of quality of life. There was no significant difference before management ($P > 0.05$). The scores of physiological function, psychological function, social function and health self-cognition in the study group were lower than those in the control group ($P < 0.05$). All the data results are indicated in Table 4.

4. Discussion

Our results suggested that the nursing satisfaction of “hospital-community-family” integrated management was upregulated in comparison with routine management. Then, the level of blood pressure after “hospital-community-family” integrated management was considerably lower than that after routine management. After “hospital-community-family” integrated management, disease awareness rate of patients in study group was obviously enhanced than that after routine management. Patients experience more significant relief from anxiety and negative emotions following “hospital-community-family” integrated management so as to improved life quality.

Hypertension is a major public health problem worldwide [16]. According to the China Cardiovascular report, the prevalence rate of hypertension among adults in China is as high as 25.2%, and the estimated number of patients has reached 270 million [17]. Hypertension can cause severe

target organ damage. Common complications include stroke, heart disease, kidney disease, peripheral vascular disease and fundus disease. About 70% of strokes and 50% of myocardial infarction are associated with high blood pressure. Once hypertension occurs with serious complications such as heart, brain and kidney, it becomes the leading cause of death from cardio-cerebrovascular diseases. At least half of the 3 million cardiovascular deaths each year are related to hypertension. Hypertension not only has a high rate of disability and mortality, but also seriously consumes medical and social resources, and its direct economic expenditure accounts for about 6.61% of the total health expenditure, bringing a heavy burden to families and countries [18]. The awareness rate, treatment rate and control rate of hypertension in people over 18 years old in China are 46.5%, 41.1% and 13.8%, respectively, which is still at a low level, and there is a large gap compared with developed countries [19]. Hypertension usually has no self-conscious symptoms, patients are easy to be ignored, can not be completely cured, and need lifelong management. Adhering to a healthy lifestyle and taking antihypertensive drugs are the main methods for the treatment of hypertension, both of which are indispensable. A healthy lifestyle is the foundation, and rational drug use is the key to achieving blood pressure standards. The two must be combined in order to effectively control hypertension. Studies have indicated that strengthening the supervision and management of patients with hypertension plays an important role in long-term control of blood pressure, reduction of clinical complications and target organ damage [20]. Therefore, strengthening the management of patients with hypertension is of great significance to promote the prognosis of patients.

For the management of hypertension, some countries mainly rely on the advantages of graded diagnosis and treatment, the United Kingdom, the United States and Canada and other countries have more mature management experience [21]. Graded diagnosis and treatment refers to the classification of diseases according to the degree of light, severe, slow, urgent and difficult. Medical institutions of different levels undertake the treatment of different levels of diseases, with a clear division of labor and reasonable medical treatment [21]. Primary health care services, namely grass-roots community health service institutions, secondary and tertiary medical services refer to specialist hospitals or general hospitals, as well as some teaching hospitals with first aid and major and difficult diseases as their main business [21, 22]. Each medical system is managed layer by layer, and the division of labor is clear. Meanwhile, a perfect regional medical information network system is established to connect personal health records, electronic medical records and hospitals, so as to realize the interconnection of networks among diagnosis and treatment institutions. Ensure smooth division of labor and cooperation and two-way referrals [22]. The community health service pays attention to all the residents of the community, carries on the disease health management to the hypertensive patients, 90% of the patients receive diagnosis and treatment in the primary health care system, and do not need to be referred to the superior organization, and the community general

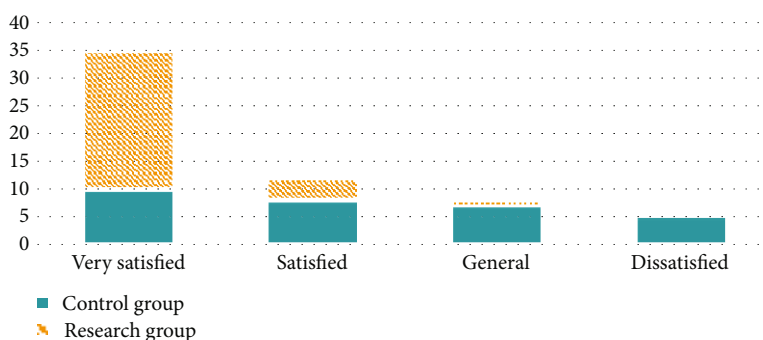


FIGURE 1: Comparison of nursing satisfaction between two groups.

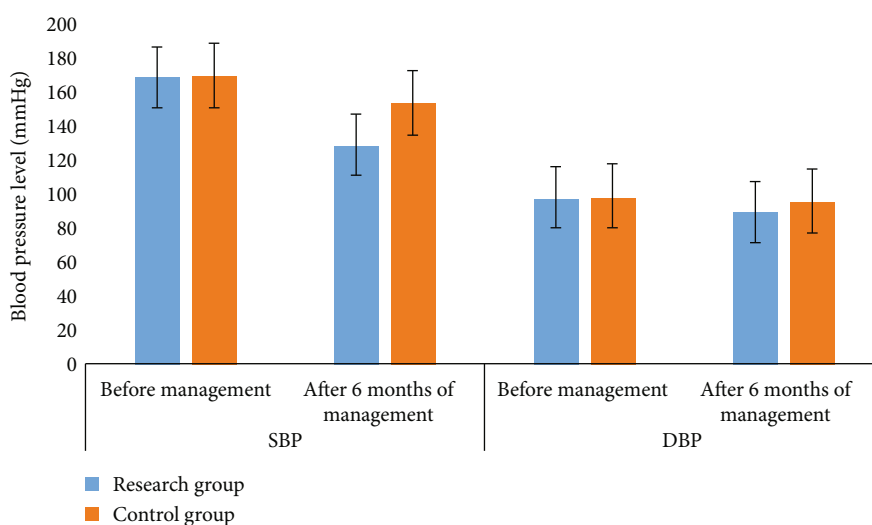


FIGURE 2: Comparison of blood pressure level between two groups of patients.

TABLE 1: Comparison of disease awareness rate between the two groups[±s, Points].

Group	N	Knowledge related to hypertension	Hypertension harmfulness	Community management method	Regular review	Blood pressure monitoring
C group	30	81.29 ± 2.42	80.59 ± 2.34	79.59 ± 3.31	80.67 ± 2.31	83.95 ± 3.31
R group	30	94.19 ± 2.44	95.12 ± 1.21	93.67 ± 1.77	92.77 ± 1.67	95.12 ± 1.22
<i>t</i>		20.560	30.210	20.545	23.250	17.343
<i>P</i>		<0.01	<0.01	<0.01	<0.01	<0.01

TABLE 2: Comparison of anxiety and depression scores between the two groups [±s, Points].

Group	N	Anxiety score		Depression score	
		Before management	After management	Before management	After management
C group	30	69.94 ± 3.41	46.48 ± 1.44	70.79 ± 4.11	47.54 ± 3.34
R group	30	69.59 ± 3.45	41.29 ± 1.21	70.31 ± 4.56	38.79 ± 3.11
<i>t</i>		0.395	15.113	0.428	10.501
<i>P</i>		>0.05	<0.01	>0.05	<0.01

practitioner acts as the “gatekeeper”. Thus, It can be seen that the daily management of hypertension in western developed countries is mainly concentrated in the community,

with the community as the main prevention and control to implement the management of chronic diseases such as hypertension [23].

TABLE 3: Comparison of disease control ability between the two groups [\pm s, Points].

Group	N	Diet management	Medication management	Behavior management	Information management	Total score
C group	30	35.39 \pm 2.45	11.69 \pm 3.21	23.62 \pm 2.45	5.79 \pm 1.21	72.94 \pm 1.35
R group	30	45.29 \pm 1.21	18.59 \pm 1.53	26.79 \pm 1.26	10.38 \pm 1.55	95.26 \pm 3.11
<i>t</i>		19.844	10.627	6.302	12.785	36.058
<i>P</i>		<0.01	<0.01	<0.01	<0.01	<0.01

TABLE 4: Comparison of quality of life scores between the two groups before treatment [\pm s, Points].

Group	N	Physiological function		Psychological function		Social function		Healthy self-cognition	
		Before management	After management	Before management	After management	Before management	After management	Before management	After management
C Group	30	15.55 \pm 4.63	13.13 \pm 2.55	16.74 \pm 3.52	14.42 \pm 4.74	18.44 \pm 3.31	16.42 \pm 2.85	15.55 \pm 3.16	13.86 \pm 1.56
R group	30	15.64 \pm 4.65	11.52 \pm 2.53	16.52 \pm 3.41	12.13 \pm 1.58	18.56 \pm 3.41	12.65 \pm 3.12	15.56 \pm 3.17	10.64 \pm 2.55
<i>t</i>		0.075	2.454	0.245	2.510	0.138	4.886	0.012	5.889
<i>P</i>		>0.05	<0.01	>0.05	<0.01	>0.05	<0.01	>0.05	<0.01

The models of community management of hypertension in some countries mainly include chronic disease care model, chronic disease self-management model, continuous nursing model, peer support management model [24]. In the community, doctors, nurses, pharmacists and other team members use clinical information systems to provide evidence-based decision support for patients, and ultimately improve patients' self-management ability [24, 25]. In addition to doctors, the team also emphasizes that nurses and pharmacists are involved in the management of high blood pressure as health care managers. At present, the control rate of hypertension in the United States has reached 50% [25]. In addition to patients' health assessment, complications examination and health education, when patients are at high risk of disease, they need to be referred to appropriate medical services. The blood pressure level of more people receiving managed treatment is under control, and the blood pressure control rate in the UK has reached (63.0 \pm 1.7) % as of 2011 [26]. Some experience indicates that the chronic disease care model is guided by the concept of graded diagnosis and treatment, based on nurses' health education, doctors deal with the abnormal value of blood pressure, and cooperate with multi-disciplinary teams. And with the help of the network platform to continuously evaluate patients' treatment compliance and drug plans, so that the treatment of a more individual telemedicine service is feasible and effective [27].

The traditional management methods implemented in our country include hierarchical management, self-management, family management and contract management. The trinity management of "hospital-community-family" is a new management mode, which means that the community health service center + secondary hospital + tertiary hospital forms a medical union, which can obtain preferential facilities from the aspects of medical treatment, referral, medication and medical insurance [28]. Different management

methods have their own advantages and disadvantages, as follows: (1) hierarchical management: establishing health files of people's condition, grading and stratifying the disease severity of patients with hypertension, and taking corresponding measures according to different levels and layers, through regular follow-up and monitoring of patients. It can dynamically understand the changes of patients' blood pressure level, so as to realize two-way referral. Some scholars have indicated that grading management can take hypertension patients as objects, classify patients, make use of existing medical resources, and consciously grade intervention, so as to promote the blood pressure control rate and awareness rate; (2) self-management: self-management refers to hypertension patients with the assistance of community medical staff, through a series of health education courses to let patients know more knowledge, skills and confidence, can help patients build confidence in overcoming the disease, reduce the workload as much as possible, and give full play to the subjective initiative and matching degree of patients. Therefore, self-management can make up for the shortcomings and disadvantages of hierarchical management, and can rely on patients and their families to actively participate in it; (3) family management: family management is very important, this is a two-way management, family-based, supplemented by doctors. Doctors can make reasonable and comprehensive intervention programs according to the level and changes of patients' blood pressure, so that patients can understand the knowledge of hypertension, correctly guide their life and diet, and realize the prevention and treatment of hypertension. Clinical studies have shown that family management intervention can fully mobilize the strength of the family, help patients develop good living habits, and ultimately improve patients' treatment compliance and self-efficacy; (4) contract management: contract management is that hypertension patients and medical staff in the community further clarify the

responsibilities and obligations of doctors and nurses through the community platform according to the voluntary principle and follow certain agreements, and formulate a targeted management plan according to the situation of patients. In order to achieve the desired management objectives. Previous studies have indicated that contract management can build a good doctor-patient relationship, help to improve patient management compliance, stabilize blood pressure, and change patients' bad living habits [29].

Changes in diet structure and lack of exercise brought about by some economic developments have led to a high incidence of hypertension, the most common chronic disease [29]. With the attention of the public to health, modern hypertension patients' excessive anxiety about their own health status, coupled with the serious complications of the disease, will affect the health and life of patients. At present, the management of hypertension in community is mainly based on the traditional management mode and the comprehensive management of the trinity of hospital, community and family [30]. The trinity integrated management of hospital-community-family is obviously more effective in the control of blood pressure and the reduction of complications. Clinically, every community doctor can actively carry out contract management on patients with hypertension and control them from the grass-roots level so as to achieve the goal of achieving blood pressure standards. The medical team, which is composed of family doctors, community nurses, public health doctors and volunteers, provides continuous health management services for patients through the mode of responsibility service. The "hospital-community-family" trinity integrated management model was first put forward in the guidance on promoting Family Doctor contract Service in June 2016, and with the deepening of the reform of the medical system, clinical management of chronic diseases has entered an era of prediction, prevention, individualized treatment and two-way referrals, which can not only meet the health needs of community residents in chronic disease management. The responsibility system of family doctors has become an important part of the comprehensive reform of community health and become the focus of the current research, and the application of family doctor responsibility system in patients with hypertension in the community is also the focus of attention [31]. In recent years, the family doctor responsibility system has been newly reported in the management of chronic diseases in the community, and achieved good results. The trinity comprehensive management of "hospital-community-family" is a new management model, which is the basis and the best choice for hypertension management. However, the management quality of patients with hypertension in the community is also affected by many factors, and the formulation of management methods should be considered and improved in many aspects and dimensions (1) Combined with the professional skills of community doctors, the professional skills training of community doctors should be strengthened, including their own professional skills, follow-up and communication skills, so as to continuously improve their own professional skills, improve patients' treatment compliance and build a good doctor-patient rela-

tionship; (2) continuously expand the number of doctors, while ensuring the number of community doctors, strengthen their management quality, let doctors and nurses master the latest management methods, and continuously improve the management quality; (3) be good at introducing new management models, actively carry out patients' self-activities, and carry out corresponding courses according to the characteristics of hypertension. With the help of Internet and multimedia technology, we should constantly update and develop new APP ports, strengthen patients' health education, change patients' bad habits and behaviors, and promote patients' awareness of self-prevention, so as to form a correct behavior and persevere, and enhance patients' survival and quality of life; (4) make full use of the medical resources of secondary and tertiary hospitals, set up chronic disease studios, and regularly consult grass-roots communities and community doctors under experts from secondary and tertiary hospitals, so as to provide high-quality and scientific management for patients. Existing practice data show that the implementation of "hospital-community-family" integrated management can significantly enhance the non-drug treatment of hypertension patients in the community. The hypertension management intervention effect of the family doctor contract model is better than the current community hypertension prevention and control follow-up management model. The same line of thinking can also be found in the study proposed by Noor A [32]. They applied new methods in their research, and their conclusions can also provide some support for this research.

Conclusively, adopting the comprehensive management of "hospital, community and family" trinity can vertically integrate medical resources and establish a truly effective hierarchical diagnosis and treatment model. At the same time, it takes advantage of the technical advantages of tertiary traditional Chinese medicine hospitals and highlights the management characteristics in the management content of the platform, which not only allows patients to Get full, seamless management to promote patient medication compliance and blood pressure control. It also enables community health care workers to improve their professional knowledge and skills. "Hospital-community-family" integrated management can promote patients' blood pressure and treatment compliance, enhance patients' self-management ability and self-confidence, and enhance the management efficiency of medical staff. Positive attitudes and high satisfaction among patients and medical staff.

Data Availability

The datasets used and analyzed during the current study are available from the corresponding author upon reasonable request.

Conflicts of Interest

The authors declare that they have no competing interests.

Authors' Contributions

Wanzhe Shi and Lei Cheng have contributed equally to this work and share first authorship.

References

- [1] N. Linda, "Managing hypertension in older people: a guide for nurses," *Independent Nurse*, vol. 2022, no. 1, pp. 613–615, 2022.
- [2] B. M. Reininger, L. A. Mitchell-Bennett, M. J. Lee et al., "Scaling a community-wide campaign intervention to manage hypertension and weight loss," *Frontiers in Medicine*, vol. 8, no. 54, pp. 55–57, 2021.
- [3] V. Tsimihodimos, C. Gonzalez-Villalpando, J. B. Meigs, and E. Ferrannini, "Hypertension and Diabetes Mellitus: Coprediction and Time Trajectories," *Hypertension*, vol. 71, no. 3, pp. 422–428, 2018.
- [4] S. Ramzi, K. Soraida, and A. S. Doaa, "Promoters of therapeutic inertia in managing hypertension: a consensus-based study," *The American Journal of Managed Care*, vol. 27, no. 11, pp. 1434–1435, 2021.
- [5] B. Uchmanowicz, A. Chudiak, I. Uchmanowicz, J. Rosińczuk, and E. S. Froelicher, "Factors influencing adherence to treatment in older adults with hypertension," *Clinical Interventions in Aging*, vol. 13, pp. 2425–2441, 2018.
- [6] P. Erietta, W. Gregoire, and B. Michel, "How Do I Manage Hypertension in Patients with Advanced Chronic Kidney Disease Not on Dialysis? Perspectives from Clinical Practice," *Vascular Health and Risk Management*, vol. 17, no. 44, pp. 41–43, 2021.
- [7] M. D.. Anderegg, T. H. Gums, L. Uribe et al., "Pharmacist Intervention for Blood Pressure Control in Patients with Diabetes and/or Chronic Kidney Disease," *Pharmacotherapy*, vol. 38, no. 3, pp. 309–318, 2018.
- [8] S. Chowdhury, C. Stephen, S. McInnes, and E. Halcomb, "Nurse-led interventions to manage hypertension in general practice: A systematic review protocol," *Collegian*, vol. 27, no. 3, pp. 340–343, 2020.
- [9] J. H. Stephens, F. Alizadeh, J. B. Bamwine et al., "Managing hypertension in rural Uganda: realities and strategies 10 years of experience at a district hospital chronic disease clinic," *PLoS One*, vol. 15, no. 6, pp. 623–624, 2020.
- [10] C. Akl, C. Akik, H. Ghattas, and C. M. Obermeyer, "The cascade of care in managing hypertension in the Arab world: a systematic assessment of the evidence on awareness, treatment and control," *BMC Public Health*, vol. 20, no. 1, pp. 131–134, 2020.
- [11] P. Zha, R. Qureshi, S. Porter et al., "Utilizing a Mobile health intervention to manage hypertension in an underserved Community," *Western Journal of Nursing Research*, vol. 42, no. 3, pp. 201–209, 2020.
- [12] T. H. Jafar, M. Gandhi, H. A. De Silva et al., "A community-based intervention for managing hypertension in rural South Asia," *The New England Journal of Medicine*, vol. 382, no. 8, pp. 164–165, 2020.
- [13] N. Gamze, L. Sarah, and C. Kaushik, "Content, structure, and delivery characteristics of yoga interventions for managing hypertension: a systematic review protocol," *International Journal of Yoga*, vol. 13, no. 2, pp. 44–45, 2020.
- [14] V. J. Bufalino, W. K. Bleser, E. A. Singletary et al., "Frontiers of Upstream Stroke Prevention and Reduced Stroke Inequity Through Predicting, Preventing, and Managing Hypertension and Atrial Fibrillation: A Call to Action From the Value in Healthcare Initiative's Predict; Prevent Learning Collaborative," *Circulation*, vol. 13, no. 7, pp. 45–46, 2020.
- [15] C. Roulet, Z. Rozsnyai, K. T. Jungo et al., "Managing hypertension in frail oldest-old-the role of guideline use by general practitioners from 29 countries," *PLoS One*, vol. 15, no. 7, pp. 431–434, 2020.
- [16] P. Crilly, "Managing hypertension: the role of diet and exercise," *The Pharmaceutical Journal*, vol. 33, no. 52, pp. 412–413, 2020.
- [17] M. J. Lee, S. Romero, H. Jia, C. A. Velozo, A. L. Gruber-Baldini, and L. M. Shulman, "Self-efficacy for managing hypertension and comorbid conditions," *World Journal of Hypertension*, vol. 9, no. 3, pp. 631–634, 2019.
- [18] M. Nichols, A. Singh, F. S. Sarfo et al., "Post-intervention qualitative assessment of mobile health technology to manage hypertension among Ghanaian stroke survivors," *Journal of the Neurological Sciences*, vol. 406, article 116462, 443 pages, 2019.
- [19] Wiley, "Best strategy for managing hypertension and pre-eclampsia at end of pregnancy," *NewsRx Health & Science*, vol. 34, no. 42, pp. 122–124, 2019.
- [20] G. Tripti, R. Tameem, and S. R. Krim, "Managing hypertension in patients with heart failure: an ongoing quandary," *Current Opinion in Cardiology*, vol. 34, no. 4, pp. 531–534, 2019.
- [21] J. Adinan, R. Manongi, G. A. Temu et al., "Preparedness of health facilities in managing hypertension & diabetes mellitus in Kilimanjaro, Tanzania: a cross sectional study," *BMC Health Services Research*, vol. 19, no. 1, pp. 56–57, 2019.
- [22] S. D. Persell, K. N. Karmali, D. Lazar et al., "Effect of Electronic Health Record-Based Medication Support and Nurse-Led Medication Therapy Management on Hypertension and Medication Self-management: A Randomized Clinical Trial," *JAMA Internal Medicine*, vol. 178, no. 8, pp. 1069–1077, 2018.
- [23] L. Xu, J. Chen, F. Guo, and C. Yi, "Complex dynamic analysis of single disease management path of hypertension in community based on system dynamics," *Chinese General Practice*, vol. 22, no. 14, pp. 1655–1662, 2019.
- [24] K. M. King-Shier, K. K. Dhaliwal, R. Puri, P. LeBlanc, and J. Johal, "South Asians' experience of managing hypertension: a grounded theory study," *Patient Preference and Adherence*, vol. Volume 13, no. 52, pp. 321–329, 2019.
- [25] L. M. Wells and C. H. Jones, "The dietary approaches to stop hypertension (DASH) diet: potential for managing hypertension in chronic kidney disease," *Journal of Clinical Nephrology and Therapeutics*, vol. 3, no. 1, pp. 552–554, 2019.
- [26] J. L. Hargraves, D. Bonollo, S. D. Person, and W. J. Ferguson, "A randomized controlled trial of community health workers using patient stories to support hypertension management: Study protocol," *Contemporary Clinical Trials*, vol. 69, pp. 76–82, 2018.
- [27] S. DeAndrade, F. El Rayess, and R. Goldman, "Perspectives on Hypertension in the New England Cape Verdean Community," *Journal of Racial and Ethnic Health Disparities*, vol. 5, no. 1, pp. 162–169, 2018.
- [28] C. P. Renfro, S. Ferreri, T. G. Barber, and S. Foley, "Development of a Communication Strategy to Increase Interprofessional Collaboration in the Outpatient Setting," *Pharmacy (Basel)*, vol. 6, no. 1, p. 4, 2018.

- [29] B. Jacobs, C. Men, M. Bigdeli, and P. S. Hill, "Limited understanding, limited services, limited resources: patients' experiences with managing hypertension and diabetes in Cambodia," *BMJ Global Health*, vol. 2, Suppl 3, pp. 412–415, 2017.
- [30] R. A. Aftab, A. H. Khan, A. S. Adnan, and N. Jannah, "A systematic review on randomized control trials on rennin angiotensin aldosterone system inhibitors role in managing hypertension among hemodialysis patients," *Renal Failure*, vol. 38, no. 3, pp. 42–44, 2016.
- [31] Cardiovascular Diseases and Conditions, "New Findings from University of Duisburg-Essen in hypertension provides new insights (the efficacy and safety of yoga in managing hypertension)," *Biotech Week*, vol. 33, no. 53, pp. 394-395, 2016.
- [32] A. Noor and A. Assiri, "A novel computational drug repurposing approach for systemic lupus erythematosus (SLE) treatment using semantic web technologies," *Saudi Journal of Biological Sciences*, vol. 28, no. 7, pp. 3886–3892, 2021.

Retraction

Retracted: The Diagnosis of Early Gastric Cancer Based on Medical Imaging Technology and Mathematical Modeling

Computational and Mathematical Methods in Medicine

Received 27 June 2023; Accepted 27 June 2023; Published 28 June 2023

Copyright © 2023 Computational and Mathematical Methods in Medicine. This is an open access article distributed under the Creative Commons Attribution License, which permits unrestricted use, distribution, and reproduction in any medium, provided the original work is properly cited.

This article has been retracted by Hindawi following an investigation undertaken by the publisher [1]. This investigation has uncovered evidence of one or more of the following indicators of systematic manipulation of the publication process:

- (1) Discrepancies in scope
- (2) Discrepancies in the description of the research reported
- (3) Discrepancies between the availability of data and the research described
- (4) Inappropriate citations
- (5) Incoherent, meaningless and/or irrelevant content included in the article
- (6) Peer-review manipulation

The presence of these indicators undermines our confidence in the integrity of the article's content and we cannot, therefore, vouch for its reliability. Please note that this notice is intended solely to alert readers that the content of this article is unreliable. We have not investigated whether authors were aware of or involved in the systematic manipulation of the publication process.

In addition, our investigation has also shown that one or more of the following human-subject reporting requirements has not been met in this article: ethical approval by an Institutional Review Board (IRB) committee or equivalent, patient/participant consent to participate, and/or agreement to publish patient/participant details (where relevant).

Wiley and Hindawi regrets that the usual quality checks did not identify these issues before publication and have since put additional measures in place to safeguard research integrity.

We wish to credit our own Research Integrity and Research Publishing teams and anonymous and named external researchers and research integrity experts for contributing to this investigation.

The corresponding author, as the representative of all authors, has been given the opportunity to register their agreement or disagreement to this retraction. We have kept a record of any response received.

References

- [1] J. Xiu, L. Ma, Y. Ding et al., "The Diagnosis of Early Gastric Cancer Based on Medical Imaging Technology and Mathematical Modeling," *Computational and Mathematical Methods in Medicine*, vol. 2022, Article ID 8721654, 7 pages, 2022.

Research Article

The Diagnosis of Early Gastric Cancer Based on Medical Imaging Technology and Mathematical Modeling

Jingying Xiu,¹ Lie Ma,² Yanping Ding,³ Yang Li,³ Lili Kan,⁴ Shi Feng,³ Fei Wu,³
Shanshan Xu,³ Xinan Lu ,³ Ting He ,³ and Zhihai Han ²

¹Beijing Tongren Hospital, Capital Medical University, 100730 Beijing, China

²Department of Pulmonary and Critical Care Medicine, The Sixth Medical Center of PLA General Hospital, 100048 Beijing, China

³ImmunoChina Pharmaceuticals Co., Ltd., 100195 Beijing, China

⁴Department of Pharmacy, Panjin Gem Flower Hospital, 124010 Panjin, Liaoning, China

Correspondence should be addressed to Xinan Lu; 164304424@stu.cuz.edu.cn, Ting He; heting@immunochina.com, and Zhihai Han; hanzhihai@hotmail.com

Received 17 August 2022; Revised 5 September 2022; Accepted 8 September 2022; Published 3 October 2022

Academic Editor: Pan Zheng

Copyright © 2022 Jingying Xiu et al. This is an open access article distributed under the Creative Commons Attribution License, which permits unrestricted use, distribution, and reproduction in any medium, provided the original work is properly cited.

The key to reducing the mortality of gastric cancer is early detection, early diagnosis, and early treatment of gastric cancer. Early diagnosis of gastric cancer is the key to early detection and diagnosis of gastric cancer. Early diagnosis and treatment of gastric cancer is of great significance for improving the curative effect and reducing mortality of gastric cancer. The purpose of this paper is to study the diagnosis of early gastric cancer based on medical imaging techniques and mathematical modeling. The effect of W-DeepLab network-assisted diagnosis of images under white light was analyzed, and the value of Narrow Band Imaging and Blue Laser Imaging in the diagnosis of early gastric cancer was compared. Because Blue Laser Imaging endoscopy can clearly observe the demarcation line and microvascular morphology; but when using Narrow Band Imaging observation, part of the demarcation line and microvascular morphology is not observed. The results show that Blue Laser Imaging is brighter than Narrow Band Imaging's endoscopic images, and it is easier to observe the microstructure of lesions under endoscopy, so as to accurately determine the nature of lesions.

1. Introduction

Gastric cancer originates from a malignant tumor of the gastric epithelium and is the second leading cause of cancer death in the world. There are large differences in the incidence of gastric cancer in countries and regions around the world [1]. Early gastric cancer usually does not have any symptoms, and even if there is, it may be caused by the combination of atrophic gastritis, Helicobacter pylori infection, or functional dyspepsia, rather than the early gastric cancer lesions themselves. When there are alarm symptoms such as aggravation of abdominal symptoms, anorexia, weight loss, anemia, and melena, most of them are advanced gastric cancer. The overall prognosis of gastric cancer in my country is poor. Because the lesions of early gastric cancer are often small, it is difficult to diagnose early gastric cancer

by regular gastroscopy. Endoscopic narrow-band imaging technology and staining technology make the gastric mucosal gland openings and microvessels of the lesions more clearly displayed under the microscope by changing the spectral and chemical staining methods, respectively, and it is easier to identify gastric cancer lesions [2, 3]. A mathematical model is an abstract description of a problem using systematic symbols and mathematical expressions. Mathematical modeling can be seen as the process of transforming a problem definition into a mathematical model. Medical imaging technology and mathematical modeling can effectively help the efficiency of early gastric cancer diagnosis.

My country is a country with a high incidence of gastric cancer. Most of the patients are in the middle and late stages when they go to the clinic. Even if they receive surgical

treatment, the survival rate and quality of life are not ideal [4]. Klimenko A A presents the most common and clinically convenient classification and staging system for gastric cancer, confirming the need for the earliest possible diagnosis and verification of the stage of the tumor process. Modern methods of gastric cancer diagnosis are considered in detail, including esophagogastroduodenoscopy (EGD) as the method of choice for the initial detection of gastric cancer, and various radiographic modalities, including multi-spiral computed tomography and endoscopic ultrasonography (EUS), combined with chromoendoscopy, narrow-band tomography, and confocal laser endoscopy [5]. Mikhaleva LM reviewed mixed gastric cancer. Compared with other types, mixed gastric cancer has the characteristics of older patients (over 65 years old), larger tumors, obvious local tumor infiltration, and high metastasis rate. Further in-depth studies of mixed-type gastric cancer in the context of its morphological histological tumor components, as well as tumorigenesis mechanisms, are warranted as they may aid in the early diagnosis of tumors and more accurate prediction of outcome and selection of appropriate management strategies, i.e., determination of the extent of surgical manipulation and further medical treatment, taking into account the molecular characteristics of the tumor and its PD-L1 status, will significantly affect the 5-year survival rate of the patient in the long run [6]. In Kumar S's study, annual endoscopic surveillance via the Cambridge protocol was recommended for patients with delayed surgery, including biopsy of any lesions and at least 30 random biopsies from the antrum, transition zone [7]. Therefore, it is of practical significance to study the diagnosis of early gastric cancer based on medical imaging technology and mathematical modeling.

Common gastroscopy combined with pathological biopsy is the main basis for the selection of early gastric cancer diagnosis and diagnosis and treatment in my country. However, endoscopic biopsy samples are shallow and few, and the biopsy process is empirical, random, and blind. Whether the focal biopsy tissue can fully reflect the overall condition of the lesion is still controversial. This paper discusses the diagnostic ability of NBI-ME, gastroscopic biopsy, and W-DeepLab modeling for early gastric cancer, in order to provide some theoretical basis for the diagnosis of early gastric cancer.

2. Research on the Diagnosis of Early Gastric Cancer Based on Medical Imaging Technology and Mathematical Modeling

2.1. Medical Imaging Technology

2.1.1. Blue Laser Imaging (BLI). BLI is a new generation of IEE for the LASEREO system, which uses lasers with two wavelengths of 410 and 450 nm as the light source [8]. As a new type of endoscope, BLI can more clearly observe the morphology of microvessels and microstructures on the surface of gastric mucosa, thereby helping to find lesions and improve the detection rate of early gastric cancer. In the BLI-bright observation mode, its bright field of view can

make subtle observations of distant lesions, while in the ME-BLI mode, the microvascular pattern, microglandular pattern, and demarcation line of the lesion can be clearly observed display. Based on the diagnostic criteria of the VS classification system, compared with WLE, BLI can clearly display the lesion boundary and provide a more accurate diagnosis of EGC [9]. Although BLI has greatly improved the diagnostic accuracy of lesion boundaries, a combined study of BLI with other IEEs is still needed to further evaluate the value of its combined application in detecting gastric lesion boundaries [10].

2.1.2. Narrow Band Imaging (NBI). Based on the VS classification and diagnosis method, ME-NBI can clearly display the structure of microglandular blood vessels and microglandular ducts on the surface of gastric mucosa. Due to differences in EGC histology and background mucosal inflammation, in undifferentiated EGCs, the cancerous tissue is often not exposed to the lesion surface. However, NBI can only obtain a more accurate diagnosis of the depth of EGC infiltration in differentiated EGC, and further studies are needed to provide evidence for undifferentiated EGC [11, 12].

ME-NBI diagnostic criteria for early gastric cancer: ME-NBI subsurface microstructure (MS) definition includes crypt opening, marginal crypt epithelium, and the part between crypt openings; surface microvascular structure (MV) subepithelial capillaries, collections Veins, and pathological microvessels [13]. According to the microstructure and vascular morphology, MS and MV were divided into three types: regular, irregular, and absent. Regular microstructure, that is, the marginal crypt epithelium shows a uniform shape such as linear, elliptical, curved, annular, and other structures, with symmetrical distribution and regular arrangement; irregular surface microstructure, that is, showing irregular linear, curved, villous, and other structures, irregular in shape, various in structure, non-uniform in structure, asymmetric in distribution, and irregular in arrangement; missing microstructure, that is, no marginal crypt structure and white opaque shape can be seen under endoscopy substance. Similarly, for regular microvessels, mucosal capillaries show a uniform shape, closed loop, or open; for irregular microvascular structure, microvessels show open, closed loop, twisted, branched, and other shapes, with different shapes. Uniform, asymmetric distribution, and irregular arrangement; missing microvessels, manifested as the disappearance of microvascular structures, are replaced by white opaque substances [14, 15]. According to the "VS classification system," early gastric cancer can be diagnosed if any of the following is satisfied; otherwise, it is a non-cancerous lesion: (1) irregular surface microstructure (IMSP) and clear demarcation line (DL); (2) irregular Microvessels (IMVP) and specific lines of differentiation (DL) [16].

2.2. W-DeepLab Modeling. Image segmentation is a critical step in image understanding. The basis of segmentation mainly includes (1) the segmented area is a homogeneous area, which can be grayscale, texture, or other specific

features; (2) the interior of the area is smooth and free of small holes; (3) the boundaries of each area are complete, the space is complete, and the location normal, no cracks [17]; (4) there should be obvious differences between adjacent areas, and a unified judgment basis should be selected.

First, perform 4 times bilinear upsampling on the features extracted by the encoder and temporarily record this result as D1; then reduce the number of channels from the feature map D2' extracted from DCNN with the same scale as D1 to obtain D2. It is obtained by 1×1 convolution with D1. The features of these scales usually have 512 or 256 channels in DCNN, but not so many feature channels are extracted by the encoder, so it is necessary to reduce the number of channels, if direct. If the connection is made without dimensionality reduction, the weight of D2' will be increased invisibly, which will greatly increase the difficulty of network training; for the subsequent work of connecting D1 and D2, the result is first recorded as D3, and the features of D3 are fine-tuned. Do the normal operation of 3×3 convolution and finally perform 4 times upsampling operation to obtain the segmentation result [18].

In this paper, the W-DeepLab network uses the cross-entropy loss function to measure the difference between the model predicted value and the actual value.

When using logistic regression to solve the binary classification problem, the known samples have m labels, the training set $[(x(1), y(1)), (x(2), y(2)), \dots, (x(m), y(m))]$, and the definable cross-entropy loss function is derived from the maximum likelihood estimation combined with the logistic classifier as:

$$J(\theta) = -\frac{1}{m} \left[\sum_{i=1}^m y^{(i)} \log h_{\theta}(x^{(i)}) + (1 - y^{(i)}) \log (1 - h_{\theta}(x^{(i)})) \right], \quad (1)$$

where $h_{\theta}(x)$ is the predicted or activation value.

The original loss function is denoted by C_0 , and the loss function after weight decay is applied to the parameter w is:

$$C = C_0 + \frac{\lambda}{2n} \sum_w w^2. \quad (2)$$

The regularization coefficient is denoted as λ , and in this paper, $\lambda=0.00004$, and the number of samples is denoted as n . Taking the derivation of the parameter w in the formula, the formula can be obtained:

$$\frac{\partial C}{\partial w} = \frac{\partial C_0}{\partial w} + \frac{\lambda}{n} w. \quad (3)$$

The learning rate is represented by η , and weight decay is added during training. At this time, the formula of the parameter w is updated to:

$$w \longrightarrow w - \eta \frac{\partial C_0}{\partial w} - \frac{\eta \lambda}{n} w = \left(1 - \frac{\eta \lambda}{n}\right) w - \eta \frac{\partial C_0}{\partial w}. \quad (4)$$

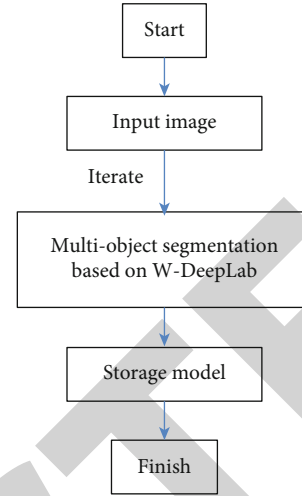


FIGURE 1: The fine-tune method initializes network parameters.

In the above formula, $1 - \eta \lambda / n$ is a coefficient less than 1, and its function is to reduce the value of w . A lower network complexity model will also fit the data better.

3. Investigation and Research on the Diagnosis of Early Gastric Cancer Based on Medical Imaging Technology and Mathematical Modeling

3.1. Research Objects. Select patients who have undergone electronic gastroscopic examinations in M Hospital from 2020 to 2021, and the nurses in the endoscopy room will number the patients in the order in which the patients made gastroscopy appointments, starting from the first patient who underwent gastroscopy on January 1, 2020; the number starts from the 1st and records the patient's name, age, gender, clinical symptoms, initial diagnosis, and contact information. According to the number, the odd-numbered patients were treated as the control group for white light endoscopy and NBI examination, and the even-numbered patients were used as the experimental group for white light endoscopy and BLI examination. The numbering nurse in the endoscopy room just numbers and does not know the grouping situation.

Inclusion criteria: (1) Patients who signed informed consent. (2) No serious infection. **Exclusion criteria:** (1) Patients with mental illness and severe heart failure. (2) Patients with a history of abdominal surgery and mucosal structures cannot be observed. (3) Patients with acute upper gastrointestinal bleeding, gastric perforation, or upper gastrointestinal obstruction. According to the inclusion and exclusion criteria, a total of 4040 people were included in this study, of which 1864 people in the control group were observed by NBI endoscopy; 2176 people in the experimental group were observed by BLI endoscopy.

3.2. Endoscopy Procedure. Choose from the GIF-H260ZNBI endoscope and the EG-L590WR blue laser endoscope. Patients undergoing gastroscopy are given an empty stomach on the day of the examination, and the oropharynx is

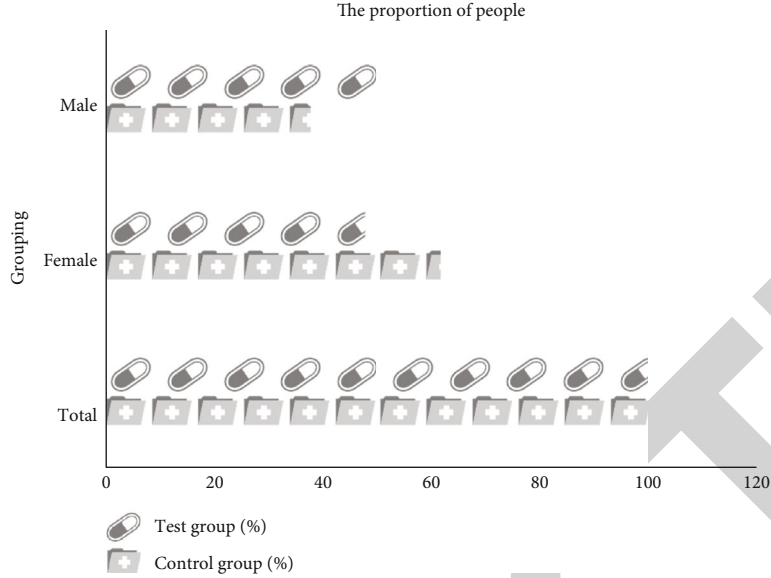


FIGURE 2: Male to female ratio.

administered local anesthesia with mucus prior to the examination. The control group underwent NBI examination, and the experimental group underwent BLI endoscopy. The control group underwent white light endoscopy to obtain clear images of the lesions. Then, after finding the lesion, switch to NBI mode to further observe the shape, boundary, and microstructure of the lesion, and make an endoscopic diagnosis. Finally, 3-5 pieces of mucosal tissue are taken from the edge of the lesion and sent for pathological biopsy. The endoscopic observation of BLI lesions in the experimental group generally adopted the following methods: first, clear images of the lesions were obtained through white light endoscopy, and the color and microscopic structure of blood vessels on the surface of the lesions were observed. After the lesions were detected, the BLI-light mode was used to observe and further analyze the histological properties of the lesions. Make a judgment, and finally use the BLI function to observe the muscle tissue and wound structure in a large picture, and make an endoscopic diagnosis of the wound. Finally, 3-5 pieces of mucosal tissue were taken at the edge of the lesion and sent for pathological biopsy.

3.3. Model Training. The ordinary white light endoscopic images studied in this paper have only 100 valid raw data before augmentation, and a new network can hardly be trained in the case of scarce data resources. Therefore, fine-tune is only performed when the parameters are initialized. In the shallow feature extraction, the existing data model is fine-tuned by combining the characteristics of ordinary white light endoscopic image data, as shown in Figure 1.

This paper proposes the W-DeepLab network for computer-aided diagnosis of intestinal metaplasia and trains it using a white light endoscopic image dataset. The dataset is randomly divided into three parts, namely, training set, validation set, and test set. The training system corresponds to the model parameters, the verification system adjusts the hyperparameters of the model, and the test system is used

TABLE 1: Gender distribution of the two groups of subjects.

Grouping	Test group (%)	Control group (%)	<i>P</i> value
Male	52	38	0.42
Female	48	62	
Total	100	100	

TABLE 2: Test results of each evaluation index.

Model	Accuracy	Sensitivity	Specificity	MIoU	Time
W-DeepLab	98%	91%	97%	88%	10frame/s
DeepLabv3+	80%	78%	93%	77%	12frame/s
FCN-32s	81%	70%	85%	62%	2frame/s

to evaluate performance, and the test system does not participate in model training and verification. This article uses the TensorFlow1.6.0 deep learning framework and the Python language program version 3.5.2 for testing. The initial learning rate is 0.0001, and the learning rate decreases according to the curve as the number of iterations increases.

4. Analysis and Research on the Diagnosis of Early Gastric Cancer Based on Medical Imaging Technology and Mathematical Modeling

4.1. Gender Composition of the Two Groups of Subjects. There were 2176 cases in the experimental group, 52% male and 48% female, and 1864 cases in the control group, as shown in Figure 2. There were 38 men and 62 women, respectively. The Pearson χ^2 test was performed on the gender of the two groups of research subjects, and there was no statistical difference in the gender composition of the two groups of subjects, as shown in Table 1.

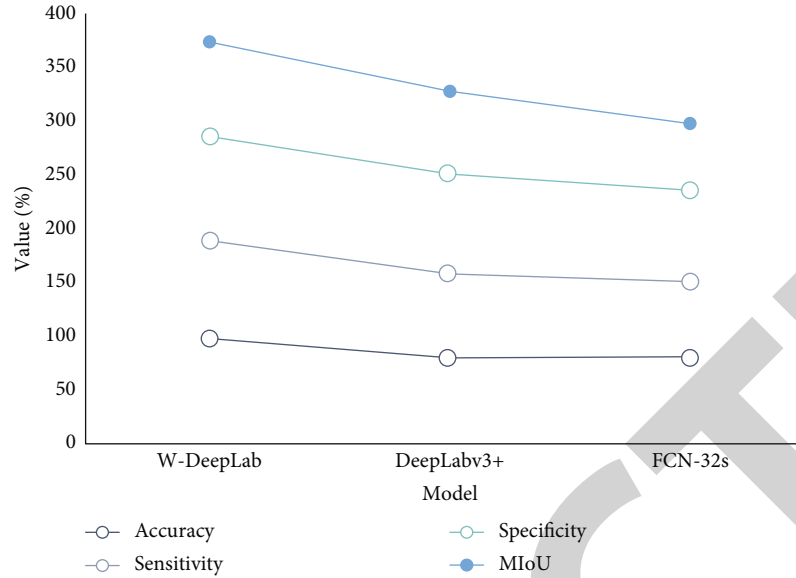


FIGURE 3: Model experimental results in the testing phase of the white light endoscopic image dataset.

4.2. *Experimental Results of Images under White Light.* The segmentation speed of FCN-32s, DeepLabv3+, and W-DeepLab was tested to enable a more comprehensive assessment of the computer-aided diagnosis network for intestinal metaplasia. The test results of each evaluation index of each network on the ordinary white light endoscopy image dataset are shown in Table 2. The better the performance of the network, the higher the specificity and sensitivity will be. From the test results, it can be clearly concluded that the specificity and sensitivity of the W-DeepLab network are better than other network models, reaching 97% and 91%, respectively, and the MIoU value of the W-DeepLab network is also the highest. The best is 88%, which is significantly higher than 62% of FCN-32s and 77% of DeepLabv3+. The most important thing is that the W-DeepLab network is as high as 98% in terms of global pixel accuracy, which is significantly better than the other two networks, as shown in Figure 3.

In the classification task of medical images, the classification accuracy is usually evaluated by the characteristic curve (ROC) index. The area enclosed by the ROC curve and the horizontal axis is called AUC. The better the classification method, the greater the AUC value. By entering the AUC value into the measurement network, the standard is to make the verification of the network proposed in this paper more comprehensive and objective. The AUC values of different models are shown in Table 3. The AUC value of the W-DeepLab network is 0.98, which is much larger than the 0.88 of FCN-32s and 0.91 of DeepLabv3+. These experiments are enough to fully demonstrate that the W-DeepLab network can make a positive contribution to the computer-aided diagnosis of intestinal metaplasia.

4.3. *Comparison of the Value of NBI and BLI in the Diagnosis of Early Gastric Cancer.* Irregular microvascular morphology and irregular surface microstructure with demarcation lines

TABLE 3: AUC values for different models.

Model	W-DeepLab	DeepLabv3+	FCN-32s
AUC	98%	91%	88%

TABLE 4: Comparison of the value of NBI and BLI in the diagnosis of early gastric cancer.

Group	Sensitivity	Specificity
NBI	79%	92%
BLI	90%	98%
P	0.018	0.44

were observed under endoscopy, which can be diagnosed as early gastric cancer. For early gastric cancer, among 1864 patients in the control group, 178 were diagnosed with early gastric cancer by NBI endoscopy. Compared with the early gastric cancer diagnosed by the pathology department, 204 patients were diagnosed by endoscopy, which was consistent with the results reported by the pathology department.

Among the 2176 patients in the experimental group, 211 patients were diagnosed with early gastric cancer by BLI endoscopy. Compared with the early gastric cancer diagnosed by the pathology department, the endoscopic diagnosis of 191 patients was consistent with the pathological report, and 7 patients were diagnosed with early gastric cancer.

The chi-square test was used to calculate the difference in sensitivity and specificity of NBI and BLI for the diagnosis of early gastric cancer, as shown in Table 4. The difference in sensitivity ($P = 0.021$) between the two was calculated to be statistically significant, while the difference in specificity ($P = 0.409$) between the two was not statistically significant, as shown in Figure 4.

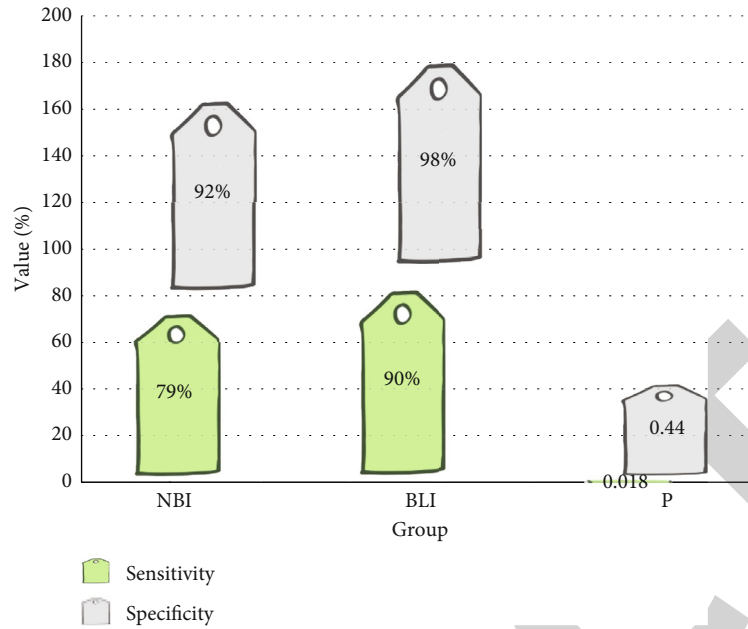


FIGURE 4: Results of the chi-square test.

5. Conclusions

The timely detection of early gastric cancer has become the key to whether patients can receive early treatment. Therefore, improving the diagnosis level of early gastric cancer will significantly reduce the mortality of gastric cancer and improve the quality of life of patients. This study compared the value of NBI and BLI in the diagnosis of early gastric cancer, but the specificity of the two was not statistically significant. All patients with correct diagnosis of early gastric cancer in the NBI picture had significant IMVP and DL or IMSP and DL. However, in 13 benign LGIN lesions, these three major structures failed NBI endoscopy. The doctor's understanding of early gastric cancer and the experience of endoscopic surgery often determine the direction of diagnosis. The missed diagnosis was due to the fact that the mucosal surface was covered with "white substances", which affected the judgment of microvessels and microstructures. Later, the images were checked and corrected to early gastric cancer. This paper also introduces the related experiments of applying W-DeepLab network in computer-aided diagnosis of intestinal metaplasia. The ordinary white light endoscopic image was selected as the image used in the data set, and then the raw data of the ordinary white light endoscopic image obtained from the Department of Gastroenterology of the First Affiliated Hospital were processed into data that could be recognized by the semantic segmentation network. It also introduces several mainstream indicators for evaluating computer-aided diagnosis ability and methods for optimizing model training; finally, the models are tested and compared on the white light endoscopy image test set. The research results show that the computer-aided diagnosis technology for intestinal metaplasia based on the W-DeepLab network has the best effect; and in the comparison between the W-DeepLab network and other semantic seg-

mentation networks, the AUC value, specificity and sensitivity, etc. properties all perform better.

The study also had some limitations. First, this study is a single-center retrospective study, which may have limitations in case selection and cannot fully cover all cases. Therefore, further verification with more cases is required. Second, endoscopic diagnostic results are not completed by the same physician, and different levels of clinical experience may affect the accuracy of endoscopic results. Finally, the diagnostic ability of BLI endoscopic mucosal microstructure typing on the differentiation degree of EGC was not further analyzed in this study, and further research is needed to determine in the future.

Data Availability

The data underlying the results presented in the study are available within the manuscript.

Conflicts of Interest

There is no potential conflict of interest in our paper. We confirm that the content of the manuscript has not been published or submitted for publication elsewhere.

Authors' Contributions

Jingying Xiu and Lie Ma contributed equally to this work. All authors have seen the manuscript and approved to submit to your journal.

References

- [1] Y. Horiuchi, T. Hirasawa, N. Ishizuka et al., "Performance of a computer-aided diagnosis system in diagnosing early gastric cancer using magnifying endoscopy videos with narrow-band

Research Article

Effect of Mirena Intrauterine Device on Endometrial Thickness, Quality of Life Score, and Curative Effect in Patients with Perimenopausal Abnormal Uterine Bleeding

Ying Yu,¹ Zhi Zhou,¹ Liping Wang,² and Jie Liu ³

¹Reproductive Medicine Center, Huanggang Central Hospital of Yangtze University, Huanggang, Hubei 438000, China

²Obstetrics and Gynecology Department, Tuanfeng Maternal and Child Health Hospital, Huanggang, Hubei 438000, China

³Obstetrics and Gynecology Department, Huanggang Central Hospital of Yangtze University, Huanggang, Hubei 438000, China

Correspondence should be addressed to Jie Liu; 2016120691@jou.edu.cn

Received 15 August 2022; Revised 25 August 2022; Accepted 19 September 2022; Published 30 September 2022

Academic Editor: Pan Zheng

Copyright © 2022 Ying Yu et al. This is an open access article distributed under the Creative Commons Attribution License, which permits unrestricted use, distribution, and reproduction in any medium, provided the original work is properly cited.

Objective. To study the effect of Mirena intrauterine device (IUD) on endometrial thickness, life quality score, and curative effect in patients with perimenopausal abnormal uterine bleeding. **Methods.** Eighty patients with perimenopausal abnormal uterine bleeding cured from January 2020 to December 2021 were enrolled as the object of study. According to random number table, the patients were classified into the study ($n = 40$) and control ($n = 40$) groups. The control cases were cured with medroxyprogesterone. The study cases were cured with Mirena IUD. The effective rate of clinical therapies was evaluated after 3 months of treatment. The endometrial thickness, menstrual volume score, and life quality score (WHOQOL-BREF) was measured after 1 month, 2 months, and 3 months of treatment. **Results.** The effective rate of patients with Mirena IUD for 3 months was higher compared to the control group ($P < 0.05$). The endometrial thickness and menstrual volume scores of study cohort after 1 month, 2 months, and 3 months following treatment were remarkably lower than those before treatment ($P < 0.05$) and were considerably lower than those of control cohort ($P < 0.05$). The hemoglobin level of the studied cases after 1 month, 2 months, and 3 months after therapy was remarkably upregulated ($P < 0.05$) and was greatly higher compared to the controlled cases ($P < 0.05$). After 3-month treatment, the WHOQOL-BREF score of the study group was higher compared to the control group ($P < 0.05$). **Conclusion.** The Mirena IUD is far more effective in the treatment of perimenopausal abnormal uterine bleeding and is helpful in reducing the thickness of the endometrium. Patients' menstrual flow can be controlled, and anemia can be corrected; thus, patients improve their quality of life and health status and can be considered for further promotion.

1. Introduction

Perimenopausal period is the temporary period from the decline of female ovarian function to 1 year after menopause [1]. The ovarian function of perimenopausal women gradually declined, the sensitivity and response of ovaries to pituitary gonadotropin decreased, and the negative feedback of estrogen and progesterone caused the increase of gonadotropin level [2]. The levels of thyroid-stimulating hormone (TSH) and luteinizing hormone (LH) increased remarkably, and the reflex of estrogen in the body increased, but it could not form a preovulatory peak, follicular development and

maturation reduced the disturbance of ovulation, and the level of progesterone was low [3]. The endometrium is affected by a single estrogen showing obvious proliferative changes, and the endometrium cannot be well transformed into the secretory phase [4–6].

The definition of abnormal uterine bleeding is inconsistent with any of the four items of normal menstrual frequency, regularity, menstrual duration, and menstrual bleeding volume, which comes from abnormal bleeding in the uterine cavity [7]. Under normal circumstances, the menstrual cycle of women is under the action of neuroendocrine regulation mechanism of reproductive axis (also called hypothalamus-

pituitary-ovary axis), and endometrium changes periodically and falls off. Under normal circumstances, the menstrual cycle appears regularly, which the average time is 23-37 days with menstrual volume of 20~60 ml for menstrual period of 3-7 days [8]. The hypothalamic-pituitary-ovarian system in perimenopausal women is prone to disruption due to reduced ovarian sensitivity and response to gonadotropins. The ovarian function shows the trend of decline, which follicular growth and development is relatively slow and ovulation dysfunction occurs, resulting in a significant decrease in progesterone secretion [9]. Endometrium is only affected by estrogen, and the lack of progesterone antagonistic effect and estrogen breakthrough uterine bleeding occurs, which is more likely to cause perimenopausal abnormal uterine bleeding [10-12]. The main clinical manifestations are irregular menstrual cycle, remarkably increased menstruation, prolonged menstruation, endless dripping, and secondary anemia accompanied by systemic symptoms such as dry skin, hot flashes, chest tightness, and irritability [13].

The therapeutic guidelines for perimenopausal abnormal uterine bleeding are to stop bleeding and correct anemia, to regulate the menstrual cycle, to prevent endometrial cancer, and to promote quality of life [14]. The traditional nonoperative treatment is mainly oral hormone drugs, such as medroxyprogesterone [15]. Medroxyprogesterone is a progesterone derivative of 17- α hydroxyprogesterone, which is a synthetic luteal progesterone. In the treatment of perimenopausal abnormal uterine bleeding, high levels of medroxyprogesterone cause endometrial atrophy and inhibit the formation of local blood vessels in the endometrium, thereby altering the uterine microenvironment and promoting blood clotting [16]. Mirena, also known as levonorgestrel intrauterine birth control system (LNG-IUS), is an efficient and safe T-shaped plastic stent contraceptive device produced by Bayer Pharmaceutical Company of Germany. It was allowed to be adopted in 1995 and has been widely applied in many European countries since 2009. Mirena contains 52 mg levonorgestrel. Its unique design structure enables it to release levonorgestrel at a uniform rate at the dose of 20 μ g/24h, which can be maintained for about 5 years. The levonorgestrel drug and the contraceptive ring are capable of acting directly on the uterine cavity, causing the expression of progesterone and estrogen receptors to be downregulated. The endometrium becomes less sensitive to estrogen and progesterone and therefore gradually shrinks and thins, eventually leading to reduced menstruation. It can be adopted for contraception and treatment of menorrhagia caused by nonorganic diseases [17]. Only 10% of levonorgestrel is absorbed into the blood circulation, so Mirena has almost no endocrine effect on ovarian function, and patients with perimenopausal abnormal uterine bleeding do not need long-term oral hormone drugs [18]. Under this background, it is very necessary to carry out related research, which can clarify the role of Mirena intrauterine device (IUD) when treating perimenopausal patients with abnormal uterine bleeding, which will provide a certain basis for clinicians to judge the condition of patients. Based on this, this study focused on 80 cases of perimenopausal abnormal uterine bleeding cured in our hospital from January 2020 to December 2021.

2. Patients and Methods

2.1. General Information. Eighty patients with perimenopausal abnormal uterine bleeding cured from January 2020 to December 2021 were enrolled in our hospital as the object of study. Eighty patients were arbitrarily classified into the study ($n = 40$) and control ($n = 40$) groups. The age of study cases was 41-55 years old; their average age was 45.36 ± 4.22 years old, and the average course of disease was 7.15 ± 4.38 months. The age of control cases was 40-56 years old; their average age was 45.42 ± 4.17 years old, and the average course of disease was 7.19 ± 4.41 months. There exhibited no significant difference in sex, age, and course of disease ($P > 0.05$). This study was approved by the Medical Ethics Society of our hospital. All patients have signed an informed consent form. Inclusion criteria are as follows: (1) the cases who met the diagnostic criteria of perimenopausal period, and their age was in perimenopausal period. Premenstrual syndrome (PMS) symptoms during perimenopause can mirror those of menopause symptoms, confusing women as to what exactly are they suffering from and what initiatives they should take to find relief. It usually starts in your mid-40s, but it can start earlier. Completing menopause before age 40 is called premature menopause; (2) the patients who were diagnosed by hysteroscopy or directly diagnosed as perimenopausal abnormal uterine bleeding after uterine curettage; (3) the patients who had no heart, liver, kidney, and other medical complications; (4) the patients without fertility requirements; (5) the patients who could successfully complete follow-up; (6) the patients cured with Mirena and medroxyprogesterone.

Exclusion criteria are as follows: (1) pregnancy-related bleeding; (2) reproductive organ tumor; (3) systemic inflammatory reaction; (4) coagulation dysfunction and liver, kidney, endocrine diseases, and abnormal development of reproductive organs; (5) irregular vaginal bleeding caused by exogenous hormones and foreign bodies; (6) gynecological infection; (7) urinary system infection; (8) history of infectious abortion within 3 months; (9) hypersensitivity to levonorgestrel and medroxyprogesterone.

2.2. Treatment Methods

2.2.1. Technical Route. The technical route of this research is displayed as indicated in Figure 1. Patients were recruited into the groups. The control group was given implementation of medroxyprogesterone treatment. The research group was given implementation of the treatment of Mirena IUD. The effective rate of clinical treatment after 3-month treatment and the endometrial thickness, menstrual volume score, and quality of life score (WHOQOL-BREF) were compared at 1 month, 2 months, and 3 months after treatment.

2.2.2. Intervention Program. After the patient completed blood routine, urine routine, blood coagulation function, liver and kidney function examination, and B-ultrasound to determine the thickness of endometrium, routine diagnostic curettage was performed. Additionally, the scraped endometrial tissue was fixed with 10% formaldehyde solution and

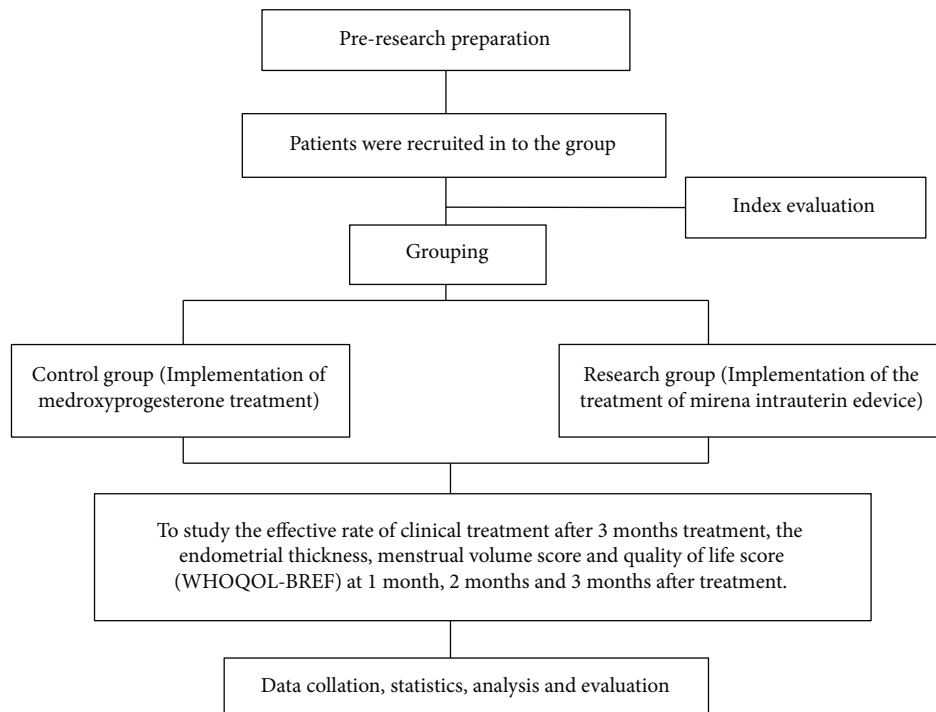


FIGURE 1: Technology roadmap.

sent for pathological examination. Endometrial malignant and precancerous lesions were excluded according to the results of pathological examination.

- (1) Control group: medroxyprogesterone (Zhejiang Xianwei Pharmaceutical Co., Ltd., specification: 2 mg/tablets) treatment; oral medroxyprogesterone 8 mg (four tablets a day) half a month after endometrial tissue curettage. The cases stopped taking medicine for 10 days and waited for endometrial exfoliation and bleeding. From the first day of bleeding, the cases would wait for half a month to start taking medicine. The continuous treatment should be last for 3 months
- (2) Study group scheme: Implement Mirena LNG-IUS was produced by Bayer, Germany, with specification 52 mg/branch. Its main composition is the chemical name of levonorgestrel D (-)-17 α --ethynyl-17 β -hydroxy-18-methylestrost-4- alkene-3- ketone; and the molecular formula is $C_{21}H_{28}O_2$. The core of Mirena is a white or quasi-white cylindrical structure, and the outer cover is fixed to the T-shaped longitudinal arm with an opaque film. The horizontal arm is folded away and placed in the placer. After the gynecological examination, the size and position of the uterus were determined. Mirena ring was placed in the uterus on the fifth day after curettage. After placing Mirena, the patients stayed in bed for 2 hours to observe the adverse reactions such as fever, abdominal pain, or vaginal bleeding. Regular follow-up observation was conducted after placement; if there was no obvious discomfort in the treatment effect

of the patient and the conscious effect was satisfactory, it can be taken out when the hormone level of the patient has reached menopause. Regular follow-up visits include understanding the patient's condition and assessing treatment; understanding the patient's behavioral changes and adjusting nonpharmacological treatment plans; understanding the patient's visits and medication use and evaluating the effectiveness of medication; supervising the patient's regular blood pressure, blood glucose, lipid, and related complications checks; and understanding and checking the patient's self-management. It can be removed at any time when the patient feels obviously uncomfortable or the therapeutic effect is not obvious during treatment

2.3. Observation Indicators

- (1) The effective rate of clinical treatment after 3 months of treatment was studied: from the beginning of the treatment, the patients will be followed up every month, and the patients will be informed to come to the hospital for reexamination on time. The curative effect was observed and blood routine examination and B-ultrasound were performed. The hemoglobin level and the thinning of endometrium were observed. In the meantime, the patient was asked whether there was irregular bleeding, nausea, vomiting and other discomfort, anemia, and if symptoms of anemia and fatigue were improved. The criterion for efficacy is return to normal menstrual cycles lasting 3-5 days each cycle after treatment. The patients with significantly reduced or amenorrhoeic

menses were deemed to be effective. Conversely, the patients whose vaginal bleeding did not change or worsened after treatment were considered ineffective

- (2) The thickness of endometrium before treatment, 1 month, 2 months, and 3 months after treatment was detected by color ultrasound
- (3) The menstrual volume scores before treatment, 1 month, 2 months, and 3 months after treatment were compared. Menstrual bleeding chart (PBLAC) was adopted to evaluate in this investigation [19]. PBLAC score (1) 0: no menstruation (amenorrhoea), (2) 1~10: drip bleeding, (3) 11~30: decreased menstruation, (4) 31~100: normal menstruation, (5) 100~150: menorrhagia, and (6) >150: menorrhagia
- (4) The hemoglobin level before treatment, 1 month, 2 months, and 3 months after treatment: venous blood was drawn to detect blood routine and count the amount of hemoglobin
- (5) The life quality score: WHOQOL-BREF score was adopted to evaluate the quality of life. The WHOQOL-BREF scale included 26 items, including physiology, psychology, social relations, and environment [20]. Each entry would be scored 1-5 points from light to heavy, and 3 items needed reverse score. The score of each field = the average score of the field to which it belongs $\times 4$. The higher the score in the field, the better the quality of life in the corresponding field

2.4. Statistical Analysis. The statistical analysis was calculated using SPSS24.0 software, and the statistical graphics were drawn by GraphPad Prism8.0. The measured data in accordance with normal distribution were presented by mean \pm standard deviation ($\bar{x} \pm s$). Paired sample t -test was adopted for intragroup comparison, and independent sample t -test was applied for intergroup comparison. $P < 0.05$ exhibited statistically significant. If it was not consistent, it was presented by the median (lower quartile to upper quartile). Paired sample nonparametric test was adopted for intragroup comparison, and independent sample nonparametric test was used for intergroup comparison. The grade data were tested by FISHER accurate method. $P < 0.05$ exhibited statistical significance.

3. Results

3.1. Effective Rate of Clinical Treatment after 3 Months of Treatment. After 3 months of treatment, the clinical effective rate of the study group was higher compared to the control group ($P < 0.05$, Table 1). The data indicated that Mirena IUD had more effective than medroxyprogesterone.

3.2. The Thickness of Endometrium before Treatment and 1 Month, 2 Months, and 3 Months after Treatment. Before treatment, there exhibited no significant difference in endometrial thickness ($P > 0.05$). The thickness of endometrium in the study group after 1 month, 2 months, and 3 months

TABLE 1: The effective rate of clinical therapies after 3 months of treatment.

Group	Effective (example/ %)	Valid (example/ %)	Invalid (example/ %)	Effective rate of clinical treatment (case/%)
C group ($n = 40$)	24/60.00	7/17.50	9/22.50	31/77.50
R group ($n = 40$)	30/75.00	8/20.00	2/5.00	38/95.00
χ^2 value				0.119
P value				0.731

treatment were remarkably thinner than that before treatment ($P < 0.05$), and they were greatly thinner lower than those in the control group ($P < 0.05$), as indicated in Table 2. The current results suggested that Mirena IUD could inhibit the growth of the thickness of endometrium compared with medroxyprogesterone treatment.

3.3. The Menstrual Volume Scores before Treatment and 1 Month, 2 Months, and 3 Months after Treatment. Before treatment, there exhibited no significant difference in menstrual volume score ($P > 0.05$). The menstrual volume scores of the study group at 1 month, 2 months, and 3 months after treatment were remarkably lower than those before treatment ($P < 0.05$), and they were remarkably lower than those in the control group ($P < 0.05$), as indicated in Table 3. The current results suggested that Mirena IUD could reduce the menstrual volume compared with medroxyprogesterone treatment.

3.4. The Hemoglobin Level before Treatment and 1 Month, 2 Months, and 3 Months after Treatment. Before treatment, there exhibited no significant difference in hemoglobin content ($P > 0.05$). The hemoglobin level of the study group after 1 month, 2 months, and 3 months of treatment was remarkably higher than that before treatment ($P < 0.05$), and they were remarkably higher than those in the control group ($P < 0.05$, Table 4). The current results showed that Mirena IUD could reduce the menstrual volume in order to maintain higher hemoglobin level compared with medroxyprogesterone treatment.

3.5. WHOQOL-BREF Score. There exhibited no significant difference in WHOQOL-BREF score before treatment ($P > 0.05$). After 3 months of treatment, the WHOQOL-BREF score of the study group was higher compared to the control group ($P < 0.05$, Table 5). The current results showed that Mirena IUD could improve the life quality of patients.

4. Discussion

Since the implementation of family planning in China, the aging population has also increased accordingly, and the number of people entering menopause is becoming larger and larger. According to a survey from the United Nations,

TABLE 2: The thickness of endometrium before treatment and 1 month, 2 months, and 3 months after treatment.

Thickness of endometrium (mm)	Before treatment	Treatment for 1 month	Treatment for 2 months	Treatment for 3 months
C group ($n = 40$)	13.54 ± 4.19	$11.82 \pm 3.11^*$	8.99 ± 3.08	$7.39 \pm 2.25^*$
R group ($n = 40$)	13.35 ± 4.12	$9.69 \pm 2.23^*$	$7.24 \pm 2.02^*$	$5.11 \pm 1.06^*$
t value	0.204	3.520	3.004	5.798
P value	0.838	<0.01	0.004	<0.01

Note: * was indicated that the values of after 1 month, 2 months, and 3 months of treatment were compared with that before treatment, $P < 0.05$.

TABLE 3: The menstrual volume scores before treatment, 1 month, 2 months, and 3 months after treatment.

Menstrual volume score (points)	Before treatment	Treatment for 1 month	Treatment for 2 months	Treatment for 3 months
C group ($n = 40$)	181.54 ± 15.19	$115.82 \pm 13.11^*$	$94.12 \pm 8.39^*$	$78.19 \pm 9.25^*$
R group ($n = 40$)	181.38 ± 15.12	$70.69 \pm 11.03^*$	$65.14 \pm 5.44^*$	$56.23 \pm 8.35^*$
t value	0.047	16.659	18.329	11.145
P value	0.963	<0.01	<0.01	<0.01

Note: * was indicated that the values of after 1 month, 2 months, and 3 months of treatment were compared with that before treatment, $P < 0.05$.

TABLE 4: The hemoglobin level before treatment, 1 month, 2 months, and 3 months after treatment.

Hemoglobin content value (score)	Before treatment	Treatment for 1 month	Treatment for 2 months	Treatment for 3 months
C group ($n = 40$)	73.52 ± 9.12	$80.24 \pm 9.22^*$	$90.29 \pm 9.64^*$	$97.59 \pm 9.32^*$
R group ($n = 40$)	73.49 ± 9.09	$85.08 \pm 10.13^*$	$99.31 \pm 10.65^*$	$111.36 \pm 10.14^*$
t value	0.015	2.235	3.971	6.323
P value	0.988	0.028	<0.01	<0.01

Note: * was indicated that the values of after 1 month, 2 months, and 3 months of treatment were compared with that before treatment, $P < 0.05$.

TABLE 5: The WHOQOL-BREF score before and after treatment.

WHOQOL-BREF score (score)	Before treatment	Treatment for 3 months	t	P value
C group ($n = 40$)	69.23 ± 8.37	82.09 ± 10.47	6.068	<0.01
R group ($n = 40$)	69.18 ± 8.42	102.25 ± 11.01	15.089	<0.01
t	0.027	8.392		
P value	0.979	<0.01		

the number of perimenopausal people was expected to reach 197 million by 2020 [21]. There is no clear age limit for perimenopausal period, and the time of ovarian function decline in women is different. Perimenopause means "around menopause" and refers to the time during which your body makes the natural transition to menopause, marking the end of the reproductive years [22]. Before menopause, some patients will develop symptoms associated with ovarian decline. The main manifestations are mental and emotional irritability and sleep disorders [23]. Additionally, some patients will show sparse menstruation or dripping, which symptoms will make people more irritable and nervous. In the perimenopausal period, there will be some other physical discomfort, such as slow intestinal peristalsis, loss of appetite, and fatigue without any inducement. The decline in estrogen levels will increase the incidence of cardiovascular

disease, and these subsequent symptoms and physical discomfort seriously plague perimenopausal women [24–28].

In the perimenopausal period, the follicles in the ovary are gradually exhausted, and the follicles are an important source of estrogen secretion in the female body [29]. Perimenopausal endometrium is stimulated by single estrogen for a long time. However, the proliferative endometrium cannot be converted to secretory phase due to the decrease of progesterone level, and the blood vessels and stroma of endometrium are easy to break and bleed [30]. Therefore, women approaching menopause are particularly prone to irregular uterine bleeding. Abnormal uterine bleeding is one of the most common gynecological problems in perimenopausal women. Most of the women approaching menopause are caused by abnormal uterine bleeding caused by ovulation disorders [31]. In the United States, gynecological diseases, including abnormal uterine bleeding, are the leading cause of hospitalization for women aged 45–54, accounting for 14% of the total hospitalization rate [32]. The annual cost of treatment for abnormal uterine bleeding is about \$100 million [33]. Therefore, our country will spend more and more on treating the diseases of perimenopausal women with the increase in the number of postmenopausal people. How to manage abnormal uterine bleeding effectively and economically is an important problem what we are facing.

Clinical studies have indicated that medroxyprogesterone could be adopted to treat perimenopausal abnormal

uterine bleeding, but patients had varying degrees of treatment dependence, easy to relapse after treatment [34]. Moreover, it is not easy for patients to master the method of medication, and it is difficult to use drugs regularly. Long-term unregulated use of medication is not conducive to improving the disease and can lead to recurrence or even aggravation. In addition, previous studies have indicated that long-term oral hormone drugs can increase the incidence of cardiovascular and cerebrovascular diseases, endometrial cancer, and breast cancer to a certain extent, which will bring great physical pain and psychological problems to patients to a certain extent [35]. Mirena LNG-IUS is produced by Bayer and contains 52 mg levonorgestrel, which can stably and slowly release levonorgestrel [36]. Through a sustained release system, levonorgestrel is continuously released into the target organ, where it is absorbed through the basal capillary network of the endometrium, inhibiting the synthesis of endometrial estrogen receptors, and thus antagonizing endometrial hyperplasia [37]. Therefore, a single-center randomized controlled trial was conducted to explore the effects of Mirena IUD on endometrial thickness, quality of life score, and efficacy in patients with perimenopausal abnormal uterine bleeding.

Our results displayed that the effective rate of patients with Mirena IUD for 3 months was greatly higher compared to the control cohort. The endometrial thickness and menstrual volume scores of study cohort after 1 month, 2 months, and 3 months following treatment were remarkably thinner than those before treatment and were considerably thinner than those of control cohort. The hemoglobin level of the studied cases after 1 month, 2 months, and 3 months after therapy was remarkably upregulated ($P < 0.05$) and was greatly higher compared to the controlled cases. After 3-month treatment, the WHOQOL-BREF score of the study group was higher compared to the control group. The results of this study further confirmed that Mirena IUD was effective when treating perimenopausal patients with abnormal uterine bleeding, which was more beneficial to enhance the thickness of endometrium, control menstrual volume, correct anemia, and promote the quality of life. This is mainly because Mirena is a new type of contraceptive, which combines ordinary birth control device with oral contraceptive, giving full play to their advantages [38]. The females with abnormal uterine bleeding in perimenopausal period are older and have relatively poor tolerance to drug metabolism and side effects. The long-term use of hormone drugs will lead to cardiovascular disease, osteoporosis, insomnia, depression, and other adverse events [39]. Moreover, 20ug levonorgestrel is released daily and directly acted on the uterine cavity following placement in the uterine cavity. Because the concentration in the serum is very low, it has almost no effect on the ovaries, and the systemic side effects will be greatly reduced.

Zhao et al. conducted a questionnaire survey on 1021 Chinese women who used Mirena in 12 different cities [40]. That results suggested 41% of the patients adopted the Mirena Ring because of abnormal uterine bleeding, most of the patients had less uterine bleeding during the use, and more than 90% of the patients consciously had better out-

comes. A study on the treatment of bleeding with medroxyprogesterone and medroxyprogesterone indicated that the Mirena group remarkably improved the hyperplasia of endometrium than the medroxyprogesterone group and the cure rate was higher than the progesterone treatment. Several studies have indicated that the endometrial thickness of the Mirena group will be further thinned during subsequent follow-up. In addition, the satisfaction of the patients and the efficacy of treatment were remarkably enhanced compared with the medroxyprogesterone group [41]. This has been consistent with the results of this study. Therefore, it can be considered that Mirena has the advantages of convenience, high compliance, and less systemic side effects when treating perimenopausal abnormal uterine bleeding. The shortcomings of this study are the small number of observed factors and the small sample size, and further clinical studies with large samples are needed.

In summary, the Mirena IUD is far more effective in the treatment of perimenopausal abnormal uterine bleeding and is helpful in reducing the thickness of the endometrium. Patients' menstrual flow can be controlled, and anemia can be corrected, and thus patients improve their quality of life and health status and can be considered for further promotion.

Data Availability

The datasets used and analyzed during the current study are available from the corresponding author upon reasonable request.

Conflicts of Interest

The authors declare that they have no conflicts of interest.

References

- [1] X. Xie and G. Wenli, *Obstetrics and Gynecology*, People's Health Publishing House, Beijing, China, 8th edition, 2014.
- [2] L. Jie, *Obstetrics and Gynecology*, People's Health Publishing House, Beijing, China, 7th edition, 2008.
- [3] J. Yu and L. Xu, "Research progress on the relationship between local endometrial microenvironment and functional uterine bleeding," *Journal of Practical Medicine*, vol. 24, no. 9, pp. 1119-1120, 2007.
- [4] M. E. D'Alton, K. M. Rood, M. C. Smid et al., "Intrauterine Vacuum-Induced Hemorrhage-Control Device for Rapid Treatment of Postpartum Hemorrhage," *Obstetrics and Gynecology*, vol. 136, no. 5, pp. 882-891, 2020.
- [5] T. A. Hunter, S. Sonalkar, C. A. Schreiber, L. K. Perriera, M. D. Sammel, and A. Y. Akers, "Anticipated Pain During Intrauterine Device Insertion," *Journal of Pediatric and Adolescent Gynecology*, vol. 33, no. 1, pp. 27-32, 2020.
- [6] S. Huiling, H. Guo, and S. Shujuan, "Clinical observation of Marvelon and norethisterone when treating peri-menopausal dysfunctional uterine bleeding," *China Health Care and Nutrition*, vol. 7, p. 204, 2012.
- [7] A. T. Evans, K. Szlachetka, and L. L. Thornburg, "Ultrasound Assessment of the Intrauterine Device," *Obstetrics and Gynecology Clinics*, vol. 46, no. 4, pp. 661-681, 2019.

- [8] X. Zhu, *Effect of Manyue Combined with Yiqi Huayu Decoction on Blood NO and Uterine Artery Blood Flow in Patients with Peri-Menopausal Dysfunctional Uterine Bleeding*, Guangzhou University of traditional Chinese Medicine, Guangzhou, China, 2014.
- [9] S. H. Averbach, Y. Ermias, G. Jeng et al., “Expulsion of intrauterine devices after postpartum placement by timing of placement, delivery type, and intrauterine device type: a systematic review and meta-analysis,” *American journal of obstetrics and gynecology*, vol. 223, no. 2, pp. 177–188, 2020.
- [10] N. Li, M. Xie, and L. Wang, “Effect of levonorgestrel intrauterine delivery system on the expression of IGF-I and IGF-II and their corresponding receptors in hyperplastic endometrium,” *Journal of practical diagnosis and Therapy*, vol. 20, no. 8, pp. 550–552, 2006.
- [11] T. Okamoto and K. Fukuda, “Bowel Perforation by Intrauterine Device,” *Clinical Gastroenterology and Hepatology*, vol. 19, no. 8, p. 79, 2021.
- [12] O. A. Adeyemi-Fowode and J. L. Bercaw-Pratt, “Intrauterine Devices: Effective Contraception with Noncontraceptive Benefits for Adolescents,” *Journal of Pediatric and Adolescent Gynecology*, vol. 32, no. 5, pp. S2–S6, 2019.
- [13] M. Enserink, “The vanishing promises of hormone replacement,” *Science*, vol. 297, no. 5580, pp. 325–326, 2002.
- [14] S. F. Peterson and L. M. Goldthwaite, “Postabortion and Postpartum Intrauterine Device Provision for Adolescents and Young Adults,” *Journal of Pediatric and Adolescent Gynecology*, vol. 32, no. 5, pp. S30–S35, 2019.
- [15] H. Yanqing, “Efficacy of Diane-35 and medroxyprogesterone when treating peri-menopausal dysfunctional uterine bleeding,” *Jilin Medicine*, vol. 43, no. 3, pp. 696–698, 2022.
- [16] L. Jie, “Comparative analysis of the efficacy of Manyue and medroxyprogesterone when treating peri-menopausal abnormal uterine bleeding,” *Chinese Practical Medicine*, vol. 16, no. 19, pp. 169–171, 2021.
- [17] M. F. Selim and A. F. Hussein, “Endothelial function in women using levonorgestrel-releasing intrauterine system (LNG-IUS),” *Contraception*, vol. 87, no. 4, pp. 396–403, 2013.
- [18] L. Gailing, “Clinical application of levonorgestrel intrauterine delivery system for non-contraception,” *International Journal of Reproductive Health/Family Planning*, vol. 29, no. 1, pp. 48–51, 2010.
- [19] Y. He, J. Qin, S. Cheng, and J. Chen, “Menstrual volume was evaluated by menstrual blood loss chart,” *Journal of Obstetrics and Gynecology*, vol. 36, no. 1, p. 51, 2001.
- [20] P. J. A. Hillard, “Practical Tips for Intrauterine Device Counseling, Insertion, and Pain Relief in Adolescents: An Update,” *Journal of Pediatric and Adolescent Gynecology*, vol. 32, no. 5, pp. S14–S22, 2019.
- [21] B. S. Shin, R. Giorgetti, and L. D. Melville, “A Woman With an Intrauterine and an Extrauterine Intrauterine Device,” *Journal of Emergency Medicine*, vol. 58, no. 5, pp. 813–814, 2020.
- [22] H. Turnbull, A. Glover, E. P. Morris, T. J. Duncan, J. J. Nieto, and N. Burbos, “Investigation and management of abnormal peri-menopausal bleeding,” *Menopause International*, vol. 19, no. 4, pp. 147–154, 2013.
- [23] H. M. Kravitz, X. Zhao, J. T. Bromberger et al., “Sleep disturbance during the menopausal transition in a multi-ethnic community sample of women,” *Sleep*, vol. 31, no. 7, pp. 979–990, 2008.
- [24] B. Yingying, “Analysis of risk factors of abnormal uterine bleeding and endometrial lesions in peri-menopausal period,” *Electronic Journal of practical Gynecology and Endocrinology*, vol. 9, no. 1, pp. 20–22, 2022.
- [25] A. J. Ti, A. H. Roe, K. C. Whitehouse, R. A. Smith, M. E. Gaffield, and K. M. Curtis, “Effectiveness and safety of extending intrauterine device duration: a systematic review,” *American Journal of Obstetrics and Gynecology*, vol. 223, no. 1, pp. 24–35, 2020.
- [26] F. Yanxia and S. Changhao, “Progress in drug treatment of peri-menopausal dysfunctional uterine bleeding,” *Journal of Clinical Military Medicine*, vol. 37, no. 3, pp. 502–504, 2009.
- [27] L. Shujuan, “Clinical research progress of Manyue when treating peri-menopausal dysovulatory abnormal uterine bleeding,” *World’s latest Medical Information Abstracts (Continuous Electronic Journals)*, vol. 20, no. 24, pp. 89–90, 2020.
- [28] S. Jianping, “Progress in drug treatment of peri-menopausal dysfunctional uterine bleeding,” *E-Journal of practical Gynecology and Endocrinology*, vol. 4, no. 25, pp. 17–19, 2017.
- [29] B. J. Van Voorhis, N. Santoro, S. Harlow, S. L. Crawford, and J. Randolph, “The relationship of bleeding patterns to daily reproductive hormones in women approaching menopause,” *Obstetrics and Gynecology*, vol. 112, no. 1, pp. 101–108, 2008.
- [30] B. I. Schwartz, M. Alexander, and L. L. Breech, “Intrauterine Device Use in Adolescents With Disabilities,” *Pediatrics*, vol. 146, no. 2, p. e20200016, 2020.
- [31] The American College of Obstetricians and Gynecologists, “Practice Bulletin No. 128,” *Obstetrics and Gynecology*, vol. 120, no. 1, pp. 197–206, 2012.
- [32] M. K. Whiteman, E. Kuklina, D. J. Jamieson, S. D. Hillis, and P. A. Marchbanks, “Inpatient hospitalization for gynecologic disorders in the United States,” *American Journal of Obstetrics and Gynecology*, vol. 202, no. 6, pp. 541.e1–541.e6, 2010.
- [33] Z. Liu, Q. V. Doan, P. Blumenthal, and R. W. Dubois, “A systematic review evaluating health-related quality of life, work impairment, and health-care costs and utilization in abnormal uterine bleeding,” *Value in Health*, vol. 10, no. 3, pp. 183–194, 2007.
- [34] J. W. Barrington, A. S. Arunkalaivanan, and M. Abdel-Fattah, “Comparison between the levonorgestrel intrauterine system (LNG-IUS) and thermal balloon ablation in the treatment of menorrhagia,” *European Journal of Obstetrics, Gynecology, and Reproductive Biology*, vol. 108, no. 1, pp. 72–74, 2003.
- [35] S. Vannuccini, S. Luisi, C. Tosti, F. Sorbi, and F. Petraglia, “Role of medical therapy in the management of uterine adenomyosis,” *Fertility and Sterility*, vol. 109, no. 3, pp. 398–405, 2018.
- [36] P. Beelen, M. J. van den Brink, M. C. Herman et al., “Levonorgestrel-releasing intrauterine system versus endometrial ablation for heavy menstrual bleeding,” *American Journal of Obstetrics and Gynecology*, vol. 224, no. 2, p. 187, 2021.
- [37] L. Polanco Pujol, E. Rodríguez Fernández, G. Bueno Chomón et al., “Intravesical migration of intrauterine device,” *Actas Urol Esp (Engl Ed)*, vol. 45, no. 1, pp. 90–91, 2021.
- [38] Y. Ma, *Clinical Study of Manyue when Treating Dysfunctional Uterine Bleeding in Peri-Menopausal Women*, Ningxia Medical University, Ningxia, China, 2015.
- [39] S. Yakun, *Satisfaction and Consultation of Levonorgestrel Intrauterine Device System*, Beijing, China, Chinese Academy of Medical Sciences, 2008.

- [40] S. Zhao, J. Deng, Y. Wang et al., "Experience and levels of satisfaction with the levonorgestrel-releasing intrauterine system in China: a prospective multicenter survey," *Patient Preference and Adherence*, vol. 8, pp. 1449–1455, 2014.
- [41] M. Karimi-Zarchi, R. Dehghani-Firoozabadi, A. Tabatabaie et al., "A comparison of the effect of levonorgestrel IUD with oral medroxyprogesterone acetate on abnormal uterine bleeding with simple endometrial hyperplasia and fertility preservation," *Clinical and Experimental Obstetrics & Gynecology*, vol. 40, no. 3, pp. 421–424, 2013.

Retraction

Retracted: Safety and Efficacy of Tirofiban Combined with Statins in the Perioperative Period of Intracranial Aneurysms: Systematic Review and Meta-Analysis

Computational and Mathematical Methods in Medicine

Received 27 June 2023; Accepted 27 June 2023; Published 28 June 2023

Copyright © 2023 Computational and Mathematical Methods in Medicine. This is an open access article distributed under the Creative Commons Attribution License, which permits unrestricted use, distribution, and reproduction in any medium, provided the original work is properly cited.

This article has been retracted by Hindawi following an investigation undertaken by the publisher [1]. This investigation has uncovered evidence of one or more of the following indicators of systematic manipulation of the publication process:

- (1) Discrepancies in scope
- (2) Discrepancies in the description of the research reported
- (3) Discrepancies between the availability of data and the research described
- (4) Inappropriate citations
- (5) Incoherent, meaningless and/or irrelevant content included in the article
- (6) Peer-review manipulation

The presence of these indicators undermines our confidence in the integrity of the article's content and we cannot, therefore, vouch for its reliability. Please note that this notice is intended solely to alert readers that the content of this article is unreliable. We have not investigated whether authors were aware of or involved in the systematic manipulation of the publication process.

In addition, our investigation has also shown that one or more of the following human-subject reporting requirements has not been met in this article: ethical approval by an Institutional Review Board (IRB) committee or equivalent, patient/participant consent to participate, and/or agreement to publish patient/participant details (where relevant).

Wiley and Hindawi regrets that the usual quality checks did not identify these issues before publication and have since put additional measures in place to safeguard research integrity.

We wish to credit our own Research Integrity and Research Publishing teams and anonymous and named external researchers and research integrity experts for contributing to this investigation.

The corresponding author, as the representative of all authors, has been given the opportunity to register their agreement or disagreement to this retraction. We have kept a record of any response received.

References

- [1] M. Hao, R. Liu, F. Yan, and Y. Luo, "Safety and Efficacy of Tirofiban Combined with Statins in the Perioperative Period of Intracranial Aneurysms: Systematic Review and Meta-Analysis," *Computational and Mathematical Methods in Medicine*, vol. 2022, Article ID 8264261, 7 pages, 2022.

Research Article

Safety and Efficacy of Tirofiban Combined with Statins in the Perioperative Period of Intracranial Aneurysms: Systematic Review and Meta-Analysis

Ming Hao,¹ Rui Liu,² Feiping Yan,³ and Youcai Luo ¹

¹Department of Neurosurgery, The Second Hospital of Yulin, Yilin City Shaanxi Province 719000, China

²Department of Neurology, The First Hospital of Yulin, Shaanxi Province 719000, China

³Department of Neurosurgery, The First Hospital of Yulin, Shaanxi Province 719000, China

Correspondence should be addressed to Youcai Luo; 1420140227@xs.hnit.edu.cn

Received 12 August 2022; Revised 25 August 2022; Accepted 5 September 2022; Published 30 September 2022

Academic Editor: Pan Zheng

Copyright © 2022 Ming Hao et al. This is an open access article distributed under the Creative Commons Attribution License, which permits unrestricted use, distribution, and reproduction in any medium, provided the original work is properly cited.

Objective. In order to verify the safety and effectiveness of tirofiban combined with statins in the perioperative period of intracranial aneurysms, this study adopts systematic review and meta-analysis, so as to comprehensively understand the situation of intracranial aneurysms in the perioperative period, and tirofiban combined with statins was finally determined as an effective treatment drug. **Methods.** This study used systematic retrospective analysis and selected 80 patients with intracranial aneurysms treated in our hospital from June 2021 to June 2022 as the research objects. Through conventional drugs and tirofiban combined with statins used in this study, the intracranial levels, the probability of aneurysm rupture, and postoperative complications of the two groups were observed and recorded. **Results.** The analysis of 80 patients with intracranial aneurysms showed that the influence of intracranial levels in the observation group was better than that in the reference group, the rupture of aneurysms in the observation group was lower than that in the reference group, and the incidence of postoperative complications in the observation group was lower than that in the reference group. **Conclusion.** Through simulation verification, it is concluded that tirofiban combined with statins is safe and effective in the perioperative application of intracranial aneurysms. This drug can improve vascular recanalization, reduce the incidence of cerebrovascular disease events, and reduce the incidence of rebleeding. Its therapeutic effect is worthy of wide clinical application and promotion.

1. Introduction

Intracranial aneurysms are tumor like protrusions caused by abnormal changes in local blood vessels of the intracranial cerebral artery wall, resulting in local vascular wall damage. Under the action of hemodynamic load and other related factors, they gradually expand and form abnormal protrusions. Aneurysm is a kind of cerebrovascular disease, which is very likely to have rupture and bleeding. Once rupture and bleeding occur, it will have a great impact on health, and there will be sequelae of nerve loss. When the amount of bleeding is large, it is easy to cause death. Tirofiban, as a more powerful antiplatelet drug, has an effect on platelet aggregation induced by various factors. It can inhibit platelet aggregation by inhibiting fibrinogen and platelet synthesis-

related receptors, so as to prolong the time of bleeding, inhibit thrombosis, or reduce the size of thrombosis. Tirofiban, as a representative inhibitor, is used in the treatment of intracranial aneurysm vascular embolism. This drug can not only be used for remedial treatment after thrombosis but also play a preventive role. Statins can effectively reduce the level of blood lipids; reduce the inflammatory response of vascular endothelial cells; regulate vascular endothelium, anti-inflammatory, and antioxidant; improve vascular reactivity; and play a positive role in reducing the incidence of cerebrovascular disease events. Statins can limit the occurrence and development of intracranial aneurysms and effectively reduce the risk of aneurysm rupture. Tirofiban combined with statins provides a new treatment method and direction for intracranial aneurysms and has a great

application prospect in perioperative treatment. Xiaojuan and Danfeng [1] discussed the effect of perioperative nursing combined with hyperbaric oxygen therapy in patients with intracranial aneurysms, which can effectively reduce the incidence of complications in patients with intracranial aneurysms, highlighting the importance of perioperative nursing. Di et al. [2] systematically evaluated the safety and effectiveness of tirofiban in the perioperative period of intracranial aneurysms, which can significantly reduce the occurrence of thromboembolic events and intracranial hemorrhage events. Therefore, they believed that the use of tirofiban antiplatelet therapy in the perioperative period is safe and effective and can provide evidence-based reference for clinical rational drug use. Weidong et al. [3] analyzed retrospectively the clinical data of perioperative patients with intracranial aneurysms in neurosurgery, evaluated the therapeutic effect of tirofiban in the perioperative period, and concluded that tirofiban is a safe and effective treatment for this disease by recording and analyzing the successful thrombolysis rate, intracranial hemorrhage, and discharge prognosis of patients after surgery. Gang et al. [4] summarized the perioperative complications of intravascular embolization for intracranial aneurysms, analyzed the high-risk related factors affecting the occurrence of complications, and retrospectively analyzed the patient's case data. Multivariate logistic regression showed that ischemia and hemorrhage were the perioperative complications of this disease, with a high risk of occurrence. Jian et al. [5] analyzed the clinical significance of the morphological and hemodynamic characteristics of the disease in predicting the risk of rupture and compared the morphological parameters and hemodynamic parameters of aneurysms, which is helpful to evaluate the risk of rupture. Binghao et al. [6] pointed out that the disease is a disease with a high mortality and disability rate among cerebrovascular diseases. Once aneurysmal hemorrhage occurs, it is extremely critical. The urgent task is to conduct rupture risk assessment, obtain morphological indicators of intracranial aneurysms, and deal with aneurysms with high rupture risk [6]. Gang [7] discussed that statins can effectively reduce the risk of cardiovascular disease, and the clinical guidelines recommend statins as the first-line treatment to prevent cardiovascular disease. This study is a cerebrovascular disease. Statins combined with other drugs can also effectively reduce the risk. Lin [8] retrospectively analyzed the compliance status and related factors of statins in secondary prevention of ischemic cerebrovascular disease and analyzed the risk of ischemic cerebrovascular disease with multiple correspondences. Jiali [9] systematically evaluated and meta analyzed the therapeutic effect of statins on aneurysmal hemorrhage. When the disease ruptures, blood flows into and accumulates in the subarachnoid space, causing a clinical syndrome, which is a common and very serious disease [9]. Zhouqin and Chunhua [10] collected the clinical research literature of patients with intracranial aneurysms, performed meta-analysis on the relevant literature that met the requirements, and systematically reviewed and evaluated the incidence of postoperative adverse reactions of patients. Kim (2022) et al. summarize the treatment effect and safety of patients when summariz-

TABLE 1: Changes of intracranial levels.

Group	Aneurysm diameter (cm)	Aneurysm wall thickness (μm)	TNF- α (ng/l)
Observation group	3.87 ± 0.23	0.78 ± 0.15	35.07 ± 3.75
Control group	4.78 ± 0.25	0.56 ± 0.13	89.73 ± 4.38
t	8.572	9.134	8.264
p	0.01	0.013	0.018

ing the thermal ablation treatment of intrahepatic cholangiocarcinoma [11], which can provide reference value for this study. Jie et al. [12] discussed the safety and effectiveness of intravenous tirofiban after intravascular treatment of acute cerebral infarction. Tirofiban can improve the discharge score of patients with intravascular. It has been proved that intravenous tirofiban is safe. Fuxing et al. [13] discussed the safety and effectiveness of aspirin in the treatment of ischemic cerebrovascular diseases. It has been proved that it can improve indicators and have significant treatment effect and high safety. In this study, aspirin was used as the conventional drug in the reference group to analyze the safety and effectiveness of other drugs in the treatment of cerebrovascular diseases. In this study, the general data of patients were systematically reviewed by multivariate logistic regression; from the statistical results, the feasibility and safety of tirofiban in treatment have been confirmed, which can reduce the incidence of bleeding. Combined with statins in the treatment of intracranial aneurysms during perioperative period, the activity of inhibitory factors can inhibit the development of aneurysms and further reduce the incidence of cerebrovascular disease events.

2. Meta-Analysis of Intracranial Aneurysms

2.1. Clinical Application of Tirofiban Combined with Statins. Tirofiban as a nonpeptide high selective antagonist can inhibit platelet aggregation and adhesion most rapidly, directly, and completely and can effectively prevent the binding of fibrinogen and receptor. Statins can effectively reduce the blood lipid level of patients and reduce the inflammatory reaction of vascular endothelial cells. Statins are not only aimed at cardiovascular diseases but also benefit the blood vessels of the whole body. They can reduce sclerotic plaque and prevent thrombosis. They can play an obvious therapeutic effect in the treatment of cerebrovascular diseases and have high safety.

2.2. Clinical Application of Conventional Drugs. The reference group of this study was treated with conventional drugs such as aspirin and nimodipine. Aspirin is an anticoagulant. For the thrombotic pathway, it can inhibit one or more of the many conduction pathways leading to platelet aggregation, so as to inhibit platelet aggregation and avoid the occurrence of thrombosis caused by platelet aggregation. Nimodipine is used to improve blood circulation and prevent and treat

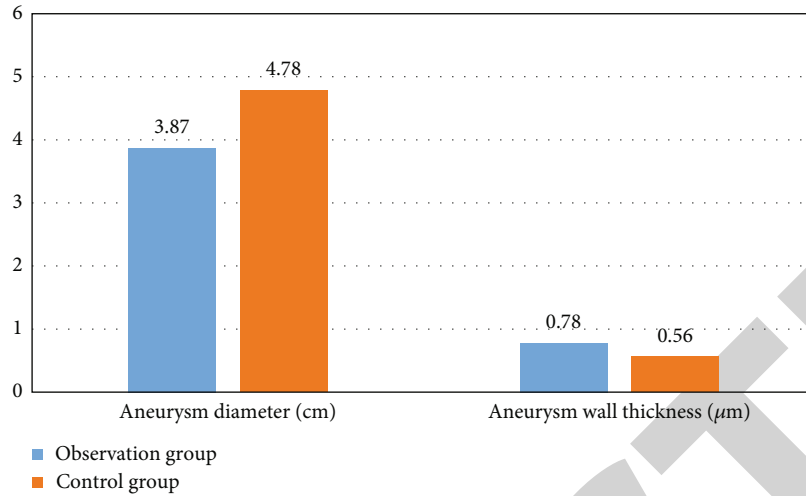


FIGURE 1: Comparison of aneurysm diameter and aneurysm wall thickness between the two groups.

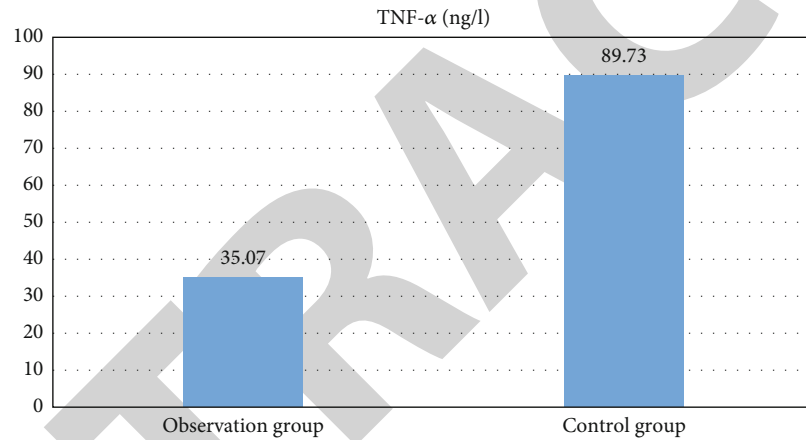


FIGURE 2: Two groups of TNF-α horizontal comparison chart.

TABLE 2: Comparison of aneurysm rupture.

Group	Intracranial hemorrhage (%)	Subarachnoid hemorrhage (%)	Head pain (%)
Observation group	2.5	3.75	5
Control group	13.75	18.75	16.25
<i>t</i>	8.453	8.612	7.685
<i>p</i>	0.015	0.009	0.02

ischemic nerve injury caused by aneurysms. The drug has a good effect on patients with vascular dementia.

2.3. Meta-Analysis of Drugs for Intracranial Aneurysms. In this study, meta-analysis was used to compare and synthesize the discussion of tirofiban combined with statins in the perioperative period of intracranial aneurysms. According to the statistical method of the research results of the problems related to the topic, relevant studies were comprehensively collected through retrieval and strictly evaluated

and analyzed one by one, and those that did not conform to the topics related to tirofiban combined statins and intracranial aneurysms, as well as the repeated publication of tirofiban combined statins. The relevant literature of intracranial aneurysms, after systematic detection, evaluation, and summary, and quantitative combined analysis in the systematic review, is helpful to explore the consistency and other differences of the therapeutic effect of tirofiban combined with statins in the treatment of intracranial aneurysms. Rigorous meta-analysis can make a more objective evaluation. The clinical similarity and methodological similarity of the included studies are good. The results of tirofiban combined with statins in the perioperative period of intracranial aneurysms in this study finally proved to be safe and effective. It has super high reliability.

3. General Information and Methods

3.1. General Information of Patients. This study adopts systematic retrospective analysis and selects 80 patients with intracranial aneurysms treated in our hospital from June

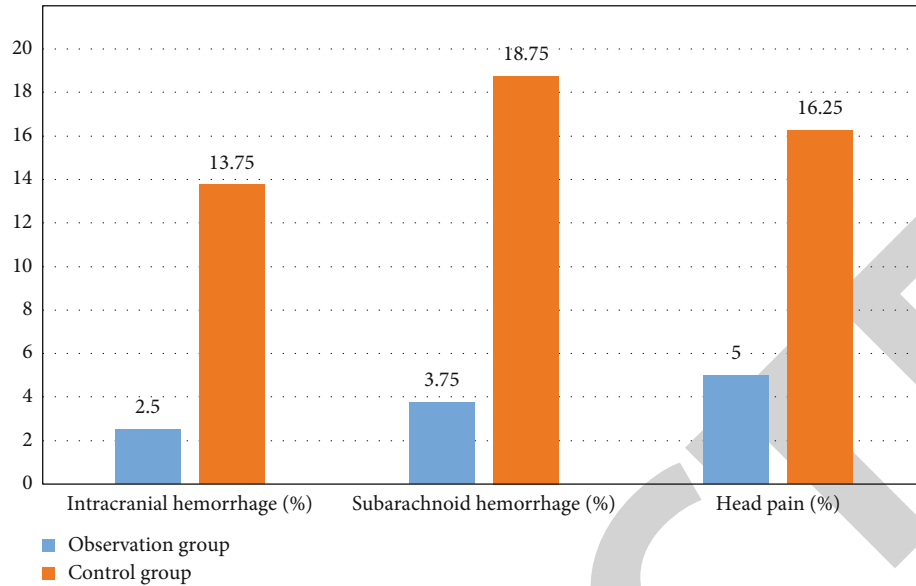


FIGURE 3: Comparison of aneurysm rupture.

TABLE 3: Comparison of postoperative complications.

Group	Hydrocephalus (%)	New cerebral infarction (%)	Recurrent aneurysm (%)
Observation group	3.75	1.25	6.25
Control group	10	13.75	16.25

2021 to June 2022 as the research object. The patients are divided into two groups according to odd and even grouping, with 40 patients in each group. Among them, 40 patients treated with conventional drugs, such as aspirin and nimodipine, were used as the reference group, including 15 male patients and 25 female patients. The age range was 40 to 75 years old, and the median age was (55.4 ± 3.8) years old; 40 patients treated with tirofiban combined with statins were used as the observation group, including 13 male patients and 27 female patients. The age range was 42 to 73 years old, and the median age was (54.1 ± 3.7) years old. After univariate t -test, the general data of the two groups were not statistically significant ($p > 0.05$), which was comparable.

3.2. Case Selection and Exclusion

3.2.1. Case Inclusion Criteria

- (1) The patient and his family members have given their informed consent and signed the informed consent form
- (2) No Alzheimer's disease or other cognitive impairment, clear consciousness, and certain expression ability
- (3) There were no other serious complications

3.2.2. Case Exclusion Criteria

- (1) Noncompliant patients
- (2) Have acute and chronic infectious diseases
- (3) Patients with a variety of basic diseases

3.3. Observation Index

- (1) Observe and record the influence of intracranial levels in the two groups
- (2) The probability of aneurysm rupture was observed and recorded in the two groups
- (3) The postoperative complications of the two groups were observed and recorded

4. Method

4.1. Perioperative Methods. Before the perioperative period, the patients were given psychological intervention to relieve the tension of the patients, explain the disease knowledge to the patients, reduce the pressure and tension of the patients, enhance the confidence of the patients, and receive treatment with the best psychological state.

After the operation of intracranial aneurysms, the patients in the reference group were treated with aspirin and nimodipine, the changes of vital signs were monitored, and the changes of the patient's condition were recorded. After the operation, the patients were asked to take an absolute lying position, and the patients were asked to relax their heads, do not use force, and do not shake their heads. Let patients have a good rest, ensure adequate nutrition and sleep, reduce intracranial pressure, pay attention to posture, and prevent rebleeding. The observation group used tirofiban combined with statins to ensure vascular recanalization. Observe and ask the patient's condition changes in time

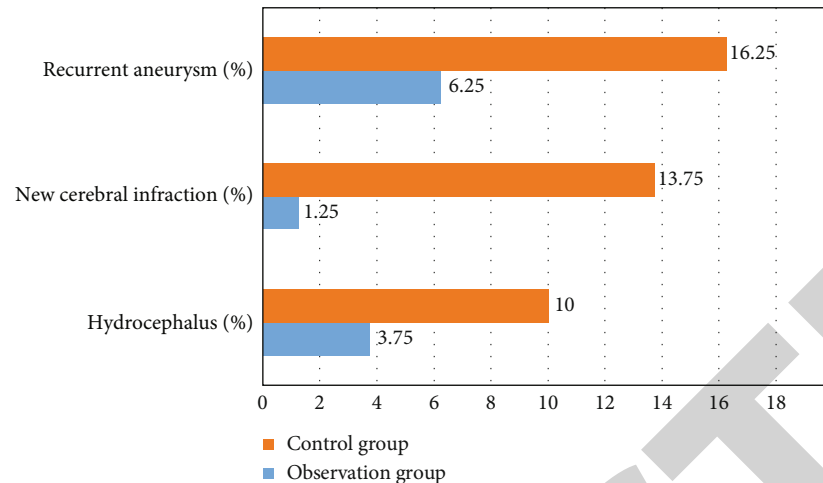


FIGURE 4: Comparison of postoperative complication rate.

during the treatment. Observe the clinical symptoms and adverse reactions of patients after medication. The effect of a reasonable safe dose of medication on a high dose will lead to aneurysm rupture. Monitor the ECG, blood vessel level, and vital signs of patients; and deal with them in time once abnormalities are found. Strictly follow the doctor's advice on medication. If the patient is found to have a slight headache, or accompanied by nausea, vomiting, and other conditions, it should be reported to the surgeon in time to check whether the patient has increased intracranial pressure.

Eat more crude fiber food, digestible food, and drink more water after operation. Drink water slowly to prevent choking reaction. Pay attention to rest, and avoid fatigue and emotional excitement. After the operation, take drugs strictly according to the doctor's advice to improve the patient's medication compliance.

4.2. Statistical Methods. The systematic review of clinical data was studied by meta-analysis using IBM SPSS 24.0 data analysis platform and Revman 5.3 software. Observe the law of data distribution, use Spearman correlation analysis method to discuss the correlation of data, and use curve estimation and linear regression analysis to observe the statistical law of data. In all analyses, the significance p value of statistical data is considered to be in the confidence space when $p < 0.05$, and the statistical result is considered to be in the absolute confidence space when $p < 0.01$.

5. Simulation Verification

5.1. Compare the Effects of the Two Methods on Intracranial Levels. After the occurrence of intracranial aneurysms, they often develop further, leading to the expansion of aneurysms, which seriously causes the injury and dysfunction of intracranial arterial endothelial cells. When drugs are used, it will have a direct impact on the diameter of aneurysm. Collagen fiber is an important part of extracellular matrix. Changes in collagen fiber synthesis will lead to changes in the thickness of aneurysm wall. Aneurysmal inflammatory factors such as TNF- α , after activation, will cause intracra-

nial inflammatory reaction. After drug treatment, it can inhibit the spread of inflammation and hinder the development of aneurysms.

At this stage, the relationship between aneurysm diameter, aneurysm wall thickness, and TNF was observed- α . The influence of intracranial level is made into Table 1 as follows.

Table 1 shows the comparison results of the two groups of data. The diameter of the aneurysm in the observation group is about 3.87 cm and that in the control group is about 4.78 cm, which is significantly smaller than that in the control group. In addition, the thickness of the aneurysm in the control group is thinner than that in the observation group, inflammatory factor TNF in control group- α More than observation group. There was a statistical relationship between $t < 10.000$ and $p < 0.05$. Through visual analysis of the above data, Figures 1 and 2 are obtained.

As shown in Figures 1 and 2, the diameter, thickness, and TNF of intracranial aneurysms in the two groups are shown- α . According to two sets of TNF- α The results of the level comparison can be seen intuitively that tirofiban combined with statins has a better therapeutic effect than conventional drugs. There is a wide gap between the two groups. This drug combined with statins can reduce inflammatory factors and improve the progress of aneurysm. All levels of intracranial are better than those of conventional drugs. It can be indirectly concluded that tirofiban combined with statins can effectively eliminate inflammation and inhibit the development of intracranial aneurysms.

5.2. Two Methods for Aneurysm Rupture. The incidence of thromboembolism in intracranial aneurysm surgery is high. Embolizing intracranial aneurysms has certain risks, and aneurysms are very fragile, so, in order to prevent and treat thromboembolism, drug intervention is needed. However, after drug intervention, platelet function will be abnormal, increasing the risk of aneurysm rupture. Tirofiban combined with statins can effectively improve the rupture of aneurysms.

Now, we study the probability of aneurysm rupture under the two methods; analyze the probability of intracranial

hemorrhage, subarachnoid hemorrhage, and head pain after rupture; and make Table 2.

As shown in Table 2, the probabilities of intracranial hemorrhage, subarachnoid hemorrhage, and head pain in the observation group were 2.5%, 3.75%, and 5%, respectively, while the probabilities of the control group were 13.75%, 18.75%, and 16.25%, respectively. There is a result of $T < 10.000$ and $p < 0.05$ between the two comparisons of the data, that is, there is a statistical difference between the data, which can be considered that different drugs have a certain impact on the rupture of aneurysms. According to the above data, Table 2 is made into a visual diagram as follows.

Tirofiban has a short half-life, and the recovery rate of platelet function is higher after the withdrawal of combined statins. According to the analysis of Figure 3, the use of tirofiban combined with statins has a small risk of aneurysm rupture, and the probability of adverse events after rupture is low. It can be considered that tirofiban combined with statins is safer than conventional drugs.

5.3. Comparison of Postoperative Complications. For intracranial aneurysms, surgery should be actively used to maintain normal blood flow. There may be a series of complications after operation, such as hydrocephalus, new cerebral infarction, or recurrent aneurysm, so drugs should be used after operation to improve the prognosis. Now compare the incidence of postoperative complications between the two groups, study and analyze the prognosis of the two groups, and make the data into Table 3.

In order to better analyze the incidence of postoperative complications in the two groups, the following Figure 4 is obtained by visualizing the data in Table 3.

Complications are the main problem after aneurysm surgery. In Table 3 and Figure 4, only one person in the observation group has a new cerebral infarction after surgery, with a probability of 1.25%, while the probability of the control group is 13.78%. The probability of complications in the observation group was significantly lower than that in the control group, and the prognosis was good. Based on the above data, it can be concluded that tirofiban combined with statins is more effective and safe in the prognosis of intracranial aneurysm surgery.

6. Summary

This study focused on the observation and analysis of the safety and effectiveness of tirofiban combined with statins in the perioperative period of intracranial aneurysms. Through statistical methods and meta-analysis, logistic regression method for systematic review and the influence data of intracranial levels in the observation group were significantly better than those in the reference group, and the aneurysm rupture rate and postoperative complication rate in the observation group were also lower than those in the reference group. It can be concluded that tirofiban combined with statins can improve vascular endothelial function, protect nerves, and resist thrombosis. It has been proved that intravenous tirofiban combined with statins is safe and effective

in the perioperative period of patients with intracranial aneurysms. Tirofiban combined with statins has an exciting prospect in the treatment of intracranial aneurysms, which can provide a good basis for subsequent treatment. To sum up, tirofiban combined with statins has an important impact on its clinical effect and has the significance of clinical treatment promotion.

Data Availability

The data underlying the results presented in the study are available within the manuscript.

Disclosure

We confirm that the content of the manuscript has not been published or submitted for publication elsewhere.

Conflicts of Interest

There is no potential conflicts of interest in our paper.

Authors' Contributions

All authors have seen the manuscript and approved to submit to your journal.

References

- [1] O. Xiaojuan and Z. Danfeng, "Effect of perioperative nursing combined with hyperbaric oxygen chamber treatment in patients with intracranial aneurysms," *Medical Equipment*, vol. 34, no. 19, pp. 189-190, 2021.
- [2] L. Di, L. Xingde, S. Cangsang, Z. Yang, and Z. Hanshu, "Meta analysis of the safety and effectiveness of tirofiban in the perioperative period of intracranial aneurysms," *China Drug Evaluation*, vol. 38, no. 5, pp. 418-424, 2021.
- [3] X. Weidong, C. Rudong, L. Hua, Z. Lingcheng, Y. Hongkuan, and Y. Jiasheng, "Tirofiban's single center experience in the treatment of stent thrombosis in intracranial aneurysms," *Chinese Journal of Stroke*, vol. 16, no. 6, pp. 556-560, 2021.
- [4] Z. Gang, Z. Xiwu, J. Che et al., "Analysis of risk factors for perioperative complications of interventional treatment of intracranial aneurysms," *Chinese Journal of Minimally Invasive Neurosurgery*, vol. 26, no. 2, pp. 58-61, 2021.
- [5] S. Jian, Z. Haihang, Y. Gongjie, T. Heping, Z. Qi, and S. Jianguo, "Clinical significance of morphological and hemodynamic characteristics of intracranial aneurysms in predicting the risk of rupture," *ECG and Circulation*, vol. 41, no. 3, pp. 272-274, 2022.
- [6] W. Binghao, S. Zhongzhou, and W. Zhi, "Research progress of morphological factors in risk assessment of intracranial aneurysm rupture," *Chinese Journal of Clinical Neurosurgery*, vol. 27, no. 3, pp. 218-220, 2022.
- [7] Z. Gang, "Reassessment of the status and significance of statins in the primary prevention of cardiovascular disease," *Chinese Journal of Cardiology*, vol. 27, no. 3, pp. 215-218, 2022.
- [8] G. Lin, "Analysis of compliance status and related factors of statins in secondary prevention of ischemic cerebrovascular disease," *Journal of Clinical Rational Drug Use*, vol. 15, no. 7, pp. 165-168, 2022.

Research Article

Deep Learning-Based Medical Data Association Rules to Explore the Connectivity and Regulation Mechanism of miRNA-mRNA Network in Myocarditis

Fang Li,¹ Jingzhe Li,² Jie Hao,¹ Jinming Liu,¹ XiuGuang Zu,¹ and Bin Wang¹ 

¹Third Division Department of Cardiology, The Second Hospital of Hebei Medical University, Shijiazhuang, Hebei 050000, China

²Clinical Medicine, Hebei Medical University, Shijiazhuang, Hebei 050017, China

Correspondence should be addressed to Bin Wang; wangbin82@hb2h.com

Received 12 August 2022; Revised 1 September 2022; Accepted 6 September 2022; Published 23 September 2022

Academic Editor: Pan Zheng

Copyright © 2022 Fang Li et al. This is an open access article distributed under the Creative Commons Attribution License, which permits unrestricted use, distribution, and reproduction in any medium, provided the original work is properly cited.

Acute, chronic myocarditis as myocardial localized or diffuse inflammation lesions is usually involving cardiac function in patients with severe adverse outcomes such as heart failure, sudden death, and no unified, but its pathogenesis clinical is mainly composed of a number of factors including infection and autoimmune defects, such as physical and chemical factors; therefore, it is of great significance to explore the regulation mechanism of myocarditis-related miRNA network connectivity and temperament for in-depth understanding of the pathogenesis of myocarditis and the direction of targeted therapy. Based on this, this study explored the miRNA network related to the pathogenesis of myocarditis through deep learning medical data association rules and analyzed its specific mechanism. The results showed that 39 upregulated miRNAs, 88 downregulated miRNAs, 109 upregulated differentially expressed miRNAs, and 589 downregulated mRNAs were obtained by data association through GSE126677 and GSE4172 databases. GO enrichment and KEGG enrichment analysis showed that the differentially expressed mRNAs were involved in the regulation of a variety of biological processes, cellular components, and molecular functions. At the same time, the miRNA with differentially expressed miRNAs and their corresponding mRNAs were connected to further clarify the specific molecular mechanism of the pathological changes of myocarditis by constructing miRNA-mRNA network. It provides effective potential molecular targets for subsequent treatment and diagnosis.

1. Introduction

As we know, the myocardium plays a role in supporting the normal work of the heart in the human body, but when it has a slight lesion, the patient's body may not feel well, and the heart function of patients with severe myocarditis will be seriously impaired, resulting in very serious consequences, such as heart failure and sudden death [1]. At present, the incidence of myocarditis is higher in winter and spring, there are different degrees of incidence probability in all age groups, and it is more common in young and middle-aged people who are usually healthy and without basic structural lesions. At the same time, there is no significant gender difference in the incidence of myocarditis, but the incidence of myocarditis is higher in long-term fatigue

group [2, 3]. At present, there is no unified conclusion on the pathogenesis of myocarditis in clinical practice, but the most common cause of myocarditis is viral infection. Second, different bacterial and fungal infections can also cause myocarditis to a certain extent, but its incidence is lower than viral infection [4]. In addition, some relevant studies have pointed out that some noninfectious factors can also cause myocarditis, such as drugs, vasculitis, and radiation [5]. The clinical manifestations and symptoms of myocarditis depend on the severity of the disease. Mild cases may have no conscious symptoms, and severe cases may even have cardiogenic shock, heart failure, severe arrhythmia, sudden death, etc. Therefore, exploring the relevant molecular mechanism of myocarditis plays an important role in preventing and organizing the progression of myocarditis [6].

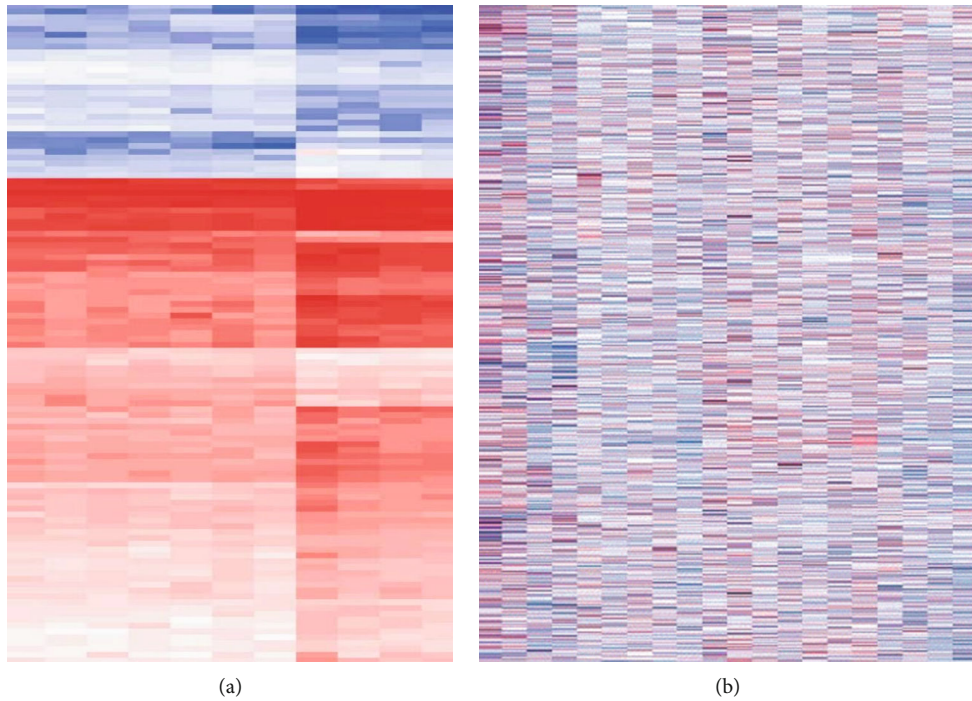


FIGURE 1: Heat map of differential expression of mRNA and miRNA.

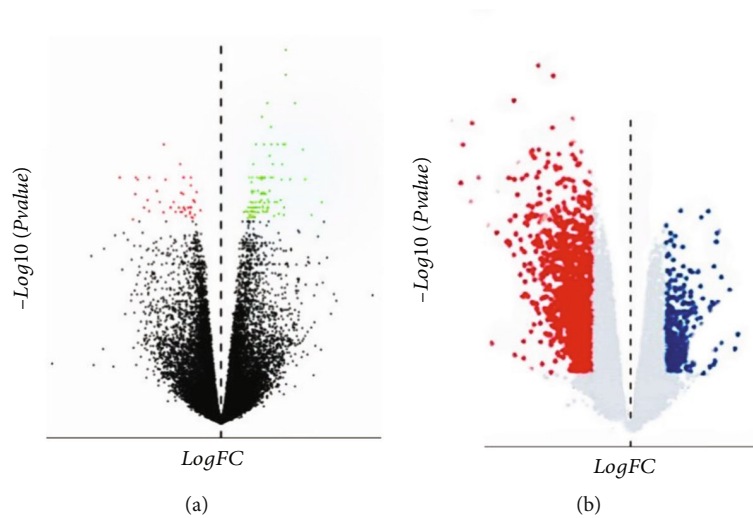


FIGURE 2: Volcano map of miRNA and mRNA differential expression. Note: (a) is the volcano map corresponding to GSE4172 database, and (b) is the volcano map corresponding to GSE126677 database. In (a) and (b), red showed high expression and blue showed low expression.

At present, with the development of gene work, the maturity of gene chip, and sequencing technology, a large amount of biological big data has been generated, which enables people's understanding of diseases to go far from the traditional pathology to the gene level and promotes the birth and development of targeted medicine [7]. Medical data are mainly based on the deep learning gene expression database (GEO) expression of disease spectrum chips on the basis of the data in the data analysis, and by using bioinformatics methods for diseases of differentially expressed genes

with the core, through the construction of protein interaction network so as to explore the pathogenesis of disease [8, 9]. At the same time, with the deepening of research, the concept of miRNA has been proposed and confirmed accordingly. As a class of noncoding RNA in cells, miRNA induces mRNA degradation or inhibits mRNA translation of its target gene by completely or incomplete binding to the 3'-untranslated region of its target gene in vivo, so as to achieve the purpose of inhibiting the expression of its target gene [10]. Current clinical research suggests the miRNA

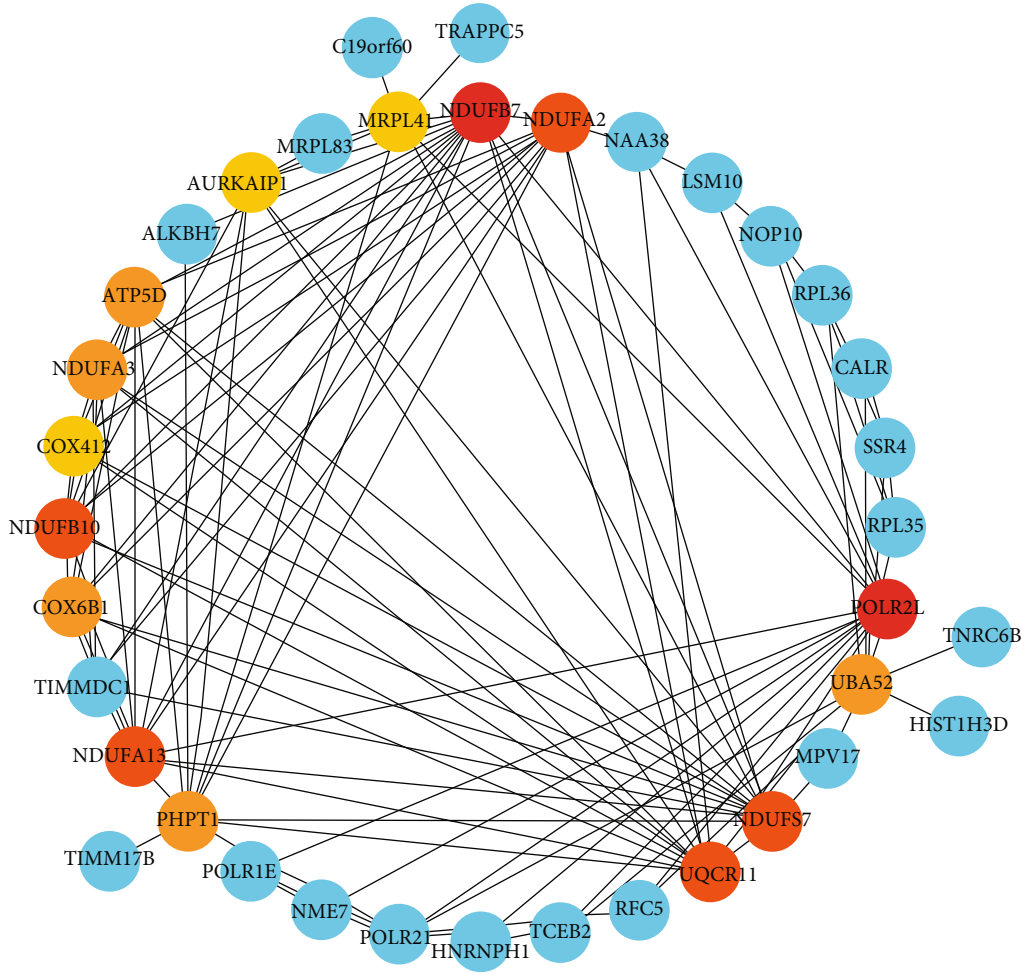


FIGURE 3: PPI network constructed by differential miRNAs.

TABLE 1: The differentially expressed mRNA data were analyzed.

Hub genes	Log FC	AveExpr	<i>t</i>	<i>P</i>
NDUFB7	-1.12	15.38	-5.83	0.001
POLR2L	-0.82	14.39	-7.53	0.008
UQCR11	-1.24	16.93	-6.43	0.042
PHPT1	-0.78	15.38	-5.93	<0.001
NDUFA3	-0.92	16.48	-5.33	0.024
AURKAIP1	-1.04	15.39	-5.82	0.019
MRPL41	-0.76	14.24	-6.93	0.005
COX4I1	-1.17	13.87	-7.38	0.027
ATP5D	-0.70	16.73	-5.61	0.031
NDUFB10	-0.87	14.38	-4.80	0.018
NDUFS7	-1.18	15.82	-6.29	<0.001
COX6B1	-0.97	14.34	-5.82	0.018
POLR2J	-0.82	15.73	-6.77	0.007

by inhibiting the expression of target genes in the body to participate in the cells of a variety of biological actions, including maintaining stem cell function, cell growth, and

apoptosis; and a growing number of studies have confirmed the miRNA can as oncogenes or tumor suppressor gene in the process of cancer development play an important role in regulation; therefore, miRNA can be used as an effective biomarker for early diagnosis, prognosis evaluation, and therapeutic effect prediction of a variety of diseases and has a wide application prospect [11].

In order to further clarify the regulatory role and mechanism of miRNAs in myocarditis, it is important to identify the differentially expressed miRNAs in myocarditis and identify their target genes. However, there are relatively few studies to analyze the relationship between miRNA-mRNA at the genome-wide level in myocarditis. Therefore, this study clarified the regulatory relationship of miRNA-mRNA in myocarditis by using in-depth medical data association rules such as gene chip and bioinformatics and did not analyze its possible molecular regulatory mechanism.

2. Data and Methods

2.1. Data Sources. The microarray dataset of gene expression profile of human myocarditis was searched in the GEO

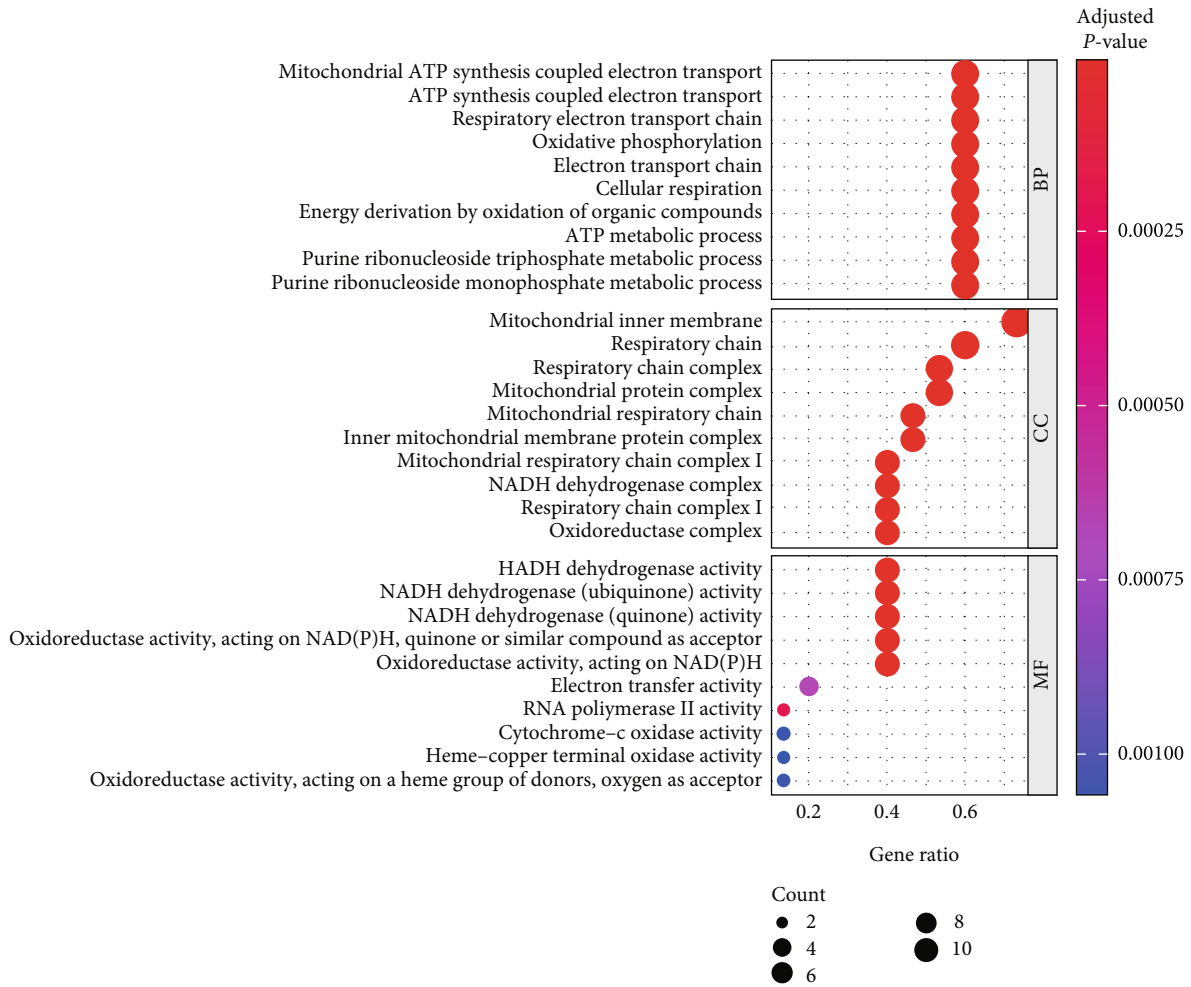


FIGURE 4: GO enrichment analysis bubble plot of miRNA differential expression.

TABLE 2: KEGG enrichment analysis.

ID	Description	P
Hsa00190	Oxidative phosphorylation	<0.001
Hsa05012	Parkinson disease	<0.001
Hsa04932	Nonalcoholic fatty liver disease	<0.001
Hsa05415	Diabetic cardiomyopathy	<0.001
Hsa03020	RNA polymerase	<0.001
Hsa04260	Cardiac muscle contraction	<0.001
Hsa04723	Retrograde endocannabinoid signaling	<0.001
Hsa05010	Alzheimer disease	<0.001
Hsa00172	Huntington disease	<0.001
Hsa05262	Pathways of neurodegeneration-multiple disease	<0.001
Hsa01824	Thermogenesis	<0.001
Hsa03745	Prion disease	<0.001
Hsa04281	Alzheimer disease	<0.001

database. The mRNA data was obtained from GSE126677, and myocardial tissue samples from 10 myocarditis patients and 5 healthy people were selected. The miRNA was derived

from the RNA sequencing data GSE4172 in the GEO database, including myocardial tissue samples from 8 myocarditis patients and 4 healthy people. The RNA was obtained

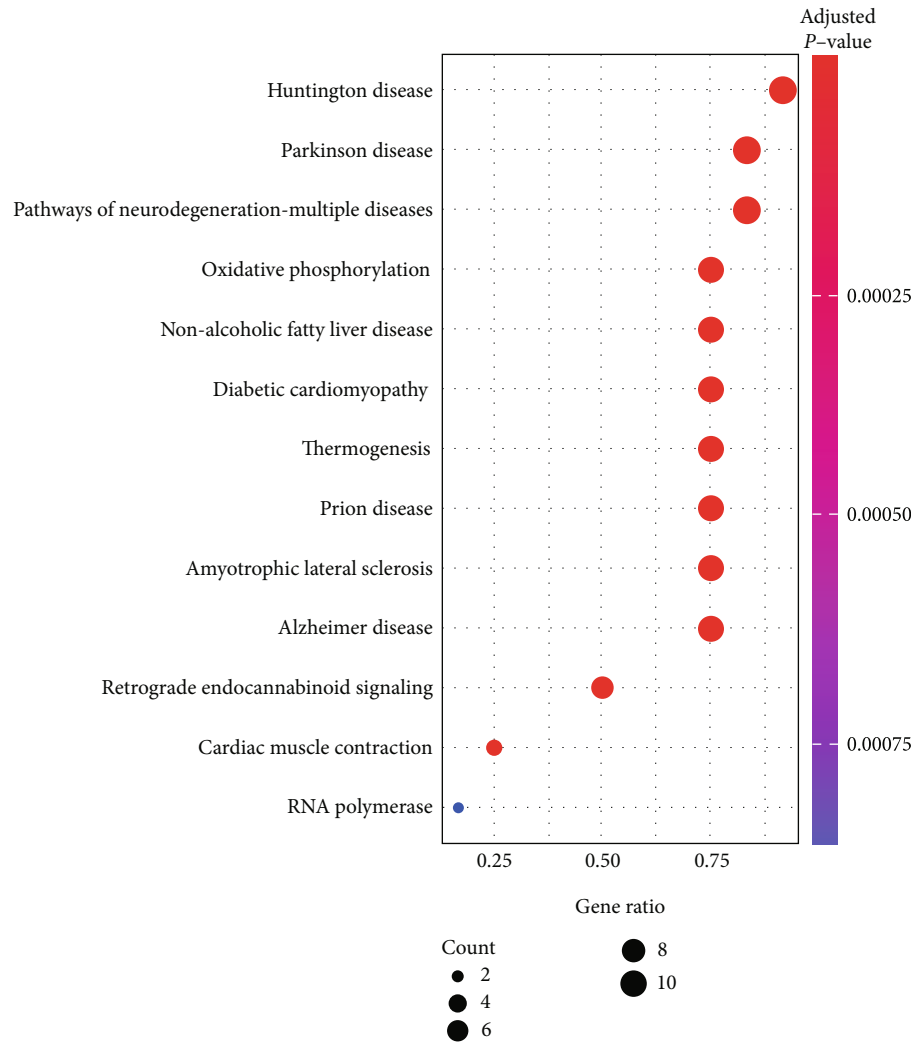


FIGURE 5: KEGG enrichment analysis bubble diagram.

from the miRNA and analyzed by gene expression profile. Affymetrix Human Genome U133 Plus 2.0 Array was used to analyze and process the gene expression profile of myocarditis, and the corresponding background correction and standardization was performed.

2.2. Methods. The differentially expressed miRNAs in myocarditis patients were analyzed by R4.0.3, and the acquired miRNA and mRNA data were standardized by Limma loading package. The differentially expressed miRNAs were obtained at $P < 0.05$, and PhestMap in R software was used to draw the required heat map. Differentially expressed miRNAs between myocarditis patients and healthy people were visualized to establish a protein-protein interaction network.

The functional enrichment analysis of differentially expressed mRNAs was annotated by biological process (BP), cell component (CC), and molecular function (MF), and the enrichment pathway of differentially expressed genes was mainly conducted by DAVID. Fun Rich3.1.3 was used to predict the target genes of differentially expressed miRNAs. The miRNA-mRNA interaction relationship was visualized by drawing Venn diagram.

2.3. Statistical Treatment. Data were analyzed by R 4.0.3, and Wilcox test was performed. Gene differential expression was analyzed by t test. $P < 0.05$ was considered statistically significant.

3. Results

3.1. Screening Differentially Expressed mRNAs and miRNAs. The results of differential gene expression analysis showed that a total of 127 miRNAs were differentially expressed in myocarditis tissues in the GSE4172 database, of which 39 were upregulated and 88 were downregulated, as shown in Figure 1(a). The GSE126677 database showed that there were 698 differentially expressed mRNAs in myocarditis tissues, of which 109 were upregulated and 589 were downregulated, as shown in Figure 1(b). The volcano plots of differential gene expression profiles were shown in Figures 2(a) and 2(b), respectively.

3.2. Construction of mRNA PPI Network and Identification of Core Genes. The constructed PPI visual network is shown in Figure 3, and a total of 13 core genes ranked

TABLE 3: miRNA and mRNA expression with potential relationship.

	Name	P	Log ₂ FC
miRNA	miR-133	<0.001	1.526
	miR-146b	<0.001	1.762
	miR-1	<0.001	2.281
	miR-146a	<0.001	1.927
	miR-27b	<0.001	1.046
	miR-320	<0.001	2.173
	miR-30a-5p	<0.001	6.423
mRNA	NDUFB7	<0.001	-1.126
	POLR2L	<0.001	-0.824
	UQCR11	<0.001	-1.246
	PHPT1	<0.001	-0.784
	NDUFA3	<0.001	-0.922
	AURKAIP1	<0.001	-1.042
	MRPL41	<0.001	-0.764
	COX411	<0.001	-1.178
	ATP5D	<0.001	-0.700
	NDUFB10	<0.001	-0.873
	NDUFS7	<0.001	-1.184
	COX6B1	<0.001	-0.973
	POLR2J	<0.001	-0.825

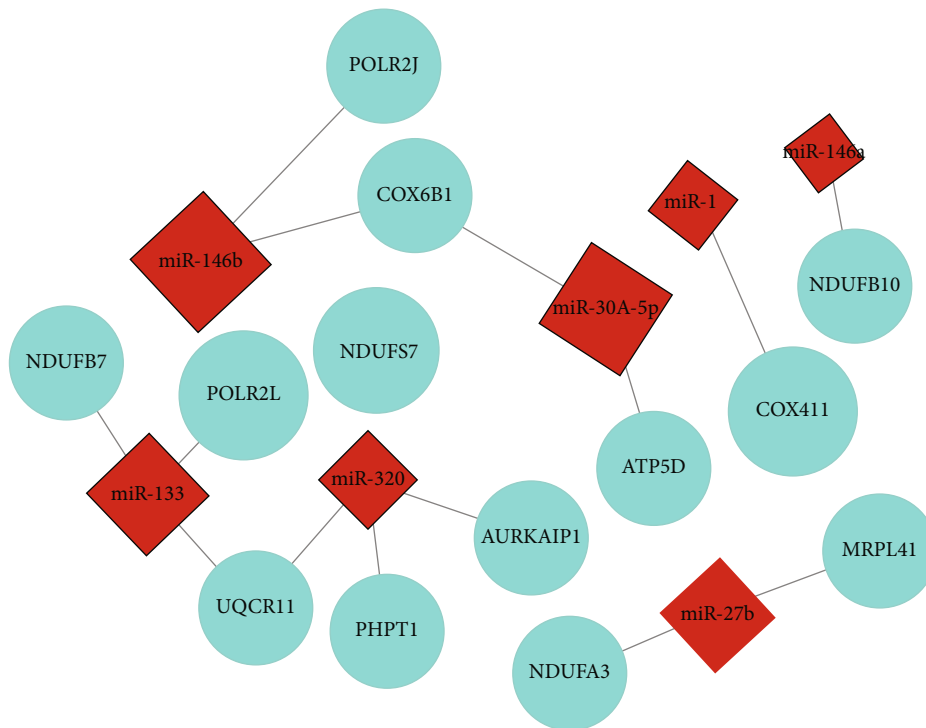


FIGURE 6: miRNA-mRNA interaction network. Note: in the figure, red represents upregulation and blue represents downregulation.

higher were screened out. The specific test data are shown in Table 1. The darker the color, the higher the degree value.

3.3. Enrichment Analysis of Differentially Expressed miRNA GO. GO analysis showed that the biological processes mainly included mitochondrial ATP synthesis coupled

electron transport, respiratory electron transport chain, oxidative phosphorylation process, cellular respiration process, and oxidative energy generation of organic compounds. Cell components include NADH dehydrogenase, mitochondrial respiratory chain complex I, and mitochondrial protein complex. Molecular functions mainly include oxidoreductase activity and NAD(P) H, RNA polymerase II activity, and cytochrome oxidase activity, as shown in Figure 4.

3.4. KEGG Enrichment Analysis. The results of KEGG enrichment of miRNAs with major differences showed that they were mainly concentrated in 13 aspects, including oxidative phosphorylation, Parkinson's disease, nonalcoholic fatty liver disease, diabetic cardiomyopathy, and myocardial contraction, as shown in Table 2 and Figure 5.

3.5. Construction of miRNA-mRNA Regulatory Network. The predicted target genes should be intersected with the downregulated differentially expressed mRNAs. A total of 13 downregulated mRNAs were obtained by drawing the Venn diagram. The expressions of related miRNAs and mRNAs are shown in Table 3, and the specific network diagram is shown in Figure 6.

4. Conclusion

Myocarditis patients according to clinical research of microRNAs can be characterized by specificity raised or lowered, with myocarditis has very close connection between onset, age is no related research illustrate myocarditis specific mechanism of the disease, but can be based on the analysis of microRNAs and mRNA expression differences on the possible molecular mechanism of speculation and provide new therapeutic targets.

4.1. The Relationship between miRNA and Myocarditis. It has been found that the upregulation of miR-21 and miR-146b can promote the differentiation of TH17 cells and increase the release of interleukin-17, thereby aggravating myocardial inflammatory response, suggesting that miR-21 and miR-146b are involved in the pathogenesis of viral myocarditis. miR-155 and miR-148a can reduce the expression of interleukin-6 and interleukin-1 β by inhibiting RelA (p65), a subunit of nuclear transcription factor κ B, while miR-146a can play a protective role in myocardium by targeting TLR3 and TRAF6 to block the nuclear transcription factor κ B pathway. miR-381 can bind to the 3'-untranslated region of COX-2 mRNA and inhibit its expression, thereby inhibiting the inflammatory response of cardiomyocytes and reducing the damage of cardiomyocytes [12, 13]. Meanwhile, in other studies, miR-34a was highly expressed in CVB3-induced myocarditis cell culture model, which resulted in the downregulation of SIRT1 expression. Other researchers have suggested that miR-217 and miR-543 have the same mechanism. SIRT1 is a core component of the SIRT1-p53 signaling pathway and an important inhibitor of apoptosis, and its downregulation further promotes apoptosis. miR-98 can affect the pathogenesis of myocarditis by binding to FAS/FASL gene targets [14, 15]. Fas is a membrane surface molecule, its ligand FASL can affect a number of apoptosis-

inducing signal transduction pathways, and miR-98 can inhibit the expression of Fas/FASL gene in cardiomyocytes by binding to Fas and FASL and then reduce cell apoptosis [16].

4.2. The Relationship between mRNA and Myocarditis. GO enrichment analysis in this study showed that the differentially expressed genes were mainly distributed in mitochondrial ATP synthesis coupled electron transport, respiratory electron transport chain, oxidative phosphorylation, respiratory chain, mitochondrial intima, NADH dehydrogenase activity, oxidoreductase activity, etc. Meanwhile, core genes were mainly enriched in oxidative phosphorylation, nonalcoholic fatty liver disease, diabetic cardiomyopathy, myocardial contraction, and other pathways. Among them, NADH is the largest protein complex in oxidative phosphorylation, and homozygous mutation in the intron of its gene will reduce the activity of the complex, thus exhibiting the clinical characteristics of hypertrophic cardiomyopathy. At the same time, Rotllan et al. [17] also pointed out that in the process of ischemia-reperfusion, if the proteolysis of NDUFS7 is increased, the activity of the complex will be reduced to varying degrees, leading to the aggravation of myocardial injury, while NDUFA13 gene knockout has a protective effect on myocardium.

COX6B1 as cytochrome magnesium sixth subcomponents, its main role is in the body by connect two cytochrome magnesium monomer into specific triggering and myocarditis, and relevant research shows COX6B1 to a certain extent can reduce the damage brought by myocardial ischemia, and the mutation can cause cardiomyopathy; however, there are relatively few basic studies on other core genes and cardiomyopathy, so the specific molecular mechanisms need to be confirmed by further studies.

In addition, KEGG analysis showed that core genes were significantly distributed in the oxidative phosphorylation pathway, suggesting that they play an important role in the process of cardiomyocyte energy metabolism. Cardiomyocyte damage is the main pathogenesis of heart failure, and the decline of cardiomyocyte function is closely related to a variety of biological processes. It is closely related to the regulation of calcium ion in cytoplasm and mitochondria, suggesting that improving the regulation of calcium ion in cardiomyocytes may be an effective therapeutic target in the clinical treatment of myocarditis.

In summary, miRNA-mRNA is involved in multiple signaling pathways that are closely related to the occurrence and development of myocarditis. Increasing the expression of miRNA-mRNA may be an effective therapeutic target for the treatment of myocarditis in clinical practice.

Data Availability

The dataset used in this paper are available from the corresponding author upon request.

Conflicts of Interest

The authors declared that they have no conflicts of interest regarding this work.

Acknowledgments

This work was sponsored in part by miR-21-5P accelerates chronic heart failure with cardiac fibrosis through activation of the STAT3 pathway (20211208).

References

- [1] M. Olejniczak, M. Schwartz, E. Webber, A. Shaffer, and T. E. Perry, "Viral myocarditis—incidence, diagnosis and management," *Journal of cardiothoracic and vascular anesthesia*, vol. 34, no. 6, pp. 1591–1601, 2020.
- [2] E. Ammirati, M. Frigerio, E. D. Adler et al., "Management of acute myocarditis and chronic inflammatory cardiomyopathy," *Circulation Heart Failure*, vol. 13, no. 11, p. e007405, 2020.
- [3] S. Dasgupta, G. Iannucci, C. Mao, M. Clabby, and M. E. Oster, "Myocarditis in the pediatric population: a review," *Congenital Heart Disease*, vol. 14, no. 5, pp. 868–877, 2019.
- [4] J. Moslehi, A. H. Lichtman, A. H. Sharpe, L. Galluzzi, and R. N. Kitsis, "Immune checkpoint inhibitor-associated myocarditis: manifestations and mechanisms," *The Journal of Clinical Investigation*, vol. 131, no. 5, article 145186, 2021.
- [5] O. Leone, M. Pieroni, C. Rapezzi, and I. Olivetto, "The spectrum of myocarditis: from pathology to the clinics," *Virchows Archiv*, vol. 475, no. 3, pp. 279–301, 2019.
- [6] C. Chen, J. Hou, J. J. Tanner, and J. Cheng, "Bioinformatics methods for mass spectrometry-based proteomics data analysis," *International Journal of Molecular Sciences*, vol. 21, no. 8, p. 2873, 2020.
- [7] R. K. Azad and V. Shulaev, "Metabolomics technology and bioinformatics for precision medicine," *Briefings in Bioinformatics*, vol. 20, no. 6, pp. 1957–1971, 2019.
- [8] D. Santesmasses, M. Mariotti, and V. N. Gladyshev, "Bioinformatics of selenoproteins," *Antioxidants & Redox Signaling*, vol. 33, no. 7, pp. 525–536, 2020.
- [9] D. Toro-Domínguez, J. Martorell-Marugán, R. López-Domínguez et al., "ImaGEO: integrative gene expression meta-analysis from GEO database," *Bioinformatics*, vol. 35, no. 5, pp. 880–882, 2019.
- [10] J. Wang and B. Han, "Dysregulated CD4+ T cells and microRNAs in myocarditis," *Frontiers in Immunology*, vol. 11, no. 11, p. 539, 2020.
- [11] Q. Q. Li, J. Xi, B. Q. Li, and N. Li, "miR-16, as a potential NF- κ B-related miRNA, exerts anti-inflammatory effects on LPS-induced myocarditis via mediating CD40 expression: a preliminary study," *Journal of Biochemical and Molecular Toxicology*, vol. 34, no. 2, p. 22426, 2020.
- [12] Y. Zhang, L. Sun, H. Sun et al., "MicroRNA-381 protects myocardial cell function in children and mice with viral myocarditis via targeting cyclooxygenase-2 expression," *Experimental and Therapeutic Medicine*, vol. 15, no. 6, pp. 5510–5516, 2018.
- [13] Y. Fei, A. Chaulagain, T. Wang et al., "miR-146a down-regulates inflammatory response by targeting TLR3 and TRAF6 in Coxsackievirus B infection," *RNA*, vol. 26, no. 1, pp. 91–100, 2020.
- [14] B. Feng, S. Chen, A. D. Gordon, and S. Chakrabarti, "miR-146a mediates inflammatory changes and fibrosis in the heart in diabetes," *Journal of molecular and cellular cardiology*, vol. 105, no. 1, pp. 70–76, 2017.
- [15] X. Chen, S. Dong, N. Zhang et al., "MicroRNA-98 plays a critical role in experimental myocarditis," *International Journal of Cardiology*, vol. 229, no. 229, pp. 75–81, 2017.
- [16] T. Liu, F. Yang, J. Liu et al., "Astragaloside IV reduces cardiomyocyte apoptosis in a murine model of coxsackievirus B3-induced viral myocarditis," *Experimental Animals*, vol. 68, no. 4, pp. 549–558, 2019.
- [17] N. Rotllan, M. Camacho, M. Tondo et al., "Therapeutic potential of emerging NAD⁺-increasing strategies for cardiovascular diseases," *Antioxidants*, vol. 10, no. 12, p. 1939, 2021.

Research Article

Weighted Gene Coexpression Network Analysis Identified IL2/STAT5 Signaling Pathway as an Important Determinant of Peri-Implantitis

Li Tang ^{1,2,3,4} Hailun Zhou ^{1,2,3,4} Donghui Chen ^{1,2,3,4} Rong Xiang ^{1,2,3,4}
and Jianjia Tang ^{1,2,3,4}

¹Department of Implant Dentistry, College of Stomatology, Guangxi Medical University, Nanning 530021, China

²Guangxi Key Laboratory of the Rehabilitation and Reconstruction of Oral and Maxillofacial Research, Nanning 530021, China

³Guangxi Colleges and Universities Key Laboratory of Treatment and Research for Oral and Maxillofacial Surgery Disease, Nanning 530021, China

⁴Guangxi Clinical Research Center for Craniofacial Deformity, Nanning 530021, China

Correspondence should be addressed to Li Tang; gxmutangli@sohu.com and Hailun Zhou; helen700229@126.com

Received 2 August 2022; Accepted 27 August 2022; Published 23 September 2022

Academic Editor: Pan Zheng

Copyright © 2022 Li Tang et al. This is an open access article distributed under the Creative Commons Attribution License, which permits unrestricted use, distribution, and reproduction in any medium, provided the original work is properly cited.

Objective. Peri-implantitis (PI) is one of the main reasons for dental implant failure. Until now, the etiology and pathogenesis of PI remain unclear. **Methods.** In this study, we used differentially expressed genes (DEGs) analysis and gene function enrichment analysis to assess the expression profile of peri-implant bone tissue and gingiva in PI public data from the Gene Expression Omnibus (GEO) database. Then, we used gingival tissues from patients with PI and healthy individual to construct gene coexpression networks to reveal the biological functions of the genes in PI using RNA sequencing data. Afterward, key gene modules were selected to reveal the critical biological process or signaling pathway using Hallmark's gene enrichment and expression analysis of the related pathway members in PI. **Results.** DEGs were enriched in the formation of cellular responses to external stimuli in bone tissue. Cytokine production, lymphocyte activation, immune response-regulating signaling pathway, and blood vessel development were the top GO biology process or pathways of the DEGs in gingival tissue. Weighted gene coexpression network analysis (WGCNA) of RNA-seq data was used to assess the results of correlation analysis between modules and traits and correlation analysis between modules and functions. kMEpurple, kMEgreen, and kMERed modules were selected as the key gene modules. Signaling pathways and gene expression analysis were performed on selected modules, such as IL2/STAT5 signaling pathway, TNF α signaling pathway via NF κ B, and angiogenesis were enriched in kMEpurple module. Hedgehog signaling pathway, Wnt β -catenin signaling pathway, and IL2/STAT5 signaling pathway were enriched in kMEgreen module. Peroxisome, IL2/STAT5 signaling pathway, and epithelial-mesenchymal transformation process were enriched in kMERed module. All the enrichment results of key modules contained IL2/STAT5 signaling pathway. **Conclusion.** Differential gene and enrichment analysis based on public data showed differences in gene expression patterns and biological process between bone and gingival tissues in PI. This spatial-temporal heterogeneity is reflected in the formation of cellular responses to external stimuli, which was enriched in bone tissue, but cytokine production, lymphocyte activation, immune response regulating signaling pathway, and blood vessel development were enriched in gingival tissue. WGCNA and Hallmark gene sets enrichment analysis of the gingival tissue expression profile and showed that IL2-mediated activation of immune cells could be a critical mechanism in PI. As a new clinical treatment alternative, we suggest that IL2/STAT5 pathway blockers could be helpful in the treatment of PI.

1. Introduction

Dental implant, because of its advantages, such as perfect retention, less damage to adjacent teeth, and less foreign body sensation, has been widely used to reconstruct aesthetic and functional problems that result from teeth loss in clinic [1]. However, peri-implantitis (PI) characterized by infection of soft tissue and bone resorption is considered to be the result of an imbalance between the bacterial challenge, and the host response can affect the long-term success rate of dental implant, which is one of the main reasons for the failure of implant [2].

Bacterial invasion in the tissue surrounding implants can trigger an immune response. This response can remove harmful substances such as bacteria and toxins. However, the cytokines, proteases, and prostaglandins produced during this process can accelerate the destruction of tissue around the implants [3]. With the growing popularity of dental implants, PI has attracted considerable attention, but the etiology and pathogenesis are still unclear [4].

Weighted gene coexpression network analysis (WGCNA) [5] aims to find gene modules for coexpression and to explore the relationship between gene networks and phenotypes of interest, as well as the hub genes in the network. WGCNA could avoid the extensive false-positive and false-negative results of prior biological methods and exclude unreasonable statistical filtering in differential gene analysis. WGCNA has been widely used in cancer research, developmental biology, and systems biology [6, 7]. However, WGCNA is rarely used in the study of oral diseases.

In this study, we analyzed the expression profiles of peri-implant bone tissue and gingiva in PI from the GEO database using differentially expressed gene analysis and gene function enrichment analysis. Then, WGCNA was used to reveal the biological functions of the genes in PI. Owing to the similarity between genes and genes in the expression profiles data of probe-based PCR microarrays, the WGCNA of microarray data was failed to screen out gene modules and gene module members with biological significance. Therefore, we collected gingival tissues from patients with PI and healthy individual to construct gene coexpression network by RNA sequencing data. Next, we selected key modules to reveal the critical biological process or signaling pathway by Hallmark gene sets enrichment analysis and expression analysis of related pathways members in PI. In this study, we wish that high-throughput sequencing technology can be used to analyze the core issues that are plaguing the study of PI. Further, avoiding problems caused by defective technical means within basic medical research of peri-implantitis.

2. Material and Methods

2.1. Microarray Data Acquisition. Gene expression data were obtained from the Gene Expression Omnibus (GEO) database (<https://www.ncbi.nlm.nih.gov/gds/>). The datasets GSE57631 and GSE33774 were queried in the database using “peri-implantitis” as the search term. GSE57631 contains 2 healthy peri-implantation bone tissues (BT_HI) and 6 peri-

implantitis bone tissues (BT_PI) of expression profiling by array. GSE33774 contains 8 healthy peri-implantation gingival tissues (GT_HI) and 7 peri-implantitis gingival tissues (GT_PI) of expression profiling by array.

2.2. Microarray Data Analysis. Z-score was used to normalize the data. Then we used the differential genes analysis of expression matrix GEO2R (<http://www.ncbi.nlm.nih.gov/geo/geo2r/>). All the genes expression profiles were normalized using the R software package. Principal component analysis (PCA) and clustering analysis of expression patterns were performed using omicshare (<http://www.omicshare.com>).

2.3. Functional Enrichment Analysis of Microarray Data. Functional enrichment analysis was performed using the Metascape database (<http://metascape.org/>). KEGG pathway, GO biological processes, reactome gene sets, canonical pathways, and CORUM ontology were selected as sources. Terms with a P value <0.01 , a minimum count of 3, and an enrichment factor >1.5 were collected and grouped into clusters based on their similarities. Kappa scores were used as a metric of similarity when performing hierarchical clustering on the enriched terms, and sub-trees with a similarity of >0.3 were considered a cluster. The most statistically significant term within a cluster was chosen to represent the cluster. All the visualizations were performed using R software.

2.4. Weighted Gene Coexpression Network Analysis of Microarray Data. WGCNA is an algorithm used in gene coexpression network identification in profiles with different traits. In this section, R software package WGCNA was used to construct weighted coexpression networks to find key gene modules of interested within different traits.

2.5. Sample Collection. Gingival tissue samples of PI and healthy individual admitted to the Affiliated Stomatological Hospital of Guangxi Medical University were collected from December 2017 to December 2018. Inclusion criteria of gingival samples were described in the consensus report of the workgroup 4 in the 2017 World Workshop on the Classification of Periodontal and Peri-Implant Diseases and Conditions [2].

To obtain PI samples, the inflamed soft tissues around the implants were removed during an open surgical debridement following currently approved protocols. Gingival tissues from patients without any clinical infection were used a control. Control patients were operated due to wisdom teeth removals or teeth needed to be removed for orthodontics.

All the patients aged 18 years and above who did not smoke or drink alcohol were included, while we excluded patients with systemic diseases and other oral diseases, such as common mucous membrane disease, jaw cyst, and tumors. This study has been reviewed and approved by the Ethics Committee of Guangxi Medical University (2017-No. 165). All the patients agreed to participate in the study and signed informed consent before surgical intervention.

2.6. RNA Sequencing. Gingival tissue gene expression profiling was performed using RNA sequencing. Library

TABLE 1: List of top 20 differentially expressed genes.

Gene	Description	logFC	P value	FDR
BT_HI-vs-BT_PI				
ZMPSTE24	Zinc metalloproteinase STE24	0.05436861	0.000425	0.418
TUBB4B	Tubulin beta 4B class IVb	0.067058028	0.000776	0.418
EIF3M	Eukaryotic translation initiation factor 3 subunit M	0.163804868	0.000305	0.418
RAB10	RAB10, member RAS oncogene family	0.144274808	0.000823	0.418
SF3A3	Splicing factor 3a subunit 3	0.040577086	0.001089	0.418
AP1G1	Adaptor related prot	0.056817586	0.001125	0.418
C20orf203	Chromosome 20 open reading frame 203	-0.129391728	0.000552	0.418
MIR15B	microRNA 15b	-0.141409803	0.000692	0.418
MIR214	microRNA 214	-0.115661557	0.000828	0.418
MIR99A	microRNA 99a	-0.073109217	0.001108	0.418
OCIAD1	OCIA domain containing 1	0.123431672	0.001013	0.418
CAV1	Caveolin 1	0.093133672	0.00071	0.418
BRK1	BRICK1 subunit of SCAR/WAVE actin nucleating complex	0.065658554	0.000527	0.418
PPP6C	Protein phosphatase 6 catalytic subunit	0.03378179	0.000684	0.418
PSMB3	Proteasome subunit beta 3	0.135521691	0.000908	0.418
PSMD10	Proteasome 26S subunit, non-ATPase 10	-0.152847334	0.000283	0.418
HIST1H2BG	Histone cluster 1 H2B family member g	0.112335029	0.000385	0.418
SNRPG	Small nuclear ribonucleoprotein polypeptide G	0.149342222	0.000241	0.418
DCTN5	Dynactin subunit 5	0.119709276	0.000526	0.418
CAPZA1	Capping actin protein of muscle Z-line subunit alpha 1	0.145481101	0.000343	0.418
GT_HI-vs-GT_PI				
NEFM	Neurofilament, medium polypeptide	-1.4062788	0.00000032	0.0106
MAPT	Microtubule associated protein tau	-1.83338262	0.00000206	0.0246
MERTK	MER proto-oncogene, tyrosine kinase	1.01973984	0.00000295	0.0246
MRC1	Mannose receptor, C type 1	1.01068439	0.00000588	0.029
GLIPR2	GLI pathogenesis related 2	0.86823054	0.00000688	0.029
SLC2A3	Solute carrier family 2 member 3	1.26464786	0.00000736	0.029
SLCO2B1	Solute carrier organic anion transporter family member 2B1	0.84589762	0.00000911	0.029
SRPX2	Sushi repeat containing protein, X-linked 2	1.27391664	0.00000938	0.029
CD14	CD14 molecule	1.33965561	0.00000996	0.029
MSR1	Macrophage scavenger receptor 1	1.17709016	0.00001044	0.029
C1QB	Complement C1q B chain	0.83761875	0.00001224	0.0313
STAC2	SH3 and cysteine rich domain 2	-1.18651859	0.00001325	0.0313
CHRNA3	Cholinergic receptor nicotinic alpha 3 subunit	-0.94702121	0.00001433	0.0313
CTGF	Connective tissue growth factor	1.32968345	0.00001505	0.0313
CASP10	Caspase 10	0.66524239	0.00001683	0.033
TLR4	Toll like receptor 4	1.40463223	0.00001948	0.036
MS4A6A	Membrane spanning 4-domains A6A	0.91872666	0.00002886	0.0494
C3AR1	Complement component 3a receptor 1	1.07948921	0.00003202	0.0494
CMAHP	Cytidine monophospho-N-acetylneuraminic acid hydroxylase, pseudogene	0.79185305	0.00003378	0.0494
SRGN	Serglycin	1.37684391	0.00003424	0.0494

construction was performed following the manufacturer's instructions provided by Illumina (San Diego, CA, USA). Samples were sequenced on an Illumina HiSeq 2500 instrument.

2.7. Weighted Gene Coexpression Network Analysis and Functional Enrichment Analysis of RNA-Seq Data. Same as

WGCNA microarray data. The number of genes arranged in the constructed modules and functional enrichment analysis was performed on genes in these modules. The corresponding genes' information was mapped to Metascape (<http://metascape.org/>).

Hallmark gene sets were used as gene annotation source. Since the construction of the Molecular Signatures Database

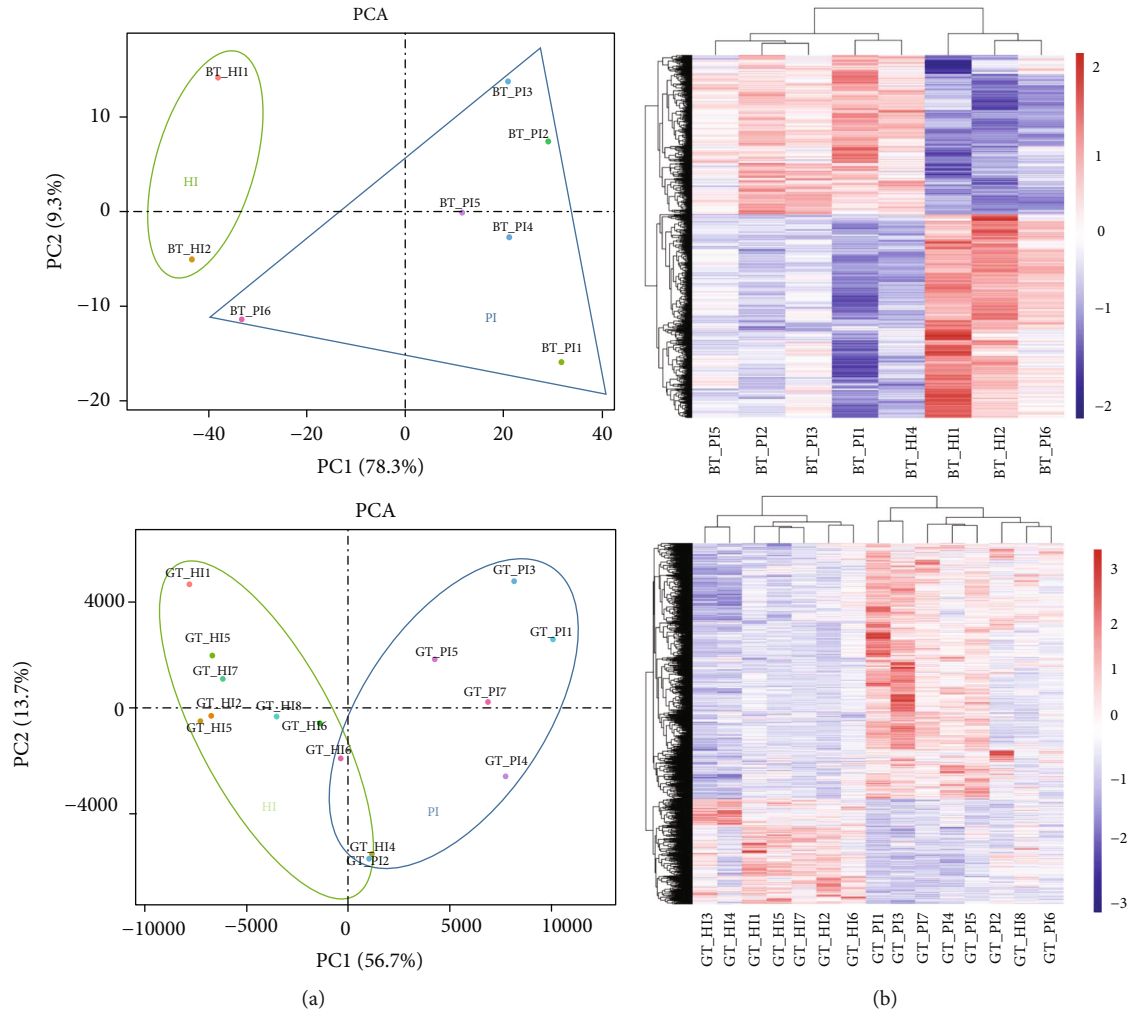


FIGURE 1: Continued.

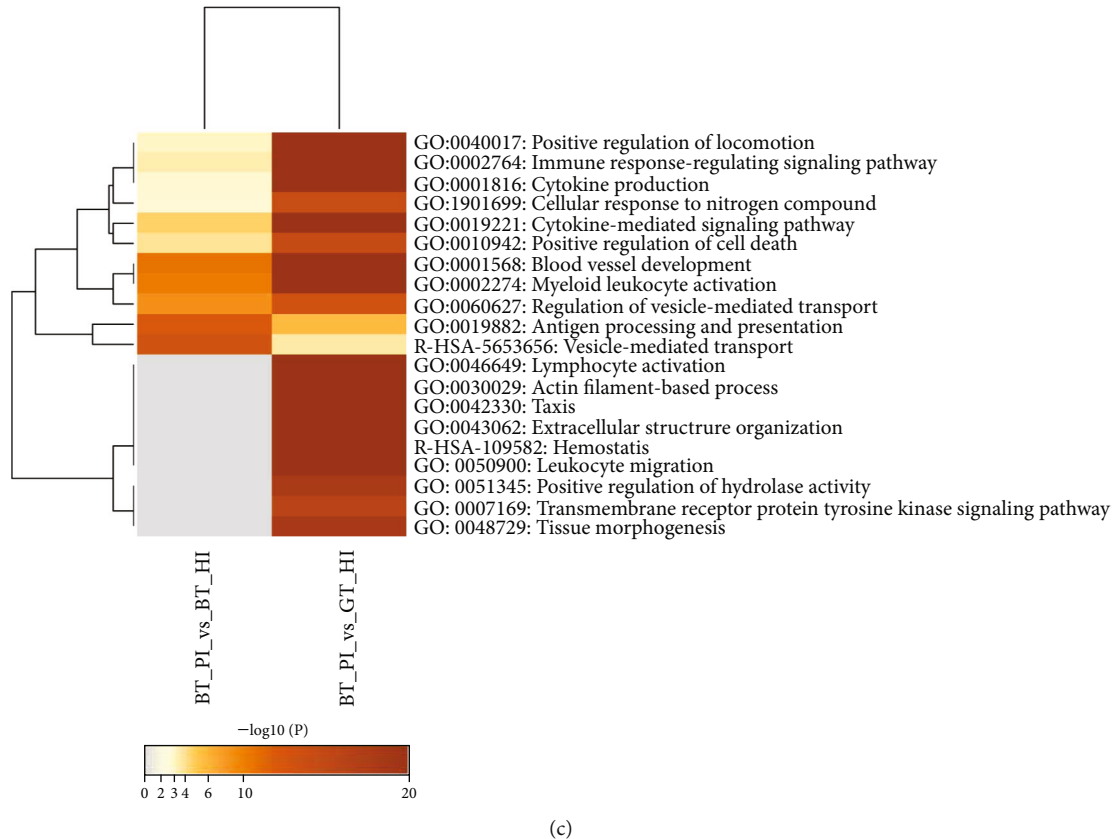


FIGURE 1: Visualization of differentially expressed gene and enrichment analysis. (a) Principal component analysis of microarray expression profiles of bone and gingival tissue. (b) Cluster analysis of microarray expression profiles of bone and gingival tissue. (c) Heatmap of enriched terms across the differentially expressed gene, colored by P values.

(MSigDB), it has been widely used as biological processes and diseases databases in metabolic disease and cancer. However, the increasing heterogeneity within gene sets is harmful to the utility of the database. Concerned with this situation, the hallmark gene sets were created as a part of MSigDB [8]. Each hallmark conveys a specific biological process and displays a coherent expression, which provides refined inputs for gene enrichment analysis. P value ≤ 0.05 after the correction was used as a threshold. The modules of interest were visualized using R software.

2.8. Statistics. The GraphPad Prism (Prism 8 for Windows, GraphPad Software Inc., San Diego, CA, USA) software was used for statistical analysis. Data obtained from the experiments are reported as the mean \pm standard deviation (SD). The difference between the two groups was determined using Student's t -test. A P value of less than 0.05 was considered statistically significant.

3. Results

3.1. Differential Expression Gene Analysis from Microarray Data. We analyzed the expression profiles of genes in 2 healthy peri-implant bone tissue samples, 6 peri-implantitis bone tissues samples, 8 healthy gingival tissue samples, and 7 peri-implantitis gingival tissues samples. The results showed that 930 upregulated mRNAs and 1189 downregu-

lated genes were identified in BT_HI-vs-BT_PI. Then 1735 significantly upregulated genes and 715 downregulated mRNAs were identified in GT_HI-vs-GT_PI. The list of top 20 DEGs is showed in Table 1.

To test the quality of the two-trait sample groups within expression profiles, the principal component analysis was used, as showed in Figure 1(a). The results of PCA analysis showed that the healthy bone tissue expression profiles and PI bone tissue of patients' expression profiles could be well distinguished, but there was a significant overlap between PI gingival tissue and healthy gingival tissue.

The expression pattern clustering the two-trait sample groups were shown in Figure 1(b). Clustering analysis of the expression patterns of genes with significant differences can adequately find the common points of expression among different genes and infer the similarity of gene functions according to the similarity of expression patterns. According to the results of the clustering analysis of expression patterns, the expression trends of gene groups with similar expression patterns in each sample can be expressed by curves. The distance calculation algorithm was used, the sample was Spearman, the gene was Pearson, and the clustering method was Hcluster.

3.2. Functional Enrichment Analysis of DEGs from Microarray Data. To test the biological function of the identified genes, information from differentially expressed genes

TABLE 2: List of top 10 enriched GO terms and pathways.

GO	Category	Description	Count	%	Log10 (P)	Log10 (q)
BT_HI-vs-BT_PI						
R-HSA-8953897	Reactome gene sets	Cellular responses to external stimuli	105	5.1	-15.97	-11.66
hsa04141	KEGG pathway	Protein processing in endoplasmic reticulum	46	2.23	-12.45	-9.03
GO:0006888	GO biological processes	ER to Golgi vesicle-mediated transport	54	2.62	-12.3	-8.94
R-HSA-6798695	Reactome gene sets	Neutrophil degranulation	86	4.18	-10.54	-7.42
R-HSA-5619115	Reactome gene sets	Disorders of transmembrane transporters	43	2.09	-9.82	-6.99
GO:0048514	GO biological processes	Blood vessel morphogenesis	105	5.1	-8.45	-5.95
GO:0006412	GO biological processes	Translation	108	5.25	-8.39	-5.91
GO:0044257	GO biological processes	Cellular protein catabolic process	110	5.34	-7.33	-5.06
R-HSA-72766	Reactome gene sets	Translation	52	2.53	-6.6	-4.44
GO:0060627	GO biological processes	Regulation of vesicle-mediated transport	81	3.93	-6.57	-4.42
GT_HI-vs-GT_PI						
GO:0002274	GO biological processes	Myeloid leukocyte activation	194	8.1	-45.73	-41.42
GO:0046649	GO biological processes	Lymphocyte activation	200	8.35	-40.59	-36.88
GO:0040017	GO biological processes	Positive regulation of locomotion	162	6.76	-33.22	-29.8
GO:0050900	GO biological processes	Leukocyte migration	143	5.97	-31.7	-28.56
GO:0001568	GO biological processes	Blood vessel development	183	7.64	-29.38	-26.44
GO:0043062	GO biological processes	Extracellular structure organization	124	5.18	-28.7	-25.81
GO:0001816	GO biological processes	Cytokine production	179	7.47	-25.89	-23.11
R-HSA-109582	Reactome gene sets	Hemostasis	147	6.14	-23.42	-20.68
GO:0002764	GO biological processes	Immune response-regulating signaling pathway	153	6.39	-22.13	-19.41
GO:0030029	GO biological processes	Actin filament-based process	164	6.84	-21.6	-18.9

were applied to the enrichment analysis using Metascape. Reactome gene sets, canonical pathways, CORUM, gene ontology (GO), and Kyoto encyclopedia of genes and genomes (KEGG) were used to obtain comprehensive functional annotations from multiple gene repositories for enrichment analysis.

The top 10 GO terms and pathways with the lowest P value of each group were shown in Table 2, and the results of the two groups enrichment were shown in Figure 1(c). DEGs were enriched in the formation of cellular responses to external stimuli in bone tissue. Moreover, cytokine production, lymphocyte activation, immune response regulating signaling pathway, and blood vessel development were the top GO biology process or pathways of DEGs in gingival tissue. It is suggested that the differential biological processes involved in the expression of gingival tissue genes and bone tissue genes may be the mechanism of spatiotemporal heterogeneity in peri-implantitis.

3.3. Weighted Gene Coexpression Network Analysis of Microarray Data. The individual gene variance in each sample was calculated according to the normalization of the expression profile. The unsigned network was constructed, selecting genes with a standard deviation higher than 1.2. The expression profiles and traits data consisted of 23 samples, 18357 genes, and 4 traits. Cluster analysis of all the samples was shown in Figure 2(a).

To ensure that the network is unsigned, the soft threshold value $\beta = 6$ was chosen. The expression profiles were transformed into the adjacency matrix and later transformed

into the topological matrix. Based on the topological overlap measure (TOM), we used the average-linkage hierarchical clustering method to cluster genes. According to the standard of a hybrid dynamic cut tree, the minimum number of bases for each gene network module was 30. After determining the gene module with a dynamic splicing method, we calculate the eigengenes of each module, then cluster the modules, merge the nearer modules into new modules, and set the height = $6.94e - 17$. Only three modules were obtained, as shown in Figure 2(b), in which the grey module is unable to aggregate into the gene set of other modules.

The gene significance of the members of module blue and turquoise was shown in Figure 2(c). The scatter plot of module kME value and gene significance value shows that higher the core value, smaller the P value, and the module members are more representative of the module characteristics.

3.4. Weighted Gene Coexpression Network Analysis of RNA-Seq Data. To test the quality of RNA sequencing within expression profiles, the principal component analysis was used, as shown in Figure 3(a). The results of PCA analysis showed that healthy gingival tissue expression profiles and PI gingival tissue of patients' expression profiles could be well distinguished, compared with the microarray data. Cluster analysis of all the samples was shown in Figure 3(b), and the gene dendrogram with traits was shown in Figure 3(c). It could be seen that genes were allocated to 11 modules, which could be used for function and module correlation analysis. According to the eigengenes of each

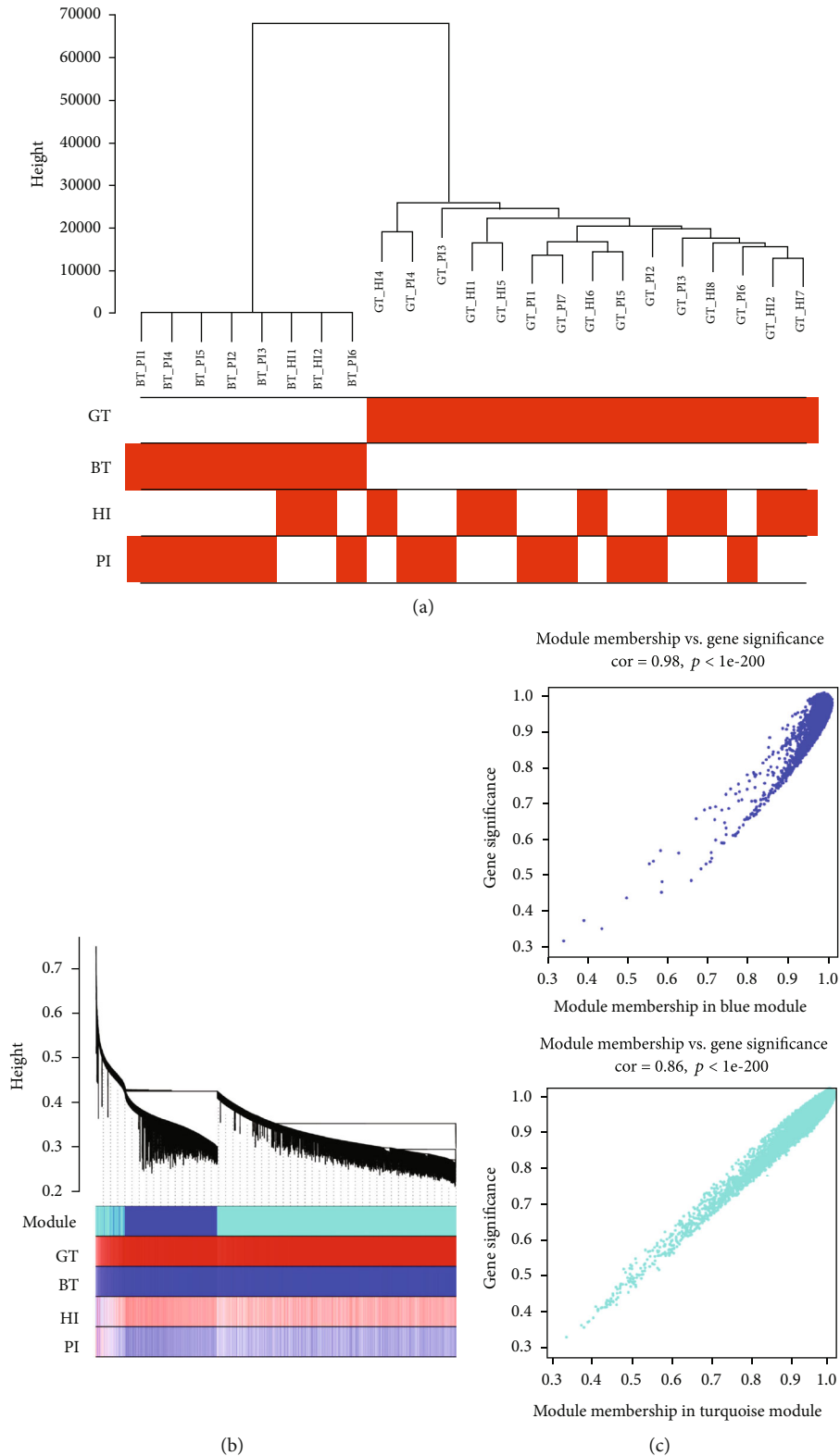


FIGURE 2: Weighted gene coexpression network analysis of microarray data. (a) Sample dendrogram and trait heatmap: the red representation in the graph is marked as nonzero samples in the trait data. (b) Gene dendrogram with trait: this figure is divided into three parts. The first part is the phylogenetic clustering tree of genes. The second part shows the module color display of the corresponding genes. The third part shows the correlation between the genes in each character-related sample and its module. The redder the color, the more positive the correlation. The negative correlation is blue. (c) Gene saliency map of module blue and turquoise members: scatter plot of module kME value and gene saliency value, higher the core value, smaller the P value, and the module members can represent the module characteristics better.

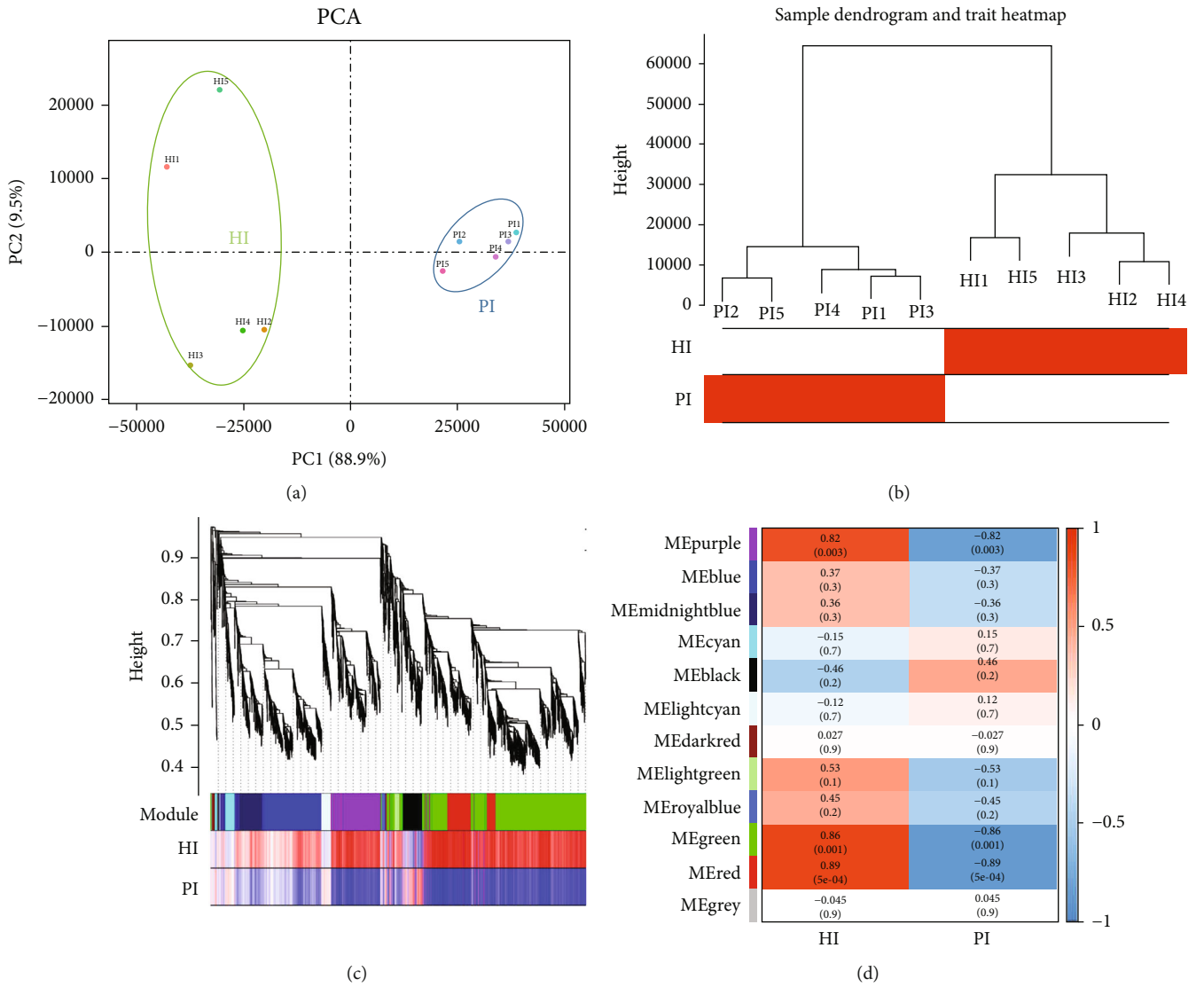


FIGURE 3: Continued.

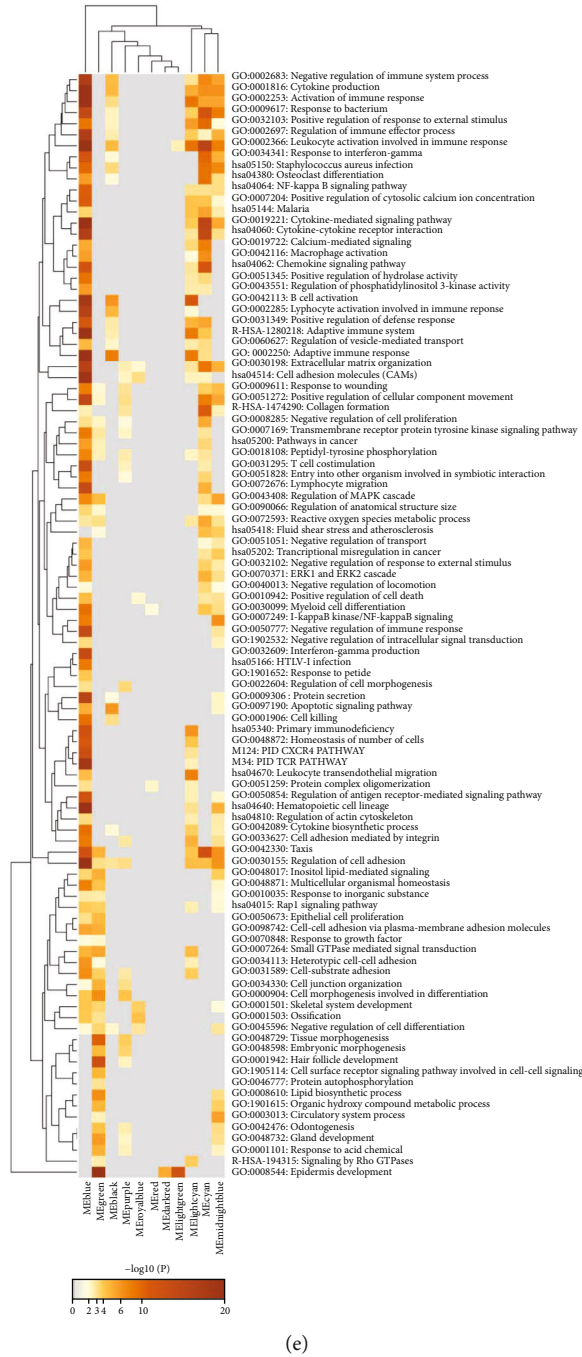


FIGURE 3: Weighted Gene coexpression network analysis of RNA-seq data. (a) Principal component analysis of RNA-seq expression profiles of gingival tissue. (b) Sample dendrogram and trait heatmap of RNA-seq data. (c) Gene dendrogram with a trait of RNA-seq data. (d) Module-trait correlation thermograms: correlation of thermograms between modules and given traits. The closer the correlation between trait and module to the absolute value of 1; the trait is related to the gene function of the module. (e) Heatmap of enriched terms across module gene members, colored by *P* values.

module, the correlation between these modules and each trait was calculated, as shown in Figure 3(d).

kME was used to evaluate the value of effective connectivity between hub genes and to identify module members. Selecting the kME > 0.7 as the members of the modules, also named hub genes, can represent better the expression trend of the entire module. To reveal the functional correlation with gene module members, all the modules hub members

were representative members of the module for gene enrichment analysis; the results were shown in Figure 3(e) and Table 3. Considering the results of the correlation analysis between modules and traits, and correlation analysis between modules and functions, the kMEpurple, kMEgreen, and kMERed modules were selected as the key gene modules. The gene significance of the members of the three modules was shown in Figure 4(a).

TABLE 3: Enrichment analysis results of modules.

Module	GO	Description	Log10 (P)
kMEblack	GO:0002250	Adaptive immune response	-7.69
	GO:0042113	B cell activation	-6.40
	GO:0097190	Apoptotic signaling pathway	-6.12
	GO:0002285	Lymphocyte activation involved in immune response	-4.83
	GO:0001816	Cytokine production	-4.63
kMEblue	GO:0001816	Cytokine production	-35.63
	GO:0030155	Regulation of cell adhesion	-33.09
	GO:0002250	Adaptive immune response	-32.10
	GO:0002366	Leukocyte activation involved in immune response	-28.75
	GO:0019221	Cytokine-mediated signaling pathway	-26.74
kMEcyan	GO:0002366	Leukocyte activation involved in immune response	-14.65
	GO:0019221	Cytokine-mediated signaling pathway	-14.53
	hsa04060	Cytokine-cytokine receptor interaction	-13.45
	GO:0042330	Taxis	-11.47
	GO:0009617	Response to bacterium	-10.84
kMEdarkred	R-HSA-6809371	Formation of the cornified envelope	-6.80
	GO:0042552	Myelination	-3.54
	GO:0008203	Cholesterol metabolic process	-3.36
	GO:0016485	Protein processing	-2.38
	M5885	NABA matrisome associated	-2.22
kMEgreen	GO:0008544	Epidermis development	-26.58
	GO:0001942	Hair follicle development	-12.11
	GO:0048729	Tissue morphogenesis	-9.51
	GO:0008610	Lipid biosynthetic process	-6.79
	GO:0000904	Cell morphogenesis involved in differentiation	-6.75
kMElightcyan	GO:0042113	B cell activation	-10.34
	GO:0002366	Leukocyte activation involved in immune response	-8.24
	GO:0002253	Activation of immune response	-8.06
	R-HSA-1280218	Adaptive immune system	-7.80
	GO:0002250	Adaptive immune response	-7.76
kMElightgreen	GO:0070268	Cornification	-13.86
	GO:0008544	Epidermis development	-11.51
	GO:0070841	Inclusion body assembly	-6.97
	R-HSA-1461957	Beta defensins	-4.12
	GO:0033559	Unsaturated fatty acid metabolic process	-2.86
kMEmidnightblue	GO:0009617	Response to bacterium	-7.61
	GO:0002366	Leukocyte activation involved in immune response	-7.51
	hsa05150	Staphylococcus aureus infection	-6.94
	GO:0007249	I-kappaB kinase/NF-kappaB signaling	-6.77
	GO:0001816	Cytokine production	-6.55
kMEpurple	GO:0000904	Cell morphogenesis involved in differentiation	-4.37
	GO:0048729	Tissue morphogenesis	-3.87
	GO:0048598	Embryonic morphogenesis	-3.62
	GO:0022604	Regulation of cell morphogenesis	-3.52
	GO:0030155	Regulation of cell adhesion	-3.29
kMERed	R-HSA-156902	Peptide chain elongation	-7.09
	R-HSA-201681	TCF dependent signaling in response to WNT	-4.97
	GO:0033131	Regulation of glucokinase activity	-3.45

TABLE 3: Continued.

Module	GO	Description	Log10 (<i>P</i>)
kMEroyalblue	GO:0051013	Microtubule severing	-3.32
	GO:0090277	Positive regulation of peptide hormone secretion	-3.28
	GO:0001503	Ossification	-4.32
	GO:0001501	Skeletal system development	-3.78
	hsa04514	Cell adhesion molecules (CAMs)	-3.35
	GO:0045596	Negative regulation of cell differentiation	-3.02
	GO:0010942	Positive regulation of cell death	-2.21

3.5. *Signaling Pathway Analysis and Gene Expression Analysis of Key Gene Modules.* The Hallmark gene sets were used as a source to reveal the critical biological process or signaling pathway of key gene modules using gene enrichment analysis. As shown in Figure 4(b), IL2/STAT5 signaling pathway, TNF α signaling pathway via NF κ B, and angiogenesis were enriched in kMEpurple module. Hedgehog signaling pathway, Wnt β -catenin signaling pathway, and IL2/STAT5 signaling pathway were enriched in kMEgreen module. Peroxisome, IL2/STAT5 signaling pathway, and epithelial-mesenchymal transformation process were enriched in kMERed module. All the enrichment results of key modules contained IL2/STAT5 signaling pathway. It is suggested that IL2-mediated activation of immune cells could be a critical mechanism in PI.

The gene expression of all the pathway members in different modules was plotted in Figure 5. The expression of some genes was inconsistent in bone and gingival tissues. More gene expressions were inconsistent in microarray and RNA sequencing data. These results confirm once again that difference in the expression of gingival tissue genes and bone tissue genes could be the mechanism of spatiotemporal heterogeneity in PI. The accuracy of gene expression profiles detected with microarray is inconsistent with RNA sequencing-based on next-generation sequencing.

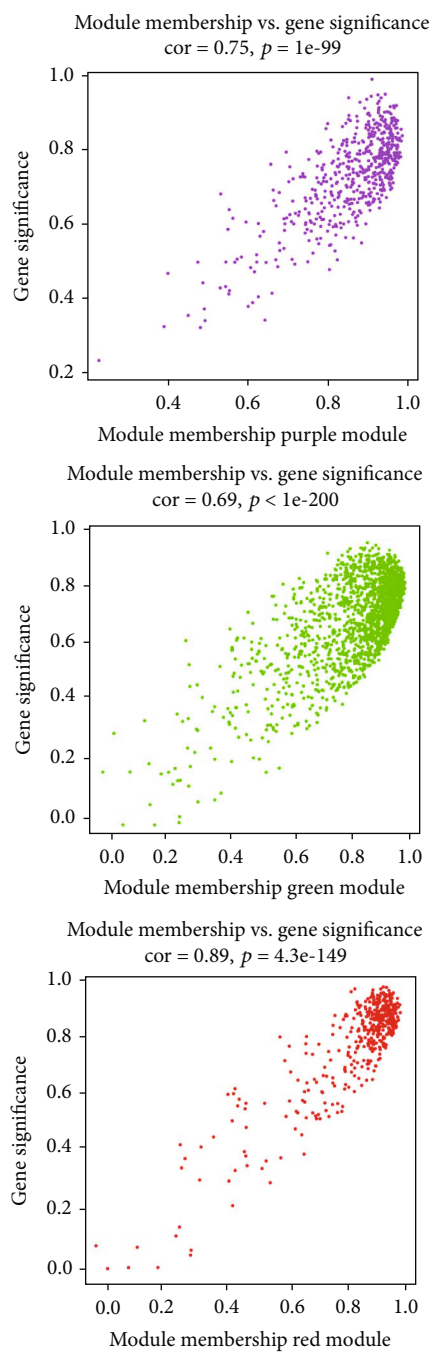
4. Discussion

The development of molecular biology and bioinformatics has revolutionized pathology. Diseases are no longer considered to be caused by abnormal expression or single genes structural changes. Dynamic network relationships between genes and multiple negative feedbacks of signal pathways are considered important regulatory models of homeostasis against pathological factors [9]. To analyze the dynamic changes of gene expression profiles, weighted gene coexpression regulation analysis was created to explore the relationship between gene networks and phenotypes. It includes three steps: calculation of correlation coefficient between genes, constructed coexpression network, and determination of gene module with traits and function [5]. In this study, we firstly used WGCNA to reveal the PI mechanism and then identified IL2/STAT5 signaling pathway as a critical element in three key modules.

Previous studies demonstrated that the expression of cytokines stimulated by exogenous factors, degradation of the extracellular matrix [10], and cellular oxidative stress

[11] is PI basic biological processes. This study confirmed these conclusions through the analysis of public databases. Moreover, through the comprehensive analysis of expression profiles, we found differences in gene expression patterns between bone and gingival tissues in PI. The differential genes of bone tissue were related to vascular growth and protein translation, processing, and transportation, while the differential genes in gingival tissues are involved in immune stress response. These differences in biological processes and cellular behavior expose the role of spatiotemporal heterogeneity in PI development. Previous studies have not considered the effects of different tissue behavior on disease occurrence. The gingival tissue is the first barrier against exogenous stimulants such as food debris, dental plaque [12], and implant dissolution [13]. It also plays a pioneering role in local tissue inflammation induced by host stress. Moreover, fibroblasts have been identified to be involved in PI pathogenesis by enhancing vascular and matrix degradation [14]. In clinical practice, uncontrolled PI has a poor prognosis leading to bone resorption, implant loosening, or loss. The proliferation of osteoclasts and apoptosis of osteoblasts is the cellular behaviors leading to this outcome. At the molecular level, active protein translation, processing, modification, and transport are the factors needed to complete this process.

The results of functional module gene enrichment analysis showed that IL2/STAT5 signaling pathway, TNF α signaling pathway via NF κ B, and angiogenesis were enriched in kMEpurple module. Hedgehog signaling pathway, Wnt β -catenin signaling pathway, and IL2/STAT5 signaling pathway were enriched in kMEgreen module. Peroxisome, IL2/STAT5 signaling pathway, and epithelial-mesenchymal transformation process were enriched in kMERed module. All the enrichment results of key modules contain IL2/STAT5 signaling pathway, has been suggested that IL2-mediated activation of immune cells play a critical mechanism in PI. IL2 receptor-dependent nuclear transcription factor STAT5 plays a key role in activating T_{reg} cells, and T_{reg} cells negatively regulate the body's immune response in vivo [15]. They usually play an important role in maintaining self-tolerance and avoiding body-injury by the immune response, but they also participate in immune surveillance and chronic infection [16, 17]. As an important pathway of host stress, the activation of Treg cells mediated by IL2/STAT5 signaling pathway is activated in PI gingival tissue. To some extent, this blocked the cascade amplification of inflammation signal and alleviated local tissue



(a)

FIGURE 4: Continued.

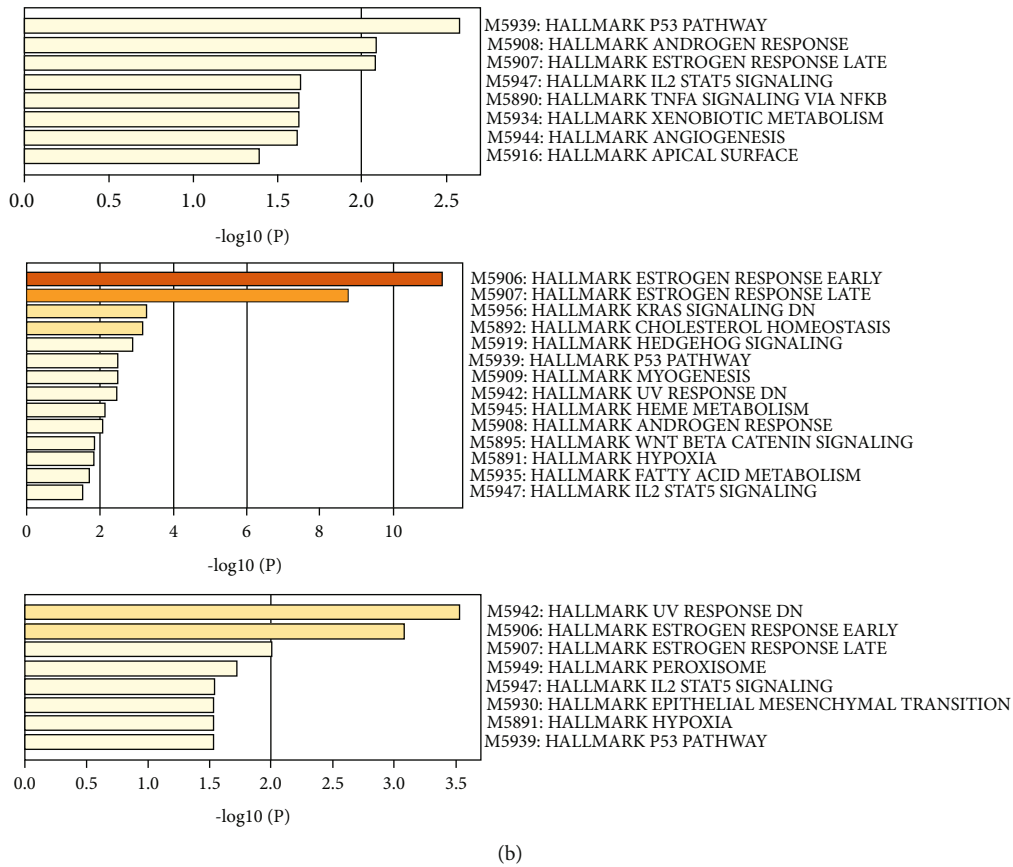


FIGURE 4: Significance analysis and signaling pathway analysis of key gene Modules. (a) Gene saliency map of module purple, green, and red members. (b) Column graphs of enriched terms across three modules genes members, colored by P values.

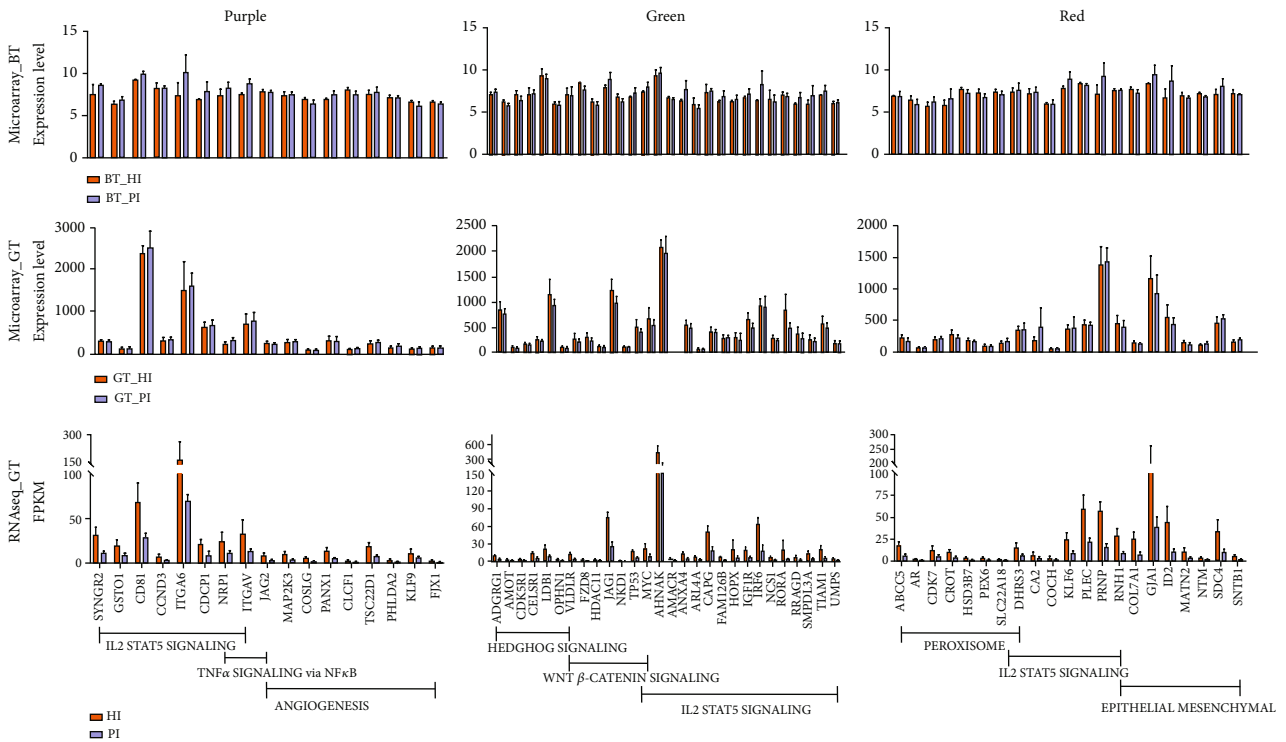


FIGURE 5: Genes expression analysis of key gene modules. Expression of key gene module members.

necrosis caused by inflammation and infection. However, this response is also an important way to induce host immune tolerance, causing persistent infection, and repeated clinical conditions [18]. This provides us with some clinical implications: IL2/STAT5 pathway blockers such as CMD178 [19] or pimozide [20] could be helpful in the PI treatment and inhibit T_{reg} cell activation at the pathway and molecular level.

In summary, there were differences in gene expression patterns and enriched biological process between bone and gingival tissues in PI, which means that biological processes and cellular behavior reveal the spatiotemporal heterogeneity in PI development. WGCNA and Hallmark gene enrichment analysis of the gingival tissue expression profile showed that IL2-mediated activation of immune cells could be a critical PI mechanism. As a new clinical treatment alternative, it is suggested that IL2/STAT5 pathway blockers could be helpful in PI treatment.

5. Conclusion

Differential gene and enrichment analysis based on public data showed differences in gene expression patterns and biological process between bone and gingival tissues in PI. This spatial-temporal heterogeneity is reflected in the formation of cellular responses to the external stimuli, which was enriched in bone tissue. In contrast, cytokine production, lymphocyte activation, immune response regulating signaling pathway, and blood vessel development were enriched in gingival tissue. WGCNA and Hallmark gene enrichment analysis of the gingival tissue expression profile showed that IL2-mediated activation of immune cells could be a critical PI mechanism. As a new clinical treatment, it is suggested that IL2/STAT5 pathway blockers could be helpful in PI treatment.

Data Availability

The datasets used and analyzed during the current study are available from the corresponding author on reasonable request.

Conflicts of Interest

The authors declare that they have no conflicts of interest.

Authors' Contributions

Li Tang and Hailun Zhou contributed equally to this work.

Acknowledgments

This study was funded by National Natural Science Foundation of China (Grant No.81460108).

References

[1] S. Jayachandran, A. D. Walmsley, and K. Hill, "Challenges in dental implant provision and its management in general dental practice," *Journal of Dentistry*, vol. 99, article 103414, 2020.

[2] T. Berglundh, G. Armitage, M. G. Araujo et al., "Peri-implant diseases and conditions: consensus report of workgroup 4 of the 2017 world workshop on the classification of periodontal and peri-implant diseases and conditions," *Journal of Clinical Periodontology*, vol. 45, Supplement 1, pp. S286–S318, 2018.

[3] Y. Wang, Y. Zhang, and R. J. Miron, "Health, maintenance, and recovery of soft tissues around implants," *Clinical Implant Dentistry and Related Research*, vol. 18, no. 3, pp. 618–634, 2016.

[4] F. Schwarz, G. Alcoforado, A. Guerrero et al., "Peri-implantitis: summary and consensus statements of group 3. The 6th EAO consensus conference 2021," *Clinical Oral Implants Research*, vol. 32, no. S21, Supplement 21, pp. 245–253, 2021.

[5] P. Langfelder and S. Horvath, "WGCNA: an R package for weighted correlation network analysis," *BMC Bioinformatics*, vol. 9, no. 1, p. 559, 2008.

[6] Z. Rezaei, J. Ranjbaran, H. Safarpour et al., "Identification of early diagnostic biomarkers via WGCNA in gastric cancer," *Biomedicine & Pharmacotherapy*, vol. 145, article 112477, 2022.

[7] X. Zhang, Y. Cui, X. Ding et al., "Analysis of mRNA-lncRNA and mRNA-lncRNA-pathway co-expression networks based on WGCNA in developing pediatric sepsis," *Bioengineered*, vol. 12, no. 1, pp. 1457–1470, 2021.

[8] A. Liberzon, C. Birger, H. Thorvaldsdóttir, M. Ghandi, J. P. Mesirov, and P. Tamayo, "The molecular signatures database hallmark gene set collection," *Cell Systems*, vol. 1, no. 6, pp. 417–425, 2015.

[9] A.-L. Barabási, N. Gulbahce, and J. Loscalzo, "Network medicine: a network-based approach to human disease," *Nature Reviews Genetics*, vol. 12, no. 1, pp. 56–68, 2011.

[10] C. Che, J. Liu, L. Ma, H. Xu, N. Bai, and Q. Zhang, "LOX-1 is involved in IL-1 β production and extracellular matrix breakdown in dental peri-implantitis," *International Immunopharmacology*, vol. 52, pp. 127–135, 2017.

[11] J. Guerrero-Gironés, S. López-García, M. R. Pecci-Lloret, M. P. Pecci-Lloret, and D. García-Bernal, "Influence of dual-cure and self-cure abutment cements for crown implants on human gingival fibroblasts biological properties," *Annals of Anatomy*, vol. 239, article 151829, 2022.

[12] A. P. V. Colombo and A.-C. R. Tanner, "The role of bacterial biofilms in dental caries and periodontal and peri-implant diseases: a historical perspective," *Journal of Dental Research*, vol. 98, no. 4, pp. 373–385, 2019.

[13] J. Chen, Q. Li, Z. Pang, M. Gong, and L. Tang, "Titanium ions promote exogenous calcium-dependent calcium influx in activated Jurkat T cells: a possible mechanism to explain its immunostimulatory properties," *Mediators of Inflammation*, vol. 2018, Article ID 3286905, 10 pages, 2018.

[14] S. Bordin, T. F. Flemmig, and S. Verardi, "Role of fibroblast populations in peri-implantitis," *The International Journal of Oral & Maxillofacial Implants*, vol. 24, no. 2, pp. 197–204, 2009.

[15] T. Chinen, A. K. Kannan, A. G. Levine et al., "An essential role for the IL-2 receptor in T_{reg} cell function," *Nature Immunology*, vol. 17, no. 11, pp. 1322–1333, 2016.

[16] Z. Liu, M. Y. Gerner, N. Van Panhuys, A. G. Levine, A. Y. Rudensky, and R. N. Germain, "Immune homeostasis enforced by co-localized effector and regulatory T cells," *Nature*, vol. 528, no. 7581, pp. 225–230, 2015.

[17] A. G. A. Kolios, G. C. Tsokos, and D. Klatzmann, "Interleukin-2 and regulatory T cells in rheumatic diseases," *Nature Reviews Rheumatology*, vol. 17, no. 12, pp. 749–766, 2021.

- [18] S. Z. Josefowicz, L. F. Lu, A. Y. Rudensky, and T. Regulatory, "Cells: mechanisms of differentiation and function," *Annual Review of Immunology*, vol. 30, no. 1, pp. 531–564, 2012.
- [19] T. Price-Troska, Z. Z. Yang, D. Diller et al., "Inhibiting IL-2 signaling and the regulatory T-cell pathway using computationally designed peptides," *Investigational New Drugs*, vol. 37, no. 1, pp. 9–16, 2018.
- [20] A. Keller, B. Wingelhofer, B. Peter et al., "The JAK2/STAT5 signaling pathway as a potential therapeutic target in canine mastocytoma," *Veterinary and Comparative Oncology*, vol. 16, no. 1, pp. 55–68, 2018.

Research Article

TAOK1 Promotes Proliferation and Invasion of Non-Small-Cell Lung Cancer Cells by Inhibition of WWC1

Lian Chen 

Department of Respiratory and Critical Care Medicine, The First Affiliated Hospital of Fujian Medical University, Fuzhou, Fujian 350000, China

Correspondence should be addressed to Lian Chen; fjfy3407@163.com

Received 7 July 2022; Revised 4 August 2022; Accepted 17 August 2022; Published 15 September 2022

Academic Editor: Pan Zheng

Copyright © 2022 Lian Chen. This is an open access article distributed under the Creative Commons Attribution License, which permits unrestricted use, distribution, and reproduction in any medium, provided the original work is properly cited.

Background. For patients with advanced non-small-cell lung cancer (NSCLC), targeted therapy significantly improves the therapeutic effect of NSCLC patients. With the development of molecular targeted therapy, more and more NSCLC-related genes have been found. Thousand and one amino-acid kinase 1 (TAOK1) has been identified as a potential target for drug research in various cancers. The main objective of this study was to explore the expression and function of TAOK1 in NSCLC. **Methods.** Western blotting was employed to assess TAOK1 expression in NSCLC cell lines. The effects of TAOK1 on biological behaviors, including proliferation, invasion, and apoptosis of NSCLC cells, were assessed. The relationship between TAOK1 and WW and C2 domain containing 1 (WWC1) was assessed by Co-IP assay. The subcutaneous injection of tumor cells in nude mice was used to verify it in vivo. **Results.** As expected, TAOK1 was increased in NSCLC cell lines. Following TAOK1 knockdown, NSCLC cells exhibited a significant decrease in the invasion and increased apoptosis in vitro. Instead, the TAOK1 elevation showed the opposite results. The Co-IP assay identified that TAOK1 specifically interacted with WWC1. Knockdown of WWC1 overturned TAOK1 silencing-mediated malignant phenotype of NSCLC cells. Additionally, subcutaneous tumorigenesis assays in nude mice confirmed that TAOK1 knockdown markedly restrained the proliferation capacity of NSCLC cells in vivo. **Conclusion.** Surprisingly, TAOK1 overexpression in NSCLC promotes tumor cell growth and invasion, which is associated with downregulation of its downstream protein WWC1, and this result might provide a robust research basis to inquire about the precise therapeutic targets for NSCLC.

1. Introduction

Despite increasing awareness and attention to physical health, lung cancer incidence is still rising. Lung cancer accounts for 13% of all cancer cases worldwide and 23% of all cancer-related deaths in 2018 worldwide [1]. According to the lung cancer classification guidelines published by the World Health Organization in 2015, lung cancer is divided into small cell lung cancer and non-small-cell lung cancer (NSCLC), which the latter accounts for more than 80% of the total incidence of lung cancer but are more abundant than the latter treatment. Due to the insidious early symptoms of lung cancer, some patients are already advanced or locally advanced at the time of diagnosis, leading to poor treatment outcomes and poor prognosis [2]. Surgical resection contributes to NSCLC patients' long-term survival,

and chemoradiotherapy is therapeutic for patients with advanced disease [3]. Consequently, it is urgent to explore NSCLC pathogenesis and new treatments.

Thousand and one amino-acid protein kinases (TAOKs) consist of three members, including TAOK1, TAOK2, and TAOK3. They are part of the step 20p protein kinase family, which plays essential roles upstream in the mitogen-activated protein kinase cascade, thus participating in multiple cellular processes [4]. TAOK1, also known as PSK2, TAO1, or MARKK, participates in apoptotic morphology through c-Jun N-terminal and Rho kinase-1 [5]. Draviam et al. reported that the interaction between TAOK1 and components of the spindle checkpoint is widely involved in mitotic progression [6]. A previous study indicated that TAOK1 is essential in neuronal function, involved in neurite outgrowth and axonal transport, and the differentiation of

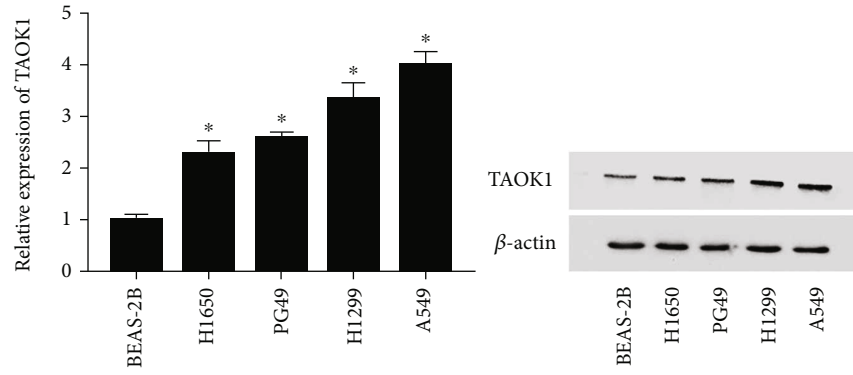


FIGURE 1: TAOK1 was highly expressed in NSCLC cell lines. (a, b) Relative TAOK1 expression in human NSCLC cell lines (H1650, PG49, H1299, and A549) and the normal lung cell line (BEAS-2B). * $P < 0.05$.

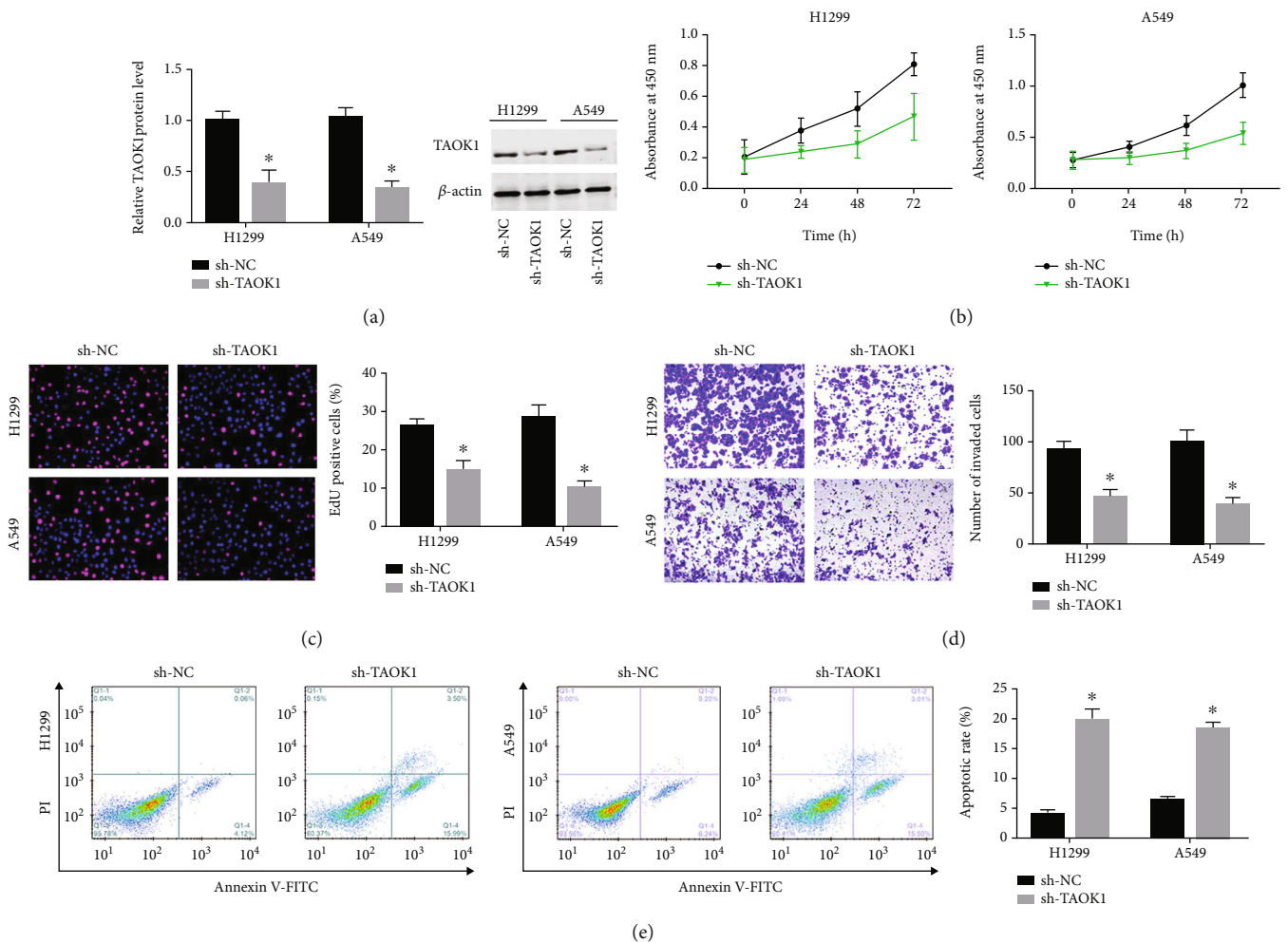


FIGURE 2: Effects of TAOK1 silencing on NSCLC cell biological behavior. A549 and H1299 cells were transfected with TAOK1 shRNA and corresponding negative controls, respectively. (a) Western blotting analysis of TAOK1 levels. (b–e) The proliferation, invasion, and antiapoptosis ability of TAOK1 silenced and control cells were detected by CCK-8, EdU, Transwell, and flow cytometry assays, respectively. * $P < 0.05$.

PC12 cells [7]. Li et al. found that TAOK1 reduces the release of inflammatory factors and the antiapoptotic ability in rats subjected to MCAO by regulating the PI3K/AKT and MAPK pathways, playing a protective role in cerebral ischemic stroke [8]. In the experimental model of inflammatory

bowel disease, TAOK1 markedly suppresses colitis by down-regulating the formation of the IL-17RA and Act1 complex [9]. According to a substantial study, TAOK1 was a downstream target for miRNA-706, and miRNA-706 inhibited hepatic fibrogenesis by downregulating TAOK1 [10].

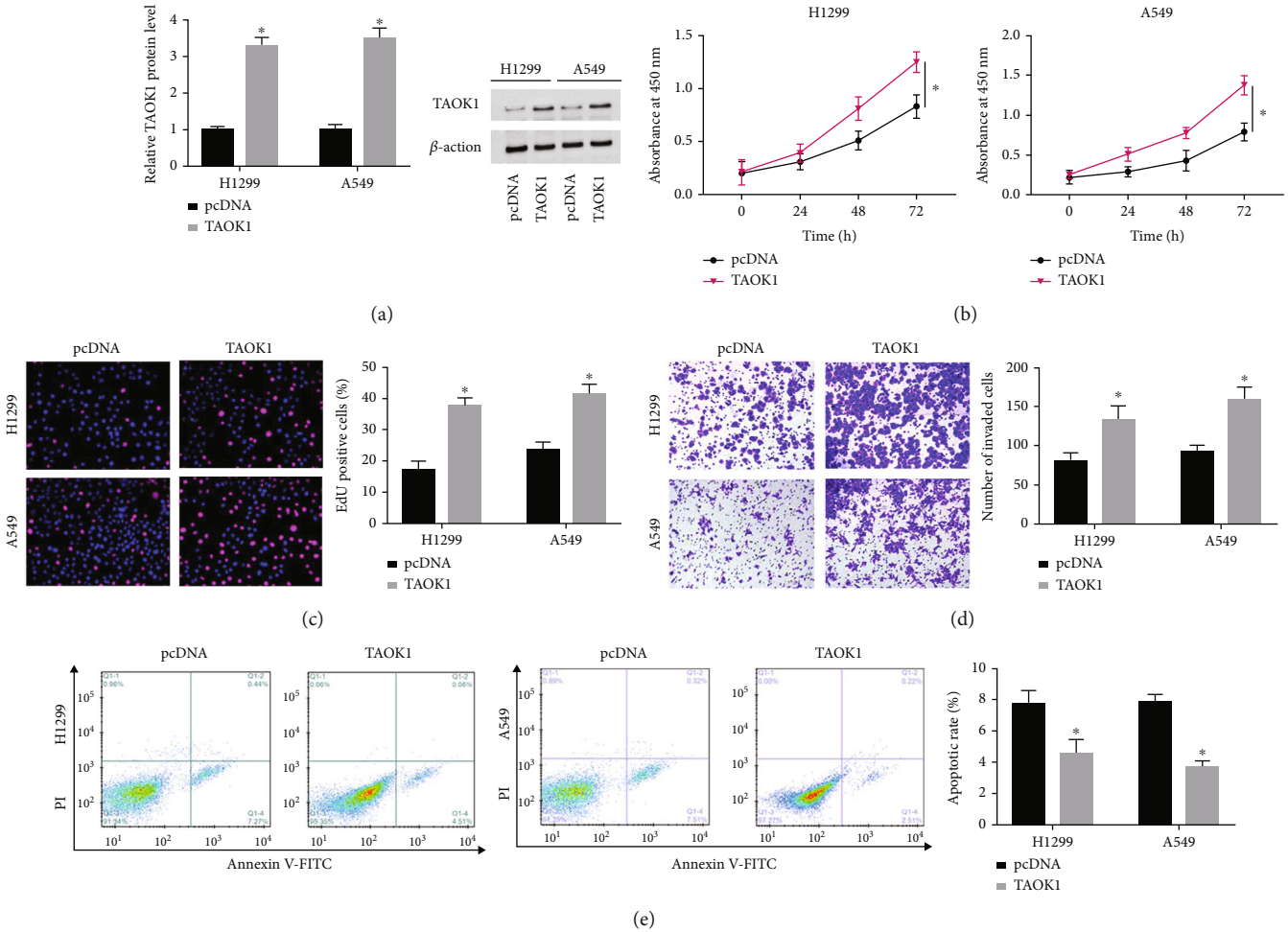


FIGURE 3: Effects of TAOK1 overexpression on NSCLC cell biological behavior. A549 and H1299 cells were transfected with pcDNA-TAOK1 and corresponding negative controls, respectively. (a) Western blotting analysis of TAOK1 levels. (b–e) The proliferation, invasion, and antiapoptosis ability of TAOK1 elevated and control cells were detected by CCK-8, EDU, Transwell, and flow cytometry assays, respectively. * $P < 0.05$.

Furthermore, current evidence demonstrated that the dysregulation of the Ste20 kinase pathway is closely related to malignant tumors, and TAOK1 inhibitors arrested NSCLC cells in G0/G1 phase and induced cell apoptosis, which indicates TAOK1 might play a crucial role in the pathogenesis of lung cancer [11]. Currently, studies targeting toak1 in NSCLC are in their infancy, and its pathophysiological functions need to be further mined.

WWC1, also known as KIBRA, is characterized by two WW domains in the amino terminus, an internal C2-like domain and a carboxy-terminal glutamic acid-rich stretch [12]. As a well-known tumor suppressor gene in various cancer, WWC1 participates in the regulation of cell proliferation, differentiation, and metastasis. However, the effect of TAOK1 on WWC1 in NSCLC progression and the potential mechanism remains unknown.

In the present study, we indicate that TAOK1 expression is upregulated in NSCLC cell lines. Functional studies showed that TAOK1 regulates NSCLC cell behavior and tumor formation in vivo. Mechanistic investigations suggest that TAOK1 interacts with WWC1 and regulates WWC1 expression, thereby promoting NSCLC progression.

2. Materials and Methods

2.1. Cell Culture and Transfection. Shanghai Cell Bank provided the NSCLC cell lines (H1650, PG49, H1299, and A549) and the normal bronchial epithelial cell line BEAS-2B. All cells were supplemented with appropriate concentrations of serum, for which BEAS-2B and A549 cells were cultured in DMEM containing 10% FBS; H1650, PG49, and 1299 cells were maintained in RPMI 1640 medium at 37°C in 5% CO₂. To keep the cells growing well, NSCLC cells were seeded in 6-well plates and cultured for 24 h. Short-hairpin RNA (shRNA) (sh-TAOK1), negative control (sh-NC), TAOK1 overexpression plasmid by pcDNA3.1 vector (pcDNA3.1-TAOK1), and negative control (pcDNA3.1-NC) (Thermo Fisher Scientific, Waltham, MA, USA) were transfected into the target cells using Lipofectamine 2000 transfection reagent (Invitrogen).

2.2. Quantitative Real-Time Polymerase Chain Reaction (qRT-PCR). Total RNA was extracted from NSCLC cells according to the TRIzol reagent instructions, reverse transcribed into cDNA according to the instructions of the

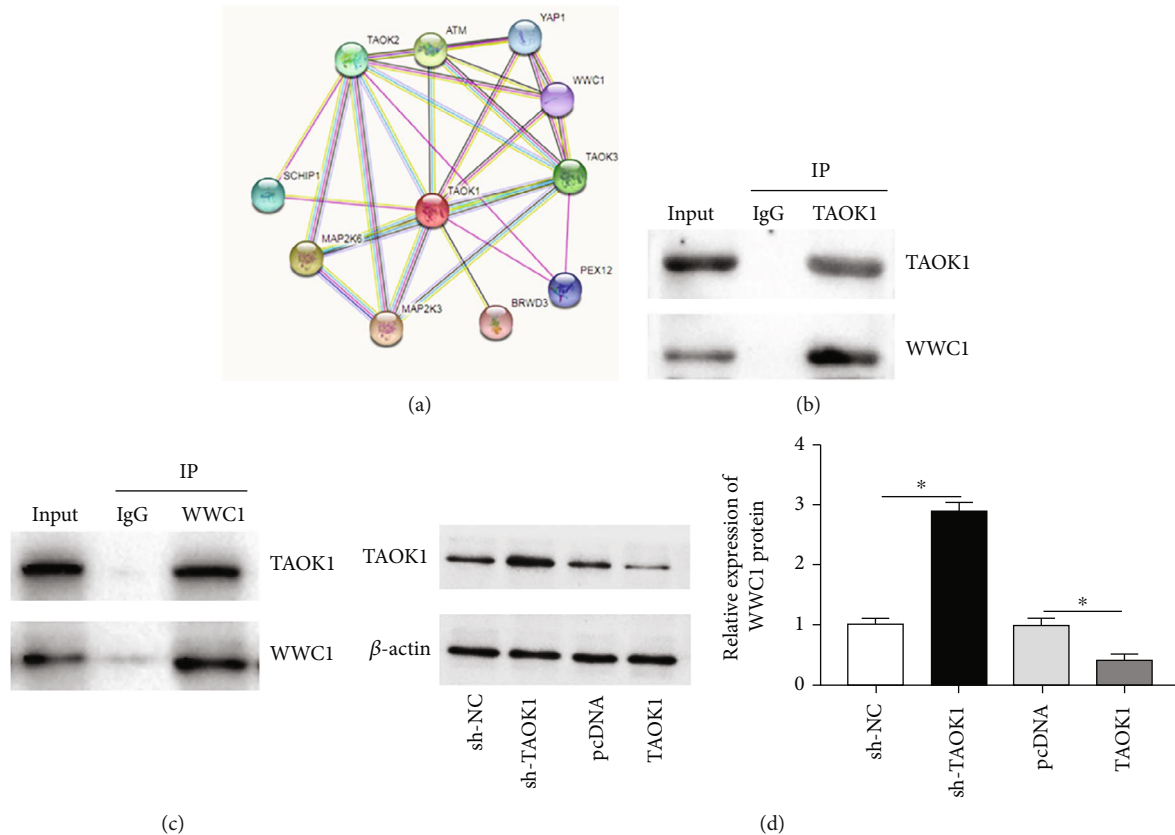


FIGURE 4: TAOK1 interacted with WWC1 and inhibited WWC1 expression. (a) Interaction network analysis diagram of TAOK1. (b, c) Co-IP assay analysis of TAOK1 and WWC1 binding. (d) Western blotting analysis of WWC1 levels. $*P < 0.05$.

reverse transcription kit (Promega, USA), and then amplified using cDNA as a template, and β -actin was used as an internal reference for qRT-PCR amplification. The relative gene expression was calculated using the $2^{-\Delta\Delta Ct}$ method. Primer sequences were as follows: GAPDH F: 5'-CCTCGT CTCATAGACAAGATGGT-3', R: 5'-GGGTAGAGTCA TACTGGAACATG-3'; TAOK1 F: 5'-AAG AGC ATC AGC TCC ACA GT-3', R: 5'-GCC GAT GTT CGT CCA TTT CT-3'; and WWC1 F: 5'-TCCGCAGTCCTGAAA CATT-3' (forward), R: 5'-GTGGATTCCCAATGAG CCGA-3'.

2.3. Western Blotting. Transfected NSCLC cells were charged, and the supernatant was collected to examine the protein concentration after adding the RIPA lysis buffer. Subsequently, electrophoretic samples were configured and added to 10% SDS-PAGE gels for electrophoresis experiments. The proteins on the gels were then transferred to PVDF membranes and blocked with 5% nonfat milk for at least 2 h. Primary antibodies (TAOK1 and WWC1) were added to the membranes and incubated for 12-16 h at 4°C, after which the membranes were washed three times for 10 min each with TTBS. The corresponding rabbit/mouse secondary antibodies were added and incubated for 2 h at room temperature, after which the membranes were re-washed three times for 10 min each. Finally, ECL reagents

were used to evaluate the grayscale of each band quantitatively.

2.4. Cell Counting Kit-8 (CCK-8) Assay. Logarithmic growth phase NSCLC cells were taken, the cell suspension was prepared, and the cells (1×10^4 cells/well) were seeded in 96-well plates and grew in a 5% CO₂ incubator for 24, 48, and 72 h, respectively. Next, 10 μ L of CCK-8 solution was added 2 h before each assay time point and placed plates in the incubator for 1 h, then placed into a microplate reader to detect absorbance values at a wavelength of 450 nm.

2.5. Ethynyl Deoxyuridine (EdU) Incorporation Assay. NSCLC cells (1×10^4 cells/well) were plated in 96-well plates. After overnight incubation, 1:1000 dilution of EDU reagent was added, cells were washed with PBS after 2 h incubation and then fixed with 3% paraformaldehyde for 10 min. Afterward, 2 mg/mL glycine was added for 5 min incubation. 0.5% Triton X-100 was added for 10 min. Apollo staining solution was added after washing and incubated for 30 min in the dark. Nuclei were then stained with Hoechst for 10 min. After washing, count the analysis after taking photographs under a microscope.

2.6. Flow Cytometry. 100 μ L of binding buffer was utilized to resuspend NSCLC cells. After adding 5 μ L Annexin V-FITC in cells for 15 min in the dark at room temperature, the PI

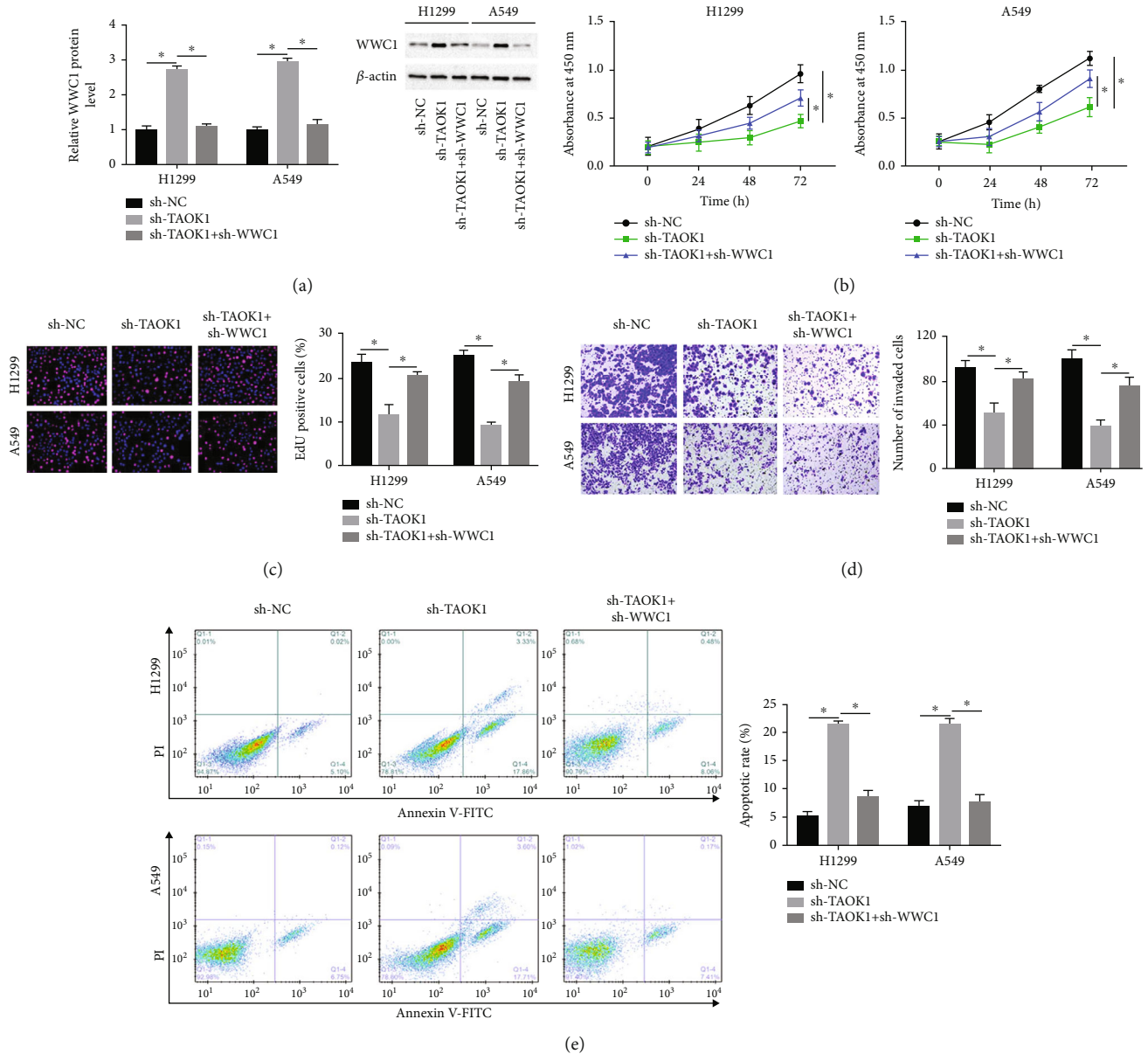


FIGURE 5: WWC1 knockdown reversed the function of TAOK1 on NSCLC cell biological behavior. A549 and H1299 cells were transfected with sh-TAOK1 alone or together with sh-WWC1. (a) Western blotting analysis of TAOK1 levels. (b–e) The proliferation, invasion, and antiapoptosis ability of TAOK1 silenced, and concurrently WWC1 silenced, and control cells were detected by CCK-8, EdU, Transwell, and flow cytometry assays, respectively. * $P < 0.05$.

solution was remixed. The apoptosis rate of each group was measured by flow cytometry.

2.7. Transwell Cell Invasion Assay. Transwell chambers were purchased from Corning with a pore size of 8.0. NSCLC cells were digested and prepared into cell suspension, counted, and the concentration was adjusted to 2×10^5 /mL and seeded in the upper chamber with coated Matrigel. Meanwhile, a complete medium was put into the lower chamber of the culture plate. Further, cells with 4% paraformaldehyde and methanol were added to the culture plate to, respectively, fixed for 20 min, and gentian violet was added to stain for 15 min. Clean the chamber upper chamber with PBS, and carefully wipe the cells on the membrane surface at the bot-

tom of the upper chamber with a wet cotton swab. After drying the chamber upper chamber, count and take photos with the burning inverted microscope.

2.8. Co-Immunoprecipitation (Co-IP). NSCLC cells are lysed in lysis buffer to obtain cell lysate, followed by incubated with agarose bead-conjugated antibodies against anti-TAOK1 and anti-WWC1 overnight. Further, the beads were washed to harvest the binding proteins. Finally, western blotting was used to assess immunoprecipitated protein.

2.9. Immunohistochemistry (IHC). Surgically resected tumor tissues were fixed in 10% formalin and processed for embedding, whereas tissue sections were made with a slice

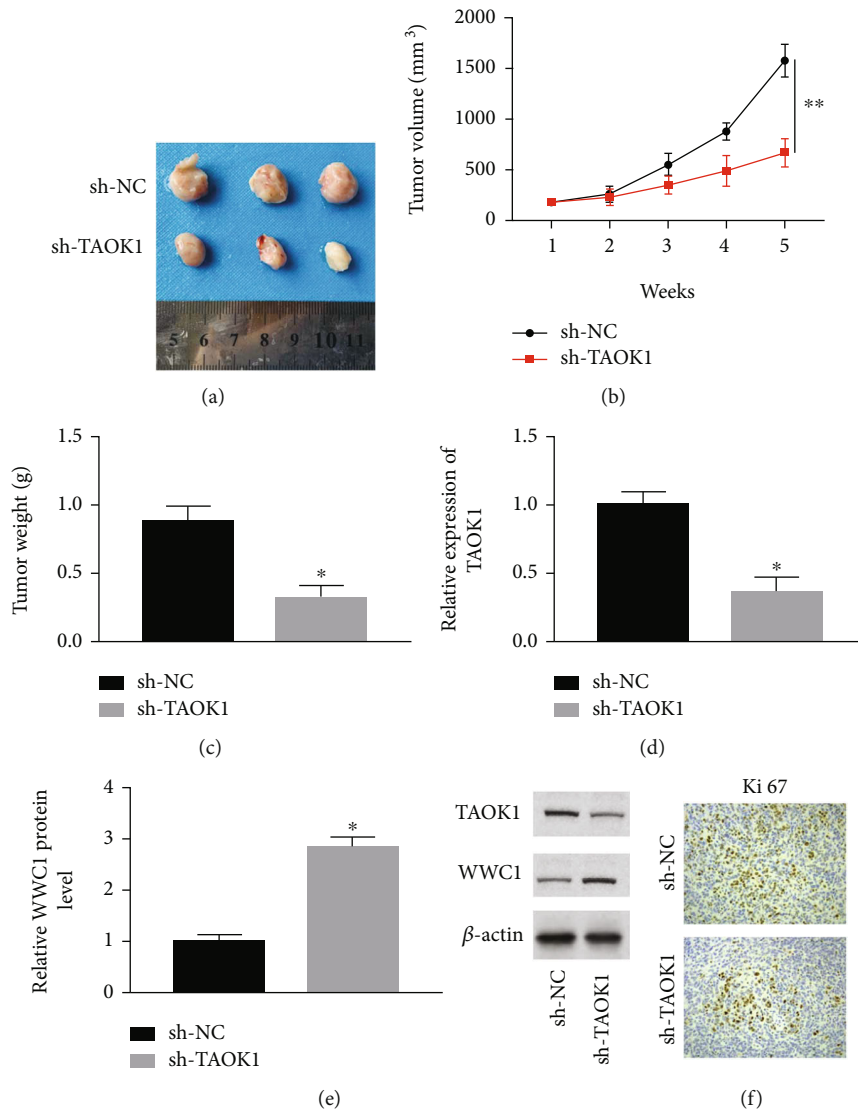


FIGURE 6: TAOK1 interference restrained tumor development in vivo. (a) The images of tumors in each group. (b, c) The volume and weight of tumor in each group. (d) Relative TAOK1 and WWC1 expression in tumor tissues in each group. (e) Immunohistochemistry analysis of each group's relative Ki-67 protein levels in tumor tissues. * $P < 0.05$.

thickness of $4\ \mu\text{M}$. Sections were deparaffinized in xylene, rehydrated, heat-fixed in sodium citrate (pH 6.0) buffer, blocked in 3% hydrogen peroxide, and incubated with a rabbit polyclonal antibody against Ki-67 at a concentration of 1:200 at 4°C for 18 h. The next day, secondary antibodies for histochemistry were added to the sections, stained with DAB, and counterstained with Mayer's hematoxylin. Sections were observed and photographed with a microscope (Nikon).

2.10. Tumor Xenograft Assay. 24 male BALB/c nude mice (four weeks old) were brought from Cavens Laboratory Animals Co., Ltd. (Changzhou, China). TAOK1 targeting shRNA (sh-TAOK1) or scrambled shRNA were transfected into A549 cells, followed by subcutaneous injection into the flanks of the nude mice at a density of 5×10^6 cells. Tumor volume was assessed by measuring tumor diameters every week.

2.11. PPI Network Construction. The PPI network was carried out using the Search Tool for the Retrieval of Interacting Genes and proteins (STRING) database (ver. 10.0, <http://www.string-db.org/>). The network visualization software Cytoscape was applied to create the PPI interaction network.

2.12. Statistical Analysis. Statistical analysis of experimental data was processed using SPSS 23.0 (SPSS Inc., Chicago, IL). Data were expressed as mean \pm SD. The significance of the variance between the two groups was determined by Student's t -test. $P < 0.05$ was considered statistically significant.

3. Results

3.1. TAOK1 Was Found to Be Increased in NSCLC Cell Lines. To examine the role of TAOK1 in CC, the expression of TAOK1 was evaluated in NSCLC cell lines by western blotting. It is worth noting that TAOK1 was highly expressed in

H1650, PG49, H1299, and A549 cells compared to the normal lung cell line (BEAS-2B) (Figure 1(a)).

3.2. TAOK1 Knockdown Reduced Proliferation, Migration, and Antiapoptotic Ability of NSCLC Cells. To explore the biological function of TAOK1, we constructed TAOK1 stably silenced H1299 and A549 cells, respectively. Western blot assay showed that TAOK1 interference effectively enhanced TAOK1 expression levels in H1299 and A549 cells (Figure 2(a)). After silencing TAOK1, the proliferation ability of H1299 and A549 cells was decreased (Figure 2(b)). We also found that cell proliferation was remarkably suppressed in TAOK1-depleted H1299 and A549 cells using the EdU assay (Figure 2(c)). Transwell assay demonstrated that TAOK1 knockdown significantly reduced the number of invading H1299 and A549 cells (Figure 2(d)). Besides, flow cytometry results indicated that TAOK1 knockdown significantly induced apoptosis (Figure 2(e)).

3.3. TAOK1 Overexpression Promoted Proliferation, Invasion, and Reduced Apoptosis of NSCLC Cells. We next elevated TAOK1 expression into H1299 and A549 cells. Using western blotting, we found that the introduction of pcDNA-TAOK1 caused an efficient increase in TAOK1 protein levels (Figure 3(a)). Compared with the pcDNA group, TAOK1 overexpression conspicuously promoted both A549 and NCI-H1299 cell proliferation (Figure 3(b)). EdU assay also revealed that TAOK1 overexpression facilitated A549 and NCI-H1299 cell growth (Figure 3(c)). Transwell assay demonstrated that the number of invaded cells elevated after TAOK1 overexpressing (Figure 3(d)). We also observed a significant decrease in apoptosis in TAOK1 overexpressing A549 and H1299 cells (Figure 3(e)).

3.4. TAOK1 Bound with WWC1 and Negatively Regulated WWC1 Expression. Given the impact of TAOK1 in NSCLC cell behavior, we performed a STRING interaction network analysis of TAOK1 and its associated significantly differentially expressed genes. The result demonstrated a potential binding relationship between TAOK1 and WWC1 proteins (Figure 4(a)). Subsequently, we investigated the interaction between TAOK1 and WWC1 by co-immunoprecipitation (Co-IP) assay. The results indicated that compared with control IgG, TAOK1-antibody could pull down WWC1. Correspondingly, WWC1-antibody also pulled down TAOK1 (Figures 4(b) and 4(c)), which indicated that TAOK1 could be intact with WWC1 in A549 cells. Besides, western blotting revealed that the TAOK1 interference restrained the WWC1 protein level in A549 cells, whereas overexpression of TAOK1 led to opposite results (Figure 4(d)).

3.5. WWC1 Knockdown Reversed TAOK1 Knockdown-Mediated Effect on Proliferation, Invasion, and Apoptosis of NSCLC Cells. To further investigate whether TAOK1 affects the NSCLC cellular fates through WWC1, TAOK1 shRNA alone, or WWC1 shRNA were transfected into A549 and H1299 cells. Western blotting results uncovered that WWC1 interference overturned the facilitation effect of TAOK1 interference on WWC1 expression (Figure 5(a)).

From the results of CCK-8, we confirmed that the capacity of cell proliferation was reduced by silencing TAOK1, whereas it was restored by WWC1 knockdown (Figure 5(b)). EdU assay also revealed that shTAOK1 inhibited A549 and NCI-H1299 cell growth (Figure 5(c)). As expected, Transwell and flow cytometry assays also indicated that TAOK1 silencing inhibited cell invasion and antiapoptosis abilities, whereas WWC1 knockdown could invert these changes (Figures 5(d) and 5(e)).

3.6. TAOK1 Knockdown Suppressed Xenograft Tumor Growth in Mice. To further detect whether TAOK1 silencing could inhibit tumor growth, A549 cells transfected with TAOK1 shRNA were subcutaneously injected into nude mice. TAOK1 knockdown significantly repressed tumor growth, reducing tumor volume and weight (Figures 6(a)–6(c)). Western blotting results revealed that TAOK1 silencing decreased TAOK1 protein expression and increased WWC1 levels in tumor tissues of rats (Figures 6(d) and 6(e)). Additionally, the immunohistochemistry assay showed that TAOK1 interference significantly attenuated the Ki-67 expression level (Figure 6(f)).

4. Discussion

The acquisition of the function of some oncogenes and the loss of the function of many tumor suppressor genes are the central links between tumor genesis and initiation. TAOK1 belongs to the mammalian STE20 kinase family, and its alteration, in turn, leads to changes in the biological behavior of cells, allowing uncontrolled cancer cell growth, aberrant proliferation, transformation and motility, and ultimately invasion and metastasis [13, 14]. Gao et al. indicated that TAOK1 inhibition or depletion effectively inhibits cell growth by arresting cell mitosis [15]. It was reported that TAOK1 expression was prominently reduced in HCC tissues and was positively correlated with immune infiltration in HCC [16]. Shi et al. validated that TAOK1 is a direct target of miR-706 cells accountable for EMT in hepatic fibrosis [16]. Meanwhile, overexpression of TAOK1 was uncovered in colorectal cancer tissues [17]. Moreover, serine/threonine kinase expression in cancers was investigated by in situ hybridization. The results suggested that increased expression of TAOK1 in lung cancer tissues showed high levels relative to lung tissues [17]. Evidence has revealed that TAOK1 might function as a Hippo pathway gene and is the main element of the susceptibility of lung cancer cells [18]. Given the above literature, an in-depth study of TAOK1 molecular expression in NSCLC and the effect of altered TAOK1 molecular expression levels on the biological behavior of NSCLC cells is essential to gain insight into the mechanism of NSCLC development and progression. Here, we uncovered that TAOK1 was upregulated in NSCLC cell lines. Subsequent functional studies revealed that knockdown of TAOK1 efficiently inhibited NSCLC cell proliferation, invasion, and induced apoptosis in vitro and suppressed NSCLC xenograft growth in vivo. Conversely, overexpression of TAOK1 promoted NSCLC cell proliferation and invasion and inhibited apoptosis.

A previous study has demonstrated that breast cancer patients with low expression WWC1 genes usually have larger tumor sizes and poor prognoses [19]. A previous study revealed that WWC1 overexpression hindered the SOX2-induced migration ability and invasive potential in esophageal squamous cell carcinoma [20]. WWC1 was low expressed in colorectal cancer tissues, and low-level WWC1 indicated worse survival of colorectal cancer patients [21]. Most importantly, WWC1 was one of the well-known upstream regulators of the Hippo signaling pathway, which contributes to the activation of the Hippo signaling pathway, resulting in YAP phosphorylation [22]. Another study has revealed that WWC1 cooperated with NF2 to mitigate the malignant progression of intrahepatic cholangiocarcinoma by activation of LATS1/2 and inhibition of YAP/TAZ activity [23]. It was reported that WWC1 was downregulated in lung adenocarcinoma tissues and cells, and WWC1 restrained proliferation and invasion and accelerated apoptosis of lung adenocarcinoma cells by Hippo signaling pathway [24]. Moreover, ACTL6A contributed to tumorigenesis in vitro and in vivo by silencing WWC1 expression and regulating Hippo/YAP signaling [25]. This study showed that TAOK1 interacted with WWC1 and negatively regulated WWC1 expression. Intriguingly, WWC1 interference restored the effects of TAOK1 knockdown on NSCLC cell proliferation, invasion, and apoptosis. However, this study still has some limitations, and it would be better to add some more animal experiments. This study lacks related clinical research, and it still needs to be further validated in a larger patient cohort.

In conclusion, our study identified that TAOK1 was low expressed in NSCLC cell lines. Furthermore, TAOK1 contributed to tumor-promoting effects, manifested by facilitating NSCLC cell proliferation, invasion, and suppressing apoptosis in vitro and accelerating xenograft formation in vivo by reducing WWC1 expression. The above findings provide a theoretical understanding of the oncogenic mechanisms of TAOK1 in NSCLC and a potential candidate for the therapy of NSCLC.

Data Availability

The labeled dataset used to support the findings of this study are available from the corresponding author upon request.

Conflicts of Interest

The author declares no competing interests.

References

- [1] F. Bray, J. Ferlay, I. Soerjomataram, R. L. Siegel, L. A. Torre, and A. Jemal, "Global cancer statistics 2018: GLOBOCAN estimates of incidence and mortality worldwide for 36 cancers in 185 countries," *CA: a Cancer Journal for Clinicians*, vol. 68, no. 6, pp. 394–424, 2018.
- [2] S. Blandin Knight, P. A. Crosbie, H. Balata, J. Chudziak, T. Hussell, and C. Dive, "Progress and prospects of early detection in lung cancer," *Open Biology*, vol. 7, no. 9, 2017.
- [3] R. Mulherkar, A. S. Grewal, and A. T. Berman, "Emerging role of immunotherapy in locally advanced non-small cell lung cancer," *Clinical Advances in Hematology & Oncology*, vol. 18, no. 4, pp. 212–217, 2020.
- [4] I. Dan, N. M. Watanabe, and A. Kusumi, "The Ste20 group kinases as regulators of MAP kinase cascades," *Trends in Cell Biology*, vol. 11, no. 5, pp. 220–230, 2001.
- [5] C. Zihni, C. Mitsopoulos, I. A. Tavares, A. J. Ridley, and J. D. H. Morris, "Prostate-derived sterile 20-like kinase 2 (PSK2) regulates apoptotic morphology via C-Jun N-terminal kinase and Rho kinase-1," *The Journal of Biological Chemistry*, vol. 281, no. 11, pp. 7317–7323, 2006.
- [6] V. M. Draviam, F. Stegmeier, G. Nalepa et al., "A functional genomic screen identifies a role for TAO1 kinase in spindle-checkpoint signalling," *Nature Cell Biology*, vol. 9, no. 5, pp. 556–564, 2007.
- [7] T. Timm, X. Y. Li, J. Biernat et al., "MARKK, a Ste20-like kinase, activates the polarity-inducing kinase MARK/PAR-1," *The EMBO Journal*, vol. 22, no. 19, pp. 5090–5101, 2003.
- [8] J. Li, Z. Liu, L. Wang, H. Xu, and Y. Wang, "Thousand and one kinase 1 protects MCAO-induced cerebral ischemic stroke in rats by decreasing apoptosis and pro-inflammatory factors," *Bioscience Reports*, vol. 39, no. 10, 2019.
- [9] Z. Zhang, Z. Tang, X. Ma et al., "TAOK1 negatively regulates IL-17-mediated signaling and inflammation," *Cellular & Molecular Immunology*, vol. 15, no. 8, pp. 794–802, 2018.
- [10] R. Yin, D. Guo, S. Zhang, and X. Zhang, "miR-706 inhibits the oxidative stress-induced activation of PKC α /TAOK1 in liver fibrogenesis," *Scientific Reports*, vol. 6, no. 1, p. 37509, 2016.
- [11] M. W. Chao, T. E. Lin, W. C. HuangFu et al., "Identification of a dual TAOK1 and MAP4K5 inhibitor using a structure-based virtual screening approach," *Journal of Enzyme Inhibition and Medicinal Chemistry*, vol. 36, no. 1, pp. 98–108, 2021.
- [12] A. Schneider, M. J. Huentelman, J. Kremerskothen, K. Duning, R. Spoelgen, and K. Nikolich, "A New Gateway to Learning and Memory?," *Frontiers in Aging Neuroscience*, vol. 2, p. 4, 2010.
- [13] W. Xiong, A. J. Knox, M. Xu et al., "Mammalian Ste20-like kinase 4 promotes pituitary cell proliferation and survival under hypoxia," *Molecular Endocrinology*, vol. 29, no. 3, pp. 460–472, 2015.
- [14] X. Gao, C. Gao, G. Liu, and J. Hu, "MAP4K4: an emerging therapeutic target in cancer," *Cell & Bioscience*, vol. 6, no. 1, p. 56, 2016.
- [15] C. Y. Koo, C. Giacomini, M. Reyes-Corral et al., "Targeting TAO kinases using a new inhibitor compound delays mitosis and induces mitotic cell death in centrosome amplified breast cancer cells," *Molecular Cancer Therapeutics*, vol. 16, no. 11, pp. 2410–2421, 2017.
- [16] Y. Shi, D. D. Zhang, J. B. Liu et al., "Comprehensive analysis to identify DLEU2L/TAOK1 axis as a prognostic biomarker in hepatocellular carcinoma," *Molecular Therapy–Nucleic Acids*, vol. 23, pp. 702–718, 2021.
- [17] M. Capra, P. G. Nuciforo, S. Confalonieri et al., "Frequent alterations in the expression of serine/threonine kinases in human cancers," *Cancer Research*, vol. 66, no. 16, pp. 8147–8154, 2006.
- [18] G. Gobbi, B. Donati, I. F. Do Valle et al., "The Hippo pathway modulates resistance to BET proteins inhibitors in lung cancer cells," *Oncogene*, vol. 38, no. 42, pp. 6801–6817, 2019.

- [19] Z. Wang, D. Katsaros, N. Biglia et al., “Low expression of WWC1, a tumor suppressor gene, is associated with aggressive breast cancer and poor survival outcome,” *FEBS Open Bio*, vol. 9, no. 7, pp. 1270–1280, 2019.
- [20] Y. Chai, Q. Li, H. Zhao et al., “SOX2 antagonizes WWC1 to drive YAP1 activation in esophageal squamous cell carcinoma,” *Cancer Medicine*, vol. 8, no. 16, pp. 7055–7064, 2019.
- [21] H. Z. Du WB, L. Luo, S. P. Tong et al., “TCF19 aggravates the malignant progression of colorectal cancer by negatively regulating WWC1,” *European Review for Medical and Pharmacological Sciences*, vol. 24, no. 2, pp. 655–663, 2020.
- [22] V. Höffken, A. Hermann, H. Pavenstädt, and J. Kremerskothen, “WWC proteins: important regulators of Hippo signaling in cancer,” *Cancers (Basel)*, vol. 13, no. 2, p. 306, 2021.
- [23] J. Park, J. S. Kim, J. H. Nahm, S. K. Kim, D. H. Lee, and D. S. Lim, “WWC1 and NF2 prevent the development of intrahepatic cholangiocarcinoma by regulating YAP/TAZ activity through LATS in mice,” *Molecules and Cells*, vol. 43, no. 5, pp. 491–499, 2020.
- [24] Y. An, Q. Zhang, X. Li, Z. Wang, Y. Li, and X. Tang, “Upregulated microRNA miR-21 promotes the progression of lung adenocarcinoma through inhibition of KIBRA and the Hippo signaling pathway,” *Biomedicine & Pharmacotherapy*, vol. 108, pp. 1845–1855, 2018.
- [25] L. Ma and L. Shan, “ACTL6A promotes the growth in non-small cell lung cancer by regulating Hippo/Yap pathway,” *Experimental Lung Research*, vol. 47, no. 5, pp. 250–259, 2021.

Retraction

Retracted: The Application of Focused Care Model in the Management of Hepatitis B Patients in a Tertiary Care Hospital and the Impact on Patients' Quality of Life

Computational and Mathematical Methods in Medicine

Received 27 June 2023; Accepted 27 June 2023; Published 28 June 2023

Copyright © 2023 Computational and Mathematical Methods in Medicine. This is an open access article distributed under the Creative Commons Attribution License, which permits unrestricted use, distribution, and reproduction in any medium, provided the original work is properly cited.

This article has been retracted by Hindawi following an investigation undertaken by the publisher [1]. This investigation has uncovered evidence of one or more of the following indicators of systematic manipulation of the publication process:

- (1) Discrepancies in scope
- (2) Discrepancies in the description of the research reported
- (3) Discrepancies between the availability of data and the research described
- (4) Inappropriate citations
- (5) Incoherent, meaningless and/or irrelevant content included in the article
- (6) Peer-review manipulation

The presence of these indicators undermines our confidence in the integrity of the article's content and we cannot, therefore, vouch for its reliability. Please note that this notice is intended solely to alert readers that the content of this article is unreliable. We have not investigated whether authors were aware of or involved in the systematic manipulation of the publication process.

In addition, our investigation has also shown that one or more of the following human-subject reporting requirements has not been met in this article: ethical approval by an Institutional Review Board (IRB) committee or equivalent, patient/participant consent to participate, and/or agreement to publish patient/participant details (where relevant).

Wiley and Hindawi regrets that the usual quality checks did not identify these issues before publication and have since put additional measures in place to safeguard research integrity.

We wish to credit our own Research Integrity and Research Publishing teams and anonymous and named external researchers and research integrity experts for contributing to this investigation.

The corresponding author, as the representative of all authors, has been given the opportunity to register their agreement or disagreement to this retraction. We have kept a record of any response received.

References

- [1] J. Zhang, Y. Wang, H. Shan, J. Duan, and J. Yu, "The Application of Focused Care Model in the Management of Hepatitis B Patients in a Tertiary Care Hospital and the Impact on Patients' Quality of Life," *Computational and Mathematical Methods in Medicine*, vol. 2022, Article ID 7770955, 11 pages, 2022.

Research Article

The Application of Focused Care Model in the Management of Hepatitis B Patients in a Tertiary Care Hospital and the Impact on Patients' Quality of Life

Jian-Wei Zhang,¹ Yan Wang,¹ Hai-Hong Shan,¹ Jia-Yu Duan,¹ and Juan Yu ²

¹Department of Infection, Shanxi Norman Bethune Hospital, Taiyuan, Shanxi Province 030000, China

²Preventive and Health Care Department, Shanxi Norman Bethune Hospital, Taiyuan, Shanxi Province 030000, China

Correspondence should be addressed to Juan Yu; 18409213@masu.edu.cn

Received 26 May 2022; Revised 30 June 2022; Accepted 6 July 2022; Published 12 September 2022

Academic Editor: Pan Zheng

Copyright © 2022 Jian-Wei Zhang et al. This is an open access article distributed under the Creative Commons Attribution License, which permits unrestricted use, distribution, and reproduction in any medium, provided the original work is properly cited.

Chronic hepatitis B is one of the common infectious diseases in the world, with a wide epidemic range and strong contagiousness, which is difficult to completely eradicate. From July 2020 to April 2022, 142 patients with hepatitis B who were admitted to tertiary hospitals were selected and randomly divided into 2 cases, with 71 cases per case. The control group adopts a conventional model, and the observation group implements a nursing model based on the control group. The management capacity and quality of life before and after the two groups of care were compared. 94 patients with chronic hepatitis B who were admitted to the hospital from July 2020 to April 2022 were selected, and 47 cases were divided into the control group and observation group according to the admission time. The control group is given a conventional model, and the observation group is given a nursing model on the basis of the control group. Both groups of patients observed anxiety self-assessment scale (SAS), depression self-assessment scale (SDS), short life span scale (SF-36) scores, and treatment conditions before and after the intervention, to explore the application of nursing model in the management of hepatitis B patients in tertiary hospitals and its impact on patient quality of life. Based on study's precare outcomes, there was no statistically significant difference between the self-administered scale (PIH) score and the quality of life measurement summary scale (QOL-BREF) score ($P > 0.05$) between the two groups. After one month of care, both groups had lower PIH scores than before care, and QOL-BREF scores were higher than before care ($P < 0.05$). After one month of treatment, the PIH score of the observation group was significantly reduced, and the QOL-BREF score after one month of treatment was significantly higher than that of the control group ($P < 0.05$). The SAS and SDS scores in the observation group were lower than those in the control group, and the quality of life scores and treatment compliance were higher than those in the control group, and the difference was statistically significant ($P < 0.05$). **Conclusions.** The nursing model can effectively improve the management and quality of life of hepatitis B patients. It also had a significant positive effect on the therapeutic capacity and quality of life of patients with hepatitis B and improved patient compliance behavior and quality of life.

1. Introduction

Chronic hepatitis is one of the most common infectious diseases in the world, with wide coverage and strong infectivity, which cannot be completely cured. According to incomplete statistics, at this stage, the world's 2.4 pieces of Wuhan city is about 100 million day and night feeling hepatitis virus infection, about 686,000 people die day and night every year in Wuhan, and there are about 93 million hepati-

tis carriers across the country. Hepatitis is a contagious disease caused by viral infection. If the treatment fails, it is likely to develop cirrhosis of the liver ascites or advanced liver cancer, which is a great threat to the patient's life. There is no reasonable treatment for this disease, and patients must take long-term medication to alleviate the disease [1].

In the process of clinical treatment, patients do not have enough grasp of the disease, have poor management methods, and have behaviors such as self-return and drug

discontinuation, resulting in ineffective disease control [2]. Relevant studies have found that better health services are conducive to improving patients' long-term self-control ability, improving clinical manifestations, alleviating disease, and improving the quality of daily life. Therefore, it is important to give the patient the necessary nursing intervention when treating the patient. At the same time, in the treatment of unrelated seriously harmful diseases in patients with hepatitis, efficient nursing interventions play a vital role in the efficacy and quality of life of patients. On this basis, this study selected 142 patients with hepatitis in tertiary hospitals to discuss the impact of care on the management level and quality of life of patients with hepatitis, and the conclusions are reported as follows [3].

The article is dedicated to discussing the impact of nursing style on the management level and quality of life of patients with hepatitis and has important research significance for the efficacy and quality of life of patients with hepatitis.

2. State-of-the-Art Technology

2.1. The Need for Health Education on Chronic Hepatitis B. Health education knowledge is also a programmatic, organized, and comprehensive science education theme activity, so that people are aware of healthy individual behaviors and lifestyles, prevent diseases, and promote the quality of health and life. At the same time, health education knowledge is conducive to patients to establish the confidence to correctly understand the disease and defeat the disease, so that patients can grasp the health care and medical expertise, closely cooperate with the treatment, and obtain medical results. The research of many scholars around the world has found that diffuse hepatitis is a typical physical and mental disease, which integrates physical diseases and psychological and social factors "three-dimensional." Prolonged negative psychological conditions can also cause diseases of the central nervous system and reduce liver volume. However, many patients with diffuse hepatitis have little understanding of life and life path. Rest and regression of exercise, dietary structure, pharmaceutical knowledge, and disease are at different stages [4]. Further reduction of the patient's immune function is not conducive to the elimination of the human body, aggravating the disease and producing a variety of negative effects, forming a vicious circle, resulting in the onset of the disease [5]. Guo Jinlong et al. investigated the level of professional knowledge of hepatitis prevention in healthy populations and found that the basic knowledge level of hepatitis prevention in healthy populations accounted for 89%, and the illiterate group only reached 11%. Through investigation and analysis, Zheng Jie et al. found that such patients understand the causes of hepatitis, medication knowledge, life care, and how to exercise, disinfect and sterilize, and protect [6].

The professional knowledge participation rate of patients with hepatitis in our country is low, usually in backward areas, because our level is low, and the level of patients in large urban areas is high. However, due to busy work and no time to take care of it, Wuhan city seriously lacks health

education knowledge about hepatitis, and the cognition of this disease is still stuck in a low level. Abnormal physiological effects, unhealthy habits, dietary mix and lifestyle, and other healing factors are ignored, causing hepatitis attacks [7]. For example, Chen Haiyan found in "Influencing Factors of Creating Healthy Behaviors and Preventive Measures for Secondary Hospitalization of Patients with Diffuse Hepatitis" that the second hospitalized patient had bad habits, living habits, and poor mentality [8]. Depending on the individual behavior of creating a healthy lifestyle for these patients, radical adherence to treatment may reduce seizures or reduce seizure levels [9]. Therefore, the implementation of dependent health education for patients with acute and chronic hepatitis and medical staff can reduce the level of healthy China and have important practical significance for reducing medical expenses and health expenditures of the broad masses of the people. This is shown in Figure 1.

2.2. Research Progress on Adherence and Its Influencing Factors in Patients with Chronic Hepatitis B. Patient compliance is defined as "the level at which the patient's behavior in the changes in medications, dietary combinations, and lifestyle habits is consistent with the doctor's order." The word "listen" was first used by Chinese experts from Ruan to teach Chinese translation applications [10]. The emphasis on adherence refers to the level at which the patient's actions are consistent with the scripting written by the doctor in advance in the treatment and prevention of the disease. Because the disease of diffuse hepatitis is very long and prone to onset, many patients have little understanding of the condition and cannot carry out outpatient follow-up visits, take medicines, and change bad eating habits and living habits according to the medical instructions of medical staff. It can be seen that the efficacy of patients with hepatitis disorders is not ideal, and it is related to the cause of the disease; in addition to the lack of efficient therapeutic drugs, a key that cannot be ignored is the poor compliance of patients [11].

Obstacles to patient compliance are numerous and complex, including patients, physicians, medical security systems, and regulatory factors that affect each other. Patient compliance depends entirely on the patient himself, and promoting patient compliance must be coordinated by patients, physicians, medical treatment, etc. and can only rely on the efforts of patients. Some experts and scholars have summarized the key obstacles that may cause a decline in compliance. It can be solved from three different levels, doctor and patient, patient and medical, and doctor and medical treatment, and promote patient compliance. At this stage, the scientific research on factors that harm patient compliance is mainly in many aspects such as high blood pressure, diabetic patients, schizophrenia, epilepsy, tuberculosis, and "kidney transplantation" [12]. When analyzing the factors that endanger the treatment compliance of patients with chronic diseases, it is emphasized that the socio-demographic economic characteristics of patients are related to treatment compliance, including the elderly, disease characteristics, surrounding environmental applicability, doctor-patient contradictions, cognitive ability of treatment and

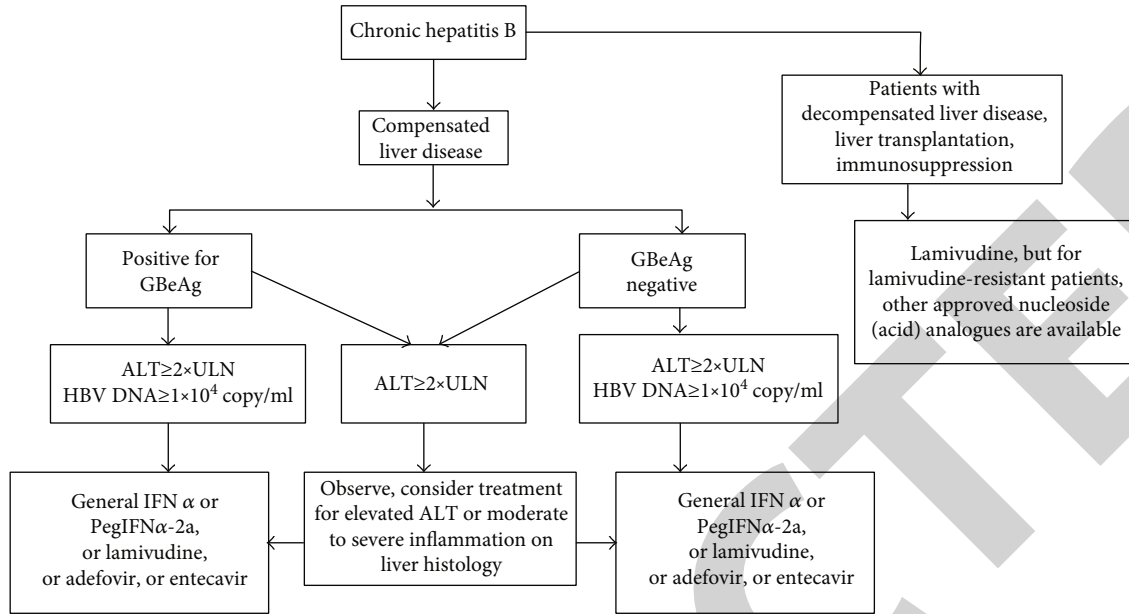


FIGURE 1: Flowchart of hepatitis B prevention and treatment.

disease, and beliefs in physical and mental health [13]. Literature data show that the current stage of treatment compliance in patients with hepatitis disorders is relatively scattered, and there is a lack of comprehensive assessment of adherence to patients with hepatitis diseases and the analysis of harmful compliance factors. Factors related to compliance have been found only in certain references. Drug use, patient perceptions of the importance and effectiveness of drugs, perceptions of the disease, concerns about adverse drug reactions, and doctor-patient conflicts may affect patients' self-adjusting personal behavior [14]. The details are shown in Figure 2.

2.3. Efficacy of Health Education on Chronic Hepatitis B. With the change of modern medical models from medicine to social medicine, doctors and nurses slowly realized that diffuse hepatitis is a typical physical and mental disease. Integrating the influencing factors of physiological diseases, psychological state, and social development, patients with diffuse hepatitis are not only physically uncomfortable but also bear various pressures in work, life, and thought, coupled with the lack of disease awareness and health care medical knowledge, repeated attacks of diseases, and long-term acceptance of therapeutic health education which has become a way for contemporary medical staff to recognize patients' diseases and health knowledge and their effectiveness [15]. This is to let people shape the concept of "better than cure," develop good living habits, correct bad habits that are harmful to health, then maintain physical health, reduce the occurrence of diseases, or maintain physical health, and reduce the production of diseases or auxiliary treatment methods for curing diseases. Specifically guide hospitalized patients to read articles health education guidelines, and carry out systematic software health education according to their specific guidance, group special lectures, etc. [16]. The results show that health education is conducive

to patients' learning knowledge and self-management ability, completing the long-term unification of professional knowledge, information content, and personal behavior in their physical and mental health. Gulalai et al. [17] carried out all-round education for hospitalized patients, so that patients could grasp the triggering elements of recurrence, grasp their own nursing knowledge, reduce the recurrence rate, and reduce the quality of life [18]. Satisfactory practical results were obtained. Through some forms of health education theme activities, patients have a better understanding of the treatment and health knowledge of acute and chronic hepatitis, and the poor living habits are greatly improved. According to health education, patients with diffuse hepatitis are made aware of the importance of medical treatment and antiviral treatment of nucleoside (acid) analogues in the infectious disease department or hepatology department of the hospital on time after the onset of the disease, especially according to health education, under the premise of timely, biochemical, excessive examination to prevent lesions, early detection of diseases, and timely treatment.

Therefore, health education for patients with diffuse hepatitis is used to grasp the factors that influence relapse, thus repairing patients' perception of life care and self-confidence in overcoming difficulties, so that they can move from passive therapeutic care to active prevention of disease and relapse [19].

2.4. Current Status of Health Education for Chronic Hepatitis B. In the past, under the influence of modern medical models and Western countries, China's health education has shown higher professional knowledge and technicality, but it does not attach great importance to service. With the change of scientific research on the meaning of physical and mental health in various countries in the world, medical personnel around the world have gradually begun to attach great importance to health education and will no longer

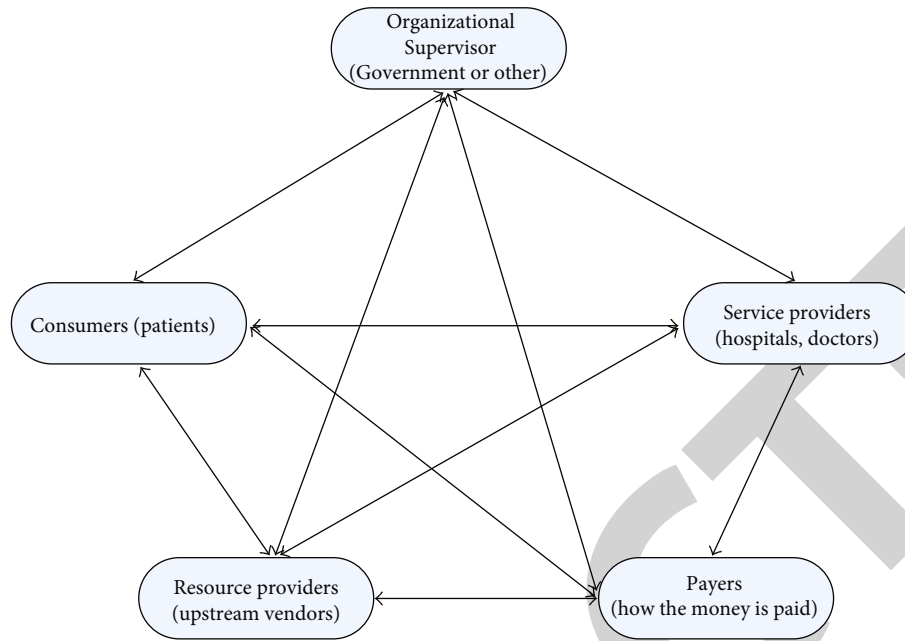


FIGURE 2: Functional role of the health system in the “five-party mode.”

regard it as a service but will closely integrate professional knowledge, technology, and services, that is, the quality and level of services to meet the needs of patients. Health education is rooted in our country, and Western theories and methods cannot be applied in a simple and mechanical way. It is necessary to combine the personality characteristics, mentality, and day and night physiological state of the Chinese nation in Wuhan City, China, and make full use of many unique health education methods created by Chinese medicine in the development of Chinese culture in the past five thousand years [20]. TCM hospital shoulders the daily task of applying TCM to prevent and treat diseases, ensure people’s health, provide TCM health care services for the people, and inherit and develop academic research talents in TCM. However, under the situation of fierce competition in the diagnosis and treatment market, the diagnosis and treatment services of Chinese medicine hospitals are significantly lower, and it is impossible to maintain survival and development. Specific performances are as follows: first, in the introduction of many outstanding talents in Western medicine, the staff of traditional Chinese medicine is gradually reduced. Second, because of the low cost of traditional Chinese medicine services, it is expected to introduce many large- and medium-sized testing instruments to increase profits and maintain the rapid development of hospitals by carrying out surgeries and treatments in Western medicine. For a long time, China’s hospitals have not had the characteristics of traditional Chinese medicine, and health education has no characteristics. The health education of patients with diffuse hepatitis in China must be closely integrated with the basic theories of traditional Chinese medicine such as “identity verification,” “future treatment,” and “four seasons of health care.” The health education of patients with chronic hepatitis should be closely related to the basic theories of traditional Chinese medicine such as

“physical fitness identification,” “treatment,” and “four-hour diagnosis and treatment” and make full use of the characteristics of traditional Chinese medicine to create health education with the characteristics of traditional Chinese medicine. Health education has become one of the disciplines of great concern to the nursing profession at this stage. Its essence is an intervention, to give people the professional knowledge, technology, and services needed to change their personal behavior and lifestyle, so that when faced with health problems such as health and disease prevention, treatment, and recovery, they can carry out personal behavior selection, remove or reduce the sources of risk affecting health, and actively adopt healthy personal behaviors and lifestyles. In general, the medical care of patients with hepatitis is not only related to hospital equipment, medical water equality, and objective reasons. It is also related to the interference of objective factors such as the psychological state of nursing staff and personal behavior. The high emphasis on nursing models and the subjective interference of medical staff in the daily life of questioning hepatitis patients is reasonable, and the relationship between the factors is shown in Figure 3.

3. Investigative Methodology

3.1. Data Collection. 142 patients with hepatitis B admitted to the hospital from July 2020 to April 2022 were studied. Selection criteria are as follows: (A) inclusion criteria: (1) CHB confirmed by serology, quantitative hepatitis B virus, and liver function; (2) have clinical symptoms such as liver discomfort, fatigue, and loss of appetite; (3) no cognitive impairment; and (4) acute medical history and (B) elimination criteria: (1) end-stage liver disease; (2) accompanied by other chronic diseases; and (3) those who do not have basic communication skills and cannot cooperate with the

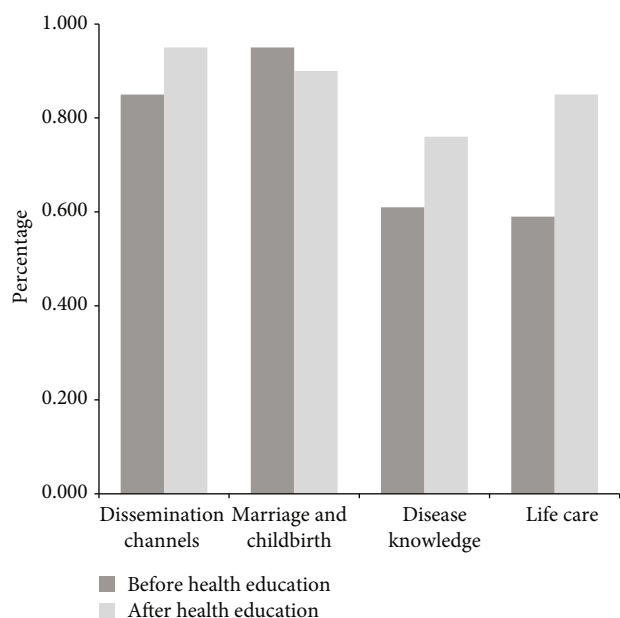


FIGURE 5: Overall improvement in cognitive awareness of hepatitis B in patients in the test group.

patients to the pathogenesis, disease regression, clinical manifestations, transmission routes, and treatment measures of hepatitis B with easy-to-understand illustrations and language, disseminate relevant disease information, combine cases and good treatment effects, and establish patient cognitive therapy. (3) Behavioral health care: it is recommended that patients choose low-fat and high-protein foods such as eggs, lean meat, and fish, eat more fruits and vegetables, and increase vitamin supplements. Eat regularly, eat lightly, eat less, avoid spicy and other irritating foods, overeat, smoke and drink alcohol, and ensure adequate sleep. Patients are encouraged to perform moderate aerobic exercise (e.g., walking and tai chi) for 30 to 50 minutes each time. (4) Out-of-hospital nursing: publish the contact information of the attending physician when discharged, guide the patient to take the medication on time and review it regularly and seek medical treatment in time under special circumstances to prevent treatment delays. Establish WeChat and QQ groups, check messages regularly every day, and answer questions from patients and their families. And timely release of the latest news related to the disease.

The two measures of cognitive and behavioral intervention are as follows: (A) cognitive intervention. Based on the results of the patient's cognitive assessment, a targeted cognitive intervention plan was developed for them. (1) Comprehensive health education: use one-on-one communication to let patients understand the causal relationship and precautions of hepatitis B. Inform the patient in detail of the stage of the current treatment goal and the benefits of actively cooperating with the care, and fully improve the patient's confidence. Strengthen the health knowledge education of patients' family lies and improve their awareness of hepatitis B, so that they can fully give patients emotional care and actively cooperate with relevant care. (2) Conduct regular missionary lectures: distribute self-made hepatitis B

publicity materials, including modules such as basic knowledge of diseases, life care, and rehabilitation exercises. At the same time, the missionary atmosphere is actively carried out, collecting each patient's questions, interacting with patients through scenario reenactment, and allowing nursing staff to record the minutes of each missionary meeting, summarize and organize them into leaflets, and send them to patients after the meeting to deepen their understanding and memory. (B) Behavioural intervention: (1) diet structure: develop a reasonable diet plan for patients, eat less and more meals, containing high protein and vitamins, etc., a balanced diet, and recommend that patients quit smoking and alcohol. (2) Exercise and rest: bed rest is the main focus of patients during acute exacerbations, avoid unnecessary activities, and ensure adequate sleep. (3) Drug intervention: during hospitalization, by quoting the opposite word, patients are instructed and advised to take the drug regularly and quantitatively and are told to stop the drug without authorization or reduce the harm caused by the use of the drug. After discharge, a love contact card is issued to each patient, which is convenient for full-time staff to make weekly telephone return visits to understand the patient's emotions and life dynamics and give timely guidance and suggestions to help patients relieve stress and emotions. Regular quarterly communication seminars are held for discharged patients to provide a platform for communication, learning, and consultation. (4) Psychological regulation: on the one hand, by creating a warm and comfortable ward environment during hospitalization, such as placing green plants, the patient's psychology can be regulated. On the other hand, nursing staff should guide patients to carry out psychological exercises in a timely manner through verbal catharsis and deep breathing methods to help patients maintain a good psychological state, as shown in Figure 5.

Both groups were given intraperitoneal drugs such as hepatoprotective, antiviral, immunomodulatory, and enzyme-lowering and were hospitalized for observation for 2 weeks. Patients in the control group were given a routine model that included explaining that heparin is B-related knowledge, daily precautions (isolating saliva and blood-related items such as toothbrushes, towels, and razors from others), following medication recommendations, maintaining a positive therapeutic mindset, and paying attention to appropriate exercise, Aphrodite spicy diet, and overeating. Instruct the patient to review regularly at the time of discharge.

3.3. *Evaluation Indicators.* (1) The self-management scale (PIH, a means of assessing the psychological state of the meditators) was used to assess the management ability of two groups of patients, including self-monitoring, disease knowledge acquisition, and core management ability, with a total score of 88 points, and the higher the score, the poorer the management. (2) Before and after 1 month of nursing, the quality of life of two groups of patients was assessed using the Quality of Life Measurement Summary Table (QOL-BREF), including four dimensions of physical, psychological, social, and environmental fields, with a score of 100 points; the higher the score, the better the quality of

life.

$$\text{SAS} = \text{Score} \times 1.25. \quad (1)$$

Patients were followed up for 1 month after discharge and compared the treatment of the two groups. (1) The anxiety self-assessment scale (SAS) was used to evaluate the patient's anxiety level, and the depression self-assessment scale (SDS) was used to evaluate the patient's depression level, using SAS20 items, each with a score of 1 to 4 points, and the total score $\times 1.25$ points: mild anxiety: 50-59 points; moderate anxiety: 60-69 points; severe anxiety: SAS ≥ 70 points; mild depression: 53-62 points; moderate depression: 63-72 points; and major depression: SDS ≥ 73 points. (2) Evaluation of patient treatment compliance: these 7 items include compliance with medication, not stopping medication without authorization, not eating and drinking, quitting smoking and alcohol, maintaining a good mental state, working and resting regularly, regularly reviewing, and those who are able to perform all of these tasks are considered fully compliant, those who cannot do any of the above are not compliant, and the rest are considered partially compliant. (3) The short life scale (SF-36) was used to evaluate the quality of life of patients. SF-36 includes 8 dimensions of general health (GH), bodily function (PF), bodily function (RP), somatic pain (BP), vitality (VT), social functioning (SF), emotional functioning (RE), and mental health (MH). Each dimension is rated from 0 to 100, and the higher the score, the better the quality of life.

$$\text{SF} = \sum_{i=1}^8 c_i \cdot \text{Score}_i. \quad (2)$$

3.4. Statistical Methods. In our research, we mainly use hypothesis tests for data processing, mainly including t -tests, Z tests, and chi-square tests. We consider the sample to conform to the normal distribution, i.e.,

$$x \sim N(\mu, \sigma^2). \quad (3)$$

First, establish the hypothesis of nothingness $H_0: \mu_1 = \mu_2$; i.e., assume that there is no significant difference between the two population means. Then calculate the statistic T -value and use different statistical calculation methods for different types of problems. If you want to determine the degree of difference between the mean of a small sample in the population and the mean of the population, the formula used to calculate the T -value of the statistic is

$$T = \frac{\bar{X} - \mu_0}{s/\sqrt{n-1}}. \quad (4)$$

If you want to determine the degree of difference between the means of the two sets of samples, the T -value

of the statistic is calculated as follows:

$$T = \frac{\bar{X}_1 - \bar{X}_2}{\sqrt{(\sum x_1^2 + \sum x_2^2)/(n_1 + n_2 - 2) \times (n_1 + n_2)/(n_1 \times n_2)}}. \quad (5)$$

The Z test is a commonly used method for large sample mean difference tests (that is, sample sizes greater than 30). It uses standard normal distribution theory to infer the probability of a difference occurring, thereby comparing whether the difference between the two means is significant.

$$Z = \frac{\bar{X} - \mu_0}{s/\sqrt{n}}, \quad (6)$$

$$Z = \frac{\bar{X}_1 - \bar{X}_2}{\sqrt{(s_1/n_1) + (s_2/n_2)}}. \quad (7)$$

Chi-square testing is a hypothesis testing method used for various counting data. It falls under the category of non-parametric tests, which are primarily compared to two or more sample rates (composition ratios) and correlation analysis of two categorical variables. The basic idea is to compare the degree of coincidence or fitting between the theoretical frequency number and the actual frequency number.

$$\chi^2 = \frac{(n-1)S^2}{\sigma^2} \sim \chi^2(n-1), \quad (8)$$

$$F = \frac{S^1/S^2}{\sigma_1^2/\sigma_2^2} \sim F(n_1 - 1, n_2 - 1). \quad (9)$$

To measure the final result, we test it with the probability P value of the sample observations or the more extreme result obtained when the null hypothesis is true; if the P value is small, the probability of the original hypothesis is very small; if it is true, then according to the principle of small probability, we have reason to reject the null hypothesis, and the smaller the P value, the more sufficient the reasons for our rejection of the null hypothesis. In summary, the smaller the P value, the more pronounced the results. However, whether the test result is "significant," "moderately significant," or "highly significant" needs to be solved according to the size of the P value and the actual problem.

$$p = \begin{cases} 2[1 - \phi(Z_0)], & p \neq p_0, \\ 1 - \phi(Z_0), & p > p_0, \\ \phi(Z_0), & p < p_0. \end{cases} \quad (10)$$

Use SPSS 23.0 statistics software to process data. The count data is expressed as n (%) \times^2 and represented by the test. The measurement data is represented by the cloud $\bar{x} \pm$, using in-depth sample t -tests between groups and paired samples within groups. $P < 0.05$ indicates that the difference is statistically significant.

TABLE 1: PICH scores ($\pm\bar{x}$, points) of self-management skills before and after nursing in two groups.

Constituencies	n	Before care	Postoperative care	t	P
Observation groups	71	66.55 \pm 2.11	25.68 \pm 4.32	71.629	0.001
Control group	71	66.23 \pm 2.12	36.31 \pm 3.55	60.972	0.001
t		0.902	16.019		
P		0.369	0.001		

TABLE 2: QOL-BREF scores before and after quality of life of patients in the two groups ($\bar{x} \pm s$, score).

Constituencies	n	Before care	Postoperative care	t	P
Observation groups	71	71.65 \pm 4.36	90.36 \pm 5.48	22.513	0.001
Control group	71	71.71 \pm 4.34	83.22 \pm 5.41	13.984	0.001
t		0.082	7.813		
P		0.935	0.001		

TABLE 3: SAS and SDS scores before and after the two groups of interventions (scores, $\bar{x} \pm s$).

Constituencies	Number of examples	SAS		Safety data sheets	
		Before intervention	After intervention	Before intervention	After intervention
Control group	47	59.5 \pm 9.7	51.3 \pm 6.2	61.7 \pm 10.6	54.9 \pm 7.3
Observation groups	47	59.6 \pm 9.8	36.8 \pm 5.2	61.7 \pm 10.5	39.8 \pm 6.3
t		0.05, >0.05	12.29, <0.01	0, >0.05	10.74, <0.01

4. Results Analysis and Discussion

4.1. Management Capabilities. Before nursing, the PIH scores of the two groups were compared, and the difference was not statistically significant ($P > 0.05$). After one month of nursing, the PIH scores of both groups were lower than before nursing care, and the PIH scores of the observation group were significantly lower than those of the control group, and the difference was statistically significant ($P < 0.05$). See Table 1.

4.2. Quality of Life. QOL-BREF scores were compared between the two groups before nursing treatment, and the difference was not statistically significant ($P > 0.05$). After one month of treatment, the QOL-BREF scores of both groups improved compared with before treatment, and the QOL-BREF scores of the observation group were significantly higher than those of the control group, and the difference was statistically significant ($P < 0.05$). See Table 2.

4.3. Changes in SAS and SDS Scores before and after the Two Groups of Interventions. The SAS and SDS scores of the two groups were close before the intervention, and the difference was not statistically significant. After the intervention, the above scores in the observation group were lower than those in the control group, and the difference was statistically significant, as shown in Table 3.

4.4. Comparison of Treatment Adherence between the Two Groups. Treatment adherence was significantly better in the observation group than in the control group, with statistically significant differences ($\chi^2 = 10.85$, $P < 0.01$), as shown in Table 4.

4.5. Changes in SF-36 Scores before and after the Two Groups of Interventions. The SF-36 scores of each dimension in the first two groups of the intervention were similar, and the difference was not statistically significant. After the intervention, the observed score was higher than that of the control group, and the difference was statistically significant, as shown in Table 5.

4.6. Analysis. Hepatitis is a chronic infectious disease that is difficult to treat. Studies have found that patient cognitive and management skills are a powerful way to prevent hepatitis. However, the existing basic methods can no longer meet the needs of hepatitis patients and their families. The nursing method can help patients recover by intervening in the cognition and life of patients with hepatitis and quickly and effectively improve the patient's management level and quality of life. The data of this scientific research shows that compared with the experimental group, after the observation group nursed 1 yuan, the management level PICH score was relatively low, the Clenlonzo score was relatively high, the difference was statistically significant, and the nursing mode used for patients with hepatitis could effectively quality their management level and life. According to the effective

TABLE 4: Comparison of treatment adherence between the two groups (cases (%)).

Constituencies	Number of examples	Fully compliant	Partial compliance	B. noncompliance
Control group	47	18 (38.3)	15 (31.9)	14 (29.8)
Observation groups	47	29 (61.7)	16 (34.0)	2 (4.3)

TABLE 5: Changes in SF-36 scores before and after the two groups ($\bar{x} \pm s$).

SF-36 rating	Control group ($n = 47$)		Observation group ($n = 47$)	
	Before intervention	After intervention	Before intervention	After intervention
Somatotropin	62.1 \pm 3.2	67.8 \pm 6.6	61.4 \pm 3.3	78.9 \pm 5.6*
Interrupter	63.1 \pm 3.3	65.4 \pm 5.2	62.8 \pm 3.3	75.3 \pm 5.2*
RP	64.9 \pm 2.8	67.7 \pm 7.2	65.8 \pm 2.6	77.1 \pm 6.5*
BP	64.8 \pm 3.4	68.5 \pm 6.3	65.3 \pm 3.5	75.9 \pm 5.4*
Interrupter	65.9 \pm 3.1	69.2 \pm 6.7	66.5 \pm 3.2	74.2 \pm 7.2*
SF	64.1 \pm 4.2	67.4 \pm 4.6	63.8 \pm 4.2	72.3 \pm 4.5*
Again	62.1 \pm 3.3	66.5 \pm 5.3	61.2 \pm 3.2	74.6 \pm 5.5*
Interrupter	61.8 \pm 3.2	67.6 \pm 6.6	62.3 \pm 3.4	77.1 \pm 5.4*

*Compared with the postintervention control group, $P < 0.05$.

intervention of patients' rest, fitness time, and dietary structure, a warm ward environment is generated to ensure adequate sleep time and balanced nutritional intake of patients and to adjust anxiety. At the same time, effective communication is establishing a good doctor-patient relationship, so that nursing staff can deeply understand the dynamics of the patient's mentality, give immediate and accurate psychological counseling to the patient, and maintain the patient's attitude of close cooperation with the treatment. In addition, cognitive behavioral care interventions include knowledge education of patients' families, enabling them to achieve a united front between relatives and caregivers. The emotional care and suggestions of family members can effectively improve the patient's mentality, reduce anxiety, antitreatment, and other negative emotions, and maximize the efficacy under the premise of active treatment of patients.

It can be seen that improving health education knowledge in the clinical medical treatment of patients with diffuse hepatitis can improve the patient's ability to adapt to treatment, maintain a stable mentality, cooperate with each other in a variety of treatment and nursing, and improve their efficacy and quality of life. Many patients with diffuse hepatitis do not have enough knowledge of disease and treatment health education, which is easy to cause misunderstandings and cognitive dissonance, and cannot adequately cooperate with each other in treatment and care. Coupled with the influence of the patient's own bad living habits, the efficacy is weak. According to the specific situation of patients, targeted health guidance is carried out, and health education knowledge is optimized from multiple aspects such as patient mentality, diet structure, drug interaction, and lifestyle. Maximize the patient's treatment and nursing requirements, ensure a better concept of mutual cooperation between treatment and nursing, improve the trust of medical staff, and closely cooperate with various types of treatment and nursing to achieve overall efficacy.

This dissertation data showed that the SAS and SDS scores in the postintervention observation group were significantly lower than those in the control experiment, showing that the comprehensive nursing intervention could effectively improve the patient's negative mood and maintain optimism and positivity. The treatment compliance and SF-36 scores of the postintervention observation group were higher than those of the control group, indicating that the integrated nursing intervention could deepen the patient's understanding of the disease, build confidence in overcoming the disease, and improve treatment compliance and quality of life. Therefore, comprehensive nursing interventions can effectively alleviate the recovery of patients with hepatitis, the personal behavior of the doctor, and the quality of life.

5. Conclusion

Hepatitis B is a common infectious disease of the Chinese biliary system software. According to the type of disease, it can be divided into diffuse and subacute. Diffuse hepatitis is a multiple disease that seriously endangers the healthy life of patients. Clinical observation is based on antiviral therapy, which is difficult to treat and easy to attack. The greater the effectiveness, the less effective it is, creating a vicious circle. How to find efficacy, it is necessary to gradually improve the relevant treatment and care plan. According to the treatment compliance of the two groups after intervention, the treatment compliance rate of the intervention group was significantly higher than that of the control experiment 70.0%, and the difference was statistically significant (Ma Yili 0.05), which was consistent with the views reported by Li Fafang and others, and the treatment difficulty coefficient and long-term treatment of comprehensive nursing intervention hepatitis were lagging behind, which was easy to cause

patients to have relatively large psychosomatic stress reactions, depression, anxiety, and other mental health problems. Reduce the patient's self-care evacuation and confidence, lead to inconfidence and frustration in daily life such as diet and difference, and reduce the patient's self-efficacy. Therefore, patients must be given the necessary psychological guidance, which is conducive to self-efficacy.

Through the implementation of comprehensive nursing interventions, this scientific research makes the patients with hepatitis have obvious nursing ability, can quietly distribute daily life, and moderately change the living methods such as avoiding alcohol, taking medicine on time, regular physical examination, and maintaining a stable mentality. This study shows that the health education knowledge level, self-awareness, self-obligation, and self-care professional skills of patients in the post-ESCA scoring intervention group are higher than those in the preintervention group and the control experiment, and the difference is statistically significant, which is consistent with the reports of Ma Yili 0.05 and Li Zhuo, indicating that the self-reliance ability of comprehensive nursing intervention is beneficial to patients with hepatitis. Takizawa Ada's self-reliance ability is positively correlated with the patient's quality of life. The greater the ability to live on its own, the higher the quality of life. This study compared the scores of 2 groups of patients. The data showed that the physical disease and psychological and social development scores of the intervention group were significantly higher than those of the preintervention group and the control experiments, and the difference was statistically significant, which was consistent with the ten million miles view, reminding that the comprehensive nursing intervention was beneficial to the quality of life of patients with hepatitis. In general, based on comprehensive nursing interventions such as reasonable diet and medication consultation, maintaining a stable psychological state, and regular review for patients with hepatitis, patients' self-restraint ability and treatment compliance have been greatly improved. We conclude that the implementation of comprehensive nursing interventions is conducive to improving the treatment compliance and self-care ability of hepatitis B patients and improving their quality of life.

Data Availability

The labeled data set used to support the findings of this study is available from the corresponding author upon request.

Conflicts of Interest

There are no conflicts of interest.

Acknowledgments

This work is supported by the Shanxi Norman Bethune Hospital.

References

- [1] S. Shrestha, P. S. Tiwari, and B. Pradhan, "Occult hepatitis B infection in end-stage renal disease patients starting maintenance hemodialysis at a tertiary care hospital: a descriptive cross-sectional study," *Journal of Nepal Medical Association*, vol. 59, no. 236, pp. 336–341, 2021.
- [2] I. Younus, M. Z. Ali, M. Ajmal, H. Akhtar, J. Ali, and F. Altaf, "Burden and baseline characteristics of patients with decompensated liver disease in Tertiary Care Hospital Gujrat," *The Professional Medical Journal*, vol. 28, no. 2, pp. 165–170, 2021.
- [3] M. Asad, S. Hameed, and M. Subhan, "Frequency of hepatitis B and C and their demographic status in voluntary blood donors in a tertiary care hospital," *AATM 2015*, vol. 12, no. 2, pp. 10–13, 2020.
- [4] N. Butt, R. Hussain, and L. Rai, "Efficacy of pegylated interferon-alpha-2a in hepatitis D infected patients," *Experience from the Tertiary Care Hospital in Karachi*, vol. 11, no. 12, pp. 25–27, 2020.
- [5] S. Khullar, R. S. Parihar, and P. K. Khatri, "Seroprevalence of hepatitis B virus and hepatitis C virus infection in haemodialysis patients at tertiary care hospital in Western Rajasthan, India," *Journal of The Academy of Clinical Microbiologists*, vol. 22, no. 1, pp. 98–103, 2020.
- [6] P. Balasundaram, V. K. Tiwari, and T. S. Raj, "Cost of treatment and consequences for chronic hepatitis B and C virus infection at a tertiary care hospital in Delhi," *Indian Journal of Public Health*, vol. 64, no. 4, pp. 409–412, 2020.
- [7] N. Omar, "Seropositivity of hepatitis B & C in hemodialysis patients at two tertiary care centers in Lahore," *BioMedica*, vol. 12, no. 4, pp. 13–21, 2021.
- [8] R. K. Deo, P. Chitalkar, S. Malla, I. Kc, B. Karki, and R. Thapa, "Epidemiology, clinico-radiological profile and management of hepatocellular carcinoma in a tertiary care center in Nepal," *Medical Journal of Shree Birendra Hospital*, vol. 20, no. 1, pp. 6–11, 2021.
- [9] S. Shrestha, S. Mahatara, S. B. Pun, M. Shrestha, R. Napit, and K. D. Manandhar, "Serological markers and molecular analysis of hepatitis B infection in a tertiary care hospital at Kathmandu, Nepal," *Indian Journal of Gastroenterology*, vol. 39, no. 4, pp. 354–361, 2020.
- [10] S. Siakavellas, J. Goulis, S. Manolakopoulos et al., "Monitoring and comorbidities in patients with chronic hepatitis B currently treated with nucleos(t)ide analogs," *Annals of Gastroenterology*, vol. 34, no. 1, pp. 73–79, 2020.
- [11] B. Alshehail, N. Alotaibi, R. Joseph, and D. Alshayban, "A quasi-experimental trial of the clinical and economic impact of implementing of hepatitis B immunoglobulin policy post needle stick and sharp injuries in reducing its unnecessary use at a tertiary care hospital," *International Journal of Clinical Practice*, vol. 75, no. 10, pp. 42–61, 2021.
- [12] B. Durga, "Knowledge and preventive practices of hepatitis B transmission among dental students and interns in a tertiary hospital: a descriptive cross-sectional study," *JNMA; Journal of the Nepal Medical Association*, vol. 58, no. 222, pp. 108–111, 2021.
- [13] A. Nn and B. Sf, "Seroprevalence of hepatitis B, hepatitis C and HIV 1/2 in patients undergoing surgery in a tertiary care hospital in north India (a hospital based study)," *Clinical Epidemiology and Global Health*, vol. 8, no. 1, pp. 45–48, 2020.

Retraction

Retracted: Design and Application of Artificial Intelligence Technology-Driven Education and Teaching System in Universities

Computational and Mathematical Methods in Medicine

Received 27 June 2023; Accepted 27 June 2023; Published 28 June 2023

Copyright © 2023 Computational and Mathematical Methods in Medicine. This is an open access article distributed under the Creative Commons Attribution License, which permits unrestricted use, distribution, and reproduction in any medium, provided the original work is properly cited.

This article has been retracted by Hindawi following an investigation undertaken by the publisher [1]. This investigation has uncovered evidence of one or more of the following indicators of systematic manipulation of the publication process:

- (1) Discrepancies in scope
- (2) Discrepancies in the description of the research reported
- (3) Discrepancies between the availability of data and the research described
- (4) Inappropriate citations
- (5) Incoherent, meaningless and/or irrelevant content included in the article
- (6) Peer-review manipulation

The presence of these indicators undermines our confidence in the integrity of the article's content and we cannot, therefore, vouch for its reliability. Please note that this notice is intended solely to alert readers that the content of this article is unreliable. We have not investigated whether authors were aware of or involved in the systematic manipulation of the publication process.

In addition, our investigation has also shown that one or more of the following human-subject reporting requirements has not been met in this article: ethical approval by an Institutional Review Board (IRB) committee or equivalent, patient/participant consent to participate, and/or agreement to publish patient/participant details (where relevant).

Wiley and Hindawi regrets that the usual quality checks did not identify these issues before publication and have since put additional measures in place to safeguard research integrity.

We wish to credit our own Research Integrity and Research Publishing teams and anonymous and named external researchers and research integrity experts for contributing to this investigation.

The corresponding author, as the representative of all authors, has been given the opportunity to register their agreement or disagreement to this retraction. We have kept a record of any response received.

References

- [1] F. Zhang, "Design and Application of Artificial Intelligence Technology-Driven Education and Teaching System in Universities," *Computational and Mathematical Methods in Medicine*, vol. 2022, Article ID 8503239, 10 pages, 2022.

Research Article

Design and Application of Artificial Intelligence Technology-Driven Education and Teaching System in Universities

Fan Zhang 

Academic Affairs Office of Minjiang University, Fuzhou 350108, China

Correspondence should be addressed to Fan Zhang; 41803307@xs.ustb.edu.cn

Received 4 August 2022; Revised 22 August 2022; Accepted 25 August 2022; Published 10 September 2022

Academic Editor: Pan Zheng

Copyright © 2022 Fan Zhang. This is an open access article distributed under the Creative Commons Attribution License, which permits unrestricted use, distribution, and reproduction in any medium, provided the original work is properly cited.

In recent years, many colleges and universities have been experimenting and exploring the evaluation of education and teaching system and have achieved certain results. In order to understand the quality of education and teaching system in colleges and universities, to improve the school conditions, and to promote the reform of teaching management, methods and means of evaluating the quality of education and teaching system in general higher education institutions are needed. Modern university education and teaching system should realize the combination of classroom teaching and practice teaching, and education and teaching system adopts the mode of the combination of on-campus practice and off-campus practice, so the design of teaching system is the key to the quality of teaching. Aiming at the current problem that talents cultivated by colleges and universities can hardly meet social demands in terms of engineering practice ability, innovation ability, and international competitiveness, this paper proposes the evaluation and adjustment of college education and teaching system driven by algorithms based on artificial intelligence (AI). By designing the teaching system of talent cultivation, and then establishing a quantitative and controllable quality assurance system for practical teaching, a new mechanism for the design of university education system is further explored. Specifically, the framework of the instructional system is built with the aid of an actor-critic algorithm in reinforcement learning, which assists in the design of the university education system, allowing students to truly understand, master and flex their knowledge, and strengthening the correct understanding of the students' internal learning mechanisms. The practical teaching effect shows that the AI-driven instructional designs are more popular with contemporary students and have higher evaluation scores. The numerical experiment results also show the stability of the instructional design, overcoming the drawbacks of traditional manual subjectivity in the design. AI-driven college education and teaching system is conducive to cultivating students' solid technical theoretical foundation. Therefore, through the AI-driven teaching system to strengthen the training of practical ability, so as to comprehensively improve students' comprehensive quality and innovation ability.

1. Introduction

Teaching education system is a unified whole composed of knowledge basic structure, frame, teaching content design, teaching method design, teaching process design, and teaching result evaluation of efficient teaching process. The traditional indoctrination teaching system based on classical conditioning and reinforcement learning theory is not fully aware of students' differences, especially the neglect of students' subjective motivation directly leads to the disengagement of students' interest in learning. The constructivist learning theory believes that learning is the process of an individual's initiative to con-

struct their own knowledge, and the learner is the center of learning [1, 2]. This coincides with the humanistic theory, which emphasizes the initiative of individuals in self-development. Therefore, the cultivation of innovative ability necessarily requires the recognition of individual differences among students in the construction of a practical education system, adhering to the student-oriented concept and highlighting the subjectivity of students' learning.

Modern university education and teaching system should realize the combination of classroom teaching and practical teaching. Classroom teaching should focus on teaching basic theoretical knowledge, and practical teaching

should focus on practical problems, and combining the two can enable students to put theory into practice [3]. The education and teaching system adopts a model combining on-campus practice and off-campus practice. The on-campus practice takes the experimental teaching in real life as the main content, and the off-campus practice takes the real-life process link as the main content to deepen students' understanding of practical applications [3]. The combination of theory and practice helps students to upgrade their theoretical knowledge to the actual production level and cultivate comprehensive talents who have a solid theoretical foundation and are capable of practical operation. In academic practice, we can verify and discover the problems or shortcomings of existing academic research and discover new academic results through scientific innovation. The experimental results generated by scientific innovation can be transformed into technology and serve production through practice [4, 5].

Universities have now come to fully understand how applicable education and teaching methods are. They have worked hard and actively pushed the development of educational and instructional systems, with some degree of success. The seamless blending of theory and practice is still not adequately accomplished [6, 7]. The flawed design of the educational system is to blame. Firstly, the practical teaching lacks the comprehensive and coordinated consideration of professional basic and core courses. Thus, the practical teaching of majors is too fragmented and discontinuous. At the same time, under the concept of constructivism and humanistic teaching theory, students are certainly the center and main body of learning, but this is not the same as ignoring the important role of teachers in teaching. At present, there are many enterprises that have signed agreements with universities to become off-campus practice education bases. However, most of these enterprises do not accept students' internships or practice. The few enterprises that accept students' participation in practice have greater limitations in terms of acceptance scale and level. Under the guidance of correct teaching methods and teaching ideas, the university education system must try new methods, adjust the teaching contents, and change the narrow inertia thinking [8]. This directly leads to the role of the off-campus practice education base not being fully utilized and losing the meaning of the original establishment of the practice base. Therefore, we need to adjust the setting of university education and the teaching system, which do not meet the current situation.

The creation of educational and teaching management ideas and concepts, together with the reform of education management, is consistently at the forefront of changes in educational ideology. Innovative teaching management concept means innovative values and talent concept of higher education. It is the forerunner and the impetus for the reform and development of college teaching as well as the theoretical basis for creating a system of college instruction [9, 10]. First of all, higher education is required to produce a large number of excellent and highly qualified innovative talents. Higher education is required to create a large number of excellent and innovative talents. The so-called excel-

lent and high quality here is a quality standard of development. The characteristics of talent training objectives should reflect comprehensive quality education, and the traditional view of knowledge quality and ability quality should be transformed into a comprehensive quality view including knowledge and ability. The positioning characteristics of talent cultivation specifications should reflect diversity. Not only should we cultivate research-oriented top-notch innovative talents, but also cultivate various types of application-oriented high-quality innovative talents [11]. The characteristics and advantages of personnel training should take innovative personnel training as the fundamental task, so as to highlight the functions of scientific research and social service. Only the organic combination of personnel training, scientific research and social services can make the three coordinated development [12, 13].

To build the teaching management execution system of universities and colleges, we should adhere to the management concept of education being people-oriented and students being the main body, the school being talent-oriented, and teachers being the main body, and take the exploration and establishment of a modern university teaching management system as the breakthrough to carry out the innovation of management system and operation mechanism. As the beginning and conclusion of teaching and management activities, talent development should emphasize the central role of students and their total development [14, 15]. The main body of education is teachers, stimulating teachers' potential as the main teaching management task, and the cohesion of human synergy as the important guarantee for the orderly operation of college teaching. By fully mobilizing the enthusiasm of professors in teaching and management, the university should enhance the quality of instruction and offer the greatest education and service for students. To achieve this, more instructors must spend their time to teaching reform and construction. We can only create a high-quality education and teaching system by allowing instructors to fully express their main spirit and by encouraging their initiative and innovation [16].

The education and teaching systems of colleges and universities serve as the specific worker to service instructors and students as well as the executor of the operation organization of education and teaching work for the talent cultivation system [17]. The teaching management organization is required to concentrate and integrate the advantageous resources of scientific research, disciplines, and talents in talent cultivation and form an innovative talent cultivation system around the knowledge, ability, and quality requirements of talents in the industry fields and positions to be served by disciplines and specialties. The design and application of higher education teaching system can also help the school improve its overall layout. A complete system design can efficiently transform the advantages of teachers and resources into the advantages of whole staff education, thus promoting the organic combination of talent cultivation and scientific research. In this way, it can enhance the level of talent cultivation and social services of the school [18, 19].

The focus and difficulty of constructing college education and teaching system lie in the specific operation mode

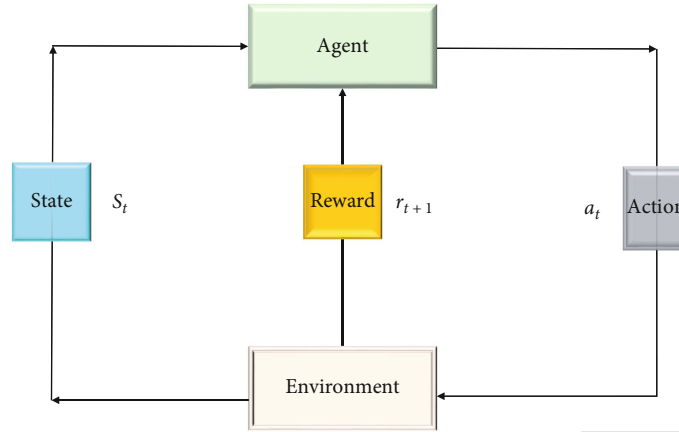


FIGURE 1: Schematic diagram of the reinforcement learning model.

and operation process. Whether the operation process is smooth and efficient depends on the rationality, feasibility, and operability of the core framework composition of teaching management execution. To address the above issues, this paper establishes a three-tier teaching system framework assisted by reinforcement learning algorithms in AI. The decision-making layer focuses on macro planning and emphasizes decision-making and innovation functions. The execution layer strengthens node control and emphasizes coordination and guidance roles. The operation layer strengthens publicity, emphasizes evaluation, and focuses on information feedback to form an efficient closed-loop control system for teaching management. Specifically in the third layer of the framework, artificial intelligence (AI) algorithm technology participates in the improvement and drives the evaluation and adjustment of the system by dynamically checking the interaction state between teachers and students, the professional learning of students, and the management effect of managers, and jointly assessing the implementation effect of the university education and teaching system. We further verify the effectiveness of AI-driven design of university education and teaching system and make some contributions to improve the design and application of university education and teaching system. AI technology assists the quality of the university education and teaching system, improves school conditions, promotes reform of teaching management, and enhances the quality of efficient education and teaching.

2. Related Works

Chen [20] conducted research and developed a proposal for a web-based system for university English-assisted teaching in order to enhance resource sharing and scheduling. A web server and an Android mobile terminal are used to implement the system, and a web-based data integration module is created. For the purpose of evaluating the effectiveness of classroom instruction in online education, Xu and Liu [21] suggested a more rigorous optimization model. He then uses this model to test its validity in a university setting. Model view controller (MVC) architecture was adopted by Sun [22]. This framework is a mobile

client running on Android that can remotely instruct and access university music as well as manage smart music. Experimental findings show that compared to traditional music lessons, online music education has a better learning impact on musical skills. On the basis of the current university curricula, Zhang and Yang [23] analyze the characteristics of the distance learning system for music and dance education and make some particular recommendations for its design. Zhang also researches the state of the art in machine learning as well as several crucial challenges in the creation of the Ologit model. According to Zhang, creating cloud-based digital teaching tools for college physical education courses can save expenses and increase the effectiveness of resource use [24].

3. Models and Evaluation Methods

3.1. Reinforcement Learning. One of the paradigms and methodologies of machine learning used to describe and solve the problem of learning strategies to maximize the reward or accomplish a particular goal during the interaction of an agent with its environment is reinforcement learning, also known as reactive learning, evaluative learning, or augmented learning. Reinforcement learning consists of an agent, an environment, a state, an action, and a reward [25, 26]. The environment will alter once an action is taken by an agent, and in response, it will send a reward signal (either a positive or negative reward) [27]. On the basis of the new state and the reward provided by the environment, the intelligence then executes a new action in accordance with a certain strategy. Through states, actions, and rewards, the intelligence and the environment interact as described above. The reinforcement learning model is shown in Figure 1.

Reinforcement learning can be modeled as a Markov decision process (MDP) [28] whose process can be represented by a five-tuple (S, A, P, R, γ) , where P is the transfer probability of each state, R is the reward value for moving on to the next state after taking an action, and γ is the discount factor. S stands for the set of environmental states.

The MDP can be expressed as

$$p(s_{t+1}|s_t, a_t, \dots, s_0, a_0) = p(s_{t+1}|s_t, a_t). \quad (1)$$

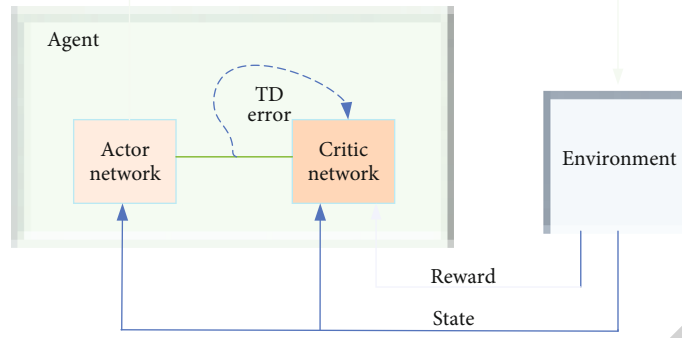


FIGURE 2: AC model framework.

One trajectory of the MDP is

$$\tau = s_0, a_0, s_1, r_1, a_1, \dots, s_{T-1}, a_{T-1}, s_T, r_T. \quad (2)$$

The probability of selection of τ is

$$p(\tau) = p(s_0, a_0, s_1, a_1, \dots) = p(s_0) \prod_{t=0}^{T-1} \pi(a_t | s_t) p(s_{t+1} | s_t, a_t). \quad (3)$$

Given the strategy $\pi(a|s)$, the cumulative reward received by the trajectory τ of an intelligent body during one interaction with the environment is a total reward of $G(\tau) = \sum_{t=0}^{T-1} \gamma^t r_{t+1}$, and $\gamma \in [0, 1]$ is the discount rate [29, 30]. When γ is close to 0, the intelligence will focus on short-term returns, while when γ is close to 1, the intelligence will focus on long-term returns.

The optimal strategy is the one that maximizes the total return obtained in each state, and the objective function of the optimal strategy is

$$J(\theta) = \mathbb{E}_{\tau \sim P_\theta(\tau)} [G(\tau)] = \mathbb{E}_{\tau \sim P_\theta(\tau)} \left[\sum_{t=0}^{T-1} \gamma^t r_{t+1} \right], \quad (4)$$

where γ is the discount factor, θ is the parameter of the policy function, τ is the behavior trajectory, and r is the current reward return value. In other words, reinforcement learning is a kind of learning that discovers how to optimize the reward by learning how to connect states to behaviors. In order to optimize the state-behavior correspondence [31, 32], delay in reward and trial and error are thus two of the most crucial aspects of reinforcement learning. Through reinforcement learning, an intelligence can learn what actions it should take to maximize its reward in what state. Reinforcement learning is a general learning framework that can be used to address general AI issues because intelligences interact with their environments in a manner similar to how humans do. Because of this, machine learning-based reinforcement learning is also referred to as a broad AI strategy [33].

The actor-critic (AC) algorithm combines policy gradients and temporal differencing to create a reinforcement learning system. The actor algorithm refers to the strategy

function $\pi_\theta(s, a)$, i.e., learning a strategy to get a higher return. The critic algorithm is represented via the value function $V_\psi(s)$, which estimates the value function of the current strategy, i.e., evaluating how good the actor algorithm is [34]. The AC method may update the parameters in a single step rather than having to repeat the process at the conclusion of each round thanks to the value function. The method based on the combination of value function and policy function is called AC algorithm. AC algorithm consists of two parts, actor and critic, where Actor is based on the policy function, which is responsible for interacting with the environment and selecting the action; critic is based on the value function, which is responsible for evaluating actor and guiding its next state action. The reinforcement learning model of the AC algorithm is shown in Figure 2.

We use here the time difference error at L steps and learn the critic function $V_\psi^{\pi_\theta}(s)$ by minimizing the square of this error, denoted as

$$\psi \leftarrow \psi - \eta \nabla J_{V_\psi^{\pi_\theta}}(\psi), \quad (5)$$

where ψ denotes the parameters of the learning critic function, η is the learning step size, and the original update function is expressed as

$$J_{V_\psi^{\pi_\theta}}(\psi) = \frac{1}{2} \left(\sum_{t=1}^{i+L-1} \gamma^{t-i} R_t + \gamma^L V_\psi^{\pi_\theta}(S') - V_\psi^{\pi_\theta}(S_i) \right)^2, \quad (6)$$

where S' is the state reached by the intelligent body after L steps under π_θ , so it can be expressed as

$$\nabla J_{V_\psi^{\pi_\theta}}(\psi) = \left(V_\psi^{\pi_\theta}(S_i) - \sum_{t=1}^{i+L-1} \gamma^{t-i} R_t - \gamma^L V_\psi^{\pi_\theta}(S') \right) \nabla V_\psi^{\pi_\theta}(S_i). \quad (7)$$

Similarly, the actor function $\pi_\theta(\cdot|s)$ determines the action taken on each state s or a probability distribution over the action space [35]. We learn this strategy function using a similar approach to the initial version of the strategy gradient:

$$\theta = \theta + \eta \nabla J_{\pi_\theta}(\theta), \quad (8)$$

where θ denotes the parameter of the actor function, η_θ is the learning step, and the formula is expressed as

$$\nabla J(\theta) = E_{\tau, \theta} \left[\sum_{i=0}^{\infty} \nabla \log \pi_\theta(A_i | S_i) \left(\sum_{t=i}^{i+L-1} \gamma^{t-i} R_t + \gamma^L V_\psi^{\pi_\theta}(S') - V_\psi^{\pi_\theta}(S_i) \right) \right]. \quad (9)$$

It is worth noting that the AC algorithm can also use the Q-value function as its criterion. In this case, the dominance function can be estimated using the following equation:

$$Q(s, a) - V(s) = Q(s, a) - \sum_a \pi(a|s) Q(s, a). \quad (10)$$

The loss function used to learn the Q-value function for this critic is

$$J_Q = (R_t + \gamma Q(S_{t+1}, A_{t+1}) - Q(S_t, A_t))^2. \quad (11)$$

Alternatively

$$J_Q = \left(R_t + \gamma \sum_a \pi_\theta(a|S_{t+1}) Q(S_{t+1}, a) - Q(S_t, A_t) \right)^2, \quad (12)$$

where action A_{t+1} is obtained by sampling the current policy π_θ in state S_{t+1} .

3.2. Design of College Education and Teaching System Driven by AI Technology. The design of higher education teaching system is similar to the process of finding the optimal strategy in a discrete space, which has natural similarity with the sequential decision making of reinforcement learning. Therefore, the design of teaching system can be transformed into a MDP, and the reinforcement learning can be better used to assist in the design of teaching system. In this way, it fully combines the characteristics of the internal management system of colleges and universities and divides tasks and roles according to decision making, implementation, monitoring, and consulting around the overall teaching goals of the school. The education and teaching system in colleges and universities is the braking force that runs through the teaching management process and is the balancer of the two forces of incentive and restraint. Innovative college education and teaching system is the basic guarantee to make school teaching in a dynamic, efficient, and conscious operation, and is the key to whether teachers can be effectively mobilized to actively participate in teaching reform and construction.

On the one hand, according to the needs and motivation characteristics of teachers, administrators, and teaching units, in addition to material incentives and institutional norms, material incentives, institutional norms, and spiritual incentives are combined by giving corresponding honors, providing opportunities to show talents, and building a platform for success. Through the promotion of typical models, exemplary demonstrations, and evaluation of excellence, we

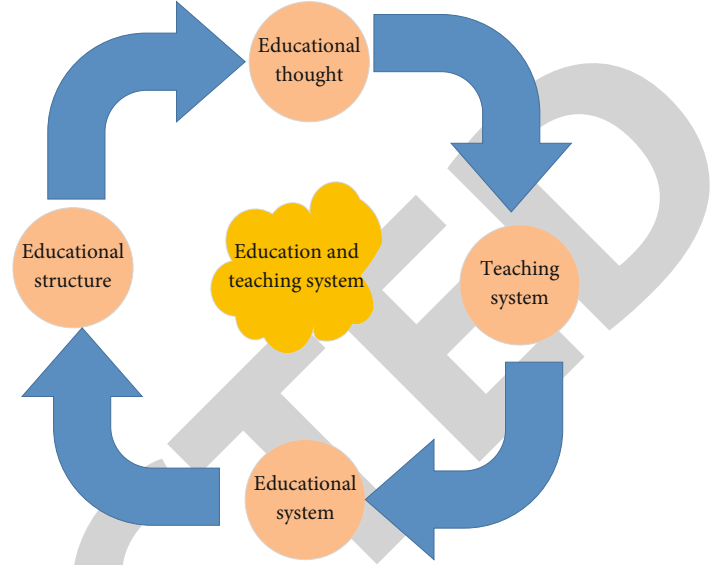


FIGURE 3: University education and the teaching system.

can stimulate the enthusiasm, initiative, and creativity of teachers, teaching managers, and teaching units to participate in teaching and teaching reform and construction.

On the other hand, by clarifying the objectives of teaching work and teaching management, establishing a scientific system of evaluation of teaching and management, and adopting a combination of rewards and punishments, reasonable pressure is formed. Teaching objectives include pressure of responsibility and pressure of competition. Only by giving full play to the competition mechanism of survival of the fittest can we establish the management system and distribution system based on the evaluation of teaching work and management work. The teaching management system is a kind of tangible specification, and the education and teaching systems of colleges and universities must be continually improved in order to guarantee that the teaching can be in outstanding condition. The construction of a complete teaching system requires colleges and universities to conform to the people-oriented concept and connotation, respect teachers' subjectivity, properly deal with contradictions and conflicts, and then form a harmonious teaching atmosphere.

In addition, a teacher-oriented system of consultation, review, and supervision of teaching should be established to promote the democratization and humanization of teaching management. Encourage and support faculty participation in teaching construction and reform, teaching management, teaching research, and teaching exchange. In turn, it provides assistance for the development of teachers who are in a position to do so; solicits rationalized suggestions from teachers on teaching and teaching management; and facilitates teachers' participation in academic activities. In summary, we will design the model of university education and the teaching system as shown in Figure 3.

The evaluation and improvement of the model of the higher education teaching system is a key step for the system to be able to work. According to the analysis of the theoretical

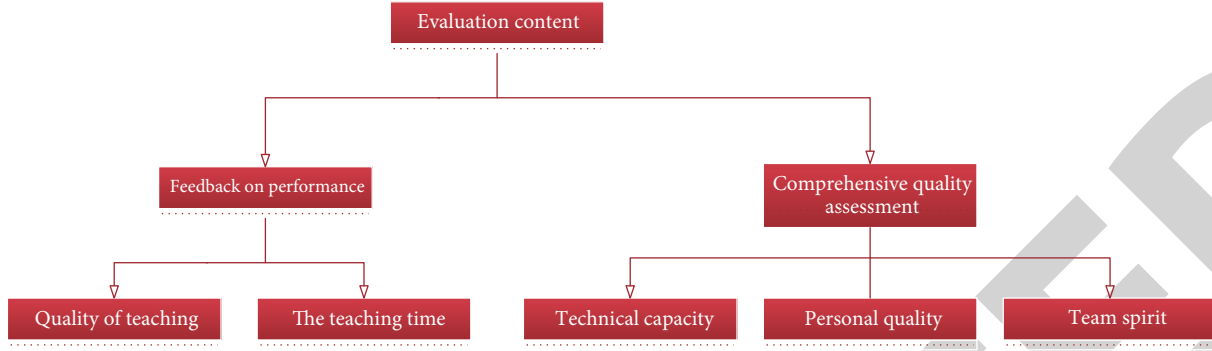


FIGURE 4: The college education and teaching system.

TABLE 1: Satisfactory evaluation of the assessment of a particular piece of data.

Effectiveness evaluation	Very satisfied	Satisfied	General	Rather poor	Poor
Operation status of teaching system		√			
Execution of teaching management			√		
The real effect of teaching management information platform	√				

structure of the education and teaching system, the core elements of the construction framework of higher education and teaching system should include five modules, including education and teaching system organization, operation mode, mechanism and system guarantee, technical platform support, and quality evaluation module. In our evaluation and feedback of the college education and teaching system, we propose AI algorithm technology to participate in the improvement and drive the evaluation and adjustment of the system by dynamically examining the interaction status of teachers and students, the professional learning of students, and the management effectiveness of managers to jointly assess the implementation effect of the college education and teaching system, as shown in Figure 4.

4. Discussion and Analysis of Results

In this paper, we test the effectiveness of our proposed AC algorithm using student evaluation scores designed by the university education and teaching system, where the data include quantitative scores in terms of operation status of teaching system, execution of teaching management, and the real effect of teaching management information platform. We run our model using a single Nvidia RTX 3060 GPU and AMD EPYC 7402 CPU in Matlab 2018b programming environment and Windows 10 OS environment. Specially, we collected 300,000 evaluations of the effectiveness of driving education and teaching system design in the context of AI in a university through a web crawler. The effectiveness of AI technology on the construction of college education system is further illustrated by simple data analysis. The data inside contains the satisfaction evaluation of different levels of students on the efficient education system, the evaluation index is divided into 5 dimensions, and the characteristics of the data collected in this paper are shown in Table 1.

In the third tier of the framework, we propose the use of AI algorithm technology to participate in the improvement of the evaluation and feedback of the efficient education and teaching system. Specifically, we evaluate the implementation effect of the university education and teaching system by dynamically examining the interaction status of teachers and students, the professional learning of students, and the system effect system examination of system providers. The evaluation and adjustment of the teaching system are driven by AI technology. Here, the loss value indicates the difference between the rating of the assisted design teaching system and the traditional teaching system. Through the continuous interaction between the intelligent body and the environment, the teaching system of AI-driven design is made closer to the real scenario. Figure 5 shows the loss values for the design of the educational system in colleges and universities with reinforced learning guidance. It can be seen that the model converges quickly to a stable value, indicating the reliability of AI techniques that facilitate the design and development of the university education system.

The foundation and key to the successful implementation of the university's talent training objectives in teaching reform and construction is an effective and organized teaching system. Figure 6 visualizes the operational status of the teaching system under the vision of big data, where the x -axis represents the initial data input (evaluation scores in 3 teaching scenarios), the y -axis represents the number of students, and the z -axis represents the teaching status evaluation score. It can be seen that the teaching process proceeds gradually and fits with the real situation, further illustrating the effectiveness of the teaching system design. In academic practice, problems or shortcomings of existing academic research are verified and discovered, and new academic results are discovered through scientific innovation. It can be transformed into technology and serve production through practice.

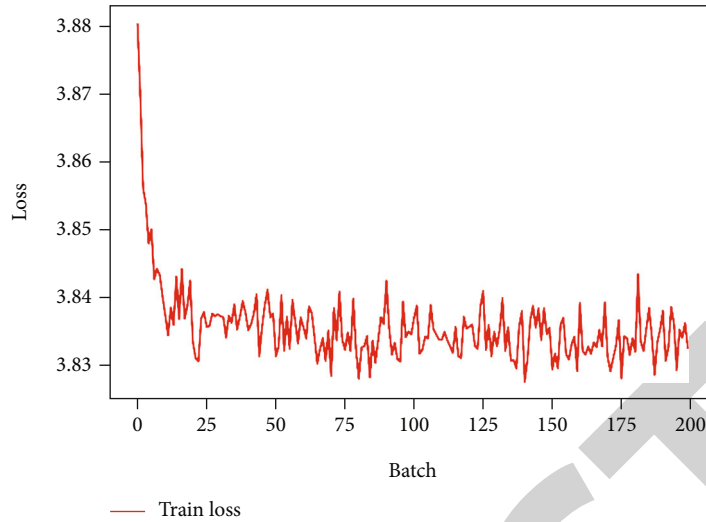


FIGURE 5: Reinforcement learning training loss value and convergence.

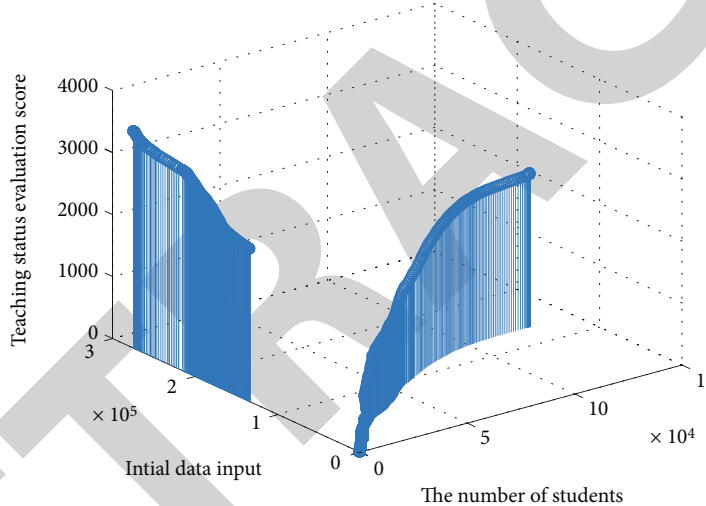


FIGURE 6: The operational state of the teaching system in the context of big data.

The sustainability of teaching management execution is fundamentally ensured by the evaluation subsystem for teaching management execution. A set of scientific and reasonable execution assessment and measurement mechanisms should be established, and tools and methods such as the target management assessment method and the key performance indicator method should be used for qualitative and quantitative analysis. Emphasis is placed on the evaluation of the teaching work of the college, highlighting the combination of daily teaching management with special projects and key work. It highlights the people-oriented approach, conducts comprehensive evaluation from multiple perspectives and levels, provides feedback through various channels, focuses on cultivation, and attracts colleges, teachers, and students to actively participate in the evaluation process. The combination of target management and day-to-day management and the establishment of information collection, analysis, feedback, and regulation form a perfect closed-loop system for teaching quality management

and evaluation. Figure 7 further validates the ability to evaluate instructional management execution. It can be seen that AI-driven instructional design has less evaluation fluctuations compared to traditional instructional design, and the evaluation design is smoothly driven by the technology of enhanced learning, which is beneficial to the implementation and popularity of higher education.

The technical support for teaching management, i.e., the construction of an information technology platform, is an important means of improving management execution. According to the needs of cultivating innovative talents, an overall design should be made to develop an informatization platform for teaching management that adapts to the teaching management mode of the school. A modern comprehensive teaching management system should be established to realize the informatization of teaching management, through which all teaching managers can carry out teaching management, realize the functions of teaching plan management, teaching task management, class scheduling

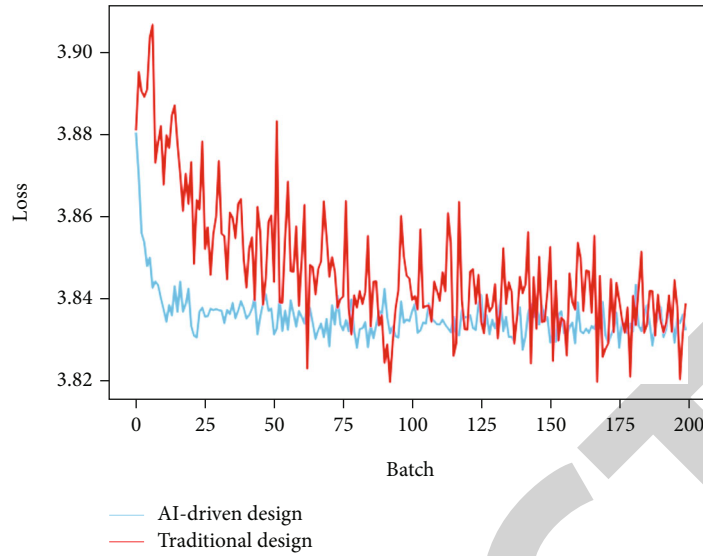


FIGURE 7: Loss value of AI-driven instructional design versus traditional instructional design.

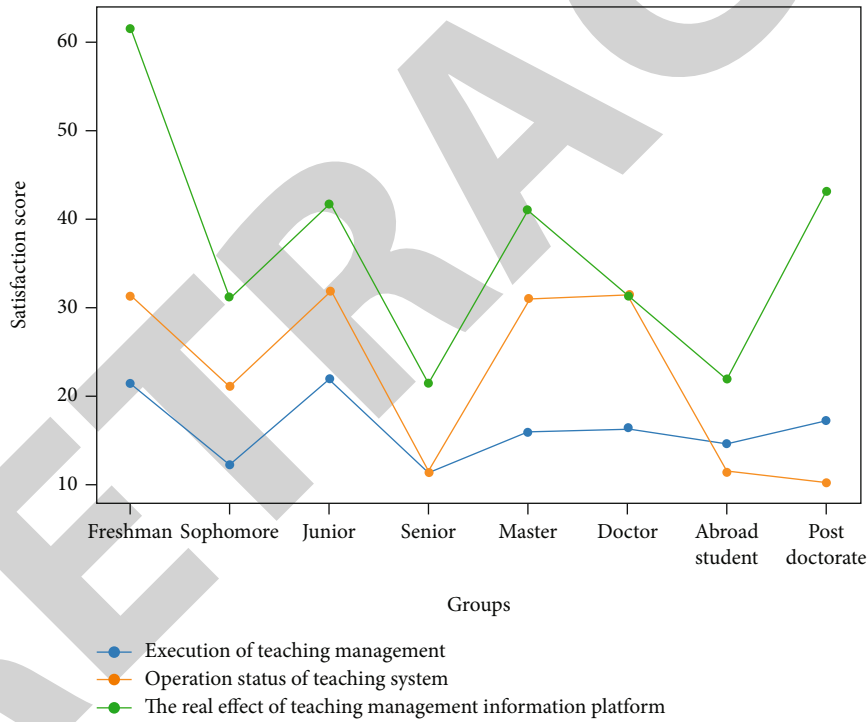


FIGURE 8: Evaluation scores of operation status of teaching system, execution of teaching management, and the real effect of teaching management information platform in different groups.

management, student registration management, grade management, data statistics and analysis, and generate various reports as needed. It is necessary to highlight the management and service functions in an all-round way, strengthen the teaching management information disclosure system for macro guidance, provide public education information, and open up teaching management information channels. Figure 8 visualizes the rating status of the AI-driven effect in teaching management technology. Including three evaluation indexes operation status of teaching system, execution of

teaching management, and the real effect of teaching management information platform, it can be seen that the overall rating of the real effect of teaching management information platform is the highest, and all ratings are evenly distributed, which indicates the effectiveness of the teaching framework designed in this paper, further promoting the standardization and standardization of teaching management, forming an efficient information transmission and feedback mechanism at the university and college levels, and improving the public service platform for teaching management.

5. Conclusions

In recent years, universities have fully recognized the importance of education and teaching system and actively promoted the design and application of education and teaching system, but in general, they still have not done a good job of seamlessly connecting theory and practice. With the continuous synthesis of technological development, there is a disconnection between the demand of society for innovative talents and the talents cultivated by colleges and universities and the society. This paper proposes an AI-based algorithm-driven evaluation and adjustment of the university education and teaching system to address the above education and teaching system design problems, design the teaching system for talent training, establish a quantitative and controllable process-oriented teaching quality assurance system, and explore a new mechanism for the design of the university education system. Specifically, the algorithm of the actor critic in reinforcement learning assists in establishing a three-tier teaching system framework, which assists in the design of the university education system, allowing students to truly understand and master as well as flex knowledge, and strengthening the correct understanding of students' intrinsic learning mechanisms. AI-driven college education system design overcomes the drawbacks of subjectivity driven by the traditional system, and colleges and universities design a reasonable teaching system to accomplish modern teaching tasks in an organized manner. And through the data of a university, we further verify the effectiveness of AI-driven college education and teaching system design and make certain contributions to improve the design and application of college education and teaching system. The experimental results show that the AI-driven instructional design can get better evaluation results, and the emerging instructional management platform is well received by the student community. The real effect of teaching management information platform has a higher score, further indicating the practicality of AI-driven instructional design. The numerical experiment results also show the stability of the instructional design, overcoming the drawbacks of traditional manual subjectivity in the design.

Data Availability

The datasets used during the current study are available from the corresponding author on reasonable request.

Conflicts of Interest

The author declares that they have no conflicts of interest.

Acknowledgments

This study was supported by the Research on the Formative Evaluation System of Applied Undergraduate Colleges and Universities Based on Intelligent Teaching Methods (Grant No. JAT190618).

References

- [1] M. H. Futrell, "Transforming teacher education to reform America's P-20 education system," *Journal of Teacher Education*, vol. 61, no. 5, pp. 432–440, 2010.
- [2] Y. F. Yang, "Developing a reciprocal teaching/learning system for college remedial reading instruction," *Computers & Education*, vol. 55, no. 3, pp. 1193–1201, 2010.
- [3] W. An, "Based on the application of deep learning in college education evaluation," *Mobile Information Systems*, vol. 2022, Article ID 2959596, 6 pages, 2022.
- [4] Z. Jojo, "Mathematics education system in South Africa," *Education Systems Around The World*, vol. 6, pp. 129–140, 2020.
- [5] J. Wei, M. Karuppiah, and A. Prathik, "College music education and teaching based on AI techniques," *Computers and Electrical Engineering*, vol. 100, article 107851, 2022.
- [6] Z. Sun, M. Anbarasan, and K. D. Praveen, "Design of online intelligent English teaching platform based on artificial intelligence techniques," *Computational Intelligence*, vol. 37, no. 3, pp. 1166–1180, 2021.
- [7] F. Liu and Q. Zhang, "A new reciprocal teaching approach for information literacy education under the background of big data," *International Journal of Emerging Technologies in Learning (ijET)*, vol. 16, no. 3, pp. 246–260, 2021.
- [8] X. Tan, "Research on college English writing teaching under the background of big data: taking Leshan Normal University as an example," *Theory and Practice in Language Studies*, vol. 9, no. 1, p. 60, 2019.
- [9] F. Dai, L. Xu, and Y. Zhu, "Higher education expansion and supply of teachers in China," *China Economic Review*, vol. 71, article 101732, 2022.
- [10] J. Liu, C. Wang, and Y. Wu, "Research on the management information system of college education and teaching based on web," *Networks*, vol. 2021, article 5090813, pp. 1–8, 2021.
- [11] A. Selvaraj, V. Radhin, K. A. Nithin, N. Benson, and A. J. Mathew, "Effect of pandemic based online education on teaching and learning system," *International Journal of Educational Development*, vol. 85, article 102444, 2021.
- [12] H. Li, H. Zhang, and Y. Zhao, "Design of computer-aided teaching network management system for college physical education," *Computer-Aided Design and Applications*, vol. 18, no. S4, pp. 152–162, 2021.
- [13] H. Yu, "Application analysis of new internet multimedia technology in optimizing the ideological and political education system of college students," *Wireless Communications and Mobile Computing*, vol. 2021, Article ID 5557343, 12 pages, 2021.
- [14] Y. Zhao, "Research on the diversified evaluation index system and evaluation model of physical education teaching in colleges and universities," *Journal of Computational and Theoretical Nanoscience*, vol. 14, no. 1, pp. 99–103, 2017.
- [15] S. P. Huang, "Effects of using artificial intelligence teaching system for environmental education on environmental knowledge and attitude," *Eurasia Journal of Mathematics, Science and Technology Education*, vol. 14, no. 7, pp. 3277–3284, 2018.
- [16] K. Zeichner, K. A. Payne, and K. Brayko, "Democratizing teacher education," *Journal of Teacher Education*, vol. 66, no. 2, pp. 122–135, 2015.
- [17] T. Duman and S. Karagöz, "An evaluation of Turkish teacher education system compared to other models in different

Retraction

Retracted: Epidural Anesthesia versus General Anesthesia for Total Knee Arthroplasty: Influences on Perioperative Cognitive Function and Deep Vein Thrombosis

Computational and Mathematical Methods in Medicine

Received 27 June 2023; Accepted 27 June 2023; Published 28 June 2023

Copyright © 2023 Computational and Mathematical Methods in Medicine. This is an open access article distributed under the Creative Commons Attribution License, which permits unrestricted use, distribution, and reproduction in any medium, provided the original work is properly cited.

This article has been retracted by Hindawi following an investigation undertaken by the publisher [1]. This investigation has uncovered evidence of one or more of the following indicators of systematic manipulation of the publication process:

- (1) Discrepancies in scope
- (2) Discrepancies in the description of the research reported
- (3) Discrepancies between the availability of data and the research described
- (4) Inappropriate citations
- (5) Incoherent, meaningless and/or irrelevant content included in the article
- (6) Peer-review manipulation

The presence of these indicators undermines our confidence in the integrity of the article's content and we cannot, therefore, vouch for its reliability. Please note that this notice is intended solely to alert readers that the content of this article is unreliable. We have not investigated whether authors were aware of or involved in the systematic manipulation of the publication process.

Wiley and Hindawi regrets that the usual quality checks did not identify these issues before publication and have since put additional measures in place to safeguard research integrity.

We wish to credit our own Research Integrity and Research Publishing teams and anonymous and named external researchers and research integrity experts for contributing to this investigation.

The corresponding author, as the representative of all authors, has been given the opportunity to register their agreement or disagreement to this retraction. We have kept a record of any response received.

References

- [1] T. Ma, G. Li, H. Zhang et al., "Epidural Anesthesia versus General Anesthesia for Total Knee Arthroplasty: Influences on Perioperative Cognitive Function and Deep Vein Thrombosis," *Computational and Mathematical Methods in Medicine*, vol. 2022, Article ID 4259499, 6 pages, 2022.

Research Article

Epidual Anesthesia versus General Anesthesia for Total Knee Arthroplasty: Influences on Perioperative Cognitive Function and Deep Vein Thrombosis

Tao Ma, Guanhua Li, Hao Zhang, Yingxin Zhang, Lei Wang, Hailong Wu, Yang Chu, Xiaoli Zhao, and Wei Wang 

Department of Anesthesiology, PLA Rocket Force Characteristic Medical Center, Beijing 100088, China

Correspondence should be addressed to Wei Wang; wangwei100088@163.com

Received 7 June 2022; Revised 4 August 2022; Accepted 23 August 2022; Published 10 September 2022

Academic Editor: Pan Zheng

Copyright © 2022 Tao Ma et al. This is an open access article distributed under the Creative Commons Attribution License, which permits unrestricted use, distribution, and reproduction in any medium, provided the original work is properly cited.

Purpose. This research mainly discussed the impacts of epidural anesthesia (EA) and general anesthesia (GA) on perioperative cognitive function (CF) and deep vein thrombosis (DVT) in patients undergoing total knee arthroplasty (TKA). **Methods.** One hundred and twenty-four patients undergoing TKA in our hospital between July 2015 and October 2021 were selected, of which 74 patients received EA (research group) and the other 50 patients received GA (control group). Perioperative CF, DVT, stress response indicators (norepinephrine, NE; cortisol, Cor), and heart rate (HR) levels were observed and compared. Risk factors affecting DVT of TKA patients were analyzed by logistic regression. **Results.** The research group had statistically better CF than the control group, with notably lower NE, Cor, and HR levels and incidence of DVT. Logistic regression analysis showed that the type of anesthesia and MoCA were risk factors for DVT in TKA patients. **Conclusion.** EA is more feasible for patients undergoing TKA, which is conducive to improving their CF, relieving stress responses, and reducing the incidence of DVT, with a certain sedative effect.

1. Introduction

With the aggravation of population aging, the elderly suffering from joint disease has become more and more common [1]. Osteoarthritis, as a commonly seen chronic disease in the elderly, has an increasing risk with age, which adversely affects the quality of life and retirement life of the elderly [2]. Total knee arthroplasty (TKA) is a surgical procedure that replaces the knee joint with artificial components and is commonly used to treat conditions such as osteoarthritis and rheumatoid arthritis [3]. According to epidemiological data, there were as many as 600,000 cases of TKA in the United States in 2012, and the number is expected to increase to 1.26 million cases per year by 2030, imposing a huge burden on the healthcare system [4]. TKA has been shown to be beneficial to relieve patients' pain and improve long-term function and life quality [5, 6]. However, this procedure is also accompanied by certain risk of complications, which may lead to postoperative cognitive dysfunction, deep

vein thrombosis (DVT), and other adverse events [7, 8]. The causes of cognitive dysfunction or DVT after TKA are complicated, and the type of anesthesia is also an influencing factor that should not be underestimated [9]. This research mainly analyzes the impacts of epidural anesthesia (EA) and general anesthesia (GA) on cognitive function (CF) and DVT of TKA patients during the perioperative period, aiming at providing novel new insights for management optimization of such patients.

GA has favorable sedative and analgesic effects, but overdose of propofol and opioids may exert inhibitory effects on the central nervous system and respiratory system, which is not conducive to hemodynamic stability [10]. GA is also known to increase the risk of cerebrovascular adverse events [11]. And despite the inhibitory action of GA on the activity of cerebral cortex and hypothalamus, it may not be effective in inhibiting traumatic stress and inflammatory indicators, which may exert adverse effects on patients' CF and induce DVT [12]. EA, as a local anesthesia method, achieves anesthesia by injecting

analgesics into the epidural space to block sensory nerves [13]. Such anesthesia not only induces vasodilation in the occluded area to increase blood flow but also preserves the patient's consciousness and provides pain relief [14, 15]. In the study of Zhu et al. [16], it was pointed out that EA significantly improved the CF of postoperative esophageal cancer patients than GA. Hafezi et al. [17] also reported that EA used in plastic surgery has a preventive effect on DVT.

Since there are few studies on the influences of GA and EA on CF and DVT in patients undergoing TKA during the perioperative period at present, this study mainly conducted in-depth analysis in this aspect and is hereby reported.

2. Data and Methods

2.1. General Data. This research has been approved by the Ethics Committee of PLA Rocket Force Characteristic Medical Center and was conducted in strict compliance with the Declaration of Helsinki. First, 124 patients undergoing TKA in the PLA Rocket Force Characteristic Medical Center from July 2015 to October 2021 were selected. Inclusion criteria are as follows: all patients were diagnosed by clinical and imaging examinations and met the surgical indications; patients and their families were clear about the purpose of this experiment and provided informed consent; American Society of Anesthesiologists (ASA) grade I-II [18]; and age > 18. Exclusion criteria are as follows: malignant tumors or severe heart, liver, and kidney diseases; mental disorders or mental illness; abnormal echocardiography (ECG) examination results; infectious diseases; previous treatment history for the disease; use of drugs in the last six months that might affect the experimental results; presence of DVT before surgery; and contraindications to anesthesia. The 124 patients with TKA were grouped according to anesthesia methods, with 74 receiving EA in the research group (RG) and 50 receiving GA in the control group (CG). The male to female ratio and mean age (years old) in RG were 41:33 and 59.50 ± 11.12 , respectively, and the data in CG were 29:21 and 57.96 ± 8.18 . RG and CG showed no evident differences in baseline data like gender and age ($P > 0.05$).

2.2. Anesthesia Methods. Both groups of subjects underwent TKA. After the preparation before anesthesia, CG received GA and RG received EA.

2.2.1. GA. 1.5-2.0 mg/kg propofol (Shanghai Yuanye Biotech, B33792-100 mg), 0.4 $\mu\text{g}/\text{mL}$ sufentanil (Sigma-Aldrich (Shanghai), S-008-1ML), 0.15-0.2 mg/kg cis-atracurium (Shenzhen Jianzhu Biotech, 30119630), and 30-50 $\mu\text{g}/\text{kg}$ midazolam (Nhwa Pharmaceutical Co. Ltd, China) were used for anesthesia induction. Then, endotracheal intubation and mechanical ventilation were performed. After successful anesthesia induction, continuous pumping of 15-75 $\mu\text{g}/\text{kg}\cdot\text{min}$ propofol and 0.05-0.15 $\mu\text{g}/\text{kg}\cdot\text{min}$ remifentanil (Sigma-Aldrich (Shanghai), R-024-1ML) was administered intraoperatively, accompanied by auxiliary inhalation of 1-2% sevoflurane (Shanghai Fuyu Biotech, FY23996-25) and intermittent addition of atracurium (Shanghai Yuanye Biotech, Y54583).

2.2.2. EA. Epidural puncture of L3-4 was performed, and 5 mL 1.5% lidocaine (Shenzhen ChemStrong Scientific, L0595000) was added, followed by catheterization. 15 mL 0.5% ropivacaine (Beijing Biolab Biotech, BP0658-FKD) was given intraoperatively.

2.3. Endpoints

2.3.1. CF. The evaluation was carried out through the Montreal Cognitive Assessment Scale (MoCA) [19]. The scale has a score ranged from 0 to 30 points, which was directly proportional to the patient's CF. The assessment was conducted before and 3 days after the surgery.

2.3.2. Heart Rate (HR) Level. HR levels were measured at the following time points: before anesthesia (T1), 30 min after anesthesia (T2), end of surgery (T3), and 2 hours after surgery (T4).

2.3.3. Stress Indexes. Norepinephrine (NE) and cortisol (Cor) of the subjects were detected at T1 and T4, using the corresponding human ELISA kits supplied by Shanghai Jianglai Industrial Limited By Share Ltd. The operation procedure strictly followed the instruction of human ELISA kits.

2.3.4. DVT. The incidence of DVT was calculated by counting the cases of DVT after operation.

2.4. Statistical Processing. Statistical analysis was performed using SPSS22.0 (Beijing Easy Bio Technology), and the significance level was $P < 0.05$. A chi-square test was employed for intergroup comparisons of count data described in the form of number of cases/percentage ($n/\%$), and the continuity correction chi-square test was adopted once the theoretical frequency of the chi-square test was < 5 . Mean \pm SEM was used to represent measurement data; the differences between groups used the independent sample t -test, and those between two time points of the two groups adopted the paired t -test. Among them, the count data involved in this study included gender, surgical site, alcoholism, and smoking, and the measurement data included mean age, disease course, body mass index (BMI), and MoCA score. Logistic multivariate regression analysis was performed to identify risk factors of DVT in TKA patients.

3. Results

3.1. The Two Cohorts of Patients Undergoing TKA Showed Comparable Baseline Data. Of the 124 patients undergoing TKA, 50 cases receiving GA were included in CG and 74 cases receiving EA were included in RG. The two cohorts were similar in gender, average age, course of disease, BMI, operation site, operation time, duration of anesthesia, alcoholism, smoking, diabetes, hypertension, and other baseline data, with compatibility ($P > 0.05$) (Table 1).

3.2. The CF Is less Affected in Patients Receiving EA during TKA. CF was assessed using the MoCA scale, and no marked difference was found between RG and CG prior to anesthesia ($P > 0.05$); but the postanesthesia score was higher in RG than in CG, with statistical significance ($P < 0.05$) (Figure 1).

TABLE 1: Baseline data of patients undergoing TKA (n , mean \pm SEM).

Factor	Control group ($n = 50$)	Research group ($n = 74$)	χ^2/lt	P
Gender (male/female)	29/21	41/33	0.082	0.775
Average age (years old)	57.96 \pm 8.18	59.50 \pm 11.12	0.838	0.404
Course of disease (years)	9.26 \pm 2.27	10.04 \pm 2.99	1.564	0.120
BMI (kg/m ²)	25.89 \pm 4.03	26.01 \pm 5.16	0.035	0.973
Surgical site (unilateral/bilateral)	26/24	32/42	0.919	0.338
Operation time (min)	99.78 \pm 28.38	95.92 \pm 31.69	0.694	0.489
Duration of anesthesia (min)	145.62 \pm 39.18	141.49 \pm 44.63	0.531	0.597
Alcoholism (yes/no)	30/20	36/38	1.544	0.214
Smoking (yes/no)	28/22	35/39	0.904	0.342
Diabetes (with/without)	23/27	32/42	0.092	0.762
Hypertension (with/without)	25/25	34/40	0.197	0.658

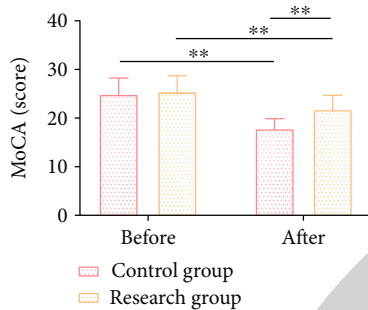


FIGURE 1: Cognitive function of TKA patients. $**P < 0.01$. Paired t -test was used to analyze the measurement data between groups before and after the intervention.

3.3. HR Level and Stress Response Changes Were Smaller in Patients Receiving EA during TKA. We evaluated the influence of two anesthesia methods on HR and stress response by measuring HR level and stress response. The data showed increased HR of the two groups at T2 and T3 compared with the value at T1; at T4, the HR level of RG was notably lower compared with T2 and T3, as well as the level of CG at T4, with statistical significance ($P < 0.05$). In terms of NE and Cor, their levels were similar in the two cohorts at T1 ($P > 0.05$), but increased markedly at T4 ($P < 0.05$), with significant differences between RG and CG at T4 ($P < 0.05$) (Figure 2).

3.4. The Incidence of DVT Was Lower in Patients Receiving EA during TKA. We recorded and compared the occurrence of DVT between groups to evaluate the influence of two anesthesia types on the incidence of DVT. DVT occurred in 12 cases in CG and 7 cases in RG, with an obvious lower incidence in RG compared with CG (9.46% vs. 24.00%, $P < 0.05$) (Figure 3).

3.5. Type of Anesthesia Is an Independent Risk Factor for DVT in TKA Patients. We included factors of differences (anesthesia type, MoCA, NE, Cor, and HR) into the analysis and assigned them as dependent variables for subsequent multivariate analysis with the logistic regression model, tak-

ing whether or not they affected the occurrence of DVT in TKA patients as the dependent variable. The results showed that the type of anesthesia ($P < 0.001$) and MoCA ($P < 0.001$) were independent risk factors for DVT in TKA patients (Table 2).

4. Discussion

For osteoarthritis, a common orthopedic disease with a sharp increase in the number of resulting fractures, TKA is undoubtedly an ideal treatment [20]. TKA is mostly performed in the elderly who are at an increased risk of perioperative cognitive dysfunction due to poor physical condition and fragile physiological function of the nervous system [21]. On the other hand, TKA patients may have varying degrees of coagulation function changes, which is one of the pathological causes of DVT [22]. This study mainly explores the influence of anesthesia on CF and DVT of TKA patients during the perioperative period.

Different anesthesia types have different effects on patients' nervous system and coagulation state, as well as CF and DVT [23]. Ishii et al. [24] also proposed that anesthesia may be a trigger for the need to prevent venous thromboembolism events. When the human body is under anesthesia, its cerebral blood flow will be reduced and the brain metabolism will be blocked, which may affect neuronal signaling [25]. GA can induce abnormal expression of brain memory protein level and serum central nervous system-specific protein S-100 β , which would adversely affect patients' central nervous system, resulting in cognitive dysfunction [26], while EA has been shown to reduce the adverse effects on the central nervous system by lowering serum S-100 β protein concentration, thus reducing the risk of postoperative cognitive dysfunction in elderly patients [10]. In our study, the MoCA score decreased statistically in both cohorts after anesthesia, with a markedly higher score in RG versus CG, suggesting that EA had little influence on the CF of TKA patients, which was consistent with the results of Ekblad [9]. Besides, we found decreased HR level at T4 in RG compared with T2 and T3 and CG at T4, as well as notably lower NE and Cor levels in RG versus

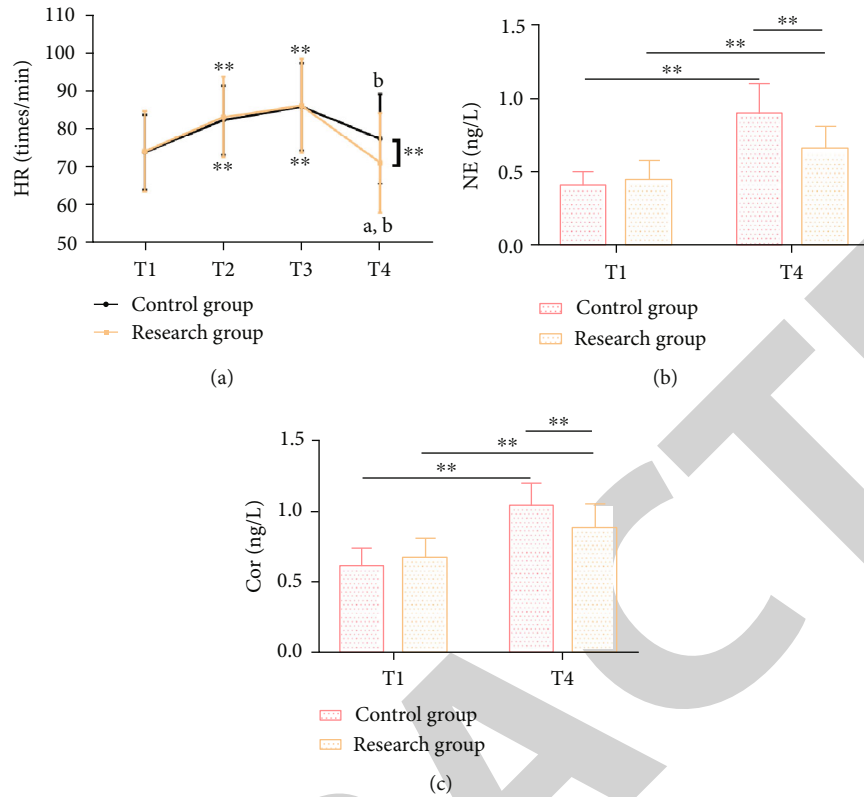


FIGURE 2: Stress response and HR level of TKA patients. (a) The HR level of TKA patients in both groups increased significantly at T2 and T3, and the HR level in the research group was lower than that in the control group at T4. (b) The NE level of TKA patients in both groups increased significantly at T4, with a lower level in the research group. (c) The Cor level of TKA patients in both groups increased significantly at T4, with a lower level in the research group. Note: $**P < 0.01$. Paired t -test was used to analyze the measurement data between groups before and after the intervention.

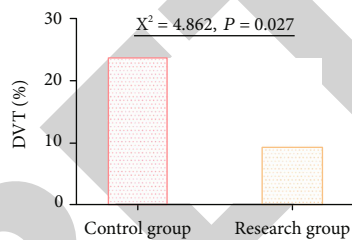


FIGURE 3: DVT in TKA patients, Chi-square test was used to analyze the incidence of DVT in both groups.

CG at T4, indicating that EA had a sedative effect on TKA patients and could alleviate their stress responses. Consistently, Li et al. [27] reported a small impact of EA on patients' stress responses in thoracic surgery for esophageal cancer. Furthermore, we found a statistically lower incidence of DVT in RG compared with CG (9.46% vs. 24.00%), suggesting that EA can reduce the risk of DVT in TKA patients, which is similar to the findings of Hafezi et al. [17]. EA may reduce the risk of DVT development by preventing postoperative hypercoagulability, thus reducing postoperative thromboembolic complications [28]. Other studies have shown that under EA, anaesthetics are absorbed into the blood through the epidural space, which can inhibit the

aggregation, release, and adhesion of platelets and improve the coagulation function of patients [29]. However, GA may activate platelet membrane glycoprotein and promote platelet aggregation, negatively influencing the body's coagulation function [29]. Finally, we conducted an in-depth exploration of the risk factors influencing the occurrence of DVT in TKA patients through logistic multivariate regression analysis. The results confirmed that the type of anesthesia and MoCA were independent risk factors for DVT in TKA patients. It has also been suggested that in order to prevent DVT after TKA, preoperative risk assessment of comorbidities in patients can be considered [30].

The novelty of this study is as follows: first, combined with indicators such as CF, HR, stress response, and incidence of DVT, it is confirmed that EA has a small impact on patients' CF during TKA and can help prevent DVT to a certain extent. Second, the logistic regression model was used for multivariate analysis, which proved that anesthesia type and MoCA were independent risk factors for DVT in TKA patients, further emphasizing the importance of anesthesia management for DVT prevention in TKA patients. But still, this research has some limitations. First of all, this is a retrospective instead of a blind or randomized study, which may lead to reporting bias. Second, this is a single-center small sample study, so the universality and accuracy of the research results may be affected to some extent. Third, inflammation, oxidative stress, and

TABLE 2: Multivariate analysis of factors affecting the occurrence of DVT in TKA patients.

Characteristic	Class	OR	95% CI	P
Anesthesia type	EA vs. GA	0.012	0.002-0.085	<0.001
MoCA	Continuous variable	0.516	0.373-0.713	<0.001
NE	Continuous variable	1.216	0.048-30.538	0.906
Cor	Continuous variable	1.691	0.062-46.102	0.755
HR	Continuous variable	1.014	0.965-1.066	0.585

coagulation indexes were not included in the analysis, nor was there supplementary follow-up to analyze the long-term CF, DVT, and other complications of patients under the two anesthesia methods. The above deficiencies will be gradually addressed in the future.

5. Conclusion

To sum up, compared with GA, EA has less influence on perioperative CF and DVT of TKA patients, with high clinical application and popularization value.

Data Availability

The labeled datasets used to support the findings of this study are available from the corresponding author upon request.

Conflicts of Interest

The authors declare no competing interests.

Authors' Contributions

Tao Ma and Guanhua Li contributed equally to this work and are co-first authors.

References

- [1] T. Muhammad, P. Maurya, and P. Sharma, "Prevalence and correlates of bone and joint diseases and its association with falls among older adults in India: evidence from LASI, 2017-18," *Geriatric Nursing*, vol. 42, no. 5, pp. 1143-1150, 2021.
- [2] N. Yukalang, N. Turnbull, W. Thongkum, A. Wongkongdech, and K. Tudpor, "Association between physical activity and osteoarthritis of knee with quality of life in community-dwelling older adults," *Studies in Health Technology and Informatics*, vol. 285, pp. 265-270, 2021.
- [3] L. A. Harvey, L. Brosseau, and R. D. Herbert, "Continuous passive motion following total knee arthroplasty in people with arthritis," *Cochrane Database of Systematic Reviews*, vol. 2, article CD004260, 2010.
- [4] A. T. Anastasio, K. X. Farley, S. D. Boden, T. L. Bradbury, A. Premkumar, and M. B. Gottschalk, "Modifiable, postoperative risk factors for delayed discharge following total knee arthroplasty: the influence of hypotension and opioid use," *The Journal of Arthroplasty*, vol. 35, no. 1, pp. 82-88, 2020.
- [5] Y. Zong, C. Hao, Y. Zhang, and S. Wu, "Quality of life assessment after total knee arthroplasty in patients with Parkinson's disease," *BMC Musculoskeletal Disorders*, vol. 23, no. 1, p. 230, 2022.
- [6] C. Chen, Y. Shi, Z. Wu et al., "Long-term effects of cemented and cementless fixations of total knee arthroplasty: a meta-analysis and systematic review of randomized controlled trials," *Journal of Orthopaedic Surgery and Research*, vol. 16, no. 1, p. 590, 2021.
- [7] S. Ren, F. Yuan, S. Yuan, C. Zang, Y. Zhang, and B. Lang, "Early cognitive dysfunction in elderly patients after total knee arthroplasty: an analysis of risk factors and cognitive functional levels," *BioMed Research International*, vol. 2022, Article ID 5372603, 9 pages, 2022.
- [8] P. Xiao, Q. Xu, W. J. Cao, X. Y. Chen, and S. L. Zhu, "Risk prediction for deep venous thrombosis after total knee arthroplasty based on modified caprini risk assessment model: a confirmatory study," *Zhongguo Gu Shang*, vol. 35, no. 3, pp. 253-257, 2022.
- [9] U. Ekblad, "The effect of oxytocin and betamimetic stimulation on prostaglandin release in perfused human fetal placenta," *European Journal of Obstetrics, Gynecology, and Reproductive Biology*, vol. 23, no. 3-4, pp. 153-158, 1986.
- [10] X. Luo and D. Li, "Effects of epidural block anesthesia combined with general anesthesia on inflammatory factors, cognitive function and postoperative pain in patients with lung cancer after thoracoscopic surgery," *American Journal of Translational Research*, vol. 13, no. 11, pp. 13024-13033, 2021.
- [11] H. Wang and L. Gao, "Association between general anesthesia and the occurrence of cerebrovascular accidents in hip fracture patients," *Journal of Healthcare Engineering*, vol. 2021, Article ID 7271136, 7 pages, 2021.
- [12] D. Milanovic, V. Pesic, N. Loncarevic-Vasiljkovic et al., "The Fas ligand/Fas death receptor pathways contribute to propofol-induced apoptosis and neuroinflammation in the brain of neonatal rats," *Neurotoxicity Research*, vol. 30, no. 3, pp. 434-452, 2016.
- [13] T. Iseri, M. Nakamori, and Y. Fujimoto, "Effects of thoracolumbar epidural anesthesia with lidocaine on the systemic hemodynamics and hepatic blood flow in propofol anesthetized dogs," *The Journal of Veterinary Medical Science*, vol. 83, no. 12, pp. 1877-1884, 2021.
- [14] H. Sayan, M. S. Aydogan, M. Bicakcioglu, H. I. Toprak, B. Isik, and S. Yilmaz, "Effects of thoracic epidural anesthesia on liver blood flow and indocyanine green clearance test in living-donor liver transplantation: a prospective, randomized, double-blind study," *Transplantation Proceedings*, vol. 47, no. 5, pp. 1462-1465, 2015.
- [15] B. Hu, H. Wang, T. Ma, Z. Fu, and Z. Feng, "Effect analysis of epidural anesthesia with 0.4% ropivacaine in transforaminal endoscopic surgery," *Journal of Healthcare Engineering*, vol. 2021, Article ID 2929843, 6 pages, 2021.
- [16] R. Zhu, J. Xiang, and M. Tan, "Effects of different anesthesia and analgesia on cellular immunity and cognitive function of patients after surgery for esophageal cancer," *Minerva Chirurgica*, vol. 75, no. 6, pp. 449-456, 2020.

Research Article

Analysis of the Preventive Action of Rivaroxaban against Lower Extremity Deep Venous Thrombosis in Patients after Laparoscopic Radical Gastrectomy

Qinhui Dong,¹ Xiayin Zhu,² Yafen Gao,¹ Zhengrong Wang,¹ Dexing Zheng,³
and Jian Zhu ⁴

¹Department of Medical Oncology, Taizhou Hospital of Zhejiang Province Affiliated to Wenzhou Medical University, Linhai, 317000 Zhejiang, China

²Department of Hematology, Taizhou Hospital of Zhejiang Province Affiliated to Wenzhou Medical University, Linhai, 317000 Zhejiang, China

³Department of Vascular Surgery, Taizhou Hospital of Zhejiang Province Affiliated to Wenzhou Medical University, Linhai, 317000 Zhejiang, China

⁴Department of Radiotherapy, Taizhou Hospital of Zhejiang Province Affiliated to Wenzhou Medical University, Linhai, 317000 Zhejiang, China

Correspondence should be addressed to Jian Zhu; ximen1987@126.com

Received 6 July 2022; Revised 4 August 2022; Accepted 17 August 2022; Published 10 September 2022

Academic Editor: Pan Zheng

Copyright © 2022 Qinhui Dong et al. This is an open access article distributed under the Creative Commons Attribution License, which permits unrestricted use, distribution, and reproduction in any medium, provided the original work is properly cited.

Background. Gastric carcinoma (GC) is a common lethal cancer in the world. Patients are prone to develop lower extremity deep venous thrombosis (LEDVT) after laparoscopic radical gastrectomy (LRG), which threatens their life and health. **Purpose.** This research is to clarify the preventive action of rivaroxaban (Riv) against LEDVT in patients undergoing LRG. **Methods.** A retrospective study was conducted on 70 patients with GC admitted for LRG between January 2019 and January 2022, including 40 patients (observation group) receiving Riv treatment and 30 patients (conventional group) treated with air wave pressure therapy apparatus. Quality of life, coagulation function, LEDVT formation, and complications were compared between groups. **Results.** The observation group had better recovery of life quality than the control group, along with more effective inhibition of coagulation disorders, less DVT formation, and fewer complications. **Conclusions.** Compared with air wave pressure therapy apparatus, Riv has better preventive action against LEDVT in GC patients after LRG.

1. Introduction

As far as the influence of gastric carcinoma (GC) on the global population is concerned, it ranks fifth in prevalence among cancers and third in cancer-related mortality [1, 2]. Various factors, including smoking, drinking, Helicobacter pylori infection, and high salt, oil, and sugar food intake, will increase the risk of GC [3–5]. Clinically, open surgery is the major approach to treat gastric adenocarcinoma, but it is prone to cause greater harm to patients [6]. In recent years, laparoscopic surgery, a procedure less invasive with milder postoperative pain and faster recovery than open surgery,

has become increasingly common [7]. However, the complexity of laparoscopic surgery for GC, improper operation of medical staff during surgery, and patient insufficient compliance can easily lead to accidents, so how to prevent all kinds of complications after surgery is critical [8, 9].

Venous thrombosis of the lower extremities is the most common adverse event after laparoscopic treatment [10]. DVT occurs when a blood clot forms in the vein of the leg. The thrombus can even rupture and travel to the lungs, resulting in potentially severe blood flow obstruction (pulmonary embolism or PE) or even death [11]. In the lower extremities, the primary route of venous blood flow

is the deep vein rather than the superficial vein. As a result, DVT causes impaired venous return of the lower extremities, resulting in limb swelling, discomfort, and gait disturbance. It is reported that nearly 2.5 to 5 percent of the population are affected by DVT at some stage in their lives [12]. Although anticoagulant therapy is widely available for the disease, more than half of patients develop postthrombotic syndrome within two years of DVT, characterized by leg pain, swelling, skin pigmentation, or venous ulcers [13, 14]. In this study, we will take rivaroxaban (Riv) as an example to explore its preventive action against lower extremity deep venous thrombosis (LEDVT) of patients after laparoscopic radical gastrectomy (LRG).

2. Methods

2.1. General Information. Seventy patients admitted and underwent LRG between January 2019 and January 2022 were selected and assigned to a control group with 30 cases and an observation group with 40 cases. The general data of the two cohorts were comparable with no statistical differences.

Patients meeting the following criteria were enrolled: ① in accordance with the World Health Organization (WHO) tumor diagnostic criteria established in the Pathology and Genetics of Tumors of the Digestive System [15], with surgical tolerance; ② preoperative diagnosis of LEDVT [16] by vascular ultrasonography; and ③ adults (age > 18). Patients were excluded according to the following criteria: ① recent active bleeding, ② blood system-related diseases or coagulopathy, ③ use of anticoagulant drugs because of other diseases, and ④ presence of LEDVT before operation.

Patients and their families were informed of this study and all signed informed consent. The Medical Ethics Committee approved the study protocol without reserves, and this study was conducted strictly following the Declaration of Helsinki.

2.2. Methods. Both groups of patients underwent LRG under general anesthesia, which was performed by the same surgical team. No hemostatics were used postoperatively. The next day after surgery, patients were instructed to ambulate to exercise their ankles, toes, knees, and other joints. In the control group, air wave pressure therapy apparatus was used to prevent LEDVT. The medical staff assisted the patient to wear the multichamber airbag leg sleeve and set the time as 30 min. The first use of the instrument followed the principle of gradually increasing the pressure, so that patients could gradually get used to it and wear it for a longer duration. The maximum tolerable pressure was determined according to patients' feelings. The observation group was given Riv (Bayer Pharmaceuticals, approval number: H20100464, specification 10 mg/tablet) for thrombosis prophylaxis, which was administered orally, 10 mg/time, once daily, for 10 days.

2.3. Outcome Measures

2.3.1. Postoperative Quality of Life (QoL). The postoperative life status of the two cohorts was observed and compared from the aspects of sleep status and activities of daily living (ADL). The sleep quality assessment used the Pittsburgh Sleep Quality Index (PSQI, score range: 0-21) [17], with

TABLE 1: General data.

Classification	Observation group ($n = 40$)	Control group ($n = 30$)	t/χ^2	P
Sex			0.33	0.568
Male	24 (60.00)	20 (66.67)		
Female	16 (40.00)	10 (33.33)		
Age (years old)	58.18 ± 6.46	58.50 ± 7.62	0.190	0.850
BMI (kg/m ²)	22.88 ± 1.18	23.23 ± 1.04	1.291	0.201
TNM staging			0.02	0.890
II	22 (55.00)	17 (56.67)		
III	18 (45.00)	13 (43.33)		
Operation plan			0.08	0.777
Total gastrectomy	16 (40.00)	11 (36.67)		
Distal gastrectomy	24 (60.00)	19 (63.33)		
Drinking			0.03	0.872
Yes	30 (75.00)	23 (76.67)		
No	10 (25.00)	7 (23.33)		
Eating habits			0.93	0.334
Heavy	32 (80.00)	21 (70.00)		
Light	8 (20.00)	9 (30.00)		

the score in inverse proportion to the sleep quality and a score greater than 7 indicating sleep disorders. As to the ADL, it was evaluated with the activity of daily living scale [18], an instrument with a score range of 0-100. The score is negatively related to self-care ability, and a score less than 60 points means that the patient needs help in life.

2.3.2. Coagulation function. Patients' venous blood was collected before and 10 days after surgery to measure the changes of fibrinogen (Fbg), activated partial thromboplastin time (APTT), prothrombin time (PT), and thrombin time (TT) using the LHOTSYS series automatic biochemical analyzer (approval number: Guangdong Food and Drug Supervision Machinery Zi 2012 no. 2400609, manufacturer: Shenzhen Glory Medical Co., Ltd., specification: BS-3600 T).

2.3.3. DVT Formation. DVT formation of patients, which was mainly judged by lower limb temperature, skin color, and swelling, was recorded and compared. For those with abnormalities and highly suspected DVT formation, immediate physical examination and color Doppler ultrasonography of the lower extremities were performed. Color Doppler ultrasonography diagnosis criteria for DVT are as follows: significant substantial echo in the lumen of lower limbs, no voluntary blood flow at the thrombus, and failure to deflate the patient's veins.

2.3.4. Complication Rate. The postoperative complications of the two groups were compared. The associated indicators included nausea, vomiting, labored breathing, and chills.

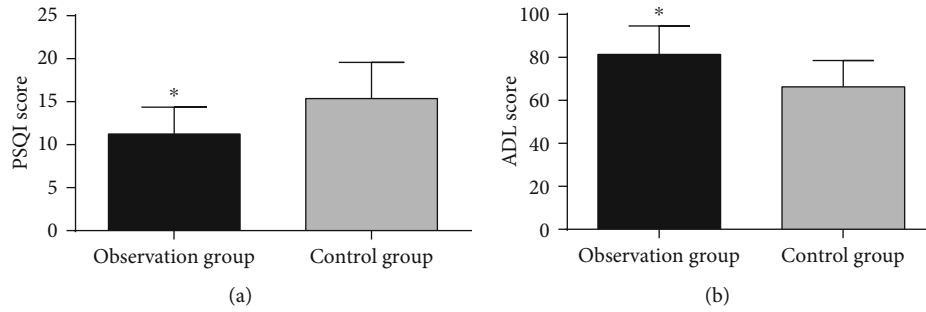


FIGURE 1: Postoperative quality of life. (a) PSQI score: an obviously lower PSQI score was determined in the observation group compared with the control group ($P < 0.05$). (b) ADL score: an obviously higher ADL score was determined in the observation group compared with the control group ($P < 0.05$). Note: compared with the control group, * $P < 0.05$.

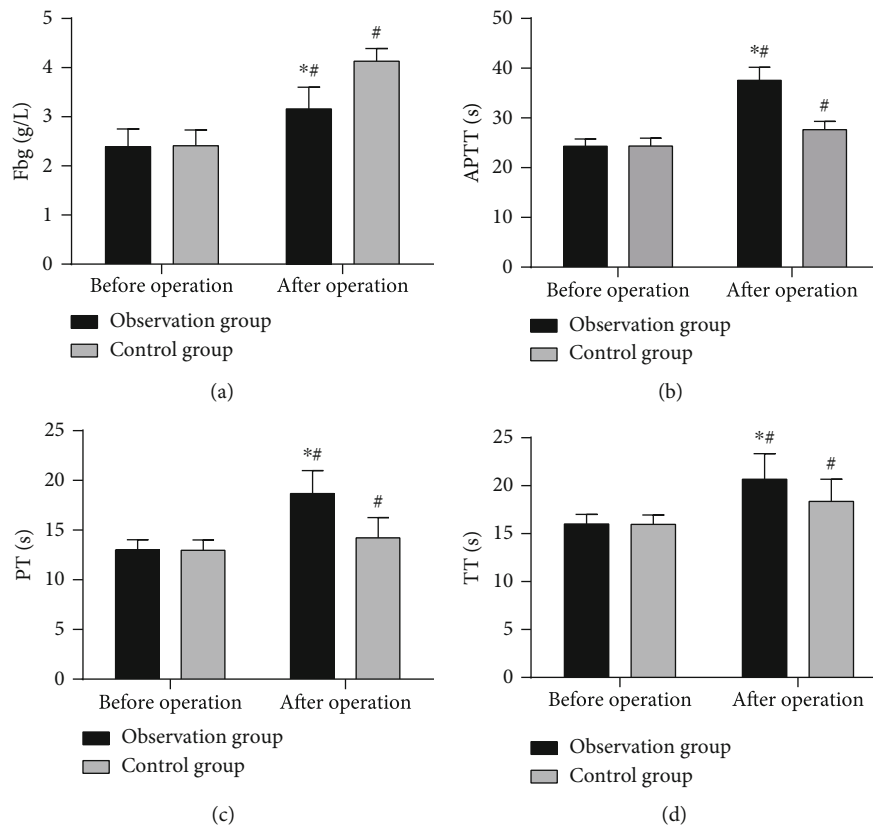


FIGURE 2: Coagulation function. (a) Fbg: significantly changed Fbg was observed in both cohorts after surgery, with a higher level in the control group as compared to the observation group ($P < 0.05$). (b) APTT: significantly changed APTT was observed in both cohorts after surgery, with a higher value in the observation group as compared to the control group ($P < 0.05$). (c) PT: markedly changed PT was observed in both cohorts after surgery, with a higher value in the observation group as compared to the control group ($P < 0.05$). (d) TT: markedly changed TT was observed in both cohorts after surgery, with a higher value in the observation group as compared to the control group ($P < 0.05$). Note: * $P < 0.05$, compared with the control group and # $P < 0.05$, compared with the posttreatment value.

TABLE 2: DVT formation in the two groups.

	Observation group ($n = 40$)	Control group ($n = 30$)	χ^2	P
Postoperative DVT	1	6	—	—
Total incidence (%)	2.50	20.00	5.83	0.016

Among the above indicators, PSQI and activity of daily living scale scores, coagulation function-related indicators (Fbg, APTT, PT, and TT), and incidence of DVT were the primary outcome measures, while the incidence of complications such as nausea, vomiting, labored breathing, and chills were the secondary ones.

2.4. Statistical Methods. Integrated data processing was done by SPSS 22.0 (Asia Analytics Formerly SPSS China). The

TABLE 3: Incidence of complications in two groups of patients.

	Observation group ($n = 40$)	Control group ($n = 30$)	χ^2	P
Nausea	1 (2.50)	0 (0.00)	—	—
Vomiting	0 (0.00)	6 (20.00)	—	—
Labored breathing	0 (0.00)	3 (10.00)	—	—
Chills	1 (2.50)	0 (0.00)	—	—
Incidence rate of complications	2 (5.00)	9 (30.00)	8.09	0.005

statistical method for categorical data (denoted by n (%)) was χ^2 ; quantitative data, denoted by $X \pm S$, were analyzed by t -test or pair t -test (before and after surgery). $P < 0.05$ was the significance level for all analyses.

3. Results

3.1. General Information. The two cohorts showed no statistical difference in sex, age, body mass index (BMI), tumor node metastasis (TNM) staging, and other general data ($P > 0.05$), see Table 1 for details.

3.2. Postoperative QoL. The comparison of patients' postoperative QoL revealed a lower PSQI score and a higher ADL score in the observation group compared with the control group, with statistical significance ($P < 0.05$, Figure 1).

3.3. Coagulation Function. Comparing patients' coagulation function, it was found that APTT, PT, and TT were significantly higher and Fbg was lower in the observation group, versus the control group, with statistical significance ($P < 0.05$, Figure 2).

3.4. DVT Formation. The intergroup comparison of DVT formation (Table 2) showed a lower overall incidence of DVT in the observation group ($P < 0.05$).

3.5. Complication Rate. The observation group had a statistical lower complication rate than the control group, as indicated by intergroup comparison data of the incidence of complications displayed in Table 3 ($P < 0.05$).

4. Discussion

Early diagnosis and treatment of GC, a highly lethal and recurrent tumor worldwide, is crucial [19]. Laparoscopic resection has recently become a common treatment for GC, but there are still many problems caused by misoperation [20–22]. After laparoscopic surgery, the incidence of DVT increases, and postthrombotic syndrome can exert a long lasting effect on the patients' daily life [23]. Therefore, DVT prophylaxis is necessary. This study mainly discusses the preventive action of Riv against postoperative thrombosis after LRG from two aspects: coagulation function and postoperative recovery.

In terms of coagulation function, the observation group using Riv was observed with an obviously better coagulation function than the control group. Riv, as a standard coagulation inhibitor, has an inhibiting effect on factor Xa and plays a vital part in various thromboembolic and atherothrombo-

tic diseases [24]. Factor Xa is essential in both intrinsic and extrinsic coagulation pathways that lead to downstream thrombin activation and clot formation [25], while Riv can reversely inhibit small molecules of the free and clot-bound factor Xa. Due to this function, Riv is not only increasingly used in various vascular diseases (coronary artery diseases, peripheral artery diseases, and thrombosis prophylaxis in particular) but also applied to the treatment of nonvalvular atrial fibrillation and DVT or venous embolism [26]. Another preventive measure, air wave pressure therapy apparatus, is often used to prevent DVT due to its ability to remove thrombosis directly by compression. However, if DVT is found to exist in lower limbs upon admission, improper prevention and control of DVT with air wave pressure therapy apparatus may induce thrombosis displacement, which may lead to PE [27]. This study showed better coagulation function in the observation group due to the use of Riv that can dissolve thrombus in a molecular mechanism. Therefore, compared with the control group which only used air wave pressure therapy apparatus to break thrombus, the coagulation function of the observation group was not significantly inhibited. Take Fbg as an example, as a glycoprotein complex, Fbg is enzymatically converted into fibrin by thrombin during tissue injury, causing blood to clot and stop bleeding. A clinical study on coronavirus disease 2019 (COVID-19) found a prothrombic diathesis in critical COVID-19 patients with significantly high Fbg levels, as well as higher Fbg levels [28]. Combining the above with our findings, we can find that compared with the control group which prevented thrombosis by compression, the observation group has lower Fbg level and less DVT formation due to the effective reduction of coagulation disorders in the molecular mechanism. In the retrospective study of Zhang et al. [29], Riv was applied to patients with severe craniocerebral injury after surgery, which also had an effective prevention effect on postoperative DVT, similar to our findings. In addition, Riv is reported to not only reduce the risk of recurrent venous thromboembolism but also have a certain preventive effect on postthrombotic syndrome [30].

When investigating patients' QoL and complications, we found that their sleep quality and life quality were effectively improved, and the incidence of complications was reduced. Consistently, Rashki Kemmak et al. reported that Riv intervention can reduce medical costs while significantly improving the QoL of patients undergoing total knee or hip arthroplasty [31]. Also, Becattini et al. [32] pointed out that Riv reduced the adverse events of patients after laparoscopic cancer surgery by 60% compared with placebo, which was

consistent with our results. Thrombosis after surgery for various types of cancer has been reported in all major clinical manifestations with a significant negative impact on patient outcomes. Both proximal and distal PE can occur after DVT [33]. To make matters worse, cancer patients will have a poor prognosis and similar symptoms after thrombosis in either deep or superficial veins [34]. As a common complication after various operations, the formation of venous thromboembolism will have a certain impact on the postoperative QoL of patients [35]. Combining these, we can find that patients in the observation group treated with Riv had a faster recovery of QoL after surgery and were safer than those in the control group due to better outcomes.

The novelty of this study lies in the following: (1) The clinical effectiveness of Riv in patients after LRG was confirmed from the perspectives of PSQI and ADL scores and coagulation function-related indicators (APTT, PT, TT, and Fbg), demonstrating that it can significantly improve patients' QoL and coagulation function. (2) From the perspective of safety, it was confirmed that Riv had a significant preventive effect on LEDVT as well as other complications in GC patients after LRG. However, there are still many deficiencies in this study. For example, we had not investigated patients' satisfaction at discharge, which is one of the defects of this study. In future experiments, we will address it and continue to improve the treatment plan, so as to make patients more satisfied. Besides, we should detect more targeted molecules or inflammatory factors related to GC, to better monitor the recovery of patients.

5. Conclusion

Conclusively, compared with air wave pressure therapy apparatus, Riv is more effective in preventing LEDVT in patients after LRG, which is worthy of further clinical promotion.

Data Availability

The labeled datasets used to support the findings of this study are available from the corresponding author upon request.

Conflicts of Interest

The authors declare no competing interests.

Authors' Contributions

Qinhui Dong and Xiayin Zhu contributed equally to this work and are co-first authors.

References

- [1] F. Bray, J. Ferlay, I. Soerjomataram, R. L. Siegel, L. A. Torre, and A. Jemal, "Global cancer statistics 2018: Globocan estimates of incidence and mortality worldwide for 36 cancers in 185 countries," *CA: a Cancer Journal for Clinicians*, vol. 68, no. 6, pp. 394–424, 2018.
- [2] J. Poorolajal, L. Moradi, Y. Mohammadi, Z. Cheraghi, and F. Gohari-Ensaf, "Risk factors for stomach cancer: a systematic review and meta-analysis," *Epidemiol Health*, vol. 42, article e2020004, 2020.
- [3] N. Putthanachote, S. Promthet, C. Hurst et al., "The XRCC 1 DNA repair gene modifies the environmental risk of stomach cancer: a hospital-based matched case-control study," *BMC Cancer*, vol. 17, no. 1, p. 680, 2017.
- [4] D. Praud, M. Rota, C. Pelucchi et al., "Cigarette smoking and gastric cancer in the stomach cancer pooling (STOP) project," *European Journal of Cancer Prevention*, vol. 27, no. 2, pp. 124–133, 2018.
- [5] Y. Minami, S. Kanemura, T. Oikawa et al., "Associations of cigarette smoking and alcohol drinking with stomach cancer survival: a prospective patient cohort study in Japan," *International Journal of Cancer*, vol. 143, no. 5, pp. 1072–1085, 2018.
- [6] T. Son and W. J. Hyung, "Laparoscopic gastric cancer surgery: current evidence and future perspectives," *World Journal of Gastroenterology*, vol. 22, no. 2, pp. 727–735, 2016.
- [7] T. K. Oh, E. Ji, and H. S. Na, "The effect of neuromuscular reversal agent on postoperative pain after laparoscopic gastric cancer surgery: comparison between the neostigmine and sugammadex," *Medicine (Baltimore)*, vol. 98, no. 26, article e16142, 2019.
- [8] K. Chen, Y. Pan, B. Zhang, H. Maher, X. F. Wang, and X. J. Cai, "Robotic versus laparoscopic gastrectomy for gastric cancer: a systematic review and updated meta-analysis," *BMC Surgery*, vol. 17, no. 1, p. 93, 2017.
- [9] K. Obama, Y. M. Kim, D. R. Kang et al., "Long-term oncologic outcomes of robotic gastrectomy for gastric cancer compared with laparoscopic gastrectomy," *Gastric Cancer*, vol. 21, no. 2, pp. 285–295, 2018.
- [10] J. E. Ha, Y. S. Lee, H. N. Lee, and E. K. Park, "Diagnostic laparoscopy of patient with deep vein thrombosis before diagnosis of ovarian cancer: a case report," *Cancer Research and Treatment*, vol. 42, no. 1, pp. 48–52, 2010.
- [11] C. Broderick, L. Watson, and M. P. Armon, "Thrombolytic strategies versus standard anticoagulation for acute deep vein thrombosis of the lower limb," *Cochrane Database of Systematic Reviews*, vol. 2021, no. 1, article CD002783, 2021.
- [12] K. A. Kim, S. Y. Choi, and R. Kim, "Endovascular treatment for lower extremity deep vein thrombosis: an overview," *Korean Journal of Radiology*, vol. 22, no. 6, pp. 931–943, 2021.
- [13] C. Kearon, E. A. Akl, J. Ornelas et al., "Antithrombotic therapy for VTE disease: chest guideline and expert panel report," *Chest*, vol. 149, no. 2, pp. 315–352, 2016.
- [14] T. Enden, Y. Haig, N. E. Klow et al., "Long-term outcome after additional catheter-directed thrombolysis versus standard treatment for acute iliofemoral deep vein thrombosis (the CaVenT study): a randomised controlled trial," *Lancet*, vol. 379, no. 9810, pp. 31–38, 2012.
- [15] T. Kahles, M. L. Mono, M. R. Heldner et al., "Repeated intravenous thrombolysis for early recurrent stroke: challenging the exclusion criterion," *Stroke*, vol. 47, no. 8, pp. 2133–2135, 2016.
- [16] B. Tutar, F. Kantarci, O. S. Cakmak, H. Yazici, and E. Seyahi, "Assessment of deep venous thrombosis in the lower extremity in Behçet's syndrome: MR venography versus Doppler ultrasonography," *Internal and Emergency Medicine*, vol. 14, no. 5, pp. 705–711, 2019.
- [17] S. H. Jeong, B. N. Jang, S. H. Kim, G. R. Kim, E. C. Park, and S. I. Jang, "Association between sedentary time and sleep

- quality based on the Pittsburgh sleep quality index among South Korean adults,” *BMC Public Health*, vol. 21, no. 1, p. 2290, 2021.
- [18] I. Ozsoy, B. Ozcan Kahraman, S. Acar, S. Ozalevli, A. Akkoclu, and S. Savci, “Factors influencing activities of daily living in subjects with COPD,” *Respiratory Care*, vol. 64, no. 2, pp. 189–195, 2019.
- [19] O. Sokolova and M. Naumann, “NF- κ B signaling in gastric cancer,” *Toxins*, vol. 9, no. 4, p. 119, 2017.
- [20] J. Yu, C. Huang, Y. Sun et al., “Effect of laparoscopic vs open distal gastrectomy on 3-year disease-free survival in patients with locally advanced gastric cancer: the class-01 randomized clinical trial,” *JAMA*, vol. 321, no. 20, pp. 1983–1992, 2019.
- [21] C. M. Lee, J. H. Park, C. In Choi et al., “A multi-center prospective randomized controlled trial (phase III) comparing the quality of life between laparoscopy-assisted distal gastrectomy and totally laparoscopic distal gastrectomy for gastric cancer (study protocol),” *BMC Cancer*, vol. 19, no. 1, pp. 1–7, 2019.
- [22] A. S. Alshahrani, G. S. Gong, and M. W. Yoo, “Comparison of long-term survival and immediate postoperative liver function after laparoscopic and open distal gastrectomy for early gastric cancer patients with liver cirrhosis,” *Gastric Cancer*, vol. 20, no. 4, pp. 744–751, 2017.
- [23] X. J. Song, Z. L. Liu, R. Zeng, W. Ye, and C. W. Liu, “A meta-analysis of laparoscopic surgery versus conventional open surgery in the treatment of colorectal cancer,” *Medicine (Baltimore)*, vol. 98, no. 17, article e15347, 2019.
- [24] W. Mueck, J. Stampfuss, D. Kubitzka, and M. Becka, “Clinical pharmacokinetic and pharmacodynamic profile of rivaroxaban,” *Clinical Pharmacokinetics*, vol. 53, no. 1, pp. 1–16, 2014.
- [25] K. P. Cabral and J. E. Ansell, “The role of factor Xa inhibitors in venous thromboembolism treatment,” *Vascular Health and Risk Management*, vol. 11, pp. 117–123, 2015.
- [26] M. Ajmal, J. Friedman, Q. Sipra, and T. Lassar, “Rivaroxaban: expanded role in cardiovascular disease management—a literature review,” *Cardiovascular Therapeutics*, vol. 2021, Article ID 8886210, 9 pages, 2021.
- [27] T. Mori, K. Yoshioka, and Y. Tanno, “Frequency of deep vein thrombosis at admission for acute stroke and associated factors: a cross-sectional study,” *Thrombosis Journal*, vol. 19, no. 1, p. 62, 2021.
- [28] I. Eljilany and A. N. Elzouki, “D-dimer, fibrinogen, and IL-6 in COVID-19 patients with suspected venous thromboembolism: a narrative review,” *Vascular Health and Risk Management*, vol. 16, pp. 455–462, 2020.
- [29] Z. L. Zhang, W. M. Liu, Y. Zhang et al., “Clinical efficacy of rivaroxaban in prevention and treatment of postoperative deep vein thrombosis for severe traumatic brain injury,” *Zhonghua Yi Xue Za Zhi*, vol. 97, no. 45, pp. 3558–3561, 2017.
- [30] C. Karathanos, P. Nana, K. Spanos et al., “Efficacy of rivaroxaban in prevention of post-thrombotic syndrome: a systematic review and meta-analysis,” *Journal of Vascular Surgery. Venous and Lymphatic Disorders*, vol. 9, no. 6, pp. 1568–1576.e1, 2021.
- [31] A. Rashki Kemma, A. Abutorabi, and V. Alipour, “Economic evaluation of rivaroxaban versus enoxaparin for prevention of venous thromboembolism after total knee replacement and total hip replacement: a systematic review,” *Clinical Drug Investigation*, vol. 40, no. 8, pp. 715–725, 2020.
- [32] C. Becattini, U. Pace, F. Rondelli et al., “Rivaroxaban for extended antithrombotic prophylaxis after laparoscopic surgery for colorectal cancer. Design of the PRO-LAPS II study,” *European Journal of Internal Medicine*, vol. 72, pp. 53–59, 2020.
- [33] H. T. Sorensen, L. Mellekjær, J. H. Olsen, and J. A. Baron, “Prognosis of cancers associated with venous thromboembolism,” *The New England Journal of Medicine*, vol. 343, no. 25, pp. 1846–1850, 2000.
- [34] A. Marin, L. Bull, M. Kinzie, and M. Andresen, “Central catheter-associated deep vein thrombosis in cancer: clinical course, prophylaxis, treatment,” *BMJ Supportive & Palliative Care*, vol. 11, no. 4, pp. 371–380, 2021.
- [35] F. Geraldini, A. De Cassai, C. Correale et al., “Predictors of deep-vein thrombosis in subarachnoid hemorrhage: a retrospective analysis,” *Acta Neurochirurgica*, vol. 162, no. 9, pp. 2295–2301, 2020.

Retraction

Retracted: The Development Relationship between Cross-Border e-Commerce and Internet of Things Technology Coupling in Digital Economy Based on Neural Network Model

Computational and Mathematical Methods in Medicine

Received 27 June 2023; Accepted 27 June 2023; Published 28 June 2023

Copyright © 2023 Computational and Mathematical Methods in Medicine. This is an open access article distributed under the Creative Commons Attribution License, which permits unrestricted use, distribution, and reproduction in any medium, provided the original work is properly cited.

This article has been retracted by Hindawi following an investigation undertaken by the publisher [1]. This investigation has uncovered evidence of one or more of the following indicators of systematic manipulation of the publication process:

- (1) Discrepancies in scope
- (2) Discrepancies in the description of the research reported
- (3) Discrepancies between the availability of data and the research described
- (4) Inappropriate citations
- (5) Incoherent, meaningless and/or irrelevant content included in the article
- (6) Peer-review manipulation

The presence of these indicators undermines our confidence in the integrity of the article's content and we cannot, therefore, vouch for its reliability. Please note that this notice is intended solely to alert readers that the content of this article is unreliable. We have not investigated whether authors were aware of or involved in the systematic manipulation of the publication process.

Wiley and Hindawi regrets that the usual quality checks did not identify these issues before publication and have since put additional measures in place to safeguard research integrity.

We wish to credit our own Research Integrity and Research Publishing teams and anonymous and named external researchers and research integrity experts for contributing to this investigation.

The corresponding author, as the representative of all authors, has been given the opportunity to register their agreement or disagreement to this retraction. We have kept a record of any response received.

References

- [1] Q. Liu, "The Development Relationship between Cross-Border e-Commerce and Internet of Things Technology Coupling in Digital Economy Based on Neural Network Model," *Computational and Mathematical Methods in Medicine*, vol. 2022, Article ID 8981618, 10 pages, 2022.

Research Article

The Development Relationship between Cross-Border e-Commerce and Internet of Things Technology Coupling in Digital Economy Based on Neural Network Model

Qi Liu 

Guangdong University of Science and Technology, Dongguan, Guangdong 523083, China

Correspondence should be addressed to Qi Liu; liuqi@gdust.edu.cn

Received 22 July 2022; Revised 12 August 2022; Accepted 22 August 2022; Published 10 September 2022

Academic Editor: Pan Zheng

Copyright © 2022 Qi Liu. This is an open access article distributed under the Creative Commons Attribution License, which permits unrestricted use, distribution, and reproduction in any medium, provided the original work is properly cited.

Compared with the traditional trading model, the problem of information asymmetry in export cross-border e-commerce (CBEC) transactions actually exists. Since the buyers and sellers of export CBEC are located in different countries, it is difficult for both parties to make accurate judgments on each other's credit. Besides, the number of export CBEC financing is relatively small, and the financing situation is not optimistic. Fortunately, the Internet of Things (IOT) technology has a wide range of applications and strong social penetration, especially in e-commerce, which can effectively improve payment, logistics, and distribution. By employing the concept of the IOT, this paper expounds the application of the IOT in the e-commerce transaction process and the impact of the IOT on the development of e-commerce. Besides, this paper also proposes some security issues in the application of the IOT in e-commerce. In addition, this paper analyzes the relationship and development trend of CBEC and IOT technology; meanwhile, it also points out the practical problems currently faced by combining the regional advantage of a certain region. The e-commerce industry develops IOT technology and drives innovation-driven development in the region. In addition, this paper builds an evaluation index system for the development of export CBEC enterprises based on the analysis of the problems and reasons by using the sample data to train the BP neural network and using the test samples to test the model. It is found that the model accuracy rate is 89.47%. Then, this paper also takes the export CBEC company A as an example to conduct empirical research and to prove the operability of the credit evaluation model. Finally, it provides relevant suggestions for improving the credit evaluation system of export CBEC enterprises.

1. Introduction

Since 2015, the market scale of China's export CBEC industry has expanded rapidly, from 4.49 trillion yuan in 2015 to 8.03 trillion yuan in 2019, maintaining a relatively fast growth rate [1, 2]. In the scale of CBEC transactions, the proportion also far exceeds that of imported CBEC. With the rapid development of market size and profitability, the times also have new requirements for all aspects of China's e-commerce industry [3, 4].

On one hand, the credit evaluation of CBEC enterprises will help further promote commercial banks to improve their credit systems, the accuracy of their credit evaluation of CBEC enterprises, and the efficiency of loan issuance,

which thereby can help to reduce their credit costs. On the other hand, it will help to further promote other evaluation institutions to improve their own evaluation systems and hence promote the sound and rapid development of the credit evaluation industry. Objective and effective credit evaluation results can also allow more investors to understand the company's situation more directly and quickly, which can bring more financing opportunities to the vast number of CBEC companies in urgent need of financing. Besides, it also can improve corporate financing efficiency and enrich corporate financing. Building an effective enterprise credit evaluation system can also supervise the enterprise itself. However, the current traditional e-commerce encounters development bottlenecks, the degree of automation

is not high, the degree of scale is not perfect, and the remote support ability is not strong, which have become the main problems affecting the development of e-commerce.

It can be seen that in cross-border export transactions, enterprises have low awareness of credit. Industry supervision is not in place; that is, it is lack of relatively complete credit reward and punishment measures, which makes credit problems occur frequently and hinders the further development of export CBEC enterprises. In order to do a good job in the credit construction of export CBEC, the most important thing is to improve the export CBEC credit evaluation system, which can clearly show the credit level of the enterprise. Therefore, investors can easily obtain the credit results of the enterprise and understand the enterprise's credit rating. Credit strengths and credit weaknesses enable them to make scientific decisions. Besides, credit strengths and credit weaknesses are also of great help to the enterprise itself. The enterprise can adjust the enterprise structure according to the credit results, so that it can develop well and quickly. At present, most of China's export CBEC enterprises have credit problems, such as inferior products and integrity issues. The number of researches on credit evaluation of export CBEC enterprises is relatively small at present, and there is a business credit issues that are not taken seriously. Therefore, exporting CBEC is an important part of Chinese goods going global, and it is very important to further improve the credit evaluation system of Chinese exporting CBEC enterprises [5, 6].

As traditional international trade continues to weaken, CBEC driven by information technology and the Internet environment will surely become another application mode of the digital economy in the field of international trade. According to the "China SME Cross-border White Paper," the current CBEC platform mainly assumes the role of matching the two sides of the trade. Meanwhile, it provides the online transaction process between the two parties, so the transaction data is available and large. With the continuous accumulation of transaction data, the interactive development of CBEC and the digital economy will surely drive the arrival of digital trade. Digital trade affects changes in transaction methods and production methods. Apart from being driven by the IOT technology, it also requires the coupled development of the economy and social environment [7, 8]. The rapid development of Internet of Things technology has brought about qualitative changes in people's lives. It is not only an opportunity for the innovation and development of the information industry but also has a significant and far-reaching impact on many fields and industries such as e-commerce.

At present, there is no uniform definition of digital trade in academia or even in the world. The US International Trade Commission defines digital trade as a transaction based on Internet technology that plays a key role in the process of ordering, producing, or delivering products and services. The organization divides digital trade into three categories: trade in goods, trade in digital services, and trade in data. In recent years, digital goods trade and CBEC led by China have been at the forefront of the world, while the United States has focused on the development of digital ser-

vice trade and the free flow of data across borders [9, 10]. This paper believes that CBEC is regarded as a part of digital trade. In the initial stage, the role of e-commerce platform is to match the information of both parties and match transactions, and other transaction links are completed offline. Changes have taken place, and cross-border trade has gradually realized the online transaction process, and the online completion mode of the transaction process is also the main mode in my country at present; finally, with the gradual accumulation and precipitation of transaction data and the development of integration of digital technology, in addition, consumers' demand preferences are diversified, and it is urgent to mine massive transaction data to achieve precise matching of supply and demand [11, 12]. Therefore, CBEC will achieve qualitative changes under the continuous accumulation of variables in cross-border trade and evolve into digital trade. In general, CBEC is the initial manifestation of digital trade, and digital trade is an inevitable trend in the development of CBEC. Using the IOT technology, combined with the operational characteristics of international trade, can reduce the supply chain of trade goods and then quickly realize the flow of goods in international trade. A complete e-commerce information platform can bring users a good experience and promote the development of e-commerce informatization. Aiming at the problems existing in the construction of information platform in current e-commerce, the use of IOT technology is the most effective strategy at present. On the one hand, the combination of IOT technology and architecture can optimize the e-commerce information platform, which can effectively improve the intelligence level of the e-commerce information system, and can well promote the e-commerce information platform to meet the needs of information development. On the other hand, the use of IOT technology can strengthen the interaction between e-commerce platforms and consumers, timely feedback consumers' opinions and needs, and improve user experience, so as to attract more consumers and promote the effective development of e-commerce [13, 14]. With the rapid development of society and economy, people's life rhythm is accelerating, and the time to go out shopping is less and less. Coupled with the popularization of computers in people's lives, online shopping has become the most convenient and popular shopping method at present, and the e-commerce industry has also become the commercial industry with the most development potential in the 21st century. After successful online shopping, consumers obtain goods in the form of express delivery through logistics companies, which requires the construction of logistics systems in the development of e-commerce, and the introduction and development of IOT technology can help e-commerce build an intelligent logistics system [15, 16]. Once the logistics company signs and receives the package, it can affix the RFID label with the package information to each package and transmit the package information to the Internet, so that consumers can track the information of their own packages anytime and anywhere, so that the information can be collected. Transparency guarantees consumers' security needs, improves consumers' trust in e-commerce, and is conducive to the sustainable development of e-commerce [17, 18].

China's e-commerce information platform started relatively late, has no rich experience, and has many problems. First of all, the sharing and transmission of e-commerce information is separated from reality, mainly because the actual operation process of e-commerce is not fully considered in the design process of the information platform architecture [19, 20]. The second is the lack of value-added services, resulting in the current Chinese e-commerce information platform unable to adapt to the development needs of the IOT technology. Finally, the operation effect of the e-commerce platform is low, and there is no efficient channel, mainly because there is no online and offline connection with the information platform in actual operation. At present, there are many technical problems in e-commerce under the IOT platform, such as chips, equipment, platform software, and hardware, which are far from other countries. Cloud computing currently has no perfect data processing model and the relationship between IPv4 and IPv6. The exchange of information between them is not yet possible. At the same time, the IOT e-commerce has not formed a mature operation plan, and it lacks competitiveness in cost control, which makes its commodity prices high, and consumers do not have enough ability to consume, resulting in a weak market [21, 22]. In addition, irregular policies and regulations, lack of security and privacy protection, and inconsistent technical standards are all problems that arise in the development of e-commerce under the current IOT technology [23, 24]. In the CBEC logistics system, there is also a complex nonlinear relationship between various risk indicators, and the genetic neural network is a mapping of a highly nonlinear relationship [25]. The neural network model optimized by the genetic algorithm can objectively evaluate the risk. BP neural network is an intelligent algorithm established by mathematical methods to process and memorize information by simulating the neural network structure of the brain. It constructs various neural networks with different topological structures according to neurons, so as to realize the simulation and approximation of the researched things. It can self-learn, self-organize, and fit arbitrary nonlinear functions, so it has a wide range of applications.

Therefore, based on the BP neural network, this paper studies the development relationship between the CBEC of the digital economy and the coupling of the IOT technology. Starting from the concept of the IOT, the article expounds the application of the IOT in the e-commerce transaction process and the impact of the IOT on the development of e-commerce and puts forward some security problems in the application of the IOT in e-commerce, so as to give some suggestions according to the problems. The application of this technology by e-commerce enterprises under the Internet of Things technology is not only an innovation of technology but also an innovation of enterprise management mode. It can break through the limitations of traditional e-commerce and conduct information interaction more efficiently and directly.

2. BP Neural Network

Through CBEC logistics risk research, it is beneficial to promote effective risk aversion between enterprises and achieve

cooperation benefits; it is beneficial to control unnecessary risk losses, missed opportunities, etc., and promote all aspects of physical logistics and CBEC lines. In addition, the operation of CBEC logistics is actually a process of collaboration and competition among various stakeholders. Through research on risks and sorting out the internal mechanism of each link, the risk management of CBEC logistics among enterprises will be more clear, and it will provide a corresponding reference for the government to further improve the CBEC logistics supervision system. Business enterprises and e-commerce platforms give relevant management inspiration. At the same time, it will further promote the control and risk aversion of information flow, capital flow, and logistics. The application of BP neural network, according to the characteristics of CBEC logistics risks and the research results of scholars, selects genetic algorithm to optimize the initial weight threshold of neural network and establishes CBEC logistics risk evaluation model and algorithm, which can effectively predict and analyze the CBEC logistics risk. The logistics risk of overseas e-commerce is minimized.

The artificial neural network operates according to the algorithm and continuously trains and learns by processing the original data to form a certain rule. After the training is completed, the original input value is reentered, and the value closest to the expected output value will be obtained. The BP algorithm includes signal forward propagation and error back propagation; that is, the direction of input to output is used when calculating the error output, and the direction of output to input is used when adjusting the weights and thresholds. During forward propagation, if there is an error between the actual output value and the expected output value, the error backpropagation will be performed, and the weights and thresholds will be continuously adjusted through the error backpropagation, and the corresponding parameter information with the smallest error will be finally determined. The BP neural network has a strong learning ability in the study of nonlinear events. Its main principle is the gradient descent method. The search target sample satisfies that the error mean square error between the actual output result of the training network and the expected output is the smallest; that is, the optimal result is obtained.

BP neural network is a multilayer feed-forward network, which is characterized by training according to the back propagation of errors, and by using the gradient search technology, the result of minimizing the error of the calculation results is achieved. The specific structure of BP neural network is shown in Figure 1.

Let the BP neural network structure be

$$n \times q \times m, \quad (1)$$

where n , q , and m are the dimensions of the network.

The network includes the weight from the i th neuron in the input layer to the j th unit in the hidden layer, which can be expressed as

$$w_{ij} \quad (i = 1, 2, \dots, n, j = 1, 2, \dots, q), \quad (2)$$

where w is the weight.

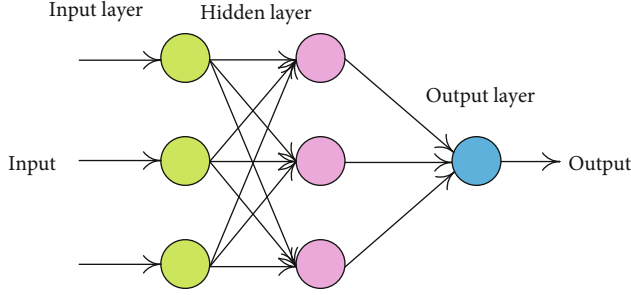


FIGURE 1: The specific structure of BP neural network.

The weight from the j th neuron in the hidden layer to the k th neuron in the output layer can be expressed as

$$w_{jk} \quad (j = 1, 2, \dots, q, k = 1, 2, \dots, m). \quad (3)$$

The steps of the BP neural network learning algorithm are as follows (Figure 2):

- (1) Initialization: set the initial values of the weights and thresholds of the network to values in the interval $[0, 1]$
- (2) Forward propagation of the network: let the input of the p th group of data samples be

$$x_p = (x_{1p}, x_{2p}, \dots, x_{np}), \quad (4)$$

where x is the variable.
Expected output is

$$t_p = (t_{1p}, t_{2p}, \dots, t_{mp}), \quad (5)$$

where t is the output.

Then, the output information of the j th neuron in the hidden layer is

$$H_{jp} = f\left(\sum_{i=1}^n w_{ij} - \theta_j\right). \quad (6)$$

The hidden layer passes the output information to the output layer, and the final output is as follows:

$$y_{kp} = f\left(\sum_{j=1}^q w_{jk} H_{jp} - \theta_k\right), \quad (7)$$

where y is the final output

- (3) Calculate the squared error E of the BP neural network: let the actual output of the p th group of samples be

$$y_p = (y_{1p}, y_{2p}, \dots, y_{mp}). \quad (8)$$

Then, the network error squared sum E can be expressed as follows:

$$E = \frac{1}{2} \sum_{p=1}^L \sum_{k=1}^m (y_{kp} - t_{kp})^2. \quad (9)$$

Judge whether the sum of squared errors E converges to the given learning accuracy ε , if $E \leq \varepsilon$, the algorithm ends, and the network stops training; otherwise, go to step (5)

- (4) Error back propagation: starting from the output layer, backpropagation layer by layer, using the steepest descent algorithm in nonlinear programming, modifying the weights of the network according to the negative gradient direction of the error function E , and adjusting the weights of the network layer by layer

$$w_{ij}(n+1) = w_{ij}(n) - \eta \frac{\partial E(n)}{\partial w_{ij}(n)}, \quad (10)$$

$$\Delta w_{ij}(n+1) = -\eta \frac{\partial E(n)}{\partial w_{ij}(n)}. \quad (11)$$

In the formula, η represents the step size or the network learning rate. The introduction of η is to speed up the convergence rate of the network. In order to increase the stability of the network learning, a momentum parameter α is usually added to the weight correction formula, then the n th learning. The modified formula of the weight is

$$\Delta w_{ij}(n+1) = -\eta \frac{\partial E(n)}{\partial w_{ij}(n)} + \alpha \Delta w(n) \quad (12)$$

- (5) Repeat steps (3) and (4) until the output error of the sample meets the predetermined condition, and the network training ends: the BP neural network algorithm is combined with the genetic algorithm, and the genetic algorithm is used as an auxiliary to optimize the connection weights between the layers of the neural network. Establish a mathematical model of cross-border e-commerce logistics risk assessment based on genetic neural network

3. Construction of CBEC Logistics Risk Evaluation Index System

The construction of the CBEC logistics risk evaluation index system is based on the identification of potential risk factors in the entire chain of CBEC enterprises in the operation of the logistics system and then overall consideration and analysis to obtain scientific and reasonable risk evaluation indicators. The construction of the risk assessment index system should follow the following principles.

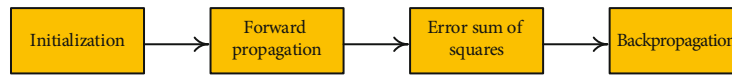


FIGURE 2: The steps of the BP neural network learning algorithm.

3.1. The Principle of Scientific Objectivity. The establishment of a CBEC logistics risk evaluation index system is based on a scientific theoretical basis and requires a large number of theories and research methods to support it, so that it can be objective and true. Cross-border logistics risk assessment needs to be carried out in different environments and under different subjects, with the participation of people from different industries, and is vulnerable to external interference. Adhere to a scientific, objective, and reasonable position to conduct scientific and objective risk assessment.

3.2. Hierarchical Progressive Principle. First of all, if risk factors exist or occur according to the different business activities of each link, it is necessary to split the CBEC logistics first to obtain a set of risk factors and then select appropriate indicators according to the principle of integrity, so that they can effectively reflect the CBEC logistics. The uniqueness of CBEC logistics can also make the entire risk index system not interfere with each other. The full consideration of multiple logistics nodes and multilevel analysis and selection makes it effective and characteristic and can cover the entire CBEC logistics system.

3.3. Practical Principles. The establishment of the CBEC logistics risk evaluation index system is not aimed at a certain enterprise but has a commonality that enables it to be effectively applied by other CBEC enterprises in the industry. The availability of index data should also be considered when establishing the index system. The availability, effectiveness, and sensitivity to risk of index data should be considered when establishing index system. Thus, we can make it more practical.

3.4. Comprehensive Comprehensiveness Principle. The risks of CBEC logistics should be taken into account both internally and externally. Different countries and external factors involved in CBEC integrated logistics should be considered comprehensively by seeking common ground while reserving differences. Therefore, the indicator system should integrate the commonalities of various risk factors but at the same time cannot be generalized.

The assumptions of this model are as follows: select indicators from the characteristics of custom clearance risk, platform risk, process risk, organizational risk, and environmental risk in the overall operation of CBEC logistics, as well as the generality of different cross-border logistics models to CBEC logistics. The commercial logistics risk evaluation index system is initially constructed. The entire risk index system consists of five aspects: platform risk, organizational risk, custom clearance risk, process risk, and environmental risk. This paper chooses the method of combining qualitative and quantitative indicators. Quantitative indicators are more scientific and rigorous, and fewer qualitative indicators

reduce the influence of subjective factors to a certain extent. Each risk index directly or indirectly evaluates the risk. Starting from the entire logistics chain, there are risk factors in each link. It is necessary to select the influencing factors that can describe the risk index in data and to comprehensively measure and comprehensively qualitative and quantitatively characterize descriptions simultaneously. There are directly influencing factors as well as the comprehensive and indirect factors affecting risk indicators. Each risk index is representative, so it can comprehensively evaluate the logistics risk of CBEC. In the custom clearance risk, it is assumed that the product custom clearance efficiency in the measurement index is calculated according to the actual custom clearance time of the product. Due to different custom clearance countries and different products, the product custom clearance efficiency cannot be comprehensively measured, so it is recommended to exclude it. The process risk mainly includes two parts: logistics and warehousing. According to the actual logistics, transportation, and distribution situation, it is recommended to add the batch rate and transfer rate at the end of distribution. This indicator can effectively reflect the efficiency of logistics and transportation and the effective times of loading, unloading, and sorting and also has a certain impact on risk evaluation. Organizational risk mainly recommends adding service satisfaction rate and effective complaint rate for service ability risk. This indicator mainly refers to the satisfaction level of logistics services provided to customers, which can intuitively reflect the quality of logistics services, and the influence of logistics service brands in the market and business development capabilities is the reflection of the risk impact of the corporate brand in the market environment.

4. Empirical Research

Before training the BP neural network, the relevant input and output values must be mastered in order to perform normal training and learning. The output value refers to the initial credit rating data of the sample. This paper selects the basic data and the expected value of credit level of representative Chinese export CBEC enterprises (self-operated export CBEC enterprises and platform-based enterprises) to train the model. Considering the availability and authenticity of the data, this paper selects the export CBEC enterprises listed on the main board, the new third board, the small- and medium-sized board, and the ChiNext as the data sample. BP neural network is an intelligent algorithm established by mathematical methods to process and memorize information by simulating the neural network structure of the brain. It constructs various neural networks with different topological structures according to neurons, so as to realize the simulation and approximation of the researched things.

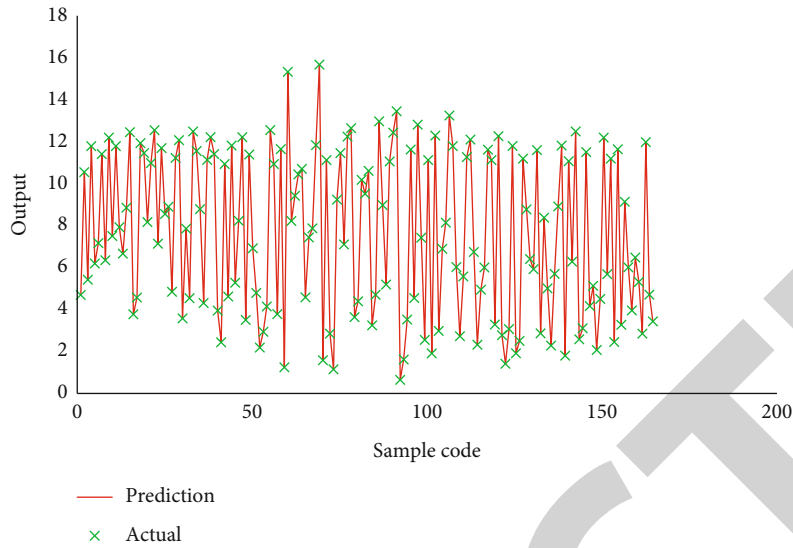


FIGURE 3: Comparison between the original output value of the training set and the real value.

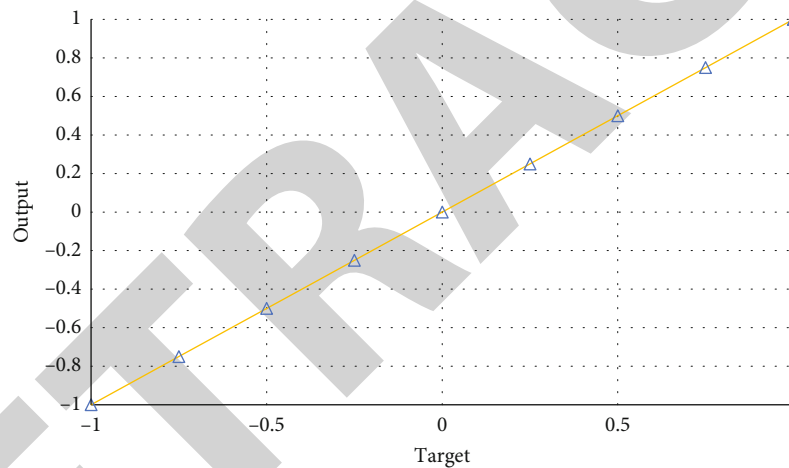


FIGURE 4: Regression fit.

Before constructing the BP neural network model, the BP neural network should be trained and learned with sample data, and the samples used for training and learning are training samples. In this paper, the input node is 32, and the output node is 1. The model is trained and debugged many times according to the previous hidden layer node empirical calculation formula. The model is trained best when the number of hidden layer nodes of the model is 10. So the final BP neural network structure is 32-10-1. Input the set training code into the MATLAB software; train 148 groups of training samples; continuously adjust the weights, thresholds, and the number of hidden layer nodes according to the training results; and finally get the best running effect. The comparison between the actual output value of the training sample and the input value of the original credit rating is shown in Figure 3, and the fitting effect is shown in Figure 4. As shown in Figures 3 and 4, the accuracy of the training model can be clearly seen, and the accuracy of the training samples has reached 100%, indicating that the train-

ing effect of the data in the BP neural network model is significant.

Firstly, genetic operations are carried out. After continuous crossover, mutation, inheritance, etc., in the sample population, the target sample individual with the greatest fitness is searched; that is, the initial weights and thresholds of each layer connection of the optimized neural network are obtained. The optimization results are assigned to the neural network, and the optimized neural network structure model is obtained after training sample data. Bring the data values of each risk measurement index of CBEC logistics into the model for training, use the data samples to first learn the nonlinear function relationship, and then use the control samples to verify and obtain the final CBEC logistics risk evaluation output value, which is the risk of CBEC logistics in this example. According to the level interval of each risk rating in the model, the risk level of CBEC logistics risk is determined by comparing with the final CBEC logistics risk value. The training results are shown in Figure 5, and the

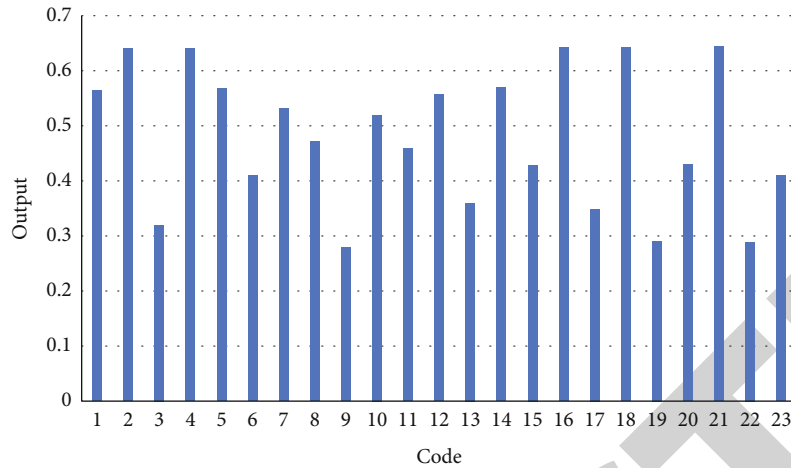


FIGURE 5: Training results.

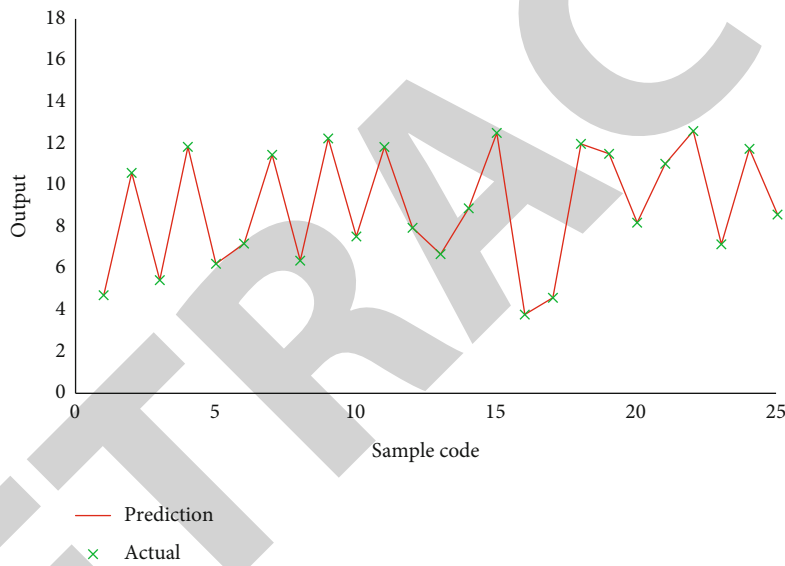


FIGURE 6: Result fit.

result fitting (Figure 6) is as follows: combining Figures 5 and 6, the actual output of the training sample and the expected output value have little difference, the fitting is well completed, and the parameter values of the neural network are further adjusted. It is again verified that the model has a good ability to learn nonlinear functional relationships.

The sensitivity analysis is carried out on the CBEC logistics risk evaluation index. On the basis of the trained genetic neural network, the sensitivity analysis is carried out on the parameters of each evaluation index in the CBEC logistics risk of enterprise A.

Knowing its risk evaluation result, reduce the value of each risk index in the network by 0.05, and keep other setting parameters unchanged. Run the operating software to obtain the risk evaluation result. When the value of any evaluation index changes, the risk evaluation result corresponding to the model is shown in Figure 7. Besides, it is also compared in Figure 8.

According to the changes of the output results, it can be reflected that the changes of the index values have little impact on the output results, and the overall sensitivity when changing the index values is low. The results of enterprise A's CBEC logistics risk evaluation, combined with the fluctuations and changes of the measurement indicators, 5-dimensional risk factors, custom clearance risk, platform risk, process risk, organizational risk, and environmental risk, correspond to 21 measurement indicators. Among them, the sensitivity of process risk measurement indicators fluctuates more than other risk measurement indicators, so enterprise A is in process risk. The transportation risk is mainly due to the long transportation distance, the number of transshipments during transportation, the combined transportation of various transportation vehicles, etc., which are the direct reasons for the high process risk. From the perspective of indicators, improve and strengthen transportation and distribution efficiency, transportation equipment

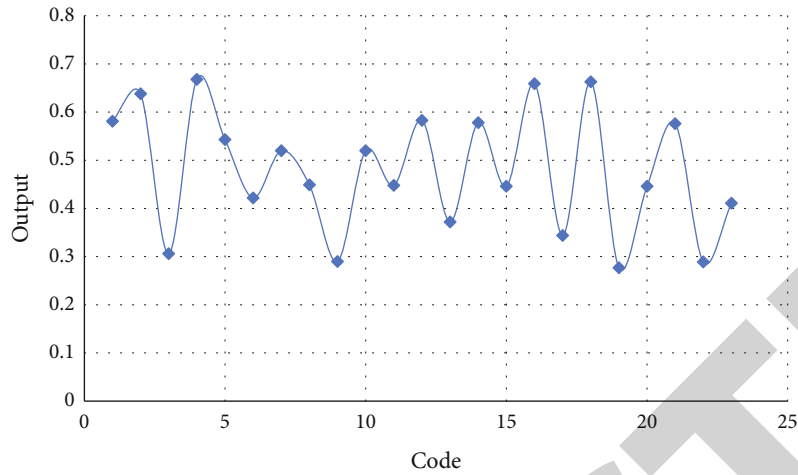


FIGURE 7: Genetic neural network risk assessment results after each index value changes.



FIGURE 8: Comparison.

utilization rate, etc. In terms of warehousing risks, it can effectively reduce the risk value; in the warehousing risk, combined with the warehousing situation of company A, its warehousing business provides overseas warehouses, bonded warehouses, etc., and for indirect transit warehouses, choose to rent third-party warehouses or build simple transit warehouses, transit stations, etc. Although there is a certain reduction in warehousing costs, its management and warehousing resource utilization directly affect the warehousing risk value. From the analysis of the results of the example, it can be concluded that warehousing resource utilization and warehousing facility management should still be the main breakthroughs to control warehousing risks. By analyzing the risk evaluation results according to the example model in organizational risk and platform risk, it can be concluded that company A has achieved relatively mature management, control, and integration between companies in terms of organiza-

tional risk. Platform risks are mainly aimed at computer technology, etc. The current results reflect well, and for the better development of enterprises, continuous breakthroughs and research in this area are still needed. The risk is analyzed according to the results of the case of enterprise A, so as to effectively control and improve the logistics risk of CBEC as a whole.

Based on the evaluation results of enterprise A's CBEC logistics risk and the research on CBEC logistics risk in this paper, CBEC logistics enterprises involve transportation and warehousing (overseas warehouses or bonded warehouses, etc.) and have independent CBEC logistics. The evaluation method of this paper can be applied according to the business modules involved in the business platform and the cooperation of many enterprises. The CBEC logistics risk evaluation model based on genetic neural network can give relevant evaluations for the risks of many CBEC logistics

enterprises. According to the evaluation results, the effective management and control of its risk matters and further risk research are used as a reference.

5. Conclusion

BP neural network has certain advantages in credit evaluation of export CBEC. The BP neural network method is used to evaluate the credit of export CBEC enterprises, and the model calculation accuracy is high. The BP neural network model itself is relatively stable, the operation speed is relatively fast, and it has advantages in processing a large amount of data, reducing human subjectivity, and being more standardized and objective. This paper uses the BP neural network to train and learn the sample data. The accuracy of the credit evaluation results is good and at a high level, which can provide scientific reference for investors and managers.

The BP neural network selected in this paper is a method suitable for a large amount of data. As the number of samples increases, its accuracy will also increase. The number of samples can be continuously increased in future research to improve the accuracy of the model.

Data Availability

The datasets used during the current study are available from the corresponding author on reasonable request.

Conflicts of Interest

The author declares that there are no conflicts of interest.

Acknowledgments

This work was supported by the Guangdong University of Science and Technology School-Level Research Project "Research on the Policy Effect of Dongguan City Comprehensive Experimental Zone for Cross-border E-Commerce" (Project No. GKY-2021KYYBW-14) and the Guangdong University of Science and Technology School-Level Research Project "Research on Cultivating Dongguan City Cross-border E-Commerce Industry Chain Based on Big Data Technology" (Project No. GKY-2021KYYBW-13).

References

- [1] L. P. Pan, X. Fu, and Y. Q. Li, "SME participation in cross-border e-commerce as an entry mode to foreign markets: a driver of innovation or not?," *Electronic Commerce Research*, vol. 2, pp. 1–30, 2022.
- [2] M. Xu and P. S. Wang, "Research on developing cross-border E-commerce and promoting the transformation and upgrading of foreign trade in Anhui Province," *International Journal of Social Science and Education Research*, vol. 5, no. 3, pp. 1–7, 2022.
- [3] G. L. Lin and D. P. Lu, "Research on countermeasures for high-quality development of cross-border E-commerce in Zhejiang Province under the background of new development pattern," *Frontiers in Economics and Management*, vol. 3, no. 3, pp. 1–10, 2022.
- [4] L. Q. Li, "Cross-border E-commerce intelligent information recommendation system based on deep learning," *Computational Intelligence and Neuroscience*, vol. 2022, Article ID 6602471, 11 pages, 2022.
- [5] J. X. Zhou, G. Q. Shen, S. H. Yoon, and X. Jin, "Customization of on-site assembly services by integrating the internet of things and BIM technologies in modular integrated construction," *Automation in Construction*, vol. 126, pp. 321–332, 2021.
- [6] N. Paudel and R. C. Neupane, "A general architecture for a real-time monitoring system based on the Internet of Things," *Internet of Things*, vol. 14, pp. 21–32, 2021.
- [7] F. Hu, L. Qiu, X. Xi et al., "Has COVID-19 changed China's digital trade?—Implications for health economics," *Frontiers in Public Health*, vol. 10, pp. 831549–831549, 2022.
- [8] K. Huang, S. Madnick, F. Zhang, and M. Siegel, "Varieties of public-private co-governance on cybersecurity within the digital trade: implications from Huawei's 5G," *Journal of Chinese Governance*, vol. 7, no. 1, pp. 81–110, 2022.
- [9] S. Shadikhodjaev, "Technological neutrality and regulation of digital trade: how far can we go?," *European Journal of International Law*, vol. 32, no. 4, pp. 1221–1247, 2021.
- [10] H. Zhang, "Trade openness and green total factor productivity in China: the role of ICT-based digital trade," *Frontiers in Environmental Science*, vol. 9, pp. 98–102, 2021.
- [11] K. M. Huang, S. Madnick, N. Choucri, and F. Zhang, "A systematic framework to understand transnational governance for cybersecurity risks from digital trade," *Global Policy*, vol. 12, no. 5, pp. 625–638, 2021.
- [12] L. Wen, "Development analysis of cross-border E-commerce logistics based on big data technology under safety law protection," *International Journal of Information Systems in the Service Sector*, vol. 14, no. 2, pp. 1–14, 2022.
- [13] N. Chen, "Analysis of the correlation between cross-border E-commerce and economic growth based on hierarchical multilevel gray evaluation model," *Journal of Mathematics*, vol. 2022, Article ID 8455404, 10 pages, 2022.
- [14] T. G. Chen, Y. Qiu, B. Wang, and J. Yang, "Analysis of effects on the dual circulation promotion policy for cross-border E-commerce B2B export trade based on system dynamics during COVID-19," *Systems*, vol. 10, no. 1, pp. 13–13, 2022.
- [15] W. Z. Mu, "Analysis and warning model of logistics risks of cross-border E-commerce," *Discrete Dynamics in Nature and Society*, vol. 2022, Article ID 5140939, 10 pages, 2022.
- [16] W. J. Jing, "Construction of an E-commerce system based on 5G and Internet of Things technology," *International Journal of Information Systems and Supply Chain Management (IJISSCM)*, vol. 15, no. 2, pp. 1–19, 2021.
- [17] J. Du and Z. Y. Yu, "Building a cross-border E-commerce ecosystem model based on block chain + Internet of Things," *Security and Communication Networks*, vol. 2021, Article ID 6451721, 7 pages, 2021.
- [18] Y. Zhang and J. T. Wen, "The IoT electric business model: using blockchain technology for the Internet of Things," *Peer-to-Peer Networking and Applications*, vol. 10, no. 4, pp. 983–994, 2017.
- [19] H. Khastavaneh and K. Ebrahimpour, "Segmentation of diabetic retinopathy lesions in retinal fundus images using multi-view convolutional neural networks," *Iranian Journal of Radiology*, vol. 16, 2019.

Retraction

Retracted: CX3CL1 Derived from Bone Marrow Mesenchymal Stem Cells Inhibits $A\beta_{1-42}$ -Induced SH-SY5Y Cell Pathological Damage through TXNIP/NLRP3 Signaling Pathway

Computational and Mathematical Methods in Medicine

Received 27 June 2023; Accepted 27 June 2023; Published 28 June 2023

Copyright © 2023 Computational and Mathematical Methods in Medicine. This is an open access article distributed under the Creative Commons Attribution License, which permits unrestricted use, distribution, and reproduction in any medium, provided the original work is properly cited.

This article has been retracted by Hindawi following an investigation undertaken by the publisher [1]. This investigation has uncovered evidence of one or more of the following indicators of systematic manipulation of the publication process:

- (1) Discrepancies in scope
- (2) Discrepancies in the description of the research reported
- (3) Discrepancies between the availability of data and the research described
- (4) Inappropriate citations
- (5) Incoherent, meaningless and/or irrelevant content included in the article
- (6) Peer-review manipulation

The presence of these indicators undermines our confidence in the integrity of the article's content and we cannot, therefore, vouch for its reliability. Please note that this notice is intended solely to alert readers that the content of this article is unreliable. We have not investigated whether authors were aware of or involved in the systematic manipulation of the publication process.

Wiley and Hindawi regrets that the usual quality checks did not identify these issues before publication and have since put additional measures in place to safeguard research integrity.

We wish to credit our own Research Integrity and Research Publishing teams and anonymous and named external researchers and research integrity experts for contributing to this investigation.

The corresponding author, as the representative of all authors, has been given the opportunity to register their agreement or disagreement to this retraction. We have kept a record of any response received.

References

- [1] C. Guo, Q. Li, J. Xiao et al., "CX3CL1 Derived from Bone Marrow Mesenchymal Stem Cells Inhibits $A\beta_{1-42}$ -Induced SH-SY5Y Cell Pathological Damage through TXNIP/NLRP3 Signaling Pathway," *Computational and Mathematical Methods in Medicine*, vol. 2022, Article ID 1949344, 12 pages, 2022.

Research Article

CX3CL1 Derived from Bone Marrow Mesenchymal Stem Cells Inhibits $A\beta_{1-42}$ -Induced SH-SY5Y Cell Pathological Damage through TXNIP/NLRP3 Signaling Pathway

Chuan Guo,^{1,2} Qinxuan Li,¹ Jiujia Xiao,¹ Xuhui Zhou,¹ Meichen Tian,¹ Lei Xie,¹ and Xun Xia^{1,2} 

¹Chengdu Medical College, Chengdu Sichuan 610500, China

²Department of Critical Care Medicine, The First Affiliated Hospital of Chengdu Medical College, Chengdu Sichuan 610500, China

Correspondence should be addressed to Xun Xia; xiacun0428@163.com

Received 8 June 2022; Revised 14 July 2022; Accepted 25 July 2022; Published 8 September 2022

Academic Editor: Pan Zheng

Copyright © 2022 Chuan Guo et al. This is an open access article distributed under the Creative Commons Attribution License, which permits unrestricted use, distribution, and reproduction in any medium, provided the original work is properly cited.

Alzheimer's disease (AD) is the most commonly seen neurodegenerative brain disorder. The paracrine effects of mesenchymal stem cells (MSCs) signify to trigger immunomodulation and neural regeneration. However, the role and mechanism of bone marrow MSC- (BMSC-) derived CX3CL1 in AD remains elusive. In this study, $A\beta_{1-42}$ -intervened SH-SY5Y cells were used for AD cell model construction. pcDNA-ligated CX3CL1 overexpression plasmids were transfected into BMSCs. The levels of soluble and membrane-bound CX3CL1 were detected by ELISA and Western blotting (WB), respectively. The growth, apoptosis, and pathology of AD model cells were evaluated by CCK-8, flow cytometry, immunofluorescence, morphology observation, biochemical examination, and WB. It was found that $A\beta_{1-42}$ significantly reduced CX3CL1 expression either in soluble or membrane-bound form, cell viability, relative protein expression of synaptic markers, SOD, CAT, and GSH-Px contents, as well as Trx protein expression; in addition, it enhanced the apoptosis rate, the relative expression of cleaved caspase-3, $A\beta$, tau, p-Tau, Iba1, MDA, TXNIP, and NLRP3 in SH-SY5Y cells; however, the above effects were prominently reversed by the coculture of BMSCs. Moreover, overexpression of CX3CL1 in BMSCs observably strengthened the corresponding tendency caused by BMSCs. In conclusion, through the TXNIP/NLRP3 pathway, CX3CL1 derived from BMSCs inhibited pathological damage in $A\beta_{1-42}$ -induced SH-SY5Y.

1. Introduction

As a progressive neurodegenerative brain disease, Alzheimer's disease (AD) is acknowledged to be the prime reason for dementia [1]. It is also the sixth main cause of death, with an estimate of about 75.6 million and 135.5 million sufferers worldwide as well as \$2.54 trillion and \$9.12 trillion costs by 2030 and 2050, respectively [2, 3]. AD is pathologically featured by the accumulation of aggregated β -amyloid ($A\beta$) plaques and neurofibrillary tangles (NFTs) that consist of hyperphosphorylated Tau proteins [4]. Thus, therapies targeting $A\beta$ and antitau agents have attracted extensive attention [5]. However, the benefits and side effects of even the promising anti- $A\beta$ drug, aducanumab, still need further investigations [6, 7]. Besides, antitau vaccine (AADvac1)

and monoclonal antitau antibodies, including gosuranemab, tilavonemab, zagotenemab, and semorinemab, have only arrived phase II at present [5]. Even several clinical drugs, such as galantamine, memantine, donepezil, and rivastigmine, only show modest benefits to symptomatic patients with AD [8]. Therefore, potential mechanisms and therapeutic strategies for AD necessitate more attention.

As a type of pluripotent progenitor cells that can be separated from various tissues like bone marrow, fatty tissue, and umbilical cord blood, mesenchymal stem cells (MSCs) have the advantages of high proliferation and easy manipulation [9]. MSCs possess multifaceted functions, such as differentiating into glial and neuronal cells, secreting growth factor and anti-inflammatory cytokines, modulating immune cells, and stimulating endogenous repair mechanisms [10, 11], making

them a novel and promising therapy for AD [12]. Bone marrow MSCs (BMSCs) are shown to alleviate cognitive decline of AD model rats [13]. Bae et al. [14] also presented that BMSCs decreased A β deposits and ameliorated synaptic transmission in AD mice models. Kim et al. [15] demonstrated the feasibility of AD treatment by human umbilical cord blood MSCs (hUC-MSCs) via stereotactic brain injection in a phase 1 clinical trial. Lee et al. [16] displayed that BMSCs induced the reduction of A β deposits and promoted microglia activation in AD mice models. Thus, MSCs are a potential and effective approach for the treatment of AD.

It has been demonstrated that the clinical efficacy of MSCs may be related to their paracrine effects on other effector cells [17]. It was found in vitro and in vivo that the suppression of BMSC-derived exosomal miR-1231 plays a role in restricting the characteristics of pancreatic cancer [18]. While supporting acute myeloid leukemia bioenergetics, BMSCs can also enhance antioxidant defense and escape from chemotherapy [19]. Meanwhile, MSCs can modulate the activation of retinal microglia by chemokine CX3CL1 signaling [20]. Moreover, CX3CL1-expressing MSCs played neuroprotective and immunomodulatory roles in the retinal degeneration rat model [21]. Also known as fractalkine, chemokine CX3CL1 is the one and only member of the CX3C family that binds to its just receptor, CX3CR1, which is expressed on the surface of microglia [22, 23]. CX3CL1 is mainly distributed in neurons within the central nervous system (CNS) [24]. Thus, there is a signaling network formed by the binding of CX3CL1 and CX3CR1 between neurons and microglia in the physiological CNS [25, 26]. There are two forms of CX3CL1 in CNS, namely, membrane-bound and soluble CX3CL1. Therein, membrane-bound CX3CL1 can be protease-cleaved to produce soluble CX3CL1 [27, 28]. Reportedly, CX3CL1 is neuroprotective via the reduced microglial generation of inflammatory factors [24]. However, the role of CX3CL1 derived from MSCs in the development and progression of AD remains elusive.

Accordingly, the motivation and novelty of this work is to clarify the role played by BMSC-derived CX3CL1 and the underlying mechanisms via A β ₁₋₄₂-induced SH-SY5Y cell model establishment. BMSC-derived CX3CL1 inhibited A β ₁₋₄₂-induced SH-SY5Y cell pathological damage via the TXNIP/NLRP3 axis.

2. Materials and Methods

2.1. Cells and Cultivation. BMSCs and the human neuroblastoma SH-SY5Y cells, supplied by Cyagen Biosciences Inc. (Guangzhou, China) and Procell (CL-0208, Wuhan, China), respectively, were cultivated under the conditions of 5% carbon dioxide (CO₂) at 37°C in a medium comprising Dulbecco's modified Eagle's medium (DMEM; Invitrogen, Carlsbad, CA, USA) as well as 10% fetal bovine serum (FBS; Gibco, Rockville, MD, USA) and 1% streptomycin-penicillin (Solarbio, Beijing, China).

2.2. BMSC Transfection. BMSCs were cultivated (5% CO₂, 37°C) after being seeded at 1×10^4 cells/cm² into the wells

of 6-well plates. When the cell confluency reached 80%, 50 ng pcDNA-ligated CX3CL1 overexpression plasmid (CX3CL1-ov) and its corresponding empty vector plasmid (NC-ov) supplied by RiboBio (Guangdong, China) were added for transfection following Lipofectamine® 3000 (Invitrogen; Thermo Fisher Scientific, Waltham, MA, USA) recommendations. The media were replaced with DMEM after 6 h of transfection, and BMSCs were then cultured for 72 h for further assays.

2.3. Experimental Groups and Treatment. SH-SY5Y cells were grouped as follows: control, A β , A β +MSC, A β +MSC-NC-ov, and A β +MSC-CX3CL1-ov. An AD cell model was built via treating SH-SY5Y with 20 μ M A β ₁₋₄₂ [29], while the control group was administrated with phosphate buffer saline (PBS) with an equal amount. Moreover, SH-SY5Y cells in A β +MSC, A β +MSC-NC-ov, and A β +MSC-CX3CL1-ov groups were coincubated with BMSCs, BMSCs transfected with NC-ov, and BMSCs transfected with CX3CL1-ov, respectively. The observation of cell morphology and axon growth was performed with a microscope (Olympus, Tokyo, Japan). After 48 h of coculture, SH-SY5Y cells at the plate bottom were trypsinized and prepared for the following assays.

2.4. Enzyme-Linked Immunosorbent Assay (ELISA). Soluble CX3CL1 concentration in cell culture supernatant, generated after 18 hours of incubation in the complete medium, was detected by commercial human fractalkine/CX3CL1 ELISA kit (ab100522, Abcam, Cambridge, UK) based on the operating instructions.

2.5. Western Blotting Analysis. SH-SY5Y cells after three PBS rinses were immersed in a RIPA lysis buffer (Boster, Wuhan, China) to obtain the total proteins. Following isolation by 10% SDS-PAGE, the protein samples were processed for electrical transfer onto PVDF membranes (EMD Millipore, Billerica, MA, USA) that were then sealed at an ambient temperature in bovine serum albumin (BSA; 3%) for 60 minutes and subsequently cultivated at 4°C with the following I antibodies all ordered from Abcam overnight: CX3CL1 (1:1000, ab25088), cleaved caspase-3 (1:500, ab2302), A β (1:1000, ab11132), tau (1:10000, ab76128), phosphorylated tau (p-Tau) (1:50000, ab109390), SNAP25 (1:1000, ab41455), Synapsin1 (1:1000, ab64581), PSD95 (1:1000, ab18258), TXNIP (1:2000, ab188865), Trx (1:1000, ab26320), and NLRP3 (1:1000, ab263899). At an ambient temperature, they were cultured with the corresponding II antibody for 60 minutes after triple PBS washes. Protein expressions were analyzed relative to β -actin. Band visualization was made with an ECL kit (EMD Millipore) based on the operating manual. Image-ProPlus (Media Cybernetics, Inc., Rockville, MD, USA) determined the gray value.

2.6. Cell Counting Kit-8 Assay. After each group of SH-SY5Y cells were planted into 96-well plates at 1×10^5 /well for overnight cultivation under the conditions of 5% CO₂ and 37°C, the cell proliferation was analyzed following the Cell Count Kit-8 (Dojindo Laboratories, Kumamoto, Japan) operating manual. A microplate reader, supplied by Thermo Fisher

Scientific, Waltham, MA, USA, was adopted to read the absorbance_{450nm}.

2.7. Flow Cytometry Assay. 90% confluent cells were washed with PBS for 2 to 3 times. Then, cell digestion with trypsin-EDTA solution and resuspension in 500 μ L binding buffer were performed. Subsequently, the cell resuspension was stained with a mixture comprising allophycocyanin (APC) and phycoerythrin (PE), both supplied by Sigma-Aldrich with an amount of 5 μ L, for 15 min at an ambient temperature in a dark environment. Flow cytometry (BD FACS-Verse, USA) determined the apoptosis rate.

2.8. Immunofluorescence Assay. Cells were maintained and adhered on chamber slides. After triple PBS rinses, they were treated with 4% paraformaldehyde fixation (10 min), 1% BSA blocking, and overnight cultivation (4°C) with the Iba1 antibody (1:1000, ab48004, Abcam). Subsequently, they were processed for triple PBS washes and 60 min of goat anti-rat IgG H&L (Alexa Fluor® 647) (1:500, ab150167, Abcam) incubation (37°C). This was followed by nuclear staining with DAPI (C1002, Beyotime, Shanghai, China), and the final image was captured with a confocal microscopy (LSM700; Zeiss, Oberkochen, Germany).

2.9. MDA, SOD, CAT, and GSH-Px Measurements. Malondialdehyde (MDA), superoxide dismutase (SOD), catalase (CAT), and glutathione peroxidase (GSH-Px) measurements used MDA (A003-1-1), total SOD (T-SOD) (A001-1-1), CAT (A007-1-1), and GSH-Px test kits (A005-1-2; all from Nanjing Jiancheng Bioengineering Institute, China), respectively, following the operating manual of the corresponding kit. The microplate reader read the absorbance of wells at 532, 560, 405, and 412 nm for MDA, SOD, CAT, and GSH, respectively.

2.10. Statistical Processing. All data collected were present in the form of the mean \pm standard deviation, and the statistical significance threshold was $p < 0.05$. Each assay was replicated 3 times. One-way analysis of variance and Duncan's test were employed to identify inter- and multigroup differences, respectively. SPSS 20.0 (SPSS Inc., Chicago, IL, USA) was used for analysis.

3. Results

3.1. BMSC-Derived CX3CL1 Reversed the $A\beta_{1-42}$ -Reduced Level of CX3CL1 in SH-SY5Y. To explore the role played by CX3CL1 derived from BMSCs in a $A\beta_{1-42}$ -induced SH-SY5Y cell model, pcDNA-ligated CX3CL1 overexpression plasmid was first transfected into BMSCs to upregulate CX3CL1 expression in BMSCs. ELISA (Figure 1(a)) and western blotting (Figures 1(b) and 1(c)) results showed that overexpression of CX3CL1 in BMSCs observably increased the levels of both soluble and membrane-bound CX3CL1, while there were no differences between the NC-ov and control groups. Besides, statistically decreased soluble and membrane-bound CX3CL1 levels were observed in SH-SY5Y under $A\beta_{1-42}$ inducement, which were significantly rescued by the coculture of BMSCs (Figures 1(d)–1(f)).

Moreover, overexpression of CX3CL1 in BMSCs further statistically enhanced CX3CL1 levels of both the soluble and membrane-bound forms, whereas transfection of NC-ov showed no statistical effect (Figures 1(d)–1(f)). These results indicated that CX3CL1 derived from BMSCs notably reversed the $A\beta_{1-42}$ -reduced CX3CL1 expression in SH-SY5Y cells.

3.2. CX3CL1 Derived from BMSCs Increased $A\beta_{1-42}$ -Induced SH-SY5Y Viability but Suppressed Apoptosis. Then, we investigated the role played by CX3CL1 derived from BMSCs in SH-SY5Y cell growth under $A\beta_{1-42}$ inducement. Statistically declined $A\beta_{1-42}$ -intervened SH-SY5Y cell viability was found compared to the control group, which was markedly inverted by the coculture of BMSCs (Figure 2(a)). Also, transfection of CX3CL1 overexpression plasmid (not empty plasmid) into BMSCs further markedly elevated SH-SY5Y cell viability compared to SH-SY5Y with $A\beta_{1-42}$ and BMSC coculture (Figure 2(a)). However, the opposite tendency was discovered in SH-SY5Y cell apoptosis, as indicated by that cocultured with BMSCs significantly reduced the $A\beta_{1-42}$ -increased apoptosis rate (Figures 2(b) and 2(c)) and the relative protein expression of cleaved caspase-3 (Figures 2(d) and 2(e)) of SH-SY5Y cells, which was prominently antagonized with the overexpression of CX3CL1 in BMSCs. These data suggested that CX3CL1 derived from BMSCs significantly enhanced $A\beta_{1-42}$ -induced SH-SY5Y cell growth but inhibited apoptosis.

3.3. CX3CL1 Derived from BMSCs Ameliorated the Pathology-Induced $A\beta_{1-42}$ in SH-SY5Y. Next, the role played by CX3CL1 derived from BMSCs in the pathology of $A\beta_{1-42}$ -induced SH-SY5Y was investigated. $A\beta$, tau, and p-Tau were found to be markedly increased with the induction of $A\beta_{1-42}$ in SH-SY5Y, which was statistically improved with the coculture of BMSCs (Figures 3(a)–3(d)). Moreover, transfection of CX3CL1 overexpression plasmid (not empty plasmid) into BMSCs further notably diminished the relative protein expression of $A\beta$, tau, and p-Tau (Figures 3(a)–3(d)). Also, similar changes were found in the relative integrated density of Iba1 (Figures 3(e) and 3(f)). Besides, coculture of BMSCs obviously improved the cell growth and axon length of $A\beta_{1-42}$ -induced SH-SY5Y, which was further ameliorated with the overexpression of CX3CL1 in BMSCs (Figure 3(g)). Furthermore, the relative protein expressions of synaptic markers, including SNAP25, Synapsin1, and PSD95, were statistically declined in SH-SY5Y with $A\beta_{1-42}$ inducement, which were notably reversed by the coculture of BMSCs (Figures 3(h)–3(k)). Consistently, upregulation of CX3CL1 in BMSCs further statistically elevated SNAP25, Synapsin1, and PSD95 protein levels (Figures 3(h)–3(k)). Taken together, these results demonstrated that CX3CL1 derived from BMSCs obviously improved the pathology-induced $A\beta_{1-42}$ in SH-SY5Y.

3.4. The Influence of BMSC-Derived CX3CL1 on $A\beta_{1-42}$ -Induced SH-SY5Y Was Associated with TXNIP/NLRP3 Axis. Furthermore, the potential mechanisms associated with the role of CX3CL1 derived from BMSCs in SH-SY5Y

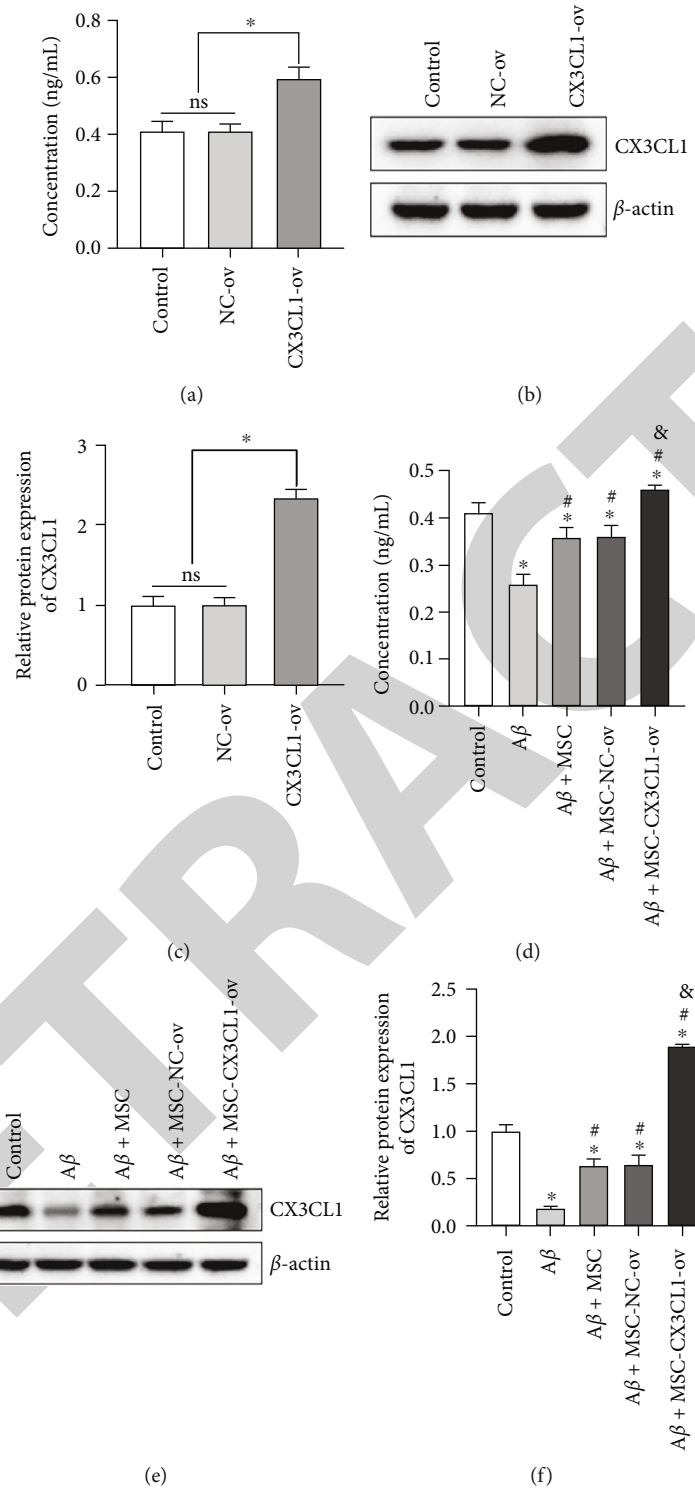


FIGURE 1: CX3CL1 derived from BMSCs significantly inverted A β_{1-42} -decreased CX3CL1 in SH-SY5Y. (a) Soluble CX3CL1 expression in BMSCs was detected by ELISA. (b and c) Western blotting determined CX3CL1 expression relative to β -actin in BMSCs. (d) ELISA measured soluble CX3CL1 levels in SH-SY5Y under different interventions. (e and f) Western blotting examined CX3CL1 expression relative to β -actin in SH-SY5Y under different interventions. ns: nonsignificance; * $p < 0.05$ versus control group; # $p < 0.05$ versus A β group; & $p < 0.05$ versus A β +MSC group.

with A β_{1-42} inducement were studied. Coculture of BMSCs markedly declined the A β_{1-42} -enhanced MDA concentration, which was further statistically decreased by overexpress-

sion of CX3CL1 in BMSCs (Figure 4(a)). On the contrary, coculture of BMSCs markedly elevated the A β_{1-42} -reduced concentrations of SOD, CAT, and GSH-Px, which was

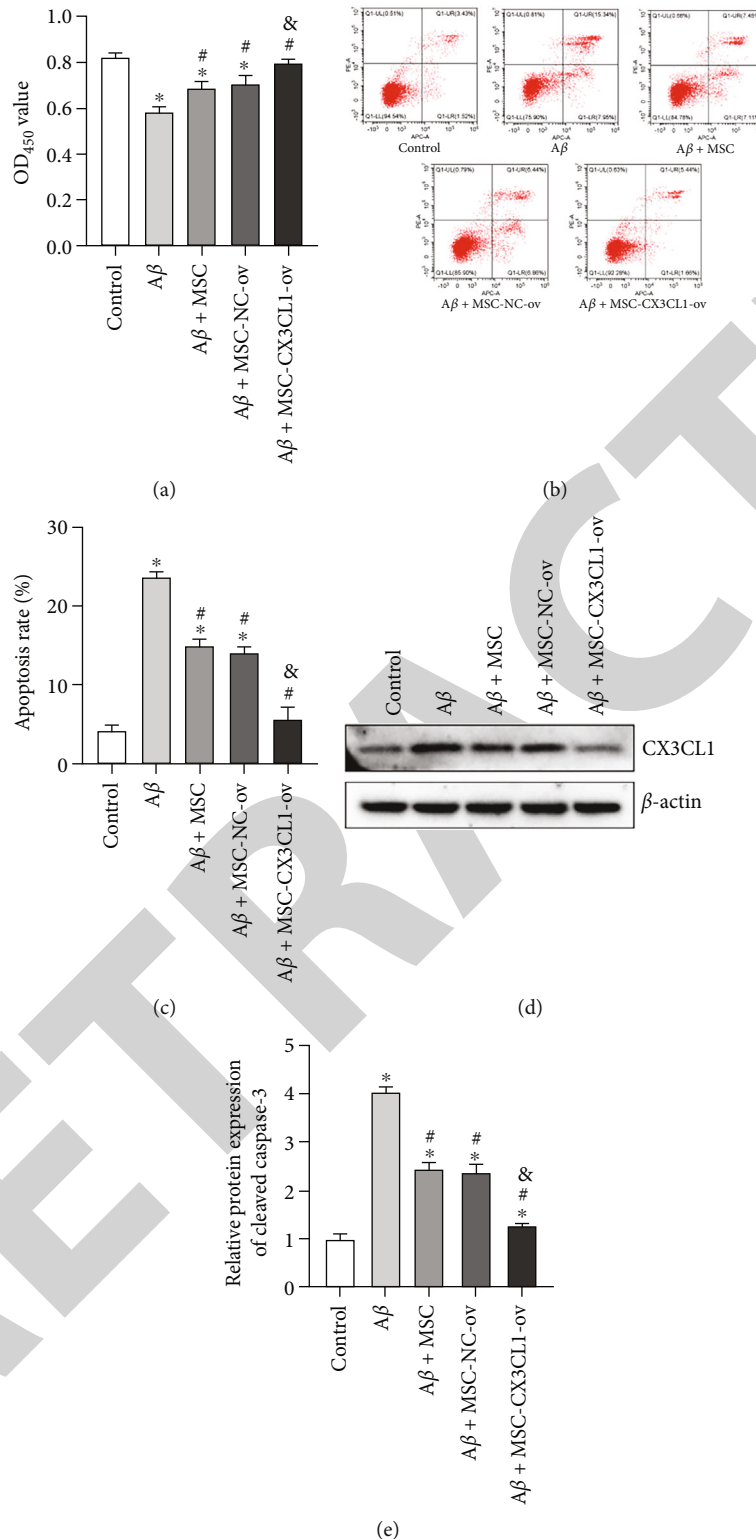


FIGURE 2: CX3CL1 derived from BMSCs statistically augmented A β_{1-42} -induced SH-SY5Y viability but repressed apoptosis. (a) CCK-8 assay assessed SH-SY5Y viability. (b and c) Flow cytometry evaluated SH-SY5Y apoptosis. (d and e) Western blotting determined cleaved caspase-3 expression relative to β -actin. * $p < 0.05$ versus control group; # $p < 0.05$ versus A β group; & $p < 0.05$ versus A β +MSC group.

further significantly increased by overexpression of CX3CL1 in BMSCs (Figures 4(b)–4(d)). Mechanically, coculture of BMSCs prominently diminished the A β_{1-42} -enhanced

TXNIP and NLRP3 protein levels while aggrandized the A β_{1-42} -attenuated Trx protein expression (Figures 4(e)–4(h)). Moreover, upregulation of CX3CL1 in BMSCs further

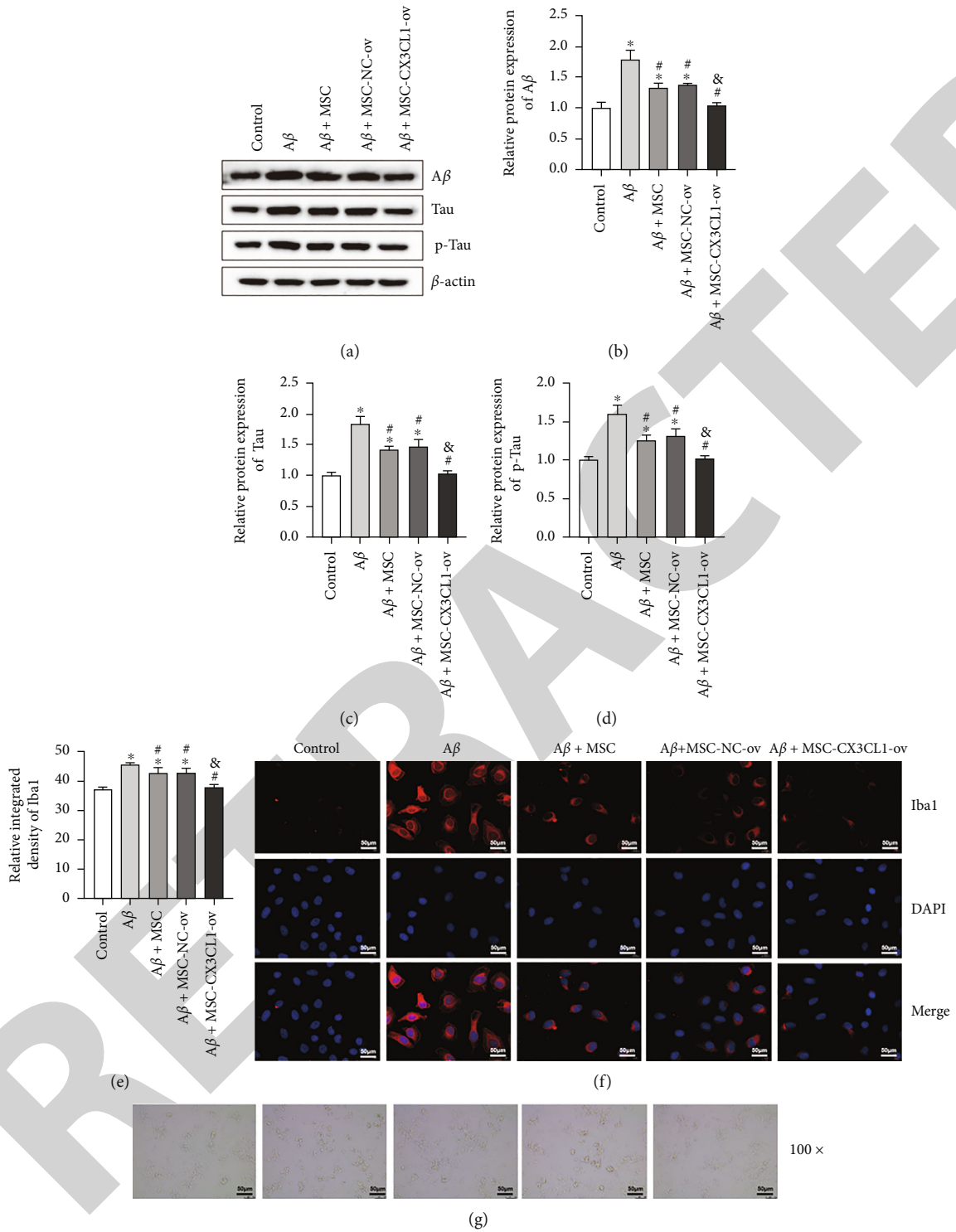


FIGURE 3: Continued.

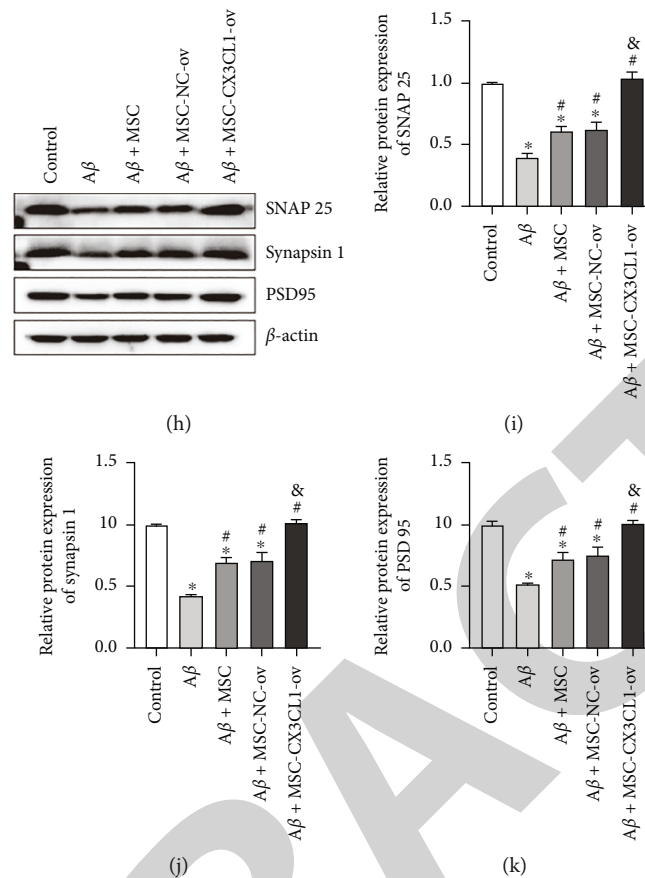


FIGURE 3: CX3CL1 derived from BMSCs alleviated the pathology-induced A β_{1-42} in SH-SY5Y. (a–d) Western blotting examined A β , tau, and p-Tau protein expressions relative to β -actin. (e and f) The relative integrated density of Iba1 was evaluated by IF. (g) The axons of SH-SY5Y cells were observed using inverted microscope. (h–k) Western blotting examined SNAP25, Synapsin1, and PSD95 protein levels relative to β -actin. * $p < 0.05$ versus control group; # $p < 0.05$ versus A β group; & $p < 0.05$ versus A β +MSC group.

statistically strengthened the corresponding tendency (Figures 4(e)–4(h)). Together, these data clarified that the effect of CX3CL1 derived from BMSCs on A β_{1-42} -induced SH-SY5Y involved the TXNIP/NLRP3 signaling axis.

4. Discussion

AD is the most prevalent neurodegenerative brain disorder that imposes a severe burden on patients and their families, even leading to social and economic losses [30]. It is demonstrated that MSC therapy is a novel and promising treatment for AD, whose paracrine action is meant to trigger immunomodulation and neural regeneration [17]. CX3CL1 is essential in the regulation of microglia activation, neuroprotection, and immunomodulation by MSCs [20, 21]. In this paper, A β_{1-42} treatment markedly reduced both soluble and membrane-bound CX3CL1 levels, cell viability, protein levels of synaptic markers (SNAP25, Synapsin1, and PSD95), SOD, CAT, and GSH-Px concentrations, and Trx protein expression, while it enhanced apoptosis, cleaved caspase-3, A β , tau, and p-Tau protein levels, relative integrated density of Iba1, MDA concentration, and TXNIP and NLRP3 protein levels in SH-SY5Y; however, the above effects were prominently reversed by the coculture of BMSCs. Moreover, we overexpressed CX3CL1 in BMSCs

and found that overexpression of CX3CL1 in BMSCs observably strengthened the corresponding tendency caused by the coculture of BMSCs.

The membrane-bound CX3CL1 and soluble CX3CL1 play diverse roles under physiological conditions. Membrane-bound CX3CL1 functions is involved in infiltrating leukocyte recruitment and adhesion [31], while soluble CX3CL1 serves as a chemoattractant associated with the cellular migration, as well as a neuroprotective signaling molecule to contribute to the sustainability of the resting state of microglia [32, 33]. Besides, soluble CX3CL1 modulates the anti-inflammatory effect in the brain, and the receptors of membrane-bound CX3CL1 are located on microglial cell surfaces [32, 34]. During fibrosis amelioration, MSCs can participate in Ly-6C-high (inflammatory) to Ly-6C low (anti-inflammatory) macrophage polarization by increasing CX3CL1 levels, exerting significant effects on ameliorating liver disease [35]. The cerebrospinal fluid CX3CL1 level is reported to be notably diminished in AD patients [36]. Also, our results revealed statistically reduced soluble and membrane-bound CX3CL1 levels in SH-SY5Y cells under A β_{1-42} inducement. However, coculture of BMSCs markedly rescued decreased CX3CL1 by A β_{1-42} in SH-SY5Y, implying that BMSCs might express and secrete CX3CL1 to compensate for the loss of CX3CL1 [37]. Overexpression of CX3CL1

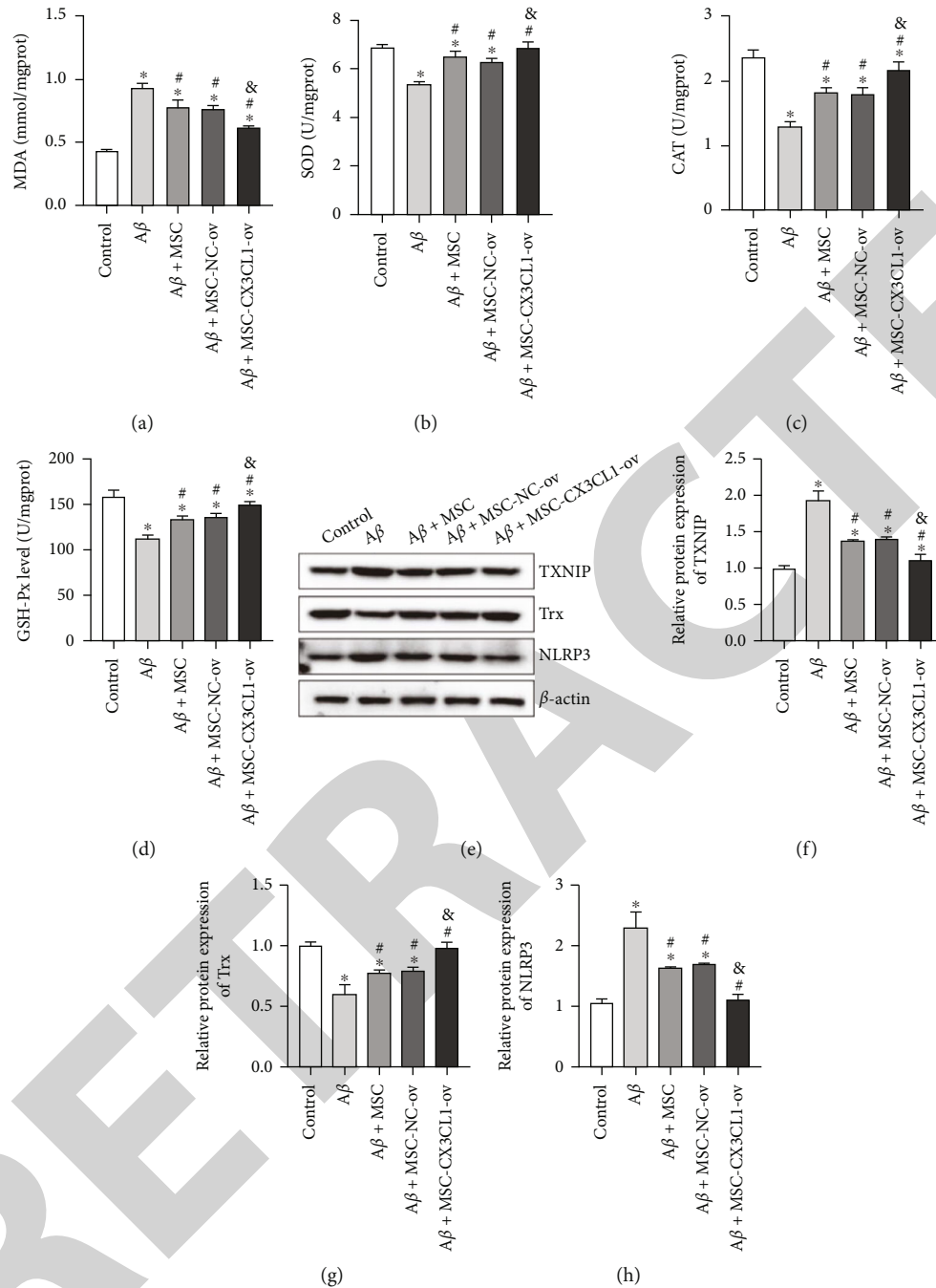


FIGURE 4: The role played by CX3CL1 derived from BMSCs in A β_{1-42} -induced SH-SY5Y was related to TXNIP/NLRP3 axis. (a–d) MDA, SOD, CAT, and GSH-Px concentrations measured by commercial kits. (e–h) Western blotting tested TXNIP, NLRP3, and Trx protein levels relative to β -actin. * $p < 0.05$ versus control group; # $p < 0.05$ versus A β group; & $p < 0.05$ versus A β +MSC group.

in BMSCs further confirmed this conclusion. Besides, we discovered that CX3CL1 derived from BMSCs significantly enhanced A β_{1-42} -induced SH-SY5Y growth but declined apoptosis rate and cleaved caspase-3 at the protein level. Cleaved caspase-3 is the activation form of caspase-3 that can regulate different phases of the apoptotic pathway [38]. Therefore, these findings elucidated that A β_{1-42} treatment resulted in low level of CX3CL1, which was positively associated with the growth and negatively related to the apoptosis of SH-SY5Y cells. Upregulation of CX3CL1 in BMSCs

obviously increased the reduced CX3CL1 and proliferation of SH-SY5Y cells but inhibited increased apoptosis by A β_{1-42} . Taken together, CX3CL1 derived from BMSCs reversed the A β_{1-42} -reduced CX3CL1, which increased the viability but suppressed the apoptosis of SH-SY5Y under A β_{1-42} inducement.

A β accumulation and hyperphosphorylated tau are the dominating pathological hallmarks of AD [39, 40], which may explain prominently high A β , Tau, and p-Tau protein levels in SH-SY5Y with A β_{1-42} inducement in this research.

Recently, Qin et al. [41] have reported that BMSC transplantation mitigated neuropathology and ameliorated cognitive deficits in AD animal models. Consistently, we found that coculture of BMSCs statistically reduced the $A\beta_{1-42}$ -increased $A\beta$, Tau, and p-Tau protein levels, which were further notably decreased by the upregulation of CX3CL1 in BMSCs. Tau and $A\beta$ are the prime suspects driving AD pathology and, as such, have become the focus of therapeutic development. There is mounting evidence that these proteins may perform many crucial physiological functions during AD pathological development that can be disrupted by $A\beta$ - or tau-lowering therapeutics [42]. In the past decades, a large number of research has demonstrated that neuroinflammation is a central risk factor of AD; thus, strategies of decreasing neuroinflammation have been regarded as the promising therapeutics for AD [43, 44]. Neuroinflammation in the brain is mediated by microglial cells, so microglial activation is a characteristic of neuroinflammation [45, 46]. Here, we observed that coculture of BMSCs significantly declined the $A\beta_{1-42}$ -enhanced relative integrated density of Iba1, a marker of microglial cells, which was further obviously diminished by the overexpression of CX3CL1 in BMSCs, indicating that CX3CL1 derived from BMSCs inhibited neuroinflammation in SH-SY5Y with $A\beta_{1-42}$ inducement. Moreover, it confirmed the fact that soluble CX3CL1 plays an anti-inflammatory role in the brain [32, 34]. In addition, it has been demonstrated that $A\beta$ and Tau oligomers, as well as neuroinflammation, can conduce to synaptic loss, which results in synaptic dysfunction [46–48]. Our findings revealed that coculture of BMSCs obviously improved $A\beta_{1-42}$ -induced SH-SY5Y cell growth and axon length, which was further notably ameliorated by the overexpression of CX3CL1 in BMSCs. Also, coculture of BMSCs statistically elevated the $A\beta_{1-42}$ -attenuated relative protein levels of SNAP25, Synapsin1, and PSD95, as well as the pre-synaptic and postsynaptic markers, which was further markedly promoted by the overexpression of CX3CL1 in BMSCs. Based on the above, we can draw the conclusion that CX3CL1 derived from BMSCs notably suppressed pathological damage in $A\beta_{1-42}$ -induced SH-SY5Y cells.

Furthermore, neuroinflammation can induce oxidative stress in the brain [48]. In the present study, $A\beta_{1-42}$ treatment remarkably reduced SOD, CAT, and GSH-Px concentrations in SH-SY5Y while enhancing MDA levels, which were prominently reversed by the coculture of BMSCs. Overexpression of CX3CL1 in BMSCs observably strengthened the corresponding tendency caused by the coculture of BMSCs, which suggested statistically inhibited oxidative stress in SH-SY5Y with $A\beta_{1-42}$ inducement by BMSC-derived CX3CL1. TrX is an intracellular antioxidative protein via thiol reduction and the scavenging of reactive oxygen species (ROS) [49]. This research identified that TrX expression was predominately decreased in SH-SY5Y with $A\beta_{1-42}$ inducement, which was in line with the reduction in AD brain regions [50]. TrX can be bound by TXNIP to dampen TrX activation and facilitate oxidative stress [51]. Oakley et al. [52] exhibited that the level of TXNIP was upregulated in the hippocampus of mice in a $5 \times$ AD mouse model. Consistently, SH-SY5Y with $A\beta_{1-42}$ inducement pre-

sented overexpressed TXNIP in our study. Moreover, TXNIP is a key link between inflammasome activation and oxidative stress [53]. Under oxidative stress, dissociated TXNIP from TrX binds to NLRP3 that conduces to inflammasome formation and activation. Consequently, a series of proinflammatory mediators are secreted to enhance neuroinflammation, which promotes synaptic dysfunction and the subsequent AD progression. Furthermore, Wang et al. [54] have reported an enhancement of binding between TXNIP and NLRP3 in the APP/PS1 mouse brain, and NLRP3 inflammasome and Nrf2/TXNIP/TrX axis are involved in the pathological changes of AD. Here, we discovered that $A\beta_{1-42}$ treatment notably decreased Trx protein expression and elevated TXNIP and NLRP3 protein levels in SH-SY5Y that were prominently reversed by the coculture of BMSCs. Upregulation of CX3CL1 in BMSCs significantly intensified the corresponding tendency caused by the coculture of BMSCs. Therefore, these results elaborated that the role of CX3CL1 derived from BMSCs in $A\beta_{1-42}$ -intervened SH-SY5Y was linked to the TXNIP/NLRP3 signaling axis.

5. Conclusion

In conclusion, our results revealed that through the TXNIP/NLRP3 signaling pathway, CX3CL1 derived from BMSCs alleviates $A\beta_{1-42}$ -induced SH-SY5Y cell injury. However, there are still some limitations in our study. First, Lee et al. [55] have reported that membrane-bound CX3CL1 but not soluble CX3CL1 mediated the $A\beta$ pathology. Our results showed that CX3CL1 derived from BMSCs reversed the $A\beta_{1-42}$ -reduced soluble and membrane-bound CX3CL1 levels; hence, whether the membrane-bound CX3CL1 consistently improved the $A\beta$ pathology or not needs further exploration in our subsequent studies. Besides, multiple research has demonstrated that the CX3CL1 is closely involved in inflammation [56–58]. However, in our study, we failed to further reveal the role of CX3CL1 derived from BMSCs in neuroinflammation. Also, the findings are not verified in vivo. Thus, more experiments are expected to be conducted in further studies to explore the underlying mechanism. In brief, it is hoped that our results can lay a foundation for AD treatment and even the management of other neurodegenerative disorders.

Data Availability

The data sets used and analyzed during the current study are available from the corresponding author on reasonable request.

Conflicts of Interest

The authors report that there are no competing interests to declare.

Authors' Contributions

CG, QL, and XX designed the experiments; CG, QL, and JX carried out the experiments; XZ, MT, and LX analyzed the

experimental results and interpreted the data; CG, QL, and XX wrote and revised the manuscript. All authors have approved the final manuscript. Chuan Guo and Qinxuan Li contributed equally to this work and are co-first authors.

Acknowledgments

The present work was supported by the Severe phenotypic transformation of microglia mediated by TLR3/TRIF signaling pathway and its regulation and mechanism on neurons after intracerebral hemorrhage, Sichuan Provincial Health Commission (No. 21PJ113); Study on the mechanism of icariin in the treatment of anti-neuro-inflammation and anti-oxidation after spinal cord injury based on Nrf2 signaling pathway, Sichuan Administration of Traditional Chinese Medicine (No. 2020JC0025); and Research on the polarization and directional induction regulation of microglia by icariin after spinal cord injury, the First Affiliated Hospital of Chengdu Medical College High-level Talents Research Start-up Fund (No. CYFY-GQ25).



References

- [1] J. Wiley, "Alzheimer's disease facts and figures," *Alzheimers Dementia*, vol. 17, 2021.
- [2] J. Jia, C. Wei, S. Chen et al., "The cost of Alzheimer's disease in China and re-estimation of costs worldwide," *Alzheimer's & Dementia*, vol. 14, no. 4, pp. 483–491, 2018.
- [3] D.-F. Zhang, M. Xu, R. Bi, and Y.-G. Yao, "Genetic analyses of Alzheimer's disease in China: achievements and perspectives," *ACS Chemical Neuroscience*, vol. 10, no. 2, pp. 890–901, 2019.
- [4] P. d'Errico and M. Meyer-Luehmann, "Mechanisms of pathogenic tau and $\alpha\beta$ protein spreading in Alzheimer's disease," *Frontiers in Aging Neuroscience*, vol. 12, p. 265, 2020.
- [5] M. Vaz and S. Silvestre, "Alzheimer's disease: recent treatment strategies," *European Journal of Pharmacology*, vol. 887, article 173554, 2020.
- [6] J. M. Long and D. M. Holtzman, "Alzheimer disease: an update on pathobiology and treatment strategies," *Cell*, vol. 179, no. 2, pp. 312–339, 2019.
- [7] J. Sevigny, P. Chiao, T. Bussière et al., "The antibody aducanumab reduces $A\beta$ plaques in Alzheimer's disease," *Nature*, vol. 537, no. 7618, pp. 50–56, 2016.
- [8] Z. Breijyeh and R. Karaman, "Comprehensive review on Alzheimer's disease: causes and treatment," *Molecules*, vol. 25, no. 24, p. 5789, 2020.
- [9] D.-C. Ding, W.-C. Shyu, and S.-Z. Lin, "Mesenchymal stem cells," *Cell Transplantation*, vol. 20, no. 1, pp. 5–14, 2011.
- [10] X. Chen, S. Wang, and W. Cao, "Mesenchymal stem cell-mediated immunomodulation in cell therapy of neurodegenerative diseases," *Cellular Immunology*, vol. 326, pp. 8–14, 2018.
- [11] V. Vasic, K. Barth, and M. H. Schmidt, "Neurodegeneration and neuro-regeneration—Alzheimer's disease and stem cell therapy," *International Journal of Molecular Sciences*, vol. 20, no. 17, p. 4272, 2019.
- [12] M. Alipour, S. M. Nabavi, L. Arab et al., "Stem cell therapy in Alzheimer's disease: possible benefits and limiting drawbacks," *Molecular Biology Reports*, vol. 46, no. 1, pp. 1425–1446, 2019.
- [13] P. Babaei, B. Soltani Tehrani, and A. Alizadeh, "Transplanted bone marrow mesenchymal stem cells improve memory in rat models of Alzheimer's disease," *Stem Cells International*, vol. 2012, Article ID 369417, 8 pages, 2012.
- [14] J. S. Bae, H. K. Jin, J. K. Lee, J. C. Richardson, and J. E. Carter, "Bone marrow-derived mesenchymal stem cells contribute to the reduction of amyloid- β deposits and the improvement of synaptic transmission in a mouse model of pre-dementia Alzheimer's disease," *Current Alzheimer Research*, vol. 10, no. 5, pp. 524–531, 2013.
- [15] H. J. Kim, S. W. Seo, J. W. Chang et al., "Stereotactic brain injection of human umbilical cord blood mesenchymal stem cells in patients with Alzheimer's disease dementia: a phase 1 clinical trial," *Alzheimer's & Dementia: Translational Research & Clinical Interventions*, vol. 1, no. 2, pp. 95–102, 2015.
- [16] J. K. Lee, H. K. Jin, and J. S. Bae, "Bone marrow-derived mesenchymal stem cells reduce brain amyloid- β deposition and accelerate the activation of microglia in an acutely induced Alzheimer's disease mouse model," *Neuroscience Letters*, vol. 450, no. 2, pp. 136–141, 2009.
- [17] D. G. Phinney and M. F. Pittenger, "Concise review: MSC-derived exosomes for cell-free therapy," *Stem Cells*, vol. 35, no. 4, pp. 851–858, 2017.
- [18] S. Shang, J. Wang, S. Chen et al., "Exosomal mirna-1231 derived from bone marrow mesenchymal stem cells inhibits the activity of pancreatic cancer," *Cancer Medicine*, vol. 8, no. 18, pp. 7728–7740, 2019.
- [19] D. Forte, M. García-Fernández, A. Sánchez-Aguilera et al., "Bone marrow mesenchymal stem cells support acute myeloid leukemia bioenergetics and enhance antioxidant defense and escape from chemotherapy," *Cell metabolism*, vol. 32, no. 5, p. 829, 2020.
- [20] L. Huang, G. Xu, J. Guo, M. Xie, L. Chen, and W. Xu, "Mesenchymal stem cells modulate light-induced activation of retinal microglia through CX3CL1/CX3CR1 signaling," *Ocular Immunology and Inflammation*, vol. 24, no. 6, pp. 684–692, 2016.
- [21] L. Huang, W. Xu, and G. Xu, "Transplantation of CX3CL1-expressing mesenchymal stem cells provides neuroprotective and immunomodulatory effects in a rat model of retinal degeneration," *Ocular Immunology and Inflammation*, vol. 21, no. 4, pp. 276–285, 2013.
- [22] C. Limatola and R. M. Ransohoff, "Modulating neurotoxicity through CX3CL1/CX3CR1 signaling," *Frontiers in Cellular Neuroscience*, vol. 8, p. 229, 2014.
- [23] P. Luo, S. F. Chu, Z. Zhang, C. Y. Xia, and N. H. Chen, "Fractalkine/CX3CR1 is involved in the cross-talk between neuron and glia in neurological diseases," *Brain Research Bulletin*, vol. 146, pp. 12–21, 2019.
- [24] K. Hatori, A. Nagai, R. Heisel, J. K. Ryu, and S. U. Kim, "Fractalkine and fractalkine receptors in human neurons and glial cells," *Journal of Neuroscience Research*, vol. 69, no. 3, pp. 418–426, 2002.
- [25] D. J. Finneran and K. R. Nash, "Neuroinflammation and fractalkine signaling in Alzheimer's disease," *Journal of Neuroinflammation*, vol. 16, no. 1, pp. 1–8, 2019.
- [26] E. Pandur, K. Tamási, R. Pap, E. Varga, A. Miseta, and K. Sipos, "Fractalkine induces hepcidin expression of BV-2 microglia and causes iron accumulation in SH-SY5Y cells," *Cellular and Molecular Neurobiology*, vol. 39, no. 7, pp. 985–1001, 2019.

- [27] K. J. Garton, P. J. Gough, C. P. Blobel et al., "Tumor necrosis factor- α -converting enzyme (ADAM17) mediates the cleavage and shedding of fractalkine (CX3CL1)," *Journal of Biological Chemistry*, vol. 276, no. 41, pp. 37993–38001, 2001.
- [28] C. Hundhausen, D. Misztela, T. A. Berkhout et al., "The disintegrin-like metalloproteinase ADAM10 is involved in constitutive cleavage of CX3CL1 (fractalkine) and regulates CX3CL1-mediated cell-cell adhesion," *Blood*, vol. 102, no. 4, pp. 1186–1195, 2003.
- [29] M. Xu, H. Huang, X. Mo et al., "Quercetin-3-O-glucuronide alleviates cognitive deficit and toxicity in A β 1-42-induced ad-like mice and SH-SY5Y cells," *Molecular Nutrition & Food Research*, vol. 65, no. 6, article e2000660, 2021.
- [30] J. Hugo and M. Ganguli, "Dementia and cognitive impairment: epidemiology, diagnosis, and treatment," *Clinics in Geriatric Medicine*, vol. 30, no. 3, pp. 421–442, 2014.
- [31] T. Imai, K. Hieshima, C. Haskell et al., "Identification and molecular characterization of fractalkine receptor CX₃CR1, which mediates both leukocyte migration and adhesion," *Cell*, vol. 91, no. 4, pp. 521–530, 1997.
- [32] J. M. Morganti, K. R. Nash, B. A. Grimmig et al., "The soluble isoform of CX3CL1 is necessary for neuroprotection in a mouse model of Parkinson's disease," *Journal of Neuroscience*, vol. 32, no. 42, pp. 14592–14601, 2012.
- [33] M. A. Ostuni, J. Guellec, P. Hermand et al., "CX3CL1, a chemokine finely tuned to adhesion: critical roles of the stalk glycosylation and the membrane domain," *Biology open*, vol. 3, no. 12, pp. 1173–1182, 2014.
- [34] K. R. Nash, P. Moran, D. J. Finneran et al., "Fractalkine over expression suppresses α -synuclein-mediated neurodegeneration," *Molecular Therapy*, vol. 23, no. 1, pp. 17–23, 2015.
- [35] K. Baghaei, P. Varjavand, A. Malmir et al., "Mesenchymal stem cells foster Ly-6C low macrophages polarization through the CX3CL1 pathway to ameliorate liver fibrosis," *Cytotherapy*, vol. 22, no. 5, p. S67, 2020.
- [36] J. R. Perea, A. Lleó, D. Alcolea, J. Fortea, J. Ávila, and M. Bolós, "Decreased CX3CL1 levels in the cerebrospinal fluid of patients with Alzheimer's disease," *Frontiers in Neuroscience*, vol. 12, p. 609, 2018.
- [37] M. Honczarenko, Y. Le, M. Swierkowski, I. Ghiran, A. M. Glodek, and L. E. Silberstein, "Human bone marrow stromal cells express a distinct set of biologically functional chemokine receptors," *Stem Cells*, vol. 24, no. 4, pp. 1030–1041, 2006.
- [38] M. Asadi, S. Taghizadeh, E. Kaviani et al., "Caspase-3: structure, function, and biotechnological aspects," *Biotechnology and Applied Biochemistry*, 2021.
- [39] M. Goedert, "Tau protein and the neurofibrillary pathology of Alzheimer's disease," *Annals of the New York Academy of Sciences*, vol. 777, no. 1, pp. 121–131, 1996.
- [40] D. M. Holtzman, E. Mandelkow, and D. J. Selkoe, "Alzheimer disease in 2020," *Cold Spring Harbor Perspectives in Medicine*, vol. 2, no. 11, article a011585, 2012.
- [41] C. Qin, Y. Lu, K. Wang et al., "Transplantation of bone marrow mesenchymal stem cells improves cognitive deficits and alleviates neuropathology in animal models of Alzheimer's disease: a meta-analytic review on potential mechanisms," *Translational Neurodegeneration*, vol. 9, no. 1, pp. 1–20, 2020.
- [42] S. A. Kent, T. L. Spire-Jones, and C. S. Durrant, "The physiological roles of tau and $\alpha\beta$: implications for Alzheimer's disease pathology and therapeutics," *Acta Neuropathologica*, vol. 140, no. 4, pp. 417–447, 2020.
- [43] A. Ardura-Fabregat, E. Boddeke, A. Boza-Serrano et al., "Targeting neuroinflammation to treat Alzheimer's disease," *CNS Drugs*, vol. 31, no. 12, pp. 1057–1082, 2017.
- [44] S. Sánchez-Sarasúa, I. Fernández-Pérez, V. Espinosa-Fernández, A. M. Sánchez-Pérez, and J. C. Ledesma, "Can we treat neuroinflammation in Alzheimer's disease?," *International Journal of Molecular Sciences*, vol. 21, no. 22, p. 8751, 2020.
- [45] L. Hamelin, J. Lagarde, G. Dorothée et al., "Distinct dynamic profiles of microglial activation are associated with progression of Alzheimer's disease," *Brain*, vol. 141, no. 6, pp. 1855–1870, 2018.
- [46] F. Regen, J. Hellmann-Regen, E. Costantini, and M. Reale, "Neuroinflammation and Alzheimer's disease: implications for microglial activation," *Current Alzheimer Research*, vol. 14, no. 11, pp. 1140–1148, 2017.
- [47] Y. Compta and T. Revesz, "Neuropathological and biomarker findings in Parkinson's disease and Alzheimer's disease: from protein aggregates to synaptic dysfunction," *Journal of Parkinson's Disease*, vol. 11, no. 1, pp. 107–121, 2021.
- [48] J. S. Rao, M. Kellom, H.-W. Kim, S. I. Rapoport, and E. A. Reese, "Neuroinflammation and synaptic loss," *Neurochemical Research*, vol. 37, no. 5, pp. 903–910, 2012.
- [49] A. Patenaude, M. Murthy, and M.-E. Mirault, "Emerging roles of thioredoxin cycle enzymes in the central nervous system," *Cellular and Molecular Life Sciences CMLS*, vol. 62, no. 10, p. 1063–1080, 2005.
- [50] M. A. Lovell, C. Xie, S. P. Gabbita, and W. R. Markesbery, "Decreased thioredoxin and increased thioredoxin reductase levels in Alzheimer's disease brain," *Free Radical Biology and Medicine*, vol. 28, no. 3, pp. 418–427, 2000.
- [51] E. Junn, S. H. Han, J. Y. Im et al., "Vitamin D3 up-regulated protein 1 mediates oxidative stress via suppressing the thioredoxin function," *The Journal of Immunology*, vol. 164, no. 12, pp. 6287–6295, 2000.
- [52] H. Oakley, S. L. Cole, S. Logan et al., "Intraneuronal beta-amyloid aggregates, neurodegeneration, and neuron loss in transgenic mice with five familial Alzheimer's disease mutations: potential factors in amyloid plaque formation," *Journal of Neuroscience*, vol. 26, no. 40, pp. 10129–10140, 2006.
- [53] R. Zhou, A. Tardivel, B. Thorens, I. Choi, and J. Tschoopp, "Thioredoxin-interacting protein links oxidative stress to inflammasome activation," *Nature Immunology*, vol. 11, no. 2, pp. 136–140, 2010.
- [54] C.-Y. Wang, Y. Xu, X. Wang, C. Guo, T. Wang, and Z.-Y. Wang, "Dl-3-n-butylphthalide inhibits nlrp3 inflammasome and mitigates Alzheimer's-like pathology via Nrf2-TXNIP-Trx axis," *Antioxidants & Redox Signaling*, vol. 30, no. 11, pp. 1411–1431, 2019.
- [55] S. Lee, G. Xu, T. R. Jay et al., "Opposing effects of membrane-anchored CX3CL1 on amyloid and tau pathologies via the p38 MAPK pathway," *Journal of Neuroscience*, vol. 34, no. 37, pp. 12538–12546, 2014.
- [56] A. Li, J. Zhao, C. Fan et al., "Delivery of exogenous proteins by mesenchymal stem cells attenuates early memory deficits in a murine model of Alzheimer's disease," *Neurobiology of Aging*, vol. 86, pp. 81–91, 2020.
- [57] S. Strobel, E. Grünblatt, P. Riederer et al., "Changes in the expression of genes related to neuroinflammation over the

Research Article

The Effect of PD-1 Inhibitor Combined with Chemotherapy on the Level of Peripheral Blood T Lymphocytes among Patients with Non-Small-Cell Lung Cancer and Its Relationship with Prognosis

Yun Zhao,¹ Jianbo He,¹ Shaozhang Zhou,¹ Ruiling Ning,¹ Wenhua Zhao,¹ Huilin Wang,¹ Cuiyun Su,¹ Wei Jiang,¹ Xiaoning Zhong^{1,2} , and Qitao Yu¹ 

¹Department of Respiratory Oncology, Guangxi Medical University Affiliated Tumor Hospital, Nanning, 530021 Guangxi, China
²Pulmonary and Critical Care Medicine, The First Affiliated Hospital of Guangxi Medical University, Nanning, 530021 Guangxi, China

Correspondence should be addressed to Xiaoning Zhong; zhongxiaoning1203@163.com and Qitao Yu; yqt178@163.com

Received 9 June 2022; Revised 14 July 2022; Accepted 21 July 2022; Published 7 September 2022

Academic Editor: Pan Zheng

Copyright © 2022 Yun Zhao et al. This is an open access article distributed under the Creative Commons Attribution License, which permits unrestricted use, distribution, and reproduction in any medium, provided the original work is properly cited.

Objective. To explore the effect of combined treatment of PD-1 inhibitor and chemotherapy on the level of peripheral blood T lymphocytes in non-small-cell lung cancer (NSCLC) patients and its relationship with prognosis. **Methods.** Retrospective analysis was conducted on 150 NSCLC patients treated in Guangxi Medical University Affiliated Tumor Hospital from June 2018 to September 2020, including 77 patients treated with PD-1 inhibitor combined with chemotherapy as the observation group (OG) and 73 patients with chemotherapy alone as the control group (CG). Therapeutic efficacy, immune function indexes, serum tumor markers, incidence of adverse reactions during hospitalization, 1-year survival rate, and life quality after 6 months of treatment were observed and compared between two groups. **Results.** Compared to the CG, the therapeutic effect of OG was evidently better. Six months after treatment, levels of CD4⁺/CD8⁺, NK cells, and CD4⁺ in two groups were elevated markedly, and indexes of OG were notably and comparatively higher than those in the other group. After treatment, OG was observed with a marked decline regarding levels of CYFRA21-1, CEA, and CA125 compared to those in the CG; and there was no notable difference in terms of adverse reaction occurrence between two groups, but the 1-year survival rate and 6-month life quality in OG over ranked those in CG. **Conclusion.** For NSCLC patients, the PD-1 inhibitor given on the basis of chemotherapy can further improve the clinical efficacy and improve immune function and long-term survival rate of patients on the premise of ensuring the safety of treatment, which is worth promoting in clinical practice.

1. Introduction

Lung cancer is one of the most common respiratory system malignant diseases with the number of new cases increasing at a rate of 3% every year, which seriously affects the health of patients [1]. It can be classified into non-small-cell lung cancer (NSCLC) and small-cell lung cancer, and the former takes up more than 80% of all cases with a deadly high mortality rate [2]. The early stage of NSCLC is usually asymptomatic, so 70% to 80% of patients are found to be in an advanced stage at the time of diagnosis [3]. Although early stage patients can be effectively treated with radical surgery combined with drugs, for patients at middle and advanced

stage, the best treatment is chemotherapy, which alleviates the disease to a certain extent, improves the life quality, and prolongs life span of patients [4]. Platinum-based chemotherapy has long been the first-line standard treatment for advanced NSCLC patients, but it would inevitably lead to high adverse reaction rate which some patients cannot tolerate, accompanying features of unsatisfactory overall response rate and survival period [5]. Hence, it is urgent and substantial to find a treatment plan with better efficacy and less side effects for NSCLC patients.

In recent years, drugs for tumor-specific immune checkpoint inhibitors have shown great potential. Programmed death-1 (PD-1), one of the cosuppressive molecules of

immune cells, can regulate immune system and upgrade self-tolerance by bringing down response of the immune system to human cells and by inhibiting T cell-mediated inflammatory activities [6]. And PD-1 prevents autoimmune diseases and also hinders the immune system from killing cancer cells, making it a novel treatment for advanced NSCLC [7]. However, some studies suggested that the response rate of PD-1 inhibitors alone was only 20% to 40%, from which most patients do not benefit. The changes of natural killer (NK) cells, T lymphocyte subsets, and inhibitory immune checkpoints in patients before and after PD-1 inhibitor treatment require further studies [8].

In the 2021 Chinese Society of Clinical Oncology (CSCO) guidelines, the PD-1 inhibitor combined with chemotherapy is the first-line class IA recommended treatment for patients with NSCLC; however, there are differences in response rates among patients treated with immune checkpoint inhibitors. Therefore, we conducted a related study on the response rate of NSCLC patients treated with inhibitors, as well as the changes in lung function and T lymphocyte subsets in patients before and after treatment. In this study, we included 150 NSCLC patients treated in our hospital from June 2018 to September 2020 and analyzed the efficacy of PD-1 inhibitor combined with chemotherapy in treating NSCLC, hopefully to provide more clinical treatment options for NSCLC patients.

2. Materials and Methods

2.1. Clinical Information. A retrospective analysis of 150 patients with NSCLC admitted to Guangxi Medical University Affiliated Tumor Hospital from June 2018 to September 2020 includes 82 male and 68 female patients. 77 patients treated with the PD-1 inhibitor combined with chemotherapy served as the observation group (OG), and 73 patients who received chemotherapy alone served as the control group (CG). The following are the inclusion criteria: (1) in line with the NSCLC diagnostic criteria established by the World Health Organization (WHO) via imaging and pathological examinations, (2) patients diagnosed with TNM stage IIIB or IV, and (3) patients with complete case data preservation. The following are the exclusion criteria: (1) patients who have received immunomodulatory therapy, (2) patients with mental illness or disturbance of consciousness, (3) patients with loss of language, cognition, and other functions and inability to communicate, (4) patients with other major physical diseases, (5) patients who have received chemotherapy and radiation therapy before surgery, (6) patients with a survival period of less than 6 months, (7) patients with abnormal liver and kidney function, (8) lactating and pregnant women, and (9) patients with another primary malignancy. This experiment has gained approval from the hospital ethics committee and complies with Helsinki Declaration, with all patients signing written informed consent concerned and their agreement for participation.

2.2. Treatment Methods. In the CG group, patients with non-squamous NSCLC were given carboplatin area under curve 5 and pemetrexed 500 mg/m² in a 3-week cycle for up to six

cycles, followed by pemetrexed maintenance, whereas squamous NSCLC were given gemcitabine 1000 mg/m² at days 1 and 8 and cisplatin 75 mg/m² or carboplatin area under curve 5 in a 3-week cycle for up to six cycles, followed by gemcitabine maintenance. On the basis of CG, OG patients were given PD-1 inhibitors by intravenous drip with the treatment of 6 cycles (21 days a cycle). If patients were to experience discomfort and adverse reactions, it should be reported to the superior physician in time with corresponding treatment measures taken.

2.3. Observation Indexes. The following are the observation indexes:

- (1) Therapeutic effect in two groups was assessed and compared according to RECIST evaluation criteria for solid tumors [9]. It is divided into complete response (CR): complete disappearance of lesions was maintained for no less than 4 weeks; partial remission (PR): the sum of tumor lesion radius was reduced by more than 30% and it can be maintained over and above 4 weeks; stable disease (SD): the sum of tumor lesion radii cannot reach PR nor PD; progressive disease (PD): the sum of tumor lesion radii rises by at least 20%, or additional lesions occur; total effective rate = (CR cases + PR cases)/total cases × 100%
- (2) Immune function indexes were compared between two groups: within 24 hours of admission and after 6 months of treatment, the venous blood was drawn in the morning, and the supernatant was collected at completion of centrifugation and then anticoagulated with EDTA. Later, CD3⁺, CD4⁺, CD8⁺, and CD56 (NK cells) were added to the flow tube to label the cloned monomers, and the serum was added and mixed and then with hemolysin and placed in the dark for 20 minutes. The levels of NK cells, CD4⁺/CD8⁺, and CD3⁺ were detected with a flow cytometer (BD Company, US)
- (3) Serum tumor markers CYFRA21-1, cytokeratin 19 fragment antigen21-1, carcinoembryonic antigen (CEA), and carbohydrate antigen 125 (CA125) before and after treatment were assessed and compared between two groups. Specifically, a patient's venous blood was taken in the morning, centrifuged at 3000 r/min for 15 min, and levels of CA125, CEA, and CYFRA21-1 were detected by electrochemiluminescence with E170 system produced by Roche Company, Switzerland
- (4) Occurrence of adverse reactions of two groups during hospitalization was compared, including rash, fever, fatigue, and gastrointestinal symptoms
- (5) Tumor-free survival rate and 1-year survival rate of two groups were compared. All patients were followed up regularly by returning to the hospital for reexamination, telephone follow-up, text message

TABLE 1: Comparison of general information [n (%)].

Factors	Observation group ($n = 77$)	Control group ($n = 73$)	t/χ^2	P
Gender			0.024	0.877
Male	40 (51.95)	37 (50.68)		
Female	37 (48.05)	36 (49.32)		
Age (years)			0.110	0.701
≤ 61	38 (49.35)	38 (52.05)		
> 61	39 (50.65)	35 (47.95)		
BMI (kg/m^2)			0.036	0.849
≤ 23	41 (53.25)	40 (54.79)		
> 23	36 (46.75)	33 (45.21)		
History of smoking			0.019	0.891
Yes	42 (54.55)	39 (53.42)		
No	35 (45.45)	34 (46.58)		
Clinical stage			0.001	0.983
Stage IIIB	36 (46.75)	34 (46.58)		
Stage IV	41 (53.25)	39 (53.42)		
Pathological type			0.057	0.972
Squamous cell carcinoma	21 (27.27)	19 (26.03)		
Adenocarcinoma	46 (59.74)	45 (61.64)		
Others	10 (12.99)	9 (12.33)		
Tumor location			0.036	0.849
Left lung	41 (53.25)	40 (54.79)		
Right lung	36 (46.75)	33 (45.21)		

TABLE 2: Comparison of therapeutic efficacy [n (%)].

Therapeutic effect	Observation group ($n = 77$)	Control group ($n = 73$)	χ^2	P
Complete remission	0	0	—	—
Partial remission	41 (53.25)	26 (35.62)	—	—
Stable disease	29 (37.66)	20 (27.40)	—	—
Disease progression	7 (9.09)	27 (36.99)	—	—
Total effective rate	41 (53.25)	26 (35.62)	9.499	0.002

follow-up, and door-to-door follow-up. The deadline was the death of the patient or March 31, 2022

- (6) QLQ-C30 quality of life scale [10] was utilized to evaluate a patient's life quality after 6 months of treatment, which includes 5 items of physical, social, emotional, role, and cognitive function. A higher score indicates better quality of life

2.4. Statistical Methods. SPSS18.0 (IBM) was used for data analysis, GraphPad Prism 8 (GraphPad Software) for figures attached, log-rank analysis for survival analysis, and Kaplan-Meier for survival curve. A chi-square test was applied for the analysis of enumeration data, and Student's t -test was

for comparison of measurement data. And $P < 0.05$ was taken to be statistically different.

3. Results

3.1. General Information Comparison. No marked differences were observed regarding gender, age, and smoking history between two groups, and subjects were comparable ($P > 0.05$, Table 1).

3.2. Comparison of Therapeutic Efficacy. The numbers of patients assessed with CR, PR, SD, and DP in OG were 0, 41, 29, and 7, respectively. And corresponding data in CG were 0, 26, 20, and 27, respectively. Statistically, OG held a strikingly higher total effective rate of treatment than that in CG ($P < 0.05$, 53.25% vs. 35.62%, Table 2).

3.3. Comparison of Immune Function Indexes. Before treatment, no marked difference was observed in levels of $\text{CD4}^+/\text{CD8}^+$, CD8^+ , CD4^+ , and NK cells between two groups ($P > 0.05$), while six months after treatment, despite CD8^+ having few fluctuations, levels of $\text{CD4}^+/\text{CD8}^+$, CD8^+ , CD4^+ , and NK cells were upregulated evidently ($P < 0.05$), and the increase in OG was markedly higher than those in OG ($P < 0.05$, Figure 1).

3.4. Comparison of Serum Tumor Markers before and after Treatment between Two Groups. Before treatment, no evident difference was observed regarding serum tumor marker levels between two groups ($P > 0.05$), while levels of

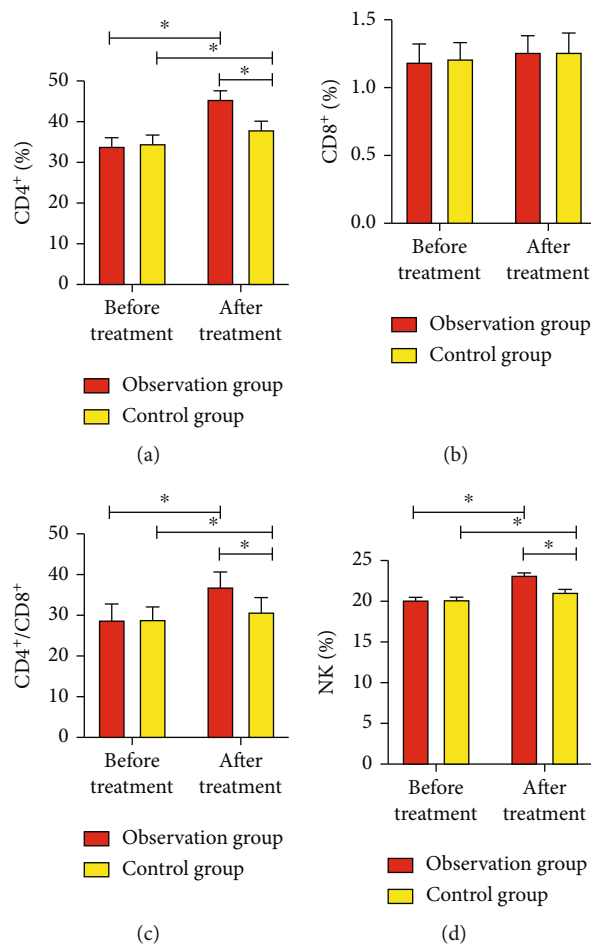


FIGURE 1: Comparison of immune function indicators between two groups; (a) comparison of CD4⁺ between two groups before and after treatment; (b) comparison of CD8⁺ between two groups before and after treatment; (c) comparison of CD4⁺/CD8⁺ between two groups before and after treatment; (d) comparison of NK cells between two groups before and after treatment. When comparing between groups or before and after treatment within a group, * indicates $P < 0.05$.

CYFRA21-1, CEA, and CA125 of both groups were down-regulated after treatment. In addition, indicators in OG were markedly lower than those in CG ($P < 0.05$, Figure 2).

3.5. Comparison of the Incidence of Adverse Reactions. The number of patients in OG who developed rash, fever, fatigue, and gastrointestinal symptoms was 3, 3, 4, and 5, respectively. Those in CG were 4, 4, 3, and 3, respectively, showing no marked difference in terms of incidence of adverse reactions when compared with that of OG ($P > 0.05$, 19.48% vs. 19.18%, Table 3). The adverse reactions of patients were treated symptomatically during the treatment and were effectively alleviated afterwards.

3.6. Comparison of 1-Year Survival Rate. The overall survival curve analysis indicated that OG patients possessed a markedly higher 1-year overall survival rate than OG (68.83% (53/77) vs. 49.32% (36/73)) ($P < 0.05$, Figure 3).

3.7. Comparison of Life Quality 6 Months Posttreatment. Compared with CG, the scores of physical, role, emotion,

cognition, and social dimensions of life quality in OG were markedly improved after treatment ($P < 0.05$, Table 4).

4. Discussion

With changes in social environment and life pressure, the incidence of lung cancer is getting higher and younger [11]. In recent years, chemotherapy has gradually become an important method for the treatment of NSCLC and has achieved good therapeutic effects. However, some patients have to forgo treatment due to multiple adverse reactions of chemotherapy [12]. Therefore, finding new treatment options is of great clinical significance. With the continuous development of molecular biology techniques, a growing number of molecular biological targets are being used in the treatment of NSCLC and have been proved to have positive therapeutic effects. PD-1, an important immunosuppressive molecule and a member of the immunoglobulin superfamily, which is one of those targets [13]. Studies have found that immunomodulation targeting PD-1 was of great significance in fighting infections, autoimmune diseases,

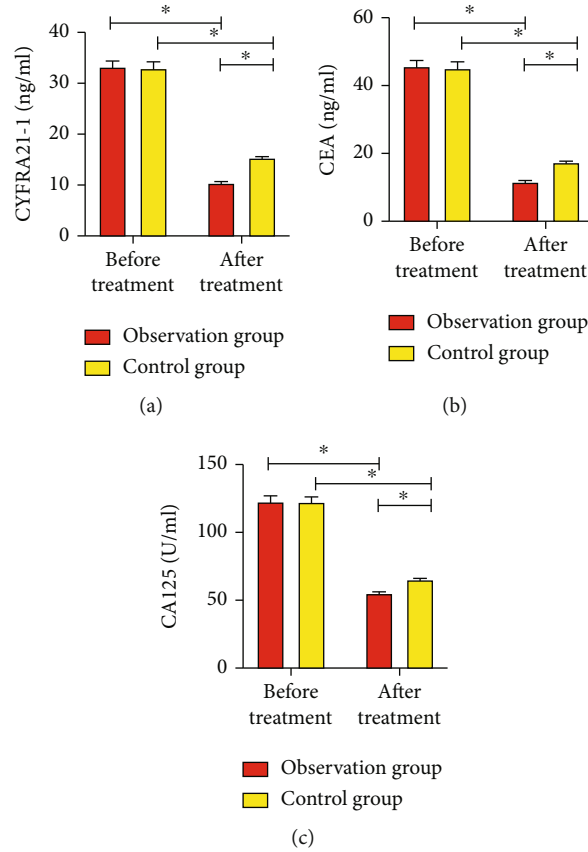


FIGURE 2: Comparison of serum tumor markers in two groups before and after treatment; (a) comparison of CYFRA21-1 between two groups before and after treatment; (b) comparison of CEA between two groups before and after treatment; (c) comparison of CA125 between two groups before and after treatment. * indicates $P < 0.05$.

TABLE 3: Comparison of incidence of adverse reactions [n (%)].

Complications	Observation group ($n = 77$)	Control group ($n = 73$)	χ^2	P
Rash	3 (3.90)	4 (5.48)	—	—
Fever	3 (3.90)	4 (5.48)	—	—
Fatigue	4 (5.19)	3 (4.11)	—	—
Gastrointestinal symptoms	5 (6.49)	3 (4.11)	—	—
Incidence of adverse reactions	15 (19.48)	14 (19.18)	0.002	0.963

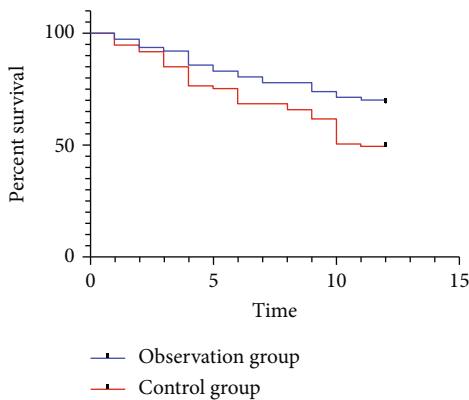


FIGURE 3: Comparison of 1-year survival rate; * indicates $P < 0.05$.

and tumors, as well as promoting the survival of transplanted organs [14]. Although the efficacy of PD-1 has been affirmed in the past, few studies have focused on the comprehensive impact of PD-1 combined with chemotherapy on NSCLC patients.

In this study, we first observed that OG patients possessed much higher total effective rate than that in CG, indicating that combined treatment of PD-1 inhibitor and chemotherapy performed better regarding short-term efficacy in the treatment of NSCLC patients. Clinically, changes of NK cells and T lymphocyte subsets are used as indicators of immune status and prognosis in NSCLC patients. $CD4^+$ is mainly a helper T lymphocyte that can promote the antitumor effect of effector cells, and $CD8^+$ is an inhibitory T lymphocyte. The two generally maintain a balanced state [15]. A study [16] has shown that the proportion of immune subsets

TABLE 4: Comparison of quality of life.

Factors	Observation group ($n = 77$)	Control group ($n = 73$)	t	P
Physical function	72.74 ± 2.75	61.91 ± 1.15	31.16	<0.001
Role function	71.12 ± 2.39	62.44 ± 1.44	26.76	<0.001
Emotional function	72.42 ± 2.3	62.09 ± 1.36	33.25	<0.001
Cognition function	72.03 ± 2.26	62.18 ± 1.24	32.84	<0.001
Social function	72.04 ± 2.21	62.4 ± 1.43	31.53	<0.001

of peripheral blood lymphocytes in lung cancer patients was abnormal, which suggested that the immune function of patients was unbalanced. However, the increase of CD8⁺ cells was the basis of cellular immune damage, and the decline of CD4⁺ cells could cause immune escape of tumor cells [17]. Results of present study suggested that CD4⁺, CD4⁺/CD8⁺, and NK cells in both groups went markedly higher after treatment, and it was notable that OG held much vivid improvement on these indicators when compared to CG, indicating that the PD-1 inhibitor combined with chemotherapy could more effectively improve the immune function of NSCLC patients than chemotherapy alone. A former study [18] found that the proportion of immune subsets of peripheral blood lymphocytes may be abnormal in NSCLC patients, of whom the peripheral blood CD8⁺ cells increased, CD4⁺ cells decreased, CD4⁺/CD8⁺ decreased, and tumor cells occurred immune escape. When the tumor burden was relieved, the abnormal lymphocyte subsets could gradually recover, which is similar to our observations. The reason for the enhanced immune function of patients in our study may also be that the PD-1 inhibitor relieving the inhibitory effect of immune checkpoints activated T lymphocytes with killing effect, thereby enhancing the immune ability and antitumor ability of the body. In addition, a study [19] showed that in the course of NSCLC, the apoptosis of tumor-specific T cells was mediated by PD-1-dependent and independent mechanisms, and the PD-1-dependent mechanism could promote the immune escape of tumor cells in NSCLC patients. This could also explain our observations.

Serum tumor markers CYFRA21-1, CEA, and CA125 are closely related to the disease progression and prognosis of NSCLC, and elevated levels of tumor markers indicate poor prognosis and short survival time. CYFRA21-1 is the most valuable serum tumor marker for NSCLC detection, a soluble acidic protein of cytokeratin detected by monoclonal antibody, and is mainly distributed in the cancerous breast and lung epithelium and released into the blood, which is of essential clinical value in judging the efficacy of NSCLC [20, 21]. CEA is a class of acidic glycoproteins located in hollow organs such as the respiratory tract and digestive tract and consists of sugar chains and peptide chains. It exists in macrophages, monocytes, and multinucleated cells, has

human embryonic epitopes, and is specific for tumor-associated antigens that are associated with tumor recurrence [22]. CA125 is a class of tumor carbohydrate antigens with high concentrations in malignant tissues and tumor cells and can be released into the blood when tumor tissues are destroyed, which is of great value in the diagnosis and prognosis of NSCLC [23]. Results of our study showed that CYFRA21-1, CEA, and CA125 in both groups all declined after treatment, and the decrease in OG was even marked, suggesting that the PD-1 inhibitor combined with chemotherapy in NSCLC treatment could better and effectively alleviate the disease than that of chemotherapy alone. In addition, long-term prognosis results of two groups showed that the 1-year overall survival rate in OG was notably higher than that in CG. This is also in line with our previous conclusion that “PD-1 inhibitor combined with chemotherapy in the treatment of NSCLC could be more effective than chemotherapy alone.” This result also showed that PD-1 did not markedly increase the related adverse reactions in patients receiving chemotherapy, suggesting that PD-1 inhibitors were generally well tolerated in NSCLC patients. Finally, we compared the life quality between two groups after treatment, and the results showed that OG patients rated a more satisfactory quality of life.

5. Conclusion

To sum up, for NSCLC patients, the PD-1 inhibitor on the basis of chemotherapy could further improve the clinical efficacy, as well as the immune function and long-term survival rate of patients on the premise of ensuring the safety of treatment, which is worthy of promotion in clinical practice. However, this study still has certain shortcomings, such as a dearth of detection of PD-L1 expression status and relevant information on the basic lung status of the patient, which may have a certain impact on the results of lung function. Due to the small sample size and limited observation time, more rigorous large-sample clinical trials are still needed in follow-up studies.

Data Availability

The labeled dataset used to support the findings of this study is available from the corresponding authors upon request.

Conflicts of Interest

The authors declare no competing interests.

Authors' Contributions

Yun Zhao and Jianbo He contributed equally to this work and are co-first authors.

References

- [1] S. Jonna and D. S. Subramaniam, “Molecular diagnostics and targeted therapies in non-small cell lung cancer (NSCLC): an update,” *Discovery Medicine*, vol. 27, no. 148, pp. 167–170, 2019.

- [2] N. Guibert, A. Pradines, G. Favre, and J. Mazieres, "Current and future applications of liquid biopsy in nonsmall cell lung cancer from early to advanced stages," *European Respiratory Review*, vol. 29, no. 155, article 190052, 2020.
- [3] T. Mitsudomi and J. Soh, "Adjuvant therapy of operable non-small cell lung cancer: an update," *Current Opinion in Oncology*, vol. 33, no. 1, pp. 47–54, 2021.
- [4] J. P. Sculier, "Non-small cell lung cancer," *European Respiratory Review*, vol. 22, no. 127, pp. 33–36, 2013.
- [5] H. Borghaei, S. Gettinger, E. E. Vokes et al., "Five-year outcomes from the randomized, phase III trials CheckMate 017 and 057: nivolumab versus docetaxel in previously treated non-small-cell lung cancer," *Journal of Clinical Oncology*, vol. 39, no. 7, pp. 723–733, 2021.
- [6] N. A. Rizvi, M. D. Hellmann, A. Snyder et al., "Mutational landscape determines sensitivity to PD-1 blockade in non-small cell lung cancer," *Science*, vol. 348, no. 6230, pp. 124–128, 2015.
- [7] M. Y. Huang, X. M. Jiang, B. L. Wang, Y. Sun, and J. J. Lu, "Combination therapy with PD-1/PD-L1 blockade in non-small cell lung cancer: strategies and mechanisms," *Pharmacology & Therapeutics*, vol. 219, article 107694, 2021.
- [8] Y. Zhang, H. Zhou, and L. Zhang, "Which is the optimal immunotherapy for advanced squamous non-small-cell lung cancer in combination with chemotherapy: anti-PD-1 or anti-PD-L1?," *Journal For Immunotherapy Of Cancer*, vol. 6, no. 1, p. 135, 2018.
- [9] S. P. L. Saw, B. H. Ong, K. L. M. Chua, A. Takano, and D. S. W. Tan, "Revisiting neoadjuvant therapy in non-small-cell lung cancer," *The Lancet Oncology*, vol. 22, no. 11, pp. e501–e516, 2021.
- [10] M. Messaggi-Sartor, E. Marco, E. Martínez-Téllez et al., "Combined aerobic exercise and high-intensity respiratory muscle training in patients surgically treated for non-small cell lung cancer: a pilot randomized clinical trial," *European Journal of Physical and Rehabilitation Medicine*, vol. 55, no. 1, pp. 113–122, 2019.
- [11] R. Pirker, "Chemotherapy remains a cornerstone in the treatment of nonsmall cell lung cancer," *Current Opinion in Oncology*, vol. 32, no. 1, pp. 63–67, 2020.
- [12] N. A. Rizvi, M. D. Hellmann, A. Snyder et al., "Cancer immunology. Mutational landscape determines sensitivity to PD-1 blockade in non-small cell lung cancer," *Science*, vol. 348, no. 6230, pp. 124–128, 2015.
- [13] N. Tsoukalas, M. Kiakou, K. Tsapakidis et al., "PD-1 and PD-L1 as immunotherapy targets and biomarkers in non-small cell lung cancer," *Journal of BUON*, vol. 24, no. 3, pp. 883–888, 2019.
- [14] J. F. Gainor, A. T. Shaw, L. V. Sequist et al., "EGFR mutations and ALK rearrangements are associated with low response rates to PD-1 pathway blockade in non-small cell lung cancer: a retrospective analysis," *Clinical Cancer Research*, vol. 22, no. 18, pp. 4585–4593, 2016.
- [15] E. Sugiyama, Y. Togashi, Y. Takeuchi et al., "Blockade of EGFR improves responsiveness to PD-1 blockade in EGFR-mutated non-small cell lung cancer," *Science Immunology*, vol. 5, no. 43, p. eaav3937, 2020.
- [16] Y. K. Chae, S. Chang, T. Ko et al., "Epithelial-mesenchymal transition (EMT) signature is inversely associated with T-cell infiltration in non-small cell lung cancer (NSCLC)," *Scientific Reports*, vol. 8, no. 1, p. 2918, 2018.
- [17] W. Dai, J. Feng, X. Hu et al., "SLC7A7 is a prognostic biomarker correlated with immune infiltrates in non-small cell lung cancer," *Cancer Cell International*, vol. 21, no. 1, p. 106, 2021.
- [18] C. Hinterleitner, J. Strähle, E. Malenke et al., "Platelet PD-L1 reflects collective intratumoral PD-L1 expression and predicts immunotherapy response in non-small cell lung cancer," *Nature Communications*, vol. 12, no. 1, p. 7005, 2021.
- [19] A. Prat, A. Navarro, L. Paré et al., "Immune-related gene expression profiling after PD-1 blockade in non-small cell lung carcinoma, head and neck squamous cell carcinoma, and melanoma," *Cancer Research*, vol. 77, no. 13, pp. 3540–3550, 2017.
- [20] M. G. Dal Bello, R. A. Filiberti, A. Alama et al., "The role of CEA, CYFRA21-1 and NSE in monitoring tumor response to Nivolumab in advanced non-small cell lung cancer (NSCLC) patients," *Journal of Translational Medicine*, vol. 17, no. 1, 2019.
- [21] L. Fu, R. Wang, L. Yin, X. Shang, R. Zhang, and P. Zhang, "CYFRA21-1 tests in the diagnosis of non-small cell lung cancer: a meta-analysis," *The International Journal of Biological Markers*, vol. 34, no. 3, pp. 251–261, 2019.
- [22] A. Mishra, N. Singh, H. Shyam et al., "Differential expression profiling of transcripts of *IDH1*, *CEA*, *Cyfra21-1*, and *TPA* in stage IIIa non-small cell lung cancer (NSCLC) of smokers and non-smokers cases with air quality index," *Gene*, vol. 766, no. 766, article 145151, 2021.
- [23] M. R. Clevers, E. A. Kastelij, B. J. M. Peters, H. Kelder, and F. M. N. H. Schramel, "Evaluation of serum biomarker CEA and Ca-125 as immunotherapy response predictors in metastatic non-small cell lung cancer," *Anticancer Research*, vol. 41, no. 2, pp. 869–876, 2021.

Retraction

Retracted: Clinical Study of Anti-PD-1 Immunotherapy Combined with Gemcitabine Chemotherapy in Multiline Treatment of Advanced Pancreatic Cancer

Computational and Mathematical Methods in Medicine

Received 27 June 2023; Accepted 27 June 2023; Published 28 June 2023

Copyright © 2023 Computational and Mathematical Methods in Medicine. This is an open access article distributed under the Creative Commons Attribution License, which permits unrestricted use, distribution, and reproduction in any medium, provided the original work is properly cited.

This article has been retracted by Hindawi following an investigation undertaken by the publisher [1]. This investigation has uncovered evidence of one or more of the following indicators of systematic manipulation of the publication process:

- (1) Discrepancies in scope
- (2) Discrepancies in the description of the research reported
- (3) Discrepancies between the availability of data and the research described
- (4) Inappropriate citations
- (5) Incoherent, meaningless and/or irrelevant content included in the article
- (6) Peer-review manipulation

The presence of these indicators undermines our confidence in the integrity of the article's content and we cannot, therefore, vouch for its reliability. Please note that this notice is intended solely to alert readers that the content of this article is unreliable. We have not investigated whether authors were aware of or involved in the systematic manipulation of the publication process.

In addition, our investigation has also shown that one or more of the following human-subject reporting requirements has not been met in this article: ethical approval by an Institutional Review Board (IRB) committee or equivalent, patient/participant consent to participate, and/or agreement to publish patient/participant details (where relevant).

Wiley and Hindawi regrets that the usual quality checks did not identify these issues before publication and have since put additional measures in place to safeguard research integrity.

We wish to credit our own Research Integrity and Research Publishing teams and anonymous and named external researchers and research integrity experts for contributing to this investigation.

The corresponding author, as the representative of all authors, has been given the opportunity to register their agreement or disagreement to this retraction. We have kept a record of any response received.

References

- [1] Y. Liu, Y. Li, S. Du, L. Fan, and J. Wang, "Clinical Study of Anti-PD-1 Immunotherapy Combined with Gemcitabine Chemotherapy in Multiline Treatment of Advanced Pancreatic Cancer," *Computational and Mathematical Methods in Medicine*, vol. 2022, Article ID 4070060, 6 pages, 2022.

Research Article

Clinical Study of Anti-PD-1 Immunotherapy Combined with Gemcitabine Chemotherapy in Multiline Treatment of Advanced Pancreatic Cancer

Yanfeng Liu,¹ Yanchuan Li,² Shan Du,³ Li Fan,³ and Junyan Wang³ 

¹General Surgery Department, The Second Affiliated Hospital of Xi'an Medical University, Xi'an, Shaanxi 710038, China

²Gynaecology and Obstetrics Department, Shaanxi Provincial People's Hospital, Xi'an, Shaanxi 710068, China

³Gastroenterology Department, The Second Affiliated Hospital of Xi'an Medical University, Xi'an, Shaanxi 710038, China

Correspondence should be addressed to Junyan Wang; wangjunyan19810914@163.com

Received 8 June 2022; Revised 13 July 2022; Accepted 1 August 2022; Published 6 September 2022

Academic Editor: Pan Zheng

Copyright © 2022 Yanfeng Liu et al. This is an open access article distributed under the Creative Commons Attribution License, which permits unrestricted use, distribution, and reproduction in any medium, provided the original work is properly cited.

Objective. This study aimed to investigate the efficacy and safety of anti-PD-1 immunotherapy combined with gemcitabine chemotherapy in multiline treatment of advanced pancreatic cancer. **Methods.** A retrospective analysis was performed on the clinical data of 32 patients with advanced pancreatic cancer treated with sintilimab regimen from January 2019 to December 2021 in our hospital. All patients were followed up until death or April 2022, in the form of outpatient, in-hospital review, or telephone follow-up. Follow-up content included routine blood, liver and kidney functions, tumor markers, plain or enhanced abdominal CT, and abdominal MRI examinations. Clinical efficacy was evaluated according to mRECIST criteria, and the severity of adverse effects was evaluated according to American Institute for Cancer Research (AICR) Standard Term for Adverse Events, Version 5.0. **Results.** During treatment, the dosage of sintilimab was halved in 2 patients due to adverse reactions. All patients were treated with sintilimab for 1~10 times, with an average of 6 ± 4 times. The total response rate (ORR) and disease control rate (DCR) were 6.25% and 12.50% and 25.00% and 37.50%, respectively, after 1 and 3 months of treatment. The mean follow-up time of 32 patients was 1-12 months, and the median follow-up time was 4 ± 3 months. By the end point of follow-up, a total of 25 patients died, and the median progression-free survival (PFS) was 3.8 (95% CI (1.85-5.63)) months. The median overall survival (OS) was 5.1 months (95% CI (3.63~7.68)). After treatment, the levels of tumor markers CA125, CEA and CA199 were partly decreased compared with those before treatment (all $P < 0.001$). After treatment, the blood routine indexes d-dimer, CRP (C-reactive protein), NLR (neutrophil to lymphocyte ratio), and MLR (monocyte to lymphocyte ratio) decreased compared with those before treatment. In 32 patients with advanced pancreatic cancer, the adverse reactions with an incidence more than 10% included fatigue, rash, hypothyroidism, hyperuricemia, and renal insufficiency. Only 2 patients showed grade 3 fatigue symptom, and all the others showed no adverse reactions of grades 3~5. In this study, all patients' adverse reactions were relieved after symptomatic treatment. **Conclusion.** Gemcitabine chemotherapy in multiline treatment of advanced pancreatic cancer with sintilimab can achieve certain clinical benefits without serious adverse reactions.

1. Introduction

Pancreatic cancer is one of the malignant tumors of the digestive system with the highest mortality, accounting for the fourth place in the cancer-related mortality [1, 2]. In recent years, epidemiology has found that the number of new pancreatic cancer cases in both male and female is increasing [3, 4]. In the USA, the number of new malignant

tumors ranks 10th in men and 9th in women among all tumors [5], and in China, the number ranks 7th in men and 11th in women [6]. The annual incidence of pancreatic cancer is 12.9 cases/100,000 person-years. However, pancreatic cancer has a poor prognosis, with a mortality rate of 11 cases/100,000 person-years [7]. Most patients are found in the middle and late stages and lose the opportunity for surgical treatment. Standardized, reasonable, and scientific drug

treatment can prolong the survival of patients with middle and advanced pancreatic cancer [8]. With the deepening of imaging, endoscopic technology and pathological research, and the continuous development of surgical treatment technology and local treatment technology, the treatment status of patients with pancreatic cancer has been significantly improved, and the number of patients with long-term survival has also been increasing [9, 10]. At present, the effective treatment of pancreatic cancer is still based on surgery, supplemented by radiation therapy and chemotherapy. With the deepening of research on tumorigenesis, development and metastasis mechanism of immune and molecular biology, gene therapy, and immunotherapy of pancreatic cancer become possible, and they also becomes new development direction of pancreatic cancer treatment [11]. Programmed death receptor-1 (PD-1) is a transmembrane protein belonging to the B7H3 immune superfamily. It is widely expressed in activated T lymphocytes, monocytes, B cells, natural killer cells, and dendritic cells and participates in immune surveillance and maintenance of immune tolerance [12, 13]. PD-1 and its ligand are also highly expressed in pancreatic cancer tumor cells [14]. Immunotherapy with PD-1 inhibitor as the main treatment scheme has achieved definite efficacy in a variety of solid tumor patients [15, 16]. Sintilimab (trade name: Daboshu) is a fully humanized IgG4 monoclonal antibody targeting PD-1. In 2018, it was approved by China's State Drug Administration (SDA) for clinical treatment of malignant tumors, and several phase I and phase II clinical trials were conducted at the same time [17–19]. At present, there are relatively few domestic clinical reports on the treatment of advanced pancreatic cancer with sintilimab combined with traditional chemotherapy drugs. This study conducted a retrospective analysis on the treatment of advanced pancreatic cancer with sintilimab in our hospital. The results are reported as follows.

2. Subjects and Methods

2.1. Research Subjects. The clinical data of patients with pancreatic cancer admitted to our hospital from January 2019 to December 2021 were retrospectively analyzed. All patients signed the informed consent form, and the study design was in line with the Declaration of Helsinki. Inclusion criteria are as follows: (1) Patients met the diagnostic criteria for pancreatic cancer in the Guidelines for Comprehensive Diagnosis and Treatment of Pancreatic Cancer in China (2020 version) [20]; (2) patients with locally advanced inoperable, metastatic, and postoperative recurrence and metastasis of pancreatic cancer; (3) the pathological type was adenocarcinoma; (4) the survival time can be followed up; (5) gemcitabine was included in the chemotherapy regimen; and (6) complete clinical data. Exclusion criteria are as follows: (1) The estimated survival was less than 3 months; (2) the tumor stage was stage IV; (3) patients had no indication of surgery or radiotherapy or who give up treatment; (4) patients had symptomatic brain metastases; (5) patients who have received chemotherapy in the past; and (6) immunodeficiency patients. A total of 32 patients with sintilimab included in the treatment regimen were selected. All patients

had not received radiotherapy and chemotherapy before enrollment.

2.2. Therapies. Sintilimab Injection (Innovent; SFDA approval number: S20180016) was administrated once every 3 weeks with a dose of 200 mg. Gemcitabine hydrochloride for injection (produced by Jiangsu Hausen Pharmaceutical Group, National drug Approval H20030104) was dissolved in 100 mL normal saline at 1000 g/m² and given intravenously for 30 min on the 1st and 8th days. Both were used until disease progression, severe adverse reactions, or self-termination of treatment.

2.3. Follow-Up and Outcome Evaluation. All patients were followed up until death or April 2022, in the form of outpatient, in-hospital review, or telephone follow-up. Follow-up content included routine blood, liver and kidney functions, tumor markers, plain or enhanced abdominal CT, and abdominal MRI examinations.

Efficacy evaluation: Clinical efficacy was evaluated according to mRECIST criteria [21]. The efficacy of CT or MRI reexamination results of patients at 1 and 3 months of treatment were divided into complete response (CR), partial response (PR), stable disease (SD), and progressive disease (PD), and the total response rate (ORR) and disease control rate (DCR) were calculated according to $ORR = CR + PR$ and $DCR = CR + PR + SD$.

Adverse reactions: The severity of toxic side effects in patients enrolled in this study was evaluated according to American Institute for Cancer Research (AICR) Standard Term for Adverse Events, Version 5.0 [22]. The toxic side effects were divided into levels 1 to 5, and the higher the level, the more serious the adverse effects were. The evaluation time was within 28 days after the last administration. The toxic side effects of included events include fatigue, skin rash, hypothyroidism, hyperuricemia, and renal insufficiency.

Two fixed physicians with extensive clinical experience evaluated efficacy and adverse effects. If there was any objection, please ask the third physician to further discuss and clarify.

2.4. Statistical Analysis. SPSS23.0 was used to analyze the collected experimental data. Mean \pm standard deviation ($X \pm S$) was used to represent the measurement data in accordance with normal distribution, and the counting data was expressed as cases or rates. Kaplan-Meier method was used to plot survival curves and count the progression-free survival (PFS) and overall survival (OS).

3. Results

3.1. Baseline Data. The baseline data of enrolled patients are shown in Table 1.

3.2. Short-Term Efficacy Evaluation. By the end of follow-up, the effective follow-up information of all 32 patients was obtained, and no one withdrew from the study due to serious adverse reactions or other reasons. During treatment, the dosage of sintilimab was halved in 2 patients due to adverse reactions. All patients were treated with sintilimab

TABLE 1: Comparison of baseline data between two groups.

Item		Sintilimab ($n = 32$)
Gender	Male	19
	Female	13
Age (years)		58.37 ± 10.53
Body mass index (kg/m^2)		22.18 ± 2.53
Complicated with diabetes		6
Complicated with hypertension		7
Tumor site	Uncinate process of pancreatic head	20
	Body and tail of pancreas	12
Nerve infiltration	Yes	14
	No	18
Degree of differentiation	Low/medium differentiation	19
	Highly differentiation	13

for 1~10 times, with an average of 6 ± 4 times. The ORRs at 1 and 3 months after treatment are 6.25% and 12.50%, respectively, and the DCRs are 25.00% and 37.50%, respectively, as shown in Table 2.

3.3. Survival Benefit Evaluation. The mean follow-up time of the 32 patients was 1-12 months, and the median follow-up time was 4 ± 3 months. By the end point of follow-up, a total of 25 patients died, with a median PFS of 3.8 (95% CI (1.85-5.63)) months and a median OS of 5.1 months (95% CI (3.63-7.68)), as shown in Figure 1.

3.4. Evaluation of Tumor Markers before and after Treatment. After treatment, the levels of tumor markers CA125, CEA, and CA199 are partly decreased compared with those before treatment (all $P < 0.001$), as shown in Table 3.

3.5. Evaluation of Blood Routine Indexes before and after Treatment. After treatment, the blood routine indexes D-dimer, CRP, NLR, and MLR all significantly decrease compared with those before treatment (all $P < 0.05$), as shown in Table 4.

3.6. Evaluation of Adverse Reactions. According to the AICR Standard Term for Adverse Events version 5.0, the adverse reactions with an incidence more than 10% in these 32 patients included fatigue, rash, hypothyroidism, hyperuricemia, and renal insufficiency. Only 2 patients showed grade 3 fatigue symptom, and all the others showed no adverse reactions of grades 3~5. All patients in this study are relieved after symptomatic treatment, as shown in Table 5.

4. Discussion

Epidemiological investigation found that the absolute and relative numbers of incidence and death of pancreatic cancer in China increased significantly in 2019 compared with 1990, with the normalized incidence and mortality increasing by 82.33% and 79.34%, indicating that the burden of pancreatic cancer on the health of Chinese residents is

gradually increasing [23, 24]. In terms of morbidity characteristics, male, age, diet, and alcohol have significant influence on the incidence of pancreatic cancer in Chinese residents [25]. As a highly invasive malignant tumor with high mortality, about 60% of them have metastasis at first diagnosis, about 30% have been in local progression at first diagnosis, and only 15% can receive radical surgery. Most patients die due to tumor metastasis or recurrence, with the 5-year survival rate being only 7% [26]. Anti-PD-1 monoclonal antibody has been approved for a short time in China, but its therapeutic effect in a variety of solid tumors has been confirmed. The present study analyzed the efficacy and safety of the multiline treatment regimen containing sintilimab in patients with advanced pancreatic cancer, with the aim of enriching the clinical data and providing a valuable reference for the promotion and application of this drug.

Studies [27, 28] found that therapies combined with immune checkpoints can regulate the immune editing process of pancreatic cancer tissues and directly affect the tumor microenvironment and immune response behavior. Drug combination can also overcome the resistance of pancreatic cancer to PD-1/PD-L1 monotherapy and promote the transformation of tumor biological behavior from nonimmunological to immunological, which maximizes the antitumor therapeutic effects of immunosuppressants [29]. The combination of PD-L1 blocker and gemcitabine has been proved to have antitumor effect in the treatment of pancreatic cancer, while the clinical response rate of the combination of pembrolizumab/gemcitabine + albumin-bound paclitaxel in the treatment of pancreatic cancer is up to 92% [29]. An in vitro study [30] found that sintilimab can specifically bind human PD-1 in high concentration and block the binding of PD-1 with PD-L1/PD-L2 ligand. When the dose of sintilimab injection is 200 mg, it can rapidly occupy more than 95% of PD-1 receptors on the surface of T cells. In addition, sintilimab can significantly increase the levels of interleukin-2 and interferon- γ in a dose-dependent manner, which may be one of the molecular mechanisms for its antitumor role [31].

TABLE 2: Short-term efficacy evaluation.

Time point	CR	PR	SD	PD	ORR	DCR
1 month	0 (0)	2 (6.25)	6 (18.75)	24 (75.00)	2 (6.25)	8 (25.00)
3 months	0 (0)	4 (12.50)	8 (25.00)	20 (62.50)	4 (12.5)	12 (37.50)

Note: CR: complete remission; PR: partial remission; SD: stable disease; PD: progressive disease; ORR: overall response rate.

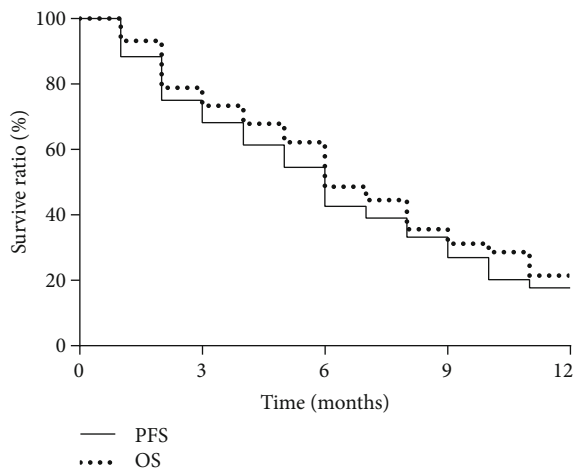


FIGURE 1: Survival curve of sintilimab immunotherapy regimen.

TABLE 3: Evaluation of tumor markers before and after treatment.

Index	Before treatment	After treatment	<i>P</i> value
CA125	10.53 ± 7.34	7.83 ± 5.83	<0.001
CEA	464.53 ± 386.74	416.34 ± 32.53	<0.001
CA199	49.37 ± 40.83	40.86 ± 38.76	<0.001

This study analyzed the clinical data of 32 patients with advanced pancreatic cancer who received sintilimab multi-line therapy in our hospital. The results showed that the dosage of sintilimab was halved in 2 patients due to adverse reactions during the treatment. The ORR of 1 month and 3 months after treatment was 6.25% and 12.50%, respectively, and the DCR was 25.00% and 37.50%, respectively. In the study of Xiao Xia et al. [32], among 8 patients with advanced pancreatic cancer treated with sintilimab, 1 patient had PR, 1 patient had SD, and 6 patients had PD. Objective remission was observed in 1 case and disease control in 2 cases. The median PFS was 2.0 months (95% CI 0.6-3.4 months), and the median OS was 3.5 months (95% CI 2.2-4.8 months), which were similar to the results of our study. However, in the study of Le et al. [33], the disease control rate in dMMR or MSI-H-positive patients with advanced metastatic pancreatic cancer treated with anti-PD-1 monoclonal antibody is up to 75%. In addition, it was reported that the disease control rate of patients with metastatic pancreatic cancer treated with pembrolizumab combined with chemotherapy is up to 100% [34]. The reasons for the differences among different studies may be related to drug dosage, heterogeneity of patients' baseline data, and differences in

TABLE 4: Evaluation of blood routine indexes before and after treatment.

Index	Before treatment	After treatment	<i>P</i> value
D-dimer	30.34 ± 13.23	22.38 ± 12.86	<0.001
CRP	28.53 ± 12.76	20.67 ± 12.78	<0.001
NLR	3.43 ± 1.86	2.80 ± 1.79	<0.001
MLR	2.86 ± 1.39	2.28 ± 1.28	<0.001

TABLE 5: Evaluation of adverse reactions (*n*, %).

Adverse reactions	Total incidence	Incidence of grades 3-5 adverse reactions
Fatigue	20 (62.50)	2 (6.25)
Rash	10 (31.25)	0 (0.00)
Hypothyroidism	8 (25.00)	0 (0.00)
Hyperuricemia	6 (18.75)	0 (0.00)
Renal insufficiency	5 (15.63)	0 (0.00)

sample size. In the present study, the mean follow-up time of 32 patients was 1-12 months, and the median follow-up time was 4 ± 3 months. By the end point of follow-up, a total of 25 patients died, with a median PFS of 3.8 (95% CI (1.85-5.63)) months and a median OS of 5.1 months (95% CI (3.63-7.68)). Compared with the results of Xiao Xia et al., both PFS and OS in our study were improved to a certain extent, suggesting that sintilimab combined with chemotherapy had certain clinical benefits in the multiline treatment of advanced pancreatic cancer.

In terms of efficacy evaluation indexes, the levels of tumor markers CA125, CEA, and CA199 decreased significantly after treatment compared with before treatment, and the blood routine indexes (D-dimer, CRP, NLR, and MLR) decreased after treatment compared with before treatment, indicating that hematological indexes had certain value in evaluating the efficacy of this treatment regimen. However, whether its application value is better than that of serum PD-1 and PD-L1 as well as the optimal threshold of single indicator and multiple indicator combination needs further discussion.

It has been reported [35] that while promoting tumor immune response, sintilimab may lead to excessive immune response, induce autoimmune response, and cause immune-related adverse events in skin, gastrointestinal tract, liver, kidney, and endocrine system. The results of our study showed that the adverse reactions with an incidence over 10% during

treatment included fatigue, rash, hypothyroidism, hyperuricemia, and renal insufficiency. Only 2 patients had grade 3 fatigue symptoms, and the rest had no grades 3-5 adverse reactions. In this study, all patients' adverse reactions were alleviated after symptomatic treatment, indicating that this treatment plan did not cause serious treatment-related adverse reactions and was safe.

Overall, the results of this study suggested that patients with advanced pancreatic cancer can benefit from the multi-line therapy with sintilimab, with no serious adverse reactions. However, according to other studies, there are still many problems with anti-PD-1 monoclonal antibody drugs in the treatment of pancreatic cancer. For example, about half of patients have poor response efficiency to pD-1/PD-L1 treatment but lack relevant evaluation markers. Anti-PD-1/PD-L1 monotherapy for solid tumors has poor efficacy and is mostly used in combination, and the optimal combination plan still needs to be discussed. In addition, the high cost of anti-PD-1/PD-L1 treatment restricts its promotion [36], which is one of the reasons for the small sample size reported in most cases. And this study lacked a noncombination control group. Interleukin-2 and interferon- γ can be detected to evaluate the antitumor effect. Future follow-up studies need to expand the sample size and follow-up time to develop the best treatment plan to maximize the clinical benefit of patients. And future follow-up studies will improve the control group settings and detect immune indicators to evaluate the antitumor effect.

Data Availability

The labeled dataset used to support the findings of this study are available from the corresponding author upon request.

Conflicts of Interest

The author declares no competing interests.

References

- [1] A. P. Klein, "Pancreatic cancer epidemiology: understanding the role of lifestyle and inherited risk factors," *Nature Reviews Gastroenterology & Hepatology*, vol. 18, no. 7, pp. 493–502, 2021.
- [2] X. Chen, F. Liu, Q. Xue, X. Weng, and F. Xu, "Metastatic pancreatic cancer: mechanisms and detection (review)," *Oncology Reports*, vol. 46, no. 5, p. 231, 2021.
- [3] J. Li, X. Chen, R. Kang, H. Zeh, D. J. Klionsky, and D. Tang, "Regulation and function of autophagy in pancreatic cancer," *Autophagy*, vol. 17, no. 11, pp. 3275–3296, 2021.
- [4] N. E. Cortez and G. G. Mackenzie, "Ketogenic diets in pancreatic cancer and associated cachexia: cellular mechanisms and clinical perspectives," *Nutrients*, vol. 13, no. 9, p. 3202, 2021.
- [5] W. Bakasa and S. Viriri, "Pancreatic cancer survival prediction: a survey of the state-of-the-art," *Computational and Mathematical Methods in Medicine*, vol. 2021, Article ID 1188414, 17 pages, 2021.
- [6] L. C. Chu, S. Park, S. Kawamoto, A. L. Yuille, R. H. Hruban, and E. K. Fishman, "Pancreatic cancer imaging: a new look at an old problem," *Current Problems in Diagnostic Radiology*, vol. 50, no. 4, pp. 540–550, 2021.
- [7] Q. Jiang and W. Zhou, "Excerpt from "2019 American preventive medicine working group expert consensus: screening for pancreatic cancer"," *Journal of Clinical Hepatobiliary Diseases*, vol. 36, no. 1, p. 3, 2020.
- [8] J. X. Huang, P. Y. Xin, Z. Y. Yang, C. X. Zhou, J. G. Lu, and G. Q. Bao, "Research progress of drug therapy for advanced pancreatic cancer," *Journal of Hepatobiliary and Pancreatic Surgery*, vol. 33, no. 8, p. 502, 2021.
- [9] L. H. Biller, B. M. Wolpin, and M. Goggins, "Inherited pancreatic cancer syndromes and high-risk screening," *Surgical Oncology Clinics of North America*, vol. 30, no. 4, pp. 773–786, 2021.
- [10] A. D. Singhi and L. D. Wood, "Early detection of pancreatic cancer using DNA-based molecular approaches," *Nature Reviews Gastroenterology & Hepatology*, vol. 18, no. 7, pp. 457–468, 2021.
- [11] W. H. Lou, "Current status, challenges and future of precision therapy for pancreatic cancer," *Chinese Journal of Practical Surgery*, vol. 41, no. 9, pp. 1014–1016, 2021.
- [12] S. Bagchi, R. Yuan, and E. G. Engleman, "Immune checkpoint inhibitors for the treatment of cancer: clinical impact and mechanisms of response and resistance," *Annual Review of Pathology*, vol. 16, no. 1, pp. 223–249, 2021.
- [13] Y. Chen, Y. Pei, J. Luo, Z. Huang, J. Yu, and X. Meng, "Looking for the optimal PD-1/PD-L1 inhibitor in cancer treatment: a comparison in basic structure, function, and clinical practice," *Frontiers in Immunology*, vol. 11, p. 1088, 2020.
- [14] S. P. Hack, A. X. Zhu, and Y. Wang, "Augmenting anticancer immunity through combined targeting of angiogenic and PD-1/PD-L1 pathways: challenges and opportunities," *Frontiers in Immunology*, vol. 11, article 598877, 2020.
- [15] D. B. Doroshow, S. Bhalla, M. B. Beasley et al., "PD-L1 as a biomarker of response to immune-checkpoint inhibitors," *Nature Reviews Clinical Oncology*, vol. 18, no. 6, pp. 345–362, 2021.
- [16] D. Bruni, H. K. Angell, and J. Galon, "The immune contexture and Immunoscore in cancer prognosis and therapeutic efficacy," *Nature Reviews Cancer*, vol. 20, no. 11, pp. 662–680, 2020.
- [17] L. X. Chen, P. Sun, and Z. Z. Hu, "Effects of sintilimab combined with chemotherapy on tumor markers and immune function of advanced non-small cell lung cancer," *Laboratory Medicine and Clinical*, vol. 19, no. 8, p. 3, 2022.
- [18] X. M. Hu, G. Y. Li, and L. Wang, "Clinical study of gemcitabine combined with sintilimab in the treatment of stage IV lung squamous cell carcinoma," *Chinese Journal of Biochemical Pharmaceutics*, 2021.
- [19] X. Xiao, Q. Wang, X. D. Guo et al., "Efficacy and safety observation of sintilimab in multi-line treatment of advanced pancreatic cancer," *Cancer Research and Clinical*, vol. 33, no. 11, p. 4, 2021.
- [20] Pancreatic Cancer committee of Chinese Anti-Cancer Association, "Guidelines for comprehensive diagnosis and treatment of pancreatic cancer in china (2020 edition)," *Chinese Journal of Surgery*, vol. 59, no. 2, p. E001, 2020.
- [21] R. Lencioni and J. M. Llovet, "Modified RECIST (mRECIST) assessment for hepatocellular carcinoma," *Seminars in Liver Disease*, vol. 30, no. 1, pp. 052–060, 2010.
- [22] A. Freitas-Martinez, N. Santana, S. Arias-Santiago, and A. Viera, "Using the common terminology criteria for adverse

Retraction

Retracted: Analysis the Innovation Path on Psychological Ideological with Political Teaching in Universities by Big Data in New Era

Computational and Mathematical Methods in Medicine

Received 27 June 2023; Accepted 27 June 2023; Published 28 June 2023

Copyright © 2023 Computational and Mathematical Methods in Medicine. This is an open access article distributed under the Creative Commons Attribution License, which permits unrestricted use, distribution, and reproduction in any medium, provided the original work is properly cited.

This article has been retracted by Hindawi following an investigation undertaken by the publisher [1]. This investigation has uncovered evidence of one or more of the following indicators of systematic manipulation of the publication process:

- (1) Discrepancies in scope
- (2) Discrepancies in the description of the research reported
- (3) Discrepancies between the availability of data and the research described
- (4) Inappropriate citations
- (5) Incoherent, meaningless and/or irrelevant content included in the article
- (6) Peer-review manipulation

The presence of these indicators undermines our confidence in the integrity of the article's content and we cannot, therefore, vouch for its reliability. Please note that this notice is intended solely to alert readers that the content of this article is unreliable. We have not investigated whether authors were aware of or involved in the systematic manipulation of the publication process.

Wiley and Hindawi regrets that the usual quality checks did not identify these issues before publication and have since put additional measures in place to safeguard research integrity.

We wish to credit our own Research Integrity and Research Publishing teams and anonymous and named external researchers and research integrity experts for contributing to this investigation.

The corresponding author, as the representative of all authors, has been given the opportunity to register their agreement or disagreement to this retraction. We have kept a record of any response received.

References

- [1] X. Luo, "Analysis the Innovation Path on Psychological Ideological with Political Teaching in Universities by Big Data in New Era," *Computational and Mathematical Methods in Medicine*, vol. 2022, Article ID 4305886, 9 pages, 2022.

Research Article

Analysis the Innovation Path on Psychological Ideological with Political Teaching in Universities by Big Data in New Era

Xiufen Luo 

Mental Health Education and Counseling Center, Hubei University of Technology, Wuhan 430068, China

Correspondence should be addressed to Xiufen Luo; z51614022@stu.ahu.edu.cn

Received 22 July 2022; Revised 12 August 2022; Accepted 18 August 2022; Published 6 September 2022

Academic Editor: Pan Zheng

Copyright © 2022 Xiufen Luo. This is an open access article distributed under the Creative Commons Attribution License, which permits unrestricted use, distribution, and reproduction in any medium, provided the original work is properly cited.

The increasing pressure of life and the rapid development of the economy have caused huge mental health situation problems for people. Mental health situation has an important relationship with one's own life values. The cognition Ideological with political is to improve people's optimistic attitude and values. The students of college will face enormous pressure from their studies, which can easily causes the mental health situation problems. However, the psychological and ideological education in universities still adopts the traditional teaching method, which reduces students' learning hobbies and learning efficiency. This also reduces students' understanding of the content of psychological ideological with political teaching. Big data theory can process complex research object data and relationships. It can help researchers discover characteristic factors related to psychological ideological with political teaching. This study uses the hole convolution in big data theory and GRU technology to analyze the three factors of student behavior characteristics, mental health situation content characteristics, and the cognition Ideological with political content characteristics in college psychological the cognition Ideological with political. The research results show that the atrous convolution and GRU methods can more accurately predict the three characteristics of psychological ideological with political teaching in universities. This is helpful for educators to discover more appropriate psychological and ideological with political teaching methods.

1. Introduction

There is a complementary relationship for the mental health situation and ideological education. A good state of mental health situation allows people to receive the cognition Ideological with political in a fuller state. The cognition Ideological with political can make students develop a positive mental state, which can reduce the occurrence of people's mental health situation diseases [1, 2]. With the increase of life pressure, people are more prone to problems with their mental health situation, which will also exacerbate the occurrence of extreme events. People need to master more mental health situation knowledge and ideological with political points [3, 4]. This is also because people lack psychological education and ideological with political knowledge. The purpose of mental health situation education is to hope that people will maintain a positive attitude and it also requires people to maintain a strong will, which can also reduce the occurrence of mental health situation problems.

The cognition Ideological with political is to let people accept more positive and optimistic knowledge through the means of political education, which is also can guide people to maintain a good attitude. In short, mental health situation and the education of ideological with political are an inseparable relationship. However, mental health situation problems are more private and difficult to cure in direct ways [5, 6]. Mental health situation problems are also different from other types of diseases, and it has an important relationship with people's living environment and life values. Positive and optimistic life values and positive and optimistic life concepts will avoid the occurrence of mental health situation problems. Positive and optimistic psychological concepts are closely related to education and life experience. The cognition Ideological with political is a positive attitude that educates people to maintain a positive and optimistic attitude, life concept, and patriotism. This shows that mental health situation and the education of ideological with political are also closely related. In today's era, many universities

have also carried out teaching work related to mental health situation and the education of ideological with political. Universities are a larger bridge connecting their study careers and social work. Students in universities will face major mental health situation problems, which requires the cognition Ideological with political [7, 8]. Since the relationship between mental health situation and ideology and politics is relatively close, universities are also places where mental health situation problems are relatively concentrated. Therefore, universities will carry out more teaching and educational work in mental health situation and ideological with political aspects. However, traditional mental health situation and the education of ideological with political is only to master the basic knowledge and relationship between the two. It is difficult to discover the relationship between mental health situation and ideological with political, and it is also difficult for students to master the relationship between mental health situation and ideological with political crowd influence [9, 10]. Therefore, people should master the teaching work of mental health situation and ideology and politics in a reasonable way.

For teaching in universities, most subjects are often taught in classrooms and textbooks. Teachers use textbooks to pass knowledge to students, but there is a lack of feedback. It is difficult to understand students' mastery, and it is also difficult to stimulate students' interest in learning. The teaching of mental health situation and ideological with political itself is a relatively boring subject. The traditional method is difficult for students to accept the relationship between mental health situation and ideology and politics, and it is also difficult for students to strengthen their positive and optimistic attitude through the cognition Ideological with political to reduce the risk of mental health situation problems [11, 12]. The purpose of mental health situation and ideological with political teaching is to let students understand the importance of ideological with political knowledge and the importance of mental health situation teaching. This will allow them to increase their interest in learning the cognition Ideological with political, which will also allow them to truly understand the purpose of the ideological with political teaching curriculum. Big data theory has been successfully applied in many feature extraction fields, which can extract complex nonlinear relationships. Similarly, the relevant characteristics of mental health situation and ideological with political teaching can be extracted and mapped by big data theory [13, 14]. This can solve the difficulties existing in mental health situation and ideological teaching tasks in traditional universities. Through big data theory, it can also improve students' learning efficiency and interest in mental health situation and ideological with political teaching.

Big data theory is good at dealing with cumbersome and extremely large data, because big data theory can use the form of weight and bias to digitize and nonlinearly process the characteristics of research objects [15, 16]. Big data theory stagnated for a while at the end of the twentieth century, because the performance of computers could not keep up with the increase in the amount of data of research objects [17, 18]. In the early stage of the development of big data

theory, it only used simple machine learning algorithms to deal with some simple research data problems. However, with the rapid development of high-performance computers, computer performance, and memory allow big data theory to deal with complex problems, which quickly derives more deep learning algorithms. Big data theory is also widely used in image recognition and video feature recognition, which also brings great convenience to people's life and production. In life, the characteristics of research objects in production or life are mainly divided into three types: spatial characteristics, temporal characteristics, and environmental characteristics [19, 20]. It also has many corresponding algorithms. These mature big data algorithms can be leveraged by researchers, and it does not require much research. For mental health situation and ideological with political teaching in universities, big data theory can also extract relevant features in the teaching process, whether it is spatial or temporal features, and then it can complete the mapping of complex relationships among teaching tasks.

This research mainly uses big data theory to study the characteristics of mental health situation and ideological with political teaching in universities. It can solve the problems of low efficiency and difficulty in arousing students' interest in mental health situation and ideological with political teaching. In the process of using big data, it mainly analyzes three aspects: student behavior information, mental health situation content characteristics, and ideological with political content characteristics in mental health situation and ideological with political teaching in universities. This study uses the atrous convolution (A-CNN) method and GRU method in big data theory to analyze these three characteristics. This research studies the application of big data theory in college teaching mental health situation and ideological with political aspects through 5 parts. Section 1 introduces the relationship between psychology and ideology and politics and the relevant background of big data theory. Section 2 analyzes the research status of mental health situation and the education of ideological with political. The design scheme of big data theory in college teaching mental health situation and ideological with political aspects is analyzed in Section 2. Section 4 explores the feasibility of ACNN and GRU technology in terms of characteristics related to teaching mental health situation and ideological with political aspects. In Section 4, this study analyzes the accuracy and feasibility of big data technology in psychology and ideological and political cognition by using the prediction error scatter plot of the three characteristics and the psychological teaching content prediction box plot. Section 5 summarizes the importance of big data theory for mental health situation and ideological with political teaching in universities.

2. Related Work

Mental health situation and the education of ideological with political are complementary contents. The cognition Ideological with political can improve people's enthusiasm, which can reduce the probability of people's mental health situation problems. Many researchers study the content of mental health situation and the education of ideological with

political. In order to solve the problems of low efficiency and poor stability of educational resources in the process of ideological with political teaching, it designs an intelligent the cognition Ideological with political resource integration model. Liu and Huang [21] use deep learning and data mining technology to integrate ideological with political-related educational resources. It uses the decision tree in data mining technology to deeply mine the content of the cognition Ideological with political resources, and then it integrates these the cognition Ideological with political resources. It also uses the LDA model to thematically define the components of ideological with political related content. The research results show that this method has relatively high accuracy and efficiency and this intelligent the cognition Ideological with political integration platform also has high stability. Mao et al. [22] believe that the cognition Ideological with political is an indispensable part of the curriculum for college students, which can cultivate college students' ideological values and positive attitudes towards life. It uses the new subject education theory to study the teaching mode of the cognition Ideological with political. It believes that the combination of collaborative education mode and ideological with political teaching can promote the innovation of the cognition Ideological with political. It establishes a synergistic effect model to solve the problems of value differences and lack of collective consciousness in the process of university teaching. There is also a feedback mechanism in this method, and the research results show that this synergistic effect model has certain universality in the cognition Ideological with political of college students in China. This method can also help college students better understand the content of the cognition Ideological with political. Lu [23] believes that the cognition Ideological with political is a carrier of teaching ideas and politics for the education of students. In order to better teach the core content and values of the cognition Ideological with political, it studies a research-based teaching model. And it uses this teaching mode to explore the theoretical basis and practical process of ideological with political teaching. It also analyzes the opportunities for mental health situation and the education of ideological with political and the challenges it faces. At the same time, it also illustrates the use and advantages of Internet technology in the process of mental health situation and ideological with political teaching. The results of the discussion show that Internet technology is helpful to students' ideological with political teaching. Hang [24] has discovered the importance of the cognition Ideological with political for college students. However, it also found that the traditional blackboard and PPT the cognition Ideological with political model are facing the risk of being eliminated, and this teaching method can no longer meet the current ideological with political teaching model. It believes that wireless communication technology and VR methods can replace blackboard and PPT teaching methods. The immersive feeling and situation of VR technology can improve the key content of the cognition Ideological with political for college students. It analyzes the application of VR technology and wireless communication technology in university ideological with political teaching. The research results show that this method of

college ideological with political teaching can change the defects of the traditional teaching mode and this method can also improve the enthusiasm and interest of college students in learning ideological with political content. He [25] mainly studies the content of ideological teaching resources sharing, and it mainly finds the problems of data interference and too long sharing time in traditional ideological with political teaching resources. It proposes an edge computing ideological with political teaching resource sharing method. This method utilizes the method of information entropy suppression, which will eliminate redundant data of ideological with political resources, which will reduce the time for resource sharing. The research results show that this method is more efficient in the content sharing of ideological with political teaching. Through the above research, it can be found that few researchers use big data to analyze the cognitive teaching of psychology and ideology in colleges and universities. This study uses big data strategies to study the relevant characteristics of psychology and ideological and political cognitive teaching, which will improve the efficiency of learning.

3. Application and Analysis of Big Data Theory in Psychological Ideological with Political Teaching in Universities

3.1. The Significance of Big Data Theory for Psychological Ideological with Political Teaching. This research mainly explores the application of big data theory in the psychological ideological with political teaching in universities. The traditional blackboard or PPT method has been difficult to meet the psychological ideological with political teaching in today's social situation. In today's social environment, the teaching mental health situation and ideological with political aspects in universities presents a multi-end and complex feature. The teaching of psychology and ideology is more complicated, and there are more psychological and ideological with political characteristics, which aggravate the psychological and ideological with political characteristics of universities. And with the development of social diversification, the content of teaching mental health situation and ideological with political aspects will be more extensive. Teaching is developing in an intelligent direction, which will increase students' interest and motivation in learning. The content of psychology and ideology and politics is a relatively subjective teaching content, unlike mathematics and physics, which are more rigorous courses. Big data theory can extract the content characteristics of psychological ideological with political teaching in universities in the form of data, and it can help students or teachers to discover more teaching content characteristics that cannot be found intuitively. The teaching content of college psychology and ideological politics can be displayed in the form of data, and big data theory can further extract and predict the characteristics of college teaching mental health situation and ideological with political aspects content, which can quantitatively analyze the teaching characteristics of college teaching mental health situation and ideological with political aspects.

3.2. *Design Scheme of Big Data Theory in Psychological Ideological with Political Teaching in Universities.* Through the above analysis and introduction, it can be found that the three key characteristics are the student behavior information, the content characteristics of psychological teaching, and the content characteristics of ideological with political teaching in psychology and ideology. These three characteristics are the key factors affecting the success of psychological ideological with political teaching in universities. Only by grasping these three key characteristics, it will more accurately grasp the development direction of college teaching mental health situation and ideological with political aspects. This will also more efficiently stimulate students' interest in learning, and it will also improve students' awareness of mental health situation content and ideological with political teaching content. Figure 1 shows the design scheme of big data theory in college teaching mental health situation and ideological with political aspects, which is an intelligent teaching design scheme. First of all, the three characteristics of psychological teaching content, ideological with political teaching content characteristics and student behavior of college teaching mental health situation, and ideological with political aspects are input into the ACNN neural network in the form of data, and the data of these three characteristics will be in the form of a matrix. The data operates through full feature extraction, convolution operations, and nonlinear feature maps. It will output content related to mental health situation and ideological with political teaching. These data will be further input into the GRU neural network, and these features will complete the extraction of temporal features. Finally, this intelligent system will map and predict the data related to psychological ideological with political teaching in universities according to the content characteristics of mental health situation and the complex relationship between the content characteristics of ideological with political teaching and student behavior. In Figure 1, the computer-aided system can display the psychological and ideological and political-related knowledge acquired by ACNN and GRU methods to students or teachers, which is also the last part of this intelligent teaching system.

3.3. *The Principle and Work-Flow of GRU Algorithm.* For the research on mental health situation and ideological with political teaching in universities, these characteristics will involve more time characteristics. For example, student behavior information is a relatively temporal feature. The LSTM method is a relatively common temporal feature extraction algorithm, which also memorizes historical state information. However, the LSTM algorithm has a lot of parameter calculations in the training process. The GRU method has the same functionality as the LSTM algorithm, but it involves fewer parameters in the training process. Figure 2 shows the relevant characteristics of the calculation method of the GRU method in the process of learning mental health situation and ideological with political teaching in universities. The GRU method has a simpler gate structure than the LSTM method, which reduces the process of parameter derivation calculation. This also reduces the use

of computer memory, which can also reduce the learning time for psychology and ideological and political cognition teaching.

In the following, this study introduces the equations of the GRU method and the workflow of the equations, which mainly include four processes: update gate, reset gate, and loss function.

- (1) Compared with the LSTM method, the GRU method improves the four-gate structure of the LSTM method into a two-gate structure, which greatly reduces the amount of parameter computation. The update gate is mainly responsible for selectively filtering historical information, and it also inputs the input data and historical selective data into the GRU structure of the next layer. Equations (1) and (2) show the calculation guidelines for the update gate

$$g_r = \sigma(W_r[h_{t-1}, x_t] + b_r), \quad (1)$$

$$\tilde{h}_t = \tanh(W_h[g_r h_{t-1}, x_t] + b_h). \quad (2)$$

- (2) Equations (3) and (4) show the calculation criterion of the GRU reset gate, which is similar to the refresh gate and output gate in LSTM. It can output historical status data as well as current status data.

$$g_z = \sigma(W_z[h_{t-1}, x_t] + b_z), \quad (3)$$

$$h_t = (1 - g_z)h_{t-1} + g_z \tilde{h}_t. \quad (4)$$

- (3) Every deep learning algorithm contains weights and biases. The nonlinear relationship of the data will be stored in the distribution of weights and biases. In the learning process of GRU, the derivation calculation methods of weights and biases are as shown in the following equations:

$$\Delta\omega_{ji} = -\eta \frac{\partial E}{\partial \omega_{ji}}, \quad (5)$$

$$\Delta u_{ij} = -\eta \frac{\partial E \partial}{\partial u_{ij}}. \quad (6)$$

- (4) The loss function is also an important part of the structure of the GRU algorithm. It will be responsible for calculating the error calculation between the predicted value and the actual value of the eigenvalues of ideological with political and psychological education. The learning process of GRU is based on

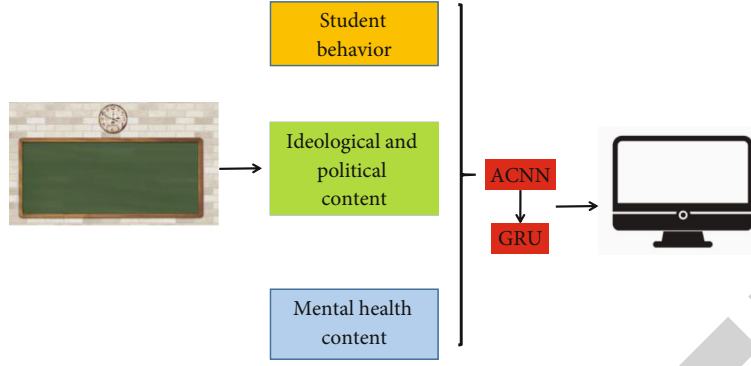


FIGURE 1: Design scheme of big data theory in psychological ideological with political teaching in universities.

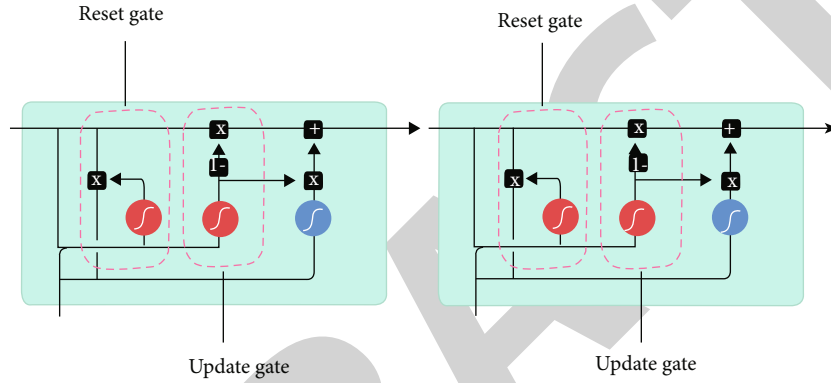


FIGURE 2: The basic principle and process of GRU algorithm.

the error of the loss function. Equation (7) shows how the loss function is calculated. In this study, the mean square error loss function was chosen. The mean square error loss function is a commonly used loss function, which has relatively high stability. It is also applicable to the data types of psychology and ideological and political cognition teaching.

$$\begin{aligned}
 E &= \frac{1}{2} \sum_{k=1}^m [d_k - f(\text{net}w_k)]^2 = \frac{1}{2} \sum_{k=1}^m \left[d_k - f \left(\sum_{j=0}^n \omega_{jk} y_j \right) \right]^2 \\
 &= \frac{1}{2} \sum_{k=1}^m \left[d_k - f \left[\left(\sum_{j=0}^n \omega_{jk} f \left(\sum_{i=0}^q u_{ij} x_i \right) \right) \right] \right]^2.
 \end{aligned} \quad (7)$$

3.4. The Role of the ACNN Method for Teaching Mental Health Situation and Ideological with Political Aspects. ACNN has specific and obvious advantages in extracting the characteristics of research objects. It can not only extract the characteristics of research objects, but also reduce the number of parameters. Compared with the CNN method, it has a higher advantage in running cost. The characteristics of college teaching mental health situation and ideological with political aspects will have a lot of parameters. If the CNN method is used, it will consume high costs and computing resources. Figure 3 shows the calculation process

and principle of ACNN. Compared with the CNN method, the ACNN method has less parameter computation, which is also the biggest advantage of the ACNN algorithm. There will be a huge amount of data in the teaching characteristics of psychology and ideological and political cognition. If the CNN method is used, more computing resources will be wasted.

Compared with the CNN method, the biggest change of the GRU algorithm is that the method of outputting features is different. Equation (8) shows the calculation equation of the output feature of the GRU algorithm, which is also a calculation method unique to ACNN:

$$S_{\text{out}} = \left\lfloor \frac{S_{\text{in}} + 2\text{padding} - S_{\text{kenal}}}{\text{step}} \right\rfloor + 1. \quad (8)$$

Equation (9) shows the computational equation for the input features of ACNN. Equation (10) shows the method of parameter adjustment of ACNN.

$$S_{\text{in}} = (S_{\text{out}} - 1) \times \text{step} + S_{\text{kenal}} - 2\text{padding}, \quad (9)$$

$$V_i = V_{i-1} + S_{\text{kenal}-i} \times \prod_{i=1}^{i-1} \text{step}_{i-1}. \quad (10)$$

During the training process of ACNN, it will have an activation function. Activation function is a process of

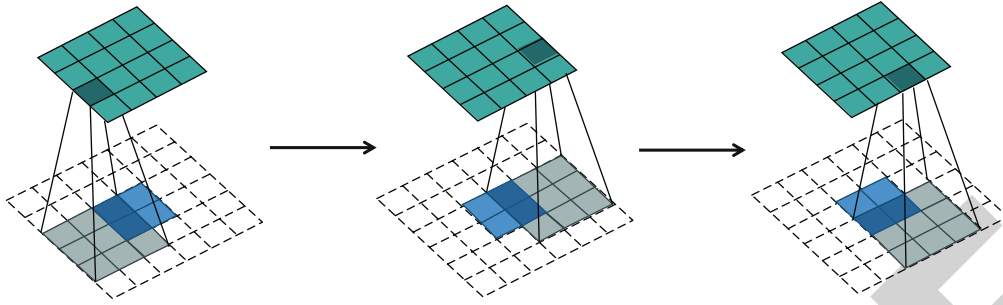


FIGURE 3: Schematic diagram and principle of the ACNN method.

nonlinear data processing. Equation (11) shows the operation process of the activation function of the ACNN algorithm:

$$a^l = \text{ReLU}(z^l) = \text{ReLU}(W^l a^{l-1} + b^l). \quad (11)$$

4. Result Analysis and Discussion

This research mainly uses big data theory to learn and map the three eigenvalues of ideological with political and psychological education in universities. This will help teachers and students to find a more suitable content and teaching methods for teaching mental health situation and ideological with political aspects. Big data theory can also find some correlations that cannot be found by artificial means about the eigenvalues of ideological with political and psychological education in universities. The traditional psychological and ideological with political teaching model only uses textbooks to teach psychological and ideological with political knowledge; it cannot show more appropriate psychological and ideological with political knowledge according to students' interests and performance. The core of big data theory is a huge amount of data, which can discover the characteristics and correlations of research objects from the data. Data sets are also an important source of big data theory. In this study, the psychological and ideological with political related data of many universities in Shanghai were selected as the data set for this study. Shanghai has more colleges and universities compared to other provinces. Moreover, the economic development of Shanghai is relatively developed, which can specify the relevant characteristics of more types of psychology and ideological and political cognitive teaching. This expands the source of the data set.

In order to further illustrate whether the three characteristics of college teaching mental health situation and ideological with political aspects have strong temporal correlations, this study first analyzed the accuracy of the single ACNN method in predicting the three eigenvalues of ideological with political and psychological education. Figure 4 shows the prediction errors of three eigenvalues of ideological with political and psychological education using a single ACNN method. In Figure 4, the area of the green area represents the data for which the prediction error of the three characteristics of psychology and ideological and political cognition teaching is within 2%. This green area can intuitively see the distribution of most of the prediction error values.

It can be seen from Figure 4 that the prediction errors of the three psychological ideological with political characteristics are all within a reasonable range. These three kinds of errors can meet the teaching reform tasks of psychology and ideology in universities. However, the values of these three errors are also in a large range, and it is also difficult to grasp the direction of the teaching tasks of psychology and ideology. In general, the largest characteristic error of teaching mental health situation and ideological with political aspects comes from the characteristics of student behavior information, which is 3.01%. The smallest error also reaches 2.67%, which is a prediction of the content characteristics of ideological with political teaching. The relationship between student behavior characteristics and time is relatively large, which is difficult to grasp only by the ACNN method.

Through the analysis of Figure 4, it can be found that only using the ACNN method to predict the three eigenvalues of ideological with political and psychological education will have a specific higher error, but it is also a usable prediction error. This study further used the ACNN-GRU method to study the accuracy of big data methods in predicting three eigenvalues of ideological with political and psychological education. Figure 5 shows the prediction errors of three eigenvalues of ideological with political and psychological education using the ACNN-GRU method. In Figure 5, each two represents a feature of psychology and ideological and political cognition teaching, and the left one represents the predicted value of psychological and ideological and political cognition teaching using the ACNN method. The predicted values on the right representing psychological and instructional cognitive teaching characteristics utilize the ACNN-GRU method. From Figure 5, it can be seen intuitively that the prediction errors of the three characteristics of psychology and ideology have been greatly reduced. For the characteristics of student behavior, the prediction error is reduced from 3.01% to 2.66%. For the characteristics of psychological teaching content, the prediction error is reduced from 2.78% to 1.96%. This shows that the ACNN-GRU method has higher accuracy compared with the ACNN method in predicting three characteristics of psychology and ideology.

Figures 4 and 5 show the average prediction error of the eigenvalues of ideological with political and psychological education in universities, which can only reflect the overall effect of the ACNN-GRU and ACNN methods in predicting

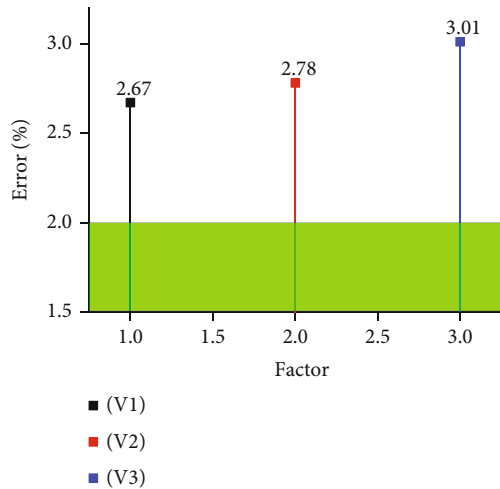


FIGURE 4: Prediction error of related eigenvalues of ideological with political and psychological education in universities using ACNN method.

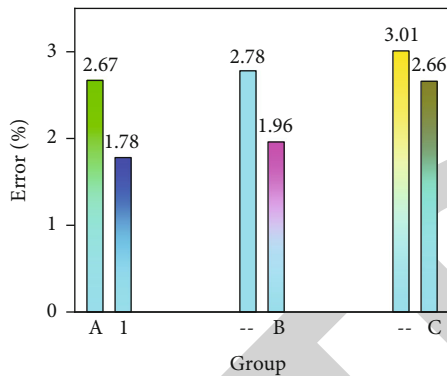


FIGURE 5: Prediction error of related eigenvalues of ideological with political and psychological education in universities using ACNN-GRU method.

the eigenvalues of ideological with political and psychological education. In order to further demonstrate the prediction effect of the ACNN-GRU method on different individual characteristics, this study selected 24 groups of ideological with political teaching content characteristics for analysis. Figure 6 shows the prediction error distribution of the content characteristics of ideological with political teaching in teaching mental health situation and ideological with political aspects. For the prediction error distribution of the content characteristics of ideological and political teaching, the reason for the large fluctuation here may be due to the relatively large fluctuation of the content characteristics of ideological and political teaching itself. Most of the feature values are close to the interval of the training set. From Figure 6, it can be seen that most of the prediction errors of the 24 groups of ideological with political teaching content characteristics are within 2%, and only one group of data has an error of more than 2%. There are also some ideological with political teaching content characteristics. The prediction error of the content characteristics is within 1%. This is

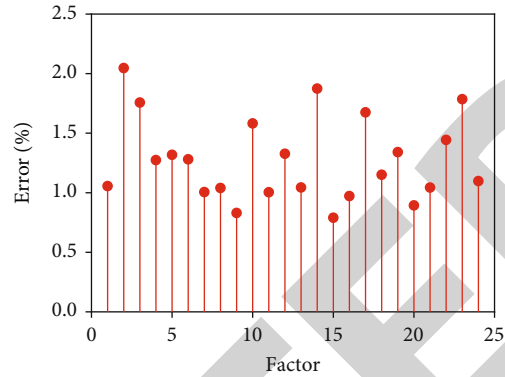


FIGURE 6: Prediction error distribution of content characteristics of ideological with political teaching.

enough to illustrate the accuracy and reliability of the ACNN-GRU method in predicting the content of ideological with political teaching. Regardless of global accuracy or individual accuracy, the ACNN-GRU method can predict the characteristics of ideological with political teaching content.

Through the previous research, it can be found that the prediction error of the content characteristics of psychological teaching is larger than the prediction error of the content characteristics of ideological with political teaching. In this study, in order to further illustrate the effectiveness of ACNN-GRU, it still selected 24 groups of characteristics of psychological teaching content for analysis. Figure 7 shows the distribution of predicted values and actual values of psychological teaching content characteristics of college teaching mental health situation and ideological with political aspects. In Figure 7, the reason for the large differences in the data sets of psychological teaching cognitive content characteristics may be due to the relatively large fluctuations in the psychological teaching cognitive content. There are great differences in the content of psychological teaching at different times. The box plot can also intuitively see the distribution of the average and extreme values of the characteristics of the psychological teaching content. From the distribution of data values of psychological teaching content features, the ACNN-GRU method can accurately predict psychological teaching content characteristics, because the size and distribution of data values are in good agreement with the actual psychological teaching content characteristics. Although there are peaks and valleys in the data distribution of psychological teaching content characteristics, the ACNN-GRU method can still perform the task of predicting psychological teaching content characteristics well. From the perspective of the average and extreme value of the characteristics of psychological teaching content, the predicted value and the actual value of the two eigenvalues are also in good agreement. This shows that the ACNN-GRU method has high reliability in predicting the characteristics of psychological teaching content.

From Figures 4 and 5, it can be seen that the prediction error of student behavior characteristics is the largest among the three psychological and ideological with political teaching characteristics. Similarly, this study also selected 24

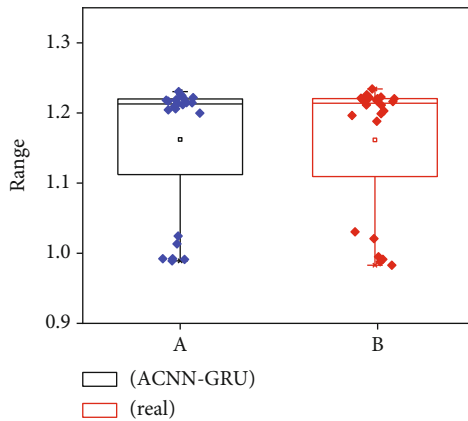


FIGURE 7: Distribution of predicted value and actual value of psychological teaching content characteristics.

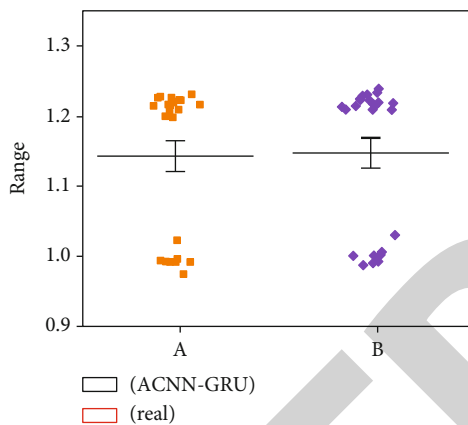


FIGURE 8: Distribution of predicted and actual values of student behavior characteristics.

groups of students' behavioral characteristics for accuracy analysis. Figure 8 shows the distribution of predicted and actual values of student behavior characteristics in teaching mental health situation and ideological with political aspects. In Figure 8, the black line represents the average value of the student behavior information feature value, which includes the average value of the predicted value and the actual value. The two ends of the black line represent the extreme values of the information characteristic of student behavior. The large differences in the data values of the student behavior characteristics may be due to the large differences in the student groups in the process of collecting the student behavior characteristic data sets. The characteristics of student behavior are similar to the characteristics of psychological teaching content, and it also has peaks and valleys. For big data theory, this distribution of peaks and valleys is more difficult to predict. However, the ACNN-GRU method can also better predict the behavioral characteristics of students in teaching mental health situation and ideological with political aspects. ACNN-GRU has already predicted the data values of student behavior characteristics, whether it is the peak value or the peak-to-valley value distribution of student

behavior characteristics. This shows that the ACNN-GRU method has high reliability for predicting the characteristics of students' behavior in psychology and ideology.

5. Conclusions

In today's era, college students will face greater academic and employment pressure, which can easily cause the mental health situation problems. Only by maintaining a positive and optimistic attitude will you avoid mental health situation problems. Mental health situation problems can easily cause the extreme events. The cognition Ideological with political can impart a positive and optimistic attitude to life and life concepts to students. Once students have a positive and objective attitude, it can also make it easier for students to receive the cognition Ideological with political. Mental health situation education and the cognition Ideological with political are a complementary relationship. However, with the advancement of technology, traditional teaching methods may not meet the needs of teachers and students to understand psychological and ideological with political knowledge. There will be a lot of cumbersome data and knowledge points in psychology and ideological and political cognition, and traditional teaching methods may be difficult to teach according to different students. Big data technology can carry out relevant psychological and ideological and political cognition teaching according to the different situations of students.

This study uses big data theory to study three characteristics of psychological teaching content, ideological with political teaching content and student behavior in college teaching mental health situation, and ideological with political aspects. First, this study analyzes the error of the ACNN method in predicting the eigenvalues of ideological with political and psychological education. Although the prediction errors of the three characteristics can meet the teaching needs of psychology and ideology, the numerical values of these three errors are relatively large. A single ACNN method has a relatively large error in predicting the relevant characteristics of psychology and ideological and political cognition, with the largest error reaching 3.01%. This error value is not conducive to college teachers and students' learning of psychology and ideological and political cognition. Then, this study analyzes the accuracy and efficiency of the ACNN-GRU method in predicting the eigenvalues of ideological with political and psychological education. Compared with the single ACNN method, the prediction accuracy of the ACNN-GRU method has been significantly improved for three eigenvalues of ideological with political and psychological education. The largest prediction error comes from the characteristics of students' behavior, and this part of the error is only 2.66%. ACNN and GRU have achieved relatively good results in predicting the psychological and ideological and political situation in colleges and universities. The model after this training can be directly applied to the actual cognitive teaching of psychology and ideological and political. This enables knowledge matching based on the needs of students and teachers.

Research Article

Influences of Ultrasonic Image-Guided Erector Spinae Plane Block on Postoperative Pulmonary Air Content of Lung Carcinoma Patients Undergoing Thoracoscopic Surgery

Xiuqing Xu, Shengrong Yang, and Pei Gao 

Department of Anesthesiology, Binhai County People's Hospital, Affiliated Hospital of Kangda College of Nanjing Medical University, Yancheng, 224500 Jiangsu, China

Correspondence should be addressed to Pei Gao; 1931011315@siit.edu.cn

Received 3 June 2022; Revised 26 June 2022; Accepted 1 August 2022; Published 6 September 2022

Academic Editor: Pan Zheng

Copyright © 2022 Xiuqing Xu et al. This is an open access article distributed under the Creative Commons Attribution License, which permits unrestricted use, distribution, and reproduction in any medium, provided the original work is properly cited.

To investigate the influences of ultrasonic image-guided erector spinae plane block (ESPB) on postoperative pulmonary air content of lung carcinoma patients undergoing thoracoscopic surgery, 42 patients performed with thoracoscopic radical surgery for lung carcinoma were selected. The patients in the experimental group were performed with ultrasound-guided unilateral ESPB and intravenous general anesthesia. The patients in the control group only underwent intravenous anesthesia. The changes in postoperative pulmonary air content between the two groups were compared. After that, all included patients were divided into the experimental (senior) group (13 cases), the experimental (adult) group (8 cases), the control (senior) group (11 cases), and the control (adult) group (10 cases) according to age. The changes in postoperative pulmonary air content of patients in the four groups were compared. The results showed that lung ultrasound score (LUS) of patients in experimental group was 6.4 ± 3.2 points 0.5 hour after catheter extraction and LUS was 4.1 ± 2.3 points 20 to 30 hours. Both scores were remarkably lower than those of patients in control group ($P < 0.05$). LUS of lower left anterior area, upper left posterior area, lower left posterior area, upper right posterior area, and lower right posterior area of patients in experimental group was all apparently lower than those in control group 0.5 hour after catheter extraction ($P < 0.05$). LUS of upper left posterior area, lower left posterior area, lower right anterior area, upper right posterior area, and lower right posterior area of patients in experimental group was all remarkably lower than those in control group 20 to 30 hours after surgery ($P < 0.05$). LUS of senile patients and middle-aged patients in experimental group 0.5 hour after catheter extraction was 8.01 ± 2.48 points and 5.93 ± 3.91 points, respectively, which were both notably lower than those in control group ($P < 0.05$). Ultrasound-guided ESPB exerted fewer influences on lung and could effectively improve postoperative pulmonary air content among patients. Hence, it was worthy of clinical promotion.

1. Introduction

Lung carcinoma is one of the commonest malignant tumors. Over the past 50 years, the incidence of lung carcinoma has been rising year by year [1]. The cause of lung carcinoma is still not very clear. As population aging and environmental pollution gradually become serious, the incidence and mortality of lung carcinoma will further increase. At present, the main clinical treatment method for lung carcinoma is surgical tumor resection. In the early stage of lung carcinoma,

therapeutic goal can be achieved by surgical treatment [2]. Thoracoscopic surgery is characterized by small incision, less trauma, and good effect. It is replacing most traditional thoracotomy incisions [3]. Thoracic surgery results in acute postoperative pain, which is related to muscle separation at incision, rib shrinkage, rib resection, and damage to the intercostal nerve. Poor pain management may aggravate postoperative pulmonary dysfunction among patients [4]. During thoracoscopic surgery, the stress reaction caused by surgical trauma is reduced. However, patients tend to

weaken the range of respiratory movement and reduce coughing, expectoration, and turning over if postoperative analgesia is poor. As a result, the risk of postoperative atelectasis and lung infection is increased [5].

After thoracic surgery, it is difficult to achieve the best analgesic effect by adopting a single analgesic program. The increase of the dose of opioids results in the growth of the incidence of nausea, vomiting, and other adverse reactions [6]. Local anesthetic shows good analgesic effect and high safety. The application of multimode analgesic methods can help patients recover as soon as possible after surgery [7]. Thoracic epidural block and thoracic paraspinous nerve block are the gold standards of regional analgesia during thoracotomy. According to relevant studies, pain score is affected to some extent [8]. In recent years, the development of ultrasound visualization technology promotes the popularization of nerve block anesthesia. With the guidance of ultrasound, nerve block takes effect in shorter time. Besides, nerve block operation is less time-consuming, success rate is increased, and the incidence of related complications is reduced [9]. Erector spinae plane block (ESPB) is explained as follows. According to different types of surgeries, the corresponding spinal nerve segment is selected, and local anesthetic is injected into fascia in erector spinae to block the nerve in the fascia using appropriate methods. As a result, analgesic effects are shown [10]. Some studies demonstrate that ultrasound-guided ESPB has the similar analgesic effect with paravertebral block. In contrast, it is easier to perform ultrasound-guided ESPB with less time [11].

Some studies show that different levels of postoperative damages to gas exchange or respiratory mechanics occur among all patients even if their pulmonary function is normal without other diseases before anesthesia surgery. The incidence of atelectasis is about 90% [12]. The main cause is that muscular relaxants used for general anesthesia, especially long-acting muscular relaxants, inhibit the function of patients' respiratory muscle, which leads to the reduction in lung air flow in patients' bodies. To deepen anesthesia, heavy use of anesthetic inhibits the excitatory response of the ventilator. In addition, the use of general anesthetic leads to the increased permeability of pulmonary capillary as well as the decreased content of macrophage in patients' bodies and inhibits the release of active substances on the surface of pulmonary alveoli [13]. In addition, adjuvant mechanical ventilation is required because anesthesia inhibits patients' respiratory function. However, respiratory system resistance is increased without muscle tone in this case. During mechanical ventilation, pulmonary alveoli collapses, shearing injury occurs, and pulmonary compliance changes abnormally. A variety of reasons lead to the reduction in patients' functional residual capacity and lung air content. What is worse, these reasons cause pulmonary vascular shunt and pulmonary gas exchange cannot occur, which further develops into atelectasis [14].

Therefore, the patients undergoing thoracoscopic radical surgery for lung carcinoma were selected and performed with ultrasound-guided ESPB anesthesia method as well as intravenous anesthesia method. The changes in postoperative lung air content of patients were compared, and the

influences of ultrasound-guided ESPB anesthesia on postoperative lung air content of patients undergoing thoracoscopic radical surgery for lung carcinoma were investigated to provide reference values for subsequent clinical surgical treatment of lung carcinoma and improve therapeutic effect.

2. Research Methods

2.1. Objects. Forty-two patients undergoing thoracoscopic radical surgery for lung carcinoma (55 ± 4.3 years old) in hospital were selected. Their body mass index (BMI) was $22 \pm 1.5 \text{ kg/m}^2$. They were randomly divided into two groups. 21 patients in control group were performed only with intravenous general anesthesia. 21 patients in experimental group underwent ultrasound-guided unilateral ESPB and intravenous general anesthesia. Further grouping: according to whether the patient was 65 years old or above, they were divided into elderly group and middle-aged group, including experimental (elderly) group (13 cases), experimental (adult) group (8 cases), control (elderly) group (11 cases), and control (adult) group (10 cases). All included research objects had signed informed consent forms, and this study had been approved by ethics committee of hospital.

Inclusion criteria: patients with American Society of Anesthesiologists (ASA) level I and II and BMI below 30 kg/m^2 ; patients with generally normal pulmonary function on admission; patients without previous history of radiotherapy and chemotherapy and using antipsychotic drug, antisympathetic drug, antipsychotic drug, and drugs interfering with adrenal function for a period of time before surgery; patients who could normally understand and be cooperative throughout the experiment.

Exclusion criteria: patients with hypertension level at II or above and complicated cerebrovascular disease; patients with complicated empyema and puncture site infection; patients with serious circulation system disease; patients with abnormal curvature of the spine and space occupying lesion of erector spinae; patients with serious liver and renal insufficiency.

2.2. Anesthesia Method. The detailed survey of patients' condition was carried out, and the risks and possible accidents of surgical anesthesia were explained to patients. Relevant knowledge about anesthesia were introduced to patients, and they were instructed to sign informed consent forms. Routine fasting lasted for 8 hours and abstinence lasted for 4 hours before surgery.

Anesthesia methods were explained as follows. After entering operating room, upper limb venous channel was routinely established. 10 ml/kg sodium lactate Ringer's injection was infused. Besides, mask oxygen inhalation was implemented, and oxygen flow was 2 L/min . Under local anesthesia, radial artery puncture was performed for invasive arterial blood pressure monitoring. Puncture and catheterization were performed for right internal jugular vein for the preparation of intraoperative fluid replenishment and venous blood extraction. Besides, electrocardio, pulse, and oxygen saturation were routinely monitored. Patients in

TABLE 1: Scoring standard for pulmonary ultrasonic images.

Image presentation	Scores (value)
Clear A line and lung sliding or 0 to 2 B lines	0
3 or more B lines or small subpleural consolidation separated by smooth pleura line	1
Multiple complicated B lines or they were thickened, and small subpleural consolidation separated by irregular pleura line	2
Solid lung disease	3

TABLE 2: General data on patients.

Groups	Experimental group (21 patients)	Control group (21 patients)
Age (years old)	54 ± 5.8	56 ± 6.2
Gender (male/female)	10/11	8/13
BMI (kg/m ²)	21 ± 3.6	22 ± 2.4
ASA level (case, I/II)	6/15	9/12
Anesthesia time (min)	128.3 ± 36.7	125.8 ± 38.2

experimental group were instructed to take lateral position and receive single ESPB at T5 horizontal transverse process under the guidance of ultrasound. 25 mL of 0.4% ropivacaine was used for local anesthesia. After 20 minutes, ice method was adopted to test block plane at the anterior axillary line of the affected side and assess if puncture was routine. If the plane was less than three segments, puncture failed and was not included in the research. The patients in control group were performed only with intravenous general anesthesia. Before the anesthesia induction, 100 mL physiological saline was injected with 0.5 $\mu\text{g}/\text{kg}$ dexmedetomidine hydrochloride, and intravenous drip was carried out within 15 minutes. After that, all patients received intravenous general anesthesia and the venous injection of 1.5-2.0 mg/kg propofol, 0.5 $\mu\text{g}/\text{kg}$ sufentanil, and 1.5 mg/kg cis-atracurium. Double lumen bronchial intubation was implemented, and adjuvant mechanical ventilation was carried out after the accurate positioning of fiber bronchoscope. Intravenous micropump was used to pump propofol (4-6 mg/kg/h) and remifentanil (0.1-1 $\mu\text{g}/\text{kg}/\text{h}$) to maintain anesthesia. Cis-atracurium was injected intermittently. According to the stimulation intensity, cyclic change, and bispectral index of intraoperative operation, the dosage of propofol and remifentanil was adjusted, and the value of bispectral index was kept between 40 and 60. Normally, blood pressure should fluctuate within $\pm 20\%$ of basic blood pressure. Insulation measure should be taken during the surgery. Target-oriented transfusion treatment was adopted, and PetCO₂ was kept between 30 and 40 mmHg. 100 g flurbiprofen axetil was offered for patients to perform analgesic cohesion half an hour before skin suture. After surgery, the patients in the two groups carried out patient-controlled intravenous analgesia (PCIA). Analgesic pump formulation was as follows. 1.0 $\mu\text{g}/\text{mL}$ sufentanil, 32 mg ondansetron hydrochloride tablets, and physiological saline were diluted to 100 mL. Background infusion was 2.5 mL/h per time

followed by 2.5 mL, and the lock time was 25 minutes. After the surgery, routine vital sign monitoring and extubation were performed according to patients' situation.

Ultrasound-guided ESPB was explained as follows. In the experiment, ultrasound-guided unilateral ESPB based on minor axis in-plane technique was utilized. Based on ultrasonic imaging, the trajectory of the needle tip in the needle track could be accurately seen. The needle tip reached the surface of transverse process and the deep surface of erector spinae safely and conventionally. Patients were asked to take lateral position. T5 spinous process was determined and then labeled. Conventional disinfection and skin preparation were performed. After that, the ultrasonic probe was placed longitudinally parallel to the spine at 2 to 3 cm outside T5 spinous process. Through ultrasonic screen imaging, trapezius muscle, rhomboideus, erector spinae, and T5 transverse process could be accurately observed from top to bottom. A 22G puncture needle was inserted from head to end. The needle tip position was determined by injecting 1-2 mL of physiological saline after no air or blood was pumped back. Next, the local anesthetic solution was injected into the surface of T5 transverse process and the deep surface of erector spinae. If the local anesthetic solution diffused in the plane of erector spinae fascia and erector spinae elevated, block operation was successful. After 20 minutes, ice method was adopted to feel and test the block plane at anterior axillary line level.

2.3. Division of Lung Ultrasound Regions. Ultrasound equipment was used. Twelve division method was adopted for examination [15, 16]. Bilateral anterior axillary line and posterior axillary line were set as the boundary. Lung area was divided into anterior, lateral, and posterior areas. Besides, bilateral nipple connection lines were set as the boundary. The anterior, lateral, and posterior areas were divided into upper left anterior area, lower left anterior area, upper left lateral area, lower left lateral area, upper left posterior area, lower left posterior area, upper right anterior area, upper right posterior area, upper right lateral area, lower right lateral area, upper right posterior area, and lower right posterior area. A low-frequency convex array probe with the frequency of 2 to 5 MHz was used to collect ultrasonic images from 12 areas of the whole lung. During the collection, the pulmonary ultrasonic images of each area were preserved for 15 s. The sites where pulmonary air content images changed most obviously were collected firstly. If the collected ultrasonic images were not clear and they could not display the real change of patients' lungs, more videos needed to be recorded or more images should be collected.

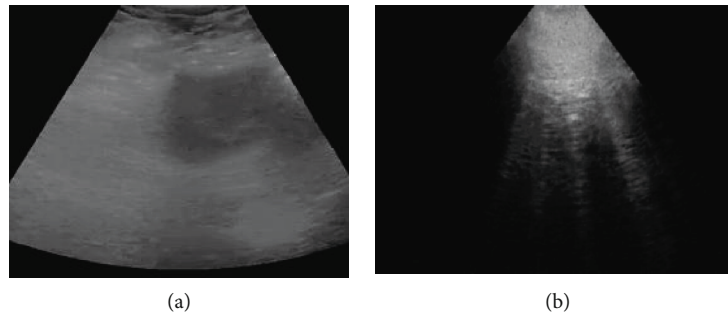


FIGURE 1: Pulmonary ultrasound. (a) Ultrasonic image 0.5 hours after extubation. (b) Ultrasonic image 20 hours after surgery.

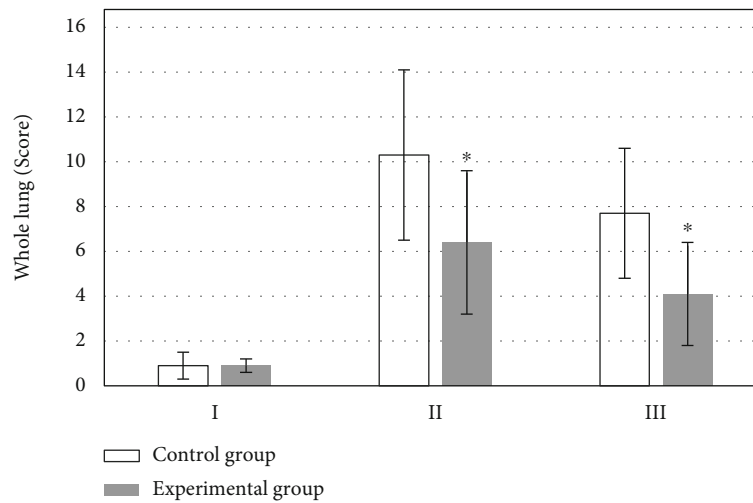


FIGURE 2: Comparison of whole lung LUS. I: the day of surgery; II: 0.5 h after extubation; III: 20-30 h after operation. *Compared with control group, $P < 0.05$.

2.4. Ultrasound Image Scoring. After imaging acquisition, the semiquantitative scoring standard was adopted to pulmonary ultrasonic signs. According to LUS, the severity of the changes in pulmonary air content was determined. The score for each pulmonary ultrasonic area ranged between 0 and 3 points. The total score of all 12 areas in the whole lung ranged between 0 and 36 points. 0 point indicated no abnormality in air content. A lower LUS suggested that the difference in the change of pulmonary air content was less significant and higher level of pulmonary air content. A higher LUS meant more remarkable reduction in pulmonary air content and worse condition, as displayed in Table 1.

2.5. Statistical Methods. SPSS 22.0 statistical software was utilized for analysis. Measurement data were expressed with mean \pm standard deviation ($\bar{x} \pm s$). General data were analyzed with independent sample t test. Paired sample t test was used to compare pulmonary LUS of healthy volunteers at different time points. $P < 0.05$ indicated that the difference showed statistical meaning.

3. Results

3.1. General Data. Age, BMI, ASA level, anesthesia time, and other general data of patients in the two groups demon-

strated no statistical differences ($P > 0.05$), as displayed in Table 2.

3.2. Lung Ultrasound Images. Images were acquired when patients were visited on the morning of surgery day or the day before surgery. In analysis of a 56-year-old male patient, images were acquired 0.5 hour after the tracheal tube was removed and postoperative extubation was indicated. Images were acquired 20 to 30 hours after surgery, indicating that ultrasound can clearly show the lung disease in the lungs (Figure 1).

3.3. Whole Lung LUS of Patients. The difference in LUS of patients in the two groups on the morning of surgery day revealed no statistical meaning ($P > 0.05$). LUS of patients in experimental group (6.4 ± 3.2 points) was remarkably lower than that of patients in control group (10.3 ± 3.8 points) 0.5 hour after catheter extraction, and the difference was significantly significant ($P < 0.05$). LUS of patients in experimental group (4.1 ± 2.3 points) was notably lower than that of patients in control group (7.7 ± 2.9 points) 20 to 30 hours after surgery, and the difference showed statistical meaning ($P < 0.05$), as illustrated in Figure 2.

3.4. LUS of 12 Pulmonary Areas of Patients in the Two Groups. Figure 3(a) is the upper left anterior region;

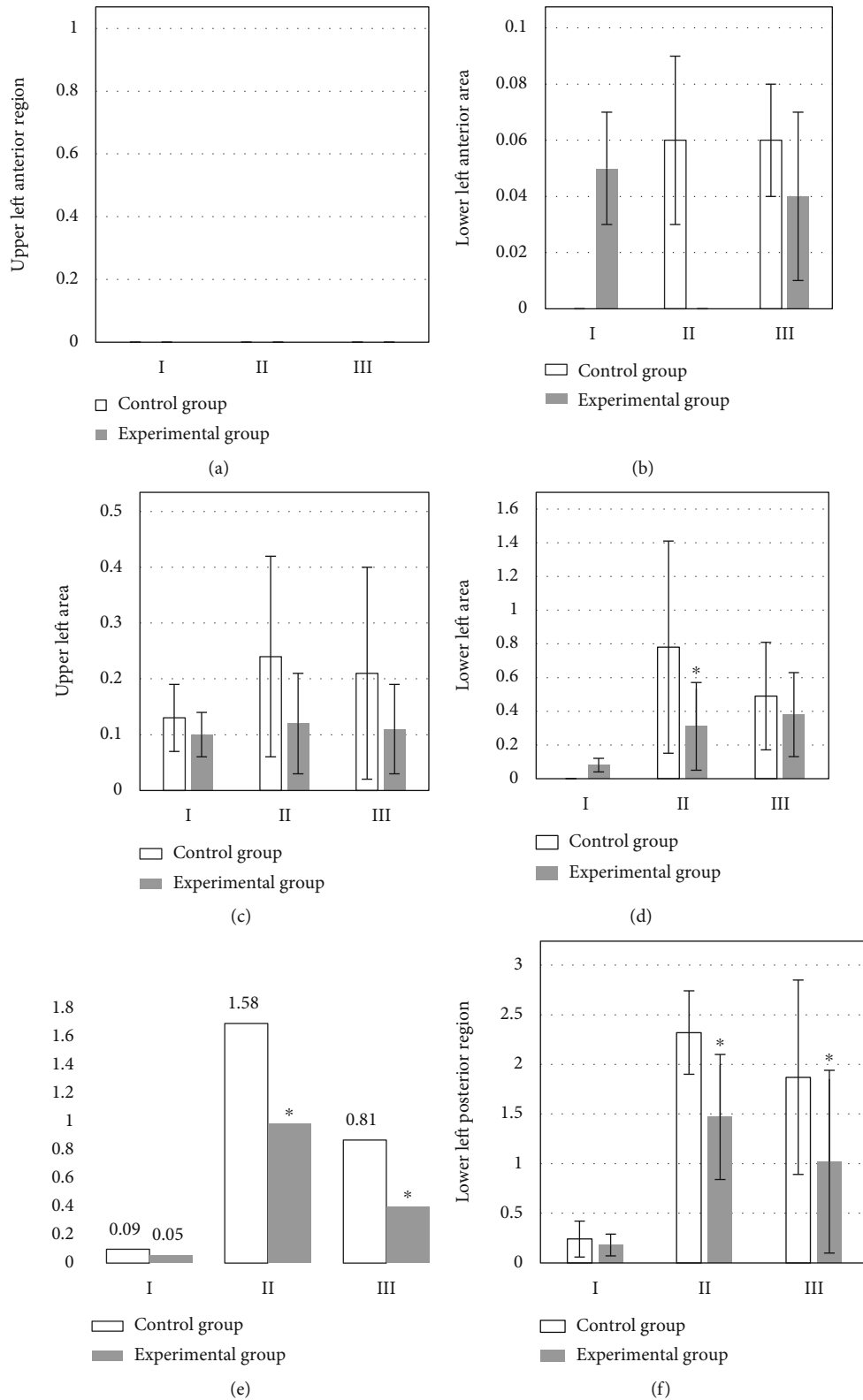


FIGURE 3: Comparison of left lung LUS scores. I: the day of surgery; II: 0.5 h after extubation; III: 20-30 h after operation. (a) The upper left anterior region. (b) The LUS score results of the lung region in the lower left region at different times. (c) The LUS score results of the lung region in the upper left region at different times. (d) The lung region in the lower left region at different times. (e) The LUS score results of the left upper posterior region at different times. (f) The LUS score results of the left lower posterior region at different times. *Compared with control group, $P < 0.05$.

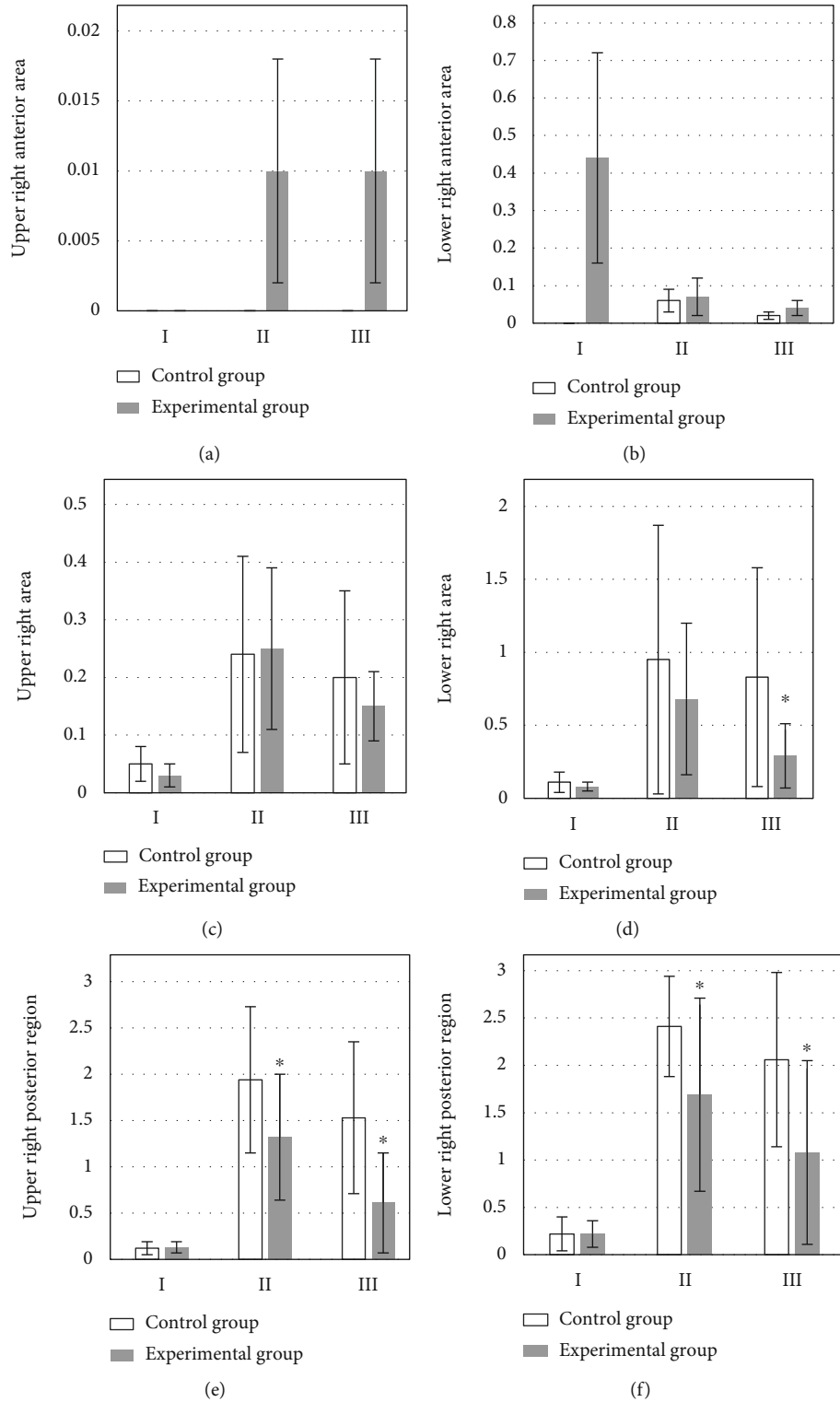


FIGURE 4: Comparison of right lung LUS scores. I: the day of surgery; II: 0.5 h after extubation; III: 20-30 h after operation. (a) The upper right anterior area. (b) The LUS score results of the lower right anterior area at different times. (c) The LUS score results of the upper right area at different times. (d) The lower right area at different times. (e) The upper right posterior area. (f) The LUS score results of the lung area at different times in the lower right posterior area. *Compared with control group, $P < 0.05$.

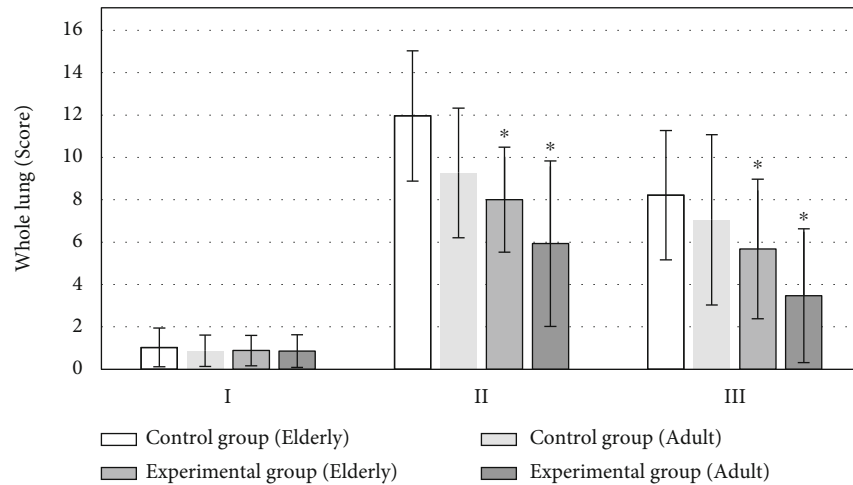


FIGURE 5: Whole lung LUS of patients at different age groups. I: the day of surgery; II: 0.5 h after extubation; III: 20-30 h after operation. * Compared with control group, $P < 0.05$.

Figure 3(b) is the LUS score results of the lung region in the lower left region at different times, 20-30 hours after the operation, the LUS score of the lower left anterior area in the control group was higher than that in the experimental group.

Figure 3(c) is the LUS score results of the lung region in the upper left region at different times. The figure shows that the upper left area of the control group is higher than that of the observation group in the three time periods.

Figure 3(d) is the lung region in the lower left region at different times. LUS score results: the figure shows that the upper left area of the control group is higher than that of the observation group in the three time periods.

Figure 3(e) is the LUS score results of the left upper posterior region at different times, the LUS score in the lower left area of the observation group was significantly lower than that of the experimental group at 0.5 hours and 20-30 hours after extubation ($P < 0.05$).

Figure 3(f) is the LUS score results of the left lower posterior region at different times. The LUS score in the lower left area of the observation group was significantly lower than that of the experimental group at 0.5 hours and 20-30 hours after extubation ($P < 0.05$).

Figure 4(a) is the upper right anterior area; Figure 4(b) is the LUS score results of the lower right anterior area at different times. The LUS score of the lower right anterior area of the observation group was higher than that of the control group at 0.5 hours after extubation and 20-30 hours after operation. Figure 4(c) is the LUS score results of the upper right area at different times. On the day of operation and 20-30 hours after extubation, the LUS score in the upper right area of the control group was higher than that of the observation group, but the LUS score of the upper right area of the control group was lower than that of the observation group at 0.5 hours after extubation. Figure 4(d) is the lower right area at different times. The LUS score results of the lung area: the lower right area of the control group was higher than that of the experimental group in the three time periods, but the experimental group was significantly lower

than the control group at 20-30 hours after surgery ($P < 0.05$). Figure 4(e) is the upper right posterior area. The LUS score in the upper right posterior area of the observation group was significantly lower than that of the control group at 0.5 h and 20-30 hours after extubation ($P < 0.05$). Figure 4(f) is the LUS score results of the lung area at different times in the lower right posterior area. The LUS score in the lower right posterior area of the observation group was significantly lower than that of the control group at 0.5 h after extubation and 20-30 hours after operation ($P < 0.05$).

3.5. *Whole Lung LUS of Patients at Different Age Groups.* The differences in LUS of patients in the four groups on the morning of surgery day all showed no statistical meaning ($P > 0.05$). LUS of elderly patients in experimental group (8.01 ± 2.48 points) was obviously lower than that of elderly patients in control group (11.96 ± 3.08 points) 0.5 hour after catheter extraction, and the difference had statistical meaning ($P < 0.05$). LUS of middle-aged patients in experimental group (5.93 ± 3.91 points) was remarkably lower than that of middle-aged patients in control group (9.27 ± 3.06 points), and the difference demonstrated statistical meaning ($P < 0.05$). LUS of elderly patients in experimental group (5.68 ± 3.29 points) was dramatically lower than that of elderly patients in control group (8.22 ± 3.05 points) 20 to 30 hours after surgery, and the difference had statistical meaning ($P < 0.05$). LUS of middle-aged patients in experimental group (3.47 ± 3.16 points) was remarkably lower than that of middle-aged patients in control group (7.05 ± 4.02 points), and the difference revealed statistical meaning ($P < 0.05$), as shown in Figure 5.

3.6. *LUS of 12 Pulmonary Areas of Patients at Different Age Groups in Experimental Group.* Figure 6(a) is the upper left anterior region; Figure 6(b) is the LUS score results of 12 lung regions of patients in different age groups in the lower left region. On the day of surgery and 20-30 hours after surgery, the LUS score of the elderly patients in the experimental group was higher than that of the young patients.

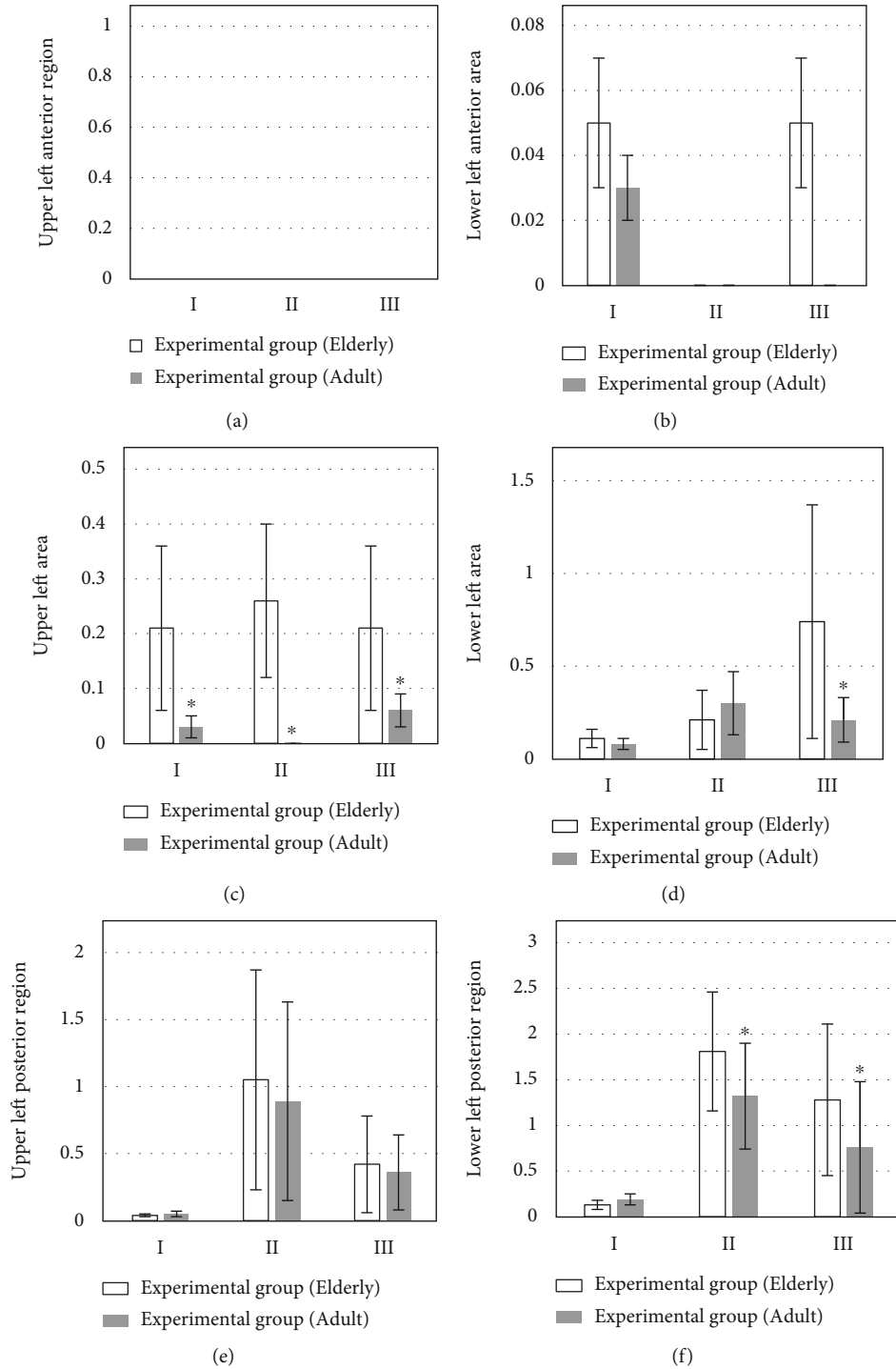


FIGURE 6: Comparison of left lung LUS scores of patients at different age groups. I: the day of surgery; II: 0.5 h after extubation; III: 20-30 h after operation. (a) The upper left anterior region. (b) The LUS score results of 12 lung regions of patients in different age groups in the lower left region. (c) The LUS score results of 12 lung regions of patients of different age groups in the upper left region. (d) The LUS score results of 12 lung areas of patients in different age groups in the lower left area. (e) The LUS score results of 12 lung areas of patients in different age groups in the upper left posterior area. (f) The LUS score of 12 lung areas of patients in different age groups in the lower left posterior area. * Compared with elderly group, $P < 0.05$.

Figure 6(c) is the LUS score results of 12 lung regions of patients of different age groups in the upper left region, the scores of the upper left area of the young patients in the experimental groups in the three time periods were significantly

cantly lower than those of the elderly patients ($P < 0.05$). Figure 6(d) is the LUS score results of 12 lung areas of patients in different age groups in the lower left area, the LUS scores in the lower left area of the young group patients

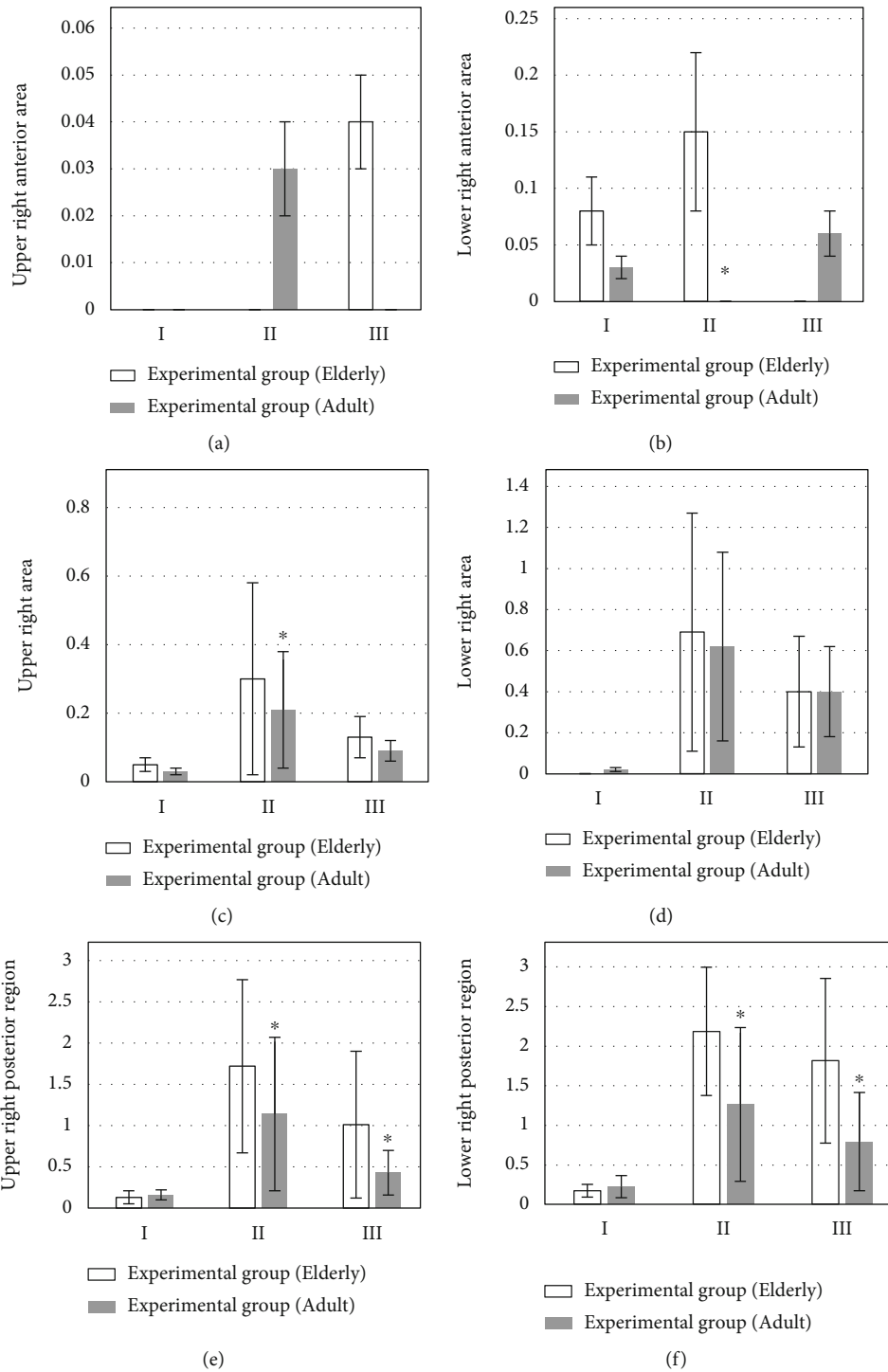


FIGURE 7: Comparison of right lung LUS of patients at different age groups. I: the day of surgery; II: 0.5 h after extubation; III: 20-30 h after operation. (a) The upper right anterior region. (b) The LUS score results of 12 lung regions of patients in different age groups in the lower right region. (c) The LUS score results of 12 lung regions of patients in different age groups in the upper right region. (d) The LUS score results of 12 lung areas of patients in different age groups in the lower right area. (e) The LUS score results of 12 lung areas of patients in different age groups in the upper right posterior area. (f) The 12 lung areas of patients in different age groups in the lower right posterior area district LUS score. *Compared with elderly group, $P < 0.05$.

were lower than those of the elderly group on the day of surgery and 20-30 hours after the operation. Figure 6(e) is the LUS score results of 12 lung areas of patients in different age groups in the upper left posterior area, 0.5 hours after

extubation and 20-30 hours after surgery, the score of the left upper posterior area in the youth group was lower than the LUS score in the elderly group. Figure 6(f) is the LUS score of 12 lung areas of patients in different age groups in

the lower left posterior area result. At 0.5 hours after extubation and at 20-30 hours after operation, the scores of the left lower posterior area of the youth group were significantly lower than the LUS scores of the elderly group ($P < 0.05$).

Figure 7(a) is the upper right anterior region. The LUS score of the upper right anterior area of the youth group was higher than that of the elderly group after extubation for half an hour, and the score of the elderly group after extubation for 20-30 hours was higher than that of the youth group; Figure 7(b) is the LUS score results of 12 lung regions of patients in different age groups in the lower right region. The LUS score of the elderly group was higher than that of the young group after half an hour of extubation, and the difference was significant ($P < 0.05$). Figure 7(c) is the LUS score results of 12 lung regions of patients in different age groups in the upper right region, in the three time periods, the scores of the upper right corner of the elderly group were higher than those of the control group, but after 0.5 hours of extubation, the difference was significant ($P < 0.05$). Figure 7(d) is the LUS score results of 12 lung areas of patients in different age groups in the lower right area. Half an hour after extubation and 20-30 minutes after the operation, the LUS score in the lower right area of the elderly group was higher than that of the young group; half an hour after extubation and 20-30 minutes after the operation, the LUS score in the lower right area of the elderly group was higher than that of the young group. Figure 7(e) is the LUS score results of 12 lung areas of patients in different age groups in the upper right posterior area; half an hour after extubation and 20-30 minutes after the operation, the LUS score in the upper right posterior area of the elderly group was higher than that of the young group, and the difference was significant ($P < 0.05$). Figure 7(f) is the 12 lung areas of patients in different age groups in the lower right posterior area district LUS score results. Half an hour after extubation and 20-30 minutes after the operation, the LUS score in the lower right posterior area of the elderly group was higher than that of the young group, and the difference was significant ($P < 0.05$).

4. Discussion

In recent years, ESPB is usually used for the combined anesthesia and multimodal analgesia for abdominal, thoracic, pediatric, and orthopedic surgery [17]. Ultrasound-guided ESPB operation is simple. However, some studies showed that pulmonary air content of most patients changed abnormally, and even atelectasis occurred after general anesthesia surgery with the continuous development and improvement of medical technology and the further study on postoperative lung complications among patients [18]. Hence, ESPB block method was adopted to investigate its influences on postoperative pulmonary air content of patients undergoing thoracoscopic surgery for lung carcinoma, which provided reference values for subsequent clinical surgical treatment for patients with lung carcinoma.

According to the research results, LUS of patients in experimental group 0.5 hour after catheter extraction and 20 to 30 hours after surgery was remarkably lower than

those of patients in control group ($P < 0.05$). LUS scoring result 0.5 hour after catheter extraction suggested that the scores for lower left lateral area, upper left posterior area, lower left posterior area, upper right posterior area, and lower right posterior area of patients in experimental group were all notably lower than those of patients in control group ($P < 0.05$). LUS scoring result 20 to 30 hours after surgery indicated that the scores for upper left posterior area, lower left posterior area, lower right lateral area, upper right posterior area, and lower right posterior area of patients in experimental group were significantly lower than those of patients in control group ($P < 0.05$). According to relevant studies, postoperative continuous adjuvant positive airway pressure ventilation could effectively reduce LUS score and prevent atelectasis [19]. Hence, ESPB could effectively improve postoperative lung air content among patients compared with single intravenous general anesthesia.

LUS of elderly patients and middle-aged patients in experimental group 0.5 hour after catheter extraction and 20 to 30 hours after surgery was remarkably lower than those of patients in control group ($P < 0.05$). LUS of upper left lateral area of adult patients in experimental group on the morning of surgery day was notably lower than that of elderly patients in experimental group. The scores for upper left lateral area, lower left posterior area, lower right anterior area, upper right lateral area, upper right posterior area, and lower right posterior area of middle-aged patients in experimental group 0.5 hour after catheter extraction were all significantly lower than those of patients in control group ($P < 0.05$). LUS scoring result 20 to 30 hours after surgery revealed that the scores for upper left lateral area, lower left lateral area, lower left posterior area, upper right posterior area, and lower right posterior area of patients in experimental group was all obviously lower than those of patients in control group ($P < 0.05$). The above research results demonstrated that the reduction in postoperative pulmonary air content among senior patients was more remarkable than that among adult patients with higher incidence. The research results were consistent with the conclusion that the incidence of postoperative pulmonary complications among senior patients was relatively higher drawn by Ledowski et al. [20].

5. Conclusion

The experiment results showed that both intravenous general anesthesia and ultrasound-guided erector spinae block anesthesia resulted different levels of reduction in pulmonary air content. Compared with that among adult patients, the incidence of the reduction in postoperative pulmonary air content was higher among senior patients. Besides, ultrasound-guided ESPB had fewer influences on postoperative pulmonary air content and improved postoperative pulmonary air content among patients. Due to the impacts of research conditions, the selected sample size is small and the research lasted for a short time, which resulted in insignificant differences between some results. Hence, further study was needed. To sum up, ultrasound-guided ESPB

was conducive to improving postoperative pulmonary air content among patients with application values.

Data Availability

The data used to support the findings of this study are available from the corresponding author upon request.

Conflicts of Interest

The authors declare no conflicts of interest.

Authors' Contributions

Xiuqing Xu and Shengrong Yang contributed equally to this work.

Acknowledgments

This work was supported by Scientific Research and Development Fund of Kangda College of Nanjing Medical University (KD2021KYJJZD116).

References

- [1] M. B. Schabath and M. L. Cote, "Cancer progress and priorities: lung cancer," *Cancer Epidemiology, Biomarkers & Prevention*, vol. 28, no. 10, pp. 1563–1579, 2019.
- [2] H. Hoy, T. Lynch, and M. Beck, "Surgical treatment of lung cancer," *Critical Care Nursing Clinics of North America*, vol. 31, no. 3, pp. 303–313, 2019.
- [3] M. Mun, M. Nakao, Y. Matsuura, J. Ichinose, K. Nakagawa, and S. Okumura, "Video-assisted thoracoscopic surgery lobectomy for non-small cell lung cancer," *General Thoracic and Cardiovascular Surgery*, vol. 66, pp. 626–631, 2018.
- [4] D. Lederman, J. Easwar, J. Feldman, and V. Shapiro, "Anesthetic considerations for lung resection: preoperative assessment, intraoperative challenges and postoperative analgesia," *Ann Transl Med.*, vol. 7, no. 15, p. 356, 2019.
- [5] G. L. Rosboch, E. Ceraolo, I. De Domenici et al., "Impact of analgesia on cancer recurrence and mortality within 5 years after stage I non-small cell lung cancer resection," *Tumori*, vol. 31, p. 3008916211020093, 2022.
- [6] K. A. Thompson-Brazill, "Pain control in the cardiothoracic surgery patient," *Critical Care Nursing Clinics of North America*, vol. 31, no. 3, pp. 389–405, 2019.
- [7] V. S. Ban, R. Bhoja, and D. L. McDonagh, "Multimodal analgesia for craniotomy," *Current Opinion in Anaesthesiology*, vol. 32, no. 5, pp. 592–599, 2019.
- [8] A. De Cassai, D. Bonvicini, C. Correale, L. Sandei, S. Tulgar, and T. Tonetti, "Erector spinae plane block: a systematic qualitative review," *Minerva Anestesiologica*, vol. 85, no. 3, pp. 308–319, 2019.
- [9] C. Kang, D. S. Hwang, J. H. Song et al., "Clinical analyses of ultrasound-guided nerve block in lower-extremity surgery: a retrospective study," *Journal of Orthopaedic Surgery (Hong Kong)*, vol. 29, no. 1, p. 2309499021989102, 2021.
- [10] S. Krishnan and M. Cascella, "Erector spinae plane block," in *StatPearls [Internet]*, StatPearls Publishing, Treasure Island (FL), 2022.
- [11] M. Saadawi, S. Layera, J. Aliste, D. Bravo, P. Leurcharusmee, and Q. Tran, "Erector spinae plane block: a narrative review with systematic analysis of the evidence pertaining to clinical indications and alternative truncal blocks," *Journal of Clinical Anesthesia*, vol. 68, article 110063, 2021.
- [12] M. A. Pritchett, K. Lau, S. Skibo, K. A. Phillips, and K. Bhadra, "Anesthesia considerations to reduce motion and atelectasis during advanced guided bronchoscopy," *BMC Pulmonary Medicine*, vol. 21, no. 1, p. 240, 2021.
- [13] C. Zeng, D. Lagier, J. W. Lee, and M. F. Vidal Melo, "Perioperative pulmonary atelectasis: part I. Biology and mechanisms," *Anesthesiology*, vol. 136, pp. 181–205, 2022.
- [14] D. Lagier, C. Zeng, A. Fernandez-Bustamante, and M. F. Vidal Melo, "Perioperative pulmonary atelectasis: part II. Clinical implications," *Anesthesiology*, vol. 136, pp. 206–236, 2022.
- [15] D. J. Doyle, A. Goyal, and E. H. Garmon, "American Society of Anesthesiologists Classification," in *StatPearls [Internet]*, StatPearls Publishing, Treasure Island (FL), 2022.
- [16] D. Haurilenka, V. Damantsevich, A. Filustsin, and A. Damantsevich, "Diagnostic value of 12-zone lung ultrasound protocol for diagnosing COVID-19-associated pneumonia in outpatients," *Journal of Ultrasonography*, vol. 21, no. 87, pp. e271–e276, 2021.
- [17] S. Bang, J. Chung, W. Kwon, S. Yoo, H. Soh, and S. M. Lee, "Erector spinae plane block for multimodal analgesia after wide midline laparotomy: a case report," *Medicine (Baltimore)*, vol. 98, no. 20, article e15654, 2019.
- [18] H. Jeong, P. Tanatporn, H. J. Ahn et al., "Pressure support versus spontaneous ventilation during anesthetic emergence-effect on postoperative atelectasis: a randomized controlled trial," *Anesthesiology*, vol. 135, no. 6, pp. 1004–1014, 2021.
- [19] C. M. Acosta, M. P. Lopez Vargas, F. Oropel et al., "Prevention of atelectasis by continuous positive airway pressure in anaesthetised children," *European Journal of Anaesthesiology*, vol. 38, no. 1, pp. 41–48, 2021.
- [20] T. Ledowski, Z. Szabó-Maák, P. S. Loh et al., "Reversal of residual neuromuscular block with neostigmine or sugammadex and postoperative pulmonary complications: a prospective, randomised, double-blind trial in high-risk older patients," *British Journal of Anaesthesia*, vol. 127, no. 2, pp. 316–323, 2021.

Research Article

Clinical Efficacy of Glucosamine plus Sodium Hyaluronate for Osteoporosis Complicated by Knee Osteoarthritis and Its Influence on Joint Function and Bone Metabolic Markers

Jing-Jin Yang¹ and Xiu-Mei Zhang² 

¹Department of Endocrinology, The First People's Hospital of Huaihua, Huaihua, 418000 Hunan, China

²Department of Gastroenterology, The First People's Hospital of Huaihua, Huaihua, 418000 Hunan, China

Correspondence should be addressed to Xiu-Mei Zhang; zhangxiumei418000@163.com

Received 9 June 2022; Revised 27 July 2022; Accepted 6 August 2022; Published 30 August 2022

Academic Editor: Pan Zheng

Copyright © 2022 Jing-Jin Yang and Xiu-Mei Zhang. This is an open access article distributed under the Creative Commons Attribution License, which permits unrestricted use, distribution, and reproduction in any medium, provided the original work is properly cited.

Background. Osteoporosis (OP) associated with knee osteoarthritis (KOA) is common in older men and postmenopausal women, and it is important to find reliable and effective treatments for this disease to improve joint function and bone metabolism in this population. **Objective.** To clarify the clinical efficacy of glucosamine (GlcN) plus sodium hyaluronate (SH) for OP complicated by KOA (OP + KOA) and its influence on joint function and bone metabolic markers (BMMs). **Methods.** Admitted from July 2019 to July 2021, 126 patients with OP + KOA were selected, including 76 cases (observation group) treated with GlcN plus SH and 50 cases (control group) given GlcN alone. The pain, joint function, BMMs, and clinical efficacy were evaluated and compared. Pain and joint function assessments employed the Visual Analogue Scale (VAS) and the Western Ontario and McMaster Universities Osteoarthritis Index (WOMAC) plus Lysholm Knee Scoring Scale, respectively. BMMs mainly measured bone gla protein (BGP), serum tartrate-resistant acid phosphatase variant (TRACP)-5b, type I collagen cross-linked C-telopeptide (CTX-1), and bone-specific alkaline phosphatase (BALP). **Results.** Higher posttreatment VAS scores were determined in observation group as compared to control group; observation group showed lower WOMAC scores of joint function and higher Lysholm scores than control group; in terms of BMMs, TRACP-5b and CTX-1 were lower while BGP and BALP were higher in observation group; the curative effect was also higher in observation group. All the above differences were statistically significant. **Conclusions.** GlcN plus SH has definite clinical efficacy in the treatment of OP + KOA, which can not only significantly improve patients' joint function and bone metabolism but also relieve pain, with high clinical popularization value.

1. Introduction

Osteoporosis (OP), a metabolic bone disease characterized by reduction of bone per unit volume and bone microstructure degeneration, has a predilection for elderly men and postmenopausal women and is associated with bone pain and fractures [1]. Knee osteoarthritis (KOA) is a degenerative joint disease in which articular cartilage is destroyed, and subchondral bone is hardened [2]. With the influence of bone degeneration factors, most patients will develop KOA accompanied by OP [3]. This is also related to the fact that the two diseases have common pathogenic factors such as gender, heredity, and inflammation [4]. Patients with OP complicated by knee

KOA (OP + KOA) will experience symptoms such as pain and limited activity, which not only affects their quality of life but also imposes certain burdens on their families and social economy [5]. At present, the treatment options for these diseases are mainly a balanced diet, calcium and vitamin D supplementation, exercise, and other lifestyle measures, as well as drug treatments such as bisphosphonates and teriparatide. The above nondrug treatment methods are challenging for patients, difficult to adhere to and slow to respond, while bisphosphonate, teriparatide, and other drug therapies have toxic side effects with contraindications in some patients [6]. Therefore, it is particularly important to find an effective method to treat OP + KOA.

Glucosamine (GlcN), a natural amino monosaccharide, is the precursor of proteoglycan synthesis and is used in various types of arthritis [7], effectively stimulating chondrocyte synthesis [8]. It has been shown to effectively inhibit granulation growth and vascular exudation in the treatment of osteoarthritis, thus inhibiting delayed allergic reaction [9]. Intra-articular injection of sodium hyaluronate (SH) is a common clinical treatment for OP + KOA [10]. SH is a component of synovial fluid and articular cartilage, which can improve the mechanical lubrication of joints. In addition, it can rebuild and repair the damaged physiological barrier, reduce articular cartilage friction-induced pain, improve joint mobility, and relieve patients' clinical symptoms [11]. Evidence has shown that the effective components of SH injection can also combine with glycoproteins in synovial fluid, thus blocking the inflammatory reaction process and effectively improving patients' diseases [12]. However, there are few studies reporting the application of GlcN plus SH in the treatment of OP + KOA. Consequently, we tested a series of indicators such as bone metabolic markers (BMMs) and joint function, to examine the efficacy of the combined treatment for the disease.

2. Data and Methods

2.1. General Case Data. This study retrospectively enrolled 126 OP + KOA patients admitted from July 2019 to July 2021, including 76 patients (observation group) treated with GlcN plus SH and 50 patients (control group) intervened by GlcN alone. This study was approved by the Academic Ethics Committee of The First People's Hospital of Huaihua. All patients participating in this study were fully aware of the purpose of this study and signed informed consent. All the enrolled cases were diagnosed as OP + KOA by X-ray plain film or CT examination [13], independent of alcohol and drugs, and could correctly understand the relevant contents of the scales used and answer the questions, with the Kellgren-Lawrence (K-L) grade I or II [14], complete general clinical data, and no recent use of other related therapeutic drugs, while those who had received knee joint replacement, with severe mental disorders, allergies to the study medication, and noncompliance with the research were excluded, as well as withdrawals and loss to follow-ups.

2.2. Therapeutic Methods. Both groups received basic treatment, including inflammatory and pain interventions. Patients in control group were treated with GlcN (Kangbide Pharmaceutical, Beijing, China, H20070173), 0.72 g each time, twice daily, for 5 weeks. On this basis, observation group was given SH injection (Bausch & Lomb Freda Pharmaceutical, Shandong, China, H10960136) once a week, 25 mg each time, also for 5 weeks.

2.3. Blood Sampling. Before and 5 weeks after treatment, 5 mL of fasting venous blood was drawn from patients in both groups at 8 am and sent to the laboratory for centrifugation, and the resulting supernatant was stored into anticoagulant tubes. All serum samples were used within 6 h.

2.4. Endpoints

- (1) Visual Analogue Scale (VAS) score [15]: patients' pain degrees were assessed before and after treatment with the VAS, an instrument with a score ranging from 0 (painless) to 10 points (unbearable pain). Higher scores indicate greater pain severity
- (2) The joint function score was evaluated by the Western Ontario and McMaster Universities Osteoarthritis Index (WOMAC, score range: 0-96 points) [16] and Lysholm Knee Scoring Scale (score range: 0-100 points) [17]. The former evaluated knee structure and function, including treatment for pain, stiffness, and joint function. A higher score indicates more severe arthritis. With the latter, patients were assessed for support, colic, locking sensation, joint instability, joint swelling, difficulty in stair-climbing, etc. Higher scores represent better recovery
- (3) Enzyme-linked immunosorbent assays (ELISAs) [18] were also carried out to measure BMMs before and after treatment: the tests were carried out strictly according to the instructions of human BGP, TRACP-5b, CTX-1, and BALP ELISA kits (Shanghai Yuanmu Biotech, Cat. Nos. YM-S0840, YM-SZ0827, YE00708, YM-SZ0822)
- (4) Efficacy evaluation: it was considered a marked response if there was significant relief in lower back and knee joint pain, with restored knee joint activity function; response was defined as alleviated lower back and knee pain compared with before treatment, with improved knee joint motion function; and nonimprovement in the patient's symptoms with aggravated pain after treatment is regarded as nonresponse. overall response rate (ORR) = (marked response + response) cases/total cases \times 100%

In this study, VAS score, WOMAC score, and Lysholm score were secondary endpoints, while BGP, TRACP-5b, CTX-1, BALP, and efficacy were primary endpoints.

2.5. Statistical Methods. Data statistical analysis and visualization adopted SPSS21.0 (SPSS, Inc., Chicago, IL, USA) and GraphPad Prism 6.0 software (GraphPad Software Inc., San Diego, CA, USA), respectively. The method for within-group comparisons of counting data recorded as the number of cases/percentage [n (%)] was the chi-square test, or chi-square continuity correction when the theoretical frequency of the former test was under 5. The mean \pm SD was used to indicate measurement data; for measurement data analysis, independent samples t -test was used for between-group comparisons, while paired t -test was used for within-group ones. The threshold of significance was $P < 0.05$ in this research.

3. Results

3.1. General Information. As shown in Table 1, the two cohorts of patients were nonsignificantly different in mean age, average course of disease, body mass index, smoking

TABLE 1: Comparison of general data [n (%)] (mean \pm SD).

Classification	Observation group ($n = 76$)	Control group ($n = 50$)	t/χ^2	P
Average age (years old)	52.07 \pm 5.07	53.14 \pm 5.39	1.130	0.261
Average course of disease (years)	3.80 \pm 1.41	3.56 \pm 1.55	0.898	0.371
Body mass index (kg/m ²)	24.70 \pm 2.54	24.04 \pm 2.11	1.523	0.130
Smoking history			2.119	0.145
Yes	45 (59.21)	23 (46.00)		
No	31 (40.79)	27 (54.00)		
Drinking history			0.007	0.935
Yes	42 (55.26)	28 (56.00)		
No	34 (44.74)	22 (44.00)		
History of hypertension			0.132	0.716
Yes	37 (48.68)	26 (52.00)		
No	39 (51.32)	24 (48.00)		
K-L grading			0.366	0.545
I	43 (56.58)	31 (62.00)		
II	33 (43.42)	19 (38.00)		

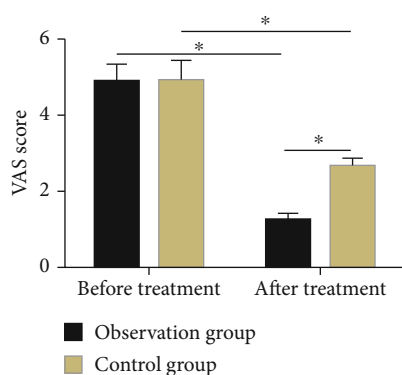


FIGURE 1: Comparison of pre- and posttreatment VAS scores. The VAS score was not statistically different between groups before treatment, but the score was significantly lower in the observation group compared with the control group after treatment. Note: * indicates $P < 0.05$ compared with before treatment or between two groups.

history, drinking history, hypertension history, K-L grading, and other general clinical baseline data ($P > 0.05$).

3.2. Comparison of Pre- and Posttreatment VAS Scores. No statistical difference was observed in the pre-treatment VAS score between control group and observation group ($P > 0.05$), but after treatment, the VAS score of the two groups was significantly improved, with a markedly lower score in observation group ($P < 0.05$) (Figure 1).

3.3. Comparison of Pre- and Posttreatment Joint Function Scores. No statistical differences were found in pretreatment WOMAC and Lysholm scores between observation group and control group ($P > 0.05$). After treatment, both the WOMAC and Lysholm scores changed significantly in the two groups, with a lower WOMAC score and a higher

Lysholm score in observation group compared with control group ($P < 0.05$) (Figure 2).

3.4. Comparison of Pre- and Posttreatment BMMs. The BMMs (BGP, TRACP-5b, CTX-1, and BALP) differed insignificantly between groups prior to treatment ($P > 0.05$). After treatment, BGP, TRACP-5b, CTX-1, and BALP of the two groups were significantly improved, with statistically lower TRACP-5b and CTX-1 while higher BGP and BALP in observation group as compared to control group (Figure 3).

3.5. Comparison of Clinical Efficacy after Treatment. After treatment, the ORR was found to be 93.42% in observation group and 78.00% in control group, with statistical significance ($P < 0.05$) (Table 2).

4. Discussion

In OP + KOA patients, the damaged articular surface will be in a state of long-term friction, which would induce a large number of wear particles and stimulation of synovial nociceptors, causing joint osteoarthritis [19]. The capsular cavity of the knee joint is abundant in blood vessels and nerves. If there is joint trauma, the synovium and ligament in the joint will be congested, and massive inflammatory exudate will be released, which will affect the knee joint function of patients [20]. At present, various treatments are available for the disease, but all with unsatisfactory curative effects [21]. Hence, this study is to observe the effect of GlcN plus SH on this disease, aiming to find a better alternative for the disease.

GlcN can effectively promote the production of glycosaminoglycans and proteoglycans to promote the synthesis of knee cartilage, with some certain anti-inflammatory effects [22], while SH can actively participate in the regulation of electrolyte and water in the extracellular fluid after entering the patient's body, which can validly lubricate

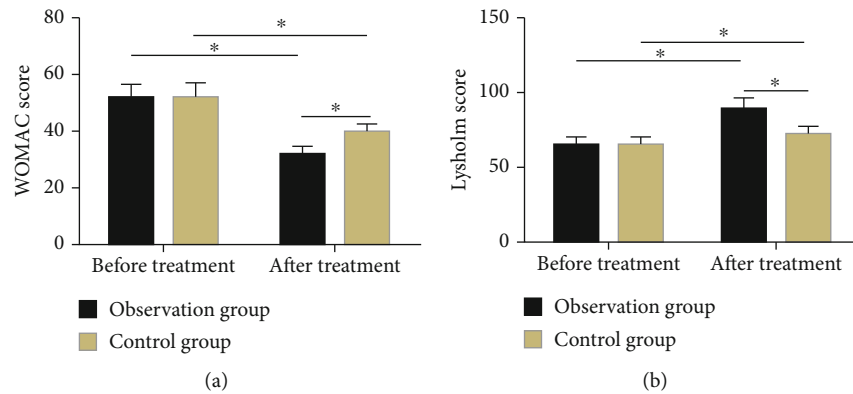


FIGURE 2: Comparison of pre- and posttreatment joint function scores. (a) The WOMAC score of the observation group was not statistically different from that of the control group before treatment, but after treatment, the score was statistically lower in the observation group. (b) The Lysholm score of the observation group was not statistically different from that of the control group before treatment, but the score was statistically higher in the observation group after treatment. Note: * indicates $P < 0.05$ compared with before treatment or between two groups.

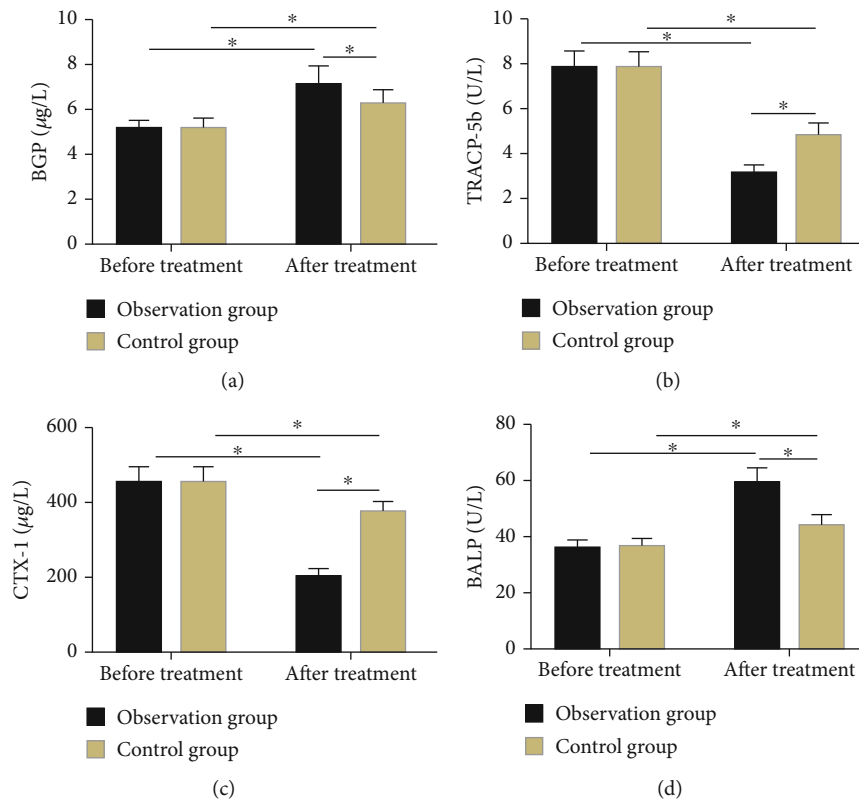


FIGURE 3: Comparison of pre- and posttreatment bone metabolism indexes. (a) The BGP of the observation group was not statistically different from that of the control group before treatment, but after treatment, the BGP was statistically higher in the observation group. (b) The TRACP-5b of the observation group was not statistically different from that of the control group before treatment, but it was statistically lower in the observation group after treatment. (c) The CTX-1 of the observation group was not statistically different from that of the control group before treatment, but after treatment, it was statistically lower in the observation group. (d) The BALP of the observation group was not statistically different from that of the control group before treatment, but it was statistically higher in the observation group after treatment. Note: * indicates $P < 0.05$ compared with before treatment or between two groups.

joints, resist infection and heal wounds, and effectively lubricate joint cavities, thus protecting joints [23]. In the research of Wang et al. [24], SH plus GlcN for KOA patients

effectively mitigated joint pain, promoted the functional recovery of knee joints, and enhanced the therapeutic effect. Alekseeva et al. [25] reported that hyaluronic acid plus

TABLE 2: Comparison of clinical efficacy after treatment [n (%)].

Groups	Marked response	Response	Nonresponse	Overall response rate (%)
Observation group (n = 76)	48 (63.16)	23 (30.26)	5 (6.58)	71 (93.42)
Control group (n = 50)	17 (34.00)	22 (44.00)	11 (22.00)	39 (78.00)
χ^2	—	—	—	6.469
P	—	—	—	0.011

chondroitin sulfate and glucosamine hydrochloride can effectively improve patients' life quality and reduce joint pain. Our study results revealed a statistically lower VAS score in observation group compared with control group after treatment. It indicates that GlcN plus SH can effectively promote articular cartilage synthesis, eliminate inflammation caused by OP + KOA, and play the role of cartilage preservation, thus effectively relieving pain. In the study of Brandt et al. [26], SH significantly reduced knee pain and stiffness of KOA patients, improved their joint function, and provided lasting benefits for those with moderate knee pain. And according to Muraleva et al. [27], the administration of GlcN to an animal model of OP reduced bone loss. In terms of joint function, our study identified that the WOMAC score was significantly lower while the Lysholm score was higher in observation group as compared to control group, demonstrating that GlcN plus SH can not only effectively relieve the pain symptoms and swelling of patients but also effectively improve their joint mobility.

Biomarkers of bone turnover can be used as a better way than radiographs to observe osteoarthritis progression [28]. BGP and BALP, as markers of bone formation, and TRACP-5b and CTX-1, as markers of bone resorption, can effectively reflect changes in bone metabolism in patients and indirectly reflect alterations in joint function [29, 30]. Our findings identified statistically lower BMMs TRACP-5b and CTX-1 while higher BGP and BALP in observation group after treatment. It indicates that after the combined treatment of GlcN and SH, bone absorption decreases, and bone formation begins to increase, which effectively corrects the imbalance of bone metabolism. It also shows that the combination therapy can effectively realize fracture healing and improve bone structure. Moreover, the curative effect was obviously higher in observation group versus control group, suggesting that GlcN plus SH has a definite clinical effect in treating OP + KOA, which can effectively reduce pain, improve knee joints, and promote rapid recovery from the disease.

Although this work has confirmed that GlcN plus SH is effective for OP + KOA, there is still some deficiencies and room for improvement. For example, we can supplement basic experiments on the therapeutic mechanisms of the two treatments to explore the risk factors that influence patient outcomes at the molecular level. Second, the sample size can be increased to improve the accuracy of experimental results. Third, prognostic analysis should be supplemented to further understand the effect of GlcN plus SH on the prognosis of such patients. We will gradually improve the research from the above perspective in the future. In addition, the innovation of this study is to compare and

analyze the clinical effects of GlcN plus SH and GlcN monotherapy in the treatment of OP + KOA in terms of pain, joint function, BMMs, clinical efficacy, etc., which confirms the clinical effectiveness of the combination therapy and provides a new direction and reliable basis for the treatment of such patients.

5. Conclusion

Taken together, GlcN plus SH is superior to GlcN monotherapy for patients with OP + KOA, which can not only significantly relieve pain, improve patients' joint function and bone metabolism but also further improve the curative effect, with high clinical promotion value.

Data Availability

The labeled dataset used to support the findings of this study are available from the corresponding author upon request.

Conflicts of Interest

The authors declare no competing interests.

Acknowledgments

This work was supported by the Hunan Key Laboratory of Metabolic Osteopathy (fund no.: 2019KF004).

References

- [1] L. S. Martin Martin, U. Massafra, E. Bizzi, and A. Migliore, "A double blind randomized active-controlled clinical trial on the intra-articular use of md-knee versus sodium hyaluronate in patients with knee osteoarthritis ("joint")," *BMC Musculoskeletal Disorders*, vol. 17, no. 1, p. 94, 2016.
- [2] H. Hsu and R. M. Siwec, *Knee Osteoarthritis*, Statpearls, Treasure Island (FL), 2022.
- [3] G. I. Im and M. K. Kim, "The relationship between osteoarthritis and osteoporosis," *Journal of Bone and Mineral Metabolism*, vol. 32, no. 2, pp. 101–109, 2014.
- [4] P. P. Geusens and J. P. van den Bergh, "Osteoporosis and osteoarthritis," *Current Opinion in Rheumatology*, vol. 28, no. 2, pp. 97–103, 2016.
- [5] X. Tang, S. Wang, S. Zhan et al., "The prevalence of symptomatic knee osteoarthritis in China: results from the China health and retirement longitudinal study," *Arthritis & Rheumatology*, vol. 68, no. 3, pp. 648–653, 2016.
- [6] C. L. Gregson, D. J. Armstrong, J. Bowden et al., "Uk clinical guideline for the prevention and treatment of osteoporosis," *Archives of Osteoporosis*, vol. 17, no. 1, p. 58, 2022.

- [7] S. Yomogida, Y. Kojima, Y. Tsutsumi-Ishii, J. Hua, K. Sakamoto, and I. Nagaoka, "Glucosamine, a naturally occurring amino monosaccharide, suppresses dextran sulfate sodium-induced colitis in rats," *International Journal of Molecular Medicine*, vol. 22, no. 3, pp. 317–323, 2008.
- [8] B. Chen, L. Fang, L. Lin et al., "Aerobic exercise combined with glucosamine hydrochloride capsules inhibited the apoptosis of chondrocytes in rabbit knee osteoarthritis by affecting trpv5 expression," *Gene*, vol. 830, article 146465, 2022.
- [9] F. Lu and H. Guo, "Study on the role of glucosamine hydrochloride in the pathogenesis of osteoarthritis," *Wei Sheng Yan Jiu*, vol. 32, no. 6, pp. 594–597, 2003.
- [10] X. Yang, W. Liang, J. Li, and P. Liu, "A meta-analysis and systematic review of the therapeutic effects of arthroscopy combined with intra-articular injection of sodium hyaluronate in the treatment of knee osteoarthritis," *Annals of Palliative Medicine*, vol. 10, no. 9, pp. 9859–9869, 2021.
- [11] A. Bronstone, J. T. Neary, T. H. Lambert, and V. Dasa, "Supartz (sodium hyaluronate) for the treatment of knee osteoarthritis: a review of efficacy and safety," *Clinical Medicine Insights: Arthritis and Musculoskeletal Disorders*, vol. 12, p. 117954411983522, 2019.
- [12] Z. Xu, Z. He, L. Shu, X. Li, M. Ma, and C. Ye, "Intra-articular platelet-rich plasma combined with hyaluronic acid injection for knee osteoarthritis is superior to platelet-rich plasma or hyaluronic acid alone in inhibiting inflammation and improving pain and function," *Arthroscopy*, vol. 37, no. 3, pp. 903–915, 2021.
- [13] F. Zhou, L. Chu, X. Liu et al., "Subchondral trabecular microstructure and articular cartilage damage variations between osteoarthritis and osteoporotic osteoarthritis: a cross-sectional cohort study," *Frontiers in Medicine*, vol. 8, article 617200, 2021.
- [14] E. S. Choi, H. D. Shin, J. A. Sim et al., "Relationship of bone mineral density and knee osteoarthritis (Kellgren-Lawrence grade): fifth Korea national health and nutrition examination survey," *Clinics in Orthopedic Surgery*, vol. 13, no. 1, pp. 60–66, 2021.
- [15] F. Li, L. Zhu, Y. Geng, and G. Wang, "Effect of hip replacement surgery on clinical efficacy, vas score and Harris hip score in patients with femoral head necrosis," *American Journal of Translational Research*, vol. 13, no. 4, pp. 3851–3855, 2021.
- [16] L. C. Walker, N. D. Clement, and D. J. Deehan, "Predicting the outcome of total knee arthroplasty using the womac score: a review of the literature," *The Journal of Knee Surgery*, vol. 32, no. 8, pp. 736–741, 2019.
- [17] T. Sueyoshi, G. Emoto, and T. Yato, "Correlation between single assessment numerical evaluation score and Lysholm score in primary total knee arthroplasty patients," *Arthroplast Today*, vol. 4, no. 1, pp. 99–102, 2018.
- [18] I. A. Tikhonova, H. Yang, S. Bello et al., "Enzyme-linked immunosorbent assays for monitoring tnf-alpha inhibitors and antibody levels in people with rheumatoid arthritis: a systematic review and economic evaluation," *Health Technology Assessment*, vol. 25, no. 8, pp. 1–248, 2021.
- [19] E. Franco-Trepat, M. Guillan-Fresco, A. Alonso-Perez et al., "Visfatin connection: present and future in osteoarthritis and osteoporosis," *Journal of Clinical Medicine*, vol. 8, no. 8, p. 1178, 2019.
- [20] S. B. Adams, L. A. Setton, R. D. Bell et al., "Inflammatory cytokines and matrix metalloproteinases in the synovial fluid after intra-articular ankle fracture," *Foot & Ankle International*, vol. 36, no. 11, pp. 1264–1271, 2015.
- [21] J. Iwamoto, Y. Sato, T. Takeda, and H. Matsumoto, "Effectiveness of exercise in the treatment of lumbar spinal stenosis, knee osteoarthritis, and osteoporosis," *Aging Clinical and Experimental Research*, vol. 22, no. 2, pp. 116–122, 2010.
- [22] S. Mondal and M. J. Swamy, "Purification, biochemical/biophysical characterization and chitoooligosaccharide binding to BGL24, a new PP2-type phloem exudate lectin from bottle gourd (*Lagenaria siceraria*)," *International Journal of Biological Macromolecules*, vol. 164, pp. 3656–3666, 2020.
- [23] M. Halici, S. Karaoglu, O. Canoz, S. Kabak, and A. Baktir, "Sodium hyaluronate regulating angiogenesis during Achilles tendon healing," *Knee Surgery, Sports Traumatology, Arthroscopy*, vol. 12, no. 6, pp. 562–567, 2004.
- [24] S. J. Wang, Y. H. Wang, and L. C. Huang, "The effect of oral low molecular weight liquid hyaluronic acid combination with glucosamine and chondroitin on knee osteoarthritis patients with mild knee pain: an 8-week randomized double-blind placebo-controlled trial," *Medicine (Baltimore)*, vol. 100, no. 5, article e24252, 2021.
- [25] L. I. Alekseeva, E. P. Sharapova, N. G. Kashevarova et al., "Use of artra msm forte in patients with knee osteoarthritis: results of a randomized open-label comparative study of the efficacy and tolerability of the drug," *Terapevticheski Arkhiv*, vol. 87, no. 12, pp. 49–54, 2015.
- [26] K. D. Brandt, J. A. Block, J. P. Michalski, L. W. Moreland, J. R. Caldwell, and P. T. Lavin, "Efficacy and safety of intraarticular sodium hyaluronate in knee osteoarthritis," *Clinical Orthopaedics and Related Research*, vol. 385, pp. 130–143, 2001.
- [27] N. A. Muraleva, E. N. Ofitserov, V. P. Tikhonov, and N. G. Kolosova, "Efficacy of glucosamine alendronate alone & in combination with dihydroquercetin for treatment of osteoporosis in animal model," *The Indian Journal of Medical Research*, vol. 135, pp. 221–227, 2012.
- [28] M. Takahashi, K. Naito, M. Abe, T. Sawada, and A. Nagano, "Relationship between radiographic grading of osteoarthritis and the biochemical markers for arthritis in knee osteoarthritis," *Arthritis Research & Therapy*, vol. 6, no. 3, pp. R208–R212, 2004.
- [29] Y. Zhou, Y. Yang, Y. Liu et al., "Irp2 knockout causes osteoporosis by inhibition of bone remodeling," *Calcified Tissue International*, vol. 104, no. 1, pp. 70–78, 2019.
- [30] Q. Liu, J. Cao, and J. Kong, "Effects of percutaneous kyphoplasty on bone metabolism and oxidative stress in elderly patients with osteoporotic spinal fractures," *Journal of the College of Physicians and Surgeons-Pakistan*, vol. 29, no. 1, pp. 37–40, 2019.

Research Article

Effects of Propofol Intravenous Anesthesia on Serum NGF, S100B Protein, and Immune Function in Patients with Bladder Cancer after Resection

Xiaohong Guan,¹ Qingxiong Peng,¹ Yongping Liu,² and Jiansong Wang³ 

¹Department of Anesthesiology, The First Hospital of Changsha, Changsha, 410011 Hunan, China

²Department of Anesthesiology, Hunan Provincial People's Hospital, The First Affiliated Hospital of Hunan Normal University, Changsha, 410005 Hunan, China

³Department of Urology, Hunan Provincial People's Hospital, The First Affiliated Hospital of Hunan Normal University, Changsha, 410005 Hunan, China

Correspondence should be addressed to Jiansong Wang; wangjsurology@hunnu.edu.cn

Received 7 June 2022; Revised 21 July 2022; Accepted 9 August 2022; Published 28 August 2022

Academic Editor: Pan Zheng

Copyright © 2022 Xiaohong Guan et al. This is an open access article distributed under the Creative Commons Attribution License, which permits unrestricted use, distribution, and reproduction in any medium, provided the original work is properly cited.

Objective. To explore the efficacy of intravenous propofol anesthesia on patients with bladder cancer after resection, as well as its effect on cognitive and immune function. **Methods.** Patients with bladder cancer and received resection of bladder cancer at our hospital from May 1, 2019, to November 30, 2021, were retrospectively retrieved and included in this study. The included patients were summarized into group A (isoflurane) and group B (intravenous propofol). The anesthesia intervention effect, serum NGF level, serum S100B protein level, and immune function before surgery, 6 h after surgery, 1 d after surgery, and 3 d after surgery were compared between the two groups. **Results.** Eighty-six patients were retrieved. The anesthesia intervention effective rate of patients in group B was significantly higher than that of patients in group A ($P < 0.01$). The serum NGF and S100B of patients in both groups were significantly lower on postsurgical day 1, but in the trend to returning to those before intervention level on day 3. There were also fluctuations in immune function represented by changes in CD3+, CD4+, CD8+, and CD4+/CD8+ T cells, which showed return of function by postsurgical day 3. **Conclusion.** The anesthetic effect of intravenous propofol in patients with bladder cancer resection is significantly more satisfactory than isoflurane, with a transient effect on serum NGF and S100B protein levels and patients' immune function, which suggests that intravenous propofol can be widely used for general anesthesia in clinical practice.

1. Introduction

Propofol and other intravenous (IV) sedative-hypnotic medications are commonly used for general anesthesia. Some studies have shown that anesthesia medications can cause postoperative cognitive dysfunction and immune dysfunction in old patients, which will seriously affect the quality of life of patients after surgery [1]. Patients with bladder cancer are diagnosed at an average of 73 years old, which is a typical group of aged population [2]. The influence of different anesthesia regimens on the cognitive function and

immune function of patients with bladder cancer resection is still concerned by clinicians around the world [3].

Some studies have shown that both serum NGF and S100B protein are key markers for evaluating whether patients' postoperative cognitive function is impaired or not [4, 5]. It was found that propofol has a rapid onset of anesthesia effect, few adverse effects, and also a minor impact on the cognitive function of patients [6, 7]. Therefore, we analyzed the anesthesia effect of propofol, its impact on serum NGF, S100B protein levels, and immune functions in patients who received bladder cancer surgery.

TABLE 1: Comparison of clinical characteristics of the two groups of patients.

Group	Case	Gender (male/female)	Age (years old)	BMI (kg/m ²)	ASA rating		
					I	II	III
Group A	43	24/19	57.87 ± 5.43	25.57 ± 4.32	25	12	6
Group B	43	25/18	58.23 ± 5.33	25.74 ± 4.44	26	13	4
χ^2/t		0.157	0.252	0.356		0.327	
<i>P</i>		0.787	0.675	0.588		0.554	

2. Materials and Methods

Patients with bladder cancer undergoing resection of bladder cancer who were treated at our hospital from May 1, 2019, to November 30, 2021, were included in this study. Patients in group A received isoflurane during the resection, while patients in group B received intravenous anesthesia with propofol. This study was approved by the institutional ethical committee of our hospital. All the included patients and their families were informed about the study and actively signed the consent form.

Inclusion criteria are as follows: (1) all the included patients met the corresponding criteria for bladder cancer resection [8], (2) aged between 18 and 85 years, and (3) the clinical data of all included patients were complete.

Exclusion criteria were as follows [9]: (1) patients had a history of allergy to the anesthetic drugs in this treatment plan, (2) patients had severe organ dysfunction, and (3) patients had severe respiratory diseases.

First, the patient was given an intramuscular infusion of atropine (Tianjin Jinyao Pharmaceutical Co., Ltd., H12020384) 0.5 mg before surgery. Secondly, the clinical signs of the patient were monitored immediately after entering the operating room, and 0.04 mg/kg midazolam (Yichang Renfu Pharmaceutical Co., Ltd., approved by H20065729) and 0.4 µg/kg fentanyl (Jiangsu Enhua Pharmaceutical Group Co., Ltd., National Medicine Zhunzi H19990027) were given for anesthesia induction, and then, tracheal intubation was performed to assist ventilation. Then, patients in group A were given 1%-3% isoflurane (Shanghai Hengrui Pharmaceutical Co., Ltd., approved by H20070172) by inhalation to maintain anesthesia, while patients in group B were given 4 mg/kg/h propofol (Xi'an Libang Pharmaceutical Co., Ltd., Chinese Medicine Zhunzi H19990282) intravenous infusion to maintain anesthesia. Finally, vecuronium bromide (Hubei Keyi Pharmaceutical Co., Ltd., H20084581) and fentanyl were intermittently administered to maintain anesthesia during the operation, and the infusion was terminated 30 minutes before the completion of the operation. Before and after the intervention, 5 ml of venous whole blood was collected from all of the included patients in the fasting state in the morning for various experiments, which was aliquoted and either used freshly or placed in a -80°C refrigerator for later use.

2.1. Evaluation of the Effect of Anesthesia Intervention. Remarkable effect: the patient's anesthesia induction state was stable, the depth of anesthesia maintenance was reasonable, and the state was stable during recovery. Normal effect:

the patient's anesthesia induction state was relatively stable, the depth of anesthesia maintenance was reasonable, and mild agitation occurred during recovery. Poor effect: the patient's state of anesthesia induction was unstable, the depth of anesthesia maintenance was unreasonable, and severe agitation occurred during recovery. The total intervention effective rate = (significant + general)/total number of cases × 100% [10, 11]. The American Society of Anesthesiologists (ASA) physical status classification system was used to evaluate the physical status of enrolled patients [12].

2.2. Detection of Serum NGF Levels. The serum nerve growth factor (NGF) levels of all included patients were detected before surgery, 6 h, 1 d, and 3 d after surgery by enzyme-linked immunosorbent assay (ELISA). The kit was purchased from Shanghai Kanu Biotechnology Co., Ltd. and operated in strict accordance with the instructions to control the intrabatch variation < 10% and the interbatch variation < 15% [13].

2.3. Detection of Serum S100B Protein Level. The serum S100B protein levels of all included patients were checked before the operation, 6 h, 1 d, and 3 d after operation by (ELISA). The kit was purchased from Shanghai Kanu Biotechnology Co., Ltd. and operated in strict accordance with the instructions to control intrabatch variation < 10% and interbatch variation < 15% [14].

2.4. Assessment of Immune Function. Each patient's whole blood sample (2 ml) was treated with heparin and put into sterile EP tubes, and one volume of PBS was added to dilute the blood. The total live cell concentration was adjusted to 2×10^6 in DMEM medium (Youkang Hengye Biotechnology (Beijing) Co., Ltd., China), followed by addition of anti-CD3+, CD4+, and CD8+ antibodies (1 µg per 10^6 cells, Abcam, China) at room temperature in the dark for 20 min. The samples were then washed three times with PBS buffer and analyzed by flow cytometry (Navios, Beckman Coulter, USA).

2.5. Statistical Methods. The data in this study were analyzed by SPSS21.0 software package (IBM Corp., Armonk, N.Y., USA). The enumeration data (%) were analyzed by χ^2 test, and the measurement data (mean ± SD) were analyzed by *t* test. A *P* < 0.05 (2-sided) means the difference is significantly different.

TABLE 2: Comparison of the effect of anesthesia intervention between the two groups (n (%)).

Group	Remarkable	Normal	Poor	Total intervention effectiveness
Group A ($n = 43$)	19 (44.18)	13 (30.95)	11 (26.19)	32 (74.41)
Group B ($n = 43$)	24 (55.81)	14 (33.33)	5 (11.91)	38 (88.37)
χ^2		—		7.325
P		—		<0.01

TABLE 3: Comparison of serum NGF levels between the two groups of patients after intervention ($\bar{x} \pm s$).

Group	Group A ($n = 43$)	Group B ($n = 43$)	t	P
Before surgery	332.38 \pm 34.67	348.21 \pm 36.83	1.664	>0.05
6 h after surgery	282.38 \pm 41.67	271.21 \pm 37.83	3.764	<0.01
1 d after surgery	295.12 \pm 37.56	287.78 \pm 30.34	2.275	<0.01
3 days after surgery	328.34 \pm 36.41	336.41 \pm 33.26	1.363	>0.05

TABLE 4: Comparison of serum S100B protein levels between the two groups of patients after intervention ($\bar{x} \pm s$).

Group	Group A ($n = 43$)	Group B ($n = 43$)	t	P
Before surgery	0.38 \pm 0.32	0.37 \pm 0.33	0.223	>0.05
6 h after surgery	0.74 \pm 0.47	0.81 \pm 0.53	0.564	<0.01
1 d after surgery	0.42 \pm 0.32	0.68 \pm 0.44	0.575	<0.01
3 days after surgery	0.37 \pm 0.33	0.36 \pm 0.34	0.225	>0.05

3. Results

3.1. Comparison of the Effect of Anesthesia Intervention. A total of 86 qualified patients (43 cases in group B and 43 matched cases in group A) were retrieved. The average age of patients was 57.87 \pm 5.43 years in group A and 58.23 \pm 5.33 years in group B. There was no difference in gender, age, BMI, or ASA rating between the two groups ($P > 0.05$ for all comparisons). The general data of the patients included in this study are shown in Table 1.

The total intervention effective rate of patients in group B was significantly higher than that of patients in group A (88.37% vs. 74.41%, $P < 0.01$, Table 2).

3.2. Comparison of Serum NGF Levels. Before surgery, the serum NGF level of patients in group B (348.21 \pm 36.83) was not significantly different from that of patients in group A (332.38 \pm 34.67) ($t = 1.664$, $P > 0.05$); 6 h and 1 d after surgery, the serum NGF levels of patients in group B were significantly lower than those of group A patients (271.21 \pm 37.83 and 287.78 \pm 30.34 vs. 282.38 \pm 41.67 and 295.12 \pm 37.56, $t = 3.764$, 2.275, $P < 0.01$, respectively). But 3 days after surgery, the serum NGF level of group B patients was not significantly different from that of group A patients (336.41 \pm 33.26 vs. 328.34 \pm 36.41, $t = 1.363$, $P > 0.05$) and has returned to the preoperative level (Table 3).

3.3. Comparison of Serum S100B Protein Levels. Before surgery, the serum S100B protein level of patients in group B was not significantly different from that in patients in group A (0.37 \pm 0.33 vs. 0.38 \pm 0.32, $t = 0.223$, $P > 0.05$); 6 h and

TABLE 5: Comparison of the immune function of the included patients between the two groups ($\bar{x} \pm s$).

Group	Group A ($n = 43$)	Group B ($n = 43$)
CD_3^+		
Before intervention	61.05 \pm 7.36	61.01 \pm 8.23
1 d after intervention	48.06 \pm 9.13 [^]	50.14 \pm 12.52 [^]
3 d after intervention	57.06 \pm 8.05 [^]	59.14 \pm 10.38
CD_4^+		
Before intervention	37.07 \pm 4.24	37.64 \pm 4.18
1 d after intervention	27.18 \pm 6.33 [^]	29.25 \pm 7.61 [^]
3 d after intervention	34.18 \pm 5.19 [^]	35.75 \pm 5.64
CD_8^+		
Before intervention	25.05 \pm 2.68	24.07 \pm 3.05
1 d after intervention	20.60 \pm 3.17 [^]	20.41 \pm 2.32 [^]
3 d after intervention	23.60 \pm 3.35 [^]	23.41 \pm 2.61
CD_4^+/CD_8^+		
Before intervention	1.66 \pm 0.13	1.63 \pm 0.14
1 d after intervention	1.38 \pm 0.15 [^]	1.37 \pm 0.25 [^]
3 d after intervention	1.48 \pm 0.17 [^]	1.57 \pm 0.16 [*]

Note: compared with the control group, $*P < 0.05$; compared with before treatment, [^] $P < 0.05$.

1 d after surgery, the serum S100B protein levels of patients in group B were significantly higher than those of patients in group A (0.81 \pm 0.53 and 0.68 \pm 0.44 vs. 0.74 \pm 0.47 and

0.42 ± 0.32 , $t = 0.564$, 0.575 , $P < 0.01$, respectively). But 3 days after surgery, the serum S100B protein level of patients in group B was not significantly different from that in patients in group A (0.36 ± 0.34 vs. 0.37 ± 0.33 , $t = 0.225$, $P > 0.05$) and has returned to the preoperative level (Table 4).

3.4. Comparison of Immune Function. Before intervention, the CD3+, CD4+, CD8+, and CD4+/CD8+ cells of group B patients were similar as those of group A patients (61.05 ± 7.36 vs. 61.01 ± 8.23 , 37.07 ± 4.24 vs. 37.64 ± 4.18 , 25.05 ± 2.68 vs. 24.07 ± 3.05 , and 1.66 ± 0.13 vs. 1.63 ± 0.14 , $P > 0.05$, respectively), whereas after intervention, the CD3+, CD4+, CD8+, and CD4+/CD8+ of patients in both groups were significantly lower on day 1, but in the trend to returning to those before intervention level on day 3 (Table 5).

4. Discussion

Cognitive impairment after resection of bladder cancer is commonly seen, especially in older patients, and the incidence is usually between 6% and 62% [15, 16]. Some researchers have claimed that cognitive function has a certain relationship with the central cholinergic system in patients, and serum NGF and S100B proteins are both serum factors that are closely related to cognitive dysfunction in patients [17, 18]. Our study indicates that propofol is effective for anesthesia intervention, which also has only transient on the serum NGF and S100B protein levels. The reason may be that propofol does not disturb the production of inflammatory chemokines in the body, thereby improving the function of the central cholinergic system [19].

CD4⁺ and CD8⁺ T cells, as key components of the immune system, can effectively reflect the changes in immune function in the body [20–22]. In this study, we found that after propofol application in groups A and B, all CD3+, CD4+, CD8+, and CD4+/CD8+ T cells changed significantly on day 1 compared with those before propofol application, then in the trend of recovery on day 3, which indicated that intravenous anesthesia by propofol had only transient effect on the immune function of patients and this was helpful for the recovery of postoperative immune function of patients. The reason for this may be that propofol is less irritating to the patient's body and will not cause too much stress and inflammatory response to the patient [23, 24].

Although propofol is an effective anesthetic reagent and has little effect on cognitive and immune functions, it still needs to be evaluated in severe clinical conditions, such as fulminant hepatitis, hypoxia brain injury, preterm labor, or intrauterine infections during pregnancy [25–33].

All in all, the anesthesia intervention effect of propofol intravenous anesthesia in patients undergoing bladder cancer resection is remarkable, with little effect on serum NGF and S100B protein levels, and does not interfere with the recovery of patients' immune function, suggesting that it can be widely used in clinical practice.

Data Availability

The data used to support the findings of this study are available from the corresponding author upon request.

Conflicts of Interest

The authors declare no conflicts of interest.

Acknowledgments

This work was supported by the Natural Science Foundation of Hunan Province (No. 2021JJ30403).

References

- [1] F. Wang, X. Y. Yao, J. Nie et al., "Effect of propofol general anesthesia on serum BDNF, S100B protein and cognitive function in senile prostate electrocision patients," *Practical Pharmacy and Clinical Remedies*, vol. 7, no. 1, pp. 125–137, 2016.
- [2] The American Cancer Society medical and editorial content team, "Risk of bladder cancer," 2022, <https://www.cancer.org/cancer/bladder-cancer/about/key-statistics.html>.
- [3] C. M. Grunewald, V. Feldmeier, T. Supprian, P. Albers, M. Giessing, and G. Niegisch, "Cognitive function in patients undergoing cystectomy for bladder cancer - results from a prospective observational study," *Therapeutic Advances in Urology*, vol. 14, p. 17562872221087660, 2022.
- [4] Y. Q. Huang, "Effect of propofol general anesthesia on neuron-specific enolase (NSE) in blood serum, S100B protein and cognitive function of gerontal patients," *Practical Pharmacy and Clinical Remedies*, vol. 17, no. 6, pp. 708–710, 2014.
- [5] L. Zhang, W. Ning, and S. Zhou, "Propofol induces proliferation and invasion of gallbladder cancer cells through activation of Nrf2," *Journal of Experimental & Clinical Cancer Research*, vol. 31, no. 1, pp. 1–8, 2012.
- [6] L. Zhan, J. Er, W. Zhai, J. Liu, and J. Han, "Overall effect of sufentanil-propofol general anesthesia combined with paravertebral block on patients with lung cancer resection," *International Journal of Clinical and Experimental Medicine*, vol. 9, no. 10, pp. 20068–20073, 2016.
- [7] S. Casellato, S. Picozzi, G. Bozzini, S. Maruccia, and L. Carmignani, "566 risks and complications of transurethral resection of bladder tumour in patients taking antiplatelet agents for cardiovascular disease," *European Urology Supplements*, vol. 1, no. 12, pp. e566–e566, 2013.
- [8] G. Li, X. Zhang, X. Guo, Y. Li, and C. Li, "Propofol inhibits the proliferation, migration, and stem-like properties of bladder cancer mainly by suppressing the hedgehog pathway," *Cell Transplantation*, vol. 30, pp. 5–9, 2021.
- [9] S. Noguchi, "Cold-cup bladder resection by topical mucosal anesthesia for the outpatients with recurrent superficial bladder cancer," *Japanese Journal of Clinical Urology*, vol. 52, no. 11, pp. 833–836, 2018.
- [10] Y. Liang, "Effect of dexmedetomidine on expression of NGF in isolated hippocampal neurons of fetal rats incubated with propofol," *Chinese Journal of Anesthesiology*, vol. 2, no. 11, pp. 1–2, 2016.
- [11] Q. Zhao, X. U. Da-Shuai, and D. O. Anesthesiology, "The effect and significance of propofol on serum NGF, NSE and S100 beta protein in elderly patients with prostate surgery," *Journal*

- of Clinical and Experimental Medicine*, vol. 56, no. 64, pp. 16–24, 2018.
- [12] D. Mayhew, V. Mendonca, and B. V. S. Murthy, “A review of ASA physical status – historical perspectives and modern developments,” *Anaesthesia*, vol. 74, no. 3, pp. 373–379, 2019.
- [13] J. Liu, W. Dong, T. Wang et al., “Effects of etomidate and propofol on immune function in patients with lung adenocarcinoma,” *American Journal of Translational Research*, vol. 8, no. 12, pp. 5748–5755, 2016.
- [14] W. Yang and D. O. Anesthesiology, “Effect analysis of mivacurium chloride used for anesthesia on electrical resection with cystoscope in the treatment of bladder cancer,” *China Modern Medicine*, vol. 49, no. 5, pp. 289–301, 2018.
- [15] Y. Koumpan, M. Jaeger, G. B. Mizubuti et al., “Spinal anesthesia is associated with lower recurrence rates after resection of nonmuscle invasive bladder cancer,” *The Journal of Urology*, vol. 199, no. 4, pp. 940–946, 2018.
- [16] H. S. Sabir, “TaG1 bladder cancer: a third of all primary tumors and 80% of all recurrences can be treated in the office using local anesthesia,” *Urology Practice*, vol. 1, no. 4, pp. 184–188, 2014.
- [17] D. Aghamohammadi, R. M. Gargari, S. Fakhari, E. Bilehjani, and S. Poorsadegh, “Classic versus inguinal approach for obturator nerve block in transurethral resection of bladder cancer under spinal anesthesia: a randomized controlled trial,” *Iranian Journal of Medical Sciences*, vol. 43, no. 1, pp. 75–80, 2018.
- [18] F. Liu, L. X. Zheng, B. Xu, and H. S. Zhou, “Effects of propofol combined with ketamin on the changes in immune function of T lymphocytes in peripheral blood from children with acute lymphocytic leukemia,” *Hainan Medical Journal*, vol. 25, no. 5, pp. 693–696, 2014.
- [19] Z. Wang and S. Zhou, “Effect of compound propofol nanoemulsion on immune function in patients with pancreatic cancer,” *Journal of Nanoscience and Nanotechnology*, vol. 21, no. 2, pp. 1390–1396, 2021.
- [20] A. Brauers and G. Jakse, “2nd resection and prognosis in primary high risk superficial bladder cancer,” *The Journal of Urology*, vol. 44, no. 57, pp. 2–8, 2021.
- [21] L. S. Zhang, “Effect of Raykeen holmium laser electric resection and conventional electric resection on malignant degree and immune function of non-invasive bladder cancer,” *Journal of Hainan Medical University*, vol. 22, no. 13, pp. 7–9, 2016.
- [22] M. Zhou, W. Liu, J. Peng, and Y. Wang, “Impact of propofol epidural anesthesia on immune function and inflammatory factors in patients undergoing gastric cancer surgery,” *American Journal of Translational Research*, vol. 13, no. 4, pp. 3064–3073, 2021.
- [23] Y. H. Cho, S. W. Kim, J. H. Kim, and M. S. Yoon, “Combination therapy with Bacillus Calmette-Guerin (BCG) and interferon-alpha in superficial bladder cancer patients,” *Immune Effector Cell Function and Toxicity*, vol. 53, no. 13, pp. 69–76, 2018.
- [24] G. Devine, M. Cheng, G. Martinez et al., “Opioid-free anesthesia for lung cancer resection: a case-control study,” *Journal of Cardiothoracic and Vascular Anesthesia*, vol. 34, no. 11, pp. 3036–3040, 2020.
- [25] L. Deng, X. Li, Z. Shi, P. Jiang, D. Chen, and L. Ma, “Maternal and perinatal outcome in cases of fulminant viral hepatitis in late pregnancy,” *International Journal of Gynecology & Obstetrics*, vol. 119, no. 2, pp. 145–148, 2012.
- [26] Y. Yang, L. Deng, X. Li et al., “Evaluation of the prognosis of fulminant viral hepatitis in late pregnancy by the MELD scoring system,” *European Journal of Clinical Microbiology & Infectious Diseases*, vol. 31, no. 10, pp. 2673–2678, 2012.
- [27] Y. Yang, L. Deng, X. Li et al., “Analysis of prognosis-associated factors in fulminant viral hepatitis during pregnancy in China,” *International Journal of Gynaecology and Obstetrics*, vol. 114, no. 3, pp. 242–245, 2011.
- [28] X. M. Li, L. Ma, Y. B. Yang, Z. J. Shi, and S. S. Zhou, “Prognostic factors of fulminant hepatitis in pregnancy,” *Chinese Medical Journal*, vol. 118, no. 20, pp. 1754–1757, 2005.
- [29] Z. Shi, L. Ma, H. Wang et al., “Insulin and hypertonic glucose in the management of aseptic fat liquefaction of post-surgical incision: a meta-analysis and systematic review,” *International Wound Journal*, vol. 10, no. 1, pp. 91–97, 2013.
- [30] X. Li, Y. Zhang, and Z. Shi, “Ritodrine in the treatment of preterm labour: a meta-analysis,” *The Indian Journal of Medical Research*, vol. 121, no. 2, pp. 120–127, 2005.
- [31] J. Vasquez-Vivar, Z. Shi, K. Luo, K. Thirugnanam, and S. Tan, “Tetrahydrobiopterin in antenatal brain hypoxia-ischemia-induced motor impairments and cerebral palsy,” *Redox Biology*, vol. 13, pp. 594–599, 2017.
- [32] J. Vasquez-Vivar, Z. Shi, J. W. Jeong et al., “Neuronal vulnerability to fetal hypoxia-reoxygenation injury and motor deficit development relies on regional brain tetrahydrobiopterin levels,” *Redox Biology*, vol. 29, article 101407, 2020.
- [33] Z. Shi, J. Vasquez-Vivar, K. Luo et al., “Ascending lipopolysaccharide-induced intrauterine inflammation in near-term rabbits leading to newborn neurobehavioral deficits,” *Developmental Neuroscience*, vol. 40, pp. 534–546, 2019.

Retraction

Retracted: Research on Land Utilization Spatial Classification Planning Method Based on Multiocular Vision

Computational and Mathematical Methods in Medicine

Received 27 June 2023; Accepted 27 June 2023; Published 28 June 2023

Copyright © 2023 Computational and Mathematical Methods in Medicine. This is an open access article distributed under the Creative Commons Attribution License, which permits unrestricted use, distribution, and reproduction in any medium, provided the original work is properly cited.

This article has been retracted by Hindawi following an investigation undertaken by the publisher [1]. This investigation has uncovered evidence of one or more of the following indicators of systematic manipulation of the publication process:

- (1) Discrepancies in scope
- (2) Discrepancies in the description of the research reported
- (3) Discrepancies between the availability of data and the research described
- (4) Inappropriate citations
- (5) Incoherent, meaningless and/or irrelevant content included in the article
- (6) Peer-review manipulation

The presence of these indicators undermines our confidence in the integrity of the article's content and we cannot, therefore, vouch for its reliability. Please note that this notice is intended solely to alert readers that the content of this article is unreliable. We have not investigated whether authors were aware of or involved in the systematic manipulation of the publication process.

Wiley and Hindawi regrets that the usual quality checks did not identify these issues before publication and have since put additional measures in place to safeguard research integrity.

We wish to credit our own Research Integrity and Research Publishing teams and anonymous and named external researchers and research integrity experts for contributing to this investigation.

The corresponding author, as the representative of all authors, has been given the opportunity to register their agreement or disagreement to this retraction. We have kept a record of any response received.

References

- [1] Z. Zhang and S. Wang, "Research on Land Utilization Spatial Classification Planning Method Based on Multiocular Vision," *Computational and Mathematical Methods in Medicine*, vol. 2022, Article ID 9300278, 13 pages, 2022.

Research Article

Research on Land Utilization Spatial Classification Planning Method Based on Multicocular Vision

Zhifei Zhang^{1,2} and Shenmin Wang³ 

¹School of Geography and Ocean Science, Nanjing University, Nanjing 210023, China

²Jiangsu Provincial Land Survey and Planning Institute, Nanjing 210093, China

³School of Geographical Science, Nanjing University of Information Science & Technology, Nanjing 210044, China

Correspondence should be addressed to Shenmin Wang; 001791@nuist.edu.cn

Received 14 July 2022; Revised 8 August 2022; Accepted 10 August 2022; Published 28 August 2022

Academic Editor: Pan Zheng

Copyright © 2022 Zhifei Zhang and Shenmin Wang. This is an open access article distributed under the Creative Commons Attribution License, which permits unrestricted use, distribution, and reproduction in any medium, provided the original work is properly cited.

With the development of China's social economy as well as the accelerating urbanization construction and the expanding scale of cities, the integration of land use and urban land classification based on land use spatial planning has become an important task for the sustainable development of China at present. Land use spatial classification planning is the basic basis for all kinds of development and protection construction activities, and government land use spatial planning at all levels plays an important role in implementing major national, provincial, and municipal strategies and promoting the rational and effective use of land use space. By briefly describing the spatial classification of land use and analyzing the idea of systematic integration of land use, this paper provides guidance and reference for exploring the construction of urban land use classification under land use spatial planning, aiming to improve the classification system of land use spatial planning. A neural network-based land use classification algorithm is proposed for the problems of few labeled samples of remote sensing images with high spatial resolution and feature deformation due to sensor height changes in land use spatial classification planning. By multiscale adaptive fusion of multiple convolutional layer features, the impact of feature deformation on classification accuracy is reduced. To further improve the classification accuracy, the depth features extracted from the pretraining network are used to pretrain the multiscale feature fusion part and the fully connected layer, and the whole network is fine-tuned using the augmented dataset. The experimental results show that the adaptive fusion method improves the fusion effect and effectively improves the accuracy of land use spatial classification planning.

1. Introduction

The current urbanization process provides great convenience for urban production and life, but the contradiction between urban and rural planning and land management has become more and more prominent. At this stage, to better promote the coordinated and unified development of the two, it is necessary not only to strengthen the coordination and cooperation among all relevant departments but also to pay more attention to the quality of urban and rural planning and construction and land management work in the process of urbanization construction. Reasonable planning is beneficial to the development of cities, but at the present

stage, there are certain problems in the process of planning for both. Based on this, this paper explores the problems and optimization measures of planning and land planning in cities analyzed under the land use space system. The land spatial planning study is shown in Figure 1.

Land planning and management land planning and management, as an important basis for urban development and construction, should fully meet the needs of urban economic development and classify land on this basis. Land resources have a leading role in coordinating economic development, population development, and environmental development in cities [1–3]. During the promotion of urban construction, rational use of land and sustainable development of land

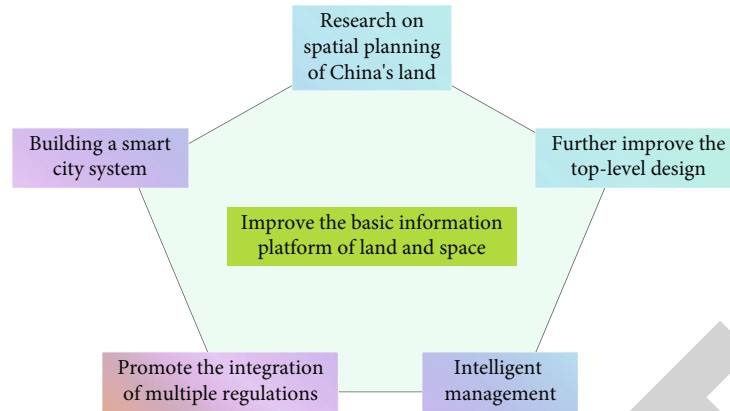


FIGURE 1: Land spatial planning study.

resources are of great significance to improve the quality of urban construction, meet the needs of urban construction, and achieve urban economic development. Under the wave of urbanization construction in China, the overall land use planning is an important guarantee to realize the smooth implementation of various national reforms. Urban land use, by coordinating the relationship between land rent and use, makes reasonable arrangements for industrial land, residential land, and other types of land to meet people's needs. In this paper, we analyze in depth from several angles to improve the efficiency of comprehensive land use and solve the contradiction between not being constrained by land use and meeting the demand for land use, and the result obtained from the overall land use planning is to realize the coordination of environmental, economic, and social benefits [4–7]. The planning and utilization of urban land resources is no longer a matter of allocating resources at present, but also a matter of coordinating with current urban construction and citizens' working and living standards. Therefore, the planning and utilization of urban land resources should be based on the two perspectives of resource allocation and land resource utilization efficiency.

As the current urbanization construction process in China is accelerating, the traditional humanistic and natural environment has been affected and even seriously damaged. The study of China's urban modernization construction process and the study of rural greening construction process to achieve green development and healthy development has become urgent [8–10]. Building green urban environment is based on optimizing urban space, planning, and designing urban environment, putting forward solutions to save material resources, hydraulic resources, and land resources in the city to achieve the purpose of environmental protection, accelerating land planning and construction, and implementing optimization of land resources, aiming to provide a harmonious living environment for urban residents and meet the needs of harmony between human and nature.

The essence of land use spatial classification planning is the optimal allocation of land use quantitative structure and spatial structure. One of the difficulties in the preparation of spatial land use classification planning is how to implement the quantitative structure of land use to a specific

geographical space to achieve the optimal allocation of land resources [11, 12]. The configuration of land use quantity structure is usually done by overlaying the current land use map with land suitability evaluation map, topographic map, town planning map, basic farmland protection zone map, nature protection zone map or other special land use planning map, etc., and then using the technical index of suitability to determine the land use of each land unit according to the overlapping situation. Although this overlay method is simple and easy to implement, the workload is large and is influenced and limited by the planner's own knowledge, experience, and preferences.

The development principle urban land use classification should focus on the functionality of land use in the context of continuous marketization and changing needs and should make full use of the actual needs of social development to reasonably increase new land use types, such as the future security type land, whose property rights attributes and operation methods are quite different from those of commercial housing, so different land use control methods should be implemented. The main purpose of urban land classification is to serve the spatial planning of the land, so the construction of the classification system needs to meet the feasibility of land classification. Therefore, it is necessary to subdivide the types of urban land space in the current situation survey and fully consider the operability of the practice [13–15].

However, there are few tools in GIS to solve the problem of land use configuration with multiple conflicting objectives, so it is especially urgent to find a method that can objectively and quantitatively optimize the configuration of land use spatial structure. How to match the quantitative structure of land use to specific land units based on the results of land suitability evaluation is a multiobjective integer planning problem with land units as the decision variables. To realize the path exploration of multicocular vision system in large-scale scenes and to provide timely feedback of the surrounding environment information, it becomes the urgent key to build an efficient, low-cost, and visualized GIS for spatial classification planning of land use. In recent years, with the development of multivision computer vision technology and related hardware processes, many classical

land use spatial classification planning methods for GIS have emerged and been applied in various fields, especially in terms of accuracy and real-time construction of 3D land use spatial classification planning in complex geographic environments. In the past, there were GIS land use spatial classification planning methods based on visual dense point clouds, but there were problems of lengthy computation and low accuracy. Nowadays, there are different types of sensors for 3D mapping, such as LIDAR and RGBD cameras. Among them, the LIDAR-based geographic mapping method obtains higher accuracy of spatial land use classification planning and is closer to the real environment, but the reconstructed effect of this method lacks texture and only reflects 3D spatial information, and the cost is higher; the reconstructed texture of RGBD camera-based method is clearer, but it is not suitable for geographically complex the large-scale mapping. In contrast, the land use spatial classification planning method of GIS based on multivision stereo matching can obtain 3D information from 2D images by simulating human binoculars and using the principle of stereo vision to adapt to complex geographic environments and has the advantages of automatic, online, noncontact detection, high flexibility, low cost, and clear texture, which can be used to build 3D land use spatial classification planning for geographically large-scale environments [16–18].

Although the method of land use spatial classification planning based on multivision GIS has many advantages, there are still problems such as long computation, low real time, and mismatching of depth values due to complex scene information when applied to geographic large-scale map building. To address the shortcomings and drawbacks of the construction of land use spatial classification planning based on multivision, this paper optimizes and improves on the basis of the original stereo matching algorithm: firstly, the original image is grayscale preprocessed and stereo corrected, and the parallax map is obtained based on the traditional matching algorithm, and the singular distortion points are detected by using left-right consistency; secondly, bilinear interpolation and median filtering are used for repair optimization; then, the method can optimize the depth calculation link in the construction of land use spatial classification planning and improve the operation speed, anti-interference, and accuracy of the system.

In recent years, China has elevated the optimization of land use spatial development pattern and the strengthening of ecological civilization construction to the national strategy. Scientific and reliable land use spatial land base data is the basis and foundation of land use spatial planning, and unified land use classification is the prerequisite for data acquisition, and land classification should be merged according to different land use characteristics, and its purpose is the key to distinguish different classification standards. However, the existing research focuses on the division of land use space into three types of space from multiple functional perspectives and multiple scales, and the research on data sources and data conversion for spatial function division is still insufficient and lacks current data support; it focuses on the functional division of land use space under a single classification system or a certain perspective and does not

make full use of the existing spatial land use classification data and does not construct effective guidelines for convergence of multiple classification systems and identification methods for multisource data fusion.

The main contributions of this paper are as follows: through comprehensive comparative analysis method and GIS spatial overlay analysis method, based on the current situation of land use spatial utilization and spatial dominant functions and on the basis of comparative analysis of the differences and discrepancies of the existing national land classification systems, we reconstruct the land use spatial land classification system for land use spatial planning, develop guidelines for the articulation of land use spatial land classification with the existing multiple national land classification systems, and explore the integration of national land. This paper provides basic data support for multiclass spatial classification, pattern optimization, and land use spatial planning. This paper addresses the problem that it is difficult to effectively match the land use quantity structure to specific land units based on the results of land suitability evaluation by conventional superposition methods and other land use allocation methods and proposes an optimal allocation method of land use spatial structure based on eye-catching vision to effectively solve the core problems of macro structure adjustment and land use zoning in land use spatial classification planning.

2. Related Work

2.1. Spatial Land Use Classification Planning. Land classification is an important basis for spatial land use planning and a scientific basis for optimizing the layout of spatial land use structure. Urban land use classification is an important means to promote the rationality of land use spatial planning and improve the value of land use, so how to systematically integrate land use and urban land use classification under land use spatial planning has become one of the main issues of current social development.

Land use spatial planning classification is to reasonably divide land into different categories according to the differences of land itself and certain rules, so that the similar attributes possessed by individual units of land in the region can be centrally summarized for better construction of corresponding functional areas. Therefore, the current land classification in China mainly includes land natural classification, land use classification, land evaluation classification, and land function classification, which provides support for land use. The natural land classification is based on the natural properties of the land, such as climate, soil, hydrology, and geomorphology, and is based on the natural laws of land classification [19, 20]. Land evaluation classification is to classify land according to the similarity and difference of evaluation indexes, such as land quality, production potential, and suitability, which is an important basis for land use planning; land function classification is to classify land according to the services or products it provides, which is essentially to classify the resource attributes of land, such as production land, living land, and ecological land, which provides a great basis and guidance for land use.

The idea of systematically integrating land use under land use spatial planning and giving full play to the support and guarantee function of land use spatial planning can optimize the urban and rural patterns in the region through reasonable land use spatial planning and promote the formation of scientific production, living, and ecological space. Moreover, it is necessary to adhere to ecological protection and protection of basic farmland, control the urban-rural development boundary, etc., fully implement the management level, promote the effective control of the total amount of land for construction and urban development intensity, and promote the balanced construction and development of infrastructure and public service facilities. On the other hand, the systematic integration of land use also requires further implementation of national land improvement and supervision of comprehensive management and ecological restoration of urban and rural land. Finally, it is necessary to actively guide the balanced development of regions through the implementation of differentiated policies to guarantee the orderly implementation of spatial planning measures for land use.

At present, countries have different standards for land classification, such as the multilevel ecological classification system in the United States, the ecological land classification system in Canada, and the land classification system in the Netherlands. And the way of land classification in China is multiple standards in parallel, showing diversified characteristics. From the perspective of land use function, the classification system of “three-living land” is constructed. We have explored a three-level comprehensive functional land use zoning system at the provincial level by integrating various types of zoning. We analyze the existing land use spatial planning land classification system and propose a land use classification system based on the problems of the existing classification system. The idea of land use division is based on the industrial structure of land use. The natural ecological spatial classification system at the city and county level is established based on the combination of land use and cover types and human activity images [21–23]. The refinement of spatial functions of land use is mainly based on three perspectives of land use, ecosystem, and landscape value, and a classification system corresponding to the functions is established.

The functional classification of the land use perspective is mainly based on the economic use of land. The sustainable development perspective classifies landscape values into five major categories and constructs a county-level classification system for the three spatial land uses by systematically classifying ecological landscapes. Inspired by the EU spatial classification, a study on the division of spatial land in Hunan Province was conducted. Based on the national standard rules of land use classification, the classification of “three spatial areas” was established. The Lorenz curve and Gini coefficient method were used to study the distribution of the three spatial areas. Based on the principle of multifunctionality of land use, the classification of “three living spaces” was constructed. In general, the existing studies have explored the spatial classification system of land use and the classification of “three living spaces” in a more system-

atic way, which is important to support the preparation of spatial land use planning.

To establish a scientific land use evaluation system and index system and management mechanism to integrate land use based on land use spatial planning system, it is necessary to improve the evaluation standards of resources, environmental carrying capacity, and spatial suitability of development to provide basic conditions for land planning layout. At the same time, we should design based on land use spatial planning, land use as the center, construction of complete infrastructure, coordination of regional development and urban-rural integration, and reasonable layout of land use planning guidance and constraint management. It is also necessary to strengthen the strength of resource protection, and the ability to control spatial utilization to ensure that land resources can be used to maximum effect. Moreover, this process needs a relatively perfect land use spatial planning standard system and land use control mechanism as a guarantee to fully guarantee the rigidity and flexibility of land use spatial planning and realize the efficient use of land.

2.2. Multiocular Vision Technology. With the rapid development of science and technology, human spatial ways and techniques of land use have been increasing. Especially with the support of aerospace technology, remote sensing imaging technology based on high-altitude overhead perspective and even outer space has come into being. Remote sensing technology perceives the characteristics of target objects and analyzes them through the propagation and reception of electromagnetic waves. In the 1970s, the world’s first remote sensing satellite was successfully launched to open a new era of remote sensing detection technology. The exploration of technology using satellites as remote sensing platforms has been favored by governments of various countries. Among the early starters, the U.S. government and some of its commercial companies have implemented multiple remote sensing satellite launch programs simultaneously in recent decades, with each series of satellite launch programs containing multiple remote sensing satellites to form a satellite constellation [24–27].

At the same time, Canada is also implementing a constellation program in which satellites will carry sophisticated LIDAR systems. When the constellation is fully launched, it will reduce the interval between revisits to Canada to less than 24 hours. In addition, the earliest started in 1974 during the Cold War with the Soviet Union’s return-type remote sensing satellite for Earth observation. Looking back at the development of remote sensing technology in China, which is also strongly supported by the government, China’s aerospace technology has also made remarkable progress since the 1980s; from the meteorological satellites in 1988 to the environmental disaster mitigation series of satellites in 2008 and the high-definition series of satellites since 2013, the development of the aerospace industry has been fruitful. By the end of April 2018, the number of remote sensing satellites worldwide increased to 684. With the deployment of so many satellite-based and airborne remote sensing platforms, countries around the world have a huge amount of remote sensing data to be processed urgently every day.

Especially for optical remote sensing data, the processing and understanding of the data has been far from keeping up with the acquisition of data. The high-resolution, large-format optical remote sensing images acquired by satellites and land types often cover a large and complex amount of ground material information. Obviously, it is no longer practical to discriminate and identify these massive data in real time through manual efforts [28]. As a result, how to use computer technology to understand and interpret optical remote sensing images has become the focus and difficult problem of current research.

Multocular stereo vision is to simulate the human visual system to construct the real world. Stereo matching, as the key to 3D reconstruction and noncontact ranging, is one of the core elements of multocular vision. Multocular vision flowchart is shown in Figure 2. It has the advantages of simple implementation, low cost, and ranging under noncontact conditions by acquiring depth through two-dimensional images and can be used in robot guidance systems for navigation judgment and target pickup, in industrial automation control systems for parts installation, quality inspection, and environmental inspection, and in security monitoring systems for human flow detection and hazard alarm [29–31]. The stereo matching algorithm is divided into region matching, feature matching, phase matching, and energy matching according to the matching primitives and methods. Area matching is influenced by image affine and radiometric distortion, difficult to choose the constraint window, and easy to produce false matches at depth discontinuities; feature matching is insensitive to image geometric transformation and has strong anti-interference and low complexity; the defect is that the parallax results are sparse and need to go through the process of interpolation and fitting; phase matching algorithm is very sensitive to rotational transformation and unstable singularities; energy matching is used to construct global energy. The energy matching algorithm obtains the parallax by constructing the global energy function, which cannot be used for large deviation images and has too much complexity.

Currently, the semiglobal stereo matching of remote sensing images combined with accelerated robust features uses feature points to guide path aggregation; the stereo matching algorithm based on AD-Census features enhances the robustness to local noisy pixels; a SURF-BRISK algorithm combining Hamming distance and affine transformation to match the localization method is proposed; the multocular stereo matching algorithm with optimized oblique planes improves the computational speed. The feature-based dense stereo matching first uses linear contrast spreading to highlight the important texture of the image, extracts feature information with accelerated segmentation detection features, relies on fast approximate nearest neighbor search library and K -nearest neighbor algorithm to achieve feature matching after accelerated robust feature description, and then uses random sampling consistency algorithm to remove false matches; the obtained exact matching point pairs are used as seed pairs based on parallax continuity. The parallax is calculated by using the simplified zero-mean normalized interrelationship number as the sim-

ilarity measure, obtaining the minimum surrogate value point pair and eliminating some of the false matches by thresholding, using the polar line constraint to reduce the search complexity, and using the two-way matching strategy to improve the matching accuracy: subpixel fitting of the parallax value to obtain the subpixel parallax to improve the parallax accuracy and make the parallax. The subpixel fitting of parallax values to obtain subpixel parallaxes improves the parallax accuracy and smooths the transition in the continuous region. The algorithm solves the shortcomings of feature matching, reduces the time complexity and noise interference, and improves the accuracy and precision, especially for the weak texture and depth discontinuity.

3. Methods

3.1. Model Architecture. The traditional CenterNet network adopts a code-decode structure to learn high-level semantic information through successive convolutional operations of the network. However, the targets in remote sensing images are small and dense, and a series of convolution will cause the aggregation of small target features, resulting in problems such as missed detection and false detection. Therefore, this paper proposes a detection model AFF-CenterNet based on CenterNet algorithm, which combines attention mechanism and parallel-layer feature sharing structure. This method combines deep features and shallow features, effectively combining the advantages of strong semantic information of deep features and strong location and texture information of shallow features, which is effective in improving small target detection. The channel attention module is added before the parallel-layer module to reduce background interference. This method adaptively calibrates the feature responses between different channels, which effectively improves the feature extraction capability of the network. The model structure diagram is shown in Figure 3.

3.2. Parallel Layer Structure. In the network structure of CenterNet algorithm, the Conv1 and Conv7 layers, Conv2 and Conv6 layers, and Conv3 and Conv5 layers are fused in this paper. Since these feature layers have different spatial sizes, they are processed by a “Feature Fusion” module before being fused. For this module, two topologies, named CenterNet-C and CenterNet-T, are designed as shown in Figure 4, where CenterNet-C has a standard 1×1 convolution to make the feature layers have the same spatial size before and after fusion, and CenterNet-T replaces the standard convolution in CenterNet-C with a hole convolution for testing. Since each feature value in different layers has a different scale, it needs to be processed by batch normalization and ReLU activation after convolution.

3.3. Channel Attention Module. The attention mechanism can focus on the local information of the image, locate the information of interest, and suppress the useless information. To make the model focus more on the channels with effective information, this paper introduces the Squeeze-Excitation Attention Module (SE-Net) before the parallel

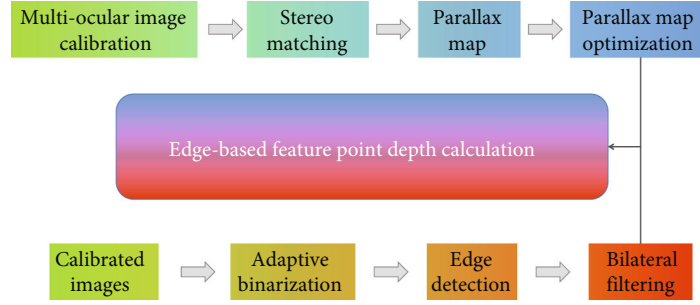


FIGURE 2: Multiocular vision flowchart.

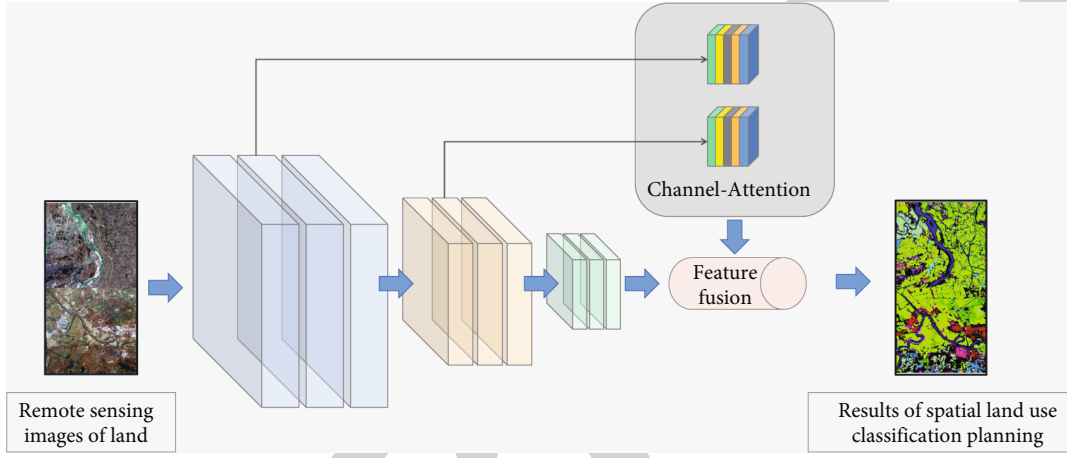


FIGURE 3: Model structure.

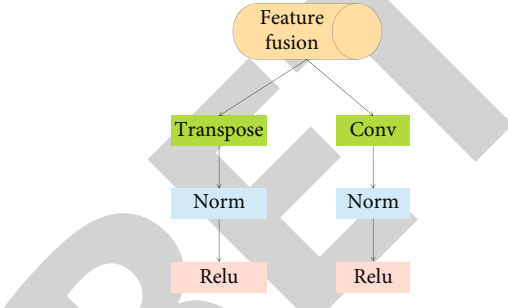


FIGURE 4: Parallel fusion module structure diagram.

feature sharing module. This module first performs a squeeze operation on the $H \times W$ feature map with the input channel number C to obtain a 1×1 feature map with the channel number C , which corresponds to the global pooling. Then, the obtained feature maps are subjected to the excitation operation to obtain the weight values between channels, which corresponds to the twice fully connected and sigmoid layers. Finally, the original feature map is multiplied by the weights of the corresponding channels through scale scaling to obtain the new feature map, to update the effective information channels, and to suppress the useless information channels.

3.4. Multiocular Visual Depth Values. Assuming a point $p(x, y, z)$ on the three-dimensional space, with the left

camera as the reference coordinate system, the projection points on the left and right lenses of the horizontally placed binocular camera are $L(x_l, y_l), R(x_r, y_r)$, and O_l, O_r which are the center points of the left and right lenses, respectively; f is the focal length of the camera, and B is the baseline of the binocular camera; according to the principle of triangular similarity of perspective transformation, it is known that

$$\frac{z}{f} = \frac{y}{y_1} = \frac{y}{y_r} = \frac{x}{x_1} = \frac{x-B}{x_r}. \quad (1)$$

The parallax under the model can be expressed as

$$d = x_1 - x_r. \quad (2)$$

From the equation, the spatial coordinates of point p and the depth value can be deduced as

$$\begin{cases} z = \frac{fB}{x_1 - x_r}, \\ x = \frac{x_1 B}{x_1 - x_r}, \\ y = \frac{y_1 B}{x_1 - x_r}. \end{cases} \quad (3)$$

TABLE 1: Software and hardware environment configuration.

Parameters	Configuration
Operating system	Ubuntu 20.04.2 LTS
CPU	Inter Core i9-10900KF
CPU memory	62.7 G
GPU	GeForce RTX 3080
GPU memory	10G
Programming language	Python
Programming platforms	Pycharm
Graphics acceleration environment	CUDA11.2, CuDNN7.6
Deep learning framework	Pytorch 1.7.0, Torchvision 0.8.1

According to the above three-dimensional spatial point coordinates and depth value solution process, in order to meet the accuracy and efficiency of octree map construction for complex environment of land use space, it is necessary to extract the two-dimensional edge feature points of the environment and solve the corresponding three-dimensional spatial coordinate points of the feature points, and the distribution of the feature points is closely related to the environmental information, and a reasonable feature point extraction method can not only maintain the integrity of the map but also reduce the system operation. A reasonable feature point extraction method can not only maintain the integrity of the map but also reduce the operation complexity of the system, thus ensuring the real-time and efficient system. Therefore, this paper proposes a method of feature point extraction based on edge binary map, by finding the coordinates of feature points of edge binary map and then obtaining the corresponding feature point parallax values from parallax map and calculating the spatial coordinates and depth values.

3.5. Loss Function. AFF-CenterNet still adopts the construction method of CenterNet loss function, which consists of three parts: centroid prediction loss L_k , bias loss L_{off} , and width-height loss L_{size} . CenterNet uses pixel-level logistic regression focal loss function to solve the problem of uneven distribution of positive and negative samples.

$$L_k = \frac{-1}{N} \sum_{xyc} \begin{cases} (1 - \hat{Y}_{xyc})^\alpha \log(\hat{Y}_{xyc}), Y_{xyc} = 1, \\ (1 - Y_{xyc})^\beta (\hat{Y}_{xyc})^\alpha \log(1 - \hat{Y}_{xyc}), \end{cases} \quad (4)$$

where α and β are the hyperparameters of focal loss, which are taken as 2 and 4, respectively, in the experiment. n is the number of key points in the image, which serves to normalize all focal losses. \hat{Y}_{xyc} is the predicted value and Y_{xyc} the true label value. When Y_{xyc} is equal to 1, for easily distinguishable samples, the predicted value \hat{Y}_{xyc} is close to 1, making $(1 - \hat{Y}_{xyc})^\alpha$ and $\log(\hat{Y}_{xyc})$ close to 0 to obtain a smaller L_k . On the contrary, for hard-to-distinguish samples, the predicted value \hat{Y}_{xyc} is close to 0, making the final L_k larger. When \hat{Y}_{xyc} is not equal to 1, the theoretical value of

the predicted value \hat{Y}_{xyc} should be 0. If this value is larger, $(\hat{Y}_{xyc})^\alpha$ will increase to serve as a penalty. If the predicted value is close to 0, then $(\hat{Y}_{xyc})^\alpha$ will be small to reduce the loss weight. And $(1 - Y_{xyc})^\beta$ serves to weaken the loss weight of negative samples around the centroid when Y_{xyc} is not equal to 1. Since the resolution of the feature map after backbone extraction network processing becomes one-fourth of the input image, which is equivalent to one pixel point of the output feature map corresponding to a 4×4 region of the original image, it causes the loss of details of the original image and makes the prediction biased. Therefore, the centroid bias value \hat{O} is introduced, and the bias value is trained using the L_1 loss function.

$$L_{\text{off}} = \frac{1}{N} \sum_p \left| \hat{O}_p - \left(\frac{p}{R} - \tilde{p} \right) \right|, \quad (5)$$

where N is the number of key points in the image, p is the target frame centroid, and R is the downsampling factor, which takes the value of 4 during the experiment. CenterNet regresses to the object size $s_k = (x_2^{(k)} - x_1^{(k)}, y_2^{(k)} - y_1^{(k)})$ for each object after predicting all the centers. To reduce the computational effort, a single size prediction \hat{S} is used for each target species, and the width-height loss L_{size} is trained using the L_1 loss function, as shown in

$$L_{\text{size}} = \frac{1}{N} \sum_{k=1}^N \left| \hat{S}_{p_k} - s_k \right|. \quad (6)$$

The total loss L_{det} is obtained from the weighted sum of the losses of the above branches, as shown in

$$L_{\text{det}} = L_k + \lambda_{\text{off}} L_{\text{off}} + \lambda_{\text{size}} L_{\text{size}}, \quad (7)$$

where the weights λ_{off} and λ_{size} are taken as 1 and 0.1, respectively.

4. Experiments and Results

4.1. Experiment Setup. In order to verify the feasibility of the proposed algorithm, the category images of an urban land

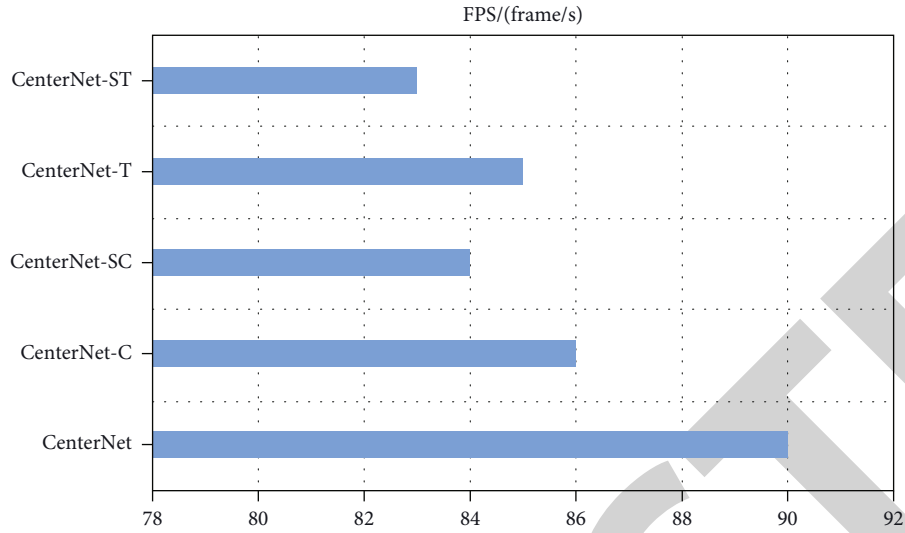


FIGURE 5: Comparison of different improved structure FPS.

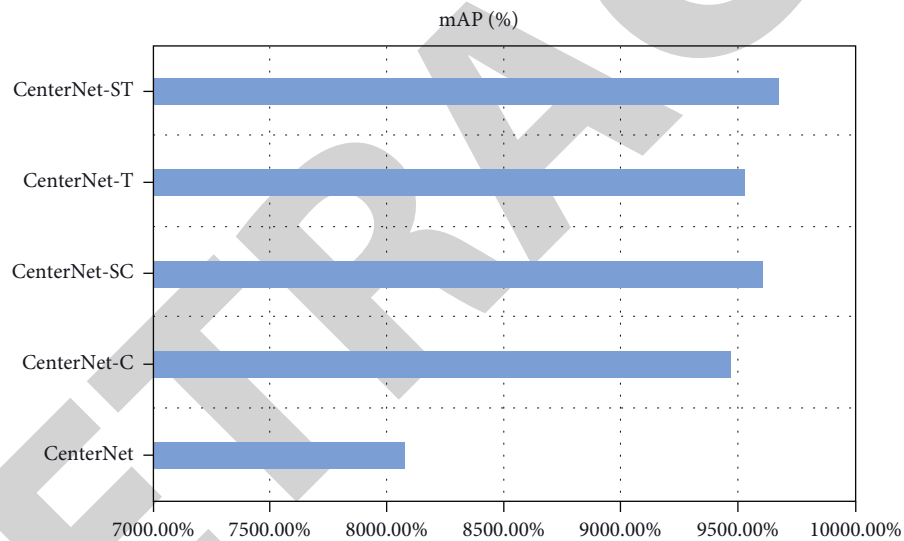


FIGURE 6: Comparison of different improved structure map.

space remote sensing image dataset in China are selected for the training and testing of the network, respectively. Among them, UCASAOD dataset is produced by the University of Chinese Academy of Sciences, which contains 1000 remote sensing images with 7482 samples, with more concentrated data and more uniform distribution of target directions. RSOD dataset contains 446 remote sensing images with 4993 samples, with diverse brightness and contrast in the images, and interference such as occlusion, shadow, and distortion. During the experiment, 10% of the images of the two datasets were randomly selected as test samples, 10% of the remaining 90% of the images were selected as the validation set, and the rest were used as the training set, and the configuration of the experimental environment is shown in Table 1.

In the experiments, the downsampling rate R is 4, and the Adam optimizer is used for iterative training, and the input images are uniformly scaled to a resolution of 512×512 . The initial learning rate is set to $1e^{-3}$, and the batch size is 4. After training 50 epochs, the learning rate is reduced to $1e^{-4}$, and then, 50 epochs are trained. In addition, to speed up the convergence, the backbone of ResNet-50 is trained using the pretrained weights obtained from the ImageNet classification task.

4.2. Experimental Results. The comparison results of several network structures before and after the improvement on the UCFAS-AOD test set are shown in Figures 5 and 6. The detection accuracy of the improved network is significantly improved while maintaining certain computational

TABLE 2: Confusion matrix for level 1 terrestrial accuracy.

Type of land use	Residential land	Commercial land	Industrial, mining, and storage land	Transportation	Land for public administration and public services	User accuracy (%)
Residential land	3573	157	1747	0	5092	33.8
Commercial land	0	10329	0	0	804	92.7
Industrial, mining, and storageland	0	0	10184	0	104	98.9
Transportation	468	0	382	669	0	44.0
Land for public administration and public services	809	570	976	792	48446	93.9
Producer accuracy (%)	73.6	93.4	76.6	45.7	60.6	33.8
Overall accuracy (%)				86.0		
Kappa coefficient				0.75		

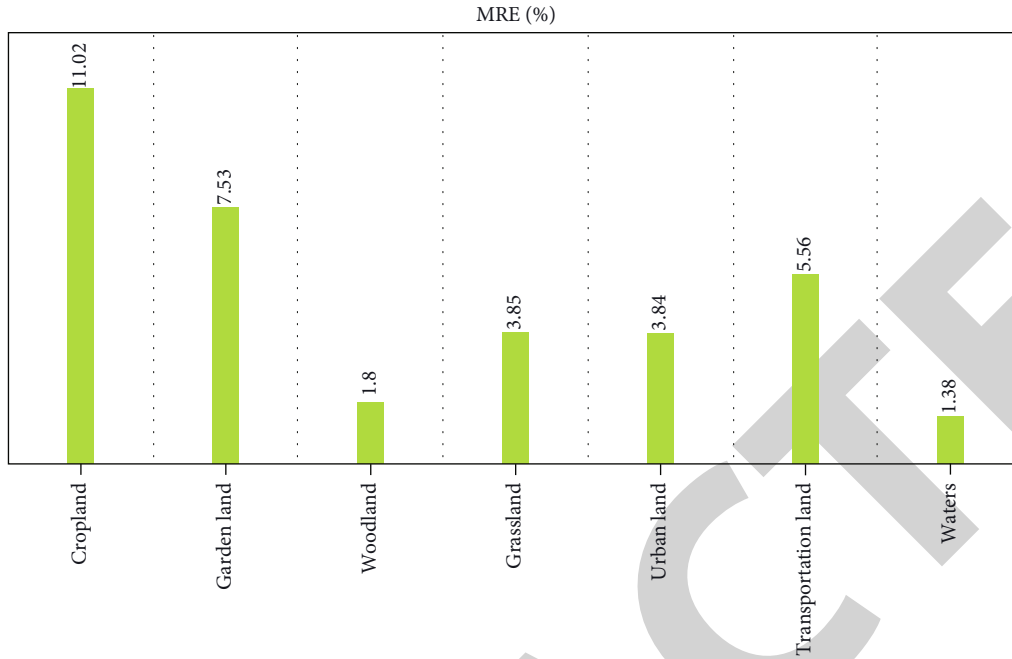


FIGURE 7: Model validation MRD statistical parameters.

efficiency. CenterNet-T with null convolution improves the detection accuracy by 0.59 percentage points compared with CenterNet-C with standard 1×1 convolution, and CenterNet-SC and CenterNet-ST improve the detection accuracy by 1.34 percentage points and 1.46 percentage points compared with CenterNet-C and CenterNet-T, respectively. CenterNet-ST, which has the best overall effect, improves the detection accuracy by 16 percentage points and 0.71 percentage points over CenterNet and CenterNet-SC, respectively, so the CenterNet-ST topology is subsequently used as the AFF-CenterNet algorithm model.

Three sets of representative images were selected from the dataset for testing and the before and after improvement comparison graphs. Because the feature extraction layer of the original network has gone through the “encoding-decoding” structure, the semantic information of small targets is seriously lost, which makes it difficult to detect small targets with similar background color, while the parallel-layer feature sharing network of AFF-CenterNet effectively fuses deep and shallow features to reduce the semantic loss, and the small targets with low contrast with the background are still detected. Small targets with low background contrast can still be effectively recognized.

Table 2 shows the confusion matrix of the accuracy of the first-level ground class, and the overall accuracy and kappa coefficient are used to determine the accuracy of the ground class. The overall accuracy of primary land class is 86.0%, and the kappa coefficient is 0.75; the overall accuracy of secondary land class is 73.9%, and the kappa coefficient is 0.69. Among them, the accuracy of commercial land user is 95.1%, and the accuracy of park and green space user is 97.1%; the accuracy of institutional land and medical and health land classification is lower, and the accuracy of the for-

mer user is 15.7%, and the latter user is 11.1%. The accuracy of the former is 15.7%, and the accuracy of the latter is 11.1%.

Figures 7, 8, and 9 present the statistical parameters of the comparison between historical and simulated values of each land use type during 2014-2020. The MRE of forest land, grassland, urban land, transportation land, and water can basically be controlled within or around 5%, while the MRE of cropland and garden land are 11.02% and 7.53%, respectively. The Nash coefficients of cropland are negative, while the Nash coefficients of other land types are greater than 0. The R^2 of grassland, urban land, and water reaches 0.99, 0.70, and 0.84, respectively, while the R^2 of other land types are not satisfactory, especially for cropland and forest land, due to the poor simulation effect of early data for model validation. Although the simulation results of the model are not satisfactory, they can still be used. Taking the model fit validation curve of cropland in Figures 7, 8, and 9 as an example, the relative error from 2009 to 2012 reached about 30%, and the simulation effect after that was very good, with only 2.24% MRE. A certain degree of error is allowed in system dynamics models, which are often used to study changes in complex systems over time series. The results of the model validation showed that the model could meet the needs of the next study.

Table 3 presents the average annual dynamic attitude of each land use type. Both urban land and transportation land in construction land show a slowing trend in growth rate. Under a series of land ecology construction policies in a city in China, forest land and water areas, which are the objects of ecological value protection, have been protected to a certain extent, and soil erosion and habitat encroachment have been effectively controlled, and the reduction of forest land and water areas is expected to be limited to 2% in the future.

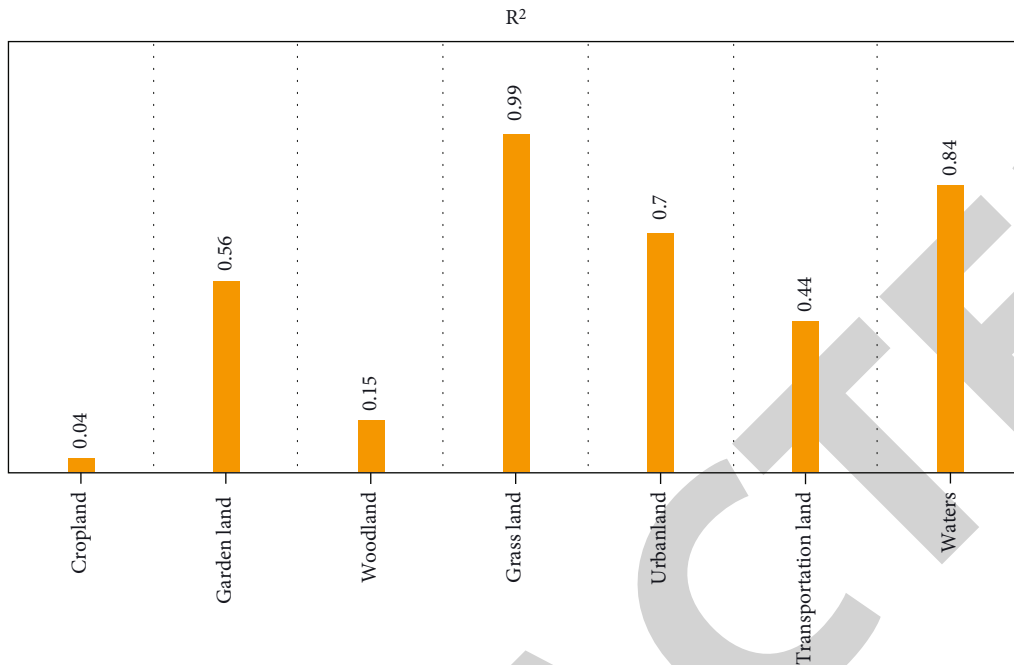


FIGURE 8: Model validation R^2 statistical parameters.

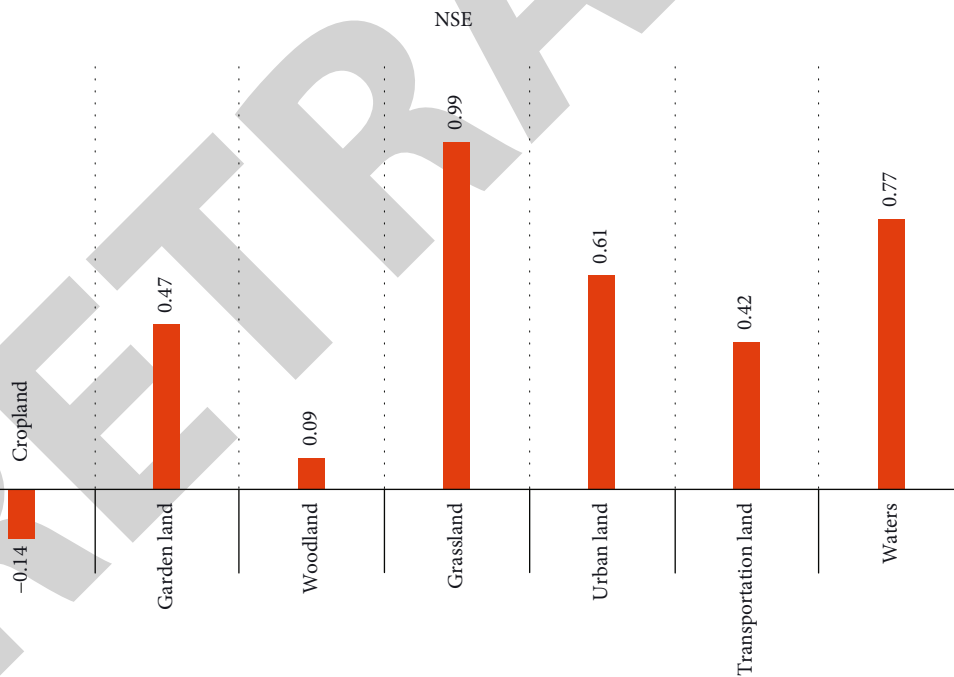


FIGURE 9: Model validation of NSE statistical parameters.

Among the agricultural land, less than 5% is arable land, but the arable land is changing drastically, and the overall trend is rapidly declining. In one Chinese city, the management of agricultural land is achieved through the establishment of a basic farmland protection system and the designation of basic farmland transformation zones. However, in the context of rapid urbanization, this reactive system of agricultural land control is seriously failing. The actual scale of popula-

tion growth in a Chinese city exceeds expectations and the total economic volume expands dramatically, which inevitably intensifies the conflict between the expansion of agricultural land and construction land around the city, and the loss of arable land, garden land, and grassland is the inevitable result. The land use map of 2014 is used as input, and the data of each land use type in 2025 predicted by the SD model is used as input to the transfer matrix of the CA model to

TABLE 3: Land use type dynamic attitude.

Land use type	Average dynamic attitude (%)		
	2004-2008	2008-2014	2014 - 2025
Cropland	-2.38	-0.14	-3.57
Garden land	-3.61	-3.03	-2.97
Woodland	-2.62	0.18	-0.91
Grassland	0.00	>100	-5.03
Urban land	2.07	1.85	2.02
Transportation land	7.46	-0.19	2.45
Waters	0.10	-0.94	-1.54

obtain the land use prediction map of 2025. This simulation scenario does not consider the effects of policies and planning, etc., and follows the current land use change trend. Table 3 integrates and compares the spatial changes of land use pattern in 2004, 2008, 2014, and the projected 2025. The overall land use structure of a city in China is basically unchanged, with construction land and forest land dominating, but there are obvious changes in the quantity and spatial distribution of each land use type. The most obvious is the outward expansion and connectivity of construction land through the encroachment of parkland and forest land, and this trend is gradually increasing, and in 2025, construction land will be more concentrated, and the distribution of agricultural land types will be more fragmented.

5. Conclusion

With the economic development of China, the differences between various regions are gradually increasing, the spatial classification of land use planning and construction has become an important measure and means to enhance the national economy and social economy, and only by vigorously promoting urban and rural construction efforts can we achieve the goal of building a well-off society and maintaining social stability. In the process of construction, land resources should be strictly managed, reasonable planning should be carried out, and corresponding measures should be taken to deal with various illegal land occupation and illegal land use in accordance with the law, so that land resources can be developed sustainably and make them fully supplied with land use space classification planning and construction. With the joint efforts of the government, the public, and the enterprises, the use of land resources will become more and more reasonable, the level of land management will be enhanced, and the speed of land use space classification planning and construction will become faster and faster.

This paper proposes that the land use spatial classification planning based on multivision has the characteristics of large scale, short period, and multiple data types, which can complete the collection and investigation of land resources and other resource information in a short time, ensure the efficiency of work and reduce the work cost, realize the real-time monitoring of land resources use and land use spatial classification quality, and provide a series of information for land use planning. It can also provide a

series of information as reference for the formulation of land use planning, which is very important for the efficient use of land resources. In the future, we plan to carry out research on spatial land use classification planning methods based on recurrent neural networks.

Data Availability

The experimental data used to support the findings of this study are available from the corresponding author upon request.

Conflicts of Interest

The authors declared that they have no conflicts of interest regarding this work.

Acknowledgments

This work was sponsored in part by Fund Project: 2017 Jiangsu Provincial Land Resources Science and Technology Plan Project "Study on Reclamation and Utilization of Industrial and Mining Wasteland" (2017048).

References

- [1] M. Zhao, C. Chen, L. Liu, D. P. Lan, and S. Wan, "Orbital collaborative learning in 6G space-air-ground integrated networks," *Neurocomputing*, vol. 497, pp. 94–109, 2022.
- [2] C. Chen, Y. Zeng, H. Li, Y. Liu, and S. Wan, "A multi-hop task offloading decision model in MEC-enabled Internet of Vehicles," *IEEE Internet of Things Journal*, vol. 8, pp. 53062–53071, 2022.
- [3] C. Chen, H. Li, H. Li, R. Fu, Y. Liu, and S. Wan, "Efficiency and fairness oriented dynamic task offloading in Internet of Vehicles," *IEEE Transactions on Green Communications and Networking*, vol. 6, pp. 1481–1493, 2022.
- [4] C. Chen, J. Jiang, Y. Zhou, N. Lv, X. Liang, and S. Wan, "An edge intelligence empowered flooding process prediction using Internet of Things in smart city," *Journal of Parallel and Distributed Computing*, vol. 165, pp. 66–78, 2022.
- [5] C. Chen, J. Jiang, R. Fu, L. Chen, C. Li, and S. Wan, "An intelligent caching strategy considering time-space characteristics in vehicular named data networks," *IEEE Transactions on Intelligent Transportation Systems*, vol. 21, pp. 1–13, 2021.

Retraction

Retracted: Clinical Study of Different Treatment Methods for Tuberculous Pleuritis Complicated with Pleural Tuberculoma

Computational and Mathematical Methods in Medicine

Received 27 June 2023; Accepted 27 June 2023; Published 28 June 2023

Copyright © 2023 Computational and Mathematical Methods in Medicine. This is an open access article distributed under the Creative Commons Attribution License, which permits unrestricted use, distribution, and reproduction in any medium, provided the original work is properly cited.

This article has been retracted by Hindawi following an investigation undertaken by the publisher [1]. This investigation has uncovered evidence of one or more of the following indicators of systematic manipulation of the publication process:

- (1) Discrepancies in scope
- (2) Discrepancies in the description of the research reported
- (3) Discrepancies between the availability of data and the research described
- (4) Inappropriate citations
- (5) Incoherent, meaningless and/or irrelevant content included in the article
- (6) Peer-review manipulation

The presence of these indicators undermines our confidence in the integrity of the article's content and we cannot, therefore, vouch for its reliability. Please note that this notice is intended solely to alert readers that the content of this article is unreliable. We have not investigated whether authors were aware of or involved in the systematic manipulation of the publication process.

In addition, our investigation has also shown that one or more of the following human-subject reporting requirements has not been met in this article: ethical approval by an Institutional Review Board (IRB) committee or equivalent, patient/participant consent to participate, and/or agreement to publish patient/participant details (where relevant).

Wiley and Hindawi regrets that the usual quality checks did not identify these issues before publication and have since put additional measures in place to safeguard research integrity.

We wish to credit our own Research Integrity and Research Publishing teams and anonymous and named external researchers and research integrity experts for contributing to this investigation.

The corresponding author, as the representative of all authors, has been given the opportunity to register their agreement or disagreement to this retraction. We have kept a record of any response received.

References

- [1] X. Zhang and J. Chi, "Clinical Study of Different Treatment Methods for Tuberculous Pleuritis Complicated with Pleural Tuberculoma," *Computational and Mathematical Methods in Medicine*, vol. 2022, Article ID 5666067, 9 pages, 2022.

Research Article

Clinical Study of Different Treatment Methods for Tuberculous Pleuritis Complicated with Pleural Tuberculoma

Xiaoling Zhang and Jingyu Chi 

Four Tuberculosis Areas, Shandong Public Health Clinical Center, Jinan, Shandong 250001, China

Correspondence should be addressed to Jingyu Chi; cjy1303@126.com

Received 28 April 2022; Accepted 29 June 2022; Published 27 August 2022

Academic Editor: Pan Zheng

Copyright © 2022 Xiaoling Zhang and Jingyu Chi. This is an open access article distributed under the Creative Commons Attribution License, which permits unrestricted use, distribution, and reproduction in any medium, provided the original work is properly cited.

Objective. To compare the clinical efficacy and adverse drug reactions of four different schemes in the treatment of pleural tuberculoma. **Methods.** A total of 120 patients with pleural tuberculoma admitted to the Tuberculosis Department of our hospital from January 2018 to January 2021 were selected as the research subjects. According to different treatment methods, the patients were divided into four groups, with 30 cases in each group. They were as follows: group A received classical HRZE regimen, group B received HRZE+pleural injection, group C received HZE+rifabutin, and group D received HZE+rifabutin+pleural injection. All patients were treated intensively for 3 months and then consolidated treatment for 6 months according to the patient's condition. The absorption of lesions in the four groups at different time was compared, and the occurrences of adverse drug reactions and treatment outcomes during treatment were recorded. **Results.** After 3 months of treatment, compared with groups A, B, and C, the number of significantly absorbed cases and effective cases in group D increased, while the number of invalid cases decreased. However, there was no statistical significance in the absorption of lesions between the four groups ($\chi^2 = 8.272$, $P = 0.507$). In addition, pairwise comparison showed no significant difference in the absorption of lesions ($P > 0.05$). After 9 months of treatment, there was no significant difference in the absorption of lesions among the four groups ($\chi^2 = 8.795$, $P = 0.185$), but the absorption of lesions in group D was significantly better than that in group A ($P < 0.05$). During treatment, the incidence of adverse reactions in the four groups was significantly different ($\chi^2 = 8.779$, $P = 0.032$). Pairwise comparison showed that the incidence of adverse reactions in groups C and D was significantly lower than that in group A ($P < 0.05$). The total treatment course of group A was 9-16 months, and 10 cases (33.33%) still had residual lesions or pleural thickening at the end of treatment. The total course of treatment in group B was 9-12 months, and 7 cases (23.33%) still had residual lesions or pleural thickening at the end of the course of treatment. The total treatment course of group C was 9-16 months, and 8 cases (26.67%) still had residual lesions or pleural thickening at the end of treatment. The total course of treatment in group D was 9-12 months, and there were still 2 cases of residual lesions (6.67%) at the end of the course. **Conclusions.** HZE+rifabutin+pleural injection against tuberculosis therapy has a significant clinical efficacy in the treatment of pleural tuberculoma, which can more effectively improve the clinical symptoms of patients, improve the efficacy, and reduce complications, with a good prognosis, worthy of clinical promotion.

1. Introduction

Tuberculous pleurisy is the second most common extrapulmonary tuberculosis after lymph node tuberculosis. It accounts for about 3% to 5% of tuberculosis in the United States and can reach 30% in countries with high tuberculosis burden [1]. As a localized lesion in the pleural cavity, pleural tuberculoma can occur in the parietal pleura or visceral pleura [2] and is one of the rare clinical diseases. At present,

its pathogenesis is not clear, and most scholars believe that it is a caseous mass wrapped in fibrous tissue formed by the concentration and drying of local tuberculosis tissue caused by fibrous connective tissue hyperplasia and pleural thickening and adhesion in the course of the development of exudative tuberculous pleuritis [3, 4]. Pleural tuberculoma can occur in all age groups but is generally believed to be more common in young adults. The incidence of pulmonary tuberculoma is 0.62%-5.7%. Most patients with pleural

tuberculoma have definite tuberculous pleurisy or pulmonary tuberculosis (75%-96%), but a small number of patients have no definite history of tuberculosis and only find the lesions during physical examination (4.0%-25%) [5-7]. Patients with tuberculous pleuritis develop pleural tuberculoma even after regular intensive antituberculosis therapy, which is classical HRZE scheme. Clinical data show that pleural tuberculoma occurs more within 3 months of antituberculosis treatment. The clinical practice is to continue the original regimen of antituberculosis treatment, and most of pleural tuberculoma can be absorbed in 3~18 months. If the disease persists or the patient requires, surgical resection is feasible [8, 9]. In recent years, we find that more and more patients developed pleural tuberculoma in the course of treatment in clinical work. Classical antituberculosis drugs are still the preferred method for the treatment of pleural tuberculoma, but they have many adverse reactions, which sometimes aggravate or prolong the disease course of patients, leading to drug resistance of tubercle bacillus in some patients and poor prognosis [10]. Rifabutin is a semi-synthetic rifamycin, similar to rifampicin, rapidly absorbed in the gastrointestinal tract, with good lipid solubility, which can be widely distributed in tissues and cells. It is well tolerated and has fewer side effects than rifampicin [11, 12]. In addition, since antituberculosis drugs are difficult to penetrate into the pleural tuberculoma lesions, the effect of chemotherapy solely relying on drugs is poor [3, 13]. On the basis of systemic antituberculosis treatment, combined with intrapleural tuberculoma injection, the drug concentration in pleural tuberculoma can be effectively increased, which is beneficial to improve the curative effect. In order to reduce complications and improve efficacy, 120 patients with pleural tuberculoma who were initially diagnosed in our hospital were treated with different treatment schemes in this study, aiming to observe the clinical efficacy of different treatment schemes and provide clinical practice for better treatment of pleural tuberculoma patients. The report is as follows.

2. Materials and Methods

2.1. Materials. A total of 120 pleural tuberculoma patients admitted to the Tuberculosis Department of our hospital from January 2018 to January 2021 were enrolled as the research subjects. Patients were randomly divided into four groups and then given different treatment regimens, 30 cases in each group. Group A was given classical HRZE regimen; group B was given HRZE+pleural cavity infusion; group C was given HZE+rifabutin; and group D was given HZE+rifabutin+pleural cavity infusion. Inclusion criteria are as follows: (1) a history of "tuberculous pleuritis," (2) suspected pleural tuberculoma, (3) complete clinical data, (4) informed consent to the study from patients and their families, and (5) patients older than 18 years old. Exclusion criteria are as follows: (1) severely infected persons; (2) patients complicated with serious cardiovascular and cerebrovascular diseases, nephropathy, and autoimmune diseases; (3) patients complicated with malignant tumor; (4) patients complicated with cognitive and behavioral ability insufficiency; (5) pregnant or lactating women; (6) patients with drug withdrawal

or change of treatment plan due to serious adverse reactions; (7) patients with previous antituberculosis treatment; and (8) patients who dropped out of the clinical study or were lost to follow-up.

2.2. Therapeutic Methods. All patients received general symptomatic treatment such as anti-infection, fluid rehydration, nutritional support, and correction of electrolyte disorders. On this basis, group A was given classical HRZE regimen. The drugs included isoniazid tablet (H) (Southwest Pharmaceutical Co., Ltd., SFDA approval number: H50020124, specification: 0.1 g/tablet, dosage: 3 tablets/time), rifampicin capsule (R) (Chengdu Tiantai Mount pharmaceutical Co., Ltd., SFDA approval number: H51022701 of specification: 0.15 g/tablet, dosage: 3 tablets/time), pyrazinamide tablets (Z) (Guangdong South China Pharmaceutical Group Co., Ltd. SFDA approval number: H44020761, Specification: 0.25 g/tablet, dosage: 3 tablets/time), and ethambutol tablets (E) (Guangdong South China Pharmaceutical Group Co., Ltd. SFDA approval number: H44020758, specification: 0.25 g/tablet, dosage: 3 tablets/time), all of which were administered orally, once a day. Group B was given HRZE+pleural cavity medicine injection regimen, a joint pleural cavity medicine injection on the basis of the treatment of group A. The specific operation was as follows: the patient underwent B-ultrasound examination to determine the puncture point; the skin was sterilized; the surgeon worn sterile gloves, covered the hole drapes, and vertically inserted the needle with 0.2% lidocaine at the upper edge of the rib at the puncture point. The B-ultrasound positioning tip was located in the center of the puncture, and 0.1 g (2 mL) isoniazid was injected locally, and the needle was removed. The patient was asked to rest in bed. Group C was given HZE+rifabutin. The drugs included isoniazid+pyrazinamide+ethambutol+rifabutin. Rifabutin (Sichuan Med-Shine Pharmaceutical Co., Ltd., SFDA approval number: H2007296, specification: 0.15 g/tablet, dosage: 2 tablets/time) was administered orally, once a day. Group D was given HZE+rifabutin+pleural infusion regimen, a joint pleural cavity medicine injection on the basis of the treatment of group C. The procedure was the same as that of group B, and patients in all four groups received intensive treatment for 3 months. If the laboratory sputum smear is still positive after 3 months of intensive treatment, the treatment would be prolonged. The four groups received the same consolidation treatment: isoniazid tablet (0.1 g/tablet) and rifampicin capsule (0.15 g/tablet), orally, three times a day, for 6 months.

2.3. Observational Indices. (1) Age, gender, complications, the levels of albumin (Alb), erythrocyte sedimentation rate (ESR), fasting blood glucose (FBG), and lactic dehydrogenase (LDH) were recorded at admission. (2) Chest CT scan features were recorded. (3) The location, number, and size of pleural tuberculoma were recorded. (4) Pleural tuberculoma absorption was compared among the four groups at the third month of treatment, and the actual course of treatment and the final treatment outcome of all patients were recorded. (5) Clinical cure rates of patients in four groups

were recorded. (6) The incidence of adverse reactions during treatment was recorded, including skin rash, liver damage (increased alanine transaminase (ALT)), cytopenia (decreased platelets (PLT)), and renal function (increased uric acid (UA)).

2.4. Evaluation Criterion. The evaluation of pleural tuberculoma absorption was carried out according to the *Clinical Diagnosis and Treatment Guidelines: Tuberculosis Volume* developed by the Chinese Medical Association [14], and the outcome of pleural tuberculoma was measured and observed by chest CT scan: (1) “significantly absorbed” refers to the complete absorption of the lesions in the lung or the reduction of the pleural tuberculoma more than 50%~80% after treatment. (2) “Effective” means the absorption of the lesion between 30% and 50%. (3) “Invalid” refers to the reduction of pleural tuberculoma in patients with less than 30% or no significant reduction. (4) “Deteriorated” refers to the trend of increasing diameter or number of pleural tuberculoma in patients. Clinical cure is as follows: complete disappearance of symptoms and signs, obvious absorption of lung lesions, and negative culture of mycobacterium tuberculosis in sputum for three consecutive times or more [15]. All patients were followed up to the end of the treatment course.

2.5. Statistical Analysis. SPSS 22.0 software was used for statistical analysis. Measurement data conformed to the normal distribution were expressed in the form of $\bar{x} \pm s$ and tested by independent sample *t*-test between two groups. Data not conformed to normal distribution were tested by the Mann-Whitney *U* rank-sum test. One-way ANOVA was used for comparison between multiple groups. Counting data were expressed as *n* (%), and the comparison between groups was performed by χ^2 test. $P < 0.05$ indicated significant difference.

3. Results

3.1. Comparison of General Data of Patients in Four Groups. Before treatment, there were no statistically significant differences in age, gender, serum biochemical indicators, and other general clinical data among the four groups (all $P > 0.05$), indicating comparability. Specific data are shown in Table 1.

3.2. Chest CT Examination. Before treatment, all patients underwent CT examination, and there were no statistical significances in the number, location, and size of pleural tuberculoma among the four groups (all $P > 0.05$), indicating comparability. Specific data are shown in Table 2.

3.3. Comparison of Absorption of Lesions at Different Time. After 3 months of treatment, the results showed that the number of significantly absorbed cases and effective cases in group D increased, while the number of invalid cases decreased compared with groups A, B, and C. However, there were no statistical significances in the absorption of lesions among the four groups ($\chi^2 = 8.272$, $P = 0.507$). In addition, pairwise comparison showed no significant differ-

ence in the absorption of lesions ($P > 0.05$). After 9 months of treatment, there was no statistically significant difference in the absorption of lesions among the four groups ($\chi^2 = 8.795$, $P = 0.185$), but the absorption of lesions in group D was significantly better than that in group A ($P < 0.05$). Specific data are shown in Table 3 and Figures 1–4.

3.4. Incidence of Adverse Reactions. During the treatment, the incidence of adverse reactions was 56.67% in group A ($n = 17$), 46.67% ($n = 14$) in group B, 30.00% ($n = 9$) in group C, and 20.00% ($n = 6$) in group D. The difference in the incidence of adverse reactions among the four groups was statistically significant ($\chi^2 = 8.779$, $P = 0.032$). Pairwise comparison showed that the incidence of adverse reactions in groups C and D was significantly lower than that in group A ($P < 0.05$). Specific data are shown in Table 4.

3.5. Actual Course of Treatment and Outcome. In group A, 19 patients maintained the original antituberculosis chemotherapy regimen, 7 patients adjusted the chemotherapy regimen and extended the treatment time due to adverse drug reactions, and 3 patients were transferred to other hospitals for surgical treatment after 9 months of treatment and continued antituberculosis chemotherapy after surgery. CT follow-up revealed significant absorption of lesions in 18 patients, effective absorption of lesions in 9 patients with improved clinical symptoms, and no significant absorption of lesions in 3 patients. The total course of treatment in group A was 9–22 months, and 10 cases (33.33%) still had residual lesions or pleural thickening at the end of the course. In group B, 26 patients continued the original treatment regimen, and 4 patients had drug withdrawal after significant pleural tuberculoma reduction. CT follow-up showed no significant change in the size and morphology of the lesions after drug withdrawal. In the end, 21 patients had the lesions significantly absorbed, while the remaining cases had lesions significantly reduced and the clinical symptoms improved. The total course of treatment in group B was 9–18 months, and 7 cases (23.33%) still had residual lesions or pleural thickening at the end of the course. In group C, 22 patients continued the original treatment regimen, and 5 patients received aminoglycoside injection on the basis of the original regimen for 2–3 months. CT follow-up showed significant pleural tuberculoma absorption in 20 patients, significant pleural tuberculoma reduction in 7 patients, and insignificant pleural tuberculoma absorption in 3 patients. The total course of treatment in group C was 9–16 months, and 8 cases (26.67%) still had residual lesions or pleural thickening at the end of the course. In group D, 28 patients continued the original treatment plan, and 2 patients stopped taking the drugs after the pleural tuberculoma shrank significantly. CT follow-up showed that the lesions were significantly absorbed in 27 patients and significantly reduced in 3 patients. The total course of treatment in group D was 9–16 months, and there were still 2 cases of residual lesions (6.67%) at the end of the treatment course.

TABLE 1: Comparison of general clinical data of patients in four groups.

Group	Group A ($n = 30$)	Group B ($n = 30$)	Group C ($n = 30$)	Group D ($n = 30$)	F / χ^2	P
Gender (male/female)	19/11	20/10	22/8	18/12	1.297	0.730
Age (years)	36.26 ± 2.41	37.31 ± 2.16	36.74 ± 2.48	37.15 ± 2.71	1.949	0.126
Alb (g/L)	37.15 ± 2.34	37.68 ± 2.44	37.43 ± 2.25	37.51 ± 2.27	1.729	0.165
ESR (mm/60 min)	18.41 ± 1.67	19.05 ± 2.10	18.57 ± 2.03	18.79 ± 1.68	0.619	0.604
BG (mmol/L)	5.92 ± 2.16	5.78 ± 2.45	5.69 ± 2.37	5.81 ± 2.43	0.855	0.467
LDH (U/L)	178.26 ± 15.30	176.52 ± 12.47	180.28 ± 14.61	179.04 ± 11.59	0.716	0.544
Complication						
Tuberculous pleuritis	30	30	30	30	—	—
Secondary pulmonary tuberculosis	12	7	15	10	4.8980	0.181
Duration of PTM					1.015	0.985
Less than 3 months	11	13	10	12		
3~6 months	13	13	14	13		
More than 6 months	6	4	6	5		

Note: group A: classical HRZE scheme; group B: HRZE+pleural cavity infusion; group C: HZE+rifabutin; group D: HZE+rifabutin+pleural cavity infusion.

TABLE 2: Comparison of CT examination results among four groups.

Group	Group A ($n = 30$)	Group B ($n = 30$)	Group C ($n = 30$)	Group D ($n = 30$)	χ^2	P
Number of pleural tuberculoma	37	40	38	35	—	—
Single lesion	23	22	24	21	0.889	0.828
Multiple lesions	7	8	6	9	1.562	1.000
Pleural tuberculoma site						
Right anterior chest wall	5	5	4	4		
Left anterior chest wall	2	3	2	2		
Right chest wall	3	4	3	3		
Left chest wall	3	5	5	4		
Right posterior chest wall	16	17	15	16		
Left posterior chest wall	8	6	7	6		
Pleural tuberculoma size (mm)						
	18.2×40.3	18.6×39.5	17.8×41.2	19.5×40.5	—	—
	40.6×25.1	41.5×58.4	38.6×67.2	41.0×64.7		

Note: group A: classical HRZE scheme; group B: HRZE+pleural cavity infusion; group C: HZE+rifabutin; group D: HZE+rifabutin+pleural cavity infusion.

TABLE 3: Comparison of absorption of lesions in four groups ($n, \%$).

Group	Time	Significant absorbed	Effective	Invalid	Deteriorated
Group A ($n = 30$)	3 months	5 (16.67)	13 (43.33)	11 (36.67)	1 (3.33)
	9 months	12 (40.00)	10 (33.33)	8 (26.67)	0
Group B ($n = 30$)	3 months	8 (26.67)	14 (46.67)	8 (26.67)	0
	9 months	14 (46.67)	10 (33.33)	6 (20.00)	0
Group C ($n = 30$)	3 months	6 (20.00)	15 (50.00)	9 (30.00)	0
	9 months	13 (43.33)	9 (30.00)	8 (26.67)	0
Group D ($n = 30$)	3 months	9 (30.00)	17 (57.67)	4 (15.26)	0
	9 months	22 (73.33)	5 (16.67)	3 (10.00)	0

Note: group A: classical HRZE scheme; group B: HRZE+pleural cavity infusion; group C: HZE+rifabutin; group D: HZE+rifabutin+pleural cavity infusion.
 $\chi^2_{A-B,3} = 2.203$, $P_{A-B,3} = 0.531$; $\chi^2_{A-C,3} = 1.434$, $P_{A-C,3} = 0.698$; $\chi^2_{A-D,3} = 5.943$, $P_{A-D,3} = 0.114$; $\chi^2_{B-C,3} = 0.379$, $P_{B-C,3} = 0.827$; $\chi^2_{B-D,3} = 1.682$, $P_{B-D,3} = 0.431$; $\chi^2_{C-D,3} = 2.648$, $P_{C-D,3} = 0.266$; $\chi^2_{A-B,9} = 0.440$, $P_{A-B,9} = 0.803$; $\chi^2_{A-C,9} = 0.093$, $P_{A-C,9} = 0.955$; $\chi^2_{A-D,9} = 6.881$, $P_{A-D,9} = 0.032$; $\chi^2_{B-C,9} = 0.375$, $P_{B-C,9} = 0.829$; $\chi^2_{B-D,9} = 4.444$, $P_{B-D,9} = 0.108$; $\chi^2_{C-D,9} = 5.730$, $P_{C-D,9} = 0.057$.

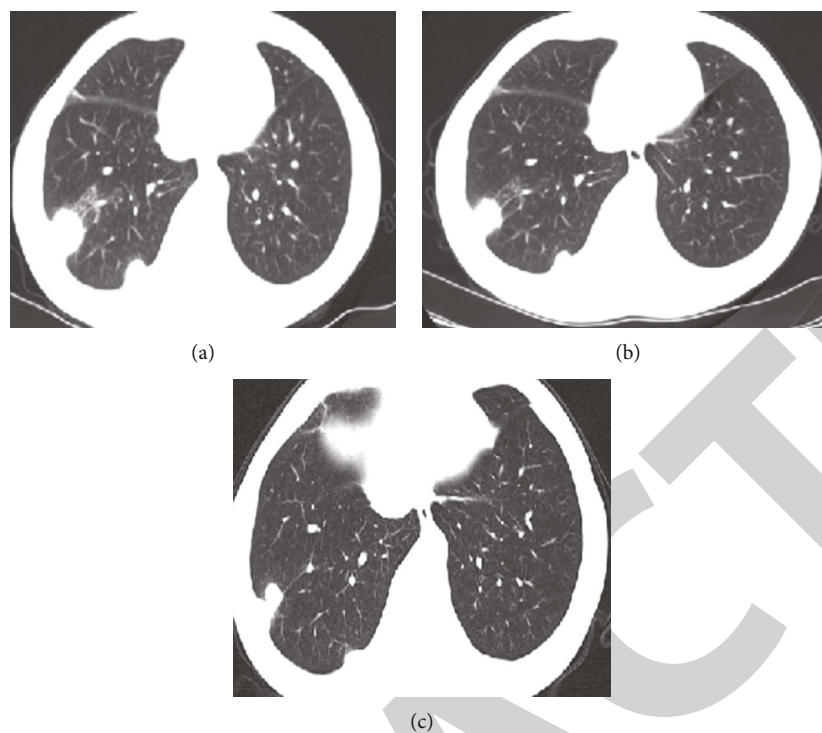


FIGURE 1: Zhao, male, 39 years old. Chest CT plain scan showed a high-density shadow on the right lung. Group A classical HRZE program was adopted. (a) Lesion 20×15 mm before treatment (December 16, 2019). (b) The lesion was reduced to 19×13 mm after 3 months of treatment (2020.3.24). (c) At the end of treatment (2021.9.13), the lesion was obviously absorbed, but there was still a residual of 14×10 mm.

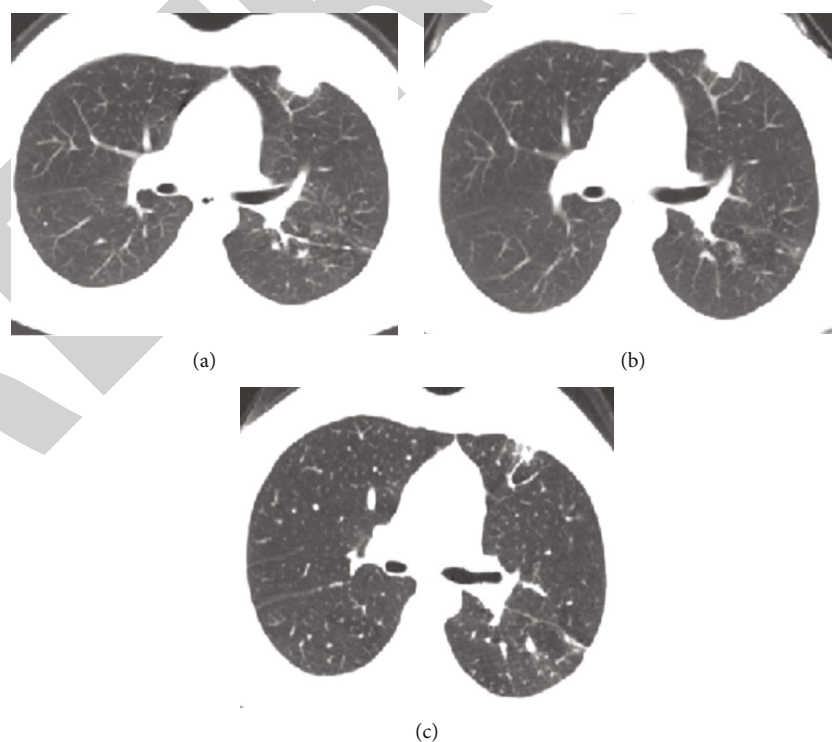


FIGURE 2: Zhang, male, 32 years old. Chest CT plain scan showed a high-density shadow in the left lung. Group B HRZE+pleural infusion was adopted for treatment. (a) Lesion 28×25 mm before treatment (2020.4.29). (b) After 3 months of treatment (2020.7.16), the lesion was reduced to 22×20 mm. (c) At the end of treatment (2021.7.7), the lesions were significantly absorbed.

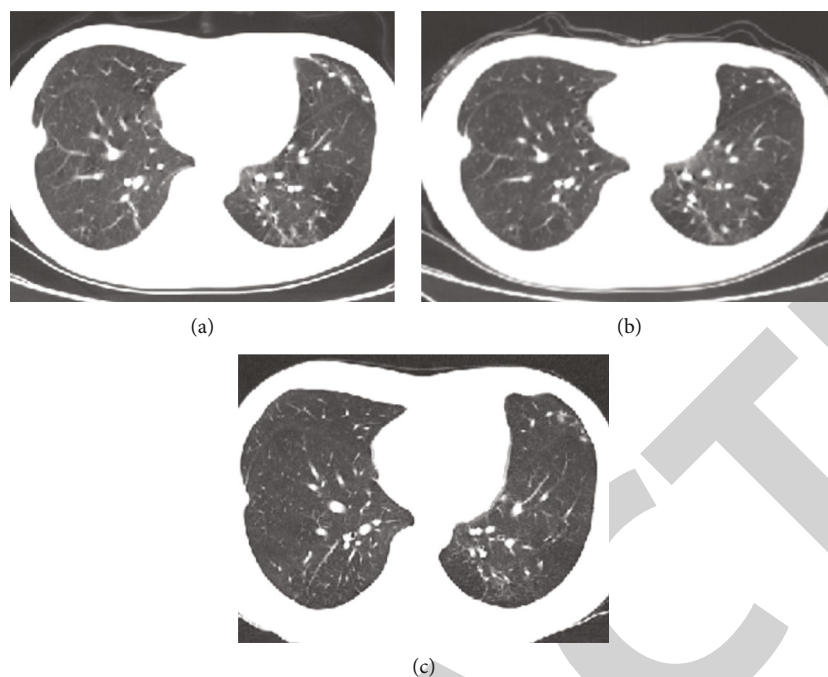


FIGURE 3: Liu, male, 42 years old. Chest CT plain scan showed two high-density shadows in the right lung, which was treated with group C HZE+rifabutin regimen. (a) Before treatment (2020.9.28), the lesion was 30×22 mm. (b) After 1 month of treatment (2020.11.02), the lesion was reduced to 22×20 mm. (c) After 5 months of treatment (2021.2.6), the lesion was reduced to 18×16 mm.

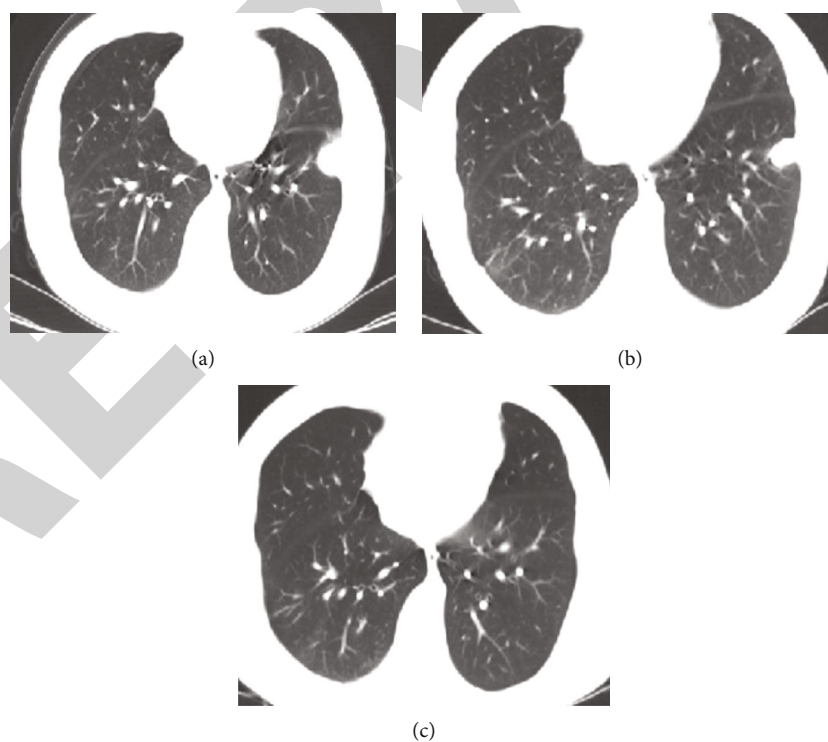


FIGURE 4: Wang, male, 47 years old. Chest CT plain scan showed a high-density shadow in the left lung. Group D HZE+rifabutin+pleural infusion was adopted for treatment. (a) The lesion was 25×18 mm before treatment (2020.9.8). (b) After 3 months of treatment (2020.11.23), the lesion was reduced to 22×13 mm. (c) The lesions were significantly absorbed after 7 months of treatment (2021.3.19).

TABLE 4: Comparison of adverse drug reactions in 4 groups.

Group	Skin rash	PLT decrease	ALT increase	UA increase	Total
Group A ($n = 30$)	6	3	10	8	17
Group B ($n = 30$)	4	5	8	5	14
Group C ($n = 30$)	3	3	6	4	9
Group D ($n = 30$)	4	2	3	4	7

Note: group A: classical HRZE scheme; group B: HRZE+pleural cavity infusion; group C: HZE+rifabutin; group D: HZE+rifabutin+pleural cavity infusion. $\chi^2_{A-B;3} = 0.601$, $P_{A-B;3} = 0.438$; $\chi^2_{A-C;3} = 4.344$, $P_{A-C;3} = 0.037$; $\chi^2_{A-D;3} = 6.944$, $P_{A-D;3} = 0.008$; $\chi^2_{B-C;3} = 1.763$, $P_{B-C;3} = 0.184$; $\chi^2_{B-D;3} = 3.590$, $P_{B-D;3} = 0.058$; $\chi^2_{C-D;3} = 0.0341$, $P_{C-D;3} = 0.559$.

4. Discussion

Pleural tuberculoma is common in the clinical treatment and follow-up of patients with tuberculous pleuritis, and a few patients have no clear history. Although pleural tuberculoma is a benign proliferative lesion, the lung can be extensively involved. Without active treatment, some lesions will continue to grow and increase in number, which seriously affects the prognosis of the disease [16]. At present, there is no unified treatment standard, and most patients have a good prognosis by extending the course of antituberculosis treatment and increasing the combination of drugs, local injection, or surgery [9, 17].

As antituberculosis drugs are difficult to penetrate in the focus, intrapleural injection of drugs on the basis of systemic antituberculosis treatment can speed up the killing of tuberculosis bacteria and shorten the course of disease [18, 19]. In addition, antituberculosis drugs have much toxic and side effects, so it is of great significance to reduce adverse reactions to improve curative effect and relieve patients' pain. Isoniazid is relatively safe among antituberculosis drugs, with few adverse reactions in conventional doses [20]. Rifampicin can cause many adverse reactions, and it mainly interferes with the combination and excretion of bilirubin and glucuronic acid through bile excretion. Patients can have joint pain, rash, PLT reduction, liver function injury, and jaundice [21, 22]. Pyrazinamide can cause arthrodynia, hyperuricemia, hepatotoxicity, and gastrointestinal reactions, which are related to dose to a certain extent, but the current conventional dose has relatively few side effects [23, 24]. The main adverse effects of ethambutol are blurred vision, eye pain, red-green color blindness, or any vision loss [25]. Rifabutin is generally well tolerated, with interruptions due to rash, gastrointestinal reactions, neutropenia, and occasionally thrombocytopenia [26].

In order to reduce complications and improve efficacy, different treatment regimens were adopted for the four groups of patients in this study. Isoniazid, pyrazinamide, and ethambutol were all given in the same dose in group A and group C. The difference was that rifampicin was used in the antituberculosis regimen in group A, while rifabutin was used in group C. Both rifampicin and rifabutin are commonly used antituberculosis drugs. A number of clinical studies have shown that rifabutin has a stronger antituberculosis effect at the same dose [27], and rifabutin also has a strong activity against strains resistant to rifampicin [28, 29]. In addition, rifabutin also has a higher lipid solubility than rifampicin and can be distributed in tissues of patients

for a longer time and at a higher concentration [30]. In this study, the absorption of lesions in group C was slightly better than that in group A at different time, but the difference was not statistically significant ($P > 0.05$), possibly due to the small sample size of this study. Group B and group D were injected with isoniazid in pleural cavity on the basis of antituberculosis drug therapy. Isoniazid is the preferred antituberculosis drug. By injecting isoniazid into the thorax, the chemotherapy drug can directly reach the interior of the lesion, and the high local drug concentration can cause tuberculoma tissue necrosis, liquefaction, tumor shrinkage, or even disappearance, improving the efficacy [31, 32]. In this study, the number of significantly absorbed cases and effective cases in group D increased, while the number of invalid cases decreased after 3 months of treatment, but there was no statistical significance in the absorption of lesions among the four groups (all $P > 0.05$). After 9 months of treatment, the absorption of lesions in group D was significantly better than that in group A ($P < 0.05$). These results indicated that HZE+rifabutin+pleural infusion antituberculosis regimen had better clinical efficacy than classical HRZE regimen in the treatment of pleural tuberculoma, which is consistent with the results of literature review. During treatment, the incidence of adverse reactions in the four groups was significantly different ($P < 0.05$), and the incidence of adverse reactions in groups C and D was significantly lower than that in group A ($P < 0.05$). These results indicated that adjusting medication regimen and replacing rifabutin with less toxic and side effects could significantly improve patients' discomfort during treatment.

In conclusion, among the four antituberculosis schemes in this study, the clinical efficacy of HZE+rifabutin+pleural infusion regimen is superior to the classical HRZE scheme, with high safety. However, the number of treatment groups in this study was relatively small, and no significant differences were observed in some results between groups. And in the course of treatment, some patients received surgical treatment, some received aminoglycoside injections for 2 to 3 months, and many patients were lost to follow-up. These would affect the research results seriously. Therefore, a large sample and multicenter study is needed to verify the accuracy of the results of this study.

Data Availability

The labeled datasets used to support the findings of this study are available from the corresponding author upon request.

Conflicts of Interest

The authors declare no competing interests.

Acknowledgments

This research was supported by the Shandong Province Medical and Health Science and Technology Development Plan Project (No. 2018WS241).

References

- [1] X. Y. Chen, "Advances in the diagnosis and treatment of tuberculous pleurisy," *Tuberculosis and Thoracic Tumors*, vol. 32, no. 1, 2016.
- [2] S. P. Cao, T. Zhang, and S. G. Qiu, "Clinical characteristics and diagnosis-treatment experience of 20 cases of pleural tuberculoma," *Clinical Misdiagnosis & Mistherapy*, vol. 32, no. 6, pp. 104–107, 2019.
- [3] G. H. Jie and C. L. Zhou, "Clinical application of CT-guided percutaneous puncture in biopsy and treatment of patients with pleural tuberculoma," *Journal of Clinical Pulmonology*, vol. 25, no. 8, pp. 1252–1253, 2020.
- [4] T. Kinjo, M. Shimoji, and J. Fujita, "Uncommon presentation of tuberculosis as an incidentally discovered solitary pleural tuberculoma," *The American Journal of Tropical Medicine and Hygiene*, vol. 106, no. 2, pp. 376–377, 2022.
- [5] S. P. Cao, T. Zhang, S. Q. Qiu, P. Clinic, and C. C. Hospital, "Clinical Characteristics and Diagnosis-treatment Experience of 20 Cases of Pleural Tuberculoma [J]," *Clinical Misdiagnosis & Mistherapy*, 2019.
- [6] R. Sumiya, S. Nagasaka, T. Ikeda, and H. Miyazaki, "Solitary pleural tuberculoma diagnosed by thoracoscopic surgical resection," *Journal of Surgical Case Reports*, vol. 2021, no. 9, 2021.
- [7] H. Wang, "Imaging diagnosis and surgical treatment of pleural tuberculosis," *Middle Journal of Advanced Study of Chinese Physicians*, vol. 31, no. 8, pp. 45–46, 2008.
- [8] L. Fan, L. P. Cheng, X. B. Ji, Z. B. Liu, X. Shi, and G. L. Mai, "Study on the risk factors of tuberculous pleurisy complicated with pleural tuberculoma," *Chinese Journal of Tuberculosis and Respiratory Medicine*, vol. 40, no. 4, pp. 306–308, 2017.
- [9] W. L. Kong and D. P. Bai, "Clinical analysis of 32 cases of pleural tuberculoma during the treatment of tuberculous pleurisy," *Chongqing Medicine*, vol. 49, no. 14, pp. 2348–2350, 2020.
- [10] Q. An, W. Song, J. Liu et al., "Primary drug-resistance pattern and trend in elderly tuberculosis patients in Shandong, China, from 2004 to 2019," *Infect Drug Resist*, vol. Volume 13, pp. 4133–4145, 2020.
- [11] M. C. Phillips, N. Wald-Dickler, K. Loomis, B. M. Luna, and B. Spellberg, "Pharmacology, dosing, and side effects of rifabutin as a possible therapy for antibiotic-resistant Acinetobacter infections," *Infectious Diseases*, vol. 7, no. 11, p. ofaa460, 2020.
- [12] L. M. Lin and H. H. Ye, "Research progress on clinical application of rifamycin in treatment of tuberculosis," *Drug Evaluation Research*, vol. 43, no. 11, pp. 2335–2339, 2020.
- [13] W. W. Gao, W. Y. Hu, and Y. L. Xu, "Research progress of pathogenesis and treatment of pleural tuberculoma," *International Journal of Respiration*, vol. 41, no. 20, pp. 1521–1525, 2021.
- [14] Chinese Medical Association, *Clinical Diagnosis and Treatment Guidelines: Tuberculosis Volume*, People's Medical Publishing House, Beijing, 2005.
- [15] L. M. Wang, "Observation of clinical features of AIDS complicated with tuberculosis," *China Practical Medicine*, vol. 14, no. 4, pp. 73–74, 2019.
- [16] W. W. Gao, W. Y. Hu, and Y. L. Xu, "Research progress on the pathogenesis and treatment of pleural tuberculoma," *International Journal of Respiratory Medicine*, vol. 41, no. 20, article 5, 2021.
- [17] X. N. Ma, N. H. Chu, and C. Liu, "Effect of intrapleural injection of glucocorticoid combined with standard quadruple anti tuberculous therapy on clinical symptoms and pulmonary function of patients with tuberculous pleurisy," *Progress in Modern Biomedicine*, vol. 15, pp. 2868–2871, 2021.
- [18] Y. Li, X. N. Liu, and X. L. Zhang, "Analysis of the influencing factors of pleural tuberculoma in patients with tuberculous pleurisy," *Journal of Anhui Medical University*, vol. 57, no. 3, p. 3, 2022.
- [19] M. Xue, L. I. Jingjing, L. Y. Zhibin et al., "Analysis of CT features and differential diagnosis of pleural tuberculoma," *Journal of Medical Imaging*, vol. 28, no. 7, p. 4, 2018.
- [20] J. R. Campbell, A. Trajman, V. J. Cook et al., "Adverse events in adults with latent tuberculosis infection receiving daily rifampicin or isoniazid: post-hoc safety analysis of two randomised controlled trials," *The Lancet Infectious Diseases*, vol. 20, no. 3, pp. 318–329, 2020.
- [21] J. I. A. N. G. Bo-feng, M. A. Chen-chen, C. H. E. N. Yang-gui et al., "Analysis on the incidence of adverse reaction and risk factors caused by anti-tuberculosis drugs," *Chinese Journal of Disease Control & Prevention*, vol. 21, no. 2, pp. 160–163, 2017.
- [22] Y. J. Ma, Q. Zhang, and W. Wu, "Research progress on adverse reactions of anti-tuberculosis drugs," *Shandong Medicine*, vol. 59, no. 32, pp. 111–113, 2019.
- [23] S. Alsayed, S. Lun, A. Payne, W. R. Bishai, and H. Gunosewoyo, "Facile synthesis and antimycobacterial activity of isoniazid, pyrazinamide and ciprofloxacin derivatives," *Chemical Biology & Drug Design*, vol. 97, no. 6, pp. 1137–1150, 2021.
- [24] P. U. Qiang-hong, L. I. Jia-meng, L. I. Fan-min, and Y. U. A. N. Shu-sheng, "Risk factors for tuberculosis chemotherapeutic drug pyrazinamide-induced hyperuricemia," *Chinese Journal of General Practice*, vol. 19, no. 12, pp. 2058–2060, 2021.
- [25] W. Y. Sheng, S. Q. Wu, L. Y. Su, and L. W. Zhu, "Ethambutol-induced optic neuropathy with rare bilateral asymmetry onset: a case report," *World Journal of Clinical Cases*, vol. 10, no. 2, pp. 663–670, 2022.
- [26] R. Haddad, J. M. Ageitos-Martínez, and N. Csaba, "Pulmonary delivery of rifabutin utilizing modified chitosan nanocapsules," 2021.
- [27] Y. L. Jian, W. U. Long-Zhang, and G. U. Zhuo-Yun, "Clinical characteristics and treatment outcomes of 18 patients with non-tuberculosis mycobacteria concerning eyes, ears, nose and throat," *Chinese Journal of Antituberculosis*, vol. 42, no. 3, article 255, 2020.
- [28] X. Wu, G. J. Yang, G. Tan et al., "Drug resistance characteristics of mycobacterium tuberculosis isolates from patients with tuberculosis to 12 antituberculous drugs in China," *Frontiers in Cellular and Infection Microbiology*, vol. 9, p. 345, 2019.
- [29] R. Chen, M. C. Li, L. L. Zhao et al., "Analysis on drug sensitivity spectrum of 167 multidrug-resistant Mycobacterium tuberculosis in China," *Chinese Journal of Epidemiology*, vol. 41, no. 5, pp. 764–769, 2020.

Research Article

Efficacy and Safety Analysis of Multislice Spiral CT-Guided Transthoracic Lung Biopsy in the Diagnosis of Pulmonary Nodules of Different Sizes

Huitong Liu , Xiao Yao, Bingqiang Xu, Wei Zhang, Yu Lei, and Xiaolong Chen 

Shaanxi Provincial People's Hospital, Xi'an, Shaanxi Province 710068, China

Correspondence should be addressed to Xiaolong Chen; chenxl1976@126.com

Received 9 June 2022; Revised 14 July 2022; Accepted 26 July 2022; Published 25 August 2022

Academic Editor: Pan Zheng

Copyright © 2022 Huitong Liu et al. This is an open access article distributed under the Creative Commons Attribution License, which permits unrestricted use, distribution, and reproduction in any medium, provided the original work is properly cited.

Objective. This study is aimed at investigating the efficacy and safety of multislice spiral CT-guided transthoracic lung biopsy in the diagnosis of pulmonary nodules of different sizes. **Methods.** Data of 78 patients with pulmonary nodules who underwent CT-guided transthoracic lung biopsy in our hospital from January 2020 to December 2021 were retrospectively analyzed, and they were divided into the small nodules group ($n = 12$), medium nodules group ($n = 35$), and large nodules group ($n = 31$) according to the diameter of pulmonary nodules. The results of puncture biopsy and final diagnosis of pulmonary nodules of different sizes were compared. The incidence of complications in patients with pulmonary nodules of different sizes was compared. Univariate analysis was used to compare the incidence of complications in 78 patients. Logistic multiple regression analysis was used to analyze the independent risk factors of pneumothorax in patients with pulmonary nodule puncture. Logistic multiple regression analysis was used to analyze the independent risk factors of pulmonary hemorrhage in patients with pulmonary nodule puncture. **Results.** The diagnostic accuracy, sensitivity, and specificity were 83.33%, 100.00%, and 77.78% in small nodules group. The diagnostic accuracy, sensitivity, and specificity of medium nodules group were 85.71%, 100.00%, and 73.68%, respectively. The diagnostic accuracy, sensitivity, and specificity of large nodules group were 93.55%, 100.00%, and 33.33%, respectively. There was no significant difference in the incidence of pneumothorax among the three groups ($P > 0.05$). The incidence of pulmonary hemorrhage in small nodule group was higher than that in the medium nodule group and large nodule group, and the difference was statistically significant ($P < 0.05$). There was no significant difference in the incidence of total complications among the three groups ($P > 0.05$). There were statistically significant differences in clinical data such as the needle tract length, the puncture position, and the distance of the puncture needle passing through the lung tissue in patients with or without pneumothorax ($P < 0.05$). There were statistically significant differences in needle tract length, distance of puncture needle passing through lung tissue, and size of pulmonary nodules in patients with or without pulmonary hemorrhage ($P > 0.05$). Logistic multivariate analysis showed that needle tract length ≤ 50 mm, lateral decubitus position, and the distance of puncture needle passing through lung tissue ≥ 14 mm were independent risk factors for pneumothorax after puncture in patients with pulmonary nodules ($P < 0.05$). The needle tract length > 50 mm, the distance of puncture needle passing through lung tissue ≥ 14 mm, and small nodules (pulmonary nodules diameter ≤ 10 mm) were independent risk factors for pulmonary hemorrhage after puncture in patients with pulmonary nodules ($P < 0.05$). **Conclusion.** Multislice spiral CT-guided transthoracic lung biopsy is effective in diagnosing pulmonary nodules of different sizes.

1. Introduction

Pulmonary nodules refer to lesions with a diameter of ≤ 30 mm in the lungs. The lung nodules are round or quasiround in shape and surrounded by air-filled lung tissue. According to CT imaging morphology, pulmonary nodules

can be divided into solid nodules, partially solid nodules, and ground glass nodules [1]. The incidence of pulmonary nodules is 35.5%, of which pulmonary nodules diagnosed as lung cancer account for 0.54%, respectively; the incidence of pulmonary nodules among people who smoke more than 30 packs per year is 25.9%, of which pulmonary nodules

diagnosed as lung cancer accounted for 1.1% [2]. The etiology of pulmonary nodules is complex and diverse, including infectious factors, tumor factors, and pulmonary infectious factors [3, 4]. It is reported that pulmonary nodules with diameter < 5 mm have a 0.4% probability of developing into carcinoma in situ, pulmonary nodules with diameter of 5–10 mm have a 1.3% probability of developing into malignancy, pulmonary nodules with diameter of 10–20 mm have a 50% probability of developing into malignancy, and pulmonary nodules with diameter > 20 mm have an 87.5% probability of developing into malignancy. Pulmonary nodules of different sizes have different probability of developing into malignancy, so early diagnosis of pulmonary nodules is very important [5]. Lung biopsy has high diagnostic accuracy and can also judge the differentiation degree of malignant tumor, which can effectively guide clinical treatment. Transthoracic lung biopsy was first applied to the microbiological diagnosis of patients with lung infection in 1882, and the first lung cancer biopsy was performed in 1886. Later, it was gradually developed to use ultrasound, CT, etc. for lung biopsy. CT is the most widely used guidance method in clinical practice, with high soft tissue contrast ability and spatial resolution. CT-guided puncture biopsy of pulmonary nodules also has high diagnostic accuracy and safety [6–9]. Multislice spiral CT refers to an imaging system with a multirow detector structure and a single exposure of the tube, which can simultaneously obtain data from multiple slices of images [10]. Compared with traditional CT-guided lung biopsy, multislice CT-guided lung biopsy has the advantages of fast scanning speed and shorter scanning time. In addition, the repeated scanning procedure of multislice spiral CT-guided lung biopsy can make the guidance easier to operate [11]. The purpose of this study was to investigate the diagnostic efficacy of multislice spiral CT-guided transthoracic lung biopsy for pulmonary nodules of different sizes. The report is as follows.

2. Materials and Methods

2.1. General Information. Data of 78 patients with pulmonary nodules who underwent multislice spiral CT-guided transthoracic lung biopsy in our hospital from January 2020 to December 2021 were retrospectively analyzed. There were 55 males and 23 females, aged from 20 to 78 years old, with an average age of 49.55 ± 5.63 years old; 12 cases with pulmonary nodule diameter ≤ 10 mm were divided into small nodule group; 35 cases with pulmonary nodule diameter ≤ 20 mm were divided into middle nodule group; 31 cases with pulmonary nodule diameter > 20 mm and ≤ 30 mm were divided into large nodule group. This study was approved by the hospital ethics committee.

2.2. Inclusion Criteria. Inclusion criteria are as follows: (1) $0 \text{ mm} < \text{pulmonary nodule diameter} \leq 30 \text{ mm}$; (2) age ≥ 18 years old; (3) no contraindications for CT-guided transthoracic lung biopsy; (4) complete clinical and imaging data; (5) the chest CT examination showed pulmonary nodules; and (6) patients volunteered to participate in this study.

2.3. Exclusion Criteria. Exclusion criteria are as follows: (1) patients with intrapulmonary vascular disease; (2) patients with pulmonary fibrosis, pulmonary hypertension, and severe emphysema; (3) patients with severe bleeding tendency or coagulation dysfunction; (4) patients who cannot cooperate with breathing; (5) the heart and blood vessels cannot be avoided during the puncture of the lesion; (6) patients with lung bullae lesions in puncture approach; (7) patients with severe pulmonary infection; and (8) there is skin infection at the site to be punctured.

2.4. Methods

2.4.1. Operation Instrument. Canon Aquilion ONE 640CT was used, and the puncture needle was a shotgun-cut biopsy needle. The imaging data of the patients were carefully observed before surgery, and the lateral, supine, and prone positions were adopted according to the size and location of the lung nodules. First, local scan of the lesion was carried out with a layer thickness of 2.7 mm. The best puncture point was selected by CT positioning ruler, and the distance between the puncture point and the edge and center of the lesion as well as the puncture direction and angle were measured. Routine disinfection and draping were performed, local anesthesia was performed, anesthesia needle was injected 1~2 cm in accordance with the expected puncture direction and angle, the puncture biopsy scanning procedure was used to scan to verify whether there was any error in puncture point, puncture direction, and angle, and the scan could be performed again after appropriate adjustment. The patient was told to keep calm breathing and hold his breath, and after confirmation, the shotgun-cut biopsy needle was used to rapidly puncture the lung lesions of the patient. After reaching the expected depth, the scan was carried out to confirm that the needle tip was in the patient's lesion. Then the patient was told to hold his breath, the lesion tissue was cut, the needle was removed quickly, and the tissue specimen was fixed with formalin and then sent for examination. If the pathologist is not satisfied, the needle biopsy should be performed again and the liquefaction necrotic area should be avoided. After surgery, the puncture site was pressed for 2~3 minutes, external dressing was applied, and then the lungs were scanned to observe whether the patient had bleeding, pneumothorax, and other complications.

2.5. Judgment Criteria for Puncture Results. (1) If the biopsy tissue is normal lung tissue and diaphragmatic muscle according to pathological results, it is regarded as failure of sampling. (2) If the pathological examination result of biopsy tissue is malignant tumor, the pathological diagnosis is definite. (3) If the pathological examination result of biopsy tissue is benign and confirmed by surgery, or the lesions disappear, shrink, and stabilize for more than half a year after treatment, it is regarded as correct pathological diagnosis. The accuracy of puncture biopsy can be obtained by comparing the final clinical examination results with the results of needle biopsy.

2.6. Observation Indicators. Observation indicators are as follows: (1) general information of all patients; (2) comparison of puncture biopsy and final diagnosis results of pulmonary nodules of different sizes; (3) comparison of the incidence of complications among patients with pulmonary nodules of different sizes; (4) univariate analysis of the incidence of complications in all patients; (5) logistic multiple regression analysis was used to analyze the independent risk factors of pneumothorax in patients with pulmonary nodule puncture; and (6) logistic multiple regression analysis was used to analyze the independent risk factors of pulmonary hemorrhage in patients with pulmonary nodule puncture.

2.7. Statistical Methods. All data in this study were input into Excel by two persons without communication and analyzed and processed by the SPSS24.0 statistical software. The measurement data were expressed as mean \pm SD ($\bar{x} \pm s$). When the data were in line with normal distribution and the variance was uniform, the t test was adopted, and one-way ANOVA was used comparison among multiple groups. Counting data were described by n and %, and disordered classification data were compared by the χ^2 test or Fisher's exact probability method. Multivariate analysis was performed by the logistic regression model. All were two-sided tests, and $P < 0.05$ was considered statistically significant.

3. Results

3.1. General Information of Patients. The general information of all patients is shown in Table 1.

3.2. Comparison of Puncture Biopsy and Final Diagnosis Results of Pulmonary Nodules of Different Sizes. In the small nodules group, the diagnostic accuracy, sensitivity, and specificity were 83.33%, 100.00%, and 77.78%, respectively, the positive prediction rate was 60.00%, the negative prediction rate was 81.82%. In the medium nodules group, the diagnostic accuracy, sensitivity, and specificity were 85.71%, 100.00%, and 73.68%, respectively, the positive prediction rate was 76.19%, and the negative prediction rate was 79.17%. In the large nodules group, the diagnostic accuracy, sensitivity, and specificity were 93.55%, 100.00%, and 33.33%, respectively, the positive prediction rate was 93.55%, and the negative prediction rate was 60.00% (see Tables 2 and 3 and Figure 1).

3.3. Comparison of Complications among the Three Groups. There was no significant difference in the incidence of pneumothorax among the three groups ($P > 0.05$); the incidence of pulmonary hemorrhage in the small nodules group was higher than that in the middle nodules group and the large nodules group, and the difference was statistically significant ($P < 0.05$). There was no significant difference in the total incidence of complications among the three group ($P > 0.05$) (see Table 4).

3.4. Univariate Analysis of Complications in 78 Patients. There were statistically significant differences in clinical data such as the needle tract length, the puncture position, and

TABLE 1: General information of patients (cases (%)).

Item	Composition ratio
Lung nodule location	
Right upper lobe	29 (37.18)
Right middle lobe	9 (11.54)
Right lower lobe	17 (21.79)
Left upper lobe	12 (15.38)
Left lower lobe	11 (14.10)
Previous tumor history	
Yes	3 (3.85)
No	75 (96.15)
Smoking history	
Yes	41 (52.56)
No	37 (47.44)
Puncture position	
Supine position	25 (32.05)
Prone position	44 (56.41)
Lateral position	9 (11.54)

the distance of the puncture needle passing through the lung tissue in patients with or without pneumothorax ($P < 0.05$). There were statistically significant differences in needle tract length, distance of puncture needle passing through lung tissue, and size of pulmonary nodules in patients with or without pulmonary hemorrhage ($P < 0.05$), as shown in Table 5.

3.5. Logistic Multivariate Regression Analysis of the Incidence of Pneumothorax in 78 Patients. Factors with statistically significant differences in the above univariate analysis of pneumothorax, including needle track length, puncture position, and distance of puncture needle passing through lung tissue, were included in the logistic regression analysis and assigned (needle track length > 50 mm = 1, ≤ 50 mm = 0; puncture position: supine position = 2, prone position = 1, and lateral position = 0; the distance of the puncture needle passing through the lung tissue < 14 mm = 1, ≥ 14 mm = 0). Logistic multivariate analysis showed that needle length ≤ 50 mm, lateral position, and the distance of puncture needle passing through lung tissue ≥ 14 mm were independent risk factors for pneumothorax after puncture in patients with pulmonary nodules ($P < 0.05$), as shown in Table 6.

3.6. Logistic Multivariate Regression Analysis of the Incidence of Pulmonary Hemorrhage in 78 Patients. Factors with statistically significant differences in the above univariate analysis of pulmonary hemorrhage, including needle track length, distance of puncture needle passing through lung tissue, and the size of the pulmonary nodule, were included in Logistic regression analysis and assigned (needle track length ≤ 50 mm = 1, > 50 mm = 0; distance of puncture needle passing through lung tissue < 14 mm = 1, ≥ 14 mm = 0; large nodule (20 mm $<$ pulmonary nodule diameter ≤ 30 mm) = 2, medium nodule (10 mm $<$ pulmonary nodule diameter ≤ 20 mm) = 1, and small nodules (pulmonary nodule diameter ≤ 10 mm) = 0).

TABLE 2: Comparison of puncture biopsy and final diagnosis results of pulmonary nodules of different sizes (cases (%)).

Group	Biopsy diagnosis result		Final diagnosis result	
	Benign	Malignant	Benign	Malignant
Small nodules group ($n = 12$)	7 (58.33)	5 (41.67)	9 (75.00)	3 (25.00)
Medium nodules group ($n = 35$)	14 (40.00)	21 (60.00)	19 (54.29)	16 (45.71)
Large nodules group ($n = 31$)	1 (3.23)	30 (96.77)	3 (9.68)	28 (90.32)
Total	22	56	31	47

TABLE 3: Comparison of diagnostic accuracy, sensitivity, specificity, positive predictive rate, and negative predictive rate of puncture biopsy among the three groups (%).

Group	Accuracy	Sensitivity	Specificity	Positive predictive rate	Negative predictive rate
Small nodules group ($n = 12$)	83.33	100.00	77.78	60.00	81.82
Medium nodules group ($n = 35$)	85.71	100.00	73.68	76.19	79.17
Large nodules group ($n = 31$)	93.55	100.00	33.33	93.33	60.00

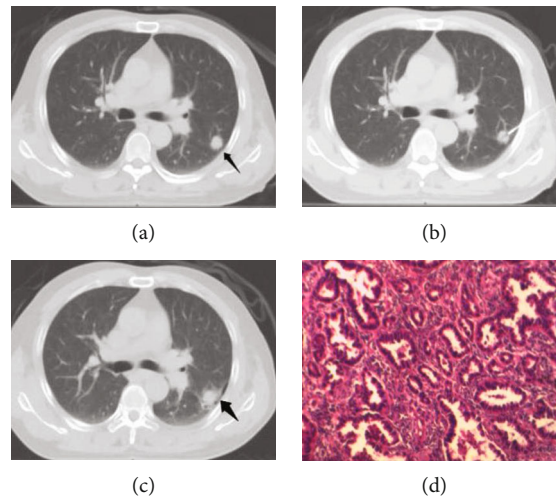


FIGURE 1: A 54-year-old male patient, with a nodule in the left lower lobe found by physical examination before 2 weeks. (a) A solid nodule in the lateral basal segment of the left lower lobe, with a diameter of about 1.3 cm (indicated by the arrow). (b) The needle was obliquely inserted from the adjacent intercostal space, avoiding the scapula. (c) After needle extraction, there was a small amount of bleeding and pneumothorax (indicated by the arrow), and the pneumothorax were absorbed after observation. (d) The surgical pathological results were the same after puncture, and invasive adenocarcinoma was considered ($\times 100$, HE staining).

TABLE 4: Comparison of the incidence of complications among the three groups (cases (%)).

Group	Pneumothorax	Pulmonary hemorrhage	Total complication rate
Small nodules group ($n = 12$)	2 (16.67)	7 (58.33)	9 (75.00)
Medium nodules group ($n = 35$)	6 (17.14)	8 (22.86)	14 (40.00)
Large nodules group ($n = 31$)	7 (22.58)	5 (16.13)	12 (38.71)

Logistic multivariate analysis results showed that the needle tract length > 50 mm, the distance of the puncture needle passing through the lung tissue ≥ 14 mm, and the small nodule (pulmonary nodule diameter ≤ 10 mm) were independent risk factor for pulmonary hemorrhage after puncture in patients with pulmonary nodules ($P < 0.05$) (see Table 7).

4. Discussion

Lung biopsy, open lung biopsy, thoracoscopy biopsy, and fiberoptic bronchoscopy biopsy can all obtain histopathological specimens of lung lesions, but open lung biopsy and thoracoscopic biopsy are more traumatic to the body, and

TABLE 5: Univariate analysis of complications in 78 patients.

Item	Pneumothorax				Pulmonary hemorrhage			
	Yes (<i>n</i> = 15)	No (<i>n</i> = 63)	<i>t</i> / χ^2 value	<i>P</i> /Fisher's exact probability value	Yes (<i>n</i> = 20)	No (<i>n</i> = 58)	<i>t</i> / χ^2 value	<i>P</i> value
Age								
<60 years old (<i>n</i> = 29)	6 (20.69)	23 (79.31)	0.063	0.801	5 (17.24)	24 (82.76)	1.708	0.191
≥60 years old (<i>n</i> = 49)	9 (18.37)	40 (81.63)			15 (30.61)	34 (69.39)		
Gender								
Male (<i>n</i> = 55)	11 (20.00)	44 (80.00)	0.071	0.790	13 (23.64)	42 (76.36)	0.393	0.531
Female (<i>n</i> = 23)	4 (17.39)	19 (82.61)			7 (30.43)	16 (69.57)		
Nodule density (cases)								
Solid (<i>n</i> = 67)	14 (20.90)	53 (79.10)	0.848	0.357	16 (23.88)	51 (76.12)	0.772	0.380
Nonsolid (<i>n</i> = 11)	1 (9.09)	10 (90.91)			4 (36.36)	7 (63.64)		
Needle track length								
≤50 mm (<i>n</i> = 17)	7 (41.18)	10 (58.82)	6.740	0.009	1 (5.88)	16 (94.12)	4.451	0.035
>50 mm (<i>n</i> = 61)	8 (13.11)	53 (86.89)			19 (31.15)	42 (68.85)		
Puncture lung lobe								
Right upper lobe (<i>n</i> = 29)	4 (13.79)	25 (86.21)	1.315	0.859	7 (24.14)	22 (75.86)	3.338	0.503
Right middle lobe (<i>n</i> = 9)	2 (22.22)	7 (77.78)			1 (11.11)	8 (88.89)		
Right lower lobe (<i>n</i> = 17)	4 (23.53)	13 (76.47)			4 (23.53)	13 (76.47)		
Left upper lobe (<i>n</i> = 12)	2 (16.67)	10 (83.33)			3 (25.00)	9 (75.00)		
Left lower lobe (<i>n</i> = 11)	3 (27.27)	8 (72.73)			5 (45.45)	6 (54.55)		
Smoking history								
Yes (<i>n</i> = 41)	8 (19.51)	33 (80.49)	0.004	0.947	11 (26.83)	30 (73.17)	0.064	0.800
No (<i>n</i> = 37)	7 (18.92)	30 (81.08)			9 (24.32)	28 (75.68)		
Puncture position								
Supine position (<i>n</i> = 25)	2 (8.00)	23 (92.00)	—	0.001	7 (28.00)	18 (72.00)	1.131	0.568
Prone position (<i>n</i> = 44)	7 (15.91)	37 (84.09)			12 (27.27)	32 (72.73)		
Lateral position (<i>n</i> = 9)	6 (66.67)	3 (33.33)			1 (11.11)	8 (88.89)		
Number of punctures								
1~3 times (<i>n</i> = 35)	7 (20.00)	28 (80.00)	0.024	0.876	10 (28.57)	25 (71.43)	0.286	0.593
≥4 times (<i>n</i> = 43)	8 (18.60)	35 (81.40)			10 (23.26)	33 (76.74)		
Distance of puncture needle passing through lung tissue (mm)	22.15 ± 2.55	13.56 ± 2.35	12.520	<0.001	24.19 ± 5.68	12.68 ± 3.25	11.101	<0.001

TABLE 6: Logistic multivariate regression analysis of the incidence of pneumothorax in 78 patients.

Factor	β	SE	Wald χ^2	OR	95% CI	<i>P</i>
Needle track length ≤ 50 mm	0.521	0.225	5.362	1.684	1.083~2.617	0.021
Lateral position	0.355	0.134	7.019	1.426	1.097~1.855	0.008
Distance of the puncture needle passing through the lung tissue ≥ 14 mm	1.526	0.554	7.587	4.600	1.553~13.624	0.006

TABLE 7: Logistic multivariate regression analysis of the incidence of pulmonary hemorrhage in 78 patients.

Factor	β	SE	Wald χ^2	OR	95% CI	<i>P</i>
Needle track length > 50 mm	1.159	0.452	6.575	3.187	1.314~7.729	0.011
Distance of puncture needle passing through lung tissue ≥ 14 mm	1.594	0.686	5.399	4.923	1.283~18.889	0.021
Small nodules	1.403	0.545	6.627	4.067	1.398~11.837	0.010

their application is limited in elderly patients and patients with cardiopulmonary dysfunction [12–14]. Lung puncture biopsy has little trauma, low cost, and less pain to patients. Some patients do not need to be hospitalized after puncture and can live a normal life the next day. In addition, CT scan has good contrast and resolution, which can clearly display the morphology, size, and adjacent important structure of lesions and can display small lesions beside the mediastinum, behind the heart shadow, and beside the spine [15, 16]. It has been reported that the accuracy of CT-guided lung biopsy in the diagnosis of benign lesions is >80% and that of malignant lesions is >90% [17]. In this study, the diagnostic efficiency of multislice spiral CT for pulmonary nodules of different sizes was observed. The results showed that the diagnostic accuracy of the small nodule group was 83.33%, the sensitivity was 100.00%, the specificity was 77.78%, the positive predictive rate was 60.00%, and the negative predictive rate was 81.82%. In the middle nodule group, the diagnostic accuracy was 85.71%, the sensitivity was 100.00%, the specificity was 73.68%, the positive predictive rate was 76.19%, and the negative predictive rate was 79.17%. In the large nodule group, the diagnostic accuracy was 93.55%, sensitivity was 100.00%, specificity was 33.33%, the positive predictive rate was 93.33%, and negative predictive rate 60.00%. Multislice spiral CT-guided lung biopsy has the highest diagnostic accuracy for diagnosing large

nodules (20 mm < pulmonary nodule diameter ≤ 30 mm). The sensitivity of multislice spiral CT-guided lung biopsy in the diagnosis of lung nodules of different sizes was up to 100.00%, indicating that multislice spiral CT-guided lung biopsy is an effective method for the diagnosis of lung cancer.

Common complications of transthoracic lung biopsy include pneumothorax, pulmonary hemorrhage, and hemoptysis, and the rare serious complications include air embolism and tumor needle passage metastasis [18, 19]. In this study, complications of multislice spiral CT-guided lung biopsy were observed, and the results showed that there was no statistical significance in the incidence of pneumothorax in groups of different sizes of pulmonary nodules. According to relevant reports, the incidence of pneumothorax of CT-guided transthoracic lung biopsy is 15.4%~42.0%, only 4.3%~7.3% patients need thoracic catheter drainage, and the incidence of hemoptysis is 0.5%~14.4%, most of which do not need intervention [20, 21]. The common risk factors of pneumothorax include long puncture path, multiple crossing of pleura, and small lesion [22, 23]. In this study, univariate and multivariate analyses were conducted on the risk factors for pneumothorax and pulmonary hemorrhage, and it was found that needle tract length ≤ 50 mm, lateral position, and the distance of puncture needle passing through lung tissue ≥ 14 mm were independent risk factors for pneumothorax after puncture in patients with pulmonary nodules. The results of this study suggest that when the puncture needle tract is ≤ 50 mm, the risk of pneumothorax increases, which is contrary to the results of previous studies [24, 25]. The reason may be that the shorter the puncture needle tract, the gas in the lung will pass through the needle in a short time, thus causing pneumothorax. In

this study, the poor postural stability of patients in lateral position also easily led to an increase in the incidence of pneumothorax after puncture. In this study, the distance of puncture needle passing through the lung tissue is closely related to the occurrence of pneumothorax, which is manifested as the greater the distance of puncture needle passing through the lung tissue, the more likely pneumothorax will occur. This may be because when people breathe, there is sliding between visceral pleura and parietal pleura, and indirect friction can be formed when the needle is fixed with chest wall muscle layer, which can lead to pneumothorax. The longer the distance of puncture needle passing through the lung tissue, the more obvious the friction effect is. Therefore, the needle tract length ≤ 50 mm, lateral position, and the distance of puncture needle passing through the lung tissue ≥ 14 mm are independent risk factors for pneumothorax in patients with pulmonary nodules after puncture. It is suggested that full attention should be paid to patients with needle tract length ≤ 50 mm, lateral position, and the distance of puncture needle passing through lung tissue ≥ 14 mm to prevent pneumothorax in time.

In this study, logistic multivariate analysis showed that the needle tract length > 50 mm, the distance of the puncture needle passing through the lung tissue ≥ 14 mm, and small nodules (pulmonary nodule diameter ≤ 10 mm) were independent risk factors for pulmonary hemorrhage after puncture in patients with pulmonary nodules ($P < 0.05$). It was reported that the incidence of pulmonary hemorrhage after puncture was 16%~33%. In this study, the incidence of pulmonary hemorrhage was higher in the small nodules group, and the overall incidence of pulmonary hemorrhage was consistent with the results of previous studies [26–28]. This study found that the longer the needle track, the easier it is to cause pulmonary hemorrhage, which is consistent with previous research results [29, 30]. The longer the needle track is, the more it passes through the lung tissue, which can lead to injury and bleeding. Therefore, the needle track length > 50 mm and the distance of the needle passing through the lung tissue ≥ 14 mm are closely related to pulmonary hemorrhage. In this study, the pulmonary nodule diameter ≤ 10 mm was an independent risk factor for pulmonary hemorrhage. This may be because when the lesion is small, the puncture process is greatly affected by breathing, and the needle needs to be adjusted several times during the puncture process, which is likely to cause pulmonary hemorrhage. In addition, if the lesion is small, normal tissue may be removed to obtain sufficient tissue specimens, resulting in increased bleeding rate. Therefore, prevention of pulmonary hemorrhage should be done well for patients with needle tract length > 50 mm, the distance of puncture needle passing through lung tissue ≥ 14 mm, and small nodules (lung nodules diameter ≤ 10 mm).

In conclusion, multislice spiral CT-guided lung biopsy has high accuracy in diagnosing pulmonary nodules, and the complication rates of pneumothorax and pulmonary hemorrhage are consistent with previous research results [31], which has clinical application value. However, in this study, the sample size is small and the classification method of nodule size is different from that of most literatures. In

future research, the sample size of the study will be further expanded and the grouping of nodule size will be improved, to provide more scientifically rigorous clinical research results in the diagnosis of pulmonary nodules by multislice spiral CT-guided lung biopsy.

Data Availability

The labeled dataset used to support the findings of this study are available from the corresponding author upon request.

Conflicts of Interest

The authors declare no competing interests.

References

- [1] S. Y. Liu, "Pay attention to the problem of over-diagnosis in the clinical management of pulmonary nodules," *Chinese Journal of Radiology*, vol. 55, no. 11, p. 4, 2021.
- [2] Lung cancer group of respiratory disease branch of Chinese Medical Association and expert group of China Lung Cancer Prevention and Control Alliance, "Chinese expert consensus on diagnosis and treatment of pulmonary nodules (2018 edition)," *Chinese Journal of Tuberculosis and Respiratory Medicine*, vol. 41, no. 10, p. 9, 2018.
- [3] Q. Wu, B. Cao, Y. Zheng et al., "Feasibility and safety of fine positioning needle-mediated breathing control in CT-guided percutaneous puncture of small lung/liver nodules adjacent to diaphragm," *Scientific Reports*, vol. 11, no. 1, p. 3411, 2021.
- [4] K. M. Bhatt, Y. K. Tandon, R. Graham et al., "Electromagnetic navigational bronchoscopy versus CT-guided percutaneous sampling of peripheral indeterminate pulmonary nodules: a cohort study," *Radiology*, vol. 286, no. 3, pp. 1052–1061, 2018.
- [5] Y. Xu, L. Lu, L. N. E et al., "Application of radiomics in predicting the malignancy of pulmonary nodules in different sizes," *AJR. American Journal of Roentgenology*, vol. 213, no. 6, pp. 1213–1220, 2019.
- [6] J. R. Andrade, R. D. Rocha, P. M. Falsarella et al., "CT-guided percutaneous core needle biopsy of pulmonary nodules smaller than 2 cm: technical aspects and factors influencing accuracy," *Jornal Brasileiro de Pneumologia*, vol. 44, no. 4, pp. 307–314, 2018.
- [7] D. Lendeckel, M. L. Kromrey, T. Ittermann, S. Schäfer, B. Mensel, and J. P. Kühn, "Pulmonary emphysema is a predictor of pneumothorax after CT-guided transthoracic pulmonary biopsies of pulmonary nodules," *PLoS One*, vol. 12, no. 6, article e0178078, 2017.
- [8] Y. Y. Chang, C. K. Chen, Y. C. Yeh, and M. H. Wu, "Diagnostic feasibility and safety of CT-guided core biopsy for lung nodules less than or equal to 8 mm: a single-institution experience," *European Radiology*, vol. 28, no. 2, pp. 796–806, 2018.
- [9] W. Wang, L. Yu, Y. Wang et al., "Radial EBUS versus CT-guided needle biopsy for evaluation of solitary pulmonary nodules," *Oncotarget*, vol. 9, no. 19, pp. 15122–15131, 2018.
- [10] Y. Q. Liu, "New progress of multi-slice spiral CT technology and clinical application," *Journal of Chinese Academy of Medical Sciences*, vol. 28, no. 1, p. 2, 2006.
- [11] S. Ruirui, "Diagnostic application of multi-planar reconstruction (MPR) technique of multi-slice spiral CT in pre-operative localization of small pulmonary nodules," *Journal of Mathematical Medicine*, vol. 35, no. 3, p. 3, 2022.
- [12] J. Hou and Z. K. Ou, "A report of 14 cases of limited thoracotomy lung biopsy," *Chinese Journal of Tuberculosis and Respiratory Diseases*, vol. 5, no. 3, pp. 139–140, 1982.
- [13] G. F. Li, Q. Y. Wang, and Y. Wang, "The application of medical thoracoscopy pleural biopsy in the diagnosis of benign and malignant pleural effusion," *Medical Equipment*, vol. 34, no. 19, p. 2, 2021.
- [14] W. J. Zhu, L. G. Shan, H. Y. Li, J. L. Peng, and Y. Zhou, "Application of high-frequency jet ventilation in painless fiberoptic bronchoscopy ultrasound positioning needle biopsy," *China Medical Device Information*, vol. 28, no. 2, p. 3, 2022.
- [15] P. C. Tsai, Y. C. Yeh, P. K. Hsu, C. K. Chen, T. Y. Chou, and Y. C. Wu, "CT-guided Core biopsy for peripheral sub-solid pulmonary nodules to predict predominant histological and aggressive subtypes of lung adenocarcinoma," *Annals of Surgical Oncology*, vol. 27, no. 11, pp. 4405–4412, 2020.
- [16] X. Xu, Y. Yao, Y. Shen, P. Zhang, and J. Zhou, "Clinical analysis of percutaneous computed tomography-guided hook wire localization of 168 small pulmonary nodules," *The Annals of Thoracic Surgery*, vol. 100, no. 5, pp. 1861–1867, 2015.
- [17] J. H. Ahn and J. G. Jang, "Initial experience in CT-guided percutaneous transthoracic needle biopsy of lung lesions performed by a pulmonologist," *Journal of Clinical Medicine*, vol. 8, no. 6, p. 821, 2019.
- [18] T. H. Yuan, B. J. Wang, X. He, C. F. Wang, and P. Nie, "Application of small field of view scanning method in CT-guided percutaneous biopsy of small pulmonary nodules and its influence on the incidence of pneumothorax and pulmonary hemorrhage," *Clinical Medicine Research and Practice*, vol. 6, no. 12, p. 3, 2021.
- [19] T. W. Du, J. Xue, and T. Wang, "Clinical application and complications of percutaneous thoracic biopsy," *Journal of Rare and Rare Diseases*, vol. 27, no. 3, p. 3, 2020.
- [20] M. Zhou, T. Wang, D. Wei et al., "Incidence, severity and tolerability of pneumothorax following low-dose CT-guided lung biopsy in different severities of COPD," *The Clinical Respiratory Journal*, vol. 15, no. 1, pp. 84–90, 2021.
- [21] M. D. Huang, H. H. Weng, S. L. Hsu et al., "Accuracy and complications of CT-guided pulmonary core biopsy in small nodules: a single-center experience," *Cancer Imaging*, vol. 19, no. 1, p. 51, 2019.
- [22] G. D. Zhang, M. Yuan, W. H. Li, Q. Mei, and Y. L. Tan, "Analysis of the main influencing factors of bleeding and pneumothorax complications in CT-guided lung biopsy," *Zhonghua General Medicine*, vol. 19, no. 5, p. 4, 2021.
- [23] C. Yang and H. Wang, "Analysis on reducing the incidence of pneumothorax by injecting a small amount of normal saline before the puncture needle in CT-guided percutaneous lung biopsy," *Modern Digestive and Interventional Diagnosis and Treatment*, vol. S01, p. 2, 2020.
- [24] C. Chen, L. Xu, X. Sun, X. Liu, Z. Han, and W. Li, "Safety and diagnostic accuracy of percutaneous CT-guided transthoracic biopsy of small lung nodules (≤ 20 mm) adjacent to the pericardium or great vessels," *Diagnostic and Interventional Radiology*, vol. 27, no. 1, pp. 94–101, 2021.

- [25] Z. G. Huang, H. L. Sun, C. L. Wang et al., “CT-guided transthoracic needle biopsy of pulmonary lesions: comparison between the cutting needle and aspiration needle,” *The British Journal of Radiology*, vol. 94, no. 1118, p. 20190930, 2021.
- [26] A. S. Elshafee, A. Karch, K. I. Ringe et al., “Complications of CT-guided lung biopsy with a non-coaxial semi-automated 18 gauge biopsy system: frequency, severity and risk factors,” *PLoS One*, vol. 14, no. 3, article e0213990, 2019.
- [27] C. Xu, Q. Yuan, C. Chi et al., “Computed tomography-guided percutaneous transthoracic needle biopsy for solitary pulmonary nodules in diameter less than 20 mm,” *Medicine (Baltimore)*, vol. 97, no. 14, article e0154, 2018.
- [28] Ö. Çakir, I. Çam, U. Koç, and E. Çiftçi, “Evaluation of major complications associated with percutaneous CT-guided biopsy of lung nodules below 3 cm,” *Turkish Journal of Medical Sciences*, vol. 50, no. 2, pp. 369–374, 2020.
- [29] C. Fontaine-Delaruelle, P. J. Souquet, D. Gamondes et al., “Predictive factors of complications during CT-guided transthoracic biopsy,” *Revue de Pneumologie Clinique*, vol. 73, no. 2, pp. 61–67, 2017.
- [30] D. Lang, V. Reinelt, A. Horner et al., “Complications of CT-guided transthoracic lung biopsy,” *Wiener Klinische Wochenschrift*, vol. 130, no. 7-8, pp. 288–292, 2018.
- [31] W. J. Heerink, G. H. de Bock, G. J. de Jonge, H. J. Groen, R. Vliegthart, and M. Oudkerk, “Complication rates of CT-guided transthoracic lung biopsy: meta-analysis,” *European Radiology*, vol. 27, no. 1, pp. 138–148, 2017.

Retraction

Retracted: Efficacy of Cetuximab in Nasopharyngeal Carcinoma Patients Receiving Concurrent Cisplatin-Radiotherapy: A Meta-Analysis

Computational and Mathematical Methods in Medicine

Received 27 June 2023; Accepted 27 June 2023; Published 28 June 2023

Copyright © 2023 Computational and Mathematical Methods in Medicine. This is an open access article distributed under the Creative Commons Attribution License, which permits unrestricted use, distribution, and reproduction in any medium, provided the original work is properly cited.

This article has been retracted by Hindawi following an investigation undertaken by the publisher [1]. This investigation has uncovered evidence of one or more of the following indicators of systematic manipulation of the publication process:

- (1) Discrepancies in scope
- (2) Discrepancies in the description of the research reported
- (3) Discrepancies between the availability of data and the research described
- (4) Inappropriate citations
- (5) Incoherent, meaningless and/or irrelevant content included in the article
- (6) Peer-review manipulation

The presence of these indicators undermines our confidence in the integrity of the article's content and we cannot, therefore, vouch for its reliability. Please note that this notice is intended solely to alert readers that the content of this article is unreliable. We have not investigated whether authors were aware of or involved in the systematic manipulation of the publication process.

Wiley and Hindawi regrets that the usual quality checks did not identify these issues before publication and have since put additional measures in place to safeguard research integrity.

We wish to credit our own Research Integrity and Research Publishing teams and anonymous and named

external researchers and research integrity experts for contributing to this investigation.

The corresponding author, as the representative of all authors, has been given the opportunity to register their agreement or disagreement to this retraction. We have kept a record of any response received.

References

- [1] L. Wang, D. Liu, and D. Wei, "Efficacy of Cetuximab in Nasopharyngeal Carcinoma Patients Receiving Concurrent Cisplatin-Radiotherapy: A Meta-Analysis," *Computational and Mathematical Methods in Medicine*, vol. 2022, Article ID 5145549, 16 pages, 2022.

Research Article

Efficacy of Cetuximab in Nasopharyngeal Carcinoma Patients Receiving Concurrent Cisplatin-Radiotherapy: A Meta-Analysis

Lin Wang,¹ Dianjun Liu,² and Deyou Wei³ 

¹Department of Pharmacy, Yantaishan Hospital, Yantai, Shandong 264001, China

²Department of Pharmacy, Yantai Hospital of Traditional Chinese Medicine, Yantai, Shandong 264001, China

³Department of Otolaryngology, Yantai Hospital of Traditional Chinese Medicine, Yantai, Shandong 264001, China

Correspondence should be addressed to Deyou Wei; weideyou7009@163.com

Received 30 May 2022; Revised 11 July 2022; Accepted 25 July 2022; Published 24 August 2022

Academic Editor: Pan Zheng

Copyright © 2022 Lin Wang et al. This is an open access article distributed under the Creative Commons Attribution License, which permits unrestricted use, distribution, and reproduction in any medium, provided the original work is properly cited.

Background. Nasopharyngeal carcinoma (NPC) is a malignant neoplasm of the nasopharyngeal epithelium. Concurrent chemoradiotherapy has been established as a standard treatment for locoregional NPC, and cisplatin is a common agent in NPC treatment. Cetuximab is a monoclonal antibody against epidermal growth factor receptor. This meta-analysis was performed to evaluate the curative effectiveness and survival outcomes of cetuximab in NPC patients who received concurrent cisplatin-radiotherapy. **Methods.** PubMed, Cochrane Library, EMBASE, China National Knowledge Infrastructure (CNKI), Wan Fang, and China Biology Medicine disc (CBM) were used to search publications studying on concurrent chemoradiotherapy and/or cetuximab in NPC. The qualities of included RCTs were assessed by the Newcastle-Ottawa Scale. STATA 14.0 was used to conduct the statistical analysis. **Results.** In total, 17 trials with 2066 patients were included in this meta-analysis. The results from this study show that cetuximab improved the therapy efficacy in NPC patients who received concurrent cisplatin-radiotherapy. Cetuximab cotreatment improved the complete response (RR = 1.92, 95% CI [1.61, 2.30]), and reduced stable disease (RR = 0.67, 95% CI [0.51, 0.88]) as well as progression disease (RR = 0.24, 95% CI [0.15, 0.40]). Besides, it also improved the overall survival (RR = 1.10, 95% CI [1.02, 1.18]), disease-free survival (RR = 1.09, 95% CI [1.03, 1.15]), metastasis-free survival (RR = 1.06, 95% CI [1.01, 1.11]), and relapse-free survival (RR = 1.04, 95% CI [1.01, 1.07]) in NPC patients. **Conclusions.** Cetuximab could improve the curative efficacy and survival outcomes of NPC patients who underwent concurrent cisplatin-radiotherapy. However, all the trials included were conducted in China; thus, the quality of the trials in this study remains doubtful. More high-quality RCTs should be included in further relevant studies.

1. Introduction

Nasopharyngeal carcinoma (NPC) is an epithelial carcinoma associated with the nasopharyngeal mucosa, and it is closely associated with Epstein-Barr virus (EBV). When comparing with other cancers, NPC is quite uncommon. In 2018, there were approximately 129,000 new cases of NPC, which represents only 0.7% of all cancer types diagnosed [1]. NPC occurs frequently in the south of China and Southeast Asian countries, and men have a higher incidence of NPC than women [2].

Advances in radiation therapy technology and concomitant chemotherapy have led to improvements in the management of NPC [3]. In comparison to traditional 2D

or 3D radiation therapy, intensity-modulated radiotherapy (IMRT) is ideally suited to the target area of the tumor, as it can deliver a high dose of radiation to NPC while protecting adjacent tissues and reduce adverse effects including neurotoxicity and dysphagia [4, 5]. NPC is a chemotherapy-sensitive disease. Combined agents, particularly cisplatin-based regimens, are highly effective in the treatment of NPC [6].

In the epoch of traditional 2D radiation therapy, studies have shown that, compared to radiation alone, simultaneous chemoradiation may significantly improve the 5-year overall survival and progression-free survival in patients with stage II NPC [7]. However, other studies have shown the opposite. Al-Sarraf et al. and Lee et al. indicated that the concomitant

chemoradiation group was not greater than those in the IMRT group in patients with NPC. Studies have confirmed that concomitant chemoradiation therapy accompanied by adjuvant chemotherapy or not could lead to better outcomes than radiotherapy alone in stage III-IV locoregionally NPC [8, 9]. On the contrary, neither adjuvant chemotherapy nor induction chemotherapy could improve the survival outcomes of radiation therapy; thus, concurrent chemoradiation therapy is considered to be the core therapy for locally advanced NPC.

Though great progression has been made in NPC treatment, there are still over 20% patients developing into recurrence and metastasis. Epidermal growth factor receptor (EGFR) is a transmembrane receptor, and it is usually involved in the cellular proliferation, migration or invasion, and other cell biological activities [10].

Increasing evidence suggests that targeting EGFR might be a potential strategy for NPC therapy, in which EGFR is highly expressed in 85% of patients with advanced NPC [11]. To date, cetuximab and nimotuzumab are the monoclonal antibodies against EGFR tested in NPC clinical trials. Studies have attempted to evaluate the efficacy and toxicity of cetuximab combined with chemoradiation therapy in the treatment of advanced NPC, but the results have been inconformity [12–15].

Based on the above reasons, we performed this meta-analysis to evaluate the efficacy of concurrent radiocisplatin therapy with/without cetuximab from the aspects of curative rate and survival outcomes.

2. Methods

2.1. Literature Search Strategy. The databases including PubMed, Cochrane Library, EMBASE, China National Knowledge Infrastructure (CNKI), Wan Fang, and China Biology Medicine disc (CBM) were used to conduct literature searches (past to May 2022). Search terms included “cetuximab” and “radiotherapy” or “radiation therapy” and “cisplatin” or “cis-platinum” or “chemotherapy” and “nasopharyngeal carcinoma”.

2.2. Selection Criteria. The final included studies should meet the following criteria: (a) trials including patients that were diagnosed with nasopharyngeal carcinoma (NPC); (b) trials including patients who received both cetuximab and concurrent chemoradiotherapy, and the chemotherapy should use cisplatin; (c) trials reported as RCTs; and (d) the literature was published in English or Chinese, and the full text was available. When it comes to redundant publications, only the most recent studies were included. Studies belong to animal or cell experiments, case report, review, letter, and conference abstract, and those without full text were out of consideration. Besides, studies that were republished or irrelevant to the subject were excluded.

2.3. Data Extraction. The retrieved data were evaluated and screened independently by Lin Wang and Deyou Wei and were determined by Deyou Wei when it comes to disagreement. Studies in this meta-analysis included the following

basic information: the name of first author, publication year and country, sample size, details of chemoradiotherapy, and outcomes (efficacy and survival).

2.4. Quality Assessment. The quality of the included trials was assessed by Newcastle-Ottawa Scale (NOS). Studies with a score above 6 are considered of high quality. All the 17 articles included in the current meta-analysis were deemed to be high-quality studies.

2.5. Statistical Analysis. All statistical analyses were performed using STATA 14.0 software (College Station, USA). For dichotomous data, relative risk (RR) and 95% confidence interval (CI) were reported. The I^2 test was taken for heterogeneity between studies. If $I^2 \leq 50\%$ or $p > 0.1$, select the fixed-effects model; otherwise, select the random-effects model. Publication bias was evaluated through Begg’s test and funnel plot, and p value less than 0.05 is considered significant.

3. Results

3.1. Study Characteristics. The literature selection process is shown in Figure 1. Initially, 763 studies were retrieved from the aforementioned databases based on the aim search terms, and 561 were left after removing duplicates. Next, 284 irrelevant studies were excluded by screening the titles or abstracts, and 75 were excluded due to ineligible data. Eventually, 17 trials were eligible for this meta-analysis. All of the 17 included studies were conducted in China, of which only 4 were published on SCI journals in English and the rest were published in Chinese journals (Table 1). In total, 2066 participants with NPC were involved in this meta-analysis. All the studies used cetuximab combined with chemoradiotherapy as observation group and chemoradiotherapy alone as the control. As for the outcomes, complete response (CR), partial response (PR), stable disease (SD), and progression disease (PD) were used to evaluate the treatment efficacy, and overall survival (OS), disease-free survival (DFS), metastasis-free survival (MFS), relapse-free survival (RFS), and progression-free survival (PFS) were used to assess the survival outcomes of the patients. NOS was used to evaluate the quality of the included literature. All 17 studies scored at least 6 and were considered high quality (Table 2).

3.2. Meta-Analysis

3.2.1. Efficacy of Cetuximab Combined with Concurrent Chemoradiotherapy in NPC Treatment. Meta-analysis showed that cetuximab improved the therapy efficacy in NPC patients undergoing concurrent chemoradiotherapy. The CR, PR, SD, and PD data of the included studies were summarized in Table 3. As shown in Figure 2(a), the CR in patients who received the combined therapy of cetuximab and concurrent chemoradiotherapy was higher than those who only received concurrent chemoradiotherapy (RR = 1.92, 95% CI [1.61, 2.30], fixed-effects model), while no significant difference was noticed in PR (Figure 2(b)) between observation and control groups (RR = 0.96, 95% CI [0.80, 1.17], fixed-effects model). In addition, both SD

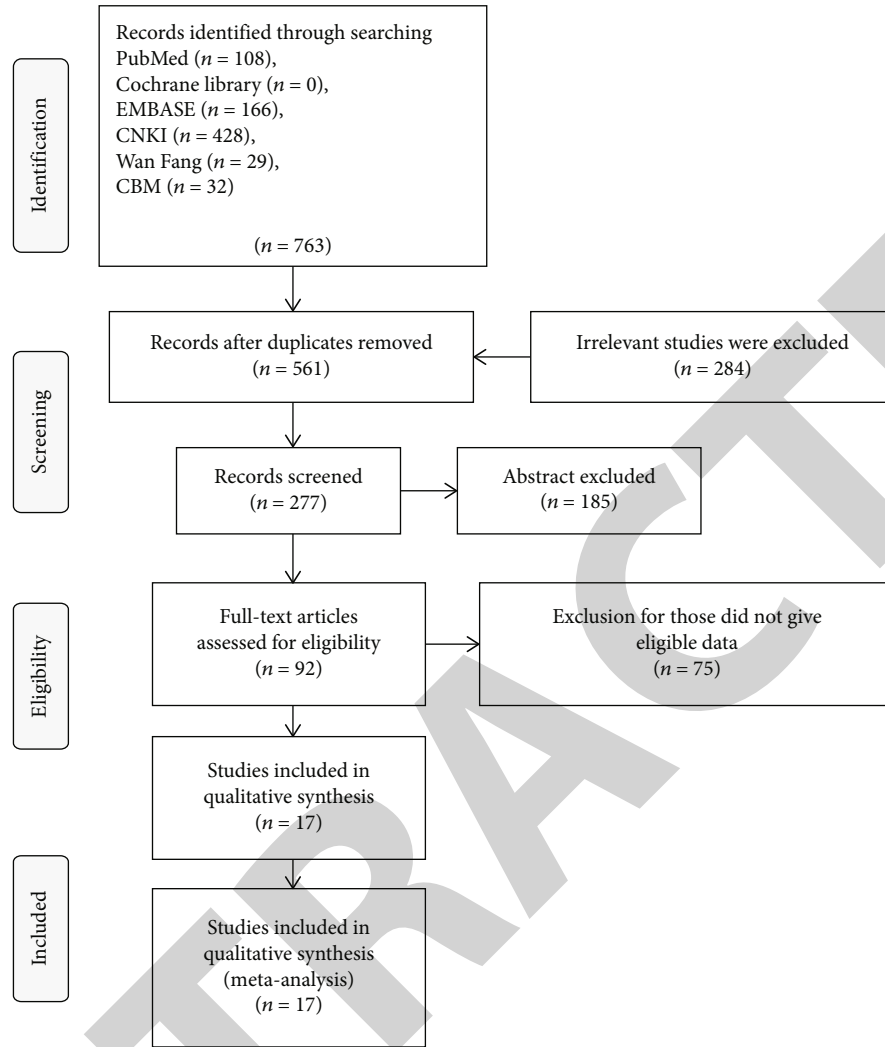


FIGURE 1: Process of study selection.

and PD (Figures 2(c) and 2(d)) were lower in concurrent chemoradiotherapy with cetuximab than that without cetuximab (SD: RR = 0.67, 95% CI [0.51, 0.88], fixed-effects model; PD: RR = 0.24, 95% CI [0.15, 0.40], fixed-effects model). Furthermore, we calculated the objective response rate (ORR) and disease control rate (DCR) by the following formulae and conducted meta-analysis according to the calculated data. As shown in Figures 2(e) and 2(f), both ORR and DCR were higher in concurrent chemoradiotherapy with cetuximab than that without cetuximab (ORR: RR = 1.38, 95% CI [1.27, 1.51], fixed-effects model; DCR: RR = 1.12, 95% CI [1.05, 1.20], random-effects model).

$$\text{ORR} = \text{CR} + \text{PR}, \quad (1)$$

$$\text{DCR} = \text{CR} + \text{PR} + \text{SD}.$$

3.2.2. Publication Bias of Treatment Efficacy. As shown in Figure 3, Begg's test was used to assess the potential publication bias. In general, funnel plots appeared symmetrical in CR, SD, PD, and DCR, and Begg's test results showed that

no significant publication bias was in CR ($p = 0.125$), SD ($p = 0.350$), PD ($p = 0.721$), and DCR ($p = 0.213$). However, publication bias was noted in the meta-analysis of PR ($p = 0.029$) and ORR ($p = 0.016$).

3.2.3. Survival Outcomes of NPC Patients Who Received Cetuximab Combined with Concurrent Chemoradiotherapy.

The survival outcomes including OS, DFS, MFS, RFS, and PFS were summarized in Table 4. The results in our study show that cetuximab improved the survival outcomes of NPC patients. As shown in Figure 4(a), NPC patients who received cetuximab therapy had a higher OS than those who did not (RR = 1.10, 95% CI [1.02, 1.18], random-effects model). Likewise, cetuximab also improved DFS, MFS, and RFS in NPC patients undergoing concurrent chemoradiotherapy (Figures 4(b)–4(d), DFS: RR = 1.09, 95% CI [1.03, 1.15], fixed-effects model; MFS: RR = 1.06, 95% CI [1.01, 1.11], fixed-effects model; RFS: RR = 1.04, 95% CI [1.01, 1.07], fixed-effects model). However, as shown in Figure 4(e), there was no significance in PFS between NPC

TABLE 1: Characteristics of the included studies.

First author	Year	Country	Sample size T E C	Chemotherapy (cisplatin)	Radiotherapy (IMRT)	Cetuximab	Efficacy	Outcomes
P Yang* [16]	2021	China	126 63 63	80 mg/m ² /3 w	66.0-75.9 Gy	400 mg/m ² loading dose and then 250 mg/m ² /w	CR, PR, SD, and PD	OS, MFS, RFS, and PFS
J Liang [17]	2019	China	40 20 20	25 mg/m ² , d ₁ -d ₃ /3 w	70 Gy	400 mg/m ² loading dose and then 250 mg/m ² /w, 7 cycles	CR, PR	—
JJ Lu [18]	2018	China	64 32 32	20 mg/m ² /3 w, 2 cycles	64-72 Gy	400 mg/m ² loading dose and then 250 mg/m ² /w	CR, PR	—
WY Li [19]	2018	China	40 20 20	3 mg/m ² , d ₁ -d ₃ /3 w	69 Gy	400 mg/m ² loading dose and then 250 mg/m ² /w, 7 cycles	CR, PR, SD, and PD	OS
Y Li* [14]	2017	China	186 62 124	80-100 mg/m ² /w, 2 cycles; 30-40 mg/m ² /w, 5-7 cycles	68-76 Gy	400 mg/m ² loading dose and then 250 mg/m ² /w, 6-7 cycles	—	OS, MFS, RFS, and PFS
WX Xia* [12]	2017	China	192 96 96	30-40 mg/m ² /w; 80-100 mg/m ² /3 w	Unclear dose	400 mg/m ² loading dose and then 250 mg/m ² /w	—	OS, DFS, MFS, and RFS
R You* [20]	2017	China	791 102 689	10 mg/m ² /3 w, 3 cycles	66-70 Gy	400 mg/m ² loading dose and then 250 mg/m ² /w	—	OS, DFS, MFS, and RFS
ZY Yang [21]	2016	China	45 22 23	40 mg/m ² /w, 6-8 cycles	73.96 Gy	400 mg/m ² loading dose and then 250 mg/m ² /w, 7 cycles	CR, PR, SD, and PD	—
XX Wang [22]	2016	China	78 36 42	40 mg/m ² /w, 6 cycles	66 Gy	40 mg/m ² /w, 6 cycles	CR, PR, SD, and PD	OS, PFS
T Zeng [23]	2016	China	138 64 74	40 mg/m ² /w, 6 cycles	76 Gy	400 mg/m ² loading dose and then 250 mg/m ² /w, 6 cycles	CR, PR, SD, and PD	OS, MFS, and RFS
XQ Cao [24]	2016	China	40 20 20	33 mg/m ² , d ₁ -d ₃ /3 w	69 Gy	400 mg/m ² loading dose and then 250 mg/m ² /w, 7 cycles	CR, PR, SD, and PD	OS
ZQ Zhao [25]	2015	China	64 32 32	20 mg/m ² /3 w, 4 cycles	64-72 Gy	400 mg/m ² loading dose and then 250 mg/m ² /w	CR, PR, SD, and PD	—
MH Fu [26]	2015	China	64 36 28	20 mg/m ² /4 w, 4 cycles	70 Gy	400 mg/m ² loading dose and then 250 mg/m ² /w	CR, PR, SD, and PD	OS, MFS, and RFS
XL Fu [27]	2015	China	40 20 20	33 mg/m ² , d ₁ -d ₃ /3 w	69 Gy	400 mg/m ² loading dose and then 250 mg/m ² /w, 6 cycles	CR, PR, SD, and PD	OS
ZH Zheng [28]	2013	China	40 20 20	80 mg/m ² /3 w, 2 cycles	69.96 Gy	400 mg/m ² loading dose and then 250 mg/m ² /w, 7 cycles	CR, PR	—
CZ Wu [29]	2013	China	68 34 34	20 mg/m ² , d ₁ -d ₄ /3 w, 2 cycles	64-68 Gy	100 mg/w, 7 cycles	CR, PR, SD, and PD	—
HY Ran [30]	2013	China	50 25 25	80 mg/m ² /3 w, 2 cycles	70 Gy	400 mg/m ² loading dose and then 250 mg/m ² /w	CR, PR, SD, and PD	—

T: total; E: experimental group; C: control group; CR: complete response; PR: partial response; SD: stable disease; PD: progression disease; OS: overall survival; DFS: disease-free survival; MFS: metastasis-free survival; RFS: relapse-free survival; PFS: progression-free survival. *Published on SCI journal in English.

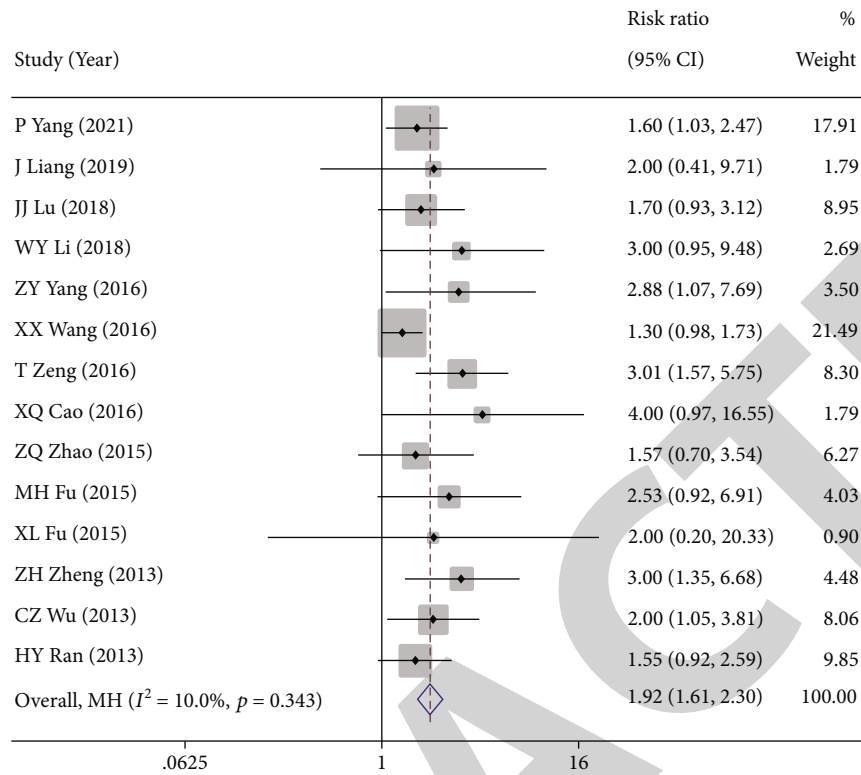
TABLE 2: Methodological quality assessment of the included studies by Newcastle-Ottawa Scale.

Study	Exposed cohort	Selection		Outcome of interest	Comparability	Assessment of outcome	Outcome Length of follow-up	Adequacy of follow-up	Total score
		Nonexposed cohort	Ascertainment of exposure						
P Yang	*	*	*	*	**	*	*	*	9
J Liang	*	*	*	*	*	*	—	—	6
JJ Lu	*	*	*	*	*	*	—	—	6
WY Li	*	*	*	*	*	*	*	*	8
Y Li	*	*	*	*	**	*	*	—	8
WX Xia	*	*	*	*	**	*	*	—	8
R You	*	*	*	*	*	*	*	—	7
ZY Yang	*	*	*	*	*	*	—	—	6
XX Wang	*	*	*	*	**	*	*	*	9
T Zeng	*	*	*	*	**	*	*	*	9
XQ Cao	*	*	*	*	**	*	*	*	9
ZQ Zhao	*	*	*	*	*	*	—	—	6
MH Fu	*	*	*	*	**	*	*	*	9
XL Fu	*	*	*	*	**	*	*	*	9
ZH Zheng	*	*	*	*	**	*	—	—	7
CZ Wu	*	*	*	*	*	*	—	—	6
HY Ran	*	*	*	*	*	*	—	—	6

TABLE 3: Efficacy of cetuximab+concurrent cisplatin-radiotherapy.

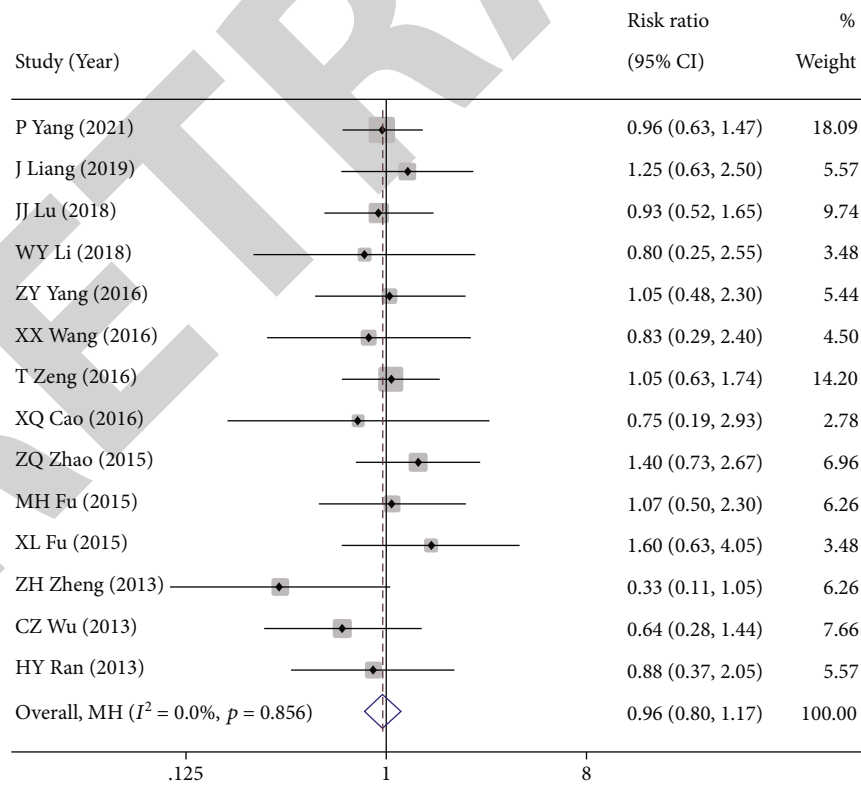
Study	CR (%)		PR (%)		SD (%)		PD (%)	
	E	C	E	C	E	C	E	C
P Yang	50.8	31.7	39.7	41.3	9.5	15.9	0	11.1
J Liang	20.0	10.0	50.0	40.0		NA		NA
JJ Lu	53.1	31.3	40.6	43.7		NA		NA
WY Li	45.0	15.0	20.0	25.0	25.0	25.0	10.0	35.0
ZY Yang	50.0	17.4	36.4	34.8	9.1	34.8	4.5	13
XX Wang	80.6	61.9	13.9	16.7	5.6	19.1	0	2.4
T Zeng	40.6	13.5	31.3	29.7	21.9	32.4	6.2	24.4
XQ Cao	40.0	10.0	15.0	20.0	35.0	30.0	10.0	40.0
ZQ Zhao	34.4	21.9	43.8	31.3	18.8	21.9	3.1	25.0
MH Fu	36.1	14.3	30.6	28.6	22.2	32.1	5.6	25.0
XL Fu	10.0	5.0	40.0	25.0	40.0	55.0	10.0	15.0
ZH Zheng	75.0	25.0	15.0	45.0		NA		NA
CZ Wu	52.9	26.5	20.6	32.4	17.6	14.7	8.8	26.5
HY Ran	68.0	44.0	28.0	32.0	4.0	24.0	0	0

E: experimental group; C: control group; CR: complete response; PR: partial response; SD: stable response; PD: progression disease; NA: not applicable.



NOTE: Weights are from Mantel-Haenszel model

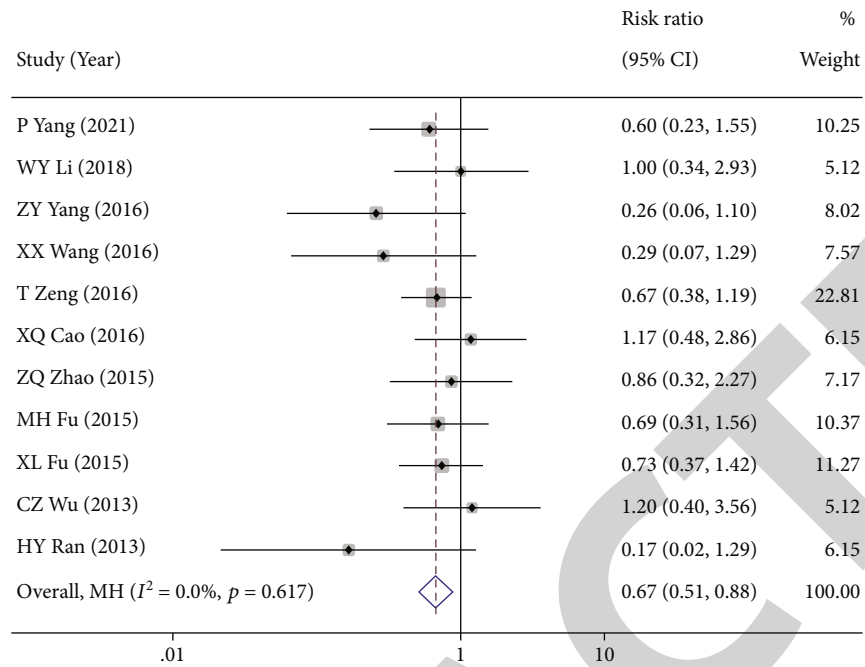
(a)



NOTE: Weights are from Mantel-Haenszel model

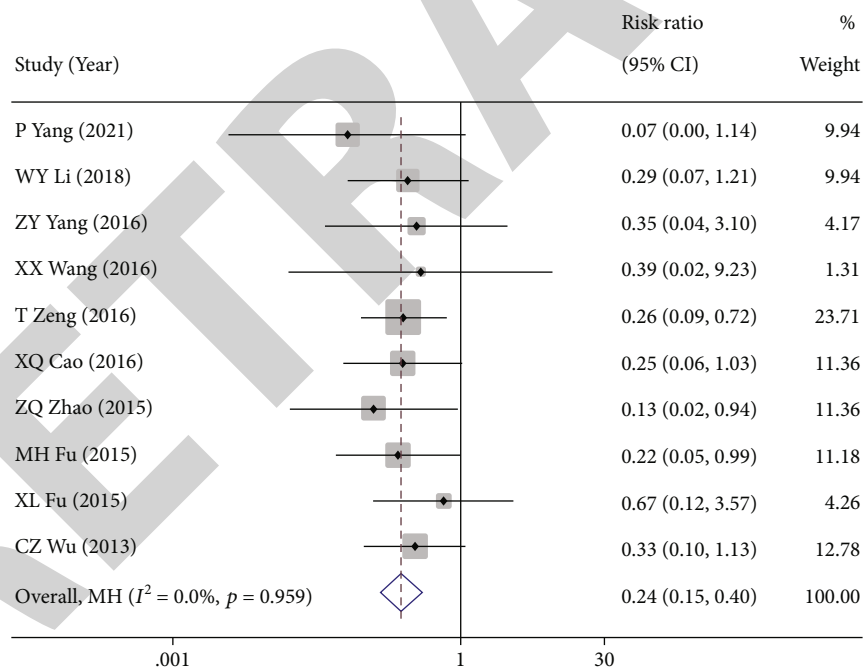
(b)

FIGURE 2: Continued.



NOTE: Weights are from Mantel-Haenszel model

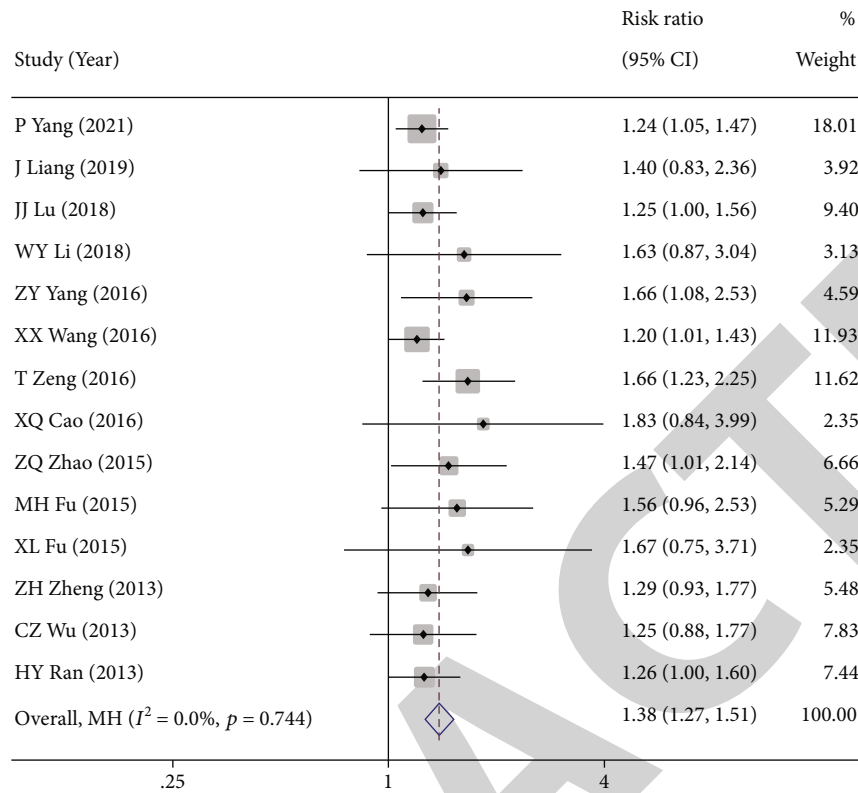
(c)



NOTE: Weights are from Mantel-Haenszel model

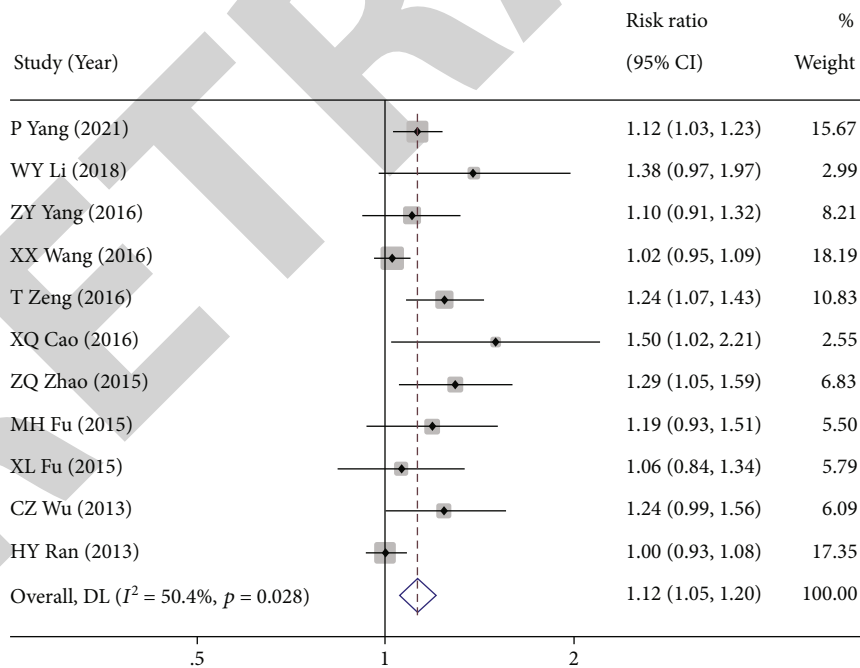
(d)

FIGURE 2: Continued.



NOTE: Weights are from Mantel-Haenszel model

(e)



NOTE: Weights are from random-effects model; continuity correction applied to studies with zero cells

(f)

FIGURE 2: Curative efficacy of cetuximab in NPC patients who received concurrent cisplatin-radiotherapy. Forest plots of (a) complete response, (b) partial response, (c) stable disease, (d) progression disease, (e) objective response rate, and (f) disease control rate.

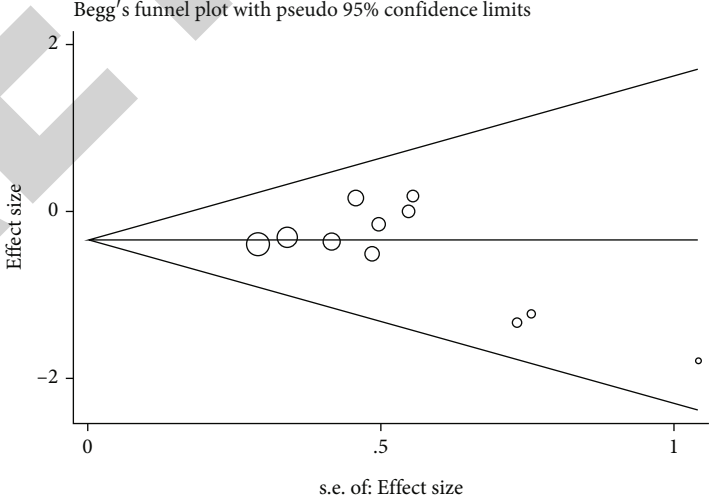
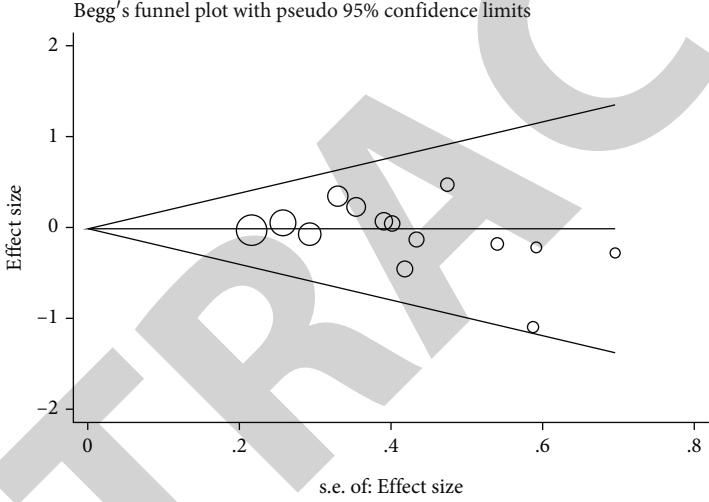
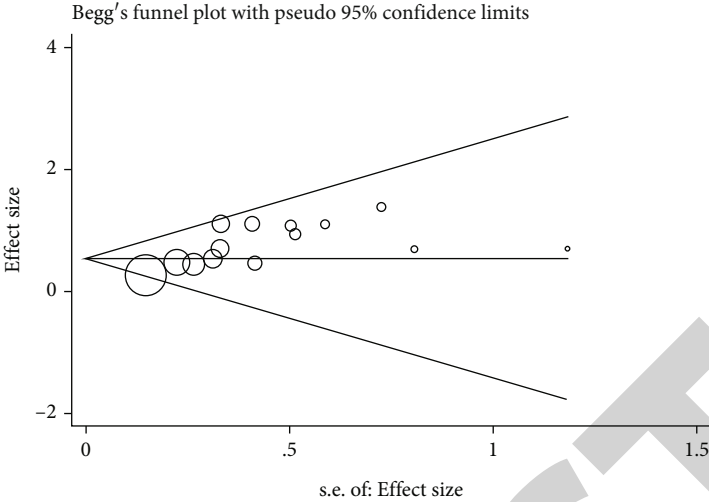


FIGURE 3: Continued.

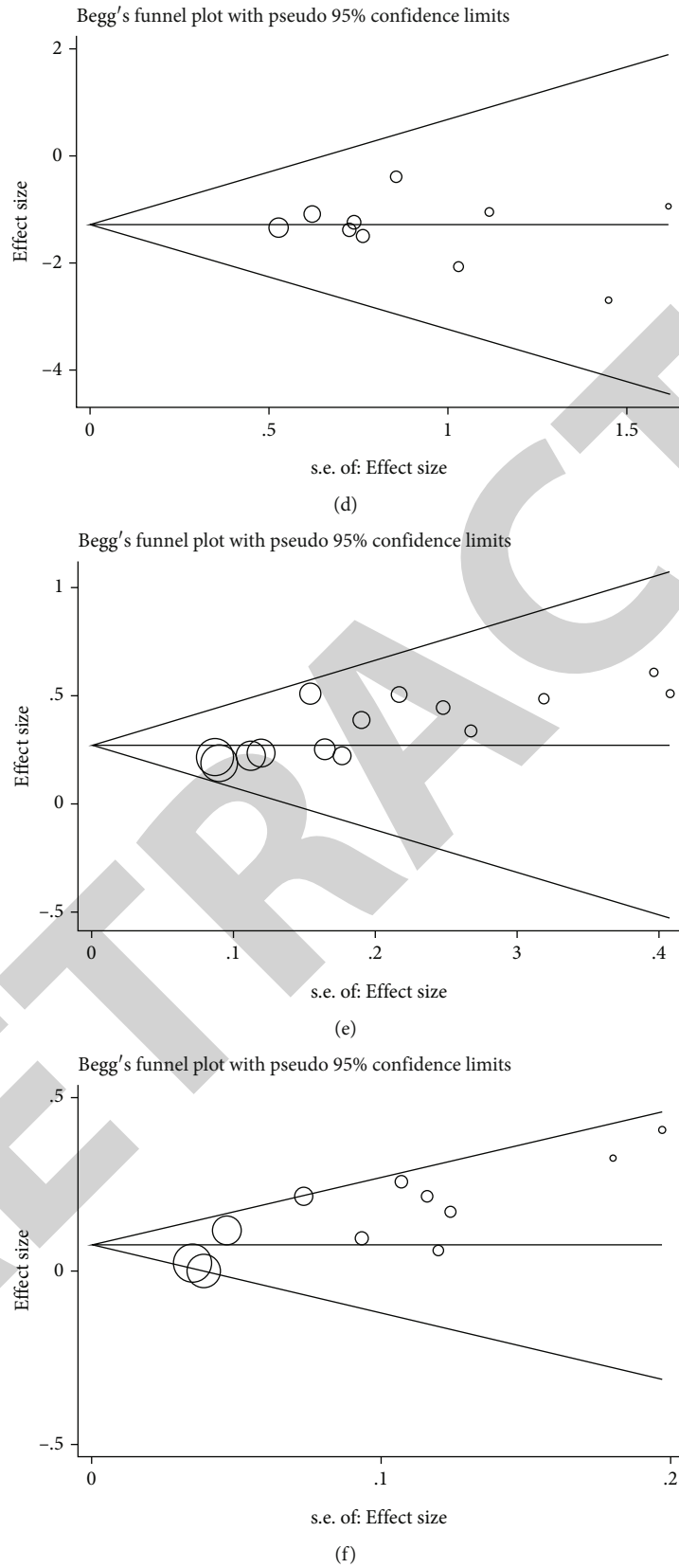
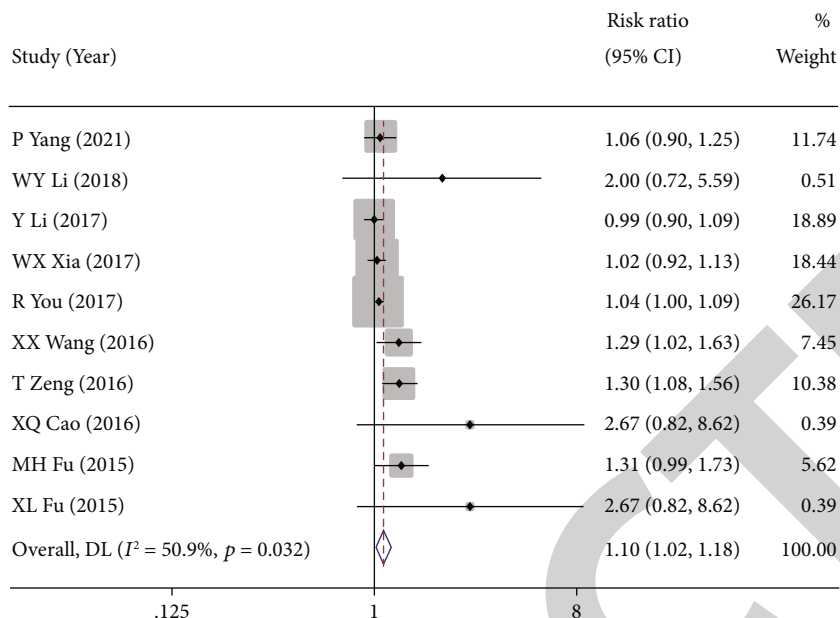


FIGURE 3: Publication bias of curative efficacy. (a) Complete response. (b) Partial response. (c) Stable disease. (d) Progression disease. (e) Objective response rate. (f) Disease control rate.

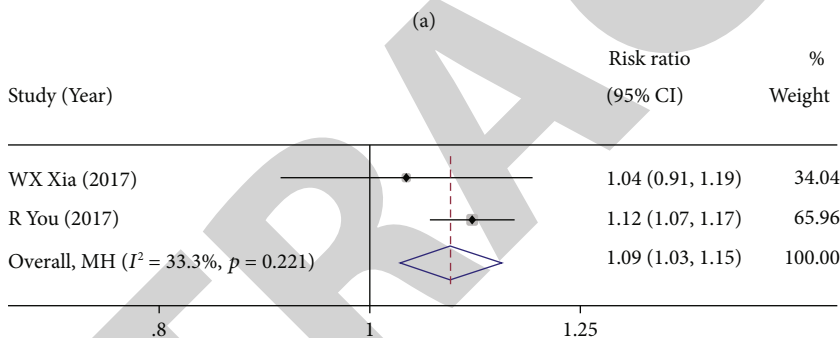
TABLE 4: Survival of cetuximab+concurrent chemoradiotherapy.

Study	OS (%)		DFS (%)		MFS (%)		RFS (%)		PFS (%)	
	E	C	E	C	E	C	E	C	E	C
P Yang	84.1	79.4	NA	NA	92.1	85.7	100	92.1	81	68.3
WY Li	40	20	NA	NA	NA	NA	NA	NA	NA	NA
Y Li	90.3	91.1	NA	NA	83.9	90.3	95.2	94.4	79	84.7
WX Xia	89.3	87.2	83.4	80.5	94.1	87.3	92.5	93.2	NA	NA
R You	96.6	92.9	93.5	86.9	94.6	89.3	97.8	94.7	NA	NA
XX Wang	88.9	69.1	NA	NA	NA	NA	NA	NA	75	59.5
T Zeng	87.5	67.6	NA	NA	78.1	64.9	87.5	81.1	NA	NA
XQ Cao	40	15	NA	NA	NA	NA	NA	NA	NA	NA
MH Fu	88.9	67.9	NA	NA	77.8	64.3	88.9	82.1	NA	NA
XL Fu	40	15	NA	NA	NA	NA	NA	NA	NA	NA

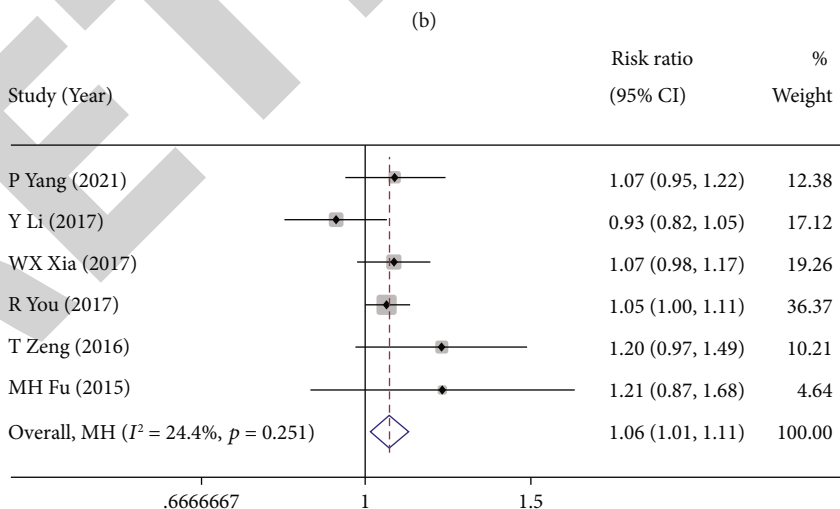
E: experimental group; C: control group; OS: overall survival; DFS: disease-free survival; MFS: metastasis-free survival; RFS: relapse-free survival; PFS: progression-free survival.



NOTE: Weights are from random-effects model



NOTE: Weights are from Mantel-Haenszel model



NOTE: Weights are from Mantel-Haenszel model

FIGURE 4: Continued.

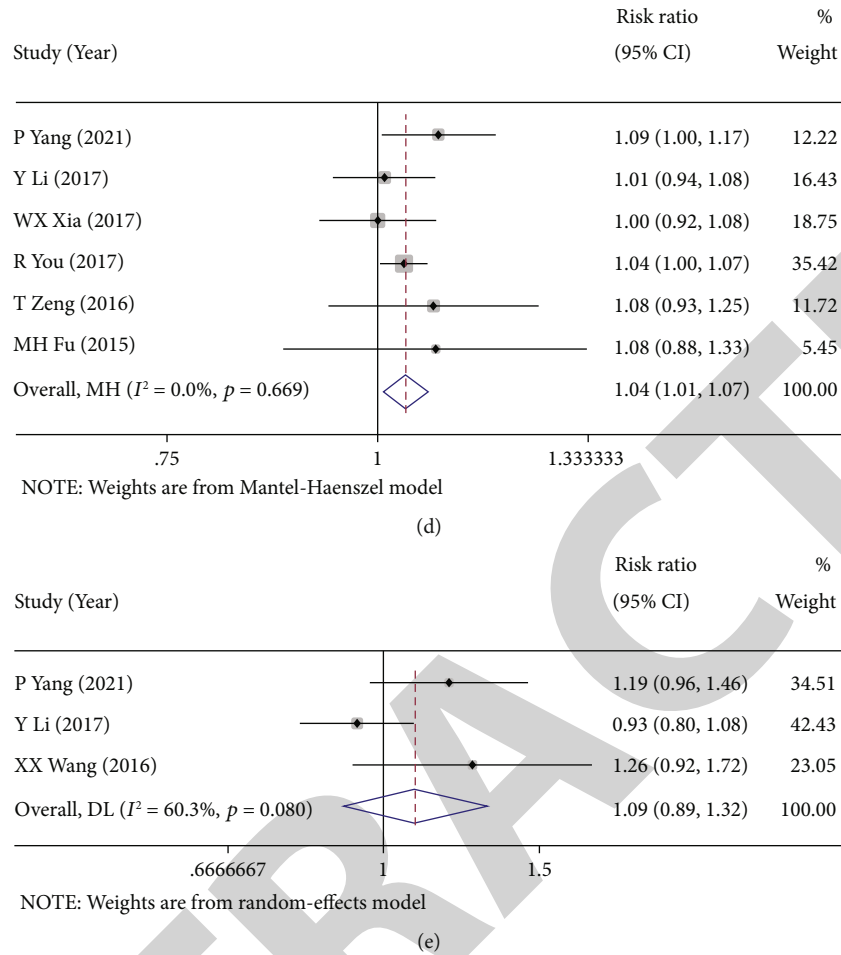


FIGURE 4: Survival outcomes of cetuximab in NPC patients who received concurrent cisplatin-radiotherapy. Forest plots of (a) overall survival, (b) disease-free survival, (c) metastasis-free survival, (d) relapse-free survival, and (e) progression-free survival.

patients receiving cetuximab and those not receiving cetuximab (RR = 1.09, 95% CI [0.89, 1.32], random-effects model).

3.2.4. *Publication Bias of Survival Outcomes.* Since only 2 studies provided DFS data and 3 offered PFS data, the publication bias towards these two outcomes was not conducted. As shown in Figure 5, funnel plots appeared symmetrical in OS, MFS, and RFS. The results of Begg’s test showed that no significant publication bias was in these outcome indicators (OS: $p = 0.060$; MFS: $p = 0.260$; RFS: $p = 1.000$).

4. Discussion

NPC is a serious malignant tumor originating from nasopharyngeal epithelium. NPC has a unique geographical and ethnic distribution, and NPC is mostly found in East and Southeast Asians. NPC is the third most common carcinoma in southern China, with an incidence rate around 1/10,000 [31]. Currently, radiotherapy is still the main curative treatment for NPC, especially IMRT. NPC is likely to infiltrate in neighbour important tissues or organs, such as the brain stem, spinal cord, and optic chiasm. IMRT can

target tumors at high doses while reducing doses to adjacent normal tissues [32]. Nevertheless, the 5-year survival rate of NPC patients with radiotherapy alone is only about 70% [33]. Thus, radiotherapy accompanied with concurrent or induction chemotherapy has been considered as a standard treatment.

Since cisplatin-based concomitant chemoradiotherapy may increase side effects in patients diagnosed with NPC; many other potential drugs in NPC treatment are under exploration. EGFR-based concomitant chemoradiation therapy is another novel alternative that may be suitable for advanced NPC treatment. Nowadays, monoclonal antibodies as well as small molecule tyrosine kinase inhibitors are used to against EGFR clinically. Cetuximab is one of the clinically used monoclonal antibodies. You et al. [20] demonstrated that concurrent chemoradiation therapy with cetuximab group exhibited better OS and DFS and distant metastasis-free survival (DMFS), while Li et al. [14] drew an opposite conclusion based on their case-control study. Due to the above paradoxes, we conducted this meta-analysis.

In total, 17 trials with 2066 patients were participated in this meta-analysis. The results in our study show that

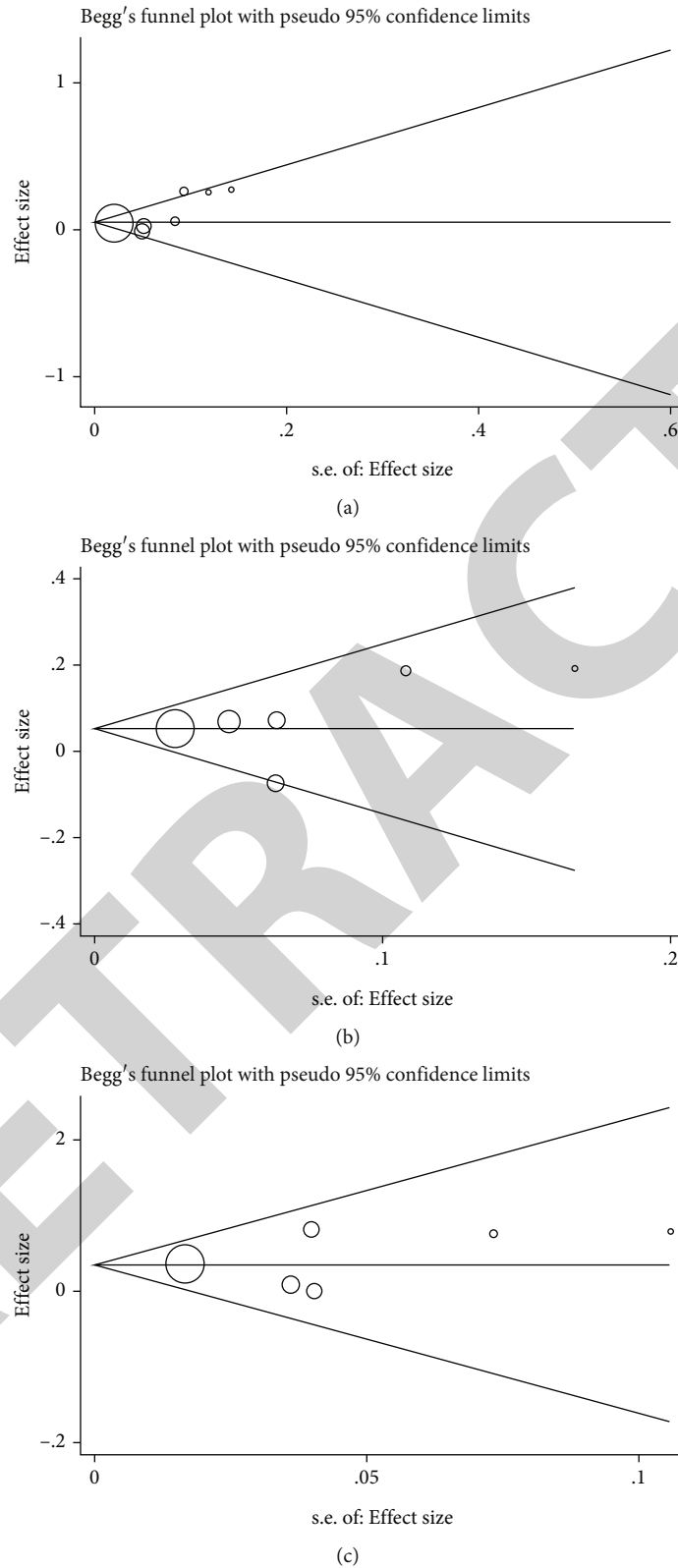


FIGURE 5: Publication bias of survival outcomes. (a) Overall survival. (b). Metastasis-free survival. (c) Relapse-free survival.

cetuximab improved the therapy efficacy in NPC patients who received concurrent cisplatin-radiotherapy. Cetuximab cotreatment improved the CR and reduced SD as well as

PD. In addition, the survival outcomes were improved by cetuximab cotreatment including OS, DFS, MFS, and RFS. The heterogeneity in this study is not significant. We only

found acceptable heterogeneity existing in the analyses of disease control rate ($I^2 = 50.4\%$, $p = 0.028$), overall survival ($I^2 = 50.9\%$, $p = 0.032$), and progression-free survival ($I^2 = 60.3\%$, $p = 0.080$).

However, the limitations of this study should be noted. First, all the included trials were conducted in China, and this may cause low study quality and regional disparity. Second, some of the included trials only provided limited data, which brings inaccuracy in subsequent meta-analysis including disease-free survival and progression-free survival. Last but not the least, publication bias was noticed in partial response and objective response rate. Nonetheless, this meta-analysis verified the positive efficacy of cetuximab in the combination of concurrent chemotherapy. It is recommended to include more high-quality studies for further evaluation.

5. Conclusions

To summarize, the results in this meta-analysis revealed that cetuximab could enhance the curative effects and improve the survival outcomes of NPC patients who received concurrent cisplatin-radiotherapy. All of the trials included were conducted in China, which may lead to low quality and regional disparity. Based on this, more trials with high quality are suggested for further assessment.

Data Availability

The labeled dataset used to support the findings of this study is available from the corresponding author upon request.

Conflicts of Interest

The authors declare that they have no conflict of interest.

Authors' Contributions

Lin Wang designed the study, Deyou Wei and Dianjun Liu conducted the literature searching and screening, Dianjun Liu did the data analysis, and Deyou Wei wrote the manuscript. All authors contributed to this work and reviewed the final version of the manuscript. Lin Wang and Dianjun Liu contributed equally to this work.

References

- [1] Y. P. Chen, A. Chan, Q. T. Le, P. Blanchard, Y. Sun, and J. Ma, "Nasopharyngeal carcinoma," *Lancet*, vol. 394, no. 10192, pp. 64–80, 2019.
- [2] S. Guan, J. Wei, L. Huang, and L. Wu, "Chemotherapy and chemo-resistance in nasopharyngeal carcinoma," *European Journal of Medicinal Chemistry*, vol. 207, article 112758, 2020.
- [3] L. L. Tang, Y. P. Chen, C. B. Chen et al., "The Chinese Society of Clinical Oncology (CSCO) clinical guidelines for the diagnosis and treatment of nasopharyngeal carcinoma," *Cancer Commun (Lond)*, vol. 41, no. 11, pp. 1195–1227, 2021.
- [4] G. Peng, T. Wang, K. Y. Yang et al., "A prospective, randomized study comparing outcomes and toxicities of intensity-modulated radiotherapy vs. conventional two-dimensional radiotherapy for the treatment of nasopharyngeal carcinoma," *Radiotherapy and Oncology*, vol. 104, no. 3, pp. 286–293, 2012.
- [5] T. Du, J. Xiao, Z. Qiu, and K. Wu, "The effectiveness of intensity-modulated radiation therapy versus 2D-RT for the treatment of nasopharyngeal carcinoma: a systematic review and meta-analysis," *PLoS One*, vol. 14, no. 7, article e219611, 2019.
- [6] M. Al-Sarraf and M. S. Reddy, "Nasopharyngeal carcinoma," *Current Treatment Options in Oncology*, vol. 3, no. 1, pp. 21–32, 2002.
- [7] Q. Y. Chen, Y. F. Wen, L. Guo et al., "Concurrent chemoradiotherapy vs radiotherapy alone in stage II nasopharyngeal carcinoma: phase III randomized trial," *Journal of the National Cancer Institute*, vol. 103, no. 23, pp. 1761–1770, 2011.
- [8] M. Al-Sarraf, M. LeBlanc, P. G. Giri et al., "Chemoradiotherapy versus radiotherapy in patients with advanced nasopharyngeal cancer: phase III randomized intergroup study 0099," *Journal of Clinical Oncology*, vol. 16, no. 4, pp. 1310–1317, 1998.
- [9] A. W. Lee, S. Y. Tung, D. T. Chua et al., "Randomized trial of radiotherapy plus concurrent-adjuvant chemotherapy vs radiotherapy alone for regionally advanced nasopharyngeal carcinoma," *Journal of the National Cancer Institute*, vol. 102, no. 15, pp. 1188–1198, 2010.
- [10] M. J. Xu, D. E. Johnson, and J. R. Grandis, "EGFR-targeted therapies in the post-genomic era," *Cancer Metastasis Reviews*, vol. 36, no. 3, pp. 463–473, 2017.
- [11] D. T. Chua, J. M. Nicholls, J. S. Sham, and G. K. Au, "Prognostic value of epidermal growth factor receptor expression in patients with advanced stage nasopharyngeal carcinoma treated with induction chemotherapy and radiotherapy," *International Journal of Radiation Oncology • Biology • Physics*, vol. 59, no. 1, pp. 11–20, 2004.
- [12] W. X. Xia, H. Liang, X. Lv et al., "Combining cetuximab with chemoradiotherapy in patients with locally advanced nasopharyngeal carcinoma: a propensity score analysis," *Oral Oncology*, vol. 67, pp. 167–174, 2017.
- [13] L. R. Wu, H. F. Zhu, J. Xu et al., "Effectiveness of cetuximab in combination with concurrent chemoradiotherapy in locoregionally advanced nasopharyngeal carcinoma: a 1: 2 propensity score-matched analysis," *Journal of Cancer*, vol. 9, no. 9, pp. 1642–1651, 2018.
- [14] Y. Li, Q. Y. Chen, L. Q. Tang et al., "Concurrent chemoradiotherapy with or without cetuximab for stage II to IVb nasopharyngeal carcinoma: a case-control study," *BMC Cancer*, vol. 17, no. 1, p. 567, 2017.
- [15] X. Zhang, L. Du, F. Zhao, Q. Wang, S. Yang, and L. Ma, "A phase II clinical trial of concurrent helical tomotherapy plus cetuximab followed by adjuvant chemotherapy with cisplatin and docetaxel for locally advanced nasopharyngeal carcinoma," *International Journal of Biological Sciences*, vol. 12, no. 4, pp. 446–453, 2016.
- [16] P. Yang, J. Liu, H. Yong, J. Ma, and X. Gao, "Effect of cetuximab combined with IMRT and concurrent chemotherapy in treating locally advanced nasopharyngeal carcinoma," *Journal Of Buon*, vol. 26, no. 1, pp. 138–144, 2021.
- [17] J. Liang and W. Lin, "Clinical observation of cetuximab combined with radiotherapy and chemotherapy in the treatment of advanced nasopharyngeal carcinoma," *Shenzhen Journal of Integrated Traditional Chinese and Western Medicine*, vol. 29, pp. 129–130, 2019.

Research Article

Effect of Ultrasound Image-Guided Nerve Block on the Postoperative Recovery Quality of Patients with Tibial Fractures Using the Concept of Enhanced Recovery after Surgery

Xiaohong Zhang, Lu He, Xiangqing Mo, Ling Jiang, and Chenhui Deng 

Department of Postanesthesia Care Unit (PACU), Zhuzhou Central Hospital, Zhuzhou, 412000 Hunan, China

Correspondence should be addressed to Chenhui Deng; 1706240507@xy.dlpu.edu.cn

Received 2 June 2022; Revised 28 July 2022; Accepted 3 August 2022; Published 22 August 2022

Academic Editor: Pan Zheng

Copyright © 2022 Xiaohong Zhang et al. This is an open access article distributed under the Creative Commons Attribution License, which permits unrestricted use, distribution, and reproduction in any medium, provided the original work is properly cited.

This study was aimed at investigating the clinical effect of ultrasound-guided nerve block based on the concept of enhanced recovery after surgery (ERAS) for postoperative anesthesia in patients with tibial fractures. The noise-reduction processing was introduced in ultrasound images to adjust the ultrasound clarity of the patient. A total of 177 patients with tibial fractures in our hospital were retrospectively analyzed and divided into OG group (general anesthesia combined with nerve block, 78 cases), C1 group (simple general anesthesia, 27 cases), C2 group (ultrasound-guided nerve block combined with general anesthesia, 10 cases), and C3 group (62 cases of spinal-epidural anesthesia). The effect of anesthesia and postoperative recovery time of patients in each group were analyzed. The wake-up time of the OG group was significantly shorter than that of the other three groups ($P < 0.05$). The doses of propofol and remifentanyl in the OG group were much lower than those in the other groups ($P < 0.05$). After the ultrasound image was processed with noise reduction, the image showed the lesion more clearly. The excellent and good rates of OG group, C1 group, C2 group, and C3 group were 89.86%, 62.73%, 75.37%, and 61.07%, respectively. The Ramsay sedation score and anesthesia satisfaction in the OG group were obviously higher than those in the other groups, but there was no significant difference ($P > 0.05$). The visual analogue scale (VAS) scores of the OG group at 12 h, 24 h, and 36 h after the surgery were 4.52 ± 0.41 , 4.72 ± 0.24 , and 4.81 ± 0.74 , respectively, which were significantly higher than those of the other three groups ($P < 0.05$). On the basis of ERAS, ultrasound-guided nerve block combined with general anesthesia can improve the perioperative pain in patients with tibial fractures and significantly shorten the time for the wake-up time. In addition, it was safe and reliable, so it was worthy of clinical promotion.

1. Introduction

The tibia and fibula are located under the human skin without muscle covering, which is a common type of long bone fractures in patients with orthopedic fractures. In recent years, the incidence has been rising, and after fracture, the skin is easily pierced by the fracture end, which can lead to traumatic arthritis over time [1]. Due to the damage of external force, the soft tissue can easily cause serious damage, which has a great impact on the health and quality of life of patients [2, 3]. Surgery is an important modality for the treatment of tibial fractures, and ensuring the safety and effectiveness of anesthesia is a very important feature. Stud-

ies have shown that nerve block anesthesia combined with general anesthesia can effectively improve myocardial oxygenation, showing a good anesthesia effect, especially for patients with underlying cardiovascular diseases [4]. The methods of intraoperative anesthesia include central nerve axon block (spinal, epidural or combined spinal-epidural block), lumbar plexus nerve block with posterior approach block (psoas compartment block), and anterior approach block (parainguinal block). Different anesthesia methods vary in terms of postoperative analgesia, type of surgery, rehabilitation, and patient satisfaction [5]. Capdevila et al. [6] showed that persistent peripheral nerve block is an effective analgesic technique for postoperative sedation of

orthopedic pain, and neurological and infectious adverse events are rare. The postoperative analgesic effect of regional nerve block is better than systemic administration of morphine, and the adverse reactions are also less than epidural anesthesia. The previous nerve blocks were all difficult to operate, and they all located the target nerve by blind detection, which could not confirm the diffusion range of anesthesia and could not guarantee the effect of the block. Even if the anesthesiologist has rich experience, there will be anatomical variations, individual differences, and other factors that may lead to inaccurate injection of anesthesia drugs and poor nerve block results [7, 8]. With the continuous development of medical technology, ultrasound-guided nerve block technology has been widely used in clinical practice. Ultrasound can visualize the positioning of nerves, accurately inject anesthetic doses, and effectively avoid damage to blood vessels and nerves, and patients do not need to change their positions. After systemic induction, the pain of patients is greatly reduced [9]. The nerve block operation under ultrasound-guided is simple and accurate, and the patient can be extubated as soon as possible after waking up. Using ultrasound-guided can not only clearly display the patient's spinal anatomy but also observe the patient's anatomical condition before puncture in real time, making it easier for physicians to understand the surgical process, ensuring the safety of the nerve block, and greatly improving the success rate of the operation [10–12].

The middle and lower third of the tibia is prone to fracture, the lower end of the calf is compressed, and severe avascular necrosis occurs. The concept of enhanced recovery surgery for the middle and lower tibia originated from cardiac surgery, and now it has been extended to vascular surgery, plastic surgery, colorectal surgery, joint surgery, hernia surgery, etc. Academician Li Jieshou's team has shown in the study of gastric cancer patients that the treatment of this concept is safe and effective [13, 14]. Anesthesia methods in the enhanced recovery surgery concept include general anesthesia, regional block, and a combination of the two. Such anesthesia method can not only meet the basic requirements of sedation, analgesia, and improve good surgical adjustment but also effectively reduce the surgical stress, which is beneficial to the postoperative recovery of patients [15]. Enhanced recovery after surgery (ERAS) refers to the clinical scientific practice of patients during the perioperative period, and evidence-based medicine has proven to be an effective measure. ERAS has been integrated into the care of many surgical diseases [16]. Nursing staff use this optimized nursing and monitoring measures to speed up the recovery of patients, shorten the hospitalization time of patients, effectively improve the patient's negative psychology, improve patient satisfaction, and have a positive impact on the incidence of postoperative complications and readmissions [17, 18]. Broadbent et al. [19] stated that it is feasible not to do routine bowel preparation before elective ERAS surgery, and it is not associated with postoperative complications.

This study investigated the effect of ultrasound image-guided nerve block on the resuscitation quality of anesthesia and resuscitation room after tibia surgery under the guidance of ERAS concept. Visualization of ultrasound-guided

nerve blocks greatly improved the success rate of nerve blocks. This study could provide a reference for the functional evaluation of patients, shorten the postoperative recovery time of patients, and analyze the anesthesia effect of ultrasound combined with nerve block on patients with tibial fracture.

2. Materials and Methods

2.1. Research Objects. There were 760 tibial fracture operations performed in 5 years from January 2017 to December 2021, and 177 patients who met the criteria of this study were selected. Among the causes of fracture, there were 66 patients with tibial fracture due to traffic accidents, 47 patients with drops, and 64 patients with falls. The patients were grouped according to the surgical method, 78 cases with general anesthesia and nerve block were OG group, 27 cases with general anesthesia (without nerve block) were group C1, 10 cases with spinal-epidural joint and nerve block were group C2, and 62 cases with spine-epidural anesthesia (without nerve block) were group C3. This study was approved by ethics committee of hospital, and the patients and their families were informed about the study and signed the informed consent.

Inclusion criteria are as follows: patient with tibial fracture on ultrasound; patients with complete clinical data; patients whose American Society of Anesthesiologists (ASA) grade was I-II; patients who were determined as tibial fracture according to the trauma history, clinical symptoms, and examination results; patients with no contraindication to surgical anesthesia; patients with no senile dementia and able to actively cooperate with medical staff in rehabilitation training; and patients not taking glucocorticoids in the past 2 months.

Exclusion criteria are as follows: those who were allergic to the anesthetics; those who were in critical condition and unable to cooperate with the investigator; patients with contraindications; patients with coagulation dysfunction; patients with systemic infection; patients with severe cardiovascular disease or abnormal liver and kidney function; and patients with old fractures.

2.2. Fast Track Surgery. Fast track surgery speeded up patient recovery and shortened surgical hospital stays. The measures used in this study to speed up recovery include the following aspects. First, it should talk with the patient before surgery, inform the patient of the surgery plan, obtain the patient's cooperation, and reduce psychological stress. Secondly, it should provide nutritional support before surgery to avoid prolonged application, oral laxatives for bowel preparation and diet control, and 250-400 mL of 10% glucose solution 2 hours before surgery. Thirdly, it should not routinely use the nasogastric tube, urinary catheter, and drainage. Fourthly, it should actively adopt minimally invasive techniques. Fifthly, it should use sedatives and pain relievers before surgery and place an epidural tube for pain relief 1-2 days before surgery. Sixthly, it can choose a reasonable anesthesia method plus general anesthesia. Finally, it can get out of bed in the early stage before surgery and get

out of bed for 6-8 hours after surgery. In addition, it should ensure the intraoperative fluid infusion, strictly control infusion volume and infusion speed, and pay attention to the intraoperative thermal insulation to adjust the room temperature to 25°C.

2.3. Research Methods. Color ultrasound scanner and high-frequency ultrasound probe were used for ultrasound-guided. After the patient entered the room, electrocardiograph (ECG) monitoring was performed. The venous access was opened, and anesthesia was used for induction. Anesthesia induction was propofol 2.0 mg/kg + fentanyl 3 µg/kg + vecuronium bromide 0.6 mg/kg + midazolam 0.03 mg/kg. When the patient did not lose consciousness and had no blinking reflex, an endotracheal intubation was adopted and connected to a ventilator for mechanical ventilation. Gastrointestinal anesthesia included remifentanyl, the drip rate was kept at 0.1 µg/(kg min), combined with intravenous infusion of propofol 3-10 mg/kg, the drip rate was maintained at 4-8 mg/(kg h), and it was stopped 10 minutes before the completion of the surgery.

For the sciatic nerve block, the patient took the affected limb to elevate, the skin was routinely disinfected at the popliteal fossa, and the ultrasound probe was placed between the biceps femoris and the semitendinosus at the proximal 7 cm of the popliteal crease. The sciatic nerve was located using an ultrasound probe and fixed to its distal bifurcation and injected with 0.375% 20 mL ropivacaine.

For the femoral nerve block, the patient was placed in the supine position, routine disinfection was performed in the groin area, and an ultrasound probe was used to place the femoral artery pulse below the inguinal ligament. According to the ultrasound-guided images, the guide needle was inserted in parallel, there was a clear sense of breakthrough, and 0.5% 10 mL ropivacaine was used for the block.

For the observation group ($n = 78$) (OG group), on the basis of general anesthesia and nerve block after induction of anesthesia, the femoral and sciatic nerves were found with the aid of ultrasound.

For the control group 1 ($n = 27$, C1 group), general anesthesia (without nerve block) and the anesthesia method were the same as that of OG group.

For the control group 2 ($n = 10$, C2 group), spinal-epidural anesthesia and nerve block anesthesia, after the patients entered the operating room, peripheral venous access was established, vital signs were detected, and oxygen inhalation nursing was given. The healthy side lying position was selected, and L1-2/L2-3 intervertebral space was determined as the puncture site. Then, it should implant an epidural catheter and inject ropivacaine hydrochloride injection (1.5-2.5 mL 5% ropivacaine after cerebrospinal fluid reflux). Surgery was performed after observing for a few minutes.

For the control group 3 ($n = 62$, C3 group), spine-epidural anesthesia, there was no nerve blocking.

During the surgery, the anesthesia level was adjusted according to the actual situation of the patient, and the dosage of anesthesia was increased according to the actual situation of the patient.

2.4. Evaluation Indicators. The related indicators of anesthesia in each group were compared, including recovery time, extubation time, dosage of propofol, and dosage of remifentanyl, and the Ramsay sedation score 10 minutes after cupping and the pain degree half an hour after extubation were compared in each group. The visual analogue scale was used to assess the degree of pain. The higher the Ramsay sedation score, the better the effect of sedation. When the score was 0, the higher the score, and the more intense the pain. The VAS score is shown in Table 1.

The adverse reactions in each group were observed, whether the patients had vomiting, nausea, dyspnea, chills, restlessness, and other adverse reactions. According to the effect of anesthesia experienced by the patient, there was no pain, irritability, or discomfort during the operation and no obvious adverse reactions. There was no obvious fluctuation in the intraoperative detection, indicating that the anesthesia was effective, mild pain, discomfort, and irritability during the surgery and no obvious adverse reactions. There was no significant fluctuation in the intraoperative detection indicators, indicating that anesthesia was ineffective.

2.5. Statistical Methods. All data in this study were established in Excel database and analyzed using the SPSS 19.0 statistical software. Measurement data were tested by t test, and the difference was statistically significant at $P < 0.05$. The enumeration data were analyzed by χ^2 test, and the enumeration data were expressed as percentage (%). It was suggested to compare the effect of anesthesia in each group by using Diehe. According to the grade data of anesthesia effect, the difference was significant at $P < 0.05$.

3. Results

3.1. Analysis of the Causes of Fractures. In this study, 177 patients who met the criteria of this study were selected. Among the causes of fracture, 66 patients suffered from tibial fracture due to traffic accident, 47 patients dropped, and 64 patients fell. Of the 78 patients in the OG group, 29 patients suffered from tibial fracture due to traffic accidents, accounting for 37.18%; 17 patients suffered from drop injury, accounting for 28.81%; and 32 patients fell, accounting for 54.24%. In the C1 group of 27 patients, 11 patients suffered tibial fracture due to traffic accidents, accounting for 40.74%; 9 patients dropped, accounting for 33.33%; and 7 patients fell, accounting for 25.93%. Among the 10 patients in group C2, 3 patients suffered tibial fracture due to traffic accident, accounting for 30%; 2 patients suffered from drop injury, accounting for 20%; and 5 patients fell, accounting for 50%. Among the 62 patients in the C3 group, 23 patients suffered from tibial fracture due to traffic accidents, accounting for 37.10%; 19 patients dropped, accounting for 30.65%; and 20 patients fell, accounting for 32.26%. There was no statistical difference among the groups ($P > 0.05$). The results are shown in Figure 1.

3.2. Analysis of Wake-Up Time. The wake-up time in different groups was compared, and the results are shown in Figure 2. The wake-up time of the OG group was

TABLE 1: VAS score.

Level	Symptoms
0 points	No pain
3 points or less	Tolerable mild pain
4-6 points	Pain interfering with sleep, but can be tolerated
7-10 points	Intense pain that was difficult to bear

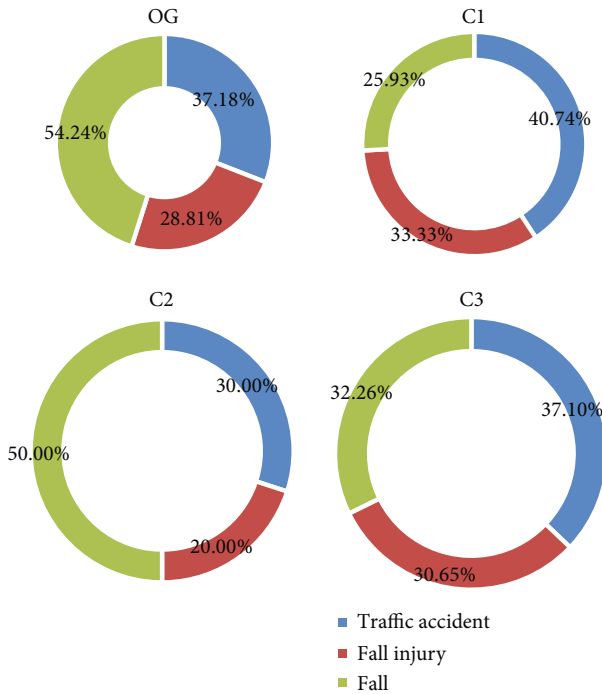


FIGURE 1: Analysis of the causes of fractures in four groups. OG: OG group; C1: C1 group; C2: C2 group; and C3: C3 group.

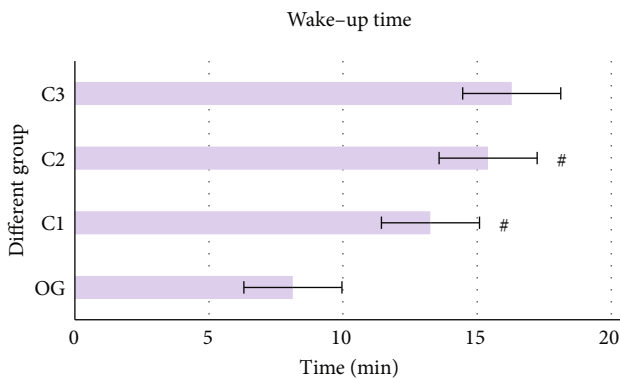


FIGURE 2: Comparison results of wake-up time in each group. OG: OG group; C1: C1 group; C2: C2 group; and C3: C3 group.

significantly less than the other three groups. There was no significant difference in wake-up time between C1 and C2 groups ($P > 0.05$).

3.3. *Comparison of Anesthesia Indicators.* Figure 3 analyzes the dosage of propofol and remifentanyl in each group, which showed that the dosage of the observation group

was significantly less than that of the other groups, and the difference was significant ($P < 0.05$). Regarding the dosage of remifentanyl, there was a significant difference between the C1 and C2 groups and the C3 group ($P < 0.05$). Propofol dosage showed the same trend. The results are shown in Figure 3.

3.4. *Comparison of Excellent and Good Rates.* The excellent and good rate was 89.86% in the observation group, 62.73% in the C1 group, 75.37% in the C2 group, and 61.07% in the C3 group. The effect of the observation group was significantly higher than that of the other three groups. The specific results are shown in Figure 4.

3.5. *Postoperative VAS Scores.* The VAS scores after 12 h, 24 h, and 36 h in the OG group were 4.52 ± 0.41 , 4.72 ± 0.24 , and 4.81 ± 0.74 , respectively. The VAS scores of C1 group after 12 h, 24 h, and 36 h after surgery were 2.21 ± 0.81 , 3.42 ± 0.94 , and 3.63 ± 0.76 , respectively. The postoperative VAS scores of C2 group after 12 h, 24 h, and 36 h were 4.31 ± 1.78 , 4.51 ± 0.94 , and 4.62 ± 0.93 , respectively; and those in the C3 group were 3.08 ± 1.42 , 3.87 ± 0.95 , and 3.96 ± 0.69 , respectively. Compared with other groups, the OG group had significant difference ($P < 0.05$). The results are illustrated in Figure 5.

3.6. *Ultrasound Images.* Figure 6(a) is an image of the sciatic nerve displayed by ultrasound, and the gray arrow indicated the position of the femoral nerve. The orange arrow in Figure 6(b) shows the femoral nerve and the femoral artery. Figure 6(c) shows the bevel of the ultrasound-guided tip indicated by the gray arrow.

3.7. *Comparisons of the Ramsay Sedation Score and Anesthesia Satisfaction.* The Ramsay sedation score and anesthesia satisfaction of the OG group were significantly higher than those of the other groups, and there was no significant difference between the OG group and the C2 group ($P > 0.05$). There was significant difference between OG group and C1 and C3 groups ($P < 0.05$). The results are shown in Table 2.

3.8. *Comparison of Adverse Reactions.* Nausea and vomiting occurred in 1.28% of the OG group. Nausea and vomiting occurred in 2 cases in the C1 group, accounting for 7.41%; chills occurred in 1 case, accounting for 3.70%, and agitation occurred in 1 case, accounting for 3.70%. There were 2 cases of nausea and vomiting in group C2, accounting for 20%, 1 case of chills in group C3, accounting for 1.61%, and 2 cases of agitation, accounting for 3.23%. The overall incidence of adverse reactions was 1 in OG, 5 in C1, 2 in C2, and 4 in C3. The observation group had the least number of patients with adverse reactions. The results are shown in Table 3.

4. Discussion

For patients in the perioperative period, it is necessary to peruse both the occurrence of complications (airway obstruction, vomiting, pain, and unstable circulatory function, etc.) and the anesthesia recovery period [20]. As stated in the ERAS application guidelines, the anesthesia management should be

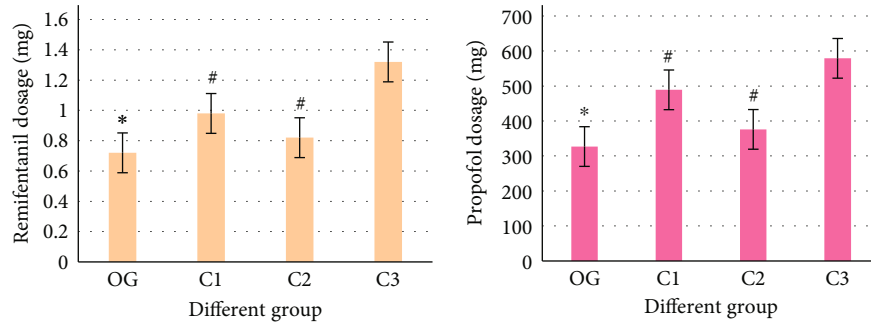


FIGURE 3: Comparison results of anesthesia-related indicators in each group. OG: OG group; C1: C1 group; C2: C2 group; and C3: C3 group. *Compared with the other three groups, $P < 0.05$; # compared with the C3 group, $P < 0.05$.

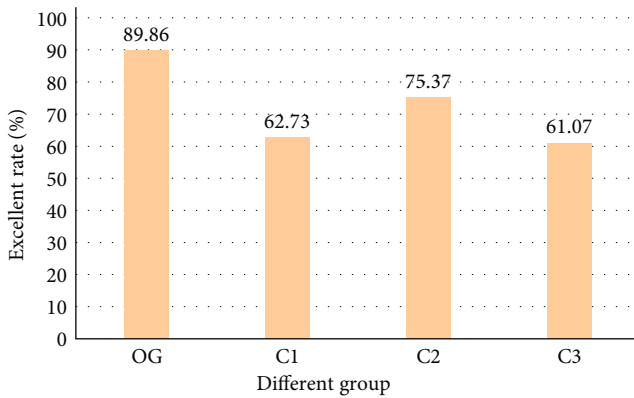


FIGURE 4: Comparison of excellent and good rates in each group. OG: OG group; C1: C1 group; C2: C2 group; and C3: C3 group.

optimized as much as possible, and short-acting anesthetics should be selected as much as possible [21]. Postoperative muscle relaxants and anesthetics have not been excreted from the body late, and the reflex phenomenon has not fully recovered. Optimizing nursing care in the recovery room can effectively avoid the occurrence of complications and promote the safety of patients through the perioperative period. ERAS advocates postoperative multimodal analgesia management, including intravenous docaine, intravenous patient-controlled analgesia management, and nonsteroidal anti-inflammatory drugs. Cheng et al. [22] proved that ultrasound-guided lower thoracic paravertebral block under the guidance of ERAS-accelerated surgery concept can provide perfect postoperative analgesia for female percutaneous nephrolithotomy, provide patients with satisfactory anesthesia and postoperative analgesia, and shorten the postoperative recovery time of patients. In the clinical nursing of postoperative resuscitation of patients with general anesthesia in the anesthesia recovery room, it is necessary to closely perfuse the patient's nervous system, respiratory system, digestive system, and circulatory system to improve symptoms and improve prognosis. In this study, 2 patients with general anesthesia had severe nausea and vomiting and arrhythmia, and 2 patients needed to be returned to the intensive care unit in time. 1 patient in the C3 group had chills, and 2 patients had agitation. The overall incidence of adverse reactions was observed, and the number of

patients with adverse reactions in the observation OG group was the least. Only 1 case of vomiting occurred, and the rest of the patients recovered smoothly. Effective nursing of patients with general anesthesia in the anesthesia recovery room can promote the safe and early recovery of patients. The nerve block is performed under ultrasound-guided, and there is no need to explore the patient's muscle twitches during the operation.

This surgery is performed in real time after induction of general anesthesia, which avoids the aggravation of pain, reduces the pain of puncture, and helps the patient to eliminate fear. Ultrasound-guided subregional nerve block anesthesia combined with spine-epidural anesthesia has a good effect. During the surgery, the emergency response of the patient's body is inhibited, the myocardial oxygenation of the patient is inhibited, and the unstable cardiac pain and other diseases will be reduced, which is beneficial to related complications such as pulmonary infection. Zhao et al. [23] pointed that ultrasound-guided nerve block anesthesia surgery can effectively improve the intraoperative anesthesia effect of patients with tibial fractures and improve the stability of intraoperative and postoperative hemodynamic indicators. Anesthesia surgery will play a positive role in postoperative pain control, reduce the risk of postoperative adverse reactions, and reduce the activity of inflammatory factors in postoperative patients. This study yielded the same effect. Zhen et al. [24] thought ultrasound-guided paravertebral nerve block anesthesia improved stress and hemodynamic responses in lung cancer thoracic surgery patients without an increase in the incidence of adverse events. Fan et al. [25] used the artificial intelligence algorithm to guide the nerve block by ultrasound images combined with general anesthesia and showed a good effect during the operation. The CNN algorithm can accurately segment the lesions in the ultrasound images of gastric cancer, which is convenient for doctors to make more accurate judgments on the lesions to provide the basis for the preoperative examination of radical gastrectomy for gastric cancer. Ultrasound-guided nerve block combined with general anesthesia can effectively improve the analgesic effect of radical gastrectomy for gastric cancer, can reduce intraoperative and postoperative adverse reactions and the dosage of analgesic drugs, and has a good effect on postoperative recovery of patients. In this study, intelligent noise-reduction processing was

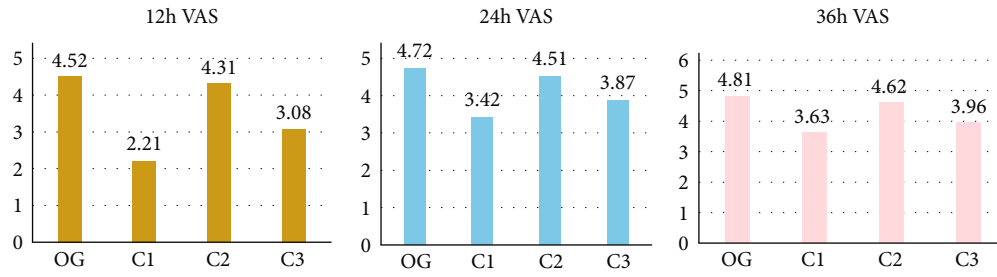


FIGURE 5: VAS scores of each group at different time periods after the surgery. OG: OG group; C1: C1 group; C2: C2 group; and C3: C3 group.

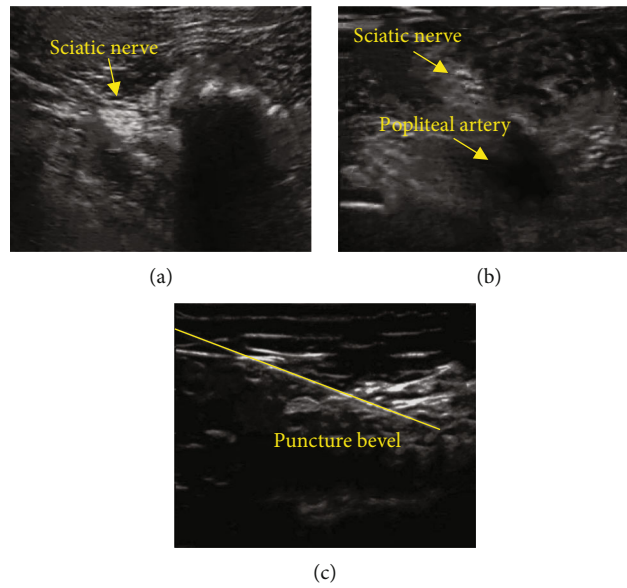


FIGURE 6: Ultrasound images. (a) Ultrasound display of the sciatic nerve; (b) ultrasound display of the femoral artery; (c) ultrasound-guided tip oblique view. The yellow arrows in the figure indicate sciatic nerve and popliteal artery, and the yellow line is puncture bevel.

TABLE 2: Comparisons of the Ramsay sedation score and anesthesia satisfaction.

Group	Cases	Ramsay sedation score	Anesthesia satisfaction score
OG	78	2.34 ± 0.71	7.81 ± 1.02
C1	27	1.96 ± 0.42	7.02 ± 0.17
C2	10	2.31 ± 0.63	6.73 ± 0.34
C3	62	2.01 ± 0.27	6.21 ± 0.28
χ^2		2.71	1.013
P		0.018	0.429

implemented in ultrasonic imaging, and the resulting ultrasonic images were clearer. This study showed that the effect was better than that of general anesthesia without nerve block, and the difference was significant ($P < 0.05$). The effect of spinal-epidural anesthesia and nerve block anesthesia was better than spine-epidural anesthesia (without nerve block), and the difference was significant ($P < 0.05$). Ultrasound-guided block combined with spine-epidural anesthesia can avoid the

TABLE 3: Comparison of adverse reactions.

Group	Cases	Nausea and vomiting	Chill	Agitation	Difficulty breathing
OG	78	1	0	0	0
C1	27	2	1	1	0
C2	10	2	0	0	0
C3	62	0	1	2	1
χ^2		0.476	1.087	1.375	
P		0.608	0.387	0.416	

adverse consequences of intraoperative regional nerve block insufficiency.

In anesthesia, the dose of drugs used in anesthesia can be reduced, which is beneficial to the stabilization of the hemodynamic indexes of patients during surgery. The VAS scores of patients with general anesthesia and nerve block were significantly higher than those of the other three groups on the basis of anesthesia induction ($P < 0.05$). It indicated that the degree of pain in all patients decreased after surgery, and the score was the highest at 36 hours after the surgery. This

further confirms that the combined anesthesia regimen under ultrasound-guided is more beneficial to improve the quality of surgical anesthesia in patients with tibial fracture.

5. Conclusion

Based on the concept of ERAS, this study adopted ultrasound-guided nerve block to analyze the postoperative anesthesia effect of patients with tibial fracture. In patients with tibia, ultrasound-guided nerve block combined with general anesthesia can ensure the effect of anesthesia, reduce the application of anesthesia dose, and improve the safety of anesthesia. The use of ERAS nursing after surgery can effectively guarantee the postoperative effect of patients, which can not only reduce the emergency response of patients but also shorten the extubation time and wake-up time. There were certain shortcomings in this study. Due to the limitation of research time and the lack of long-term follow-up of patients, long-term follow-up of patients was required in the later stage to further verify the long-term efficacy. Next, different anesthesia methods can be compared by analyzing the patient's hemodynamic indicators. It was believed that in the future, clinical applications would have better anesthesia effects for the treatment of tibial fractures.

Data Availability

The data used to support the findings of this study are available from the corresponding author upon request.

Conflicts of Interest

The authors declare no conflicts of interest.

References

- [1] D. Wang, J. Yang, X. Dong, S. Zhou, and C. Wang, "Incidence and predictive factors of tibial fracture with occult posterior ankle fractures," *Journal of Healthcare Engineering*, vol. 2021, Article ID 4392595, 6 pages, 2021.
- [2] R. Morris, I. Pallister, and R. W. Trickett, "Measuring outcomes following tibial fracture," *Injury*, vol. 50, no. 2, pp. 521–533, 2019.
- [3] Y. Jang, G. Gaski, R. Natoli, W. Virkus, and T. Mckinley, "Tibial fracture healing score: a novel tool to predict tibial non-union," *Orthopedics*, vol. 43, no. 4, pp. e323–e328, 2020.
- [4] L. Lin, Y. Liu, C. Lin et al., "Comparison of three fixation methods in treatment of tibial fracture in adolescents," *ANZ Journal of Surgery*, vol. 88, no. 6, pp. E480–E485, 2018.
- [5] Q. Liu, Y. M. Sun, H. Huang et al., "Sirtuin 3 protects against anesthesia/surgery-induced cognitive decline in aged mice by suppressing hippocampal neuroinflammation," *Journal of Neuroinflammation*, vol. 18, no. 1, p. 41, 2021.
- [6] L. L. Wu, C. H. Xi, Y. Yin et al., "Comparison of the postoperative analgesic effect of ultrasound-guided serratus anterior plane block combined with pectoral nerves block I and thoracic paravertebral block in radical mastectomy," *Zhonghua Yi Xue Za Zhi*, vol. 101, no. 27, pp. 2147–2151, 2021.
- [7] G. B. Reahl, D. Marinos, N. N. O'Hara et al., "Risk factors for knee stiffness surgery after tibial plateau fracture fixation," *Journal of Orthopaedic Trauma*, vol. 32, no. 9, pp. e339–e343, 2018.
- [8] H. Shokri and A. A. Kasem, "Sciatic obturator femoral technique versus spinal anaesthesia in patients undergoing surgery for fixation of open tibial fractures using Ilizarov external fixator. A randomised trial," *BMC anaesthesiology*, vol. 20, no. 1, 2020.
- [9] T. F. Bendtsen, T. Parras, B. Moriggl et al., "Ultrasound-guided pudendal nerve block at the entrance of the pudendal (Alcock) canal: description of anatomy and clinical technique," *Regional Anesthesia and Pain Medicine*, vol. 41, no. 2, pp. 140–145, 2016.
- [10] A. Anugerah, K. Nguyen, and A. Nader, "Technical considerations for approaches to the ultrasound-guided maxillary nerve block via the pterygopalatine fossa: a literature review," *Regional Anesthesia and Pain Medicine*, vol. 45, no. 4, pp. 301–305, 2020.
- [11] M. G. Lee, S. U. Choi, J. K. Lim et al., "Ultrasound-guided sciatic nerve block at the midhigh level in a porcine model: a descriptive study," *Veterinary Medicine and Science*, vol. 6, no. 3, pp. 543–549, 2020.
- [12] M. M. Moake, B. C. Presley, and R. M. Barnes, "Ultrasound-guided posterior tibial nerve block for plantar foot foreign body removal," *Pediatric Emergency Care*, vol. 36, no. 5, pp. 262–265, 2020.
- [13] A. D. Kaye, R. D. Urman, E. M. Cornett et al., "Enhanced recovery pathways in orthopedic surgery," *Journal of Anaesthesiology Clinical Pharmacology*, vol. 35, no. 5, pp. S35–S39, 2019.
- [14] J. Zhou, S. Lin, S. Sun, C. Zheng, J. Wang, and Q. He, "Effect of single-incision laparoscopic distal gastrectomy guided by ERAS and the influence on immune function," *World Journal of Surgical Oncology*, vol. 19, no. 1, p. 307, 2021.
- [15] G. Nelson, J. Bakkum-Gamez, E. Kalogera et al., "Guidelines for perioperative care in gynecologic/oncology: Enhanced Recovery After Surgery (ERAS) Society recommendations-2019 update," *International Journal of Gynecological Cancer*, vol. 29, no. 4, pp. 651–668, 2019.
- [16] A. Ashok, D. Niyogi, P. Ranganathan et al., "The enhanced recovery after surgery (ERAS) protocol to promote recovery following esophageal cancer resection," *Surgery today*, vol. 50, no. 4, pp. 323–334, 2020.
- [17] A. D. Kaye, D. J. Chernobylsky, P. Thakur et al., "Dexmedetomidine in enhanced recovery after surgery (ERAS) protocols for postoperative pain," *Current Pain and Headache Reports*, vol. 24, no. 5, p. 21, 2020.
- [18] E. Melloul, K. Lassen, D. Roulin et al., "Guidelines for perioperative care for pancreatoduodenectomy: Enhanced Recovery After Surgery (ERAS) Recommendations 2019," *World Journal of Surgery*, vol. 44, no. 7, pp. 2056–2084, 2020.
- [19] E. Broadbent, A. Kahokehr, R. J. Booth et al., "A brief relaxation intervention reduces stress and improves surgical wound healing response: a randomised trial," *Brain, behavior, and immunity*, vol. 26, no. 2, pp. 212–217, 2012.
- [20] N. Dietz, M. Sharma, S. Adams et al., "Enhanced recovery after surgery (ERAS) for spine surgery: a systematic review," *World Neurosurgery*, vol. 130, pp. 415–426, 2019.
- [21] M. J. Scott, G. Baldini, K. C. Fearon et al., "Enhanced recovery after surgery (ERAS) for gastrointestinal surgery, part 1: pathophysiological considerations," *Acta Anaesthesiologica Scandinavica*, vol. 59, no. 10, pp. 1212–1231, 2015.

- [22] C. Long, Z. Shaoqiang, Z. Yao, and W. Geng, "Application of ultrasound-guided thoracic paravertebral block in percutaneous nephrolithotomy for women under the guidance of enhanced recovery surgery concept," *China Medical Journal*, vol. 55, no. 11, pp. 1232-1233, 2020.
- [23] Y. Zhao, H. Zhang, and M. Song, "Clinical observation of ultrasound-guided nerve block anesthesia on postoperative pain control of fracture patients," *Journal of Healthcare Engineering*, vol. 2022, Article ID 9510669, 6 pages, 2022.
- [24] S. Q. Zhen, M. Jin, Y. X. Chen, J. H. Li, H. Wang, and H. X. Chen, "Ultrasound-guided paravertebral nerve block anesthesia on the stress response and hemodynamics among lung cancer patients," *World Journal of Clinical Cases*, vol. 10, no. 7, pp. 2174–2183, 2022.
- [25] W. Fan, L. Yang, J. Li, and B. Dong, "Ultrasound image-guided nerve block combined with general anesthesia under an artificial intelligence algorithm on patients undergoing radical gastrectomy for gastric cancer during and after operation," *Computational and Mathematical Methods in Medicine*, vol. 2022, Article ID 6914157, 7 pages, 2022.

Retraction

Retracted: Exploration of Landscape Lighting Design Based on Interactive Genetic Algorithm

Computational and Mathematical Methods in Medicine

Received 27 June 2023; Accepted 27 June 2023; Published 28 June 2023

Copyright © 2023 Computational and Mathematical Methods in Medicine. This is an open access article distributed under the Creative Commons Attribution License, which permits unrestricted use, distribution, and reproduction in any medium, provided the original work is properly cited.

This article has been retracted by Hindawi following an investigation undertaken by the publisher [1]. This investigation has uncovered evidence of one or more of the following indicators of systematic manipulation of the publication process:

- (1) Discrepancies in scope
- (2) Discrepancies in the description of the research reported
- (3) Discrepancies between the availability of data and the research described
- (4) Inappropriate citations
- (5) Incoherent, meaningless and/or irrelevant content included in the article
- (6) Peer-review manipulation

The presence of these indicators undermines our confidence in the integrity of the article's content and we cannot, therefore, vouch for its reliability. Please note that this notice is intended solely to alert readers that the content of this article is unreliable. We have not investigated whether authors were aware of or involved in the systematic manipulation of the publication process.

Wiley and Hindawi regrets that the usual quality checks did not identify these issues before publication and have since put additional measures in place to safeguard research integrity.

We wish to credit our own Research Integrity and Research Publishing teams and anonymous and named external researchers and research integrity experts for contributing to this investigation.

The corresponding author, as the representative of all authors, has been given the opportunity to register their agreement or disagreement to this retraction. We have kept a record of any response received.

References

- [1] H. Shi and J. Zheng, "Exploration of Landscape Lighting Design Based on Interactive Genetic Algorithm," *Computational and Mathematical Methods in Medicine*, vol. 2022, Article ID 1771617, 11 pages, 2022.

Research Article

Exploration of Landscape Lighting Design Based on Interactive Genetic Algorithm

Haixiao Shi and Jie Zheng 

Art School of Jiangsu University, Zhenjiang 212000, China

Correspondence should be addressed to Jie Zheng; qiuyan@ujs.edu.cn

Received 29 June 2022; Revised 21 July 2022; Accepted 28 July 2022; Published 22 August 2022

Academic Editor: Pan Zheng

Copyright © 2022 Haixiao Shi and Jie Zheng. This is an open access article distributed under the Creative Commons Attribution License, which permits unrestricted use, distribution, and reproduction in any medium, provided the original work is properly cited.

There are many problems in the practical application of landscape lighting design. In order to solve these problems more specifically, based on the relevant theories of interactive genetic algorithm, radial basis function and hesitation degree are introduced into genetic algorithm. Through the analysis and processing of the data to get the optimized interactive genetic algorithm, the algorithm can analyze and optimize the landscape lighting design. Based on this model, the lighting design can be predicted and analyzed, and the prediction result is relatively good. Relevant studies show that the interactive genetic algorithm can be divided into three typical change stages according to the different results of intensity calculation, of which the first stage mainly presents the trend of gradual decline. The fluctuation phenomenon is obvious in the second paragraph. The third paragraph shows a gradual increasing trend of change. The corresponding relationship between the two fitness functions is obvious. With the increase of experts in independent variables, the corresponding fitness values show a trend of gradual decline on the whole. Through the calculation and analysis of five different indicators of landscape lighting by using interactive genetic algorithm, it can be seen that electrification has a relatively small impact on landscape lighting. The results of intelligent and environmental protection calculation are relatively high, and the corresponding range of change is relatively large, which shows that these two indicators are very important for improving the lighting design level of landscape. Finally, the model is verified by comparing data and model curves. Interactive genetic algorithm is very important to improve the lighting design of landscape, and the optimization model can be widely used in other fields.

1. Introduction

Interactive genetic algorithm has a wide application prospect in different fields, including portfolio optimization [1], clothing customization [2], communication system combination [3], gene selection [4], and information storage [5]. In view of the existing problems in genetic target combination optimization, fuzzy neural network and intelligent recognition model were used to extract the original data based on the relevant theories of interactive genetic algorithm [6]. The optimized interactive genetic algorithm model can analyze the genetic content under different combinations and verify the accuracy of the model with relevant data. In order to improve the accuracy of controller identification, interactive genetic algorithm can be used to analyze the relevant data and calculation process of controller in segments

[7]. Finally, accurate calculation results were obtained, and the superiority of the model was verified by data. Hull structure optimization was an important research subject. In order to further improve the stability of hull structure, model analysis method was adopted to calculate and solve relevant data based on interactive genetic algorithm theory [8]. Thus, a new optimization model can be obtained, and the model can predict and analyze the data.

The above research mainly analyzes interactive genetic algorithm from different fields. In order to further improve the application field of interactive genetic algorithm, it was introduced into landscape lighting. Based on the relevant theories of interactive genetic algorithm, radial basis function proxy analysis method was used to optimize the model parameters. By adjusting the indexes of interactive hesitancy, the optimized interactive genetic algorithm was obtained.

The algorithm can provide theoretical support for landscape lighting design and finally use the method of data calculation to optimize and predict the model. The results show that the model can provide guidance for the prediction of landscape lighting design. Therefore, interactive genetic algorithms can provide different guidance and optimization analysis for other fields of design and analysis.

2. The Basic Research Content of Interactive Genetic Algorithm

Interactive genetic algorithm can also be called human-computer interaction evolutionary optimization algorithm; that is, in the process of evolutionary computation, people can realize the intervention and guidance of the evolutionary process by interacting with the computer according to the needs [9, 10]. In the field of general interaction design, interaction design system usually consists of five elements: user, behavior, scene of interaction activity, technology of interaction activity and product itself, and product subject. So it can solve a kind of implicit performance index optimization problem which cannot be solved by traditional genetic algorithm. With the participation of human, genetic algorithm has been well expanded, and it no longer simply depends on dry fitness function, thus greatly broadening the application field of traditional genetic algorithm [11, 12]. The main characteristics of interactive genetic algorithm are as follows: (1) individual adaptive value is uncertain: since the user's evaluation of individuals is based on the user's cognition of the evaluated object. (2) The individual evaluation process is difficult to be durable: frequent human-computer interaction makes the evaluation results easy to fatigue. (3) Non-uniqueness of optimization results: the preferences of users' evaluation lead to certain individuality of optimization results.

Interactive genetic algorithms are widely used in many fields. In order to further analyze the main research contents and ideas of interactive genetic algorithm, the main calculation process of interactive genetic algorithm is obtained by analyzing and summarizing relevant literature, as shown in Figure 1. Through the analysis and calculation of the interactive genetic algorithm, the specific calculation process is shown as follows: firstly, the corresponding data of the main contents of the interactive research should be encoded. Then, the corresponding data can be imported through coding, and the relevant model parameters can be set through data import and analysis. After setting the relevant parameters, the initial population of the relevant research object is generated, so as to generate the corresponding initial population. On the basis of initializing the population, the related parameters of decoding individuals are solved. The accuracy of the interactive genetic algorithm is further improved by decoding individual parameters, and then, the adaptive value of the model is evaluated. Finally, the results of the model are judged: if they meet the requirements, they are directly derived. If the requirements are not met, further iterations are required. It is worth explaining that the judgment criteria includes two parts: (1) whether the requirements are met and (2) whether it conforms to relevant standards. Based

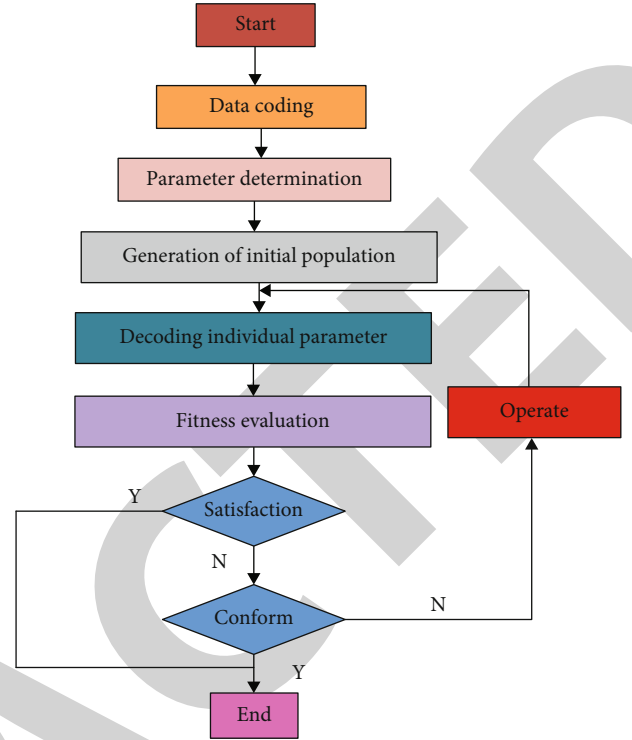


FIGURE 1: Basic flow chart of interactive genetic algorithm.

on the standpoint of interaction design and the description of interaction design methods, interaction design of product interaction interface is generally considered in four cases: (1) user-centered design, (2) activity-centered design, (3) system design, and (4) genius design.

2.1. Radial Basis Function Proxy Process. Radial basis function neural network is a kind of feedforward neural network, which is characterized by optimal approximation in function approximation. In the aspect of searching range, its remarkable characteristic is global optimum [13, 14]. Compared with the hidden layer of neural network, the completion of linear fitting of radial basis function requires more complex hidden layer neurons to be added, so as to facilitate the overfitting of trained samples [15, 16]. The forward network of RBF neural network is composed of three layers: input layer, hidden layer, and output layer. The radial basis function acts as an excitation function by acting on the hidden layer. The functional relationship between the input and output of the radial basis function neural network is as follows:

$$y_i(X) = \sum_{j=1}^M \omega_{ij} \varphi_j(X) + b_j \quad (i = 1, 2, \dots, n), \quad (1)$$

where X is the input vector, y_i is the output value of the i th output unit, M is the number of centers, ω_{ij} is the weight from the j th hidden neuron to the i th output unit, b_j is the offset value, and $\varphi_j(X)$ is the nonlinear transfer function of the radial basis function layer.

In the calculation of interactive genetic algorithm, nonlinear basis function should be selected to calculate and analyze the model [17, 18]. The nonlinear basis function is a very important function form, which is very important to improve the accuracy and precision of the model. Gaussian function has good transfer accuracy in linear transfer process, and its calculation steps are relatively few, which can meet the calculation requirements of the algorithm. By referring to relevant research content, this paper chooses Gaussian function as nonlinear basis function:

$$\varphi_j(X) = \exp\left(-\frac{\|x-c_j\|}{2\sigma_j^2}\right), \quad (2)$$

where c_j is the center of the radial basis function and σ is the width parameter. Width parameter belongs to hidden layer neural network, which can adjust the sensitivity of neurons in interactive genetic algorithm. And it can influence the concrete form of nonlinear function to some extent.

The Gaussian function corresponding to the nonlinear basis function is obtained through the above analysis and solution. It can be seen from the calculation formula of Gaussian function that the final value of Gaussian function is related to the center value and width parameters of the corresponding radial basis function. To further analyze the effect of these two parameters on the function, the curve of the transfer function is drawn (Figure 2). With the gradual increase of independent variable X , the corresponding center distance shows a trend of gradual decline. In the early stage of its decline, the decline law is more obvious, which belongs to the linear decline stage. With the gradual increase of parameters, the corresponding decrease shows obvious fluctuation; with the further increase of independent variable x , the corresponding center distance data shows a relatively stable trend of change. With the gradual increase of independent variable x , the curve drops slowly at first, and the corresponding drops are basically the same, indicating that the decline conforms to the rule of linear decline. When the corresponding function value reaches the minimum value, the curve shows a trend of slow rise with the gradual increase of independent variable. When the corresponding independent variable x belongs to 240, the data corresponding to the curve increases rapidly and reaches a high level. This indicates that there is variation or change of parameters in the calculation process, which leads to differences in the corresponding nonlinear calculation results. With the further increase of independent variable x , the curve first shows a linear decline and then gradually tends to gentle. However, the curve fluctuates to a certain extent at a higher level, which indicates that the influence of width parameters is more obvious than that of center distance.

The radial basis function layer transfer function $\varphi_j(X)$ is generally a Gaussian function, and the output function is

$$y_i(X) = \sum_{j=1}^M \omega_{ij} \exp\left(-\frac{\|x-c_j\|}{2\sigma_j^2}\right) + b_j. \quad (3)$$

The learning of radial basis function neural network parameters consists of two parts: one is the determination of hidden layer neuron center vector c and normalized parameter vector σ , and the other is the determination of output layer weight matrix ω .

Through the above analysis, the corresponding calculation relation of output function can be obtained, and the different combination of direction vector will have a certain degree of influence on the specific calculation result. In order to further optimize the data of the corresponding output function, it is necessary to analyze the change rule of the vector and obtain the change curve under the action of the corresponding independent variable output function through analysis and calculation, as shown in Figure 3. It can be seen from the different change curves in the figure that the output results of the vector function under the action of the combination of vectors in different directions have different changing trends. Specifically, it can be divided into five different types: in the first case, with the gradual increase of independent variable X , the corresponding curve first shows a stable change and then slowly increases. The slope of the corresponding curve is gradually decreasing, and the slope is gradually approaching zero. The curve tends to be flat as the corresponding slope approaches zero. After a long period of stability, the curve slowly decreases, the overall change in a small range. This shows that the influence of the first combination on the output function is relatively limited. Under the action of the second combination, with the gradual increase of x , the corresponding output function as a whole shows a relatively constant change. Only under the action of individual independent variables, certain fluctuations will occur, and the fluctuation range is relatively small, indicating that the second combination is an inherent attribute of the output function. Under the action of the third type, the corresponding value of the output function increases slowly first and then tends to be stable with the gradual increase of the independent variable x . Then, with the further increase of independent variables, the corresponding results show obvious fluctuation phenomenon, and the corresponding time of fluctuation phenomenon lasts longer. Note that the parameter jumps during the calculation, resulting in fluctuations in the corresponding output. Under the action of the fourth combination, the corresponding curve increases linearly first and then slowly. When the corresponding independent variable gradually increases, the corresponding curve will decline slowly and finally tends to flat. The stage of the curve is obvious, indicating that the combination has a good generalization of the influence on the output result. Under the action of the fifth combination, the corresponding output results decline slowly at first and then gradually tend to flat. The final curve shows a U-shaped trend. It can be seen from the above analysis that five different combinations represent five different curve types, respectively. In actual selection, specific combination modes of calculation need to be selected according to the size of computation and specific types.

2.2. Interactive Hesitation Adjustment. The most important characteristic of interactive genetic algorithm is that its

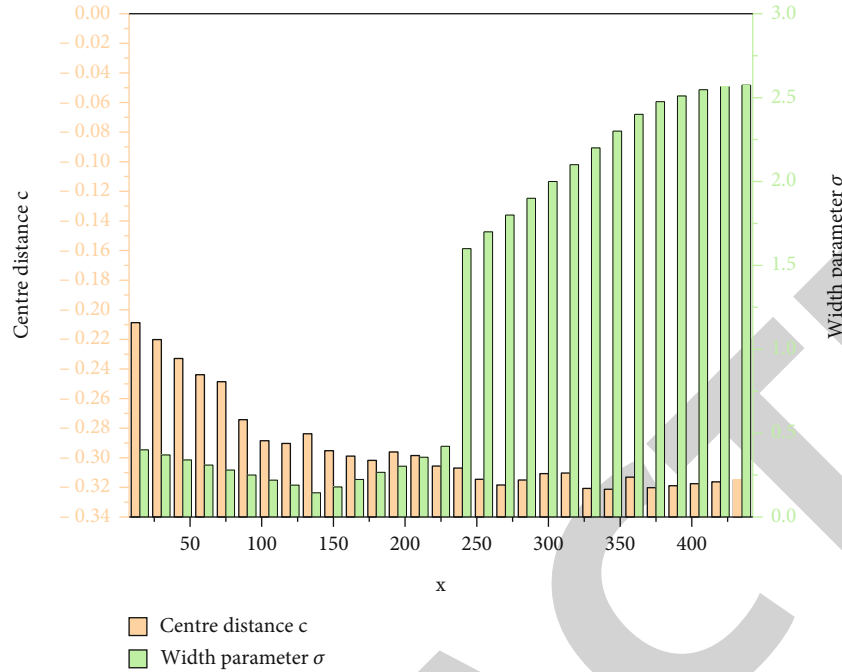


FIGURE 2: Transfer function change curve.

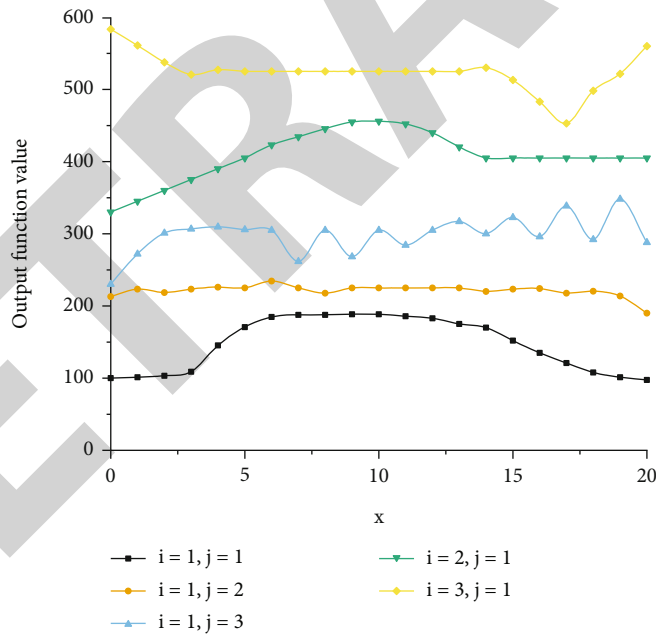


FIGURE 3: The influence of independent variables on the output function curve.

individual adaptive value is not obtained by adaptive function, but from human evaluation. The advantage of this is that it can solve the optimization problem of implicit indicators [19, 20]. However, due to human subjective factors and the increase of fatigue, the same individual may have different adaptive values in different evaluation stages [21, 22]. The existence of model deviation will lead to slow evolution speed and relatively low satisfaction of final results and then lead to long evaluation time, resulting in fatigue problem.

Therefore, it is very important to study how to reduce model error.

Errors in the interactive genetic algorithm can be divided into the following two types: (1) inaccuracy of individual adaptive values due to the addition of corresponding calculation process without full consideration of the actual situation in the actual calculation process. Finally, the calculated results differ greatly from the actual situation. (2) Due to the relatively large amount of calculation time and data,

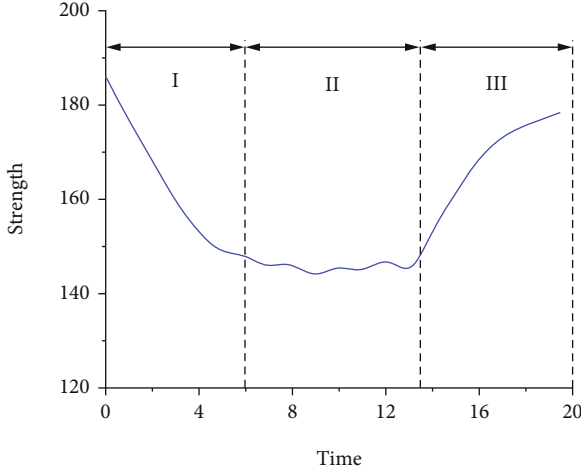


FIGURE 4: Algorithm change phase.

there are different degrees of deviation in the data calculation process, and finally, the jump point in the calculation process is relatively large. According to the length of interaction time, the evaluation process of interactive genetic algorithm can be divided into three different types of change stages according to the trend of specific data in the change process.

Through the above analysis, the relevant calculation process and proxy process of interactive genetic algorithm can be obtained. In order to further analyze the change process of interactive genetic algorithm, we drew the change curve of the algorithm through calculation, as shown in Figure 4. The curve can be divided into typical three-stage change trends according to different change forms. In the first stage, with the gradual increase of time, the corresponding algorithm strength first presents an approximate linear downward trend, and its overall variation range is relatively large. In the later stage of the first stage, the downward trend of the curve gradually changed into a gentle change, and the curve entered the second stage. In the second stage, the corresponding curve shows a trend of fluctuation, and its variation range is relatively small. This indicates that the influence of the corresponding data of the curve at this stage is relatively stable, when the corresponding iteration time exceeds 13. In the third stage, the increase of iteration time leads to a gradual linear increase in the strength of model parameters and then gradually tends to a gentle change trend. On the whole, the curve shows an approximate U-shaped change. Through the above analysis, it can be seen that the interactive genetic algorithm has both linear and nonlinear change process, indicating that the algorithm can better describe the linear and nonlinear change.

As can be seen from the changes in the calculated data, the error intensity corresponding to the curve calculation is relatively high in the initial stage, which is because the calculation model fails to specify specific objectives at the beginning of individual evaluation, so the calculation results lack certain reference. As a result, the ideal individual does not have a clear target, so some data containing the ideal individual elements will be compared and jump, resulting in dif-

ferent degrees of error. When the second stage is reached, the model has sufficient calculation and analysis of data changes, so that the calculation results can better reflect the actual change process. Therefore, it is necessary to have a clear understanding of ideal data, so the model has a strong purpose when evaluating sample data, which makes the error of calculation results relatively small. In the final stage of the model calculation, the volatility of the calculated data is obvious, which makes the calculation results appear errors in a certain range.

The expression hesitation $h_i(t)$ specifically means the position of the evaluation time of $x_i(t)$ of the i th individual of the generation t in all the individuals of this generation and the comparison with the average evaluation time. The intensity of hesitancy of $x_i(t)$, the i th individual in generation t , is expressed by hesitancy $h_i(t)$:

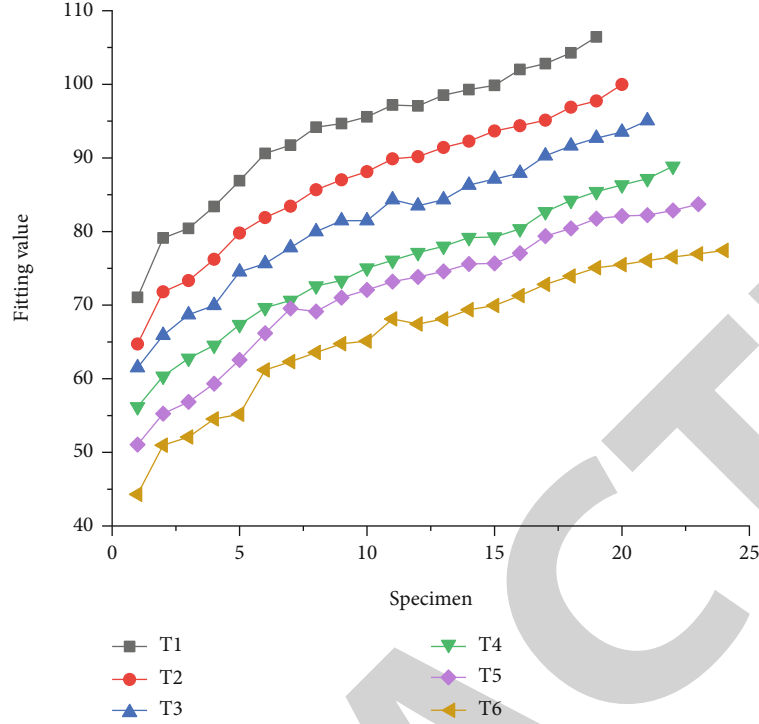
$$h_i(t) = \frac{1}{n_g} \sum_{j=1}^{n_g} a(T_i(t), T_j(t)) + \frac{T_i(t) - \bar{T}(t)}{\bar{T}(t)}, \quad (4)$$

where n_g is the number of models, $T_i(t)$ refers to the evaluation time of the i th individual, and $T_j(t)$ refers to the evaluation time of the j th individual, in which $a(T_i(t), T_j(t))$ is a piecewise function and $\bar{T}(t)$ refers to the average evaluation time. The corresponding functions are as follows:

$$a(T_i(t), T_j(t)) = \begin{cases} 1, & T_i(t) > T_j(t), \\ 0, & T_i(t) \leq T_j(t), \end{cases} \quad (5)$$

$$\bar{T}(t) = \frac{1}{n_g} \sum_{j=1}^{n_g} T_j(t). \quad (6)$$

Through the above analysis, different interactive hesitation curve can be obtained, and different calculation and evaluation time can be obtained by adjusting the change of hesitation. It can be seen from the analysis that the evaluation time has a great influence on the result of hesitation. In order to analyze the fitting curve of evaluation time under the action of different samples, the convergence curve under the action of parameter T was drawn through analysis and calculation in Figure 5. The six different types of change curves drawn have different fitting degrees. With the gradual increase of samples, the corresponding quasisum value shows an overall change trend of slow increase at first, then linear increase, and finally slow increase. This shows that the increase of sample size will lead to an obvious increase in the time fitting curve of interactive genetic algorithm. And when the specimen is fixed, the corresponding evaluation time will gradually decrease. This indicates that when the sample is constant, the decrease of evaluation time will lead to the gradual improvement of corresponding fitting data. Therefore, both the increase of sample time and the decrease of evaluation time can promote the development of the fitting curve.

FIGURE 5: Convergence analysis of parameter T .

2.3. Optimized Interactive Genetic Algorithm. When users hesitate about individual $x_j(t)$, it is easy to produce deviation in their evaluation of the adaptive value [23, 24]. In order to further analyze the calculation process of the optimized interactive genetic algorithm, firstly, each individual x_j contains n fragments x_{jm} [25, 26]. Each fragment x_{jm} corresponds to the phenotype of a specific module, and the corresponding calculation formula is obtained through analysis:

$$\max f(x) = \text{s.t. } x \in S, \quad (7)$$

where $f(x)$ is the adaptive value evaluated by users for individual x and S is the search space of individual x .

$$d(x_i(t), x_i) = \frac{1}{n} \sum_{j=1}^n b_m(x_i(t), x_i), \quad (8)$$

$$b_m(x_i(t), x_i) = \begin{cases} 0, & x_{im}(t) = x_{jm}, \\ 1, & x_{im}(t) \neq x_{jm}, \end{cases} \quad (9)$$

where the actual meaning of $d(x_i(t), x_i)$ is the distance between two individuals $x_i(t)$ and x_j . Through the change of distance, we can get the set of individuals close to hesitating individual $x_i(t)$:

$$L(x_i(t)) = \{x_j | d(x_i(t), x_j) \leq d_0, x_j \in N_e\}, \quad (10)$$

where N_e is the set of evaluated individuals and d_0 is the critical value reflecting the distance between two individuals.

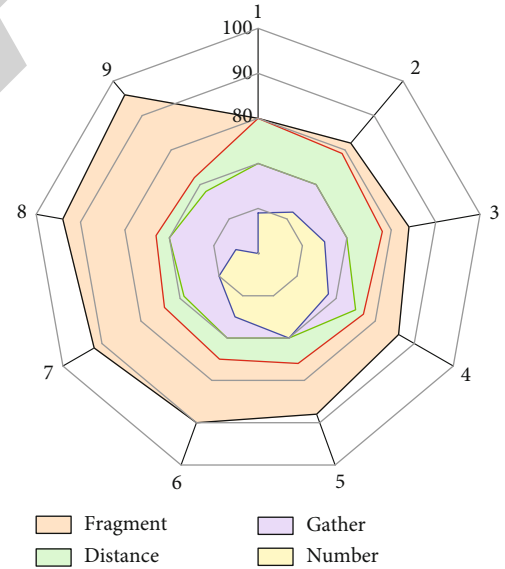


FIGURE 6: Hesitation parameter variation curve.

Several typical parameters were selected through analysis: fragment, distance, set, and data. The influence of the above-mentioned parameters on hesitation has different forms. The change curves of corresponding hesitation parameters were obtained through calculation and solution, as shown in Figure 6. The four different factors have different changing trends, indicating that the influences of different factors on the model have different forms of expression. From the changes of curves, it can be seen from the fragments that, with the gradual increase of samples, the

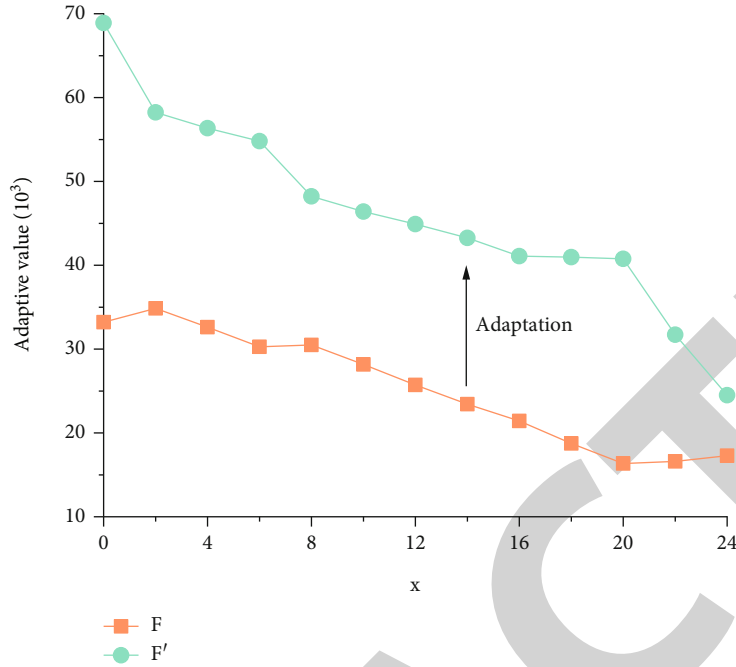


FIGURE 7: Functional correspondence.

corresponding model fragments show a trend of gradual increase, and the increase amount is basically the same. With the increase of samples, the corresponding hesitation data showed a relatively obvious linear change characteristics. As can be seen from the change curve of distance, with the increase of samples, the hesitation index corresponding to distance shows a trend of gradual decline. And it can be seen from the corresponding amount of decline that it conforms to the characteristics of linear decline. It can be seen that the slope corresponding to the fragment curve is greater than that corresponding to the distance curve through the slope of the two kinds of descending and ascending curves. It can be seen from set elements that, with the increase of samples, the corresponding set shows a relatively stable trend of change. It can be seen from the number element that it shows a different trend of gradual rise and then gradual decline. From the above analysis, it can be seen that different elements have different influences on hesitation. Through analysis and calculation, the average adaptive value of individuals in the set is obtained:

$$f'(x_i(t)) = \frac{1}{n_l} \sum_{j=1}^{n_l} f(x_j), x_j \in L(x_i(t)). \quad (11)$$

Approximate true fitness $f'(x_i(t))$ of hesitating individual $x_i(t)$. Finally, this value is used to adjust the adaptation value of sample $x_i(t)$:

$$f(x_i(t)) = f'(x_i(t)). \quad (12)$$

Through this process, we can identify the individual users who are causing hesitation, and the approximate true adaptation $f'(x_i(t))$ can be obtained by calculating the aver-

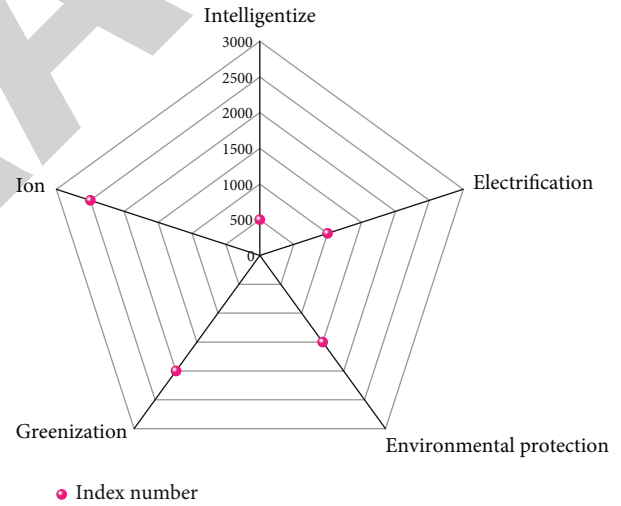


FIGURE 8: Garden landscape lighting index analysis.

age adaptation of similar individuals. Then, adjust its adaptive value, so as to reduce the positive and negative deviation, speed up the algorithm, and reduce user fatigue.

Through analysis, it can be seen that there is a one-to-one correspondence between the real adaptive value and the approximate real adaptive value. To research the corresponding relationship between the two functions, the corresponding curves of the two functions are obtained through calculation in Figure 7. The two different forms of change function have different forms of expression. First of all, it can be seen from the real adaptation value that with the gradual increase of independent variable x , the corresponding curve drops rapidly first, then slowly, and then rapidly. The three stages of decline all show a linear decline process,

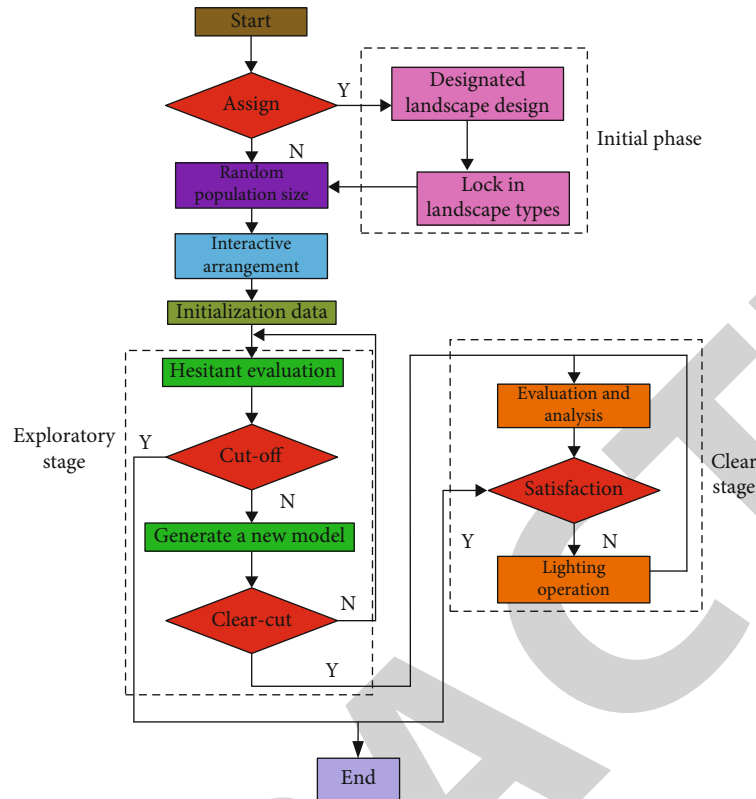


FIGURE 9: Landscape lighting design flow chart based on interactive genetic algorithm.

and the overall linear characteristics of the curve is obvious. This indicates that the increase of independent variable x will lead to certain changes in the corresponding adaptive values, and the linear characteristics of each stage are also obvious. The overall variation range of the corresponding curve is relatively small, and the overall linear characteristics are also obvious. But as the sample size increases, the curve fluctuates to a certain extent. Finally, when the independent variable x exceeds 20, the curve shows a gradually increasing trend of change, which is contrary to the real data. This shows that the corresponding relationship between the two functions needs to be considered comprehensively in the actual calculation process.

3. Landscape Lighting Design and Research Based on Interactive Genetic Algorithm

3.1. The Main Characteristics of Landscape Lighting. Landscape lighting design is a very complex process, which has different characteristics of change. Landscape, as a very important culture and landscape, plays an irreplaceable role in the field of culture. Therefore, in the design of its lighting process needs to consider the geological characteristics of landscape, landscape location, use methods, and lighting characteristics of different aspects of the impact. In order to further analyze this characteristic, five different indexes are selected to analyze the design of landscape lighting in detail. These five indicators are, respectively, intelligent, electric, environmental protection, green, and energy saving, respectively, representing five different factors. The specific

distribution of indicators is shown in Figure 8. In order to further analyze the overall situation of different indicators of garden landscape lighting, the analysis chart of garden landscape indicators as shown in Figure 8 is drawn. It can be seen from the figure that the total amount of intelligent indicators is the smallest, only 500. The electrification target is 1000. The corresponding environmental protection index is 1500. The greenness index is 2000, and energy-saving index is the highest, about 2500.

3.2. Application of Interactive Genetic Algorithm in Landscape Lighting Design. Interactive genetic algorithm has been widely used in different fields, and its application prospect is relatively good [27, 28]. The radial basis function and calculation process of interactive genetic algorithm have good operability. In order to further apply interactive genetic algorithm to landscape design, the radial basis function and interactive hesitancy were analyzed, and the relevant indexes of landscape design were introduced into radial basis function [29, 30]. The interactive hesitancy is optimized, and a new interactive genetic algorithm is obtained. Thus, the landscape design process based on interactive algorithm is obtained, as shown in Figure 9. It can be seen from the calculation results in the figure that the calculation process is mainly divided into three modules: initial stage, exploration stage, and definite stage. The corresponding data should be imported first. If it meets the requirements of the specified model, it should be imported into the initial stage for the design of the specified landscape and the analysis of the locked landscape type. Then, it is imported into the random

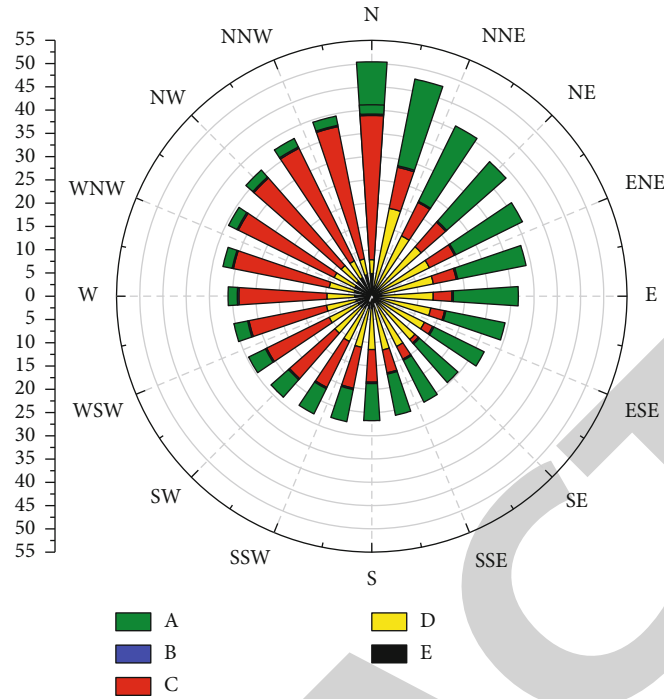


FIGURE 10: Landscape lighting design calculation diagram based on interactive genetic algorithm.

population module; if it does not meet the requirements, it is directly imported into the random population module, through the calculation of the random population module and then interactive arrangement. The initial initialization parameters are obtained by interactive arrangement, sorted and analyzed, and then imported into the exploration phase. In the exploration stage, hesitancy discrimination is firstly carried out, through which it can be seen that if the data meets the cut-off requirements, it will be imported to the definite stage; if it does not meet the cut-off requirements, a new model needs to be generated, and further discrimination needs to be carried out in the generation of a new model. If the criterion does not meet the clear criteria, it needs to be imported into the hesitation analysis for a new iteration; if it meets the hesitation criterion, it needs to be imported into the clear stage. In the definite stage, the first step is evaluation and analysis, through which the parameters of the model are evaluated and analyzed, and then, further satisfaction discrimination is carried out. If it does not meet the requirements, it will be reiterated. If it meets the requirements, lighting operation will be carried out, so as to export the corresponding data.

The garden landscape lighting design flow chart based on the interactive genetic algorithm can be further analyzed and studied on the lighting equipment related to the garden landscape. Through calculation and analysis, the calculation results of landscape lighting design based on interactive genetic algorithm are obtained, as shown in Figure 10. It can be seen from the curve in the figure that five different indicators represent A, B, C, D, and E, respectively. It can be seen from the curve that different indicators have different trends in different calculation processes. Firstly, with the gradual increase in the number of iterations, the corre-

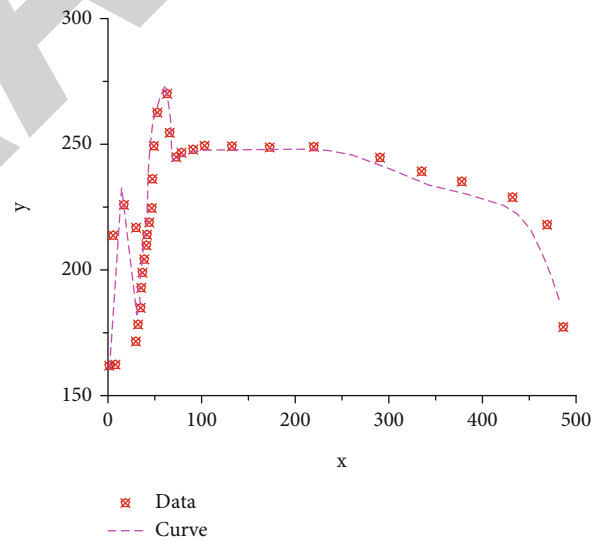


FIGURE 11: Diagram of model validation results.

sponding indicator shows A trend of gradual decline, and its corresponding change diagram shows A trend of global fluctuation that gradually increases first and then gradually declines. It can be seen from indicator B that the proportion of corresponding curves is relatively small. The curve corresponding to index C shows a U-shaped trend of slow decline at first and then gradual increase. It can be seen from indicator D that it is in a stable decline stage, and the corresponding slope is basically the same, indicating that it conforms to the change trend of linear decline. It can be seen from index E that its variation range is relatively small, and the overall trend is relatively constant. From the above analysis, it can be seen that the five different indicators have different

change properties. It can also be explained from the side that the five indicators can better reflect the interactive genetic algorithm, which can well reflect the characteristics of specific indicators in landscape design under the action of interactive genetic algorithm.

4. Discussion

The above is mainly through calculating the specific data of landscape lighting and then importing it into the radial basis function for further analysis, so that the interactive genetic algorithm can be adjusted, and then, the optimized interactive genetic algorithm can be obtained. Finally, the flow chart of landscape design under the action of interactive genetic algorithm and the corresponding calculation results are obtained. A comparison diagram of corresponding test data and model curve was drawn (Figure 11). The corresponding test data shows a trend of rapid increase first, then gradual decline, and then rapid increase to the maximum value. The corresponding curve shows a stable downward trend. When it reaches a high value of independent variable, the corresponding curve drops rapidly, indicating that the linear and nonlinear characteristics of the curve are relatively obvious. The corresponding model curve can better reflect the specific characteristics of the test data. As can be seen from its specific changes, the model can not only reflect the changing trend of the test data but also better reflect the specific values of the test data at some key nodes, so it can be seen that the accuracy of the optimization model is relatively good. It can be shown that the model based on interactive genetic algorithm can better reflect the specific changes of landscape design.

5. Conclusion

- (1) With the gradual increase of the independent variable, the corresponding center distance shows a slow decline with a relatively small decline range. On the other hand, the corresponding width parameter shows a slow decrease and then a gradual increase, with a wide range of variation, which indicates that the width parameter has a high influence on the transfer function
- (2) The five different combination forms of direction vectors have different ranges of variation, and their influences on the output function also have different forms. Among them, the second combination type belongs to the inherent attribute of the output function, and its variation range is relatively small
- (3) The fitting data increases slowly at first and then rapidly, indicating that the number of samples can promote the development of fitting data. However, the corresponding evaluation time showed a decreasing trend for fitting data, indicating that sample size and evaluation time had opposite effects on fitting data
- (4) The hesitation curve corresponding to the four different parameter indexes is different, among which

the fragment curve rises gradually. The corresponding distance curve decreases gradually, while the stability of set curve is relatively good, and the fluctuation of number curve is obvious

Data Availability

The datasets used during the current study are available from the corresponding author on reasonable request.

Conflicts of Interest

The authors declare that they have no conflict of interest.

Acknowledgments

This work was supported by the National Natural Science Foundation of China (2345678).

References

- [1] M. Sasaki, A. Laamrani, M. Yamashiro, C. Alehegn, and A. Kamoyedji, "Portfolio optimization by fuzzy interactive genetic algorithm," *Journal of Advanced Management Science*, vol. 42, no. 32, pp. 124–131, 2018.
- [2] X. Zhu, X. Li, Y. Chen, J. Liu, X. Zhao, and X. Wu, "Interactive genetic algorithm based on typical style for clothing customization," *Journal of Engineered Fibers and Fabrics*, vol. 15, no. 10, p. 155892502092003, 2020.
- [3] S. V. Kuzmin, K. O. Korovin, and T. R. Raimzhanov, "An implementation of interactive application for the synthesis of communication systems with antenna arrays," *Journal of the Russian Universities Radioelectronics*, vol. 23, no. 2, pp. 46–54, 2020.
- [4] G. Qi, Y. Zheng, and F. Lin, "EigenGWAS: an online visualizing and interactive application for detecting genomic signatures of natural selection," *Molecular Ecology Resources*, vol. 10, no. 12, pp. 7236–7258, 2021.
- [5] D. Xia, W. He, and A. Fan, "Research on interactive data packet storage using genetic algorithm under hadoop cloud computing platform," *Paper Asia*, vol. 10, no. 7, pp. 85–88, 2018.
- [6] N. Benabbou, C. Leroy, and T. Lust, "An interactive regret-based genetic algorithm for solving multi-objective combinatorial optimization problems," *Proceedings of the AAAI Conference on Artificial Intelligence*, vol. 34, no. 3, pp. 2335–2342, 2020.
- [7] V. Ramasamy, R. K. Sidharthan, R. Kannan, and G. Muralidharan, "Optimal tuning of model predictive controller weights using genetic algorithm with interactive decision tree for industrial cement kiln process," *PRO*, vol. 7, no. 12, pp. 938–946, 2019.
- [8] T. Muttaqie, H. P. Sang, and S. R. Cho, "Optimisation of the design of a steel-welded pressure hull structure based on interactive nonlinear collapse strength analyses," *Ships and Offshore Structures*, vol. 10, no. 12, pp. 146–158, 2020.
- [9] X. Xue, X. Wu, and J. Chen, "Optimizing ontology alignment through an interactive compact genetic algorithm," *ACM Transactions on Management Information Systems*, vol. 12, no. 2, pp. 1–17, 2021.

Retraction

Retracted: Analysis of Efficacy, Complications, and Inflammatory Reactions of Bridge Combined Internal Fixation System for Periarticular Fractures of the Shoulder

Computational and Mathematical Methods in Medicine

Received 27 June 2023; Accepted 27 June 2023; Published 28 June 2023

Copyright © 2023 Computational and Mathematical Methods in Medicine. This is an open access article distributed under the Creative Commons Attribution License, which permits unrestricted use, distribution, and reproduction in any medium, provided the original work is properly cited.

This article has been retracted by Hindawi following an investigation undertaken by the publisher [1]. This investigation has uncovered evidence of one or more of the following indicators of systematic manipulation of the publication process:

- (1) Discrepancies in scope
- (2) Discrepancies in the description of the research reported
- (3) Discrepancies between the availability of data and the research described
- (4) Inappropriate citations
- (5) Incoherent, meaningless and/or irrelevant content included in the article
- (6) Peer-review manipulation

The presence of these indicators undermines our confidence in the integrity of the article's content and we cannot, therefore, vouch for its reliability. Please note that this notice is intended solely to alert readers that the content of this article is unreliable. We have not investigated whether authors were aware of or involved in the systematic manipulation of the publication process.

Wiley and Hindawi regrets that the usual quality checks did not identify these issues before publication and have since put additional measures in place to safeguard research integrity.

We wish to credit our own Research Integrity and Research Publishing teams and anonymous and named external researchers and research integrity experts for contributing to this investigation.

The corresponding author, as the representative of all authors, has been given the opportunity to register their agreement or disagreement to this retraction. We have kept a record of any response received.

References

- [1] H. Xu, Y. Fan, J. Lu, Y. Wu, and X. Feng, "Analysis of Efficacy, Complications, and Inflammatory Reactions of Bridge Combined Internal Fixation System for Periarticular Fractures of the Shoulder," *Computational and Mathematical Methods in Medicine*, vol. 2022, Article ID 5048172, 6 pages, 2022.

Research Article

Analysis of Efficacy, Complications, and Inflammatory Reactions of Bridge Combined Internal Fixation System for Periarticular Fractures of the Shoulder

Haiyun Xu, Youliang Fan, Jiajun Lu, Yixiong Wu, and Xiaoguang Feng 

Department of Orthopedics, The Fourth People's Hospital of Changzhou, Changzhou, 213100 Jiangsu, China

Correspondence should be addressed to Xiaoguang Feng; yamadis2022@163.com

Received 24 May 2022; Revised 4 July 2022; Accepted 3 August 2022; Published 21 August 2022

Academic Editor: Pan Zheng

Copyright © 2022 Haiyun Xu et al. This is an open access article distributed under the Creative Commons Attribution License, which permits unrestricted use, distribution, and reproduction in any medium, provided the original work is properly cited.

Objective. The aim of the present research is to analyze the impact of the bridge combined internal fixation system (BCFS) on efficacy, complications, and inflammatory reactions of periarticular fractures of the shoulder. **Methods.** A retrospective analysis was performed on 100 patients with periarticular fractures of the shoulder admitted between January 2016 and January 2020. Patients were assigned to the observation group (OG) and control group (CG) according to different treatment schemes, with 50 cases in each group. Patients in OG were intervened by BCFS, while those in CG were routinely given plate fixation. The treatment outcome, complications, and inflammatory reaction of the two groups were compared. **Results.** The results showed better treatment outcome, shoulder joint function recovery, and inflammatory reaction alleviation of OG compared with CG. Besides, statistically shorter fracture healing and hospitalization time as well as fewer complications were determined in OG. **Conclusion.** These results demonstrate that compared with the plate fixation system, BCFS can significantly improve the surgical efficacy and healing efficiency and alleviate the inflammatory response of patients, with a low complication rate, all of which contribute to faster recovery of periarticular fractures of the shoulder. Hence, BCFS is an ideal choice for periarticular fractures of the shoulder that deserves clinical promotion.

1. Introduction

Fractures are common injuries that occur at all ages, usually triggered by collisions, stress, or diseases [1]. As a kind of fractures, periarticular fractures of the shoulder joint include clavicle and scapula fractures, fractures of the upper end of the humerus and of the outer clavicle with coracoclavicular ligament rupture, displaced fractures of the outer 1/3 of the clavicle, open fractures, and fractures combined with vascular and nerve injuries, usually requiring surgical treatment [2]. However, fracture healing, a complex process that takes time, is affected by the blood supply, bone stability, and inflammation at the fracture site [3]. Besides, improper fixation material selection or inadequate fixation adversely influences functional recovery and fracture healing of the affected limb [4]. According to relevant epidemiological data, about

4.3% of the elderly in the United States have another shoulder fracture within one year after surgery [5]. Therefore, this study starts with the fixation of the periarticular fracture of the shoulder, aiming at finding a more ideal treatment.

Internal fixation is currently the major surgical treatment for fractures [6], which has been shown to prompt patients to regain their mobility and reduce the occurrence of serious complications [7]. When dealing with different clinical types of fractures, choosing an appropriate internal fixation method to maximize patients' recovery has become the key to clinical work [8]. The bridge combined fixation system (BCFS), a novel type of internal fixation device independently developed by Professor Xiong Ying from Yan'an Hospital affiliated to Kunming Medical University [9], has the advantages of small volume, firm fixation, simple operation, few postoperative complications, and promising

clinical application potential [10]. Guo et al. [11] reported that BCFS is effective and safe for severe comminuted femoral fractures.

At this stage, BCFS is primarily used in the treatment of pelvic and femoral fractures, but little is known regarding its application in periarticular fractures of the shoulder. Accordingly, this paper mainly discusses the efficacy, complications, and inflammatory reactions of BCFS in the treatment of periarticular fractures of the shoulder, hoping to provide a new reference for the management of such fractures.

2. Data and Methods

2.1. General Data. This retrospective study selected 100 patients with periarticular fractures of the shoulder treated between January 2016 and January 2020. According to different fixation schemes, 50 patients treated with BCFS were set as the observation group (OG), and another 50 cases with routine plate fixation were used as the control group (CG). CG comprised 28 males and 22 females whose age range was (37.06 ± 9.14) years old; the fractures were attributed to car accidents in 22 cases, falls in 11 cases, crushes in 12 cases, and others in 5 cases. In OG, the male-female ratio and age range were 31:19 and (37.32 ± 8.47) years old, respectively, and the causes of injuries were car accidents in 18 cases, falls in 16 cases, crushes in 5 cases, and others in 11 cases. The two cohorts of patients were clinically comparable with no statistical difference in sex, age, cause of injury, and other baseline data ($P > 0.05$). This research was conducted after obtaining approval from the Ethics Committee of the Fourth People's Hospital of Changzhou and informed consent from patients and their families.

2.2. Eligibility Criteria. Inclusion criteria were as follows: diagnosis of periarticular fractures of the shoulder by clinical X-ray examination, age: 20-65, no relevant history of periarticular fractures of the shoulder, informed consent provided, and active cooperation with the study.

Exclusion criteria were as follows: old fractures or pregnant/lactating women; diseases of vital organs, clotting disorders, or inability to tolerate surgery; severe mental illness; inconsistency with the inclusion criteria; and uncooperative patients or those with defective case records that affected the curative effect judgment.

2.3. Treatment Methods. CG (plate fixation group) was as follows: plate fixation was used to treat patients in this group. The patient was placed in the lateral decubitus position for general anesthesia and routine disinfection. After incision, a 6-8-hole steel plate was used for fixation, and routine orthopedic nursing was performed postoperatively.

OG (BCFS group) was as follows: patients in this study were treated with BCFS. The patient's posture, anesthesia, disinfection, and postoperative care were all consistent with those of CG. Attention was paid to protecting important nerves and blood vessels during the operation. The fixation rod was then remodeled according to the fracture site and shape, and the appropriate fixation position was selected

by rotating and sliding the connecting block on the fixation rod to ensure the fixation effect.

2.4. Efficacy Assessment. Marked effectiveness: the function of the affected limb returned to normal, with pain disappeared, anatomically reduced fracture, and well aligned fracture showed by X-ray film

Effectiveness: the function of the affected limb basically returned to normal, with basically disappeared pain, reduced fracture, and X-ray indicating over 1/3 alignment of the fracture

Ineffectiveness: the function of the affected limb has not returned to normal, with no reduction of the fracture or slow healing and even the occurrence of other complications

2.5. Endpoints

- (1) Curative effect: please refer to efficacy assessment for the evaluation standard of curative efficacy. The overall response rate (ORR) is the percentage of the sum of markedly effectiveness+effectiveness cases in all cases
- (2) Clinical indices: clinical indices (fracture healing time and length of hospital stay [LOS]) were recorded
- (3) Complication rate: complications, including healing deformity, blood ooze, and infection, were observed and recorded during postoperative recovery
- (4) Shoulder joint function score: the Constant-Murley Scale (CMS; score range: 0-100 points) was used before and 6 months after operation, assessing patients' shoulder joint function from pain (15 points), shoulder joint mobility (40 points), power (25 points), and activity of daily living (ADL; 20 points), with higher scores indicating better shoulder joint function
- (5) Serum inflammatory indicators: serum was extracted, and enzyme-linked immunosorbent assay (ELISA) [12] was utilized to test pre- and posttreatment alterations of serum inflammatory factors like tumor necrosis factor α (TNF- α), interleukin (IL)-1 β , and IL-6. The operation steps strictly followed human TNF- α , IL-1 β , and IL-6 ELISA kits supplied by Wuhan Fine Biotech

2.6. Statistical Processing. SPSS 21.0 (SPSS, Inc., Chicago, IL, USA) and GraphPad Prism 6 (GraphPad Software, San Diego, USA) were responsible for data analysis and visualization, respectively. $P < 0.05$ was supposed to indicate statistical significance. The χ^2 test was used for intergroup comparisons of enumeration data (sex, age, etc.) represented by number of cases/percentage ($n/\%$). For the quantitative data (mean age, fracture healing time, etc.) given mean \pm SEM, independent sample t -test and paired t -test were employed for between-group and within-group comparisons, respectively.

TABLE 1: Baseline data of patients with periarticular fractures of the shoulder (n (%), mean \pm SEM).

Factor	n	Control group ($n = 50$)	Observation group ($n = 50$)	χ^2/t	P
Sex				0.372	0.542
Male	59	28 (56.00)	31 (62.00)		
Female	41	22 (44.00)	19 (38.00)		
Age (years old)				1.073	0.300
<35	37	21 (42.00)	16 (32.00)		
≥ 35	63	29 (58.00)	34 (68.00)		
Average age (years old)	100	37.06 \pm 9.14	37.32 \pm 8.47	0.148	0.883
Cause of injury				6.458	0.091
Car accidents	40	22 (44.00)	18 (36.00)		
Falls	27	11 (22.00)	16 (32.00)		
Crushes	17	12 (24.00)	5 (10.00)		
Others	16	5 (10.00)	11 (22.00)		
Education level				0.360	0.548
Technical secondary school or above	49	23 (46.00)	26 (52.00)		
Technical secondary school below	51	27 (54.00)	24 (48.00)		
Drinking history				1.051	0.305
No	39	22 (44.00)	17 (34.00)		
Yes	61	28 (56.00)	33 (66.00)		
Residence				0.877	0.349
Urban areas	76	40 (80.00)	36 (72.00)		
Rural areas	24	10 (20.00)	14 (28.00)		
Marital status				0.735	0.391
Single	32	14 (28.00)	18 (36.00)		
Married	68	36 (72.00)	32 (64.00)		

3. Results

3.1. Baseline Data of Patients with Periarticular Fractures of the Shoulder. The analysis of patients' general data (Table 1) revealed comparability between the two groups, as no statistical difference was found in sex, age, average age, cause of injury, education level, drinking history, place of residence, marital status, etc. ($P > 0.05$).

3.2. Clinical Indices of Patients with Periarticular Fractures of the Shoulder. We recorded patients' fracture healing time and LOS to compare and analyze the influences of the two fixation methods on the clinical indices of patients with periarticular fractures of the shoulder (Table 2). It was found that the fracture healing time and LOS were statistically shorter in OG versus CG ($P < 0.05$).

3.3. Curative Effect of Patients with Periarticular Fractures of the Shoulder. We analyzed patients' outcomes to assess the impacts of the two treatments on patients with periarticular fractures of the shoulder (Table 3). Data showed an ORR of 96.00% in OG and 80.00% in CG, with statistical significance ($P < 0.05$).

3.4. Complication Rate in Patients with Periarticular Fractures of the Shoulder. By comparing and analyzing the incidence of complications in terms of healing deformity, blood ooze, and infection (Table 4), we found that the total

complication rate was statistically lower in OG compared with CG (4.00% vs. 22.00%, $P < 0.05$).

3.5. Patient's Shoulder Joint Function Scores. We recorded the shoulder joint function (CMS) scores before and 6 months after operation (Figure 1). Data showed no statistical difference in pretreatment CMS scores between the two groups ($P > 0.05$); the posttreatment scores elevated in both cohorts ($P < 0.05$), and the improvement degree of shoulder joint function was more obvious in OG ($P < 0.05$).

3.6. Serum Inflammatory Indicators (TNF- α , IL-1 β , and IL-6) in Patients. We examined TNF- α , IL-1 β , and IL-6 concentrations in patients' serum (Figure 2). Data showed no statistical difference in pretreatment TNF- α , IL-1 β , and IL-6 between groups ($P > 0.05$). Evident decreases were observed in the above three indexes in posttreatment ($P < 0.05$), and the improvement degree was more significant in OG ($P < 0.05$).

4. Discussion

Periarticular fractures of the shoulder are a condition including fractures of the clavicle and scapula around the shoulder joint [13]. For such fractures, conservative treatment methods, such as arm sling and spica bandages, are usually used [14]. However, the application of these traditional

TABLE 2: Clinical indices of patients with periarticular fractures of the shoulder.

Groups	<i>n</i>	Fracture healing time (weeks)	Length of hospital stay (d)
Control group	50	13.00 ± 1.59	12.88 ± 1.30
Observation group	50	10.40 ± 1.29	9.50 ± 0.95
<i>t</i> value	—	8.979	14.843
<i>P</i> value	—	<0.001	<0.001

TABLE 3: Curative effect of patients with periarticular fractures of the shoulder (*n* (%)).

Groups	<i>n</i>	Marked effectiveness	Effectiveness	Ineffectiveness	Total effective rate (%)
Control group	50	22 (44.00)	18 (36.00)	10 (20.00)	40 (80.00)
Observation group	50	31 (62.00)	17 (34.00)	2 (4.00)	48 (96.00)
χ^2 value	—	—	—	—	6.061
<i>P</i> value	—	—	—	—	0.014

TABLE 4: Incidence of complications in patients with periarticular fractures of the shoulder (*n* (%)).

Categories	Control group (<i>n</i> = 50)	Observation group (<i>n</i> = 50)	χ^2 value	<i>P</i> value
Healing deformity	2 (4.00)	1 (2.00)	—	—
Blood ooze	7 (14.00)	1 (2.00)	—	—
Infection	2 (4.00)	0 (0.00)	—	—
Total incidence	11 (22.00)	2 (4.00)	7.162	0.007

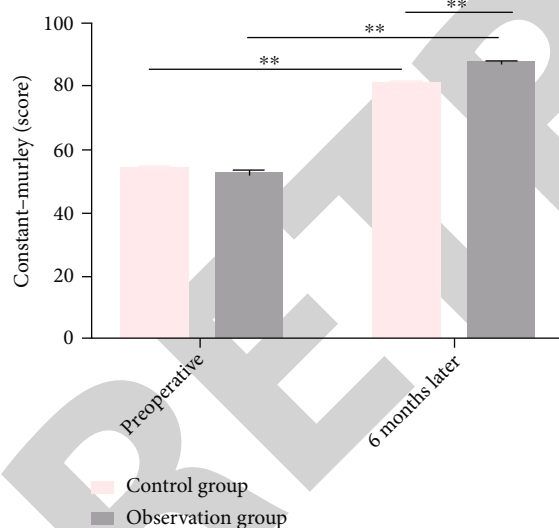


FIGURE 1: Shoulder joint function score of patients with periarticular fractures of the shoulder. Shoulder function (Constant-Murley Scale) scores of patients in both groups before and 6 months after operation. Note: $**P < 0.01$.

treatments has limitations such as poor efficacy, bone fragment movement, and nursing difficulties [15]. Therefore, it is of great practical significance to change the treatment methods to improve the curative effect and safety in view of various hindrances in the past treatment of such fractures.

BCFS is a novel type of clamp-rod internal fixation device that is commonly used for the fixation of upper

and lower extremity or pelvic fractures [16]. Previous biomechanical and clinical analysis shows that BCFS is also effective in treating long bone fractures [17]. BCFS has certain advantages in treating periarticular fractures of the shoulder, as it has little contact with the bone surface and can minimize the damage of periosteal perfusion [18]. A total of 100 subjects were enrolled in this study and were assigned to two groups (CG and OG) based on the difference in treatment methods. CG was treated with plate fixation, while OG was treated with BCFS. The results showed a statistically higher ORR in OG compared with CG (96.00% vs. 80.00%), which suggested that BCFS treatment was helpful to improve the curative effect of such patients. Then, we recorded patients' clinical indices such as fracture healing time and found faster fracture healing and shorter LOS in OG, suggesting higher recovery efficiency in patients with periarticular fractures of the shoulder treated with BCFS. In the biomechanical study of BCFS, Wang et al. [19] pointed out that BCFS could more firmly fix the fracture and maintain the stability of the fracture end, with a positive effect on the fracture healing of patients. Shoulder function was also assessed in this study using the CMS, one of the most commonly used tools, which includes the measurement of patients' mobility, pain, power, and ADL [20]. The data showed significantly better shoulder joint function improvement in OG at 6 months postoperatively, which was mutually verified with the efficacy of this procedure and the results of clinical indices. In the study of Niu et al. [21] on clinical application of BCFS in mid-clavicular fractures, the postoperative CMS score is similar to that of this study.

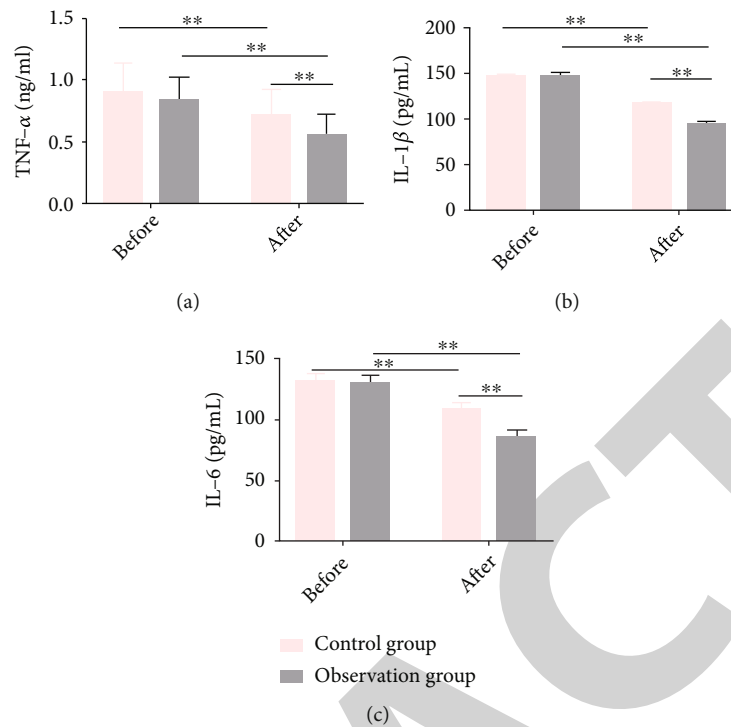


FIGURE 2: Serum inflammatory indicators (TNF- α , IL-1 β , and IL-6) in patients. (a) TNF- α levels before and after treatment in the two groups. (b) IL-1 β levels before and after treatment in the two groups. (c) IL-6 levels before and after treatment in the two groups. Note: ** $P < 0.01$.

The incidence of complications such as healing deformity, bleeding, and infection was also compared, and the results revealed a statistically lower incidence in OG as compared to CG (4.00% vs. 22.00%), which indicated that BCFS was safer than plate fixation in the treatment of periarticular fractures of the shoulder. Wang et al. [17] applied BCFS to treat femoral fractures, and no postoperative implant fracture, wound infection, or other serious complications occurred, similar to our research results. Finally, we detected three serum proinflammatory markers, namely, TNF- α , IL-1 β , and IL-6; the three are highly correlated with patients' immune response, and their increased concentrations will reduce patients' immune function [22]. The results showed that postoperatively, the three indexes in OG were significantly lower than those before treatment and CG, which suggested that BCFS had an inhibitory effect on the inflammatory response of patients with periarticular fractures of the shoulder. In the study of inflammatory cytokines after fracture, Wahl et al. [23] pointed out that the proinflammatory environment brought about by inflammatory factors such as TNF- α , IL-1 β , and IL-6 may be the catalyst for the development of postfracture complications; so, the inhibition of the inflammatory response of patients plays an auxiliary role in reducing complications.

Although this study confirmed that BCFS applied to patients with periarticular fractures of the shoulder can contribute to accelerated fracture healing, faster recovery of shoulder function, better improvement of serum inflammatory indicators, and reduction of complication rate, there are still some deficiencies. Considering the

limited number of cases ($n = 100$) included, we need to expand the sample size to improve the accuracy of the research results. Second, fracture healing is a slow process, while there is no follow-up investigation in the study design. So, increasing the follow-up of 8-24 months after surgery is needed to more intuitively track patients' recovery. The above two shortcomings will be addressed in future research.

5. Conclusion

Conclusively, BCFS is more effective, safer, and simpler in operation than plate fixation in treating periarticular fractures of the shoulder, with good clinical application potential and value for clinical use.

Data Availability

The labeled dataset used to support the findings of this study are available from the corresponding author upon request.

Conflicts of Interest

The authors declare no competing interests.

References

- [1] Y. Lang, Q. Sun, L. M. Zhu et al., "miR-25 overexpression promotes fracture healing by activating the wnt signaling pathway," *European Review for Medical and Pharmacological Sciences*, vol. 23, pp. 7200-7208, 2019.

Research Article

Discussion on Repolarization Reserve between Patients with Coronary Heart Disease and Normal Controls

Rubing Kang,¹ Yitong Li,² Chunmei Gao,³ Jianhui Li,¹ Cheng Zhang,⁴ and Junli Wang¹ 

¹Department of Cardiology, Heji Hospital Affiliated to Changzhi Medical College, Changzhi, 046011 Shanxi, China

²Guizhou Medical University, Guiyang, 550025 Guizhou, China

³Department of ECG Diagnosis, Second Hospital of Shanxi Medical University, Taiyuan, 030001 Shanxi, China

⁴Department of Cardiology, Binhai Hospital of Peking University (Tianjin Fifth Central Hospital), Tianjin 300450, China

Correspondence should be addressed to Junli Wang; choudanfadaicai@163.com

Received 9 June 2022; Revised 20 July 2022; Accepted 29 July 2022; Published 18 August 2022

Academic Editor: Pan Zheng

Copyright © 2022 Rubing Kang et al. This is an open access article distributed under the Creative Commons Attribution License, which permits unrestricted use, distribution, and reproduction in any medium, provided the original work is properly cited.

Objective. To investigate the repolarization reserve of normal controls (NCs) and patients with coronary heart disease (CHD). **Methods.** From January 1st, 2010 to December 31st, 2018, 200 age- and gender-matched inpatients in the Second Hospital of Shanxi Medical University and Heji Hospital Affiliated to Changzhi Medical College were selected for treadmill exercise test (TET), including 67 patients in the myocardial ischemia group, 66 patients in the suspected myocardial ischemia group, and 67 patients in the normal control group. Coronary angiography (CAG) was performed on 49 of 133 patients in the myocardial ischemia group and the suspected myocardial ischemia group, and 9 positives and 40 negatives were identified. The heart rate (HR) and QT interval of TET examiners before exercise, during exercise (90 beats/min, 120 beats/min, maximum HR), and in the recovery period (1 minute and 3 minutes after exercise) were reviewed, and QTc values were calculated after being corrected by Bazett's. **Results.** The mean QTc values in NCs were all below 452 ms, before exercise, during exercise (90 beats/min, 120 beats/min and maximum HR), and during the recovery period (1 minute and 3 minutes after exercise). The comparison results of the RR interval between the two groups revealed $P > 0.05$, indicating no statistical significance. Significant differences were present when comparing the QT intervals when the HRs were 90 beats/minute and 120 beats/minute during exercise ($P < 0.05$). And comparing the QTc values, it was found that the QTc values during different exercise periods were statistically different between groups ($P < 0.05$). **Conclusions.** NCs have good repolarization reserve. CAG can confirm true myocardial ischemia patients (i.e., patients with CHD) among myocardial ischemia and suspected myocardial ischemia patients screened by TET. Patients with positive CAG have poor repolarization reserve as QT interval represents ventricular repolarization adaptability.

1. Introduction

It is well known that human ventricular repolarization (interval) is inversely proportional to heart rate [1, 2]. When the heart rate is fast, the ventricular repolarization period is shortened while significantly prolonged when the heart rate is slow [3, 4]. This kind of frequency adaptability of ventricular repolarization which is called ventricular repolarization reserve, also known as ventricular repolarization adaptability, is of great significance to the automatic regulation and effectiveness of ventricular contraction and relaxation under physiological conditions [5, 6]. In recent years, evidences

have shown that the inward late sodium current in the plateau phase of cell membrane plays a key role in the frequency adaptation of ventricular repolarization [7–9]. Meanwhile, we also found that the late sodium current, as an important inward current in the plateau phase of action potential, is very sensitive to the stimulation frequency [10]. When the stimulation frequency is fast, the current is small; otherwise, it is the opposite [11].

A large number of studies have shown that myocardial ischemia from different causes, such as heart failure [12], myocardial infarction [13], cardiomyopathy [14], and myocarditis [15], can lead to the reduction of repolarization

reserve capacity, which becomes acquired long QT syndrome [16]. The primary reason for this was that slow delayed rectifier potassium current (I_{ks}) is an important repolarization reserve of human cardiomyocytes [17]. The decrease of outward current or the increase of inward current caused by myocardial ischemia, or both, can reduce the ventricular reserve function and prolong the interval [18]. Moreover, the formation of late sodium current and the change of early and late depolarization potential can synergistically lead to malignant arrhythmia and eventually cardiac death on the basis of the reduction of existing myocardial repolarization reserve [19].

The treadmill exercise test [20] in this study is a simple and relatively safe, noninvasive test for the diagnosis of myocardial ischemia, and it is a test to increase cardiac load through exercise. The functional state of the heart was determined by the principle that the body should increase coronary blood flow correspondingly when exercising, which can find myocardial ischemia caused by various reasons. The novelty and motivation of this study is to use such principle to make the patients stop when the maximum heart rate of the exercise test reaches the symptom limitation by means of passive exercise and compares the interphase changes and change rules of the patients in the recovery period before exercise and after exercise to determine whether the function of repolarization reserve is impaired. The research results are reported as follows.

2. Methods

2.1. Research Participants. From January 1st, 2010 to December 31st, 2018, 200 inpatients in the Second Hospital of Shanxi Medical University and Heji Hospital Affiliated to Changzhi Medical College were selected for treadmill exercise test (TET), including 67 patients in the myocardial ischemia group (positive group), 66 patients in the suspected myocardial ischemia group (suspected positive group), and 67 patients in the normal control group (negative group). Forty-nine of the 133 cases in the myocardial ischemia group and suspected myocardial ischemia group underwent coronary angiography (CAG), of which 9 cases were positive and 40 cases were negative. This study was approved by the Ethics Committee of Heji Hospital affiliated to Changzhi Medical College.

2.2. Data Collection. The heart rate (HR) and QT interval of TET examiners before exercise, during exercise (90 beats/min, 120 beats/min, maximum HR), and during the recovery period (1 minute and 3 minutes after exercise) were reviewed, and QTc values were calculated after Bazett's correction. CAG, the "golden standard" for diagnosing coronary heart disease (CHD), has been extensively used in clinical practice, by which positive and negative patients were further diagnosed in this study. The repolarization reserve function of positive and negative patients was judged by the comparison of RR interval, QT interval, and QTC values. In the following, the repolarization reserve of normal controls (NCs) and the difference between patients with

TABLE 1: RR interval and QT intervals as well as QTc values of normal controls during different exercise periods ($\bar{x} \pm s$).

Index	Value
Number	67
Age	52.22 \pm 9.31
Before exercise	
RR interval	777.79 \pm 118.74
QT interval	399.07 \pm 31.44
QTc value	454.78 \pm 27.16
90 beats/minute during exercise	
RR interval	663.79 \pm 3.91
QT interval	371.90 \pm 19.11
QTc value	456.39 \pm 23.89
120 beats/minute during exercise	
RR interval	498.13 \pm 5.53
QT interval	335.42 \pm 16.25
QTc value	475.36 \pm 22.97
Maximum heart rate during exercise	
RR interval	432.13 \pm 46.63
QT interval	307.34 \pm 22.49
QTc value	467.76 \pm 28.01
During the recovery period (1 minute after exercise)	
RR interval	511.06 \pm 70.03
QT interval	330.93 \pm 28.25
QTc value	466.72 \pm 22.92
During the recovery period (3 minute after exercise)	
RR interval	647.28 \pm 121.96
QT interval	368.19 \pm 31.27
QTc value	461.49 \pm 28.14

positive CAG and those with negative CAG were studied by TET.

2.3. Instruments and Methods

2.3.1. Treadmill Exercise Test. Q-stress Treadmill produced by Quinton, USA was used. Medication that may cause abnormal ST segment changes and elevated myocardial oxygen consumption was discontinued three days before the examination, and smoking and alcohol were prohibited after meals or 2 hours before meals. The Bruce's protocol was adopted, that is, the test was terminated at 85% of the expected maximum HR for age ($220 - \text{age}$). Multidirectional and multiangle selective left and right CAG was performed by percutaneous puncture into the femoral artery of the lower extremities with the use of a C-arm machine. The left coronary artery was projected in at least four positions, with at least two positions of the coronary artery, and additional positions as necessary to fully reveal the segments of the coronary artery. Diagnostic criteria are as follows: CHD

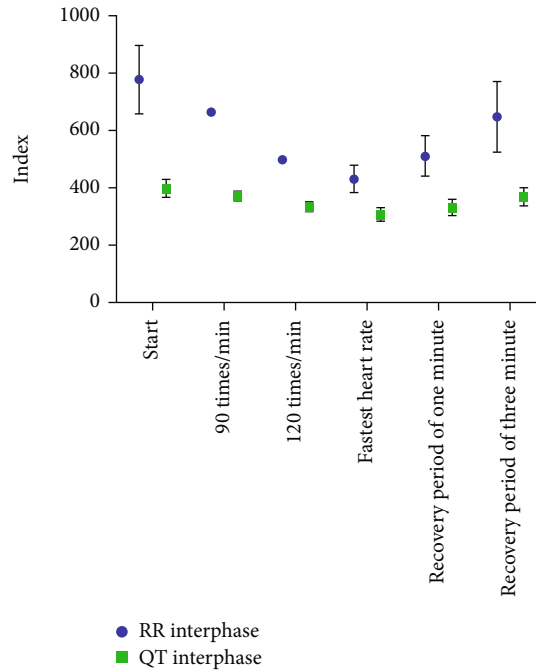


FIGURE 1: Change trends during RR and QT in the normal group.

was confirmed if the CAG showed at least 1 lumen stenosis $\geq 50\%$ in the left main artery, left anterior descending artery, left circumflex artery, and right coronary artery.

2.3.2. Repolarization Reserve. The HR and QT intervals of TET examiners were measured before exercise, during exercise (90 beats/minute, 120 beats/minute and maximum HR), and in the recovery period (1 minute and 3 minutes after exercise), and their changes were compared. $QTc = QT \text{ interval} / \sqrt{RR \text{ interval}}$; the smaller the QTc value, the better the repolarization reserve.

2.3.3. Measurement Methods. In all the three groups, consecutive RR intervals before exercise, during exercise (90 beats/min, 120 beats/min, maximum HR), and in the recovery period (1 minute and 3 minutes after exercise) were selected for manual measurement of RR and QT intervals. The lead with T wave amplitude at least greater than 2 mm and clear T wave end in the routine-lead was selected. For the same patient, the same lead was always measured. In some cases where the end of T wave was difficult to identify (biphasic T wave, T wave notch, T-U wave fusion, etc.), a tangent line was drawn from the steepest part of the descending branch of T wave crest, and the intersection of this tangent line and equipotential line was considered the end of T wave. In patients with bundle branch block, the QRS time difference before and after block was subtracted to adjust the QT interval.

2.4. Statistical Processing. Data analysis was performed by SPSS17.0. Categorical data were expressed by mean \pm standard deviation (SD), while measurement data were expressed by n (%). The differences in the RR interval, QT interval, and QTc values among two groups were identified

TABLE 2: Comparison of age and sex composition between two groups ($\bar{x} \pm s$).

	Age	Gender (male/female)
Negative coronary angiography ($n = 40$)	55.18 ± 10.20	22/18
Positive coronary angiography ($n = 9$)	51.44 ± 14.22	5/4
t/χ^2	0.923	0.001
P	0.361	0.976

There was no significant difference between the two groups ($P > 0.05$).

by the independent sample t -test; statistical comparisons of the groups were conducted using one-way ANOVA, with $P < 0.05$ as the significance level.

3. Results

3.1. RR Interval, QT Interval, and QTc Values in Normal Controls. In NCs, RR interval and QT interval were shortened with the increase of treadmill speed. However, as the postexercise recovery period increased, RR interval and QT interval were gradually prolonged. The mean QTc values were all below 452 ms (Table 1 and Figure 1).

3.2. Comparison of Age and Sex Composition between Groups. This study also compared the age and gender composition between NCs and patients with positive CAG for statistical analysis. The results showed $P > 0.05$, indicating no significant difference between groups (Table 2).

TABLE 3: Comparison of RR interval, QT interval, and QTc value between patients with positive and negative coronary angiography ($\bar{x} \pm s$).

Index	Negative CAG ($n = 40$)	Positive CAG ($n = 9$)	t	P
Initial heart rate (before exercise)				
RR interval	751.38 \pm 75.82	750.33 \pm 109.20	0.035	0.973
QT interval	389.30 \pm 25.05	419.22 \pm 48.78	2.665	0.011
QTc value	451.25 \pm 37.63	485.56 \pm 31.67	2.535	0.014
90 beats/minute during exercise				
RR interval	663.43 \pm 3.90	665.22 \pm 4.06	1.235	0.223
QT interval	367.25 \pm 13.23	387.78 \pm 18.34	4.132	0.000
QTc value	450.93 \pm 16.42	475.22 \pm 23.39	3.699	0.001
120 beats/minute during exercise				
RR interval	499.85 \pm 4.67	498.11 \pm 4.94	0.999	0.323
QT interval	323.30 \pm 11.27	342.56 \pm 20.34	3.937	0.000
QTc value	457.43 \pm 16.11	485.33 \pm 27.78	4.061	0.000
Maximum heart rate during exercise				
RR interval	414.08 \pm 31.85	419.56 \pm 54.31	0.405	0.687
QT interval	291.60 \pm 26.14	308.89 \pm 24.47	1.812	0.076
QTc value	448.75 \pm 20.53	476.67 \pm 24.50	3.560	0.001
During the recovery period (1 minute after exercise)				
RR interval	514.03 \pm 65.06	504.56 \pm 85.01	0.373	0.711
QT interval	319.30 \pm 23.44	331.11 \pm 31.40	1.282	0.206
QTc value	446.75 \pm 23.69	470.00 \pm 25.98	2.615	0.012
During the recovery period (3 minute after exercise)				
RR interval	643.92 \pm 116.71	643.00 \pm 98.91	0.022	0.983
QT interval	351.75 \pm 30.23	381.44 \pm 41.30	2.485	0.017
QTc value	442.50 \pm 28.80	474.44 \pm 27.89	3.022	0.004

There were significant differences in QTc values among the three groups ($P < 0.05$).

3.3. RR and QT Intervals and QTc Values of Patients with Normal Control and Negative and Positive CAG. The RR interval differences between the normal control group and negative CAG and positive CAG patients before exercise, when the HR was 90 beats/min during exercise, 120 beats/min during exercise or with maximum HR during exercise, all showed no statistical significance ($P > 0.05$). However, the RR intervals of the patients with negative CAG were significant lower than those in the normal control group ($P < 0.05$). One minute after exercise and at 3 minutes after exercise, the RR intervals of the normal control group and patients with negative and positive CAG suggested the absence of statistical significance ($P > 0.05$).

The comparison of preexercise QT intervals in the normal control and negative and positive CAG patients indicated statistical significance ($P < 0.05$). While the QT intervals in the normal control and negative and positive CAG patients with different HRs during exercise showed that the QT interval at the HR of 90 beats/minute and 120 beats/minute during exercise was statistically different between three groups ($P < 0.05$), the data showed no obvious difference in the QT interval between three groups at one minute after exercise ($P > 0.05$) and obvious difference in 3 minutes after exercise.

The differences of preexercise QTc values in the control, negative, and positive CAG patients indicated the presence of statistical significance ($P < 0.05$). It also showed that the QTc values were statistically different between patients with negative CAG and those with positive CAG during exercise ($P < 0.05$). The QTc values in patients at one minute after exercise showed obvious difference between groups ($P < 0.05$), while the data at 3 minutes after exercise presented no obvious difference between groups ($P > 0.05$), as shown in Tables 3 and 4 and Figure 2.

4. Discussion

The generation of myocardial action potential is the result of sequential activation and deactivation of inward sodium and calcium ion currents and various outward potassium currents on myocardial cell membrane [21]. Experimental studies in the 1980s [22–25] have reached an important conclusion, that is, when the outward current decreases and/or the inward current increases, early postdepolarization will occur, resulting in the prolongation of action potential duration. At the same time, it is recognized that window calcium current plays an important role [26]. In this case, the L-type calcium channels may reactivate and reverse repolarization

TABLE 4: Comparison of RR interval, QT interval, and QTc value between patients with normal control, positive, and negative coronary angiography ($\bar{x} \pm s$).

Index	Normal control ($n = 67$)	Negative CAG ($n = 40$)	Positive CAG ($n = 9$)	F	P
Initial heart rate (before exercise)					
RR interval	777.79 \pm 118.74	751.38 \pm 75.82	750.33 \pm 109.20	0.906	0.407
QT interval	399.07 \pm 31.44	389.30 \pm 25.05	419.22 \pm 48.78 ^b	3.686	0.028
QTc value	454.78 \pm 27.16	451.25 \pm 37.63	485.56 \pm 31.67 ^{ab}	4.475	0.014
90 beats/minute during exercise					
RR interval	663.79 \pm 3.91	663.43 \pm 3.90	665.22 \pm 4.06	0.768	0.466
QT interval	371.90 \pm 19.11	367.25 \pm 13.23	387.78 \pm 18.34 ^{ab}	5.241	0.007
QTc value	456.39 \pm 23.89	450.93 \pm 16.42	475.22 \pm 23.39 ^{ab}	4.690	0.011
120 beats/minute during exercise					
RR interval	498.13 \pm 5.53	499.85 \pm 4.67	498.11 \pm 4.94	1.434	0.243
QT interval	335.42 \pm 16.25	323.30 \pm 11.27 ^a	342.56 \pm 20.34 ^b	10.580	0.000
QTc value	475.36 \pm 22.97	457.43 \pm 16.11 ^a	485.33 \pm 27.78 ^b	11.450	0.000
Maximum heart rate during exercise					
RR interval	432.13 \pm 46.63	414.08 \pm 31.85 ^a	419.56 \pm 54.31	2.308	0.104
QT interval	307.34 \pm 22.49	291.60 \pm 26.14 ^a	308.89 \pm 24.47	5.809	0.004
QTc value	467.76 \pm 28.01	448.75 \pm 20.53 ^a	476.67 \pm 24.50 ^b	8.651	0.000
During the recovery period (1 minute after exercise)					
RR interval	511.06 \pm 70.03	514.03 \pm 65.06	504.56 \pm 85.01	0.073	0.930
QT interval	330.93 \pm 28.25	319.30 \pm 23.44 ^a	331.11 \pm 31.40	2.452	0.091
QTc value	466.72 \pm 22.92	446.75 \pm 23.69 ^a	470.00 \pm 25.98 ^b	9.983	0.000
During the recovery period (3 minute after exercise)					
RR interval	647.28 \pm 121.96	643.92 \pm 116.71	643.00 \pm 98.91	0.013	0.987
QT interval	368.19 \pm 31.27	351.75 \pm 30.23 ^a	381.44 \pm 41.30 ^b	4.911	0.009
QTc value	461.49 \pm 28.14	442.50 \pm 28.80 ^a	474.44 \pm 27.89 ^b	7.694	0.000

Note: ^acomparison with the normal control, $P < 0.05$; ^bcomparison with negative CAG, $P < 0.05$.

during action potential platform [27]. Physiologically, potassium ion current constitutes the main ion current of repolarization and exits through different potassium ion channels on the cell membrane. It is the repolarization potential of these different potassium ion currents that constitutes the basic repolarization reserve [28]. Under normal circumstances, human ventricular repolarization period (QT interval) is directly proportional to RR interval and inversely proportional to HR, that is, the ventricular repolarization period is shortened when the HR is fast, and significantly prolonged when the HR is slow [29]. The findings of this study fully conform to this law. Patients with myocardial ischemia and suspected myocardial ischemia were screened by TET, and the true positives were further confirmed by CAG. Significant differences were found when retrospectively comparing the QTc values of patients with positive and negative CAG. Since QT interval represents ventricular repolarization adaptability, this result indicates that patients with positive CAG have poor repolarization reserve capacity. This is because the main current of action potential repolarization of ventricular myocytes is formed by potassium ions flowing out of different kinds of potassium channels. Phase-

1 repolarization is participated by IKto (instantaneous outward potassium current); phase-2 and 3 repolarization involves IKR (rapidly delayed rectifier potassium current) and IKS (slow delayed rectifier potassium current), and; phase-3 and 4 repolarization consists of IK1 (inward rectifier potassium current)[30]. The main factor affecting potassium efflux is the functional state of potassium channels, which can determine the characteristics of cell action potential repolarization and reduce potassium efflux by inhibiting the function of potassium channels. There is remodeling of cardiac repolarization in myocardium of myocardial ischemia caused by various reasons, and repolarization originates from the remodeling of ion channels and ion currents in cardiomyocytes [31]. Moreover, the current remodeling of ion channels in ischemic cardiomyocytes is mainly due to the reduction and downregulation of Ito and Ik1 currents, especially the slow activation of Iks channels, which can cause the change of cardiac repolarization into acquired long QT syndrome and reduce repolarization reserve [32].

In this study, we used the treadmill exercise test for the diagnosis of myocardial ischemia, and it is a test to increase cardiac load through exercise. However, when conducting

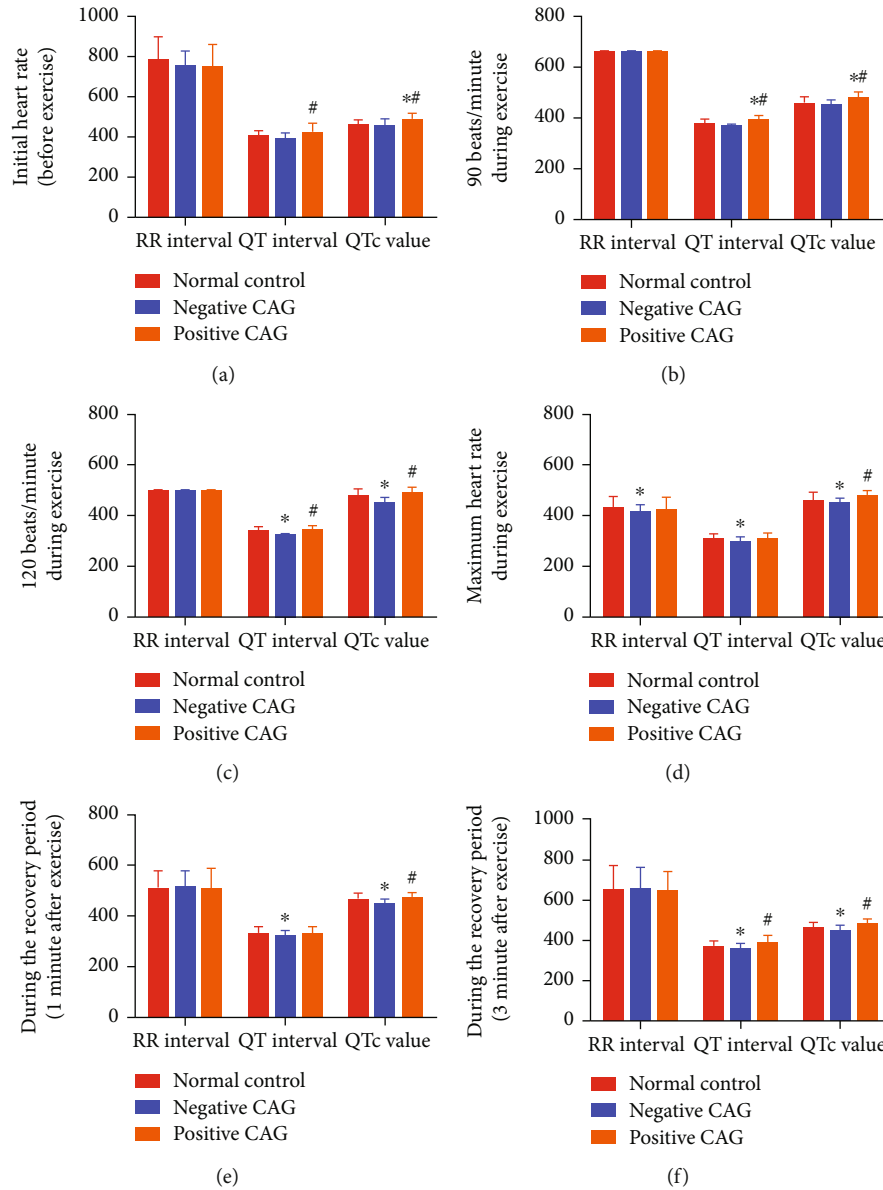


FIGURE 2: Comparison of RR interval, QT interval, and QTc value between patients with the normal control and positive and negative coronary angiography ($\bar{x} \pm s$). (a) Initial heart rate before exercise. (b) 90 beats/minute during exercise. (c) 120 beats/minute during exercise. (d) Maximum heart rate during exercise. (e) During the recovery period 1 minute after exercise. (f) During the recovery period 3 minute after exercise. * $P < 0.05$, compared to the normal control group; # $P < 0.05$, compared to the negative CAG group).

exercise tests, the inadaptability to exercise or excessive load will produce undefined changes, which will affect the test results. Therefore, whether the test is carried out on the treadmill or on the circulatory power meter, it must always adapt to the clinical and biomechanical conditions of patients, so as to accurately explain the clinical variables.

5. Conclusion

The QT interval of patients with positive CAG does not decrease with the increase of ventricular rate, that is, the ventricular repolarization period is inversely proportional to the HR. When the HR increases, the ventricular repolarization period does not shorten correspondingly, but pro-

longs, indicating poor repolarization reserve capacity in patients with positive CAG.

Data Availability

The labeled datasets used to support the findings of this study are available from the corresponding author upon request.

Conflicts of Interest

The authors declare no competing interests.

Authors' Contributions

Rubing Kang and Yitong Li contributed equally to this work and are co-first authors.

References

- [1] S. Ahnve and H. Vallin, "Influence of heart rate and inhibition of autonomic tone on the QT interval," *Circulation*, vol. 65, no. 3, pp. 435–439, 1982.
- [2] F. Galetta, F. Franzoni, P. Fallahi et al., "Changes in heart rate variability and qt dispersion in patients with overt hypothyroidism," *European Journal of Endocrinology*, vol. 158, no. 1, pp. 85–90, 2008.
- [3] M. K. Lahiri, A. Chicos, D. Bergner et al., "Recovery of heart rate variability and ventricular repolarization indices following exercise," *Annals of Noninvasive Electrocardiology*, vol. 17, no. 4, pp. 349–360, 2012.
- [4] C. Pérez, E. Pueyo, J. P. Martínez, J. Viik, and P. Laguna, "Characterization of impaired ventricular repolarization by quantification of QT delayed response to heart rate changes in stress test," in *2020 Computing in Cardiology Conference (CinC)*, pp. 1–4, Rimini, Italy, December 2020.
- [5] K.-J. Axelsson, L. Gransberg, G. Lundahl, F. Vahedi, and L. Bergfeldt, "Adaptation of ventricular repolarization time following abrupt changes in heart rate: comparisons and reproducibility of repeated atrial and ventricular pacing," *American Journal of Physiology-Heart and Circulatory Physiology*, vol. 320, no. 1, pp. H381–HH92, 2021.
- [6] A. Harvey, D. Curnier, P. Dodin, S. Abadir, V. Jacquemet, and M. Caru, "The influence of exercise and postural changes on ventricular repolarization in the long QT syndrome: a systematic scoping review," *European Journal of Preventive Cardiology*, 2022.
- [7] Y. Zhu, X. Ai, R. A. Oster, D. M. Bers, and S. M. Pogwizd, "Sex differences in repolarization and slow delayed rectifier potassium current and their regulation by sympathetic stimulation in rabbits," *Pflügers Archiv - European Journal of Physiology*, vol. 465, no. 6, pp. 805–818, 2013.
- [8] L. Wu, J. Ma, H. Li et al., "Late sodium current contributes to the reverse rate-dependent effect of IKr inhibition on ventricular repolarization," *Circulation*, vol. 123, no. 16, pp. 1713–1720, 2011.
- [9] D. Guo, J. Lian, T. Liu et al., "Contribution of late sodium current (I_{Na-L}) to rate adaptation of ventricular repolarization and reverse use-dependence of QT-prolonging agents," *Heart Rhythm*, vol. 8, no. 5, pp. 762–769, 2011.
- [10] R. Coppini, C. Ferrantini, L. Yao et al., "Late sodium current inhibition reverses electromechanical dysfunction in human hypertrophic cardiomyopathy," *Circulation*, vol. 127, no. 5, pp. 575–584, 2013.
- [11] B. Trenor, K. Cardona, J. F. Gomez et al., "Simulation and mechanistic investigation of the arrhythmogenic role of the late sodium current in human heart failure," *PLoS One*, vol. 7, no. 3, article e32659, 2012.
- [12] B. R. Pagliaro, F. Cannata, G. G. Stefanini, and L. Bolognese, "Myocardial ischemia and coronary disease in heart failure," *Heart Failure Reviews*, vol. 25, no. 1, pp. 53–65, 2020.
- [13] M. Smit, A. R. Coetzee, and A. Lochner, "The pathophysiology of myocardial ischemia and perioperative myocardial infarction," *Journal of Cardiothoracic and Vascular Anesthesia*, vol. 34, no. 9, pp. 2501–2512, 2020.
- [14] M. S. Maron, I. Olivotto, B. J. Maron et al., "The case for myocardial ischemia in hypertrophic cardiomyopathy," *Journal of the American College of Cardiology*, vol. 54, no. 9, pp. 866–875, 2009.
- [15] M. J. L. Magalhães, L. de Pádua Gomes de Farias, L. de Pádua Silva Baptista et al., "Acute myocarditis associated with acute myocardial infarction," *Radiology: Cardiothoracic Imaging*, vol. 3, no. 1, article e200469, 2021.
- [16] N. El-Sherif, G. Turitto, and M. Boutjdir, "Acquired long qt syndrome and torsade de pointes," *Pacing and Clinical Electrophysiology*, vol. 41, no. 4, pp. 414–421, 2018.
- [17] T. G. Diness, Y. H. Yeh, X. Y. Qi et al., "Antiarrhythmic properties of a rapid delayed-rectifier current activator in rabbit models of acquired long QT syndrome," *Cardiovascular Research*, vol. 79, no. 1, pp. 61–69, 2008.
- [18] L. Belardinelli, W. R. Giles, S. Rajamani, H. S. Karagueuzian, and J. C. Shryock, "Cardiac late Na^+ current: proarrhythmic effects, roles in long QT syndromes, and pathological relationship to CaMKII and oxidative stress," *Heart Rhythm*, vol. 12, no. 2, pp. 440–448, 2015.
- [19] Z. Zhao, Y. Xie, H. Wen et al., "Role of the transient outward potassium current in the genesis of early afterdepolarizations in cardiac cells," *Cardiovascular Research*, vol. 95, no. 3, pp. 308–316, 2012.
- [20] P. R. Vehrs, J. D. George, G. W. Fellingham, S. A. Plowman, and K. Dustman-Allen, "Submaximal treadmill exercise test to predict VO_2 max in fit adults," *Measurement in Physical Education and Exercise Science*, vol. 11, no. 2, pp. 61–72, 2007.
- [21] G. W. Beeler and H. Reuter, "Reconstruction of the action potential of ventricular myocardial fibres," *The Journal of Physiology*, vol. 268, no. 1, pp. 177–210, 1977.
- [22] B. P. Damiano and M. R. Rosen, "Effects of pacing on triggered activity induced by early afterdepolarizations," *Circulation*, vol. 69, no. 5, pp. 1013–1025, 1984.
- [23] E. Marban, S. W. Robinson, and W. G. Wier, "Mechanisms of arrhythmogenic delayed and early afterdepolarizations in ferret ventricular muscle," *The Journal of Clinical Investigation*, vol. 78, no. 5, pp. 1185–1192, 1986.
- [24] D. S. Bailie, H. Inoue, S. Kaseda, J. Ben-David, and D. P. Zipes, "Magnesium suppression of early afterdepolarizations and ventricular tachyarrhythmias induced by cesium in dogs," *Circulation*, vol. 77, no. 6, pp. 1395–1402, 1988.
- [25] C. T. January, J. M. Riddle, and J. J. Salata, "A model for early afterdepolarizations: induction with the Ca^{2+} channel agonist Bay K 8644," *Circulation Research*, vol. 62, no. 3, pp. 563–571, 1988.
- [26] C. January, V. Chau, and J. C. Makielski, "Triggered activity in the heart: cellular mechanisms of early after-depolarizations," *European Heart Journal*, vol. 12, Supplement F, pp. 4–9, 1991.
- [27] P. C. Viswanathan and Y. Rudy, "Pause induced early afterdepolarizations in the long qt syndrome: a simulation study," *Cardiovascular Research*, vol. 42, no. 2, pp. 530–542, 1999.
- [28] M. B. Thomsen, "Kv7.1 isoform gradients in the heart: new potential approach to alter repolarization reserve," *Heart Rhythm*, vol. 10, no. 8, pp. 1229–1230, 2013.
- [29] P. Kligfield, K. G. Lax, and P. M. Okin, "QT interval-heart rate relation during exercise in normal men and women: definition by linear regression analysis," *Journal of the American College of Cardiology*, vol. 28, no. 6, pp. 1547–1555, 1996.

- [30] T. Lewalter and B. Lüderitz, “Historical milestones of electrical signal recording and analysis,” in *Cardiac Repolarization*, pp. 7–21, Springer, 2003.
- [31] Z. Qu, L. H. Xie, R. Olcese et al., “Early afterdepolarizations in cardiac myocytes: beyond reduced repolarization reserve,” *Cardiovascular Research*, vol. 99, no. 1, pp. 6–15, 2013.
- [32] J. Biermann and T. S. Faber, “Ventrikuläre tachykardien unter belastung,” *Herzschrittmachertherapie & Elektrophysiologie*, vol. 24, no. 4, pp. 197–201, 2013.

Retraction

Retracted: Application of Digital Orthopedic Technology in Orthopedic Trauma

Computational and Mathematical Methods in Medicine

Received 26 September 2023; Accepted 26 September 2023; Published 27 September 2023

Copyright © 2023 Computational and Mathematical Methods in Medicine. This is an open access article distributed under the Creative Commons Attribution License, which permits unrestricted use, distribution, and reproduction in any medium, provided the original work is properly cited.

This article has been retracted by Hindawi following an investigation undertaken by the publisher [1]. This investigation has uncovered evidence of one or more of the following indicators of systematic manipulation of the publication process:

- (1) Discrepancies in scope
- (2) Discrepancies in the description of the research reported
- (3) Discrepancies between the availability of data and the research described
- (4) Inappropriate citations
- (5) Incoherent, meaningless and/or irrelevant content included in the article
- (6) Peer-review manipulation

The presence of these indicators undermines our confidence in the integrity of the article's content and we cannot, therefore, vouch for its reliability. Please note that this notice is intended solely to alert readers that the content of this article is unreliable. We have not investigated whether authors were aware of or involved in the systematic manipulation of the publication process.

In addition, our investigation has also shown that one or more of the following human-subject reporting requirements has not been met in this article: ethical approval by an Institutional Review Board (IRB) committee or equivalent, patient/participant consent to participate, and/or agreement to publish patient/participant details (where relevant).

Wiley and Hindawi regrets that the usual quality checks did not identify these issues before publication and have since put additional measures in place to safeguard research integrity.

We wish to credit our own Research Integrity and Research Publishing teams and anonymous and named external researchers and research integrity experts for contributing to this investigation.

The corresponding author, as the representative of all authors, has been given the opportunity to register their agreement or disagreement to this retraction. We have kept a record of any response received.

References

- [1] J. Lin, J. Ge, J. Gong, H. Hong, and C. Jiang, "Application of Digital Orthopedic Technology in Orthopedic Trauma," *Computational and Mathematical Methods in Medicine*, vol. 2022, Article ID 3157107, 11 pages, 2022.

Research Article

Application of Digital Orthopedic Technology in Orthopedic Trauma

Jiangtao Lin, Junbo Ge, Jinpeng Gong, Huanyu Hong, and Chuanqiang Jiang 

The First Ward of Trauma Orthopedics, Yantaishan Hospital, Yantai 264003, China

Correspondence should be addressed to Chuanqiang Jiang; 18409144@masu.edu.cn

Received 8 June 2022; Revised 30 June 2022; Accepted 13 July 2022; Published 16 August 2022

Academic Editor: Pan Zheng

Copyright © 2022 Jiangtao Lin et al. This is an open access article distributed under the Creative Commons Attribution License, which permits unrestricted use, distribution, and reproduction in any medium, provided the original work is properly cited.

In order to solve the limitation of auxiliary treatment means in the process of orthopedic trauma surgery, and further improve the effective integration of orthopedic trauma clinical surgery and computer technology, a new orthopedic trauma auxiliary treatment means based on digital orthopedic technology was proposed with the aid of virtual digital technology. The method builds a 3D model of fracture fragments through 3D orthopedic modeling and obtains a high-quality 3D model through processing. Later clinical tests verify the feasibility of this auxiliary treatment method. The test results show that the precision of the 3D reconstruction model based on custom option fitting is higher than that based on optimal option fitting, and the precision difference is within 0.2%. This result also indicates that the 3D model obtained by 3D reconstruction has higher accuracy. The results show that three-dimensional finite element modeling technology can accurately simulate the stress of the spine of orthopedic patients and can reduce the incidence of complications through preoperative diagnosis, curative effect prediction, and trauma surgery, which has a good aid for postoperative recovery.

1. Introduction

In recent years, with the rapid development of digital technology, it provides a new technical means for the basic research of clinical treatment of orthopedic diseases, especially through the mutual integration and mutual influence of traditional orthopedic theory, gradually forming a modern digital orthopedic treatment technology with digital characteristics. At present, the techniques applied in orthopedic surgery mainly include medical image processing and 3D modeling, 3D virtual simulation and visualization, computer-aided design, finite element technology, mechanical simulation of human skeletal muscle system in robot-assisted treatment, etc. These techniques have greatly improved the therapeutic effect and technical level of orthopedic surgery. As a special type of orthopedics, traumatic orthopedics has different characteristics from spinal surgery and joint surgery, and the integration of digital technology and traumatic orthopedics is becoming more and more extensive. In this study, higher quality 3D models were obtained by constructing 3D orthopedic models. With the support of 3D finite element modeling

technology, the feasibility of digital orthopedic-assisted therapy was verified through clinical tests.

2. Literature Review

Yang and others say that in traditional orthopedic research, surgeons have to rely solely on images of patients to determine surgical procedures in their heads [1]. Wang et al. say that the advantages of digital orthopedic techniques over traditional orthopedic models lie in preoperative planning for a three-dimensional anatomical model of the site. The 3D model of the affected area was printed by 3D and the operation was simulated directly [2]. Wang et al. say that finite element analysis can provide biomechanical support for surgical protocols [3]. Back and Pfringer said that foreign studies include the following: in a proposed train-oriented simulation framework for temporal bone surgery, the system allows two users to observe and operate a common model in different locations to perform an operation and allows each user to experience the influence of the force generated by the contact of other users with the bone surface [4]. Adam and others say the system also allows teachers to

observe students remotely and provide real-time feedback and demonstrations. Virtual reality software and workflow applications were used for radiotherapy, treatment planning, and evaluation using virtual linear accelerators [5]. The result is that it is possible to simulate most radiotherapy workflows and tasks. Rawal and others say the method saves time and is relatively safe, allowing for a good understanding and experience of clinical procedures in advance. A new haptic surgical simulator for cerebral aneurysms was developed, and its role in neurosurgical residency training was evaluated [6]. Stogov et al. say that surgical treatment of cerebral aneurysms is complex and rare and that a simulation-based tool is needed to educate future neurosurgeons to operate on cerebral arteries [7]. The simulator is a virtual reality aneurysm surgery simulator based on real-time haptic feedback. It adopts an immersive touch platform to provide aneurysm and vessel volume deformation and aneurysm rupture during surgery with haptic feedback. Ow et al. said that 17 neurosurgeons who tested the simulator in three ways said it was very similar to actual aneurysm surgery [8]. Doctors believe that the simulator provides immersive anatomical details for surgical dissection and accurate guidance and is useful for preoperative surgical practice and neurosurgical training. Hamsen and others say that 3D printing is based on digital model files, which use adhesive materials such as powdered metal or plastic to print layer by layer until the desired object is constructed. It is a digital technology [9]. 3D printing technology can provide a more complete personalized solution for the medical industry. Typical applications include 3D printing of preoperative planning models, surgical guides, prosthetic implants, and medical rehabilitation instruments such as hearing aids. Good preoperative planning is the key to successful operation. In particular, for difficult and high-risk operations or new operations, preoperative planning is particularly important. Compared to 2D data, 3D data is more realistic, and the 3D model is printed by a 3D printer. It can not only assist doctors to carry out accurate surgical planning and formulate more accurate and detailed surgical plans to improve the success rate of surgery but also facilitate doctors to have better intuitive communication with patients and their families on surgical plans. Hang and others say biomedical 3D printing in China, while still in its infancy, is becoming more widely used. Due to the individual characteristics of different patients, preoperative simulation can be customized, and the customized characteristics of 3D printing technology bring great convenience to personalized treatment. Academician Dai Zhirong believes that 3D printing technology has brought good news to the medical field (see [10]). Taking orthopedic implants as an example, complex porous structures integrated with the implants can be directly printed on the surface of the implants by 3D printing technology. These structures are conducive to bone growth and patient rehabilitation. Denture processing, for example, allows dental scanners and 3D printers to print denture models of multiple patients at the same time, freeing dentists from the role of artisans making plaster casts by hand and freeing them up to spend precious time on treatment. Take surgery, for example, by combining medical image data design soft-

ware with 3D printing, doctors can not only see a three-dimensional model of the patient on a computer but also 3D print the model and use the physical model for precise surgical planning and practice. It can help doctors develop a more accurate surgical plan; thus, the operation time is shortened and the success rate of the operation is improved. For the clinical treatment of developmental hip dysplasia (DDH), 3D printing technology was used to print the lesion models of 10 patients with DDH. Computer-aided measurement was used to simulate the operation, measure the size of the used prosthesis, and compare it with the actual postoperative value. The results showed that there was no significant difference between the measured values of acetabular diameter lines and the actual values, the acetabular rotation center was found accurately, and the use of the prosthesis was consistent with the preoperative plan. In the 3D printing group, intraoperative blood loss, operative time, postoperative drainage, postoperative complication rate, and so on were better than those of conventional surgery. 3D printing technology can improve the precision and efficacy of DDH joint replacement surgery. China's first 3D-printed orthopedic implant 3D-printed artificial hip product applied by Peking University Third Hospital, one of the supporting units of the TCT Asian exhibition, has been approved by the State Food and Drug Administration. The Third Affiliated Hospital of Southern Medical University (Guangdong Orthopaedic Hospital) carried out the first 3D-printed artificial vertebra implantation operation in Guangdong Province, successfully implanted the 3D-printed artificial vertebra in a patient with chordoma. Kang Yujian, an academician of the American Academy of Toxicology, said that 3D printing has changed the traditional medical operation mode and realized customized medical precision medicine, which means that customized health is no longer far away from us. The application of digital orthopedic technology in orthopedic trauma is shown in Figure 1.

3. Method

The finite element method regards the whole structure as a geometric entity connected by finite elements, and the assembly effect of the mechanical characteristics of each small element reflects the overall mechanical properties of the structure. The finite element analysis process is composed of algebraic equations to solve a series of problems, as shown in the following formula:

$$[K]\{U\} = \{Q\}. \quad (1)$$

The finite element analysis process is composed of algebraic equations to solve a series of problems, as shown in Formula (1).

These quantities are indeterminate and are described quantitatively depending on the problem to be solved. The theoretical stress analysis is to analyze the stress distribution by mathematical models, while the finite element method is to divide the elements. It simulates the real structure to some extent and describes all aspects of the structure numerically. The accuracy of its description depends on the degree of unit

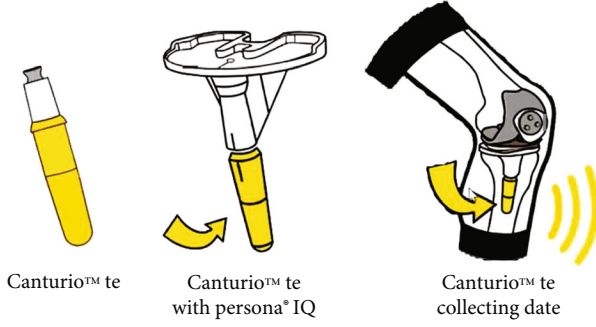


FIGURE 1: Application of digital orthopedic technology in orthopedic trauma.

subdivision, often based on experimental data. In the process of solving the problem, the structure description is combined with the algebraic equation of solid mechanics theory to find the stress and displacement of the required solution. The application process of the finite element method includes the following three main parts: data input, operation, and data output [11].

Adaptability to complex geometric configurations: a unit can be one-dimensional, two-dimensional, or three-dimensional in space, and each kind of unit can have a different shape, for example, a three-dimensional unit can be tetrahedral pentahedron or hexahedron. At the same time, different connection methods can be adopted between various elements. For example, the field function can be kept continuous between two surfaces, the derivative of the field function can also be kept continuous, or only the normal component of the field function can be kept continuous. *Applicability to various physical problems:* since the unknown field functions in the whole solution domain are represented by fragments of approximate functions in cells, there is no restriction on the form of equations that the field functions satisfy, nor on the same form of equations corresponding to each cell. Therefore, although the finite element method was initially proposed for linear elastic stress analysis, it soon developed elastoplastic problems, viscoelastoplastic problems, dynamic problems, buckling problems, etc. [12].

On the basis of previous studies, some scholars proposed to establish a three-dimensional model of implant-bone interface by using microscopic slices. The advantage of this method is that the thickness of the section is uniform, and the bone density and interface bonding of the trabecular bone can be reflected. The data are accurate and reliable. The disadvantages are that it takes a long time to complete, and it takes 2 months to process an implant image. The modeling methods of the finite element method can be the grinding disc method and CT scanning tomography, and their characteristics are shown in Table 1.

Load has three elements: size direction and point of operation. A static load is a load that increases gradually from zero to a final value with little or no change. The load that does not meet the static load condition is called a dynamic load. Under the dynamic load, the component produces an acceleration field which cannot be neglected

[13, 14]. The dynamic load can be divided into inertial force and impact load; the latter is closely related to oral biomechanics. The relation between impact load and static load is shown in the following formula:

$$P_d = KP. \quad (2)$$

P_d is the impact load, P is the static load, and K is the impact dynamic load coefficient.

E_f and μ_f are set as the elastic modulus and Pearson's ratio of the femur of knee joint occlusal elastomer, respectively. Here, f represents the femur, and E_t and μ_t represent the elastic modulus and Pearson's ratio of the tibia of knee joint occlusal elastomer, respectively. Here, t represents the tibia, and R_f and R_f' are two principal curvature semimeridions of the contact surface of the elastic femur occlusal. R_t and R_t' , respectively, are the two principal radii of curvature of the contact surface of the tibial occlusal of elastomer. a and b , respectively, are the major semiaxis and the minor semiaxis of the elastic contact surface of the tibial joint of the knee joint. δ is the relative displacement of the elastic center of femur and tibia, q_0 is the maximum compressive stress of the elastic contact surface of tibial articulation of the knee joint, and P is the axial static pressure. Thus, according to the Hertz theory, the fixed solution of the maximum compressive stress elastic contact area and deformation of the articulation contact area of the knee joint can be deduced, as shown in the following formula:

$$q_0 = \frac{3P}{2\pi ab}. \quad (3)$$

The maximum compressive stress occurs in the center of the contact surface. As can be seen from the above equation, the maximum compressive stress is 1.5 times of the average compressive stress on the elastic contact surface of the tibial articulatory joint of the knee joint. To calculate this compressive stress, two half axes a and b in the elliptic contact area of the knee joint must be worked out first, and the derivation results are shown in the following formulas:

$$a = \delta \sqrt[3]{\frac{3P}{4A} \left(\frac{1 - \mu_f^2}{E_f} + \frac{1 - \mu_t^2}{E_t} \right)}, \quad (4)$$

$$b = \beta \sqrt[3]{\frac{3P}{4A} \left(\frac{1 - \mu_f^2}{E_f} + \frac{1 - \mu_t^2}{E_t} \right)}, \quad (5)$$

$$\delta = \lambda \sqrt[3]{\frac{9}{128} AP^2 \left(\frac{1 - \mu_f^2}{E_f} + \frac{1 - \mu_t^2}{E_t} \right)}. \quad (6)$$

Here is shown in the following formulas:

$$A = \frac{1}{2} \left(\frac{1}{R_f} + \frac{1}{R_f'} + \frac{1}{R_t} + \frac{1}{R_t'} \right), \quad (7)$$

TABLE 1: Comparison of modeling methods.

Grinding method	CT tomography method
Advantages: accurate information of model section geometry and accurate distribution of bone trabecula can be obtained	Advantages: (1) the section geometry is accurate, and it can be quickly and accurately digitized, reducing the error; (2) the integrity of the model is not damaged; (3) the nonuniformity of the section of bone tissue material can be reflected
Disadvantages: (1) the model is destroyed and bone tissue is lost due to cutting; (2) it is difficult to obtain a consistent thickness of the section when the section is very thin; (3) sufficient time is required to prepare the model, and the section geometry is digitized with large error	Disadvantages of nonuniformity of material cross-section: (1) it is difficult to determine the alignment direction of bone trabecula; (2) CT scanning requires multiple channels

$$B = \frac{1}{2} \left[\left(\frac{1}{R_f} - \frac{1}{R'_f} \right)^2 + \left(\frac{1}{R_t} - \frac{1}{R'_t} \right)^2 + 2 \left(\frac{1}{R_f} - \frac{1}{R'_f} \right) \left(\frac{1}{R_t} - \frac{1}{R'_t} \right) \cos 2\Phi \right]^{1/2}, \quad (8)$$

$$\cos \theta = \frac{B}{A}. \quad (9)$$

Φ is the included angle between R_f and R_t , the plane where the two main radii of curvature are located; α , β , and λ are the coefficients; and the value of θ can be calculated according to Formula (9) and obtained by referring to the table.

3.1. Mathematical Description of Elastic Occlusal Surface of Knee Joint. Since it is still difficult to establish a network for the accurate mathematical description of the real 3D articulation surface of the knee joint, polynomial numerical approximation is used to describe the femoral surface and tibial surface of the knee joint elastic occlusion. Assuming that both surfaces are continuous and smooth functions, they can be expressed in polynomial form as follows.

For the tibial occlusal surface, it is shown in the following formula:

$$f_T(x, y, z) = xe_x + y(x, z)e_y + ze_z. \quad (10)$$

T is the tibial surface, as shown in the following formula:

$$x, y = y(x, z), z. \quad (11)$$

The above formula is the coordinates of points on the tibial occlusal surface, and y can be obtained through multiple approximation as shown in the following formula:

$$y = y(x, z) = \sum_{i=0}^n \sum_{j=0}^{n-1} a_{ij} x^i z^j. \quad (12)$$

In the above formula, a_{ij} can be determined by the following least square method as shown in the following formula:

$$\sum_{r=1}^m \{y_r - y(x_r, z_r)\}^2 = \sum_{r=1}^m \left\{ y_r - \sum_{i=0}^n \sum_{j=0}^{n-1} a_{ij} x_r^i z_r^j \right\}^2. \quad (13)$$

It is shown in the following formula:

$$r = r(x_r, y_r, z_r). \quad (14)$$

The above formula is the coordinate of measuring point r of the tibial occlusal surface, while m is the number of points measured by the tibial occlusal surface.

In the same way, the femur surface equation of knee elastic occlusion can be determined as shown in the following formula:

$$f_F(x', y', z') = x' e'_x + y' (x', z') e'_y + z' e'_z. \quad (15)$$

Combined with formulas (12)–(15), it can be seen that the accuracy of the two surfaces of knee elastic occlusal contact, namely, tibial occlusal surface and femur occlusal surface, depends on the number of corresponding measurement points and the number of polynomial items selected.

The object of the study was fresh sheep femur, which was selected because it was widely available and easily accessible. In the smooth middle section of the femur of the fresh sheep, the length was 50 mm, and two through holes with diameters of 5 mm were made for calibration. The purpose of doing this is as follows: first, it is relatively easy to carry out CMM for the smooth femur segment of sheep; second, a reference is established after calibration to ensure the accuracy of comparison.

3.2. Three-Dimensional Reconstruction of Sheep Femur from CT Scan. Mask 1 of sheep femur with CT scan interval of 0.6 mm was extracted from Mimics16.0, namely, the initial mask. The initial mask is copied and edited to obtain the mask of the calibration segment, that is, the processed mask. Then, select Calculate 3D option and reconstruct the 3D reconstruction model with initial mask processing. The same method was used to compare contours under different fitting options, and the polar coordinate gap (d/mm) was outputted to sort out the data. Shown in Tables 2–8 are the polar coordinate gaps of different contours under different fitting options.

The corresponding histogram of the sheep femur contour at different heights can be found in that when the fitting option is High Medium, the corresponding point difference of the sheep femur 3D reconstruction model is significantly greater than when the fitting option is Optimal Custom.

TABLE 2: The gap of polar coordinates under different fitting options when $Z = 15$ mm.

Fit method	Medium	High	Optimal	Custom
Point 1	0.532	0.320	0.051	0.080
Point 2	0.559	0.388	0.142	0.161
Point 3	0.572	0.282	0.051	0.002
Point 4	0.676	0.402	0.122	0.159
Point 5	0.679	0.490	0.214	0.200
Point 6	0.563	0.293	0.137	0.143
Point 7	0.639	0.425	0.198	0.183
Point 8	0.760	0.420	0.124	0.075
Mean distance	0.631	0.378	0.168	0.164
Standard deviation	0.066	0.077	0.087	0.089

TABLE 3: The gap of polar coordinates under different fitting options when $Z = 20$ mm.

Fit method	Medium	High	Optimal	Custom
Point 1	0.497	0.191	0.068	0.049
Point 2	0.551	0.209	0.087	0.036
Point 3	0.535	0.258	0.044	0.045
Point 4	0.705	0.387	0.131	0.120
Point 5	0.596	0.286	0.006	0.031
Point 6	0.511	0.395	0.172	0.174
Point 7	0.483	0.365	0.149	0.133
Point 8	0.523	0.374	0.055	0.012
Mean distance	0.545	0.333	0.128	0.121
Standard deviation	0.106	0.084	0.100	0.103

TABLE 4: The gap of polar coordinates under different fitting options when $Z = 25$ mm.

Fit method	Medium	High	Optimal	Custom
Point 1	0.334	0.127	0.059	0.078
Point 2	0.500	0.232	0.106	0.097
Point 3	0.62	0.386	0.319	0.320
Point 4	0.599	0.306	0.188	0.175
Point 5	0.678	0.359	0.326	0.343
Point 6	0.631	0.425	0.165	0.174
Point 7	0.696	0.440	0.159	0.155
Point 8	0.709	0.442	0.158	0.133
Mean distance	0.630	0.379	0.169	0.165
Standard deviation	0.104	0.102	0.120	0.124

When the fitting option was Optimal, the corresponding point gap of the sheep femur 3D reconstruction model was close to that of the sheep femur 3D reconstruction model when the fitting option was Custom. The accuracy of the 3D reconstruction model of fresh sheep femur was defined as follows: the percentage of the polar coordinate difference

TABLE 5: The gap of polar coordinates under different fitting options when $Z = 30$ mm.

Fit method	Medium	High	Optimal	Custom
Point 1	0.463	0.256	0.099	0.100
Point 2	0.427	0.119	0.095	0.082
Point 3	0.582	0.370	0.176	0.176
Point 4	0.454	0.089	0.083	0.083
Point 5	0.622	0.407	0.158	0.146
Point 6	0.558	0.154	0.038	0.045
Point 7	0.693	0.445	0.256	0.241
Point 8	0.681	0.375	0.248	0.258
Mean distance	0.625	0.385	0.193	0.194
Standard deviation	0.081	0.120	0.070	0.070

TABLE 6: The gap of polar coordinates under different fitting options when $Z = 35$ mm.

Fit method	Medium	High	Optimal	Custom
Point 1	0.456	0.275	0.128	0.159
Point 2	0.470	0.200	0.008	0.003
Point 3	0.660	0.488	0.215	0.234
Point 4	0.667	0.282	0.001	0.008
Point 5	0.528	0.500	0.186	0.179
Point 6	0.662	0.335	0.137	0.114
Point 7	0.582	0.253	0.073	0.069
Point 8	0.605	0.311	0.102	0.101
Mean distance	0.597	0.346	0.119	0.123
Standard deviation	0.074	0.124	0.070	0.102

TABLE 7: The gap of polar coordinates under different fitting options when $Z = 40$ mm.

Fit method	Medium	High	Optimal	Custom
Point 1	0.566	0.416	0.103	0.115
Point 2	0.614	0.273	0.062	0.165
Point 3	0.624	0.477	0.201	0.111
Point 4	0.740	0.465	0.076	0.103
Point 5	0.658	0.373	0.103	0.105
Point 6	0.693	0.455	0.175	0.103
Point 7	0.648	0.416	0.163	0.130
Point 8	0.655	0.475	0.296	0.298
Mean distance	0.628	0.387	0.148	0.138
Standard deviation	0.048	0.066	0.065	0.056

(d/mm) and the corresponding polar coordinate (D/mm) of the corresponding points.

Combined with the above table, the d/mm histogram of the polar coordinate distance at different heights under different fitting options is presented for intuitive observation as shown in Figure 2.

TABLE 8: Polar distance at different points of the femur of fresh sheep at different heights.

Height	Z = 15	Z = 20	Z = 25	Z = 30	
Point 1	8.971	8.670	8.503	8.403	
Point 2	8.657	8.922	8.759	8.499	
Point 3	9.502	8.519	8.514	8.966	
Polar gap (d/mm)	Point 4	9.570	8.547	8.981	8.532
	Point 5	8.931	9.285	8.784	8.794
	Point 6	8.895	9.209	8.577	8.637
	Point 7	9.138	8.688	8.351	8.700
	Point 8	8.456	8.453	8.376	8.586
Mean distance	8.892	8.673	8.526	8.553	
Standard deviation	0.334	0.276	0.218	0.229	

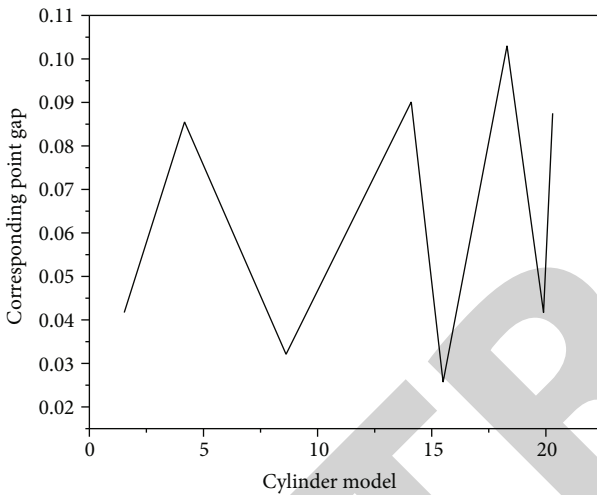


FIGURE 2: Histogram of corresponding point difference of cylinder model under different 3D printing processing technology.

The load deformation generated after the cylinder compression test is shown in Figure 3.

By analyzing the above two tables and Figures 2 and 3, it can be seen that the quality of the 3D model is Optimal > High > Medium, and the minimum accuracy of the 3D reconstruction model of sheep femur fitted by the Optimal option is 4.208%, which is within an acceptable range due to the particularity of the skeleton. The 3D reconstruction model of sheep femur fitted by the Optimal option is 2.0% larger than that of fresh sheep femur, that is, about 0.16 mm. The CT scan data of fresh sheep femur used in this study have high pixels, and the 3D reconstruction model precision fitted by the Custom option is higher than that fitted by the Optimal option; the difference is within 0.2%. This means that the quality of the CT scan data is good. The 3D model obtained by 3D reconstruction based on the gray value has higher accuracy. Considering that the running speed and storage space of the computer and the accuracy difference between the two is within 0.2%, 3D reconstruction based on Contour is a better comprehensive

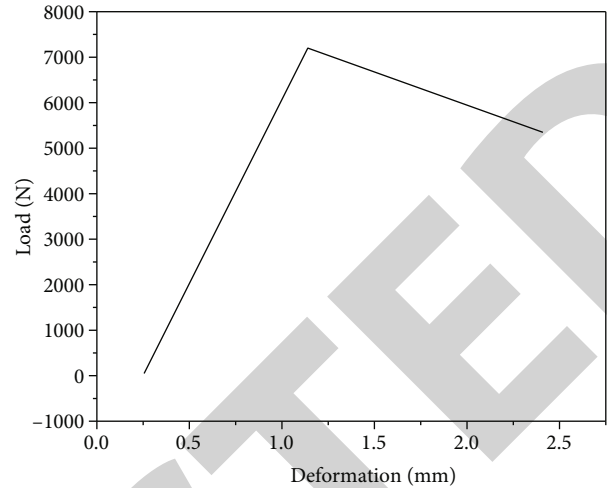


FIGURE 3: Load-deformation curve of the sample.

consideration and the Optimal fitting method is superior Custom Indicates the fitting method.

4. Experiments and Analysis

Here, Mimics software is used to build a Pilon fracture 3D model through Pilon fracture CT data, demonstrating the specific steps of model building, reflecting the unique characteristics and advantages of digital orthopedics, and demonstrating its application value in clinical orthopedics. At the same time, the Pilon fracture was classified on the generated 3D model and compared with its own X-ray film to verify the accuracy of the X-ray film diagnosis [15]. The technical route is shown in Figure 4.

Mimics16.0 was imported into the DICOM medical image and Thresholding-Bone (CT) option. Due to the different gray values of the bone and soft tissue, the two can be separated and the ankle initial mask can be obtained through Region Growing. Then, the discrete elements were accurately separated by the Region Growing option, and the foot bone mask was obtained through which to reconstruct the overall 3D model of the initial foot and ankle fractures [16, 17].

In the preoperative simulation, it is essential to effectively separate the fracture fragments from the fracture. It is crucial to separate fracture fragments accurately. Because the fragments are in contact with each other and overlap, the surgeon needs to be involved in this stage to ensure that the fragments are separated correctly. The process of separating the boundary of the fracture fragment is the process of carefully editing each layer mask of the fragment. After correctly separating the first fracture fragment, Boolean Operations can quickly and accurately separate the remaining bone fragment. According to the above method, all the fracture fragments were separated in turn, including the parts without fracture such as the foot scaphoid. Since preoperative simulation was not affected, it was possible to complete the separation of the mask of each fracture fragment without separating it and then establish a 3D model

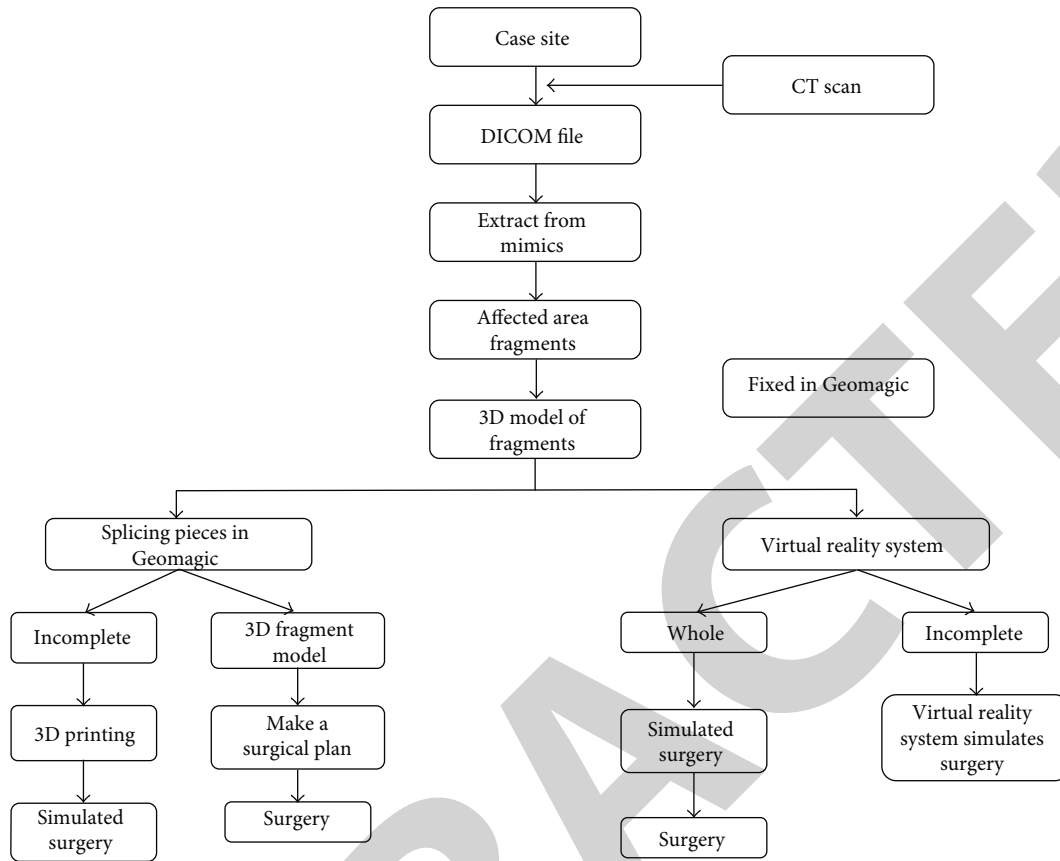


FIGURE 4: Technical route.

with Calculate 3D-Optimal and use different colors to represent each fracture fragment for convenient observation [18].

Due to the cancellous bone structure in the distal tibia bone, there are many honeycomb holes in the reconstructed 3D model. The large number of holes increases the number of features in the 3D model and complicates the model. In the process of preoperative simulation, the holes in the 3D model will not affect the accuracy of preoperative simulation but will occupy a large amount of computer memory [19, 20]. In the process of the 3D printing model, the complexity of the 3D model makes it more difficult to print data, and the internal holes will generate redundant support and materials cannot be processed in the printing process, which increases the difficulty of 3D printing. To improve the model quality, the reconstructed 3D model is outputted as an STL file and imported into Geomagic Studio to process each fracture fragment model.

The VR operating system includes hardware devices and software devices, as shown in Figure 5.

Mapping tools are used such as a steel ruler vernier caliper and caliper inside and outside, according to the real object for reverse modeling, in UG to build a pedicle screw (6.5 mm × 45 mm), crosslink interbody fusion device (length 22 mm × width 10 mm × high 12 mm), 3D model, and simplified model. Pedicle screw interbody fusion devices are all produced by the Beijing Riebel Company [21]. The actual pedicle screw structure is complex, with many threads and tightening devices. These structures

are not the focus of biomechanical analysis but will greatly increase the workload of finite element analysis, which is prone to collapse of finite element analysis or nonconvergence of results. Therefore, it is necessary to simplify the model of interbody fusion screw rod system.

The total spinal data of a 41-year-old normal male (scanning parameters: 120 kV, 166 mAs, layer thickness: 0.8 mm) were scanned by the SOMATOM Definition dual-source, CT machine, row 64, manufactured by Siemens in Germany. The CT data were imported into the Mimics software in DICOM format, and the vertebral body boundary was accurately differentiated and separated manually in the image processing stage. The method was the same as the Pilon fracture treatment in the previous chapter, and the single vertebral body spinal model of the C7-S1 segment was extracted, which was convenient for subsequent three-dimensional reconstruction, and the three-dimensional spinal model was obtained [22].

In finite element analysis, the quality and quantity of the mesh directly affect the accuracy of calculation results and solving time. In general, the more the number of mesh (mesh) with a higher density, the greater the precision of the results of the analysis, but eventually, at the same time, the solving time will increase; to solve the problem, the equipment, such as computers, will require higher performance requirements, so the correct selection of meshing quantity can better coordinate calculation accuracy and computation time, both to achieve the optimum [23, 24].

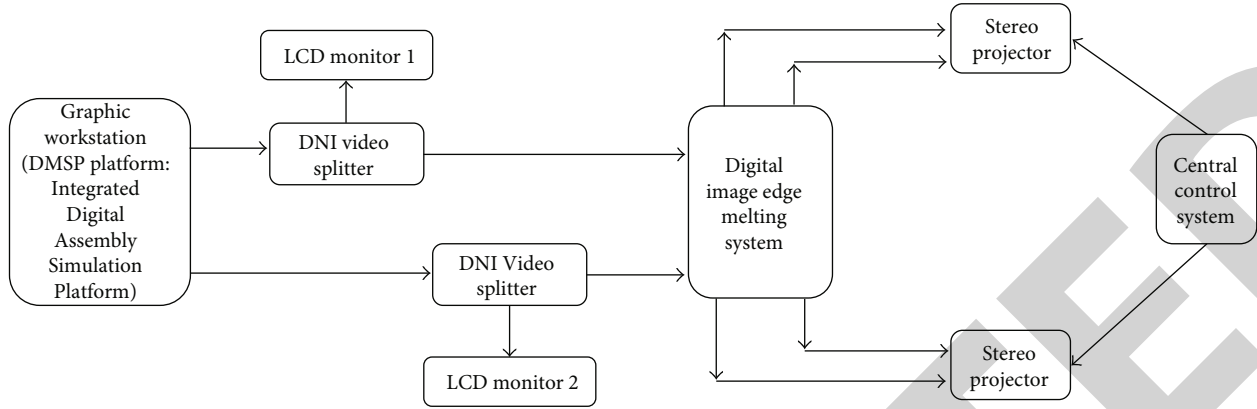


FIGURE 5: Schematic diagram of virtual reality system.

Figure 3 shows the relationship between solution accuracy (u), calculation time (t), and mesh number (n) in finite element analysis. Curve 1 shows the relationship between the solution accuracy (u) and the number of meshing (n). It can be seen from curve 1 that, within a certain range of solution accuracy, the solution accuracy increases significantly with the increase of meshing density, namely, the increase of the meshing number. However, in the second half of curve 1, it can be seen that the curve has a very flat trend, and the solution accuracy can be obtained beyond a certain range. As the number of grids continues to increase, the solution accuracy will hardly change; curve 2 shows the relationship between the calculation time (t) and the number of meshing (n). In a certain solution time interval, the solution time does not change significantly with the increase of the number of meshing. For example, when the first half of curve 2 exceeds a certain solution time, the solution time increases rapidly with the continuous increase of the number of grids, and the second half of curve 2 becomes steeper. Meanwhile, the performance configuration requirements of the solver computer also increase greatly.

The selection of mesh size is also an important factor affecting the solution accuracy in the later stage. Generally speaking, for simple statics analysis, if we pay more attention to the solution results of displacement variation, the finite element mesh can be divided into larger ones. The same solution model can divide different grid sizes for different structures according to different demands. For nonconcerned structures, the grid size can be appropriately larger, such as the vertebral structure in the spin-rod system in this study. As stress is emphasized in this paper, the grid control of the displacement structure should be smaller, such as the pedicle screw of the spin-rod system. Meanwhile, the specific grid size can also be set by referring to previous literatures with the same structure and verified solution results [25, 26].

In the process of finite element analysis, material properties have a great influence on the accuracy of analysis results. Many researchers outside China have proposed many reliable methods for human bone attachment materials. Among them, DICOM data and gray scale assignment is the most common one. The material process is completed in the FEA module of Mimics software [27]. In this finite element

TABLE 9: Finite element model parameters.

Materials	Poisson ratio	Elasticity modulus (MPa)	Density (kg/m^3)
Cortical bone	0.3	1200	1700
Cancellous bone	0.25	100	1100
Fibre ring	0.45	4.2	1050
Nucleus pulposus	0.5	1.0	

analysis of human spinal interbody fusion screw system, the gray value material assigning method was used to assign materials to open the model in Mimics software, and materials were attached in the FEA module. The parameters are shown in Table 9.

The interbody fusion screw rod system includes the pedicle screw crosslinking device, which is made of medical titanium alloy (Ti-6Al-4V). The material of the interbody fusion device is PEEK (polyetheretherketone), as shown in Table 10.

Among them, the mask of each vertebral body of the human spine is attached with material according to the gray value, and the nail bar system of intervertebral fusion is attached with a single material by the three-dimensional model.

Select Supports>Fixed Supports from the menu of Supports>Fixed Supports under the Static Structural environment, light the Face option, select the lower surface of the sacrum of each set of models, and fix it to ANSYS. The static analysis of Workbench 15.0 provides five common contact types, which are summarized in Table 11.

The finite element model established in this study simulated the stress state of the vertebral disc screw system in the standing posture of the human body. The trend was close to the actual stress in the standing posture of the human body. Qian et al. believed that the gravity line of the human body passed through the 7th cervical vertebra, the 1st lumbar vertebra, and the 1st sacral vertebra in the upright posture. According to the study by Pierre et al., the gravity line of the human body varies widely due to individual differences and does not completely coincide with the plumb line of cervical vertebra 7. Generally speaking, the gravity line of young

TABLE 10: Titanium alloy, PEEK material parameters.

Name	Directivity	Poisson ratio	Elasticity modulus (MPa)	Density (kg/m ³)
Medical titanium alloys	Isotropy	0.34	110000	4.5
PEEK	Isotropy	0.1	3800	

TABLE 11: Contact types and properties.

Contact type	Iterations	Normal behavior (separation)	Tangential behavior (sliding)
Bonded	1	Nondisjunction	Nonslip
No separation	1	Nondisjunction	Allow the sliding
No separation	Many times	Clearance allowed	Allow the sliding
Rough	Many times	Clearance allowed	Nonslip
Frictional	Many times	Clearance allowed	Allow the sliding

people is generally behind, while the gravity line of older people is slightly ahead. According to the above theory, we assumed that the gravity line passed through the 7th cervical vertebra and applied a load of 500 N perpendicular to the ground on the 7th cervical vertebra, so as to simulate the gravity line when normal people stand as much as possible, and then calculated the force on the spine and the stress changes of different interbody fusion materials. The force on the spine is obviously different with the human posture. After loading 500 N force on the back of the cervical 7 spine in the four groups to simulate the normal human gravity line, the stress of the interbody fusion material in the whole and lumbar 2-lumbar 5 spine screw system was analyzed [28].

Equivalent compressive stress of the l4-l5 vertebral body-combined screw rod system: the maximum compressive stress of model A, model B, and model C was all in the pedicle of L5—A: 188.24 MPa, B: 184.76 MPa, and C: 187.03 MPa, respectively; in model D, the maximum compressive stress is in the connecting rod part, which is much larger than the first three groups, at 348.19 MPa.

The maximum compressive stresses of the nail rod system are all in front of the connecting rod—model A: 36.43 MPa; model B: 21.81 MPa; model C: 33.48 MPa; and model D goes up to 348.19 MPa.

The equivalent compressive stress between waist 4 and waist 5 is as follows: model A is basically distributed in the rear of the annulus fibrosus, and the maximum compressive stress is 0.92 MPa. The maximum compressive stress of model B and model C is at the back of the fusion material—model B: 6.31 MPa; model C: 73.35 MPa. The stress value of the intervertebral body is less than the limit stress of the corresponding material, and the effective strength support can be achieved within the online elastic range. The maximum compressive stress of lumbar 2/3 and 3 and 4 intervertebral discs was 2.57 MPa and 4.91 MPa, respectively. The maximum compressive stress in the third lumbar spine was 3.62 MPa at the posterior edge of the vertebral body, and the maximum compressive stress in the fourth lumbar spine was 19.71 MPa around the pedicle.

The maximum compressive stresses in model A, model B, and model C were all located at the pedicle of L5 with

similar values, while the maximum compressive stress in model D was located at the lumbar connecting rod, which largely indicated that a large part of compressive stress after l4/5 fusion was transmitted to L5 through the bilateral connecting rod in the upright state. On the pedicle of the vertebral body, the conduction force through the vertebral body was reduced compared with that without surgery. The working compressive stresses of the screw rod system in model A, model B, and model C were all small and close in value, which was much smaller than that in model D with blank intervertebral space, indicating that most of the loads in the first three models were dispersed and transmitted through the annulus fibrosus nucleus pulposus bone crusher and PEEK fusion device. Although the maximum compressive stress of the intervertebral section in the first three models is different, the load through the intervertebral material conduction is not different in general. In this chapter, DICOM medical images were used to establish four groups of finite element models of human vertebra-interbody fusion screw rod system for different materials used in posterior lumbar surgery, and stress changes of different materials used in human spine were analyzed under standing posture and compared with normal the human body. The following conclusions were drawn:

- (1) The three-dimensional finite element method is used to model the force applied in the direction of gravity and calculate the force on the normal spine
- (2) Pure spinous process lamina can be used to achieve effective mechanical support in posterior sublumbar interbody fusion

5. Conclusion

In this paper, the basic problems of isodigital orthopedic technology in orthopedic assisted therapy were studied, and the main conclusions were as follows:

- (1) Within a certain range, the lower the CT scan interval is, the higher the accuracy of 3D reconstruction model is. In the software Mimics, optimal is the

fitting option to obtain the best accuracy of the 3D model. Different 3D processing processes produce different reasons for the error of the model. Environmental temperature and other factors have an impact on the model. For the bone, it is not the highest accuracy of the processing method. The shape of the skeleton and the purpose of the printing model should be considered to select the appropriate printing method

- (2) In surgical operations, the application of VR 3D printing technology to preoperative simulation can allow doctors to truly observe the structure of the surgical site and provide a reliable basis for clinicians to choose the correct treatment and surgical methods, so as to provide preoperative diagnosis. It can shorten the operation time, minimize the surgical incision, and reduce the incidence of surgical complications, which has very important practical significance
- (3) The three-dimensional finite element method was used to model the load applied in the direction of gravity and calculate the force of the normal spine. Effective mechanical support strength can be achieved in posterior sublumbar interbody fusion with pure spinous process lamina. On the basis of the above findings, further study is necessary for the following two questions:
 - (i) When the same 3D printing process is adopted, do different slicing methods (i.e., printing directions) have any influence on the accuracy of the 3D printing model of bone, and what kind of influence will it have
 - (ii) The finite element model of the human spine does not consider the ligaments around the vertebral body, and the finite element model can be further improved to analyze the stress changes of the human spine at different postures

Data Availability

The labeled data set used to support the findings of this study is available from the corresponding author upon request.

Conflicts of Interest

There are no conflicts of interest.

Acknowledgments


This work is supported by Yantaishan Hospital.

References

- [1] Y. Yang, A. Yu, W. Xiao, Z. Sun, F. Liu, and F. Wu, "Strategies suggested for emergency diagnosis and treatment of traumatic orthopedics in the epidemic of COVID-19," *Chinese Journal of Orthopaedic Trauma*, vol. 22, no. 2, pp. 123–127, 2020.
- [2] X. Wang and T. Wang, "Current situation and prospect of technical standard system of trauma treatment under the background of disaster emergency," *Journal of Emergency Management and Disaster Communications*, vol. 2, no. 2, pp. 225–238, 2021.
- [3] C. L. Wang, L. L. Bo, J. J. Bian, and X. M. Deng, "Application of ultrasonic visualization technology in the treatment of war trauma," *Academic Journal of Second Military Medical University*, vol. 41, no. 7, pp. 885–890, 2020.
- [4] D. A. Back and D. Pfringer, "Digitalisierung in der orthopädie und unfallchirurgie," *Der Unfallchirurg*, vol. 123, no. 11, p. 829, 2020.
- [5] M. Adam, E. Alkaramany, A. Alhamoud, J. Derbas, A. Murshid, and G. A. Alhaneedi, "Appropriateness of the post-operative rehabilitation of low energy hip fractures in elderly in comparison with the aaos appropriate use criteria at a level one trauma center," *European Journal of Orthopaedic Surgery & Traumatology*, vol. 32, no. 2, pp. 219–227, 2022.
- [6] M. Rawal, T. S. Kathayet, N. Mahaseth, P. K. Rokaya, and S. Mahat, "Orthopaedic and trauma services during COVID 19 at Karnali Academy of Health Sciences: an early experience," *Journal of Karnali Academy of Health Sciences*, vol. 3, pp. 1–6, 2020.
- [7] M. V. Stogov, D. V. Smolentsev, and E. A. Kireeva, "Bone xenografts in trauma and orthopaedics (analytical review)," *Traumatology and Orthopedics of Russia*, vol. 26, no. 1, pp. 181–189, 2020.
- [8] Z. Ow, C. K. Cheong, Y. H. Chin, and B. Z. Chin, "A look at the global impact of SARS CoV-2 on orthopedic services," *Journal of Clinical Orthopaedics and Trauma*, vol. 12, no. 1, pp. 33–39, 2021.
- [9] U. Hamsen, C. Waydhas, J. Bayer et al., "Trauma patients with SARS-CoV-2 in German ICUs during the 2nd wave of the COVID-19 pandemic," *European Journal of Trauma and Emergency Surgery*, vol. 48, no. 2, pp. 827–831, 2022.
- [10] K. Hang, L. Ying, J. Bai et al., "Knockdown of SERPINB2 enhances the osteogenic differentiation of human bone marrow mesenchymal stem cells via activation of the wnt/ β -catenin signalling pathway," *Stem Cell Research & Therapy*, vol. 12, no. 1, pp. 1–12, 2021.
- [11] A. Barié, T. Sprinckstüb, J. Huber, and A. Jaber, "Quadriceps tendon vs. patellar tendon autograft for ACL reconstruction using a hardware-free press-fit fixation technique: comparable stability, function and return-to-sport level but less donor site morbidity in athletes after 10 years," *Archives of Orthopaedic and Trauma Surgery*, vol. 140, no. 10, pp. 1465–1474, 2020.
- [12] L. Leppik, K. Oliveira, M. B. Bhavsar, and J. H. Barker, "Electrical stimulation in bone tissue engineering treatments," *European Journal of Trauma and Emergency Surgery*, vol. 46, no. 2, pp. 231–244, 2020.
- [13] A. R. Arain, C. T. Adams, S. F. Haddad, M. Moral, and A. J. Rosenbaum, "Diagnosis and treatment of peritalar injuries in the acute trauma setting: a review of the literature," *Advances in Orthopedics*, vol. 2020, Article ID 1852025, 8 pages, 2020.
- [14] O. V. Syniachenko, V. G. Klymovytsky, M. V. Yermolaeva, S. M. Verzilov, and K. V. Liventsova, "History of orthopedics in the mirror of numismatics," *Trauma*, vol. 21, no. 5, pp. 48–53, 2020.

Research Article

The Effect on Quality of Life after Three-Dimensional Intensity-Modulated Radiation Therapy in Patients with Low-Grade Glioma

Huili Chen, He Rao, and Yong Huang 

Department of Head and Neck Breast Chemoradiotherapy, Zhongnan Hospital of Wuhan University, Hubei Province 430071, China

Correspondence should be addressed to Yong Huang; t0211117@163.com

Received 16 June 2022; Revised 29 June 2022; Accepted 6 July 2022; Published 13 August 2022

Academic Editor: Pan Zheng

Copyright © 2022 Huili Chen et al. This is an open access article distributed under the Creative Commons Attribution License, which permits unrestricted use, distribution, and reproduction in any medium, provided the original work is properly cited.

Objective. To investigate the effect of three-dimensional intensity-modulated radiation therapy (IMRT) that accurately target delineation on quality of life (Qol) in patients with low-grade gliomas. **Methods.** From February 2015 to December 2019, 100 patients with low-grade gliomas were randomly divided into three-dimensional conformal radiotherapy control group ($n = 50$) and three-dimensional IMRT research group ($n = 50$). The scores of the Mini-Cog Assessment (Mini-Cog) and Montreal Cognitive Assessment Scale (MoCA), the self-care ability score (BI), and the effect of symptom improvement and the quality of life SF-36 score were compared between the two groups. **Results.** After radiotherapy, the self-care ability of patients in the two groups was significantly improved, and the improvement of study group was better than that of the control group ($P < 0.05$). The Mini-Cog and MOCA scores in the study group were significantly higher than those in the control group ($P < 0.05$). In addition, the symptom improvement effect and quality of life of the patients in the study group were also significantly better than those in the control group ($P < 0.05$). The scores of SDS and SAS of patients who underwent three-dimensional conformal IMRT were significantly lower than those of the control group. There was no significant difference in mortality between the two groups. **Conclusion.** Three-dimensional conformal intensity-modulated radiation therapy can delineate the target volume more accurately, regulate the intensity of radiation, and improve the symptoms and quality of life of patients with low-grade gliomas.

1. Introduction

Glioma is the most common primary brain tumor in adults. WHO classifies glioma into four grades, and clinically, gliomas of grades I to II are called low-grade gliomas (LGG), including low-grade malignant astrocytoma, oligodendrogliomas, and mixed gliomas [1, 2]. The clinical course of LGG is generally less aggressive than that of primary glioblastoma, with its incidence peaking in the third and fourth decade of life [3]. The natural history of tumors is largely determined by the tumor's histological subtype and genetic characteristics. Many patients live 15 years or more, while others die from the disease within a few years. Therefore, individualizing treatment remains a challenge.

Surgery is usually the preferred treatment. Although some patients can be cured, there are still some patients with

postoperative recurrence, or most tumors cannot be completely resected due to the limitation of the principle of tumor location and maximum protection of neurological function, and it is easy to transform from low-grade glioma to high-grade glioma [4]. Therefore, in addition to surgical resection, a variety of adjuvant treatments are also required, such as postoperative observation, radiotherapy, chemotherapy, and comprehensive treatment [5]. Adjuvant radiation therapy, as one of the current standard treatment options, has negative short- and long-term impacts on patients' neurocognitive function and health-related quality of life [6]. Three-dimensional conformal radiotherapy is a relatively advanced radiotherapy method, which focuses the radiation on the target area of the tumor according to the main shape of the tumor, so as to avoid unnecessary radiation to the surrounding normal tissues and organs, thus reducing the

complications of radiotherapy. Studies [7] have shown that, compared with low dose radiotherapy (45.0 Gy), higher dose radiotherapy (59.4 Gy) has a negative impact on LGG patients' quality of life in the short term. Since patients with low-grade glioma have a longer survival time than patients with high-grade glioma, the choice of treatment should take into account the quality of life of patients, so the relevant follow-up adjuvant radiotherapy has always been a controversial issue. In addition, due to the existence of edema area and the changes of normal anatomical structure after surgery, there are generally large errors in the determination of the target volume of postoperative radiotherapy, especially the definition of clinic target volume (CTV). In recent years, intensity-modulated radiation therapy (IMRT) has been favored because of its better conformity to the radiotherapy target volume and uniform dose distribution, which can better protect normal tissues around the target volume while treating tumors [8, 9]. Due to traumatic brain anatomical site of the specific tumor, with the brain tissue damage of tumor patients, the cognitive function, behavior, and ability are gradually decreased. In addition, radiation therapy is harmful to patients, and radiation damages brain and cognitive function, resulting in pain, severe helplessness, and despair of glioma patients, causing serious damage to their society and family, and even leading to rest and abandonment of treatment. So glioma patients have very low subjective experience of quality of life. With the development of modern medicine, clinical treatment is no longer limited to improving the survival rate and prolonging the survival period, meeting the physiological and psychological needs of postoperative patients, reducing functional sequelae, and improving the quality of life which has become a new trend in clinical research [10, 11]. With the development of the medical model to the biological, psychological, and social medical model, the evaluation index of treatment effect is no longer the single survival time as the only standard, and how to relieve patients' pain and symptoms and improve patients' psychological and life quality has become an important research topic. In the current patient-centered medical situation, efforts to maintain an acceptable quality of life for patients have become the primary goal of cancer treatment, and it is also a secondary indicator of most clinical oncology interventions. Therefore, in this study, 100 patients with low-grade glioma were selected as experimental subjects to explore the impact of IMRT on patients' quality of life.

2. Materials and Methods

2.1. General Information. In this study, 100 patients with low-grade glioma admitted to our hospital from February 2015 to December 2019 were selected as the research subjects. The average age of patients in the control group was 34.06 ± 5.81 years and a male to female ratio of 15:12. The average age of patients in the research group was 38.63 ± 8.21 years and a male to female ratio of 12:15. There were no significantly different ($P > 0.05$; Table 1). They were randomly divided into two groups by random number table method, with 50 patients in each group. Inclusion criteria are as follows: (1) patients with clinically diagnosed low-

TABLE 1: Comparison of the general information of the two groups of patients.

Group	Cases	Age	Gender (male/female)
Control group	50	34.06 ± 5.81	26.76 ± 2.02
Research group	50	38.63 ± 8.21	27.82 ± 1.43
<i>T</i> value		1.671	2.018
<i>P</i> value		0.831	0.994

grade glioma according to the guideline for diagnosis and treatment of glioma of central nervous system in China (2015); (2) normal blood routine, biochemical, electrocardiogram, chest X-ray, and abdominal color Doppler ultrasound results before treatment; (3) no lesions in the brain stem; and (4) both patients had clear consciousness and clear complaints before and after treatment. Exclusion criteria are as follows: (1) patients with mental disorders, (2) patients with other tumors, and (3) patients with allergic constitution. This study passed the ethical review of our hospital on January 5, 2015. Before enrollment, we informed patients of the purpose and process of the experiment, obtained informed consent from patients, and signed informed consent.

2.2. Research Methods. The control group received conventional three-dimensional conformal radiotherapy. According to the patient's condition, 5-7 irradiation fields were selected for irradiation. The area of glioma expanded by 2 cm was selected as CTV, and the radiation dose for the radical target volume was 66 to 72 Gy, with a total of 33 to 36 times. After operation, the radiotherapy dose for low-risk target volume was 50~54 Gy, with a total of 25~27 times. The radiotherapy dose of high-risk target volume was 56~60 Gy, with 28~30 times in total, once a day, with separated irradiation, 5 times for each week.

In the research group, three-dimensional conformal IMRT was used, and the radiation dose of each site should be controlled. The target volumes of the brain, face, lower neck, and supraclavicular region should be irradiated in a targeted manner. During radiotherapy, the thermoplastic mask was used for fixation, and thin layer (2-3 mm) CT scan was performed with a mesh head frame. CT data were transmitted to Peacock workstation to delineate target volumes and important anatomical structures. According to the location of lesions, the positional relationship between nerves and blood vessels, the tumor volume of patients, the total treatment dose, and the treatment times of patients were input into the workstation for reverse calculation. 80% to 90% were wrapped around the tumor or within the range of 1-2 cm outside the tumor with an isodose curve, and 4-21 treatments were performed with a single dose of 2.5-8 Gy, 3-5 times per week. Both groups of patients were treated with mannitol and hormone therapy after radiotherapy to reduce radiation nerve damage.

2.3. Observation Indicators and Curative Effect Standards. (1) The cognitive function of the two groups of patients was analyzed by the Mini-Cog Assessment (Mini-Cog) and the Montreal Cognitive Assessment (MoCA). The Mini-

Cog consisted of three-item recall and clock drawing from the Cognitive Abilities Screening Instrument (CASI). In three-item recall, 3 points were calculated for the immediate recall and 3 points for the short-term delayed recall. In clock drawing, a 3-point approach was applied for scoring: 1 point for drawing a circle, 1 point for drawing correct clock numbers, and 1 point for drawing precise clock period. Regular clock drawing was measured when all time criterions were precise, and the hand point was reliable with the indicated time. The MoCA evaluation indexes included executive and visual-spatial function, attention, naming, abstract thinking, linguistic expression, delayed recall, and orientation, with a total score of 0 to 30 points. The higher the score, the better the cognitive function. All the above tests were performed by the same attending physician with relevant training when the patient's mood was stable. (2) Barthel Index (BI) was used to compare patients' self-care ability. The scale mainly included 10 items, including eating, bathing, dressing, self-care of defecation and urination, toileting, bed to chair shifting, walking on level ground, and stair climbing, with a total of 25 items with a full score of 100 points. The higher the score, the stronger the self-care ability. (3) Quality of life questionnaire QLQ-H&N35 scale was used to evaluate the improvement effect of symptoms, including cough, pain, dry mouth, sticky saliva, dysphagia, and eating difficulty. The measurement time was 3 months after treatment; the lower the score was, the lighter the symptoms were. (4) The health survey short form SF-36 scale was used to evaluate the improvement effect of quality of life, including physiological function, role physical, physical pain, general health, energy, social function, emotional function, and mental health. The measurement time was 3 months after treatment; the higher the score, the better the quality of life. (5) Self-Rating Depression Scale (SDS) score and Self-Rating Anxiety Scale (SAS) score were used to evaluate the psychological state of the patients, and the measurement time was 3 months after treatment. SDS and SAS scores are as follows: less than 50 points indicates no depression/anxiety; a score of 50 to 60 indicates mild depression/anxiety; a score of >60 to 70 indicates moderate depression/anxiety. A score of >70 indicates severe depression/anxiety. (6) The mortality and disability rates of the two groups were observed during 2-year follow-up.

2.4. Statistical Analysis. SPSS 26.0 software was used for statistical analysis of data in this study. Measurement data were expressed by $\bar{x} \pm s$, and t test was used for the comparison between the two groups. The count data were expressed as rate (%) and were compared using χ^2 test. $P < 0.05$ was considered statistically significant.

3. Results

3.1. Mini-Cog and MoCA Scores of the Two Groups of Patients. The Mini-Cog and MoCA scores of the patients in the research group were 26.24 and 27.82, respectively, showing significant differences ($P < 0.05$) compared with the 25.19 and 26.76 scores in the control group, as shown in Table 2.

TABLE 2: Comparison of Mini-Cog and Mo CA scores between the two groups of patients ($\bar{x} \pm s$, points).

Group	Cases	Mini-Cog	MoCA
Control group	50	5.46 \pm 0.76	26.76 \pm 2.02
Research group	50	7.59 \pm 0.83	27.82 \pm 1.43
T value		-1.083	-3.028
P value		0.001	0.003

TABLE 3: Comparison of self-care ability scores between the two groups of patients ($\bar{x} \pm s$, points).

Group	Cases	Before radiotherapy	After radiotherapy
Control group	50	71.22 \pm 12.23	72.54 \pm 7.69
Research group	50	70.16 \pm 15.12	76.89 \pm 9.87
T value		0.385	-2.458
P value		0.701	0.016

3.2. The Self-Care Ability Scores of the Two Groups of Patients. Before radiotherapy, the self-care ability scores of the control group and the research group were 71.22 points and 70.16 points, and there was no significant difference between them ($P > 0.05$). After radiotherapy, the self-care ability score of patients in the research group was 76.89 points, significantly higher than 72.54 points in the control group ($P < 0.05$), as shown in Table 3.

3.3. Symptom Improvement Effect of Two Groups of Patients. The QLQ-H&N35 questionnaire scores of the patients in the research group were significantly lower than those in the control group in terms of cough, pain, dry mouth, sticky saliva, dysphagia, and eating difficulty ($P < 0.05$), as shown in Table 4.

3.4. The Improvement Effect of Quality of Life of the Two Groups of Patients. The scores of patients in the research group were higher than those in the control group in terms of physiological function, role physical, physical pain, general health, energy, social function, emotional function, and mental health, with significant differences ($P < 0.05$), as shown in Table 5.

3.5. Comparison of the SDS Score and SAS Score between Two Groups of Patients. The SDS score of the patients in the research group before radiotherapy was 76.62, and the SDS score of the patients in the control group before radiotherapy was 74.56. There was no significant difference between them ($P > 0.05$). After radiotherapy, the SDS scores of the patient in the research group and the control group were 58.18 and 66.39, respectively, showing significant differences ($P < 0.05$). Before radiotherapy, the SAS score of the patient in the research groups and the control groups was 71.60 and 72.89. There was no significant difference between them ($P > 0.05$). After radiotherapy, the SAS scores of the patient in the research group and the control group were 58.16 and 65.72, respectively, showing significant differences ($P < 0.05$), as shown in Table 6.

TABLE 4: Comparison of symptom improvement effect between two groups of patients ($\bar{x} \pm s$, points).

Group	Cases	Cough	Pain	Dry mouth	Sticky saliva	Dysphagia	Eating difficulty
Control group	50	1.21 \pm 0.30	4.24 \pm 0.87	2.25 \pm 0.48	1.25 \pm 0.22	5.65 \pm 1.27	2.05 \pm 0.38
Research group	50	0.91 \pm 0.23	4.03 \pm 0.62	1.86 \pm 0.39	1.03 \pm 0.31	4.79 \pm 1.12	1.95 \pm 0.51
<i>T</i> value		3.741	2.603	3.316	2.232	3.591	1.112
<i>P</i> value		0.001	0.011	0.001	0.028	0.001	0.269

TABLE 5: Comparison of the improvement of quality of life between the two groups of patients ($\bar{x} \pm s$, points).

(a)

Group	Cases	Physiological function	Role physical	Physical pain	General health
Control group	50	84.34 \pm 5.12	72.12 \pm 6.33	73.76 \pm 7.45	73.87 \pm 8.45
Research group	50	87.41 \pm 7.34	76.37 \pm 7.12	78.41 \pm 9.19	77.56 \pm 7.04
<i>T</i> value		-2.426	-3.154	-2.779	-2.372
<i>P</i> value		0.017	0.002	0.007	0.020

(b)

Group	Cases	Energy	Social function	Emotional function	Mental health
Control group	50	66.67 \pm 7.88	79.54 \pm 9.03	82.56 \pm 6.31	81.56 \pm 6.78
Research group	50	71.12 \pm 7.81	86.11 \pm 8.23	85.77 \pm 5.92	85.72 \pm 7.01
<i>T</i> value		-2.836	-3.082	-2.623	-3.061
<i>P</i> value		0.006	0.001	0.010	0.003

TABLE 6: Comparison of the SDS score and SAS score between two groups of patients ($\bar{x} \pm s$, points).

Group	Cases	SDS score before radiotherapy	SDS score after radiotherapy	SAS score before radiotherapy	SAS score after radiotherapy
Control group	50	74.56 \pm 5.12	66.39 \pm 6.18	72.89 \pm 6.53	65.72 \pm 5.50
Research group	50	76.62 \pm 5.94	58.18 \pm 5.84	71.60 \pm 5.98	58.16 \pm 7.52
<i>T</i> value		1.204	8.206	0.840	8.682
<i>P</i> value		0.207	<0.001	0.873	0.006

TABLE 7: Comparison of the mortality rate between two groups of patients (n , %).

Group	Cases	Death
Control group	50	2 (4%)
Research group	50	1 (2%)
χ^2 value		4.321
<i>P</i> value		0.701

3.6. *Comparison of the Mortality Rate between Two Groups of Patients.* The mortality of the control group was higher than that of the research group, but the difference was not statistically significant ($P > 0.05$), as shown in Table 7.

4. Discussion

Brain glioma is a malignant tumor disease. At present, with the change of people's living habits, the incidence of brain

glioma is increasing [12]. Although surgical resection of glioma lesions is the first choice in clinical practice, tumor cells grow in an infiltrative manner, and patients with surgery alone have a poor prognosis. Multiple adjuvant therapy methods are needed to further inhibit the malignant proliferation and metastasis of tumor cells.

Relevant studies [13] have shown that head and neck tumors are moderately sensitive to radiotherapy. Compared with conventional radiotherapy, three-dimensional conformal radiotherapy can avoid irradiation of 30% to 40% of normal brain tissue, thus effectively improving the local control rate of brain tumor and patient survival rate, and has become the first choice for brain tumor radiotherapy. Although it has good therapeutic effect, there are still problems such as incomplete target delineation and difficulty in meeting the uniformity of intensity, resulting in severe damage to peripheral lesions and affecting the quality of life of patients. Accurately delineating the target volume and adjusting the radiation dose are crucial for glioma patients

[14, 15]. IMRT is an in vitro stereotactic radiotherapy developed on the basis of three-dimensional conformal radiotherapy, including photon beams, proton beams, and heavy ion beams. The method is based on the preoperative CT results of patients to develop targeted targets, and the targeted area is analyzed anatomically, and then, the intensity of radiation is adjusted to accurately deliver radiation to the lesions. It can not only increase the conformal degree of the target volume but also has the characteristics of scientific dose distribution, uniform dose in the radiation field, and compact dose gradient, which can effectively improve the tumor radiotherapy dose and reduce the radiation dose of normal tissues around the target volume, enhance the therapeutic effect, and improve the efficacy and safety of treatment [16]. Cancer patients have a series of psychological disorders due to the sudden knowledge of the disease and the worry about the disease in the hospital treatment process, the fear of bringing huge economic burden to the family, the fear of surgery, etc., which is not conducive to the postoperative rehabilitation of patients, affecting the quality of life of patients.

Quality of life is an indicator system that reflects the long-term impact of internal and external environment on human physiology, psychological, social activities, and life satisfaction. As an important part of the function of various organs, once the brain tissue is damaged, it will have a negative impact on the quality of life of patients. With the continuous development of diagnosis and treatment technology, as well as the continuous improvement of people's medical awareness, while focusing on the prognosis, more attention is paid to the quality of life of patients [17]. Improving the patient's quality of life means a positive change in both physical and psychological status, which is also a clinically accepted standard of prognosis. Therefore, how to improve the postoperative quality of life of patients through treatment is an important goal of intracranial tumor treatment [18]. In addition, most patients have a variety of nervous anxiety about the brain tumor, coupled with the various symptoms caused by the tumor, so that patients are prone to a variety of bad emotions during hospitalization, which have a negative impact on the prognosis of patients [19]. In addition to the highest dose of radiation irradiation at the primary tumor site, the surrounding adjacent tissues also inevitably received higher doses, leading to acute side reactions such as oral mucositis, oral pain, dry mouth, dysphagia, difficulty in opening the mouth, and decreased taste during radiotherapy [20]. Related studies suggest that there is a significant negative relationship between symptom severity and its quality of life in each time period before and after radiotherapy [21].

In this study, we found that the scores of self-care ability of patients who underwent three-dimensional conformal IMRT were significantly higher than those of the control group. In the results of the quality of life questionnaire, patients in the three-dimensional conformal IMRT research group had significantly less symptoms such as cough, pain, dry mouth, sticky saliva, dysphagia, and eating difficulty. This is because IMRT can protect the brain stem, spinal cord, and parotid gland, increase the conformal degree of target volume, and thus have a low impact on patients' normal self-care life and reduce the adverse reaction symptoms in the process of radiotherapy. It is well known that advanced radiation encephalop-

athy caused by radiation therapy can seriously affect the quality of life of patients. In our results, the improvement of quality of life in the research group was similar to the quality of life assessment results of children with brain tumor undergoing proton beam radiotherapy in Massachusetts General Hospital, USA, and the scores of 4 out of 5 assessment items in the proton beam radiotherapy group were similar to those in the healthy control group [22]. The research of M.D. Anderson Cancer Center also showed that proton beam radiotherapy is more beneficial to the protection of children's neurocognitive function and avoid intellectual impairment [23].

Due to the lack of understanding of the disease and the worry about treatment effect, cost, and other aspects, most patients with craniocerebral tumor have varying degrees of anxiety and depression, resulting in patients unable to actively cooperate with the treatment. Negative emotions also tend to lead to patients with reduced immunity, endocrine disorders, energy deficiency, and other serious impact on patients' quality of life. It affects the treatment and prognosis of patients [24]. Our study found that the scores of SDS and SAS of patients who underwent three-dimensional conformal IMRT were significantly lower than those of the control group. These results suggest that the negative emotions of patients in the research group have been improved.

This is consistent with our conclusion; namely, patients receiving three-dimensional conformal IMRT had higher Mini-Cog and MoCA scores, the scores of physiological functions, role physical, physical pain, general health, energy, social function, emotional function, and mental health were higher than those of the control group, and the negative effects on patients' functions were lower. Age and education had little effect on Mini-Cog. And it reduced the error caused by age and educational background [25]. The negative effects were due to irradiation of specific radiation-sensitive areas, such as the hippocampus, and the lasting effects of increased treatment. This is because the dose intensity and range of three-dimensional conformal IMRT are mainly adjusted according to the three-dimensional shape of the patient's target volume, the relationship between target volume and organ, and the anatomical relationship between target volume and organ, so as to avoid great damage to normal organs and tissues. These results suggest that controlling the dose of radiation to a specific target volume and uniform dose of irradiation can prevent brain injury and subsequent negative effects on patient's function. There was no significant difference in mortality between the two groups, possibly due to insufficient follow-up and the lower mortality rate of low-grade gliomas compared to high-grade gliomas.

In conclusion, three-dimensional conformal IMRT can delineate the target volume more accurately and regulate the radiation intensity, which has a positive effect on the improvement of symptoms and quality of life of patients with low-grade glioma, and is safe and effective.

Data Availability

The labeled datasets used to support the findings of this study are available from the corresponding author upon request.

Conflicts of Interest

The authors declare no competing interests.

References

- [1] N. Samudra, T. Zacharias, A. Plitt, B. Lega, and E. Pan, "Seizures in glioma patients: an overview of incidence, etiology, and therapies," *Journal of the Neurological Sciences*, vol. 404, pp. 80–85, 2019.
- [2] D. J. Brat, R. G. W. Verhaak, K. D. Aldape, W. K. A. Yung, and J. Zhang, "Comprehensive, integrative genomic analysis of diffuse lower-grade gliomas," *New England Journal of Medicine*, vol. 372, no. 26, pp. 2481–2498, 2015.
- [3] M. Ceccarelli, F. P. Barthel, T. M. Malta et al., "Molecular profiling reveals biologically discrete subsets and pathways of progression in diffuse glioma," *Cell*, vol. 164, no. 3, pp. 550–563, 2016.
- [4] L. Baohui, H. Dong, W. Hu, Z. Na, O. H. XieBaojun, and C. Qianxue, "The necessity and strategy of multidisciplinary diagnosis and treatment of glioma," *Chinese Journal of Clinical Neurosurgery*, vol. 25, pp. 731–733, 2020.
- [5] T. J. C. Wang and M. P. Mehta, "Low-grade glioma radiotherapy treatment and trials," *Neurosurgery Clinics of North America*, vol. 30, no. 1, p. 111, 2019.
- [6] L. Dirven, J. C. Reijneveld, M. J. Taphoorn et al., "Impact of radiation target volume on health-related quality of life in patients with low-grade glioma in the 2-year period post treatment: a secondary analysis of the EORTC 22033-26033," *International Journal of Radiation Oncology • Biology • Physics*, vol. 104, no. 1, pp. 90–100, 2019.
- [7] F. Pignatti, M. van den Bent, D. Curran et al., "Prognostic factors for survival in adult patients with cerebral low-grade glioma," *Journal of Clinical Oncology*, vol. 20, no. 8, pp. 2076–2084, 2002.
- [8] H. Dai, J. Huang, L. Chen, L. Z. Zhong, and Y. B. Zhou, "Dosimetric comparison of RapidArc and IMRT in hippocampus sparing during postoperative radiotherapy for glioma," *Chinese journal of Medical Physics*, vol. 35, no. 12, pp. 1404–1407, 2018.
- [9] P. Liu, G. Liu, G. H. Wang et al., "Comparison of dosimetric gains provided by intensity-modulated radiotherapy, volume-modulated arc therapy, and helical tomotherapy for high-grade glioma," *BioMed Research International*, vol. 2020, 9 pages, 2020.
- [10] A. S. Jakola, S. Gulati, C. Weber, G. Unsgård, and O. Solheim, "Postoperative deterioration in health related quality of life as predictor for survival in patients with glioblastoma: a prospective study," *PLoS One*, vol. 6, no. 12, 2011.
- [11] G. Lombardi, E. Bergo, P. Del Bianco et al., "Quality of life perception, cognitive function, and psychological status in a real-world population of glioblastoma patients treated with radiotherapy and temozolomide: a single-center prospective study," *American Journal of Clinical Oncology*, vol. 41, no. 12, pp. 1263–1271, 2018.
- [12] C. Xiaoye, "Difficulties and research progress of comprehensive diagnosis and treatment of brain glioma," *China Medical Information Herald*, vol. 35, p. 20, 2020.
- [13] S. Yao, K. Shi, and Y. Zhang, "Advances in hyperprogressive disease in patients with advanced non-small cell lung cancer treated with immunotherapy," *Zhongguofei ai za zhi=Chinese journal of lung cancer*, vol. 24, no. 4, pp. 271–278, 2021.
- [14] C. X. Ni, Y. Wang, T. G. Yu, J. Y. Zhou, X. F. Sheng, and G. Meng, "Primary study of DWI in the delineation of radiotherapy target volume of glioma," *Chinese Computed Medical Imaging*, vol. 24, no. 2, p. 4, 2018.
- [15] D. M. Li, X. H. Wu, and X. X. Zhu, "Impact of MRI-CT image registration on target delineation of postoperative radiotherapy for gliomas," *Chinese Journal of Cancer*, vol. 27, no. 5, pp. 544–548, 2008.
- [16] S. Philip, K. Ronny, F. John, E. Johnathan, and H. Dwight, "Clinical and molecular recursive partitioning analysis of high-grade glioma treated with IMRT," *American journal of clinical oncology*, vol. 42, no. 1, pp. 27–35, 2019.
- [17] D. Sabina, J. R. Shinn, S. Justin, R. William Russell, and S. J. Stephan, "Peri-incisional botulinum toxin therapy for treatment of intractable head pain after lateral skull base surgery: a case series," *Headache*, vol. 59, no. 9, pp. 1624–1630, 2019.
- [18] P. Sthl, B. Fekete, I. Henoch et al., "Health-related quality of life and emotional well-being in patients with glioblastoma and their relatives," *Journal of Neuro-Oncology*, vol. 149, no. 2, pp. 347–356, 2020.
- [19] P. O. Valko, A. Siddique, C. Linsenmeier, K. Zaugg, U. Held, and S. Hofer, "Prevalence and predictors of fatigue in glioblastoma: a prospective study," *Neuro-Oncology*, vol. 17, no. 2, pp. 274–281, 2015.
- [20] A. R. Giovagnoli, R. F. Meneses, A. Silvani et al., "Quality of life and brain tumors: what beyond the clinical burden?," *Journal of Neurology*, vol. 261, no. 5, pp. 894–904, 2014.
- [21] J. G. Vartanian, A. L. Carvalho, B. Yueh et al., "Long-term quality-of-life evaluation after head and neck cancer treatment in a developing country," *Otolaryngology - Head and Neck Surgery*, vol. 130, no. 10, pp. 1209–1213, 2004.
- [22] T. I. Yock, S. Bhat, J. Szymonifka et al., "Quality of life outcomes in proton and photon treated pediatric brain tumor survivors," *Radiotherapy and Oncology*, vol. 113, no. 1, pp. 89–94, 2014.
- [23] L. S. Kahalley, R. Peterson, M. D. Ris, L. Janzen, and D. Mabbott, "Superior intellectual outcomes after proton radiotherapy compared with photon radiotherapy for pediatric medulloblastoma," *Journal of Clinical Oncology*, vol. 38, no. 5, pp. 454–461, 2020.
- [24] F. W. Boele, W. Hoeben, K. Hilverda et al., "Enhancing quality of life and mastery of informal caregivers of high-grade glioma patients: a randomized controlled trial," *Journal of Neuro-oncology*, vol. 111, no. 3, pp. 303–311, 2013.
- [25] L. Xueyan, D. Jie, and Z. Shasha, "Comparison of the value of Mini-Cog and MMSE screening in the rapid identification of Chinese outpatients with mild cognitive impairment," *Medicine*, vol. 97, no. 22, article e10966, 2018.

Retraction

Retracted: A Method for Evaluating the Quality of Mathematics Education Based on Artificial Neural Network

Computational and Mathematical Methods in Medicine

Received 27 June 2023; Accepted 27 June 2023; Published 28 June 2023

Copyright © 2023 Computational and Mathematical Methods in Medicine. This is an open access article distributed under the Creative Commons Attribution License, which permits unrestricted use, distribution, and reproduction in any medium, provided the original work is properly cited.

This article has been retracted by Hindawi following an investigation undertaken by the publisher [1]. This investigation has uncovered evidence of one or more of the following indicators of systematic manipulation of the publication process:

- (1) Discrepancies in scope
- (2) Discrepancies in the description of the research reported
- (3) Discrepancies between the availability of data and the research described
- (4) Inappropriate citations
- (5) Incoherent, meaningless and/or irrelevant content included in the article
- (6) Peer-review manipulation

The presence of these indicators undermines our confidence in the integrity of the article's content and we cannot, therefore, vouch for its reliability. Please note that this notice is intended solely to alert readers that the content of this article is unreliable. We have not investigated whether authors were aware of or involved in the systematic manipulation of the publication process.

Wiley and Hindawi regrets that the usual quality checks did not identify these issues before publication and have since put additional measures in place to safeguard research integrity.

We wish to credit our own Research Integrity and Research Publishing teams and anonymous and named external researchers and research integrity experts for contributing to this investigation.

The corresponding author, as the representative of all authors, has been given the opportunity to register their

agreement or disagreement to this retraction. We have kept a record of any response received.

References

- [1] F. Bao and C. Wang, "A Method for Evaluating the Quality of Mathematics Education Based on Artificial Neural Network," *Computational and Mathematical Methods in Medicine*, vol. 2022, Article ID 6976654, 11 pages, 2022.

Research Article

A Method for Evaluating the Quality of Mathematics Education Based on Artificial Neural Network

Fuli Bao ¹ and Chong Wang²

¹Department of Ideology and Politics, Inner Mongolia Vocational and Technical College of Communications, Chifeng 024005, China

²School of Mathematical Sciences, Daqing Normal University, Daqing 163712, China

Correspondence should be addressed to Fuli Bao; z51414035@stu.ahu.edu.cn

Received 23 June 2022; Revised 16 July 2022; Accepted 20 July 2022; Published 12 August 2022

Academic Editor: Pan Zheng

Copyright © 2022 Fuli Bao and Chong Wang. This is an open access article distributed under the Creative Commons Attribution License, which permits unrestricted use, distribution, and reproduction in any medium, provided the original work is properly cited.

Teaching quality evaluation (TQE) is an important link in the process of school teaching management. Evaluation indicators and teaching quality have a complicated and nonlinear connection that is influenced by several variables. Some of these drawbacks include too much subjectivity and unpredictability, difficulty in defining index weights, sluggish convergence, and weak computer capacity. The current assessment techniques and models have these issues as well. This research uses an ANN model to assess the quality of mathematics instruction at colleges and universities (CAU) in order to address the challenging nonlinear issue of TQE and completes the following tasks. (1) The background and significance of TQE research are analyzed, and the domestic and foreign research status of TQE and neural network is systematically expounded. (2) The technical principle of DNN is introduced and the DDAE-SVR DNN model is constructed, and then, the evaluation index system of mathematics teaching quality is constructed. (3) The DDAE-SVR DNN model is put out as a potential alternative. The Adam method is used in the unsupervised training process to dynamically modify the learning step size for each training parameter. The spatial properties of the original data may be modified several times such that the reconstruction can be completed after many hidden layers have been applied. Data essentials such as precision, accuracy, and consistency are prioritized above all other considerations when generating the final product. Unsupervised prediction uses SVR and maps the complicated nonlinear connection into high-dimensional space in order to attain linearity in low-dimensional space, which is the goal of the supervised prediction process. The usefulness and benefits of the model provided in this research in the mathematics TQE may be verified by tests including the use of the TQE dataset and comparisons with other shallow models.

1. Introduction

Since our country's reform and opening up, we have seen remarkable growth in every sector. Every day, the need for skills grows, and the quality of a country's talent pool is linked to its overall competitiveness in the global marketplace [1]. The popularization of higher education is also related to the cultivation and reserve of talents. In order to narrow the gap between the educational level of our country and foreign countries and improve the quality of the people in an all-round way, our country has expanded the scale of college enrollment since 1999. Since the first full implementation of online enrollment in 2002, as of 2003, the number of undergraduate and junior college stu-

dents in general CAU nationwide has exceeded 10 million [2]. Quality teaching is a critical component of a school's overall administration, and it serves as a crucial indication for determining whether or not a school is succeeding. Teachers' TQE enables school leaders and managers comprehend the extent to which teaching goals have been met, as well as thoroughly and properly grasp the school's teaching work and enhance the quality of teaching [3]. TQE related to teaching quality will also become a very important task. TQE constitutes the basis of teaching activities in CAU and is the basic link to ensure the quality of personnel training in CAU. There are a number of ways in which the TQE may be used to improve teaching quality and promote change, and it has a significant

impact on overall educational quality. However, because teaching is a kind of mental labor, there is no fixed process, and the TQE system often contains nonquantitative factors, which constitutes the complexity and difficulty of TQE. The teaching process includes teaching and learning. A teacher's TQE is much more complicated than the quality evaluation of a product [4]. There are numerous aspects that go into the teaching process, which is a two-way street between the instructor and learner. There is a wide range of topics to consider when assessing a teacher's ability to instruct effectively. How to establish a scientific and reasonable TQE system so that it can evaluate the teaching quality objectively and fairly is a very meaningful subject. According to reference [5], the integration of information technology into higher education, the modernisation of educational material, and the general development of the quality of higher education should be a primary goal of this research. It is imperative that we tackle the challenge of evaluating the teaching quality at CAU in a fair and accurate manner in order to further the higher education reform and enhance CAU's teaching goals and quality. That is why studying ways to improve teaching quality at CAU has emerged as an essential research issue in the effort to make education and training more scientific and standardized. An ANN is a nonlinear system made up of a large number of computational neurons arranged in layers that may be altered in many ways. Large-scale parallel processing, self-organizing white learning, and nonlinear capabilities make it an attractive alternative to traditional computing methods in many situations. There are many applications where ANN may be used that standard techniques and models cannot, and the results are excellent. ANN is a mathematical model for processing computation. Gradient-descent correction is used in BPNN to rectify the error signal produced during forward propagation until the accuracy objective or the number of iterations is satisfied [6]. As time went on, researchers discovered that every closed interval continuous function could be approximated by a BPNN hidden layer, meaning that any three-layer BPNN could complete any n -to- m -dimensional mapping [7]. A deep learning structure called a multilayer perceptron, which has numerous hidden layers, may be utilized to handle increasingly difficult nonlinear problems [8]. Layer-by-layer unsupervised greedy training using DBN is being proposed by researchers. Multiple restricted Boltzmann machines (RBM) in sequence stack a DBN into a deep structure in the method, which offers promise for tackling optimization difficulties connected to deep structures. A deep structural model based on a multilayer auto-encoder is presented [9, 10]. There was a spike in DNN research when the findings were released, and neural network models' number of layers and size have both increased dramatically since then. A complete assessment of instructional activities is thus necessary, and this study suggests the DDAE-SVR DNN model as a solution for the limitations of the current methodologies and models. In order to improve the teaching quality to promote the reform and development of CAU, establish a scientific

TQE system in CAU to strengthen the teaching management of CAU.

2. Related Work

For a long time, many educators in our country have been constantly studying how to construct an objective and scientific TQE system and improve it. However, Western nations began sooner than my country and experienced some successes, which led to the development of more effective approaches such as multiple intelligences' theory and constructivism. Taylor assessment model was also developed [11]. Since the concept of TQE was formed in the second half of the 19th century, it can be divided into five stages: examination, test, description, reflection, and construction according to the characteristics of each period [12]. The initial TQE exists in the form of examinations, and the results are largely influenced by teachers' subjective judgments. In the 1930s, in order to strengthen the objectivity and rationality of evaluation, educators put forward the term test and formed the concept of educational evaluation. At this time, the achievement of educational goals is evaluated through the description of students' learning behavior. It can be said that this is a breakthrough development of pedagogical evaluation methods. Since the rapid economic growth of China has supplied the necessary conditions and materials for the development of Chinese education, a wide range of theoretical studies into TQE has been conducted. There have been several teaching assessment methods presented by educators throughout the years. Reference [13] established a TQE system using fuzzy algorithms to improve the quality evaluation of schools. It can also conduct self-evaluation in stages according to the actual situation of students. Reference [14] used the analytic hierarchy process (AHP) to quantitatively evaluate the teaching quality of CAU and formed a corresponding evaluation system. Reference [15] constructed a set of teaching quality monitoring system based on the concept of "people-oriented, three-dimensional integration." The "people-oriented" in the system mainly refers to teachers and students-oriented, while "three-dimensional" refers to the top-level dimension (school), the middle dimension (second-level college), and the basic dimension (teacher). Reference [16], under the guidance of the national dual innovation and development strategy, adopts the mathematical fuzzy AHP and introduces diversified evaluation methods to change the supervision function and solve the problems existing in the TQE. Reference [17] designs the implementation process of the blended teaching model and builds a blended TQE model according to the teaching results, which has achieved good results in practical applications. To guarantee that the quality of teaching is maintained, a variety of types of higher teaching assessment have been established across the globe and play a more active part in the teaching process. Because it is a nonlinear classification issue, assessing the quality of higher education instruction is complex. So while developing a TQE system, it is important to identify the most fundamental elements that may immediately represent the quality of teaching. With the development of computer technology and information

technology, many scholars have adopted a mathematical model to directly establish a TQE system. The content and methods of assessment are also diverse among CAUs because of their differing views on teaching excellence [18]. Reference [19] applied a multilevel evaluation model of type II fuzzy sets to the performance TQE. Reference [20] applied AHP and neural network in the TQE model. Reference [21] developed a TQE model by combining the fuzzy AHP with the fuzzy comprehensive assessment approach, giving higher education administrators another instrument for raising the level of teaching quality. Reference [22] applied the TOPSIS method of multiattribute decision-making in TQE for research. Reference [23] uses BPNN and related theories to formulate the evaluation index system, constructs an effective computer graphics TQE model, and uses this model to evaluate the actual teaching situation of related courses. Reference [24] proposed an optimized BP algorithm, and the results after applying it to actual training show that the evaluation model established by this algorithm has fast convergence speed and high accuracy and has broad application prospects in teaching evaluation problems in higher education. Reference [25] combined AHP and neural network, combined the advantages of the two, added a screening process in the evaluation, and finally got the AHP-BPNN evaluation model. Using the PSO method, Reference [26] establishes a complete model for evaluating college professors' teaching quality by optimizing a neural network and finding the global optimum network parameters. By using ANN theory in TQE, not only are the difficulties of qualitative and quantitative indicators in a complete evaluation index system solved but also are the challenges of establishing complicated mathematical models and analytical expressions inside a conventional evaluation process resolved. It also reduces the impact of human error on the assessment process, resulting in more precise and effective findings. The TQE model developed by neural network theory is a useful tool for TQE.

3. Method

3.1. Deep Neural Network Theory

3.1.1. Deep Neural Networks. DNN is a deepening structure of ANN, and its network structure contains multiple hidden layers, which can better obtain learning features from input sample data. Since the 1940s, a large number of scholars and research institutions have devoted themselves to the research of ANN models, but most of the models are shallow models containing only one hidden layer, for example, three-layer BPNN model, maximum entropy model, traditional Markov model, and conditional random field. The hidden layer of the model converts the original data information input into the network through the input layer into the feature space required by a specific problem or target, which is the key to information processing. It is mainly used in classification, regression, pattern recognition, and other problems. However, since the shallow neural network model has only one hidden layer, its computing power, efficiency, and modeling ability will be limited in the face of high-

order complex nonlinear functions. Therefore, the DNN that contains multiple hidden layer neural networks to better obtain the feature vectors of the sample data has become the focus of researchers. The training of neural network models with deep structures is not easy, and the mappings produced by deep models are nonconvex functions, which are extremely difficult to study theoretically. The proposal of DBN and unsupervised greedy layer-by-layer training algorithm has opened up the research wave of DNN model. The multiple hidden layers of the DNN model have good feature learning ability, and the acquired data features can well represent the nature of the data. In the training process of the DNN model, the unsupervised greedy layer-by-layer learning algorithm initializes the deep structure layer by layer and then uses the supervised algorithm to fine-tune the model parameters. This method overcomes the problems encountered in the training process of traditional models and improves the efficiency of DNN models. By designing multiple hidden layers, the DNN performs multiple feature space transformations on the sample data, obtains good data feature vectors, and realizes the fitting of complex nonlinear mapping relationships. The arrival of the era of big data has provided many datasets for the training of DNN models, such as ImageNet image recognition dataset and Project Gutenberg language model dataset.

3.1.2. Basic Model of Deep Neural Network. DNN may be implemented in a variety of ways. There are two primary models discussed here: the RBM model and the autoencoder model.

- (1) Autoencoder model: in 1986, the idea of an autoencoder was initially put out. It is an algorithm that is used mostly for data reduction and feature extraction. There are two networks that make up the autoencoder: one to encode and one to decode. There are three layers to this model. Error propagation utilizing the BP technique is the underlying premise, and network weights and thresholds are constantly updated to recreate the original data. In order to generate a copy of the original data, the final output data are trimmed. First, the encoder network transforms the input data, such as reducing the number of dimensions in the input data. By first synthesizing the original input data using a decoding network and then using an error function to assess how much of the original input data is being incorrectly reproduced, this may be done. In order to provide an output that is as close to the input as feasible, an autoencoder must find an approximation identity function. For example, if the input data feature vector is h in the hidden layer and the output feature vector is y , the decoder from the middle hidden layer to the output layer and the autoencoder from the input data feature vector to the middle hidden layer are used, respectively, to decode x and encode h , mapped using the following mathematical expression:

$$\begin{aligned} h &= f(x_i) = A_f(W_f x_i + p_i), \\ y &= g(h_i) = A_g(W_g x_i + p_j), \end{aligned} \quad (1)$$

where f and g are the encoding function and decoding function, respectively; A_f and A_g are the activation functions of encoding and decoding, respectively, which are generally nonlinear functions; W_f and W_g and p_i and p_j are the weight matrix and threshold value matrix of the network, respectively.

It is common for autoencoders to use the gradient descent approach in order to fine-tune layer weights and thresholds in order to reduce the amount of error in reassembling the original input data. MSE or cross-entropy loss (CEL) functions are often used as the cost function, and the expression is as follows:

$$\begin{aligned} L(x, y) &= \frac{1}{n} \sum_{i=1}^n (y_i - x_i)^2, \\ L(x, y) &= \frac{1}{n} \sum_{i=1}^n x_i \log(y_i) + (1 - x_i) \log(1 - y_i). \end{aligned} \quad (2)$$

- (2) RBM model: the RBM model is an improvement of the BM. An undirected two-layer graph model is used. Nodes between the visible and hidden layers are connected by the RBM model, while all other nodes are left unconnected. Boltzmann machine units are connected only between neighboring layers, and the cross-layer unit is not connected to the same layer unit. RBM's bipartite graph model assumes that the units in its visible and hidden layers may be distributed arbitrarily exponentially, $v_i \in \{0, 1\}$, $h_j \in \{0, 1\}$, where $(i = 1, 2, 3, \dots, n; j = 1, 2, 3, \dots, m)$. To determine the RBM model, we only need to get $\theta = \{w_{ij}, a_i, b_j\}$, where w_{ij} is the connection weight between the visible layer and the hidden layer unit and a_i and b_j represent the visible layer and the hidden layer, respectively, offset of the unit. For a given set of states (v, h) , the energy formulation of the RBM is as follows:

$$E(v, h|\theta) = - \sum_{i=1}^n a_i v_i - \sum_{j=1}^m b_j h_j - \sum_{i=1}^n \sum_{j=1}^m v_i w_{ij} h_j. \quad (3)$$

The joint probability distribution (v, h) of the visible layer unit and the hidden layer unit in a specific state may be determined by exponentiating and regularizing the energy function.

$$\begin{aligned} P(v, h|\theta) &= \frac{e^{-E(v, h|\theta)}}{Z(\theta)}, \\ Z(\theta) &= \sum_{v, h} e^{-E(v, h|\theta)}. \end{aligned} \quad (4)$$

This yields the marginal distribution of visible and buried layer unit sizes, with $Z(\theta)$ serving as a normalization factor. By using a greedy learning technique to train several RBMs, the DBN model may be thought of as a Bayesian probabilistic generative model.

3.2. DDAE-SVR Deep Neural Network Model

3.2.1. Deep Denoising Autoencoder. DDAE is a typical neural network architecture consisting of many DAE layered; therefore, it includes several hidden layers. In order to avoid overfitting during the training process, after unsupervised training, a model with strong robustness and generalization emerges from the DAE's addition of noise to the original input dataset. Dataset denoising is the first step in training a deep noise reduction autoencoder. Input nodes are often set to 0 with a specified frequency as a generic processing strategy. Once the dataset has been denoised, it is sent into the first DAE to perform the data feature modification. The output of the first DAE's hidden layer is utilized as the input feature vector for the second autoencoder's second autoencoding layer. Until all DAEs have been trained, the output of the preceding DAE's hidden layer is utilized as the input feature vector for the succeeding DAE. To put it another way, when the original data has been denoised, the data feature conversion is completed by training each hidden layer one by one, unsupervised. An error function may be used to calculate the difference between a reconstructed dataset and the original dataset. In order to complete the reconstruction of the original input dataset, error propagation and option weight and threshold adjustments are made using BP in order to lower the overall error. As an unsupervised training approach, this portion of the DDAE introduces the Adam method. A classification or regression prediction may be improved by changing the parameters of a classifier or predictor in the DDAE's actual output layer, which is a virtual representation of the DDAE's virtual output layer neurons.

3.2.2. Support Vector Regression. SVM is a machine learning technique based on statistical theory. As a decision surface, a categorization hyperplane is needed to separate positive and negative occurrences of the same notion more effectively. Classification, pattern recognition, and return are some of the most common uses for it. Some of the advantages of SVMs in dealing with complex nonlinear issues and high-dimensional pattern recognition may be attributed to the use of a limited number of learned patterns. It is difficult to represent in mathematical analysis the complicated nonlinear connection between the evaluation indicators and the TQE findings at CAU since there are numerous indications of teaching quality assessment. Although SVR has an excellent nonlinear function fitting ability, this issue may be solved by using it. As a result, in order to assess and forecast teaching quality, the output layer of the DNN model is predicted using SVR in this chapter. In multidimensional space, the SVR is divided into linear regression and nonlinear regression, which are then combined. SVR's nonlinear regression is the emphasis of this part, since the quality of

CAU's instruction is a complex nonlinear problem to solve. To achieve a linearization connection comparable to the low-dimensional space, SVR uses nonlinear regression to transfer a complicated nonlinear relationship onto a high-dimensional space. A nonlinear mapping function should be used to map the dataset S to a high-dimensional space, and the linear regression characteristics of the feature space H should be taken into consideration when setting up the mapping function for the dataset S that cannot be linearly separated in the original space R^n . As a result, to describe nonlinear issues linearly, do linear regression in H first in the feature space before returning to R^n , the original space. Given a kernel function $K(x_i, x) = (\mathcal{O}(x_i), \mathcal{O}(x))$, the representation of the built nonlinear function is as follows:

$$f(x) = \sum_{i=1}^s (\alpha_i - \alpha_i^*) K(x_i, x) + b. \quad (5)$$

3.2.3. DDAE-SVR Deep Neural Network Model. Low-level noise reduction due to the restricted computational and modeling capability of the shallow neural network model, the DDAE-SVR DNN model uses an unsupervised training layer and SVR as a prediction output layer to solve complicated nonlinear issues or analyze large-scale datasets. Instead of relying on techniques like first- and second-order moment estimation and second-order moment estimation, unsupervised training utilizes the Adam optimization methodology to boost convergence and processing power. After the input dataset has been denoised using a DDAE, the model is trained using unsupervised layer-by-layer learning. Make sure the unsupervised training data is as close to the original dataset as possible when generating feature vectors for the original input. An input feature vector created from the model's final output layer is fed into SVR as a predictor, and SVR is used as a predictor for the final output layer. The DDAE-SVR DNN model's two most important features are as follows.

- (1) For the DDAE-SVR DNN model, the original input data will be weighted according to a set percentage before being fed into the unsupervised layer-by-layer training technique to prevent overfitting. The characteristics have been set to 0 in order to improve the model's robustness and generalizability. Deep noise reduction autoencoders are mostly used during the unsupervised training phase of the learning process. Using the result of the first DAE as an input feature vector, the data from the input layer is sent into the second DAE for training, and so on. Each DAE becomes a hidden layer of DDAE once it has been trained. Iterate the Adam algorithm until a specified accuracy or number of iterations is attained, or until a specific number of iterations has been completed
- (2) The final output layer of the DDAE-SVR DNN model uses the feature vector from the DDAE's final hidden layer as an input feature vector for the supervised fine-tuning procedure. SVR, a supervised algo-

rithm, serves as the predictor in the final output layer. Predictive accuracy and efficiency are improved in this supervised prediction process by tuning parameters relevant to SVR

3.3. DDAE-SVR DNN Mathematics Education Quality Evaluation Model. It is possible to extract characteristics from the original sample data using the deep-structured neural network model's many hidden layers. To solve complex nonlinear issues or deal with the in-depth structure of large datasets, the neural network model introduced in this chapter is used by CAU. This is a normalized evaluation index sample data collection, and we have n samples in it. Assuming W is the weight matrices of the DDAE model's various layers, p is the threshold matrices, and \mathcal{O} is the DDAE model itself. As a result, once \mathcal{O} processes the incoming dataset, its expression is as follows.

$$\theta = \phi(WX + p), \quad (6)$$

where θ represents the output feature vector of the deep noise reduction autoencoder model, θ is input into the SVR model for evaluation and prediction, and f is used as a function of the SVR model; the expression is as follows.

$$y_d = f(\theta). \quad (7)$$

This chapter recommends that the evaluation sample data be divided into two sets: one for training and one for testing. The model is then trained using the training dataset. The test dataset is used to verify the model's performance in the TQE issue after developing a stable and optimal model. Figure 1 depicts the DDAE-SVR DNN model's flowchart for assessing the validity of the mathematical reasoning.

3.4. Mathematical TQE Index System. Multilevel and multi-objective optimization is the name of the game when it comes to the CAU TQE. As a result, the assessment indicators should not only represent the teaching process in its whole and objectively but also limit the number of evaluation indicators as much as feasible. Both "teaching" and "learning" are important concepts in classroom discussions. Both the students' and the teachers' evaluation indicators are based on input from those who are most acquainted with the teaching process and its distinctive features, namely, the students' and the teachers' evaluation indicators from the teaching supervision group. Students' evaluations of instructors might best represent the issues with educational activities since they serve as the major body of learning. The evaluation indicators are shown in Table 1.

Since the input data of the network has different dimensions and physical meanings, the input features have different numerical ranges and the numerical ranges between different features vary greatly, so the sample data is normalized and preprocessed. After normalization, the data is converted into $[0, 1]$ to reduce the difficulty of weight correction due to the large variation of the input value. On the other hand, the excitation function of the BPNN is a sigmoid function, and the derivative of the function changes in $[0, 1]$ in a

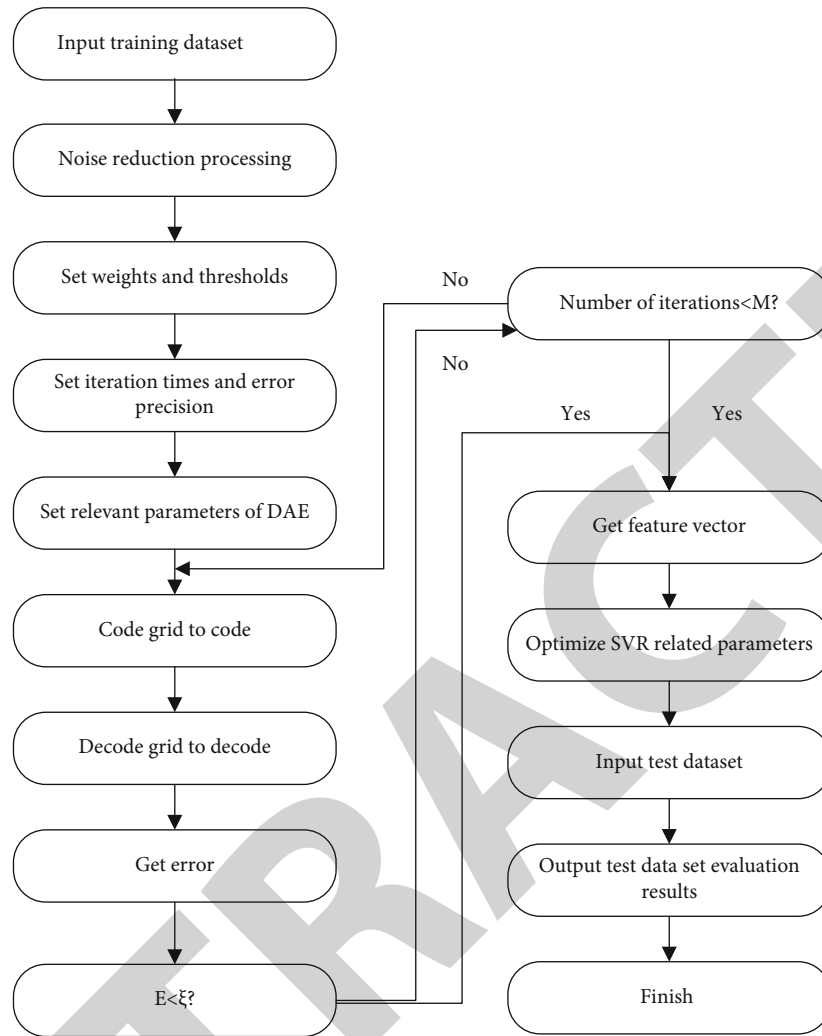


FIGURE 1: Flowchart of DDAE-SVR DNN model for evaluating mathematical quality.

TABLE 1: Mathematical TQE index system.

Index	Label
Lectures on time, dedicated to work	B1
Full of energy, serious, and contagious in class	B2
Openly listen to opinions and improve teaching methods and content	B3
Treat students equally	B4
Emphasis on basic theoretical knowledge and teaching of methods	B5
Difficulties are highlighted, and the details are appropriate	B6
Combining theory with practice	B7
Expand the frontiers of disciplinary knowledge	B8
Teaching students according to their aptitude and stimulating interest	B9
Explain clearly and logically	B10
Effective use of multimedia aids in teaching	B11
Satisfied with the teacher's attitude and methods	B12
Master most of the theoretical knowledge of course teaching	B13
Learn to analyze and solve problems independently	B14
Patiently answer students' questions	B15

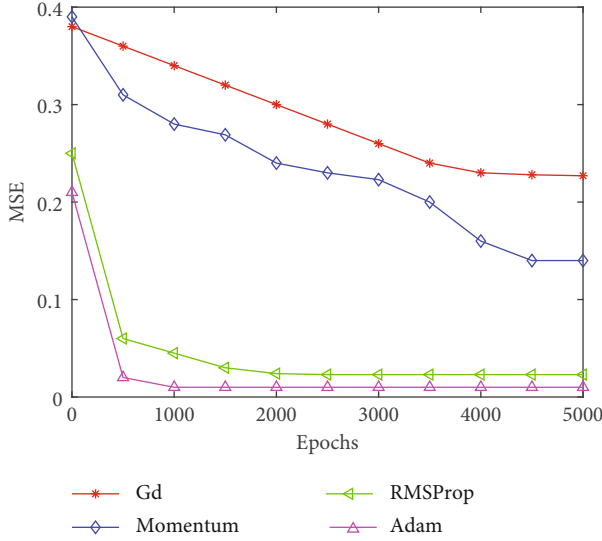


FIGURE 2: Comparison of training errors of different optimization algorithms.

large definition domain. The normalization of the sample data helps the network to converge as soon as possible, thereby improving the computational efficiency of BPNN. The method used in this article is as follows:

$$x_i = \frac{x - x_{\min}}{x_{\max} - x_{\min}}, \quad (8)$$

where x_{\max} represents the maximum value in the data, x_{\min} represents the minimum value in the data, and x and x_i represent the data before processing and the output data after processing.

4. Experiment and Analysis

4.1. Dataset Sources and Evaluation Indicators. This research uses data from a university's educational administration system to compile an assessment dataset for math courses taught between 2012 and 2018, totaling 1685 samples. Data gathered from students' evaluations of a teacher's teaching process is utilized as an input value in the assessment model. In order to ensure model verification, the comprehensive score is employed as the model's goal predicted output value based on the numerous lecture recordings of teaching supervision group instructors. A total of 1520 sample data were collected after analyzing the dataset and removing the data with high, low, and inconsistent evaluations. The resultant data samples are then subjected to normalization preprocessing.

As part of the DDAE, a new method known as the Adam algorithm is implemented, which minimizes output data error while preserving as many of the original data's key properties as possible. In order to increase the model's accuracy in making predictions, the key SVR parameters are tweaked in the supervised output layer. Performance comparison measurements are used to compare this model to other shallow models. Model assessment and prediction

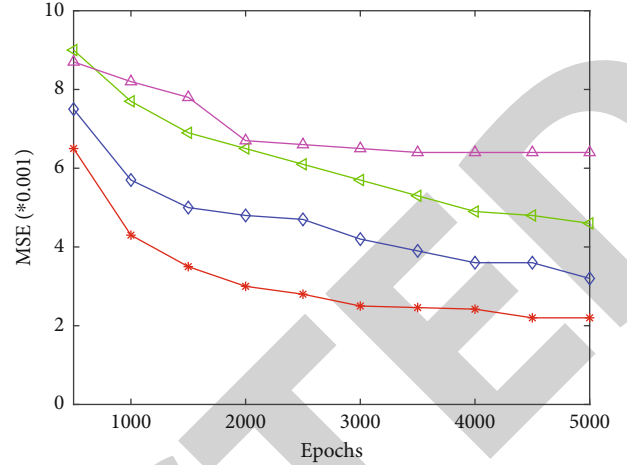


FIGURE 3: Comparison of layer errors of different hidden layers.

accuracy are evaluated using MAPE, MSE, SMAPE, and RMSE in this chapter's DDAE-SVR DNN model, which gives more advantages than other models in terms of mathematical quality evaluation. These are the formulas they use. This includes test data's sample size (n), actual value of the data (p_i), and its model's anticipated value (r_i).

$$\text{MAPE} = \frac{1}{n} \sum_{i=1}^n \left| \frac{r_i - p_i}{r_i} \right|,$$

$$\text{MSE} = \frac{1}{n} \sum_{i=1}^n (p_i - r_i)^2,$$

$$\text{SMAPE} = \frac{1}{n} \sum_{i=1}^n \frac{|r_i - p_i|}{(|r_i| + |p_i|)/2},$$

$$\text{RMSE} = \sqrt{\frac{1}{n} \sum_{i=1}^n (p_i - r_i)^2}.$$

(9)

4.2. Model Parameter Analysis. To get the most out of a TQE model, it is necessary to identify the model's important parameters. For the time being, much of it takes the shape of experiments. Throughout the experiment, model parameters are regularly changed to improve computing capacity and forecast accuracy and to discover the greatest possible combination of model parameters. In order to improve the model's accuracy in making predictions about the quality of the teaching process, this section employs both unsupervised learning training and supervised prediction output.

- (1) There are a variety of methods utilized in the neural network model's training phase, including the gradient descent and RMSProp techniques. Gradient descent has become a common optimization technique for neural network models with several hidden layers because of its slow convergence as it approaches the lowest value and its ease of slipping

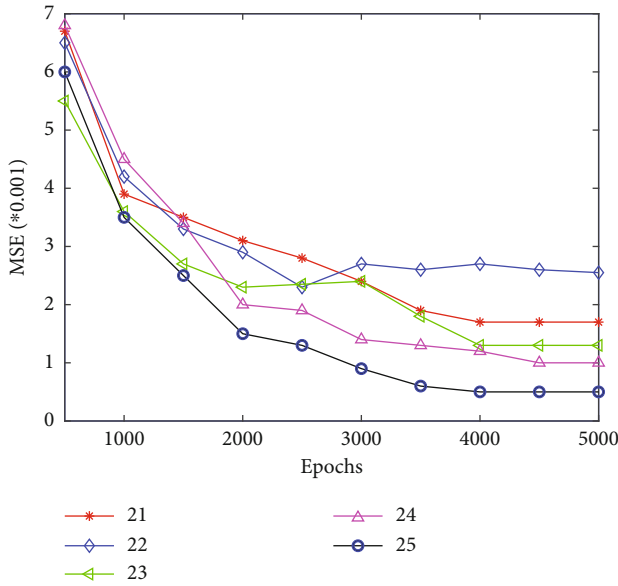


FIGURE 4: Selection of different numbers of neurons in the hidden layer.

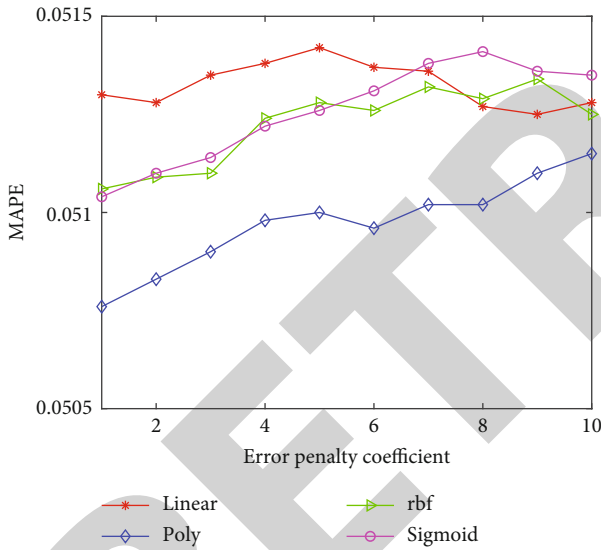


FIGURE 5: Selection of kernel function and penalty coefficient.

into the local minimum value. As a result, the Adam method is introduced in this part as an optimization strategy for the DDAE-SVR DNN model's unsupervised learning training. The Adam method dynamically adjusts the learning step size of each parameter using first- and second-order moment estimations of the gradient. Because of this, the settings are more or less constant between iterations. It is the MSE function and gradient descent that is used to figure out the error between unsupervised training output and input data in the DDAE-SVR DNN model, assuming there are three hidden layers and 20 neurons in each hidden layer. There are four optimization methods used to train and compute the

error: the RMSProp algorithm, momentum algorithm, and Adam algorithm. Their error change curves are given in Figure 2. According to Figure 2, the GD and momentum algorithms have been decreasing in efficiency, although at a slow pace and with an increasing number of rounds. Figure 2 illustrates a slow convergence rate. In the first 500 iterations, error in feature vectors generated by RMSProp and Adam algorithms may be quickly decreased utilizing these techniques. Regardless how many iterations are performed, the convergence of error tends to stay flat. The Adam algorithm is used as the optimal approach for unsupervised learning training because it is the most successful at recreating the original input data

Determine how many hidden layers a DNN model needs, and take into account the size of its evaluation dataset. The hidden layer has a total of 20 neurons and may have anywhere from 2 to 5 hidden layers. Unsupervised learning training uses the Adam algorithm as an optimization tool. The evaluation sample dataset is used to train the DDAE-SVR DNN model. We trained an unsupervised DDAE, and the resulting reconstructed feature vector differed significantly from the original input dataset, as seen in Figure 3. With more repetitions of training, it can be seen that there is a decrease in the error between output data and original input data. With a constant number of repetitive training, the error rises with each additional hidden layer. So, after unsupervised training, the DDAE-SVR DNN model with two hidden layers minimizes error between the reconstructed output data and the original input data.

The DDAE-SVR DNN model uses a range of 21 to 25 neurons in each hidden layer to arrive at the final number. Unsupervised learning is used in conjunction with two hidden layers and an optimization strategy in the Adam approach to build the model. Each time an evaluation sample dataset is introduced into the model during training, the hidden layer's number of neurons is modified to account for the changes. By training the DDAE unsupervised, the DDAE is able to rebuild the error curve between output data and the original input data, as illustrated in Figure 4. The error between the reconstructed output data and the original input data decreases while the number of neurons in the hidden layer stays constant. The more neurons in the hidden layer there are, the more effective iterative training is at correcting this error. DDAE-SVR DNN uses 25 hidden layers to provide output data with the lowest feasible error margin when compared to original input data.

- (2) Final hidden layer neurons may be acquired using DDAE-SVR DNN model's unsupervised learning and training approach, which reduces the error between the output data reconstructed from final hidden layer and original input data. For the model prediction output layer, a feature vector is utilized as an input. The model's final output prediction layer evaluates and predicts the TQE using the SVR prediction period. In terms of SVR performance, error

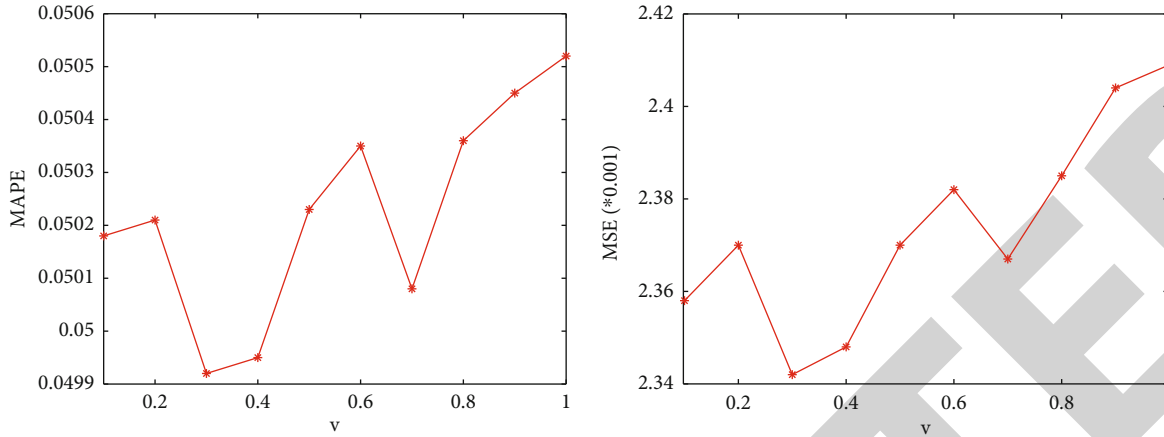


FIGURE 6: MAPE and MSE variation for different parameters v .

TABLE 2: Comparison of the results of various indicators of different models.

Model	MAPE	MSE	SMAPE (%)	RMSE	Training time (s)
Standard-BP	0.06856	47.52	1.52	6.89	16.37
SVM	0.04725	28.37	1.15	4.59	0.326
Adaptive BP	0.04673	26.56	1.12	4.45	0.535
DDAE-SVR	0.0451	24.12	1.11	4.28	5.126

penalty coefficient v and kernel function type are two of the most important considerations to make. This model’s complexity and risk may be changed by adjusting its mistake penalty coefficient. In the model, the number of support vectors and training errors is determined by the variable V , which has a range of $(0, 1)$. The distribution of sample data in high-dimensional space is controlled by the kernel function type. As a result, improving SVR’s prediction efficiency and accuracy requires tweaking these three key parameters. Kernel function types include linear, polynomial, sigmoid, and radial basis functions; the error penalty coefficient range is set at $[1, 10]$, $v = 0$, in light of the sample dataset’s size. Unsupervised training is the only way to uncover the last layer of information. As part of the DDAE-SVR DNN model’s prediction assessment, the output feature vector is utilized as an input feature vector for DDAE-SVR DNN model’s output feature layer. The SVR is then used to evaluate prediction accuracy. Figure 5 illustrates this. The MAPE error of the evaluation prediction increases as the error penalty coefficient increases, as can be shown in the figure. This is true regardless of the SVR kernel function employed as the error penalty coefficient. Due to the short sample size of the assessment dataset, an increase in the penalty coefficient will result in

an excessive penalty, which in turn will raise the MAPE. Using a polynomial function as a kernel function rather than the other three functions improves the SVR model’s prediction accuracy; hence, the error penalty coefficient for the SVR model has been set to 1

v , the training error parameter, is controlled by a polynomial kernel function, and an error penalty coefficient of 1 is used in this DNN model. The optimal value for $[0.1, 1]$ may be used to regulate the number of support vectors and training error. We use a feature vector from the model’s final hidden layer neuron that was trained without supervision to acquire the input feature vector for SVR. MAPE and MSE values both exhibit a decreasing and subsequently increasing pattern with respect to time as seen in Figure 6. If v is 0.3, this chapter’s model has the least prediction error and the highest accuracy.

4.3. *Comparison with Other Models.* According to this chapter’s hypothesis, the DDAE-SVR DNN model provided in this chapter has a better TQE than other models; hence, this chapter optimizes the model’s parameters. For comparison, three models of the conventional BPNN, SVM, and adaptive BPNN were built. To train and evaluate the model, input the evaluation sample dataset and denormalize the prediction and evaluation outcomes. Comparisons are made using performance measures like MAPE and MSE. Table 2 shows the comparing findings. There are several advantages to this neural network model; however, it takes longer to train than other neural network models, as seen in this table. Thus, this paper’s model has been shown to be successful.

5. Conclusion

High-quality talent is the primary aim of higher education, and teaching quality is an essential way of achieving this goal. The TQE at CAU is a crucial strand in the web of educational administration. Every day, college professors are evaluated on their ability to teach in an objective and fair manner using objective, scientific methods. It is a useful tool for assessing how well the school’s teachers are doing their

jobs. In order to increase the quality of instruction, managers may learn from teachers' classroom activities how well their teaching strategies are working in practice. However, TQE is mostly a nonlinear classification problem. It is a multifactor complex system with qualitative and quantitative indicators. Because the indicators are multilevel and complex, it is hard to put a finger on it using a predetermined mathematical model. TQE makes use of a number of well-established assessment techniques, including the weighted mean method, AHP, and the fuzzy comprehensive judgment approach, among others. Although some achievements have been achieved, there are still many defects, such as lack of self-learning ability, and it is difficult to make accurate evaluations. When determining the weight of each evaluation index, it is often estimated by experience, which leads to the subjective evaluation and cannot solve the problem well. Therefore, this paper builds a DDAE-SVR DNN model to evaluate the quality of mathematics teaching and completes the following tasks. (1) The background and significance of TQE research are analyzed, and the domestic and foreign research status of TQE and neural network is systematically expounded. (2) The technical principle of DNN is introduced and the DDAE-SVR DNN model is constructed, and then, the evaluation index system of mathematics teaching quality is constructed. (3) The DDAE-SVR DNN model is put out as a potential alternative. The Adam method is used in the unsupervised training process to dynamically modify the learning step size for each training parameter. The spatial properties of the original data may be modified several times such that the reconstruction can be completed after many hidden layers have been applied. Data essentials such as precision, accuracy, and consistency are prioritized above all other considerations when generating the final product. Unsupervised prediction uses SVR and maps the complicated nonlinear connection into high-dimensional space in order to attain linearity in low-dimensional space, which is the goal of the supervised prediction process. The usefulness and benefits of the model provided in this research in the mathematics TQE may be verified by tests including the use of the TQE dataset and comparisons with other shallow models. Лысенко

Data Availability

The datasets used during the current study are available from the corresponding author on reasonable request.

Conflicts of Interest


The authors declare that they have no conflict of interest.

References

- [1] E. I. Berseneva, O. N. Buzan, E. V. Lysenko, K. K. Khismatulina, and E. A. Tsapodoy, "Talent management as a new concept of human resource management: comparative analysis of best practices," *Management of the Personnel and Intellectual Resources in Russia*, vol. 8, no. 4, pp. 74–82, 2019.
- [2] T. H. Wong, "College admissions, international competition, and the Cold War in Asia: the case of overseas Chinese students in Taiwan in the 1950s," *History of Education Quarterly*, vol. 56, no. 2, pp. 331–357, 2016.
- [3] L. Zhou, H. Li, and K. Sun, "Teaching performance evaluation by means of a hierarchical multifactorial evaluation model based on type-2 fuzzy sets," *Applied Intelligence*, vol. 46, no. 1, pp. 34–44, 2017.
- [4] Y. Feng, Y. U. Gan, and H. Zhou, "Teaching quality evaluation model based on neural network and analytic hierarchy process," *Computer Engineering and Applications*, vol. 49, no. 17, pp. 235–3068, 2013.
- [5] M. Yuan and C. Li, "Research on global higher education quality based on BP neural network and analytic hierarchy process," *Journal of Computer and Communications*, vol. 9, no. 6, pp. 158–173, 2021.
- [6] N. Li, "A fuzzy evaluation model of college English teaching quality based on analytic hierarchy process," *International Journal of Emerging Technologies in Learning (ijET)*, vol. 16, no. 2, pp. 17–30, 2021.
- [7] W. Dai and P. Hu, "Application of BP neural network in the analytic hierarchy process of person-post evaluation model," *The Journal of Supercomputing*, vol. 76, no. 2, pp. 897–914, 2020.
- [8] Y. Zhou, Y. Niu, Q. Luo, and M. Jiang, "Teaching learning-based whale optimization algorithm for multi-layer perceptron neural network training," *Mathematical Biosciences and Engineering*, vol. 17, no. 5, pp. 5987–6025, 2020.
- [9] H. Zhang, T. Huang, S. Liu et al., "A learning style classification approach based on deep belief network for large-scale online education," *Journal of Cloud Computing*, vol. 9, no. 1, pp. 1–17, 2020.
- [10] J. Wang, "Speech recognition of oral English teaching based on deep belief network," *International Journal of Emerging Technologies in Learning*, vol. 15, no. 10, 2020.
- [11] W. X. Jiang and Y. Z. Zhong, "Research of teaching evaluation model based on ID3 decision making tree for polytechnic," *Journal of Applied Science and Engineering Innovation*, vol. 4, no. 3, pp. 95–98, 2017.
- [12] E. Lejonberg, E. Elstad, and K. A. Christophersen, "Teaching evaluation: antecedents of teachers' perceived usefulness of follow-up sessions and perceived stress related to the evaluation process," *Teachers and Teaching*, vol. 24, no. 3, pp. 281–296, 2018.
- [13] Y. Jiang and Y. Wang, "Evaluation of teaching quality of public physical education in colleges based on the fuzzy evaluation theory," *Journal of Computational and Theoretical Nanoscience*, vol. 13, no. 12, pp. 9848–9851, 2016.
- [14] H. Raharjo, M. Xie, T. N. Goh, and A. C. Brombacher, "A methodology to improve higher education quality using the quality function deployment and analytic hierarchy process," *Total Quality Management*, vol. 18, no. 10, pp. 1097–1115, 2007.
- [15] B. Zhong, Q. Wang, J. Chen, and Y. Li, "An exploration of three-dimensional integrated assessment for computational thinking," *Journal of Educational Computing Research*, vol. 53, no. 4, pp. 562–590, 2016.
- [16] Q. W. Dong, S. M. Wang, F. J. Han, and R. D. Zhang, "Innovative research and practice of teachers' teaching quality evaluation under the guidance of 'innovation and entrepreneurship'," *Procedia Computer Science*, vol. 154, pp. 770–776, 2019.

Review Article

Efficacy of Postoperative Analgesia by Erector Spinal Plane Block after Lumbar Surgery: A Systematic Review and Meta-analysis of Randomized Controlled Trials

Xiao Xiao,¹ Tingting Zhu,¹ Lin Wang,² Hongmei Zhou,¹ and Yanli Zhang¹ 

¹Department of Anesthesiology, The Second Hospital of Jiaying, China

²Department of Anesthesia Operating Room, The Second Hospital of Jiaying, China

Correspondence should be addressed to Yanli Zhang; 2016122558@jou.edu.cn

Received 7 June 2022; Revised 25 June 2022; Accepted 15 July 2022; Published 11 August 2022

Academic Editor: Pan Zheng

Copyright © 2022 Xiao Xiao et al. This is an open access article distributed under the Creative Commons Attribution License, which permits unrestricted use, distribution, and reproduction in any medium, provided the original work is properly cited.

Background. In recent years, erector spinae plane block (ESPB) has been increasingly used as a new regional block technique for postoperative analgesia; however, little is known on its benefits. Therefore, we performed a systematic review and meta-analysis to investigate the efficacy and safety of ESPB in lumbar spine surgery. **Methods.** Databases including PubMed, Embase, Cochrane Library, and Web of Science were systematically searched for randomized controlled trials (RCTs) comparing ESPB with no block in lumbar spine surgery until September 30, 2021. The primary outcome was opioid consumption after surgery. The Cochrane Collaboration's tool for assessing the risk of bias was used to evaluate the quality of included studies. **Results.** Fifteen RCTs involving 980 patients were included in the study. Opioid consumption 24 hours after surgery was significantly lower in the ESPB group standardized mean difference (SMD = -2.27, 95% confidence interval (95% CI) (-3.21, -1.32); $p < 0.01$). ESPB reduced pain scores at rest and on movement within 48 hours after surgery and the incidence of the postoperative rescue analgesia (RR = 0.32, 95% CI (0.31, 0.80); $p = 0.02$), while it significantly prolonged time to first rescue analgesia (SMD = 4.87, 95% CI (2.84, 6.90); $p < 0.01$). Moreover, significantly better patient satisfaction was associated with ESPB (SMD = 1.89, 95% CI (1.03, 2.74); $p < 0.01$). **Conclusion.** ESPB provides effective and safe postoperative analgesia after lumbar spine surgery.

1. Introduction

Severe postoperative pain after spinal surgery is a major factor affecting postoperative recovery and is associated with increased postoperative opioid use and prolonged hospitalizations [1]. The erector spinae plane block (ESPB) is a novel regional analgesia technique whereby local anesthesia (LA) is injected into the fascial plane deep into the erector spinae muscles and is considered a relatively safe and simple technique [2, 3]. First described in 2016 by Forero et al. [2], ESPB has been demonstrated to provide effective postoperative analgesia in thoracic and breast surgery [4]. A growing number of studies validated the benefits of ESPB, including

reduced postoperative pain scores, postoperative opioid consumption, and postoperative nausea and vomiting (PONV) risk [4, 5]. In recent years, some randomized controlled trials (RCTs) [6–8] have been published on the use of ESPB after lumbar spine surgery; however, the robustness of the findings was questionable due to the limited sample size. Herein, we conducted a meta-analysis to explore the efficacy and safety of ESPB in adult patients who received general anesthesia (GA) for lumbar spine surgery. Our primary outcome was postoperative opioid consumption. Secondary outcomes included postoperative pain score, time to first rescue analgesia, number of patients requiring rescue analgesia, patient satisfaction, the length of hospitalization, and adverse reactions.

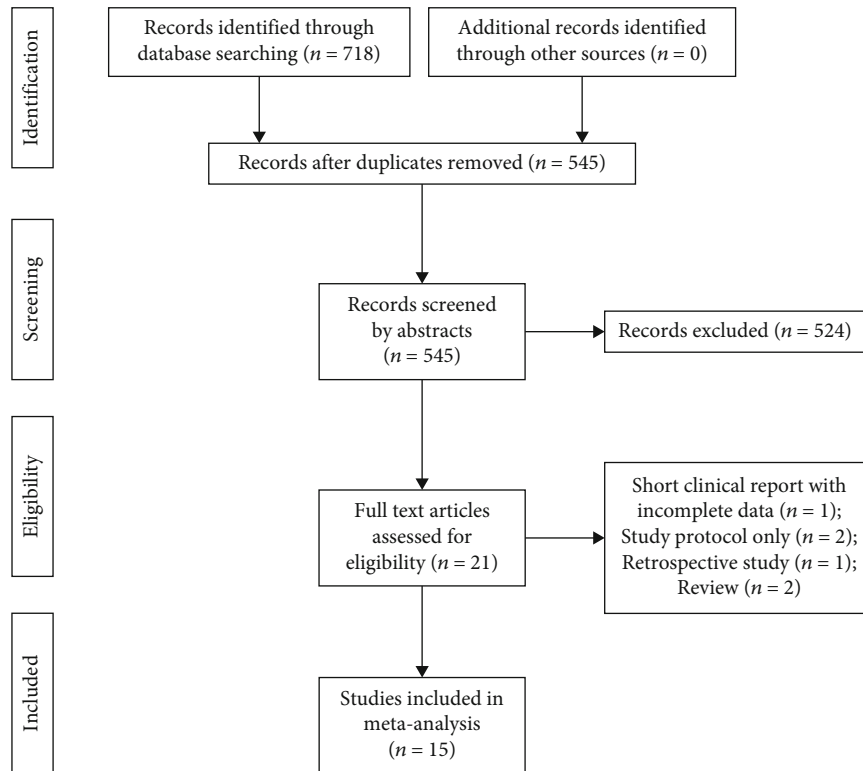


FIGURE 1: PRISMA flow diagram of the literature selection. Records excluded during screening step: no postoperative opioid consumption, letters, retrospective studies, case reports, reviews, incomplete clinical trials, studies without control groups, studies without full text, and conference abstracts were also excluded.

2. Methods

This systematic review and meta-analysis was based on the guidelines recommended by the Preferred Reporting Items for Systematic Reviews and Meta-Analyses (PRISMA) [9] and registered at the PROSPERO database (CRD42021276713).

2.1. Search Strategy. PubMed, Embase, the Cochrane Library, and Web of Science were systematically searched for relevant studies up to September 1, 2021, using the terms: (“Erector Spinae Plane Block” OR “Erector Spinae Plane Blocks” OR “Regional Anesthesia” OR “Regional Analgesia”) AND (“Lumbar Disc Disease” OR “Lumbar Spinal Surgery” OR “Lumbar surgery” OR “Lumbar fusion surgery” OR “Lumbar discectomy”). No restriction was made with respect to language. Additionally, reference lists of studies meeting the above criteria were reviewed to identify additional relevant articles that could be included.

2.2. Study Selection Criteria. Three authors (Z. YL., XX., and W. L.) independently searched the literature, and any point of disagreement was solved by a discussion with a fourth author (Z.TT). Search results were imported into EndNote X9, and duplicates were removed. All published RCTs with full text available that compared ESPB with no block after lumbar spine surgery were included in this study. Trials that did not report postoperative opioid consumption were excluded. Letters, retrospective studies, case reports, reviews,

incomplete clinical trials, studies without control groups, studies without full text, and conference abstracts were also excluded.

2.3. Data Extraction and Quality Assessment. Two authors (Z. YL. and X.X.) extracted the following information: first author, published year, type of surgery, techniques, concentration and volume of local anesthesia, postoperative analgesia, rescue analgesia, postoperative pain scores, postoperative opioid analgesic consumption, adverse reactions, etc.

To facilitate data analysis, we calculated the median and interquartile range (IQR) as described by Luo et al. [10] and the standard deviation (SD) as defined by Wan et al. [11]. For studies where the original data were presented in graphical format, the GetData graph digitizer was used to extract numerical data. The pain scores 48 hours after surgery at rest and on movement were extracted. If not otherwise stated, we assumed that pain scores were assessed at rest. Methodological quality assessment was independently done by the two authors (Z. YL. and X.X.) using Cochrane Collaboration’s tool for assessing risk of bias. We evaluated the quality of all studies based on seven aspects: trials were considered low quality if at least one category was graded “high risk of bias” while trials were considered high quality if the randomization and allocation concealment were both graded “low risk of bias,” and other items were graded “low risk of bias” or “uncertain risk of bias.” Finally, trials were considered moderate quality if no criteria for high or low risk of bias were met.

2.4. *Statistical Analysis.* Review Manager (RevMan, version 5.3, The Nordic Cochrane Centre, The Cochrane Collaboration, Copenhagen, Denmark) was used for this meta-analysis. For continuous data, the standardized mean difference (SMD) and 95% confidence intervals (CI) were calculated using random-effect model while for dichotomous data, the Mantel-Haenszel method was used to calculate the relative ratio (RR) and 95% CIs. The I^2 statistic was used to quantify statistical heterogeneity. If significant heterogeneity was observed ($I^2 < 50\%$), a fixed-effect model was adopted; otherwise, a random-effect model was applied. $p < 0.05$ (2-sided) was considered statistically significant. Funnel plots were used to evaluate the publication bias.

3. Results

3.1. *Results of Literature Search and Characteristics.* The initial search yielded 718 references, with no additional records from other sources. The records were imported into End-Note X9, and 524 unqualified records were excluded. After reading the title and abstracts, only 21 articles remained. Finally, 15 trials involving 980 participants met the inclusion criteria. A flowchart of the literature screening process is shown in Figure 1. The Cochrane Collaboration risk of bias tool (Figure 2) was used to determine the risk of bias in included studies.

Of the 15 trials included [6–8, 12–23], one [17] involved free-hand ESPB, while the others [6–8, 12–16, 18–23] were ultrasound-guided (USG-guided) ESPB. The main local anesthetics used included bupivacaine [6–8, 12–14, 16, 18, 19], ropivacaine [20–23], levobupivacaine [15], and mixtures of bupivacaine and lidocaine [17]. The features of the included trials are shown in Table 1.

3.2. *Primary Outcomes.* All trials [6–8, 12–23] reported postoperative opioid consumption; however, only one trial [13] reported opioid consumption 8 hours after surgery. The pooled analysis showed that ESPB could reduce 4 to 12 hours (SMD = -2.46, 95% CI (-3.62, -1.29); $p < 0.01$; Figure 3), 24 hours (SMD = -2.27, 95% CI (-3.21, -1.32); $p < 0.01$; Figure 4), and 48 hours (SMD = -0.83, 95% CI (-1.05, -0.60); $p < 0.01$; Figure 5) postoperative opioid consumption.

3.3. *Secondary Outcomes.* Moreover, ESPB significantly reduced postoperative pain scores at rest (PACU: SMD = -1.86, 95% CI (-2.59, -1.13); $p < 0.01$; 2 h: SMD = -1.73; 95% CI (-2.70, -0.75); $p < 0.01$; 4 h: SMD = -1.38, 95% CI (-2.15, 0.61); $p < 0.01$; 6 h: SMD = -2.26, 95% CI (-3.54, -0.99); $p < 0.01$; 12 h: SMD = -0.69, 95% CI (-1.14, -0.24); $p < 0.01$; 24 h: SMD = -0.52, 95% CI (-0.75, -0.29); $p < 0.01$; 48 h: SMD = -0.33, 95% CI (-0.61, -0.06); $p = 0.02$) and on movement (PACU: SMD = -1.31, 95% CI (-2.14, -0.48); $p < 0.01$; 4 h: SMD = -1.20, 95% CI (-2.31, -0.09); $p = 0.03$; 6 h: SMD = -8.24, 95% CI (-13.40, -3.08); $p < 0.01$; 12 h: SMD = -3.21, 95% CI (-5.67, -0.75); $p = 0.02$; 24 h: SMD = -1.05, 95% CI (-1.94, -0.17); $p = 0.02$; 48 h: SMD = -0.70, 95% CI (-1.05, -0.35); $p < 0.01$). Importantly, ESPB could significantly prolong time to first rescue analgesia (SMD = 4.87, 95% CI (2.84, 6.90); $p < 0.01$),

	Random sequence generation (selection bias)	Allocation concealment (selection bias)	Blinding of participants and personnel (performance bias)	Blinding of outcome assessment (detection bias)	Incomplete outcome data (attrition bias)	Selective reporting (reporting bias)	Other bias
Ciftci 2021	+	?	?	+	+	+	+
Eskin 2020	+	+	?	+	+	+	+
Ghamry 2019	+	+	?	+	+	+	+
Goel 2021	+	?	?	+	+	+	+
Siam 2020	+	+	?	?	+	+	+
Singh 2019	+	?	?	+	+	+	+
Wahdan 2021	+	?	+	+	+	+	+
Yayik 2019	+	?	?	+	+	+	+
Yesiltas 2021	+	?	+	+	+	+	+
Yörükoğlu 2021	+	?	+	+	+	+	+
Yu 2021	+	?	+	+	+	+	+
Zhang J 2021	+	+	?	+	+	+	+
Zhang Q 2021	+	+	?	+	+	+	+
Zhang T 2020	+	+	?	+	+	+	+
Zhu 2021	+	?	?	+	+	+	+

FIGURE 2: Methodological quality and bias risk in included trials. Green, yellow, and red represent low, unclear, and high risk of bias, respectively.

reduce intraoperative opioid consumption (SMD = -1.48, 95% CI (-2.35, -0.6); $p < 0.01$), and reduce the number of patients requiring rescue analgesia (RR = 0.32, 95% CI (0.13, 0.80); $p = 0.02$). Furthermore, ESPB could reduce the incidence of PONV (RR = 0.35, 95% CI (0.22, 0.55); $p < 0.01$), shorten the length of hospitalization (MD = -1.80, 95% CI (-3.21, -0.39); $p = 0.01$), and improve patient satisfaction (SMD = 1.89, 95% CI (1.03, 2.74); $p < 0.01$). Detailed information on the secondary outcomes is presented in Table 2.

TABLE 1: The features of the included trials.

Author/ year	Participants (<i>n</i>)	Age	Type of surgery	Techniques	ESPB group	Control group	Postoperative analgesia	Rescue analgesia
Ciftci et al. (2021) [6]	60	18– 65 years	1-level lumbar discectomy and hemilaminectomy surgery	USG- guided ESPB	40 mL of 0.25% bupivacaine	No block	PCIA fentanyl, 1 g paracetamol every 6 hours	Meperidine (0.5 mg/kg)
Eskin et al. (2020) [7]	80	18– 80 years	1- or 2-level lumbar decompression surgery	USG- guided ESPB	20 mL of 0.25% bupivacaine	No block	PCIA tramadol	Meperidine (0.5 mg/kg)
Elgebaly et al. (2019) [8]	60	18– 60 years	2-level lumbar spondylolisthesis (L3-L5)	USG- guided ESPB	20 mL of 0.25% bupivacaine	Sham blocks (20 ml normal saline)	Paracetamol 1 gm/6 hours and ketorolac 30 mg loading dose then 15 mg/8 hours	Morphine 0.1 mg/kg iv. VAS > 30
Goel et al. (2021) [12]	100	18– 78 years	1-level transforaminal lumbar interbody fusion surgery	USG- guided ESPB	20 mL of 0.25% bupivacaine	No block	1 gm paracetamol iv. Sixth hourly, 30 mg iv. ketorolac eighth hourly, pregabalin capsule 75 mg once a day	Fentanyl 1 mcg/kg iv. VAS ≥ 5
Siam et al. (2020) [13]	30	>18 years	Lumbar spine surgery	USG- guided ESPB	20 mL of 0.25% bupivacaine	Ketorolac 0.75 mg/kg and paracetamol 10 mg/kg	—	0.5 mg/kg peridine VAS > 4
Singh et al. (2019) [14]	40	18– 65 years	Lumbar spine surgery	USG- guided ESPB	20 mL of 0.5% bupivacaine	No block	iv. diclofenac 1.5 mg/ kg every 8 hours	iv. morphine 3 mg on demand or NRS ≥ 4
Finnerty and Buggy (2021) [15]	140	18– 65 years	2-level lumbar spine surgery	USG- guided ESPB	20 mL of 0.25% levobupivacaine	20 mL of normal saline 0.9%	iv. ketorolac 30 mg every 8 hourly, PCIA morphine	iv. Morphine VAS ≥ 4
Yayik et al. (2019) [16]	60	18– 65 years	1- or 2-level open lumbar decompression surgery	USG- guided ESPB	20 mL of 0.025% bupivacaine	No block	400 mg IV ibuprofen 12 hourly; PCIA tramadol	25 mg pethidine VAS ≥ 4
Yeşiltaş et al. (2021) [17]	56	>18 years	Open posterior instrumentation and fusion	Free-hand ESPB	20 mL (1 : 1) mixture solution of 0.25% bupivacaine and 1.0% lidocaine	Sham blocks (20 mL physiological saline)	iv. 1 mg/kg tramadol, 1 g paracetamol	25 mg pethidine VAS ≥ 4
Yörükoğlu et al. (2021) [18]	54	18– 65 years	1-level lumbar microdiscectomy	USG- guided ESPB	20 mL of 0.25% bupivacaine	Sham blocks (20 mL normal saline)	Tramadol (100 mg) and paracetamol (1 g), PCIA morphine	Tenoxicam 20 mg IV (NRS was >3)
Yu et al. (2021) [19]	80	26– 67 years	1-level lumbar fracture	USG- guided ESPB	30 mL of 0.25% bupivacaine	Sham blocks (normal saline)	PCIA sufentanil and flurbiprofen	im. pethidine (NRS was >4)
Zhang et al. (2021) [20]	60	18– 75 years	Lumbar spine surgery	USG- guided ESPB	25 mL of 0.3% ropivacaine	No block	PCIA morphine	PCIA bolus

TABLE 1: Continued.

Author/year	Participants (n)	Age	Type of surgery	Techniques	ESPB group	Control group	Postoperative analgesia	Rescue analgesia
Zhang et al. (2021) [21]	60	20–75 years	Open posterior lumbar spinal fusion surgery	USG-guided ESPB	20 mL 0.4% ropivacaine	Sham blocks	iv. flurbiprofen 300 mg, PCIA sufentanil	PCIA bolus
Zhang et al. (2020) [22]	60	18–80 years	Open posterior lumbar spinal fusion surgery	USG-guided ESPB	25 mL of 0.3% ropivacaine	No block	PCIA morphine	PCIA bolus
Zhu et al. (2021) [23]	40	45–70 years	Lumbar fusion	USG-guided ESPB	20 mL of 0.375% ropivacaine	Sham blocks (normal saline)	iv. sufentanil 5 µg, flurbiprofen 50 mg, PCIA oxycodone	iv. sufentanil 5 µg

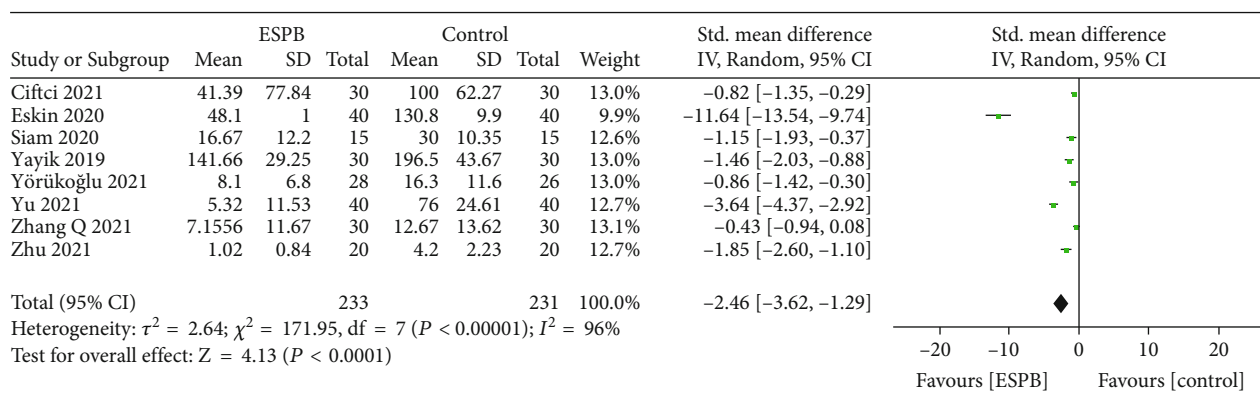


FIGURE 3: Forest plots of opioid consumption 4 to 12 hours after surgery.

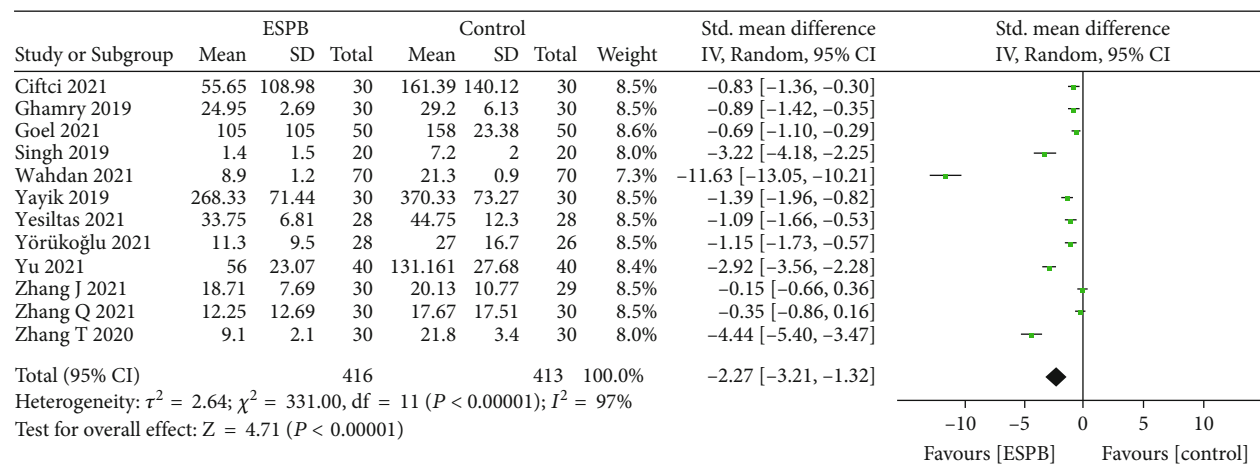


FIGURE 4: Forest plots of opioid consumption 24 hours after surgery.

3.4. *Quality Assessment and Publication Bias.* All trials described the random sequence generation methodology, and six trials [7, 8, 10, 13, 20–22] described allocation concealment methods used. Four trials [15, 17–19] described the blinding of participants and personnel, while one trial [13] did not mention blinding of outcome assessment. Complete data were available in all included studies, with no selective reporting or bias. Quality assessment results are displayed in Figure 2. No publication bias was found by visual inspection of funnel plots (Figure 6).

4. Discussion

Herein, we sought to investigate whether ESPB offered superior analgesia after lumbar spine surgery by pooling data of 15 RCTs that involved 980 participants. Importantly, we found that ESPB could significantly reduce postoperative opioid consumption in this patient population. Additionally, ESPB helped prolong the time to first rescue analgesia and reduced postoperative acute pain scores, intraoperative opioid consumption, the number of patients requiring

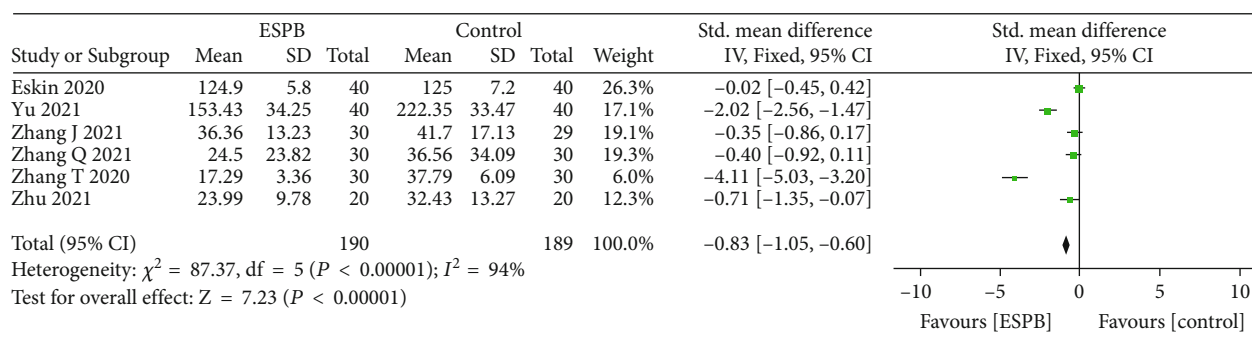


FIGURE 5: Forest plots of opioid consumption 48 hours after surgery.

TABLE 2: Secondary outcomes of RCTs included in meta-analysis.

Outcomes	Studies include	RR or SMD 95% CI	<i>p</i> value for statistical significance	<i>p</i> value for statistical heterogeneity	<i>I</i> ² test for heterogeneity
VAS/NRS scores at the PACU (at rest)	9	-1.86 (-2.59, -1.13)	<0.01	<0.01	93%
VAS/NRS scores at the PACU (on movement)	3	-1.31 (-2.14, -0.48)	<0.01	<0.01	82%
VAS/NRS scores at 2 h (at rest)	7	-1.73 (-2.70, -0.75)	<0.01	<0.01	95%
VAS/NRS scores at 2 h (on movement)	2	-1.88 (-4.04, 0.27)	0.09	<0.01	95%
VAS/NRS scores at 4 h (at rest)	8	-1.38 (-2.15, 0.61)	<0.01	<0.01	94%
VAS/NRS scores at 4 h (on movement)	3	-1.20 (-2.31, -0.09)	0.03	<0.01	91%
VAS/NRS scores at 6 h (at rest)	8	-2.26 (-3.54, -0.99)	<0.01	<0.01	96%
VAS/NRS scores at 6 h (on movement)	3	-8.24 (-13.40, -3.08)	<0.01	<0.01	98%
VAS/NRS scores at 12 h (at rest)	9	-0.69 (-1.14, -0.24)	<0.01	<0.01	83%
VAS/NRS scores at 12 h (on movement)	5	-3.21 (-5.67, -0.75)	0.02	<0.01	94%
VAS/NRS scores at 24 h (at rest)	14	-0.52 (-0.75, -0.29)	<0.01	<0.01	66%
VAS/NRS scores at 24 h (on movement)	7	-1.05 (-1.94, -0.17)	0.02	<0.01	94%
VAS/NRS scores at 48 h (at rest)	7	-0.33 (-0.61, -0.06)	0.02	0.04	51%
VAS/NRS scores at 48 h (on movement)	5	-0.70 (-1.05, -0.35)	<0.01	0.07	53%
Time to first rescue analgesic	9	4.87 (2.84, 6.90)	<0.01	<0.01	98%
Intraoperative opioid consumption	8	-1.48 (-2.35, -0.6)	<0.01	<0.01	94%
Number of patients rescue analgesia (<i>n</i>)	10	0.32 (0.13, 0.80)	0.02	<0.01	97%
PONV (postoperative nausea and vomiting)	13	0.35 (0.22, 0.55)	<0.01	0.27	18%
The length of hospitalize	5	-1.80 (-3.21, -0.39)	0.01	<0.01	97%
Patient satisfaction	5	1.89 (1.03, 2.74)	<0.01	<0.01	92%

postoperative rescue analgesia, the incidence of PONV, and shortened the length of hospitalization. These parameters contributed to better patient satisfaction. Given that the pooled estimates showed a high degree of heterogeneity, the quality of evidence of our outcomes was low to moderate.

The ESPB technique involves the injection of LA into the fascial planes between the erector spinae muscles and the transverse process. The mechanisms underlying the efficacy of ESPB remain unclear. Few studies have examined LA diffusion in ESPB and have not suggested an acceptable predictable diffusion [24]. Potential mechanisms of ESPB have been proposed: during ultrasound-guided ESPB, the local anesthetic drug has been found to spread from the injection site to the three upper vertebral body planes and four lower

caudal paravertebral planes [25]. Interestingly, unilateral ESPB has been shown to exert a contralateral blockade effect, which may be accounted for by the spread of local anesthetic drug in the epidural membrane [26–28]. In addition, some evidence suggested that LA had dorsal branch diffusion [29]. Furthermore, it has been reported that ESPB can be used in posterior spinal surgery, possibly exerting analgesic effects by blockade of the posterior ramus of the spinal nerve [15]. Moreover, in recent years, ESPB has been evolving as an effective technique that can significantly reduce the risk of spinal cord or nerve roots injury and has huge prospects in replacing epidural analgesia for postoperative analgesia.

Severe postoperative pain associated with lumbar spine surgery is an important factor affecting the recovery of patients. Current evidence demonstrated that implementing

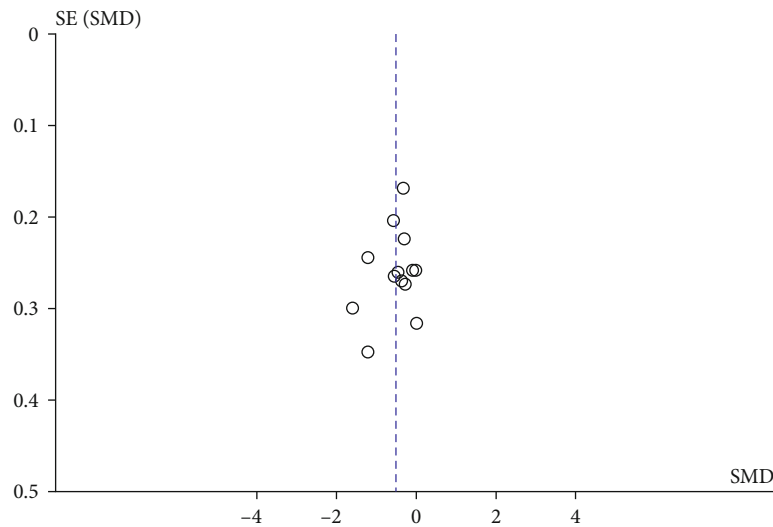


FIGURE 6: Funnel plots detecting publication bias.

Enhanced Recovery After Surgery (ERAS) programs after lumbar spine surgery may improve functional recovery and reduce the length of hospitalization, opioid consumption, complications, and unplanned readmission rate [30]. Postoperative analgesia is an important part of ERAS programs. In recent years, the implementation of ESPB has been documented to exert an effective postoperative analgesic effect, especially with ultrasound guidance [31–34]. Two recent meta-analyses [35, 36] have demonstrated the efficacy of ESPB for postoperative analgesia; however, they included fewer randomized controlled trials, smaller sample sizes, and significant heterogeneity in their results.

Herein, we demonstrated that ESPB reduced postoperative opioid consumption, which objectively reflected the efficacy of ESPB in postoperative analgesia. In this regard, ESPB could significantly lower pain scores during the first postoperative 48 hours at rest and on movement, but not the postoperative 2-hour pain score on movement. This finding may be accounted for by a high dose of rescue analgesia administered within 2 hours after surgery which lowered the pain scores. Moreover, few trials have evaluated postoperative 2-hour pain scores on movement. The traditional methods of postoperative analgesia rely mainly on postoperative opioid-based patient-controlled intravenous analgesia (PCIA). However, patients may experience adverse reactions, such as nausea and vomiting, dizziness, and constipation, while some patients even give up opioid-based PCIA. Side effects caused by postoperative opioid consumption lead to poor postoperative experience and low patient satisfaction and are not conducive to rapid recovery [37]. Alleviating acute postoperative pain is an important part of ERAS. In this regard, we found that ESPB could significantly reduce the length of hospitalization, which meets the requirements of ERAS. In addition, reducing the incidence of PONV in this patient population may improve satisfaction rates.

In recent years, ultrasound-guided ESPB has been increasingly used during clinical practice, and most of the trials ($n = 14/15$) included in our study used ultrasound-

guided ESPB. In one study where intraoperative freehand bilateral ESPB was used [17], the authors documented significant benefits in terms of postoperative opioid consumption, time to first rescue analgesia, the number of rescue analgesia, and postoperative length of hospital stay. Importantly, freehand ESPB was simpler and safer, reduced serious complications, and did not require additional time to preparation compared with ultrasound-guided might provide a new idea for analgesia after lumbar surgery.

In one [19] of the included studies, the effects of ESPB in reducing the incidence of chronic pain after surgery were investigated. However, fewer cases with postoperative chronic pain were present in the ESPB group which could explain for the absence of statistically significant difference. However, in a pooled analysis of case reports by Viderman and Sarria-Santamera [38], effective pain relief was reported in 43 patients with documented chronic severe pain that underwent ESPB, suggesting that ESPB may be a new approach for the treatment of chronic pain.

The literature contains limited information on complications associated with ESPB. Tulgar et al. [39] reported bilateral postoperative quadriceps weakness in a 29-year-old patient that underwent bilateral ESPB for cesarean section and myomectomy. To the best of our knowledge, no block-related complications such as spinal nerve injury, lower extremity sensory or motor dysfunction, local anesthetic toxicity, and infection have been documented. Nonetheless, high-quality multicenter studies with large sample sizes are required to confirm the safety of ESPB.

This study has the following limitations. First, significant heterogeneity in the ESPB procedure was observed as different local anesthetics and methods were used in the included studies to evaluate acute pain. Furthermore, opioid consumption and pain scores were not presented as means and standard deviation but as medians and interquartile range or graphs. In addition, different types of opioids for analgesia accounted for high interstudy heterogeneity, and most of the outcomes had high heterogeneity. Moreover, a

relatively small number of studies were included, and their quality was not high. In certain severe clinical situations [40–46], the effectiveness and safety of ESPB still need to be evaluated.

In conclusion, ESPB is effective and safe for postoperative analgesia after lumbar spine surgery. ESPB can reduce postoperative opioid consumption, improve patient satisfaction, and shorten the length of hospitalization. However, more high-quality trials are needed to substantiate our findings.

Data Availability

The data used to support the findings of this study are available from the corresponding author upon request.

Conflicts of Interest

There are no conflict of interest between the authors.

Authors' Contributions

Z.YL. and X.X. were responsible for the assumptions. Z.YL. and W.L. dealt the data of the study. X.X. was responsible for the analysis. Z.YL. and Z.TT. were responsible for the methodology. Z.Y.L. was responsible for the writing—original draft. Z.HM and X.X. were responsible for the writing—review and editing. All authors have read and agreed to the published version of the manuscript.

References

- [1] J. P. Melvin, R. J. Schrot, G. M. Chu, and K. J. Chin, “Low thoracic erector spinae plane block for perioperative analgesia in lumbosacral spine surgery: a case series,” *Canadian Journal of Anaesthesia*, vol. 65, no. 9, pp. 1057–1065, 2018.
- [2] M. Forero, S. D. Adhikary, H. Lopez, C. Tsui, and K. J. Chin, “The erector spinae plane block,” *Regional Anesthesia and Pain Medicine*, vol. 41, no. 5, pp. 621–627, 2016.
- [3] K. El-Boghdadly and A. Pawa, “The erector spinae plane block: plane and simple,” *Anaesthesia*, vol. 72, no. 4, pp. 434–438, 2017.
- [4] W. Huang, W. Wang, W. Xie, Z. Chen, and Y. Liu, “Erector spinae plane block for postoperative analgesia in breast and thoracic surgery: a systematic review and meta-analysis,” *Journal of Clinical Anesthesia*, vol. 66, article 109900, 2020.
- [5] Q. Cai, G. Q. Liu, L. S. Huang et al., “Effects of erector spinae plane block on postoperative pain and side-effects in adult patients underwent surgery: a systematic review and meta-analysis of randomized controlled trials,” *International Journal of Surgery*, vol. 80, pp. 107–116, 2020.
- [6] B. Ciftci, M. Ekin, E. C. Celik, A. M. Yayik, M. E. Aydin, and A. Ahiskalioglu, “Ultrasound-guided erector spinae plane block versus modified-thoracolumbar interfascial plane block for lumbar discectomy surgery: a randomized, controlled study,” *World Neurosurgery*, vol. 144, pp. e849–e855, 2020.
- [7] M. B. Eskin, A. Ceylan, M. Ö. Özhan, and B. Atik, “Ultrasound-guided erector spinae plane block versus mid-transverse process to pleura block for postoperative analgesia in lumbar spinal surgery,” *Der Anaesthetist*, vol. 69, no. 10, pp. 742–750, 2020.
- [8] A. S. Elgebaly, A. G. Anwar, M. N. Shaddad, and M. R. El Ghamry, “Ultrasound-guided erector spinae plane block for acute pain management in patients undergoing posterior lumbar interbody fusion under general anaesthesia,” *Southern African Journal of Anaesthesia and Analgesia*, vol. 25, no. 6, pp. 26–31, 2019.
- [9] J. P. Higgins, D. G. Altman, P. C. Gøtzsche et al., “The Cochrane Collaboration’s tool for assessing risk of bias in randomised trials,” *BMJ*, vol. 343, no. oct18 2, article d5928, 2011.
- [10] D. Luo, X. Wan, J. Liu, and T. Tong, “Optimally estimating the sample mean from the sample size, median, mid-range, and/or mid-quartile range,” *Statistical Methods in Medical Research*, vol. 27, no. 6, pp. 1785–1805, 2018.
- [11] X. Wan, W. Wang, J. Liu, and T. Tong, “Estimating the sample mean and standard deviation from the sample size, median, range and/or interquartile range,” *BMC Medical Research Methodology*, vol. 14, no. 1, p. 135, 2014.
- [12] V. K. Goel, M. Chandramohan, C. Murugan et al., “Clinical efficacy of ultrasound guided bilateral erector spinae block for single-level lumbar fusion surgery: a prospective, randomized, case-control study,” *The Spine Journal*, vol. 21, no. 11, pp. 1873–1880, 2021.
- [13] E. M. Siam, M. Abo Aliaa Doaa, E. Sally, and M. E. Abdelaa, “Erector spinae plane block combined with general anaesthesia versus conventional general anaesthesia in lumbar spine surgery,” *Egyptian Journal of Anaesthesia*, vol. 36, no. 1, pp. 201–226, 2020.
- [14] S. Singh, N. K. Choudhary, D. Lalin, and V. K. Verma, “Bilateral ultrasound-guided erector spinae plane block for postoperative analgesia in lumbar spine surgery: a randomized control trial,” *Journal of Neurosurgical Anesthesiology*, vol. 32, no. 4, pp. 330–334, 2020.
- [15] D. T. Finnerty and D. J. Buggy, “Efficacy of the erector spinae plane (ESP) block for quality of recovery in posterior thoracolumbar spinal decompression surgery: study protocol for a randomised controlled trial,” *Trials*, vol. 22, no. 1, p. 150, 2021.
- [16] A. M. Yayik, S. Cesur, F. Ozturk et al., “Postoperative analgesic efficacy of the ultrasound-guided erector spinae plane block in patients undergoing lumbar spinal decompression surgery: a randomized controlled study,” *World Neurosurgery*, vol. 126, pp. e779–e785, 2019.
- [17] S. Yeşiltaş, A. Abdallah, Ö. Uysal, S. Yılmaz, İ. Çinar, and K. Karaaslan, “The efficacy of intraoperative freehand erector spinae plane block in lumbar spondylolisthesis,” *Spine*, vol. 46, no. 17, pp. E902–E910, 2021.
- [18] H. U. Yörükoğlu, D. İçli, C. Aksu, S. Cesur, A. Kuş, and Y. Gürkan, “Erector spinae block for postoperative pain management in lumbar disc hernia repair,” *Journal of Anesthesia*, vol. 35, no. 3, pp. 420–425, 2021.
- [19] Y. Yu, M. Wang, H. Ying, J. Ding, H. Wang, and Y. Wang, “The analgesic efficacy of erector spinae plane blocks in patients undergoing posterior lumbar spinal surgery for lumbar fracture,” *World Neurosurgery*, vol. 147, pp. e1–e7, 2021.
- [20] J. J. Zhang, T. J. Zhang, Z. Y. Qu, Y. Qiu, and Z. Hua, “Erector spinae plane block at lower thoracic level for analgesia in lumbar spine surgery: a randomized controlled trial,” *World Journal of Clinical Cases*, vol. 9, no. 19, pp. 5126–5134, 2021.
- [21] Q. Zhang, Y. Wu, F. Ren, X. Zhang, and Y. Feng, “Bilateral ultrasound-guided erector spinae plane block in patients undergoing lumbar spinal fusion: a randomized controlled trial,” *Journal of Clinical Anesthesia*, vol. 68, article 110090, 2021.

- [22] T. J. Zhang, J. J. Zhang, Z. Y. Qu, H. Y. Zhang, Y. Qiu, and Z. Hua, "Bilateral erector spinae plane blocks for open posterior lumbar surgery," *Journal of Pain Research*, vol. Volume 13, no. 13, pp. 709–717, 2020.
- [23] L. Zhu, M. Wang, X. Wang, Y. Wang, L. Chen, and J. Li, "Changes of opioid consumption after lumbar fusion using ultrasound-guided lumbar erector spinae plane block: a randomized controlled trial," *Pain Physician*, vol. 24, no. 2, pp. E161–E168, 2021.
- [24] S. Tulgar, M. E. Aydin, A. Ahiskalioglu, A. De Cassai, and Y. Gurkan, "Anesthetic techniques: focus on lumbar erector spinae plane block," *Local and Regional Anesthesia*, vol. - Volume 13, no. 13, pp. 121–133, 2020.
- [25] K. J. Chin, S. Adhikary, N. Sarwani, and M. Forero, "The analgesic efficacy of pre-operative bilateral erector spinae plane (ESP) blocks in patients having ventral hernia repair," *Anaesthesia*, vol. 72, no. 4, pp. 452–460, 2017.
- [26] A. Schwartzmann, P. Peng, M. A. Maciel, and M. Forero, "Mechanism of the erector spinae plane block: insights from a magnetic resonance imaging study," *Canadian Journal of Anaesthesia*, vol. 65, no. 10, pp. 1165–1166, 2018.
- [27] S. Tulgar, O. Selvi, A. Ahiskalioglu, and Z. Ozer, "Can unilateral erector spinae plane block result in bilateral sensory blockade?," *Canadian Journal of Anaesthesia*, vol. 66, no. 8, pp. 1001–1002, 2019.
- [28] B. Altuparmak, M. Korkmaz Toker, and A. İ. Uysal, "Potential mechanism for bilateral sensory effects after unilateral erector spinae plane blockade in patients undergoing laparoscopic cholecystectomy," *Canadian Journal of Anaesthesia*, vol. 67, no. 1, pp. 161–162, 2020.
- [29] M. W. Harbell, D. P. Seamans, V. Koyyalamudi, M. B. Kraus, R. C. Craner, and N. R. Langley, "Evaluating the extent of lumbar erector spinae plane block: an anatomical study," *Regional Anesthesia and Pain Medicine*, vol. 45, no. 8, pp. 640–644, 2020.
- [30] N. Dietz, M. Sharma, S. Adams et al., "Enhanced recovery after surgery (ERAS) for spine surgery: a systematic review," *World Neurosurgery*, vol. 130, pp. 415–426, 2019.
- [31] C. Aksu, A. Kuş, H. U. Yörükoğlu, C. T. Kılıç, and Y. Gürkan, "The effect of erector spinae plane block on postoperative pain following laparoscopic cholecystectomy: a randomized controlled study," *Journal of Anesthesiology and Reanimation Specialists' Society*, vol. 27, no. 1, pp. 9–14, 2019.
- [32] Y. Gürkan, C. Aksu, A. Kuş, U. H. Yörükoğlu, and C. T. Kılıç, "Ultrasound guided erector spinae plane block reduces post-operative opioid consumption following breast surgery: a randomized controlled study," *Journal of Clinical Anesthesia*, vol. 50, pp. 65–68, 2018.
- [33] M. M. Abu Elyazed, S. F. Mostafa, M. S. Abdelghany, and G. M. Eid, "Ultrasound-guided erector spinae plane block in patients undergoing open epigastric hernia repair: a prospective randomized controlled study," *Anesthesia and Analgesia*, vol. 129, no. 1, pp. 235–240, 2019.
- [34] M. A. Hamed, A. S. Goda, M. M. Basiony, O. S. Fargaly, and M. A. Abdelhady, "Erector spinae plane block for postoperative analgesia in patients undergoing total abdominal hysterectomy: a randomized controlled study original study," *Journal of Pain Research*, vol. Volume 12, no. 12, pp. 1393–1398, 2019.
- [35] Y. Qiu, T. J. Zhang, and Z. Hua, "Erector spinae plane block for lumbar spinal surgery: a systematic review," *Journal of Pain Research*, vol. Volume 13, no. 13, pp. 1611–1619, 2020.
- [36] M. J. Liu, X. Y. Zhou, Y. B. Yao, X. Shen, R. Wang, and Q. H. Shen, "Postoperative analgesic efficacy of erector spinae plane block in patients undergoing lumbar spinal surgery: a systematic review and meta-analysis," *Pain and therapy*, vol. 10, no. 1, pp. 333–347, 2021.
- [37] G. Graffigna and S. Barello, "Patient health engagement (PHE) model in enhanced recovery after surgery (ERAS): monitoring patients' engagement and psychological resilience in minimally invasive thoracic surgery," *Journal of Thoracic Disease*, vol. 10, Suppl 4, pp. S517–S528, 2018.
- [38] D. Viderman and A. Sarria-Santamera, "Erector spinae plane block in chronic pain management: a scoping review," *Tumori*, vol. 107, no. 5, pp. 458–467, 2021.
- [39] S. Tulgar, O. Selvi, O. Senturk, T. E. Serifsoy, and D. T. Thomas, "Ultrasound-guided erector spinae plane block: indications, complications, and effects on acute and chronic pain based on a single-center experience," *Cureus*, vol. 11, no. 1, article e3815, 2019.
- [40] J. Vasquez-Vivar, Z. Shi, K. Luo, K. Thirugnanam, and S. Tan, "Tetrahydrobiopterin in antenatal brain hypoxia-ischemia-induced motor impairments and cerebral palsy," *Redox Biology*, vol. 13, pp. 594–599, 2017.
- [41] J. Vasquez-Vivar, Z. Shi, J. W. Jeong et al., "Neuronal vulnerability to fetal hypoxia-reoxygenation injury and motor deficit development relies on regional brain tetrahydrobiopterin levels," *Redox Biology*, vol. 29, article 101407, 2020.
- [42] L. Deng, X. Li, Z. Shi, P. Jiang, D. Chen, and L. Ma, "Maternal and perinatal outcome in cases of fulminant viral hepatitis in late pregnancy," *International Journal of Gynecology & Obstetrics*, vol. 119, no. 2, pp. 145–148, 2012.
- [43] Y. Yang, L. Deng, X. Li et al., "Analysis of prognosis-associated factors in fulminant viral hepatitis during pregnancy in China," *International Journal of Gynaecology and Obstetrics*, vol. 114, no. 3, pp. 242–245, 2011.
- [44] Y. Yang, L. Deng, X. Li et al., "Evaluation of the prognosis of fulminant viral hepatitis in late pregnancy by the MELD scoring system," *European Journal of Clinical Microbiology & Infectious Diseases*, vol. 31, no. 10, pp. 2673–2678, 2012.
- [45] X. M. Li, L. Ma, Y. B. Yang, Z. J. Shi, and S. S. Zhou, "Prognostic factors of fulminant hepatitis in pregnancy," *Chinese Medical Journal*, vol. 118, no. 20, pp. 1754–1757, 2005.
- [46] X. Li, Y. Zhang, and Z. Shi, "Ritodrine in the treatment of preterm labour: a meta-analysis," *The Indian Journal of Medical Research*, vol. 121, no. 2, pp. 120–127, 2005.

Research Article

Ultrasound Evaluation of Pelvic Floor Function after Transumbilical Laparoscopic Single-Site Total Hysterectomy Using Deep Learning Algorithm

Yan Zhu,¹ Jiamiao Zhang,¹ Zhonglei Ji,¹ Wen Liu,¹ Mingyue Li,¹ Enhui Xia,² Jing Zhang,¹ and Jianqing Wang¹ 

¹Department of Obstetrics and Gynecology, The Yancheng Clinical College of Xuzhou Medical University, The First People's Hospital of Yancheng, Yancheng, 224001 Jiangsu, China

²Department of Ultrasound, The Yancheng Clinical College of Xuzhou Medical University, The First People's Hospital of Yancheng, Yancheng, 224001 Jiangsu, China

Correspondence should be addressed to Jianqing Wang; 1526410103@st.usst.edu.cn

Received 2 June 2022; Revised 6 July 2022; Accepted 15 July 2022; Published 10 August 2022

Academic Editor: Pan Zheng

Copyright © 2022 Yan Zhu et al. This is an open access article distributed under the Creative Commons Attribution License, which permits unrestricted use, distribution, and reproduction in any medium, provided the original work is properly cited.

This study was aimed at investigating the ultrasound based on deep learning algorithm to evaluate the rehabilitation effect of transumbilical laparoscopic single-site total hysterectomy on pelvic floor function in patients. The bilinear convolutional neural network (BCNN) structure was constructed in the ultrasound imaging system. The spatial transformer network (STN) was used to preserve image information. Two algorithms, BCNN-R and BCNN-S, were proposed to remove sensitive information after ultrasonic image processing, and then, subtle features of the image were identified and classified. 80 patients undergoing transumbilical laparoscopic single-site total hysterectomy in hospital were randomly divided into a control group and a treatment group, with 40 cases in each group. In the control group, conventional ultrasound was used to assess the image of pelvic floor function in patients undergoing laparoendoscopic single-site surgery (LESS); in the observation group, ultrasound based on deep learning algorithm was used. The postoperative incision pain score, average postoperative anus exhaust time, average hospital stay, and postoperative satisfaction of the two groups were evaluated, respectively. The highest accuracy of constructed network BCNN-S was 88.98%; the highest recall rate of BCNN-R was 88.51%; the highest accuracy rate of BCNN-R was 97.34%. The operation time, intraoperative blood loss, and exhaust time were similar between the two groups, and the difference had no statistical significance ($P > 0.05$). The numerical rating scale (NRS) scores were compared, the observation group had less pain, the difference between the two groups had statistical significance ($P < 0.05$), and the postoperative recovery was good. The BCNN based on deep learning can realize the imaging of the uterus by ultrasound and realize the evaluation of pelvic floor function, and the probability of pelvic floor dysfunction is small, which is worthy of clinical promotion.

1. Introduction

Pelvic floor disease is a degenerative lesion including urinary incontinence and pelvic organ prolapse [1]. In the United States, nearly 400,000 patients undergo surgery due to pelvic floor dysfunction each year, and 300,000 cases occur during hospitalization. Each year, 33% of women have different pelvic floor dysfunction (PFD) before the age of 60 and require hysterectomy [2]. Hysterectomy is closely related to PFD, which can improve the risk of postoperative pelvic floor dys-

function and affect the quality of life of patients [3]. The pelvic floor function of normal women mainly relies on intact muscle strength, nerves, and ligaments. The interaction of various organs allows the pelvic floor structure to reach a normal dynamic balance state [4]. The hysterectomy can damage the neural tissue, impair vascular nutrition, and severely destroy important supporting structures such as muscles, ligaments, fascia, and connective tissue [5, 6]. PFD in women is usually judged based on the patient's clinical symptoms as well as the corresponding examination

results, and the examinations include finger pressure test, urodynamic examination, and magnetic resonance imaging, but these modalities have the disadvantage of poor reproducibility and cannot comprehensively evaluate the pelvic floor function of the anatomy for dynamic imaging, safety, and repeated procedures [7, 8]. At present, transperineal pelvic floor ultrasound is increasingly loved by researchers to evaluate the dynamic changes of pelvic floor function. Pelvic floor ultrasound enables real-time observation of pelvic anatomy and function and enables dynamic imaging, which has become a major modality for assessing pelvic floor ultrasound [9, 10].

Transumbilical laparoendoscopic single-site surgery (TU-LESS) is a surgical technique performed using surgical instruments through the pore channel, mainly using the umbilicus to place multiple operating pore channels as well as the operating platform of the laparoscope in the abdomen, which can reduce abdominal infections caused by gastrointestinal tract as well as transapproach surgery, with the characteristics of mild pain, rapid recovery, no earthworm-like scar left in the abdomen, safety, and minimal invasion. In this process, it can also use the natural wrinkle site of the umbilicus to cover the surgical incision, which can meet the requirements of women for abdominal “scarless” cosmetology [11, 12]. Compared with traditional multiport laparoscopy, TU-LESS is easier to perform in total hysterectomy, can shorten gastrointestinal recovery time and postoperative ambulation time, and can remove the uterus through a single port at the umbilicus and through an approach in a manner similar to “apple cutting.” “Chopstick effect” between instruments is one reason for prolonged operation time [13, 14].

With the advantages of high sensitivity, noninvasion, easy operation, and low cost of ultrasound imaging, real-time three-dimensional (four-dimensional) ultrasound imaging has become an effective diagnostic tool in imaging systems in the 21st century [15]. Ultrasound is widely used in obstetrics and gynecology without ionizing radiation, cost-effective, and easy to approach, for example, abdominal ultrasound, cardiovascular ultrasound, electrocardiogram, and prenatal diagnostic ultrasound, but the presence of pseudonoise in ultrasound imaging causes reduced imaging quality and is also a challenge in ultrasound; relying only on the experience of doctors, as well as the proficiency of operators, there are significant differences in results in different institutions as well as different ultrasound systems [16, 17]. This requires the use of advanced intelligent ultrasound image analysis algorithms to intervene imaging quality. Deep learning technology has made it successful for natural image recognition in the construction of large-scale image datasets, and high-resolution ultrasound imaging equipment has accumulated many ultrasound image data, which also makes deep learning possible for the auxiliary diagnosis of images [18, 19]. The bilinear convolutional neural network (BCNN) enables a good classification of images [20]. Yosinski et al. [21] pointed out when learning the features of the underlying CNN that the CNN network can get distinct features with increasing depth, and the closer to the input end, the more specific information the feature displays.

The ultrasonic transverse section of patients with total hysterectomy was identified, and the BCNN was used to identify the ultrasonic transverse section of the uterus.

The innovation is that the intelligent algorithm is used to identify high resolution the transverse section, and the extracted features are fused, which is helpful to retain the subtle features. It is hoped that it can provide reference for ultrasound evaluation of pelvic floor function in patients with transumbilical laparoscopic single-site total hysterectomy and provide theoretical basis for clinical work.

2. Materials and Methods

2.1. Subjects. Eighty patients admitted to hospital from June 2018 to June 2020 who underwent transumbilical laparoscopic single-site total hysterectomy were selected. The age of the study subjects ranged from 32 to 50 years, with an average of 42.5 ± 3.61 years and BMI of 23.67 ± 1.2 kg/m². There were 28 cases of uterine fibroids, 19 cases of endometrial lesions, and 33 cases of adenomyosis. The patients were randomly divided into the control group ($n = 40$) and the treatment group ($n = 40$) by random number table method. There was no significant difference in basic information between the two groups ($P > 0.05$). Preoperative gynecological examination of the uteri was less than 4 months of gestation with good range of motion, and the operation was completed by the same physician. This study had been approved by the ethics committee of the hospital, and the patients and their families signed the informed consent form.

Inclusion criteria: patients with uterine fibroids or adenomyosis diagnosed by routine cervical biopsy or cervical liquid-based cytology before surgery; patients with complete clinical data; patients without cervical malignant lesions or uterine prolapse; patients without fertility requirements, nonpregnant patients; patients without serious medical and surgical diseases and a history of repeated surgery.

Exclusion criteria: patients who are allergic to the drugs used; patients who are critically ill and unable to cooperate; patients with chronic diseases such as heart, brain, liver, and kidney; patients with mental diseases; patients with systemic infection.

2.2. Treatment Methods. Ultrasonic diagnostic apparatus was used. The intestinal tract of the patient with the probe frequency of 4-8H was emptied, the patient laid on the examination bed, and the probe coated with coupling agent and covered with disposable film gloves was placed at the perineum to clearly show the uterine condition. In the Valsalva state and at rest, distance from the bladder neck to the posteroinferior border of the pubic symphysis (BNSD), distance from the external cervical orifice to the posteroinferior border of the pubic symphysis (CSD), posterior urethrovesical angle (PUA), and bladder neck mobility and the difference in the distance from the bladder neck to the posteroinferior border of the pubic symphysis (BND) under the maximum Valsalva state and at rest were compared between two groups. For measurements in both states, all data were measured in triplicate by 3 examining physicians and then averaged.

The patient was anesthetized by endotracheal intubation. The bladder lithotomy position was taken, and the uterine lifting device was placed. The patient's posture was low head and high foot. The longitudinal incision (about 10 mm) was made from the center of the umbilical to the lower edge of the umbilical wheel, and then, the self-made operation platform was implanted through the umbilicus. The external diameter of 10 mm and 5 mm instruments and camera lens were implanted at the finger end of the glove. After successfully entering the abdominal cavity, the pneumoperitoneum was established, the pressure was 12-14 (mmHg), the patient's body position was adjusted to 30°, the head was low, and the hip was high, so as to use the uterine lifting device. The pelvic cavity was evaluated by laparoscopy. Bipolar electrocoagulation was used to shorten the isthmus of the fallopian tube, the round ligament of the uterus, and the inherent ligament of the ovary, and then, the broad ligaments in the anterior and posterior parts and the peritoneal reflection of the bladder were opened, respectively. Bipolar electrocoagulation of bilateral uterine arteries and veins was performed. The cervical stump 1-10# absorption suture was selected to stop bleeding, and the uterus was removed at vertebral body and parallelly at the isthmus above the uterine vascular suture. After cervical reduction, the tract mucosa and pelvic peritoneum were sutured. Before the end of the operation, the pelvic wound was examined, and repeated washing was performed to stop bleeding. After incision suture, the operation ended.

Hardware platform: Ubuntu 16.04 operating system, deep learning framework is Pytorch-1.2.0. Python 3.6 is the development language, memory 128 GB, central processor is IntelXeon (R) Silver 4110CPU@2.10 GHz×32, and image processor is NVIDIA 1080Ti.

2.3. Observation Indicators. The intraoperative blood loss, postoperative pain score, postoperative fever, postoperative exhaust time, conversion operation, and operation time were recorded.

Pain degree: numerical rating scale (NRS) score was used (Table 1).

2.4. BCNN Structure. The BCNN structure is shown in Figure 1. In this algorithm, after optimizing the minimum loss, the two networks supervised each other, and it did not require a lot of time to adjust the parameters. Finally, the accurate recognition results were obtained. The parallel network of CNN Stream A and CNN Stream B extracted the cross-sectional features with high recognition in the input network image. The features extracted by CNN Stream A and CNN Stream B were fused, which helped to identify subtle features.

The image processing technology of deep learning used superimposing multiple convolutions to obtain image characteristics and then used multilayer perceptron to classify them. In clinical practice, the standard constrained deep network was used to realize the transverse section of ultrasound imaging. The doctor needed to spend a lot of experience in finding the horizontal transverse section during the examination, which was particularly important to have a standard

TABLE 1: NRS.

Score	Symptoms
0	Painless
1-3	Mild pain, sleep unaffected
4-6	Moderate pain, sleep affected
7-10	Severe pain, sleep affected seriously

access that can accurately identify the transverse section of the uterus. BCNN-S and BCNN-R were proposed to identify the transverse section of uterine ultrasound. First, image processing was performed, then the high transverse section was identified, and finally the features were fused. After obtaining the subtle features, the identification and classification were performed, and finally, the accurate identification of the horizontal direction of the transverse section of uterus was obtained.

The algorithm was optimized. The initial learning efficiency was set to 1, the weight attenuation was set to $1e-5$, the momentum attenuation was set to 0.9, and the learning rate of each epoch was multiplied by 0.1. The gradient was updated after algorithm optimization, which was more stable and smoother. The default parameters can make the model reach a stable level (Table 2).

2.5. Space Conversion Module. Through the attention mechanism, the space transformer networks (STN) can convert the spatial information in the original image to another space to retain key information. The spatial transformer (ST) was proposed. The spatial domain information in the image is transformed to extract key information. The trained STN can find out the areas that need to be concerned in the image information. ST has the function of scaling and rotation. The local information of the image can be extracted by transformation. ST module is input to the existing network structure. The model input equation is shown as follows.

$$Q \in R^{H \times W \times C}. \quad (1)$$

W represents the width, H represents the height of the output tensor of the upper layer, and C represents the channel. Different convolution kernels and basic three channels of the image produce different channel information. The input image enters the double-stream route, and the transformed image is obtained through matrix change.

$$V' \in R^{H \times W \times C}. \quad (2)$$

V' represents the transformed image features, and the positioning network learns a set of parameters \mathbb{X} . This parameter generates a sampling signal through the parameters of the grid generator, which is essentially the transformation of the matrix image.

The sampling matrix generated by STN can extract the key information in the original image. One is the sampling matrix for scaling and rotation transformation, and the

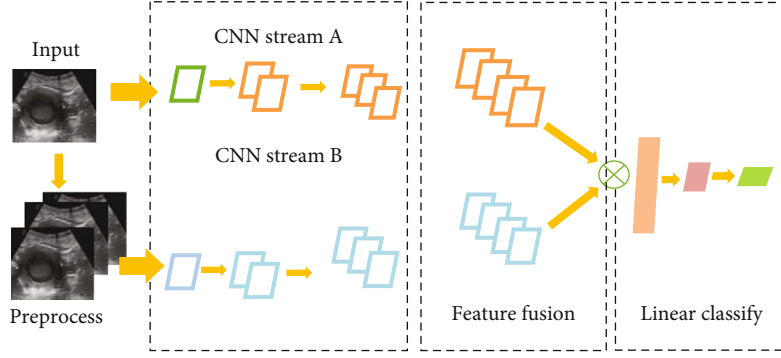


FIGURE 1: BCNN structure.

TABLE 2: BCNN parameters.

Layer name	Kernel	Layer name	Kernel
	BCNN-R		BCNN-S
Conv 1	$7 \times 7, 64, \text{stride } 2$	Conv 1	
	$1 \times 1, 64$		$1 \times 1, 3 \times 3, 64$
Block 1	$3 \times 3, 64$	Fire 1-3	$1 \times 1, 3 \times 3, 64$
	$1 \times 1, 256$		$1 \times 1, 3 \times 3, 256$
	$1 \times 1, 128$		$1 \times 1, 3 \times 3, 256$
Block 2	$3 \times 3, 128$	Fire 4-7	$1 \times 1, 3 \times 3, 384$
	$1 \times 1, 512$		$1 \times 1, 3 \times 3, 512$
	$1 \times 1, 256$		
Block 3	$3 \times 3, 256$		$1 \times 1, 3 \times 3, 512$
	$1 \times 1, 1024$		
	$1 \times 1, 512$		$2 \times 2, \text{maxpool, stride } 2$
Block 4	$3 \times 3, 512$	Fire 8	$1 \times 1, 3 \times 3, 512$
	$1 \times 1, 2048$		
Pool		Outer product	

other is the unit matrix, which is expressed as follows.

$$\begin{pmatrix} X_i^s \\ Y_i^s \\ 1 \end{pmatrix} = T_\theta(Gi) = AZ_\theta \begin{pmatrix} X_i^s \\ Y_i^s \\ 1 \end{pmatrix} = \begin{pmatrix} \theta_{11} & \theta_{12} & \theta_{13} \\ \theta_{21} & \theta_{22} & \theta_{23} \end{pmatrix} \begin{pmatrix} X_i^s \\ Y_i^s \\ 1 \end{pmatrix}. \quad (3)$$

\boxtimes matrix is the corresponding sampling matrix. This module can identify the key information of the module on the upper layer. It is also a matrix that can be differentiated. It uses the kernel function to represent the complex change information.

$$V_i^c = \sum_n \sum_m B_{nm}^c T(x_i^s - m; \psi x) * (y_i^s - n; \psi y). \quad (4)$$

T is the conversion kernel function, B represents the information before conversion, and V represents the information after conversion.

Classification network has strong feature representation ability and good recognition ability for conventional images. In target recognition, the difference between different targets is very small, but it is not ideal to classify directly in conventional images. In the debugging of fine-grained classification network, the loss measurement function is introduced. There will be three weight shared networks q , m , and s when three samples are input each time. The accumulated three network outputs obtain the loss, and in addition to the use of softmax loss function, the three characteristic outputs constitute the Triplet loss.

$$F = \lambda_s F_s(q) + (1 - q) F_t(q, m, s). \quad (5)$$

$F_s(q)$ represents the loss obtained by the softmax loss function, which represents the overall category information of the image so that the network can be optimized to the real category. $F_t(q, m, s)$ belongs to the Triplet error of three sub networks f_q, f_m, f_s with shared parameters. In order to increase the recognition ability of the same category and different samples of the network, the distance between classes is

calculated. The two loss functions restrict each other, and the performance of the model is significantly improved.

When detecting the target, CNN can train through the object frame and component annotation in the fine-grained training image, including object head detection, fine-grained object level detection, and trunk detection. Ideal object detection results can be obtained by using position geometric constraints.

After the residual attention module can strengthen the attention and image features, the features are input into the next module at the same time. The $W_i, c(x)$ function represents different functions and has different attention domains. The equation is as follows.

$$W_1(x_{i,c}) = \frac{1}{1 + \exp(-x_{i,c})}, \quad (6)$$

$$W_2(x_{i,c}) = \frac{x_{i,c}}{\|x_i\|}, \quad (7)$$

$$W_3(x_{i,c}) = \frac{1}{1 + \exp(-(x_{i,c} - \text{mean}_c)/\text{std}_c)}. \quad (8)$$

W_1 indicates that the Sigmoid function directly activates the image feature tensor, W_2 indicates that the image feature tensor is globally averaged and pooled to obtain channel domain attention, and W_3 indicates the average number of Sigmoid functions activating the image feature tensor to obtain spatial domain attention.

2.6. Performance Evaluation Indicators. Reasonable evaluation of performance indicators can effectively evaluate the performance of the algorithm. The cross section of ultrasonic image is evaluated as a binary classification problem. The prediction category and real category of the model are divided into true negative (TN), false positive (FP), true positive (TP), and false negative (FN).

The accuracy calculation is shown in Equation (9). The higher the accuracy of classification, the better the performance of the algorithm. Precision refers to the proportion of TP in all samples predicted to be positive. Recall indicates the proportion of samples predicted to be positive in positive samples. When the recall rate and accuracy rate are high, the average will be higher. If one of them is low, it will lower the average, and its value will be close to the low number, as shown in Equation (12).

$$\text{Accuracy} = \frac{\text{TP} + \text{TN}}{\text{TP} + \text{FP} + \text{TN} + \text{FN}}, \quad (9)$$

$$\text{Precision} = \frac{\text{TP}}{\text{TP} + \text{FP}}, \quad (10)$$

$$\text{Recall} = \frac{\text{TP}}{\text{TP} + \text{FN}}, \quad (11)$$

$$F1 = \frac{2PR}{P + R}. \quad (12)$$

It is required to make evaluation on the overall mean Intersection over Union (mIoU) and mean Dice of graph.

mIoU predicts the intersection of the target area and the real target area. The higher the value of mIoU, the higher the correlation. mDICE is used to calculate the similarity between two samples. It is a geometric similarity measurement function. GT in Equation (14) denotes the true region, and Pre denotes the predicted region.

$$\text{IOU} = \frac{\text{GT} \cap \text{Pre}}{\text{GT} + \text{Pre}}, \quad (13)$$

$$\text{DICE} = \frac{2|\text{GT} \cap \text{Pre}|}{|\text{GT}| + |\text{Pre}|}. \quad (14)$$

The experimental environment hardware: platform memory (RAM) is 128 GB, the image processor (GPU) is NVIDIA 1080Ti $\times 2$, the central processing unit (CPU) is Intel Xeon®Silver4110 CPU@2.10 GHz $\times 32$, and the operating system is Ubuntu 16.04. The deep learning framework is Pytorch1.2.2, and Python 3.6 is selected as the development language.

2.7. Statistical Methods. The database of all data was established by Excel, and SPSS 19.0 statistical software was adopted. Measurement data were expressed as mean \pm standard deviation ($\bar{x} \pm s$), enumeration data were analyzed by the χ^2 test, and enumeration data were expressed as percentage (%). $P < 0.05$ was considered to indicate a significant difference.

3. Results

3.1. Training and Test Data Results. In this study, 3619 ultrasound images were obtained from the public dataset HC18 and the self-built dataset JFU19 after preprocessing, which were divided into training set and data set according to a certain proportion, and a certain number of training sets were drawn to evaluate the model, it was shown the model had a good recognition effect, and the three positions of horizontal, vertical, and right-angle lines were trained, respectively, and the results are shown in Figure 2. The test of the training set revealed that the model showed a good performance.

3.2. Parameter Information of BCNN. In this study, BCNN-R and BCNN-S feature images were extracted to analyze the performance of the algorithm. The resulting feature is shown in Figure 3. The feature image has distinct activation regions, which also indicates that there are many features that can be used for network identification and classification. Compared with BCNN-S B, BCNN-R A has more activated regions, which also obtains more identification ability. The ultrasound image in Figure 3(c) has more noise and reverberation than that in Figure 3(d). BCNN-R has a more complex structure and is inevitably subjected to a lot of noise.

3.3. Algorithm Performance Comparison. Comparing the algorithm performance of BCNN-R and BCNN-S with that in References [22–24], the highest accuracy of BCNN-S was 88.98%, followed by 85.62% of BCNN-R. BCNN-R had the highest recall rate of 88.51%, followed by BCNN-S

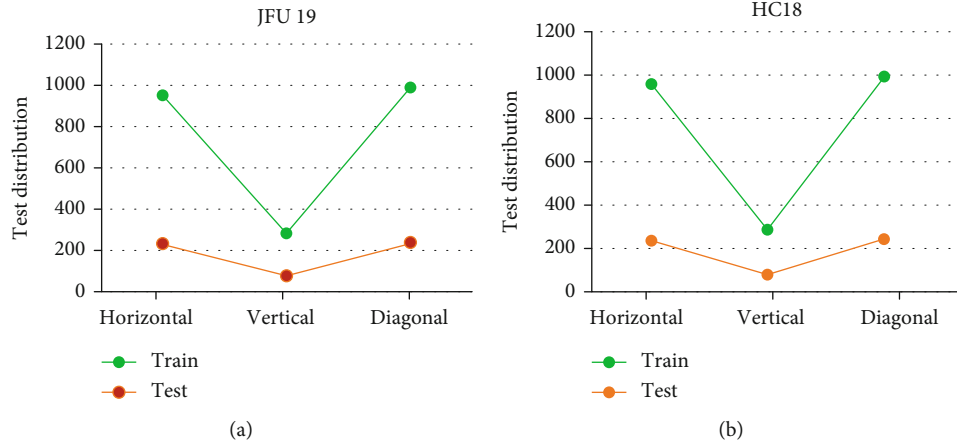


FIGURE 2: The comparison results between training set and test set. (a) The processing results of the public dataset HC8 for ultrasonic images. (b) The processing results of JFU19 for ultrasonic images.

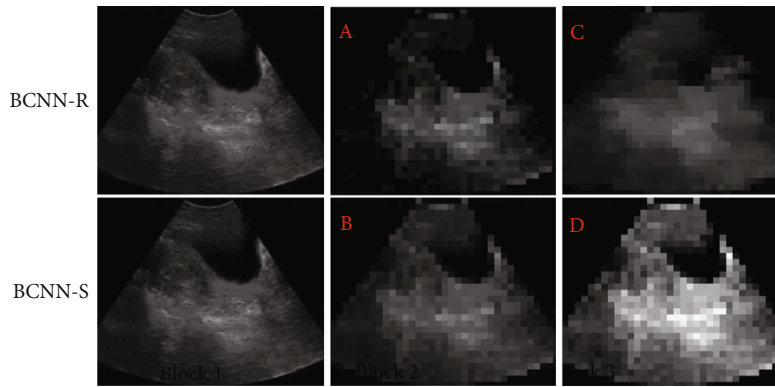


FIGURE 3: BCNN-R and BCNN-S feature images. (a) The activation region shown in the BCNN-R feature image. (b) The activation region shown in the BCNN-S feature image. (c) The activation process of region classification by BCNN-R feature map. (d) The activation process of region classification by BCNN-S feature image.

of 87.54%; the highest accuracy of BCNN-R was 97.34%, followed by 91.67% of BCNN-S (Figure 4).

3.4. Experimental Results of Semantic Segmentation. In order to explore the change of the algorithm with epoch and the performance of the algorithm in ultrasonic image segmentation, the mIoU and mDICE evaluation indexes were analyzed. The results were as follows. Compared with mIoU and mDICE in Reference [24], mIoU and mDICE in BCNN had higher convergence performance, which can increase the robustness of the network to a certain extent and inhibit overfitting (Figure 5).

3.5. Ultrasound Results. The ultrasound parameters BNSD, CSD, PUA, bladder neck mobility, and BND under the maximum Valsalva state and at rest were compared between the two groups. It had a reduced BNSD under Valsalva state compared with that under at rest (Table 3).

3.6. Comparison of Surgical Conditions. The operation time, NRS score, intraoperative blood loss, and exhaust time of the two groups were compared. The operation time, intraoperative blood loss, and exhaust time of the two groups were

similar, and the difference was not statistically significant ($P > 0.05$). In the NRS score, the pain of the observation group was mild, and the difference was significant ($P < 0.05$) (Table 4).

3.7. Comparison of Hospitalization Time and Satisfaction. The satisfaction score of the observation group was 5.32 ± 0.16 , and that of the control group was 4.96 ± 0.21 . The hospitalization time of the observation group was 6.72 ± 2.32 days, and that of the control group was 8.13 ± 2.18 days. The difference between the groups was statistically significant ($P < 0.05$) (Figure 6).

3.8. Postoperative Comparison. Abdominal infection, hematoma, incision bleeding, and incision infection did not occur in both groups after operation, and the patients recovered well. However, in the control group, one patient had active bleeding in the umbilical region after operation, and the dressing became dry after hemostasis with pressurized sand. The incidence of fever in the observation group was 1 case (2.5%), and that in the control group was 3 cases (7.5%). The fever rate in the control group was significantly higher than that in the observation group ($P < 0.05$) (Figure 7).

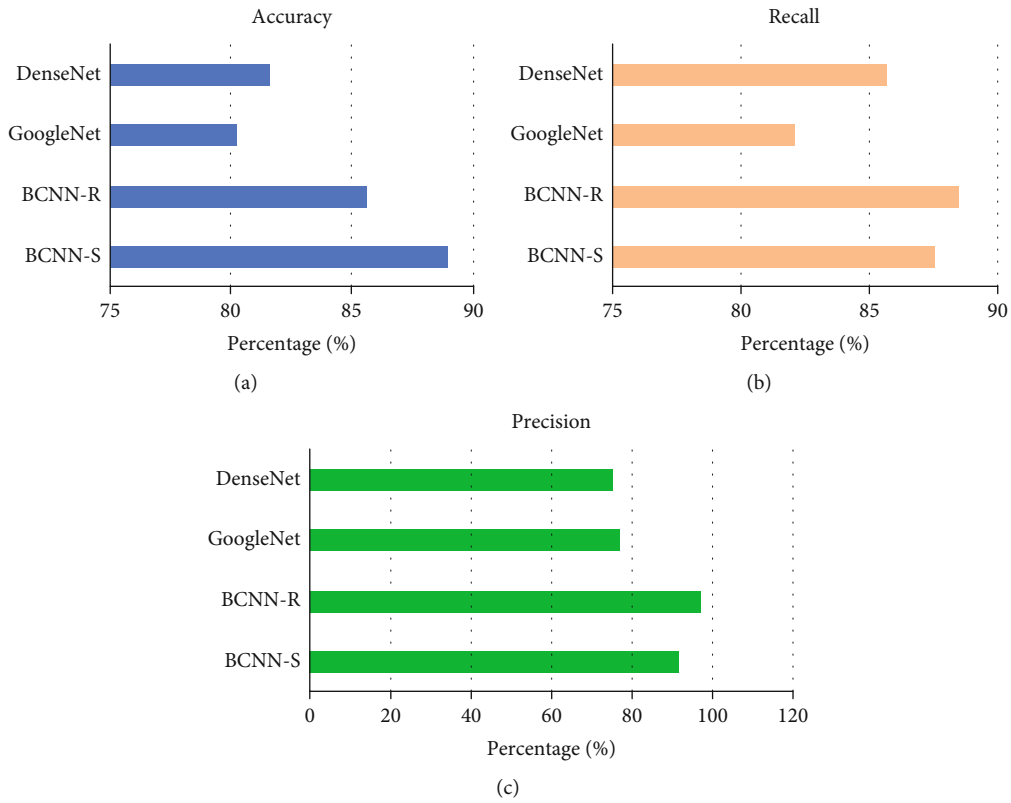


FIGURE 4: Performance comparison of algorithms. (a) Comparison results of four algorithms in accuracy. (b) Comparison results of four algorithms in recall. (c) Comparison results of four algorithms in precision.

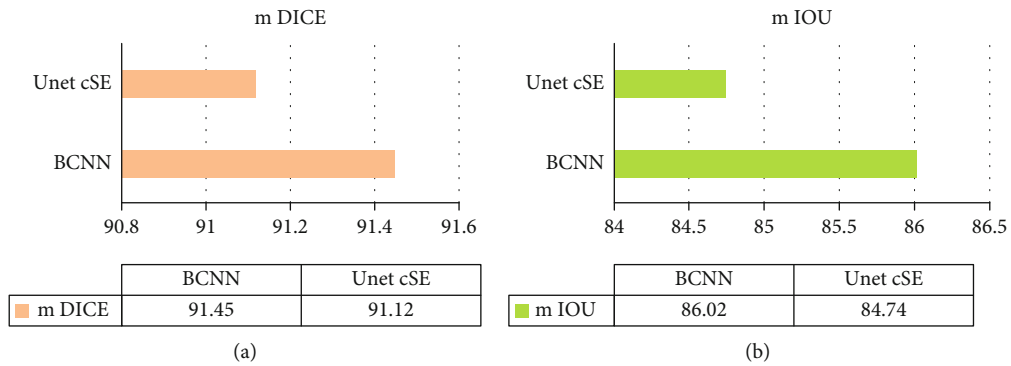


FIGURE 5: Performance comparison of algorithms. (a) The comparison between BCNN and UnetcsE algorithm in mDICE. (b) The comparison between BCNN and UnetcsE algorithm in mIoU.

TABLE 3: Result comparison between the two groups under at rest and Valsalva state.

Group	Number	BNSD	CSD	PUA	BND
Observation group	At rest	25.34 ± 3.12	31.87 ± 2.31	101.3 ± 8.41	7.12 ± 3.8
	Valsalva state	19.87 ± 4.5	32.7 ± 3.18	121.87 ± 12.6	8.7 ± 1.31
Control group	At rest	22.87 ± 2.8	31.87 ± 2.31	98.5 ± 7.86	6.1 ± 4.3
	Valsalva state	18.17 ± 2.31	30.87 ± 3.17	119.7 ± 9.38	8.67 ± 2.2

TABLE 4: Comparison of surgical conditions.

Group	Number	Operation time (min)	NRS cores	Exhaust time (h)	Intraoperative blood loss (ml)
Observation group	40	87.4 ± 9.76	1.87 ± 0.31*	30.3 ± 2.41	112.1 ± 10.8
Control group	40	80.1 ± 8.3	2.29 ± 0.15	32.5 ± 1.86	153.1 ± 18.3
<i>P</i>		>0.05	<0.05	>0.05	>0.05

Note: *compared with the control group, $P < 0.05$.

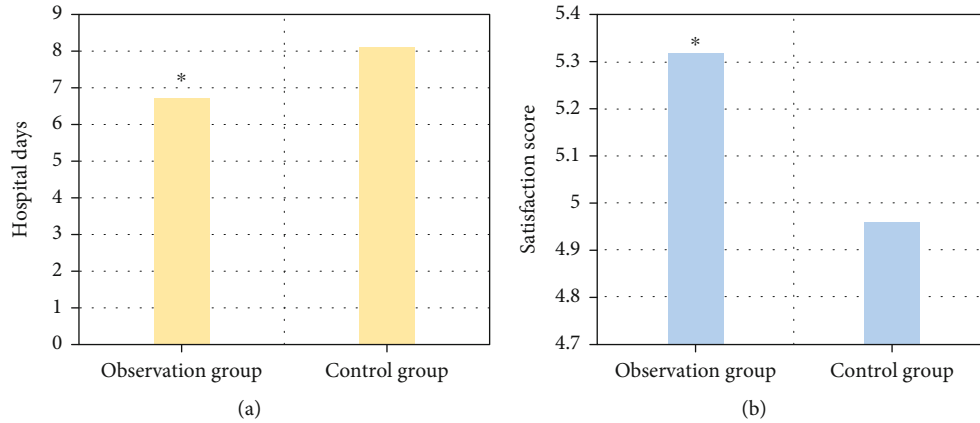


FIGURE 6: Comparison of hospitalization time and satisfaction between the two groups. (a) Comparison result of hospitalization time between the two groups. (b) Satisfaction score of two groups. *Compared with the control group, $P < 0.05$.

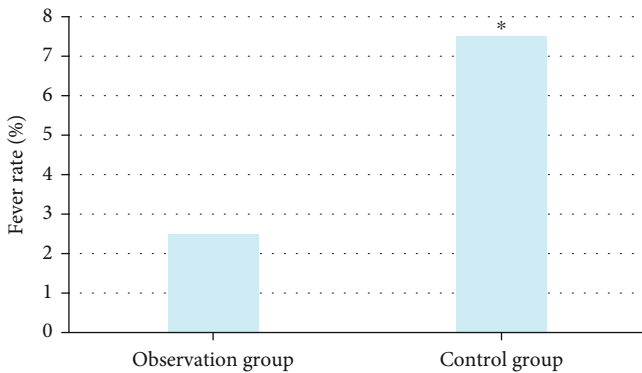


FIGURE 7: Comparison of postoperative fever rate. *Compared with the control group, $P < 0.05$.

4. Discussion

Total hysterectomy is a relatively common gynecological surgery. After hysterectomy, the whole physiological state and overall structure of pelvic floor will change, which may produce PDF. Female pelvic floor is intricate, and it is important to find a noninvasive, reproducible, and simple diagnostic method for assessing pelvic floor function. With the rapid development of surgical abdominal surgery, LESS, with the natural approach, is widely used in clinical practice and is easier to understand and accept for some gynecological patients who meet the surgical criteria [25]. Compared with traditional hysterectomy, laparoendoscopic single-site total hysterectomy reduced hospital stay and postoperative

blood loss, the two groups of patients had similar operation time, intraoperative blood loss, and exhaust time, and the difference had no statistical significance ($P > 0.05$); in the NRS score, the pain of the observation group was mild, and the difference had statistical significance ($P < 0.05$). Chung [26] compared single-site laparoscopic total hysterectomy with conventional laparoscopic total hysterectomy, there was no difference in pain scores between the two groups, and the operation time was significantly longer in single-site laparoscopic total hysterectomy group. In the observation group, intelligent algorithm was added in the ultrasound imaging, and there was no significant difference in the operation time. One patient had active bleeding at the umbilicus after surgery, and the dressing became dry after hemostasis with pressurized sand.

Ultrasonic technique of the BCNN model based on deep learning is accurate for evaluating pelvic floor function. Yu et al. [27] evaluated the effect of laparoscopic hysterectomy based on artificial intelligence imaging; ultrasound imaging based on ISCB algorithm can high-quality display the pelvic floor structure of patients undergoing total laparoscopic hysterectomy, improve the diagnostic rate of doctors, accelerate postoperative rehabilitation of patients, reduce postoperative pain, and improve patient satisfaction. In this experiment, BCNN-S had the highest accuracy of 88.98%; BCNN-R had the highest recall of 88.51%; and BCNN-R had the highest precision of 97.34%. The proposed algorithm shows high convergence performance in ultrasonic image segmentation. This experiment also shows that the intelligent algorithm of deep learning can effectively improve the efficacy of hysterectomy patients. Compared with mIoU and mDICE in

Reference [24], mIoU and mDICE in BCNN had higher convergence performance, which can increase the robustness of the network to a certain extent and inhibit overfitting.

5. Conclusion

Eighty patients undergoing transumbilical single-site laparoscopic total hysterectomy in hospital were randomly divided into the treatment group and the control group to investigate the efficacy and safety of ultrasound based on deep learning for pelvic floor function in patients undergoing LESS. Ultrasound technology can be used to dynamically observe the anatomy of female pelvic floor organs; ultrasound technology of BCNN model based on deep learning has no significant toxic and side effects, with higher accuracy for evaluating the pelvic floor function. The incidence of pelvic floor dysfunction after hysterectomy is small, and attention should be paid to pelvic floor disorders and the image of sexual function during surgery, which is more conducive to the recovery of physical and mental health and normal life of patients. There are some shortcomings, due to the limitation of time, there is a lack of long-term follow-up, so long-term follow-up to patients is needed at a later stage to further verify the long-term efficacy. It is believed that it can provide some ideas and experimental support for the recovery of pelvic floor function in patients undergoing LESS.

Data Availability

The data used to support the findings of this study are available from the corresponding author upon request.

Conflicts of Interest

The authors declare no conflicts of interest.

Authors' Contributions

Yan Zhu and Jiamiao Zhang contributed equally to this work.

References

- [1] K. Louis-Charles, K. Biggie, A. Wolfenbarger, B. Wilcox, and C. M. Kienstra, "Pelvic floor dysfunction in the female athlete," *Current Sports Medicine Reports*, vol. 18, no. 2, pp. 49–52, 2019.
- [2] R. C. Ramdhan, M. Loukas, and R. S. Tubbs, "Anatomical complications of hysterectomy: a review," *Clinical Anatomy*, vol. 30, no. 7, pp. 946–952, 2017.
- [3] B. Berghmans, "Physiotherapy for pelvic pain and female sexual dysfunction: an untapped resource," *International Urogynecology Journal*, vol. 29, no. 5, pp. 631–638, 2018.
- [4] F. Sendag, A. Akdemir, B. Zeybek, A. Ozdemir, I. Gunusen, and M. K. Oztekin, "Single-site robotic total hysterectomy: standardization of technique and surgical outcomes," *Journal of Minimally Invasive Gynecology*, vol. 21, no. 4, pp. 689–694, 2014.
- [5] E. J. Nam, S. W. Kim, M. Lee et al., "Robotic single-port transumbilical total hysterectomy: a pilot study," *Journal of Gynecologic Oncology*, vol. 22, no. 2, pp. 120–126, 2011.
- [6] R. Sinha, M. Sundaram, C. Mahajan et al., "Single-incision total laparoscopic hysterectomy," *Journal of Minimal Access Surgery*, vol. 6, no. 4, pp. 168–182, 2010.
- [7] L. Chen, Y. Zheng, L. Min, and S. M. Dong, "Clinical cohort study of total hysterectomy via transvaginal natural orifice transluminal endoscopic surgery and transumbilical laparoendoscopic single site surgery," *Zhonghua fu Chan ke za zhi*, vol. 55, no. 12, pp. 843–847, 2020.
- [8] S. L. Wallace, L. D. Miller, and K. Mishra, "Pelvic floor physical therapy in the treatment of pelvic floor dysfunction in women," *Current Opinion in Obstetrics & Gynecology*, vol. 31, no. 6, pp. 485–493, 2019.
- [9] S. Lawson and A. Sacks, "Pelvic floor physical therapy and women's health promotion," *Journal of Midwifery & Women's Health*, vol. 63, no. 4, pp. 410–417, 2018.
- [10] Y. W. Jung, Y. T. Kim, D. W. Lee et al., "The feasibility of scarless single-port transumbilical total laparoscopic hysterectomy: initial clinical experience," *Surgical Endoscopy*, vol. 24, no. 7, pp. 1686–1692, 2010.
- [11] S. A. Prendergast, "Pelvic floor physical therapy for vulvodynia: a clinician's guide," *Obstetrics and Gynecology Clinics of North America*, vol. 44, no. 3, pp. 509–522, 2017.
- [12] S. Chen, Y. Wang, F. Yang, K. Wang, and Y. Zheng, "WITHDRAWN: Transumbilical laparoendoscopic single-site surgery (TU-LESS) extraperitoneal approach for lymphadenectomy: an innovative method," *Journal of Gynecologic Oncology*, vol. 32, 2021.
- [13] A. Akdemir, N. Yildirim, B. Zeybek, S. Karaman, and F. Sendag, "Single incision trans-umbilical total hysterectomy: robotic or laparoscopic?," *Gynecologic and Obstetric Investigation*, vol. 80, no. 2, pp. 93–98, 2015.
- [14] H. H. Cai, M. B. Liu, and Y. L. He, "Treatment of early stage endometrial cancer by transumbilical laparoendoscopic single-site surgery versus traditional laparoscopic surgery: a comparison study," *Medicine (Baltimore)*, vol. 95, no. 14, article e3211, 2016.
- [15] L. Huang, L. He, L. Zhang et al., "Application of the prone position in myomectomy by transvaginal natural orifice transluminal endoscopic surgery," *Videosurgery and Other Minimally Invasive Techniques*, vol. 16, no. 1, pp. 234–242, 2021.
- [16] S. H. Saravelos, K. Jayaprakasan, K. Ojha, and T. C. Li, "Assessment of the uterus with three-dimensional ultrasound in women undergoing ART," *Human Reproduction Update*, vol. 23, no. 2, pp. 188–210, 2016.
- [17] A. T. Evans, K. Szlachetka, and L. L. Thornburg, "Ultrasound assessment of the intrauterine device," *Obstetrics and Gynecology Clinics of North America*, vol. 46, no. 4, pp. 661–681, 2019.
- [18] Z. Lv and L. Qiao, "Analysis of healthcare big data," *Future Generation Computer Systems*, vol. 109, pp. 103–110, 2020.
- [19] S. Xie, Z. Yu, and Z. Lv, "Multi-disease prediction based on deep learning: a survey," *Computer Modeling in Engineering & Sciences*, vol. 128, no. 2, pp. 489–522, 2021.
- [20] Z. Yu, S. U. Amin, M. Alhussein, and Z. Lv, "Research on disease prediction based on improved DeepFM and IoMT," *IEEE Access*, vol. 9, pp. 39043–39054, 2021.
- [21] Y. S. Choi, J. N. Park, Y. S. Oh, K. S. Sin, J. Choi, and D. S. Eun, "Single-port vs. conventional multi-port access laparoscopy-assisted vaginal hysterectomy: comparison of surgical

- outcomes and complications,” *European Journal of Obstetrics & Gynecology and Reproductive Biology*, vol. 169, no. 2, pp. 366–369, 2013.
- [22] M. Tobias-Machado, F. A. Chicoli, R. M. Costa Jr et al., “LESS sacrocolpopexy: step by step of a simplified knotless technique,” *International braz j urol*, vol. 38, pp. 859–860, 2012.
- [23] G. Huang, Z. Liu, G. Pleiss, L. Van Der Maaten, and K. Weinberger, “Convolutional networks with dense connectivity,” *IEEE Transactions on Pattern Analysis and Machine Intelligence*, pp. 1–1, 2019.
- [24] N. Toussaint, B. Khanal, M. Sinclair et al., “Weakly supervised localization for fetal ultrasound images,” in *Deep Learning in medical image analysis and multimodal learning for clinical decision support*, pp. 192–200, Springer, 2018.
- [25] S. J. Oh, S. Y. Lee, W. Y. Kim et al., “Comparison between transumbilical and transvaginal morcellation of a large uterus during single-port-access total laparoscopic hysterectomy,” *Obstetrics & Gynecology Science*, vol. 63, no. 3, pp. 379–386, 2020.
- [26] J. H. Chung, J. M. Baek, K. Chung et al., “A comparison of postoperative pain after transumbilical single-port access and conventional three-port total laparoscopic hysterectomy: a randomized controlled trial,” *Acta Obstetrica et Gynecologica Scandinavica*, vol. 94, no. 12, pp. 1290–1296, 2015.
- [27] H. Yu, Z. Zhao, X. Duan, J. Zhou, and D. Su, “Ultrasound image under artificial intelligence algorithm to evaluate the intervention effect of accelerated rehabilitation surgery nursing on laparoscopic hysterectomy,” *Computational Intelligence and Neuroscience*, vol. 2022, Article ID 9042954, 11 pages, 2022.

Research Article

Anatomical and Imaging Study on the Optimum Entry Point and Trajectory for Anterior Transpedicular Root Screw Placement into the Lower Cervical Spine

Jihui Zhang,¹ Liujun Zhao ,¹ Jingfei Xu,² Yongjie Gu,¹ and Liang Yu¹

¹Department of Spinal Surgery, Ningbo No. 6 Hospital, Ningbo, 315040 Zhejiang Province, China

²Department of Medical Insurance, Ningbo No. 6 Hospital, Ningbo, 315040 Zhejiang Province, China

Correspondence should be addressed to Liujun Zhao; zhaoliujun55555@sina.com

Received 6 May 2022; Revised 16 June 2022; Accepted 27 June 2022; Published 9 August 2022

Academic Editor: Pan Zheng

Copyright © 2022 Jihui Zhang et al. This is an open access article distributed under the Creative Commons Attribution License, which permits unrestricted use, distribution, and reproduction in any medium, provided the original work is properly cited.

Objective. To study the optimum entry point and trajectory for anterior transpedicular root screw (ATPRS) placement into the lower cervical spine (LCS), so as to provide a basis for clinical application. **Methods.** A retrospective analysis of cervical CT images of patients who underwent cervical CT examination in the Spinal Surgery of Ningbo No. 6 Hospital from January 2020 to August 2021 was conducted. The data were obtained and modeled. On the coronal plane, the vertebral body (VB) between the anterior midline of cervical vertebral segments C₃₋₇ and the left P line (by drawing the line parallel to the anterior midline of the VB at the intersection of the anterior edge of the Luschka's joint and the upper endplate) was equally divided into 9 zones (a-i). The ideal entry point and path of cervical ATPRS were designed and recorded. Additionally, 7 cadaveric specimens were selected, and the screw placement parameters were regenerated according to the above methods for screw placement. **Results.** Zone i of each segment, with the longest screw length, was the best area for screw placement. In all patients, the horizontal angles of vertebrae C₃₋₇ in zones a, d, and g, zones b, e, and h, and zones c, f, and i showed a gradually decreasing trend. The sagittal angle range of C₃₋₇ in all patients showed a gradually increasing trend in zones a-c, d-f, and g-i. The distance from the anterior midline of C₃₋₇ to the P line increased in all patients, and the distance was longer in males than in females, with statistical significance. Pedicle screws were successfully inserted in all the 7 cadaveric specimens. **Conclusions.** ATPRS placement can be used for LCS internal fixation, and the precise screw placement parameters can be simulated by the software, which provides theoretical basis for its future clinical application.

1. Introduction

The change of lifestyle in modern society has driven the continuously rising incidence of cervical spine injury (CSI), with degenerative diseases, trauma, and infection of the lower cervical spine (LCS) frequently occurring in the anterior column of the vertebral body (VB) [1, 2]. Clinically, surgical treatment is mainly adopted to relieve spinal cord and nerve root compression, restore the normal sequence and physiological curvature of cervical spine (CS), and rebuild the stability of CS. Anterior cervical decompression and fusion is a common method to treat lower cervical diseases [3, 4], most of which are fixed with unicortical cervical vertebral screws, with a good fixation effect for patients with single-

level cervical diseases. However, a combination of anterior and posterior surgery is usually required for those with single-level three-column injury or multilevel anterior compression treated by anterior vertebral screws, with anterior surgery for decompression and posterior surgery for fixation. However, the biomechanical stability of traditional anterior cervical plate and screw fixation is not satisfactory [5, 6]. Although posterior pedicle screws or lateral mass screws can provide sufficient stability for patients with multilevel internal fixation, this procedure undoubtedly lengthens the operative time of patients and increases surgical trauma, complications, and costs [7–9].

There are two anterior cervical internal fixation methods: vertebral screws, which are widely used in clinical

practice, and pedicle screws, which are limited by difficulty in screw placement [10, 11]. Therefore, how to achieve the dual purpose of decompression and fixation at the same time in LCS surgery through anterior approach has become a research hotspot in recent years. As an alternative, the anterior transpedicular screw (ATPS) technique, applied clinically by Aramomi et al. [12], has gradually been extensively used for cervical stabilization due to the combination of the advantages of anterior approach with superior biomechanical properties of cervical pedicle fixation [10, 13, 14]. In general, pedicle fixation is considered risky because of the anatomical relationship of the cervical pedicle, which is close to important structures such as vertebral arteries, spinal cord, and nerve roots [15, 16].

Therefore, precise screw insertion is the key to successful clinical application of ATPS. Under this circumstance, we proposed a novel anterior screw technique called anterior transpedicular root screws (ATPRSs) for anterior cervical arch foundation, which is also the novelty of this study. At the same time, due to ethnic anatomical differences, there are limited anatomical and imaging studies related to this technique in China. Thus, the motivation of this paper is to study and measure the applied anatomy and CT of the lower cervical vertebra from the anterior approach, in order to provide anatomical and imaging-related parameters for ATPRS implantation in the LCS.

2. Data and Methods

2.1. General Information of Samples Collected In Vivo. Cervical CT images of patients undergoing cervical CT examination in the Spinal Surgery of Ningbo No. 6 Hospital from January 2020 to August 2021 were collected. Inclusion criteria: Adult patients who visited Spinal Surgery and underwent cervical CT examination, with no obvious LCS deformity or history of cervical surgery (to eliminate the measurement error caused by the interference of surgery or internal fixation), and complete imaging data were enrolled. Exclusion criteria: Patients with fracture, deformity, tumor, and obvious degeneration or previous cervical surgery history were excluded, as well as those aged under 25 or over 70. According to the inclusion and exclusion criteria, 39 patients were finally enrolled, including 22 males and 17 females, with an age range of 28-66 years (mean: 39.3 ± 8.9). This study was approved by the hospital Ethics Committee (Ethics Number: NBU-2021-021). Because of the retrospective nature of this study, the requirement for informed consent was waived.

2.2. Model Reconstruction. The original CS CT data of 39 patients in Dicom format were imported into the Mimic 17.0 software (Mimics 17.0, Materialize, Belgium) for analysis. After reading CT sequence images, the threshold value of CS was selected to obtain the original mask. Then, three-dimensional (3D) reconstruction was performed to establish 3D images of vertebrae C_{3-7} successively through multilayer mask processing. After smoothing and triangular patch (Tri-Patch) trimming, the complete 3D images of vertebrae C_{3-7} were obtained and saved.

2.3. Virtual Screw Placement and Data Measurement. In order to avoid measurement biases caused by subjective factors of the gauger, all the following data were repeatedly measured by two researchers skilled in the operation of mimics software, and the measured data results were averaged as the final data.

The retrieved 3D images of C_{3-7} levels were displayed with the highest transparency to establish contour lines. On the coronal plane, a line parallel to the anterior midline of the VB at the intersection of the anterior edge of the Luschka's joint (uncovertebral joint, UVJ) and the superior endplate was made, which is called the P line, and the VB between the anterior midline of the C_{3-7} levels to the left P line was evenly divided into 9 zones (a-i), by referring to our previous study [17]. Then, a cylinder with a diameter of 3.5 mm was drawn by MEDcad module instead of screws for simulation of screw placement. Pedicle screw placement: After transparentizing the 3D reconstruction of the VB, the posterior wall of the VB was used as a reference to make it perpendicular to the screen, with the overlap of the upper and lower edges of the posterior wall of the VB and no lateral inclination as the standard. Then, the VB was restrained. The transverse distance of the vertebral canal was used to locate the central line of the VB, and the horizontal vertical line perpendicular to the central line was established by the anterior edge of the VB. The VB was then rotated to show its sagittal view. Then, the posterior wall of the VB was made perpendicular to the lower edge of the screen, and the projection line of the posterior wall was overlapped and constrained again to make a vertical line perpendicular to the center line. The horizontal, coronal, and sagittal planes of the VB were determined by the principle of two lines determining one side through the center line, the horizontal vertical line, and the vertical line. In the viewing window, the VB was set to a horizontal plane in which the VB was rotated so that the pedicle was perpendicular to the lower edge of the screen to facilitate screw placement. The cylinder was moved slowly to ensure that it was embedded in the vertebra. Fine-tuning was performed in sagittal, coronal, and horizontal windows to make the simulated screw placement in the best position. That is, the head of the screw was located at the intersection of the posterolateral edge of the VB and the axis of the pedicle on the horizontal plane and at the lower edge of the pedicle on the sagittal position. The caudal end of the screw was located at the center point of 9 zones equally divided between the midline of the anterior edge of VB and the left P line. The method of bilateral screw implantation was consistent.

Through the measurement module of the Mimics software, the measurement file was established to determine the position and length of the screw. The horizontal plane angle (α), sagittal plane angle (β) of the anterior pedicle screw, and the distance from the midline of anterior edge of VB to the P line were measured. Related data of each VB was recorded using the Excel software.

2.4. Nailing of Cadaveric Specimens. Seven adult cervical vertebra specimens treated with formaldehyde were selected, including 4 males and 3 females aged from 29 to 58 years

TABLE 1: Comparison of screw lengths in different levels and zones of cervical vertebrae (cm).

	C ₃		C ₄		C ₅		C ₆		C ₇	
	Male (n = 22)	Female (n = 17)	Male (n = 22)	Female (n = 17)	Male (n = 22)	Female (n = 17)	Male (n = 22)	Female (n = 17)	Male (n = 22)	Female (n = 17)
a	18.1 ± 0.7	17.0 ± 1.1*	18.7 ± 1.0	17.9 ± 1.1*	18.9 ± 1.3	18.2 ± 1.0	20.5 ± 0.8	19.3 ± 1.1*	22.2 ± 1.3	20.9 ± 1.0*
b	19.2 ± 0.8	18.3 ± 0.8*	20.0 ± 1.0	19.1 ± 0.7*	20.3 ± 0.6	19.4 ± 0.6*	22.2 ± 1.2	20.4 ± 1.1*	23.4 ± 1.0	22.3 ± 1.3*
c	20.5 ± 0.7	19.3 ± 0.6*	21.1 ± 0.9	20.5 ± 0.5*	21.6 ± 0.8	20.3 ± 1.0*	23.0 ± 0.9	21.9 ± 1.1*	24.7 ± 0.9	23.0 ± 0.7*
d	18.5 ± 1.0	17.3 ± 1.2*	19.1 ± 1.0	18.0 ± 0.7*	19.5 ± 1.2	18.3 ± 1.0*	21.2 ± 1.4	19.5 ± 1.2*	22.3 ± 1.4	21.0 ± 1.1*
e	19.8 ± 1.1	18.4 ± 0.8*	20.7 ± 1.1	19.4 ± 1.0*	20.9 ± 0.7	19.5 ± 1.3*	22.4 ± 1.4	20.8 ± 1.0*	24.0 ± 0.9	22.6 ± 1.2*
f	20.8 ± 0.7	19.3 ± 1.1*	21.4 ± 1.1	20.5 ± 0.9*	21.8 ± 1.3	20.7 ± 0.9*	23.1 ± 1.3	21.9 ± 0.5*	25.0 ± 0.8	23.5 ± 0.9*
g	20.2 ± 0.5	18.9 ± 1.1*	20.3 ± 0.8	19.0 ± 0.8*	21.1 ± 1.0	19.4 ± 1.0*	22.4 ± 1.1	20.3 ± 0.9*	23.8 ± 1.5	22.4 ± 0.8*
h	21.5 ± 1.1	19.7 ± 0.9*	21.7 ± 0.8	20.1 ± 1.2*	22.4 ± 0.9	20.8 ± 0.5*	23.8 ± 1.2	21.5 ± 0.9*	25.1 ± 1.1	23.6 ± 1.4*
i	22.4 ± 0.8	20.6 ± 1.2*	23.1 ± 0.8	21.2 ± 1.0*	23.5 ± 0.8	21.7 ± 1.1*	24.9 ± 1.1	22.6 ± 0.8*	26.2 ± 1.1	24.7 ± 0.7*

Notes: * $P < 0.05$ vs. male.

(mean: 43.7 ± 10.1). After eliminating bone defects, deformities, and obvious degeneration by CT examination, the soft tissue in front of the cervical VB was gradually and thoroughly removed, the prevertebral fascia was incised, and the VB was exposed, with the strip width to the bilateral UVJs. The prepared specimens were refrigerated at -20°C and taken out 24 hours before the formal experiment.

Seven CS specimens were randomly numbered and scanned by CT, and the related parameters were measured by the Mimics software in the same way as adult CS CT images. After thawing the specimen at room temperature and fully exposing the VB and other bone structures, the screws were gradually inserted under the guidance of C-arm X-ray machine and Kirschner wires, and ATPRS were placed under X-ray fluoroscopy. Subsequently, the screw trajectory was observed to determine whether the screw was located in the bone. After confirming that the upper wall of the channel and the left and right lateral walls were not damaged, the safety of screw placement was reconfirmed by anteroposterior-lateral fluoroscopy. Following screw placement, a CT scan was performed to determine the position of the screw and whether the screw was inserted safe and effective. Also, the specimen was dissected along the screw with a pendulum saw to check whether the screw penetrated the bone surface or damaged the surrounding structure, and the screw trajectory was observed.

2.5. Statistical Processing. Statistical analysis was made by SPSS 22.0 (IBM, NY, USA). Mean \pm SD was used to indicate the measurement data of normal distribution, and an independent samples t -test was performed. For the intragroup comparison of screw placement zones, a paired sample t -test was used. A significance level of two-tailed $\alpha = 0.05$ was used in all analyses.

3. Results

3.1. Screw Lengths in Each Zone of Cervical Levels C₃₋₇. After software simulation of screw placement, it was found that the APSs could be placed at the cervical levels C₃₋₇ in all

patients. The optimal areas were screw lengths over 22 mm for males and 20 mm for females, as shown in Table 1.

3.2. Horizontal Angles of APSs in Each Zone of Cervical Levels C₃₋₇. The screw horizontal angles of all patients are shown in Table 2. The horizontal angle differed significantly between males and females at different cervical levels ($P < 0.05$). However, no significant difference was present in angles between zones a, d, and g of C₃₋₇ segments in all patients ($P > 0.05$). Nor was there any obvious difference in the horizontal angle between zones b, e, and h and zones c, f, and i ($P > 0.05$), all of which showed a decreasing trend in the angle.

3.3. Sagittal Plane Angles of APSs in Each Region of Cervical Levels C₃₋₇. The sagittal angle showed significant differences between male and female at different cervical levels ($P < 0.05$). However, there was no significant difference in the angle between zones a, b, and c of C₃₋₇ segments in all patients ($P > 0.05$). Also, zones d, e, and f were not evidently different from zones g, h, and i in the sagittal angle ($P > 0.05$), all of which showed an increasing trend (see Table 3).

3.4. Distance from Midline of Anterior Edge to P Line at Cervical Vertebra C₃₋₇. As shown in Table 4, from C₃ to C₇, the distance from the anterior midline of the VB to the P line increased gradually, with that of C₇ being the longest and a distance shorter in females than in males ($P < 0.05$). Subsequently, screw placement was carried out on cadaveric specimens according to simulated nail placement parameters, which proved the feasibility of nail placement, as shown in Figure 1.

4. Discussion

At present, anterior CS plate fixation is widely used, in which 13-15 mm vertebral mono- or bicortical screws are mostly used as the fixation screws, with better fixation strength for patients undergoing single-level surgery [18]. However, for senile osteoporosis patients and those with cervical multilevel decompression, this procedure can easily

TABLE 2: Comparison of horizontal angles of screws in different segments and regions (°).

	C ₃		C ₄		C ₅		C ₆		C ₇	
	Male (n = 22)	Female (n = 17)	Male (n = 22)	Female (n = 17)	Male (n = 22)	Female (n = 17)	Male (n = 22)	Female (n = 17)	Male (n = 22)	Female (n = 17)
a	45.4 ± 5.1	43.5 ± 2.8	45.2 ± 3.2	43.1 ± 3.5	44.0 ± 3.8	40.5 ± 2.4*	43.4 ± 3.2	42.8 ± 3.3	45.7 ± 4.0	43.7 ± 4.1
b	41.1 ± 3.2	38.6 ± 2.8*	39.4 ± 2.9	35.0 ± 3.4*	36.4 ± 2.3	35.2 ± 3.8	36.4 ± 2.5	35.2 ± 3.0	38.5 ± 2.5	35.7 ± 4.2*
c	34.1 ± 3.1	31.7 ± 2.6*	33.2 ± 2.5	30.2 ± 3.8*	34.0 ± 3.5	30.6 ± 3.4*	33.0 ± 2.7	30.6 ± 2.3*	33.1 ± 3.0	30.9 ± 4.0
d	46.2 ± 3.5	45.2 ± 2.9	44.1 ± 3.2	42.1 ± 2.6*	44.1 ± 2.8	41.5 ± 4.0*	43.5 ± 3.6	42.9 ± 3.8	44.7 ± 2.4	44.5 ± 3.7
e	41.5 ± 2.0	38.2 ± 4.1*	40.3 ± 2.2	35.9 ± 3.9*	36.2 ± 3.7	36.1 ± 2.9	35.9 ± 3.2	35.4 ± 4.1	37.4 ± 2.9	36.9 ± 3.2
f	36.4 ± 2.5	33.7 ± 3.5*	34.5 ± 2.3	30.8 ± 3.7*	33.4 ± 3.6	31.5 ± 3.6	31.6 ± 2.1	30.1 ± 2.8	33.8 ± 2.3	31.7 ± 3.4*
g	44.2 ± 2.9	45.5 ± 2.4	47.1 ± 3.2	43.2 ± 3.8*	45.8 ± 2.4	44.1 ± 2.1*	44.8 ± 2.7	44.9 ± 3.3	46.2 ± 3.6	45.1 ± 4.2
h	41.2 ± 2.4	38.5 ± 3.9*	40.8 ± 3.8	35.5 ± 2.4*	39.3 ± 2.7	37.5 ± 2.2*	38.6 ± 3.1	36.2 ± 2.5*	38.3 ± 3.8	36.2 ± 4.2
i	36.8 ± 2.2	33.6 ± 2.9*	35.2 ± 3.4	33.5 ± 1.9*	34.4 ± 2.9	34.5 ± 3.2	33.8 ± 2.6	32.6 ± 3.4	34.2 ± 4.3	32.9 ± 3.4

Notes: *P < 0.05 vs. male.

TABLE 3: Comparison of sagittal angles of screws in different segments and zones (°).

	C ₃		C ₄		C ₅		C ₆		C ₇	
	Male (n = 22)	Female (n = 17)	Male (n = 22)	Female (n = 17)	Male (n = 22)	Female (n = 17)	Male (n = 22)	Female (n = 17)	Male (n = 22)	Female (n = 17)
a	86.2 ± 4.9	86.5 ± 5.2	86.5 ± 4.6	85.3 ± 4.2	93.2 ± 5.0	85.4 ± 5.7*	92.1 ± 5.2	87.9 ± 4.9*	86.7 ± 4.5	87.4 ± 4.9
b	85.6 ± 5.2	87.3 ± 4.8	93.2 ± 4.0	83.5 ± 4.3*	95.6 ± 4.5	86.2 ± 4.3*	94.5 ± 5.0	89.0 ± 5.7*	89.3 ± 5.7	87.2 ± 3.9
c	86.2 ± 4.8	86.5 ± 5.0	92.7 ± 5.1	82.1 ± 4.1*	97.2 ± 5.3	89.1 ± 4.2*	91.8 ± 4.6	85.5 ± 3.6*	86.4 ± 4.9	87.4 ± 4.2
d	104.2 ± 4.9	105.4 ± 5.1	106.7 ± 3.9	105.5 ± 4.1	110.4 ± 3.5	105.5 ± 3.8*	109.2 ± 4.2	102.3 ± 3.7*	104.3 ± 5.1	103.4 ± 4.0
e	106.7 ± 4.5	107.2 ± 5.3	107.5 ± 3.9	106.0 ± 4.4	113.4 ± 3.6	108.2 ± 4.3*	111.3 ± 3.8	105.2 ± 2.9*	107.5 ± 4.2	109.6 ± 4.8
f	101.3 ± 5.1	105.5 ± 3.8*	108.1 ± 4.6	104.8 ± 4.5*	112.0 ± 4.2	106.8 ± 3.8*	110.6 ± 4.2	106.8 ± 3.1*	109.4 ± 4.9	108.2 ± 4.5
g	121.4 ± 2.0	120.9 ± 5.2	123.7 ± 3.9	121.6 ± 4.2	124.9 ± 4.6	122.3 ± 4.9	124.5 ± 3.5	120.3 ± 4.6*	116.2 ± 4.2	121.8 ± 3.8*
h	122.4 ± 4.8	124.0 ± 4.1	125.4 ± 3.7	123.8 ± 4.0	125.4 ± 4.3	122.9 ± 5.6	123.4 ± 4.0	123.8 ± 3.8	119.0 ± 4.1	121.9 ± 4.0*
i	122.6 ± 4.2	125.7 ± 5.3*	125.2 ± 4.4	122.1 ± 4.7*	128.3 ± 5.1	125.5 ± 5.0	122.2 ± 4.5	125.1 ± 5.2	123.8 ± 4.1	124.5 ± 3.9*

Notes: *P < 0.05 vs. male.

lead to loosening of internal fixation. Currently, there is no relatively stable and reliable fixation method in clinical practice [19]. Biomechanical studies have shown that the pedicle is the toughest part of the vertebrae, and its cortical bone is cylindrical with a small amount of cancellous bone in the middle. This structure has a good holding force on screws, and the stability provided by pedicle screw fixation is obviously better than that provided by anterior cervical locking plate system, posterior spinous process wire fixation, and transarticular plate/screw fixation [19–22]. Due to the special anatomical characteristics of the pedicle of the LCS, any deviation during the operation will cause serious consequences. If the screw path is too high, it is easy to damage the nerve root, while too internal a screw path is prone to spinal cord injury; if the screw path is too lateral, it can easily damage the vertebral artery [23]. As the application of anterior cervical pedicle screw internal fixation technology is still in its initial stage, there have been no reports of injury of arterial spinal cord and nerve roots or failure of internal fixation. Similar to posterior cervical pedicle screw fixation, anterior pedicle screw fixation has the risk of complications such as damage to vertebral artery spinal cord and nerve

roots, as well as complications such as hoarseness, esophageal injury, cerebrospinal fluid leakage, and internal fixation failure caused by traditional anterior surgery [24, 25]. At the same time, most scholars believe that successful pedicle screw placement depends on three factors [26], namely, the location of the entry point, the appropriate placement angle in the transverse and sagittal planes, and the appropriate screw diameter and length. Hence, precise measurement of parameters related to these elements becomes the key to ensuring surgical success.

In this study, the Mimics software is used to carry out 3D reconstruction with CT images to realize simulation operation and 3D measurement. The simulation of screw placement can be repeated in the software, which is helpful to the study of the best entry area and trajectory of screw placement. The basic research of anterior pedicle screw placement using the Mimics software involves the question of reliability in comparison with the real thing. The samples included in the research were 3D models reconstructed by CT scanning. Although there is a certain difference between the surface treatment and the real object, there is no distortion in the angle; moreover, this technology is a CT scan orientation,

TABLE 4: Comparison of distance from the anterior midline of the VB to the P line at each segment (mm).

	C ₃	C ₄	C ₅	C ₆	C ₇
Male ($n = 22$)	8.2 ± 0.4	9.0 ± 0.5	9.3 ± 0.3	10.2 ± 0.3	14.1 ± 0.5
Female ($n = 17$)	7.5 ± 0.3	8.5 ± 0.3	9.1 ± 0.2	9.7 ± 0.4	12.8 ± 0.4
t	6.0184	3.6413	2.3685	4.4647	8.7624
P	<0.0001	0.0008	0.0232	<0.0001	<0.0001



FIGURE 1: Screw placement in cadaveric specimens.

so the distribution of the spatial structure of the model is consistent with the real object. At present, a large number of studies have used the Mimics software to build cervical VB for finite element analysis and clinical surgical procedures [27–29]. In this study, the screw placement area was refined and divided into 9 zones, and the screw placement parameters of each zone were analyzed. The results indicated that screws larger than 22 mm could be placed in men and more than 20 mm in women. Zone i was the optimal entry point among all the 9 zones, with the longest screw length. The screw diameter, however, is mainly determined by the pedicle width. Generally, the screw diameter should be smaller than the pedicle width of the corresponding segment and larger than the relatively small cancellous bone core, so that the thread can be cut into the cortical bone, thus maximizing the pull-out force and bending strength. In this study, the screw placement was set to 3.5 mm and its feasibility was demonstrated. The pedicle screw diameter can therefore be selected as a baseline safe value of 3.5 mm and adjusted as appropriate. This study also found no statistical significance in the horizontal angle of C₃₋₇ on the same sagittal plane. But the horizontal angle of different sagittal planes showed statistically significant differences with a gradually decreasing trend, among which the angles of zones a, d, and g were the largest. Therefore, when nailing in these areas, the inclination angle should be the largest. The sagittal angle at the same level had no statistically significant difference, but the sagittal angle at different levels showed a statistically significant difference with a gradually increasing trend, which is similar to our previous findings [30]. The method used here was first proposed in our previous research [17] and was first applied on cadaveric specimens in this study. Before surgery, the CT data of patients was imported into the software, and the screw placement was

simulated in the optimal area to determine the final entry area and trajectory. It was also observed in this study that the distance from the midline of the anterior edge of C₃₋₇ to the anterior edge of the UVJ gradually increased. Finally, we further applied this method to cadaveric specimens and confirmed its feasibility. However, this study mainly used fluoroscopy-guided free-hand screw placement, and despite successful placement in cadaveric specimens, the study demonstrated a 21.7% incidence of critical pedicle rupture in the axial plane [13]. Patton et al. [11] found that catastrophic screw placement occurred in 33.3% of the patients with fluoroscopy-guided free-hand screw placement, compared with a significantly lower but still high incidence of 16.7% in the image-guided group. It is shown that patient-specific drill templates (PDTs) made by three-dimensional printing technology (3DP) had favorable effectiveness and accuracy in assisting cervical transpedicular screw placement [31, 32].

This study still shows room for improvement. First of all, the data collected are all from CT reconstruction images, which inevitably leads to human errors. Besides, in the actual clinical operation, it is relatively difficult to find the optimum entry point in clinical screw placement because most patients requiring surgery had CS degeneration of varying degrees. And in view of the accuracy of this screw placement method, it is necessary to strictly study and analyze the patients with surgical indications. Moreover, the sample size of this study is small, so it is necessary to further study the biomechanical stability and accuracy of this screw placement method. In a word, ATPRS placement into the LCS is a feasible internal fixation technique, but its clinical application value needs further systematic analysis and research.

5. Conclusion

In summary, anatomical and radiographic measurements demonstrate that ATPRS can be used as a means of internal fixation of the lower CS in clinical practice. Due to the accuracy of this operation, it should not be used as a routine operation, and patients with surgical indications should be strictly selected. But we think that as research continues and technology advances, ATPRS will be further promoted and applied.

Data Availability

The labeled dataset used to support the findings of this study are available from the corresponding author upon request.

Conflicts of Interest

The authors declare no competing interests.

Authors' Contributions

Jihui Zhang and Liujun Zhao contributed equally to this work and are co-first authors.

Acknowledgments

This experimental study on a new type of anterior lower cervical pedicle base screw (ATPRS) screw-plate system was supported by the Zhejiang Provincial Public Welfare Technology Research Project (LGF18C100004).

References

- [1] P. Bovonratwet, M. C. Fu, V. Tyagi et al., "Incidence, risk factors, and clinical implications of postoperative hematoma requiring reoperation following anterior cervical discectomy and fusion," *Spine*, vol. 44, no. 8, pp. 543–549, 2019.
- [2] T. Ihalainen, I. Rinta-Kiikka, T. M. Luoto et al., "Risk factors for laryngeal penetration-aspiration in patients with acute traumatic cervical spinal cord injury," *The Spine Journal*, vol. 18, no. 1, pp. 81–87, 2018.
- [3] L. Jiang, M. Tan, L. Dong et al., "Comparison of anterior decompression and fusion with posterior laminoplasty for multilevel cervical compressive myelopathy," *Journal of Spinal Disorders & Techniques*, vol. 28, no. 8, pp. 282–290, 2015.
- [4] B. Xiao, B. Wu, T. Rong, W. Cui, D. Sang, and B. Liu, "Clinical impact of 3-level anterior cervical decompression and fusion (ACDF) on the occipito-atlantoaxial complex: a retrospective study of patients who received a zero-profile anchored spacer versus cage-plate construct," *European Spine Journal*, vol. 30, no. 12, pp. 3656–3665, 2021.
- [5] N. E. Epstein, "Reoperation rates for acute graft extrusion and pseudarthrosis after one-level anterior corpectomy and fusion with and without plate instrumentation: etiology and corrective management," *Surgical Neurology*, vol. 56, no. 2, pp. 73–80, 2001.
- [6] P. Ouyang, T. Lu, X. He, Z. Gao, X. Cai, and Z. Jin, "Biomechanical comparison of integrated fixation cage versus anterior cervical plate and cage in anterior cervical corpectomy and fusion (ACCF): a finite element analysis," *Medical Science Monitor*, vol. 25, pp. 1489–1498, 2019.
- [7] A. C. Lau and M. Y. Wang, "The clinical and economic costs of treating cervical radiculopathy: the age-old question of the anterior versus posterior approach," *Journal of Neurosurgery: Spine*, vol. 27, no. 6, pp. 617–619, 2017.
- [8] A. He, D. Xie, X. Cai et al., "One-stage surgical treatment of cervical spine fracture-dislocation in patients with ankylosing spondylitis via the combined anterior-posterior approach," *Medicine*, vol. 96, no. 27, p. e7432, 2017.
- [9] U. G. Longo, M. Loppini, S. Petrillo, A. Berton, N. Maffulli, and V. Denaro, "Management of cervical fractures in ankylosing spondylitis: anterior, posterior or combined approach?," *British Medical Bulletin*, vol. 115, no. 1, pp. 57–66, 2015.
- [10] H. Koller, A. Hempfing, F. Acosta et al., "Cervical anterior transpedicular screw fixation. Part I: study on morphological feasibility, indications, and technical prerequisites," *European Spine Journal*, vol. 17, no. 4, pp. 523–538, 2008.
- [11] A. G. Patton, R. P. Morris, Y.-F. Kuo, and R. W. Lindsey, "Accuracy of fluoroscopy versus computer-assisted navigation for the placement of anterior cervical pedicle screws," *Spine*, vol. 40, no. 7, pp. E404–E410, 2015.
- [12] M. Aramomi, Y. Masaki, S. Koshizuka et al., "Anterior pedicle screw fixation for multilevel cervical corpectomy and spinal fusion," *Acta Neurochirurgica*, vol. 150, no. 6, pp. 575–582, 2008.
- [13] H. Koller, F. Acosta, M. Tauber et al., "Cervical anterior transpedicular screw fixation (ATPS)—part II. Accuracy of manual insertion and pull-out strength of ATPS," *European Spine Journal*, vol. 17, no. 4, pp. 539–555, 2008.
- [14] H. Koller, W. Hitzl, F. Acosta et al., "In vitro study of accuracy of cervical pedicle screw insertion using an electronic conductivity device (ATPS part III)," *European Spine Journal*, vol. 18, no. 9, pp. 1300–1313, 2009.
- [15] Z. Zhang, Z. Mu, and W. Zheng, "Anterior pedicle screw and plate fixation for cervical facet dislocation: case series and technical note," *The Spine Journal*, vol. 16, no. 1, pp. 123–129, 2016.
- [16] K. Kotil, M. A. Akçetin, and Y. Savas, "Neurovascular complications of cervical pedicle screw fixation," *Journal of Clinical Neuroscience*, vol. 19, no. 4, pp. 546–551, 2012.
- [17] L. Zhao, J. Zhang, Y. Gu et al., "Study on the best entry region and trajectory of anterior transpedicular root screws," *Zhonghua Yi Xue Za Zhi*, vol. 100, no. 41, pp. 3235–3239, 2020.
- [18] J. D. Oliver, S. Goncalves, P. Kerezoudis et al., "Comparison of outcomes for anterior cervical discectomy and fusion with and without anterior plate fixation," *Spine*, vol. 43, no. 7, pp. E413–E422, 2018.
- [19] Y. Do Koh, T.-H. Lim, J. W. You, J. Eck, and H. S. An, "A biomechanical comparison of modern anterior and posterior plate fixation of the cervical spine," *Spine*, vol. 26, no. 1, pp. 15–21, 2001.
- [20] K. Li, W. Zhang, D. Liu et al., "Pedicle screw fixation combined with intermediate screw at the fracture level for treatment of thoracolumbar fractures: a meta-analysis," *Medicine*, vol. 95, no. 33, p. e4574, 2016.
- [21] J. Wang, X. He, and T. Sun, "Comparative clinical efficacy and safety of cortical bone trajectory screw fixation and traditional pedicle screw fixation in posterior lumbar fusion: a systematic review and meta-analysis," *European Spine Journal*, vol. 28, no. 7, pp. 1678–1689, 2019.
- [22] G. Keorochana, S. Pairuchvej, W. Trathitaphun, A. Arirachakaran, P. Predeeprompan, and J. Kongtharvonskul, "Comparative outcomes of cortical screw trajectory fixation and pedicle screw fixation in lumbar spinal fusion: systematic review and meta-analysis," *World Neurosurgery*, vol. 102, pp. 340–349, 2017.
- [23] M. Miyazaki, T. Ishihara, S. Kanazaki, N. Notani, T. Abe, and H. Tsumura, "Relationship between vertebral morphology and the potential risk of spinal cord injury by pedicle screw in adolescent idiopathic scoliosis," *Clinical Neurology and Neurosurgery*, vol. 172, pp. 143–150, 2018.
- [24] K. N. Fountas, E. Z. Kapsalaki, T. Machinis, and J. S. Robinson, "Extrusion of a screw into the gastrointestinal tract after anterior cervical spine plating," *Clinical Spine Surgery*, vol. 19, no. 3, pp. 199–203, 2006.
- [25] R. Kapu, M. Singh, A. Pande, M. C. Vasudevan, and R. Ramamurthi, "Delayed anterior cervical plate dislodgement with pharyngeal wall perforation and oral extrusion of cervical

- plate screw after 8 years: a very rare complication,” *Journal of Craniovertebral Junction and Spine*, vol. 3, no. 1, pp. 19–22, 2012.
- [26] N. A. Ebraheim, R. Xu, T. Knight, and R. A. Yeasting, “Morphometric evaluation of lower cervical pedicle and its projection,” *Spine*, vol. 22, no. 1, pp. 1–5, 1997.
- [27] A. Kashyap, S. Kadur, A. Mishra, G. Agarwal, A. Meena, and L. Maini, “Cervical pedicle screw guiding jig, an innovative solution,” *Journal of Clinical Orthopaedics and Trauma*, vol. 9, no. 3, pp. 226–229, 2018.
- [28] W. Wu, Z. Han, B. Hu et al., “A graphical guide for constructing a finite element model of the cervical spine with digital orthopedic software,” *Annals of Translational Medicine*, vol. 9, no. 2, p. 169, 2021.
- [29] M. Athari, M. Golbakhsh, A. Mirbolook et al., “Posterior first and second cervical vertebrae fusion by screw fixation technique using the modern pre-fabricated template method on cadaver samples,” *Malaysian Orthopaedic Journal*, vol. 15, no. 3, pp. 58–64, 2021.
- [30] L. Zhao, G. Li, J. Liu et al., “Radiological studies on the best entry point and trajectory of anterior cervical pedicle screw in the lower cervical spine,” *European Spine Journal*, vol. 23, no. 10, pp. 2175–2181, 2014.
- [31] X. Sun, E. Yang, C. Zhao et al., “Progress in the Application of 3D Printing Technology in Spine Surgery,” *Journal of Shanghai Jiaotong University (Science)*, vol. 26, pp. 352–360, 2021.
- [32] C.-E. Heyde, G. Osterhoff, S. Uja, A. Völker, N. von der Höh, and J. Jarvers, “Patient-matched 3-D-printed guides for the insertion of cervical pedicle screws in tumor surgery,” *Case Reports in Surgery*, vol. 2021, Article ID 8135996, 9 pages, 2021.

Research Article

Early Diagnosis and Treatment of Coronary Heart Disease with Image Features of Optical Coherence Tomography under Adaptive Segmentation Algorithm

Chaozhang Lin 

Medical Section, Hainan Tunchang People's Hospital, Tunchang, 571600 Hainan, China

Correspondence should be addressed to Chaozhang Lin; 20148113@stu.sicau.edu.cn

Received 10 June 2022; Revised 2 July 2022; Accepted 15 July 2022; Published 8 August 2022

Academic Editor: Pan Zheng

Copyright © 2022 Chaozhang Lin. This is an open access article distributed under the Creative Commons Attribution License, which permits unrestricted use, distribution, and reproduction in any medium, provided the original work is properly cited.

This research was aimed at exploring the application value of optical coherence tomography (OCT) images under adaptive segmentation algorithm in the early diagnosis of coronary heart disease (CHD). Eighty-two patients with CHD were included, who were to undergo coronary angiography (CAG) to confirm their condition. According to the diagnostic criteria of CHD in the American Coronary Artery Surgery Study (CASS), the patients were divided into the stable plaque group (41 cases) and unstable plaque group (41 cases). Besides, 20 healthy volunteers were selected as the control group, and all of them underwent OCT scans. On the basis of a fourth-order partial differential equation (PDE) and active contour (AC) model, a novel adaptive image segmentation algorithm PDE-AC was constructed and used for OCT image processing. No significant difference was found in general clinical data and serological indicators in the control group compared to the other two groups ($P > 0.05$). The lipid plaque length, degree of stenosis, and lipid pool angle, macrophages and intimal erosion, and plaque fissure in the unstable plaque group were highly greater than those in the stable plaque group. The fibrous cap thickness (FCT) was significantly thinner than that in the stable plaque group ($P < 0.05$). The diagnostic sensitivity, specificity, and accuracy of OCT under PDE-AC algorithm for CHD (91.53%, 84.08%, and 95.38%) were markedly higher than those of single OCT (83.46%, 75.11%, and 88.02%) ($P < 0.05$). In summary, OCT images under PDE-AC algorithm did better than simple OCT images in the diagnosis of CHD. Lipid plaque length, degree of stenosis, and lipid pool angle, macrophage and intimal erosion, plaque fissure, and FCT were important indicators for judging plaque stability, having the better clinical application value.

1. Introduction

Coronary heart disease (CHD) is a heart disease caused by coronary atherosclerosis that narrows or blocks the lumen, leading to myocardial ischemia, hypoxia, or necrosis. It is the most common organ disease caused by atherosclerosis, and males have an earlier onset than females. CHD is more common in adults over 40 years old, showing a younger trend in recent years; it is one of the major diseases threatening human health [1–3]. The clinical paradigms of CHD mainly include latent CHD, angina pectoris CHD, myocardial infarction CHD, sudden death CHD, and heart failure and arrhythmia CHD [4, 5]. The main risk of CHD is the rupture of sclerotic plaques, which induces platelet aggregation to form thrombus, resulting in acute myocardial infarction.

Treatment methods include controlling factors that damage blood vessels and stopping or delaying the progression of plaques. The plaque stability is increased, and the risk of myocardial infarction can be minimized. The platelet aggregation function is inhibited, and platelet aggregation can be prevented when plaque ruptures, thereby avoiding thrombosis. If CHD is not controlled in time, angina pectoris, myocardial infarction, etc. may occur in the long-term development, which can be life-threatening in severe cases. Therefore, once many patients suffer from CHD, they will become very depressed and even maybe cannot face life positively [6]. Most people do not have any symptoms ordinarily, and their work, study, and life go as usual. But there are often signs of myocardial ischemia, such as feeling unwell of the precordium, or symptoms of fatigue. Although

the symptoms are very mild, myocardial ischemia can be detected if an electrocardiogram is performed in time, so that it can be prevented as early as possible [7, 8].

As an important clinical auxiliary department, medical imaging plays an irreplaceable role for clinicians to assess the conditions. With the help of imaging, the diagnosis accuracy and efficiency of clinicians can be greatly improved. The current clinical imaging diagnostic methods for CHD mainly consists of coronary angiography (CAG), computed tomography (CT), magnetic resonance imaging (MRI), and optical coherence tomography (OCT) [9]. CAG has always been the gold standard for the diagnosis of CHD, but its diagnostic accuracy is poor, and the degree of coronary stenosis can only be roughly judged by experienced physicians [10, 11]. Coronary CT is a common method for CHD screening in the department of cardiology. It mainly develops images by injecting a contrast agent into the vein and then scans the structure of the coronary artery through CT scanning. Finally, three-dimensional reconstruction is made to get coronary images, so as to determine whether there is coronary stenosis [12]. Therefore, this is a noninvasive examination to initially determine the condition of coronary artery disease through CT scanning; but, CAG is traumatic as it needs to puncture the artery. MRI can objectively reflect myocardial perfusion and myocardial transmural degree and is the most sensitive for subendocardial myocardial lesions, but it takes a long time and is expensive [13, 14]. OCT is the latest intravascular optical scanning tomography technology used in clinical practice. It utilizes the different optical features reflected from the tissue by low-coherence near-infrared light to perform tissue analysis and imaging, and the imaging speed is fast. The greatest advantage of OCT is its high resolution. So far, it is the intravascular imaging technology with the highest resolution, which allows accurate observation of the subintimal lesions or plaques. It can be applied to identify various intravascular microstructures such as unstable plaques, stable plaques, calcification, thrombus, and dissection. Besides, OCT is expected to become an ideal method for evaluating unstable plaques in the future [15].

The quality of images is an important factor affecting the accuracy of doctors' judgment, so the enhancement of medical images is critical. The quality of the image preprocessing algorithm is directly related to the effect of subsequent image processing, like image segmentation, target recognition, and edge extraction. For high-quality digital images, it is often necessary to denoise the images, while maintaining the integrity of the original information as much as possible and removing the useless information in the signals [16]. In recent years, the partial differential equation (PDE) method derived from constrained optimization, energy minimization, and calculus of variations has been widely used in image processing. In particular, active contour (AC) has become one of the common methods of image segmentation. The PDE-AC model links the prior knowledge of the image region with the constraints of the image data, so that the AC can maintain the continuity and smoothness during the evolution process. It can well solve the issue that the initial position affects the convergence speed [17].

However, few existing studies have applied the PDE-AC algorithm to OCT image processing. In this research, patients with CHD who met the requirements were divided into two groups, and 20 healthy people were selected as the control group. The application value of OCT images under adaptive segmentation algorithm was comprehensively evaluated in the early diagnosis of CHD. Thereout, this research provided an effective solution for the clinical diagnosis and treatment of CHD.

2. Materials and Methods

2.1. Research Objects. Eighty-two CHD patients were collected as the research objects, who were scheduled to have CAG in the hospital from February 2015 to August 2020. According to the diagnostic criteria for CHD of American Coronary Artery Surgery Study (CASS), the patients were divided into the stable plaque group and unstable plaque group, with each 41 cases. In addition, 20 healthy volunteers having physical examination during the same period were included in the control group. This research had been approved by the ethics committee of the hospital. The patients and their families were informed about the research and signed the informed consent forms.

Inclusion criteria are follows: Patients had the angina pectoris CHD or myocardial infarction CHD, with typical symptoms of chest pain, having complete clinical data, and aged over 18 years old.

Exclusion criteria are as follows: (1) Patients were complicated with psychiatric diseases. (2) Patients had a stenosis rate of less than 50%. (3) Patients suffered from severe liver and kidney insufficiency. (4) Patients did not complete follow-up and lost contact midway. (5) Patients were complicated with hematological diseases. (6) Patients could not receive OCT examination for the complete coronary occlusion. (7) Patients got acute myocardial infarction.

2.2. Image Examination Methods. A digital subtraction system was used for performing CAG on the patients. The main projection positions included left anterior oblique+cranial position, spider position, liver position, and right anterior oblique+cranial position. After CAG, OCT scanning was performed with optical coherence tomography scanner, and 1800UI heparin was added. First, the imaging catheter was taken out and wiped with wet gauze. 2.5 mL of contrast agent was injected after the hydrophilic coating was activated. Then, system calibration was performed, and the 6F guiding catheter was inserted into the target coronary artery to lesion location. The optical display lens was adjusted to 5 mm of the proximal marker of the catheter, and the position of the 6F guiding catheter was also adjusted until smoke was emitted. The contrast medium was injected fast in a pellet manner, the light microscope was back-tested, and the system was turned off after the surgery. The acquired images were sent to the workstation for processing, and two experienced senior physicians were selected to interpret the OCT images.

2.3. Adaptive Image Segmentation Algorithm. In this research, the fourth-order PDE and AC model were introduced for a novel adaptive image segmentation algorithm. The energy functional of this model could be expressed as

$$F^* = \alpha F^k + (1 - \alpha) F^h + \beta F^i + \lambda F^j. \quad (1)$$

In equation (1), F^k denoted the global term, F^h denoted the local term, F^i was the regularization constraint term, and F^j was the length constraint term. α , $1 - \alpha$, β , and λ represented the global term parameter, the local term parameter, the regularization constraint term parameter, and the length constraint term parameter, respectively. Then, the edge-guided image was used to replace the original grayscale image in the AC model, and the edge-guided (EG) image could be expressed as

$$EG = \sqrt{Ex^2 + Ey^2}. \quad (2)$$

Ex represented the gradient of the x -axis of the image, while Ey represented the gradient of the y -axis of the image. Ex and Ey could be expressed as

$$Ex = h \cdot px, \quad (3)$$

$$Ey = h \cdot py. \quad (4)$$

In equations (3) and (4),

$$px = \begin{bmatrix} 20 - 2 \\ 2\sqrt{2} \ 0 \ 2\sqrt{2} \\ 20 - 2 \end{bmatrix}, \quad (5)$$

$$py = \begin{bmatrix} 2 \ 2\sqrt{2} \ 1 \\ 0 \ 0 \ 0 \\ -2 - 2\sqrt{2} - 2. \end{bmatrix}. \quad (6)$$

The global energy term F^k of the AC model was defined as

$$F^k = \kappa_1 \int |EG(x) - k_1|^2 dx + \kappa_2 \int |EG(x) - k_2|^2 dx. \quad (7)$$

In equation (7), $EG(x)$ represented the value of the x th pixel in the EG image, k_1 was the value of the pixel of the EG image within the evolution curve, and k_2 represented the value of the pixel of the EG image outside the evolution curve.

The local energy term F^h of the AC model was defined as

$$F^h = \kappa_1 \int S \bullet |EG(x) - l_1|^2 dx + \kappa_2 \int S \bullet |EG(x) - l_2|^2 dx. \quad (8)$$

In equation (8), l_1 and l_2 were smooth functions, and S meant a Gaussian kernel function.

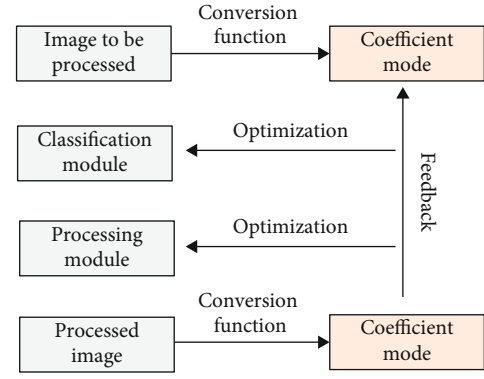


FIGURE 1: Image processing process under PDE-AC.

The regularization term F^i of the AC model was defined as

$$F^i = \int \frac{|\nabla\varphi(x) - 1|^2}{2} dx. \quad (9)$$

In the AC model, length constraint term F^j was defined as

$$F^j = \int \Omega |\nabla\varphi(x)|^2 dx. \quad (10)$$

Therefore, the energy functional of the model was updated to be

$$\begin{aligned} F^* = & \alpha \kappa_1 \int |EG(x) - k_1|^2 dx + \kappa_2 \int |EG(x) - k_2|^2 dx \\ & + (1 - \alpha) \kappa_1 \int S \bullet |EG(x) - l_1|^2 dx \\ & + \kappa_2 \int S \bullet |EG(x) - l_2|^2 dx + \beta \int \frac{|\nabla\varphi(x) - 1|^2}{2} dx \\ & + \lambda \int \Omega |\nabla\varphi(x)|^2 dx. \end{aligned} \quad (11)$$

Finally, the adaptive image segmentation algorithm PDE-AC under the fourth-order PDE as well as AC model was worked out.

2.4. Image Evaluation Indicators and Observation Indicators. The geometric active contour (GAC) model [18] and the advanced modeled iterative reconstruction algorithm (ADMIRE) [19] were introduced to compare with the PDE-AC algorithm in this research. The correct classification ratio (CCR), Dice similarity coefficient (DISC), and average segmentation time (AST) were adopted as the evaluation indicators of image segmentation results. The CCR and DISC were calculated as the following:

$$CCR = \frac{|P \cap Q|}{|P|}, \quad (12)$$

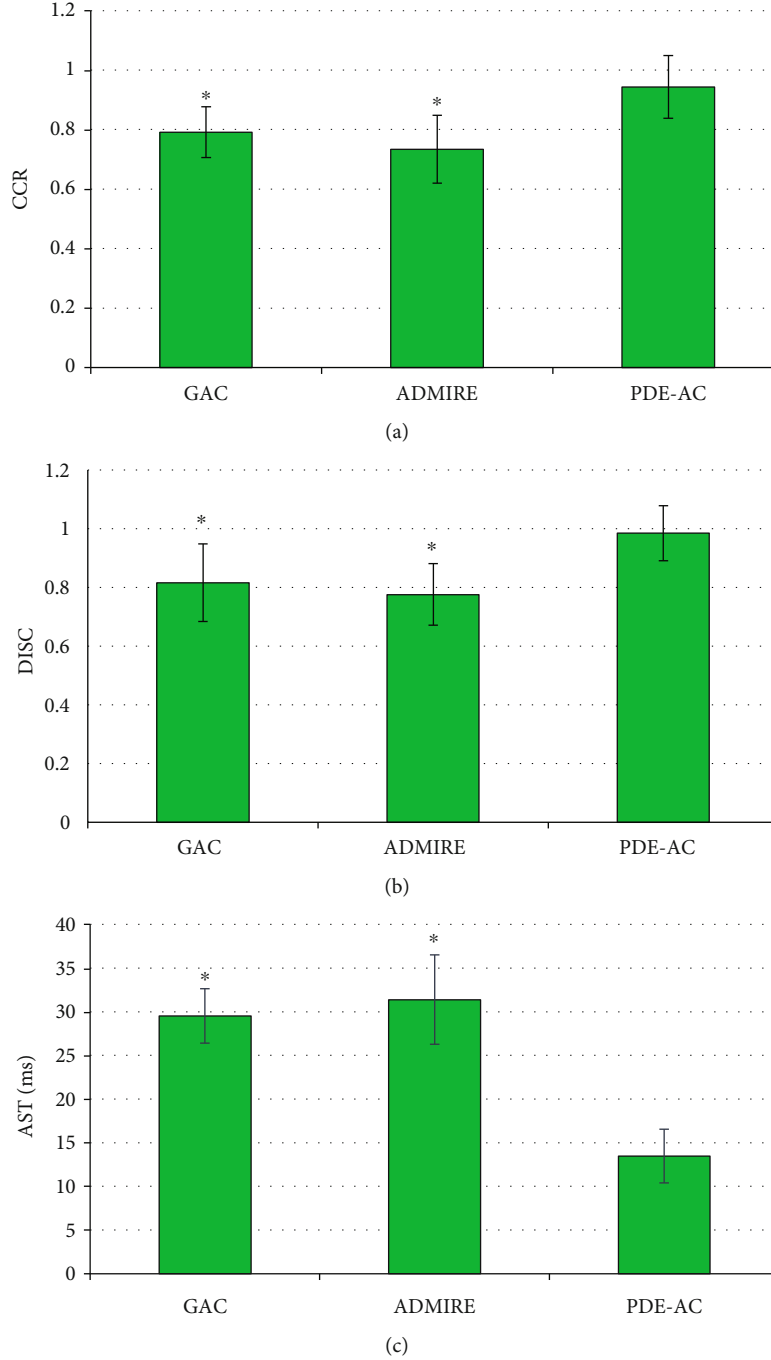


FIGURE 2: Comparison of segmentation outcome indicators under different algorithms. (a-c) CCR, DISC, and AST, respectively. * Compared with PDE-AC algorithm, $P < 0.05$.

$$\text{DISC} = 2 \times \frac{|P \cap Q|}{|P| + |Q|}. \quad (13)$$

In the equations above, P represented the segmentation outcome of the PDE-AC algorithm on the image and Q represented the segmentation outcome of the gold standard. The basic flow of image processing was shown as Figure 1.

The observation indicators were as follows. The basic information of patients (age, body mass index (BMI), number of male and female cases, hypertension, diabetes, smok-

ing, drinking, triglyceride, total cholesterol, low-density lipoprotein, and high-density lipoprotein) were collected. Serological indicators of patients, including matrix metalloproteinase 7 (MMP7), matrix metalloproteinase 9 (MMP9), and matrix metalloproteinase 12 (MMP12) levels, were counted. These serological indicators were determined using the double-antibody sandwich enzyme-linked immunosorbent assay (ELISA). The OCT images obtained by scanning were sent to the workstation for processing, and related quantitative indicators were measured. Fibrous cap

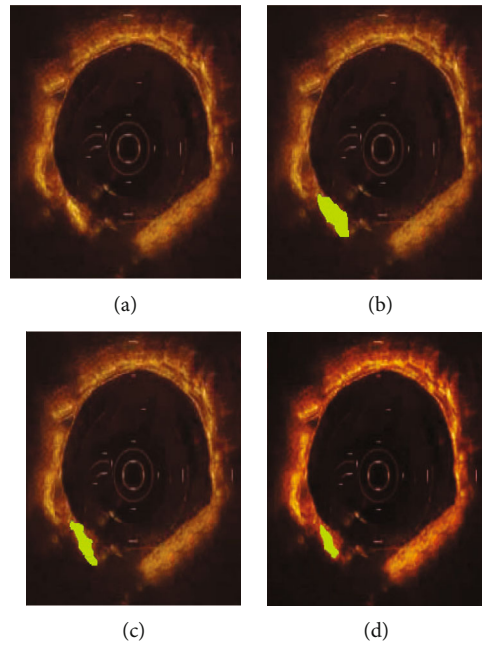


FIGURE 3: Segmentation and reconstruction outcomes of OCT images by different algorithms. (a) The original image. (b) Under GAC algorithm. (c) Under ADMIRE algorithm. (d) Under PDE-AC algorithm. The green area in the picture is a calcified plaque.

thickness (FCT), lipid plaque length, degree of stenosis, lipid pool angle, macrophages, intimal erosion, plaque fissure, plaque calcification, intraplaque microchannels, and thrombotic conditions were included. The results of CAG were as the gold standard, and the accuracy, sensitivity, and specificity of both OCT images under the PDE-AC algorithm and simple OCT images were calculated.

2.5. Statistical Methods. All the data were statistically analyzed using SPSS 19.0. The measurement data were expressed as mean + standard deviation ($\bar{x} \pm s$), while the enumeration data were statistically inferred using χ^2 test. The measurement data conformed to normal distribution, and tested by t -test. $P < 0.05$ was considered to be statistically significant.

3. Results

3.1. Comparison of Segmentation Results of Different Algorithms. As shown in Figure 2, the CCR (0.943 ± 0.105) and DISC (0.985 ± 0.094) of the images segmented and reconstructed by the PDE-AC algorithm were significantly higher than those of the GAC and ADMIRE algorithms, with statistically observable differences ($P < 0.05$). AST (13.482 ± 3.076 ms) of the reconstructed image segmented by the PDE-AC algorithm was statistically lower than that of the GAC algorithm and ADMIRE algorithm ($P < 0.05$).

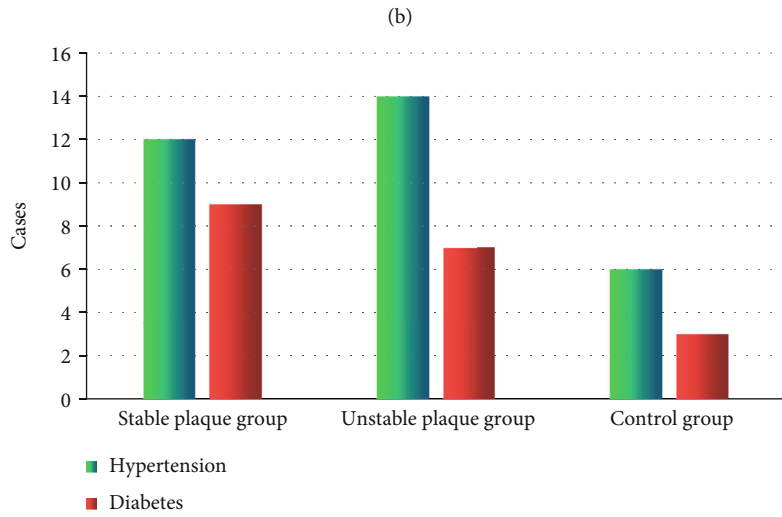
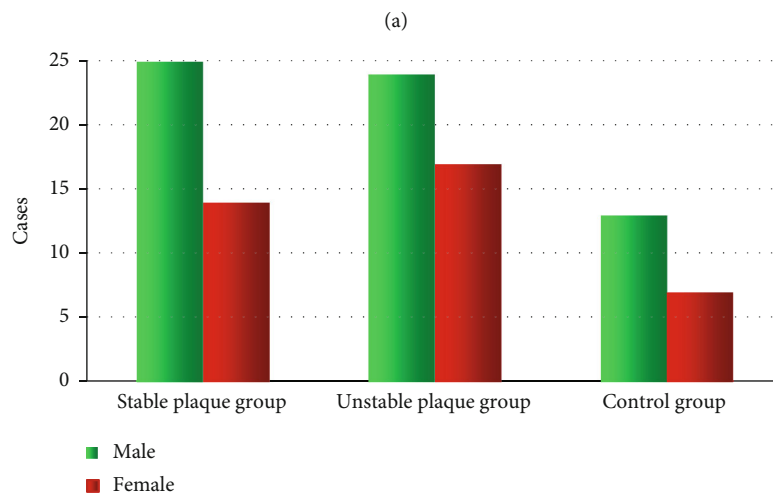
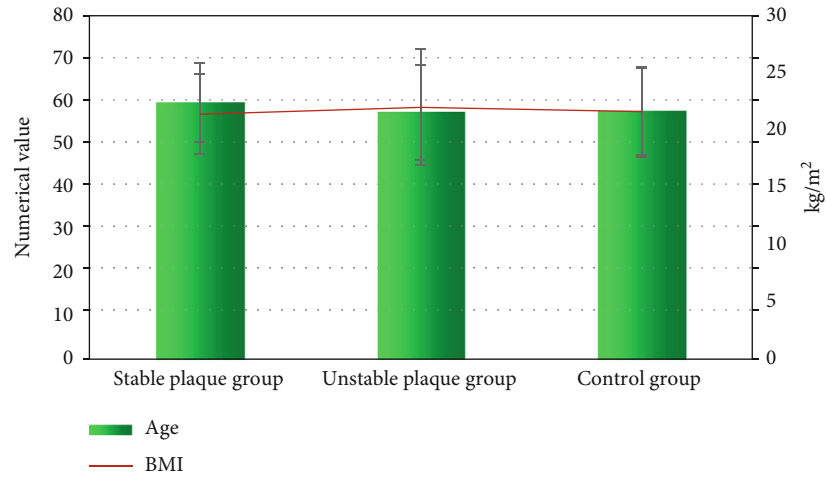
Figure 3 showed the segmentation and reconstruction results of OCT images by different algorithms. The image quality after processing by the GAC, ADMIRE, and PDE-AC algorithms was improved compared with the original images. In the images processed by the PDE-AC algorithm, artifacts and noise were greatly reduced, and the clarity

was also significantly improved. The overall quality was better than the images processed by GAC or ADMIRE.

3.2. Comparison of Basic Clinical Data of Patients. Figure 4 displayed the comparisons of the basic clinical data among three groups of patients. Not a statistically significant difference was shown in their age, BMI, number of males and females, hypertension, diabetes, smoking, drinking, triglyceride, total cholesterol, low-density lipoprotein, and high-density lipoprotein in the three groups ($P > 0.05$).

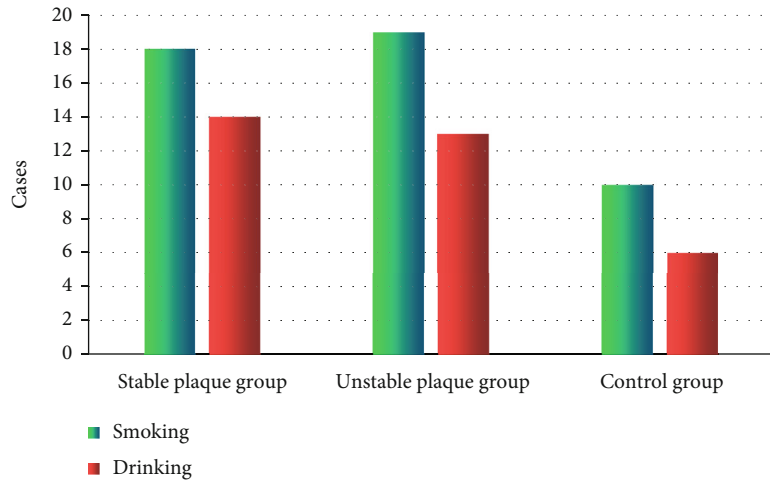
3.3. Imaging Manifestations of Cases. As shown in Figure 5, a typical 3-layer structure consisting of the intima, media, and adventitia could be observed in the OCT images of healthy volunteers. The intima was shown as bright bands with high signal, the media showed dark bands with low signal, and the adventitia showed an extracellular matrix and outer elastic lamina. Compared with the OCT images of healthy volunteers, in the OCT images of the patients, the macrophages showed dot-like or strip-like structures of high reflection and strong attenuation, the fibrous cap was intact, and the lumen surface was irregular. The lesions were accompanied by thrombosis, with no superficial lipid and calcification in the proximal or distal to the thrombus.

3.4. Comparison of Serological Indicators. In Figure 6, there was not a significant difference in the level of MMP12 among the three groups of patients ($P > 0.05$). The levels of MMP7 and MMP9 in the unstable plaque group were remarkably higher than those in the stable plaque group and control group; the differences were of statistical significance ($P < 0.05$). The levels of MMP7 and MMP9 were not statistically different between the stable plaque group and control group ($P > 0.05$).

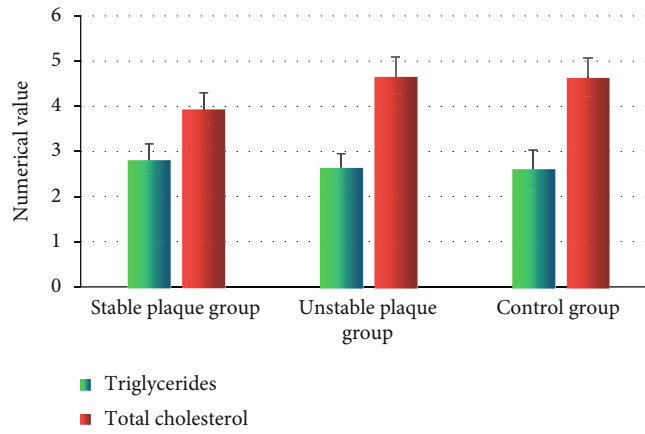


(c)

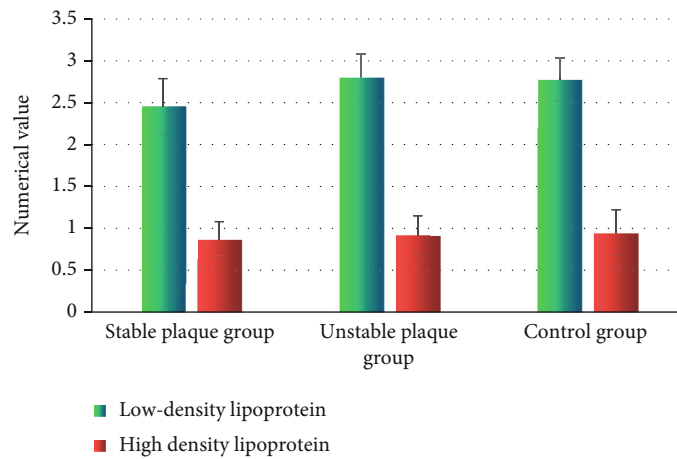
FIGURE 4: Continued.



(d)



(e)



(f)

FIGURE 4: Comparison of basic data of three groups of patients. (a) Age and BMI. (b) The number of male and female cases. (c) Hypertension and diabetes. (d) Smoking and drinking. (e) Triglycerides and total cholesterol. (f) Low-density lipoprotein and high-density lipoprotein.

3.5. Comparison of OCT Quantitative Indicators between Stable Plaque Group and Unstable Plaque Group. As presented in Figure 7, there was no remarkable difference in plaque calcification, intraplaque microchannels, and throm-

bus between the stable plaque group and the unstable plaque group ($P > 0.05$). Lipid plaque length, degree of stenosis, and lipid pool angle, macrophages and intimal erosion, and plaque fissure in the unstable plaque group were considerably

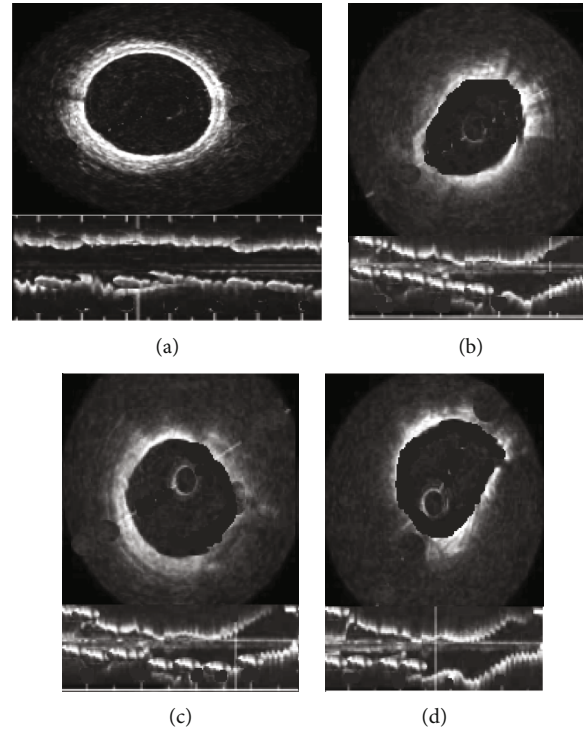


FIGURE 5: Imaging manifestations of the cases. Male patient, 67-year-old, with unstable angina pectoris. (a) OCT image of a healthy volunteer. (b–d) OCT images.

greater than those in the stable plaque group, with the differences of statistical significance ($P < 0.05$). The FCT of the unstable plaque patients was significantly smaller than that in the stable plaque group, showing a statistically significant difference ($P < 0.05$).

3.6. Comparison of Diagnostic Effect between OCT Images under PDE-AC Algorithm and Simple OCT Images. In Figure 8, the diagnostic sensitivity of OCT images under the PDE-AC algorithm for CHD was 91.53%, the diagnostic specificity was 84.08%, and the diagnostic accuracy was 95.38%. The diagnostic sensitivity, specificity, and accuracy of the simple OCT images for CHD were 83.46%, 75.11%, and 88.02%, respectively. The diagnostic sensitivity, specificity, and accuracy of OCT images under the PDE-AC algorithm were all markedly higher than those of simple OCT images with differences of statistical significance ($P < 0.05$).

4. Discussion

The gold standard for clinical diagnosis of CHD is CAG. CAG is an interventional examination that can intuitively reflect the stenosis of cardiac vessels. It is currently the most reliable method for diagnosing CHD. However, the invasiveness of CAG to patients limits its development, and it is necessary to seek more scientific diagnostic methods [20, 21]. Thus, 82 CHD patients who were going to undergo CAG for confirming the condition were included in this research as the research objects. According to the CASS diagnostic criteria for CHD, the patients were divided into the stable plaque group with 41 cases and the unstable plaque group

with the other 41 cases. Furthermore, 20 healthy volunteers having physical examination during the same period were chosen as the control group, and all the patients as well as volunteers underwent OCT. For the improvement of quality of OCT images, the fourth-order PDE and AC model were also introduced in this research, to construct a novel adaptive image segmentation algorithm PDE-AC. The PDE-AC algorithm was then compared with the GAC algorithm and ADMIRE algorithm. The GAC algorithm is on the basis of the methods of curve evolution and level set. It implicitly expresses the two-dimensional evolution curve as a three-dimensional continuous function and follows certain rules to continuously update the level set function. Thus, the implicit closed curve can be evolved [22]. ADMIRE is a third-generation MRI technology that compares the virtual raw data generated by forward projection with the projection data actually collected by the detector for multiple times, to eliminate artifacts and reduce noise [23]. The CCR (0.943 ± 0.105) and DISC (0.985 ± 0.094) of the segmented and reconstructed images by the PDE-AC algorithm were statistically higher than those of the GAC and ADMIRE algorithms ($P < 0.05$). Such a result was similar to the findings of Gu et al. [24], indicating that the PDE-AC algorithm proposed in this research was better than the traditional algorithm for segmentation of OCT images. Thus, the PDE-AC algorithm had a certain clinical application value. In addition, the AST (13.482 ± 3.076 ms) of the reconstructed image segmented by the PDE-AC algorithm was statistically and significantly lower than that of GAC and ADMIRE ($P < 0.05$). Compared with PDE-AC, the shortcomings of the other two algorithms were also quite

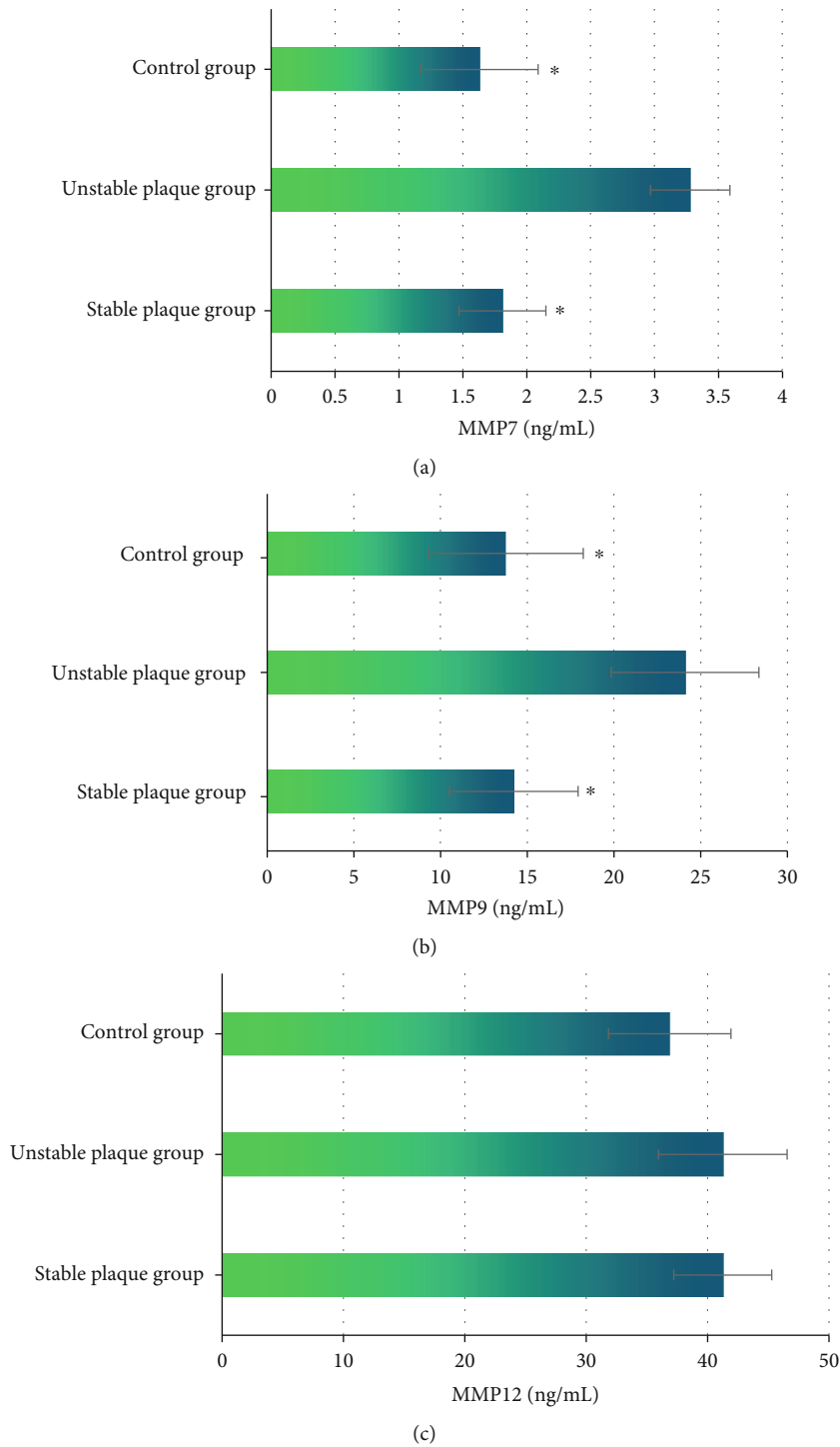


FIGURE 6: Comparison of serological indicators among three groups. (a–c) MMP7, MMP9, and MMP12, respectively. *Compared with the levels in the unstable plaque group, $P < 0.05$.

obvious. For example, the constant evolution speed needed to be manually determined according to the position of the initial curve, adaptive segmentation could not be achieved, and boundary leakage was prone to occur. While the PDE-AC algorithm could achieve adaptive segmentation, and the evolution speed changed with the position of the evolution curve, which avoided boundary leakage to a certain extent and had a better performance.

In this research, the basic clinical data of three groups of patients were first compared. None of statistically significant difference was discovered in the pairwise comparisons of their age, BMI, number of males and females, hypertension, diabetes, smoking, drinking, triglyceride, total cholesterol, low-density lipoprotein, and high-density lipoprotein ($P > 0.05$). This result provided feasibility for follow-up study. Then, the quantitative data indicators of OCT of the

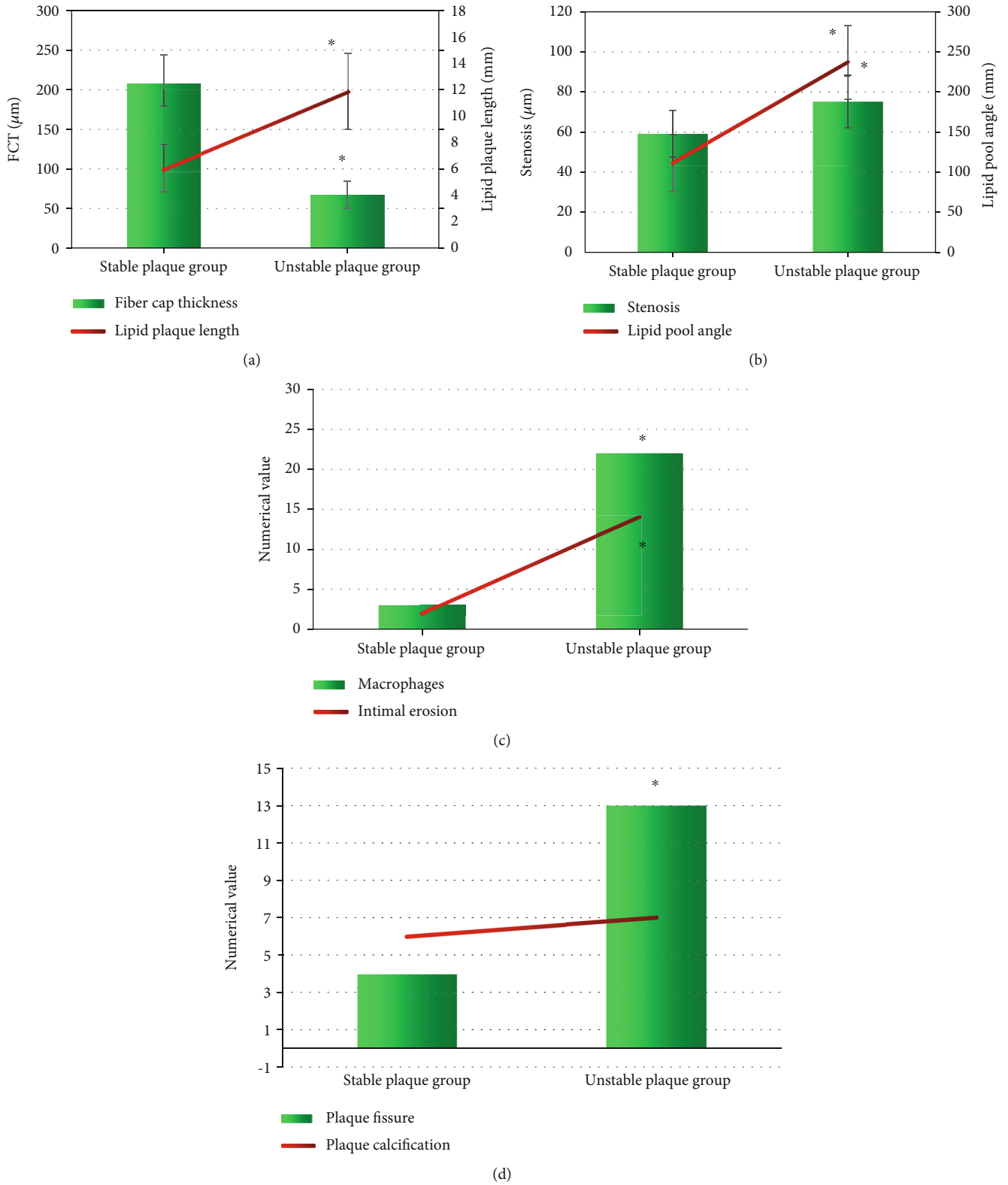


FIGURE 7: Continued.

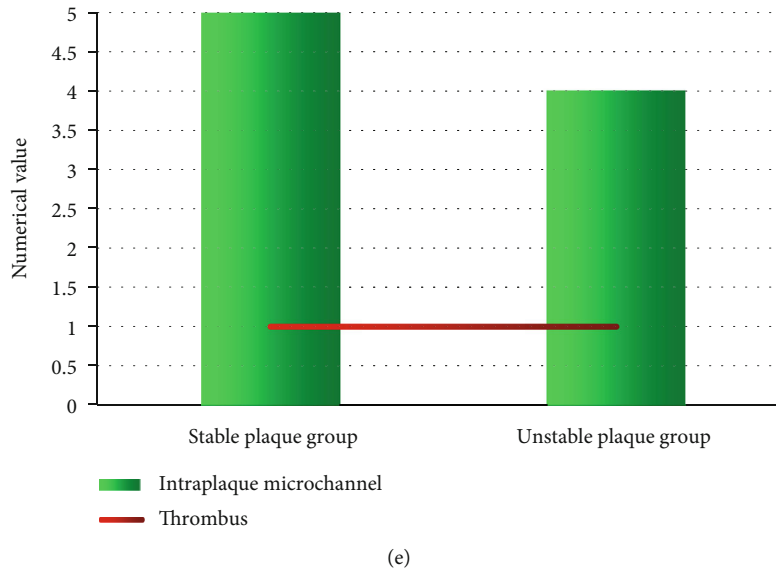


FIGURE 7: Comparison of lesion volume between the two groups before and after treatment. (a) FCT and the lipid plaque length. (b) Degree of stenosis and the angle of the lipid pool. (c) Macrophages and intimal erosion. (d) Plaque fissure and plaque calcification. (e) Comparison in intraplaque microchannel and thrombus. * Compared with the stable plaque group, $P < 0.05$.

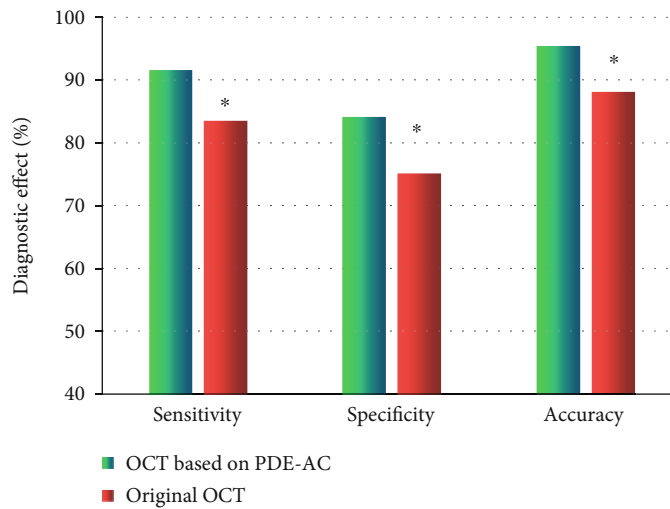


FIGURE 8: Comparison of the diagnostic effect between the PDE-AC algorithm-based OCT images and simple OCT images. * Compared with origin OCT images, $P < 0.05$.

patients were compared. The lipid plaque length, degree of stenosis, lipid pool angle, macrophages, intimal erosion, and plaque fissure of the unstable plaque group were statistically markedly greater than those of the stable plaque group, while FCT was statistically thinner ($P < 0.05$). There-out, it was indicated that the lipid plaque length, the degree of stenosis, the angle of lipid pool, macrophages and intimal erosion, plaque fissure, and FCT were important indicators for interpreting the presence of unstable plaques [25, 26]. With micron-scale axial resolution, OCT could accurately determine FCT and the cellular composition of the fibrous cap in vulnerable plaques formed by lipids on the vessel wall. It was also more sensitive in detecting thrombi and dissections. The image features of OCT scans could determine

the stability of plaques in patients with CHD and help physicians to assess the progress of the disease timely. Specificity and accuracy of OCT images under PDE-AC algorithm for diagnosing CHD were statistically and significantly higher than those of simple OCT images ($P < 0.05$). This further revealed that the PDE-AC algorithm-based OCT images were superior to simple OCT images in the diagnosis of CHD, deserving a better clinical application value.

5. Conclusion

In this research, OCT scans were performed on all three groups of objects, and the images were segmented by the PDE-AC adaptive algorithm. The PDE-AC algorithm not

only showed excellent image segmentation effect but also had high operating efficiency and good comprehensive performance. OCT images under the PDE-AC algorithm were better than simple OCT images in the diagnosis of CHD. Lipid plaque length, degree of stenosis, lipid pool angle, macrophage and intimal erosion, plaque fissure, and FCT were important indicators for judging plaque stability, having the better clinical application value. However, due to time and budget constraints, this research included a small size of samples from a single source. Meanwhile, in view of safety, acute myocardial infarction cases were not included, so there was a certain selection bias. Reinclusion of CHD patient samples would be considered in the future, to further analyze the application value of OCT images under the PDE-AC algorithm. In conclusion, this research gave a reference for the imaging diagnosis of clinical CHD.

Data Availability

The data used to support the findings of this study are available from the corresponding author upon request.

Conflicts of Interest

The author declares no conflicts of interest.

References

- [1] R. Y. Khamis, T. Ammari, and G. W. Mikhail, "Gender differences in coronary heart disease," *Heart*, vol. 102, no. 14, pp. 1142–1149, 2016.
- [2] P. H. Wirtz and R. von Känel, "Psychological stress, inflammation, and coronary heart disease," *Current Cardiology Reports*, vol. 19, no. 11, p. 111, 2017.
- [3] Y. Tian, P. Deng, B. Li et al., "Treatment models of cardiac rehabilitation in patients with coronary heart disease and related factors affecting patient compliance," *Reviews in Cardiovascular Medicine*, vol. 20, no. 1, pp. 27–33, 2019.
- [4] J. D. Sara, M. Prasad, M. F. Eleid, M. Zhang, R. J. Widmer, and A. Lerman, "Association between work-related stress and coronary heart disease: a review of prospective studies through the job strain, effort-reward balance, and organizational justice models," *Journal of the American Heart Association*, vol. 7, article e008073, 2018.
- [5] H. Liu, J. Zhuang, P. Tang, J. Li, X. Xiong, and H. Deng, "The role of the gut microbiota in coronary heart disease," *Current Atherosclerosis Reports*, vol. 22, no. 12, p. 77, 2020.
- [6] Y. Wu, B. Zhu, Z. Chen et al., "New insights into the comorbidity of coronary heart disease and depression," *Current Problems in Cardiology*, vol. 46, no. 3, article 100413, 2021.
- [7] P. A. Ades and D. E. Gaalea, "Coronary heart disease as a case study in prevention: potential role of incentives," *Preventive Medicine*, vol. 55, pp. S75–S79, 2012.
- [8] P. Milani, F. Scotti, and F. Bergamini, "Comment on: Diagnostic algorithm utilising multimodal imaging including optical coherence tomography angiography for the detection of myopic choroidal neovascularization," *Eye*, vol. 35, no. 1, pp. 349–350, 2021.
- [9] Y. Kim, G. I. Jung, D. Jeon et al., "Non-invasive optical coherence tomography data-based quantitative algorithm for the assessment of residual adhesive on bracket-removed dental surface," *Sensors*, vol. 21, no. 14, p. 4670, 2021.
- [10] M. Huang, H. Zhao, S. Gao et al., "Identification of coronary heart disease biomarkers with different severities of coronary stenosis in human urine using non-targeted metabolomics based on UPLC-Q-TOF/MS," *Clinica Chimica Acta*, vol. 497, pp. 95–103, 2019.
- [11] SCOT-HEART investigators, "CT coronary angiography in patients with suspected angina due to coronary heart disease (SCOT-HEART): an open-label, parallel-group, multicentre trial," *The Lancet*, vol. 385, no. 9985, pp. 2383–2391, 2015.
- [12] J. L. Mega, N. O. Stitzel, J. G. Smith et al., "Genetic risk, coronary heart disease events, and the clinical benefit of statin therapy: an analysis of primary and secondary prevention trials," *The Lancet*, vol. 385, no. 9984, pp. 2264–2271, 2015.
- [13] X. Jiang, M. Shen, L. Wang et al., "Validation of a novel automated algorithm to measure drusen volume and area using swept source optical coherence tomography angiography," *Translational Vision Science & Technology*, vol. 10, no. 4, p. 11, 2021.
- [14] J. Wang, L. Jia, X. Li et al., "New insights into the association between fibrinogen and coronary atherosclerotic plaque vulnerability: an intravascular optical coherence tomography study," *Cardiovascular Therapeutics*, vol. 2019, Article ID 8563717, 12 pages, 2019.
- [15] A. Sharma and A. Arbab-Zadeh, "Assessment of coronary heart disease by CT angiography: current and evolving applications," *Journal of Nuclear Cardiology*, vol. 19, no. 4, pp. 796–806, 2012.
- [16] C. Li, Z. Zhu, H. Yuan et al., "Improved retinal microcirculation after cardiac surgery in patients with congenital heart disease," *Frontiers in Cardiovascular Medicine*, vol. 8, article 712308, 2021.
- [17] Y. Zhu, L. Lin, C. Wang et al., "Impact of statins therapy on morphological changes in lipid-rich plaques stratified by 10-year Framingham risk score: a serial optical coherence tomography study," *Oncotarget*, vol. 8, no. 16, pp. 27401–27411, 2017.
- [18] C. Li, P. Zhong, H. Yuan et al., "Retinal microvasculature impairment in patients with congenital heart disease investigated by optical coherence tomography angiography," *Clinical & Experimental Ophthalmology*, vol. 48, no. 9, pp. 1219–1228, 2020.
- [19] W. Wang, Y. Wang, X. Gao et al., "Association between food and nutrients intakes and coronary plaque vulnerability in patients with coronary heart disease: an optical coherence tomography study," *Nutrition, Metabolism, and Cardiovascular Diseases*, vol. 31, no. 1, pp. 201–208, 2021.
- [20] J. Wang, J. Jiang, Y. Zhang, Y. W. Qian, J. F. Zhang, and Z. L. Wang, "Retinal and choroidal vascular changes in coronary heart disease: an optical coherence tomography angiography study," *Biomedical Optics Express*, vol. 10, no. 4, pp. 1532–1544, 2019.
- [21] C. Chezar-Azerrad, H. M. Garcia-Garcia, K. Dan et al., "Optical coherence tomography based treatment approach for patients with acute coronary syndrome," *Expert Review of Cardiovascular Therapy*, vol. 19, no. 2, pp. 141–149, 2021.
- [22] W. Zhang, X. Wang, P. Zhang, and J. Chen, "Global optimal hybrid geometric active contour for automated lung segmentation on CT images," *Computers in Biology and Medicine*, vol. 91, pp. 168–180, 2017.

- [23] J. T. Stranix, C. S. Stern, M. Rensberger et al., “A virtual surgical planning algorithm for delayed maxillomandibular reconstruction,” *Plastic and Reconstructive Surgery*, vol. 143, no. 4, pp. 1197–1206, 2019.
- [24] S. Gu, M. W. Jenkins, L. M. Peterson, Y. Q. Doughman, A. M. Rollins, and M. Watanabe, “Optical coherence tomography captures rapid hemodynamic responses to acute hypoxia in the cardiovascular system of early embryos,” *Developmental Dynamics*, vol. 241, no. 3, pp. 534–544, 2012.
- [25] H. Yano, S. Horinaka, and T. Ishimitsu, “Effect of evolocumab therapy on coronary fibrous cap thickness assessed by optical coherence tomography in patients with acute coronary syndrome,” *Journal of Cardiology*, vol. 75, no. 3, pp. 289–295, 2020.
- [26] Y. Homma, Y. Hayabuchi, A. Ono, and S. Kagami, “Pulmonary artery wall thickness assessed by optical coherence tomography correlates with pulmonary hemodynamics in children with congenital heart disease,” *Circulation Journal*, vol. 82, no. 9, pp. 2350–2357, 2018.

Retraction

Retracted: Effect of Propofol Intravenous Anesthesia Combined with Press-Needle Therapy on Analgesic Effect during Painless Abortion

Computational and Mathematical Methods in Medicine

Received 27 June 2023; Accepted 27 June 2023; Published 28 June 2023

Copyright © 2023 Computational and Mathematical Methods in Medicine. This is an open access article distributed under the Creative Commons Attribution License, which permits unrestricted use, distribution, and reproduction in any medium, provided the original work is properly cited.

This article has been retracted by Hindawi following an investigation undertaken by the publisher [1]. This investigation has uncovered evidence of one or more of the following indicators of systematic manipulation of the publication process:

- (1) Discrepancies in scope
- (2) Discrepancies in the description of the research reported
- (3) Discrepancies between the availability of data and the research described
- (4) Inappropriate citations
- (5) Incoherent, meaningless and/or irrelevant content included in the article
- (6) Peer-review manipulation

The presence of these indicators undermines our confidence in the integrity of the article's content and we cannot, therefore, vouch for its reliability. Please note that this notice is intended solely to alert readers that the content of this article is unreliable. We have not investigated whether authors were aware of or involved in the systematic manipulation of the publication process.

Wiley and Hindawi regrets that the usual quality checks did not identify these issues before publication and have since put additional measures in place to safeguard research integrity.

We wish to credit our own Research Integrity and Research Publishing teams and anonymous and named external researchers and research integrity experts for contributing to this investigation.


The corresponding author, as the representative of all authors, has been given the opportunity to register their agreement or disagreement to this retraction. We have kept a record of any response received.

References

- [1] X. Zhu, X. He, B. Fan et al., "Effect of Propofol Intravenous Anesthesia Combined with Press-Needle Therapy on Analgesic Effect during Painless Abortion," *Computational and Mathematical Methods in Medicine*, vol. 2022, Article ID 6543211, 10 pages, 2022.

Research Article

Effect of Propofol Intravenous Anesthesia Combined with Press-Needle Therapy on Analgesic Effect during Painless Abortion

Xia Zhu ^{1,2}, Xueming He,² Baojun Fan,^{1,2} Jing Liu,^{1,2} Shuqing Wu,^{1,2} Hongli Wang,^{1,2} and Chunwei Chen^{1,2}

¹Department of Anesthesiology, The Affiliated Lianyungang Oriental Hospital of Xuzhou Medical University, Lianyungang, Jiangsu 222042, China

²Center for Clinical Research and Translational Medicine, The Affiliated Lianyungang Oriental Hospital of Kangda College of Nanjing Medical University, Lianyungang, Jiangsu 222042, China

Correspondence should be addressed to Xia Zhu; 710020210049@xzhmu.edu.cn

Received 19 May 2022; Revised 15 June 2022; Accepted 27 June 2022; Published 8 August 2022

Academic Editor: Pan Zheng

Copyright © 2022 Xia Zhu et al. This is an open access article distributed under the Creative Commons Attribution License, which permits unrestricted use, distribution, and reproduction in any medium, provided the original work is properly cited.

Objective. To discover the effect of propofol intravenous anesthesia along with press-needle therapy on analgesic effect during painless abortion. **Methods.** A total of 128 cases who experienced painless abortion in our hospital from January 2019 to August 2021 were recruited as the research subjects. They were categorized into control and observation groups through the haphazard number table approach, with 64 patients in each group. Propofol intravenous anesthesia was given to the control group, and the observation group was given combined anesthesia with press-needle on this basis. Ramsay score, hemodynamic indexes, operation-related indexes, and postoperative recovery were studied between the two groups before anesthesia (T0), at the time of uterine aspiration (T1), promptly following the operation (T2), and at the recovery time of directional force (T3). The stress state and the level of pain mediators in the two groups of sufferers were observed at each time period, and the visual analogue scale (VAS) was employed to assess the degree of postoperative uterine contraction pain. **Results.** Ramsay score at T1 and T2 time points in observation group was lesser than that in control group ($P < 0.05$). There existed no meaningful discrepancies in operation time and recovery time between both groups ($P > 0.05$). The total dosage of propofol in the observation group was lesser compared to that in the control group, and the recovery time of directional force was much shorter compared to that in the control group ($P < 0.05$). There existed no meaningful discrepancies in perioperative diastolic blood pressure (DBP), systolic blood pressure (SBP), and heart rate (HR) between both groups ($P > 0.05$). The levels of norepinephrine (NE), cortisol (Cor), glucose (GLU) and substance P (SP), prostaglandin E2 (PGE2), and 5-hydroxytryptophan (5-HT) in the observation group were lesser than those in the control group immediately after surgery and 24 hours following the operation ($P < 0.05$). There existed no meaningful discrepancies in vaginal bleeding time, endometrial thickness 3 weeks after operation, and time to start menstruating between both groups ($P > 0.05$). The score of VAS for the observation group was lesser than that of the control group at 10 min and 30 min after operation ($P < 0.05$). There existed no substantial discrepancy in the incidence of negative reactions between both groups ($P > 0.05$). **Conclusion.** Propofol intravenous anesthesia combined with press-needle therapy can ameliorate the analgesic impacts during painless abortion, reduce postoperative uterine contraction pain, inhibit the release of postoperative pain mediators, and improve the stress state of the body.

1. Introduction

Abortion surgery refers to the use of surgical methods to terminate a pregnancy, that is, “artificial” termination of pregnancy [1]. Abortion is one of the most common methods of

pregnancy termination and a remedy for unsuccessful contraception. Very recently, painless abortion has been widely used in clinical practice. Clinically, it is generally believed that the use of appropriate anesthetic drugs during surgery can not only achieve better anesthesia effect and relieve

TABLE 1: Comparison of the general outcomes for the two groups of patients.

Item	Observation group ($n = 64$)	Control group ($n = 64$)	χ^2/t value	P value
Age (years)	28.15 \pm 3.02	28.71 \pm 3.15	1.027	0.307
Body mass index (kg/m ²)	21.73 \pm 1.85	21.59 \pm 1.73	0.442	0.659
ASA grading (numbers)				
Grade I	37	39	0.130	0.719
Grade II	27	25		
Gestational age (weeks)	6.09 \pm 1.12	5.94 \pm 1.16	0.744	0.458
Gravidity (frequencies)	1.83 \pm 0.21	1.76 \pm 0.23	1.798	0.075
Parity (frequencies)	1.02 \pm 0.15	1.05 \pm 0.13	1.209	0.229

Note: ASA: American Society of Anesthesiologists [11].

patients' intraoperative and postoperative pain but also ensure the smooth operation [2, 3]. Propofol is a regularly implemented anesthetic drug in abortion operation. It has the advantages of fast onset and short half-life. However, it has been reported that its anesthetic effect is not ideal [4, 5]. Auricular acupoint press-needle therapy is a micro-needle therapy guided by the holographic theory of auricular acupoints. It is a method to bury the microneedle into the auricular acupoint and stimulate the acupoint to achieve the therapeutic effect. The press-needle is an intradermal needle, characterized by light and shallow. The needle tip penetrates the superficial skin, which not only has the effect of acupuncture but also can avoid the phenomenon of complicated needling operation [6, 7]. In this study, the subcortical, Shenmen, and sympathetic acupoints in the ear were selected. Among them, the subcortical acupoint can regulate the excitation and inhibition of the cerebral cortex, the Shenmen acupoint can relieve pain and calm the mind, and the sympathetic acupoint has the functions of dredging Qi, promoting blood circulation, and relieving pain [8]. Ashi acupoint can regulate Qi and blood and reduce the influence caused by blood stasis, and the combination of multiple acupoints can adjust the pain threshold of the central nervous system and analgesic and antispasmodic effects [9, 10]. However, the application value of this analgesic method combined with propofol anesthesia in painless abortion is still in the exploratory stage. Therefore, the target of the present exploration is to discover the influence of propofol intravenous anesthesia combined with press-needle therapy on analgesic effect during painless abortion and to present reference for the choice of anesthesia methods for patients.

2. Materials and Methods

2.1. Clinical Data. A total of 128 patients who experienced painless abortion in our hospital from January 2019 to August 2021 were recruited as the research targets, and they were categorized into the observation and control groups through the haphazard number table approach, with 64 cases in each group. There existed no meaningful discrepancy in general outcomes between both groups ($P > 0.05$), as shown in Table 1.

2.2. The Criteria of Inclusion

- (1) Cases who underwent painless abortion
- (2) The present research was confirmed through the Ethics Committee of our hospital, and the contributors presented the letter of satisfaction and signed the consent letter
- (3) Patients with ASA grade of I-II

2.3. The Criteria of Exclusion

- (1) Cases with hemorrhagic diseases
- (2) Cases with skin diseases such as skin damage of outer ear and eczema
- (3) Cases with infectious diseases
- (4) Cases with a history of chronic pain and analgesic drug dependence
- (5) Cases combined with kidney and liver and other important organ dysfunction
- (6) Cases with a history of alcohol or drug abuse
- (7) Cases with mental illness
- (8) Cases with other uterine diseases
- (9) Those who are allergic to narcotics

2.4. Methods. Patients in both groups were deprived of water for 2 hours and fasted for 8 hours before surgery. After the bladder was emptied, venous channels were established, and vital signs were detected by ECG monitoring. The control group was given intravenous anesthesia with propofol (Xi'an Libang Pharmaceutical Co., Ltd., batch number: H19990282), using manual intravenous bolus of propofol, the induction dose was 2.5 mg/kg, and an additional 30 mg of propofol was added when the eyelash reflex disappeared.

The observation group was processed with press-needle therapy in accordance with the control group, and bilateral uterine, pelvic, endocrine, subcortical, Shenmen, sympathetic, and Ashi acupoints were selected according to the positioning standard of "Nomenclature and location of auricular points GBT 13734-2008." The ear skin was

disinfected with 75% ethanol, the auricle was fixed with the left thumb and index finger, the back of the ear at the acupuncture site was supported by the middle finger, the annular needle handle of sterile press-needle (Hua Tuo brand, Batch No. 20182270591, specification: 0.22 mm*1.5 mm) was taken with tweezers with the right hand, and the tape was removed, and it was inserted into the acupoint. After the acupuncture was fixed, the acupoints were pressed with the thumb abdomen. When pressing, the pressure was moderate, from light to heavy, and one is tight and one is loose, with the patient having acid, numbness, and swelling pain as the appropriate degree. When pressing, if the patient did not feel comfortable, the operation should be stopped immediately, with 60~90 times/min, and each acupoint was lasted for 20~30s. It should be noted that the press-needle treatment should be avoided for patients with skin allergy and hemorrhagic diseases, and at the same time, the red and swollen and purulent parts of the ear skin should be avoided. During treatment, routine disinfection of needles, tweezers, and the patient's auricular points should be performed. During operation, the patient should be informed to keep the auricle clean and dry and remove needles immediately if redness occurs.

2.5. Observation Indicators

2.5.1. Analgesic Influence. Ramsay score was implemented to appraise the analgesic effect of patients before anesthesia (T0), at the time of uterine aspiration (T1), immediately after surgery (T2), and at the time of directional force recovery (T3) [12]. One point indicated fidgety; 2 points indicated quiet, awake, and cooperative; 3 points indicated drowsiness and quick responses to commands; 4 points indicated light sleep state and can be awakened quickly; 5 points indicated falling asleep and unresponsive to calls; 6 points indicated deep sleep and no response to calls.

2.5.2. Surgery-Related Indicators. The operation time, recovery time, total dosage of propofol, and recovery time of directional force were compared between the two groups.

2.5.3. Hemodynamic Indicators. Philips MT50 monitor was used for detecting systolic blood pressure (SBP), diastolic blood pressure (DBP), and heart rate (HR) of patients at T0, T1, T2, and T3 time points.

2.5.4. Stress Indicators. 5 ml of venous blood was recruited from cases prior to surgery, immediately following the surgery and 24 hours after surgery, centrifuged at a rate of 3000 r/min, serum was separated, and high-performance liquid chromatography (HPLC) was used to detect norepinephrine (NE) level; cortisol (Cor) levels were detected by radioimmunoassay. Glucose (GLU) level was measured by glucokinase method.

2.5.5. Pain Mediators. Prostaglandin E2 (PGE2), serum substance P (SP), and 5-hydroxytryptamine (5-HT) levels were discerned through enzyme-linked immunosorbent assay (ELISA) before surgery, immediately following the surgery,

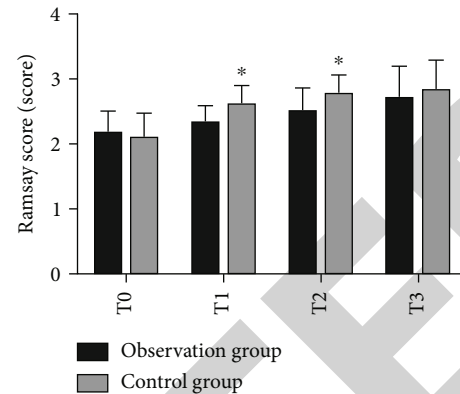


FIGURE 1: Comparison of analgesic influences between both groups (note: * indicated $P < 0.05$ when compared to the observation group).

and 24 hours after surgery. The kit was provided by Shenzhen Jingmei Biological Engineering Co., Ltd.

2.5.6. Postoperative Recovery. The vaginal bleeding time, endometrial thickness 3 weeks after operation, and time to start menstruating were compared between the two groups. The endometrial thickness was examined by color Doppler ultrasound diagnostic apparatus of GE Company of the United States.

2.5.7. Postoperative Uterine Contraction Pain. The visual analogue scale (VAS) was employed to assess the postoperative uterine contraction pain of patients [13]. A scale with a length of 10 cm was used for evaluation. Patients selected a number on the scale to represent their own pain sensation, with the score ranging from 0 to 10 points. The greater the score, the more potent the pain sensation of patients.

2.5.8. Adverse Reactions. The incidence of anesthesia-related adverse reactions, for instance, nausea and vomiting, body movement, and respiratory depression, were analyzed in both groups.

2.6. Statistical Processing. SPSS22.0 computer program was employed to evaluate the outcomes, count achievements were presented as percentage (%), and discrepancies between groups were studied through χ^2 analysis; assessment outcomes were presented as $\bar{x} \pm s$ after normality test, and discrepancies between groups were studied through t analysis. $P < 0.05$ demonstrated that the discrepancy was statistically meaningful.

3. Results

3.1. Comparison of Analgesic Influences between Both Groups. The Ramsay scores in the observation group at T1 and T2 time points were lesser than those in the control group ($P < 0.05$), as demonstrated in Figure 1.

3.2. Comparison of Surgery-Related Indicators between Both Groups. There were no substantial differences in operation time and recovery time between both groups ($P > 0.05$).

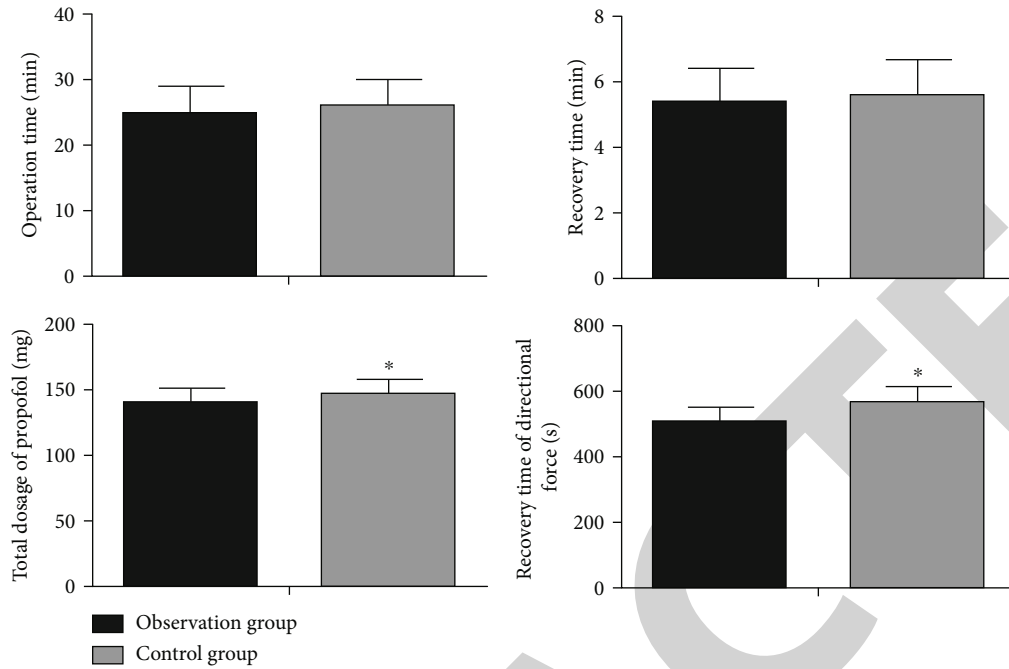


FIGURE 2: Comparison of surgery-related indicators between both groups (note: * indicated $P < 0.05$ when compared to the observation group).

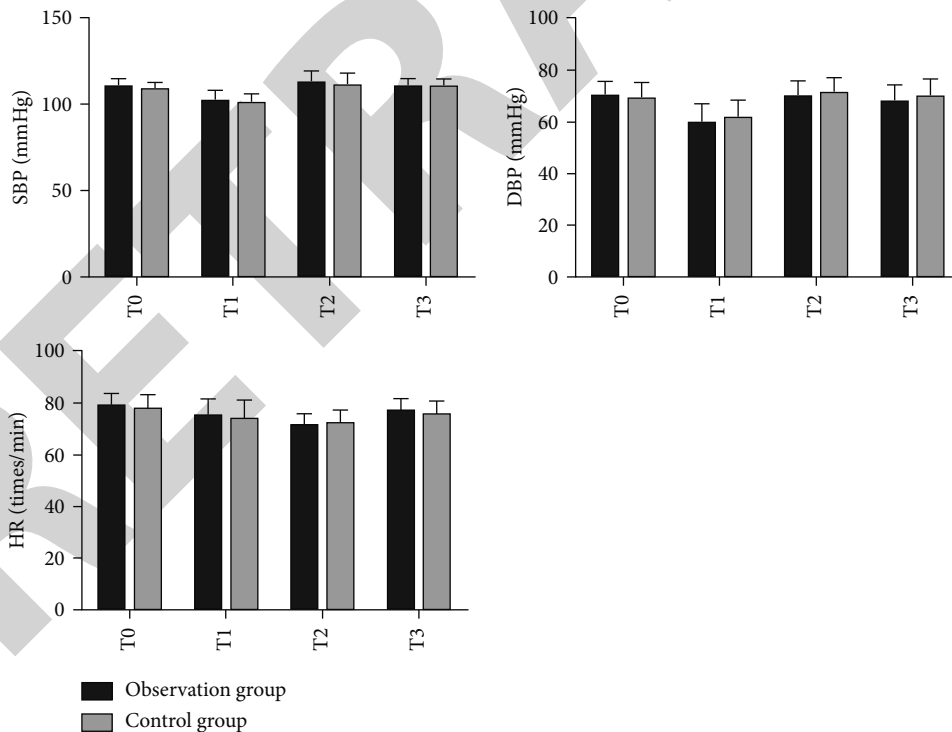


FIGURE 3: Modifications in hemodynamic indexes in the two groups.

The total dosage of propofol in the observation group was lesser compared to that in the control group, and the recovery time of directional force was shorter than that in the control group ($P < 0.05$), as demonstrated in Figure 2.

3.3. Changes in Hemodynamic Indexes in Both Groups. There existed no meaningful discrepancy in perioperative SBP, DBP, and HR between both groups ($P > 0.05$), as demonstrated in Figure 3.

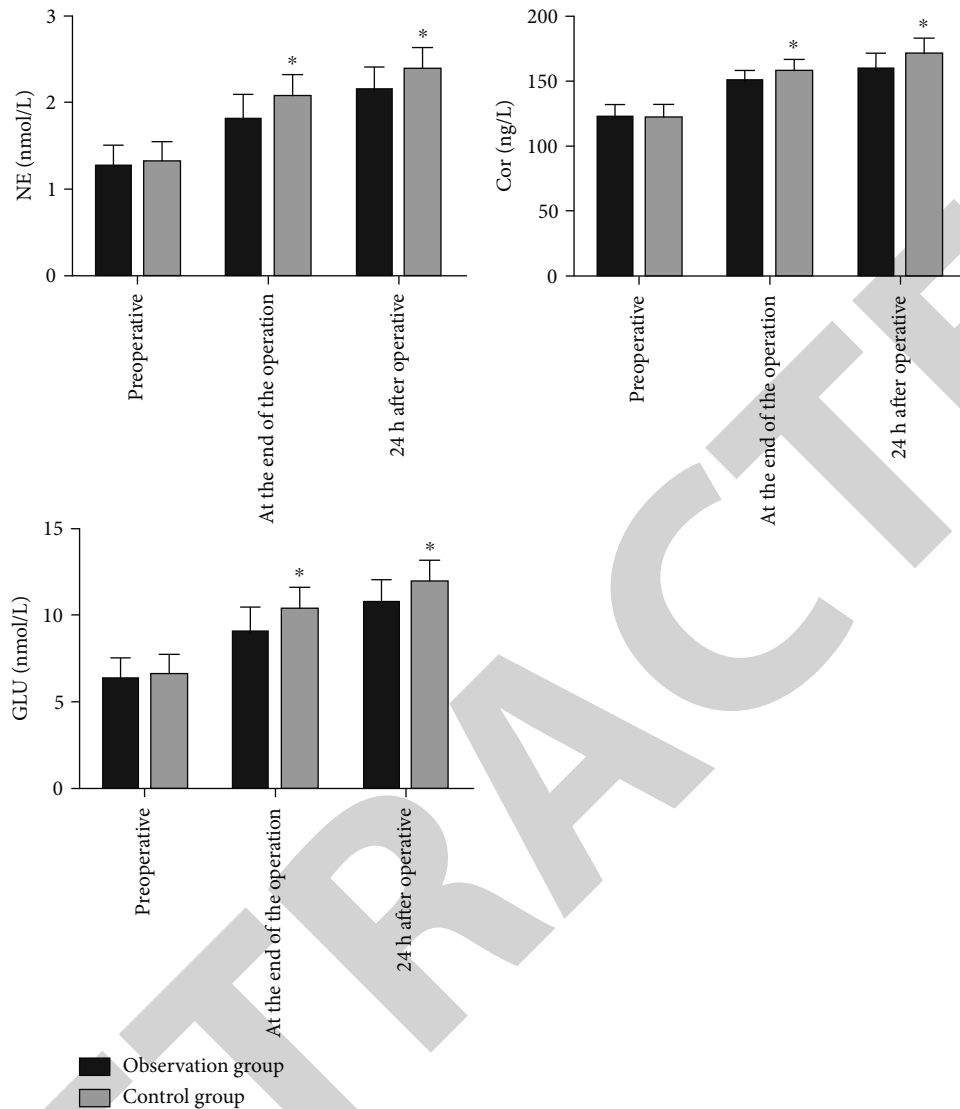


FIGURE 4: Comparison of stress indicators between both groups (note: * indicated $P < 0.05$ when compared with the observation group).

3.4. Comparison of Stress Indicators between Both Groups.

There existed no meaningful discrepancy in the levels of NE, Cor, and GLU before the operation between both groups ($P > 0.05$); the levels of NE, GLU, and Cor in the observation group promptly following the surgery and 24 hours after the operation were lesser than those in the control group ($P < 0.05$), as demonstrated in Figure 4.

3.5. Comparison of Pain Mediators between Both Groups.

There existed no meaningful discrepancy in the levels of SP, PGE2, and 5-HT before operation between both groups ($P > 0.05$); the levels of SP, PGE2, and 5-HT in the observation group promptly following the surgery and 24 hours following the surgery were lesser than those in the control group ($P < 0.05$), as demonstrated in Figure 5.

3.6. Comparison of Postoperative Recovery between Both Groups. There existed no meaningful discrepancy in vaginal bleeding time, endometrial thickness 3 weeks after opera-

tion, and time to start menstruating between both groups ($P > 0.05$), as demonstrated in Figure 6.

3.7. Comparison of Postoperative Uterine Contraction Pain between Both Groups. The VAS score of the observation group at 10 min and 30 min following the surgery was lower than that of the control group ($P < 0.05$), as demonstrated in Figure 7.

3.8. Comparison of the Incidence of Anesthesia-Related Adverse Reactions between the Two Groups. There was no significant difference in the incidence of negative reactions between both groups ($P > 0.05$), as demonstrated in Table 2.

4. Discussion

Abortion is an important way to terminate early pregnancy. Compared with medical abortion, abortion has the advantages of high success rate of pregnancy termination and

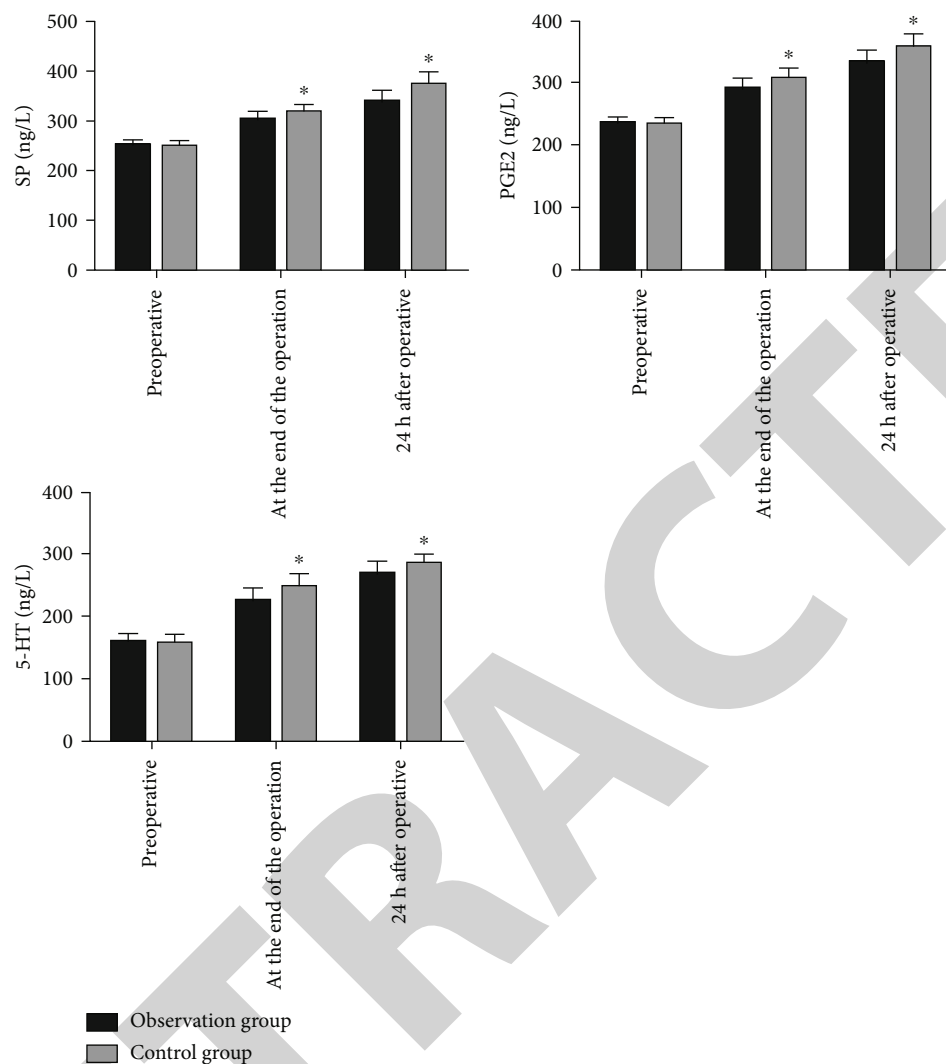


FIGURE 5: Comparison of pain mediators between both groups (note: * indicated $P < 0.05$ when compared to the observation group).

fewer complications [14, 15]. At present, it is believed that anesthesia for painless induced abortion requires short-acting, adequate analgesia and sedation and requires the patient to wake up quickly after the operation, restoring directional force and consciousness quickly, without drug residues and aftereffects [16, 17]. Propofol is a short-acting intravenous anesthetic employed for induction and maintaining general anesthesia. Relevant investigations have pointed out that propofol used in painless abortion has the advantages of short-acting sedation, quick onset, and short half-life, but single-drug anesthesia has disadvantages of long postoperative recovery time and high incidence of postoperative uterine contraction pain [18]. It has been reported that combined anesthesia on this basis can further improve the anesthetic effect [19]. Auricular point analgesia has been used in a variety of surgeries or operations that require anesthesia and analgesia. As a new type of intradermal needle, press-needle has acupuncture effect. Compared with the traditional filiform needle, it does not damage the ear cartilage. Compared with the traditional ear point pressing with bean, press-needle can produce stronger benign stimulation to the

ear acupoint and strengthen the therapeutic effect. At the same time, the ear press-needle is buried in the skin, which can stimulate the auricular point more accurately, and the paste is firm and stable [20]. In this study, bilateral uterus, pelvic cavity, and Shenmen acupoints were selected based on the bioholographic theory of the auricle, and corresponding acupoints were selected according to the lesion site, namely, the positive reaction point of the lesion. Shenmen acupoint was located in the fourth area of triangular fossa of the ear, slightly above the fork of the upper and lower crura of antihelix. Relevant investigations have emphasized that acupuncture of Shenmen acupoint is able to calm the mood and relieve spasm and pain [21]. The pelvic cavity and uterine acupoints are located in the triangular fossa, and various benign afferent impulses are generated based on stimulation by press-needle, which can participate in the regulation of cranial nerves, that is, the excitation and inhibition of the cerebral cortex, block pathological nerve impulses and sympathetic nerve efferent impulses, or inhibit pathological excitatory foci and restore its normal physiological function. Subcortical, endocrine, and sympathetic

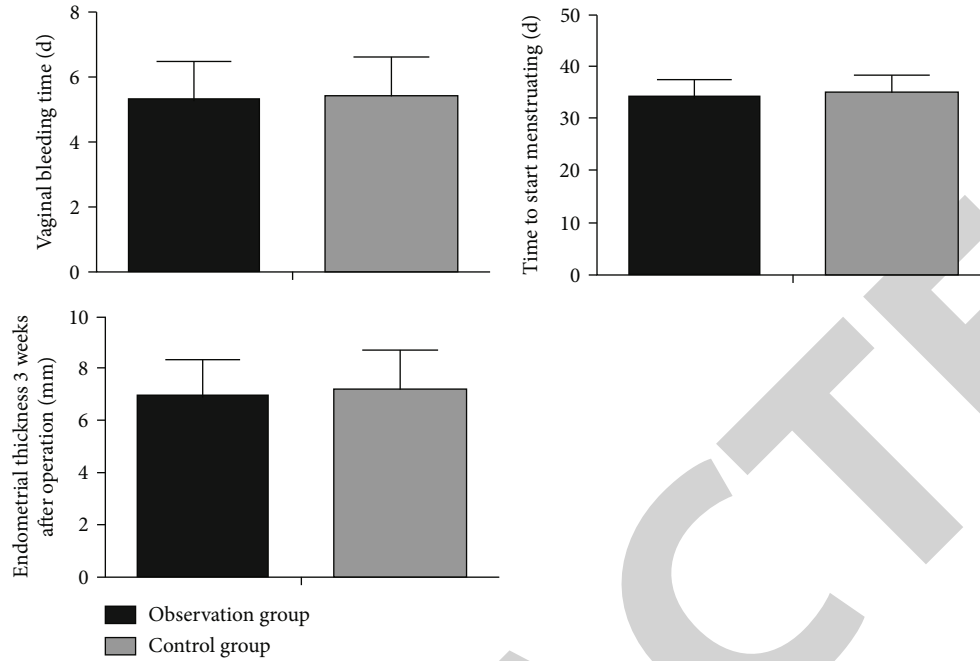


FIGURE 6: Comparison of postoperative recovery between both groups.

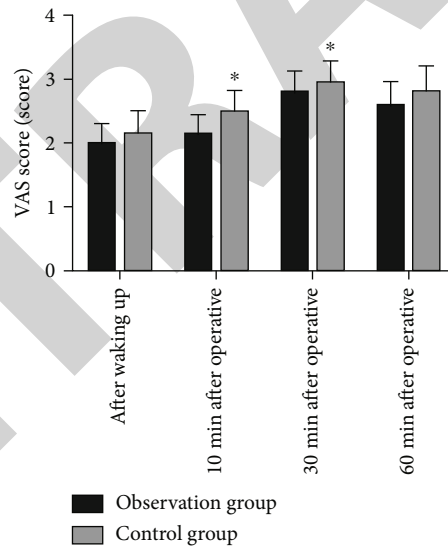


FIGURE 7: Comparison of postoperative VAS scores between both groups (note: * indicated $P < 0.05$ when compared to the observation group).

acupoints are named in combination with modern anatomy and physiology, and their effects are similar to physiological functions [22, 23]. Subcortical acupoint has the effect of sedation and analgesia, which can regulate the excitation and inhibition process of cerebral cortex and subcortical plant nerve center [24]. Endocrine acupoint can regulate the endocrine system, have anti-inflammatory and analgesic, and enhance immune regulation effects [25]. Sympathetic acupoint can calm the mood and relieve pain, invigorate Qi, and reduce inversion and can regulate the vasomotor function and adjust the visceral function [26]. The results of the present research illustrated that the Ramsay scores

in the observation group at T1 and T2 time points were lesser than those in the control group, the total dosage of propofol was less than that in the control group, and the recovery time of directional force was shorter than that in the control group. The results showed that propofol anesthesia in combination with press-needle therapy is capable of improving the anesthetic influence, decreasing the dosage of anesthetic drugs, and promoting the rapid recovery of postoperative directional force.

Under stress, the body's sympathetic nerves are excited, which promotes the production of NE and Cor and increases blood sugar [27, 28]. Abortion requires cervical forceps to

TABLE 2: Comparison of the incidence of anesthesia-related negative reactions between both groups (cases, %).

Group	<i>n</i>	Body movement	Respiratory depression	Bradycardia	Nausea and vomiting	Overall incidence
Observation group	64	1	0	1	2	6.25
Control group	64	3	1	2	3	14.06
χ^2						2.141
<i>P</i>						0.143

stretch and expand the cervix and use a curette to scratch the uterine wall, which can cause local pain, lead to sympathetic nerve excitation, and increase the synthesis of catecholamines, resulting in hemodynamic fluctuations [29]. The use of anesthetic drugs is very important to maintain hemodynamic stability and ensure the safety of patients. This study found that there were no meaningful discrepancies in perioperative SBP, DBP, and HR between both groups, indicating that single-drug anesthesia and combined anesthesia with press-needle had little effect on hemodynamics. In addition, this study found that the levels of NE, Cor, and GLU in the observation group immediately after the operation and 24 hours after the operation were lower than those in the control group, illustrating that combined anesthesia with press-needle is capable of reducing the stress state of patients undergoing abortion. This is mainly because the auricular acupoint has a benign bidirectional regulation function. The tiny nerve branches weave a network in the auricle, and a considerable number of sympathetic nerves are distributed on the auricle. Stimulation of auricular acupoint can cause the thalamus to regulate the excitation of sympathetic and parasympathetic nerves of the body, inhibit the stress response of the sympathetic nucleus on pain, promote the release of antipain neurotransmitters, improve the pain threshold, and reduce the body's sensitivity to pain [30].

SP, PGE2, and 5-HT are pain mediators related to the occurrence and intensification of pain [31]. SP is a neuropeptide with injury-stimulating properties that widely exists in the systemic system and can aggravate pain by promoting the release of pain-causing factor 5-HT and also plays a role in transmitting pain information [32]. PGE2 is an inflammatory medium that can enhance the excitability of receptors and enhance the sensitivity of nerves to painful stimuli, thus producing lasting pain [33]. 5-HT is distributed in the central nervous system and has a direct pain-causing effect, which can act locally through second messengers and stimulate sensory nerve endings to produce pain [34, 35]. Relevant studies have pointed out that stimulating auricular acupoints can regulate inflammatory factors and relieve pain caused by the release of inflammatory mediators [36]. The findings of the current survey illustrated that the levels of SP, PGE2, and 5-HT in the observation group immediately after the operation and 24 hours after the operation were lower than those in the control group, indicating that combined analgesia with press-needle with may inhibit the release of pain mediators, which may be an important reason why this method can relieve pain in patients. The reason is that press-needle therapy stimulates the nerve endings, makes

the nerves excited, and then travels along the corresponding nerve conduction pathway to the central nervous system, thereby activating the regulation of the nervous system and stimulating the release of prostaglandins and other chemicals, thereby affecting blood circulation, in order to achieve analgesic effect. Acupuncture at pelvis and uterus acupoints can block pathological nerve impulses and sympathetic nerve efferent impulses and inhibit pathological excitatory foci. Therefore, the authors believe that press-needle acupuncture at this acupoint may help restore its normal physiological function. However, the outcomes of this research illustrated that there existed no substantial discrepancies between both groups in the vaginal bleeding time, endometrial thickness 3 weeks after operation, and time to start menstruating, indicating that the propofol intravenous anesthesia combined with press-needle therapy would not affect the uterine recovery of patients after painless abortion.

Press-needle acupuncture at multiple acupoints can enhance the analgesic effect, relieve the nervous state of the brain, and reduce the sensitivity of the patient's response to pain. This study found that combined anesthesia can reduce the severity of postoperative uterine contraction pain, which further confirmed that this method can relieve postoperative pain. Relevant studies have pointed out that press-needle analgesia can reduce adverse reactions such as nausea and vomiting caused by stimulation of the vagus nerve [37]. However, the outcomes of the current research illustrated that there existed no meaningful discrepancy in the incidence of postoperative negative reactions between both groups, demonstrating that press-needle analgesia had little effect on the adverse reactions related to anesthesia in patients, which was consistent with the above study results, which could be relevant to the small size of cases included in this research, so further analysis is needed in the later stage.

In conclusion, propofol combined with press-needle anesthesia can improve the analgesic effect of painless abortion during operation, relieve the uterine contraction pain after operation, inhibit the release of postoperative pain media, and improve the stress state of body. However, the observation group was given acupuncture therapy, while the control group was not given the corresponding acupuncture treatment, which could not really prove that acupuncture on the corresponding acupoints had an effect, and the placebo effect could not be ruled out. In addition, the effect of acupuncture may be closely related to the practice of acupuncturists, so multiple acupuncturists may have a certain impact on the results. In future research, we will further expand the sample size and set up a better corresponding control group to improve this research.

Data Availability

The labeled dataset used to support the findings of this study are available from the corresponding author upon request.

Conflicts of Interest

The authors declare no competing interests.

Authors' Contributions

Xia Zhu and Xueming He contributed equally to this work.

Acknowledgments

This study was supported by the Medical Research Project Fund of Jiangsu Provincial Health Commission (Project No. Z2021066).

References

- [1] Y. X. Cheng, H. P. Chang, J. Zhang, Y. Liu, and S. Zhao, "Efficacy and safety of combined intravenous anesthesia with nalbuphine and propofol during painless induced abortion surgery," *Journal of Hebei Medical University*, vol. 38, no. 11, p. 1324, 2018.
- [2] H. Xie, W. Chen, J. Liu, J. Li, and S. Li, "Changes of analgesia/nociception index under different surgical steps in abortion under general anesthesia: a prospective clinical study," *Journal of clinical anesthesia*, vol. 66, no. 11, article 109898, 2020.
- [3] F. Yao, A. B. Zhu, S. J. Xu, W. J. Zhang, H. P. Xiong, and M. K. Shen, "Effects of different doses of oxycodone on uterine contraction pain and emotional scale after painless abortion," *Journal of Clinical Anesthesiology*, vol. 35, no. 1, pp. 12–16, 2019.
- [4] X. Chen, D. Wang, S. H. Shu, and X. Q. Chai, "The half effective effect room target concentration of remifentanyl in inhibiting body movement during hysteroscopy when combined with propofol," *Journal of Clinical Anesthesiology*, vol. 36, no. 4, pp. 394–395, 2020.
- [5] M. Hunie, E. Fenta, S. Kibret, and D. Teshome, "The current practice of aspiration prophylaxis in obstetric anesthesia: a survey among non-physician anesthetic providers working in hospitals in Ethiopia," *BMC Anesthesiology*, vol. 21, no. 1, pp. 256–259, 2021.
- [6] Y. F. Zhu, H. Y. Wang, X. H. Yu et al., "Influence of auricular acupuncture and acupuncture adjuvant therapy on drug analgesia in patients after rotator cuff repair," *China Rural Medicine*, vol. 28, no. 5, pp. 17–18, 2021.
- [7] X. Chen, W. Huang, Y. T. Jin et al., "Prescription analysis of electroacupuncture for simple obesity based on complex network technology," *China Acupuncture*, vol. 38, no. 3, pp. 331–336, 2018.
- [8] S. Peng, Y. L. Wang, S. Q. Zhang et al., "Analysis of auricular point sticking and acupoint selection rules for postoperative pain based on data mining," *Journal of Nursing*, vol. 28, no. 5, p. 5, 2021.
- [9] X. G. Liu, Q. C. Wang, and X. Zhou, "A brief analysis of the clinical application of Ashi point," *Diet Health*, vol. 5, no. 14, p. 25, 2018.
- [10] Y. Zhang, "Observation on the application effect of multi-acupoint stimulation on the body surface in natural labor analgesia," *Chinese Community Physician*, vol. 36, no. 28, p. 2, 2020.
- [11] J. L. Apfelbaum, C. A. Hagberg, R. A. Caplan et al., "Practice guidelines for management of the difficult airway: an updated report by the American Society of Anesthesiologists Task Force on Management of the Difficult Airway," *Anesthesiology*, vol. 78, no. 2, pp. 251–270, 2003.
- [12] R. Riessen, R. Pech, P. TrNkle, G. Blumenstock, and M. Haap, "Comparison of the Ramsay score and the Richmond agitation sedation score for the measurement of sedation depth," *Critical Care*, vol. 16, no. S1, pp. 31–35, 2012.
- [13] G. B. Langley and H. Sheppard, "The visual analogue scale: its use in pain measurement," *Rheumatology International*, vol. 5, no. 4, pp. 145–148, 1985.
- [14] N. Lince-Deroche, D. Constant, J. Harries et al., "The costs and cost effectiveness of providing second-trimester medical and surgical safe abortion services in Western Cape province, South Africa," *PLoS One*, vol. 13, no. 6, article e0197485, 2018.
- [15] C. Li, J. Gao, and J. Liu, "Repeat abortion and associated factors among women seeking abortion services in northwestern China: a cross-sectional study," *BMC Public Health*, vol. 21, no. 1, pp. 1626–1629, 2021.
- [16] Y. L. Wang, H. Li, and G. Y. Guo, "Anesthesia effect of nalbuphine combined with propofol for painless induced abortion and its influence on patient stress and inflammatory response," *Shandong Medicine*, vol. 59, no. 26, pp. 54–56, 2019.
- [17] J. B. Hou, H. X. Wang, X. Wan et al., "Selection of optimal dose of pentazocine in painless induced abortion guided by Narcotrend index," *Journal of Practical Medicine*, vol. 34, no. 24, pp. 4098–4101, 2018.
- [18] X. H. You and Z. J. Chen, "Comparison of the application effect of nitrous oxide and propofol in painless artificial abortion," *Chongqing Medical Journal*, vol. 46, no. 30, pp. 4272–4273, 2017.
- [19] W. F. Yang, C. J. Chen, Y. Li, and C. Q. Duan, "Comparison of anesthesia effect and postoperative inflammatory response of alfentanil and sufentanil in painless induced abortion," *Chinese Journal of Family Planning*, vol. 29, no. 10, pp. 2056–2059, 2021.
- [20] J. Z. Zhou, H. L. Cheng, H. Chen et al., "Based on the autonomic nerves to discuss the regulating effect of auricular acupuncture on the gastrointestinal tract," *Shanghai Journal of Acupuncture*, vol. 41, no. 1, pp. 107–110, 2022.
- [21] X. J. Zhang, R. Zhao, Y. Chen et al., "The application of analgesic needles in in vitro fertilization-embryo transfer transvaginal ultrasound oocyte retrieval," *China Clinical Research*, vol. 35, no. 2, pp. 230–233, 2022.
- [22] J. R. Chen, S. Y. Gao, X. P. Liu et al., "Effect of uterine massage combined with psychological nursing on postpartum uterine contraction pain," *Shenzhen Journal of Integrated Traditional Chinese and Western Medicine*, vol. 31, no. 24, p. 3, 2021.
- [23] L. S. Wan, W. S. Li, W. Y. Li, and G. C. Li, "Observation on the anesthesia effect of general anesthesia assisted by auricular-plaster therapy in gynecological surgery," *China Acupuncture*, vol. 33, no. 3, pp. 237–240, 2013.
- [24] L. Jiexuan, *Research on the Effect of Auricular Point Sticking on the Anxiety of College Sprinters before Competition*, Guangzhou University of Traditional Chinese Medicine, 2019.
- [25] Y. Zhong, S. F. Niu, Z. F. Wen et al., "Efficacy of auricular acupuncture combined with acupuncture at Sanyinjiao in the

Retraction

Retracted: Effects of Dapagliflozin in Combination with Metoprolol Sustained-Release Tablets on Prognosis and Cardiac Function in Patients with Acute Myocardial Infarction after PCI

Computational and Mathematical Methods in Medicine

Received 27 June 2023; Accepted 27 June 2023; Published 28 June 2023

Copyright © 2023 Computational and Mathematical Methods in Medicine. This is an open access article distributed under the Creative Commons Attribution License, which permits unrestricted use, distribution, and reproduction in any medium, provided the original work is properly cited.

This article has been retracted by Hindawi following an investigation undertaken by the publisher [1]. This investigation has uncovered evidence of one or more of the following indicators of systematic manipulation of the publication process:

- (1) Discrepancies in scope
- (2) Discrepancies in the description of the research reported
- (3) Discrepancies between the availability of data and the research described
- (4) Inappropriate citations
- (5) Incoherent, meaningless and/or irrelevant content included in the article
- (6) Peer-review manipulation

The presence of these indicators undermines our confidence in the integrity of the article's content and we cannot, therefore, vouch for its reliability. Please note that this notice is intended solely to alert readers that the content of this article is unreliable. We have not investigated whether authors were aware of or involved in the systematic manipulation of the publication process.

In addition, our investigation has also shown that one or more of the following human-subject reporting requirements has not been met in this article: ethical approval by an Institutional Review Board (IRB) committee or equivalent, patient/participant consent to participate, and/or agreement to publish patient/participant details (where relevant).

Wiley and Hindawi regrets that the usual quality checks did not identify these issues before publication and have since put additional measures in place to safeguard research integrity.

We wish to credit our own Research Integrity and Research Publishing teams and anonymous and named external researchers and research integrity experts for contributing to this investigation.

The corresponding author, as the representative of all authors, has been given the opportunity to register their agreement or disagreement to this retraction. We have kept a record of any response received.

References

- [1] H. Zhang and Z. Liu, "Effects of Dapagliflozin in Combination with Metoprolol Sustained-Release Tablets on Prognosis and Cardiac Function in Patients with Acute Myocardial Infarction after PCI," *Computational and Mathematical Methods in Medicine*, vol. 2022, Article ID 5734876, 8 pages, 2022.

Research Article

Effects of Dapagliflozin in Combination with Metoprolol Sustained-Release Tablets on Prognosis and Cardiac Function in Patients with Acute Myocardial Infarction after PCI

Hao Zhang  and Zeyan Liu

Department of Emergency Medicine, The Second Affiliated Hospital of Anhui Medical University, Hefei, Anhui 230601, China

Correspondence should be addressed to Hao Zhang; haozhys@163.com

Received 6 June 2022; Revised 6 July 2022; Accepted 11 July 2022; Published 3 August 2022

Academic Editor: Pan Zheng

Copyright © 2022 Hao Zhang and Zeyan Liu. This is an open access article distributed under the Creative Commons Attribution License, which permits unrestricted use, distribution, and reproduction in any medium, provided the original work is properly cited.

Objective. To find the effects of dapagliflozin in combination with metoprolol sustained-release tablets on cardiac function and prognosis in acute myocardial infarction patients after PCI. **Methods.** A total of 84 patients with myocardial infarction who experienced PCI from February 2020 to February 2022 were included and allocated into 3 groups: groups A, B, and C ($n = 28$ /per group). Group A was given dapagliflozin combined with metoprolol sustained-release tablets, group B was given dapagliflozin, and group C was given the placebo. Left ventricular end diastolic diameter (EDD), left ventricular ejection fraction (LVEF), and end systolic diameter (ESD) were measured before and after treatment in all groups; myocardial infarction areas were matched among all three groups at 3 months posttreatment. The serum concentrations of interleukin-6 (IL-6), hypersensitive C-reactive protein (hs-CRP), superoxide dismutase (SOD), and malondialdehyde (MDA) were detected in all three groups before and after treatment. The levels of N-terminal probrain natriuretic peptide (NT-pro BNP), lipoprotein (a) (Lp(a)), ischemia-modified albumin (IMA), and secreted frizzled-related protein 5 (SFRP5) were also detected in the serum of all groups. Adverse reactions and cardiovascular adverse events were matched between all groups. **Results.** The levels of LVEF in groups A and B were increased after treatment, while the levels of EDD and ESD were decreased. The improvement degree of LVEF and EDD levels in groups A and B was found greater compared to group C ($P < 0.05$). No significant difference was found in myocardial infarction area among the three groups at 3 months postoperation ($P > 0.05$). Serum concentrations of MDA, hs-CRP, IL-6, IMA, NT-proBNP, and Lp(a) were found to decrease in all three groups after treatment, while the levels of SOD and SFRP5 were increased. The improvement degree of serum hs-CRP, IL-6, SOD, MDA, IMA, NT-proBNP, Lp(a), and SFRP5 levels was greater in both groups A and B compared to group C. The improvement degree of serum hs-CRP, SOD, MDA, IMA, Nt-probNP, Lp(a), and SFRP5 levels was significantly greater in group A compared to group B ($P < 0.05$). No adverse effect was observed in all three groups ($P > 0.05$). Total occurrence of cardiovascular adverse effects such as stent thrombosis, heart failure, ventricular fibrillation, and death was 10.71% in group A, 25.00% in group B, and 53.75% in group C. There was statistical significance in the onset of cardiovascular adverse effects 3 months postoperation among all three groups ($P < 0.05$). **Conclusion.** Dapagliflozin with metoprolol sustained-release tablets can be effective in improving the heart function, inflammatory response, oxidative stress response, and prognosis in patients after PCI.

1. Introduction

Persistent myocardial ischemia and hypoxia caused by coronary artery occlusion can lead to acute myocardial infarction. According to relevant studies, the number of new acute myocardial infarction cases in China can reach 500,000 every year, and the onset age tends to be younger.

Percutaneous coronary intervention (PCI) is often used in clinical treatment of acute myocardial infarction, which can quickly open blocked vessels and restore myocardial blood supply. According to the registration data of coronary intervention in mainland China in 2020, there were 968,651 patients undergoing coronary intervention in my country in 2020, ranking first in the world [1]. However, some patients

treated with PCI still have poor cardiac function recovery, so it is very important to improve the prognosis of patients with acute myocardial infarction treated with PCI [2–4]. Metoprolol sustained-release tablet is a selective β -receptor blocker. According to relevant studies, β -blockers can effectively block myocardial inflammation caused by adrenergic receptor activation and can effectively reduce ventricular rate and myocardial oxygen consumption in patients with ischemic cardiomyopathy. They are often used in combination with angiotensin-converting enzyme inhibitors/angiotensin receptor antagonists and other conventional drugs [5, 6]. Dapagliflozin was initially widely used as a hypoglycemic drug in clinic. The mechanism of action of dapagliflozin is that sodium-glucose cotransporter 2 (SGLT2) is expressed in the proximal renal tubules, for the major transporter responsible for glucose reabsorption in renal tubular filtration [7]. According to relevant studies, in addition to its hypoglycemic effect, dapagliflozin can lower blood pressure, diuretic, inhibit myocardial fibrosis, and improve myocardial metabolism and homeostasis [8, 9]. In this study, dapagliflozin combined with metoprolol sustained-release tablets was used in patients with acute infarction undergoing PCI, in order to explore its clinical efficacy.

2. Materials and Methods

2.1. General Information. A total of 84 patients with myocardial infarction who had undergone PCI from February 2020 to February 2022 were included and randomly separated into three groups: A, B, and C, with 28 patients per group. Four females and 24 males of age from 23 to 87 years were included in group A; the average age was 56.32 ± 12.19 years; 11 cases had diabetes mellitus; 10 cases had heart failure; 11 cases had ventricular arrhythmia; 14 cases had angina pectoris; 12 cases had smoking history. In group B, there were 20 males and 8 females, age from 23 to 86 years old, with an average of 57.68 ± 11.49 years old; 8 cases had diabetes mellitus; 12 cases had heart failure; 15 cases had ventricular arrhythmia; 9 cases had angina pectoris; 16 cases had smoking history. Two females and 26 males of age from 24 to 80 years were included in group C, and the average age was 56.25 ± 12.04 years; 13 cases had diabetes mellitus; 9 cases had heart failure; 10 cases had ventricular arrhythmia; 12 cases had angina pectoris; 15 cases had a smoking history. The three groups' overall data were compared ($P > 0.05$). The present study has been approved by the Hospital Ethics Board.

2.2. Inclusion Criteria. ① All met the Chinese Medical Association's diagnostic criteria for acute myocardial infarction and were confirmed through imaging. ② The New York Heart Association (NYHA) Classification was grades II to IV. ③ The PCI was carried out within 24 hours of its occurrence. ④ Estimated survival time ≥ 1 year. ⑤ The clinical and imaging data were complete. ⑥ All of them volunteered to participate.

2.3. Exclusion Criteria. These are as follows: ① patients allergic to drugs used in this study, ② people with a history of

myocardial infarction, ③ patients with severe renal and liver dysfunction, ④ patients with a history of PCI treatment, ⑤ patients with mechanical complications after acute myocardial infarction, ⑥ patients with contraindications to the study drug, and ⑦ patients lost to follow-up.

2.4. Methods. Immediately after admission, the patients received general treatment, including ECG, blood pressure, and oxygen saturation detection, bed rest, establishment of venous channels, oxygen inhalation, and correction of water, electrolyte balance, and acid-base balance disorders. Meanwhile, atorvastatin or rosuvastatin was used for plaque stabilization in all three groups. All patients were given oral 300 mg of aspirin (Bayer Health Care Co., Ltd., National drug approval number: J20080078) and 180 mg of ticagrelor (AstraZeneca AB, National drug approval number: J20130020) and then underwent emergency PCI. After PCI, aspirin (100 mg/d) and ticagrelor (180 mg/d) were routinely taken orally. Group C was given placebo, and group B was given dapagliflozin (AstraZeneca Pharmaceuticals Co., Ltd., National drug approval number: J20170040), 10 mg/time, once a day. Group A was given dapagliflozin combined with metoprolol succinate sustained-release tablets (AstraZeneca Pharmaceuticals Co., Ltd., National Drug approval number: J20150044), dapagliflozin was given as group B, and metoprolol succinate sustained-release tablets were given orally, 11.875–47.5 mg/time, once a day. All three groups were treated continuously for 3 months.

2.5. Observation Indicators. These are as follows: (1) comparison of the levels of cardiac function ultrasound indexes. Left ventricular end diastolic diameter (EDD), left ventricular ejection fraction (LVEF), and end systolic diameter (ESD) were estimated by Siemens PRIME ACUSON ES2000 and Philips EPIQ 7C Doppler ultrasound. (2) Comparison of myocardial infarction area. Myocardial ECT was used to reconstruct the tomographic images of the heart in three mutually vertical directions: horizontal long axis, vertical long axis, and short axis. The infarction area components of each tomography were measured and recorded as S_x , S_y , and S_z , and the total infarction area was recorded as S . According to $S = \sqrt{(S_x^2 + S_y^2 + S_z^2)/2}$, S_x is the infarction area component in the long axis direction, S_y is the infarction area component in the short axis direction, and S_z is the infarction area component in the horizontal axis direction. The calculation method of S_x was to measure the length of the damaged myocardium on the long axis of each tomographic image, respectively, as $A_1 B_1, A_2 B_2, A_3 B_3 \dots A_n B_n$, and the vertical distance between adjacent tomographic image was denoted as d , $S_x = (A_1 B_1 + A_2 B_2) \times d/2 + (A_2 B_2 + A_3 B_3) \times d/2 + \dots$. The algorithm of S_y and S_z was the same as that of S_x , and the myocardial infarction area was compared between the three groups at 3 months postoperation. (3) Comparison of the levels of inflammatory and oxidative stress indexes in all three groups. Venous blood (5 ml) was collected from each patient in fasting before and after treatment and then centrifuged at 2500 r/min for 15 min, and then, the supernatant was removed and cryopreserved for testing. The serum

TABLE 1: Comparison of cardiac function ultrasound index levels among three groups ($\bar{x} \pm s$).

Group	LVEF (%)		EDD (mm)		ESD (mm)	
	Before treatment	After treatment	Before treatment	After treatment	Before treatment	After treatment
Group A ($n = 28$)	46.40 \pm 5.44	58.60 \pm 4.47 ^{ac}	58.86 \pm 4.46	54.01 \pm 4.93 ^{ac}	47.49 \pm 2.95	44.15 \pm 3.31 ^a
Group B ($n = 28$)	46.44 \pm 5.14	57.48 \pm 5.58 ^{ac}	59.46 \pm 5.14	55.22 \pm 4.98 ^{ac}	47.59 \pm 4.28	45.25 \pm 5.45 ^a
Group C ($n = 28$)	45.10 \pm 3.90	51.06 \pm 4.52 ^a	58.64 \pm 7.80	58.13 \pm 7.13	46.53 \pm 4.22	46.28 \pm 4.31

^aSame group comparison before treatment ($P < 0.05$). ^bComparison with group B ($P < 0.05$). ^cComparison with group C ($P < 0.05$).

levels of interleukin-6 (IL-6) and high-sensitivity C-reactive protein (hs-CRP) were determined by the Enzyme-Linked Immunosorbent Assay (ELIZA). The serum levels of malondialdehyde (MDA) and superoxide dismutase (SOD) were determined by double-antibody sandwich ELIZA. (4) Comparison of the serum levels of N-terminal probrain natriuretic peptide (NT-pro BNP), lipoprotein (a) (Lp(a)), ischemia-modified albumin (IMA), and secreted frizzled-related protein 5 (SFRP5) in all three groups. The serum levels of NT-pro BNP, IMA, and SFRP5 were determined by ELIZA, and the Lp(a) level was measured by automatic biochemical analyzer. (5) Comparison of the onset of adverse effects among all groups. (6) Comparison of the occurrence of cardiovascular adverse events among the three groups.

2.6. Statistical Methods. To process and analyze the data, statistical software (SPSS 20.0) was used. Data of measurement were represented as $\bar{x} \pm s$. For intergroup comparison, an independent sample *T*-test was applied. To compare before and after treatment effects, paired *T*-test was applied. χ^2 test was used for comparison. Count data represented as frequency and constituent ratio. $P < 0.05$ was considered statistically significant.

3. Results

3.1. Comparison of Cardiac Function Ultrasound Index Levels among the Three Groups. No significant difference was found in LVEF, EDD, and ESD levels ($P > 0.05$) before treatment. However, the levels of LVEF and EDD in groups A and B were increased significantly after treatment, while the levels of EDD and ESD decreased. The improvement degree of LVEF and EDD levels in groups A and B was greater compared to group C ($P < 0.05$) as indicated in Table 1.

3.2. Comparison of Myocardial Infarction Area 3 Months after Operation among the Three Groups. There was no significant difference in the myocardial infarction area 3 months after operation among the three groups ($P > 0.05$), as shown in Table 2.

3.3. Comparison of Inflammation and Oxidative Stress Levels among the Three Groups before and after Treatment. Before treatment, no significant difference was found in the levels of SOD and MDA and hs-CRP and IL-6 between all groups ($P > 0.05$). The serum concentrations of MDA and hs-CRP and IL-6 were decreased after treatment in all three groups; however, the SOD level was increased. The improvement

TABLE 2: Comparison of myocardial infarction area 3 months after operation among the three groups ($\bar{x} \pm s$, cm²).

Group	Myocardial infarction area 3 months after operation
Group A ($n = 28$)	8.03 \pm 1.66
Group B ($n = 28$)	8.87 \pm 1.53
Group C ($n = 28$)	8.24 \pm 2.14

^aSame group comparison before treatment ($P < 0.05$). ^bComparison with group B ($P < 0.05$). ^cComparison with group C ($P < 0.05$).

degree of serum hs-CRP, IL-6, SOD, and MDA levels in groups A and B was greater than that in group C, and the improvement degree of serum hs-CRP, SOD, and MDA was higher in group A compared to group B ($P < 0.05$), as indicated in Table 3.

3.4. Comparison of Serum IMA, NT-proBNP, and Lp(a) Levels among the Three Groups. Before treatment, no significant difference was found in the levels of IMA, NT-proBNP, Lp(a), and SFRP5. The levels of IMA, NT-proBNP, and Lp(a) were decreased in all groups after treatment, while the levels of SFRP5 were increased. The improvement in the serum levels of IMA, NT-proBNP, Lp(a), and SFRP5 was higher in both groups A and B compared to group C. The improvement in serum levels of IMA, NT-proBNP, Lp(a), and SFRP5 was increased in group A than in group B ($P < 0.05$) as indicated in Table 4.

3.5. Comparison of the Occurrence of Adverse Reactions among the Three Groups. No adverse effect was observed in all three groups.

3.6. Comparison of Cardiovascular Adverse Events 3 Months after Surgery among the Three Groups. The total occurrence of cardiovascular adverse reactions such as stent thrombosis, cardiac failure, ventricular fibrillation, and death was 10.71% in group A, 25.00% in group B, and 53.75% in group C. The onset of cardiovascular adverse effects 3 months postoperation was significantly different among the three groups ($\chi^2 = 12.757$, $P < 0.05$) as indicated in Table 5.

4. Discussion

Dapagliflozin is a novel sodium-glucose cotransporter 2 inhibitor, which was initially marketed as a hypoglycemic drug in China. However, in subsequent studies, dapagliflozin was found to have antihypertensive and diuretic effects,

TABLE 3: Changes in the inflammation and oxidative stress levels before and after treatment in the three groups ($\bar{x} \pm s$).

Group	hs-CRP (mg/l)		IL-6 (ng/l)		SOD (U/ml)		MDA (nmol/l)	
	Before treatment	After treatment	Before treatment	After treatment	Before treatment	After treatment	Before treatment	After treatment
Group A (n = 28)	13.82 ± 2.54	6.18 ± 1.16 ^{abc}	14.81 ± 3.29	5.84 ± 0.73 ^{ac}	41.16 ± 4.50	64.42 ± 5.52 ^{abc}	8.17 ± 1.85	3.37 ± 1.65 ^{abc}
Group B (n = 28)	13.07 ± 2.57	7.88 ± 1.24 ^{ac}	14.64 ± 3.71	6.15 ± 1.18 ^{ac}	40.92 ± 5.90	59.29 ± 5.06 ^{ac}	8.03 ± 1.62	5.30 ± 1.40 ^{ac}
Group C (n = 28)	13.85 ± 3.58	10.14 ± 2.73 ^a	15.12 ± 4.53	9.04 ± 1.68 ^a	40.74 ± 4.13	50.33 ± 7.01 ^a	8.76 ± 1.86	6.42 ± 1.58 ^a

^aSame group comparison before treatment ($P < 0.05$). ^bComparison with group B ($P < 0.05$). ^cComparison with group C ($P < 0.05$).

TABLE 4: Comparison of serum of IMA, NT-proBNP, Lp(a), and SFRP5 levels among the three groups ($\bar{x} \pm s$).

Group	IMA (U/ml)		NT-proBNP (pg/ml)		Lp(a) (mg/l)		SFRP5 (ng/ml)	
	Before treatment	After treatment	Before treatment	After treatment	Before treatment	After treatment	Before treatment	After treatment
Group A ($n = 28$)	91.01 \pm 8.68	35.64 \pm 2.92 ^{abc}	3686.42 \pm 499.58	2079.91 \pm 322.45 ^{abc}	332.47 \pm 37.33	264.46 \pm 32.41 ^{abc}	21.13 \pm 3.72	84.03 \pm 8.20 ^{abc}
Group B ($n = 28$)	90.49 \pm 7.90	42.69 \pm 7.62 ^{ac}	3670.94 \pm 517.82	2411.84 \pm 523.83 ^{ac}	334.76 \pm 46.72	284.89 \pm 36.59 ^{ac}	21.81 \pm 2.45	59.90 \pm 6.95 ^{ac}
Group C ($n = 28$)	91.22 \pm 10.03	58.62 \pm 5.03 ^a	3634.97 \pm 451.28	2846.79 \pm 415.30 ^a	332.61 \pm 29.12	304.22 \pm 29.83 ^a	22.37 \pm 2.88	41.73 \pm 6.19 ^a

^aSame group comparison before treatment ($P < 0.05$). ^bComparison with group B ($P < 0.05$). ^cComparison with group C ($P < 0.05$).

TABLE 5: Comparison of cardiovascular adverse events 3 months after surgery among the three groups ($n(\%)$).

Group	Heart failure	Ventricular fibrillation	Death	Total incidence of cardiovascular adverse events
Group A ($n = 28$)	3 (10.71)	0 (0.00)	0 (0.00)	3 (10.71) ^c
Group B ($n = 28$)	4 (14.29)	2 (7.14)	1 (3.57)	7 (25.00) ^c
Group C ($n = 28$)	9 (32.14)	3 (10.71)	3 (10.71)	15 (53.57)

^aSame group comparison before treatment ($P < 0.05$). ^bComparison with group B ($P < 0.05$). ^cComparison with group C ($P < 0.05$).

improve osmotic pressure, inhibit myocardial fibrosis, improve myocardial energy metabolism, and improve myocardial homeostasis in addition to hypoglycemic effects [10, 11]. In addition, dapagliflozin can reduce the body mass of patients, 60%~70% of which is adipose tissue, including visceral tissue and subcutaneous tissue, and reduce the accumulation and inflammation of epicardial adipose tissue, which can be used for the treatment of cardiovascular diseases [12]. At present, the mechanism of dapagliflozin in the treatment of cardiovascular diseases has not been fully clarified, which may include a variety of mechanisms. The initial study believed that dapagliflozin could reduce the toxicity of glucose to the heart through the hypoglycemic effect, so dapagliflozin is used more in patients with cardiovascular disease complicated by diabetes [13–15]. Studies suggest that dapagliflozin may increase the synthesis of the hepatic ketone body, enhance myocardial energy metabolism, and improve cardiac function. In addition to the common hypoglycemic effects, dapagliflozin also has the effects of hypotension, diuresis, improvement of ventricular remodeling, and myocardial cell homeostasis. Besides, it can also improve arterial stiffness, which is beneficial to the treatment of cardiovascular diseases [16]. Metoprolol sustained-release tablets are selective β_1 -receptor blockers with antisymphatic effects, which can block myocardial inflammatory response caused by receptor activation and reduce ventricular remodeling. In addition, the use of beta-blockers can reduce cardiac oxygen consumption and improve myocardial perfusion in patients with cardiovascular disease. However, the application of β -blockers can cause hemodynamic instability and lead to severe bronchial asthma, and the dosage of β -blockers is limited [17–19]. In this study, the combined application of dapagliflozin and metoprolol may reduce the dose of metoprolol sustained-release tablets and also decrease the onset of complications by ensuring therapeutic effects.

Coronary atherosclerotic plaque rupture and accompanying mural thrombus may be the main pathogenesis of acute coronary syndrome (ACS), and the activation of inflammatory response may be the main factor leading to atherosclerotic plaque instability [20]. Serum hs-CRP, IL-6, SOD, and MDA levels can indicate the degree of inflammatory response and oxidative stress response in acute myocardial infarction patients [21]. In the present study, the level of LVEF in groups A and B was increased after treatment, while the levels of EDD and ESD were decreased. The improvement degree of LVEF and EDD in groups A and B was greater compared to group C. There was no significant difference in the myocardial infarction area 3 months post-operation between all groups. Serum concentrations of MDA, hs-CRP, and IL-6 were decreased after treatment in

all three groups, while the levels of SOD increased. The concentrations of SOD, MDA, and hs-CRP, IL-6 were increased in the serum of both groups A and B compared to group C. Serum concentrations of SOD, MDA, and HS-CRP were higher in group A compared to group B. It indicates that dapagliflozin combined with metoprolol sustained-release tablets can effectively improve cardiac function, inflammatory response, and oxidative stress response in myocardial infarction patients post-PCI. The combined treatment group has better effect on improving inflammation and oxidative stress response than that of doxycycline alone. The improvement effect of cardiac function, inflammation, and oxidative stress in group B with dapagliflozin alone was also better compared to group C, showing that dapagliflozin may improve the cardiac function, inflammatory response, and oxidative stress in myocardial infarction patients post-PCI, but dapagliflozin in combination with metoprolol has better efficacy. Dapagliflozin and prolonged release metoprolol tablets improve cardiac function, reduce inflammation, and reduce the response to oxidative stress. The combined treatment plays a synergistic role and has a better effect on improving cardiac function. At present, no clinical study has applied dapagliflozin combined with metoprolol in patients with myocardial infarction after PCI, and the mechanism involved in this is yet to be explored.

IMA is a marker of myocardial infarction and is closely related to the degree of myocardial ischemia. It can be produced by human serum albumin during myocardial ischemia and increases rapidly when myocardial injury occurs. When the body tissue is ischemia, blood supply and oxygen supply are reduced, cells undergo anaerobic metabolism, lactic acid accumulation, and superoxide radical (O_2^-) formation, which is dismutated into hydrogen peroxide (H_2O_2) and oxygen through superoxide dismutase, and finally, IMA can be formed in the presence of metal ions. Patients after PCI are prone to myocardial ischemic injury, and IMA is a common marker of myocardial ischemia [22, 23]. NT-proBNP is the product of BNP precursor (proBNP) after cleavage into BNP, secreted by ventricular cells, which has the role of balancing water and sodium metabolism and dilating blood vessels [24, 25]. Myocardial ischemia and hypoxia can lead to increased myocardial tension and activation of excitatory neurohumoral factors and stimulate the generation of myocardial cells, leading to the increase in the level of NT-proBNP; the higher the level of serum NT-proBNP, the greater the myocardial ischemia area [26]. According to relevant studies, serum Lp(a) can induce platelet activation by promoting the formation of arterial plaque, trigger thrombosis, and accelerate the progression of coronary atherosclerosis [27]. Studies have shown that the serum

level Lp(a) increases with increased coronary lesions [28]. SFRP5 can regulate lipid metabolism and inflammatory response through Wnt signal transduction pathway, which is closely related to myocardial cell injury and cardiovascular ischemic injury [29]. In this study, the levels of IMA, NT-proBNP, and Lp(a) were decreased in all three groups after treatment, while the levels of SFRP5 were increased. The improvement degree of IMA, NT-proBNP, Lp(a), and SFRP5 was higher in both the groups A and B compared to group C. The improvement degree of IMA, NT-proBNP, Lp(a), and SFRP5 levels was higher in group A compared to group B. It shows that dapagliflozin may improve the serum level of cardiac function markers in myocardial infarction patients who undergone PCI, and dapagliflozin combined with metoprolol sustained-release tablets is more effective. This may be because dapagliflozin can improve myocardial energy metabolism, improve myocardial homeostasis, and relieve myocardial ischemia and hypoxia, and metoprolol sustained-release tablets can reduce myocardial oxygen consumption and improve myocardial perfusion in cardiovascular patients; the combined application of the two can effectively improve myocardial ischemia and hypoxia and effectively regulate the serum level of cardiac function indicators. Also, we did not observe any adverse effects in all three groups, indicating that the addition of drugs in groups A and B did not cause serious adverse reactions, indicating that the medication was safe. Comparing the onset of cardiovascular adverse effects 3 months postoperation among all groups, it showed that the occurrence of cardiovascular events was 10.71%, 25.00%, and 53.75% in groups A, B, and C, respectively. It shows that dapagliflozin in combination with metoprolol can effectively reduce the incidence of cardiovascular adverse events in myocardial infarction patients post-PCI. Previously, it has been revealed that β -blockers improve the prognosis in myocardial infarction patients post-PCI [30]. We suggest that the dapagliflozin and metoprolol combined use had a better effect in improving prognosis.

In conclusion, dapagliflozin in combination with metoprolol may improve cardiac function, reduce the inflammatory response and oxidative stress response, improve myocardial ischemia and hypoxia state, and improve prognosis in myocardial infarction patients post-PCI, which has clinical application value. However, this study has the following shortcomings, including the small sample size and the lack of metoprolol group. In future studies, the sample size of the study should be further expanded and the metoprolol group should be set up.

Data Availability

The labeled dataset used to support the findings of this study are available from the corresponding author upon request.

Conflicts of Interest

The authors declare no competing interests.

References

- [1] "The 24th National Interventional Cardiology Forum," 2021.
- [2] G. Marquis-Gravel, M. Zeitouni, A. Kochar et al., "Technical consideration in acute myocardial infarction with cardiogenic shock: a review of antithrombotic and PCI therapies," *Catheterization and Cardiovascular Interventions*, vol. 95, no. 5, pp. 924–931, 2020.
- [3] Y. Honda, "Intravascular imaging to guide PCI for acute myocardial infarction: shifting from "whether" to "how,"" *JACC. Cardiovascular Interventions*, vol. 14, no. 22, pp. 2444–2446, 2021.
- [4] K. H. Cho, X. Han, J. H. Ahn et al., "Long-term outcomes of patients with late presentation of ST-segment elevation myocardial infarction," *Journal of the American College of Cardiology*, vol. 77, no. 15, pp. 1859–1870, 2021.
- [5] M. C. Bahit, A. Kochar, and C. B. Granger, "Post-myocardial infarction heart failure," *JACC Heart Fail.*, vol. 6, no. 3, pp. 179–186, 2018.
- [6] J. Kim, D. Kang, H. Park et al., "Long-term β -blocker therapy and clinical outcomes after acute myocardial infarction in patients without heart failure: nationwide cohort study," *European Heart Journal*, vol. 41, no. 37, pp. 3521–3529, 2020.
- [7] J. Ma, "Application progress of dapagliflozin in the treatment of patients with type 2 diabetes," *Modern Diagnosis and Treatment*, vol. 32, no. 16, p. 3, 2021.
- [8] R. H. M. Furtado, M. P. Bonaca, I. Raz et al., "Dapagliflozin and cardiovascular outcomes in patients with type 2 diabetes mellitus and previous myocardial infarction," *Circulation*, vol. 139, no. 22, pp. 2516–2527, 2019.
- [9] D. von Lewinski, M. Benedikt, N. Tripolt, M. Wallner, H. Sourij, and E. Kolesnik, "Can sodium-glucose cotransporter 2 inhibitors be beneficial in patients with acute myocardial infarction?," *Kardiologia Polska*, vol. 79, no. 5, pp. 503–509, 2021.
- [10] C. H. Guo and X. Y. Gao, "The effect of dapagliflozin on metabolic indexes in patients with type 2 diabetes mellitus and metabolic syndrome," *Journal of Clinical Military Medicine*, vol. 46, no. 5, p. 3, 2018.
- [11] P. Z. Miao, "Research progress on the role of dapagliflozin in cardiovascular disease," *Internal Medicine Theory and Practice*, vol. 15, no. 2, p. 5, 2020.
- [12] M. Zhang, W. Liang, and X. Xu, "Comparison of the efficacy and safety of dapagliflozin and sitagliptin in the treatment of overweight and obese type 2 diabetes mellitus," *Journal of Practical Medicine*, vol. 37, no. 9, p. 5, 2021.
- [13] A. Odutayo, B. R. da Costa, T. V. Pereira et al., "Sodium-glucose cotransporter 2 inhibitors, all-cause mortality, and cardiovascular outcomes in adults with type 2 diabetes: a Bayesian meta-analysis and meta-regression," *Journal of the American Heart Association*, vol. 10, no. 18, article e019918, 2021.
- [14] S. R. Kalluri, T. H. Bhutta, H. Hannoodee et al., "Do SGLT2 inhibitors improve cardio-renal outcomes in patients with type II diabetes mellitus: a systematic review," *Cureus.*, vol. 13, no. 9, article e17668, 2021.
- [15] H. F. Lee, S. W. Chen, J. R. Liu et al., "Major adverse cardiovascular and limb events in patients with diabetes and concomitant peripheral artery disease treated with sodium glucose cotransporter 2 inhibitor versus dipeptidyl peptidase-4 inhibitor," *Cardiovascular Diabetology*, vol. 19, no. 1, p. 160, 2020.

Retraction

Retracted: Impacts of Low-Dose Total Glycosides of *Tripterygium wilfordii* plus Methotrexate on Immunological Function and Inflammation Level in Patients with Rheumatoid Arthritis

Computational and Mathematical Methods in Medicine

Received 27 June 2023; Accepted 27 June 2023; Published 28 June 2023

Copyright © 2023 Computational and Mathematical Methods in Medicine. This is an open access article distributed under the Creative Commons Attribution License, which permits unrestricted use, distribution, and reproduction in any medium, provided the original work is properly cited.

This article has been retracted by Hindawi following an investigation undertaken by the publisher [1]. This investigation has uncovered evidence of one or more of the following indicators of systematic manipulation of the publication process:

- (1) Discrepancies in scope
- (2) Discrepancies in the description of the research reported
- (3) Discrepancies between the availability of data and the research described
- (4) Inappropriate citations
- (5) Incoherent, meaningless and/or irrelevant content included in the article
- (6) Peer-review manipulation

The presence of these indicators undermines our confidence in the integrity of the article's content and we cannot, therefore, vouch for its reliability. Please note that this notice is intended solely to alert readers that the content of this article is unreliable. We have not investigated whether authors were aware of or involved in the systematic manipulation of the publication process.

Wiley and Hindawi regrets that the usual quality checks did not identify these issues before publication and have since put additional measures in place to safeguard research integrity.

We wish to credit our own Research Integrity and Research Publishing teams and anonymous and named external researchers and research integrity experts for contributing to this investigation.

The corresponding author, as the representative of all authors, has been given the opportunity to register their agreement or disagreement to this retraction. We have kept a record of any response received.

References

- [1] Y. Han, J. Jin, F. Wu, and Z. Wang, "Impacts of Low-Dose Total Glycosides of *Tripterygium wilfordii* plus Methotrexate on Immunological Function and Inflammation Level in Patients with Rheumatoid Arthritis," *Computational and Mathematical Methods in Medicine*, vol. 2022, Article ID 7523673, 7 pages, 2022.

Research Article

Impacts of Low-Dose Total Glycosides of *Tripterygium wilfordii* plus Methotrexate on Immunological Function and Inflammation Level in Patients with Rheumatoid Arthritis

Yong Han¹,^{ORCID} Jingri Jin,² Fushun Wu,¹ and Zhiwei Wang²

¹Department of Immunology, Yanbian University Hospital, Yanji, 133000 Jilin, China

²Department of Osteology, Yanbian University Hospital, Yanji, 133000 Jilin, China

Correspondence should be addressed to Yong Han; hanyonghy82@163.com

Received 10 May 2022; Revised 29 June 2022; Accepted 7 July 2022; Published 1 August 2022

Academic Editor: Pan Zheng

Copyright © 2022 Yong Han et al. This is an open access article distributed under the Creative Commons Attribution License, which permits unrestricted use, distribution, and reproduction in any medium, provided the original work is properly cited.

Purpose. This research mainly clarifies the impacts of low-dose- (LD-) total glycosides of *Tripterygium wilfordii* (GTW) plus methotrexate (MTX) on immunological function and inflammation level in patients with rheumatoid arthritis (RA). **Methods.** We enrolled 106 RA patients treated in Yanbian University Hospital between July 2019 and July 2021, including 56 cases (research group) intervened by LD-total GTW plus MTX and 50 cases (control group) treated with MTX, in addition to conventional treatment given to both groups. The improvement in immunological function (immunoglobulin (Ig) A, IgG, and IgM), inflammatory cytokines (ICs; C-reaction protein (CRP), tumor necrosis factor- α (TNF- α), and interleukin-6 (IL-6)), incidence of adverse reactions (ARs), joint function, and patient satisfaction were observed and compared. **Results.** Statistical better improvements of immunological function, ICs, and joint function were observed in the research group compared with the control group. Besides, patient satisfaction was higher and the incidence of ARs was lower in the research group. **Conclusions.** LD-total GTW plus MTX is highly effective and safe in enhancing the immunity, lowering the inflammation level, and improving the joint function of RA patients.

1. Introduction

Rheumatoid arthritis (RA), one of the most commonly seen chronic inflammatory diseases, is a chronic autoimmune condition affecting joints. It is characterized by progressive and symmetrical inflammation of the affected joints, leading to cartilage destruction, bone erosion, and ultimately disability [1]. In the later stages of the disease, many joints are involved with extra-articular symptoms in most cases [2]. The incidence of RA varies by gender, age, and patient group [3]. The prevalence of this connective tissue disease, which is associated with reduced quality of life, poor functional status, and increased mortality, has increased over the past two decades, further increasing the disease burden [4]. The condition of RA is prone to fluctuate with the aggravation of episodes. Without optimal treatment, the patient's symptoms can progressively worsen until the joints are irreversibly damaged and physical and mental functions are

affected [5]. In addition, the complications and comorbidities of RA can reduce life expectancy by several years [6, 7]. For these reasons, the treatment of RA needs a careful selection. In this study, we take drugs such as total glycosides of *Tripterygium wilfordii* (GTW) and methotrexate (MTX) as examples to study the drug treatment of RA, aiming to provide new reference for the treatment of RA and the improvement of patients' condition.

Tripterygium glycosides (TG) are a kind of natural active ingredient extracted from *Tripterygium wilfordii*, a southern Chinese vine that has long been used in traditional Chinese medicine [8]. Due to diverse pharmacological effects such as detoxification, blood-activating, inflammation prevention, and antiproliferation, the drug has been widely used to treat various types of inflammation [9]. It works by inhibiting dihydroorotate dehydrogenase, even in the treatment of active moderate-to-severe RA [10]. Another long widely used drug for severe RA, MTX, inhibits inflammation by

suppressing dihydrofolate reductase. MTX treatment, however, often comes with side effects [11]. Therefore, MTX needs to be combined with other drugs during treatment. However, for RA, there are few related studies on the combination treatment of the above two drugs. The purpose of this study is to study the impact of low-dose- (LD-) total GTW combined with MTX on RA patients through immunity- and inflammation-related indicators.

2. Methods

2.1. General Information. The study population comprised 106 cases of RA treated in Yanbian University Hospital from July 2019 to July 2021. According to different treatment methods, they were assigned to either the control group or the research group. The research group, with 56 cases, was treated with LD-total GTW plus MTX and conventional treatment, while the control group (50 cases) received MTX and routine treatment. The two cohorts showed no significant differences in general data ($P > 0.05$), with comparability. Inclusion criteria are as follows: all patients were diagnosed as RA in our hospital and were mentally normal that could accurately express their discomfort, with no history of drug allergy related to this study. Exclusion criteria are as follows: serious heart, liver, kidney, and other organ diseases; pregnant or lactating woman; use of immunosuppressants within 30 days before enrollment; and missing or incomplete clinical records.

The family members of patients gave their consent for patients' participation in this study and signed the relevant agreement. This study has obtained approval from the Medical Ethics Committee of Yanbian University Hospital.

2.2. Treatment Methods. Both groups received routine treatment. Oral indomethacin (Guangdong Huanan Pharmaceutical Group, SFDA Approval No. H44020701) was administered 0.1 g once, 3 times/d. Additionally, a reasonable diet was adopted, and high-fat and high-cholesterol foods were avoided as much as possible. On this basis, the control group was given 15 mg MTX (SFDA Approval No. H31020644, specification: 2.5 mg \times 100 tablets) produced by Shanghai Pharmaceuticals Sine, per os, once a week. The research group was given oral LD-total GTW and MTX. 10 mg total GTW (Jiangsu Meitong Pharmaceutical Co., Ltd., SFDA Approval No. Z32021007) was administered 3 times per day and 7.5 mg MTX was given once a week. Both groups were treated for 3 months, and the dosage of indomethacin was halved after 1 month of treatment and stopped after 2 months of treatment.

2.3. Measurement Indicators. Before the detection of immunological function and inflammatory cytokines (ICs) in patients, we collected 5 mL of fasting cubital venous blood from patients before and after treatment and extracted serum by 10 min of centrifugation at $1500 \times g$ and 4°C .

2.3.1. Immunological Function. Serum immunoglobulins of both cohorts of patients were quantified before and after treatment. Immunoglobulin (Ig) A, IgG, and IgM contents

were measured using a spectrophotometer (Shanghai Hui-cheng Biotech, C001-96T-1).

2.3.2. ICs. Serum ICs in both cohorts were measured before and three days after treatment. C-reaction protein (CRP), tumor necrosis factor- α (TNF- α), and interleukin-6 (IL-6) concentrations were detected by enzyme-linked immunosorbent assay (ELISA). The assay was carried out strictly following the instructions of the corresponding human ELISA kit (Wuhan Fine Biotech, EH2643, AQ-H0302-B, AQ-H0201).

2.3.3. Incidence of Adverse Reactions (ARs). The incidence of ARs in the two groups was detected and compared, and the related indicators were nausea, belching, abdominal pain, and mucosal ulcer.

2.3.4. Evaluation of Joint Function. Patients' joint function after treatment was compared. The joint function was evaluated according to the "Joint Dysfunction Grading Standard" [12]: (1) Grade I: patients can carry out daily life and work. (2) Grade II: patients can carry out general daily life and some professional work, but with confined activity. (3) Grade III: patients can carry out general daily life, but cannot participate in certain work or projects, with activity limitations. (4) Grade IV: patients cannot take care of themselves in daily life, with limited working ability.

2.3.5. Patient Satisfaction. We also compared patients' satisfaction with the nursing, using the nursing satisfaction questionnaire with the test contents and evaluation criteria all designed by our hospital. On a 100-point scale, 100-85, 60-84, and below 60 indicated satisfied, 60-84 basically satisfied, and dissatisfied, respectively. Satisfaction = (satisfied cases + basically satisfied cases)/total cases \times 100%.

2.4. Statistical Methods. SPSS22.0 (Asia Analytics formerly SPSS China) was used for the statistical processing of comprehensive data. Enumeration data were tested by χ^2 , while quantitative data denoted by ($X \pm S$) were verified by the t -test, with $P < 0.05$ as the significance threshold.

3. Results

3.1. General Information. The research group and the control group were not statistically different in a series of general data such as gender, age, body mass index (BMI) ($P > 0.05$). See Table 1 for details.

3.2. Immunological Function. The immunoglobulin levels differed insignificantly between research group and the control group prior to treatment ($P > 0.05$). The posttreatment IgG, IgA, and IgM levels decreased compared with their pretreatment levels, and the improvement of the above indexes was more obvious in the research group ($P < 0.05$; Figure 1).

3.3. ICs. Similarly, ICs were not notably different between groups prior to treatment ($P > 0.05$). And statistical decreases were observed in CRP, TNF- α , and IL-6 in both cohorts of patients after treatment, with more significant improvement of the above indexes in the research group compared to the control group ($P < 0.05$; Figure 2).

TABLE 1: General data.

Classification	Research group (n = 56)	Control group (n = 50)	t/χ^2	P
Sex			0.03	0.872
Male	30	26		
Female	26	24		
Age (years old)	61.77 ± 7.36	60.84 ± 7.15	0.66	0.512
BMI (kg/m ²)	26.06 ± 2.87	25.26 ± 2.97	1.41	0.162
Work location			0.40	0.528
Urban areas	38	31		
Rural areas	18	19		
Smoking			0.11	0.743
Yes	41	38		
No	15	12		
Drinking			0.07	0.792
Yes	35	30		
No	21	20		

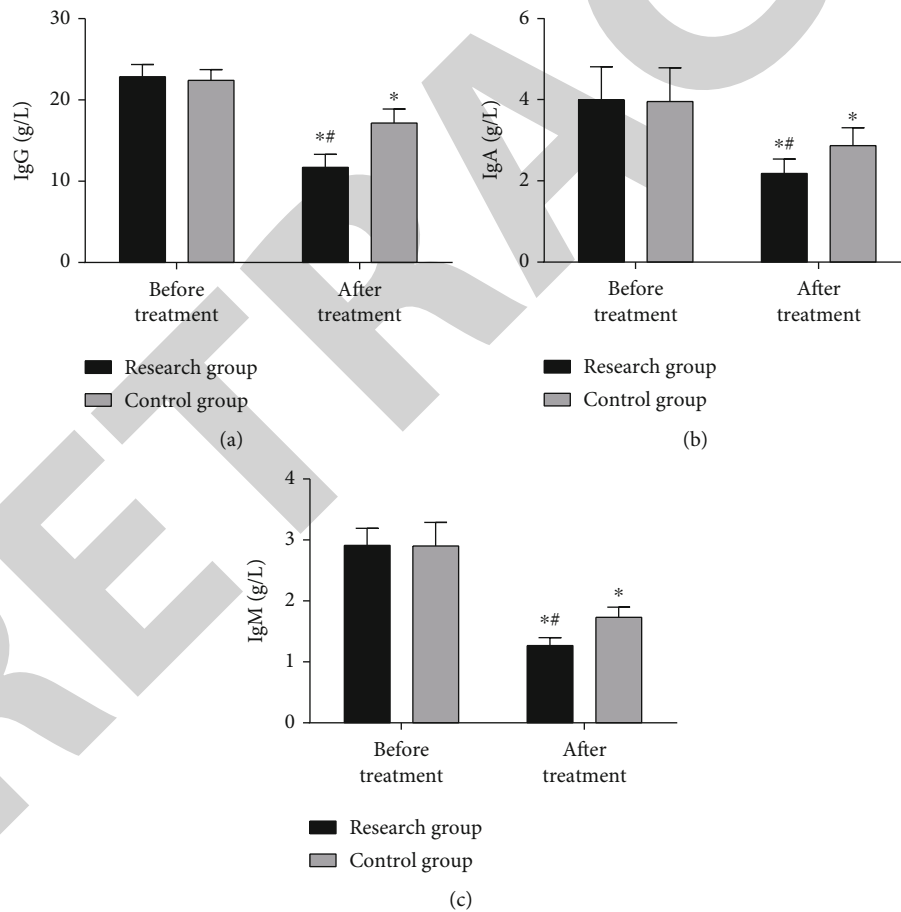


FIGURE 1: Immunoglobulins of the two groups of patients: (a) IgG levels in the two groups, (b) IgA levels in the two groups, and (c) IgM levels in the two groups. * means $P < 0.05$ compared with before treatment, and # means $P < 0.05$ compared with the control group.

3.4. *Incidence of ARs.* After investigating ARs in the two groups, it was found that the incidence was significantly lower in the research group compared with the control group ($P < 0.05$). Please see Table 2 for details.

3.5. *Joint Function Evaluation.* As shown in Table 3, the proportion of grade I joint dysfunction in the research group increased significantly after treatment compared with the control group ($P < 0.05$), but there was no significant

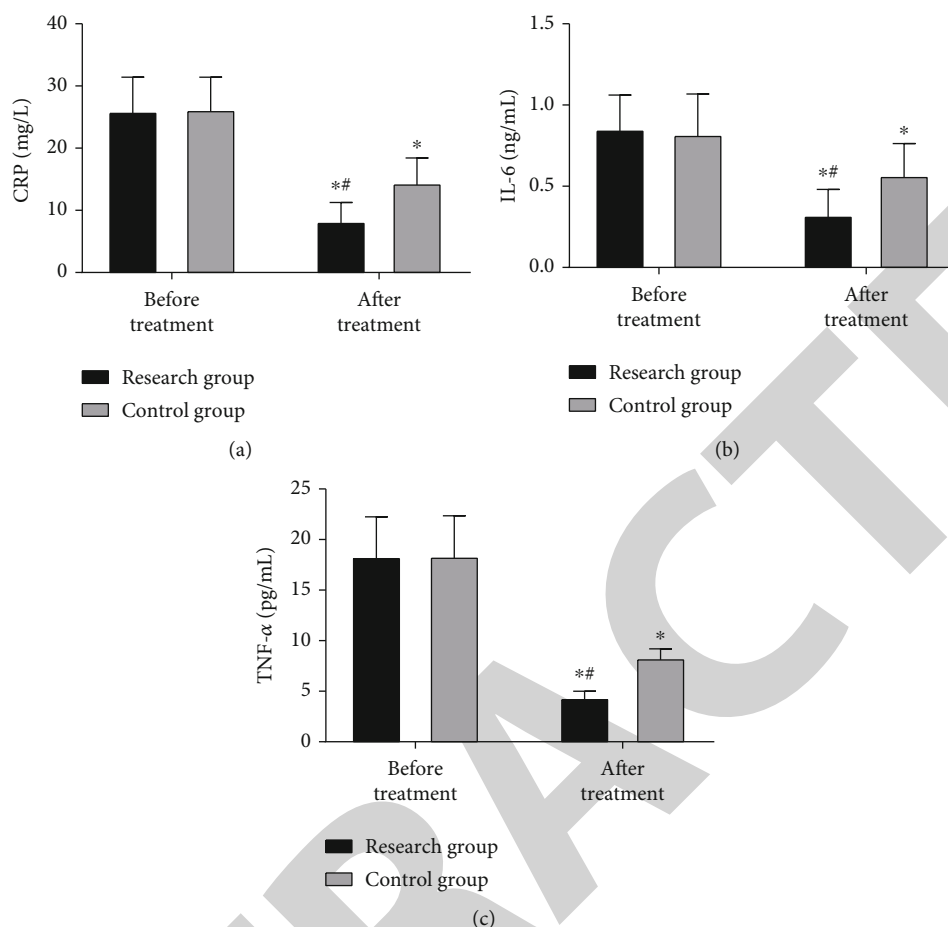


FIGURE 2: Inflammatory cytokines of the two groups of patients: (a) CRP levels in the two groups, (b) IL-6 levels in the two groups, and (c) TNF- α levels in the two groups. * means $P < 0.05$ compared with before treatment, and # means $P < 0.05$ compared with the control group.

TABLE 2: Incidence of adverse events.

Classification	Research group ($n = 56$)	Control group ($n = 50$)	χ^2	P
Nausea	2 (3.57)	3 (6.00)		
Eructation	0 (0.00)	1 (2.00)		
Abdominal pain	2 (3.57)	1 (2.00)		
Mucosal ulcer	0 (0.00)	6 (12.00)		
Incidence of adverse reactions (%)	4 (7.14)	11 (22.00)	5.86	0.012

TABLE 3: General data.

Classification	Research group ($n = 56$)	Control group ($n = 50$)	χ^2	P
Grade I	33 (58.93)	19 (38.00)	4.63	0.031
Grade II	18 (32.14)	21 (42.00)	1.10	0.294
Grade III	5 (8.93)	10 (20.00)	2.67	0.103

difference between groups in the proportions of grade II and grade III joint dysfunction ($P > 0.05$).

3.6. Patient Satisfaction. The investigation of patient satisfaction revealed a higher satisfaction degree in the research group as compared to the control group ($P < 0.05$; Table 4).

4. Discussion

As a disease of unknown origin, RA causes inflammatory changes in synovial tissues, cartilage, and hard bones of joints and, less commonly, in the extra-articular sites. Patients with RA mainly present with joint pain, swelling, and subsequent

TABLE 4: Satisfaction of the two groups of patients.

Classification	Research group ($n = 56$)	Control group ($n = 50$)	χ^2	P
Satisfied	36 (64.29)	22 (44.00)	—	—
Basically satisfied	18 (32.14)	18 (36.00)	—	—
Dissatisfied	2 (3.57)	10 (20.00)	—	—
Satisfaction (%)	54 (96.43)	40 (80.00)	7.45	0.006

cartilage and bone destruction, as well as systemic manifestations caused by arachidonic acid metabolites and various ICs [13]. There is currently no cure for such a systemic inflammatory disease, and because of its heterogeneity, variability, and multilevel nature, there is no a unified description of its pathogenesis, so the treatment of it is still a difficulty [14]. In this section, we will discuss the impacts of the two-drug combination therapy on the immunological function and inflammation level of RA based on the results obtained.

According to the results, the research group that used the combination of the two drugs had significantly better immunological function recovery than the control group. In the study of Dong et al. [15], the application of GTW to patients with RA could significantly reduce IgA and IgG levels in patients, similar to our findings. Liu et al. [16] also pointed out that GTW and MTX had significant inhibitory effects on the levels of IgG, IgA, and IgM in RA patients with anemia, which was consistent with our results. A combination therapy of MTX with other drugs can significantly improve patients' immunological function. This is because when combined with other drugs, it inhibits tyrosine kinases that affect immunological function while reducing the production of pyrimidine and dihydroorotate dehydrogenase to inhibit DNA synthesis, enabling it to exert a pharmacodynamic mechanism on lymphocyte activation and immune response, thus enhancing the immunity of patients [17–19]. On the other hand, MTX, when used alone, brings many side effects and has a poor effect on lymphocyte proliferation of the immune system. Therefore, it is necessary to combine with other drugs to inhibit lymphocyte proliferation and finally improve the abnormal immune response of RA patients [20–22]. As an extract of Chinese herbal medicine, total GTW is effective in the treatment of various systemic diseases [23]. Tripterygium glycosides belong to a nonsteroidal immunosuppressant, which can effectively inhibit cellular immunity and humoral immunity [8, 24]. Currently, the drug is extensively used to treat autoimmune diseases, including RA, primary glomerulonephritis, and immune-related nephritis [25, 26]. According to the characteristics of the two drugs, the combination of total GTW can effectively make up for the deficiency of MTX and adjust patients' immunity.

In terms of inflammation, more significantly reduced levels of ICs were determined in the research group after treatment. In the treatment of various types of arthritis, the antifolic acid mechanism of MTX has historically been related to the treatment of neoplastic (lymphoblastic) diseases. The immunosuppression brought by LD-MTX therapy can even play an anticancer role, which mainly depends on the inhibition of the enzyme 5-aminoimidazole-4-carboxamide ribonucleoside (AICAR) transformylase

(ATIC), resulting in a higher level of AICAR inhibition of adenosine monophosphate deaminase and adenosine deaminase. This leads to higher extracellular levels of adenine, which is further converted into adenosine, thus playing an anti-inflammatory role through adenosine receptors. It also reduces downstream inflammatory signaling via the nuclear factor kappa B (NF κ B) [27]. However, the antifolate effects of MTX also contribute to most of its side effects and result in it having little effect on inhibiting other anti-inflammatory pathways [28], which may explain the limited decrease of ICs in the control group using MTX alone. As mentioned above, *Tripterygium wilfordii* has anti-inflammatory action, which can be enhanced if MTX is combined. Combining the conclusions of previous literature with our findings, we can conclude that the combination of the two drugs can effectively improve patient's immunological function and relieve inflammation, which can facilitate patients' rehabilitation and improved limb recovery. And because of the combination of the two, the side effects of MTX can even be effectively reduced, contributing to higher patient safety, fewer ARs, and higher patient satisfaction. In the report of Wang et al. [29], GTW plus MTX in patients with RA significantly inhibited the level of CRP without increasing the complication rate, which is consistent with our findings. Wang et al. [30] also pointed out that compared with MTX alone, GTW combined with MTX intervention can significantly improve the clinical manifestations of joint swelling and tenderness in RA patients, indicating higher efficacy of the combined treatment in improving patients' joint function, which can support our results. Chen et al. [31] also reported a higher compliance degree in RA patients treated with GTW and MTX combination therapy compared with those receiving MTX monotherapy, which reflected that the satisfaction rate of RA patients with combined therapy may be relatively higher.

The innovation of this study lies in the comparative evaluation of the clinical effects of LD-total GTW combined with MTX combined with MTX and MTX monotherapy in the treatment of RA from the perspectives of immunological function, ICs, incidence of ARs, joint function, and patient satisfaction. This study confirmed the efficacy and safety of the combination therapy for patients with RA, providing a new basis for the treatment of such patients. However, there are many shortcomings in this study. We failed to effectively observe patients' treatment compliance during the treatment process nor have we investigated the psychological anxiety and depression of them. In future research, we will continue to address the above deficiencies, and constantly improve the treatment methods to make patients satisfied.

Conclusively, this research believes that LD-total GTW combined with MTX can significantly improve RA patients' immunity, reduce inflammation, and improve their joint function with higher safety.

Data Availability

The labeled datasets used to support the findings of this study are available from the corresponding author upon request.

Conflicts of Interest

The authors declare no competing interests.

References

- [1] Y. J. Lin, M. Anzaghe, and S. Schulke, "Update on the pathomechanism, diagnosis, and treatment options for rheumatoid arthritis," *Cells*, vol. 9, no. 4, 2020.
- [2] E. A. Littlejohn and S. U. Monrad, "Early diagnosis and treatment of rheumatoid arthritis," *Primary Care*, vol. 45, no. 2, pp. 237–255, 2018.
- [3] J. S. Smolen, D. Aletaha, and I. B. McInnes, "Rheumatoid arthritis," *Lancet*, vol. 388, no. 10055, pp. 2023–2038, 2016.
- [4] A. J. Esposito, S. G. Chu, R. Madan, T. J. Doyle, and P. F. Delaripa, "Thoracic manifestations of rheumatoid arthritis," *Clinics in Chest Medicine*, vol. 40, no. 3, pp. 545–560, 2019.
- [5] N. Chaurasia, A. Singh, I. L. Singh, T. Singh, and T. Tiwari, "Cognitive dysfunction in patients of rheumatoid arthritis," *Journal of Family Medicine and Primary Care*, vol. 9, no. 5, pp. 2219–2225, 2020.
- [6] M. N. Lassere, J. Rappo, I. J. Portek, A. Sturgess, and J. P. Edmonds, "How many life years are lost in patients with rheumatoid arthritis? Secular cause-specific and all-cause mortality in rheumatoid arthritis, and their predictors in a long-term Australian cohort study," *Internal Medicine Journal*, vol. 43, no. 1, pp. 66–72, 2013.
- [7] A. F. Radu and S. G. Bungau, "Management of rheumatoid arthritis: an overview," *Cells*, vol. 10, 2021.
- [8] X. Xu, Q. J. Li, S. Xia, M. M. Wang, and W. Ji, "Tripterygium glycosides for treating late-onset rheumatoid arthritis: a systematic review and meta-analysis," *Alternative Therapies in Health and Medicine*, vol. 22, no. 6, pp. 32–39, 2016.
- [9] Y. Jin, Y. Wang, S. Wang, Q. Zhao, D. Zhang, and X. Feng, "The efficacy of Tripterygium glycosides combined with LMWH in treatment of HSPN in children," *Evidence-Based Complementary and Alternative Medicine*, vol. 2021, Article ID 7223613, 6 pages, 2021.
- [10] Y. J. Yang, Y. Deng, L. L. Liao, J. Peng, Q. H. Peng, and Y. H. Qin, "Tripterygium glycosides combined with leflunomide for rheumatoid arthritis: a systematic review and meta-analysis," *Evidence-Based Complementary and Alternative Medicine*, vol. 2020, Article ID 1230320, 11 pages, 2020.
- [11] B. Friedman and B. Cronstein, "Methotrexate mechanism in treatment of rheumatoid arthritis," *Joint, Bone, Spine*, vol. 86, no. 3, pp. 301–307, 2019.
- [12] C. B. Outzen, D. Maron, J. Nissen et al., "The influence of a novel edge enhancement software on image quality of DR hand images of patients with rheumatoid arthritis," *Radiography (Lond)*, vol. 27, no. 3, pp. 877–882, 2021.
- [13] H. U. Scherer, T. Haupl, and G. R. Burmester, "The etiology of rheumatoid arthritis," *Journal of Autoimmunity*, vol. 110, article 102400, 2020.
- [14] L. A. Ridgley, A. E. Anderson, and A. G. Pratt, "What are the dominant cytokines in early rheumatoid arthritis?," *Current Opinion in Rheumatology*, vol. 30, no. 2, pp. 207–214, 2018.
- [15] W. Z. Dong, J. Liu, L. Xin, Y. Y. Fang, and J. T. Wen, "Effect of Tripterygium glycosides tablets on immune-induced liver and kidney function in patients with rheumatoid arthritis based on data mining," *Zhongguo Zhong Yao Za Zhi*, vol. 44, pp. 3526–3532, 2019.
- [16] J. Liu, H. Li, and X. Chen, "Effects of traditional Chinese medicine for invigorating spleen to resolve dampness and dredging collaterals on patients with rheumatoid arthritis and anemia," *Zhong Xi Yi Jie He Xue Bao*, vol. 4, no. 4, pp. 348–354, 2006.
- [17] R. F. van Vollenhoven, E. C. Keystone, V. Strand et al., "Efficacy and safety of tregalizumab in patients with rheumatoid arthritis and an inadequate response to methotrexate: results of a phase IIb, randomised, placebo-controlled trial," *Annals of the Rheumatic Diseases*, vol. 77, no. 4, pp. 495–499, 2018.
- [18] J. S. Smolen, A. Szumski, A. S. Koenig, T. V. Jones, and L. Marshall, "Predictors of remission with etanercept-methotrexate induction therapy and loss of remission with etanercept maintenance, reduction, or withdrawal in moderately active rheumatoid arthritis: results of the preserve trial," *Arthritis Research & Therapy*, vol. 20, no. 1, p. 8, 2018.
- [19] H. Wijesinghe, P. Galappathy, R. de Silva et al., "Leflunomide is equally efficacious and safe compared to low dose rituximab in refractory rheumatoid arthritis given in combination with methotrexate: results from a randomized double blind controlled clinical trial," *BMC Musculoskeletal Disorders*, vol. 18, no. 1, p. 310, 2017.
- [20] A. Bilger, J. Plowshay, S. Ma et al., "Leflunomide/teriflunomide inhibit Epstein-Barr virus (EBV)-induced lymphoproliferative disease and lytic viral replication," *Oncotarget*, vol. 8, pp. 44266–44280, 2017.
- [21] M. Schultz, S. O. Keeling, S. J. Katz, W. P. Maksymowych, D. T. Eurich, and J. J. Hall, "Clinical effectiveness and safety of leflunomide in inflammatory arthritis: a report from the RAPPORT database with supporting patient survey," *Clinical Rheumatology*, vol. 36, no. 7, pp. 1471–1478, 2017.
- [22] C. Qu, Y. Lu, and W. Liu, "Severe bone marrow suppression accompanying pulmonary infection and hemorrhage of the digestive tract associated with leflunomide and low-dose methotrexate combination therapy," *Journal of Pharmacology and Pharmacotherapeutics*, vol. 8, no. 1, pp. 35–37, 2017.
- [23] J. Lu, W. Wu, M. Zhang, P. Wang, M. Niu, and X. Yang, "Wells syndrome successfully treated with Tripterygium glycosides," *Clinical, Cosmetic and Investigational Dermatology*, vol. 14, pp. 1029–1031, 2021.
- [24] L. J. Ho, W. L. Chang, A. Chen, P. Chao, and J. H. Lai, "Differential immunomodulatory effects by Tripterygium wilfordii Hook f-derived refined extract PG27 and its purified component PG490 (triptolide) in human peripheral blood T cells: potential therapeutics for arthritis and possible mechanisms explaining in part Chinese herbal theory "Junn-Chenn-Zuou-SS"," *Journal of Translational Medicine*, vol. 11, p. 294, 2013.
- [25] G. Z. Zhu, X. C. Han, H. Z. Wang, Y. Z. Yang, Y. Gao, and H. L. Wang, "Effect of Tripterygium glycosides tablets in treating rheumatoid arthritis: a systematic review and meta-analysis," *Zhongguo Zhong Yao Za Zhi*, vol. 44, pp. 3358–3364, 2019.

Research Article

Therapeutic Effect of Ultrasound-Guided Peripherally Inserted Central Catheter Combined with Predictive Nursing in Patients with Large-Area Severe Burns

Baiyan He,¹ Aiqiong Zhang,² and Shuting He ¹

¹Department of Burn and Plastic Surgery, Central Hospital of the First People's Hospital, Chenzhou, 423000 Hunan, China

²Intervention Room, South Hospital of the First People's Hospital, Chenzhou, 423000 Hunan, China

Correspondence should be addressed to Shuting He; 1514410525@st.usst.edu.cn

Received 4 June 2022; Revised 7 July 2022; Accepted 16 July 2022; Published 31 July 2022

Academic Editor: Pan Zheng

Copyright © 2022 Baiyan He et al. This is an open access article distributed under the Creative Commons Attribution License, which permits unrestricted use, distribution, and reproduction in any medium, provided the original work is properly cited.

This study was aimed to explore the application value of ultrasound-guided peripherally inserted central catheter (PICC) combined with predictive nursing in the treatment of large-area severe burns. 88 patients with large-area severe burns who visited hospital were chosen as the research objects. They were randomly divided into the observation group and the control group, with 44 cases in each. The patients in the observation group were treated with ultrasound-guided PICC combined with predictive nursing, while those in the control group were treated with traditional PICC and nursing methods. Then, the anxiety of patients was compared between groups by the Self-rating Anxiety Scale (SAS), while the depression was compared by the Self-rating Depression Scale (SDS). The pain of the patients was analyzed by the McGill Pain Questionnaire (MPQ), and a self-made nursing satisfaction questionnaire was adopted to evaluate the nursing satisfaction. The surgery-related indicators of the patients were detected and recorded (the success rate of one-time puncture, the success rate of one-time catheter placement, incidence of complications, heart rate, blood pressure, etc.). The success rates of one-time puncture (93% vs. 86%) and of catheter placement (95% vs. 81%) in the observation group were significantly higher than those in the control group, $P < 0.05$. The pain scores of the observation group were much lower than those of the control group at each time period, $P < 0.05$. The number of patients with negative emotions such as anxiety and depression in the observation group was markedly less than that in the control group. The incidence of complications in the observation group was notably lower than that in the control group (4.5% vs 18%), $P < 0.05$. The nursing satisfaction of the observation group was significantly higher than that of the control group (93% vs 79.5%), $P < 0.05$. In conclusion, ultrasound-guided PICC and predictive nursing had high clinical application values in the treatment of patients with large-area severe burns.

1. Introduction

Burns bring patients a huge impact on health, life, work, and study. It will weaken the social labor force and increase the economic burden on the family and society. Statistics show that the incidence of burns in China is much higher than that in oversea countries [1]. Generally, burns are classified into four grades: first-degree burns, superficial second-degree burns, deep second-degree burns, and third-degree burns. The specific clinical manifestations of each grade are as follows. For the first-degree burns, the mild burns are generally characterized by mild redness, swelling, and heat

pain, with no blisters and no skin damage. It can usually recover to normal within a week without any scarring, but the color of local skin may be darker in a short term. For superficial second-degree burns, blisters of different sizes are formed, and the blister fluid is clear and transparent, which is pale yellow or egg white-like fluid. The ruptured blisters expose a rosy and moist wound [2]. Patients may experience significant pain and local redness and swelling. The wound usually heals in 1-2 weeks without scarring, but sometimes the newly grown skin may have pigment changes. For deep second-degree burns, there is local swelling, and the epithelial tissue turns to be white or brownish-

yellow. There are also scattered small blisters; the wound of the ruptured blisters is slightly wet with the color of red and white or red in white. Many red dots or small vascular branches can be observed, the cutaneous sensation is insensitive, and the pain is not obvious. If there is no infection, the healing generally takes about 3-4 weeks. In the event of infection, not only the healing time will be prolonged but also scars will be left after healing. For the third-degree burns, the wound surface is dry and is in waxy white, brown, or charcoal black, with no blisters and no pain. It is tough and leather-like, and thick vascular network coagulates under the eschar, which is caused by venous embolism in the fat layer. In summary, the second- and third-degree burns pose a serious threat to the life and health of patients. In addition, the prognosis of patients is generally very poor, and the treatment time is relatively long. Therefore, the treatment and nursing for burns take a long-term and difficult process [3].

Since burns can cause extensive damage to the protective barrier of the skin, further loss of body fluids can occur. Clinically, long-term fluid supplementation, anti-infection, and postoperative repair are often required for patients. This process typically takes months or even years. Intravenous infusion is commonly used for fluid supplementation in clinical practice. However, the scarred skin formed in burn patients often makes it difficult to find veins, which increases the difficulty of venipuncture. The general puncture requires alternation repeatedly [4]. These can cause great suffering to patients and increase the difficulty of clinical nursing. Therefore, finding a method that can relieve the pain of patients and enable long-term infusion administration is a hot topic of current clinical research [5]. For peripherally inserted central catheter (PICC), the tip of the catheter is located in the superior vena cava, which can quickly dilute the drug. Thus, it can avoid problems such as phlebitis and drug leakage caused by tissue necrosis [6, 7]. In addition, PICC also has the advantages of long indwelling time as well as no risk of pneumothorax and arterial injury [8, 9]. With the development of imaging technologies such as ultrasound, the improved Seldinger PICC placement technique under ultrasound guidance has been gradually derived [10]. A large number of clinical studies have shown that the success rate of traditional PICC placement is only 78%, the success rate of PICC placement using optimized Seldinger technique alone is 84%, and that of optimized ultrasound-guided Seldinger PICC placement reaches 98%. In general, ultrasound-guided optimized Seldinger technique for PICC placement has the wide and good clinical applications. However, there is no direct report worldwide about its application in patients with large-area severe burns [11]. Therefore, further in-depth research is needed on its application effect in patients with large-area severe burns.

There are also some defects and deficiencies in the optimized Seldinger PICC placement technique guided by ultrasound. For example, venipuncture and blade dilation are required during catheter placement, which can cause local tissue damage and pain in patients [12]. Pain caused by ultrasound-guided optimized Seldinger PICC placement can lead to a series of physiological and pathological

changes, and these changes are important factors causing postoperative complications. Therefore, it is necessary and urgent to take appropriate nursing intervention methods to improve the quality of life and prognosis of severely burned patients. Predictive nursing is a method that is widely used worldwide and has been recognized and confirmed by many scholars [13]. Predictive nursing, conducted by some foreign scholars, has reduced the incidence of coronary heart disease by 50%. For patients with advanced head and neck tumors, some scholars have adopted predictive enteral nutrition support nursing, and found that this nursing measure can make the patients with neck tumors nourished. Researches by domestic scholars show that predictive nursing can improve the comfort, satisfaction, and compliance of clinical treatment. There are many similar studies [14]. From the above, predictive nursing has achieved good outcomes in clinical work and has been widely promoted. It can effectively relieve the negative moods of patients and reduce the incidence of complications. However, all the existing related researches in the world directly reported the application of predictive nursing in the PICC of burn patients under the ultrasound-guided modified Seldinger technique. As for the application effect of the modified Seldinger technique in the PICC of burn patients under the guidance of ultrasound, further research is needed [15].

The patients with large-area severe burns were pre-selected as the research objects in this research, so as to explore the application value of ultrasound-guided PICC placement combined with predictive nursing in the treatment. It was expected to provide reference and basis for the clinical treatment of related diseases as well as the application of related technologies.

2. Research Methods

2.1. Objects. In this study, 100 patients with severe burn admitted to the hospital from July 2020 to January 2022 were selected and randomly divided into control group and observation group, with 50 cases in each. The ultrasound-guided PICC combined with predictive nursing was given in the observation group, while the control group received traditional PICC combined with nursing. Inclusion criteria required the patients had an age of 18-66 years old, no skin damage to the auricle, no history of alcohol allergy, and PICC placement for the first time. Besides, the patients were suitable for the indications of PICC; they had no mental illness and could correctly express pain. No systemic or local pain relief measure was taken for 24 hours before PICC placement. Exclusion criteria were as follows. The patients received deep venous catheter placement (intravenous access port, subclavian or internal jugular, and femoral venous catheter placement). The diameter of the basilic vein, brachial vein, and median cubital vein under B-mode ultrasound was $<5\text{ mm}^2$. The patients suffered from upper extremity hemiplegia, had a history of surgery, or had an unsuccessful one-time venipuncture. They received radiotherapy, chemotherapy, drugs, surgery, or other treatments that could relieve pain during the research. The informed

consent forms were obtained from patients, and this study had been approved by ethics committee of hospital.

2.2. PICC Puncture Methods. In the control group, ordinary deep vein puncture was adopted for PICC placement. A disposable puncture catheter was used, the patient was in a supine position, the arm to be catheterized was abducted by 90°, and the vein below the elbow was selected for puncture. After the blood vessel is selected, sterilization and draping were carried out. Puncture was performed with a puncture needle, the needle core was withdrawn after the venous return was observed, and the catheter was sent into along the outer cannula of the puncture needle until to the predetermined length. Then, the guide wire was withdrawn, the catheter was connected to the installer, and the sterile saline gauze was used to clean the skin around the puncture point. The puncture point was covered with sterile gauze and fixed with transparent application. After the catheter was fixed, it was positioned under X-ray.

In the observation group, the patients underwent PICC placement using the ultrasound-guided technique. The body position and disinfection method were the same as those in the control group. The vein below the elbow was selected for puncture. The approximate position of the vein was displayed on the transverse section under color Doppler ultrasonic apparatus. Then, the longitudinal section was scanned to observe the blood flow, wall thickness, and blood vessel diameter of the vein. It was turned to the transverse section, the midpoint of the probe was located at the same point as the transverse section of the vein, and this point was marked, which was just the position on the body surface of the vein. This point was as the starting point, and a point was located after detection every 1 cm. A total of 3 points were located, and the 3 points were kept on the same straight line. After routine disinfection and draping, the lowest located point was the needle insertion point of puncture. The probe was at right angles to the vein as well as to the skin. Under the guidance of ultrasound, the puncture needle and the vein were advanced in parallel. After good blood return was obtained, the position of the needle core was kept unchanged, and the guide wire was put into for 10 cm. After, the puncture angle was reduced, and it was continued to insert the guide wire. The needle core was then withdrawn, the catheter sheath was advanced, and the catheter was placed well.

2.3. Nursing Intervention. The patients in the control group received routine nursing. The nursing mainly included admission introduction, medication guidance, routine observation, auxiliary treatment, health education, and other basic nursing care.

The patients in the observation group were given with predictive nursing. A predictive nursing intervention team was established. The team organized team members for nursing knowledge training every week and conducted regular assessments. The specific interventions were as follows. (1) On the basis of fully understanding of the patients' acquisition of knowledge, a systematic knowledge theory system was constructed. Through repeated communications, distribution of brochures, and other methods, the correct

cognition of disease understanding in patients was deepened and strengthened. The patients were also helped to establish correct beliefs and attitudes. (2) During the treatment and nursing period, the Self-rating Anxiety Scale (SAS) and the Self-rating Depression Scale (SDS) were adopted for observing and evaluating whether the negative situation occurred in patients. If the patient had depression, anxiety, etc., it was necessary to give a targeted psychological intervention measure, and the intervention was carried out every 7 days for 25 minutes each time. (3) Patients with severe burns might need to stay in bed for a long time, and some negative emotions could also affect the vagus nerve, resulting in constipation. Nursing intervention team needed to carry out reasonable dietary intervention for patients. (4) For nursing after catheter placement, chitin-type wound dressings should be used for fixation, to promote hemostasis and healing at the puncture point as soon as possible. Relevant information was recorded in detail on the catheter maintenance record sheet, including catheter model, batch number, the position of catheter placement, catheter placement length, and other information. The precautions, possible adverse reactions, daily life precautions, and common sense of self-maintenance after catheter placement were explained in detail to the patients and their families. The importance of regularly maintaining the catheter and keeping the catheter in good condition was also expounded.

2.4. Observation Indicators. *Pain score:* The McGill pain questionnaire (MPQ) was used for estimation. With standards of the pain rating index (PRI) score (0-3 points), 0 point stood for no pain, 1 point for mild pain, 2 points for moderate pain, and 3 points for severe pain. Under the Present Pain Intensity (PPI) scoring (0-5 points), no pain, mild pain, pain causing discomfort, moderate pain, severe pain, and unbearable pain were indicated by 0, 1, 2, 3, 4, and 5 points, respectively. The observation and comparison were at six time points, including local anesthesia, venipuncture, withdrawal of puncture needle, blade expansion, vascular sheath insertion, and vascular sheath withdrawal.

Anxiety situation: The SAS was adopted for the evaluation of patients' anxiety, with a score of 0 to 100. The SAS standard score <50 indicated no anxiety, 50-59 indicated mild anxiety, 60-69 meant moderate anxiety, and 70 and above represented severe anxiety. The comparison was made before nursing and 15 days after nursing intervention, respectively.

Depression: As SDS was used for evaluation, SDS standard score <53 meant no depression. 53-62, 63-72, and ≥73 were denoted as mild depression, moderate depression, and severe depression, respectively. It was compared before nursing as well as 15 days after nursing intervention.

Surgery-related indicators: The success rate of one-time puncture, the success rate of one-time catheter placement, the incidence of complications, and the basic physiological indicators such as heart rate (measured by the doctors using a stethoscope) and blood pressure (measured with a sphygmomanometer) of the patients in the two groups were recorded. These were compared 15 days after nursing intervention.

TABLE 1: General information of patients in the two groups.

Items	Observation group ($n=50$ cases)	Control group ($n=50$ cases)	X^2/t value	P
Gender			0.388	0.614
Male	28	30		
Female	22	20		
Age (years old)			0.120	0.133
	44.2 ± 9.8	55.3 ± 11.3		
Nationality			2.131	1.810
Han Chinese	36	38		
Minorities	14	12		
Education level			0.335	0.198
Primary school and below	8	9		
Junior high school	13	11		
High school or technical secondary school	20	21		
College and above	9	9		
Marital status			0.512	0.837
Married	23	25		
Single	17	16		
Divorced	5	4		
Widowed	5	5		
Monthly income per capita (yuan)			0.383	0.193
<1,000	11	10		
1,000-3,000	18	16		
3,001-5,000	16	17		
>5,000	5	7		
Payment method			0.449	0.527
Urban medical insurance	20	21		
Rural cooperative medical care	22	18		
Commercial insurance	5	6		
Self-paying	3	5		

Bacterial culture: The condition of bacterial infection was compared between the two groups during the nursing intervention period.

2.5. Statistical Methods. The observed data were filled in the observation table, and the values were entered into the SPSS11.0 software for statistical analysis. The data were statistically described by the mean ± standard deviation, and the measurement data were analyzed by t test. The scores before and after nursing intervention were compared using paired-sample T test within the same group, while the scores were compared using the independent-sample T test between the groups. $P < 0.05$ meant a difference was statistically significant.

3. Results

3.1. General Information. The general data of the two groups of patients are listed in Table 1. The observation group included 28 male patients and 22 female patients, with an average age of 44.2 ± 9.8 years old. In the control group, 30 male patients and 20 female patients were included, having an average age of 55.3 ± 11.3 years old. There was no sta-

tistical difference in these general data between two groups, $P < 0.05$.

3.2. Comparison of the Success Rates of Puncture and Catheter Placement. The success rates of puncture and catheter placement were compared between the two groups as shown in Figure 1. The number of successful one-time puncture was 48 (96%) and 41 (82%), respectively, in the two groups. The success rate of one-time catheter placement was 47 (94%) and 39 (78%), respectively. The success rates of both one-time puncture and one-time catheter placement were markedly higher in the observation group than those in the control group, $P < 0.05$.

3.3. Comparison of Pain Scores. The comparison results of the MPQ pain scores in the two groups are displayed in Figure 2. The MPQ scores of the two groups of patients were 36.3 ± 9.88 and 35.5 ± 11.3 , respectively, before nursing intervention, with no significant difference, $P > 0.05$. The MPQ scores after nursing intervention turned to be 18.6 ± 7.11 and 28.9 ± 6.3 , respectively. After intervention, the MPQ score of the observation group was greatly lower than that of the control group, $P < 0.05$.

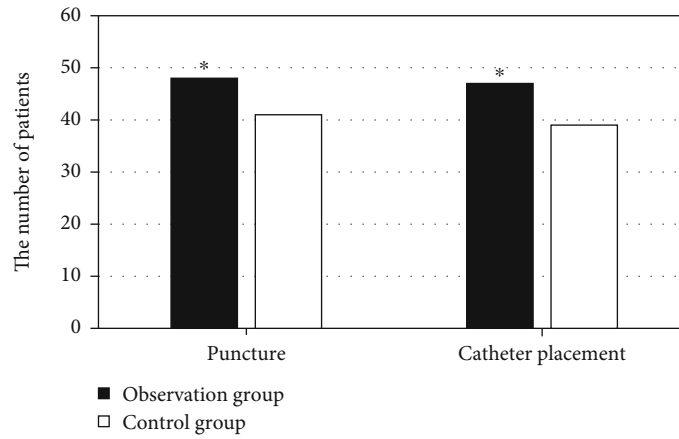


FIGURE 1: Comparison of the success rates of puncture and catheter placement in two groups. *Compared with control group, $P < 0.05$.

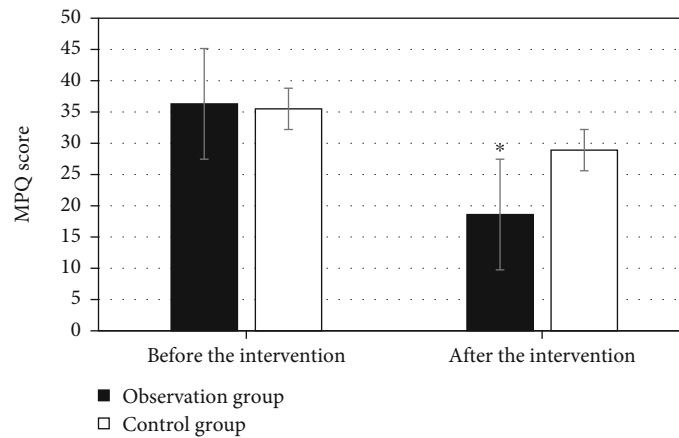


FIGURE 2: Comparison of MPQ pain scores of patients between the two groups. *Compared with control group, $P < 0.05$.

3.4. Comparison of Anxiety and Depression. The anxiety condition of the two groups of patients is presented in Figure 3. Before intervention, the number of patients without anxiety, mild anxiety, moderate anxiety, and severe anxiety were counted as 6, 24, 18, and 2, respectively, in the observation group. Those were 7, 23, 19, and 1, respectively, in the control group. The SAS scores of the two groups were 55.3 ± 11.3 and 56.1 ± 9.6 , respectively, having no statistical difference in anxiety between the two groups, $P > 0.05$. After nursing intervention, there were 18, 30, 2, and 0 patients with no anxiety, mild anxiety, moderate anxiety, and severe anxiety, respectively, in the observation group, while 13, 16, 19, and 2 patients in control group, respectively. The SAS scores of the two groups became 40.3 ± 8.7 and 55.1 ± 10.2 , respectively. The anxiety of patients in the observation group was pretty milder than that of the control group, $P < 0.05$.

The comparative results of depression of patients in the two groups are displayed in Figure 4. The number of patients with no, mild, moderate, and severe depression was counted to be 11, 30, 5, and 4, respectively, before intervention in the observation group. 13, 28, 6, and 3 patients got no, mild, moderate, and severe depression, respectively, in the control group. The SDS scores of the two groups were 60.2 ± 9.9 and

62.2 ± 10.2 , respectively, before intervention, without a statistical difference in anxiety between the two groups as $P > 0.05$. After nursing intervention, 25, 20, 4, and 1 patient in the observation group and 8, 10, 30, and 2 patients in the control group had no depression, mild depression, moderate depression, and severe depression, respectively. The SDS score was 48.8 ± 9.9 in the observation group while 60.2 ± 11.2 in the control group. The depression status of patients in the observation group was remarkably milder than that in the control group, $P < 0.05$.

3.5. Comparison of Physiological Indicators. The physiological indicators of patients in the two groups are compared in Figure 5. The systolic blood pressure before nursing intervention was 115 ± 11.3 mmHg in the observation group and 116 ± 10.2 mmHg in the control group, showing no significant difference between the groups. After intervention, the systolic blood pressure turned to be 110 ± 8.8 mmHg and 125 ± 9.3 mmHg, respectively, in the observation and control groups. The diastolic blood pressure before intervention was 68.8 ± 5.2 mmHg and 69.3 ± 6.7 mmHg, respectively; not a significant difference was found between the groups. The diastolic blood pressure after intervention was 69.3 ± 10.2 mmHg and 73.8 ± 11.4 mmHg in the observation and

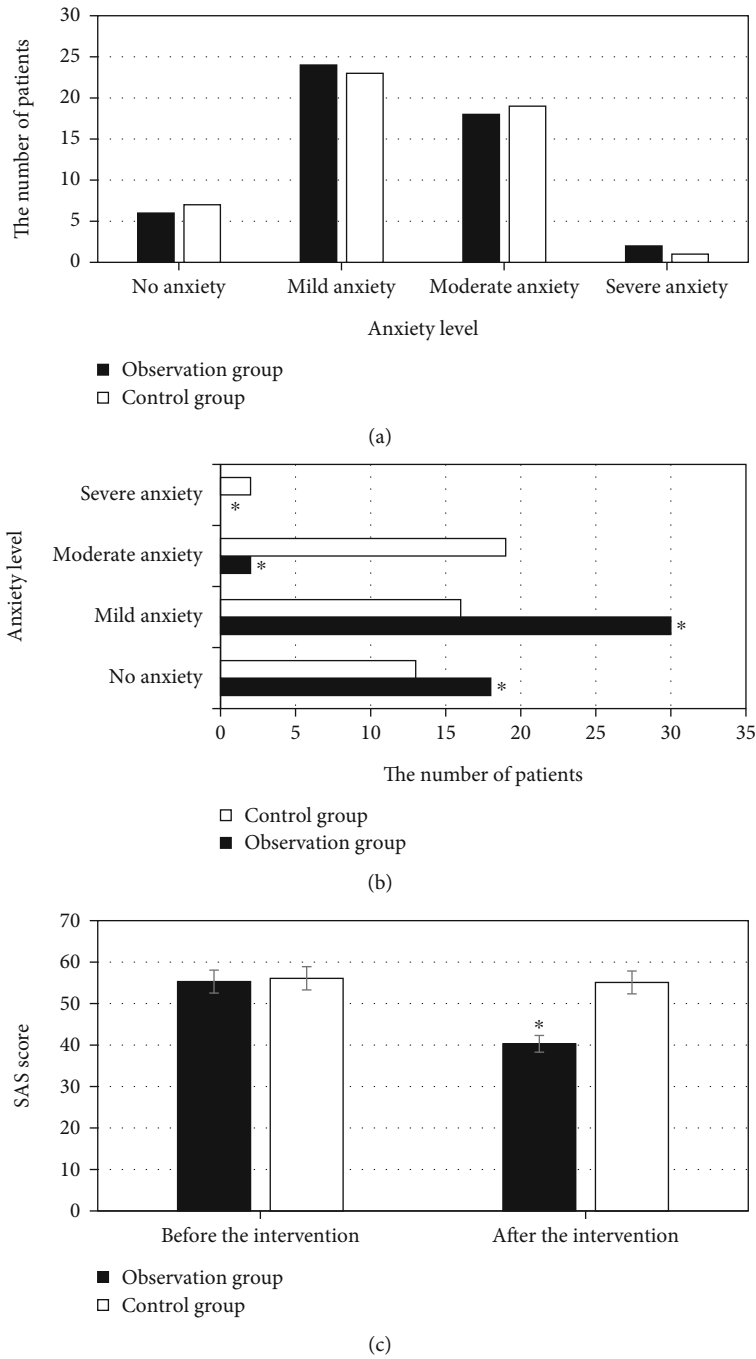


FIGURE 3: Comparison results of anxiety of patients between two groups. (a), (b), and (c) represented before intervention, after intervention, and SAS score, respectively. * Compared with control group, $P < 0.05$.

control groups, respectively; a significant difference was shown between groups, $P < 0.05$. The heart rates were 70.3 ± 4.4 beats/min and 70.8 ± 5.2 beats/min before intervention in the two groups, suggesting no significant difference between groups. The heart rates after intervention were 70.8 ± 3.8 beats/min and 79.3 ± 3.7 beats/min, respectively, in the observation and the control groups, with a significant difference between groups for $P < 0.05$.

3.6. *Comparison of Complications.* The incidence of complications in the two groups is shown in Figure 6. There were 0,

1, 1, and 0 patients with local hematoma, local infection, thrombosis, and phlebitis, respectively, in the observation group. The incidence of complications was counted to be 4.5% in the observation group. 2, 3, 2, and 1 patient got the complications, respectively, in the control group; there-out, the incidence of complications was 18%.

3.7. *Comparison of Nursing Satisfaction.* The comparative results of nursing satisfaction in the two groups are presented in Figure 7. There were 36, 11, and 3 patients satisfied, basically satisfied, and dissatisfied, respectively, in the

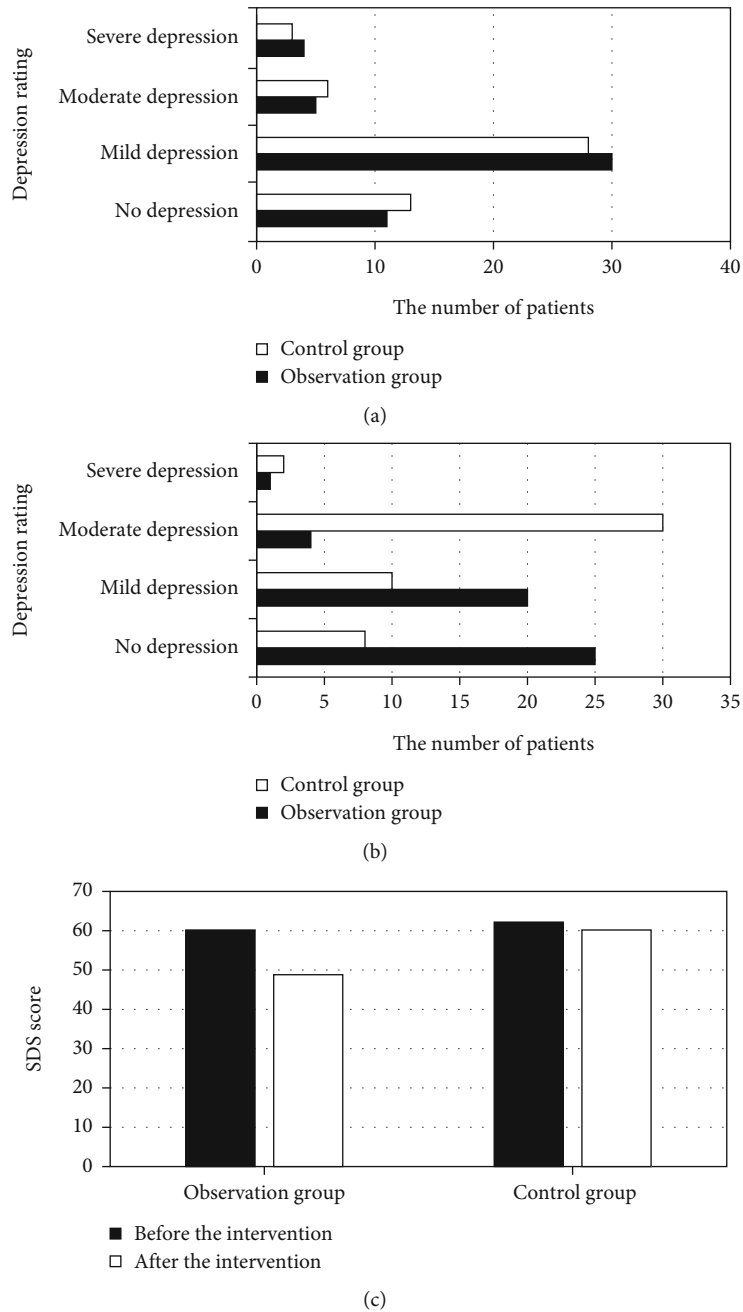


FIGURE 4: Comparison results of depression status of patients in two groups. (a) Before intervention. (b) After intervention. (c) SDS score. * Compared with control group, $P < 0.05$.

observation group. The satisfied rate reached 94%. In the control group, 24, 17, and 9 patients were satisfied, basically satisfied, and dissatisfied, respectively, with the satisfied rate of 82%. The satisfaction of the observation group was observably higher than that of the control group, $P < 0.05$.

3.8. Comparison of the Incidence of Bacterial Infection. The incidence of bacterial infection was compared between the two groups. 3 (6%) patients got bacterial infection in the observation group, while bacterial infection occurred in 9 (18%) patients in the control group. The number of patients

with bacterial infection in the observation group was considerably less than that in the control group, $P < 0.05$.

4. Discussion

Not only affect burns life and health but even destroy the patients' life, work, and study. Burns will weaken the social labor force and also lay an increased economic burden on the family and the society [16, 17]. The protective barrier of large areas of the skin is damaged when a burn occurs, which can lead to a massive loss of body fluids. Thus,

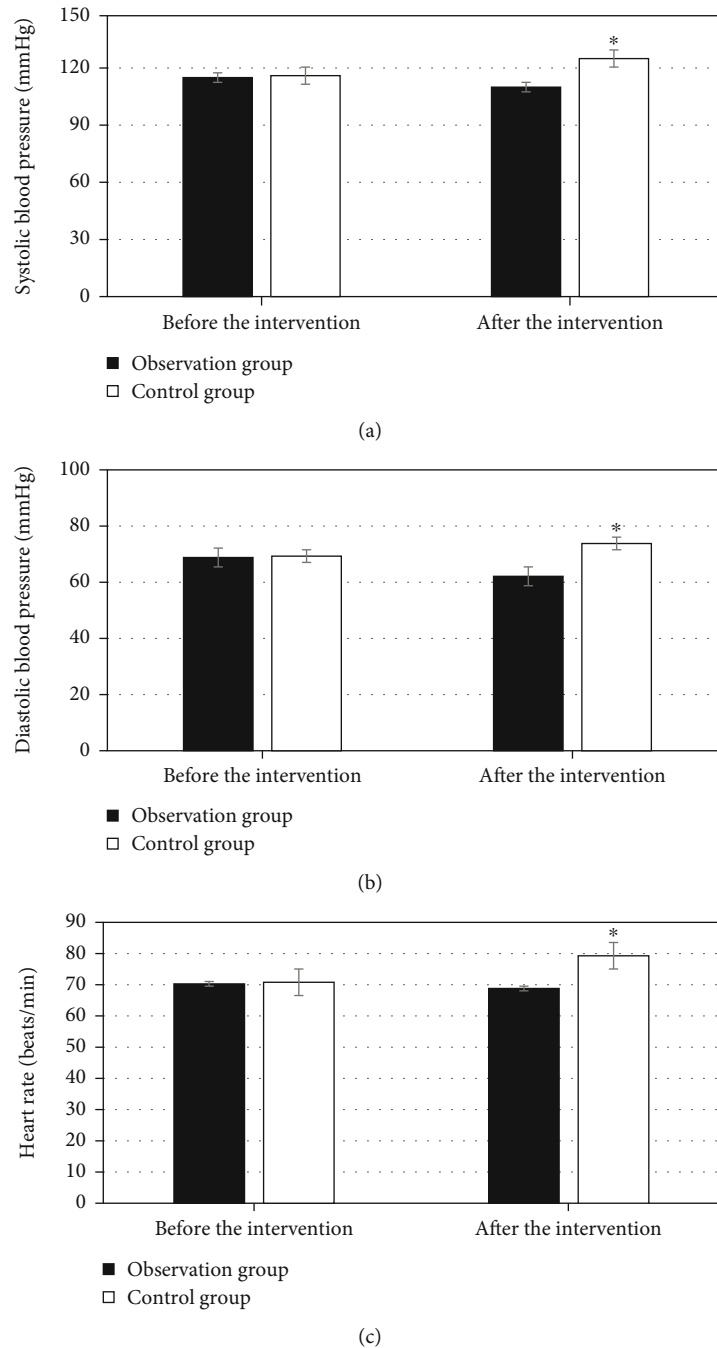


FIGURE 5: Comparison of physiological indicators between two groups. (a), (b), and (c) represented systolic blood pressure, diastolic blood pressure, and heart rate, respectively. *Compared with control group, $P < 0.05$.

long-term fluid supplementation, anti-infection, and postoperative repair are often required for patients in clinical practice. Typically, this course takes months or even years. These procedures are generally completed by intravenous infusion. However, burn patients generally have scarred skin, which makes the veins difficult to find, greatly increasing the difficulty of venipuncture. In addition, conventional puncture or central venous catheter requires repeated alternation and replacement in a short time period [18]. These problems and shortcomings often bring pain to patients and increase the difficulty of clinical nursing. On the basis of the treat-

ment characteristics of burns, it is indispensable and urgent to find a method that can relieve the pain of patients, avoid local skin infection, and achieve good long-term infusion administration as well [19].

PICC refers to the technique of inserting a central venous catheter through peripheral vein puncture, so that the tip of the catheter reaches the superior vena cava or subclavian vein [20–22]. As the tip of PICC is in the superior vena cava, the drugs can be quickly diluted, thus avoiding tissue necrosis caused by phlebitis and drug leakage [23, 24]. Moreover, PICC placement is generally operated

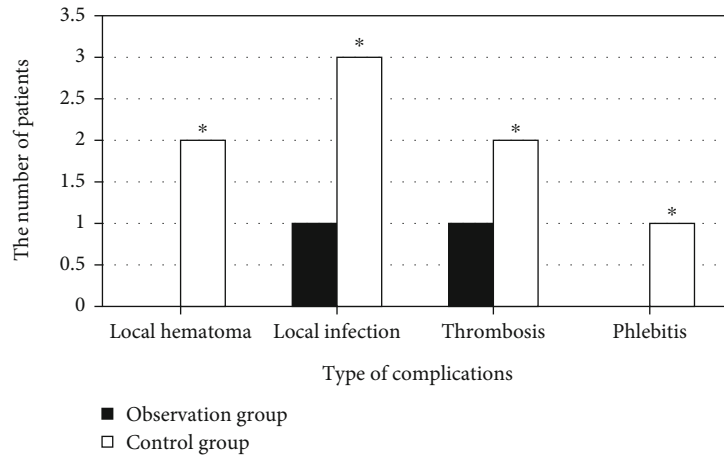


FIGURE 6: Comparison of the incidence of complications in two groups. * Compared with control group, $P < 0.05$.

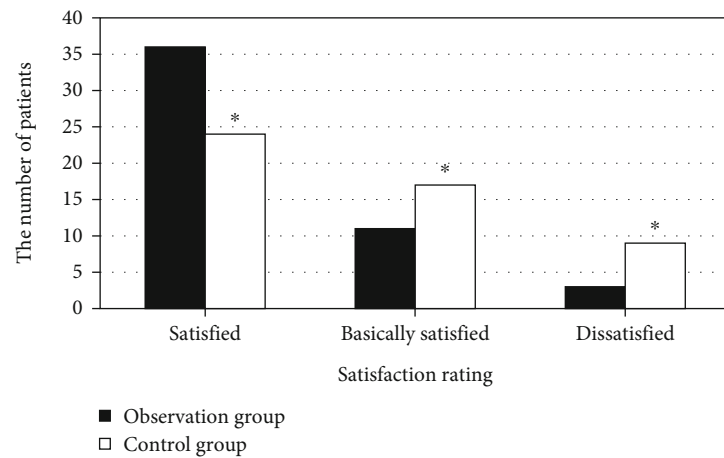


FIGURE 7: Comparison of nursing satisfaction of patients in two groups.

independently by a professional nurse, having the advantages of long indwelling time and no risk of pneumothorax as well as arterial injury. With the development of imaging technologies including ultrasound, the optimized Seldinger PICC placement technique has been derived gradually under ultrasound guidance [25]. In a large number of clinical studies, the success rate of traditional PICC placement is only 78%, that rises to 84% as modified Seldinger technique was used, and reaches 98% using optimized ultrasound-guided Seldinger PICC placement [26, 27]. The ultrasound-guided optimized Seldinger technique has a wide range of great clinical applications for PICC placement. Thereout, PICC placement has a high application value in burn treatment. Therefore, in this work, patients with severe burns were selected as the research objects, and were randomly divided into the observation group and the control group. In the observation group, ultrasound-guided PICC technology was utilized for catheter placement, while traditional PICC was adopted in the control group. The success rate of one-time puncture (93% vs. 86%) and the success rate of one-time catheter placement (95% vs. 81%) in the observation group were notably higher than those in the control group, $P < 0.05$. It suggested that the application value of ultrasound-guided

PICC technology was much higher than that of traditional catheter placement technology in the treatment of severe burns. This was consistent with the findings of previous related studies.

In spite of many advantages of the ultrasound-guided optimized Seldinger technique for PICC placement, it also has some flaws and deficiencies. Venipuncture, blade dilation, etc. are needed during catheter placement, and these PICC operations can cause local tissue damage as well as pain to the patients [28]. With the continuous development of pain specialty, pain has become the fifth vital sign after the four vital signs of breathing, pulse, blood pressure, and body temperature [29]. Pain caused by PICC placement can bring about a series of physiological and pathological changes, which are important factors for postoperative complications. Therefore, taking appropriate nursing intervention methods is necessary and urgent for severely burned patients, to promote their quality of life and prognosis. Predictive nursing is widely applied and has been recognized by numerous scholars across the world [30]. In this work, patients with large-area severe burns were included as the research objects. The patients were randomly divided into the observation group and the control group. The observation group

received ultrasound-guided PICC technology combined with predictive nursing, while traditional PICC combined with traditional nursing was adopted in the control group. The MPQ scores of the observation group were significantly lower than those of the control group at each time period, $P < 0.05$. The patients in the observation group had significantly fewer negative emotions such as anxiety and depression than the control group. The incidence of complications in the observation group was significantly lower than that in the control group (4.5% vs 18%), $P < 0.05$. The nursing satisfaction in the observation group was greatly higher than that of the control group (93% vs 79.5%), $P < 0.05$. In summary, ultrasound-guided PICC and predictive nursing had high clinical application value in the treatment of patients with large-area severe burns. This was consistent with the predictions.

5. Conclusion

The patients with severe burns were selected as the research objects and were randomly divided into the observation and the control groups. In the observation group, patients received ultrasound-guided PICC with predictive nursing, while traditional PICC and traditional nursing were given to the control group. The ultrasound-guided PICC and predictive nursing showed high clinical application values in treating large-area severe burns; thus, this work provided a reference and basis for the clinical treatment. However, due to the limited samples and text space, this work still had certain defects. In the future, the samples would be expanded for further research.

Data Availability

The data used to support the findings of this study are available from the corresponding author upon request.

Conflicts of Interest

The authors declare no conflicts of interest.

Acknowledgments

This work was supported by Chenzhou First People's Hospital in Hunan (N2021-20).

References

- [1] B. Galen, S. Baron, S. Young, A. Hall, L. Berger-Spivack, and W. Southern, "Reducing peripherally inserted central catheters and midline catheters by training nurses in ultrasound-guided peripheral intravenous catheter placement," *BMJ Quality and Safety*, vol. 29, no. 3, pp. 245–249, 2020.
- [2] F. Grasso, A. Capasso, D. Pacella et al., "Ultrasound guided catheter tip location in neonates: a prospective cohort study," *The Journal of Pediatrics*, vol. 244, pp. 86–91.e2, 2022.
- [3] W. Xiao, Q. Lin, S. Chen et al., "Catheterization of PICC through a superficial femoral vein for patients with superior vena cava syndrome using ECG positioning and ultrasound-guided technologies," *The Journal of Vascular Access*, vol. 27, 2021.
- [4] K. Choi, M. A. Keum, M. S. Kim et al., "Feasibility of the ultrasound-guided insertion of the peripherally inserted central catheter (PICC) by the vascular surgeon at the bedside in the trauma intensive care unit," *Annals of Vascular Surgery*, vol. 80, pp. 143–151, 2022.
- [5] R. Sabouneh, P. Akiki, A. Al Bizri, S. El Helou, S. Zeidan, and H. D. Al, "Ultrasound guided central line insertion in neonates: pain score results from a prospective study," *Journal of Neonatal-Perinatal Medicine*, vol. 13, no. 1, pp. 129–134, 2020.
- [6] J. V. Suell, M. Meshkati, C. Juliano, and A. Groves, "Real-time point-of-care ultrasound-guided correction of PICC line placement by external manipulation of the upper extremity," *Archives of Disease in Childhood - Fetal and Neonatal Edition*, vol. 105, no. 1, p. 25, 2020.
- [7] R. Jørgensen, C. B. Laursen, L. Konge, and P. I. Pietersen, "Education in the placement of ultrasound-guided peripheral venous catheters: a systematic review," *Scandinavian Journal of Trauma, Resuscitation and Emergency Medicine*, vol. 29, no. 1, p. 83, 2021.
- [8] Y. O. Kim, C. R. Chung, E. Gil, C. M. Park, G. Y. Suh, and J. A. Ryu, "Safety and feasibility of ultrasound-guided placement of peripherally inserted central catheter performed by neurointensivist in neurosurgery intensive care unit," *PLoS One*, vol. 14, no. 5, article e0217641, 2019.
- [9] C. M. Fung, D. R. Stayer, J. J. Terrasi et al., "Extended dwell and standard ultrasound guided peripheral intravenous catheters: Comparison of durability and reliability," *The American Journal of Emergency Medicine*, vol. 47, pp. 267–273, 2021.
- [10] S. Park, S. Moon, H. Pai, and B. Kim, "Appropriate duration of peripherally inserted central catheter maintenance to prevent central line-associated bloodstream infection," *PLoS One*, vol. 15, no. 6, article e0234966, 2020.
- [11] S. H. Ji, S. J. Yoo, S. A. Cho et al., "Ultrasound-guided insertion of peripherally inserted central catheter after anesthetic induction in children undergoing surgery for moyamoya disease - thirty cases report," *Anesthesia and Pain Medicine*, vol. 16, no. 3, pp. 273–278, 2021.
- [12] P. E. J. Fridolfsson, "Ultrasound-guided peripherally inserted central catheter placement in extremely low birth weight neonates," *Neonatal Network*, vol. 41, no. 1, pp. 21–37, 2022.
- [13] N. Moureau and E. G. Gregory, "Survey of ultrasound-guided peripheral intravenous practices: a report of supply usage and variability between clinical roles and departments," *British Journal of Nursing*, vol. 29, no. 19, pp. S30–S38, 2020.
- [14] A. Greca, E. Iacobone, D. Elisei et al., "ECHOTIP: a structured protocol for ultrasound-based tip navigation and tip location during placement of central venous access devices in adult patients," *The Journal of Vascular Access*, vol. 8, 2021.
- [15] G. Zito Marinosci, D. G. Biasucci, G. Barone et al., "ECHO-TIP-Ped: a structured protocol for ultrasound-based tip navigation and tip location during placement of central venous access devices in pediatric patients," *The Journal of Vascular Access*, vol. 13, 2021.
- [16] S. Cho, "Peripherally inserted central catheter procedure at the bedside by a nephrologist is safe and successful," *Kidney Research and Clinical Practice*, vol. 40, no. 1, pp. 153–161, 2021.
- [17] F. X. Li, Y. F. Hao, M. J. Tian, Y. P. Li, and H. Y. Zhang, "A comparison of lower limb peripherally inserted central catheter and deep venous catheterisation," *Journal of the College of Physicians and Surgeons Pakistan*, vol. 31, no. 12, pp. 1478–1481, 2021.

- [18] A. E. Amick, S. E. Feinsmith, J. Sell et al., "Ultrasound-guided peripheral intravenous catheter insertion training reduces use of midline catheters in hospitalized patients with difficult intravenous access," *Journal of Patient Safety*, vol. 18, no. 3, pp. e697–e703, 2022.
- [19] V. Chasseigne, A. Larbi, J. Goupil et al., "PICC management led by technicians: establishment of a cooperation program with radiologists and evaluation of complications," *Diagnostic and Interventional Imaging*, vol. 101, no. 1, pp. 7–14, 2020.
- [20] G. Scoppettuolo, D. G. Biasucci, and M. Pittiruti, "Vascular access in COVID-19 patients: smart decisions for maximal safety," *The Journal of Vascular Access*, vol. 21, no. 4, pp. 408–410, 2020.
- [21] S. Bing, C. Smotherman, R. G. Rodriguez, D. J. Skarupa, J. H. Ra, and M. L. Crandall, "PICC versus midlines: comparison of peripherally inserted central catheters and midline catheters with respect to incidence of thromboembolic and infectious complications," *American Journal of Surgery*, vol. 223, no. 5, pp. 983–987, 2022.
- [22] S. Kwon, S. M. Son, S. H. Lee et al., "Outcomes of bedside peripherally inserted central catheter placement: a retrospective study at a single institution," *Acute and Critical Care*, vol. 35, no. 1, pp. 31–37, 2020.
- [23] M. Ostroff, K. Aberger, and N. Moureau, "Case report: end of life care via a mid-thigh femoral midline catheter," *The Journal of Vascular Access*, vol. 31, 2021.
- [24] J. Zhang, N. Zhao, F. Liu, K. Qian, and R. Jiang, "Application of modified microbubble test in peripherally inserted central venous catheters tip positioning," *Zhonghua Wei Zhong Bing Ji Jiu Yi Xue*, vol. 31, no. 9, pp. 1149–1153, 2019.
- [25] C. Liu, T. Jin, A. Meng, J. Mao, R. Shi, and L. Liu, "An ECG method for positioning the tip of a PICC in "mirror people" with dextrocardia: a case report," *The Journal of Vascular Access*, vol. 12, 2021.
- [26] G. Villa, C. Chelazzi, R. Giua et al., "The Valsalva manoeuvre versus tourniquet for venipuncture," *The Journal of Vascular Access*, vol. 19, no. 5, pp. 436–440, 2018.
- [27] S. C. Rainey, G. Deshpande, H. Boehm et al., "Development of a pediatric PICC team under an existing sedation service: a 5-year experience," *Clinical Medicine Insights: Pediatrics*, vol. 13, 2019.
- [28] M. A. A. Bayoumi, R. van Rens, P. Chandra et al., "Peripherally inserted central catheters versus non-tunnelled ultrasound-guided central venous catheters in newborns: a retrospective observational study," *BMJ Open*, vol. 12, no. 4, article e058866, 2022.
- [29] L. Li, Z. Gao, and L. Guo, "Comfort status and its influencing factors in patients with gastrointestinal cancer after PICC catheterization," *Hu Li Za Zhi*, vol. 67, no. 6, pp. 32–39, 2020.
- [30] C. Jie, P. Chunxue, X. Jiawei, L. Hongmei, and Q. Huohong, "Multidisciplinary cooperative mode led by infusion nurse specialists used to ensure the nursing quality of peripherally inserted central catheters in China: a 5-year retrospective study," *The Journal of Vascular Access*, vol. 21, 2021.

Research Article

Construction and Validation of Prediction Model of Severe Abdominal Pain Post-Transarterial Chemoembolization in Patients with HBV-Associated Primary Liver Cancer

Yaobo Yang,¹ Sipan Chen ,¹ Zhaoyong Yan ,¹ Yang Jiao,¹ Xiang Yan,² and Yulong Li³

¹Department of Interventional Radiology, Shaanxi Provincial People's Hospital, Xi'an, Shaanxi 710068, China

²Department of Hepatobiliary Surgery, Shaanxi Provincial People's Hospital, Xi'an, Shaanxi 710068, China

³Department of Gastroenterology, Shaanxi Provincial People's Hospital, Xi'an, Shaanxi 710068, China

Correspondence should be addressed to Sipan Chen; panda_spph@163.com

Received 26 May 2022; Revised 27 June 2022; Accepted 11 July 2022; Published 30 July 2022

Academic Editor: Pan Zheng

Copyright © 2022 Yaobo Yang et al. This is an open access article distributed under the Creative Commons Attribution License, which permits unrestricted use, distribution, and reproduction in any medium, provided the original work is properly cited.

Objective. This study is aimed at constructing and evaluating a prediction model of severe abdominal pain post-transcatheter arterial chemoembolization in patients with HBV-related primary liver cancer. **Methods.** Patients with HBV-associated primary liver cancer who received transarterial chemoembolization (TACE) from March 2019 to March 2022 in the Interventional Therapy Department of our hospital were selected as the subjects, and the included 160 patients were randomly divided into modeling group ($n = 120$) and validation group ($n = 40$) in a ratio of 3:1. Visual analog scale (VAS) was used to assess pain severity. 120 patients in the modeling group were divided into no/mild abdominal pain group and severe abdominal pain group. The clinical data of the patients, including gender, age, TACE treatment history, vascular invasion, maximum diameter of tumor, infarction degree, preoperative Eastern Oncology Collaboration Group (ECOG) score, and Lipiodol dosage, were analyzed. Receiver operating characteristic (ROC) curve was used to evaluate the predictive value of the prediction model for severe abdominal pain post-TACE. **Results.** A total of 116 patients (72.50%) had severe abdominal pain after TACE. Univariate analysis showed that severe abdominal pain after TACE in the modeling group was associated with TACE treatment history, maximum tumor diameter, infarction degree, and preoperative ECOG score (all $P < 0.05$), but not related to gender, age, vascular invasion, and Lipiodol dosage (all $P > 0.05$). Logistic regression analysis showed that TACE treatment history, maximum tumor diameter, infarction degree, and preoperative ECOG score were all independent influencing factors for acute abdominal pain post-TACE in HBV-HCC patients (all $P < 0.05$). The prediction model equation was $Y = -3.673 + 1.722 \times \text{TACE treatment history} + 1.175 \times \text{tumor maximum diameter} + 2.064 \times \text{infarction degree} + 1.555 \times \text{preoperative ECOG score}$. Goodness-of-fit test results showed no significant difference between the established prediction model and the observed value ($\chi^2 = 1.645$, $P = 0.560$) and $R^2 = 0.821$, suggesting that the prediction ability of the model was relatively accurate. ROC analysis results showed that the area under the curve (AUC) of severe abdominal pain after TACE was 0.916 (0.862–0.970) and 0.902 (95% CI: 0.841–0.963) in the modeling group and the verification group, respectively. **Conclusion.** TACE treatment history, tumor maximum diameter, infarction degree, and preoperative ECOG score are independent influencing factors for severe abdominal pain post-TACE in patients with HBV-HCC, and the prediction model established on this basis has good application value.

1. Introduction

Primary liver cancer is one of the most common malignant tumors in China, with 410,000 new cases and 390,000 deaths in 2020, ranking the fourth in the incidence of malignant tumors and adversely affecting the health of Chinese resi-

dents, with a 5-year survival rate of only 14.1% [1, 2]. According to pathological characteristics, primary liver cancer can be divided into hepatocellular carcinoma (HCC), intrahepatic cholangiocarcinoma, and mixed HCC-cholangiocarcinoma, among which HCC is the most common, accounting for more than 75% [3]. Among the known

causes, chronic hepatitis B, chronic hepatitis C, and nonalcoholic steatohepatitis are the most common causes of primary liver cancer [4, 5]. According to the report, the proportion of liver cancer caused by hepatitis B is as high as 92.05% [6]. With the advancement of surgical treatment, radiotherapy, chemotherapy, immunotherapy, targeted therapy, and liver transplantation, the expected survival and quality of life of HCC patients were significantly improved [7]. However, since most patients with liver cancer have been in the middle-late stage at diagnosis and unable to accept surgery treatment, interventional treatment become one of the main treatment approaches for patients with liver cancer. Interventional therapies include transarterial chemoembolization (TACE) and hepatic arterial infusion chemotherapy (HAIC) [8, 9]. Among them, TACE is widely used. TACE can increase the concentration of chemotherapy drugs exposed to tumors by injecting large doses of chemical drugs locally to the tumor target lesions, promoting tumor embolization infarction or necrosis [10, 11]. Postembolic syndromes, including acute abdominal pain, nausea, and vomiting, are common after TACE, which is an important reason for prolonged hospital stay, decreased treatment effect, and interruption of treatment [12]. At present, clinical studies have reported that the incidence and severity of abdominal pain vary greatly in different cohorts of HCC patients after TACE treatment [13, 14]. This study analyzed the occurrence characteristics of severe abdominal pain in HBV-related primary liver cancer patients in our hospital, explored its influencing factors, and constructed a clinical prediction model, aiming to provide valuable reference for the risk classification of severe abdominal pain in patients, strengthening targeted intervention, and improving pain management.

2. Subjects and Methods

2.1. Subjects. Patients with HBV-related primary liver cancer who received TACE from March 2019 to March 2022 in the Interventional Therapy Department of our hospital were selected as the study subjects. Inclusion criteria are as follows: (1) primary liver cancer was confirmed by pathology and met the diagnostic criteria [15]; (2) >20 years of age; (3) the tumor was consistent with <70% liver, in line with TACE criteria; (4) no extrahepatic metastasis before surgery, and the estimated survival time > 3 months; (5) HBV-related primary liver cancer; and (6) complete clinical data. Exclusion criteria are as follows: (1) severe abdominal pain before surgery or a history of long-term use of painkillers, (2) complicated with other malignant tumors, (3) non-HBV-related primary liver cancer, (4) abdominal pain caused by complications in addition to TACE, and (5) confused patients such as hepatic encephalopathy. 160 patients meeting the above criteria were randomly divided into the modeling group ($n = 120$) and the validation group ($n = 40$) according to the ratio of 3:1. All the subjects in this study signed informed consent for the study, and this study was approved by the medical ethics committee of the hospital.

2.2. Pain Assessment. Referring to “Expert Consensus on Pain Management after Adult Surgery” [16], the trained professional physicians of hepatology evaluated the severity of

severe abdominal pain at 1 h, 6 h, 12 h, and 24 h after TACE for HBV-HCC patients by using visual analogue scale (VAS) [14]. The assessment tool was a scale without any mark on the patient’s surface. The scale of the physician’s surface was 1-100 mm, with one end marked with “no pain” and the other marked with “most severe pain.” The corresponding score was obtained according to the pain intensity of the patient. Pain severity assessment is as follows: 0 is no pain; 1~3 is mild pain, manifested as discomfort, heavy pressure pain, dull pain, etc.; 4~6 is moderate pain, manifested as jumping pain, burning sensation, spasm, etc.; and 7~10 is severe pain, which interferes with normal activities. 120 patients in the modeling group were divided into no/mild abdominal pain group and severe abdominal pain group (moderate/severe abdominal pain). During the patient’s abdominal pain, an appropriate amount of short-acting analgesics would be used, which were in line with humanistic care and ethics, but the effect of the selected analgesics generally lasted for 4-6 hours, so as not to affect the assessment of abdominal pain at subsequent time points.

2.3. Clinical Data Collection. According to the requirement that the variables in the risk factor survey should be 5~10 times the sample size, this study included 8 variables through previous research reports and clinical practice, including gender, age, TACE treatment history, vascular invasion, tumor maximum diameter, infarction degree, preoperative ECOG score [17], and Lipiodol dosage. All data were obtained through the hospital patient medical record management system. Data entry was performed by two people at the same time to ensure the accuracy of information. Scorings were done by fixed staffs, and the principle of blinding was adopted.

2.4. Statistical Analysis. SPSS21.0 was used to analyze the collected experimental data. The measurement data in accordance with the normal distribution were represented by $\bar{X} \pm S'$. The comparison of measurement data between two groups was performed by the group t -test. The counting data were represented by the number of cases or rates. The comparison of counting data between two groups was performed by the χ^2 test. The variables with statistical significance in the univariate analysis were assigned and included in the multivariate analysis. Multivariate analysis was conducted by logistic regression model, and ROC curve was used to evaluate the predictive value of the model for predicting severe abdominal pain post-TACE. ROC curve plotting was performed using the GraphPad 6.0 software. The goodness-of-fit test method was used to test the difference between the model established in this study and the actual observation. $P > 0.05$ indicated that the model has good feasibility. $P < 0.05$ was considered statistically significant.

3. Results

3.1. Features of Severe Abdominal Pain Post-TACE. A total of 116 of 160 patients developed severe abdominal pain after TACE, with an incidence of 72.50%. The duration of pain in patients with severe abdominal pain was 55-220 min, with an average of 125 ± 36 min. The number of patients who

TABLE 1: Features of severe abdominal pain post-TACE (VAS, points (%)).

Timing	0 points	1 ~ 3 points	4 ~ 6 points	7 ~ 9 points	10 points
1 h	3 (1.88)	21 (13.13)	100 (62.50)	26 (16.25)	10 (6.25)
6 h	7 (4.38)	43 (26.88)	83 (51.88)	27 (16.88)	6 (3.75)
12 h	13 (8.13)	66 (41.25)	62 (38.75)	19 (11.88)	0 (0.00)
24 h	19 (11.88)	82 (51.25)	53 (33.13)	6 (3.75)	0 (0.00)

scored 4-6 points in VAS at 1 h and 6 h after TACE was relatively high, and the number of patients who scored 1-3 points in VAS at 12 h and 24 h after TACE was relatively high (Table 1).

3.2. Comparison of Clinical Data between the Modeling Group and the Validation Group. There were no significant differences between the modeling group and the validation group in gender, age, TACE treatment history, vascular invasion, tumor maximum diameter, infarction degree, preoperative ECOG score, and Lipiodol dosage (all $P > 0.05$, Table 2).

3.3. Univariate Analysis of Severe Abdominal Pain Post-TACE in the Modeling Group. Univariate analysis showed that severe abdominal pain post-TACE in the modeling group was associated with TACE treatment history, maximum tumor diameter, infarction degree, and preoperative ECOG score (all $P < 0.05$), but not related to gender, age, vascular invasion, and Lipiodol dosage (all $P > 0.05$, Table 3).

3.4. Multivariate Logistic Regression Analysis of the Factors Influencing Severe Abdominal Pain Post-TACE. The significant variables in single-factor analysis, including TACE treatment history, maximum tumor diameter, infarction degree, and preoperative ECOG score, were included in the multivariate regression analysis model. The variables assigning was as follows: TACE treatment history (yes = 1, no = 0), maximum tumor diameter (≥ 5 cm = 1, < 5 cm = 0), infarction degree (complete = 1, incomplete = 0), and preoperative ECOG score (2 = 1, 0-1 = 0). The final logistic regression analysis results showed that TACE treatment history, maximum tumor diameter, infarction degree, and preoperative ECOG score were all independent factors influencing severe abdominal pain post-TACE in HBV-HCC patients (all $P < 0.05$, Table 4).

3.5. Prediction Model Establishment and ROC Evaluation. According to the risk factors in Table 3, the prediction model of severe abdominal pain after TACE was constructed: $P = 1/(1 + e^{-Y})$, where P is the probability of severe abdominal pain after TACE, e is the natural logarithm, and $Y = -3.673 + 1.722 \times \text{TACE treatment history} + 1.175 \times \text{maximum tumor diameter} + 2.064 \times \text{infarction degree} + 1.555 \times \text{preoperative ECOG score}$. Goodness-of-fit test results showed that there was no significant difference between the prediction model of severe abdominal pain post-TACE and the observed value ($\chi^2 = 1.645$, $P = 0.560$), and $R^2 = 0.821$, suggesting that the prediction ability of the model was relatively accurate. ROC analysis results showed that the AUC of severe abdominal pain post-TACE in the modeling group and the verification group was 0.916 (0.862~0.970) and 0.902 (95% CI: 0.841~0.963), respectively (Table 5 and Figure 1).

4. Discussion

With the change of living standard and lifestyle, the incidence and mortality of liver cancer are increasing year by year. According to the report of the International Agency for Research on Cancer (IARC), there were 841,000 cases and 781,000 deaths about liver cancer worldwide in 2018 [18, 19]. The incidence and deaths of liver cancer in my country account for more than half of the world, and the proportion of liver cancer in my country caused by hepatitis B is as high as 90% [20]. Currently, for patients with primary liver cancer, TACE is commonly used clinically to block tumor blood supply and deposit chemotherapy drugs around the tumor so as to play a role of local chemotherapy. TACE is carried out 600,000 to 800,000 times per year in China [21]. TACE is helpful to improve the survival benefit of patients with primary liver cancer. However, in clinical practice, severe abdominal pain post-TACE will prolong the hospital stay of patients, affect their postoperative recovery, and even interrupt the treatment in severe cases [22, 23]. In the present study, 116 of 160 patients developed severe abdominal pain after TACE, with an incidence of 72.50%. The duration of pain in patients with severe abdominal pain was 55-220 min, with an average of 125 ± 36 min. The number of patients with 4-6 points in VAS at 1 h and 6 h post-TACE was relatively high, and the number of patients with 1-3 points in VAS at 12 h and 24 h post-TACE was relatively high. These suggested that the incidence of severe abdominal pain was relatively high at the early stage of TACE, and that the number of severe abdominal pain gradually decreased with the increase of time.

Previous studies [24, 25] have found that TACE treatment experience, liver cancer surgery or transplantation history, diabetes, chronic liver disease history, pain history, CRP level, ECOG score, preoperative anxiety, and postoperative TACE are risk factors for severe abdominal pain post-TACE. Severe abdominal pain post-TACE has a high incidence and has many influencing factors, so it is particularly important to actively prevent abdominal pain. Multivariate logistic regression analysis of this study showed that TACE treatment history, maximum tumor diameter, infarction degree, and preoperative ECOG score were independent risk factors for the occurrence of severe abdominal pain post-TACE. Specifically, the larger the tumor diameter is, the more embolization agents such as Lipiodol are used in TACE, and the greater the tumor embolization degree is, the more severe the abdominal pain reaction caused by ischemic necrosis in a short period of time [26]. However, patients with a history of TACE are relatively less sensitive to repeated same irritant pain. Research [27, 28] shows that

TABLE 2: Comparison of clinical data between the modeling group and the validation group.

Factor	Classification	Modeling group ($n = 120$)	Validation group ($n = 40$)	χ^2 value	P value
Gender	Male	65	25	0.847	0.358
	Female	55	15		
Age (years)	≥ 60	43	18	1.069	0.301
	< 60	77	22		
TACE treatment history	Yes	46	17	0.218	0.640
	No	74	23		
Vascular invasion	Yes	62	23	0.410	0.522
	No	58	17		
Maximum diameter of tumor (cm)	< 5	75	27	0.325	0.569
	≥ 5	45	13		
Infarction degree	Incomplete	103	33	0.261	0.609
	Complete	17	7		
Preoperative ECOG score (points)	0 ~ 1	99	30	1.080	0.299
	2	21	10		
Lipiodol dosage (mL)	< 10	86	28	0.041	0.840
	≥ 10	34	12		

TABLE 3: Univariate analysis of severe abdominal pain post-TACE in the modeling group.

Factor	Classification	No/mild abdominal pain group ($n = 35$)	Severe abdominal pain group ($n = 85$)	χ^2 value	P value
Gender	Male	20	45	0.176	0.675
	Female	15	40		
Age (years)	≥ 60	13	30	0.037	0.848
	< 60	22	55		
TACE treatment history	Yes	5	41	12.091	< 0.001
	No	30	44		
Vascular invasion	Yes	22	40	2.478	0.116
	No	13	45		
Maximum diameter of tumor (cm)	< 5	7	38	6.456	0.011
	≥ 5	28	47		
Infarction degree	Incomplete	1	16	5.198	0.023
	Complete	34	69		
Preoperative ECOG score (points)	0 ~ 1	33	66	4.754	0.029
	2	2	19		
Lipiodol dosage (mL)	< 10	10	24	0.001	0.970
	≥ 10	25	61		

TABLE 4: Multivariate logistic regression analysis of the factors influencing severe abdominal pain post-TACE.

Risk factor	B value	SE value	Wald value	OR value	95% CI	P value
TACE treatment history	1.722	0.631	7.443	5.593	1.624~ 19.265	0.016
Maximum tumor diameter	1.175	0.583	4.055	3.235	1.032~ 1.142	0.035
Infarction degree	2.064	0.672	9.437	7.880	2.111~ 29.413	< 0.001
Preoperative ECOG score	1.555	0.615	6.391	4.734	1.418~ 15.803	0.023

TABLE 5: Prediction model establishment and ROC evaluation.

Index	AUC	Sensitivity (%)	Specificity (%)	95% CI	Standard error	P value
Modeling group	0.916	90.10	87.16	0.862~0.970	0.028	<0.001
Validation group	0.902	89.67	86.55	0.841~0.963	0.031	<0.001

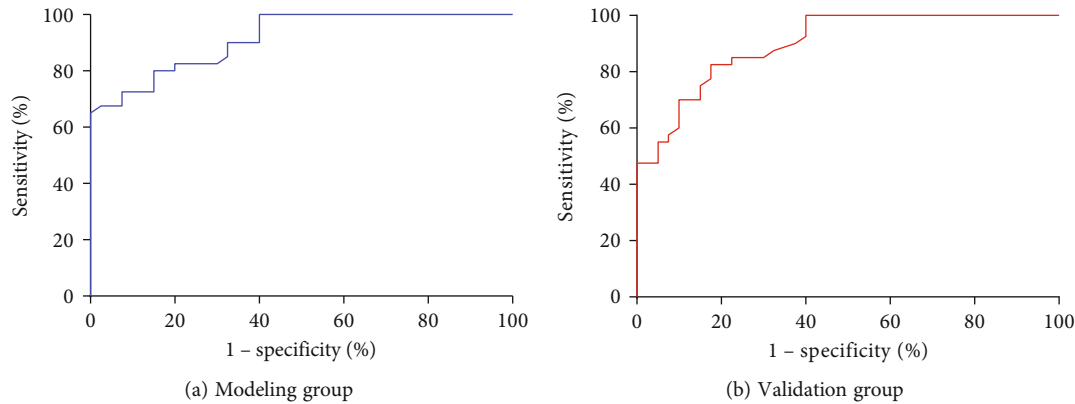


FIGURE 1: ROC analysis of the model's predictive value in predicting severe abdominal pain in the modeling group and validation group.

patients with a history of TACE are 7.931 times more sensitive to abdominal pain than those without TACE, which is similar to the results of the present study. The higher the ECOG score, the more advanced or larger the liver cancer of the patient is, and the more embolic agents such as Lipiodol used in TACE are correspondingly larger, resulting in more severe abdominal pain.

In this study, prediction model was established. The AUC of severe abdominal pain after TACE in the modeling group and the validation group was 0.916 (0.862~0.970) and 0.902 (95% CI: 0.841~0.963), respectively, indicating that the prediction model established in this study had a high predictive value for severe abdominal pain post-TACE. At present, severe abdominal pain post-TACE has a high incidence and has certain subjectivity with the existence of misdiagnosis and missed diagnosis. The present model can directly predict the risk factors of severe abdominal pain post-TACE without the influence of blood environment and exogenous factors. The application of this model combined with clinical indicators can improve the sensitivity of diagnosis and help patients to detect severe abdominal pain post-TACE at an early stage, so that treatment and control measures can be adopted as soon as possible to avoid further development and aggravation of the disease.

In conclusion, severe abdominal pain post-TACE is associated with multiple factors including TACE treatment history, maximum tumor diameter, infarction degree, and preoperative ECOG score. In this study, the logistic regression risk prediction model of postoperative severe abdominal pain post-TACE established based on the above factors has a good prediction effect, and clinical intervention can be carried out according to the above risk factors to reduce the incidence of postoperative severe abdominal pain. However, this study also has shortcomings such as small sample size and only the visual analog scale (VAS) used to assess the severity of pain. In the future, the research sample can

be further expanded, and multiple means of assessing pain severity can improve the reliability of the study to provide more support for clinical application.

Data Availability

The labeled datasets used to support the findings of this study are available from the corresponding author upon request.

Conflicts of Interest

The authors declare no competing interests.

References

- [1] H. Sun, Q. Meng, C. Shi et al., "Hypoxia-inducible exosomes facilitate liver-tropic premetastatic niche in colorectal cancer," *Hepatology*, vol. 74, no. 5, pp. 2633–2651, 2021.
- [2] Y. Meng, Q. Zhao, L. An et al., "A TNFR2–hnRNPK axis promotes primary liver cancer development via activation of YAP signaling in hepatic progenitor cells," *Cancer Research*, vol. 81, no. 11, pp. 3036–3050, 2021.
- [3] W. Q. He, X. Gao, L. Gao, Y. Ma, D. Sun, and J. Sun, "Contrasting trends of primary liver cancer mortality in Chinese Mongol and non-Mongol," *Asian Pacific Journal of Cancer Prevention*, vol. 22, no. 9, pp. 2757–2763, 2021.
- [4] Z. Fu, X. Li, J. Zhong et al., "Lenvatinib in combination with transarterial chemoembolization for treatment of unresectable hepatocellular carcinoma (uHCC): a retrospective controlled study," *Hepatology International*, vol. 15, no. 3, pp. 663–675, 2021.
- [5] Y. Y. Zhang, X. Guan, and X. P. Ren, "Research progress on etiological morphology and prevention strategies of viral hepatitis-cirrhosis-primary liver cancer," *Cancer Progress*, vol. 19, no. 17, p. 4, 2021.

- [6] F. Li, "Correlation between hepatitis B virus DNA load and immune function in patients with hepatitis B primary liver cancer," *Modern Oncology*, vol. 28, no. 14, p. 4, 2020.
- [7] J. Heianna, W. Makino, M. Toguchi et al., "Transarterial chemoembolization for the palliation of painful bone metastases refractory to first-line radiotherapy," *Journal of Vascular and Interventional Radiology*, vol. 32, no. 3, pp. 384–392, 2021.
- [8] H. Ghanaati, M. Mohammadifard, and M. Mohammadifard, "A review of applying transarterial chemoembolization (TACE) method for management of hepatocellular carcinoma," *Journal of Family Medicine and Primary Care*, vol. 10, no. 10, pp. 3553–3560, 2021.
- [9] J. Titano, A. Noor, and E. Kim, "Transarterial chemoembolization and radioembolization across Barcelona clinic liver cancer stages," *Seminars in Interventional Radiology*, vol. 34, no. 2, pp. 109–115, 2017.
- [10] S. Miyayama, "Ultrasensitive conventional transarterial chemoembolization: when and how?," *Clinical and Molecular Hepatology*, vol. 25, no. 4, pp. 344–353, 2019.
- [11] X. Ding, W. Sun, W. Li et al., "Transarterial chemoembolization plus lenvatinib versus transarterial chemoembolization plus sorafenib as first-line treatment for hepatocellular carcinoma with portal vein tumor thrombus: a prospective randomized study," *Cancer*, vol. 127, no. 20, pp. 3782–3793, 2021.
- [12] L. F. Bian, X. H. Zhao, B. L. Gao et al., "Predictive model for acute abdominal pain after transarterial chemoembolization for liver cancer," *World Journal of Gastroenterology*, vol. 26, no. 30, pp. 4442–4452, 2020.
- [13] A. Pachev, L. Raynaud, L. Paulatto et al., "Predictive factors of severe abdominal pain during and after transarterial chemoembolization for hepatocellular carcinoma," *European Radiology*, vol. 31, no. 5, pp. 3267–3275, 2021.
- [14] C. S. Cheng, L. Chen, J. Xie, and Z. Chen, "Multimodality palliative treatment with transarterial chemoembolization and high-intensity focused ultrasound for gastric leiomyosarcoma multiple liver metastasis pain: a case report," *Medicine*, vol. 98, no. 39, article e17328, 2019.
- [15] Z. Li and J. Y. Zhu, "Interpretation of Guidelines for Diagnosis and Treatment of Primary Liver Cancer (2022 Edition)," *Journal of Clinical Hepatobiliary Diseases*, vol. 38, no. 5, pp. 1027–1029, 2022.
- [16] J. G. Xu, "Expert consensus on post-operative pain management in adults," *Journal of Clinical Anesthesiology*, vol. 33, no. 9, pp. 911–917, 2017.
- [17] C. D. Bergerot, E. J. Philip, P. G. Bergerot et al., "Discrepancies between genitourinary cancer patients' and clinicians' characterization of the eastern cooperative oncology group performance status," *Cancer*, vol. 127, no. 3, pp. 354–358, 2021.
- [18] L. Kong, G. Wei, T. Lv et al., "Outcome of TACE treatment in HIV infected patients with hepatocellular carcinoma," *Scientific Reports*, vol. 11, no. 1, p. 696, 2021.
- [19] P. Zhao, D. M. Jiang, L. F. Xian et al., "Mortality analysis of primary liver cancer in the mainland of China from 2004 to 2018," *Shanghai Journal of Preventive Medicine*, pp. 881–886, 2021.
- [20] K. Li, H. B. Ning, and J. Shang, "The latest progress in clinical research on hepatitis B virus infection and liver cancer," *Journal of Southwest Medical University*, vol. 44, no. 6, p. 5, 2021.
- [21] M. Shaghaghi, M. AliyariG hasabeh, S. Ameli et al., "Role of tumor margin and ADC change in defining the need for additional treatments after the first TACE in patients with unresectable HCC," *European Journal of Radiology*, vol. 133, article 109389, 2020.
- [22] K. M. Lwin, Y. K. S. Dee, and Y. H. Linn, "The effects of supplement therapy on HCV-related HCC: a case report of a patient who had undergone TACE for six times," *Journal of Gastrointestinal Cancer*, vol. 52, no. 2, pp. 802–808, 2021.
- [23] H. Li, F. Wu, M. Duan, and G. Zhang, "Drug-eluting bead transarterial chemoembolization (TACE) vs conventional TACE in treating hepatocellular carcinoma patients with multiple conventional TACE treatments history: a comparison of efficacy and safety," *Medicine*, vol. 98, no. 21, article e15314, 2019.
- [24] A. Chiarotto, L. J. Maxwell, R. W. Ostelo, M. Boers, P. Tugwell, and C. B. Terwee, "Measurement properties of visual analogue scale, numeric rating scale, and pain severity subscale of the brief pain inventory in patients with low Back pain: a systematic review," *The Journal of Pain*, vol. 20, no. 3, pp. 245–263, 2019.
- [25] A. L. Feng, J. K. Zhu, Y. Yang et al., "Repeated postoperative adjuvant TACE after curative hepatectomy improves outcomes of patients with HCC," *Minimally Invasive Therapy & Allied Technologies*, vol. 30, no. 3, pp. 163–168, 2021.
- [26] P. Viveiros, A. Riaz, R. J. Lewandowski, and D. Mahalingam, "Current state of liver-directed therapies and combinatory approaches with systemic therapy in hepatocellular carcinoma (HCC)," *Cancers*, vol. 11, no. 8, pp. 1085–1100, 2019.
- [27] F. Yang, S. N. Markovic, J. R. Molina et al., "Association of sex, age, and eastern cooperative oncology group performance status with survival benefit of cancer immunotherapy in randomized clinical trials: a systematic review and meta-analysis," *JAMA Network Open*, vol. 3, no. 8, pp. 1–10, 2020.
- [28] R. Iezzi, A. Posa, A. Tanzilli, F. Carchesio, M. Pompili, and R. Manfredi, "Balloon-occluded MWA (b-MWA) followed by balloon-occluded TACE (b-TACE): technical note on a new combined single-step therapy for single large HCC," *Cardiovascular and Interventional Radiology*, vol. 43, no. 11, pp. 1702–1707, 2020.

Research Article

Efficacy of Gamma Globulins in Children with Kawasaki Disease and Factors Influencing Children's Short-Term Prognosis

Hao Sun , Huimin Lu, and Yunhong Wu

Department of General Paediatrics, Children's Hospital of Shanxi, Taiyuan City, 030000 Shanxi, China

Correspondence should be addressed to Hao Sun; sunhao9068@163.com

Received 7 June 2022; Revised 4 July 2022; Accepted 11 July 2022; Published 30 July 2022

Academic Editor: Pan Zheng

Copyright © 2022 Hao Sun et al. This is an open access article distributed under the Creative Commons Attribution License, which permits unrestricted use, distribution, and reproduction in any medium, provided the original work is properly cited.

Purpose. To explore and analyze the therapeutic effect of gamma globulins (GG) on Kawasaki disease (KD) in children and the influencing factors of short-term prognosis. **Methods.** First, 90 pediatric KD patients admitted between January 2019 and January 2021 were selected and divided into a control group ($n = 40$) and a research group ($n = 50$) according to the difference in treatment. In addition to routine treatment and nursing given to both groups, control group was given aspirin (ASA), based on which research group was supplemented with GG therapy. The treatment outcome and adverse events (AEs) of the two cohorts of patients were analyzed and compared, and the influencing factors of children's short-term prognosis were analyzed by logistics multivariate analysis. **Results.** Research group had a statistical higher overall response rate than control group, with significantly fewer cases suffering from AEs such as nausea and vomiting, diarrhea, rash, dizziness and headache, and coronary artery injury. On the other hand, logistics multivariate analysis identified that gender, body mass index (BMI), onset time, platelet (PLT), and treatment mode all independently influence the short-term prognosis of children with KD. **Conclusions.** GG therapy is effective in treating pediatric KD patients and can effectively prevent AEs. In addition, gender, BMI, onset-to-treatment time, PLT, C-reactive protein (CRP), and treatment methods are independent risk factors for short-term prognosis of children with KD.

1. Introduction

Kawasaki disease (KD) is an acute systemic vasculitis with complex pathological triggers, usually occurring in children under the age 5 [1]. According to KD epidemiological data, the median diagnosis age of the disease is 1.4 years old, with a predilection for boys and the rainy season as the peak period [2]. The disease mainly has a negative impact on children's medium-sized arteries, especially the coronary arteries [3]. The main clinical presentations of KD are fever, rash, cervical lymph node enlargement, and oral mucosal erythema [4]. For pediatric KD patients, delayed treatment and intervention can result in 25% of them developing coronary artery injury that may consequently lead to adverse events (AEs) such as coronary artery aneurysm, ischemic heart disease, or sudden death [5, 6]. Therefore, optimizing treatment strategies for pediatric KD patients is of great significance for improving patient prognosis and optimizing clinical management of the disease.

Though not completely clarified, the pathological mechanism of KD is shown to be associated with immune system activation and inflammatory cascade caused by unknown stimuli [7]. Aspirin (ASA), or acetylsalicylic acid, in combination with gamma globulins (GG), constitutes a key part of the standard treatment plan for KD, which can exert synergistic systemic anti-inflammatory effects and reduce coronary artery injury [8, 9]. ASA is known to induce the production of some proresolving lipid-derived mediators, the secretion of which is used by the immune system to control the inflammatory response associated with injury stimuli, endowing ASA with anti-inflammatory effects [10]. Additionally, it has analgesic, antipyretic, and antiplatelet pharmacological actions [11]. GG, on the other hand, is an immunoglobulin G (IgG) mixed preparation made from the plasma purification of thousands of healthy donors, which can be used to treat autoimmune diseases and inflammatory diseases [12]. GG is shown to exert anti-inflammatory effects via blocking Fc receptors, neutralizing

pathogenic products of unknown infectious agents, and regulating inflammatory cytokines [13].

Considering that the curative effect of GG therapy in children with KD and the influencing factors of children's short-term prognosis have not been fully clarified, this research conducts relevant analyses to provide new insights into the treatment of pediatric KD.

2. Data and Methods

2.1. General Data. This research, ratified by Children's Hospital of Shanxi Ethics Committee, enrolled 90 children with KD from January 2019 to January 2021 and assigned them to a control group ($n = 40$) and a research group ($n = 50$) according to the difference in treatment. In addition to routine treatment and nursing in both groups, control group was given ASA, based on which research group was supplemented with GG therapy. Control group comprised 25 boys and 15 girls, aged 2.47 ± 0.90 years, with the onset-to-treatment time of 6.57 ± 1.55 days. Research group had 30 boys and 20 girls, aged 2.43 ± 1.47 years, with the onset-to-treatment time of 6.90 ± 1.52 days. The two cohorts showed no distinct differences in baseline data ($P > 0.05$). All subjects' legal guardians were fully informed of the purpose of the study and provided informed consent.

2.2. Inclusion and Exclusion Criteria. All the included children had confirmed the first episode of KD and met the indications of GG and ASA, with normal growth and development and intact medical records.

Children were excluded from this study if they had infectious diseases, rash and fever illness, vital organ-associated diseases, congenital heart disease, chronic obstructive pulmonary disease, or drug allergies.

2.3. Treatment Methods. Children in control group were given 30-50 mg/kg ASA (Beijing Kangruina Biotechnology Co., Ltd., A1189) that was divided into 2-3 oral doses every day. The dose was gradually reduced after the body temperature recovered for 3 days. About 2 weeks after treatment, ASA was reduced to 3-5 mg/kg per day and administered orally for 6-8 weeks.

Research group was given intravenous GG (Shanxi Kangbao Biological Products Co., Ltd., S19994004) in addition to the above treatment, that is, 1.0 g/kg/d GG was given 5 days after the onset of the disease with the infusion time of 8-12 h, for 2 days.

2.4. Curative Effect Evaluation. If the child's symptoms such as fever, lymph node swelling, congestion of conjunctiva, and pharyngeal mucosa disappear, and the area of macula recovers by 90% or more, it is regarded as cured; if the above-mentioned symptoms disappear and the macula area recovers by 75-89%, it is considered markedly effective; if the child's symptoms have improved but not completely disappeared, with the macula area recovered by 30-74%, it is considered effective; if the child has no change in the above symptoms with the macula area recovered $< 30\%$, it was regarded as ineffective.

2.5. Outcome Measures

2.5.1. Curative Effect. The corresponding cases of cured, effective, and ineffective patients were recorded according to the above evaluation criteria, and the percentage of the sum of cured, effective, and effective in the total cases was the total effective rate.

2.5.2. Incidence of AEs. The incidence of AEs (chills, nausea and vomiting, dizziness, and headache) was recorded.

2.5.3. Coronary Artery Injury. Coronary artery injury of children was evaluated by echocardiography, and the incidence of mild, moderate, and severe coronary artery injury and the total incidence were recorded. The criteria are as follows: mild injury: coronary artery diameter 2.5-4.0 mm; moderate injury: coronary artery diameter 4.0-6.0 mm; severe injury: coronary artery diameter ≥ 7 mm.

2.5.4. Short-Term Prognosis. Events such as ineffective treatment, adverse reactions, and coronary artery injury during treatment were considered as poor short-term outcomes.

The primary outcome measures of this study are curative effect and incidence of adverse reactions, and the secondary ones are coronary artery injury and short-term outcome.

2.6. Statistical Analysis. We analyzed the data and obtained corresponding pictures with GraphPad Prism 6 (GraphPad Software Inc., USA). The enumeration data, recorded as the number of cases/percentage ($n/\%$), were analyzed via the chi-square test or the chi-square continuity correction when the theoretical frequency of the former test was below 5. Mean \pm SEM was used to indicate the measurement data, and the independent sample t -test was used for comparison of data between groups. Univariate and multivariate analyses of independent risk factors affecting the short-term prognosis of children with KD were performed using the SPSS Regression SPSS22.0 (SPSS, Inc., Chicago, IL, USA) models. $P < 0.05$ was the statistical significance level for all tests in this study.

3. Results

3.1. Baseline Data of Pediatric KD Patients. By analyzing the general data of 90 pediatric KD patients (Table 1), we found that control group and research group had no statistical difference in sex, age, onset-to-treatment time, duration of fever, body temperature, KD type, overweight, platelet (PLT), C-reactive protein (CRP), alanine aminotransferase (ALT), and aspartate aminotransferase (AST), which were comparable ($P > 0.05$).

3.2. Therapeutic Effect of Pediatric KD Patients. We analyzed the curative effect of two groups to evaluate the influence of the two interventions on KD patients. According to the data (Table 2), the cure rate of research group was 34.00% that of the control group (22.50%). In addition, the total effective rate was 90.00% in the research group and 72.50% in the control group, with statistical significance between them ($P < 0.05$).

TABLE 1: Baseline data of pediatric KD patients [n , mean \pm SEM].

Factor	Control group ($n = 40$)	Research group ($n = 50$)	χ^2/t	P
Gender (male/female)	25/15	30/20	0.058	0.809
Age (years old)	2.47 \pm 0.90	2.43 \pm 1.47	0.151	0.880
Onset-to-treatment time (d)	6.57 \pm 1.55	6.90 \pm 1.52	1.015	0.313
Duration of fever (d)	3.37 \pm 0.72	3.60 \pm 0.74	1.483	0.142
Body temperature ($^{\circ}$ C)	38.90 \pm 0.45	39.09 \pm 0.71	1.472	0.145
Type of KD (complete/incomplete)	18/22	25/25	0.223	0.637
Overweight (yes/no)	27/13	40/10	1.825	0.177
PLT ($10^9/L$)	372.49 \pm 124.89	379.80 \pm 141.42	0.257	0.798
CRP (mg/L)	76.07 \pm 16.35	82.41 \pm 18.02	1.728	0.088
ALT (U/L)	35.45 \pm 11.76	35.94 \pm 13.68	0.180	0.858
AST (U/L)	32.89 \pm 17.45	34.90 \pm 14.51	0.597	0.552

TABLE 2: Therapeutic effect of pediatric KD patients [n (%)].

Groups	n	Cured	Markedly effective	Effective	Ineffective	Total effective rate (%)
Control group	40	9 (22.50)	12 (30.00)	8 (20.00)	11 (27.50)	29 (72.50)
Research group	50	17 (34.00)	15 (30.00)	13 (26.00)	5 (10.00)	45 (90.00)
χ^2 value	—	—	—	—	—	4.656
P value	—	—	—	—	—	0.031

TABLE 3: Incidence of adverse events in pediatric KD patients [n (%)].

Categories	Control group ($n = 40$)	Research group ($n = 50$)	χ^2 value	P value
Chills	5 (12.50)	2 (4.00)	—	—
Nausea and vomiting	1 (2.50)	0 (0.00)	—	—
Dizziness and headache	4 (10.00)	0 (0.00)	—	—
Total incidence	10 (25.00)	2 (4.00)	8.481	0.004

3.3. *Incidence of AEs in Pediatric KD Patients.* We compared and analyzed the incidence of AEs in terms of chills, nausea and vomiting, dizziness, and headache and found that the total incidence was significantly lower in research group compared with control group (4.00% vs. 25.00%, $P < 0.05$; Table 3).

3.4. *Incidence of Coronary Artery Injury in Pediatric KD Patients.* We also recorded the occurrence of coronary artery injury in both groups of KD patients, so as to compare and analyze the influence of the two interventions on coronary artery injury. The results revealed that more patients in control group suffered from coronary artery injury of various severity, with a higher overall incidence compared with research group (22.50% vs. 4.00%, $P < 0.05$). See Table 4.

3.5. *Analysis of Influencing Factors of Short-Term Prognosis of Pediatric KD Patients.* The influencing factors of short-term prognosis in 90 pediatric KD patients were analyzed by univariate analysis. The data showed that the adverse fac-

TABLE 4: Incidence of coronary artery injury in pediatric KD patients [n (%)].

Categories	Control group ($n = 40$)	Research group ($n = 50$)	χ^2 value	P value
Mild	4 (10.00)	2 (4.00)	—	—
Moderate	3 (7.50)	0 (0.00)	—	—
Severe	2 (5.00)	0 (0.00)	—	—
Total incidence	9 (22.50)	2 (4.00)	7.089	0.008

tors significantly affecting the short-term prognosis of children with KD included sex, onset-to-treatment time, overweight, PLT, CRP, and treatment methods ($P < 0.05$). Multivariate logistic regression analysis further confirmed that gender, onset-to-treatment time, overweight, PLT, CRP, and treatment mode were significantly and independently associated with poor short-term prognosis of children with KD ($P < 0.05$; Tables 5 and 6).

4. Discussion

KD, as a self-limiting childhood disease, can be divided into complete KD and incomplete KD, in which the former meets the diagnostic criteria of KD, while the latter does not fully meet [14]. This may lead to difficult diagnosis and delayed treatment in children with incomplete KD, increasing the risk and mortality of coronary artery aneurysm, myocardial suppression, arrhythmia, and other diseases [15]. The etiology of KD remains to be defined and may be related to respiratory disease-associated pathogens

TABLE 5: Assignment of logistic multivariate regression analysis.

Factors	Variables	Assignment
Sex	X1	Male = 0, female = 1
Age (years old)	X2	Continuous variable
Onset-to-treatment time (d)	X3	Continuous variable
Fever time (d)	X4	Continuous variable
Body temperature (°C)	X5	Continuous variable
KD type	X6	Complete = 0, incomplete = 1
Be overweight	X7	Yes = 0, no = 1
PLT (10 ⁹ /L)	X8	Continuous variable
CRP (mg/L)	X9	Continuous variable
ALT (U/L)	X10	Continuous variable
AST (U/L)	X11	Continuous variable
Treatment methods	X12	Aspirin = 0, aspirin + GG = 1

TABLE 6: Univariate and multivariate logistic analysis of short-term prognosis of pediatric KD patients.

Characteristic	Univariate		Multivariate	
	OR (95% CI)	P	OR (95% CI)	P
Sex	1.304 (1.039-1.632)	0.024	2.113 (1.354-3.304)	0.002
Age (years old)	2.034 (0.960-1.547)	0.068		
Onset-to-treatment time (d)	2.315 (1.124-4.875)	0.023	2.279 (1.290-4.061)	0.007
Duration of fever (d)	2.109 (0.926-4.453)	0.057		
Body temperature (°C)	1.556 (0.913-2.684)	0.114		
Types of KD	1.009 (0.987-1.003)	0.356		
Overweight	2.872 (1.425-4.826)	<0.001	1.854 (1.013-3.397)	0.045
PLT (10 ⁹ /L)	2.541 (1.149-3.751)	<0.001	2.105 (1.127-3.915)	0.019
CRP (mg/L)	2.213 (1.123-3.985)	0.009	2.319 (1.305-4.228)	0.005
ALT (U/L)	1.011 (0.008-1.750)	0.525		
AST (U/L)	1.058 (0.356-1.167)	0.308		
Treatment methods	3.754 (1.319-10.522)	0.012	3.061 (2.245-5.467)	0.029

such as coronavirus, rhinovirus, and adenovirus [16]. This report mainly analyzes the curative effect and short-term prognosis of children with KD, hoping to make a contribution to optimizing the treatment and improving the prognosis of KD.

This research included 90 pediatric KD patients who were assigned to the control group treated with ASA and the research group additionally treated with GG. In our study, the total effective rate of treatment was obviously higher in research group than in control group (90.00% vs. 72.50%), indicating that GG intervention can significantly improve the clinical efficacy of children with KD. In addition, 10.00% of the children in research group did not respond to GG therapy and had GG resistance, which was consistent with the report of McCrindle et al. [17]. In terms of safety, chills, dizziness, and headache were the main AEs in control group versus chills alone in research group; the overall incidence of AEs was obviously lower in research group compared with control group (4.00% vs. 25.00%), suggesting that in treating pediatric KD patients, GG has a certain safety that is better than ASA alone. Mohammadzadeh

et al. [18] reported that GG combined with ASA reduced the complication rate from 47% at the onset of pediatric KD to 7% at the sixth month, similar to our findings. In the evaluation of coronary artery injury, research group was found with fewer cases of mild, moderate, and severe coronary artery injury and a notably lower overall incidence compared with control group (4.00% vs. 22.50%). In the research of Galeotti et al. [12], GG effectively prevented KD complicated artery injury in children and reduced the risk of coronary artery disease from as high as 25% to 2-4%, which is consistent with our research results. Coronary artery injury is mainly attributed to KD, accompanied by thrombosis and distal embolism, for which ASA, an anti-thrombotic drug, shows some certain preventive effect [19]. Finally, we confirmed through univariate and multivariate logistic regression analyses that gender, onset-to-treatment time, overweight, PLT, and treatment methods were independent risk factors for poor short-term prognosis of children with KD, similar to the results of Qiu et al. [20]. The report of Huang et al. [21] confirmed that PLT, CRP, neutrophil percentage, serum albumin, serum sodium, etc. were

the risk factors of GG resistance in children with KD, which confirms the accuracy of our findings. Hu and Ren [22] also pointed out that immunoglobulin M (IgM), IgA, and the number of coronary arteries involved (NCAI) are the adverse prognostic factors of coronary artery injury in children with KD.

The novelty of this study lies in that it demonstrates the effectiveness and safety of GG treatment in children with KD from the perspectives of efficacy and incidence of adverse reactions and confirms that GG treatment has a certain protective effect on the prognosis of children with KD from the aspects of the occurrence of coronary artery injury and the short-term prognostic factors. The above provides new insights into the management optimization of pediatric patients with KD. However, there are still some limitations. First, it is a single-center research, which is prone to information bias. Second, the basic experimental analysis of related therapeutic mechanisms can be supplemented to further clarify the anti-KD mechanism of GG and the prevention mechanism of KD-related coronary artery injury. Finally, if children's long-term prognosis can be discussed in future research, the influence of the two intervention methods on the long-term prognosis of children with KD will be further understood. We will continue to improve the research project from the above aspects.

5. Conclusion

Our data indicate that GG treatment is effective in the treatment of children with KD, which can effectively reduce the incidence of AEs and help prevent coronary artery injury. On the other hand, the poor short-term prognosis of some children with KD may be related to factors such as sex, onset-to-treatment time, overweight, PLT, and treatment methods. In clinical practice, reasonable intervention measures can be formulated according to the above factors to improve the short-term prognosis of children with KD.

Data Availability

The labeled dataset used to support the findings of this study are available from the corresponding author upon request.

Conflicts of Interest

The authors declare no competing interests.

References

- [1] L. Meng, Z. Zhen, Q. Jiang et al., "Predictive model based on gene and laboratory data for intravenous immunoglobulin resistance in Kawasaki disease in a Chinese population," *Pediatric Rheumatology Online Journal*, vol. 19, no. 1, p. 95, 2021.
- [2] M. N. Mat Bah, E. Y. Alias, H. Razak, M. H. Sopian, F. H. Foo, and N. Abdullah, "Epidemiology, clinical characteristics, and immediate outcome of Kawasaki disease: a population-based study from a tropical country," *European journal of pediatrics*, vol. 180, no. 8, pp. 2599–2606, 2021.
- [3] M. Piram, "Epidemiology of Kawasaki disease in Europe," *Frontiers in Pediatrics*, vol. 9, article 673554, 2021.
- [4] K. Rajak, A. R. Twayana, R. Shrestha, P. Amatya, and C. Ghimire, "Prevalence of Kawasaki disease in a tertiary care hospital: a descriptive cross-sectional study," *JNMA; Journal of the Nepal Medical Association*, vol. 57, no. 220, pp. 408–411, 2019.
- [5] G. B. Kim, "Reality of Kawasaki disease epidemiology," *Korean Journal of Pediatrics*, vol. 62, no. 8, pp. 292–296, 2019.
- [6] C. Li, Y. Du, H. Wang, G. Wu, and X. Zhu, "Neonatal Kawasaki disease: case report and literature review," *Medicine (Baltimore)*, vol. 100, no. 7, article e24624, 2021.
- [7] E. Rife and A. Gedalia, "Kawasaki disease: an update," *Current Rheumatology Reports*, vol. 22, no. 10, p. 75, 2020.
- [8] Y. Lin, Y. Li, J. Ma, A. Li, Y. Liu, and L. Shi, "Aspirin-induced delayed urticaria in children with Kawasaki disease: a retrospective case-control study," *International Journal of General Medicine*, vol. Volume 14, pp. 8211–8216, 2021.
- [9] F. Sanati, M. Bagheri, S. Eslami, and A. Khalooei, "Evaluation of high-dose aspirin elimination in the treatment of Kawasaki disease in the incidence of coronary artery aneurysm," *Annals of Pediatric Cardiology*, vol. 14, no. 2, pp. 146–151, 2021.
- [10] A. P. Cadavid, "Aspirin: the mechanism of action revisited in the context of pregnancy complications," *Frontiers in Immunology*, vol. 8, p. 261, 2017.
- [11] H. Helgadottir, T. Tropea, S. Gizurarson, and M. Mandala, "Endothelium-derived hyperpolarizing factor (edhf) mediates acetylsalicylic acid (aspirin) vasodilation of pregnant rat mesenteric arteries," *International Journal of Molecular Sciences*, vol. 22, no. 18, p. 10162, 2021.
- [12] C. Galeotti, S. V. Kaveri, R. Cimaz, I. Kone-Paut, and J. Bayry, "Predisposing factors, pathogenesis and therapeutic intervention of Kawasaki disease," *Drug Discovery Today*, vol. 21, no. 11, pp. 1850–1857, 2016.
- [13] P. Buda, J. Friedman-Gruszczynska, and J. Ksiazek, "Anti-inflammatory treatment of Kawasaki disease: comparison of current guidelines and perspectives," *Frontiers in Medicine*, vol. 8, article 738850, 2021.
- [14] T. Li, J. Feng, N. Li, and T. Liu, "Correct identification of incomplete Kawasaki disease," *The Journal of International Medical Research*, vol. 49, 2021.
- [15] B. O. Kilic, S. Baysun, T. C. Goksen, I. Akinbingol, and Z. Arslan, "An unusual presentation of Kawasaki disease: gallbladder hydrops and acute cholestatic hepatitis," *Case Reports in Medicine*, vol. 2018, Article ID 4930234, 2 pages, 2018.
- [16] B. Hu, Y. Li, G. Wang, and Y. Zhang, "The blood gene expression signature for Kawasaki disease in children identified with advanced feature selection methods," *BioMed Research International*, vol. 2020, Article ID 6062436, 6 pages, 2020.
- [17] B. W. McCrindle, A. H. Rowley, J. W. Newburger et al., "Diagnosis, treatment, and long-term management of Kawasaki disease: a scientific statement for health professionals from the American Heart Association," *Circulation*, vol. 135, p. e927, 2017.
- [18] I. Mohammadzadeh, S. Noei, K. Babazadeh, H. Zamani, R. Barari-Savadkoohi, and R. Alizadeh-Navaei, "Comparison of early and late intravenous gamma globulin treatment of Kawasaki disease on fever and cardiovascular complications," *Caspian Journal of Internal Medicine*, vol. 7, no. 3, pp. 211–216, 2016.
- [19] C. H. Lu, C. W. Fang, H. M. Chen et al., "Prescribing patterns of coronary artery aneurysm in Taiwan," *BMC Cardiovascular Disorders*, vol. 19, no. 1, p. 188, 2019.

- [20] H. Qiu, C. Jia, Z. Wang et al., “Prognosis and risk factors of coronary artery lesions before immunoglobulin therapy in children with Kawasaki disease,” *Balkan Medical Journal*, vol. 37, no. 6, pp. 324–329, 2020.
- [21] H. Huang, J. Jiang, X. Shi et al., “Nomogram to predict risk of resistance to intravenous immunoglobulin in children hospitalized with Kawasaki disease in eastern China,” *Annals of Medicine*, vol. 54, no. 1, pp. 442–453, 2022.
- [22] J. Hu and W. Ren, “Analysis of the risk factors in prognosis of Kawasaki disease with coronary artery lesions,” *Frontiers in Pediatrics*, vol. 9, article 798148, 2021.

Research Article

Application Value of Evidence-Based Care in Patients with Lung Cancer Chemotherapy

Ying Chen,¹ Hong Xu,¹ Yun Cheng,¹ and Yuan Qian ²

¹Tumor Building, Affiliated Hospital of Jiangnan University, Wuxi City, 214061 Jiangsu Province, China

²Tumor Building, Nursing Department, Affiliated Hospital of Jiangnan University, Wuxi City, 214061 Jiangsu Province, China

Correspondence should be addressed to Yuan Qian; money528-yuan@sohu.com

Received 8 June 2022; Revised 6 July 2022; Accepted 11 July 2022; Published 30 July 2022

Academic Editor: Pan Zheng

Copyright © 2022 Ying Chen et al. This is an open access article distributed under the Creative Commons Attribution License, which permits unrestricted use, distribution, and reproduction in any medium, provided the original work is properly cited.

Objective. The present research project is aimed at elucidating the application value of evidence-based care (EBC) in patients with lung cancer (LC) chemotherapy. **Methods.** Ninety-four advanced LC patients visited between March 2019 and February 2021 were retrospectively selected. Based on the type of care, 44 cases who used routine nursing were set as the control group (CG), and 50 patients who received EBC were included in the research group (RG). The pain degree, adverse mood, and individual fatigue of patients were assessed, using the Visual Analogue Scale (VAS), Self-Rating Anxiety/Depression Scale (SAS/SDS), and Cancer Fatigue Scale (CFS), respectively. Besides, patients were assessed for treatment compliance, self-efficacy, and life quality using the treatment compliance questionnaire, General Self-Efficacy Scale (GSES), and Quality of Life Questionnaire Core 30 (QLQ-C30), respectively. **Results.** The VAS, SAS, and SDS scores were lower in RG versus CG after nursing intervention. RG scored lower in the dimensions of physical, affective, and cognitive fatigue in terms of individual fatigue assessed by the CFS and higher in various domains of the QLQ-C30 score after nursing intervention. Besides, higher treatment compliance and self-efficacy were determined in RG as compared to CG. **Conclusions.** In addition to improving the treatment compliance, self-efficacy, and life quality of patients with LC chemotherapy, EBC can effectively alleviate their pain, adverse psychological mood, and individual fatigue, which deserves to be promoted in clinical application.

1. Introduction

Lung cancer (LC) is a fatal cancer represented by non-small-cell lung cancer (NSCLC), which causes approximately 2 million deaths worldwide every year [1]. The disease, originated from the bronchial epithelium or glands of the lungs, has the characteristics of high incidence and recurrence rate, with a five-year survival of merely 16.6% [2]. LC patients generally present with no obvious early symptoms, resulting in the fact that most of them are diagnosed in the middle and late stages with clinical presentations such as chest pain, hemoptysis, cough, and dyspnea [3]. Chemotherapy, a common treatment for patients with advanced LC, may also lead to adverse emotions such as irritability, depression, and cancer-related fatigue [4, 5], all of which will not only exert varying degrees of negative effects on the self-efficacy and life quality of LC patients undergoing chemotherapy but also reduce patients' treatment compliance that lowers their

treatment compliance [6, 7]. This puts forward a demand for the management optimization of patients with LC chemotherapy, and exploring an effective and reliable high-quality nursing model is of positive significance for the rehabilitation of such patients [8].

Routine nursing intervention for LC patients undergoing chemotherapy often neglects psychological support, comfort care, pain threshold management, etc., which is difficult to mobilize patients' confidence to overcome the disease, resulting in a treatment outcome far from satisfactory [9]. Evidence-based care (EBC) is an intervention model that continuously improves nursing guidance and adjusts the practice process based on credible and scientific research results and past clinical experience [10]. Previous studies have shown that EBC has been recognized in different disease settings such as acute cerebral infarction, acute coronary syndrome, and postpartum depression, playing an active part in the treatment of patients, promoting

patients' rehabilitation, and improving their treatment experience [11–13]. In addition, EBC has been applied clinically in LC patients receiving combined chemotherapy, which not only helps to reduce pain but also improves patients' quality of life and clinical satisfaction [14]. Nowadays, EBC has become a global nursing standard, which has the necessity and guiding advantages for healthcare systems, patients, and medical staff. However, its application in nursing practice is still relatively slow [15]. Therefore, in this study, we will compare the application value of EBC with conventional nursing in patients with LC chemotherapy, so as to verify its application advantages in such a medical background, and make a contribution to the clinical promotion of EBC and the management optimization of patients with LC chemotherapy.

2. Materials and Methods

2.1. General Case Data. This research was conducted after obtaining approval from the Affiliated Hospital of Jiangnan University Ethics Committee. Ninety-four advanced LC patients visited between March 2019 and February 2021 were retrospectively selected and grouped according to different nursing patterns, with 44 cases receiving conventional care included in the control group (CG) and 50 cases receiving EBC assigned to the research group (RG). CG included 24 males and 20 females, with an average age of 59.86 ± 8.37 years and a disease course of 4.66 ± 2.03 years, while RG was composed of 29 males and 21 females that averagely aged 60.18 ± 10.68 with a disease course of 4.84 ± 2.24 years. The two cohorts were comparable in gender, age, disease course, and other general data ($P > 0.05$). The subjects not only knew the research purpose but also signed and provided the informed consent form.

2.2. Eligibility Criteria. The following are the inclusion criteria: diagnosis of advanced LC, age ≥ 18 , voluntary chemotherapy and regular treatment in our hospital, normal cognitive and communication skills, in line with the chemotherapy indications, and life expectancy > 6 months.

The following are the exclusion criteria: severe organ diseases, other malignant tumors, presence of mental illness or history of mental illness, and patients with limited mobility or otherwise unable to complete all methods of care. The patient selection flowchart can be seen in Figure 1.

2.3. Nursing Measures. CG received routine care. Patients were required to follow the doctor's instructions for appropriate treatment and care. During the treatment, the nursing staff paid close attention to patients' vital signs and made strict records and gave pain-relieving and targeted interventions to those with severe pain and complications. Meanwhile, the nurses distributed disease guidebooks to patients, patiently imparting their knowledge of health education and explaining precautions related to disease and treatment.

RG received EBC, the details of which are as follows:

- (1) Team building and scheme formulation: an EBC team composed of professional nurses and doctors

was set up, and the team members were given professional training in EBC. Members of the team recorded patients' clinical data, reviewed relevant literature, and understood patients' nursing needs to develop reasonable nursing plans for them based on professional knowledge and disease analysis

- (2) Summary of nursing experience: according to previous medical records of LC patients undergoing chemotherapy, the possible complications, treatment methods, and corresponding causes of complications were summarized, and nursing experience was summed up to find potential solutions
- (3) Health education: health education related to disease and chemotherapy was given to patients, and the characteristics, symptoms, treatment, prognosis, and other knowledge related to LC were told to patients in an easy-to-understand language, so as to establish disease-related awareness for patients to cope with the disease more calmly. Prior to receiving chemotherapy, patients were popularized about chemotherapy drugs and frequency of use and other related information. Moreover, the medical staff patiently listened to and answered the questions raised by patients
- (4) Nursing of complications: according to the related risk factors and past pathology of patients with LC chemotherapy, preventive measures were taken to minimize the risk of complications
- (5) Psychological nursing: patients were given personalized psychological interventions taking their family, educational background, and disease development into consideration. Through strengthening communication, patients' emotions were appeased in time to reduce their psychological pressure. And by giving positive psychological hints and encouragement, patients were helped to build confidence in overcoming diseases and eliminate negative emotions and resistance to treatment as far as possible
- (6) Pain care: pain assessment was performed on all the enrolled patients. Besides, patients were briefed on pain and pharmacological remission and were told to follow the doctor's advice to take analgesics. The pain threshold of patients was also raised through distraction when they were in pain
- (7) Posture nursing: the medical staff gave patients guidance on postures and appropriately assisted patients to be in a comfortable position to avoid pressure ulcers
- (8) Exercise and diet care: patients were given scientific and appropriate exercise guidance based on their personal information and condition, so as to help them improve immunity and accelerate recovery. In addition, nurses gave corresponding dietary guidance to patients according to their eating habits and

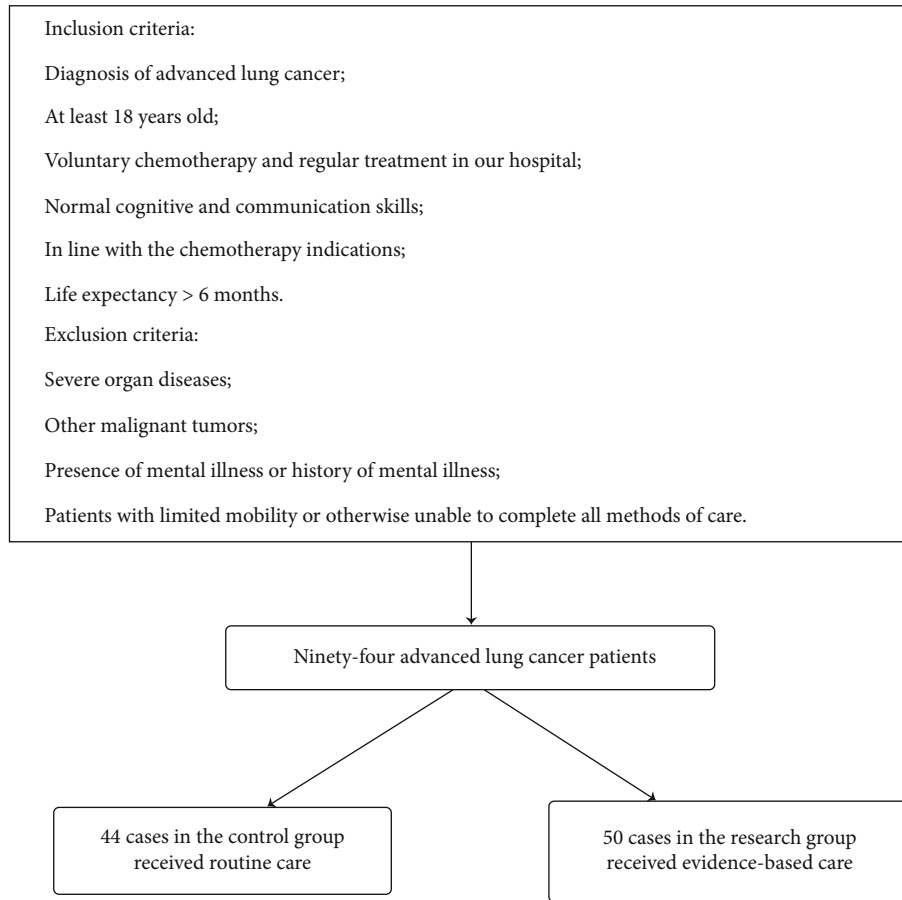


FIGURE 1: Patient selection flowchart.

advised them to eat more high-protein foods and fruits

- (9) Discharge guidance: upon discharge, patients were instructed to take medicine scientifically and avoid increasing or decreasing the dosage or discontinuing the drugs by themselves. Besides, they were reminded that optimistic attitude, peaceful mood, and good living habits were the keys to stabilizing the condition and promoting rehabilitation. Patients were also told to see a doctor in time in case of any abnormalities

2.4. Endpoints

- (1) Degree of pain: the Visual Analogue Scale (VAS) [16], with a score of 0-10 and the score directly proportional to the pain degree, was used for pain assessment
- (2) Adverse mood: the Self-Rating Anxiety/Depression Scale (SAS/SDS) [17], both with a score ranging from 0 to 100 and the score directly proportional to negative emotions, were adopted for adverse mood evaluation

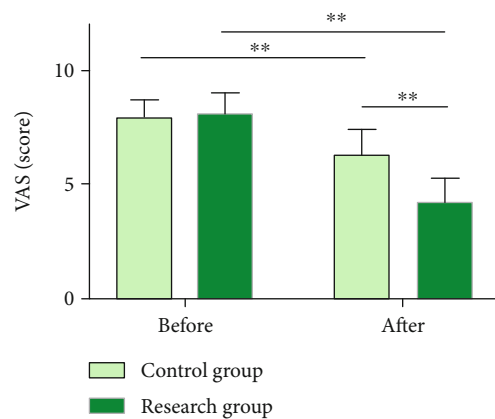


FIGURE 2: Pain levels of patients with lung cancer undergoing chemotherapy. The VAS score of the research group after nursing was significantly lower than that before nursing and the control group. Note: $**P < 0.01$. Independent sample *t*-test was used for data comparison between groups and paired *t*-test for data comparison before and after nursing.

- (3) Individual fatigue: the Cancer Fatigue Scale (CFS) [18], which included three dimensions of physical (0-28 points), emotional (0-16 points), and cognitive

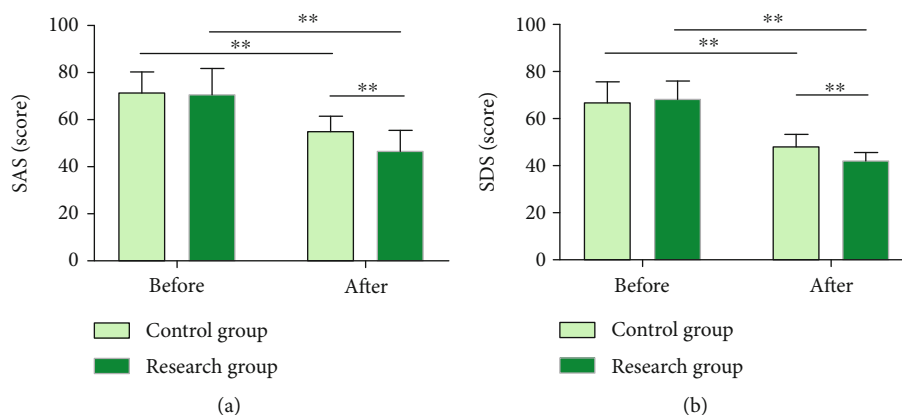


FIGURE 3: SAS and SDS scores of patients with lung cancer undergoing chemotherapy. (a) The SAS score of the research group after nursing was lower than that before treatment and the control group. (b) The SDS score of the research group after nursing was lower than that before treatment and the control group. Note: $**P < 0.01$. Data comparison between groups and that before and after nursing were performed by independent sample t -test and paired t -test, respectively.

fatigue (0-16 points), was employed for individual fatigue assessment. The score was positively related to the degree of fatigue

- (4) Treatment compliance: patients' treatment compliance was evaluated by the questionnaire of treatment compliance. Complete compliance was indicated if the patient was highly cooperative with the guidance of nurses and completed the guidance on time; basic cooperation with the guidance of nurses was regarded as partial compliance; failure to cooperate fully with the nursing staff and avoidance of nursing guidance is considered noncompliance
- (5) Self-efficacy: patients' self-efficacy was assessed by the General Self-Efficacy Scale (GSES) [19], a measurement with a score ranging from 0 to 145 and the score positively proportional to the level of self-efficacy
- (6) Life quality: the Quality of Life Questionnaire Core 30 (QLQ-C30) was used to evaluate patients' quality of life from five domains [20]: role, physical, social, cognitive, and emotional functioning. The score of each domain ranges from 0 to 100, and the score is proportional to the quality of life level

Among the above measures, the degree of pain, adverse mood, and individual fatigue were primary endpoints, while the others were secondary endpoints. In addition, all the above indicators were tested before and 6 months after nursing.

2.5. Statistics and Methods. GraphPad Prism 6 (GraphPad Software, San Diego, USA) was used for data analysis and image export. The counting data were represented as case/percentage (n (%)), and a chi-square test was employed for intergroup comparisons. Denoted by mean \pm SD, the measurement data were compared by independent sample t -test

between groups and by the paired t -test among different time periods. A significance level of $P < 0.05$ was used in all analyses.

3. Results

3.1. EBC Effectively Alleviates Pain of Patients with LC Chemotherapy. We compared and analyzed the pain levels of two groups of patients after nursing intervention by the VAS (Figure 2), in order to evaluate the impact of the two nursing methods on the relief of pain symptoms in patients with LC chemotherapy. The results showed no significant difference in VAS scores between groups prior to intervention ($P > 0.05$), while significant pain relief was observed in both cohorts after intervention ($P < 0.01$), with lower VAS scores in RG as compared to CG ($P < 0.01$).

3.2. EBC Significantly Mitigates Adverse Mood in LC Patients Undergoing Chemotherapy. SAS and SDS scores in both groups were recorded before and after nursing intervention (Figure 3). Similarly, the two scores were nonsignificantly different between groups prior to intervention ($P > 0.05$) and decreased notably in both cohorts after that ($P < 0.01$). The postintervention SAS and SDS scores were statistically lower in RG versus CG ($P < 0.01$).

3.3. EBC Significantly Reduces Individual Fatigue Degree and Improves Self-Efficacy of LC Patients Undergoing Chemotherapy. We evaluated patients' individual fatigue level and self-efficacy after nursing intervention by using CFS and GSES, respectively (Figure 4). The two scores differed insignificantly between groups before intervention ($P > 0.05$), while after intervention, the scores of physical, emotional, and cognitive fatigue in terms of individual fatigue assessed by the CFS were lower ($P < 0.05$) and the GSES score was higher in RG ($P < 0.01$), with statistical significance as compared to CG.

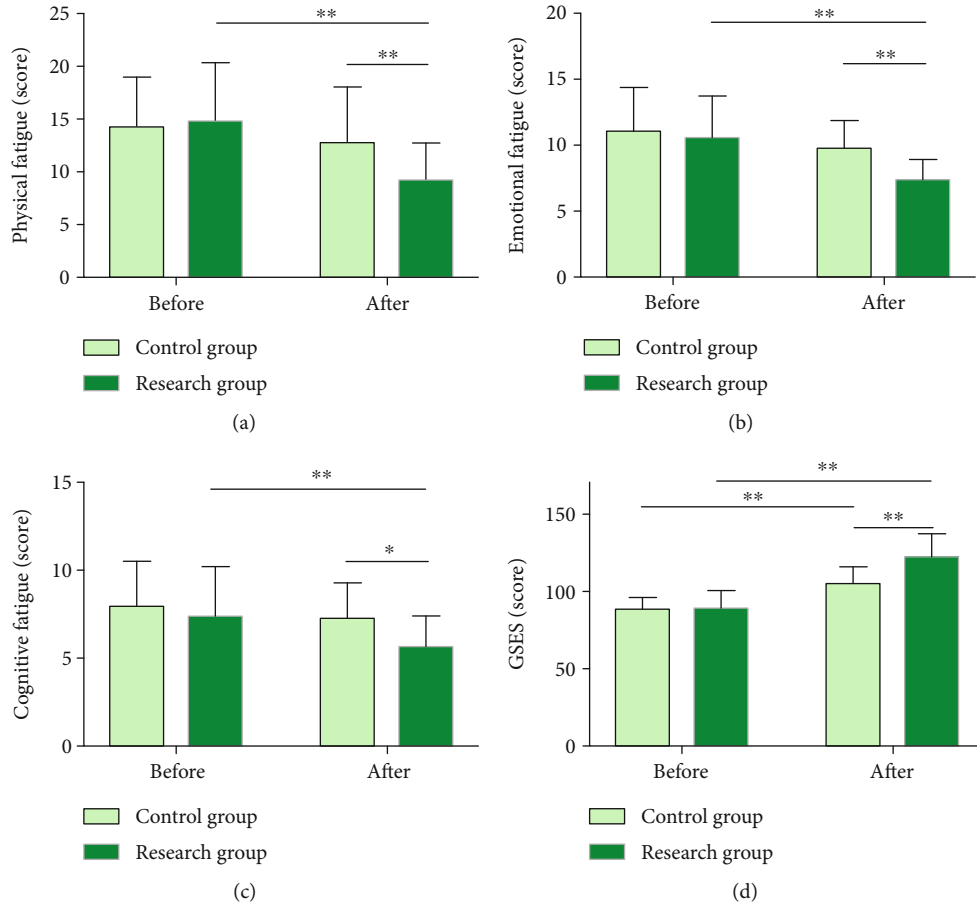


FIGURE 4: CFS and GSES scores of patients. (a) Physical fatigue scores of two groups of patients after nursing intervention. (b) Emotional fatigue scores of two groups of patients after nursing intervention. (c) Cognitive fatigue scores of two groups of patients after nursing intervention. (d) GSES scores of two groups of patients after nursing intervention. Note: * $P < 0.05$ and ** $P < 0.01$. Data comparison between groups and that before and after nursing was performed by independent sample t -test and paired t -test, respectively.

3.4. *EBC Significantly Improves Treatment Compliance of Patients with LC Chemotherapy.* Patients' compliance with treatment was evaluated through the compliance questionnaire (Table 1). RG using EBC was found with higher treatment compliance than CG treated with routine care ($P < 0.05$).

3.5. *EBC Effectively Enhances Life Quality of Patients with LC Chemotherapy.* The QLQ-C30 scores were measured before and after intervention to analyze the impact of the two models of care on patients' life quality (Figure 5). The data also determined no statistical difference in QLQ-C30 scores between groups prior to intervention ($P > 0.05$), while the score of each domain of the QLQ-C30 in RG after intervention was significantly higher than that before intervention and CG ($P < 0.01$).

4. Discussion

LC is one of the prime reasons for global cancer-related deaths, with most patients being not diagnosed at an early stage due to the presence of nonspecific clinical manifestations [21]. The common clinical treatments for patients with

TABLE 1: Treatment compliance of two groups (n (%)).

Groups	n	Complete compliance	Partial compliance	Noncompliance
CG	44	18 (40.91)	14 (31.82)	12 (27.27)
RG	50	28 (56.00)	18 (36.00)	4 (8.00)
χ^2 value	—	6.317		
P value	—	0.043		

Note: data differences between groups were analyzed by the chi-square test.

nonearly LC are radiotherapy and chemotherapy [22]. Although chemotherapy provides some benefits for LC patients, it may also lead to more serious complications that make patients overwhelmed [23], which will further affect their confidence to overcome the disease and cause certain psychological pressure, posing varying degrees of threat to patients' treatment compliance and self-efficacy [24]. We believe that providing high-quality EBC services to patients with LC chemotherapy will be more conducive to promoting their recovery, and we hereby report our findings.

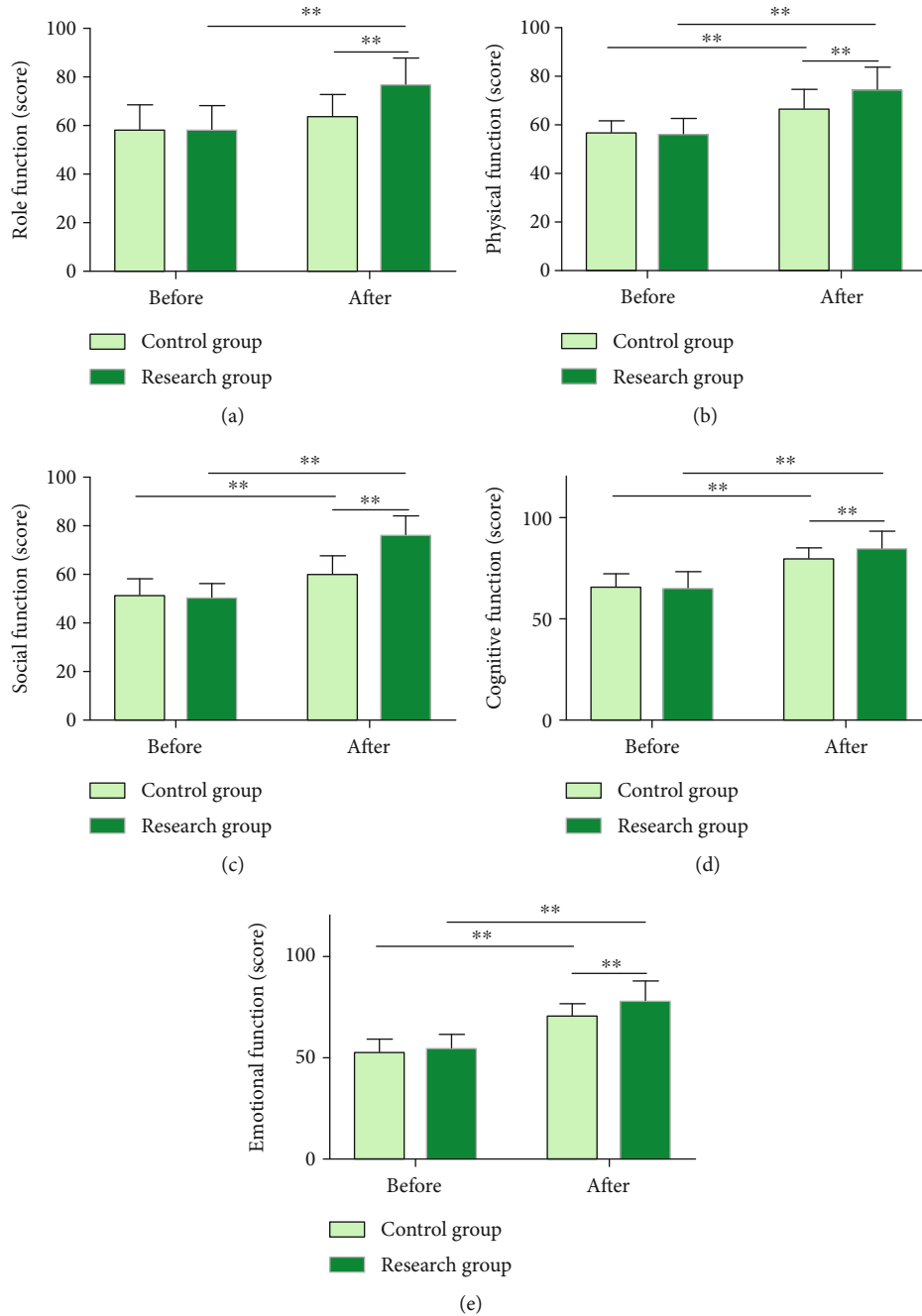


FIGURE 5: Quality of life scores of lung cancer patients undergoing chemotherapy. (a) Role function scores of two groups of patients after intervention. (b) Physical function scores of two groups of patients after intervention. (c) Social function scores of two groups of patients after intervention. (d) Cognitive function scores of two groups of patients after intervention. (e) Emotional function scores of two groups of patients after intervention. Note: $**P < 0.01$. Data comparison between groups and that before and after nursing was performed by independent sample t -test and paired t -test, respectively.

LC patients will experience physiological pain caused by chemotherapy during the treatment process. In addition, chemotherapy will kill a large number of healthy cells while destroying cancer cells, which will lead to decreased immunity, organ dysfunction, nausea, vomiting, fatigue, hair loss, and other adverse events [25, 26]. In our study, both nursing methods played a certain role in relieving pain in patients with LC chemotherapy, but the VAS score of RG under

EBC intervention was significantly lower compared with CG, suggesting that EBC has better pain-relieving effects than conventional nursing for such patients, consistent with the study of Liu et al. [14]. In the research of Zhang et al. [27], it is also pointed out that EBC is helpful to alleviate the eating pain of children with severe hand-foot-mouth disease. This is because under EBC intervention, medical staff will not only give pain assessment and analgesics but also

conduct pain threshold and in vitro management of patients, all of which contributes to minimized pain degree in patients [28]. On the other hand, LC patients are prone to adverse mood after receiving chemotherapy, which is not only detrimental to the patient's recovery but also adversely affects treatment compliance, leading to an increased risk of relapse [29]. We observed lower SAS and SDS scores in RG after nursing compared with CG, indicating that EBC can significantly improve the adverse psychology of patients with LC chemotherapy, similar to the findings of Shen et al. [28]. EBC for LC patients undergoing chemotherapy also includes interventions for psychological disorders. Medical staff will provide personalized psychological interventions in combination with patients' personal information and do their best to help relieve patients' psychological stress and other adverse mood. In terms of individual fatigue and self-efficacy, RG exhibited lower CFS scores in the dimensions of physical, emotional, and cognitive fatigue than CG, as well as higher GSES scores, demonstrating that EBC is helpful to mitigate individual fatigue and enhance self-efficacy of LC patients undergoing chemotherapy. In addition, RG that received the EBC intervention also demonstrated higher treatment adherence. The above results are all consistent with those reported by Zhang et al. [30]. Under EBC, LC patients can gain a higher sense of self-esteem, because medical staff give patient responses, as well as disease-related cognition popularization, exercise, diet, and discharge guidance. Undoubtedly, professional support in all of the above aspects exerts positive effects on the alleviation of individual patient fatigue, and improvement self-efficacy, treatment compliance, and quality of life. Finally, through the QLQ-C30 scale, we also confirmed that the QLQ-C30 score of LC chemotherapy patients under EBC intervention improved more significantly in terms of role, physical, social, cognitive, and emotional functioning, better than the conventional nursing, suggesting that EBC was also significantly superior to conventional nursing in improving patients' quality of life.

Still, there are some limitations to be addressed in this study. First, the analysis of sleep quality and respiratory function of patients with LC chemotherapy should be supplemented to help further understand the potential advantages of EBC. Second, the sample size of the experimental subjects is small, and increasing the sample size will help to further improve the universality of research results. Finally, the evaluation indexes of pain degree, individual fatigue, treatment compliance, self-efficacy, and quality of life of LC patients undergoing chemotherapy are relatively single. The nursing strategy can be further optimized if we can supplement relevant analysis of influencing factors on the treatment compliance of patients with LC chemotherapy. Future studies will be gradually refined from the above angles. In addition, the contribution of this study to the subject area and its novelty is as follows: first, starting from the common negative states of LC patients undergoing chemotherapy, such as pain, adverse mood, and individual fatigue, it is confirmed that EBC has a significant inhibitory effect on the above aspects; that is, it can significantly reduce patients' pain, bad mood, and individual fatigue. Second, in terms of

self-efficacy, treatment compliance, and quality of life, it is proved that EBC has a significant positive impact on the above aspects; namely, it can significantly enhance patients' self-efficacy and treatment compliance, contributing to improved life quality of such patients. The above provides a new theoretical basis for the nursing choice of patients with LC chemotherapy.

All in all, EBC is effective in the treatment of patients with LC chemotherapy, which can significantly reduce their pain and discomfort, relieve adverse mood and individual fatigue, and improve their treatment compliance, self-efficacy, and quality of life.

Data Availability

The labeled datasets used to support the findings of this study are available from the corresponding author upon request.

Conflicts of Interest

The authors declare no competing interests.

Acknowledgments

This study was funded by the Wuxi Municipal Health Commission, MS201928, Study on the effect of memory training under intelligent software on cognitive impairment in patients with whole brain radiotherapy.

References

- [1] A. Gonzalez-Marron, J. C. Martin-Sanchez, Q. Miro et al., "Relation between tobacco control policies and population at high risk of lung cancer in the European Union," *Environmental Research*, vol. 179, article 108594, 2019.
- [2] Y. Li, L. Zu, H. Wu et al., "MiR-192/NKRF axis confers lung cancer cell chemoresistance to cisplatin via the NF- κ B pathway," *Thorac Cancer*, vol. 13, no. 3, pp. 430–441, 2022.
- [3] M. E. Cooley, E. Mazzola, N. Xiong et al., "Clinical decision support for symptom management in lung cancer patients: a group rct," *Journal of Pain and Symptom Management*, vol. 63, no. 4, pp. 572–580, 2022.
- [4] L. Zhao, P. Shi, X. Xiong, and J. Zeng, "Nonpharmacological interventions for cancer-related fatigue in lung cancer patients: a protocol for an evidence map of overview of a network meta-analysis of existing trials," *Medicine*, vol. 100, no. 32, article e26864, 2021.
- [5] X. Lv, Y. Zhao, and Y. Wu, "Effects of the training of aerobic function on clinical symptoms and quality of life in patients with medium and advanced lung cancer," *Journal of Healthcare Engineering*, vol. 2022, 2022.
- [6] J. Mou and S. Zheng, "Effects of adopt-based breathing training combined with continuous nursing on quality of life, mental health, and self-efficacy in lung cancer patients undergoing chemotherapy: based on a retrospective cohort study," *Computational and Mathematical Methods in Medicine*, vol. 2022, 2022.
- [7] B. H. Kim, J. S. Kim, K. H. Kim, H. J. Moon, and S. Kim, "Clinical significance of radiation dose-volume parameters and functional status on the patient-reported quality of life changes

- after thoracic radiotherapy for lung cancer: a prospective study," *La Radiologia Medica*, vol. 126, no. 3, pp. 466–473, 2021.
- [8] J. Yu, T. Huang, J. Xu, J. Xiao, Q. Chen, and L. Zhang, "Effect of nursing method of psychological intervention combined with health education on lung cancer patients undergoing chemotherapy," *Journal of Healthcare Engineering*, vol. 2022, 2022.
- [9] S. Yang, L. Zheng, Y. Sun, and Z. Li, "Effect of network-based positive psychological nursing model combined with elemene injection on negative emotions, immune function and quality of life in lung cancer patients undergoing chemotherapy in the era of big data," *Frontiers in Public Health*, vol. 10, article 897535, 2022.
- [10] S. Y. Ma, "Evaluating the impact of evidence-based nursing in combination with clinical nursing pathway for nursing care of patients with stroke," *Medicine*, vol. 101, no. 2, article e28278, 2022.
- [11] Y. Liu, M. Qu, N. Wang, and L. Wang, "Effects of an evidence-based nursing intervention on neurological function and serum inflammatory cytokines in patients with acute cerebral infarction: a randomized controlled trial," *Restorative Neurology and Neuroscience*, vol. 39, no. 2, pp. 129–137, 2021.
- [12] J. Meng, J. Du, X. Diao, and Y. Zou, "Effects of an evidence-based nursing intervention on prevention of anxiety and depression in the postpartum period," *Stress and Health*, 2021.
- [13] J. Liu, Z. Zhong, S. Ou, and K. Peng, "Application effect of evidence-based nursing in perioperative period of acute coronary syndrome," *American Journal of Translational Research*, vol. 13, pp. 2653–2661, 2021.
- [14] S. Liu, X. Huang, J. Wen, F. Fu, and H. Wang, "Application of evidence-based nursing intervention in the treatment of advanced squamous cell carcinoma of the lung by erlotinib combined with tegafur, gimeracil, and oteracil potassium and its influence on quality of life," *Journal of Healthcare Engineering*, vol. 2021, Article ID 6801779, 2021.
- [15] Y. Zhou and X. Li, "Effect assessment of the application value of evidence-based nursing intervention in operating room nursing: a protocol for a systematic review and meta-analysis," *Medicine*, vol. 100, no. 32, article e26867, 2021.
- [16] H. Tang, L. Chen, Y. Wang, Y. Zhang, N. Yang, and N. Yang, "The efficacy of music therapy to relieve pain, anxiety, and promote sleep quality, in patients with small cell lung cancer receiving platinum-based chemotherapy," *Support Care Cancer*, vol. 29, no. 12, pp. 7299–7306, 2021.
- [17] W. Wang, G. Lou, and Y. Zhang, "Olanzapine with ondansetron and dexamethasone for the prevention of cisplatin-based chemotherapy-induced nausea and vomiting in lung cancer," *Medicine*, vol. 97, no. 37, article e12331, 2018.
- [18] X. Wang and J. You, "Treating cancer-related fatigue after chemotherapy in lung cancer patients by yiqi jianpi recipe: a clinical study," *Zhongguo Zhong Xi Yi Jie He Za Zhi*, vol. 35, no. 9, pp. 1069–1073, 2015.
- [19] Q. Deng, L. Kang, S. Zhu et al., "Effects of nursing based on Orem's self-care model on self-care efficacy, quality of life and adverse emotions in patients with advanced lung cancer," *American Journal of Translational Research*, vol. 13, no. 4, pp. 2983–2989, 2021.
- [20] X. F. Liu, H. Lin, Q. Wang et al., "Drug-eluting bead bronchial arterial chemoembolization vs. chemotherapy in treating advanced non-small cell lung cancer: comparison of treatment efficacy, safety and quality of life," *European Review for Medical and Pharmacological Sciences*, vol. 25, pp. 2554–2566, 2021.
- [21] A. Romaszko, E. Swietlik, A. Doboszynska, P. Szpruch, and J. Luks, "Lung cancer and multiple neoplasms: a retrospective analysis," *Advances in Experimental Medicine and Biology*, vol. 911, pp. 53–58, 2016.
- [22] B. Dong, J. Wang, X. Zhu et al., "Comparison of the outcomes of stereotactic body radiotherapy versus surgical treatment for elderly (≥ 70) patients with early-stage non-small cell lung cancer after propensity score matching," *Radiation Oncology*, vol. 14, no. 1, p. 195, 2019.
- [23] A. Pearce, M. Haas, R. Viney et al., "Incidence and severity of self-reported chemotherapy side effects in routine care: a prospective cohort study," *PLoS One*, vol. 12, no. 10, article e0184360, 2017.
- [24] R. T. Jomar, R. A. F. Gomes, D. C. Leite, H. F. Gomes, E. M. Peres, and E. F. P. Junior, "Nursing diagnoses in adult/elderly patients undergoing outpatient antineoplastic chemotherapy: a review," *Ecancer Medical Science*, vol. 11, p. 736, 2017.
- [25] M. Quist, S. W. Langer, C. Lillelund et al., "Effects of an exercise intervention for patients with advanced inoperable lung cancer undergoing chemotherapy: a randomized clinical trial," *Lung Cancer*, vol. 145, pp. 76–82, 2020.
- [26] C. H. Wright, J. Wright, G. Cioffi et al., "Association of cancer center type with treatment patterns and overall survival for patients with sacral and spinal chordomas: an analysis of the national cancer database from 2004 to 2015," *Journal of Neurosurgery. Spine*, vol. 32, pp. 311–320, 2019.
- [27] Z. Zhang, M. Dong, Y. Han et al., "Application effect of medical care integration combined with family intervention under the evidence-based nursing mode on child patients with severe hand-foot-mouth disease and its influence on intestinal function," *Evidence-based Complementary and Alternative Medicine*, vol. 2021, 2021.
- [28] Y. Shen, Y. Zhou, J. Hou, and J. Hu, "Application effects of evidence-based nursing in pain nursing of advanced lung cancer," *American Journal of Translational Research*, vol. 13, no. 8, pp. 9479–9484, 2021.
- [29] C. Zhou, J. Tang, F. Sun, L. Huang, M. Liu, and D. Kuang, "Continuity of care plus whole process psychological intervention for lung cancer patients undergoing chemotherapy," *Evidence-based Complementary and Alternative Medicine*, vol. 2022, 2022.
- [30] T. Zhang, J. Lu, Y. Fan, and L. Wang, "Evidence-based nursing intervention can improve the treatment compliance, quality of life and self-efficacy of patients with lung cancer undergoing radiotherapy and chemotherapy," *American Journal of Translational Research*, vol. 14, no. 1, pp. 396–405, 2022.

Research Article

Tandem Mass Tag Analysis of the Effect of the Anterior Cingulate Cortex in Nonerosive Reflux Disease Rats with Shugan Jiangni Hewei Granules Treatment

Tianzuo Wang,¹ Jing Li,² Yuebo Jia,¹ Jiaqi Zhao,¹ Meijun He,¹ and Guang Bai² 

¹Liaoning University of Traditional Chinese Medicine, Shenyang, Liaoning 110847, China

²Department of Gastroenterology, Affiliated Hospital of Liaoning University of Traditional Chinese Medicine, Shenyang, Liaoning 110033, China

Correspondence should be addressed to Guang Bai; 18004018638@163.com

Received 10 June 2022; Revised 7 July 2022; Accepted 11 July 2022; Published 30 July 2022

Academic Editor: Pan Zheng

Copyright © 2022 Tianzuo Wang et al. This is an open access article distributed under the Creative Commons Attribution License, which permits unrestricted use, distribution, and reproduction in any medium, provided the original work is properly cited.

Objective. The current study aims to analyze the improvement mechanism of visceral hypersensitivity (VH) and targets of Shugan Jiangni Hewei granules (SJHG) for nonerosive reflux disease (NERD) treatment as well as to offer an experimental foundation for its clinical use. **Methods.** Healthy male Sprague–Dawley rats ($n = 36$) were acquired in the current study that was further split into three groups: blank, model, and drug (SJHG). Subsequently, differentially expressed proteins and bioinformatics analysis were performed on the collected tissue samples acquired from the anterior cingulate cortex of the model and SJHG rat groups using a tandem mass tag- (TMT-) based proteomics. Eventually, the obtained data from the bioinformatic analysis was further verified through western blotting. **Results.** From the bioinformatics analysis, only 64 proteins were differentially expressed between the NC and SJHG groups. These molecules were found to be highly expressed in immunological response and neural signal transmission. Finally, we confirmed three therapeutic targets of SJHG, namely, kininogen 1 (Kng1), junctional adhesion molecule A (JAM-A), and the PI3K/Akt signaling pathway. **Conclusions.** SJHG is effective in treating VH, Kng1 and JAM-A may be therapeutic targets of SJHG, and the therapeutic mechanism of SJHG may be realized by influencing immune response or transmission of neural signals.

1. Introduction

Gastroesophageal reflux disease (GERD) is described as a chronic condition via the Montreal Consensus report in which the reflux of stomach contents into the oesophagus causes a variety of linked symptoms, the most prominent of which are acid reflux and heartburn [1]. GERD is very common in the community, and the incidence of GERD in China is 8.2%–17.3% [2, 3]. Current information on the phenotypic manifestations of GERD indicates that there are two main phenotypic manifestations—namely, erosive and nonerosive reflux disease (NERD) [4]. NERD also has symptoms such as acid reflux and heartburn; however, no erosion or damage to the esophageal mucosa was observed with traditional endoscopy [5]. It is worth noting that recent studies found that esophageal-dilated intercellular spaces (DIS)

could be found in NERD patients under electron microscopy [6]. Clinically, the incidence of NERD is significantly higher than that of the other subtype of GERD, accounting for about 70% of GERD cases [7, 8]. Visceral hypersensitivity (VH) is a phenomenon in which the threshold of uncomfortable visceral stimulation or abnormal pain decreases, or the viscera reacts strongly to traumatic stimulation or demonstrates discomfort with physiological stimulation, which is considered to be an important pathological mechanism of NERD [9]. NERD is often accompanied by psychological symptoms such as anxiety, depression, and panic, which are thought to be related to the sensory enhancement triggered by the central mechanism of VH [10, 11]. Interestingly, the effect is mutual; several studies have found that irritability, anxiety, and other psychological effects of long-term stimulation can make the central nervous system

(CNS)—including the anterior cingulate gyrus, amygdala, insula, hypothalamus, prefrontal cortex, and other brain areas—show abnormal activation, thereby aggravating the degree of VH [12, 13]. Mechanical stimulation of the colon results in persistent hyperactivation of the middle cingulate cortex; in acute colitis, downregulation of anterior cingulate cortex excitability successfully attenuates visceral hypersensitivity, anxiety-like behaviors, and visceral motor response [14]. CNS neurons in a VH state demonstrated increased release of a variety of neurotransmitters, which are mostly encapsulated in vesicles for transport [15]. In addition, c-fos is a nucleophosmin whose positive expression is highly correlated with visceral sensitivity and is considered a biomarker of VH [16].

NERD is classified under the umbrella of “swallowing acid” conditions by traditional Chinese medicine (TCM) theory, and its pathogenesis has been defined by liver qi stagnation, stomach discomfort, and adverse stomach qi rising [17]. Clinical manifestations of NERD include belching, throat discomfort, liver depression, and qi stagnation as the primary symptoms. Therefore, Shugan Jiangni Hwei granules (SJHG) were produced as a possible therapeutic agent according to the principle of “disperse and rectify the depressed liver-energy, harmonize the stomach, and regulate vital energy.” Its ingredients include 9 g of Radix Bupleuri (Chaihu), 12 g of Arum Ternatum Thunb (BanXia), 9 g of Chuanxiong Rhizoma (ChuanXiong), 12 g of Aurantii Fructus (ZhiQiao), 12 g of Citrus Reticulata (ChenPi), 9 g of licorice (GanCao), 9 g of Cyperi Rhizoma (XiangFu), 9 g of Inulae Flos (XuanFuHua), 30 g of Reddle (DaiZheShi), and 10 g of Scutellariae Radix (HuangQin) [18]. In our previous study, compared to standard drug therapy, we found that SJHG not only more effectively improved the symptoms of acid reflux and heartburn in NERD patients but also significantly reduced the scores of anxiety and depression in patients [19]. As a result, it was hypothesized that SJHG may cause a decrease in neurosensitivity in NERD patients’ brains. Differentially expressed molecules in the anterior cingulate gyrus were screened via tandem mass tag- (TMT-) labeled proteomics and the activities of these proteins were examined using bioinformatics tools to investigate the possible mechanism of SJHG in enhancing VH in NERD. Eventually, a western blot experiment was performed to confirm essential molecules. The objective of this research was to discover how VH causes NERD in the brain, as well as its possible treatment targets.

2. Materials and Methods

2.1. SJHG Preparation. SJHG is composed of 11 herbal medicines (see Table 1). Tian Jiang Pharmaceutical Co. Ltd. (Jiangsu, China) supplied all of the herbs used in this composition study. The firm produced inspection report certifications for all herbs, and all fulfilled the *Chinese Pharmacopoeia’s* criteria (2020).

2.2. Animals. The experimental animal center of Liaoning University of Traditional Chinese Medicine (no. 210726211100566367), China, provided 40 male Sprague-

TABLE 1: Components of SJHG.

Latin name	Chinese name	Amount used
Radix Bupleuri	Chaihu	9 g
Cyperi Rhizoma	XiangFu	9 g
Arum Ternatum Thunb	BanXia	12 g
Citrus Reticulata	ChenPi	12 g
licorice	GanCao	9 g
Inulae Flos	XuanFuHua	9 g
Aurantii Fructus	ZhiQiao	12 g
Reddle	DaiZheShi	30 g
Scutellariae Radix	HuangQin	10 g
Chuanxiong Rhizoma	ChuanXiong	9 g

Dawley rats (of particular pathogen-free grade, weighing 250 ± 20 g) for this study. The dietary intake of these rats was set as 25 g/day, with unrestricted drinking water access at the experimental animal facility, which had a temperature range of 22°C – 25°C , a relative humidity range of 45–60%, and a light cycle of 12/12 hours. All of the methods for the experiments were carried out in accordance with a plan authorized by the Experimental Animal Ethics Committee of Liaoning University of Traditional Chinese Medicine (animal ethics no. 21000042021049). Eventually, the rats were divided into three research groups randomly after the adaptive feeding for one week. The normal control (NC) group rats were fed generally for four weeks and then received intraperitoneal injections of normal saline on the 14th day of the experiment and a gavage of 1.5 mL normal saline in the last two weeks of the experiment. There was no additional intervention in this group. Separately, rats in a NERD group were treated to chronic random stress for 21 days and were then exposed to 1–2 forms of stress stimulation each day following adaptive feeding for 1 week, as described below: (1) Fasting for <20 h, (2) 17 h of water cut-off, (3) swimming for 5 min at 4°C , (4) 17 h 45° cage tilt, (5) shaking stress (high-speed shaking) for 10 min, (6) binding stress for 2 h, (7) wet cushion material exposure (200 mL of water and 100 g of sawdust) for 5 h, or (8) tail-clamping for 2 min. It was opted to inject ovalbumin (#A8040; Solarbio, Beijing, China) and aluminum hydroxide adjuvant (#77161; Thermo Fisher Scientific, Waltham, MA, USA) mixture with a 1:2 ratio intraperitoneally on day 14 of the experiment. In the NERD group, from week 3, normal saline was administered intragastrically for 14 days. On day 29, esophageal acid perfusion was performed. The methods of esophageal acid infusion were as follows: the rats were fasted for 24 h before acid infusion, and each rat’s head was raised 20° – 30° in the supine position after anesthesia with urethane (IE0570; solarbio, Beijing, China). The abdominal wall was cut open to expose the stomach wall, and a small round hole was cut near the cardia, through which the drainage tube was placed to collect fluid from the perfusion. During the surgical experiment, rats were given morphine (2 mg/Kg) for pain relief after anesthesia. The other end of a single-cavity perfusion tube was attached to a continuous-perfusion pump and was orally put in the oesophagus, fixed

2–3 cm above the oesophagus and stomach junction. Subsequently, for 50 minutes, 10 mL/h of 0.1 mol/L hydrochloric acid (KDX007; Shanghai Kehua Bio-Engineering Co., Shanghai, China) was dropped. Finally, in the SJHG group, at week 3, a gastric gavage was performed with SJHG granular solvent (4 g/kg, the human-equivalent dose) instead of normal saline, while the rest of the process was the same as that in the NERD group. During the experiment, the rats' water intake, hair, and emotional condition were all monitored. Finally, the rats were slaughtered, and substantial pieces of their brains, oesophagus mucosa, and spinal cord were removed for further research.

2.3. Transmission Electron Microscopic Observation. Tissue blocks of ≤ 1 mm³ diameter were immediately cut from the rats' spinal cord and oesophagus after they had been slaughtered by a sharp blade within 1–3 minutes. These blocks were further transferred to an Eppendorf tube containing freshly prepared TEM fixative (G1102, Servicebio, Wuhan, China) for further fixation at 4°C for preservation and transportation before being placed in an ice bath for preservation and transportation. Post-fixation, the tissues were maintained away from light in PB with 0.1 M concentration (pH 7.4) containing 1% OsO₄ at room temperature for 2 hours. The tissue samples were then rinsed thrice with PB after OsO₄ removal for 15 minutes each time.

Using acetone as an intermediate solvent, the dehydration of fixed tissue samples was performed in an ethanol series before being embedded in EMBed 812 resin (90529-77-4; SPI). Furthermore, these resin blocks were cut to a thickness of 60–80 nm using an ultra-microtome (UC7; Leica, Wetzlar, Germany). Afterwards, ultra-pure water was used to rinse thrice with 2% uranium acetate saturated alcohol solution and 2.6% of lead citrate to avoid light and CO₂ staining for 8 minutes. The cuprum grids were initially dried through filter paper and then placed on the grids board to dry overnight. The dried grids were further visualized through a transmission electron microscope and obtained results were saved in image format.

2.4. Immunohistochemical Analysis. Additionally, for histochemistry analysis, 4 m slices of the paraffin tissue block were cut. The c-fos (cat. #11069.1 : 500; Servicebio) antibody drips were prepared in a specific proportion with phosphate-buffered saline on the blocks and incubated overnight at 4°C. The tissue was coated with a secondary antibody that was horseradish peroxidase- (HRP-) labeled (HRP-labeled goat anti-rabbit, cat. #G23303.1 : 200; Servicebio). An automated image analysis system (Servicebio, Wuhan, China) was used to read the tissue measurement area. This system divided the positive grade as 0, 1, 2, and 3 points for without staining, weak positive light yellow, medium positive tan, and strong positive tan, respectively. On the immunohistochemistry slices, these images were obtained employing a tissue slice digital scanner.

2.5. TMT Proteomics. Before being placed into a 5 mL centrifuge tube, the tissue sample was pulverized into cell powder using liquid nitrogen. The cell powder was then sonicated

TABLE 2: The average weight (g) of rats belonged to the normal group and the model group ($\bar{x} \pm s$).

Group	Baseline	14th day	28th day
Normal	270.33 ± 13.05	325.67 ± 12.00	365.25 ± 16.98
Model	275.00 ± 9.682 [#]	327.09 ± 10.45 [#]	333.8 ± 16.61*

thrice on ice with a four volume of lysis buffer (8 M urea, 1% protease inhibitor cocktail) using a high-intensity ultrasonic processor (Scientz, Ningbo, China). The remaining debris was removed by centrifugation at 12,000 g for 10 minutes at 4°C. Finally, the supernatant was collected, and the protein content was measured using a bicinchoninic acid kit, as directed by the manufacturer.

The protein solution was reduced with 5 mM dithiothreitol for 30 min at 56°C whereas was alkylated with 11 mM iodoacetamide for 15 min at room temperature in darkness for digestion. After that, the protein sample was diluted by adding 100 mM TEAB to a urea concentration of <2 M. Finally, trypsin was added at 1 : 50 and a 1 : 100 trypsin-to-protein mass ratio for the overnight and 4 h digestion, respectively. The peptides were then desalted using a C18 SPE column.

The tryptic peptides were first dissolved in 0.5 M of TEAB before being used. After each peptide channel had been tagged with its appropriate TMT reagent (Thermo Fisher Scientific), it was incubated for 2 h at room temperature. For determining the labeling efficiency, five mL of each sample were desalted, pooled, and evaluated via mass spectrometry (MS). Following the evaluation of labeling efficiency, samples were quenched with a 5% hydroxylamine solution. Subsequently, the pooled samples were desalted and dried through Strata X C18 SPE column (Phenomenex, Torrance, CA, USA) and vacuum centrifugation.

The peptides were separated on a 300 Extend C18 column (5 m grain size, 4.6 mm inner diameter, 250 mm length; Agilent Technologies, Santa Clara, CA, USA) using high-pH reversed-phase high-performance LC. The setting for the procedure was set at 9 pH, 8%–32% acetonitrile as the peptide gradient. The 60 components were separated in 1 h, and the peptide was then consolidated into nine components and freeze-dried in a vacuum for future procedures.

The peptides were separated using the EASY-NLC 1200 ultra-high-performance LC system (Thermo Fisher Scientific) after being dissolved by mobile phase A (aqueous solution 2% acetonitrile and containing 0.1% formic acid). The mobile phase was prepared in an aqueous solution having 90% acetonitrile and 0.1% formic acid. The procedure for establishing a liquid-phase gradient was as 7%–22%; 22%–32%; 32%–80%, and 80% B from 0 to 40, 40 to 53 min, 53 to 57 min, 57 to 60 min, respectively. The flow rate remained constant at 500 nL/min. The peptides were separated using an ultra-high-performance liquid-phase system before being fed into an NSI ion source and analyzed with the Q-EXactive HF-X mass spectrometer (Thermo Fisher Scientific). The ion source voltage was set to 2.1 kV, and the peptide parent ions and secondary fragments were identified and analyzed using the high-resolution Orbitrap system. The first- and

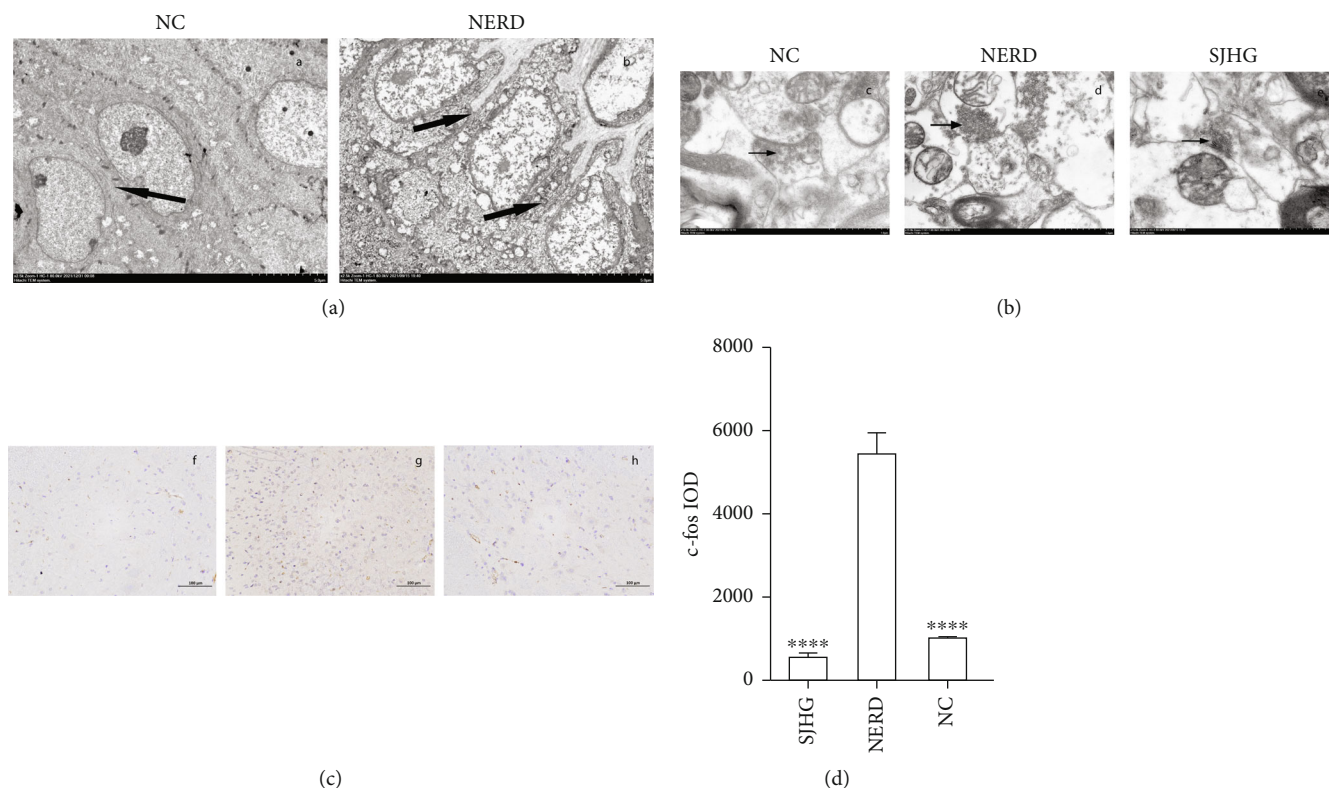


FIGURE 1: Electron microscopy and immunohistochemical results. (a) Intercellular spaces of epithelia of the esophageal mucosa as observed by TEM ($\times 2.5K$). (a. NC group, b. NERD group; black arrows indicate the interstitial space). (b) Synaptic vesicles as observed by TEM ($\times 15K$). (c. NC group, d. NERD group, e. SJHG group; black arrows indicate synaptic vesicles). (c) Expression of *c-fos* protein in the spinal cords of rats (immunohistochemical staining, $\times 200$) (f. group, g. NERD group, h. SJHG group). (d) IOD values of *c-fos* protein in the spinal cord of rats in the 3 groups. *** $P < 0.0001$, compared with the NERD group.

second-level MS scanning ranges were set as 350–1600 m/z , and 100 m/z , with a scanning resolution of 120,000 and 30,000, respectively. Following the completion of the first level of scanning, the parent ions of the top 20 peptide segments in terms of signal strength were selected to enter the high-energy collision dissociation (HCD) collision cell in sequence. During the data-collection mode, they were splintered using 28% of the fragmentation energy. Similarly, the MS analysis at the second level was carried out in this sequence. To reduce the number of times that parent ions were repeatedly scanned, the automatic gain control was set to $1E5$, the signal threshold was set to $8.3E4$ ions/s, the maximum injection length was set to 60 ms, and the dynamic exclusion period of the MS/MS scan was set to 30 seconds.

The MaxQuant search engine (version 1.6.15.0) was used to carry out the processing of the MS/MS data that was produced. These are the settings for the retrieval parameters: the database that was utilized was *Rattus norvegicus* 10116 PR 20210721.fasta (29934 items), and the reverse database was included so that the false-positive rate that is produced by random matching may be determined. A common contamination database has been introduced to the database to reduce the impact of contaminated proteins on the identification findings of the proteins under investigation. Trypsin/P was chosen as a cleavage enzyme because it allows for up

to two missed cleavages to occur. Mass tolerance for precursor ions was set at 20 ppm in the first search and 5 ppm in the main search, while mass tolerance for fragment ions was set at 0.02 Da. The bacterial carbamidomethylation of Cys was characterized as a fixed change, whilst the acetylation of the protein's N-terminal and the oxidation of Met were, respectively, regarded as changeable alterations. The percentage of cases involving false positives has been brought down to 1%.

2.6. Bioinformatics Analysis. Moreover, the UniProt-GOA database (<http://www.ebi.ac.uk/GOA/>) was accessed to retrieve the Gene Ontology (GO) annotation proteome. The IDs were transferred to detected proteins via UniProt identifiers and further mapped to GO identifiers based on the protein identifier. All protein GO functions were annotated using InterProScan for those proteins that failed to be annotated through the UniProt-GOA database. Furthermore, GO annotation for proteins was characterized based on their molecular function, biological process, and cellular component. Additionally, the clustering functional characterization of homologous proteins was performed. The COG (cluster of orthologous groups) refers to the protein lineal homologs in COG/clusters of orthologous groups for eukaryotic complete genomes (KOG) function. COG is a database maintained by the NCBI and classified into two

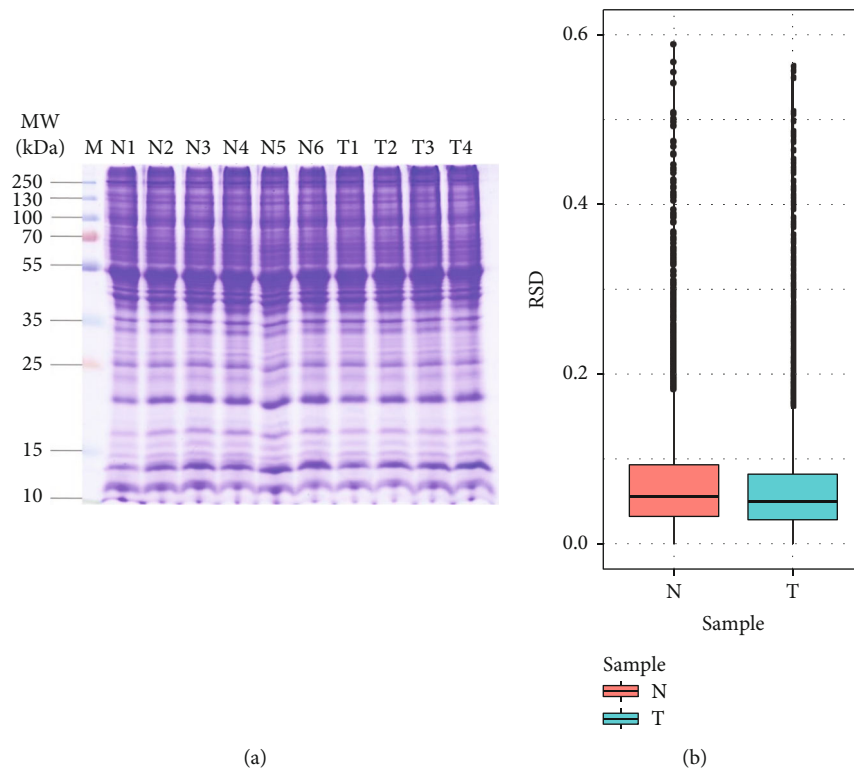


FIGURE 2: Quality control of the samples. (a) SDA-PAGE diagram. (b) Protein RSD distribution between repeated samples. Note: N means model group, T means SJHG group.

categories: prokaryotes (COG database) and eukaryotes (KOG database). Database evaluation and analysis were used to compare and analyze DEPs for COG/KOG functional classification. It was discovered that proteins in eukaryotic tissue cells may attach to certain types of membranes, which allowed to map them to specific parts of the cell. Therefore, the Wolf Psort program was used to annotate the proteins' subcellular locations in the cytoplasm, Golgi apparatus, nuclear matrix, extracellular region, endoplasmic reticulum, ribosome, and vacuole, mitochondria, nucleus, peroxisome, and cytoskeleton.

A protein domain is a segment of a protein with a conserved sequence that can operate independently in most cases. It is made up of 25–500 amino acids and is the structural component of molecular function. These regions are small in size, have a stable structure, and can be folded into functioning structures independently. A domain may be found in numerous proteins, and a domain can be found in multiple proteins. Protein-domain annotation was done for identified proteins in the project data using the Pfam database and the PfamScan program. Protein pathways were annotated using the Kyoto Encyclopedia of Genes and Genomes (KEGG) database. The KAAS server of KEGG was employed to annotate proteins whereas the KEGG mapper was accessed to map the annotation result onto the KEGG pathway database. The bubble plot revealed a considerable enrichment of these annotated DEPs.

At least one ≥ 1 functional classification substantially enriched in the proteome was filtered out ($P < 0.05$) using GO functional classification information and P -value

enrichment of the related proteome. The chosen P -value data matrix was first changed using the $-\log_{10}$ logarithm transformation, and further categorization of different functions was performed through Z transformation. Finally, for unilateral clustering analysis, the hierarchical clustering approach was applied. Additionally, the association among clusters was highlighted as a heat map generated through a `heatmap.2` function from the R package. The horizontal heat map depicts the results of various groups' enrichment tests, while the vertical heat map depicts the description of differentially expressed enrichment-related functions. The degree of enrichment is shown by the DEPs in distinct categories and the accompanying color blocks of functional descriptions such as red and blue color indicate the high and low levels of enrichment.

PPIs were found by searching all DEP sequences or accessions against the STRING (version 11.5) database. Only interactions between proteins in the search data set were used to exclude external candidates. We used STRING's "confidence score" metric to find all interactions with a "high confidence" value of ≥ 0.7 . Subsequently, the R tool `networkD3` was used to display the STRING PPI network.

2.7. Statistical Analysis. The processing and analysis of obtained data were carried out using SPSS 17 (IBM Corporation, Armonk, NY, USA). It was determined to express the measurement data in terms of the mean \pm standard error of the mean values. To compare the features of the samples between the two groups, Student's t -test was utilized. $P < 0.05$ was considered a statistically significant cutoff.

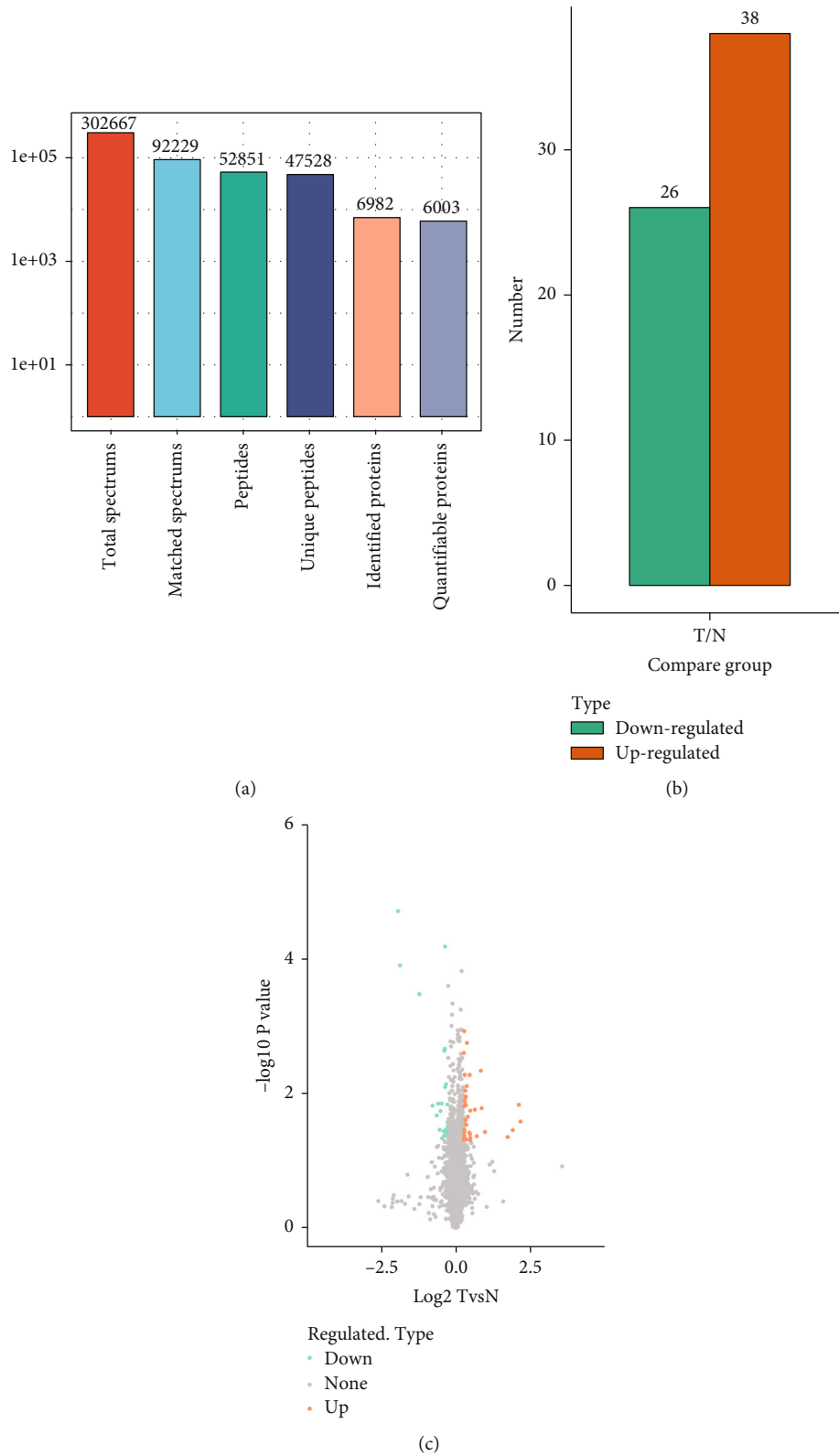
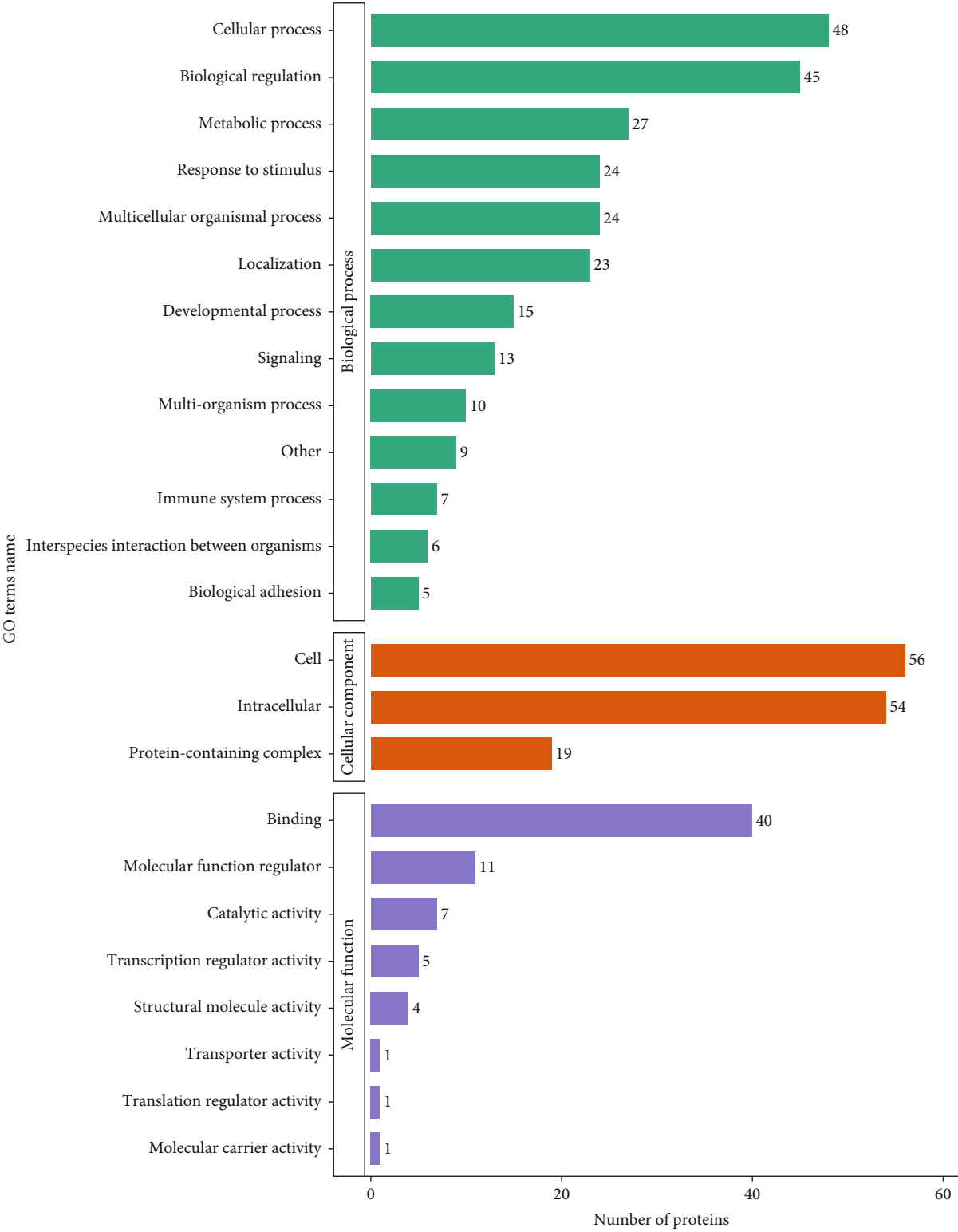


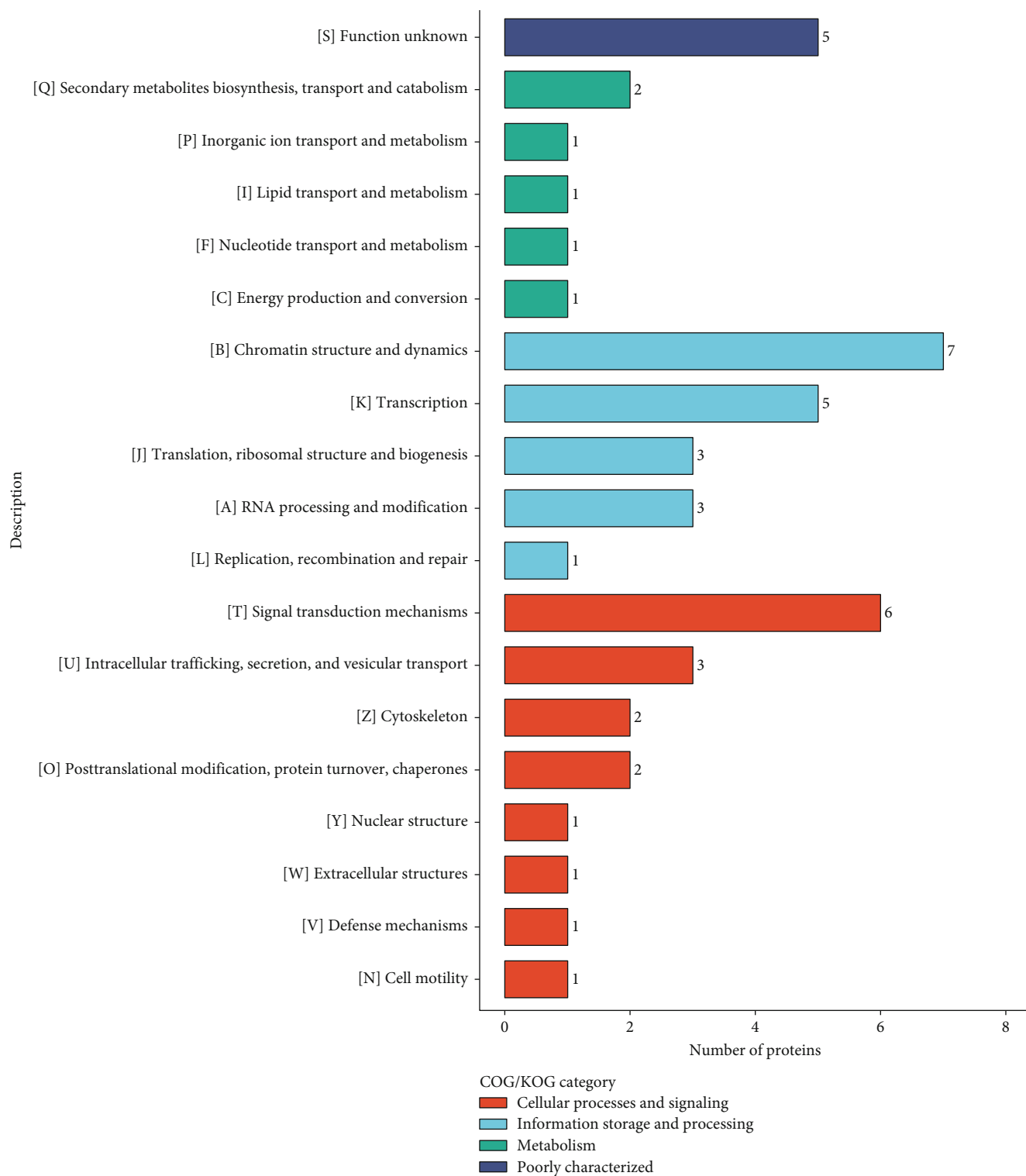
FIGURE 3: Results of the LC-MS/MS study. (a) MS data fundamental statistics. (b) DEP quantity dispersion. (c) DEPs volcano diagram.

2.8. *Verification by Western Blot Analysis.* An assay buffer (G2002; Servicebio) was used to extract protein from the Cingulate Gyrus and Spinal Dorsal Horn nerve tissue, and the bicinchoninic acid protein assay (G2026; Servicebio)

was used to measure the concentration of proteins. To separate the same number of proteins and transfer them to a polyvinylidene difluoride membrane, we used an SDS-PAGE gel (S8010-500g; Solarbio) electrophoresis. This



(a)
FIGURE 4: Continued.



(b)

FIGURE 4: Continued.

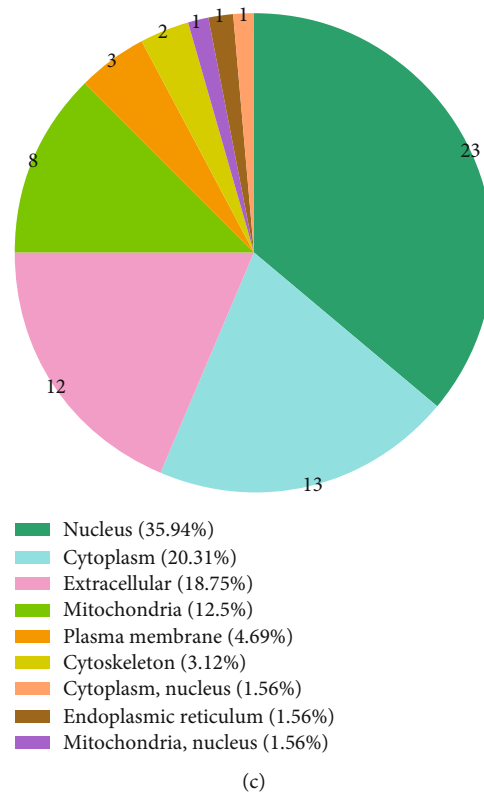


FIGURE 4: Functional annotation of DEPs. (a) GO term's function annotations. (b) COG/KOG function. (c) DEPs localization in subcellular compartments.

membrane was incubated overnight with the corresponding primary antibody (anti-kininogen 1 [Kng1]: cat.#DF6544, 1:1000 from Affinity Biosciences, Cincinnati, OH, USA; anti-junctional adhesion molecule A [JAM-A]: cat.#DF63731:1000 from Affinity Biosciences; and anti- β -actin cat.#GB15001, 1:2000 at 4°C from Servicebio), further incubated with HRP-conjugated secondary antibody (cat.#GB25301,1:5000; Servicebio). After chemiluminescence treatment, Photoshop (Adobe, San Jose, CA, USA) and Alpha (AlphaEase FC, version 6.0.0) software processing were used to analyze the optical density of the film.

3. Results

3.1. Rats' General Health State. There were no fatalities in the control group throughout the trial; however, two rats died in the model group and three rats died in the SHJG group. Each group of rats had a healthy mental condition, lustrous hair, and typical drinking behavior prior to modeling. Rats in groups other than the normal group exhibited a weaker mental state, lower feeding and drinking habits, and yellow and withered hair, and were more irritable when the stressor was administered. At the end of the 28th day, the weights of rats in the normal and model groups were statistically substantially different, with the normal group being heavier ($P < 0.05$, see Table 2).

Note: * $P < 0.05$; # $P > 0.05$, compared to the normal group.

3.2. VH and NERD Signs. Changes in esophageal epithelial cells and the synaptic cleft of the spinal cord dorsal horn were observed by TEM. Under 2.5-K electron microscopy, the NERD group's epithelia had much wider intercellular gaps than those in the control group (see Figure 1(a)). Synaptic vesicles in the spinal dorsal horn of rats in the NERD group increased under the 15-K electron microscope compared to those in the NC and SJHG groups (see Figure 1(b)). Figure 1(c) shows the immunohistochemical outcomes. The content of c-fos in the spinal cords of rats in the NERD group was higher ($P < 0.0001$) than in the NC group, according to the integrated optical density. Meanwhile, the SJHG group's c-fos content was substantially reduced ($P < 0.0001$) as compared to the NERD group. The NERD with VH model caused by stress was also validated by these data.

3.3. Sample Quality Control. SDS-PAGE electrophoresis was performed to evaluate the protein's quality control. Figure 2(a) shows that the protein bands were clean, homogeneous, and free of degradation, indicating that they would be suitable for use in the experiment. The reproducibility of protein quantification was evaluated using the RSD technique. Smaller RSD values indicate better quantitative repeatability. The RSD was found to be $< 10\%$, showing that the quantitative technique was accurate and consistent (see Figure 2(b)).

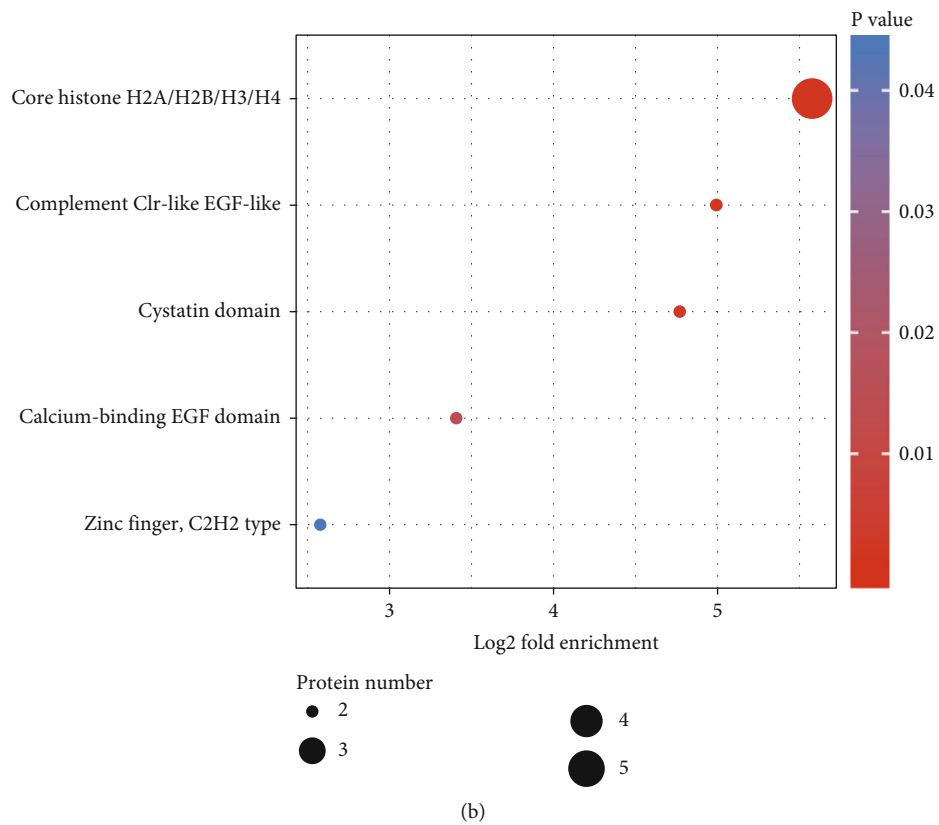
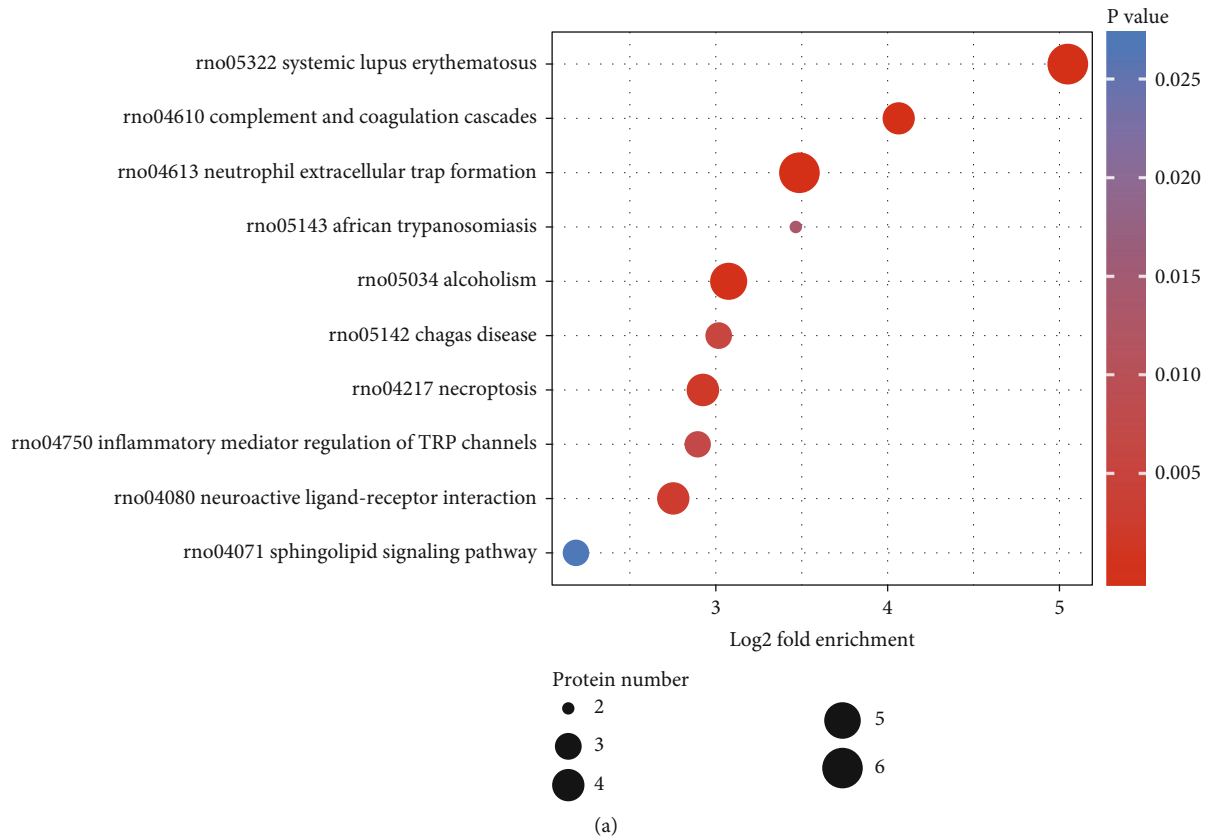
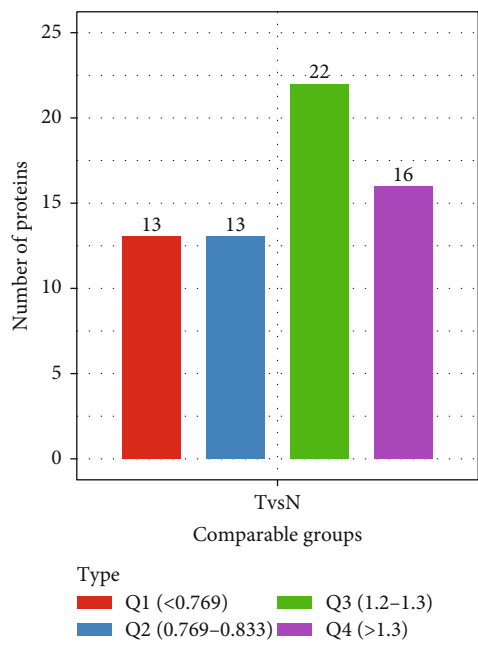
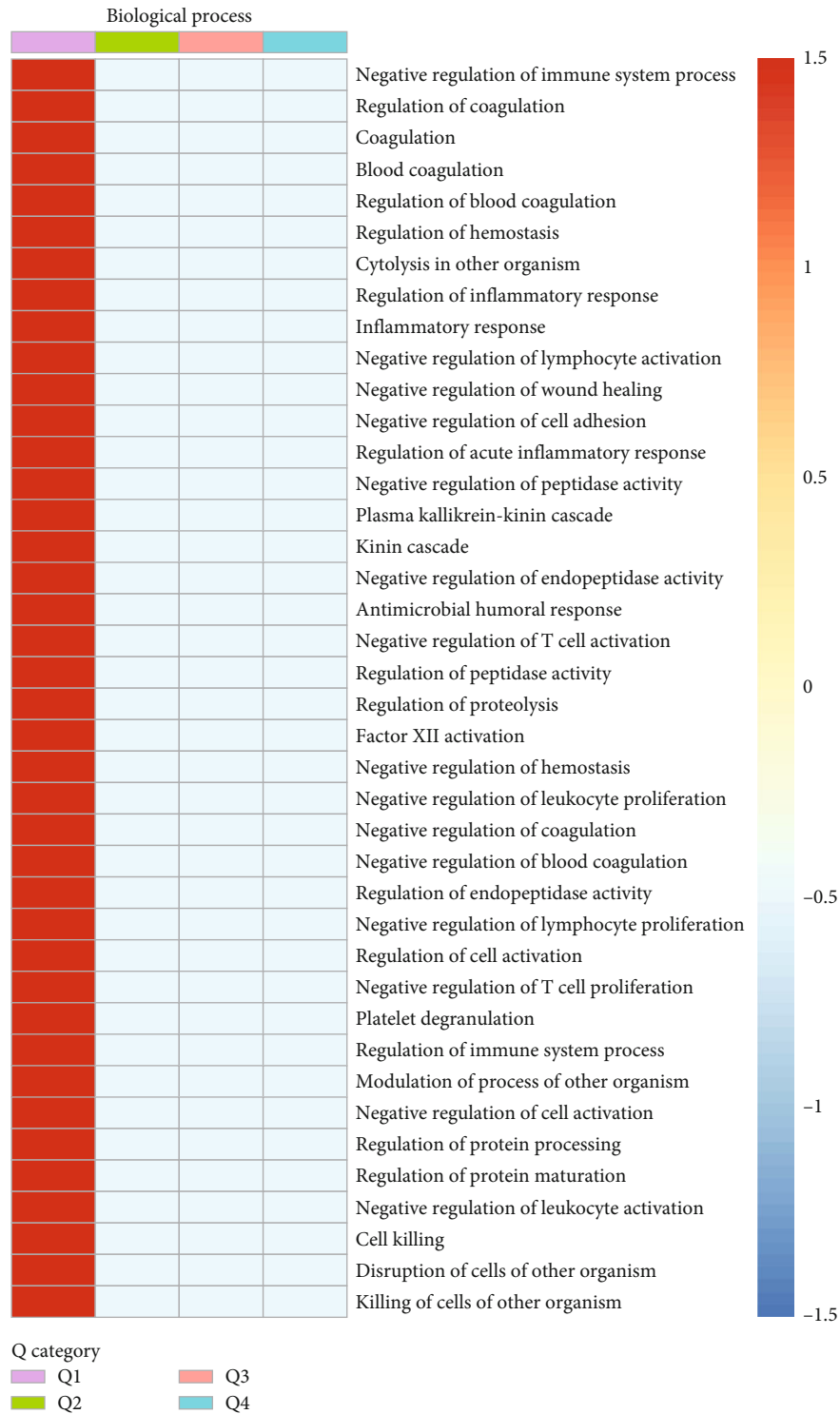


FIGURE 5: (a) KEGG pathways of DEPs. (b) Protein domains of DEPs.



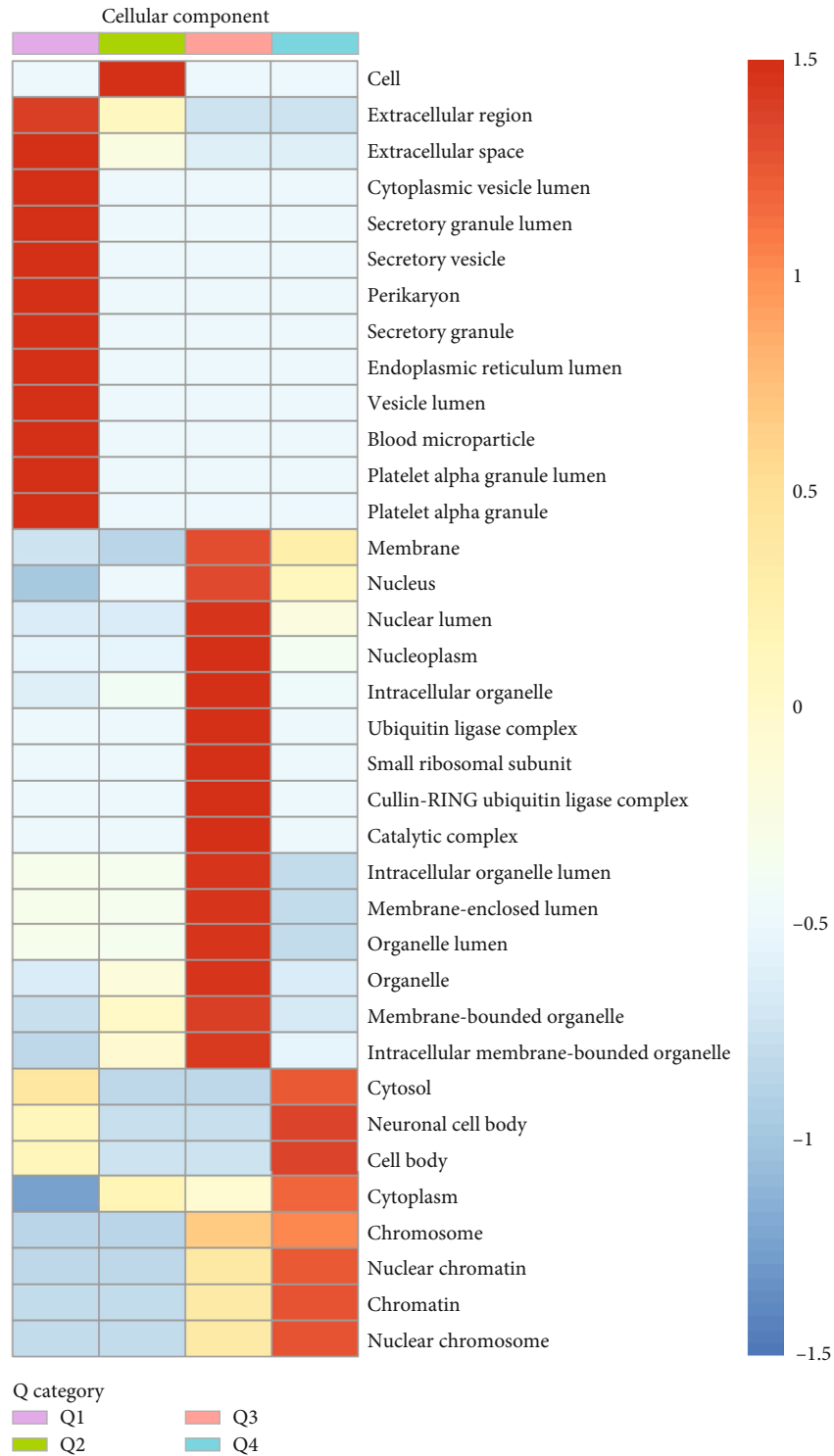
(a)

FIGURE 6: Continued.



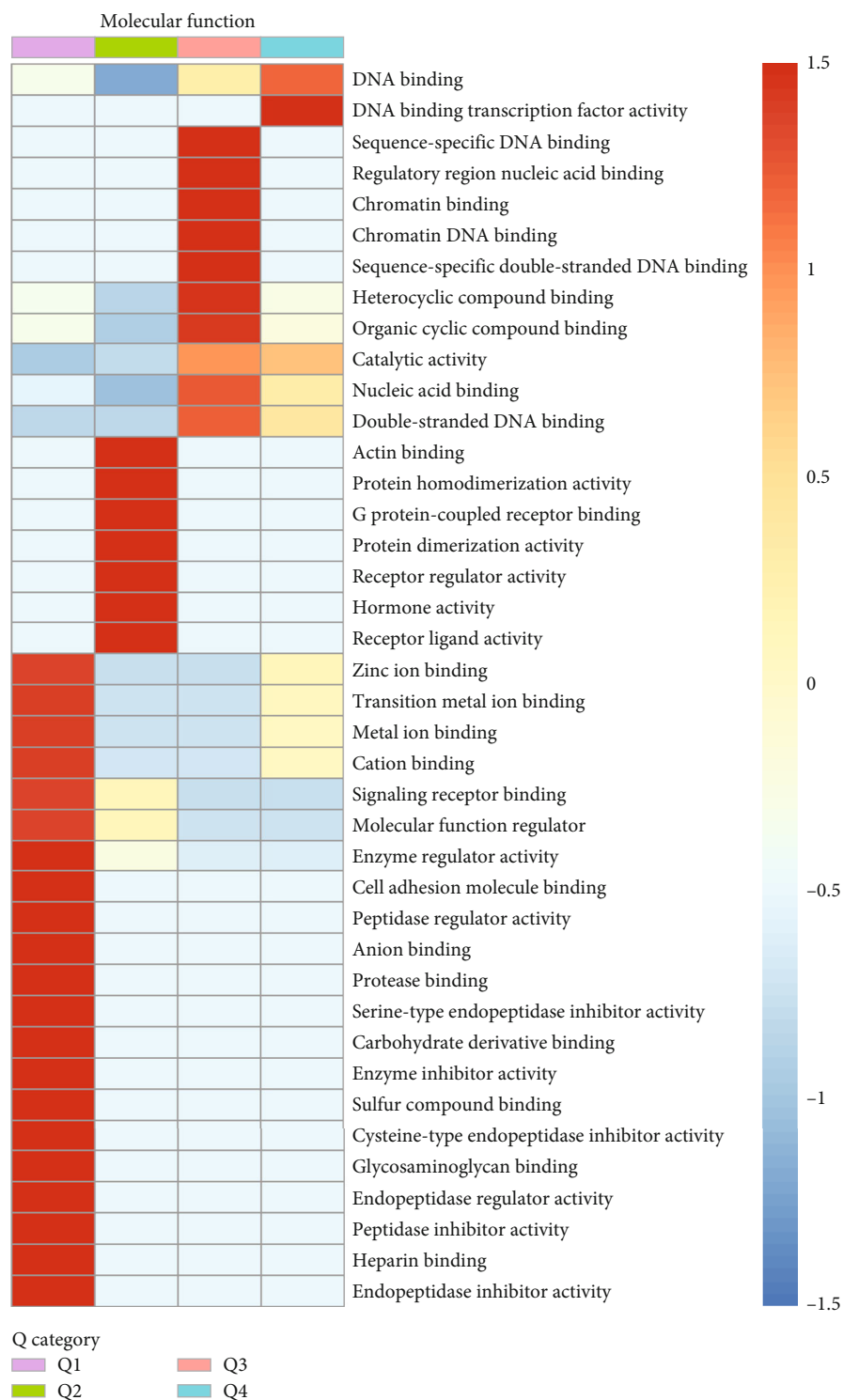
(b)

FIGURE 6: Continued.



(c)

FIGURE 6: Continued.



(d)

FIGURE 6: Cluster analysis of GO functional enrichment of DEPs. (a) The distribution of DEPs in Q1–Q4. (b) Biological processes. (c) Cell composition. (d) Molecule function.

3.4. LC-MS/MS Analysis. MS was used to produce 302,667 secondary spectrograms for the current study. After examining the protein theory database, 92,229 valid mass spectrograms were discovered, with a 30.47% usage rate. A total of

52,851 peptides were found using spectrographic analysis, with 47,528 of them being specific. A total of 6,982 proteins were discovered, with 6,003 of these being measurable (see Figure 3(a)). Consequently, only 64 differentially expressed

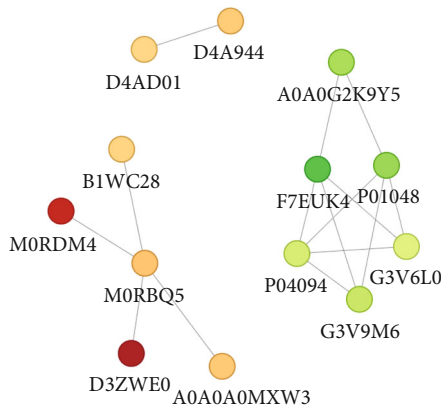


FIGURE 7: The network of protein-protein interactions that occur between the different proteins.

proteins were predicted with the cutoff criterion set as fold change = 1.2 and $P < 0.05$, including 38 upregulated proteins and 26 downregulated proteins (see Figures 3(b) and 3(c)).

3.5. Functional Classification of DEPs. GO functional categorization revealed that the differential molecules were mostly involved in cellular activities, biological control, metabolic processes, reaction to stimuli, immune system processes, and biological adhesion (see Figure 4(a)). Secondary metabolite production, transport and catabolism, chromatin structure and dynamics, transcription, and signal transduction pathways were all implicated in these differentially expressed molecules according to the COG/KOG categorization system (see Figure 4(b)). DEPs were found in the nucleus in 35.94% ($n = 23$) of the samples, in the cytoplasm in 20.31% ($n = 13$), and in the extracellular space in 18.75% ($n = 12$) of the samples. In addition to mitochondria and plasma membranes, there were others (see Figure 4(c)).

3.6. DEPs Protein Domains and Pathway Enrichment Analysis. Bubble plots were used to show protein domains and KEGG pathway enrichment. DEP enrichment was shown in the image by the circles. DEP enrichment is very significant ($P < 0.01$) in red, significant ($P > 0.05$) in yellow, and nonsignificant ($P < 0.05$) in blue. The fold enrichment is represented by the size of the circle. The components of DEPs centered on the complement Clr-like EGF-like, cystatin domain, core histone H2A/H2B/H3/H4, and calcium-binding EGF domain, according to protein-domain enrichment analysis. Systemic lupus erythematosus, neutrophil extracellular trap formation, complement and coagulation cascades, African trypanosomiasis, necroptosis, alcoholism, Chagas disease, inflammatory mediator-regulation of TRP channels, neuroactive ligand-receptor interaction, and sphingolipid signaling pathway were identified as significant enrichment signal pathways of DEPs by KEGG analysis (see Figure 5).

3.7. DEPs Cluster Analysis. DEPs were classified into four categories based on the AF/SR ratio (Q1, 0.769, Q2, 0.769–0.833, Q3, 1.2–1.3, and Q4, > 1.3). (see Figure 6). Q3 and

Q4 constitute the majority of upregulated proteins, and these proteins were localized in the nucleus and organelle lumens of the cell (see Figure 6(c)) and primarily various epigenetic regulatory molecules (e.g., histone H2A, histone H2B, ribonucleoprotein complex, nuclear factor 1) (see Figure 6(d)). The proteins that were downregulated (Q1) were mostly localized in the extracellular compartment involved in the negative control of biological immune responses and the activation of associated proteins. The molecular function of downregulated proteins is mainly to bind with a variety of metal ions and regulate the activity of peptidase inhibitors and endopeptidase inhibitors (see Figures 6(b)–6(d)).

3.8. PPI Network Analysis of DEPs. We generated a PPI network of the differential proteins to better illustrate the interrelationships between them. Circles with green DEPs and red DEPs indicate DEPs, which are the proteins that have been downregulated. The results showed that there were six important node proteins, as follows: kinogen-1 (Kng1, F7EUK4), four nodes; T-Kng1 (Map1, P01048), four nodes; histone H2B (Hist3h2bb, M0RBQ5), four nodes; proenkephalin-A (Penk, P04094), four nodes; pro-MCH (Pmch, G3V6L0, CPB1), three nodes; and fibrillin 1 (Fbn1, G3V9M6, TTR), three nodes (see Figure 7).

3.9. Validation of the Differently Expressed Proteins by Western Blotting. Figure 8 shows that compared to the NC group, the Kng1 protein level in the cingulate gyrus increased in the NERD group, while the JAM-A protein level did not change significantly. Moreover, the SHJG group's JAM-A protein level increased significantly in comparison to the NERD group, while the Kng1 protein level decreased.

4. Discussion

There is mounting evidence to support the idea that VH plays a significant part in the etiology of NERD; nevertheless, the research that has been conducted so far on VH has not been sufficient, such as by providing an explanation for why VH causes mental abnormalities. We found that the proteomics of brain tissue in NERD has not been studied yet, which is crucial for understanding the pathogenesis of NERD. However, the effects of NERD on brain tissue may be multifaceted and complex, which may lead to a significant decrease in the accuracy of prediction. According to TCM, NERD is mainly caused by “liver qi stagnation, stomach discomfort, and adverse rising of the stomach qi” [20]. At the same time, TCM believes that VH and function of “liver” are closely related [21]. Therefore, we choose to treat liver depression, qi stagnation of traditional Chinese medicine formula for research.

We confirmed whether the disease model was successfully established by TEM and IHC analysis. After induction of emotional stress, the c-fos protein level and synaptic vesicle release increased in the dorsal horn of the spinal cords of rats but decreased after treatment with SHJG. This indicated that splanchnic hypersensitivity was observed in NERD model rats and that this central nervous sensitivity could

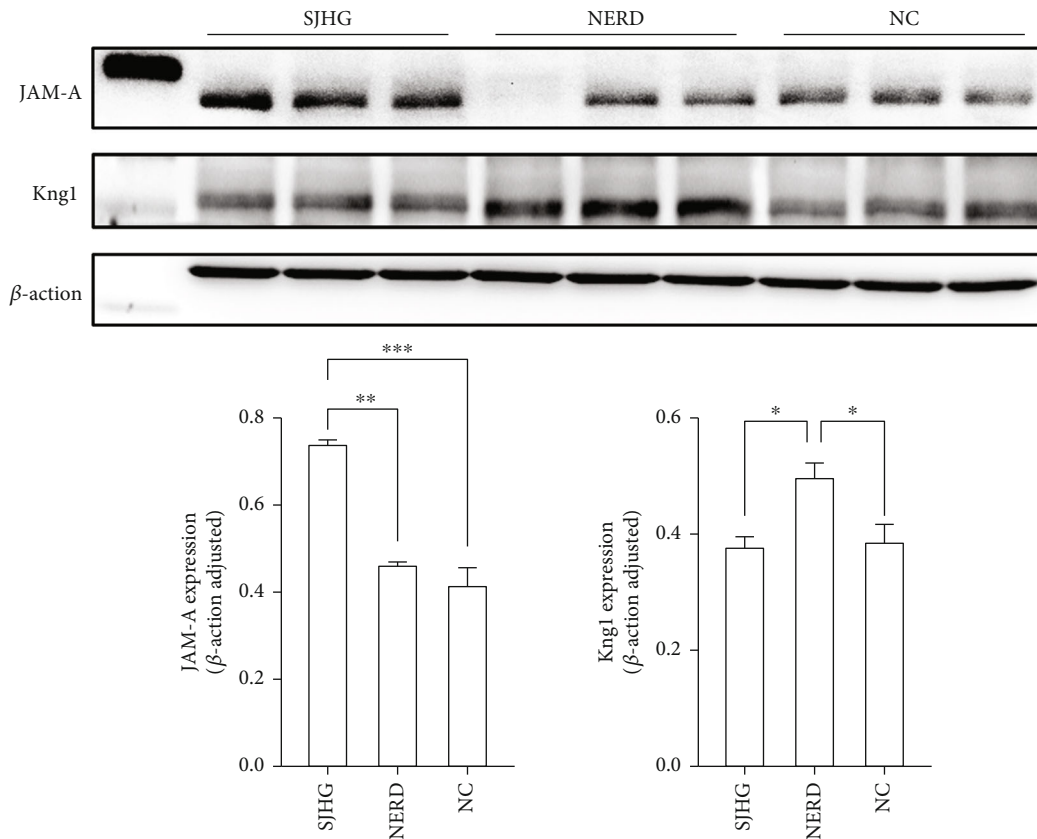


FIGURE 8: Protein expressions of JAM-A and Kng1 among the groups. The expression level of JAM-A and Kng1 were analyzed through western blot analysis. *** $P < 0.001$, ** $P < 0.01$, * $P < 0.05$.

be improved by SJHG. In addition, the esophageal mucosa of rats was observed by TEM, and the DIS in the esophageal submucosa was confirmed in NERD model rats. SJHG's validity was proven by the aforementioned findings, which showed that the NERD model had been effectively created.

To further understand the mechanism by which SJHG improves VH in brain tissue, we analyzed the molecular profile of rat cingulate gyrus tissue using a TMT proteomics system and found 64 proteins with distinct expression differences. We discovered that these differentially expressed molecules in the nucleus, extracellular area, and cytoplasm were linked to biological regulation, cellular processes, metabolic processes, stimulus response, immune system processes, and biological adhesion through classification and functional enrichment analysis. In addition, four of the ten significant signaling pathways, including systemic lupus erythematosus, neutrophil extracellular trap formation, inflammatory mediator–regulation of TRP channels, and complement and coagulation cascades, were associated with the immune system. The transmission of brain signals is mediated by three pathways: inflammatory mediator–TRP channel regulation, neuroactive ligand–receptor interaction, and the sphingolipid signaling route. Other signal pathways include necroptosis, alcoholism, Chagas disease, and African trypanosomiasis. The differential molecules involved include Kng1, JAM-A, phosphatidylinositol 3-kinase regulatory subunit beta (Pik3r2), complement component C9, Map1, Penk, and histone H2A. These results suggest that SJHG may

improve VH by regulating the inflammatory response of brain tissue or by inhibiting the abnormal activation of various nerve cells. We discovered six critical hub proteins, each with ≥ 3 nodes, using PPI network analysis. By analyzing the differentially expressed histones in the network, we found that five differentially expressed histones in the network were involved in DNA modification, affecting epigenetic inheritance. In addition, we found interactions between some immune-associated molecules and molecules related to neuroactive ligand–receptor interaction, such as Kng1, Pmch, Hrg, Map1, and Penk. These results suggest that SJHG treatment of VH may be accomplished by influencing the interaction between the immune and nervous systems. At the same time, these regulatory effects may be accomplished through histone modifications.

Through a bioinformatics analysis and literature review, we found that Kng1 and JAM-A proteins might be related to the mechanism of VH, so we verified the proteomics results by WB and confirmed that Kng1 and JAM-A protein levels had significant changes. Kng1 was significantly upregulated in the NERD group, while SJHG could restore Kng1 protein expression to normal levels. Meanwhile, JAM-A protein levels were upregulated in the NERD group and SJHG group.

High- and low-molecular-weight Kng (HMWK and LMWK) are two proteins with distinct structures that may be produced by varied shearing in the presence of a Kng1 protein [22]. HMWK, as a precursor protein of the

kallikrein–kinin system (KKS), is essential for the maintenance of the functional stability of the KKS [23, 24]. Composed of proteolytic enzymes and biogenic peptide cascades, KKS is widely distributed throughout the brain and is involved in the progression of various neurological diseases [24]. On the other hand, HMWK can release bradykinin after enzymatic catalysis to reduce the hypersensitivity of pain in nerve pain model rats [25]. These consequences propose that the abnormal expression of Kng1 may be a cause of VH in rats with NERD disease, and SJHG may treat NERD by reducing Kng1 [26]. JAM-A is a kind of adhesion protein containing a PDZ domain on its cell membrane. Currently, JAM-A is found in the nerve, epithelium, endothelium, and blood cells. It crosses the cell membrane and is divided into two parts: extramembrane and intramembrane. The extramembrane portion of JAM-A acts as a “fence” that regulates cell adhesion and migration [27, 28]. JAM-A is an important protein that constitutes the tight junction between cells, which maintains the integrity of the blood–brain barrier and prevents inflammatory factors from entering the brain through this barrier [28, 29]. Moreover, adhesion receptors on adjacent cells can adapt to changes in the microenvironment because of the information conveyed by adhesion receptors on their cells. Adhesion receptors use their cytoplasmic domains (including FERM, proline-rich motifs, PDZ domains, and phosphorylation sites) to bind to appropriate specific interaction motifs in cytoplasmic proteins and transmit intercellular signals [30–32]. SJHG’s therapy of VH may be based on the hypothesis that JAM-A expression is being increased.

Finally, in this study, SJHG reduced the expression level of Pik3r2, which was of interest to us. Pik3r2 is a protein that is involved in the PI3K/Akt signaling pathway, which is a signaling pathway that has been implicated in the proliferation and survival of neurons in the central nervous system [33, 34]. Indirectly, the PI3K/Akt signaling system regulates autophagy, resulting in the PI3K/Akt signaling pathway associated with neuronal survival [35]. This route is used by a variety of neuroendocrine substances to exhibit neuroprotective effects, such as brain-derived neurotrophic factor (BDNF). The PI3K/Akt signaling pathway is important in the development of cognitive capacities as well as the maintenance of synaptic plasticity in studies [36–38]. SJHG therapy for VH seems to be associated with alterations in the PI3K/Akt signaling pathway in the rat’s cingulate gyrus, according to the findings of this study.

5. Conclusions

In the cingulate gyrus of NERD rats, SJHG treatment altered the expression levels of several proteins. The differential molecules involved include Kng1, JAM-A, Pik3r2, complement component C9, Map1, Penk, and histone H2A. And these molecules were significantly enriched in immune response and the transmission of neural signals. These results suggest that SJHG may improve VH by regulating the inflammatory response of brain tissue or by inhibiting the abnormal activation of various nerve cells. These results provide new evidence of SJHG treatment of NERD by ame-

liorating VH. In addition, we found two therapeutic targets of SJHG—namely, Kng1 and JAM-A. And SJHG may influence autophagy through the PI3K/Akt signaling pathway. However, there are some shortcomings of this study. SJHG is a compound preparation. Although possible targets of action were found, it cannot explain what specific components play a role and cannot clarify the specific mechanism of action. Relevant experiments were not performed to verify that SJHG affects the PI3K/Akt signaling pathway. There may be discoveries in NERD diagnosis and treatment utilizing vast numbers of samples and in-depth mechanism studies of the molecules uncovered by this work, even if they are not yet understood how well these differential molecules are involved in the pathogenic processes of VH.

Data Availability

The labeled dataset used to support the findings of this study is available from the corresponding author upon request.

Conflicts of Interest

The authors declare no conflict of interest.

Authors’ Contributions

Bai G and Li J have made substantial intellectual contributions to the conception and design of this study. Wang TZ, Jia YB, Zhao JQ, and He MJ carried out the experiments. Wang TZ, Jia YB, Li J, and He MJ contributed to the experiment conduction and data analysis of this study. Wang TZ participated in the manuscript writing and approved the final version.

Acknowledgments

We would like to thank Jingjie PTM BioLab (Hangzhou) Co. Inc. for quantitative proteomic analysis assistance and thank LetPub (<http://www.letpub.com>) for its linguistic assistance during the preparation of this manuscript. The study was supported by the Living Inheritance of Shengjing Spleen and Stomach Academic School [No. LiaoWeiZongHeZi(2021)19] and the third TCM Master Inheritance Studio and the national famous TCM Inheritance Studio construction project [LiaoZhongYiYaoHanZi(2018)76].

References

- [1] N. Vakil, S. V. van Zanten, P. Kahrilas, J. Dent, R. Jones, and the Global Consensus Group, “The Montreal definition and classification of gastroesophageal reflux disease: a global evidence-based consensus,” *The American Journal of Gastroenterology*, vol. 101, no. 8, pp. 1900–1920, 2006, quiz 43.
- [2] K. Wang, L. Zhang, Z. H. He et al., “A population-based survey of gastroesophageal reflux disease in a region with high prevalence of esophageal cancer in China,” *Chinese Medical Journal*, vol. 132, no. 13, pp. 1516–1523, 2019.
- [3] X. Fang, L. Zhu, D. Wu et al., “Natural history of gastroesophageal reflux: a prospective cohort study in a stratified,

- randomized population in Beijing,” *Journal of Digestive Diseases*, vol. 20, no. 10, pp. 523–531, 2019.
- [4] Y. C. Shi, S. T. Cai, Y. P. Tian et al., “Effects of proton pump inhibitors on the gastrointestinal microbiota in gastroesophageal reflux disease,” *Genomics, Proteomics & Bioinformatics*, vol. 17, no. 1, article S1672022919300658, pp. 52–63, 2019.
- [5] K. M. Hedayat, J. C. Lapraz, and B. Schuff, “Gastroesophageal reflux disease (GERD),” *The Theory of Endobiogeny*, vol. 115, no. 3, pp. 214–218, 2020.
- [6] H. V. Malenstein, R. Farré, and D. Sifrim, “Esophageal dilated intercellular spaces (DIS) and nonerosive reflux disease,” *The American Journal of Gastroenterology*, vol. 103, no. 4, pp. 1021–1028, 2008.
- [7] R. L. Cui, L. Y. Zhou, S. R. Lin, and Y. Xue, “A study on the light microscopic measurement of intercellular space of squamous epithelium in lower-esophagus to diagnose gastroesophageal reflux disease,” *Zhonghua Nei Ke Za Zhi*, vol. 48, no. 3, pp. 208–212, 2009.
- [8] E. Savarino, E. Marabotto, G. Bodini et al., “Epidemiology and natural history of gastroesophageal reflux disease,” *Minerva Gastroenterologica e Dietologica*, vol. 63, no. 3, pp. 175–183, 2017.
- [9] C. Xu and X. Niu, “Progress on the mechanism of visceral hypersensitivity in nonerosive reflux disease,” *Gastroenterology Research and Practice*, vol. 2022, Article ID 4785077, 7 pages, 2022.
- [10] A. D. Farmer, J. K. Ruffle, and Q. Aziz, “The role of esophageal hypersensitivity in functional esophageal disorders,” *Journal of Clinical Gastroenterology*, vol. 51, no. 2, pp. 91–99, 2017.
- [11] J. Tack, “Is there a unifying role for visceral hypersensitivity and irritable bowel syndrome in non-erosive reflux disease?,” *Digestion*, vol. 78, Supplement 1, pp. 42–45, 2008.
- [12] W. D. Gunter, J. D. Shepard, R. D. Foreman, D. A. Myers, and M. B. Greenwood-Van, “Evidence for visceral hypersensitivity in high-anxiety rats,” *Physiology & Behavior*, vol. 69, no. 3, article S0031938499002541, pp. 379–382, 2000.
- [13] F. Zeng, W. Qin, F. Liang et al., “Abnormal resting brain activity in patients with functional dyspepsia is related to symptom severity,” *Gastroenterology*, vol. 141, no. 2, article S0016508511006202, pp. 499–506, 2011.
- [14] L. Brenner, L. Zerlin, and L. L. Tan, “Functional disruption of cortical cingulate activity attenuates visceral hypersensitivity and anxiety induced by acute experimental colitis,” *Scientific Reports*, vol. 11, no. 1, article 81256, p. 2103, 2021.
- [15] B. Feng, J. H. La, E. S. Schwartz, and G. F. Gebhart, “Neural and neuro-immune mechanisms of visceral hypersensitivity in irritable bowel syndrome,” *American Journal of Physiology-Gastrointestinal and Liver Physiology*, vol. 302, no. 10, pp. G1085–G1098, 2012.
- [16] Q. Yang, Y. Yao, D. Zhao et al., “LncRNA H19 secreted by umbilical cord blood mesenchymal stem cells through microRNA-29a-3p/FOS axis for central sensitization of pain in advanced osteoarthritis,” *American Journal of Translational Research*, vol. 13, no. 3, pp. 1245–1256, 2021.
- [17] J. Y. Zhang, J. Y. Li, H. Shen et al., “Research progress of gastroesophageal reflux disease in Chinese medicine,” *Acta Chinese Medicine and Pharmacology*, vol. 49, no. 3, pp. 115–119, 2021.
- [18] M. J. He, G. Bai, J. Li, Z. H. Meng, T. Z. Wang, and Y. N. Chen, “Discussion on the mechanism of central sensitization in non-erosive reflux disease based on theory of “liver-brain related,” *CHINESE Archives Of Traditional Chinese Medicine*, vol. 40, no. 3, pp. 163–166, 2022.
- [19] G. Z. Ma, P. Liu, and G. Bai, “Effects of Shugan Jiangni Hewei granules on the expression of esophageal mucoproteinase-activated receptor-2 and cyclooxygenase-2 in patients with gastroesophageal reflux disease with liver-stomach discord syndrome,” *World Chinese Medicine*, vol. 13, no. 10, p. 4, 2018.
- [20] L. Li, “Trace the TCM ancient literature of gastroesophageal reflux disease,” *Global Traditional Chinese Medicine*, vol. 4, no. 1, pp. 11–15, 2011.
- [21] M. He, J. Li, Z. Meng et al., “Discussion on the mechanism of central sensitization in non-erosive reflux disease based on theory of “liver-brain related,”” *Chinese Archives of Traditional Chinese Medicine*, pp. 1–10, 2021.
- [22] M. B. Ponczek, “High molecular weight Kininogen: a review of the structural literature,” *International Journal of Molecular Sciences*, vol. 22, no. 24, article ijms222413370, p. 13370, 2021.
- [23] B. Wang, A. Yang, Z. Zhao et al., “The plasma Kallikrein-Kininogen pathway is critical in the pathogenesis of colitis in mice,” *Frontiers in Immunology*, vol. 9, p. 21, 2018.
- [24] A. Nokkari, H. Abou-El-Hassan, Y. Mechref et al., “Implication of the Kallikrein-Kinin system in neurological disorders: quest for potential biomarkers and mechanisms,” *Progress in Neurobiology*, vol. 165–167, pp. 26–50, 2018.
- [25] S. Yamaguchi-Sase, I. Hayashi, H. Okamoto et al., “Amelioration of hyperalgesia by kinin receptor antagonists or kininogen deficiency in chronic constriction nerve injury in rats,” *Inflammation Research*, vol. 52, no. 4, article JCL5BUD1CC54EJ8K, pp. 164–169, 2003.
- [26] K. Czubak-Prowizor, A. Babinska, and M. Swiatkowska, “The F11 Receptor (F11R)/Junctional Adhesion Molecule-A (JAM-A) (F11R/JAM-A) in cancer progression,” *Molecular and Cellular Biochemistry*, vol. 477, no. 1, article 4259, pp. 79–98, 2022.
- [27] W. Jia, R. Lu, T. A. Martin, and W. G. Jiang, “The role of claudin-5 in blood-brain barrier (BBB) and brain metastases (review),” *Molecular Medicine Reports*, vol. 9, no. 3, pp. 779–785, 2014.
- [28] C. Collins and W. J. Nelson, “Running with neighbors: coordinating cell migration and cell-cell adhesion,” *Current Opinion in Cell Biology*, vol. 36, article S0955067415000794, pp. 62–70, 2015.
- [29] T. Keiper, S. Santoso, P. P. Nawroth, V. Orlova, and T. Chavakis, “The role of junctional adhesion molecules in cell-cell interactions,” *Histology and Histopathology*, vol. 20, no. 1, pp. 197–203, 2005.
- [30] J. Nomme, A. S. Fanning, M. Caffrey, M. F. Lye, J. M. Anderson, and A. Lavie, “The Src homology 3 domain is required for junctional adhesion molecule binding to the third PDZ domain of the scaffolding protein ZO-1*,” *The Journal of Biological Chemistry*, vol. 286, no. 50, article S0021925820870501, pp. 43352–43360, 2011.
- [31] C. K. Campla, H. Mast, L. Dong et al., “Targeted deletion of an NRL- and CRX-regulated alternative promoter specifically silences FERM and PDZ domain containing 1 (Frmpd1) in rod photoreceptors,” *Human Molecular Genetics*, vol. 28, no. 5, pp. 804–817, 2019.
- [32] N. R. Chandan, S. Abraham, S. SenGupta, C. A. Parent, and A. V. Smrcka, *Identification of G Protein α I Signaling Partners by Proximity Labeling Reveals a Network of Interactions that Includes PDZ-RhoGEF*, BioRxiv preprint, 2021.

- [33] T. Ali, S. U. Rahman, Q. Hao et al., “Melatonin prevents neuroinflammation and relieves depression by attenuating autophagy impairment through FOXO3a regulation,” *Journal of Pineal Research*, vol. 69, no. 2, article e12667, 2020.
- [34] C. W. Keller and J. D. Lünemann, “Autophagy and autophagy-related proteins in CNS autoimmunity,” *Frontiers in Immunology*, vol. 8, p. 165, 2017.
- [35] D. Heras-Sandoval, J. M. Pérez-Rojas, J. Hernández-Damián, and J. Pedraza-Chaverri, “The role of PI3K/AKT/mTOR pathway in the modulation of autophagy and the clearance of protein aggregates in neurodegeneration,” *Cellular Signalling*, vol. 26, no. 12, article S0898656814002848, pp. 2694–2701, 2014.
- [36] Y. Hu, W. Chen, L. Wu et al., “TGF- β 1 restores hippocampal synaptic plasticity and memory in Alzheimer model via the PI3K/Akt/Wnt/ β -catenin signaling pathway,” *Journal of Molecular Neuroscience*, vol. 67, no. 1, article 1219, pp. 142–149, 2019.
- [37] Y. Zhong, Y. Zhu, T. He, W. Li, Q. Li, and Y. Miao, “Brain-derived neurotrophic factor inhibits hyperglycemia-induced apoptosis and downregulation of synaptic plasticity-related proteins in hippocampal neurons via the PI3K/Akt pathway,” *International Journal of Molecular Medicine*, vol. 43, no. 1, pp. 294–304, 2019.
- [38] F. Chu, K. Li, X. Li, L. Xu, J. Huang, and Z. Yang, “Graphene oxide ameliorates the cognitive impairment through inhibiting PI3K/Akt/mTOR pathway to induce autophagy in AD mouse model,” *Neurochemical Research*, vol. 46, no. 2, article 3167, pp. 309–325, 2021.

Research Article

A Nomogram Model for Individualized Prediction of the Risk of Respiratory Tract Infection within Six Months after Diagnosis in Patients with Primary Immune Thrombocytopenia

Jinhua Wei,¹ Weiwei Pan,¹ Feng Luo,¹ Fengnian Tang,¹ Jiashi Wei,¹ Siwen Fang,¹ and Honglian Huang² 

¹Department of Hematology, Department of Rheumatology and Immunology, The People's Hospital of Hechi, Hechi, 547000 Guangxi, China

²Department of Gynecology, The People's Hospital of Hechi, Hechi, 547000 Guangxi, China

Correspondence should be addressed to Honglian Huang; hchuanghonglian@163.com

Received 20 May 2022; Revised 16 June 2022; Accepted 11 July 2022; Published 28 July 2022

Academic Editor: Pan Zheng

Copyright © 2022 Jinhua Wei et al. This is an open access article distributed under the Creative Commons Attribution License, which permits unrestricted use, distribution, and reproduction in any medium, provided the original work is properly cited.

The risk factors of upper respiratory tract infection (URI) within 6 months after diagnosis in patients with idiopathic thrombocytopenic purpura (ITP) were analyzed, and the nomogram model was established and verified, with 242 and 50 ITP patients as the training and validation set, respectively. The patients were followed up for six months after the diagnosis of ITP. The clinical data of patients were collected, and the risk factors of URI in ITP patients within six months after diagnosis were analyzed using univariable, followed by multivariable logistic regression. Among the 242 ITP patients in the training set, 52 cases (21.49%) had URI, including 24 cases of viral infection, 11 cases of *Mycoplasma pneumoniae* infection, and 17 cases of bacterial infection. Logistic regression analysis showed that advanced age, use of glucocorticoid, smoking history, platelet count, serum CRP level, and lymphocyte subsets CD_4^+ and CD_8^+ were all risk factors for ITP patients to develop symptoms within six months after diagnosis ($P < 0.05$). Using the above five indicators, a nomogram prediction model was built for URI occurrence in patients with ITP within half a year after diagnosis, and the results showed an AUC, a sensitivity, and a specificity of 0.936 (95% CI: 0.878-0.983), 0.942, and 0.865, respectively. The nomogram model was internally verified by the bootstrap method for 500 self-sampling times, and the prediction of the calibration curve was in high consistency with the real results. External validation of the nomogram model resulted in an AUC, a sensitivity, and a specificity of 0.890 (95% CI: 0.757-0.975), 0.949, and 0.727, respectively. The nomogram model of URI in ITP patients within half a year after diagnosis based on logistic regression analysis has good discrimination and prediction accuracy. This provides important guidance value for individualized prediction of URI in ITP patients.

1. Introduction

Primary immunologic thrombocytopenic purpura (ITP) accounts for about 30% of all bleeding disorders [1], and its main clinical manifestations are decreased platelet count and severe bleeding. According to statistics, the global incidence of ITP was between 1.5 and 3.0‰ [2]. The incidence rate among adults in Europe was about 1.8‰ [3], and the incidence rate in China was 2.8‰ [4], which is higher than that in Europe. Glucocorticoids are the main drug treatment for ITP at present, but the risk of respiratory tract infection

is high when taking the drugs [5]. It has been reported that the incidence of respiratory tract infection during treatment in ITP patients is as high as 5 times that of healthy people, and the mortality rate within 1 year of treatment is as high as 0.9%. The majority of deaths were from upper respiratory tract infection (URI) [6]. Therefore, while paying close attention to complications such as severe bleeding in ITP, we must also pay attention to the prevention and treatment of respiratory tract infections. At present, there is no analysis on the risk factors of URI in ITP patients within half a year after diagnosis; so, for ITP prevention and treatment, it is

very important to identify relevant risk factors for URI within half a year after ITP diagnosis to screen out high-risk patients. How to realize the individualized prediction of the risk of ITP patients within six months after diagnosis is a difficulty that needs to be urgently solved, and there are few relevant reports at home and abroad.

A nomogram integrates relevant risk factors and visualizes risk values [7]. Based on this, this study analyzed the clinical data of ITP patients to explore the risk factors of URI within six months after diagnosis and built and validated a nomogram model for individualized prediction of URI risk in ITP patients within six months after diagnosis.

2. Materials and Methods

2.1. Study Population. A training set and a validation set, which included 242 ITP patients visited the Hechi People's Hospital between January 2019 and June 2020 and 50 ITP patients admitted between July 2020 and December 2020, respectively, were set up. Inclusion criteria for training and validation sets were as follows: (1) meet the clinical diagnostic criteria of "Chinese Expert Consensus on Diagnosis and Treatment of ITP in Adults 2016 Edition" [8], no less than two routine blood tests showed a decrease in platelet count, and bone marrow test showed an increase in the number of megacaryocyte and a mature disorder; (2) antibiotic treatment and splenectomy were performed after diagnosis; (3) those suffering from ITP for the first time; (4) age ≥ 18 years old; (5) the follow-up time is not less than six months; and (6) the patient voluntarily participated in this research with informed consent provided. Exclusion criteria were as follows: (1) patients with secondary thrombocytopenia; (2) patients treated with antiplatelet aggregation, anticoagulation, and other drugs; (3) patients with passive participation in this study; and (4) patients who were lost to follow-up and whose follow-up data were incomplete. The present study was a retrospective study.

2.2. Collect Patient Data. The Hospital Information System (HIS) was used to collect and summarize the clinical information of ITP patients on admission, including gender, age, drinking history (female drinking > 70 g pure alcohol/week, male > 140 g pure alcohol/week), smoking history (smoking more than 100 cigarettes or cumulative smoking of more than six months), pathogens, combined anemia, glucocorticoids, splenectomy therapy, rituximab, serum C-reactive protein (CRP) levels, natural killer (NK) cells, lymphocyte subpopulations CD_3^+ , CD_4^+ , CD_8^+ , B lymphocyte, and platelet counts.

2.3. Grouping. All cases were followed up for half a year, and the follow-up was conducted in the form of outpatient review. Patients visited the hospital for reexamination every 1 month after discharge. According to the diagnostic criteria of acute upper respiratory tract infection [9], the patient had pharyngeal itching, dry throat, symptoms of upper respiratory catarrh or fever, headache, and other symptoms. Physical examination showed that the pharynx, nasal mucosa congestion, secretions, and edema were diagnosed as URI. The ITP patients in the modeling set who developed URI

within half a year after diagnosis were assigned to the infected group, and those who did not were assigned to the uninfected group.

2.4. Statistics and Methods. SPSS 23.0 analyzed the original data. Continuous variables that obeyed the normal distribution were denoted by (mean \pm standard deviation), and *t*-test conducted intergroup comparisons. The categorical variables was represented by *n* (%), and the chi-square test or rank-sum test conducted intergroup comparisons. Univariate and multivariate logistic regression were employed to identify prognostic factors of patients. URI risk in ITP patients within six months after diagnosis was analyzed using the logistic regression model, based on which a nomogram prediction model was built. The discriminative ability of the model was evaluated by calculating the area under the curve (AUC) and 95% confidence interval (CI), and internal validation with 500 iterations of bootstrap was used to evaluate the calibration effect through unreliability tests and calibration curves. *R* software (v4.1.2; <https://www.r-project.org>) was used. A *P* value < 0.05 was interpreted as statistical significance.

3. Result and Discussion

3.1. Univariate Analysis of the Onset of Symptoms in ITP Patients within Half a Year after Diagnosis. Among the 242 ITP patients in the modeling set, 52 had URI, accounting for 21.49%, including 24 cases of viral infection, 11 cases of *Mycoplasma pneumoniae* infection, and 17 cases of bacterial infection. Statistically significant differences were present in age, use of glucocorticoid, smoking, platelet count, serum CRP level, and lymphocyte subsets CD_4^+ and CD_8^+ between infected and noninfected groups ($P < 0.05$), as shown in Table 1.

3.2. Multivariate Analysis of URI in Patients with ITP within Half a Year after Diagnosis. The dependent variable was the occurrence of URI (1 = yes, 0 = no) within six months after diagnosis of ITP patients, and the independent variables were the statistically significant features in Table 1. The categorical data was assigned a value (glucocorticoid application (1 = yes, 0 = no)), and the original value of the measurement data was entered. As indicated by the multivariate logistic regression analysis with results presented in Table 2, age, smoking history, glucocorticoid use, platelet count, serum CRP level, and lymphocyte subsets CD_4^+ and CD_8^+ were all risk factors for URI in patients with ITP within half a year after diagnosis ($P < 0.05$).

3.3. Establishment and Validation of the Risk Nomogram Model for URI in ITP Patients within Half a Year after Diagnosis. Seven independent risk factors obtained by logistic regression analysis were used for a nomogram model construction (Figure 1). Internal validation found that the predicted AUC, sensitivity, and specificity of the nomogram model for ITP patients with URI within six months after diagnosis were 0.936 (95% CI: 0.878-0.983), 0.942, and 0.865, respectively (Figure 2(a)). It suggests that the nomogram model has better discriminative ability. Hosmer-Lemeshow test for the deviation between the predicted value

TABLE 1: Single factor analysis that may affect the onset of symptoms in patients with ITP within half a year after diagnosis.

Clinical information	Noninfected group ($n = 190$)	Infected group ($n = 52$)	χ^2/t	P
Gender				
Male	112 (58.95)	26 (50.0)		
Female	78 (41.05)	26 (50.0)	1.334 ^b	0.248
Age (years)	59.45 ± 8.45	64.85 ± 10.92	3.815 ^a	<0.001
Drinking history				
Yes	56 (29.47)	20 (38.46)		
No	134 (70.53)	32 (61.54)	1.531 ^b	0.216
Smoking history				
Yes	71 (37.37)	37 (71.15)		
No	119 (62.63)	15 (28.85)	18.858 ^b	<0.001
Pathogen				
Virus	108 (56.84)	37 (71.15)		
Germ	82 (43.16)	15 (28.85)	3.482 ^b	0.062
Combined anemia				
Yes	67 (35.26)	22 (42.31)		
No	123 (64.74)	30 (57.69)	0.871 ^b	0.351
Use of glucocorticoid				
Yes	96 (50.53)	40 (76.92)		
No	94 (49.47)	12 (23.08)	11.557 ^b	0.001
Splenectomy treatment				
Yes	56 (29.47)	12 (23.08)		
No	134 (70.53)	40 (76.92)	0.827 ^b	0.363
CRP(mg/L)	3.19 ± 0.78	3.77 ± 0.85	4.659 ^a	<0.001
CD ₃ ⁺ (%)	74.39 ± 9.78	72.88 ± 9.22	0.998 ^a	0.319
CD ₄ ⁺ (%)	39.23 ± 6.59	34.74 ± 7.33	4.248 ^a	<0.001
CD ₈ ⁺ (%)	27.88 ± 6.64	34.78 ± 6.95	6.573 ^a	<0.001
Platelet count ($\times 10^9/L$)	25.25 ± 5.24	21.20 ± 6.85	4.610 ^a	<0.001

Note: CRP: C-reactive protein; CD₃⁺: CD3-positive T-lymphocytes; CD₄⁺: CD4-positive T-lymphocytes; CD₈⁺: CD8-positive T-lymphocytes. ^b stands for χ^2 test, and ^a stands for t -test.

TABLE 2: Logistic regression analysis of the onset of symptoms in ITP patients within half a year after diagnosis.

Variable	β	SE	Wald χ^2	P	OR (95% CI)
Age	0.095	0.028	11.320	0.001	1.100 (1.041, 1.163)
Smoking history	2.078	0.526	15.616	<0.001	7.987 (2.850, 22.383)
Glucocorticoid	1.853	0.551	11.328	0.001	6.378 (2.168, 18.763)
Blood platelet count	-0.138	0.045	9.393	0.002	0.871 (0.797, 0.951)
CRP	0.892	0.308	8.399	0.004	2.441 (1.335, 4.462)
CD ₄ ⁺	-0.108	0.038	8.399	0.004	0.897 (0.833, 0.967)
CD ₈ ⁺	0.203	0.040	26.022	<0.001	1.225 (1.133, 1.324)

Note: CRP: C-reactive protein; CD₄⁺: CD4-positive T-lymphocytes; CD₈⁺: CD8-positive T-lymphocytes.

of the model and the actual value (chi – square = 14.249, $P = 0.075$) indicates that the prediction model has a good calibration ability. The mean absolute error (MAE) of the calibration curve from 500 samplings by the bootstrap method was 0.013, indicating that the occurrence risk predicted by model is in good agreement with the actual occurrence risk (Figure 2(b)).

The validation set (50 cases, of which 39 cases did not have upper symptoms and 11 cases of upper symptoms) was used to externally validate the model, and an AUC of 0.890 (95% CI: 0.757-0.975), a sensitivity of 0.949, and a specificity of 0.727 were determined (Figure 3(a)), demonstrating favorable prediction accuracy of the nomogram model. The calibration curve is close to the ideal curve,

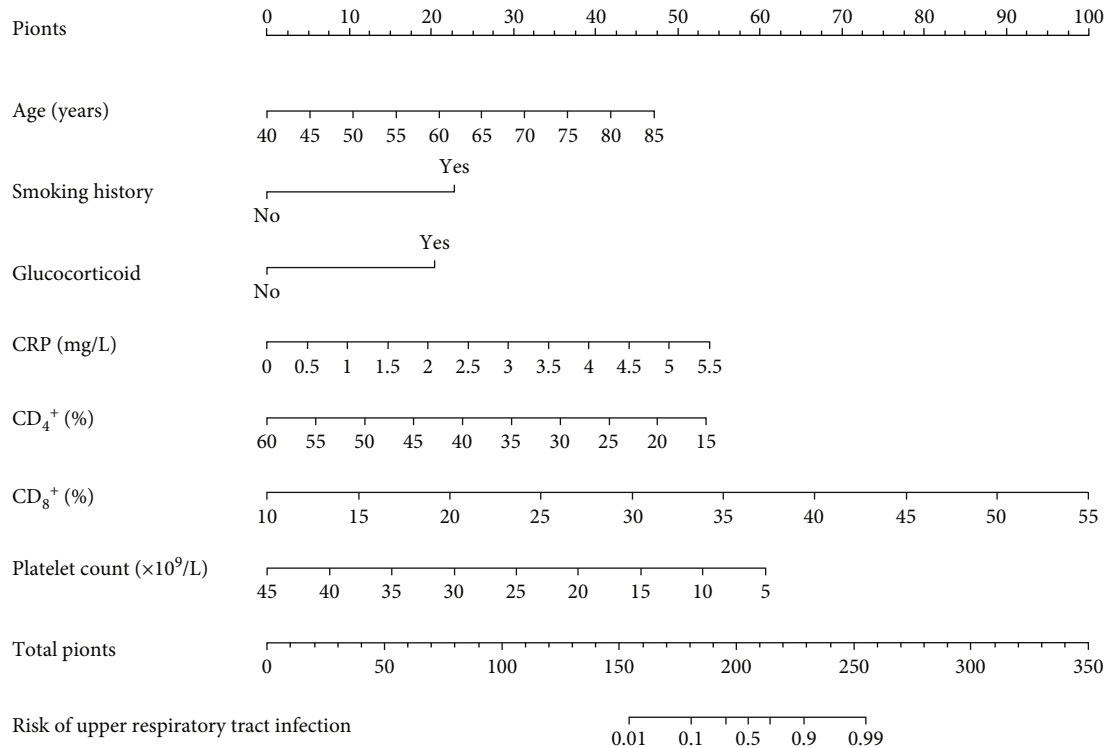


FIGURE 1: Nomogram model for predicting the risk of ITP patients to develop upper respiratory tract infection within half a year after diagnosis. CRP: C-reactive protein; CD₄⁺: CD4-positive T-lymphocytes; CD₈⁺: CD8-positive T-lymphocytes.

indicating that the predicted probability of the nomogram is basically consistent with the measured value (Figure 3(b)).

4. Discussion

With complex pathogenesis, ITP is generally believed to be linked to the reduction of platelet production and the excessive clearance of platelets by macrophages [10]. Studies have shown that [11], ITP patients with a history of respiratory tract infection in the first half of the month, the infection risk of ITP patients is much higher than that of the general population. Infection will increase the Fc and C3b receptors of macrophages, resulting in an increase in their affinity, and platelets are more easily destroyed [12]. ITP widely acknowledged to be associated with immune cell dysfunction and immune dysfunction [13]. Immune cell dysfunction and immune dysfunction are closely related to RTI [14]. However, the mechanism of the onset of symptoms in ITP patients within six months after diagnosis is unclear. Therefore, early and effective identification of ITP patients who are at risk of developing hypersensitivity is extremely important.

Among the 242 ITP patients, URI occurred in 52 cases, with an incidence rate of 21.49%, which was basically consistent with the results of domestic and foreign studies [15]. In this study, the age, using glucocorticoid, smoking, platelet count, serum CRP level, and lymphocyte subsets CD₄⁺ and CD₈⁺ were all influencing factors of ITP patients developing upper respiratory tract infection within half a year after diagnosis. Elderly patients are often accompanied by other underlying diseases and may take a variety of drugs at the same time, resulting in

a decline in body function and body resistance. Therefore, for elderly patients, follow-up should be strengthened, and preventive measures should be taken. For smokers, it is necessary to inform them of the dangers of smoking and instruct them to quit smoking. Because long-term smoking can easily lead to abnormal lung function in patients, the longer smoking time is, the easier it is to increase the risk of secondary respiratory tract infection in patients with ITP [16]. In the process of using glucocorticoid therapy, blood sugar will increase, which can cause the body's defense function to decline, and viruses and bacteria are more likely to invade the body at this time [17]. On the other hand, hormones can also affect the function of lymphocytes and monocytes, resulting in a decrease in the body's ability to resist infection, which leads to a greater susceptibility to upper respiratory tract infections [18]. Kimura and Kishimoto [19] analyzed the medical records of 1805 ITP patients exposed to glucocorticoids and found that secondary respiratory infections were closely related to the recent use of glucocorticoids, and even low-dose applications had certain risks.

CRP level is an important indicator for judging URI. When the body is injured or infected, the level of CRP will rise rapidly, and it will fall back quickly after the patient's condition improves [20]. CRP levels in children with ITP are negatively correlated with platelet counts, and elevated CRP predicts lower platelet counts [21]. Kapur et al. [22] found a close association between CRP levels and antiplatelet antibodies in children's ITP. This study confirmed that elevated CRP was a risk factor for the development of upper respiratory tract infection. The dysfunction of T lymphocyte subsets is involved in the occurrence and development of URI, and

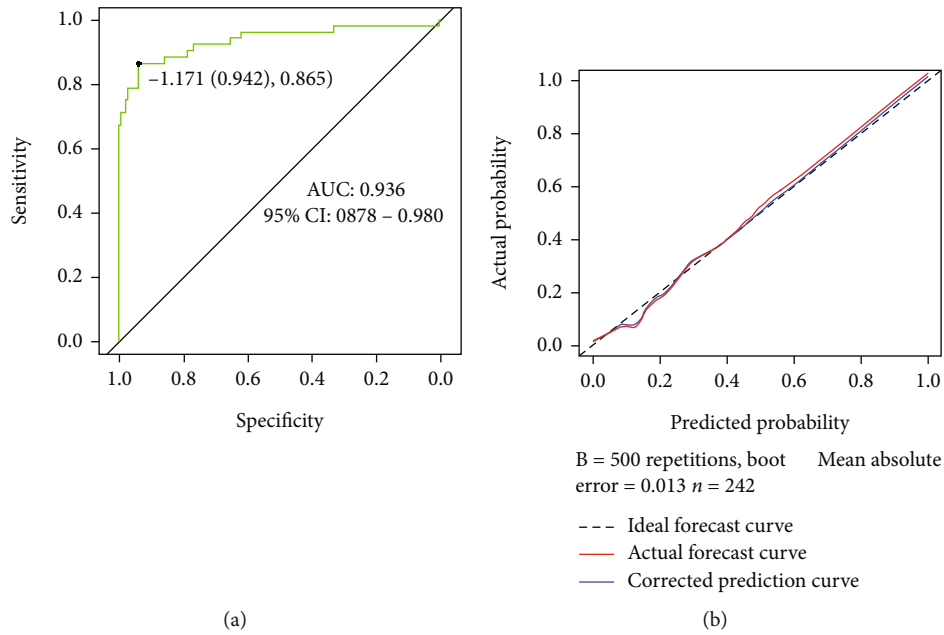


FIGURE 2: Internal verification of the nomogram model. (a) Risk of respiratory tract infection within six months after diagnosis in patients with primary immune thrombocytopenia by ROC curve. (b) Calibration curve of the nomogram model for training set. The Y- and X-axis represent the actual rate and the predicted risk of respiratory tract infection, respectively. The dotted line represents a perfect prediction made by an ideal model. The red line represents the actual model performance, and the closer it fits to the dotted line, the better the prediction.

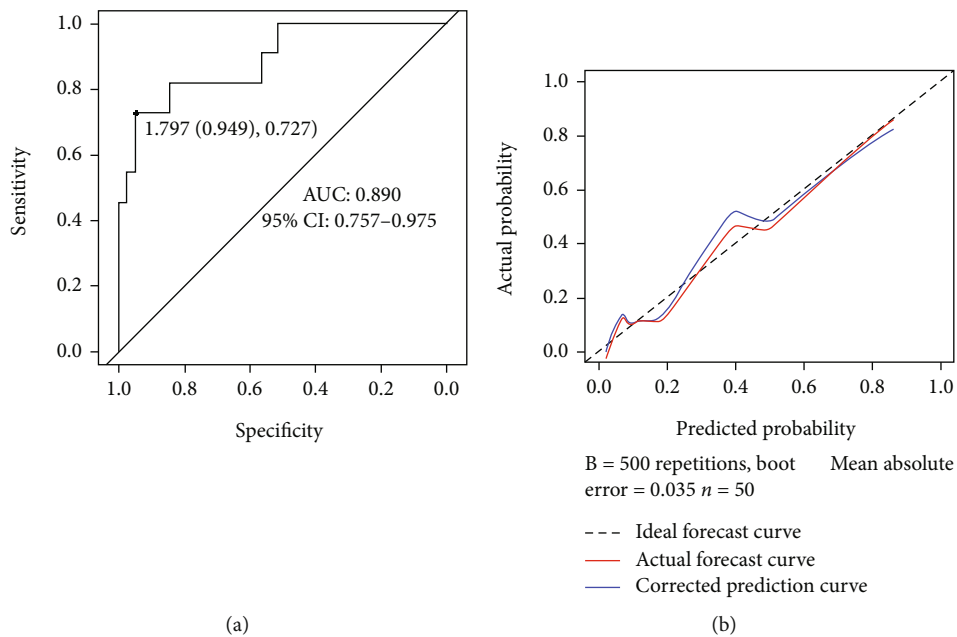


FIGURE 3: External verification of the nomogram model. (a) ROC curve of model evaluation for validation set. (b) Calibration curve of the nomogram model for validation set. The Y- and X-axis represent the actual rate and the predicted risk of respiratory tract infection, respectively. The dotted line represents a perfect prediction made by an ideal model. The red line represents the actual model performance, and the closer it fits to the dotted line, the better the prediction.

its dysfunction and low immune function are closely related to URI [23]. T lymphocyte subsets are important indicators for judging the immune function of the body. Mature T lymphocytes can be divided into CD_4^+ and CD_8^+ subsets according to surface markers [24]. The synergistic effect of CD_4^+

and antigen stimulates B cells to secrete plasma cells, and the CD_4^+ T cells in some ITP patients are destroyed, resulting in decreased cellular immune function, which may increase the risk of URI [25]. In this study, the CD_4^+ level was statistically significant in the multivariate analysis,

consistent with previous studies. CD_8^+ is a subset of cytotoxic cells or suppressor cells, an increase in the number indicates that the immune function is inhibited, and it is easy to cause a URI [26]. Platelets have a large number of receptor molecules on their surfaces, allowing them to rapidly sense invading pathogens and inflammation caused by infections [27]. Studies have shown [28] that respiratory tract infection is not only related to the immunomodulatory treatment of ITP patients but also to the platelet count of the disease itself. A compromised immune system can make patients more susceptible to infections before and after ITP develops. For bacterial infection, Gram-negative bacilli infection causes the release of endotoxin in the blood, which greatly enhances the phagocytosis of autoantibody-coated bacteria and accelerates the destruction of platelets [29]. For patients with low platelet levels, glucocorticoids, prednisone, dexamethasone, recombinant human thrombopoietin, and other drugs can be used for treatment. Doctors should adjust the treatment plan in a timely manner according to each patient's specific condition to ensure that the patient can get more benefits from the treatment.

Most of the previous research models are presented in the form of formulas, and the calculation process is complicated; not only there is the risk of calculation errors but also the workload of medical workers is increased. A good model should be effective, practical, and simple. The nomogram model can evaluate the prognosis intuitively, concisely, and accurately, which helps medical staff make better clinical decisions. Besides, the nomogram can uniquely reveal the correlation between relevant risk factors and outcome events [30]. In this study, a nomogram was built based on the abovementioned risk factors for URI in ITP patients within half a year after diagnosis, namely, age, corticoid application, smoking, serum CRP levels, and T lymphocyte subsets CD_4^+ , CD_8^+ , and internal verification was performed. The results showed that the model $AUC = 0.936$, sensitivity = 0.942, and specificity = 0.865 suggest that the nomogram model has better discriminative ability. After being verified by the validation set data, the predicted value of the model has a high consistency with the actual value, indicating that it has a good predictive ability. The limitation of this study is that this study is a single-center study, not a multicenter large-sample epidemiological survey. The data are from the same medical center, and there may be case selection bias. In the follow-up research work, this research group plans to cooperate with other centers to use its clinical data to further improve and improve the predictive value of the model.

5. Conclusion

Advanced age, use of glucocorticoid, smoking history, low platelet count, high CRP level, and low CD_4^+ and high CD_8^+ T cells were all risk factors for URI in patients with ITP within half a year after diagnosis. Based on logistic regression analysis, the nomogram model of the onset of symptoms in ITP patients within half a year after diagnosis has good discrimination and prediction accuracy. It can provide guidance for clinically accurate and personalized prediction of ITP patients.

Data Availability

The labeled dataset used to support the findings of this study are available from the corresponding author upon request.

Conflicts of Interest

The authors declare no competing interests.

Acknowledgments

The authors would like to express their gratitude for the support from the Science and Technology Plan Project of Hechi City (AB193632).


References

- [1] R. L. Wasserman, "Gammaplex® 5 and 10% in the treatment of primary immunodeficiency and chronic immune thrombocytopenic purpura," *Immunotherapy*, vol. 9, no. 13, pp. 1071–1088, 2017.
- [2] G. Bahoush, A. Poorasgari, and M. Nojomi, "Relationship of primary immune thrombocytopenic purpura and atopia among children: a case control study," *Scientific Reports*, vol. 10, no. 1, p. 11717, 2020.
- [3] A. M. Zahran and K. I. Elsayh, "CD4+ CD25+high Foxp3+ regulatory T cells, B lymphocytes, and T lymphocytes in patients with acute ITP in Assiut children hospital," *Clinical and Applied Thrombosis/Hemostasis*, vol. 20, no. 1, pp. 61–67, 2014.
- [4] R. T. Wang, X. G. Liu, Y. Hou, and M. Hou, "A physician-patient survey for primary immune thrombocytopenia: Chinese subgroup analysis of I-WISH International Survey," *Zhonghua Xue Ye Xue Za Zhi*, vol. 42, no. 5, pp. 369–375, 2021.
- [5] K. Reich, K. Kabashima, K. Peris et al., "Efficacy and safety of Baricitinib combined with topical corticosteroids for treatment of moderate to severe atopic dermatitis: a randomized clinical trial," *JAMA Dermatology*, vol. 156, no. 12, pp. 1333–1343, 2020.
- [6] X. Lin, H. Q. Zhang, L. H. Shou, X. L. Shen, and Z. X. Zhang, "Efficacy of vitamin D plus calcium with/without alendronate on bone metabolism in immunologic thrombocytopenic purpura patients with steroid treatment: nine-month results of a randomized, double-blinded, controlled trial," *Experimental and Therapeutic Medicine*, vol. 18, no. 2, pp. 1391–1398, 2019.
- [7] M. Wang, W. Liu, Y. Xu et al., "Predicting bleeding risk in a Chinese immune thrombocytopenia (ITP) population: development and assessment of a new predictive nomogram," *Scientific Reports*, vol. 10, no. 1, p. 15337, 2020.
- [8] Thrombosis and hemostasis Group, Hematology Society, and Chinese Medical Association, "Consensus of Chinese experts on diagnosis and treatment of adult primary immune thrombocytopenia (version 2016)," *Zhonghua Xue Ye Xue Za Zhi*, vol. 37, no. 2, pp. 89–93, 2016.
- [9] L. Li, X. Liao, J. Zhao, and Y. M. Xie, "Interpretation of chinese clinical guidelines for acute upper respiratory tract infection in children," *Zhongguo Zhong Yao Za Zhi*, vol. 42, no. 8, pp. 1510–1513, 2017.
- [10] G. Kistangari and K. R. McCrae, "Immune thrombocytopenia," *Hematology/Oncology Clinics of North America*, vol. 27, no. 3, pp. 495–520, 2013.

- [11] R. Kado and W. J. McCune, "Treatment of primary and secondary immune thrombocytopenia," *Current Opinion in Rheumatology*, vol. 31, no. 3, pp. 213–222, 2019.
- [12] D. Y. Cui, J. Zhang, Q. Zhang, H. F. Hao, Q. Q. Wu, and L. F. Sun, "Immunological damage effects of cytomegalovirus infection on bone marrow hematopoietic cells," *Zhonghua Yi Xue Za Zhi*, vol. 99, no. 22, pp. 1727–1730, 2019.
- [13] S. Audia, M. Mahévas, M. Samson, B. Godeau, and B. Bonnotte, "Pathogenesis of immune thrombocytopenia," *Autoimmunity Reviews*, vol. 16, no. 6, pp. 620–632, 2017.
- [14] P. C. Calder, A. C. Carr, A. F. Gombart, and M. Eggersdorfer, "Optimal nutritional status for a well-functioning immune system is an important factor to protect against viral infections," *Nutrients*, vol. 12, no. 4, p. 1181, 2020.
- [15] H. Eddou, A. Zinebi, A. Khalloufi et al., "Un purpura thrombopénique amégacaryocytaire acquis qui cache une leucémie aigue myéloblastique," *The Pan African Medical Journal*, vol. 26, p. 32, 2017.
- [16] J. J. Zuo, Y. Xi, M. X. Zhu et al., "Advances of studies on the occurrence of the upper respiratory disease correlative with immunity and tobacco," *Lin Chung Er Bi Yan Hou Tou Jing Wai Ke Za Zhi*, vol. 33, no. 10, pp. 1003–1008, 2019.
- [17] L. Cheng, C. Liu, F. Li et al., "The prediction value of Treg cell subtype alterations for glucocorticoid treatment in newly diagnosed primary immune thrombocytopenia patients," *Thrombosis Research*, vol. 181, pp. 10–16, 2019.
- [18] J. M. Ehrchen, J. Roth, and K. Barczyk-Kahlert, "More than suppression: glucocorticoid action on monocytes and macrophages," *Frontiers in Immunology*, vol. 10, p. 2028, 2019.
- [19] A. Kimura and T. Kishimoto, "IL-6: regulator of Treg/Th17 balance," *European Journal of Immunology*, vol. 40, no. 7, pp. 1830–1835, 2010.
- [20] M. Aronen, L. Viikari, I. Kohonen et al., "Respiratory tract virus infections in the elderly with pneumonia," *BMC Geriatrics*, vol. 19, no. 1, p. 111, 2019.
- [21] Y. Rama Kishore, B. Prashantha, M. Girish, and B. Manaswitha, "Increased C-reactive protein levels at diagnosis negatively predict platelet count recovery after steroid-treatment in newly diagnosed adult immune thrombocytopenia patients," *Thrombosis Research*, vol. 152, pp. 61–63, 2017.
- [22] R. Kapur, K. M. Heitink-Pollé, L. Porcelijn et al., "C-reactive protein enhances IgG-mediated phagocyte responses and thrombocytopenia," *Blood*, vol. 125, no. 11, pp. 1793–1802, 2015.
- [23] P. Han, Y. Hou, Y. Zhao et al., "Low-dose decitabine modulates T-cell homeostasis and restores immune tolerance in immune thrombocytopenia," *Blood*, vol. 138, no. 8, pp. 674–688, 2021.
- [24] N. H. Overgaard, J. W. Jung, R. J. Steptoe, and J. W. Wells, "CD4+/CD8+ double-positive T cells: more than just a developmental stage?," *Journal of Leukocyte Biology*, vol. 97, no. 1, pp. 31–38, 2015.
- [25] Z. Liu, W. Long, M. Tu et al., "Lymphocyte subset (CD4+, CD8+) counts reflect the severity of infection and predict the clinical outcomes in patients with COVID-19," *The Journal of Infection*, vol. 81, no. 2, pp. 318–356, 2020.
- [26] M. E. Schmidt and S. M. Varga, "The CD8 T cell response to respiratory virus infections," *Frontiers in Immunology*, vol. 9, p. 678, 2018.
- [27] V. I. Kullaya, Q. de Mast, A. van der Ven et al., "Platelets modulate innate immune response against human respiratory syncytial virus in vitro," *Viral Immunology*, vol. 30, no. 8, pp. 576–581, 2017.
- [28] G. Lippi, M. Plebani, and B. M. Henry, "Thrombocytopenia is associated with severe coronavirus disease 2019 (COVID-19) infections: a _meta_ -analysis," *Clinica Chimica Acta*, vol. 506, pp. 145–148, 2020.
- [29] H. Liu, X. L. He, B. Zhang, N. G. Xiao, Y. L. You, and Z. J. Duan, "Viral etiology in children with acute lower respiratory tract infections plus platelet disorders in Changsha, China: an analysis of 255 cases," *Zhongguo Dang Dai Er Ke Za Zhi*, vol. 16, no. 4, pp. 406–409, 2014.
- [30] L. Cai, X. Zhou, M. Wang et al., "Predictive nomogram for severe COVID-19 and identification of mortality-related immune features," *The Journal of Allergy and Clinical Immunology. In Practice*, vol. 9, no. 1, pp. 177–184.e3, 2021.

Research Article

Correlation Analysis of Computed Tomography Features and Pathological Types of Multifocal Ground-Glass Nodular Lung Adenocarcinoma

Jieli Kou,^{1,2} Xiaofei Gu,² and Liqing Kang^{1,3} 

¹Graduate School, Tianjin Medical University, Tianjin 300070, China

²Medical Imaging Center, Cangzhou People's Hospital, Cangzhou 061000, China

³Department of Magnetic Resonance Imaging, Cangzhou Central Hospital, Cangzhou 061014, China

Correspondence should be addressed to Liqing Kang; 201812210204015@zcmu.edu.cn

Received 3 June 2022; Revised 24 June 2022; Accepted 1 July 2022; Published 26 July 2022

Academic Editor: Pan Zheng

Copyright © 2022 Jieli Kou et al. This is an open access article distributed under the Creative Commons Attribution License, which permits unrestricted use, distribution, and reproduction in any medium, provided the original work is properly cited.

To investigate the correlation between computed tomography (CT) image characteristics of multiple lung ground-glass nodules (GGNs) and pathological classification, the CT image data of multiple lung GGN patients confirmed by pathology ($n = 132$) in our hospital were collected. The imaging features of GGNs were analyzed by qualified physicians, including lesion size (diameter, volume, and mass), location, CT values (mean and relative CT values), lesion morphology (round and irregular), marginal structure (pagination and burr), internal structure (bronchial inflation sign), and adjacent structure (pleural depression). CT imaging analysis was performed for the subtype of infiltrating adenocarcinoma (IAC). In CT findings, GGNs were greatly different from adenomatous hyperplasia (AAH), pure GGN adenocarcinoma in situ (AIS), and microinvasive adenocarcinoma (MIA) in terms of marginal structure, lesion morphology, internal structure, adjacent structure, and size ($P < 0.05$). The mean and relative CT values of mural adenocarcinoma, acinar adenocarcinoma, and papillary adenocarcinoma of IAC subtypes were greatly different from those of AAH/AIS/MIA ($P < 0.05$). In summary, the CT images of GGNs can be used as the basis for the differentiation of AAH, AIS, and MIA early noninvasive types and IAC invasive types, and the CT value of the IAC subtype can be used as the basis for the classification and differentiation of IAC pathological subtypes.

1. Introduction

Lung cancer is a relatively common malignant tumor with the highest morbidity and mortality throughout the year [1]. Although smoking is the main risk factor accounting for 80% to 90% of all lung cancer diagnoses [2], in recent years, the incidence among young and nonsmoking people has also shown an increasing trend, posing a serious threat to the health of Chinese people [3]. Lung cancer can be mainly classified into non-small-cell lung cancer (NSCLC) and small-cell lung cancer (SCLC). Among all lung cancers, NSCLC accounts for approximately 85-88%, and SCLC accounts for approximately 12-15% [4]. NSCLC is classified into three types according to its characteristics and treatment measures, namely, adenocarcinoma (55%), squamous

cell carcinoma (35%), and large cell carcinoma (10%) [5]. The probability of malignancy varies with the density of pulmonary nodules. Pulmonary nodules are classified into three types according to density, namely, ground-glass nodules (GGNs), solid nodules (SNs), and partial solid nodules (PSNs) [6]. The malignant probability from high to low is partially solid nodules, GGNs, and solid nodules [7].

GGN refers to the fuzzy nodules in the lung. The density of nodules is slightly higher than that of the surrounding lung parenchyma, but the outline of blood vessels and bronchus within the nodules can be seen [8]. Causes of GGN include inflammation, pulmonary fibrosis, and the most common early lung adenocarcinoma [9]. The study found that simple GGNs gradually evolved into lung adenocarcinoma (LA) during long-term follow-up, and lung

adenocarcinoma was classified into atypical adenomatous hyperplasia (AAH), adenocarcinoma in situ (AIS), minimally invasive adenocarcinoma (MIA), and invasive adenocarcinoma (IAC) [10]. Lung adenocarcinoma is more likely to metastasize earlier than lung squamous cell carcinoma, so lung adenocarcinoma has a poor prognosis and needs early diagnosis and treatment [11]. The pathological degree of early GGN was sorted according to the degree of malignancy, degree of invasion, and prognosis. AAH had the smallest volume, the lowest surgical trauma, and the lowest degree of malignancy, and the prognosis was the best without considering complications. Sometimes, after long-term observation, it is found that AAH does not change much and does not require treatment [12]. AIS has basically no difference in size compared with AAH, and the degree of malignancy is poor. Some lesions are slightly infiltrated, so they are difficult to identify, and the prognosis is better than that of MIA [13]. MIA is mainly mural growth, and the pathological differentiation between MIA and IAC mainly includes invasion of blood vessels and lymphatics, invasion of the pleura and airway, tumor necrosis, and airway transmission [14]. IAC is the final stage in the transformation of lung cancer, and there are five subtypes, namely, apical, acinar, papillary, solid, and micropapillary. The adherent type corresponds to high differentiation, acinar and papillary types correspond to medium differentiation, and solid and micropapillary types correspond to low differentiation. The higher the degree of differentiation, the better the prognosis, and the higher the proportion of the micropapillary type and solid type, the worse the prognosis.

After the widespread use of low-dose computed tomography (CT) in lung cancer examination, the number of GGNs detected has increased. Preoperative detection and positioning of GGNs by CT to identify the subtypes of early lung adenocarcinoma is crucial for accurate preoperative pathological diagnosis of patients by clinical staff [15]. However, how to distinguish infiltrating lesions from non- or microinfiltrating lesions according to CT images and enable patients to receive surgical treatment as soon as possible is the research focus of radiologists. The CT features of GGNs are related to the pathology of lung adenocarcinoma GGNs. With the development and popularization of high-resolution computed tomography (HRCT), the positional relationship between GGNs and surrounding capillaries and bronchi can be clearly displayed [16]. HRCT has obvious application value in the identification of GGNs and makes it possible to determine the pathological subtypes of lung adenocarcinoma with the CT features of GGNs. Clinicopathological diagnosis is the gold standard for differentiating cancer, and no CT, MRI, or other examination can ultimately determine the nature and type of lesions. Therefore, the study of the relationship between CT examination and pathological diagnosis is helpful to continuously improve the diagnostic accuracy of clinicians [17]. At present, there is no unified diagnostic standard for CT diagnosis of GGNs in clinical practice. In this study, the CT image features of GGNs were analyzed to distinguish different pathological subtypes of IAC and to study the relationship between the CT features of GGNs and pathological types of lung adenocarcinoma.

TABLE 1: Clinical data information of patients.

GGN type	Cases	Age	Sex	
			Male	Female
AAH	19	46.14 ± 5.78	10	9
AIS	23	46.01 ± 6.02	13	10
MIA	25	45.34 ± 5.14	12	13
IAC	65	51.76 ± 4.99*	29	36

* Compared with the noninfiltrating AAH/AIS/MIA group, $P < 0.05$.

TABLE 2: Clinical data of IAC subtype.

IAC subtype classification	Cases	Age	Sex	
			Male	Female
Adherent growth IAC	38	51.72 ± 4.99	18	20
Acinar IAC	18	50.01 ± 5.06	8	10
Papillary IAC	9	51.66 ± 5.18	3	6

2. Materials and Methods

2.1. General Information. In this study, 132 patients with chest CT examination and pathologically confirmed GGNs in hospital from May 2020 to May 2021 were enrolled. Inclusion criteria are as follows: complete and clear preoperative CT images of patients can be harvested through picture archiving and communication system (PACS); there were at least two GGNS with maximum diameters of no less than 25 mm in both lungs; postoperative pathology required thoracoscopic or thoracoscopic resection and staining, which was reviewed by at least one senior pathologist with 10 years of experience in diagnosis of tumor pathology, and pathological subtypes were classified according to the new classification in 2015. Exclusion criteria are as follows: patients unable to undergo surgical treatment and patients with incomplete imaging data. At the beginning of this study, patients or their families signed informed consent. This study was approved by the ethics committee of the hospital.

2.2. Examination Methods. 64-slice spiral CT machine was employed. Breath-holding training was performed before scanning, and the breath-holding state under breathing was calm during scanning. The supine position was the dominant position, and some patients were in the prone position. First, the whole lung was scanned with a thickness of 5-10 mm, including the axilla and chest wall on both sides. After GGN was found, a CT scan was performed again. The layer thickness was 1.25 mm target scan, and the standard algorithm and bone algorithm were reconstructed. The target scanning parameters were as follows. The collimator was 1.25 mm, the pitch was 1.375, the tube voltage was 120 kV, the tube current was 250-350 mAs, the field of vision was 16-24 cm, and the matrix was 512×512 . MPR was performed on all patient raw data at a 1.25 mm layer thickness on an ADW 4.5 or 4.7 workstation. The accompanying signs of GGN were displayed, with emphasis on the walking,

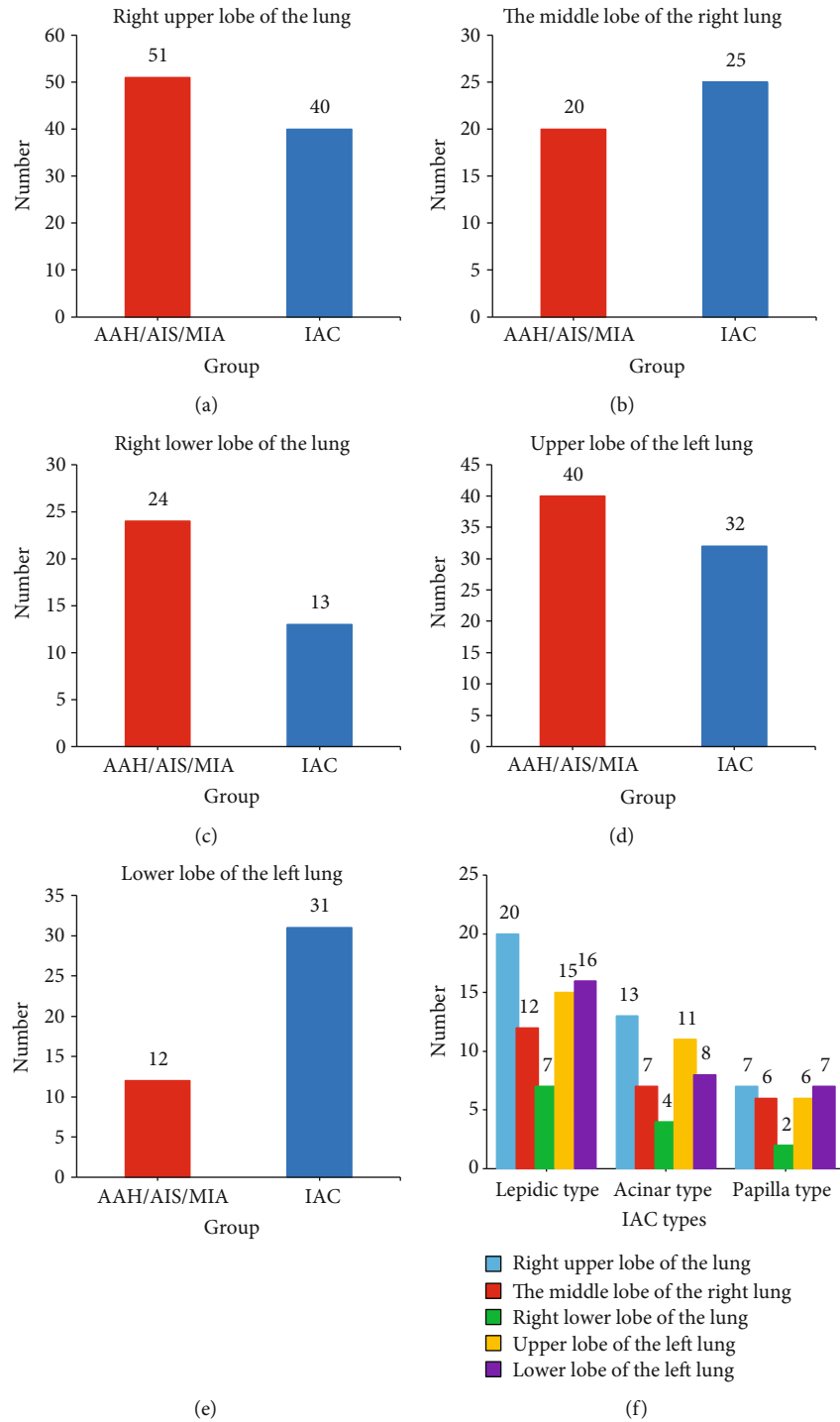


FIGURE 1: GGN location statistics. a–f showed the GGN location statistics of the upper lobe of the right lung, middle lobe of the right lung, lower lobe of the right lung, upper lobe of the left lung, lower lobe of the left lung, and various pathological subtypes of IAC, respectively.

morphology, and lumen of the relevant bronchi, and the relationship between them and lesions was recorded.

2.3. CT Scanning and Image Processing. The images were analyzed separately by two highly qualified physicians in the Department of Radiology, and the results were statistically analyzed. If there was any deviation in the analysis, the consensus of the two physicians was taken as the result.

2.4. Evaluation Content. The evaluation included location (right upper lobe, right middle lobe, right lower lobe, left upper lobe, and left lower lobe), lesion morphology (round and irregular), marginal lobulation and burr, internal structure (air bronchial sign), bronchial truncation, adjacent structure (pleural depression), lesion size (diameter and volume and mass), mean CT value, and relative CT value. Diameter was the average diameter of GGN, that is, the

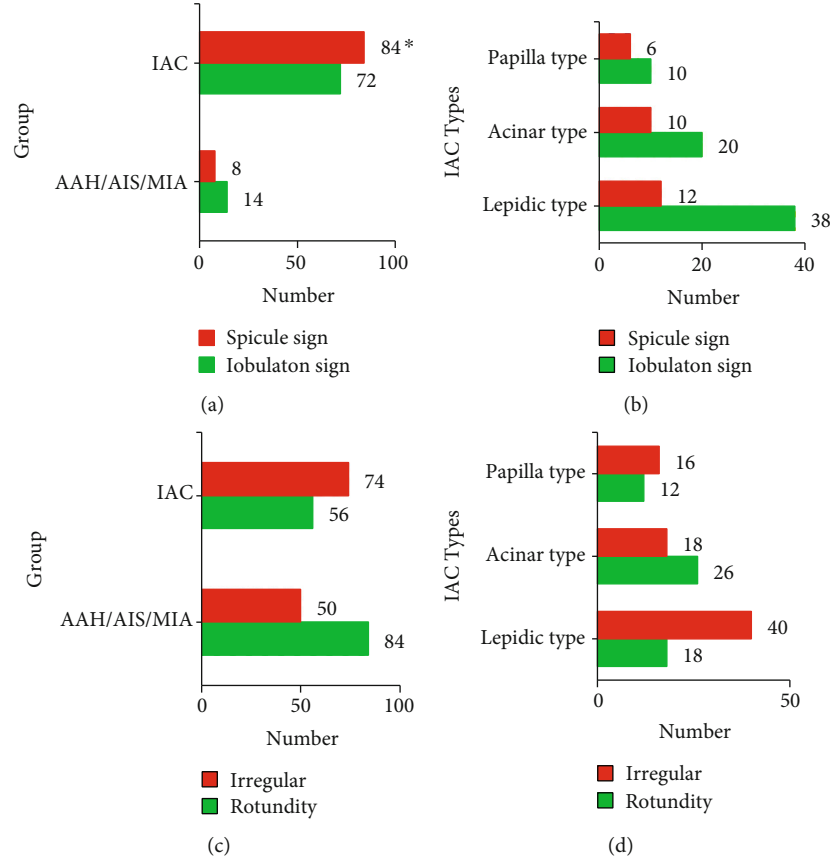


FIGURE 2: The marginal condition and lesion morphology of GGNs. (a–d) The pagination and burr at the edges of noninvasive GGNs and invasive GGNs, edge morphology of each pathological subtype of IAC, round and irregular lesion morphology of noninvasive GGNs and invasive GGNs, and lesion morphology of each pathological subtype of IAC, respectively. *Compared with the noninfiltrating AAH/AIS/MIA group, $P < 0.05$.

average of long diameter + short diameter on the largest layer of GGN in CT images. The maximum layer length L , short diameter W , and thickness T (number of nodular layers \times layer thickness) of GGNs were calculated, and the volume was calculated according to Equation (1). The mass was calculated according to Equation (2) [18].

$$V = \frac{1}{6} \pi \times L \times W \times T, \quad (1)$$

$$g = \frac{V \times (1000 + \text{CT value})}{10^6}. \quad (2)$$

The average CT value was measured at the corresponding GGN position three times and averaged. The relative CT value was the ratio of the average CT value of the largest layer of GGNs in the CT lung window to the average CT value of normal lung tissue in the same plane. When the GGN looks like a wave or shell edge, it is called a leaf-splitting sign. The burr mark is a nodular shadow with tubercle margins not reaching the pleura. Vacuolar sign refers to small round vacuoles appearing in nodules, while bronchial aeration sign refers to GGN signs containing gas in bronchioles that cross nodules. Therefore, it is difficult

to distinguish between the two images, so the experiment was combined with statistics.

2.5. Postoperative Pathological Analysis. After surgical resection, the lesions were fixed with paraformaldehyde and embedded in paraffin. Hematoxylin-eosin staining and immunohistochemical staining were performed after sectionalization. Classification and classification statistics were carried out according to the pathological classification method of lung adenocarcinoma subtype published by the World Health Organization (WHO) in 2015 [19].

2.6. Statistical Methods. SPSS 22.0 was used for data processing. ANOVA was used for measurement data. The Kruskal-Wallis H test was used when the samples did not conform to a normal distribution. The χ^2 test was used for technical data. $P < 0.05$ indicated that the difference was statistically significant.

3. Results

3.1. Statistical Results of Clinical Data. The patients were divided into two groups according to the degree of invasion. Sixty-seven patients had preinvasive lesions of lung adenocarcinoma (AAH/AIS/MIA group). There were 65 patients

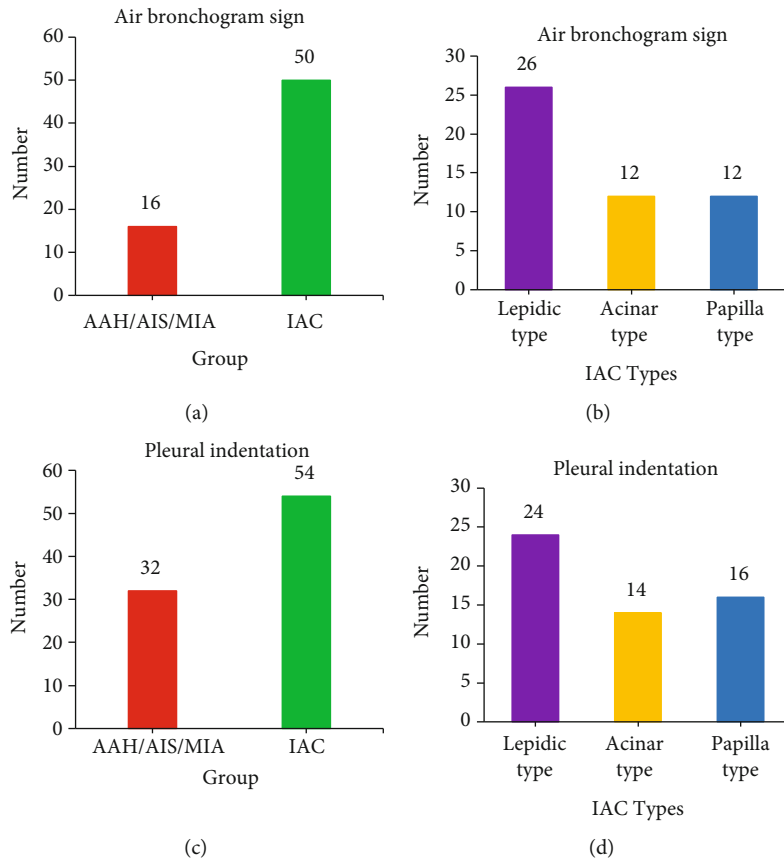


FIGURE 3: GGN internal structure and adjacent structure statistics. (a–d) The number of bronchial inflation signs in noninvasive GGNs and invasive GGNs, the internal structure of each pathological subtype of IAC, the number of noninvasive and invasive GGNs whose adjacent structures were pleural depressions, and the statistical analysis of adjacent structures of various pathological subtypes in IAC, respectively. *Compared with the noninfiltrating AAH/AIS/MIA group, $P < 0.05$.

with infiltrating adenocarcinoma (IAC group). In the IAC group, there were three subtypes, including 38 cases of adherent growth type IAC, 18 cases of acinar IAC, and 9 cases of papillary IAC. The clinical data of all GGN cases are shown in Table 1. The age of patients with IAC was higher than that of AAH, AIS, and MIA, and the difference was statistically significant ($P < 0.05$). The data of various pathological subtypes of IAC are shown in Table 2, and there was no significant difference between the data of various pathological subtypes of IAC ($P > 0.05$).

3.2. GGN Site Statistics Result. In Figure 1, there was no significant difference in GGN location between the AAH/AIS/MIA group and the IAC group ($P > 0.05$). There was no significant difference in the location of each pathological subtype of IAC ($P > 0.05$).

3.3. GGN Margin and Lesion Morphology. In Figure 2, the comparison of noninvasive and invasive GGN margins found that the number of GGNS with pagination and burrs in IAC margins was much higher than that in AAH/AIS/MIA ($P < 0.05$), and there was no significant difference among IAC subgroups. Comparison of noninvasive and invasive GGN lesions showed no significant

difference between IAC and AAH/AIS/MIA or between IAC subgroups.

3.4. GGN Internal Structure and Adjacent Structure. Since the bronchial inflation sign and air bubble sign are not easy to judge, both were counted as bronchial inflation signs in this experiment. In Figure 3, the number of bronchial inflation signs and pleural depression signs in IAC was much higher than that in AAH/AIS/MIA, and the difference was statistically significant ($P < 0.05$). There were no significant differences among the IAC subgroups.

3.5. Diameter, Volume, and Mass of GGNs. In Figure 4, the diameter, volume, and mass of infiltrating GGNs were much higher than those of noninfiltrating GGNs, and the difference was statistically significant (all $P < 0.05$). There was no significant difference between IAC subtypes (all $P > 0.05$).

3.6. Mean and Relative CT Values. In Table 3, both CT values and relative CT values of pathological subtypes in the IAC group were significantly different from those in the noninvasive AAH/AIS/MIA group ($P < 0.05$).

3.7. CT Features and HE Staining Analysis of GGNs. Atypical adenoma hyperplasia (Figure 5(a)) is a benign hyperplastic

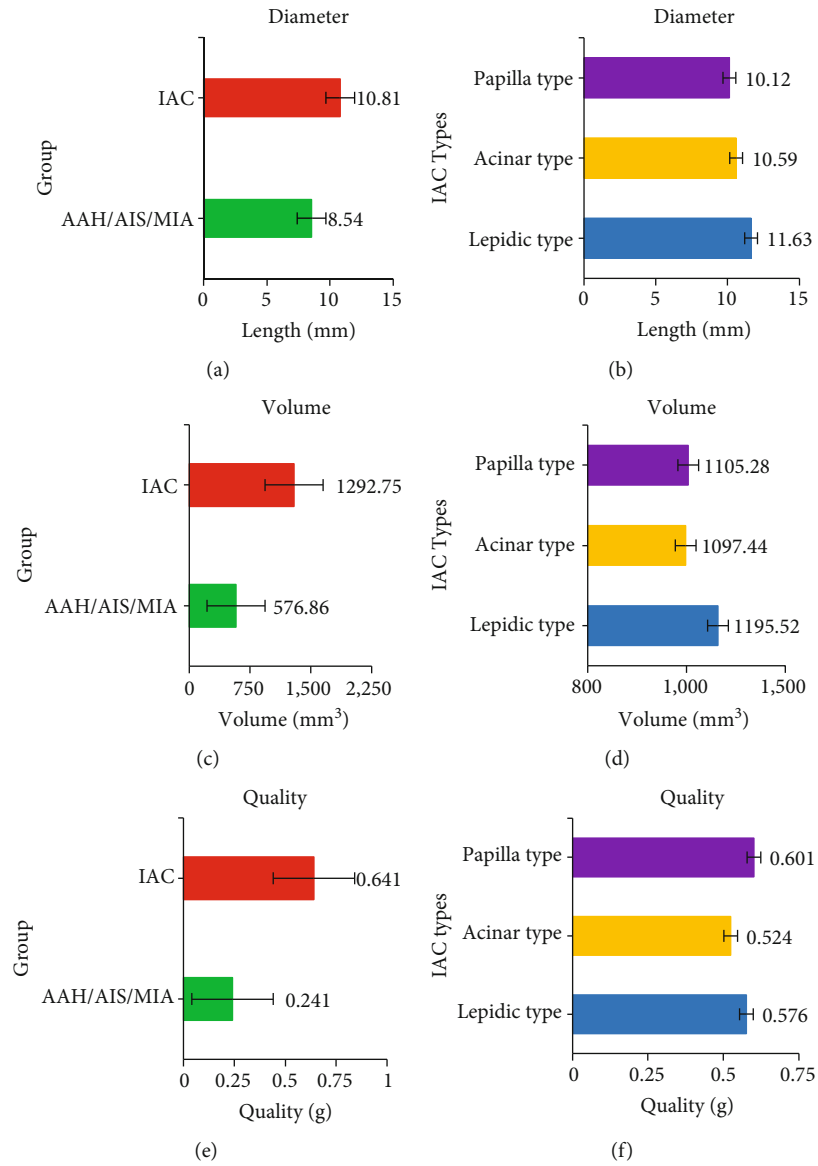


FIGURE 4: Diameter, volume, and mass statistics of GGNs. (a–f) The diameter of the noninfiltrating type and infiltrating type GGN, diameter of each pathological subtype of IAC, volume of the noninfiltrating type and infiltrating type GGN, volume of each pathological subtype of IAC, mass of the noninfiltrating type and infiltrating type GGN, and mass of each pathological subtype of IAC, respectively. *Compared with the noninfiltrating AAH/AIS/MIA group, $P < 0.05$.

TABLE 3: Comparison of mean and relative CT values between the infiltrating IAC group and the noninfiltrating AAH/AIS/MIA group.

Type	AAH/AIS/MIA	Pathological subtypes of IAC		
		Adherent growth IAC	Acinar IAC	Papillary IAC
CT value (HU)	-651 ± 103	$-603 \pm 76^*$	$-589 \pm 89^*$	$-565 \pm 73^*$
Relative CT value (HU)	0.77 ± 0.05	$0.63 \pm 0.12^*$	$0.65 \pm 0.11^*$	$0.53 \pm 0.14^*$

*Compared with the AAH/AIS/MIA group, $P < 0.05$.

disease that is also considered a precancerous lesion and may become cancerous if left untreated. Atypical adenomatous hyperplasia is a millimeter micronodular lesion that is indistinguishable from normal lung tissue in color and texture. It occurred in the central area of the acinar near the

respiratory bronchioles and consisted of mild-to-moderate atypia of type II alveolar cells or Clara cells growing along the alveolar wall (Figure 5(i)), which can form inconspicuous pseudopapillae. Nonmyxoid AIS showed nonsolid ground glass shadows (Figure 5(b)), which was histologically

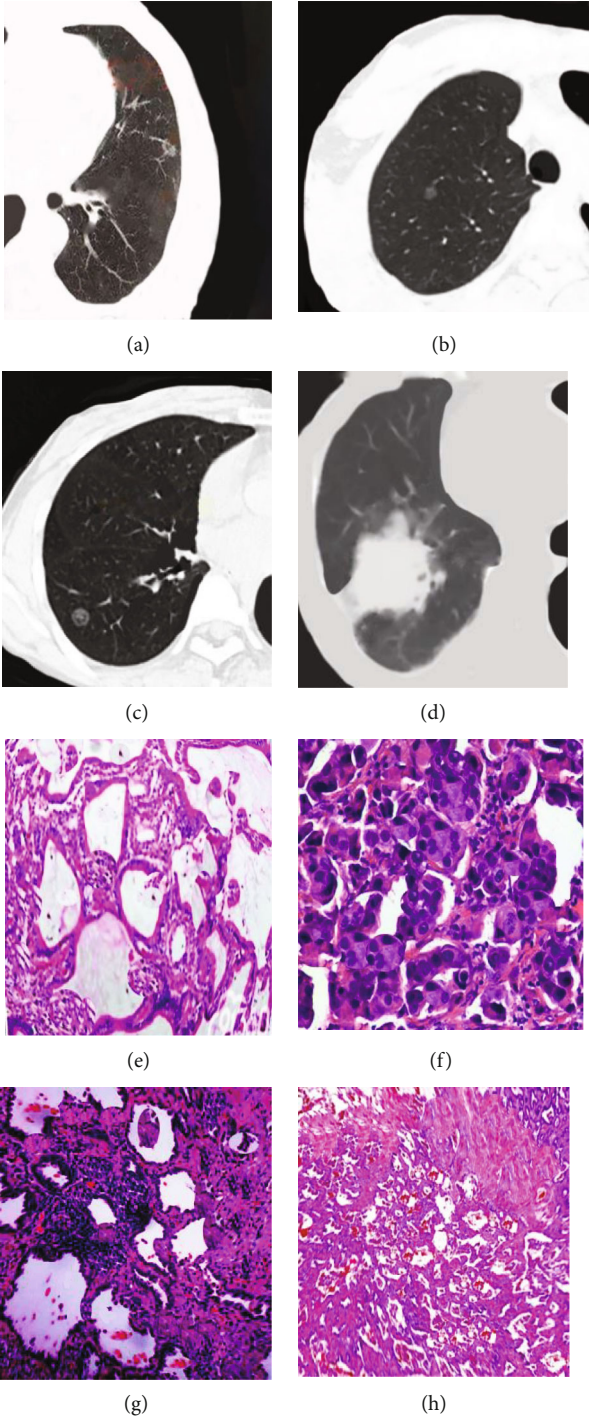


FIGURE 5: Continued.

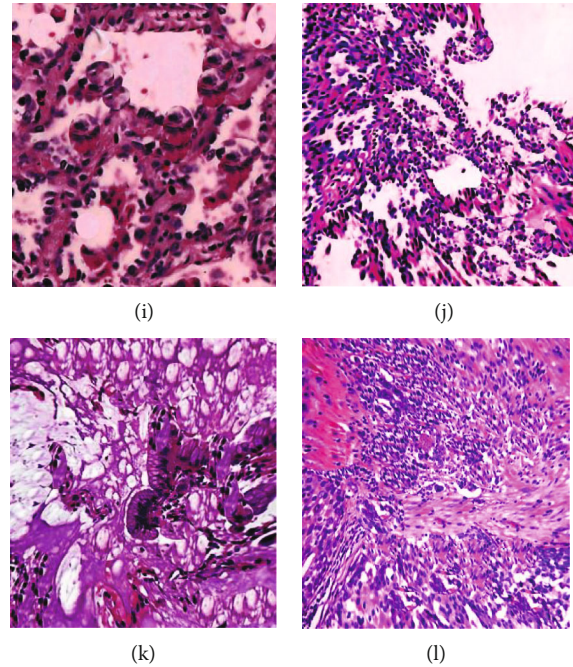


FIGURE 5: CT features of different GGNS and HE staining of infiltrating lung adenocarcinoma. (a) A CT scan of atypical adenomatous hyperplasia in the lower lobe of the patient's left lung; (b) a CT scan of a pure GGN in situ adenocarcinoma in the upper lobe of the patient's right lung; (c) an MIA in the middle lobe of the patient's right lung; (d) an invasive adenocarcinoma in the lower lobe of the patient's right lung; (e) the HE $\times 200$ staining diagram of invasive lung adenocarcinoma; (f) the HE $\times 200$ staining diagram of papillary lung adenocarcinoma; (g) the HE $\times 100$ staining diagram of acinar lung adenocarcinoma; (h) the HE $\times 100$ staining diagram of mural lung adenocarcinoma; (i) the HE $\times 200$ staining of atypical cell lung cancer; (j) the HE $\times 100$ staining of nonmucinous in situ lung adenocarcinoma; (k) the HE $\times 200$ staining of mucinous in situ lung adenocarcinoma; (l) the HE $\times 100$ staining of MIA.

similar to atypical adenomatous hyperplasia. The tumor cells in situ were denser, crowded, and lacked intercellular spaces (Figure 5(j)). Mucinous in situ adenocarcinoma often presents as solid nodules. Tall columnar tumor cells grow adherents with nuclei in the basement and a large amount of mucus in the cytoplasm (Figure 5(k)), similar to goblet cells, and the nuclei may be completely free of atypia. Chest CT of an MIA showed a small and impure GGN (Figure 5(c)) with a growth pattern other than adherence infiltrating into the stroma containing myofibroblasts (Figure 5(l)). Infiltrating adenocarcinoma presented irregular nodular shadows accompanied by vascular cluster signs and pleural depression signs (Figure 5(d)). Generally, HE staining (Figure 5(e)) showed three different subtypes, namely, the papillary type (Figure 5(f)), acinar type (Figure 5(g)), and mural type (Figure 5(h)).

4. Discussion

Lung cancer is more insidious than other cancers, and once symptoms appear, it is basically at an advanced stage, so physical examination is an effective means to find early lung cancer. CT is the most commonly used method for the diagnosis of lung cancer at present, which also leads to the delayed early diagnosis of lung cancer, so early CT detection is crucial [20]. GGN, as a CT imaging manifestation of early lung cancer, has received increasing attention. However, low-dose CT also detected massive GGNS. Classification of

GGNs and subtypes of lung adenocarcinoma cases by CT can help improve the accuracy of clinical staff's preoperative diagnosis of patients and select more accurate treatment methods for lesions [21]. The histological growth pattern and biological function of lung adenocarcinoma determine the gradual increase in density and change in morphology in the development process, so the manifestation on CT shows that GGN develops into PSN and SN.

Pathological studies of lung cancer have found that the increase in density and size of lesions is often a symbol of malignant lesions, so the size, volume, and mass of lesions are correlated with the degree of malignancy of lesions [22]. Three-dimensional GGN statistics have good repeatability and are most sensitive to changes in GGN volume with high specificity. Therefore, the GGN quality calculated by the volume of GGN can also well reflect the volume and density changes of GGN, with stronger accuracy and objectivity, which is of great significance to evaluate the pathology of GGN [23]. Some studies have found that the higher the diameter and execution composition of GGNS are, the higher the degree of malignancy of the tumor [24]. This study also found that the diameter, volume, and mass of IAC infiltrating lesions were much higher than those of noninfiltrating lesions, and the differences were statistically significant. The morphology of GGNS showed that the pagination morphology of IAC lesions was higher than that of noninvasive lesions, and the difference was statistically significant. The main reason for this phenomenon is the

diversity of cell growth in GGNs with different growth rates. Some cells with faster growth rates are blocked by adjacent lung tissues or interstitium, resulting in growth restriction and lobular signs [25]. Vacuolar or bronchoinflated signs appear histologically because tumor cells spread along the lung interstitium and the bronchial wall, mainly in the form of mural growth. This growth mode is more likely to invade the alveolar structure and fuse with the alveolar or bronchial wall to form an air cavity [26]. The number of cases with vacuolar or bronchoinflated signs of IAC was greater than that of non-IAC, and the difference was statistically significant. The pleural depression sign lesion was close to the pleura, and there was a contractile force, resulting in the adjacent pleura being pulled so that it was pulled to the side of the lesion. The occurrence of pleural depression indicates that the degree of malignancy of tumors is generally high. In this study, it was also found that the incidence of pleural depression in IAC infiltrating lesions was significantly higher than that in noninfiltrating lesions. In addition, the age of patients with AAH/AIS/MIA noninvasive surgery was lower than that of patients in the IAC group. This may be related to the pathological development of GGNs. The younger the patients are, the more benign the pathological type of GGN, while the older the patients are, the more likely the GGN pathology is malignant [27]. The progression of CT imaging manifestations of GGNs from AAH to IAC also means an increase in the execution components, density, and CT value, which also suggests the progression trend of pathological types of the lesions. This in turn explains why the age of onset in the IAC group was older than that in the preinvasive or MIA group. In general, the more real components of the GGN, the higher the CT value. This study found that the average CT value of each subgroup with IAC infiltration was higher than that of AAH/AIS/MIA, and the difference was statistically significant. This is related to the higher proportion of GGN solid components in each pathological subtype. The subtypes of IAC, if ordered by mean CT value, were found to have the lowest mean CT value in the mural growth type and vascular or lymphatic invasion. There was less pleural invasion or cellular airway spread or necrosis, and the average CT value of acinar type IAC was lower than that of papillary type. In addition, papillary IAC is more prone to vascular invasion or lymphatic invasion, pleural invasion, or cellular airway spread or necrosis, especially the airway spread of tumor cells, due to its histological morphology [28, 29].

5. Conclusion

In this study, CT features and pathological features of multiple GGN were used to explore the correlation between the two. It was found that the imaging features of GGN could be used as a reliable basis for the identification of AAH, AIS, MIA, and IAC, which were especially effective in the features of GGN's edge structure, lesion morphology, internal structure, adjacent structure, and size. The pathological subtypes of IAC can be distinguished by the mean CT value and relative CT value in early noninvasive lung adenocarcinoma of AAH, AIS, and NIA. However, the deficiency of

this study is that the number of patient samples is small, which cannot reflect the actual situation more objectively. More experimental cases should be included in subsequent studies. In addition, follow-up was not considered in this retrospective study, and multiple GGNS proved to be atypical adenomatous hyperplasia, AIS, microinvasive adenocarcinoma, and invasive adenocarcinoma after thoracoscopic or thoracotomy resection was included. The included samples were somewhat deviated, and isolated GGNS were not considered. In conclusion, this study is helpful for surgeons and radiologists to distinguish between patients with invasive and noninvasive lesions before surgery and to adopt different treatment regimens to improve patient outcomes.

Data Availability

The data used to support the findings of this study are available from the corresponding author upon request.

Conflicts of Interest

The authors declare no conflicts of interest.

References

- [1] N. Duma, R. Santana-Davila, and J. R. Molina, "Non-small cell lung cancer: epidemiology, screening, diagnosis, and treatment," *Mayo Clinic Proceedings*, vol. 94, no. 8, pp. 1623–1640, 2019.
- [2] M. B. Schabath and M. L. Cote, "Cancer progress and priorities: lung cancer," *Cancer Epidemiology, Biomarkers & Prevention*, vol. 28, no. 10, pp. 1563–1579, 2019.
- [3] S. Dubin and D. Griffin, "Lung cancer in non-smokers," *Molecular Medicine Reports*, vol. 117, no. 4, pp. 375–379, 2020.
- [4] Y. Wang, S. Zou, Z. Zhao, P. Liu, C. Ke, and S. Xu, "New insights into small-cell lung cancer development and therapy," *Cell Biology International*, vol. 44, no. 8, pp. 1564–1576, 2020.
- [5] R. Ruiz-Cordero and W. P. Devine, "Targeted therapy and checkpoint immunotherapy in lung cancer," *Surgical Pathology Clinics*, vol. 13, no. 1, pp. 17–33, 2020.
- [6] L. Sucony, D. M. Rassl, A. P. Barker, F. M. McCaughan, and R. C. Rintoul, "Adenocarcinoma spectrum lesions of the lung: detection, pathology and treatment strategies," *Cancer Treatment Reviews*, vol. 99, article 102237, 2021.
- [7] D. R. Baldwin and M. E. J. Callister, "Physician assessment of pretest probability of malignancy and adherence to guidelines for pulmonary nodule evaluation," *Chest*, vol. 152, no. 2, pp. 447–448, 2017.
- [8] B. Liu, "Diagnosis and treatment of pulmonary ground-glass nodules," *Zhongguo Fei Ai Za Zhi*, vol. 22, no. 7, pp. 449–456, 2019.
- [9] T. Xia, M. Cai, Y. Zhuang et al., "Risk factors for the growth of residual nodule in surgical patients with adenocarcinoma presenting as multifocal ground-glass nodules," *European Journal of Radiology*, vol. 133, p. 109332, 2020.
- [10] M. Yotsukura, H. Asamura, N. Motoi et al., "Long-term prognosis of patients with resected adenocarcinoma in situ and minimally invasive adenocarcinoma of the lung," *Journal of Thoracic Oncology*, vol. 16, no. 8, pp. 1312–1320, 2021.
- [11] B. Y. Wang, J. Y. Huang, H. C. Chen et al., "The comparison between adenocarcinoma and squamous cell carcinoma in

- lung cancer patients,” *Journal of Cancer Research and Clinical Oncology*, vol. 146, no. 1, pp. 43–52, 2020.
- [12] C. Nguyen, N. K. Larsen, N. Dietz, G. Sirineni, and M. Balters, “Pulmonary atypical adenomatous hyperplasia: diagnostic and therapeutic implications,” *Cureus*, vol. 11, no. 11, article e6079, 2019.
- [13] H. Xie and G. Chen, “The earliest stage of lung adenocarcinoma: the pathological diagnosis and clinical significance of adenocarcinoma in situ,” *Zhongguo Fei Ai Za Zhi*, vol. 24, no. 11, pp. 753–755, 2021.
- [14] M. Nie, K. Yao, X. Zhu et al., “Evolutionary metabolic landscape from preneoplasia to invasive lung adenocarcinoma,” *Nature Communications*, vol. 12, no. 1, p. 6479, 2021.
- [15] W. C. Hsu, P. C. Huang, K. T. Pan et al., “Predictors of invasive adenocarcinomas among pure ground-glass nodules less than 2 cm in diameter,” *Cancers*, vol. 13, no. 16, p. 3945, 2021.
- [16] Y. Meng, C. L. Liu, Q. Cai, Y. Y. Shen, and S. Q. Chen, “Contrast analysis of the relationship between the HRCT sign and new pathologic classification in small ground glass nodule-like lung adenocarcinoma,” *La Radiologia Medica*, vol. 124, no. 1, pp. 8–13, 2019, Epub 2018 Sep 6.
- [17] Y. Jin, Z. Chen, Q. Chen, L. Sha, and C. Shen, “Role and significance of bioactive substances in sputum in the diagnosis of lung cancer,” *Zhongguo Fei Ai Za Zhi*, vol. 24, no. 12, pp. 867–873, 2021.
- [18] G. Tao, L. Zhu, Q. Chen et al., “Prediction of future imagery of lung nodule as growth modeling with follow-up computed tomography scans using deep learning: a retrospective cohort study,” *Translational Lung Cancer Research*, vol. 11, no. 2, pp. 250–262, 2022.
- [19] A. G. Nicholson, M. S. Tsao, M. B. Beasley et al., “The 2021 WHO classification of lung tumors: impact of advances since 2015,” *Journal of Thoracic Oncology*, vol. 17, no. 3, pp. 362–387, 2022.
- [20] H. Kadara, L. M. Tran, B. Liu et al., “Early diagnosis and screening for lung cancer,” *Cold Spring Harbor Perspectives in Medicine*, vol. 11, no. 9, article a037994, 2021.
- [21] R. M. Hoffman, R. P. Atallah, R. D. Struble, and R. G. Badgett, “Lung cancer screening with low-dose CT: a meta-analysis,” *Journal of General Internal Medicine*, vol. 35, no. 10, pp. 3015–3025, 2020.
- [22] H. Hashimoto, J. Matsumoto, M. Murakami et al., “Progressively increasing density of the solid center of a ground-glass nodule in a solitary pulmonary capillary hemangioma: a case report,” *Pathology International*, vol. 70, no. 8, pp. 568–573, 2020.
- [23] Y. Yoshida, M. Yanagawa, A. Hata et al., “Quantitative volumetry of ground-glass nodules on high-spatial-resolution CT with 0.25-mm section thickness and 1024 matrix: phantom and clinical studies,” *European Journal of Radiology Open*, vol. 8, article 100362, 2021.
- [24] X. Shao, R. Niu, Z. Jiang, X. Shao, and Y. Wang, “Role of PET/CT in management of early lung adenocarcinoma,” *AJR. American Journal of Roentgenology*, vol. 214, no. 2, pp. 437–445, 2020.
- [25] R. Niu, X. Shao, X. Shao, J. Wang, Z. Jiang, and Y. Wang, “Lung adenocarcinoma manifesting as ground-glass opacity nodules 3 cm or smaller: evaluation with combined high-resolution CT and PET/CT modality,” *AJR. American Journal of Roentgenology*, vol. 213, no. 5, pp. W236–W245, 2019.
- [26] Y. Zhang, Y. Shen, J. W. Qiang, J. D. Ye, J. Zhang, and R. Y. Zhao, “HRCT features distinguishing pre-invasive from invasive pulmonary adenocarcinomas appearing as ground-glass nodules,” *European Radiology*, vol. 26, no. 9, pp. 2921–2928, 2016.
- [27] Q. Du, J. Peng, X. Wang, M. Ji, Y. Liao, and B. Tang, “Dynamic observation of lung nodules on chest CT before diagnosis of early lung cancer,” *Frontiers in Oncology*, vol. 12, article 713881, 2022.
- [28] Z. Wang, W. Zhu, Z. Lu, W. Li, and J. Shi, “Invasive adenocarcinoma manifesting as pure ground glass nodule with different size: radiological characteristics differ while prognosis remains the same,” *Translational Cancer Research*, vol. 10, no. 6, pp. 2755–2766, 2021.
- [29] M. Yoshida, M. Yuasa, H. Ogawa et al., “Can computed tomography differentiate adenocarcinoma in situ from minimally invasive adenocarcinoma?,” *Thoracic Cancer*, vol. 12, no. 7, pp. 1023–1032, 2021.

Research Article

Efficacy Analysis of Endovascular Therapy for Nonthrombotic Iliac Vein Compression Syndrome Combined with Chronic Venous Insufficiency

Renda Zhu , Xiaodong Jin, and Jiayi Shen

Department of General Surgery, Haining People's Hospital, Zhejiang Province, Haining, 314400 Zhejiang, China

Correspondence should be addressed to Renda Zhu; zjzhudada@hotmail.com

Received 27 May 2022; Revised 6 July 2022; Accepted 14 July 2022; Published 26 July 2022

Academic Editor: Pan Zheng

Copyright © 2022 Renda Zhu et al. This is an open access article distributed under the Creative Commons Attribution License, which permits unrestricted use, distribution, and reproduction in any medium, provided the original work is properly cited.

Purpose. This research is aimed at elucidating the clinical efficacy of balloon dilatation (BD) plus stent implantation for nonthrombotic iliac vein compression syndrome (NIVCS) combined with chronic venous insufficiency (CVI) in different compression positions. **Methods.** Sixty-five NIVCS patients comorbid with CVI admitted between December 2015 and April 2020 were selected and assigned to two groups according to different iliac vein compression positions. Both groups of patients received iliac vein BD + stent implantation, with the difference lying in that the tip of the stent was inserted 0.5-1 cm into the inferior vena cava (IVC) in the experimental group versus 2-3 cm in the control group. The technical success rate, the postoperative venous clinical severity score (VCSS), and the incidence of complications were compared. **Results.** The technical success rate of both groups was 100%. Patients were followed up for 12-36 months (average: 25.5 ± 6.2). Decreases in VCSS were observed in both cohorts at 3, 6, 12, 24, and 36 months postoperatively compared with the preoperative scores, but with no statistical difference. There was no death, nor related complications such as restenosis and lower limb deep vein thrombosis during the follow-up period, with no statistical difference in the incidence of complications between groups. **Conclusions.** BD + stent implantation is a safe and effective treatment for NIVCS with few complications and remarkable short-term and medium-term effects.

1. Introduction

Nonthrombotic iliac venous compression syndrome (NIVCS) refers to a condition in which the left common iliac vein or inferior vena cava (IVC) is compressed by the right common iliac artery and the fifth lumbar vertebra simultaneously, causing the venous return disorder of the left lower extremity [1, 2]. It is usually manifested as chronic venous insufficiency (CVI) such as superficial varicose veins, swelling, pain, and skin ulcers of the lower extremities, especially in the left lower limb [3]. According to clinical symptoms, it can be divided into either asymptomatic, CVI, or iliofemoral venous thrombosis type, among which the first two types belong to NIVCS [4]. According to relevant epidemiological data, about 24% of patients with iliac venous compression syndrome (IVCS) are asymptomatic, and clinical symptoms may appear when the disease is severe, posing a serious

threat to the physical and mental health and quality of life of such patients [5, 6]. Iliac vein balloon dilatation (BD) and stent implantation, which can correct obstructive lesions, relieve clinical symptoms, and reduce the risk of secondary deep vein thrombosis of lower limbs with a high mid- and long-term patency rate [7], have gradually become the preferred treatment for iliac vein stenosis and occlusion. In recent years, endovascular technology has become the preferred choice for NIVCS because of its advantages of minimal invasiveness, obvious clinical efficacy, few complications, and high technical success rate. At present, there is a growing consensus on endovascular treatment and primary stent implantation after BD [8-11]. But still, there are controversies about the positioning of the tip of stent implantation and the length of stent implantation into the IVC due to the difference of the iliac vein compression sites or the anatomical position of the iliac vein compression

point [12], which may lead to different postoperative complications. This study retrospectively analyzed the postoperative efficacy of 65 patients undergoing endovascular treatment for NIVCS in the Department of Vascular Surgery, Haining People's Hospital, from December 2015 to April 2020, and conducted a single-center efficacy analysis for endovascular treatment of NIVCS, aiming to provide reliable clinical evidence for the optimization of treatment techniques and improve the prognosis of such patients.

2. Materials and Methods

2.1. General Information. A total of 65 patients, including 40 males and 25 females, aged 36-81 years (mean: 64.2 ± 11.4), were diagnosed with left lower limb lesions, mainly presenting with varying degrees of chronic CVI symptoms such as pain, edema, varicose veins, pigmentation, and ulcer of the affected limb. All cases underwent digital subtraction angiography (DSA), the recognized gold standard for the diagnosis of IVCS [13], because DSA can clearly display the anatomical structure of the stenotic segment of the iliac vein and the function of deep vein valves and venous reflux of lower extremities and more intuitively show the degree and causes of stenosis. Generally, the diagnosis can be made by lower extremity DSA. And femoral vein catheterization was performed if DSA failed to diagnose the disease, and the diagnosis was based on the widening of left and right diameters of the iliac vein, weak contrast agent at the compression site, reduction of anterior and posterior diameters, and establishment of pelvic collateral circulation. Patients' enrollment criteria are as follows: (1) patients with C3 grade or above CVI according to the Clinical-Etiologic-Anatomic-Pathophysiologic (CEAP) classification [14], (2) iliac vein compression by more than 50% as indicated by intraoperative venography, (3) development of collateral circulation vessels, and (4) Patients who undergo surgical treatment with the consent for operation obtained from patients themselves or their families. Exclusion criteria are as follows: (1) lower extremity deep vein thrombosis (LEDVT) or postthrombotic syndrome; (2) presence of pelvic space-occupying lesions as indicated by pelvic color Doppler ultrasound, computerized tomography (CT), or magnetic resonance imaging (MRI); (3) patients with surgical intolerance due to heart, lung, liver, and renal insufficiency; and (4) patients with allergies to contrast agents or contraindications to anticoagulation. Patients were assigned to two groups according to the way of endovascular treatment, including 39 cases (experimental group) who underwent BD+stent implantation with the tip of the stent inserted 0.5-1 cm into the IVC and 26 cases (control group) who underwent the same procedure but with the tip of the stent inserted 2-3 cm into the IVC. The experimental group and control group were not statistically different in age, gender, CEAP classification, lesion side, and preoperative venous clinical severity score (VCSS) and were therefore comparable (Table 1). Exclusion criteria are as follows: acute LEDVT, LEDVT syndrome, pelvic space-occupying lesions, active bleeding, renal failure, patients who refuse endovascular treatment, elderly patients who cannot tolerate surgery, and those with a life expectancy less than 1 year.

2.2. Methods. Iliac vein compression was confirmed in both groups by preoperative lower limb venography. In the supine position, ipsilateral femoral vein puncture was performed on the affected side of the femoral vein, and a 10F vascular sheath was placed. The diagnosis and lesion were further confirmed by sheath angiography, and the guide wire was introduced to open the stenosis or occlusion segment. After confirmation, the pressure difference between the two ends of the stenosis was measured to be greater than 2 mmHg (1 mmHg = 0.133 kPa). According to the stenosis degree of the iliac vein lesion and the diameter of the proximal and distal veins of the diseased segment, a P3 (Cordis Company, USA) or 8-14mm charge balloon (Boston Scientific, USA) was selected to fully predilate the stenosis occlusion segment step by step in both groups, until the angiography showed that the stenosis of the iliac vein lesion was less than 30%, the peripheral collateral circulation was significantly reduced, and the pressure difference between the two ends of the stenosis was less than 2 mmHg. Then, primary Wallstent (Boston Scientific, USA) implantation was performed, with the diameter of the stent 1-2mm larger than the iliac vein, the length completely covering the diseased segment, and the proximal end exceeding the diseased segment by 5-10mm. Due to intraoperative displacement and contraction of the stent, the ejector rob of the delivery sheath was gently pushed forward every 3-4 cm during the stent release after positioning, so that the stent can be fully deployed as far as possible until it is completely released and completely attached to the iliac vein, so as to reduce the occurrence of postoperative stent displacement. It is advisable for the stent tip not to touch the opposite side wall of the IVC. After releasing the stent, radiography was performed in the anteroposterior-lateral position to confirm whether the stent was well opened, and if not, a balloon of appropriate size was selected for postexpansion. Subcutaneous injection of low molecular weight heparin was routinely administered once a day since the 1st postoperative day. Patients were required to wear elastic socks for 6 months after discharge and were given oral rivaroxaban 20 mg once a day for 3 months. The coagulation function was tested regularly.

2.3. Evaluation Methods. Technical success was defined as intraoperative angiography indicating smooth blood back-flow to the iliac vein and IVC, good stent opening without obvious displacement, and significantly less peripheral collateral circulation than before surgery, with the pressure difference between the two ends of stenosis less than 2 mmHg. The preoperative and postoperative VCSS, postoperative complications (stent thrombosis, bilateral LEDVT, stent displacement, etc.), and deaths in two groups were recorded and compared. The VCSS score ranges from 0 to 30, which is proportional to the venous clinical severity.

2.4. Statistical Methods. The data was statistically analyzed by the SPSS 20.0 (SPSS, Inc., Chicago, IL, USA) statistical software. The analyses of counting data recorded as % and measurement data expressed as $\bar{x} \pm s$ were performed by the χ^2 test and t -test, respectively, with $P < 0.05$ as the level of significance.

TABLE 1: Comparison of general data between two groups of patients.

General data	Control group ($n = 26$)	Experimental group ($n = 39$)	P value
Males (n (%))	18 (69.23)	22 (56.41)	>0.05
Age ($\bar{x} \pm s$, years old)	65.2 \pm 8.4	63.7 \pm 7.2	>0.05
Lesion side (n (%))			
Left side	26 (100)	39 (100)	>0.05
CEAP classification (n)			>0.05
C3	5 (19.23)	8 (20.51)	
C4	8 (30.77)	13 (33.33)	
C5	9 (34.62)	11 (28.21)	
C6	4 (15.38)	7 (17.95)	
Preoperative VCSS ($\bar{x} \pm s$, points)	14.3 \pm 2.28	14.54 \pm 2.76	

TABLE 2: Comparison of related results of patients with different types of compression.

Results	Left common iliac vein compression	Left common iliac and inferior vena cava compression
Lesion length (cm)	2.1 \pm 0.62	3 \pm 0.41
Stent diameter (mm)	14.15 \pm 0.45	14.31 \pm 0.62
Stent length	90	90
Patency degree	39 (100)	26 (100)

3. Results

In this study, there were 39 cases (60%) of left common iliac vein compression and 26 cases (40%) of IVC combined with left common iliac vein compression. The technical success rate of both groups was 100%, with no death, and the majority of patients experienced significant relief or disappearance of lower limb pain 1-3 days after endovascular treatment. The lower extremity pain relief rate, swelling relief rate, and ulcer healing rate in the experimental group were 90% (18/20), 100% (39/39), and 85.7% (6/7), respectively, while those in the control group were 86.7% (13/15), 100% (26/26), and 75% (3/4), respectively, with no statistical significance between groups. The success rate of endovascular surgery was 100%. The diameter of the implanted stent was 12-16 mm, mostly 14 mm (93.8%), and the length was 90 mm. Elastic stockings were used for treatment for at least 3 months after surgery. Patients all recovered well during the 12-36 (mean: 25.5 \pm 6.2) months of follow-up. Follow-up ultrasound examination showed 100% patency rate of the iliac vein, no stent displacement, stent thrombosis, or bilateral LEDVT. The results of lesion length, as well as stent diameter, stent length, and patency of patients with different types of compression, are shown in Table 2. No statistical differences were found in stent diameter, stent length, and postoperative patency between groups ($P > 0.05$). Follow-up showed that the patency rates of patients with stent diameters of 12 mm, 14 mm, and 16 mm were 100% (2 cases),

100% (60 cases), and 100% (3 cases), respectively, also showing no significant difference ($P > 0.05$). The VCSS also differed insignificantly between groups at 3, 6, 12, 24, and 36 months postoperatively ($P > 0.05$) (see Table 3 for details).

4. Discussion

The occurrence of iliac vein compression syndrome is a chronic process with the main clinical symptoms of lower limb swelling, varicose veins, pigmentation, lower limb ulcers, etc., which can be complicated by LEDVT and post-thrombotic syndrome in severe cases [7]. Current studies suggest that correcting iliac vein compression can improve the clinical presentations of patients with CVI, irrespective of the presence of venous reflux disorder [15]. However, instead of large-sample multicenter clinical analysis of iliac vein endovascular treatment in China, most of the current studies are single-center ones.

BD and stent implantation can significantly reduce lower limb pain, edema, and ulcers, while lowering the recurrence rate of venous reflux diseases. The purpose of stent implantation is to prevent venous elastic retraction and reduce the impact of the endovascular structure damaged by percutaneous endovascular angioplasty on blood flow, so as to reduce the risk of thrombosis. Regarding the indication of stent implantation in the treatment of NIVCS, Ming et al. [16] reported that this procedure was safe and effective with a high patency rate, despite the high incidence of iliac vein stenosis. However, not all patients with iliac vein stenosis need stenting, so the indications for iliac vein stenting should be strictly followed. First of all, DSA of the iliac vein of the lower limbs should be performed to widen the left and right diameters, weaken the contrast agent at the compression site, reduce the front and back diameters, and establish the pelvic collateral circulation, with the pressure difference between the two ends of the stenosis greater than 2 mmHg at rest. At the same time, the clinical symptoms of lower limbs, mainly including CEAP grading of CVI > grade 3, obvious swelling, pigmentation, or ulcers, should be taken into consideration. Most iliac vein lesions can be diagnosed by intravascular ultrasound [17] with a positive rate significantly higher than that of angiography. The area measurement provided by intravascular ultrasound is of great significance for diagnosing iliac vein occlusion and

TABLE 3: Comparison of postoperative follow-up VCSS between two groups ($\bar{x} \pm s$), points.

Group	Follow-up time				
	3 months	6 months	12 months	24 months	36 months
Experimental group	6.41 \pm 1.47*	5.32 \pm 1.02*	4.23 \pm 1.15*	3.57 \pm 1.53*	2.35 \pm 1.30*
Control group	6.53 \pm 2.13*	5.67 \pm 1.34*	4.37 \pm 1.60*	3.69 \pm 1.23*	2.24 \pm 1.24*
<i>P</i> value	>0.05	>0.05	>0.05	>0.05	>0.05

*Compared with the preoperative value, $P < 0.05$.

guiding stent placement, but this procedure has not been carried out in most primary hospitals in China at present. The second is the choice of stents. Currently, Wallstents, which are the only stents that can be implanted into the venous system and the exact one we used in our center, are used in most vascular surgeries in China. The third is the positioning of the stent. Raju et al. [18] and Professor Lu Xingwu from Shanghai Ninth People's Hospital believe that the stent should be inserted into the IVC for 3-5 cm to prevent the proximal end of the stent from collapsing and stent displacement. A research found that the implantation of an excessively long stent in the IVC may affect the contralateral iliac vein blood backflow and increase the incidence of contralateral LEDVT [19], although the actual clinical incidence is not high. In the actual clinical work, intraoperative angiography found that there was compression of both the IVC and the left common iliac vein in some patients, and a simple stent entering the IVC by 10 mm could not completely cover the stenosis segment, or the tip just covered the lesion segment. The total length of a Wallstent into the IVC may be 20-30 mm because it risks stent retraction. Some vascular surgeons perform simultaneous angiography of bilateral iliac veins before stent implantation and then released the stent under the roadmap, which is more conducive to the precise positioning of the stent. We believe that this method is more effective and feasible and can be popularized in primary hospitals.

Our center summarized the reasons for the failure of stent placement in other central iliac vein occlusions in the past. In order to prevent the potential risk of too much stent implantation into the IVC that affects the contralateral blood, some surgeons did not cover venous lesions before the primary stent implantation or made the tip of the stent exceeds the lesion too little, resulting in stent tip retraction, surgical failure, and even stent thrombosis and deep venous thrombosis of the affected lower extremity. Therefore, according to our experience, the tip of a Wallstent generally needs to exceed the proximal end of the compression point by 10 mm, as there is a risk of intraoperative and postoperative displacement because of its weak radial support but good flexibility. The diameter of the selected stent is generally 12-16 mm, and the length is mostly 90 mm. Intraoperative balloon is required to fully preexpand the stenosis or occlusion segment. On the basis of completely covering the diseased segment, a 90 mm long stent is preferred to reduce the possibility of displacement. During the release process, the joystick should be gently pushed forward every 3-4 cm of release to make the mesh of the stent open as completely as possible, so that the stent can fully adhere to the iliac vein and reduce intraoperative and postoperative stent displacement.

In this way, our center had significantly reduced intraoperative and postoperative stent displacement. This study determined no significant difference in stent length between different compression types. Therefore, different compression types do not seem to affect the short- and medium-term patency rate of stents, provided that the stent diameter is matched to fully cover the lesion, but follow-up reports on long-term outcomes are still lacking. The fourth issue is the diameter of the stent. It has been reported in the literature that the stent diameter has no significant impact on the patency rate and the relief of patients' symptoms [20]. The results of this study also confirm similar short- and medium-term patency rates of stents with different diameters. The size of the iliac vein stent should be avoided to be too small to cause residual symptoms. Generally, a dilatation balloon of the largest diameter corresponding to the diameter of the stent is selected in our center. The fifth is the patency of the stent. The iliac vein is prone to thrombosis due to its low pressure and slow flow rate. However, iliac vein stents have a high long-term patency rate, and the stent thrombosis rate is less than 5% for nonthrombotic iliac vein stenosis [21].

All the iliac vein stent thrombosis in our hospital were postsurgical patients with postthrombotic syndrome. None of the 65 patients included in this study had serious complications such as death, venous thromboembolism, severe bleeding at the puncture site, vascular rupture during dilatation, or operation-related infection. During the 12-36 months of follow-up, most of the venous functions of the lower limbs were significantly improved, with no serious complications (stent thrombosis, contralateral iliac femoral vein thrombosis, etc.). Therefore, it is considered that it is safe for stents to enter 3 cm of the IVC on the basis of completely covering the diseased segment. Limited by the characteristics of retrospective study, the sample size of this study was small and only supported by data from a single center, resulting in data collection bias. Besides, the habits of different surgeons may also affect the stent implantation and patency rate.

The innovations of this study are as follows: first, it confirms the efficacy, reliability, and safety of iliac vein BD plus stent implantation in the treatment of NIVCS patients with CVI from the aspects of technical success rate, VCSS scale, and safety. Second, related parameters and surgical details of this treatment technique were optimized by summarizing the reasons for previous failures of stent implantation of other central iliac vein occlusions, providing optimization means and clinical reference for the management of NIVCS patients with CVI.

5. Conclusion

In a word, BD combined with stent implantation is a safe and effective treatment for NIVCS with few complications and remarkable short- and medium-term effects. But there are still some controversies about the positioning before implantation and the length of the stent inserted into the IVC. We believe that full coverage of the diseased segment of the ipsilateral iliac vein and avoiding excessive length of stent insertion into the IVC should be considered at the same time during stent implantation. Large-sample studies are still required to further determine the patency rate of stents in the long term, as well as the effects of stents on complications associated with contralateral blood flow.

Data Availability

The labeled dataset used to support the findings of this study are available from the corresponding author upon request.

Conflicts of Interest

The authors declare no competing interests.

References

- [1] L. K. Tu, M. L. Nie, J. Fu et al., "Comparing the efficacy of endovascular treatment for iliac vein compression syndrome with or without acute deep venous thrombosis: a single-center retrospective study," *Vascular*, vol. 30, no. 2, pp. 341–348, 2022.
- [2] J. Birn and S. Vedantham, "May-Thurner syndrome and other obstructive iliac vein lesions: meaning, myth, and mystery," *Vascular Medicine*, vol. 20, no. 1, pp. 74–83, 2015.
- [3] N. Sermsathanasawadi, K. Pruekprasert, W. Pitaksantayothin et al., "Prevalence, risk factors, and evaluation of ilio caval obstruction in advanced chronic venous insufficiency," *Journal of Vascular Surgery: Venous and Lymphatic Disorders*, vol. 7, no. 3, pp. 441–447, 2019.
- [4] H. Che, G. Liu, Y. Yu, G. Sang, and X. Zhang, "Guidance of venous stent implantation after catheter-directed thrombolysis in patients with acute left lower extremity deep venous thrombosis based on pressure gradient differences between the iliac vein and inferior vena cava: a single-center retrospective study," *Annals of Vascular Surgery*, vol. 59, pp. 217–224, 2019.
- [5] Q. Radaideh, N. M. Patel, and N. W. Shamma, "Iliac vein compression: epidemiology, diagnosis and treatment," *Vascular Health and Risk Management*, vol. 15, pp. 115–122, 2019.
- [6] Y. C. Hsu, Y. K. Huang, L. S. Hsu, P. Y. Chen, and C. W. Chen, "Using non-contrast-enhanced magnetic resonance venography for the evaluation of May-Thurner syndrome in patients with renal insufficiency: a case report," *Medicine*, vol. 98, no. 52, article e18427, 2019.
- [7] A. M. Qian, Z. X. Cai, S. Zhang et al., "Endovascular treatment for non-thrombotic right iliac vein compression syndrome with intravascular ultrasound," *Zhonghua Yi Xue Za Zhi*, vol. 99, pp. 3633–3637, 2019.
- [8] H. F. Sang, J. H. Li, X. L. Du et al., "Diagnosis and endovascular treatment of iliac venous compression syndrome," *Phlebology*, vol. 34, no. 1, pp. 40–51, 2019.
- [9] J. Kong, P. Liu, J. Li et al., "Surgical treatment of recurrent varicose veins in the lower limbs associated with endovascular treatment of iliac vein stenosis," *International Journal of Surgery*, vol. 50, pp. 110–113, 2018.
- [10] Y. Zhu, L. Li, Z. Liu, and X. Cai, "Single-stage treatment of AngioJet rheolytic thrombectomy and stenting for iliac vein compression syndrome with secondary acute iliofemoral deep vein thrombosis," *Annals of Vascular Surgery*, vol. 61, pp. 384–393, 2019.
- [11] M. K. W. Lichtenberg, R. de Graaf, W. F. Stahlhoff, A. Ozkapi, T. Rassaf, and F. Breuckmann, "Venovo venous stent in the treatment of non-thrombotic or post-thrombotic iliac vein lesions - short-term results from the Arnsberg venous registry," *VASA*, vol. 48, no. 2, pp. 175–180, 2019.
- [12] L. D. S. Rodrigues, M. Bertanha, R. El Dib, and R. Moura, "Association between deep vein thrombosis and stent patency in symptomatic iliac vein compression syndrome: systematic review and meta-analysis," *Journal of Vascular Surgery: Venous and Lymphatic Disorders*, vol. 9, no. 1, pp. 275–284, 2021.
- [13] M. Li, L. Zhang, K. Zhang et al., "An efficacy and safety study of rivaroxaban for the prevention of deep vein thrombosis in patients with left iliac vein compression treated with stent implantation (plicts): study protocol for a prospective randomized controlled trial," *Trials*, vol. 21, no. 1, p. 811, 2020.
- [14] F. Kilinc, A. Akbas, S. Sener, Y. Hayran, and A. Aktas, "Cutaneous findings in patients with chronic venous insufficiency," *Journal of Cosmetic Dermatology*, vol. 21, no. 5, pp. 2106–2112, 2022.
- [15] S. Raju and P. Neglen, "High prevalence of nonthrombotic iliac vein lesions in chronic venous disease: a permissive role in pathogenicity," *Journal of Vascular Surgery*, vol. 44, no. 1, pp. 136–144, 2006.
- [16] Z. B. Ming, W. D. Li, R. F. Yuan, X. Q. Li, and W. B. Ding, "Effectiveness of catheter directed thrombolysis and stent implantation on iliofemoral vein thrombosis caused by iliac vein compression," *Journal of Thrombosis and Thrombolysis*, vol. 44, no. 2, pp. 254–260, 2017.
- [17] F. H. Rossi, A. M. Kambara, T. O. Rodrigues et al., "Comparison of computed tomography venography and intravascular ultrasound in screening and classification of iliac vein obstruction in patients with chronic venous disease," *Journal of Vascular Surgery: Venous and Lymphatic Disorders*, vol. 8, no. 3, pp. 413–422, 2020.
- [18] S. Raju, S. McAllister, and P. Neglen, "Recanalization of totally occluded iliac and adjacent venous segments," *Journal of Vascular Surgery*, vol. 36, no. 5, pp. 903–911, 2002.
- [19] O. Hartung, A. D. Loundou, P. Barthelemy, D. Arnoux, M. Boufi, and Y. S. Alimi, "Endovascular management of chronic disabling ilio-caval obstructive lesions: long-term results," *European Journal of Vascular and Endovascular Surgery*, vol. 38, no. 1, pp. 118–124, 2009.
- [20] U. B. Jeon, J. W. Chung, H. J. Jae et al., "May-Thurner syndrome complicated by acute iliofemoral vein thrombosis: helical CT venography for evaluation of long-term stent patency and changes in the iliac vein," *AJR. American Journal of Roentgenology*, vol. 195, no. 3, pp. 751–757, 2010.
- [21] M. Yin, X. Huang, C. Cui et al., "The effect of stent placement for May-Thurner syndrome combined with symptomatic superficial venous reflux disease," *Journal of Vascular Surgery: Venous and Lymphatic Disorders*, vol. 3, no. 2, pp. 168–172, 2015.

Research Article

Intelligent Three-Dimensional Reconstruction Algorithm-Based Ultrasound-Guided Nerve Block in Intraoperative Anesthesia and Postoperative Analgesia of Orthopedic Surgery

Cuijie Liu, Lin Li, Xuan Zhou, and Xiuyan Wang 

Department of Anesthesiology, Affiliated Hongqi Hospital of Mudanjiang Medical University, Mudanjiang, 157011 Heilongjiang, China

Correspondence should be addressed to Xiuyan Wang; 201630204011@stu.swun.edu.cn

Received 4 June 2022; Revised 24 June 2022; Accepted 4 July 2022; Published 22 July 2022

Academic Editor: Pan Zheng

Copyright © 2022 Cuijie Liu et al. This is an open access article distributed under the Creative Commons Attribution License, which permits unrestricted use, distribution, and reproduction in any medium, provided the original work is properly cited.

This research was aimed at analyzing the role of ultrasound-guided nerve block based on intelligent three-dimensional (3D) reconstruction algorithm in intraoperative anesthesia and postoperative analgesia of orthopedic surgery. 68 elderly patients were undergoing orthopedic surgery on the lower extremities, and they were randomly rolled into two groups with 34 patients in each group. The patients in control group received sciatic nerve block anesthesia (SNBA), and the patients in the experimental group received ultrasound-guided SNBA (UG-SNBA) under 3D reconstruction algorithm to analyze and compare the anesthesia effect and the postoperative analgesia effect. The results showed that compared with other algorithms, the evaluation index of ultrasound images processed by the 3D reconstruction algorithm was better. In terms of anesthesia effect, there was no significant difference in systolic blood pressure, diastolic blood pressure, and heart rate between the two groups before surgery ($P > 0.05$). Intraoperative and postoperative indicators of the experimental group were significantly better than those of the control group; the drug dosage (61 mg) was less than that of the control group (78 mg). In addition, the onset time of anesthesia, the time of pain blockade, and the postoperative awake time (5 minutes, 8 minutes, and 8 minutes, respectively) were shorter than those in the control group (13 minutes, 15 minutes, and 15 minutes, respectively). The visual analogue scale (VAS) scores of the experimental group were better than those of the control group on the day after surgery, one day after surgery, two days after surgery, and three days after surgery, with significant differences ($P < 0.05$). In summary, 3D reconstruction algorithm-based ultrasound image effect was clearer, the effect of UG-SNBA was more stable, and the postoperative analgesic effect was better. This work provided a higher reference for the selection of safe and effective anesthesia options in orthopedic surgery.

1. Introduction

Orthopedic surgery is clinically divided into four levels, ranging from simple to complex. The first-level surgery mainly refers to debridement, and the second-level surgery mainly refers to traumatic tendon repair. The third-level surgery mainly refers to complicated internal fixation of limbs, bone shaft fractures, and intra-articular fractures, and the fourth-level surgery mainly refers to the surgery of the cervical spine [1, 2]. The elderly are the main patients suffering from orthopedic diseases, especially the lower limb bones. The main reason is that with age, the loss of calcium

in the body leads to osteoporosis, which makes the incidence of orthopedic diseases in the elderly dramatically higher than patients of other ages. For the elderly patients during orthopedic surgery, more requirements are required during the surgery due to their weaker functions in all aspects of the body, so that the anesthesia effect of the elderly patients can be more secure in surgery [3, 4].

When elderly patients undergo anesthesia surgery on the lower extremities, sciatic nerve block anesthesia (SNBA) is generally performed, which is one of the local anesthesia. The principle of nerve block anesthesia is described as follows. The local anesthesia drug was injected near the

peripheral nerve trunk to block the conduction of nerve impulses, thereby making this part of the nerve controlled area anesthesia [5]. The sciatic nerve is composed of the fourth lumbar to the three anterior branches of the sacrum and is the largest body nerve. It ranges from the foramen of the piriformis muscle out of the pelvis, goes to the deep surface of the gluteus maximus, then passes through the greater trochanter and ischial tuberosity, and then, descends to the back of the thigh, which mainly affects the calf and foot. When the SNBA is adopted, the puncture point is often used between the piriformis muscle and the superior muscle. There are two methods of anesthesia, namely, the lateral position sciatic nerve block method and the supine position sciatic nerve block method [6, 7]. In anesthesia, the anesthesia teacher usually finds a suitable puncture location based on his own past experience. However, due to the large differences in the body of elderly patients, there are different signs on the body surface, which makes the difficulty of puncture success increase, decreasing the success rate of anesthesia. The introduction of ultrasound technology to assist anesthesia in orthopedic surgery can improve the success rate of puncture and make the anesthesia effect better [8].

Ultrasound technology to guide the nerve tissue is a new and innovative technology. Ultrasound interacts with human tissue to form information and then enlarges the information [9] to form an image, which is used to determine the specific location of human tissue, so as to assist doctors in better treatment of patients [10]. Due to the low time efficiency of traditional ultrasound technology, the image quality is relatively unclear. With the development of information technology, modern medical imaging technologies such as computed tomography and ultrasound have also developed. Compared with other imaging technologies, ultrasound is less harmful to the human body, and the speed of ultrasound imaging is faster. In addition, it shows the characteristics of real-time, which can give the doctor a timely response to the patient's tissue location and pathology [11, 12]. On this basis, great progress has been made in medical diagnosis and treatment technology. However, two-dimensional (2D) images can only express the anatomical information of a certain section and cannot determine the three-dimensional (3D) structure of the tissue and the relationship between them. Therefore, it is necessary to display the 3D structure and shape of human organs and obtain structural information that cannot be provided by traditional methods [13]. The 3D reconstruction algorithm of medical images can convert 2D images into 3D images with intuitive 3D effects, showing the 3D shape of human tissue. The region of interest can be observed from multiple directions and angles to obtain more information, which is of great significance for clinicians to formulate more scientific surgical plans [14, 15]. The introduction of the ultrasound-guided nerve block of the intelligent 3D reconstruction algorithm in the anesthesia during orthopedic surgery can better assist in the orthopedic surgery. There have been many reports on the ultrasound image of 3D reconstruction algorithm, but there are few studies on its application to guided nerve block in orthopedic surgery anesthesia and postoperative analgesia effect. In this study, the role of ultrasound-

guided SNBA (US-SNBA) based on the intelligent 3D reconstruction algorithm in orthopedic surgery anesthesia and postoperative analgesia effect was explored, aiming to provide a theoretical guidance for clinical orthopedic surgery.

2. Materials and Methods

2.1. Objects and Grouping. In this study, 68 elderly patients who underwent orthopedic surgery on the lower extremities in hospital from January 2019 to January 2020 were selected as subjects, including 36 males and 32 females. The patients who did not cooperate in the whole process in the later period were excluded. They were randomly divided into two groups, with 34 people in each group. Subjects in the experimental group were 20 males and 14 females, and there were 16 males and 18 females in the control group. The patients in control group received sciatic nerve block anesthesia (SNBA), and those in the experimental group received ultrasound-guided SNBA (UG-SNBA) under 3D reconstruction algorithm to analyze and compare the anesthesia effect and the postoperative analgesia effect. This study had been approved by ethics committee of the hospital. The patients and their families had signed the relevant informed consents.

Inclusion criteria are as follows: the age range was between 60 and 80 years old; the patients were clinically diagnosed to be able to undergo orthopaedic surgery; and the patients had not undergone other surgical treatment recently.

Exclusion criteria are as follows: patients with other organic diseases, patients with incomplete clinical data acquisition, and patients who did not cooperate with the whole treatment.

2.2. Principles of 3D Reconstruction Algorithm. 3D reconstruction is the main purpose of human vision and the main research direction of computer vision. It represents the process of recovering the 3D coordinates of spatial points from a single image plus scene constraints and two or more images (Figure 1).

3D reconstruction requires depth measurement. Firstly, the depth information of the object or scene was obtained, and then, the 3D modeling was performed to form a 3D representation of the object or scene. The flowchart was shown in Figure 2 below.

3D scene reconstruction includes surface reconstruction and weight reconstruction. Surface reconstruction describes the 3D structure of the object through the splicing of geometric units to fit the surface of the object. There are polygonal mesh surfaces, curved surfaces, tensor product surfaces, and superquadric. The surface patch was expressed by a polynomial, and the plane was shown in Equation (1); the bilinear surface, hyperboloid patch, bicubic surface, and sub-surface patch were shown in Equations (2)–(5), respectively. In the below equations, Z was the surface patch, a referred to the coefficient, and x and y represented the coordinate axes.

$$Z_1 = a_0 + a_1x + a_2y, \quad (1)$$

$$z_3 = z_2 + a_4x^2 + a_5y^2, \quad (2)$$

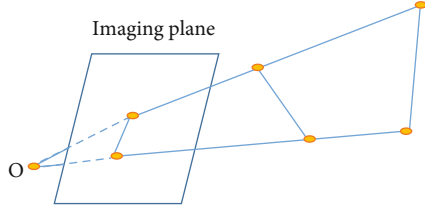


FIGURE 1: Schematic diagram of image reconstruction.

$$z_2 = z_1 + a_3xy, \quad (3)$$

$$z_4 = z_3 + a_6x^3 + a_7x^2y + a_8xy^2 + a_9y^3, \quad (4)$$

$$z_5 = z_4 + a_{10}x^4 + a_{11}x^3y + a_{12}x^2y^2 + a_{13}xy^3 + a_{14}y^4. \quad (5)$$

For triangular surface interpolation, the image plane coordinates were calculated for a point (a, b) in the image, and the x coordinate and y coordinate were expressed in Equation (6) and Equation (7), respectively.

$$x_b = b - \frac{m-1}{2}, \quad (6)$$

$$y_a = -a + \frac{n-1}{2}. \quad (7)$$

The three noncollinear points of the store in the depth image were obtained, and the plane corresponding to the three points were calculated. The depth value of (a, b) on the plane was calculated with

$$z_{ab} = a_0 + a_1x_b + a_2y_a. \quad (8)$$

When a 3D image was constructed, its linear interpolation can be used to model the surface patch through a binary linear function, as shown in

$$f(x, y, z) = a_0 + a_1x + a_2y + a_3z + a_4xy + a_5yz. \quad (9)$$

The minimum median square rule and the resampling strategy were adopted to achieve robust regression, as shown in Equation (10), in which c and a in the above equation both represented coefficients.

$$\operatorname{argmin}|\operatorname{med}[z_a - f(x_a, y_b); c]|. \quad (10)$$

When the surface was approximated, the model of the reconstructed surface was set as

$$z = f(x, y; a_0, a_1, \dots, a_{m-1}). \quad (11)$$

The surface reconstruction is actually a regression of determining the parameters of the surface model for the most suitable data. The regression function was shown in

$$\chi^2 = \sum_{a=0}^{n-1} (z - f(x, y; a_0, a_1, \dots, a_{m-1}))^2. \quad (12)$$

When the function was regularized, an approximation

constraint function can be added to make the surface you selected, and there was a unique solution for the function, as shown in

$$\chi^2 = \sum_{a=0}^{n-1} \left(z_a - f(x_a, y_b)^2 + \alpha^2 \iint \left(\frac{\partial^2 f}{\partial x^2} + 2 \frac{\partial f}{\partial x} \frac{\partial f}{\partial y} + \frac{\partial^2 f}{\partial y^2} \right) dx dy \right). \quad (13)$$

The result of the trilinear interpolation was shown in Equation (14), and the isosurface was defined as Equation (15), in which c was a constant.

$$f(x, y, z) = a_0 + a_1x + a_2y + a_3z + a_4xy + a_5yz + a_6zx + a_7xyz, \quad (14)$$

$$(x, y, z) | f(x, y, z) = c. \quad (15)$$

2.3. Surgical Procedure. For all patients, it should establish intravenous access, closely monitor the vital signs, intravenously inject 0.5 mg penehyclidine hydrochloride injection, and take nerve block anesthesia after anesthesia induction took effect. The control group was anesthetized by sciatic nerve block under the guidance of nerve stimulator. Using the midpoint of the line connecting the most prominent part of the ischial tubercle and the greater trochanter of the femur as the puncture point, the 21 G puncture needle was vertically pierced into the skin. The current of the nerve stimulator was adjusted to 1.0 mA, and the current was adjusted to 0.4 mA after the motor response of the peroneal or tibial nerve was generated. In addition, it should inject 20 mL of 0.4% acid ropivacaine injection.

The research group performed ultrasound-guided sciatic nerve block anesthesia. The patient was placed in the lateral decubitus position, and ultrasound probe was placed between the femoral tubercle and the greater trochanter in the subgluteal region and was closely attached to the lower part of the gluteal groove and perpendicular to the long axis of the thigh. The direction of the probe was adjusted, and the sciatic nerve was identified in the hyperechoic greater trochanter, between the ischial tuberosity, deep gluteus maximus, and between the quadratus femoris, and showed a hyperechoic honeycomb image. A 21 G puncture needle was used to insert the needle in the plane to the side of the sciatic nerve, and then 20 mL of 0.4% ropivacaine was injected to complete the block anesthesia.

2.4. Image Evaluation Indicators. For the effect evaluation of ultrasound images, peak signal-to-noise ratio (PSNR) and structural similarity (SSIM) were used. PSNR was a measure of image quality and was often expressed in logarithmic decibel (dB) units. The calculation of PSNR first needed to know the calculation of mean square error (MSE). It was assumed that two $m \times n$ monochrome images were I and K , if one was similar to the noise of the other, then its MSE was defined as follows:

$$\operatorname{MSE} = \frac{1}{mn} \sum_{i=0}^{m-1} \sum_{j=0}^{n-1} [I(i, j) - K(i, j)]^2. \quad (16)$$

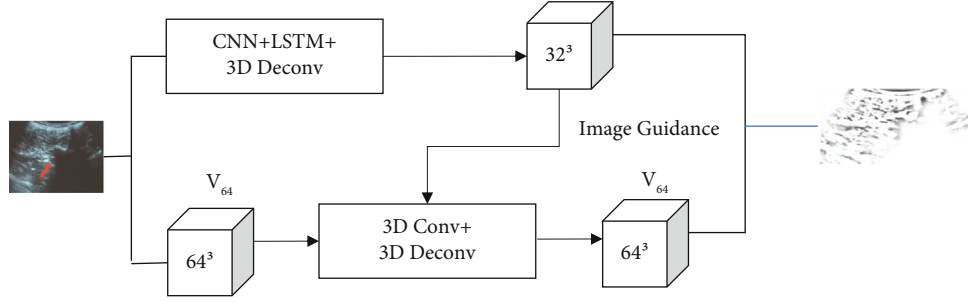


FIGURE 2: Flow chart of 3D reconstruction.

MSE was a common loss function, and PSNR was obtained through MSE. The equation was as follows:

$$\text{PSNR} = 10 \cdot \log_{10} \left(\frac{\text{MAX}_I^2}{\text{MSE}} \right) = 20 \cdot \log_{10} \left(\frac{\text{MAX}_I}{\sqrt{\text{MSE}}} \right). \quad (17)$$

PSNR higher than 40 dB indicated that the image quality was excellent, that is, very close to the original image. 30-40 dB usually indicated good image quality (i.e., distortion is perceptible but acceptable), 20-30 dB indicated poor image quality; and PSNR below 20 dB indicated unacceptable image quality.

SSIM was an indicator that measures the similarity of two pictures and was often used for the evaluation of image quality. The input of SSIM was two images. It was assumed that the two input images were x and y , respectively, and the equation was as follows:

$$\text{SSIM}(x, y) = [l(x, y)]^\alpha [c(x, y)]^\beta [s(x, y)]^\gamma. \quad (18)$$

In the above equation, $l(x, y)$ referred to the brightness comparison, $c(x, y)$ was the contrast comparison, and $s(x, y)$ was the structural comparison. SSIM was a number between 0 and 1. The larger the value, the smaller the gap between the output image and the undistorted image, that is, the better the image quality.

2.5. Observation Indicators. The difference between the ultrasound image under the 3D reconstruction algorithm and the traditional image was compared and analyzed, and then, the systolic blood pressure (SBP), diastolic blood pressure (DBP), and heart rate of the experimental group and the control group were compared before, during, and after the surgery. When the anesthesia effect was analyzed, the drug dosage, anesthesia onset time, pain block time (PBT), and postoperative wakefulness time (PWT) were compared between the two groups. After the surgery, the effect of postoperative analgesia effect was analyzed using the visual analogue scale (VAS). The VAS scoring criteria were shown in Figure 3. 0-2 means “comfortable,” 3-4 means “mild discomfort,” 5-6 means “moderate discomfort,” 7-8 means “severe discomfort,” and 9-10 means “extremely discomfort.”

2.6. Statistical Methods. The data of this experimental study was analyzed and processed using SPSS 19.0 version statistical software. The measurement of the data was expressed in

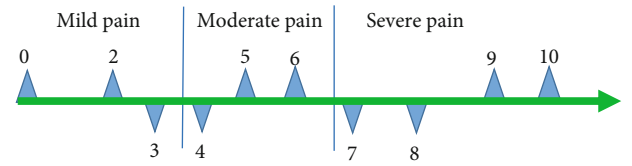


FIGURE 3: The VAS scoring criteria.

the form of the mean \pm standard deviation ($\bar{x} \pm s$), and the analysis of the count data was expressed by the percentage (%). The pairwise comparison between the data was realized using analysis of variance. $P < 0.05$ indicated that the difference was statistically significant.

3. Results

3.1. Ultrasound Images under 3D Reconstruction Algorithm.

The following were two typical cases. Patient A, male, 60 years old, underwent internal fixation of a tibial fracture and underwent ultrasound-guided sciatic nerve + common peroneal nerve block. Patient B, male, 54 years old, underwent unilateral below-knee surgery with ultrasound-guided sciatic nerve + femoral nerve block. Figure 4 showed ultrasound images of two patients.

Because it was necessary to determine the position of the surrounding blood vessels during the lower limb bone surgery, Figure 5 showed the blood vessel ultrasound image of three random patients. The blood vessel image near the lower limb bone under the ultrasound guidance of the intelligent 3D reconstruction algorithm showed clearer image.

3.2. Comparison of Processing Effects of Different Algorithms.

The effect of the algorithm applied in this work was compared with that of BM3D, DnCNN, and Red-Net algorithms. As shown in Table 1, the PSNR and SSIM of the 3D reconstruction algorithm were better than other algorithms, and the difference was significant ($P < 0.05$).

3.3. Comparison on SBP, DBP, and Heart Rate.

As shown in Figure 6, the SBPs were 135 ± 5.67 mmHg, 138 ± 5.27 mmHg, and 141 ± 5.87 mmHg for three preoperative measurements, 120 ± 4.89 mmHg, 124 ± 4.86 mmHg, and 119 ± 4.37 mmHg for three intraoperative measurements, and 129 ± 6.35 mmHg, 131 ± 6.64 mmHg, and 133 ± 6.26 mmHg for three postoperative measurements in the experimental group. The SBPs were

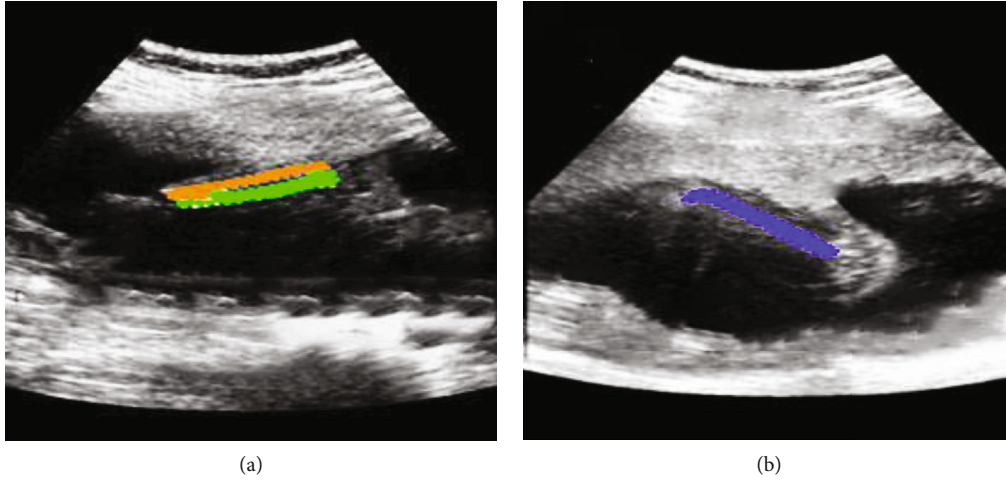


FIGURE 4: The traditional ultrasound images. (a) Fibula is marked in orange and tibia in green; (b) Femur is shown in blue.

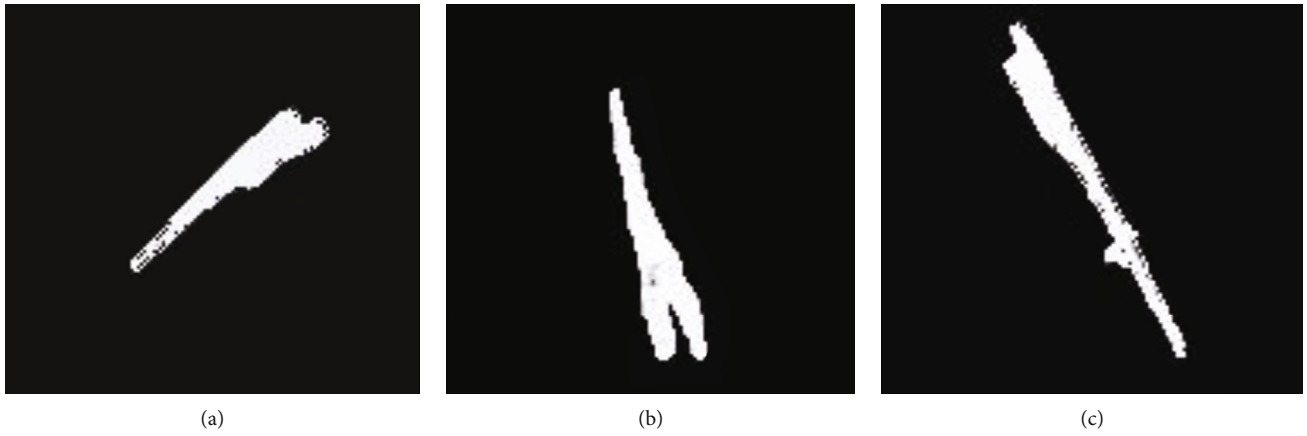


FIGURE 5: The blood vessel ultrasound images under intelligent 3D reconstruction. (a–c) The blood vessel images of three random patients, respectively.

137 ± 6.38 mmHg, 139 ± 6.45 mmHg, and 136 ± 6.32 mmHg for three preoperative measurements; 130 ± 5.03 mmHg, 129 ± 5.25 mmHg, and 128 ± 5.28 mmHg for three intraoperative measurements; and 149 ± 5.98 mmHg, 151 ± 5.86 mmHg, and 143 ± 5.15 mmHg for three postoperative measurements.

As shown in Figure 7, the DBPs were 89 ± 2.37 mmHg, 87 ± 2.48 mmHg, and 91 ± 2.74 mmHg for three preoperative measurements; 80 ± 2.74 mmHg, 84 ± 2.69 mmHg, and 81 ± 2.85 mmHg for three intraoperative measurements; and 87 ± 3.06 mmHg, 88 ± 3.05 mmHg, and 86 ± 3.14 mmHg for three postoperative measurements in the experimental group. The DBPs were 93 ± 2.48 mmHg, 87 ± 2.86 mmHg, and 89 ± 2.57 mmHg for three preoperative measurements; 68 ± 2.46 mmHg, 71 ± 2.63 mmHg, and 73 ± 2.74 mmHg for three intraoperative measurements; and 96 ± 3.33 mmHg, 92 ± 3.26 mmHg, and 95 ± 3.37 mmHg for three postoperative measurements.

As shown in Figure 8, the three preoperative heart rate measurements were 81 ± 3.36 beats/sec, 80 ± 3.67 beats/sec, and 77 ± 3.84 beats/sec; the intraoperative measurements

TABLE 1: Comparison of the effects of different algorithms.

Algorithm	PSNR (dB)	SSIM (dB)
BM3D algorithm	24.374	0.587
DnCNN algorithm	30.287	0.638
Red-Net algorithm	29.498	0.737
3D reconstruction algorithm	35.216*	0.853*

*Compared with other algorithms, $P < 0.05$.

were 75 ± 4.02 beats/sec, 73 ± 4.04 beats/sec, and 76 ± 4.24 beats/sec; and the postoperative measurements were 77 ± 4.68 times/second, 79 ± 4.74 times/second, 78 ± 4.23 times/second, respectively. The heart rate of the patients in the control group was measured three times, and the values were 80 ± 3.47 beats/sec, 79 ± 3.75 beats/sec, and 76 ± 3.55 beats/sec before the surgery; 69 ± 3.97 beats/sec, 71 ± 3.79 beats/sec, and 68 ± 3.85 beats/sec during the surgery; and 87 ± 3.98 times/sec, 88 ± 3.74 times/sec, and 85 ± 3.64 times/sec after the surgery.

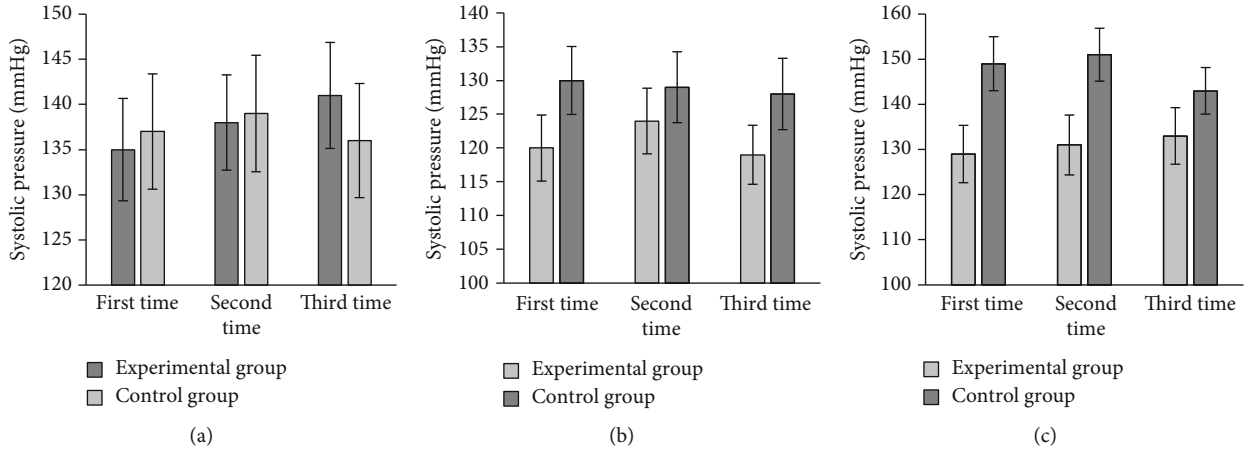


FIGURE 6: Comparison on SBP of patients in two groups. (a-c) The SBP values before, during, and after the surgery, respectively.

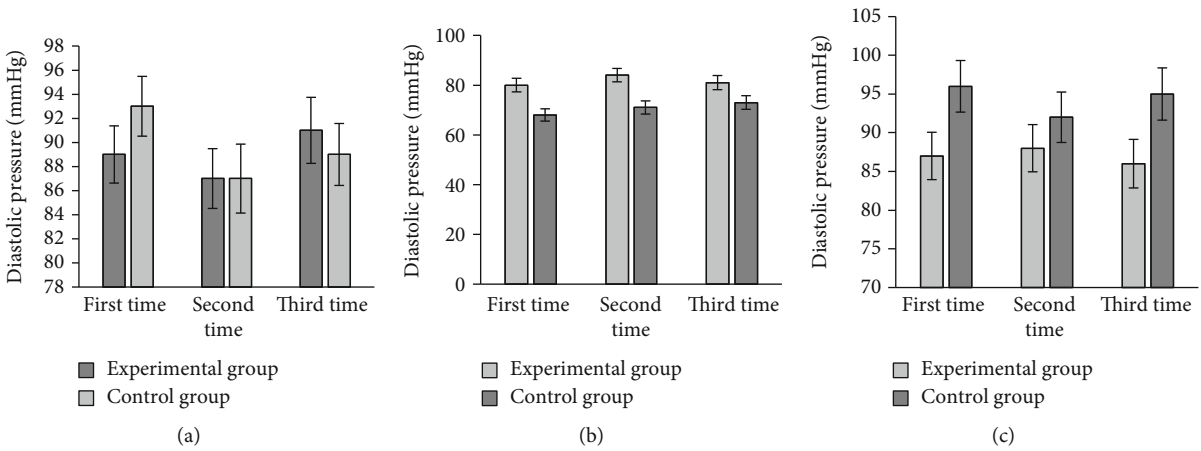


FIGURE 7: Comparison on DBP of patients in two groups. (a-c) The DBP values before, during, and after the surgery, respectively.

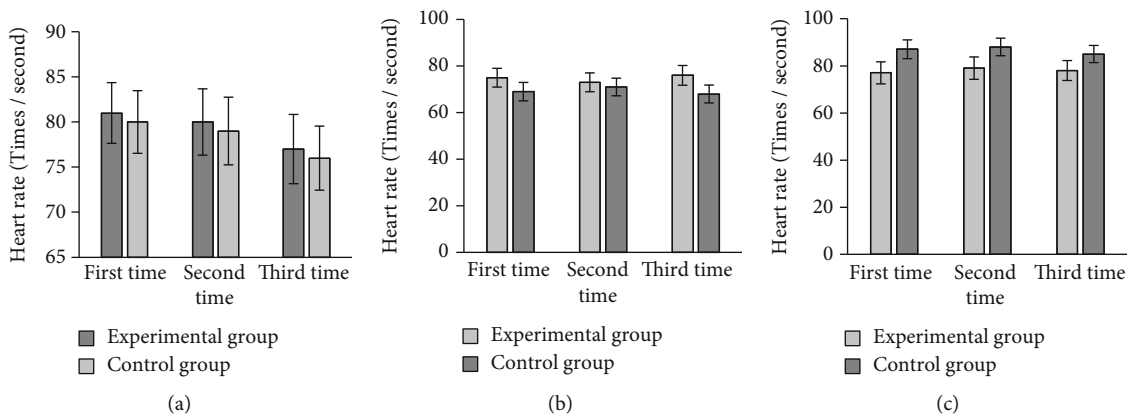


FIGURE 8: Comparison on heart rate of patients in two groups. (a-c) The heart rates before, during, and after the surgery, respectively.

In Figure 9, P1, P2, and P3 referred to preoperative, intraoperative, and postoperative, respectively; (a-c) patient's SBP, DBP, and heart rate, respectively. The average values of SBP measured before, during, and after the surgery of the experimental group were 138 ± 6.46 mmHg,

121 ± 6.36 mmHg, and 131 ± 6.63 mmHg, respectively, while those in the control group were 137 ± 6.24 mmHg, 129 ± 6.85 mmHg, and 148 ± 6.47 mmHg, respectively. The average values of DBP measured before, during, and after the surgery were 89 ± 5.47 mmHg, 81 ± 5.94 mmHg, and 87 ± 5.25

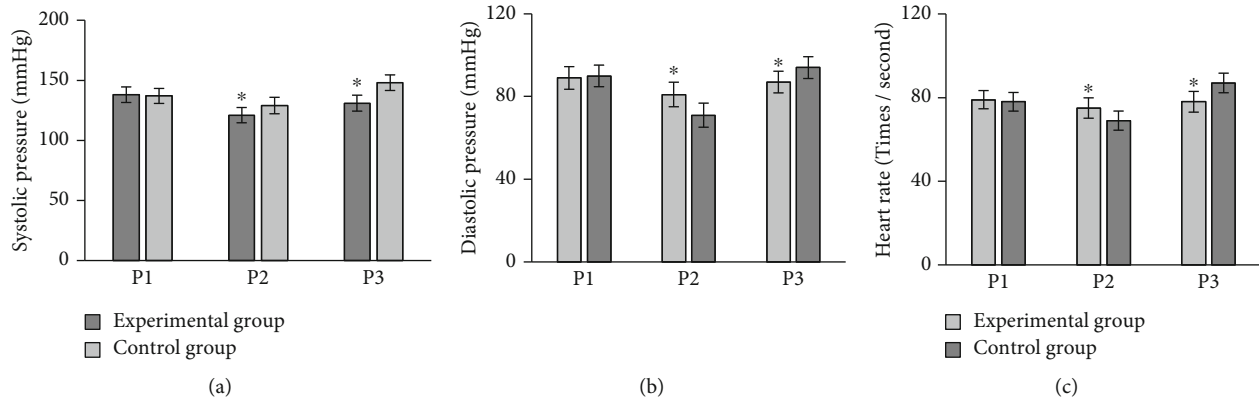


FIGURE 9: Comparison on different parameters of patients in different groups. (a–c) The comparisons of SBP, DBP, and heart rate, respectively. *Compared with control group, $P < 0.05$.

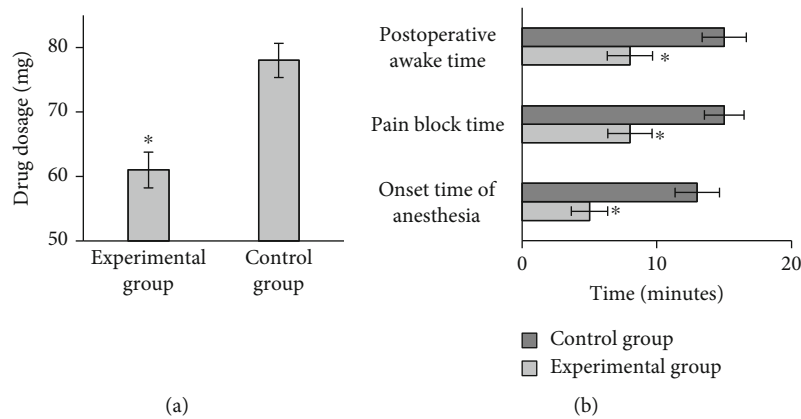


FIGURE 10: Comparison on intraoperative anesthesia effect. (a) The comparison on average drug dosage; (b) the comparisons on anesthesia onset time, PBT, and PWT, respectively. *Compared with control group, $P < 0.05$.

mmHg of the experimental group, respectively, while those were 90 ± 5.24 mmHg, 71 ± 5.83 mmHg, and 94 ± 5.27 mmHg in the control group. The average heart rate values measured before, during, and after the operation were 79 ± 4.36 beats/sec, 75 ± 4.86 beats/sec, and 78 ± 4.95 beats/sec in the experimental group and 78 ± 4.45 beats/sec, 69 ± 4.58 beats/sec, and 87 ± 4.69 beats/sec in the control group, respectively. The differences between the two groups before surgery were not remarkable ($P > 0.05$), but they were statistically obvious during and after the surgery ($P < 0.05$).

3.4. Intraoperative Anesthesia Effect. When the anesthesia effect was analyzed, the average drug dosage of the experimental group was 61 ± 2.78 mg, and that in the control group was 78 ± 2.65 mg (as shown in Figure 10(a)). As illustrated in Figure 10(b) below, the average anesthesia onset time, the average PBT, and the average PWT of patients in the experimental and control groups were 5 ± 1.35 minutes vs. 13 ± 1.65 minutes, 8 ± 1.64 minutes vs. 15 ± 1.47 minutes, and 8 ± 1.68 minutes vs. 15 ± 1.64 minutes, respectively. Therefore, the differences between two groups were obvious statistically ($P < 0.05$).

3.5. Postoperative Analgesia Effect. The average VAS scores of the two groups were compared within three days after operation, and the results were given in Figure 11. The VAS scores in experimental group and the control group were 0.8 ± 0.45 and 3.3 ± 0.68 on the day of surgery, 2.5 ± 0.32 and 4.9 ± 0.85 on the day after surgery, 1.5 ± 0.24 and 3 ± 0.47 on the two days after surgery, and 1.3 ± 0.53 and 2.3 ± 0.74 on the three days after surgery, showing statistically notable differences ($P < 0.05$).

4. Discussion

Elderly patients have poor body tolerance; the function of various organs declines and often accompanied by a variety of underlying diseases. In this case, clinical lower extremity fracture surgery is performed, so there is a higher requirement for intraoperative anesthesia [16]. Traditional orthopedic surgery anesthesia mostly uses general anesthesia, which is convenient for ventilation and management, so it is widely used in clinical practice. However, intubation and extubation may increase myocardial oxygen consumption, increase heart rate and blood pressure, and increase

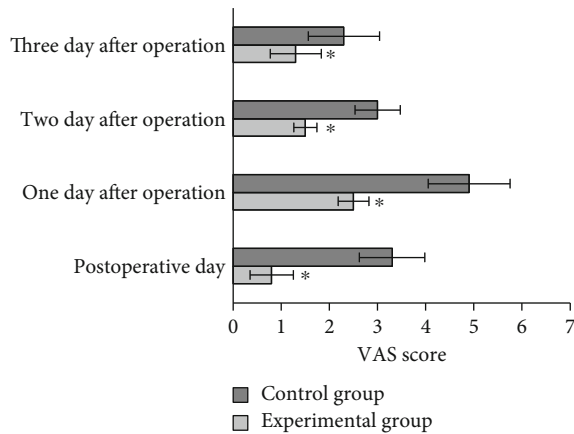


FIGURE 11: Comparison on VAS scores of patients in different groups. *Compared with control group, $P < 0.05$.

the cardiovascular burden of patients [17]. The key to nerve block anesthesia is nerve positioning. The nerve stimulation needle is accurately placed near the target nerve, which can reduce the damage to nerves and blood vessels, and the anesthesia effect can be fully exerted. Nerve stimulator belongs to the traditional anatomical positioning method of nerve block anesthesia. Although the positioning is accurate, it requires high operator skills and experience. Otherwise, it is difficult to identify the diffusion of anesthetics and affect the blocking effect [18]. In recent years, with the development of ultrasound technology, its application in internal medicine has become more and more extensive, which also provides support for the application in the anatomical positioning of nerve block anesthesia. Using ultrasound guidance, not only can accurately locate but also facilitate the observation of drug diffusion [19].

In this work, the intelligent 3D reconstruction algorithm was used to optimize the ultrasound, and at the same time, it was used as a guide for nerve block in the orthopedic surgery of elderly patients in the control group and the experimental group. In addition, the effect of anesthesia and postoperative analgesia was analyzed. The results showed that the ultrasonic image evaluation index (PSNR: 35.216 and SSIM: 0.853) of the intelligent 3D reconstruction algorithm was better than other algorithms. After ultrasound guidance, according to the observation records, there was no significant difference in the systolic blood pressure, diastolic blood pressure, and heart rate between the two groups before operation. The indexes of the experimental group during operation and after operation were better than those of the control group ($P < 0.05$), and the anesthesia effect was more stable. This is consistent with the results of Li et al. [20]. The position of the sciatic nerve is shallow, and the algorithm-optimized ultrasound guidance can clearly display the target nerve structure, as well as the local drug diffusion, observe the path of the nerve stimulation needle, avoid nerve damage, and improve the effect of nerve block anesthesia. The drug dosage of the experimental group (61 mg) was also less than that of the control group (78 mg). The onset time of anesthesia, pain block time, and postoperative awakening time (5 minutes, 8 minutes, and 8 minutes) were all shorter

than those of the control group (13 minutes, 15 minutes, and 15 minutes). The VAS scores of the experimental group were better than those of the control group on the day after surgery, one day after surgery, two days after surgery, and three days after surgery, with significant differences ($P < 0.05$). This point was also mentioned in the article of Selame et al. [21]. The application of ultrasound guidance in sciatic nerve block anesthesia can improve the safety of the block and the success rate of the block. Because the application of the nerve stimulator has a certain blind spot, it is difficult to observe the target nerve and drug diffusion. Ultrasound-guided nerve block anesthesia can observe the scope of drug injection in real time and make timely adjustments to ensure the effect of anesthesia. This anesthesia method can also effectively avoid nerve and blood vessel damage. Therefore, it is necessary to pay attention to the design of anesthesia plan in the process of lower extremity fracture surgery, so as to reduce the impact on the patient's breathing and blood circulation and improve the success rate and safety of anesthesia.

5. Conclusion

In this study, ultrasound-guided nerve block anesthesia based on three-dimensional reconstruction algorithm was used to analyze the effect of anesthesia and postoperative analgesia. The results showed that the ultrasonic images processed by the algorithm were clearer, and the anesthesia effect of orthopedic surgery under the guidance of the algorithm was more stable and obvious, and the analgesic effect was stronger. The disadvantage was that the patient sample in this work was small, and the experimental results would be biased in this case. Therefore, the selection of sample size should be increased in future experimental research, and the anesthesia and postoperative analgesia effects of ultrasound-guided nerve block based on 3D reconstruction algorithm in orthopedic surgery should be further analyzed and compared. In conclusion, this study provides data support and theoretical basis for the anesthesia scheme of clinical orthopedic surgery.

Data Availability

The data used to support the findings of this study are available from the corresponding author upon request.

Conflicts of Interest

The authors declare no conflicts of interest.

References

- [1] K. A. Abdullah, M. F. McEntee, W. Reed, and P. L. Kench, "Evaluation of an integrated 3D-printed phantom for coronary CT angiography using iterative reconstruction algorithm," *Journal of Medical Radiation Sciences*, vol. 67, no. 3, pp. 170–176, 2020.
- [2] K. J. Hua and B. G. Ma, "EVR: reconstruction of bacterial chromosome 3D structure models using error-vector resultant algorithm," *BMC Genomics*, vol. 20, no. 1, p. 738, 2019.

- [3] J. S. Burgdorf, S. M. Brudzynski, and J. R. Moskal, "Using rat ultrasonic vocalization to study the neurobiology of emotion: from basic science to the development of novel therapeutics for affective disorders," *Current Opinion in Neurobiology*, vol. 60, pp. 192–200, 2020.
- [4] V. Kapilevich, S. Seno, H. Matsuda, and Y. Takenaka, "Chromatin 3D reconstruction from chromosomal contacts using a genetic algorithm," *IEEE/ACM Transactions on Computational Biology and Bioinformatics*, vol. 16, no. 5, pp. 1620–1626, 2019.
- [5] W. Kampitak, A. Tanavalee, S. Ngarmukos, and S. Tantavisut, "Motor-sparing effect of iPACK (interspace between the popliteal artery and capsule of the posterior knee) block versus tibial nerve block after total knee arthroplasty: a randomized controlled trial," *Regional Anesthesia and Pain Medicine*, vol. 45, no. 4, pp. 267–276, 2020.
- [6] G. S. Hussey, D. G. Nascari, L. T. Saldin et al., "Ultrasonic cavitation to prepare ECM hydrogels," *Acta Biomaterialia*, vol. 108, pp. 77–86, 2020.
- [7] Q. Li and L. Shen, "3D neuron reconstruction in tangled neuronal image with deep networks," *IEEE Transactions on Medical Imaging*, vol. 39, no. 2, pp. 425–435, 2020.
- [8] Q. Jiang, M. Zhang, and B. Xu, "Application of ultrasonic technology in postharvested fruits and vegetables storage: a review," *Ultrasonics Sonochemistry*, vol. 69, p. 105261, 2020.
- [9] M. Contreras, J. Benedito, and J. V. Garcia-Perez, "Ultrasonic characterization of salt, moisture and texture modifications in dry-cured ham during post-salting," *Meat Science*, vol. 172, article 108356, 2021.
- [10] A. Pryor Jr., Y. Yang, A. Rana et al., "GENFIRE: a generalized Fourier iterative reconstruction algorithm for high-resolution 3D imaging," *Scientific Reports*, vol. 7, no. 1, article 10409, 2017.
- [11] M. Rowlands, G. V. Walt, J. Bradley et al., "Femoral nerve block intervention in neck of femur fracture (FINOF): a randomised controlled trial," *BMJ Open*, vol. 8, no. 4, article e019650, 2018.
- [12] A. Delbos, M. Philippe, C. Clément, R. Olivier, and S. Coppens, "Ultrasound-guided ankle block. History revisited," *Best Practice & Research. Clinical Anaesthesiology*, vol. 33, no. 1, pp. 79–93, 2019.
- [13] Z. Jing, G. Qiang, H. Fang, L. Zhan-Li, L. Hong-An, and S. Yu, "A novel 3D reconstruction algorithm of motion-blurred CT image," *Computational and Mathematical Methods in Medicine*, vol. 2020, Article ID 9324689, 13 pages, 2020.
- [14] Q. Cheng, P. Sun, C. Yang, Y. Yang, and P. X. Liu, "A morphing-based 3D point cloud reconstruction framework for medical image processing," *Computer Methods and Programs in Biomedicine*, vol. 193, article 105495, 2020.
- [15] Y. Xie, H. Liao, D. Zhang, L. Zhou, and F. Chen, "Image-based 3D ultrasound reconstruction with optical flow via pyramid warping network," *Annual International Conference of the IEEE Engineering in Medicine and Biology Society*, vol. 2021, pp. 3539–3542, 2021.
- [16] M. McKendrick, A. Sadler, A. Taylor et al., "The effect of an ultrasound-activated needle tip tracker needle on the performance of sciatic nerve block on a soft embalmed Thiel cadaver," *Anaesthesia*, vol. 76, no. 2, pp. 209–217, 2021.
- [17] G. A. McLeod, M. McKendrick, A. Taylor et al., "An initial evaluation of the effect of a novel regional block needle with tip-tracking technology on the novice performance of cadaveric ultrasound-guided sciatic nerve block," *Anaesthesia*, vol. 75, no. 1, pp. 80–88, 2020.
- [18] M. K. Karmakar, M. A. Reina, R. K. Sivakumar, P. Areeruk, J. Pakpirom, and X. Sala-Blanch, "Ultrasound-guided subparaneural popliteal sciatic nerve block: there is more to it than meets the eyes," *Regional Anesthesia and Pain Medicine*, vol. 46, no. 3, pp. 268–275, 2021.
- [19] M. G. Lee, S. U. Choi, J. K. Lim et al., "Ultrasound-guided sciatic nerve block at the midhigh level in a porcine model: a descriptive study," *Veterinary Medicine and Science*, vol. 6, no. 3, pp. 543–549, 2020.
- [20] Y. Li, Q. Zhang, Y. Wang et al., "Ultrasound-guided single popliteal sciatic nerve block is an effective postoperative analgesia strategy for calcaneal fracture: a randomized clinical trial," *BMC Musculoskeletal Disorders*, vol. 22, no. 1, 2021.
- [21] L. A. Selame, K. McFadden, N. M. Duggan, A. J. Goldsmith, and H. Shokoohi, "Ultrasound-guided transgluteal sciatic nerve block for gluteal procedural analgesia," *The Journal of Emergency Medicine*, vol. 60, no. 4, pp. 512–516, 2021.

Research Article

The Value of 320-Slice Spiral Computed Tomography Perfusion Imaging in Staging and Long-Term Dynamic Evaluation of Breast Cancer

Hequn Geng¹,¹ Zhilin Zhang,² Xiaochen Zhang,¹ Zhandong Liang,¹ Yong Li,¹ and Shujun Cui¹

¹Department of Medical Imaging, The First Affiliated Hospital of Hebei North University, Zhangjiakou, 075000 Hebei, China

²Department of Radiotherapy, The First Affiliated Hospital of Hebei North University, Zhangjiakou, 075000 Hebei, China

Correspondence should be addressed to Hequn Geng; 20148369@stu.sicau.edu.cn

Received 3 June 2022; Revised 24 June 2022; Accepted 6 July 2022; Published 21 July 2022

Academic Editor: Pan Zheng

Copyright © 2022 Hequn Geng et al. This is an open access article distributed under the Creative Commons Attribution License, which permits unrestricted use, distribution, and reproduction in any medium, provided the original work is properly cited.

The value of 320-slice spiral computed tomography (CT) perfusion imaging in staging and long-term dynamic evaluation of breast cancer was explored. 120 breast cancer patients who underwent preoperative CT examination and were confirmed by surgery and pathology were selected. All patients underwent preoperative TNM staging of breast cancer, with 120 cases in each stage. According to the results of 320-slice spiral CT, the postoperative pathology and surgical methods were compared and analyzed. CT diagnosis of breast cancer showed that T1 sensitivity was 71% and accuracy was 61%, T2 sensitivity was 74% and accuracy was 64%, T3 sensitivity was 94% and the accuracy was 84%, and the T4 sensitivity was 100% and the accuracy was 91%. The sensitivity of N1 stage was 71%, and the accuracy was 61%; and the sensitivity of N2~N3 stage was 81%, and the accuracy was 76%. There were 7 cases of M1 with distant metastasis, the sensitivity was 71%, and the accuracy was 71%. At T1 stage, blood flow (BF) was 39.2 ± 16.7 mL/min/100 g, blood volume (BV) was 2.66 ± 1.4 mL/100 g, mean transit time (MTT) was 8.16 ± 2.7 s, and permeability surface (PS) was 16.6 ± 9.7 mL/min/100 g. 320-slice spiral CT perfusion imaging technology provided a new diagnostic mode for everyone, which can quantitatively identify breast cancer with multiple parameters, which was of great significance for clinical auxiliary diagnosis.

1. Introduction

Breast cancer is one of the most common malignant tumors in women worldwide, and accurate preoperative staging is the key to its treatment effect. Breast cancer accounts for about 20% of new cancers, and about 15% of the mortality rate [1]. Due to changes in people's lifestyles and reproductive patterns, its prevalence has continued to rise significantly in China in recent years, and it also tends to be younger [2]. Statistics show that the incidence of breast cancer in Beijing, China, is about 44/100,000, which is close to the incidence of moderately developed countries [3]. In addition, timely and accurate diagnosis of breast lesions, and given standardized treatment, can greatly reduce the mortality rate of patients, improve the survival rate of patients, and significantly improve the quality of life of

patients [4]. Therefore, it is of great necessity and urgency to take early measures to prevent and closely monitor high-risk groups of breast cancer, and to achieve early detection, early diagnosis, and early treatment of breast cancer, and it will also bring great clinical and social value.

The role of imaging examinations in the screening and early diagnosis of breast diseases is crucial. The most common imaging examination methods include ultrasound, mammography, and magnetic resonance imaging (MRI) imaging techniques [5]. Ultrasound and mammography have certain defects in the detection and characterization of breast lesions. Although ultrasonography is inexpensive, easy to operate, and has high repeatability, it has limitations such as different resolutions of instruments, great differences in operator experience, and inconsistent objective diagnostic criteria [6]. Mammography is sensitive to radiotherapy and

chemotherapy, but lesions located deep in the glands of dense breasts and multifocal lesions have poor display ability and are easy to be misdiagnosed and missed. Its sensitivity is about 68~91%, and its sensitivity to lesions in dense breast will be greatly reduced, about 48% [7]. Compared with MRI perfusion imaging, breast CT perfusion imaging has the advantages of being simpler and faster, and this technique can be used for quantitative examination in different body positions [8]. Because of its faster scanning speed than ordinary computed tomography (CT), helical CT can have multiphase scanning and reconstruction in any direction and can completely display the morphology and structure of lymph nodes, which significantly enhances the accuracy of preoperative staging of breast cancer [9]. Breast disease CT perfusion imaging technology can detect changes in breast morphology and hemodynamic changes at an early stage. According to the changes of various perfusion parameters, it can indicate the probability of the existence of early lesions, distinguish benign and malignant lesions, and further help determine the nature of lesions according to the differences in perfusion parameters between breast cancer and benign lesions (such as breast hyperplasia and fibroadenoma) [10–12]. The theoretical basis of CT perfusion imaging is the principle of radiotracer dilution in nuclear medicine and the central volume law (mean transit time (MTT) = blood volume (BV)/blood flow (BF)). It refers to the continuous multiple scans of the same slice at the selected slice while the contrast agent is injected intravenously, and the TDC of each pixel in the slice is obtained, which reflects the changes in the perfusion volume of tissues and organs [13].

Due to the increasing incidence of breast cancer patients, many complications, and poor prognosis, some patients are detected late, which brings serious life and economic burden to patients and the country. Therefore, it is necessary to take early measures to prevent and closely monitor high-risk groups of breast cancer, so as to achieve early detection, early diagnosis, and early treatment of breast cancer. This is important for improving patient outcomes and quality of life. It is very necessary and urgent to evaluate the value of 320-slice spiral CT perfusion scanning in the preoperative staging of breast cancer, the way and regularity of its metastasis, and its long-term dynamic evaluation. It will also bring greater clinical value and social value [14]. The objective of this work was to investigate the value of various perfusion parameters of breast cancer in the diagnosis of breast cancer by 320-slice spiral CT perfusion imaging, combined with the clinical data and pathological confirmation data of patients after surgery, so as to evaluate the value of 320-slice spiral CT perfusion in preoperative staging, metastasis pathway, regularity, and long-term dynamic evaluation of breast cancer, providing imaging basis for the diagnosis and treatment of breast cancer.

2. Materials and Methods

2.1. Research Subjects. Data of 120 breast cancer patients who underwent preoperative CT examination and were confirmed by surgery and pathology in hospital from January

2016 to January 2017 were included. Ages ranged from 25 to 58, with an average age of 42. The preoperative tumor node metastasis (TNM) staging of breast cancer was performed for all patients. There were 120 cases in each stage. Inclusion criteria were given as follows: patients with no allergy to iodine-containing contrast agents, patients with no renal insufficiency (creatinine level < 1.5 mg/dL), patients with no pregnancy, and patients with complete image data. Exclusion criteria were set as follows: patients who were lactating and pregnant women and patients without pathological diagnosis. This work was approved by ethics committee of hospital, and the families of the patients included signed the informed consent.

2.2. Breast Cancer Pathological TNM Staging Criteria. The 7th edition of breast pTNM staging jointly developed by the American Joint Committee on Cancer (AJCC) and the Union for International Cancer Control (UICC) was adopted [15]. The criteria were as follows:

- (1) Primary tumor (T): Tx: primary tumor cannot be assessed; T0: no evidence of primary tumor; Tis: carcinoma in situ; T1: maximum tumor diameter \leq 20 mm; T2: maximum tumor diameter > 20 mm and \leq 50 mm; T3: maximum tumor diameter > 50 mm; and T4: direct invasion of the chest wall or skin regardless of tumor size
- (2) Regional lymph nodes (N): Nx: regional lymph nodes cannot be assessed; N0: no regional lymph node metastases on histological examination; N1: micrometastases; or 1-3 ipsilateral axillary lymph nodes; transfer; N2: 4-9 ipsilateral axillary lymph node metastasis; or clinically found ipsilateral internal mammary lymph node metastasis without axillary lymph node metastasis; N3: 10 or more ipsilateral axillary lymph node metastasis; or subclavian lymph node metastasis; or clinically found ipsilateral internal mammary lymph node metastasis, with 1 or more ipsilateral axillary lymph node metastasis; Or 3 or more ipsilateral axillary lymph node metastasis, with no clinical findings, ipsilateral internal mammary lymph node metastasis confirmed by sentinel lymph node biopsy; or ipsilateral supraclavicular lymph node metastasis
- (3) Distant metastasis (M): M0: no metastases were found on clinical and imaging examinations; M1: distant metastases detected by clinical or imaging methods, or metastases > 0.2 m confirmed by histology

2.3. Imaging Examinations. In this study, Toshiba Aquilion 320-slice spiral CT, double-barrel high-pressure syringe, and vitrea workstation were adopted. The patient was placed in the prone position, the chest-neck junction and abdomen were elevated, and both breasts sagged naturally. The scanning range was from the top of the armpit to the lower edge of the breasts. Initially, the plane was selected by plain scan, and the middle plane was selected at the center of the lesion.

The scanning parameters were set as follows: 121 kV, 201 mA, delay 7 s, slice thickness 6 mm, and 90 consecutive scans per slice. In the same way (with the consent and supervision of the patient), the enlarged lymph nodes and metastases were selectively scanned, and the nonionic contrast medium was injected through the cubital vein with a flow rate of 4.0 mL/s and a total volume of 51 mL. The patient was breathing calmly throughout the perfusion scan. All patients underwent 320-slice spiral CT scan before surgery, and the pathology and scan results were compared after operation. TNM staging was determined by 2 senior radiologists based on preoperative CT findings.

2.4. Postprocessing of Images. Image postprocessing was performed using the body tumor perfusion software in the vitrea workstation. The thoracic aorta was defined as the input artery, and the lesion area was set as the region of interest to calculate the four perfusion parameters, including blood flow (BF), blood volume (BV), mean transit time (MTT), and permeability surface (PS), in the region of interest (ROI).

The segmentation of the tumor ROI was all performed by one professional physician, and two physicians were responsible for the interpretation of the clinical results of the patients. In this work, it only performed retrograde anatomy and deep feature extraction on the largest tumor lesion in each patient. The pulsed phase images were selected for segmentation analysis, because the enhanced breast adenoma lesions in the pulsed phase were significantly different from adjacent normal glandular tissues. To obtain the depth features, the ROI was manually delineated along the tumor boundary at the largest tumor slice on CT arterial-phase enhanced axial images.

2.5. Long-Term Evaluation. All patients underwent CT scan before the surgery, and the pathology and scan results were compared after the surgery. It should file and track all patients, instruct them to review regularly, perform perfusion scanning for breast cancer metastases, and summarize the final results of distant metastasis in 6 months, 1 year, and 1.5 years.

2.6. Collection of Clinical Data. Methods of checking blood routine indexes were described as follows. The routine blood tests of patients were performed using an automatic blood cell analyzer. The five blood routine indexes were collected, including white blood count (WBC), red blood count (RBC), platelet (PLT), neutrophil absolute value (NEU), and lymphocyte absolute value (LYM).

2.7. Statistical Analysis. All data were analyzed by SPSS 19.0 software. Numerical data were expressed as $(\bar{x} \pm s)$, and categorical data were expressed as percentages. The data conforming to the normal distribution were analyzed by *t*-test and analysis of variance, and the nonnormally distributed data were analyzed by the Wilcoxon nonparametric test. The enumeration data were analyzed by the chi-square test. Correlation analysis was performed using the Spearman correlation analysis. $P < 0.05$ was considered statistically significant.

TABLE 1: The general information of included patients.

Stage	Age (years old)	Number of births	Breastfeeding (cases)	Family history of breast cancer (cases)
T1	26-52	0-1 times	21	2
T2	27-58	1-2 times	19	1
T3	25-57	1-2 times	22	3
T4	24-55	0-1 times	18	2
N0	24-53	1-2 times	17	1
N1	26-54	0-1 times	20	2
N2-N3	25-52	1-2 times	18	2

3. Results

3.1. Clinical Characteristics. 120 patients were included in this work, ranging in age from 25 to 58 years, with an average age of 42 years. The differences in age, number of births, breastfeeding, and family history of breast cancer among breast cancer patients in T stage, N stage, and M stage were shown in Table 1. The differences between the blood routine indexes of breast cancer patients with different T stages and N stages were shown in Table 2.

3.2. Comparison of Perfusion Parameters in Different Stages of Breast Cancer Patients. The comparison of perfusion parameters (mean \pm standard deviation) of breast cancer patients with different stages was shown in Table 3.

3.3. Examination Results. According to the new TNM staging criteria of the International Association against Cancer, the findings were as follows (Figure 1). In 41 cases of T1 stage, the lesions were enhanced on CT enhanced scan, and the lesions were small nodules or small round masses, less than 2.1 cm, the sensitivity was 71%, and the accuracy was 61%. 34 cases of T2 stage lesions were nodular or round-like, with diameters ranging from 2.1 to 5.1 cm, with blurred borders (some cases were still clear), and the length and thickness of the burrs varied. Enhanced lesions enhanced, CT value increased by 31~51 Hu, the sensitivity was 74%, and the accuracy was 64%. In 27 cases of T3 stage, the sensitivity was 94% and the accuracy was 84%. In 18 cases of T4 stage, the lesions invaded the muscle layer or chest wall, the sensitivity was 100%, and the accuracy was 91%. The CT value results of patients with different T stages were shown in Figure 2.

There were 63 cases in N0 stage (no lymph node metastasis) and 41 cases in N1 stage (ipsilateral axillary lymph node enlargement, and the sensitivity and accuracy were 71% and 61%, respectively). In 16 cases of N2~N3 stage, the lymph nodes showed heterogeneous enhancement after CT enhanced scan, some showed ring enhancement, the CT value increased by 32-52 Hu (1 case had no enhancement). The sensitivity was 81%, and the accuracy was 76%. The above results were shown in Figure 3. The CT value results of patients with different N stages were shown in Figure 4.

TABLE 2: Differences in blood routine indexes of breast cancer patients with different T stages and N stages.

Stage	WBC ($\times 10^9/L$)	RBC ($\times 10^{12}/L$)	PLT ($\times 10^9/L$)	NEU ($\times 10^9/L$)	LYM ($\times 10^9/L$)
T1	5.26	4.58 \pm 0.3	226.5 \pm 54.2	3.53	1.35
T2	5.47	4.66 \pm 0.4	229.7 \pm 50.3	3.92	1.54
T3	6.03	4.71 \pm 0.3	231.8 \pm 44.4	4.22	1.63
T4	6.67	4.78 \pm 0.5	235.7 \pm 56.7	4.51	1.87
N0	5.33	4.35 \pm 0.7	227.5 \pm 52.1	3.42	1.38
N1	5.46	4.58 \pm 0.6	229.3 \pm 45.7	3.87	1.79
N2-N3	6.82	4.62 \pm 0.9	236.6 \pm 38.2	4.46	1.88

TABLE 3: The comparison of perfusion parameters (mean \pm standard deviation) of breast cancer patients with different stages.

Stage	BF (mL/min/100 g)	BV (mL/100 g)	MTT (s)	PS (mL/min/100 g)
T1	39.2 \pm 16.7	2.66 \pm 1.4	8.16 \pm 2.7	16.6 \pm 9.7
T2	40.5 \pm 18.3	3.23 \pm 1.6	8.88 \pm 3.6	17.3 \pm 8.9
T3	42.4 \pm 16.9	3.85 \pm 1.5	9.06 \pm 3.8	18.7 \pm 9.8
T4	45.7 \pm 19.7	3.91 \pm 1.4	9.43 \pm 3.5	19.5 \pm 9.5

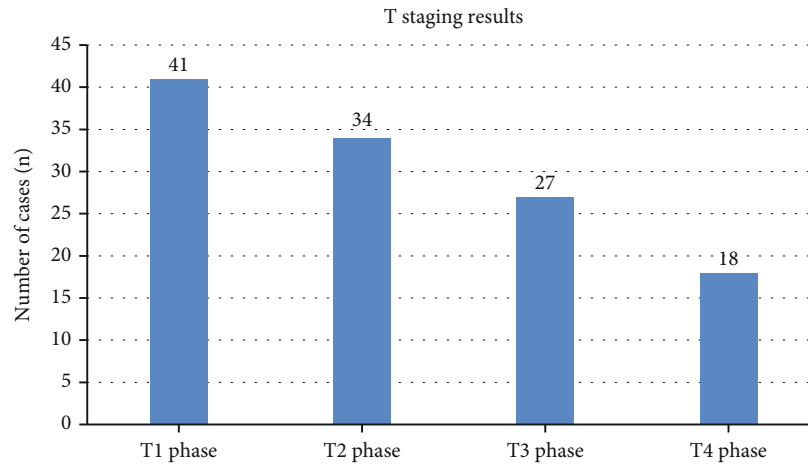


FIGURE 1: Results of T stage under CT imaging.

There were 113 cases in M0 and 7 cases in M1. The supraclavicular lymph nodes of patients with distant metastases beyond the ipsilateral breast showed heterogeneous enhancement after enhancement, and the CT value increased by 31 to 51 Hu, with a sensitivity of 71% and an accuracy of 71%. Differences in CT values between patients with and without distant metastases were shown in Figure 5. The 6-month, 1-year, and 1.5-year follow-up results were as follows: 2 cases of distant metastasis at 6 months, 3 cases of distant metastasis at 1 year, and 3 cases of distant metastasis at 1.5 years, as showed in Figure 6. Among the 8 cases of metastases, 2 cases were transferred to the contralateral breast endolymphatic chain, the systemic lymph nodes were enlarged, 2 cases were bone metastases, 2 cases were brain-lung metastases, and 2 cases were bone-lung metastases.

4. Discussion

Most breast adenocarcinoma patients will undergo CT examination before surgery, which can not only be used to assess the extent of breast adenocarcinoma lesions. In addition, it can also detect the presence of metastases in many organs and bone masses such as distant skin, chest wall, regional lymph nodes (axillary, internal mammary, and supraclavicular lymph nodes), so as to make systematic preoperative clinical staging and arrange follow-up treatment plans [16]. 320-slice spiral CT is an auxiliary diagnostic imaging tool, which has strong clinical value in the preoperative evaluation of breast adenocarcinoma. Many studies have shown that multiscale and multifeature combination has strong predictive value than a single feature, and

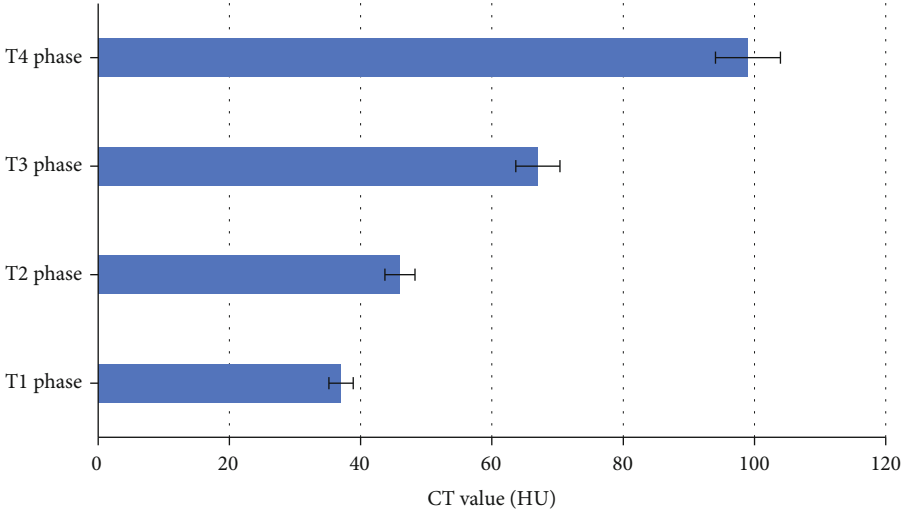


FIGURE 2: CT value results of patients with different T stages.

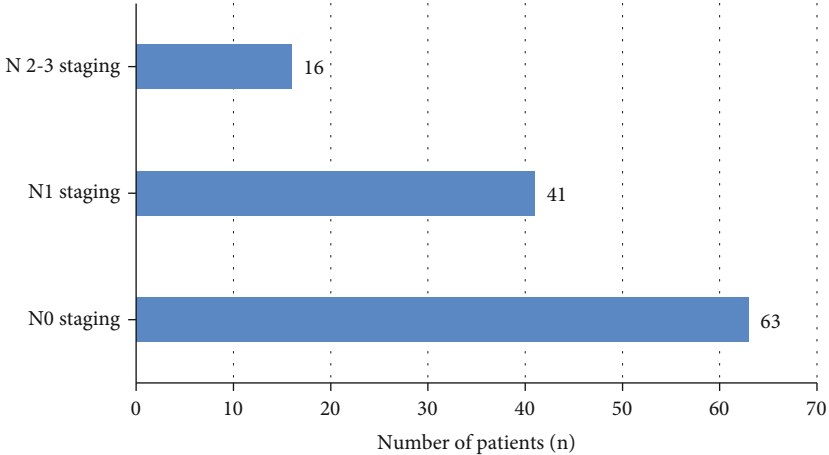


FIGURE 3: Results of N stage under CT imaging.

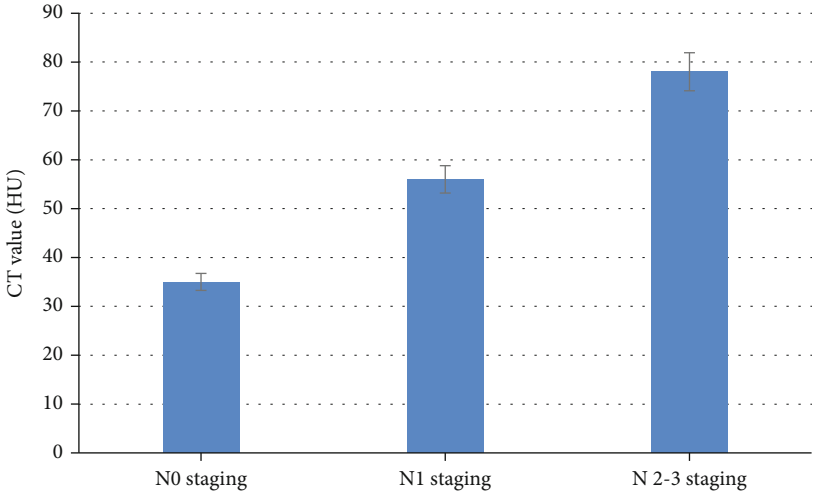


FIGURE 4: CT value results of patients with different N stages.

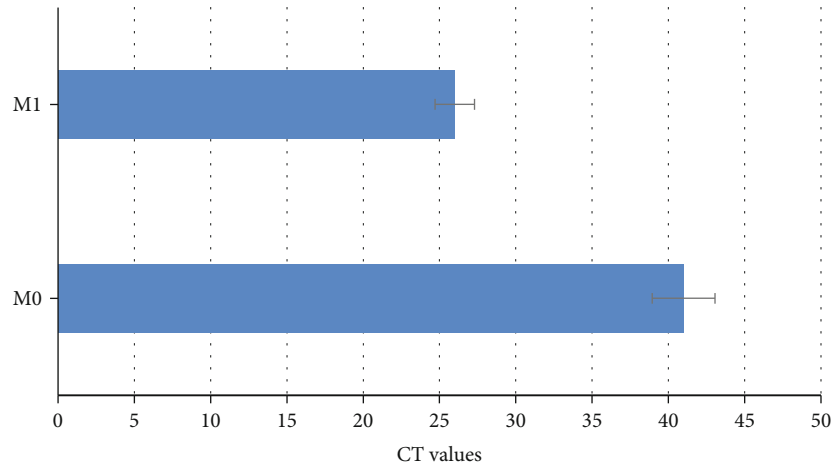


FIGURE 5: CT values of patients with or without distant metastasis.

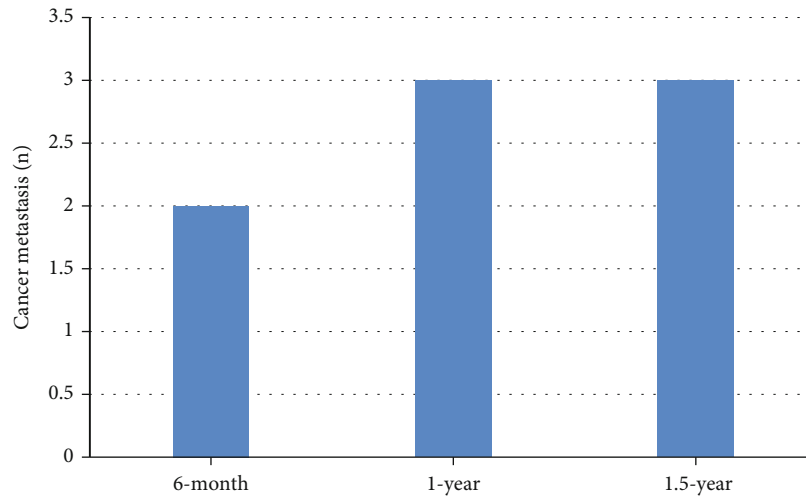


FIGURE 6: Results of distant metastasis on CT imaging.

multifeature combination analysis is more conducive to individualized management of patients [17, 18].

The advantage of dynamic helical CT enhanced scanning lies in the use of multilayer structures at different scanning rates to reflect the layered structure [19]. 41 cases of early breast cancer in T1 stage in this work, obvious enhancement appeared in the arterial phase, and the CT value increased >4.1 Hu. The lesions in the parenchymal phase also enhanced significantly, and they regressed significantly in the equilibrium phase, but the lesions in T2 ~ T4 phases all enhanced in the equilibrium phase, so the arterial phase was used to detect early breast cancer. A study has shown that the CT value of advanced breast cancer is higher than that of early breast cancer [20]. In stage t4, the skin and chest wall are involved, the fat layer is blurred and disappears, and the ribs can be destroyed. The lymph nodes of each group in N staging were significantly enhanced in the arterial and venous phases after CT enhanced scanning, especially in the venous phase, and the CT value increased by 31~51 Hu [21]. 320-slice spiral CT perfusion is helpful for preoperative lymph node analysis.

A study dissected 1,248 axillary lymph nodes of 72 patients with breast cancer and found that axillary lymph nodes with a length of less than 5.1 mm still had a 10.1% metastasis rate, the LNM rate of 5.2-9.1 mm was 17.4%, and the LNM rate of 10.2-20.1 mm was 19.8%. In addition, the rate of LNM with a long diameter greater than 19 mm was 41%, and there was no correlation between lymph node metastasis and the size and histological grade of the primary tumor [22, 23]. Combining with the literature, it can be concluded that axillary lymph node diameter > 1.2 cm can be classified as metastasis, but lymph nodes < 1.2 cm cannot be excluded. Patients in M stage were supraclavicular LNM or distant metastasis in this work. 320-slice spiral CT has become a common method for diagnosing liver, lung, and supraclavicular lymph nodes in breast cancer patients. In this work, among the 8 cases of metastasis, 2 cases were metastasized to the contralateral breast endolymphatic chain, the systemic lymph nodes were enlarged, 2 cases were bone metastases, 2 cases were brain-lung metastases, and 2 cases were bone-lung metastases.

5. Conclusion

The results in this work showed that 320-slice spiral CT thin slice scan can be used for preoperative staging and long-term dynamic evaluation of breast cancer and can accurately assess the extent and location of breast cancer, as well as the condition of thoracic and axillary lymph nodes at one time. There were also many problems and deficiencies in this work. The sample size was relatively small, and more experimental people should be included, not in a single area or in a small area. Clinical trials should be conducted in multicenter, large-sample hospitals. In conclusion, 320-slice spiral CT can be used to assist in the diagnosis and evaluation of breast cancer and had reference value.

Data Availability

The data used to support the findings of this study are available from the corresponding author upon request.

Conflicts of Interest

The authors declare no conflicts of interest.

Acknowledgments

This work was supported by the 2017 key project plan of medical science research in Hebei Province (20170792).

References

- [1] M. Bergamino, L. Bonzano, F. Levrero, G. L. Mancardi, and L. Roccatagliata, "A review of technical aspects of T_1 -weighted dynamic contrast-enhanced magnetic resonance imaging (DCE-MRI) in human brain tumors," *Physica Medica*, vol. 30, no. 6, pp. 635–643, 2014.
- [2] E. Nagel, C. Klein, I. Paetsch et al., "Magnetic resonance perfusion measurements for the noninvasive detection of coronary artery disease," *Circulation*, vol. 108, no. 4, pp. 432–437, 2003.
- [3] J. H. Shepherd, K. Ballman, M. C. Polley et al., "CALGB 40603 (alliance): long-term outcomes and genomic correlates of response and survival after neoadjuvant chemotherapy with or without carboplatin and bevacizumab in triple-negative breast cancer," *Journal of Clinical Oncology*, vol. 40, no. 12, pp. 1323–1334, 2022.
- [4] A. L. Mitchell, A. Gandhi, D. Scott-Coombes, and P. Perros, "Management of thyroid cancer: United Kingdom national multidisciplinary guidelines," *The Journal of Laryngology & Otology*, vol. 130, no. S2, pp. S150–S160, 2016.
- [5] Á. Sávolt, G. Péley, C. Polgár et al., "Eight-year follow up result of the OTOASOR trial: the optimal treatment of the axilla - surgery or radiotherapy after positive sentinel lymph node biopsy in early-stage breast cancer: a randomized, single centre, phase III, non-inferiority trial," *European Journal of Surgical Oncology*, vol. 43, no. 4, pp. 672–679, 2017.
- [6] M. C. T. Batenburg, M. L. Gregorowitsch, W. Maarse et al., "Patient-reported cosmetic satisfaction and the long-term association with quality of life in irradiated breast cancer patients," *Breast Cancer Research and Treatment*, vol. 179, no. 2, pp. 479–489, 2020.
- [7] K. L. Cooper, Y. Meng, S. Harnan et al., "Positron emission tomography (PET) and magnetic resonance imaging (MRI) for the assessment of axillary lymph node metastases in early breast cancer: systematic review and economic evaluation," *Health Technology Assessment*, vol. 15, no. 4, 2011.
- [8] A. D. Resende, S. Leal, C. Batista-Pinto, F. Garcez, and S. I. Sá, "Hepatic effects of long-term tamoxifen administration to cycling female rats," *Journal of Biochemical and Molecular Toxicology*, vol. 33, no. 5, p. e22293, 2019.
- [9] E. K. Vos, G. J. Litjens, T. Kobus et al., "Assessment of prostate cancer aggressiveness using dynamic contrast-enhanced magnetic resonance imaging at 3 T," *European Urology*, vol. 64, no. 3, pp. 448–455, 2013.
- [10] M. Playdon, L. M. Ferrucci, R. McCorkle et al., "Health information needs and preferences in relation to survivorship care plans of long-term cancer survivors in the American Cancer Society's Study of Cancer Survivors-I," *Journal of Cancer Survivorship*, vol. 10, no. 4, pp. 674–685, 2016.
- [11] C. De Angelis, M. Di Maio, A. Crispo et al., "Luminal-like HER2-negative stage IA breast cancer: a multicenter retrospective study on long-term outcome with propensity score analysis," *Oncotarget*, vol. 8, no. 68, pp. 112816–112824, 2017.
- [12] R. Rabinovitch, J. Moughan, F. Vicini et al., "Long-term update of NRG oncology RTOG 0319: a phase 1 and 2 trial to evaluate 3-dimensional conformal radiation therapy confined to the region of the lumpectomy cavity for stage I and II breast carcinoma," *International Journal of Radiation Oncology • Biology • Physics*, vol. 96, no. 5, pp. 1054–1059, 2016.
- [13] G. F. Liu, Q. Yang, B. G. Haffty, and M. S. Moran, "Clinical-pathologic features and long-term outcomes of tubular carcinoma of the breast compared with invasive ductal carcinoma treated with breast conservation therapy," *International Journal of Radiation Oncology • Biology • Physics*, vol. 75, no. 5, pp. 1304–1308, 2009.
- [14] N. Tamirisa, S. M. Thomas, O. M. Fayanju et al., "Axillary nodal evaluation in elderly breast cancer patients: potential effects on treatment decisions and survival," *Annals of Surgical Oncology*, vol. 25, no. 10, pp. 2890–2898, 2018.
- [15] S. Y. Park, Y. Y. Cho, H. I. Kim et al., "Clinical validation of the prognostic stage groups of the eighth-edition TNM staging for medullary thyroid carcinoma," *The Journal of Clinical Endocrinology & Metabolism*, vol. 103, no. 12, pp. 4609–4616, 2018.
- [16] A. A. Yassine, W. C. Y. Lo, T. Saeidi et al., "Photodynamic therapy outcome modelling for patients with spinal metastases: a simulation-based study," *Scientific Reports*, vol. 11, no. 1, p. 17871, 2021.
- [17] G. Manca, D. Volterrani, S. Mazzarri et al., "Sentinel lymph node mapping in melanoma," *Quarterly Journal of Nuclear Medicine and Molecular Imaging*, vol. 39, no. 7, pp. e346–e354, 2014.
- [18] R. Seifert, A. Küper, M. Tewes et al., "[18 F]-Fluorodeoxyglucose positron emission tomography/CT to assess the early metabolic response in patients with hormone receptor-positive HER2-negative metastasized breast cancer treated with cyclin-dependent 4/6 kinase inhibitors," *Oncology Research and Treatment*, vol. 44, no. 7-8, pp. 400–407, 2021.
- [19] A. N. Shah and M. Cristofanilli, "The growing role of CDK4/6 inhibitors in treating hormone receptor-positive advanced breast cancer," *Current Treatment Options in Oncology*, vol. 18, no. 1, p. 6, 2017.

- [20] S. You, T. H. Kim, D. K. Kang, K. J. Park, Y. S. An, and J. S. Sun, "Usefulness of staging chest CT in breast cancer: evaluating diagnostic yield of chest CT according to the molecular subtype and clinical stage," *Current treatment options in oncology*, vol. 10, no. 5, p. 906, 2021.
- [21] L. Beaton, A. Bergman, A. Nichol et al., "Cardiac death after breast radiotherapy and the QUANTEC cardiac guidelines," *Clinical and Translational Radiation Oncology*, vol. 19, pp. 39–45, 2019.
- [22] R. Minamimoto, M. Senda, K. Uno et al., "Performance profile of FDG-PET and PET/CT for cancer screening on the basis of a Japanese Nationwide Survey," *Annals of Nuclear Medicine*, vol. 21, no. 9, pp. 481–498, 2007.
- [23] M. Franchi, A. Trama, I. Merlo et al., "Cardiovascular risk after adjuvant trastuzumab in early breast cancer: an Italian population-based cohort study," *Oncologist*, vol. 25, no. 10, pp. e1492–e1499, 2020.

Retraction

Retracted: Efficacy of Gamma Globulin Combined with Azithromycin Sequential Therapy in the Treatment of RMPP and Its Effect on Th1/Th2 Cytokine Levels

Computational and Mathematical Methods in Medicine

Received 27 June 2023; Accepted 27 June 2023; Published 28 June 2023

Copyright © 2023 Computational and Mathematical Methods in Medicine. This is an open access article distributed under the Creative Commons Attribution License, which permits unrestricted use, distribution, and reproduction in any medium, provided the original work is properly cited.

This article has been retracted by Hindawi following an investigation undertaken by the publisher [1]. This investigation has uncovered evidence of one or more of the following indicators of systematic manipulation of the publication process:

- (1) Discrepancies in scope
- (2) Discrepancies in the description of the research reported
- (3) Discrepancies between the availability of data and the research described
- (4) Inappropriate citations
- (5) Incoherent, meaningless and/or irrelevant content included in the article
- (6) Peer-review manipulation

The presence of these indicators undermines our confidence in the integrity of the article's content and we cannot, therefore, vouch for its reliability. Please note that this notice is intended solely to alert readers that the content of this article is unreliable. We have not investigated whether authors were aware of or involved in the systematic manipulation of the publication process.

In addition, our investigation has also shown that one or more of the following human-subject reporting requirements has not been met in this article: ethical approval by an Institutional Review Board (IRB) committee or equivalent, patient/participant consent to participate, and/or agreement to publish patient/participant details (where relevant).

Wiley and Hindawi regrets that the usual quality checks did not identify these issues before publication and have since put additional measures in place to safeguard research integrity.

We wish to credit our own Research Integrity and Research Publishing teams and anonymous and named external researchers and research integrity experts for contributing to this investigation.

The corresponding author, as the representative of all authors, has been given the opportunity to register their agreement or disagreement to this retraction. We have kept a record of any response received.

References

- [1] J. Qi, F. Jia, H. Tian, and S. Yang, "Efficacy of Gamma Globulin Combined with Azithromycin Sequential Therapy in the Treatment of RMPP and Its Effect on Th1/Th2 Cytokine Levels," *Computational and Mathematical Methods in Medicine*, vol. 2022, Article ID 5162768, 5 pages, 2022.

Research Article

Efficacy of Gamma Globulin Combined with Azithromycin Sequential Therapy in the Treatment of RMPP and Its Effect on Th1/Th2 Cytokine Levels

Jie Qi, Fang Jia, Hui Tian, and Shengmei Yang 

Special Needs Ward, Shanxi Children's Hospital, Taiyuan 030013, China

Correspondence should be addressed to Shengmei Yang; shengmeiyang@stu.ahu.edu.cn

Received 27 April 2022; Revised 17 June 2022; Accepted 27 June 2022; Published 20 July 2022

Academic Editor: Pan Zheng

Copyright © 2022 Jie Qi et al. This is an open access article distributed under the Creative Commons Attribution License, which permits unrestricted use, distribution, and reproduction in any medium, provided the original work is properly cited.

Objective. To investigate the efficacy of gamma globulin combined with azithromycin sequential therapy in the treatment of children with refractory mycoplasma pneumonia and its effect on Th1/Th2 cytokine levels. **Method.** From January 2021 to January 2022, 100 children diagnosed with refractory mycoplasma pneumonia were randomly divided into 2 groups (50 cases in each one), the control group was treated with azithromycin plus comprehensive basic treatment, and the treatment group was treated with combined treatment on the basis of the control group, gamma globulin therapy; the treatment effect and cytokine levels of the two groups were compared. **Results.** Th1, Th2, and Th1/Th2 before treatment were not significantly different between the two groups. Th1, Th2, and Th1/Th2 in the treatment group were significantly downregulated compared with those in the control group after treatment. The levels of IgG, IgA, and IgM in the treatment group were not significantly different from those in the control group before treatment but were significantly upregulated after treatment. IL-10, IL-6, and IL-2 levels were also significantly increased in the treatment group. The disappearance time of clinical symptoms such as fever, cough, and pulmonary rales in the treatment group was significantly shorter than that in the control group, and the cure rate in the treatment group was significantly better than that in the control group. **Conclusion.** The clinical effect of gamma globulin combined with azithromycin sequential therapy in the treatment of children with refractory mycoplasma pneumonia is remarkable, which can reduce inflammatory factors, improve patients' immunity, and promote disease recovery.

1. Introduction

Refractory Mycoplasma pneumoniae pneumonia (RMPP) mainly refers to mycoplasma pneumonia characterized by persistent fever, progressive aggravation of clinical symptoms, and related imaging manifestations after 1 week of standard macrolide therapy [1]. Acquired pneumonia with unknown clinical etiology changes rapidly, and extensive pulmonary inflammation can occur in a relatively short period of time, often accompanied by complications such as massive pleural effusion, pleural thickening, lung abscess, and pneumothorax. In more severe cases, children may develop bronchiolitis obliterans, atelectasis, and sys-

temic inflammatory response syndrome, posing serious health risks [2]. At present, the treatment of refractory Mycoplasma pneumoniae pneumonia mainly adopts antibacterial, inhibiting overactive immune response and bronchoalveolar lavage, but the clinical efficacy is still poor [3]. In recent years, azithromycin is clinically combined with basic therapy. It has been reported that the pathogenesis of severe Mycoplasma pneumoniae pneumonia is related to cell-mediated immunity, and corticosteroid therapy may be effective. Intravenous immunoglobulin (IVIG) has been used as a potent immunomodulator for Kawasaki disease and other immune-mediated diseases [4]. Intravenous immune globulin can also be used to treat refractory

Mycoplasma pneumoniae pneumonia. Therefore, this study is aimed at investigating the treatment options for refractory mycoplasma pneumonia in children.

2. Materials and Methods

2.1. Patients. From January 2021 to January 2022, 100 pediatric patients diagnosed with refractory mycoplasma pneumonia were randomly divided into 2 groups (50 cases in each). All patients in this study gave informed consent, and the patients themselves or their representatives signed the relevant consent forms. The details of the baseline data of the included subjects are summarized in Table 1.

2.2. Inclusion and Exclusion Criteria. The inclusion criteria for this study were (1) meeting the diagnostic criteria for refractory mycoplasma pneumonia in "Practical Internal Medicine" and (2) no related treatment was performed before inclusion in the study.

The exclusion criteria were (1) combined with other respiratory diseases, (2) related to malignant tumors and other diseases, and (3) suffering from mental illness or drug allergy.

2.3. Interventions. The children in the control group were treated with conventional treatment measures such as fever reduction, oxygen inhalation, atomization, cough relief, phlegm reduction, and azithromycin. Administer 10 mg/kg body weight on the first day, the maximum daily dose does not exceed 0.5 g, and on the 2nd to 5th days, administer oral 5 mg/kg body weight; the maximum dose does not exceed 0.25 g. Continue treatment for 2 weeks. The patients in the treatment group were given routine basic therapy at the same time, gamma globulin combined with azithromycin. The gamma globulin was dissolved in normal saline for intravenous infusion.

2.4. Observation Indicator. The clinical efficacy of the two groups of patients was compared. T lymphocyte factors Th1, Th2, and Th1/Th2; inflammatory factors IL-10, IL-6, and IL-2; and immunoglobulin levels IgG, IgA, and IgM were determined by commercial ELISA kits (Abcam, USA).

2.5. Statistical Analysis. The experimental data was analyzed by SPSS21.0 software (SPSS, Chicago, USA), the count data was analyzed by χ^2 (%), the measurement value was analyzed by t test, and two-sided $P < 0.05$ was used to judge whether there was a statistically significant difference.

3. Results

3.1. Comparison of Th1, Th2, and Th1/Th2 between the Two Groups before and after Treatment. As shown in Table 2, Th1 (0.53 ± 0.15), Th2 (0.47 ± 0.13), and Th1/Th2 (1.41 ± 0.20) in the treatment group were compared with those in the control group Th1 (0.57 ± 0.16), Th2 (0.46 ± 0.14), and Th1/Th2 (1.43 ± 0.15) which had no significant difference ($t = 2.019, 1.631, \text{ and } 1.461$; $P = 0.245, 0.131, \text{ and } 0.102$). After treatment, Th1 (0.16 ± 0.14), Th2 (0.18 ± 0.07), and Th1/Th2 (0.39 ± 0.16) in the treatment

group were lower than those in the control group Th1 (0.37 ± 0.2), Th2 (0.31 ± 0.06), and Th1/Th2 ($0.58 \pm 0.58 \pm 0.18$), and the difference was significant ($t = 15.943, 12.005, \text{ and } 13.325$; $P = 0.001, 0.005, \text{ and } 0.005$).

3.2. Comparison of Serum Immunoglobulin Levels between the Two Groups before and after Treatment. As shown in Table 3, before treatment, IgG (8.50 ± 1.40), IgA (1.40 ± 0.20), and IgM (1.50 ± 0.30) in the treatment group were compared with IgG (8.30 ± 1.60), IgA (1.20 ± 0.30), and IgM (1.50 ± 0.20) in the control group, and there was no significant difference ($t = 1.568, 1.064, \text{ and } 1.263$; $P = 0.712, 0.070, \text{ and } 0.065$). After treatment, IgG (11.20 ± 1.60), IgA (2.20 ± 0.30), and IgM (1.70 ± 0.10) in the treatment group were significantly higher than those in the control group in terms of IgG (9.50 ± 1.80), IgA (1.80 ± 0.40), and IgM (1.60 ± 0.30 , $t = 12.018, 11.935, \text{ and } 10.881$; $P = 0.001, 0.003, \text{ and } 0.001$).

3.3. Comparison of Inflammatory Factors before and after Treatment in the Two Groups. After treatment, IL-10 (30.20 ± 5.23), IL-6 (40.52 ± 2.83), and IL-2 (30.61 ± 1.50) in the treatment group were significantly lower than those in the control group IL-10 (19.91 ± 5.40) and IL-6 (48.21 ± 1.50) and IL-2 (21.20 ± 2.41), and the difference was significant ($t = 12.583, 8.934, \text{ and } 10.033$; $P = 0.011, 0.001, \text{ and } 0.005$) as shown in Table 4.

3.4. Comparison of the Disappearance Time of Clinical Symptoms in Two Groups of Patients. As shown in Table 5, compared with the control group, the time to disappearance of clinical symptoms such as fever (2.18 ± 0.01), cough (4.36 ± 1.89), and pulmonary rales (3.86 ± 0.51) in the treatment group was significantly reduced, and the difference was significant ($t = 7.943, 11.274, \text{ and } 9.538$; $P = 0.0001, 0.005, \text{ and } 0.006$).

3.5. Comparison of Clinical Efficacy between Two Groups of Patients. The cure rate in the treatment group was 76.00% (38/50), which was significantly better than that in the control group (48.00% (24/50)), with a significant difference ($\chi^2 = 11.724, P < 0.001$). The total effective rate in the treatment group was 92.00% (46/50), which was significantly better than that in the control group (80.00% (40/50)), with a significant difference ($\chi^2 = 9.458, P = 0.015$, Table 6).

4. Discussion

Mycoplasma pneumoniae (MP) is one of the common pathogens causing community-acquired pneumonia (CAP) in children. More than 10%-40% of CAP is caused by MP. MP pneumonia (MPP) may develop into life-threatening severe pneumonia in some cases, although it is usually a benign self-limiting disease [5]. As the treatment of choice for MP infections in children, macrolides have been used for MP treatment for many years. However, many clinical isolates of MP cases show resistance to macrolides [6]. However, for the treatment of refractory *Mycoplasma pneumoniae* in children, the application of immunoglobulin still lacks evidence-based medical evidence.

TABLE 1: General information of 2 groups.

Group	Average age (year old)	BMI (kg/m ²)	Disease duration (d)
Treatment (50)	10.43 ± 1.39	23.81 ± 3.26	6.36 ± 1.56
Control (50)	10.51 ± 1.92	23.31 ± 3.32	6.42 ± 1.59
t/χ^2	2.371	3.374	1.856
P	0.382	0.593	0.895

TABLE 2: Comparison of Th1, Th2, and Th1/Th2 between the two groups of patients.

Group	n	Th1		Th2		Th1/Th2	
		Before	After	Before	After	Before	After
Treatment	50	0.53 ± 0.15	0.16 ± 0.14	0.47 ± 0.13	0.18 ± 0.07	1.41 ± 0.20	0.39 ± 0.16
Control	50	0.57 ± 0.16	0.37 ± 0.21	0.46 ± 0.14	0.31 ± 0.06	1.43 ± 0.15	0.58 ± 0.18
t	/	2.019	15.943	1.631	12.055	1.461	13.325
P	/	0.245	0.001	0.131	0.005	0.102	0.005

TABLE 3: Comparison of serum immunoglobulin levels before and after treatment between the two groups of patients.

Group	n	IgG		IgA		IgM	
		Before	After	Before	After	Before	After
Control	50	8.30 ± 1.60	9.50 ± 1.80	1.20 ± 0.30	1.80 ± 0.40	1.50 ± 0.20	1.60 ± 0.30
Treatment	50	8.50 ± 1.4	11.20 ± 1.60	1.4 ± 0.20	2.20 ± 0.30	1.50 ± 0.30	1.70 ± 0.10
t		1.568	12.018	1.064	11.935	1.263	10.881
P		0.112	0.001	0.070	0.003	0.065	0.001

TABLE 4: Changes of inflammatory factor levels in patients before and after treatment.

Group	n	IL-10		IL-6		IL-2	
		Before	After	Before	After	Before	After
Treatment	50	42.60 ± 6.71	30.20 ± 5.23	85.92 ± 5.20	40.52 ± 2.83	67.80 ± 6.31	30.61 ± 1.50
Control	50	41.52 ± 5.90	19.91 ± 5.40	85.71 ± 4.93	48.21 ± 3.80	65.62 ± 2.84	21.20 ± 2.41
t		1.532	12.583	1.202	8.934	2.075	10.033
P		0.596	0.011	0.840	0.001	0.940	0.005

TABLE 5: Comparison of the disappearance time of clinical symptoms in the two groups of patients.

Group	Fever	Cough	Pulmonary rales
Control ($n = 50$)	4.28 ± 1.33	6.27 ± 1.57	5.86 ± 0.57
Treatment ($n = 50$)	2.18 ± 0.01	4.36 ± 1.89	3.86 ± 0.51
t	7.943	11.274	9.538
P	0.001	0.005	0.006

Mycoplasma pneumoniae is a common pathogen that causes community-acquired pneumonia. In the past, *Mycoplasma pneumoniae* was sensitive to macrolide antibiotics, and *Mycoplasma pneumoniae* pneumonia (MPP) was usually a benign self-limiting disease [7]. However, despite appropriate antibiotics, persistent fever and clinical deterioration can lead to severe illness. Two major complications that may be encountered clinically are macrolide-resistant

mycoplasma pneumoniae and refractory *mycoplasma pneumoniae* [8]. Macrolide-resistant *mycoplasma pneumoniae* manifests with persistent fever and/or no radiographic resolution to macrolide antibiotics and may even develop into severe and complex pneumonia. Tetracycline (doxycycline or minocycline) or fluoroquinolones are alternative treatments for macrolide-resistant *mycoplasma pneumoniae*. Refractory *mycoplasma pneumoniae* is characterized by an excessive immune response to the pathogen [9]. In this context, corticosteroids are considered an immunomodulatory agent for downregulating an overactive host immune response. Macrolide overuse may lead to macrolide resistance, which in turn leads to an increase in macrolide-resistant *mycoplasma pneumoniae* [10].

The host innate and adaptive immune systems work together to combat damage caused by *mycoplasma* infection. However, the clinical course of pneumonia may worsen when the inflammatory response is overamplified. In

TABLE 6: Comparison of clinical efficacy between the two groups of patients.

Group	Healing	Show effect	Effective	Ineffective	Total effective	Total efficiency
Treatment ($n = 50$)	16 (32.00)	22 (44.00)	8 (16.00)	4 (8.00)	38 (76.00)	46 (92.00)
Control ($n = 50$)	10 (20.00)	14 (28.00)	16 (32.00)	10 (20.00)	24 (48.00)	40 (80.00)
χ^2		/			11.724	9.458
P		/			<0.001	0.015

refractory mycoplasma pneumonia, the host immune response may lead to lung injury rather than direct microbial damage [11–13]. Therefore, refractory mycoplasma pneumonia is to some extent an immune-mediated disease, and immunosuppressive therapy may therefore be a reasonable approach [14]. Several studies reported the use of immunosuppressive agents, such as corticosteroids or intravenous immunoglobulin, in selected patients. Cell-mediated immunity has been shown to play an important role in the progression of mycoplasma infection [15]. Interleukin (IL) 2, IL8, IL5, IL6, IL18, and other cytokines may be involved in Mycoplasma pneumoniae infection and induce inflammatory response. A high immune response of T cells may lead to the destruction of lung tissue. The immune response produces many inflammatory mediators that may lead to more severe lung damage. Excessive cell-mediated immune and cytokine responses play important roles in refractory mycoplasma pneumonia. Refractory mycoplasma pneumonia is not only an infection but also an immune-mediated disease [16]. Corticosteroids can modulate immunity to inflammatory responses. Corticosteroids have been shown to be effective in improving the clinical manifestations and lung injury of M. pneumoniae infection in children and adults, reducing lung histopathological scores and reducing mortality in severe pneumonia by reducing cytokines and reducing inflammatory responses [17]. Clinical progress has been made in the immunotherapy of refractory mycoplasma pneumonia. Immunoglobulins are considered potent immunomodulators for various immune-mediated diseases, and it has marked activity against Mycoplasma pneumonia and provide additional protection, especially in patients who do not respond well to antibiotic therapy. Immunoglobulins have been reported to be effective in the treatment of many autoimmune and systemic inflammatory diseases [18–20]. Immunoglobulins have significant effects on different immune system effector cells (such as B and T lymphocytes and dendritic cells) and regulate a wide range of genes.

Although only a few studies have reported the use of immunoglobulins in refractory mycoplasma pneumonia, our trial suggests that azithromycin in combination with immunomodulatory therapy is an effective treatment. After treatment in this study, the Th1 (0.16 ± 0.14), Th2 (0.18 ± 0.07), and Th1/Th2 (0.39 ± 0.16) of the study group were compared with those of the control group Th1 (0.37 ± 0.2), Th2 (0.31 ± 0.06), and Th1/Th2 (0.58 ± 0.18), and the decrease was more obvious. Compared with the control group, the immunoglobulin IgG, IgA, and IgM of the

study group increased significantly. After treatment, the reduction of inflammatory factors in the study group was more significant than that in the control group. The disappearance time of clinical symptoms and the total effective rate of treatment in the study group were significantly better than those in the control group. The data show that sequential therapy with immunoglobulin combined with azithromycin can effectively improve the cure rate of children with refractory mycoplasma pneumonia. The data analysis shows that the combined medication can significantly shorten the duration of fever in children, improve cough symptoms, promote the absorption of lung inflammation, shorten the hospital stay, reduce the level of inflammatory factors, and regulate the immune system of the body, to achieve the purpose of improving the curative effect.

In conclusion, gamma globulin combined with azithromycin sequential therapy has significant clinical effect in the treatment of children with refractory mycoplasma pneumonia, which can reduce inflammatory factors, improve patients' immunity, and promote disease recovery.

Data Availability

All data was provided in the manuscript.

Conflicts of Interest

The authors declare that they have no conflicts of interest.

References

- [1] S. S. Shah, "Mycoplasma pneumoniae as a cause of community-acquired pneumonia in children," *Clinical Infectious Diseases: an Official Publication of the Infectious Diseases Society of America*, vol. 68, no. 1, pp. 13–14, 2018.
- [2] C. J. Gross, J. J. Porter, S. C. Lipsett, M. C. Monuteaux, A. W. Hirsch, and M. I. Neuman, "Variation in management and outcomes of children with complicated pneumonia," *Hospital Pediatrics*, vol. 11, no. 3, pp. 207–214, 2021.
- [3] T. A. Tsai, C. K. Tsai, K. C. Kuo, and H. R. Yu, "Rational stepwise approach for Mycoplasma pneumoniae pneumonia in children," *Journal of Microbiology, Immunology, and Infection*, vol. 54, no. 4, pp. 557–565, 2021.
- [4] Y. C. Lee, C. H. Chang, W. J. Lee et al., "Altered chemokine profile in refractory Mycoplasma pneumoniae pneumonia infected children," *Journal of Microbiology, Immunology, and Infection*, vol. 54, no. 4, pp. 673–679, 2021.
- [5] H.-K. Cho, "Consideration in treatment decisions for refractory mycoplasma pneumoniae pneumonia," *Clinical and Experimental Pediatrics*, vol. 64, no. 9, pp. 459–467, 2021.

Retraction

Retracted: Serum Adiponectin Level in Different Stages of Type 2 Diabetic Kidney Disease: A Meta-Analysis

Computational and Mathematical Methods in Medicine

Received 27 June 2023; Accepted 27 June 2023; Published 28 June 2023

Copyright © 2023 Computational and Mathematical Methods in Medicine. This is an open access article distributed under the Creative Commons Attribution License, which permits unrestricted use, distribution, and reproduction in any medium, provided the original work is properly cited.

This article has been retracted by Hindawi following an investigation undertaken by the publisher [1]. This investigation has uncovered evidence of one or more of the following indicators of systematic manipulation of the publication process:

- (1) Discrepancies in scope
- (2) Discrepancies in the description of the research reported
- (3) Discrepancies between the availability of data and the research described
- (4) Inappropriate citations
- (5) Incoherent, meaningless and/or irrelevant content included in the article
- (6) Peer-review manipulation

The presence of these indicators undermines our confidence in the integrity of the article's content and we cannot, therefore, vouch for its reliability. Please note that this notice is intended solely to alert readers that the content of this article is unreliable. We have not investigated whether authors were aware of or involved in the systematic manipulation of the publication process.

Wiley and Hindawi regrets that the usual quality checks did not identify these issues before publication and have since put additional measures in place to safeguard research integrity.

We wish to credit our own Research Integrity and Research Publishing teams and anonymous and named external researchers and research integrity experts for contributing to this investigation.

The corresponding author, as the representative of all authors, has been given the opportunity to register their agreement or disagreement to this retraction. We have kept a record of any response received.

References

- [1] L. Li, J. Shi, and G. Wu, "Serum Adiponectin Level in Different Stages of Type 2 Diabetic Kidney Disease: A Meta-Analysis," *Computational and Mathematical Methods in Medicine*, vol. 2022, Article ID 1863243, 11 pages, 2022.

Research Article

Serum Adiponectin Level in Different Stages of Type 2 Diabetic Kidney Disease: A Meta-Analysis

Li Li ¹, Jilai Shi ¹ and Guoliang Wu²

¹Department of Endocrinology, The Affiliated Hospital of Shandong University of Traditional Chinese Medicine, Jinan, Shandong 250014, China

²Department of Anorectal Surgery, The First Affiliated Hospital of Shandong First Medical University, Jinan, Shandong 250014, China

Correspondence should be addressed to Jilai Shi; 974070133@qq.com

Received 13 May 2022; Revised 29 June 2022; Accepted 4 July 2022; Published 15 July 2022

Academic Editor: Pan Zheng

Copyright © 2022 Li Li et al. This is an open access article distributed under the Creative Commons Attribution License, which permits unrestricted use, distribution, and reproduction in any medium, provided the original work is properly cited.

Background. Biomarkers in predicting the stages of nephropathy associated with type 2 diabetes mellitus are urgent, and adiponectin may be a promising biomarker. This meta-analysis examined the association of serum adiponectin level with the stages of type 2 diabetic nephropathy. **Methods.** Databases including PubMed, Cochrane Library, EMBASE, China National Knowledge Infrastructure (CNKI), and Wan Fang were searched for published studies on adiponectin and type 2 diabetic kidney disease. The Newcastle-Ottawa scale was used to assess the quality of the literature. STATA 14.0 was used to conduct the statistical analysis. **Results.** Thirty-four studies with 5254 patients were included in this meta-analysis. The results of this study show that there was no significant difference in serum adiponectin level between normoalbuminuria and the control group (mean difference = -0.42 , 95% CI $[-1.23, 0.40]$), while serum adiponectin level was positively correlated with the severity of type 2 diabetic kidney disease. The serum adiponectin level in type 2 diabetic kidney disease patients ranks as macroalbuminuria > microalbuminuria > normoalbuminuria. **Conclusions.** Serum adiponectin level might be an important marker to predict the progression of type 2 diabetic kidney disease.

1. Introduction

Hyperglycemia is the defining feature of diabetes mellitus (DM). Currently, DM is classified into two forms: type 1 (T1) and type 2 (T2) DM. T1DM is caused by the absolute lack of insulin which ensues consequent pancreatic beta cell destruction, while T2DM is mainly due to insulin resistance [1]. WHO reported that there were around 422 million people living with DM in 2018, and T2DM accounts for over 90% among these people [2]. Obesity is an important risk factor for T2DM [3]. The DM complications attack almost every body tissue, and DM is a leading cause of cardiovascular morbidity and mortality, blindness, renal failure, and amputations. Besides, the early diagnosis of T2DM in young people has been linked to a more aggressive form of the disease [4].

Long-term DM is closely related to microvascular complications, especially diabetic kidney disease (DKD). DKD is the most common complication of T2DM, which develops

in around 40% of diagnosed patients [5, 6]. In addition, it is the leading cause of end-stage renal disease all over the world [7]. The definition DKD is based on current guidelines using four main criteria: a decline in renal function, proteinuria, and a reduction in glomerular filtration rate (GFR) [8]. DKD was divided into three stages according to albumin-to-creatinine ratio (ACR): normoalbuminuria ($ACR < 30$ mg/g), microalbuminuria ($30 \text{ mg/g} \leq ACR < 300$ mg/g), and macroalbuminuria ($ACR \geq 300$ mg/g). It is crucial to diagnose patients who are more sensible to develop DKD for better control of the process of disease. Albuminuria has been one of the biomarkers to screen renal function; however, it has lots of limitations such as large variability and low sensitivity, and it may not be detectable in early stage [9, 10].

Biomarkers may allow earlier diagnosis and treatment for DKD, thereby slowing disease progression and raising life expectancy among patients [11]. Biomarkers are

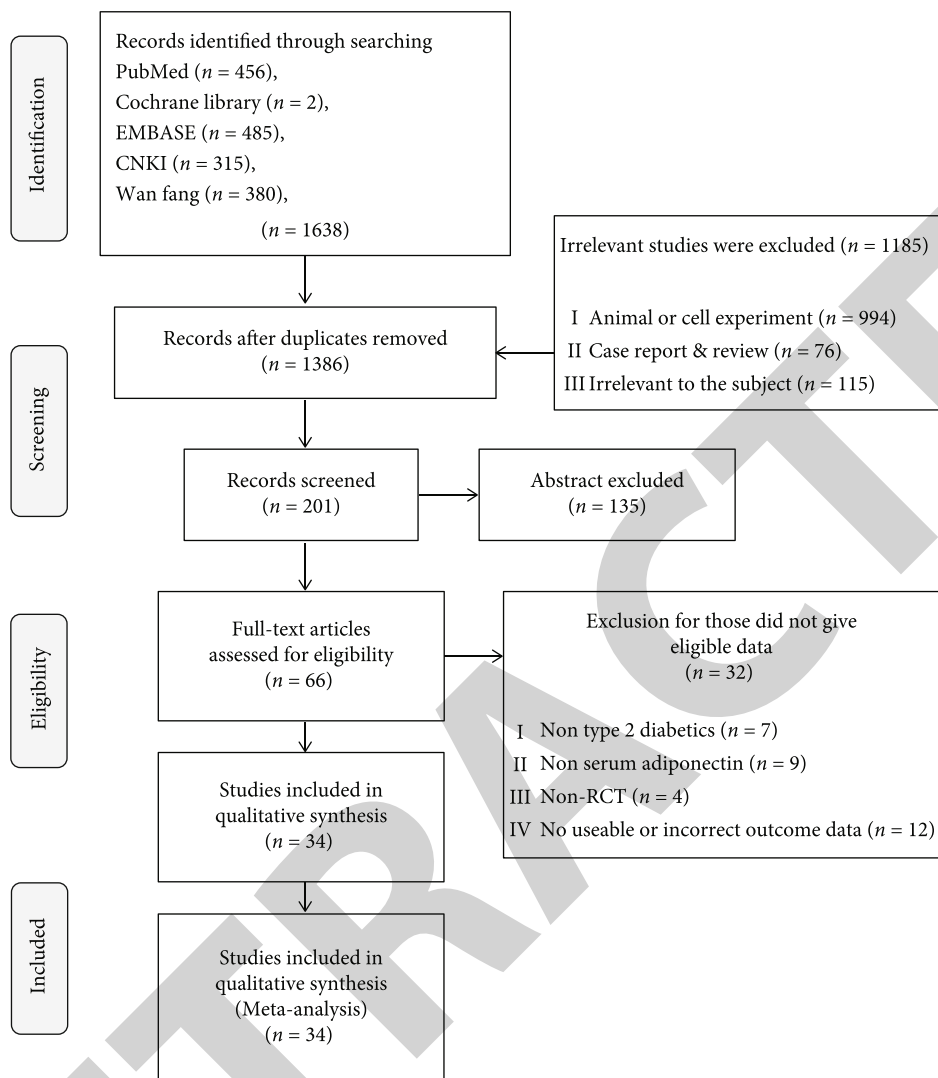


FIGURE 1: Flowchart of literature selection.

characteristic factors that can be measured and assessed as an indicator for normal physiologic or pathogenic processes. Examples of biomarkers are proteins, lipids, microRNAs, genomic, etc. Plenty of biomarkers associated with DKD were found in recent years, such as serum cystatin C, neutrophil gelatinase-associated lipocalin (NGAL), N-acetyl- β -D-glucosaminidase (NAG), and serum homocysteine (Hcy) [12].

Adiponectin (ADP) may play a role in DKD [13]. ADP is a small collagen-like protein expressed by adipocytes, which has been shown to have functions as anti-inflammation and insulin-sensitizing [14–17]. Reports of ADP effects on DKD have been variable; thus, a meta-analysis to obtain more precise evaluations is in need. This meta-analysis reveals the association between serum ADP levels and the severity of T2DKD. Results in this study may provide evidence to whether ADP can be a potential biomarker for DKD.

2. Methods

2.1. Data Source and Search Strategy. We identified studies published in PubMed, Cochrane Library, EMBASE, China

National Knowledge Infrastructure (CNKI), and Wan Fang (last search date: April 24, 2022). The search terms included “adiponectin” and “diabetes mellitus” or “type 2 diabetes mellitus” or “type 2 diabetes” or “type 2 diabetics” or “ketosis-resistant diabetes mellitus” or “non-insulin-dependent diabetes mellitus” and “diabetic nephropathy” or “diabetic kidney disease” or “Kimmelstiel-Wilson disease”.

2.2. Data Extraction and Eligibility Criteria. Two investigators (Li Li and Guoliang Wu) independently extracted data and reached consensus, and the disagreement was determined by the third investigator (Jilai Shi). For each eligible literature, the following information was extracted: the first author’s name, publication year, country, sample size, and data for ADP concentration.

Studies eligible for this meta-analysis should meet the following criteria: (a) the study included a control group (healthy people) and observation groups (DM patients with/without DKD); (b) observation groups including patients that were diagnosed as T2DM; (c) trials reported

TABLE 1: Characteristics of studies included.

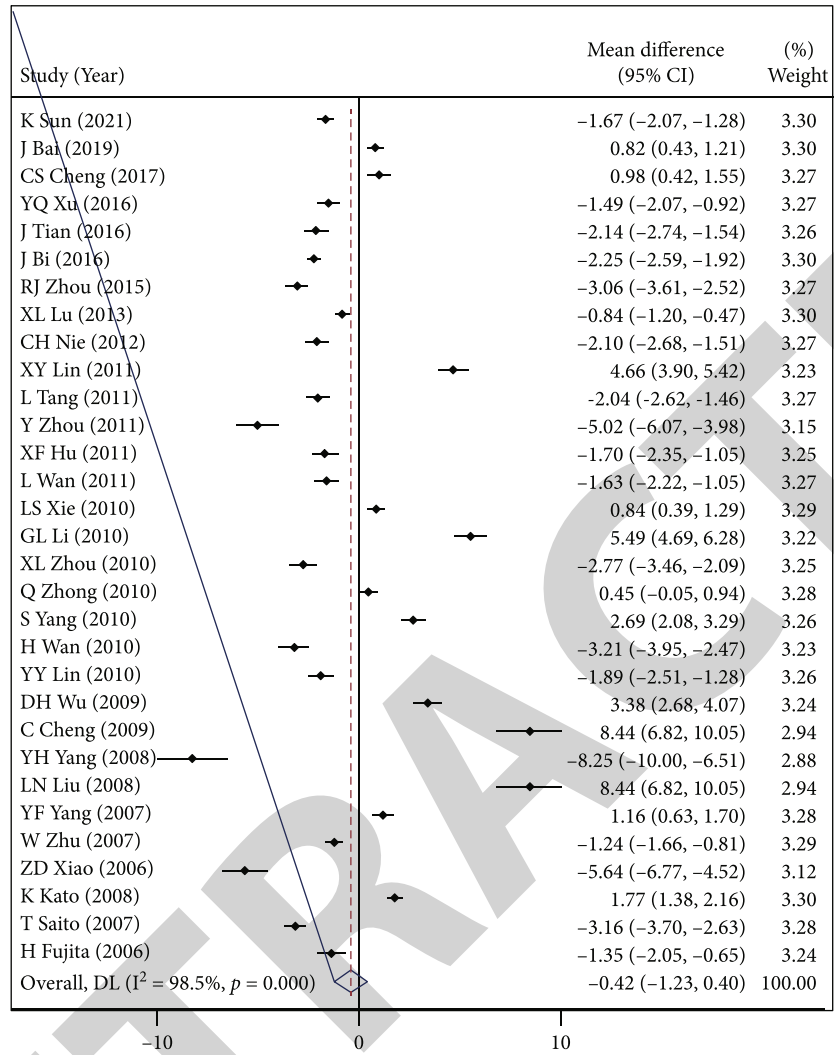
Study	Year	Total sample size	Control			Normoalbuminuria			Microalbuminuria			Macroalbuminuria			NOS
			Sample size	Mean	SD	Sample size	Mean	SD	Sample size	Mean	SD	Sample size	Mean	SD	
Sun [18]	2021	226	60	15.10	1.20	74	12.90	1.40	66	8.70	1.70	26	4.50	1.90	7
Bai [19]	2019	190	50	3.19	1.26	61	4.25	1.33	44	6.34	1.27	35	13.41	2.62	8
Cheng [20]	2017	112	30	6.72	2.70	25	9.57	3.12	27	12.87	3.46	30	17.97	3.84	6
Xu [21]	2016	113	30	11.80	4.20	30	6.70	2.40	25	12.60	4.10	28	18.50	7.90	7
Tian [22]	2016	128	34	12.50	4.80	34	4.90	1.50	29	15.60	1.40	31	25.50	2.10	8
Bi [23]	2016	470	100	13.10	4.90	122	4.90	2.10	123	16.10	2.10	125	26.10	1.90	7
Zhou [24]	2015	172	85	73.40	9.90	37	39.40	13.50	30	54.40	10.20	20	67.80	11.30	6
Lu [25]	2013	258	62	10.22	2.13	62	8.55	1.86	70	5.93	1.64	64	3.58	1.37	7
Nie [26]	2012	140	35	9.72	4.30	35	3.27	0.68	35	10.88	2.85	35	12.75	2.46	8
Lin [27]	2011	200	50	9.58	1.33	50	16.88	1.77	50	22.54	1.86	50	28.12	2.11	6
Tang [28]	2011	132	35	12.70	5.00	35	5.10	1.70	30	15.80	1.60	32	25.70	2.30	8
Zhou [29]	2011	120	30	12.95	2.14	30	3.77	1.45	30	5.12	1.34	30	8.68	1.12	7
Hu [30]	2011	100	25	6.20	3.39	25	2.07	0.54	25	3.62	0.78	25	5.46	1.82	8
Wan [31]	2011	120	30	10.51	3.91	30	5.93	0.67	30	7.75	1.21	30	9.32	3.36	8
Xie [32]	2010	165	40	8.10	2.80	42	10.10	1.90	41	18.20	1.30	42	24.90	3.10	6
Li [33]	2010	220	51	9.69	1.26	67	16.92	1.36	57	21.34	1.67	45	26.21	1.95	8
Zhou [34]	2010	119	30	73.59	10.18	35	39.36	13.92	32	54.38	10.14	22	67.74	14.89	7
Zhong [35]	2010	130	45	5.63	1.16	25	6.28	1.87	31	9.28	2.59	29	11.15	3.18	7
Yang [36]	2010	150	40	5.15	1.99	40	10.12	1.70	40	16.58	2.68	30	7.40	1.28	6
Wan [37]	2010	130	30	11.20	3.50	36	3.40	0.80	34	9.60	2.20	30	14.30	5.60	8
Lin [38]	2010	120	30	6.44	3.11	30	2.21	0.55	30	3.62	0.80	30	5.31	1.86	6
Wu [39]	2009	151	47	10.10	1.82	32	16.41	1.94	40	18.32	1.30	32	25.52	3.19	7
Cheng [40]	2009	120	30	10.51	0.91	30	17.62	0.77	30	23.32	0.36	30	25.75	0.21	8
Yang [41]	2008	90	30	8.81	1.22	20	0.82	0.31	20	2.32	0.36	20	5.22	1.04	7
Liu [42]	2008	120	30	10.51	0.91	30	17.62	0.77	30	22.32	0.36	30	25.75	0.21	7
Yang [43]	2007	117	30	4.25	1.62	33	5.81	1.03	28	6.31	1.99	26	11.32	2.13	8
Zhu [44]	2007	213	50	14.69	7.12	52	7.78	3.55	57	10.15	5.83	54	153.98	6.33	8
Xiao [45]	2006	90	30	9.69	2.23	32	0.74	0.47	14	2.52	0.61	14	5.32	1.86	8
Kato [46]	2008	192	116	6.92	0.43	47	7.68	0.43	24	9.51	0.87	5	16.00	4.43	8
Yilmaz [47]	2008	123	N/A	N/A	N/A	38	24.10	6.10	40	16.80	2.70	45	13.30	3.10	7
Saito [48]	2007	259	49	8.99	1.12	76	6.38	0.56	106	7.67	1.25	28	5.75	0.97	6
Fujita [49]	2006	73	20	10.14	3.12	19	6.44	2.29	18	7.16	2.25	16	11.77	8.01	8
Komaba [50]	2006	153	N/A	N/A	N/A	86	7.08	5.47	44	10.65	6.07	23	14.14	8.71	6
Koshimura [51]	2004	38	N/A	N/A	N/A	18	6.50	2.10	7	7.90	3.80	13	11.00	5.50	6

Mean: $\mu\text{g/ml}$; SD: standard deviation; N/A: not applicable.

as RCTs (randomized controlled trials); (d) the literature reported the data for ADP concentration; (e) the literature was published in English or Chinese and the full text was available. Studies were excluded from our meta-analysis if they (a) did not report ADP concentrations in patients; (b) are animal or cell experiments, case report, review, letter, conference abstract, and those without full text; (c) are republished studies with similar data or patient; and (d) are irrelevant to the subject.

2.3. Quality Assessment. Quality of the studies included in this meta-analysis was evaluated by the Newcastle-Ottawa scale (NOS) assessment tool. These studies were judged based on three broad perspectives: selection, comparability, and exposure outcome. Studies with a score over 6 are considered of high quality.

2.4. Statistical Analysis. The relationship between adiponec-
tin and diabetic kidney disease was reported as mean

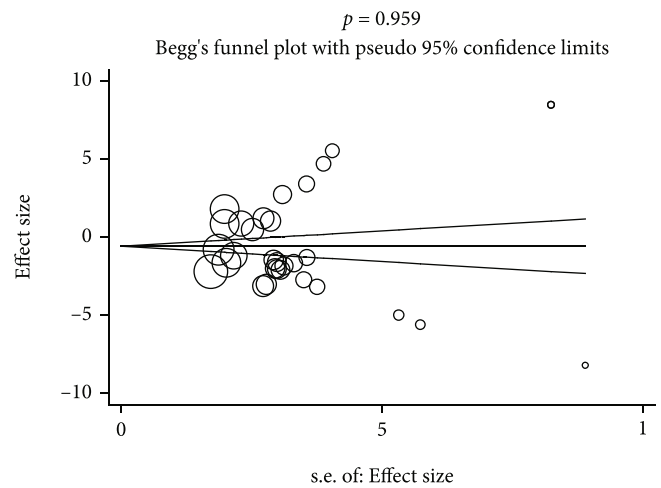


NOTE: Weights are from random-effects model

(a)

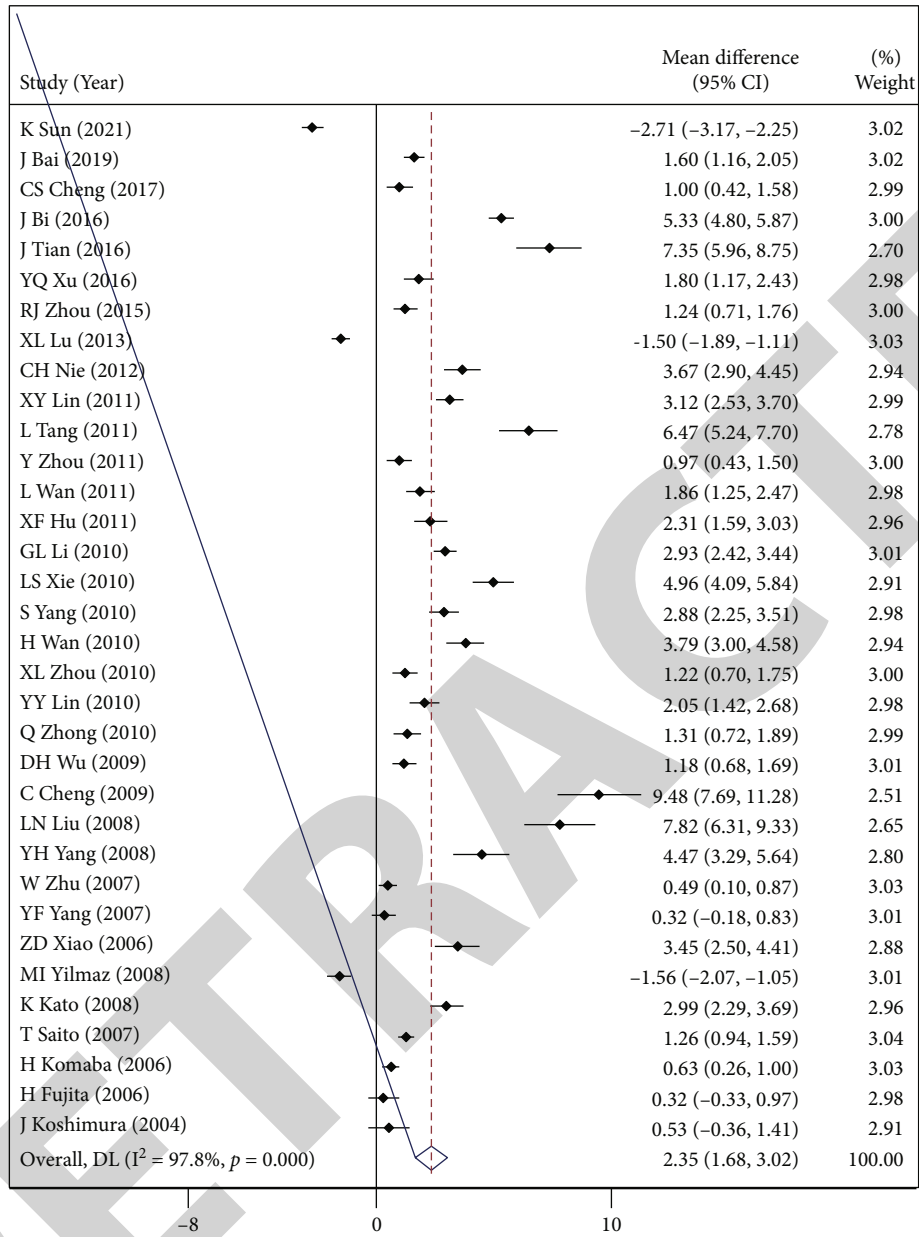
Subgroup	I^2	p	Mean difference (95% CI)
<i>Sample size</i>			
> 100	99.0%	0.001	0.03 (-1.38, 1.44)
< 100	98.1%	0.001	-0.64 (-1.68, 0.41)
<i>China</i>			
Yes	98.4%	0.001	-0.36 (-1.22, 0.49)
No	99.1%	0.001	-0.91 (-4.15, 2.33)

(b)



(c)

FIGURE 2: Meta-analysis of the relationship between serum adiponectin and type 2 diabetic kidney disease (normoalbuminuria vs. control): (a) mean difference of serum adiponectin level; (b) subgroup analysis; (c) publication bias.



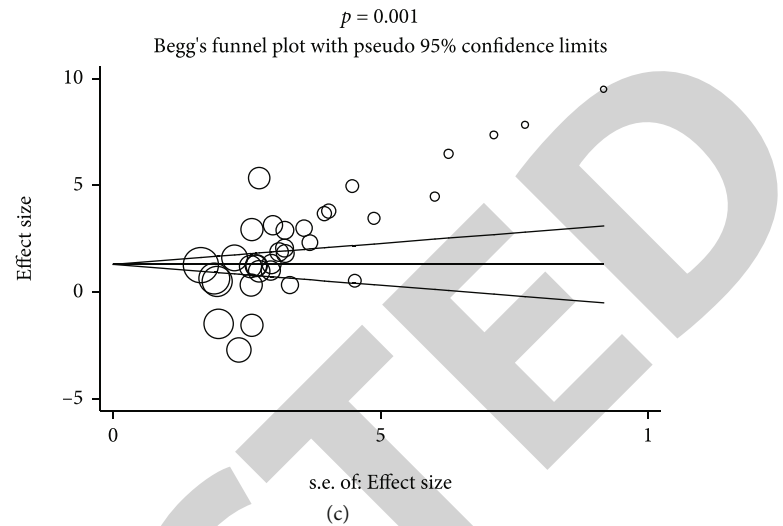
NOTE: Weights are from random-effects model

(a)

FIGURE 3: Continued.

Subgroup	I^2	p	Mean difference (95% CI)
<i>Sample size</i>			
> 100	99.0%	0.001	1.23 (-0.17, 2.64)
< 100	96.4%	0.001	2.75 (2.03, 3.48)
<i>China</i>			
Yes	98.0%	0.001	2.73 (1.93, 3.53)
No	96.2%	0.001	0.69 (-3.07, 1.74)

(b)



(c)

FIGURE 3: Meta-analysis of the relationship between serum adiponectin and type 2 diabetic kidney disease (microalbuminuria vs. normoalbuminuria): (a) mean difference of serum adiponectin level; (b) subgroup analysis; (c) publication bias.

difference (MD) and 95% confidence intervals (CI) for continuous data using STATA 14.0 software (College Station, TX, USA). MD estimates were considered as significant if CI did not cross zero and $p < 0.05$. Pooled estimate was using a fixed-effect (absence of heterogeneity) or a random-effect (presence of heterogeneity) model. Heterogeneity between the studies was tested by Q test and I^2 test. If $I^2 \leq 50\%$ or $p(Q \text{ test}) > 0.1$, then no significant heterogeneity existed. Subgroup analyses were conducted to explore the potential sources of heterogeneity. Publication bias was assessed by Begg's test and funnel plot, and it was considered to be significant when $p < 0.05$. Pooled estimates were subjected to sensitivity analysis which involved excluding one study at a time and recalculating the summary effects to test the robustness of the results.

3. Results

3.1. Search Outcomes and Study Characteristics. Figure 1 outlines the study selection process in a flowchart following PRISMA guidelines. A total of 1638 literatures during the initial search were followed by omissions, and eventually, 34 studies were considered eligible and left for this meta-analysis.

The characteristics of the included studies are featured in Table 1. Overall, the total sample size included in this meta-analysis was 5254 with a wide range among patients across all studies (38 to 470). Of the included studies, 28 were conducted in China and published in Chinese, and the other 6 were conducted out of China and published in English. The mean NOS score was 7.15 ± 0.82 , and all the included studies were of high quality with NOS scores above 6.

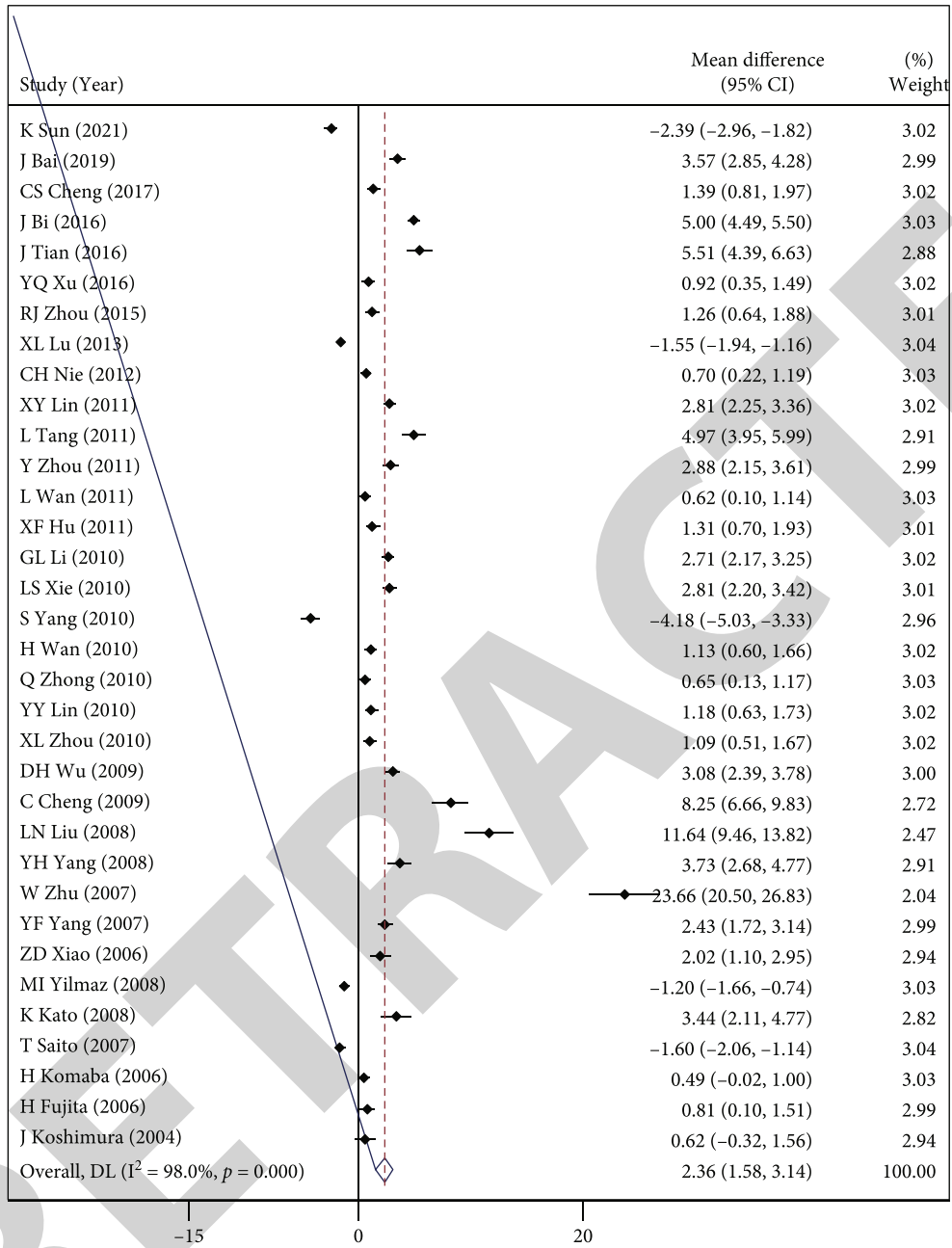
3.2. Meta-Analysis of the Relationship between Serum ADP and T2DKD

3.2.1. Normoalbuminuria versus Control. In total, 31 studies were included in this meta-analysis, with 1354 healthy peo-

ple and 1296 T2DM patients with normoalbuminuria. First, as depicted in Figure 2(a), there was a severe heterogeneity of these trials by comparing the MD of serum ADP ($I^2 = 98.5\%$, $p = 0.001$, random-effect model). The meta-analysis result indicates that there was no significant difference in serum ADP level between normoalbuminuria and the control group (MD = -0.42 , 95% CI [$-1.23, 0.40$]). To explore the potential sources of the existed heterogeneity, subgroup analyses on sample size and nation (the study was performed in China or not) were performed. However, the heterogeneity still existed in either subgroup of sample size or nation (Figure 2(b)). Next, Begg's test was used to assess the potential publication bias. As shown in Figure 2(c), the funnel plot appeared symmetrical, and Begg's test result showed that no significant publication bias was in here ($p = 0.959$).

3.2.2. Microalbuminuria versus Normoalbuminuria. In this meta-analysis, all the 34 trials were included, including 1337 patients with T2DM with microalbuminuria and 1438 with normoalbuminuria. As shown in Figure 3(a), a significant heterogeneity (random-effect model) existed with $I^2 = 97.8\%$ and $p = 0.001$. Meta-analysis result shows that the level of serum ADP was higher in patients with microalbuminuria than those with normoalbuminuria (MD = 2.35 , 95% CI [$1.68, 3.02$]). A subgroup analysis was also conducted here to find the potential sources of heterogeneity, and we found that the heterogeneity still existed in all the subgroups (Figure 3(b), sample size and nation). However, the combined effect changed in the large sample size subgroup (MD = 1.23 , 95% CI [$0.17, 2.64$]) and the subgroup of trials that were not conducted in China (MD = 0.69 , 95% CI [$-3.07, 1.74$]). As shown in Figure 3(c), the funnel plot appeared asymmetrical, and Begg's test result showed that there was a significant publication bias ($p = 0.001$).

3.2.3. Macroalbuminuria versus Microalbuminuria. Similar results as *microalbuminuria versus normoalbuminuria* were



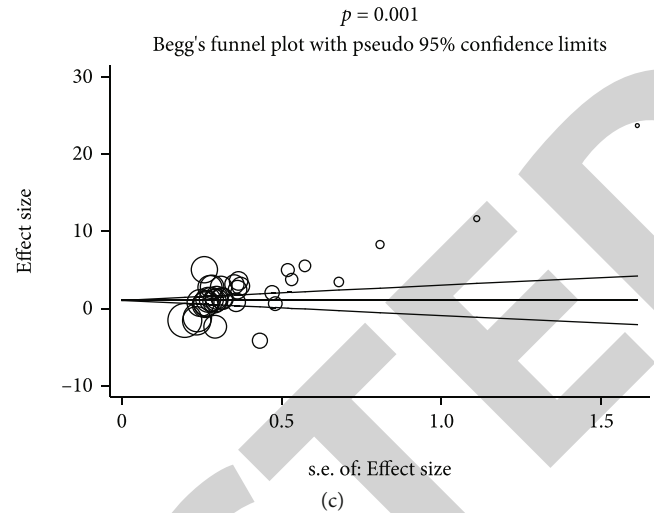
NOTE: Weights are from random-effects model

(a)

FIGURE 4: Continued.

Subgroup	I^2	p	Mean difference (95% CI)
<i>Sample size</i>			
> 100	99.2%	0.001	5.00 (2.63, 7.36)
< 100	96.8%	0.001	1.70 (0.98, 2.42)
<i>China</i>			
Yes	98.1%	0.001	2.80 (1.92, 3.68)
No	94.9%	0.001	0.33 (-0.80, 1.46)

(b)



s.e. of: Effect size

(c)

FIGURE 4: Meta-analysis of the relationship between serum adiponectin and type 2 diabetic kidney disease (macroalbuminuria vs. microalbuminuria): (a) mean difference of serum adiponectin level; (b) subgroup analysis; (c) publication bias.

found in this part. All the 34 trials were included in this meta-analysis, 1125 patients diagnosed as T2DM with macroalbuminuria and 1337 with microalbuminuria. As shown in Figure 4(a), a significant heterogeneity (random-effect model) existed here with I^2 and p values of 98.0% and 0.001, respectively. In addition, the serum ADP level in patients with macroalbuminuria was higher than those with microalbuminuria (MD = 2.36, 95% CI [1.58, 3.14]). Subgroup analyses on sample size and nation did not eliminate the heterogeneity. However, the combined effect changed in the subgroup of trials that were conducted out of China (Figure 4(b), MD = 0.33, 95% CI [-0.80, 1.46]). Besides, the funnel plot of this meta-analysis appeared asymmetrical (Figure 4(c)), and Begg's test result showed that there was a significant publication bias ($p = 0.001$).

3.2.4. Sensitivity Analysis. Since we found significant publication bias in the above studies (*microalbuminuria* versus *normoalbuminuria* and *macroalbuminuria* versus *microalbuminuria*), a sensitivity analysis was conducted by excluding one study at a time and recalculating the summary effects. As shown in Table 2, there is no obvious deviation or even reversal in the results obtained. The above data indicates that though significant heterogeneity existed in the study, the results are quite robust.

4. Discussion

T2DM accounts for more than 90% of all the DM patients worldwide. The complications of T2DM nearly affect all the body tissues, including kidney. It is worth noting that DKD is the most common complication of T2DM. Early diagnosis of DKD allows slow disease progression and relatively high life expectancy. Biomarkers provide the possibility for early diagnosis of DKD. ADP is a small collagen-like protein which has functions of anti-inflammation and insulin-sensitizing. Studies have shown that ADP may play a role in DKD; however, the relationship between them

remains unclear and variable. Noel et al. [52] conducted a meta-analysis on this subject, and they had similar results as ours. They found that there is no significant difference in ADP levels between healthy people and DM patients with microalbuminuria. Besides, ADP levels were positively correlated with the severity of DKD. However, the amount of included studies was limited. Totally, 13 trials were included in their study, and only 6 of them were related to T2DM. In addition, Wang et al. [53] also performed a meta-analysis about this issue, and their findings were published in Chinese. In their study, 38 studies were included (both T1DM and T2DM) and all of them were conducted in China. Their results also reached a consensus that ADP levels were positively correlated with DKD severity. However, they pointed out the difference in ADP levels between healthy people and DM patients with normoalbuminuria which was not figured out in our study. Their results indicated that the concentration of serum ADP was higher in healthy people than normoalbuminuria DM patients (MD = -1.03, 95% CI [-1.76, -0.30]). The above reasons compelled us to conduct this meta-analysis.

In total, 34 trials with 5254 T2DM patients were included in this meta-analysis. The results of this study show that there was no significant difference in serum ADP level between normoalbuminuria and the control group (MD = -0.42, 95% CI [-1.23, 0.40]), while serum ADP level was positively correlated with the severity of T2DKD. The serum ADP level in T2DKD patients ranks as macroalbuminuria > microalbuminuria > normoalbuminuria.

The following are the limitations of this meta-analysis that should not be ignored. Most of the included studies were extracted from Chinese literature databases and were all published in Chinese. Though the other 6 literature were published in English, 5 of them were conducted in Japan, and thus, the quality of these trials remains doubtful. Besides, high heterogeneity and publication bias also brought limitation to the reliability of this meta-

TABLE 2: Sensitivity analysis.

Excluded study	Normoalbuminuria vs. control			Microalbuminuria vs. normoalbuminuria			Macroalbuminuria vs. microalbuminuria		
	I^2	p	Mean difference (95% CI)	I^2	p	Mean difference (95% CI)	I^2	p	Mean difference (95% CI)
Sun [18]	98.5%	0.001	-0.37 (-1.22, 0.47)	97.3%	0.001	2.50 (1.87, 3.12)	97.9%	0.001	2.50 (1.73, 3.27)
Bai [19]	98.5%	0.001	-0.46 (-1.30, 0.39)	97.9%	0.001	2.38 (1.68, 3.08)	98.0%	0.001	2.32 (1.54, 3.11)
Cheng [20]	98.5%	0.001	-0.46 (-1.30, 0.37)	97.9%	0.001	2.40 (1.71, 3.09)	98.1%	0.001	2.40 (1.60, 3.20)
Xu [21]	98.5%	0.001	-0.38 (-1.22, 0.46)	97.9%	0.001	2.37 (1.68, 3.06)	98.1%	0.001	2.41 (1.61, 3.22)
Tian [22]	98.5%	0.001	-0.36 (-1.19, 0.47)	97.8%	0.001	2.21 (1.55, 2.88)	98.0%	0.001	2.26 (1.48, 3.04)
Bi [23]	98.4%	0.001	-0.35 (-1.20, 0.49)	97.5%	0.001	2.25 (1.61, 2.89)	97.8%	0.001	2.26 (1.51, 3.01)
Zhou [24]	98.4%	0.001	-0.33 (-1.15, 0.50)	97.9%	0.001	2.39 (1.70, 3.09)	98.1%	0.001	2.40 (1.60, 3.21)
Lu [25]	98.5%	0.001	-0.40 (-1.26, 0.46)	97.5%	0.001	2.47 (1.81, 3.12)	97.8%	0.001	2.48 (1.70, 3.25)
Nie [26]	98.5%	0.001	-0.36 (-1.20, 0.47)	97.8%	0.001	2.31 (1.63, 2.99)	98.1%	0.001	2.42 (1.61, 3.23)
Lin [27]	98.3%	0.001	-0.59 (-1.38, 0.21)	97.8%	0.001	2.33 (1.65, 3.01)	98.0%	0.001	2.35 (1.55, 3.15)
Tang [28]	98.5%	0.001	-0.36 (-1.20, 0.47)	97.8%	0.001	2.23 (1.57, 2.90)	98.0%	0.001	2.28 (1.50, 3.06)
Zhou [29]	98.4%	0.001	-0.27 (-1.09, 0.55)	97.9%	0.001	2.40 (1.71, 3.09)	98.1%	0.001	2.35 (1.55, 3.14)
Hu [30]	98.5%	0.001	-0.37 (-1.21, 0.46)	97.9%	0.001	2.36 (1.67, 3.04)	98.1%	0.001	2.40 (1.60, 3.20)
Wan [31]	98.5%	0.001	-0.38 (-1.21, 0.46)	97.9%	0.001	2.37 (1.68, 3.06)	98.1%	0.001	2.43 (1.62, 3.23)
Xie [32]	98.5%	0.001	-0.46 (-1.30, 0.38)	97.8%	0.001	2.27 (1.60, 2.94)	98.1%	0.001	2.35 (1.56, 3.15)
Li [33]	98.3%	0.001	-0.62 (-1.40, 0.17)	97.8%	0.001	2.34 (1.65, 3.02)	98.0%	0.001	2.36 (1.56, 3.15)
Zhou [34]	98.5%	0.001	-0.34 (-1.17, 0.49)	97.9%	0.001	2.39 (1.70, 3.09)	98.1%	0.001	2.41 (1.60, 3.21)
Zhong [35]	98.5%	0.001	-0.45 (-1.29, 0.40)	97.9%	0.001	2.39 (1.70, 3.08)	98.1%	0.001	2.42 (1.62, 3.23)
Yang [36]	98.4%	0.001	-0.52 (-1.34, 0.29)	97.8%	0.001	2.34 (1.65, 3.02)	97.9%	0.001	2.55 (1.78, 3.31)
Wan [37]	98.5%	0.001	-0.32 (-1.15, 0.50)	97.8%	0.001	2.31 (1.63, 2.99)	98.1%	0.001	2.41 (1.60, 3.22)
Lin [38]	98.5%	0.001	-0.37 (-1.20, 0.47)	97.9%	0.001	2.36 (1.68, 3.05)	98.1%	0.001	2.41 (1.60, 3.21)
Wu [39]	98.4%	0.001	-0.55 (-1.35, 0.26)	97.9%	0.001	2.39 (1.70, 3.09)	98.1%	0.001	2.34 (1.55, 3.13)
Cheng [40]	98.4%	0.001	-0.69 (-1.49, 0.12)	97.8%	0.001	2.17 (1.50, 2.83)	98.0%	0.001	2.19 (1.42, 2.96)
Yang [41]	98.4%	0.001	-0.19 (-1.00, 0.62)	97.8%	0.001	2.29 (1.61, 2.97)	98.1%	0.001	2.32 (1.53, 3.11)
Liu [42]	98.4%	0.001	-0.69 (-1.49, 0.12)	97.8%	0.001	2.20 (1.54, 2.87)	98.0%	0.001	2.12 (1.35, 2.89)
Yang [43]	98.5%	0.001	-0.47 (-1.30, 0.36)	97.9%	0.001	2.42 (1.73, 3.11)	98.1%	0.001	2.36 (1.57, 3.16)
Zhu [44]	98.5%	0.001	-0.39 (-1.24, 0.46)	97.9%	0.001	2.42 (1.72, 3.12)	97.8%	0.001	1.91 (1.17, 2.65)
Xiao [45]	98.4%	0.001	-0.25 (-1.06, 0.56)	97.9%	0.001	2.32 (1.64, 3.00)	98.1%	0.001	2.37 (1.58, 3.17)
Kato [46]	98.4%	0.001	-0.49 (-1.32, 0.33)	97.9%	0.001	2.33 (1.65, 3.02)	98.1%	0.001	2.33 (1.54, 3.12)
Yilmaz [47]	N/A	N/A	N/A	97.9%	0.001	2.47 (1.81, 3.14)	98.0%	0.001	2.47 (1.68, 3.26)
Saito [48]	98.4%	0.001	-0.33 (-1.15, 0.50)	97.9%	0.001	2.40 (1.68, 3.11)	97.9%	0.001	2.48 (1.70, 3.26)
Fujita [49]	98.5%	0.001	-0.39 (-1.22, 0.45)	97.9%	0.001	2.42 (1.73, 3.11)	98.1%	0.001	2.42 (1.62, 3.22)
Komaba [50]	N/A	N/A	N/A	97.9%	0.001	2.41 (1.71, 3.12)	98.1%	0.001	2.43 (1.62, 3.24)
Koshimura [51]	N/A	N/A	N/A	97.9%	0.001	2.41 (1.72, 3.09)	98.1%	0.001	2.42 (1.62, 3.21)

Random-effect model used; N/A: not applicable.

analysis. Fortunately, the sensitivity analysis indicated the robustness of our results. Based on the above reasons, more high-quality trials conducted and published in other countries are recommended in further evaluation.

5. Conclusions

In summary, our meta-analysis indicated that serum ADP levels were positively correlated with the severity of T2DKD. Therefore, serum ADP level might be an important

marker to predict the progression of T2DKD. However, although quite a lot studies were included in this meta-analysis, heterogeneity and publication bias still existed, which affected the reliability of the results. Thus, more high-quality trials are recommended in further assessment.

Data Availability

The labeled dataset used to support the findings of this study is available from the corresponding author upon request.

Conflicts of Interest

The authors declare that they have no conflict of interest.

Authors' Contributions

Li Li designed the study; Li Li, Guoliang Wu, and Jilai Shi conducted the literature searching and screening; Guoliang Wu and Li Li did the data analysis; and Li Li wrote the manuscript. All authors contributed to this work and reviewed the final version of the manuscript.

Acknowledgments

This work was supported by the clinical medical science and technology innovation program funded by the Jinan Science and Technology Bureau (No. 202019104).

References

- [1] American Diabetes Association, "Classification and diagnosis of diabetes," *Diabetes Care*, vol. 38, pp. S8–S16, 2015.
- [2] X. X. Zhang, J. Kong, and K. Yun, "Prevalence of diabetic nephropathy among patients with type 2 diabetes mellitus in China: a meta-analysis of observational studies," *Journal Diabetes Research*, vol. 2020, article 2315607, 11 pages, 2020.
- [3] A. M. Schmidt, "Highlighting diabetes mellitus: the epidemic continues," *Arteriosclerosis, Thrombosis, and Vascular Biology*, vol. 38, no. 1, pp. e1–e8, 2018.
- [4] N. Lascar, J. Brown, H. Pattison, A. H. Barnett, C. J. Bailey, and S. Bellary, "Type 2 diabetes in adolescents and young adults," *The Lancet Diabetes and Endocrinology*, vol. 6, no. 1, pp. 69–80, 2018.
- [5] A. N. Long and S. Dagogo-Jack, "Comorbidities of diabetes and hypertension: mechanisms and approach to target organ protection," *Journal of Clinical Hypertension (Greenwich, Conn.)*, vol. 13, no. 4, pp. 244–251, 2011.
- [6] R. Z. Alicic, M. T. Rooney, and K. R. Tuttle, "Diabetic kidney disease," *Clinical Journal of the American Society of Nephrology*, vol. 12, no. 12, pp. 2032–2045, 2017.
- [7] U. Maggiore, K. Budde, U. Heemann et al., "Long-term risks of kidney living donation: review and position paper by the ERA-EDTA DESCARTES working group," *Nephrology, Dialysis, Transplantation*, vol. 32, no. 2, pp. 216–223, 2017.
- [8] S. Bermejo, J. Pascual, and M. J. Soler, "The large spectrum of renal disease in diabetic patients," *Clinical Kidney Journal*, vol. 10, no. 2, pp. 255–256, 2017.
- [9] R. Liu, G. Li, X. F. Cui et al., "Methodological evaluation and comparison of five urinary albumin measurements," *Journal of Clinical Laboratory Analysis*, vol. 25, no. 5, pp. 324–329, 2011.
- [10] B. Jim, J. Santos, F. Spath, and J. Cijiang He, "Biomarkers of diabetic nephropathy, the present and the future," *Current Diabetes Reviews*, vol. 8, no. 5, pp. 317–328, 2012.
- [11] S. J. Thornton, J. Sullivan, and E. van Eijndhoven, "Lifetime benefits of early detection and treatment of diabetic kidney disease," *PLoS One*, vol. 14, no. 5, article e217487, 2019.
- [12] S. Thipsawat, "Early detection of diabetic nephropathy in patient with type 2 diabetes mellitus: a review of the literature," *Diabetes & Vascular Disease Research*, vol. 18, no. 6, article 147916412110588, 2021.
- [13] D. Zha, X. Wu, and P. Gao, "Adiponectin and its receptors in diabetic kidney disease: molecular mechanisms and clinical potential," *Endocrinology*, vol. 158, no. 7, pp. 2022–2034, 2017.
- [14] K. Maeda, K. Okubo, I. Shimomura, T. Funahashi, Y. Matsuzawa, and K. Matsubara, "Reprint of cDNA cloning and expression of a novel adipose specific collagen-like factor, apM1 (diseost abundant gene transcript 1)," *Biochemical and Biophysical Research Communications*, vol. 425, no. 3, pp. 556–559, 2012.
- [15] D. R. Gable, S. J. Hurel, and S. E. Humphries, "Adiponectin and its gene variants as risk factors for insulin resistance, the metabolic syndrome and cardiovascular disease," *Atherosclerosis*, vol. 188, no. 2, pp. 231–244, 2006.
- [16] P. Bjornstad, L. Pyle, G. Kinney et al., "Adiponectin is associated with early diabetic kidney disease in adults with type 1 diabetes: a coronary artery calcification in type 1 diabetes (CACTI) study," *Journal of Diabetes and its Complications*, vol. 31, no. 2, pp. 369–374, 2017.
- [17] C. Menzaghi, V. Trischitta, and A. Doria, "Genetic influences of adiponectin on insulin resistance, type 2 diabetes, and cardiovascular disease," *Diabetes*, vol. 56, no. 5, pp. 1198–1209, 2007.
- [18] K. Sun, "Application value of combined detection of FGF21, APN, VEGF and RBP in early diagnosis of type 2 diabetic nephropathy," *Chinese Practical Medicine*, vol. 16, no. 30, pp. 44–46, 2021.
- [19] J. Bai, J. F. Liu, and W. Bai, "Changes in serum, peptide and adiponectin levels and their correlation with renal arterial blood flow resistance index in patients with diabetic nephropathy," *International Journal of Laboratory Medicine*, vol. 40, no. 12, pp. 1467–1470, 2019.
- [20] C. S. Cheng and G. Li, "Expression and clinical significance of adiponectin and soluble vascular cell adhesion molecule-1 in patients with different stages of diabetic nephropathy," *Jilin Medical*, vol. 38, no. 12, pp. 2274–2275, 2017.
- [21] Y. Q. Xu and Y. F. Sun, "Application of hepatic fatty acid binding protein and adiponectin in early diagnosis and severity assessment of type 2 diabetic nephropathy," *Guangdong Medical*, vol. 37, no. 9, pp. 1344–1346, 2016.
- [22] J. Tian, "Changes in adiponectin and c-reactive protein levels in patients with type 2 diabetic nephropathy and their clinical significance," *New World of Diabetes*, vol. 19, no. 1, pp. 65–67, 2016.
- [23] J. Bi, "Study on the role of serum adiponectin, adiponectin and C-reactive protein in the development of type 2 diabetic nephropathy," *Labeled Immunoassay and Clinical*, vol. 23, no. 7, pp. 770–772, 2016.
- [24] R. J. Zhou, X. Li, and W. Zhang, "Analysis of serum adiponectin level and its influencing factors in patients with type 2 diabetic nephropathy at different stages," *Chinese Practical Medicine*, vol. 10, no. 25, pp. 42–43, 2015.
- [25] X. L. Lu, "Correlation between serum adiponectin and vascular endothelial growth factor levels and oxidative stress in diabetic nephropathy," *Chinese Journal of Practical Diagnosis and Therapy*, vol. 27, no. 2, pp. 147–149, 2013.
- [26] C. H. Nie, "Correlation between serum cystatin C and adiponectin levels and diabetic nephropathy," *Laboratory Medicine and Clinical Practice*, vol. 9, no. 17, pp. 2149–2150, 2012.
- [27] X. Y. Lin, "Clinical significance of serum adiponectin detection in patients with type 2 diabetic nephropathy," *Inner Mongolia Traditional Chinese Medicine*, vol. 30, no. 3, pp. 107–108, 2011.
- [28] L. Tang, C. L. Chen, and G. L. Su, "Clinical significance of serum interleukin-18 and adiponectin detection in patients

Retraction

Retracted: Research on the Effect of Nursing Methods for Gestational Diabetes Mellitus Based on Comprehensive Nursing Intervention

Computational and Mathematical Methods in Medicine

Received 26 September 2023; Accepted 26 September 2023; Published 27 September 2023

Copyright © 2023 Computational and Mathematical Methods in Medicine. This is an open access article distributed under the Creative Commons Attribution License, which permits unrestricted use, distribution, and reproduction in any medium, provided the original work is properly cited.

This article has been retracted by Hindawi following an investigation undertaken by the publisher [1]. This investigation has uncovered evidence of one or more of the following indicators of systematic manipulation of the publication process:

- (1) Discrepancies in scope
- (2) Discrepancies in the description of the research reported
- (3) Discrepancies between the availability of data and the research described
- (4) Inappropriate citations
- (5) Incoherent, meaningless and/or irrelevant content included in the article
- (6) Peer-review manipulation

The presence of these indicators undermines our confidence in the integrity of the article's content and we cannot, therefore, vouch for its reliability. Please note that this notice is intended solely to alert readers that the content of this article is unreliable. We have not investigated whether authors were aware of or involved in the systematic manipulation of the publication process.

In addition, our investigation has also shown that one or more of the following human-subject reporting requirements has not been met in this article: ethical approval by an Institutional Review Board (IRB) committee or equivalent, patient/participant consent to participate, and/or agreement to publish patient/participant details (where relevant).

Wiley and Hindawi regrets that the usual quality checks did not identify these issues before publication and have since put additional measures in place to safeguard research integrity.

We wish to credit our own Research Integrity and Research Publishing teams and anonymous and named external researchers and research integrity experts for contributing to this investigation.

The corresponding author, as the representative of all authors, has been given the opportunity to register their agreement or disagreement to this retraction. We have kept a record of any response received.

References

- [1] X. Ren, J. Jin, Y. Chen, and J. Jin, "Research on the Effect of Nursing Methods for Gestational Diabetes Mellitus Based on Comprehensive Nursing Intervention," *Computational and Mathematical Methods in Medicine*, vol. 2022, Article ID 2396658, 10 pages, 2022.

Research Article

Research on the Effect of Nursing Methods for Gestational Diabetes Mellitus Based on Comprehensive Nursing Intervention

Xueqiong Ren , Jianing Jin, Yaer Chen, and Jing Jin

The Affiliated Hospital of Medical School of Ningbo University, Ningbo 315020, China

Correspondence should be addressed to Xueqiong Ren; rxq761231@163.com

Received 6 May 2022; Revised 30 May 2022; Accepted 2 June 2022; Published 14 July 2022

Academic Editor: Pan Zheng

Copyright © 2022 Xueqiong Ren et al. This is an open access article distributed under the Creative Commons Attribution License, which permits unrestricted use, distribution, and reproduction in any medium, provided the original work is properly cited.

In order to explore the effective way of gestational diabetes care, this paper applies comprehensive nursing to gestational diabetes care. In terms of nursing intervention for pregnant women with gestational diabetes mellitus, combining the phased changes of pregnant women's physiological and psychological needs during pregnancy, this paper comprehensively implements health education, diet intervention, exercise intervention, pregnancy monitoring, psychological intervention, infection prevention, and perinatal monitoring and other nursing interventions in a selective and focused manner. This makes the intervention measures at each stage focused, intersecting, interpenetrating, and continuing to play a role, which can effectively improve the implementation effect of the intervention measures and better promote the effective improvement of pregnancy outcomes. In addition, this paper studies the effect of gestational diabetes care based on comprehensive nursing intervention through a controlled trial, and the study verifies that comprehensive nursing has a good effect in gestational diabetes care.

1. Introduction

At present, more and more studies have begun to find that if gestational diabetes patients receive correct and timely intervention during pregnancy, the prognosis of mother and baby can be significantly improved, and the incidence of complications can be significantly reduced. Moreover, a large number of studies have proved that actively cooperating with treatment is easier to control blood sugar within a satisfactory range, and effective diet and blood sugar intervention measures are the key to the treatment of gestational diabetes mellitus and the reduction of maternal and infant complications [1]. At the same time, if gestational diabetes patients are given early health education, guidance on diet, exercise, self-glucose monitoring, and insulin treatment to improve pregnant women's awareness of the disease, it can encourage patients to actively cooperate with treatment and significantly improve pregnancy outcomes. Gestational diabetes is more harmful to pregnant women and perinatal infants and will seriously affect the life safety of pregnant women and perinatal infants. In addition, the prepregnancy weight of pregnant women and the increase of weight during preg-

nancy have a great relationship with the occurrence of gestational diabetes mellitus. If the disease is not treated in time, it can lead to adverse pregnancy outcomes [2]. Therefore, early intervention and scientific management of gestational diabetes mellitus can reduce the perinatal morbidity. The main effects of the disease on the perinatal period include gestational hypertension, infection, polyhydramnios, macrosomia, fetal dysplasia, stillbirth, neonatal hypoglycemia, and neonatal respiratory distress syndrome. In addition, a number of studies have shown [3] that if gestational diabetes mellitus patients are diagnosed and treated promptly and correctly during pregnancy, the prognosis of mother and baby will be significantly improved, and the incidence of serious complications can be significantly reduced. Literature [4] has shown that timely and effective intervention and treatment for pregnant women with gestational diabetes can reduce the incidence of maternal and infant complications. Moreover, it is of great significance for improving the systematic management of pregnant and lying-in women, improving the quality of obstetric prevention and treatment, and reducing the "three rates," namely, maternal mortality, perinatal mortality, and birth rate of sick and

disabled children. Early intervention in pregnant women with gestational diabetes mellitus to control blood sugar within a satisfactory range is the key to improving pregnancy outcomes. Literature [5] also showed that the probability of early and midterm nursing intervention to control blood sugar at normal levels was 86.8% and 84.1%, respectively, and that of late intervention was 42.1%. It can be seen that the treatment of gestational diabetes should be detected and treated early in order to minimize the adverse effects on pregnant women, fetuses, and newborns.

With the increasing awareness of gestational diabetes, pregnant women generally attach great importance to the changes in their bodies during pregnancy, which lays a good foundation for strengthening nursing interventions during pregnancy. How to control and manage the amniotic fluid index, body weight, blood sugar, and other indicators during pregnancy is of great significance to ensure the health of mothers and babies. Some studies believe that after gestational diabetes is diagnosed, timely health education interventions will lay the foundation for the implementation of other interventions in the later stages of pregnant women with gestational diabetes [6]. Health education during pregnancy can help pregnant women and their families understand the dangers of gestational diabetes to maternal and child health, understand the common symptoms and treatment methods of gestational diabetes, and actively cooperate with various inspections, which are helpful for early detection and active cooperation. Studies have shown that the needs of gestational diabetes patients and their families for health education are urgent and multifaceted [7]. By explaining the impact of gestational diabetes on pregnant women, fetuses and newborns in simple terms, pregnant women, and their families should pay more attention to this disease. Related research believes that for gestational diabetes, health education is more important than drug treatment [8]. Research results show that implementing health education can help pregnant women with gestational diabetes to better cooperate with treatment, effectively control blood sugar, and improve pregnancy outcomes, thereby ensuring maternal and child health [9].

Health education intervention can effectively improve the diet, exercise, and personal hygiene habits of pregnant women with gestational diabetes mellitus, improve the compliance of pregnant women with gestational diabetes mellitus [10], and significantly improve pregnancy outcomes. Dietary intervention is the foundation and the most important factor in the treatment of gestational diabetes. Through dietary intervention, indicators such as weight gain during pregnancy and delivery weight can be effectively managed and controlled, thereby effectively improving pregnancy outcomes. At the same time, because dietary intervention is greatly affected by factors such as the pregnant woman herself and her family's living habits, the intervention process has many troublesome factors, and it is difficult to implement. Therefore, the simultaneous use of dietary intervention and health education and other interventions has a greater impact on improving pregnancy outcomes for a significant effect [11]. Dietary and nutritional care for gestational diabetes patients is very important. Through

reasonable dietary intervention, it is beneficial to maintain the blood sugar level in a reasonable range. Dietary intervention is very necessary and very important for pregnant women with gestational diabetes mellitus. However, when implementing dietary intervention for pregnant women with gestational diabetes mellitus, the daily calorie intake should be reasonably determined based on the specific situation of each pregnant woman, while ensuring the effective supply of nutrients and heat energy for the healthy growth and development of pregnant women and their fetuses, avoiding starvation ketone bodies and postprandial hyperglycemia to occur [12]. Therefore, dietary nursing intervention plays an important role in the comprehensive nursing intervention for pregnant women with gestational diabetes mellitus. At the same time, some researchers believe that reasonable diet plus exercise therapy is the first choice for the treatment of gestational diabetes mellitus. About 75%-80% of pregnant women with gestational diabetes mellitus can adjust their blood sugar levels through lifestyle adjustments such as diet and exercise ideal range [13]. The results of the literature [14] show that nursing interventions have a positive impact on the prognosis of gestational diabetes mellitus, and its intervention effect is not inferior to the simple endocrinologist's treatment. The study of literature [15] showed that after implementing diet and exercise nursing intervention, the incidence of maternal and infant complications in the nursing intervention group was significantly lower than that in the control group in 100 pregnant women with gestational diabetes mellitus in the intervention group compared with the control group. Pregnant women with gestational diabetes have many influences and constraints during pregnancy, so a single nursing intervention is easily interfered by other factors, thus affecting the intervention effect. Judging from the current domestic and foreign research, for pregnant women with gestational diabetes mellitus, comprehensive and systematic intervention measures are more likely to produce synergistic effects and then play the best intervention effect [16].

With the rapid development of economy and society and the continuous improvement of medical level, people's attention to health and material level has also increased rapidly [17]. Pregnant women with gestational diabetes and their families pay more and more attention to the quality of pregnant women during pregnancy, and health education plays an important role in hospital management. It has been fully implemented, and dietary intervention has become a commonly accepted nursing intervention for most pregnant women, and exercise therapy is more likely to be adopted by pregnant women [18]. Nursing interventions such as psychological intervention, monitoring during pregnancy, and infection prevention are gradually being effectively applied in most studies [19]. The effect of exercise therapy for gestational diabetes patients cannot be ignored. Pregnant women with gestational diabetes maintain proper exercise, which is not only beneficial to the health of mothers and babies, but also to better control of blood sugar levels, because the exercise of but also help to improve the sensitivity of insulin and gender receptor binding [20]. Improving glucose tolerance and reducing insulin requirements in

patients with gestational diabetes can be achieved through appropriate exercise. Studies have shown that exercise has a positive effect on enhancing the sensitivity of peripheral tissues to insulin, improving the uptake and utilization of glucose by muscle cells, and eliminating insulin resistance. Upper extremity exercise intervention can help improve the pregnancy outcomes of pregnant women with high risk factors for diabetes [21]. Safe and effective exercise can help rationally control the blood sugar level of pregnant women with gestational diabetes. However, the specific exercise method and single exercise time need to be combined. Each pregnant woman's own conditions are specifically determined.

Prevention is the main strategy for disease control. The realization of early prevention and control of GDM will effectively delay or avoid the occurrence of GDM, improve maternal and infant outcomes, and reduce social burden. In the research on GDM intervention, both foreign and domestic, most of them implement comprehensive nursing measures such as health education, diet, and exercise intervention, mainly through knowledge lectures, outpatient consultation, telephone follow-up, etc. After a period of follow-up, the intervention of the effect is analyzed. Most of these studies focus on groups with GDM, lack of early intervention for high-risk groups of GDM, and the intervention measures are mostly formed on the basis of previous summary, and the measures lack evidence-based support. Effective intervention needs to be based on the corresponding theory. The previous research lacks an effective theoretical basis for the discussion of why the intervention, why the individual changes, how the intervention can improve the individual's cognition, and how to ensure the compliance and continuity of the intervention.

Pregnancy is a special physiological stage for women. Patients with gestational diabetes will have a series of physiological pressures and pathogenic anxiety. If diabetes during pregnancy is not paid enough attention or treated in time, it will often bring adverse consequences to mothers and babies. To establish a harmonious and effective relative network, family members must create a good family atmosphere, be good at understanding the psychological activities of patients, patiently listen to the requirements or questions raised by patients, and provide targeted explanations and guidance, so that patients can get the system of family, friends, and medical staff. Support and timely eliminate the doubts in the heart, so as to relieve the negative emotions such as tension and fear to achieve the purpose of reducing clinical medication.

In order to improve the nursing effect of gestational diabetes mellitus, this paper applies comprehensive nursing to gestational diabetes mellitus nursing, explores the effect of comprehensive nursing, and effectively improves the nursing effect of gestational diabetes mellitus.

2. Materials and Methods

In this study, patients diagnosed with gestational diabetes mellitus by glucose screening in the outpatient department of obstetrics and gynecology of the hospital were selected

as samples. The appropriate pregnant women who voluntarily received comprehensive nursing intervention were selected as the experimental group. The remaining gestational diabetes patients who did not receive comprehensive nursing intervention or were unwilling to receive comprehensive nursing intervention served as the control group. The relevant study design was approved by the ethics committee. Inclusion criteria are as follows: control group: pregnant women with gestational diabetes mellitus who were diagnosed with gestational diabetes mellitus in the obstetrics and gynecology outpatient clinic of the hospital according to gestational age and parity and were hospitalized in the obstetrics and gynecology department. Moreover, they did not receive or were reluctant to undertake comprehensive nursing interventions. Experimental group: the research subjects were pregnant women who underwent glucose screening in the outpatient department of obstetrics and gynecology of the hospital for less than 28 weeks of gestation and were diagnosed with gestational diabetes mellitus. Before this pregnancy, there was no threatened miscarriage, threatened premature birth, heart disease, hypertension, placenta previa, intrauterine growth retardation, etc. Those with education level above junior high school voluntarily accept comprehensive nursing intervention. The diagnostic criteria of the two groups of pregnant women were in line with the diagnostic criteria of gestational diabetes mellitus in the seventh edition of the *Obstetrics and Gynecology Textbook of the People's Medical Publishing House*. Exclusion criteria are as follows: pregnant women with gestational diabetes mellitus who failed to complete comprehensive nursing interventions such as health education, diet intervention, exercise intervention, and perinatal monitoring.

Comprehensive nursing intervention measures were taken for pregnant women with gestational diabetes mellitus included in the experimental group, and the implementation of intervention measures was divided into three stages. The first stage is when the gestational age is less than 28 weeks, and the experiment focused on health education, supplemented by diet control and exercise intervention. The second stage is from 28 to 36 gestational weeks. The experiment focused on diet intervention, exercise intervention, pregnancy care and self-monitoring, and health education and psychological counseling for pregnant women. The third stage is from 36 gestational weeks to postpartum. While focusing on psychological intervention, infection prevention, and perinatal monitoring, the experiment continued to carry out health education, dietary control, and maternal blood glucose monitoring. The intervention measures in the above three stages are focused on, intersect, penetrate each other, and continue to play a role in different stages. During the nursing intervention process, the pregnant women should be followed up every two weeks for dietary intervention, exercise intervention, nursing during pregnancy, self-monitoring, and blood sugar control. At the same time, it is necessary to communicate and solve new problems with pregnant women in a timely manner, so as to improve the compliance of pregnant women with nursing intervention, in order to achieve the best nursing intervention effect. Blood sugar control standard is as

follows: fasting blood sugar less than 5.3 mmol/L, 2 hours postprandial blood sugar less than 6.7 mmol/L. Pregnant women and newborns with gestational diabetes mellitus included in the control group were treated with traditional nursing methods. By comparing the differences in maternal and infant outcomes between the experimental group and the control group, the effect of comprehensive nursing intervention on the pregnancy outcomes of the most gestational diabetes mellitus was systematically reviewed.

During pregnancy, pregnant women with gestational diabetes are prone to a series of special changes in physiology and psychology due to lack of effective understanding of pregnancy and fear of gestational diabetes, resulting in elevated blood sugar, which threatens and affects the health of mothers and babies. Therefore, timely health education intervention can enable pregnant women to have a comprehensive understanding of pregnancy and diabetes and improve the compliance of pregnant women and their families with dietary intervention and exercise intervention. Furthermore, it helps to adjust and improve the pregnancy environment of pregnant women with gestational diabetes mellitus and helps to promote good outcomes for mothers and infants. In the early stage of health education intervention in this study, a professional gestational diabetes health education group was established, which consisted of senior obstetrics and gynecology experts, obstetric nurses, endocrinology experts, and nutritionists. For the gestational diabetes patients and their families in the experimental group, we formulated a targeted health education intervention plan based on the actual situation of each pregnant woman. In addition, the experiment carried out publicity and education on gestational diabetes related knowledge through multimedia teaching, mobile phone text messages, establishment of WeChat groups, health education video clips, and bedside one-on-one. At the same time, we introduced knowledge about gestational diabetes to patients, so that they can understand that appropriate scientific intervention can greatly improve adverse pregnancy outcomes, so as to ensure good compliance among educated people. In addition, we guided pregnant women to understand the disease comprehensively, objectively, and correctly, improve the negative emotions of pregnant women with gestational diabetes mellitus, maintain a good and stable psychological state, and promote smooth and healthy childbirth. In addition, we organize and carry out collective psychological counseling, give full play to the role of collective education, and organize pregnant women in the experimental group to participate in weekly knowledge counseling and expert lectures for gestational diabetes patients. Further, we try to guide the group to create a good atmosphere and psychological orientation of optimism and face up to reality, to encourage them to support and encourage each other, and to ensure that the interventions of diet and exercise are put into place. According to the specific conditions of each pregnant woman in the experimental group, such as blood sugar level and body mass index, a personalized dietary intervention plan was reasonably determined to ensure the effective supply of nutrients needed by pregnant women during pregnancy and healthy growth and development of the fetus. We educated pregnant

women with gestational diabetes mellitus in the experimental group to combine their own physical conditions with appropriate exercise. At the same time, we educated them to pay close attention to their own feelings, scientifically grasp the time and intensity of each exercise, ensure that the exercise is safe, effective, and reasonable, and avoid exercising on an empty stomach as much as possible. Moreover, we instructed pregnant women with gestational diabetes mellitus in the experimental group to master their own methods of checking blood sugar and make records. In addition, we educate and guide pregnant women with gestational diabetes mellitus, adhere to regular weight measurement, master weight changes, adhere to regular daily blood pressure measurement, observe blood pressure fluctuations, and make relevant records carefully. After the gestational age reached 28 weeks, we taught the pregnant women in the experimental group how to count fetal movements and record them. If there is a decrease in fetal movement, the number of fetal movements per hour is less than 4 times, or the fetal movement is too frequent, and the number of fetal movements per 12 hours exceeds 40 times; the pregnant woman should go to the hospital for examination and treatment in time accompanied by her family to effectively rule out intrauterine distress. In addition, we instructed the pregnant women in the experimental group to develop good hygiene habits, pay attention to indoor hygiene, change and wash intimate clothing every day, especially pay attention to strengthening personal oral hygiene, and pay attention to maintaining perineal hygiene to effectively enhance their own resistance. If pregnant women find symptoms of infection during pregnancy, they should contact the competent doctor in time and take effective treatment measures in time, so that the symptoms of infection can be effectively controlled in time to avoid the expansion of infection.

In the second and later stages of pregnancy, through the intervention of health education in the previous stage, pregnant women have a certain understanding of pregnancy and diabetes. On this basis, combined with the staged needs of pregnant women and fetuses for healthy development, dietary intervention, exercise intervention, and pregnancy monitoring were implemented. At the same time, health education interventions need to continue to be carried out to ensure the effective implementation of dietary interventions, exercise interventions, and pregnancy monitoring. Through a full range of comprehensive nursing interventions, pregnant women are guided to achieve good physical and psychological outcomes.

3. Result

The amniotic fluid index, BMI, weight gain during pregnancy, delivery weight, fasting blood sugar, and 2h postprandial blood sugar in the experimental group of pregnant women with gestational diabetes are lower/lower than those in the control group. The results of statistical analysis show that the differences between the experimental group and the control group in the above indicators are statistically significant ($P < 0.05$), as shown in Tables 1–6, and the corresponding statistical graphs are shown in Figures 1–6.

TABLE 1: Comparison table of amniotic fluid index.

Number	Test group (mm)	Control group (mm)
1	107.03	172.97
2	117.96	77.59
3	125.28	85.91
4	100.30	80.93
5	80.80	164.31
6	99.40	123.96
7	132.38	143.18
8	90.80	154.63
9	100.71	165.31
10	95.07	77.64
11	107.68	102.38
12	114.18	112.90
13	103.34	90.70
14	94.96	110.48
15	109.01	102.24
16	96.91	149.07
17	108.92	75.00
18	107.65	107.06
19	111.35	155.72
20	90.42	168.96
21	104.12	129.11
22	123.87	111.67
23	94.35	138.21
24	80.80	100.56
25	120.54	143.04
26	125.74	82.57
27	132.14	136.48
28	110.22	100.65
29	113.57	109.97
30	113.07	144.23
31	103.70	161.84
32	114.06	92.76
33	117.03	149.19
34	86.49	146.41
35	115.53	122.26
36	93.94	112.31
37	116.73	85.12
38	86.40	151.97
39	121.13	163.18
40	126.77	81.72

TABLE 2: Comparison table of BMI.

Number	Test group (kg/m ²)	Control group (kg/m ²)
1	18.86	18.94
2	20.31	18.05
3	21.71	17.78
4	20.21	17.62
5	19.77	22.92
6	19.74	24.54
7	20.18	20.96
8	20.91	19.28
9	19.86	20.49
10	20.06	24.36
11	20.52	17.40
12	18.84	17.50
13	20.34	18.48
14	21.51	20.26
15	20.54	24.45
16	19.62	24.18
17	20.16	17.51
18	21.15	19.37
19	20.87	20.70
20	21.65	17.59
21	19.66	23.71
22	21.94	22.96
23	19.93	18.34
24	20.13	19.30
25	21.75	18.65
26	20.31	24.05
27	20.29	21.95
28	19.43	23.32
29	21.52	20.42
30	19.42	18.62
31	20.36	23.70
32	19.27	21.47
33	21.65	24.66
34	21.22	22.20
35	19.40	24.66
36	20.17	24.42
37	20.68	19.25
38	19.64	19.60
39	20.46	19.02
40	19.18	18.09

4. Analysis and Discussion

The comparison of pregnancy outcome indicators between the experimental group and the control group shows that there are no cases of gestational hypertension in the experimental group, while many cases of gestational hypertension occurred in the control group. The comparison of pregnancy outcome indicators between the experimental group and the control group shows that there are no cases of gestational

hypertension in the experimental group, while many cases of gestational hypertension occurred in the control group. There is statistically significant difference in the incidence of gestational hypertension between the two groups ($P < 0.05$). Regarding the preterm birth index, the preterm birth rate of the experimental group and the control group in the control group is higher than that in the experimental group, and the statistical analysis showed that the difference is statistically significant ($P < 0.05$). The comparison result

TABLE 3: Comparison table of weight gain during pregnancy.

Number	Test group (kg)	Control group (kg)
1	18.69	20.97
2	15.98	18.64
3	15.69	16.94
4	17.37	21.65
5	15.61	16.60
6	16.68	14.86
7	17.37	19.39
8	18.37	13.99
9	15.65	17.33
10	17.18	20.54
11	15.46	16.81
12	18.15	12.69
13	19.22	16.35
14	15.53	13.68
15	17.96	21.65
16	18.15	22.28
17	15.53	18.83
18	17.53	23.24
19	15.49	12.60
20	15.73	21.94
21	17.22	22.70
22	17.93	22.35
23	18.37	23.18
24	17.12	13.36
25	18.79	22.74
26	17.96	12.63
27	19.38	18.10
28	16.11	20.88
29	17.71	22.03
30	15.73	13.84
31	16.05	16.14
32	18.76	20.91
33	15.32	16.38
34	19.31	12.44
35	17.38	14.99
36	19.27	22.00
37	17.46	13.40
38	17.32	14.14
39	15.86	13.98
40	17.04	22.12

TABLE 4: Comparison table of weight at delivery.

Number	Test group (kg)	Control group (kg)
1	68.99	70.59
2	64.77	76.99
3	64.09	62.18
4	67.84	76.46
5	62.16	68.01
6	68.15	72.15
7	73.71	73.02
8	62.39	62.25
9	72.89	78.20
10	64.04	67.86
11	73.50	74.61
12	61.66	75.61
13	64.26	61.24
14	73.78	65.98
15	64.89	69.54
16	64.34	75.81
17	62.16	66.62
18	67.23	69.21
19	62.26	79.12
20	74.48	70.56
21	74.62	68.94
22	66.68	62.07
23	62.56	79.27
24	68.67	67.18
25	63.42	62.55
26	64.98	67.50
27	67.93	73.76
28	74.35	65.81
29	61.29	74.25
30	74.73	77.00
31	72.70	63.62
32	73.28	71.97
33	74.04	68.85
34	66.15	69.77
35	63.39	66.84
36	72.13	64.00
37	65.93	65.78
38	68.30	74.39
39	61.31	66.17
40	73.50	67.24

of the cesarean section rate shows that the control group was higher than the experimental group, and the statistical analysis showed that the difference is statistically significant ($P < 0.05$).

The comparison of the incidence of polyhydramnios shows that the control group was higher than the experimental group, and the statistical analysis shows that the difference was statistically significant ($P < 0.05$). The comparison results of fetal distress rate show that the real control

group was higher than the experimental group, and the statistical analysis shows that the difference was statistically significant ($P < 0.05$). The comparison of postpartum hemorrhage rate shows that the control group is higher than the experimental group, and the statistical analysis shows that the difference is statistically significant ($P < 0.05$). The comparison of urinary system infection rate shows that the control group is higher than the experimental group, and the statistical analysis showed that the difference is

TABLE 5: Comparison table of fasting blood glucose.

Number	Test group (mmol/L)	Control group (mmol/L)
1	4.48	5.49
2	4.59	6.09
3	5.32	6.09
4	4.26	5.93
5	4.68	5.40
6	4.43	6.12
7	4.77	5.29
8	5.29	5.24
9	4.41	5.37
10	5.23	4.98
11	4.13	6.08
12	5.10	4.90
13	5.30	5.82
14	3.97	5.23
15	4.81	5.75
16	4.36	5.67
17	4.89	5.78
18	4.50	5.65
19	5.02	5.95
20	4.08	5.66
21	5.07	5.38
22	4.68	5.59
23	4.71	5.90
24	4.52	4.70
25	5.09	5.37
26	4.95	6.17
27	5.31	5.72
28	4.88	5.32
29	4.64	5.81
30	5.24	5.92
31	4.24	5.84
32	5.06	5.46
33	4.36	5.31
34	5.08	4.80
35	4.82	5.30
36	4.02	4.86
37	4.13	4.79
38	5.20	4.97
39	4.65	5.43
40	5.26	4.74

TABLE 6: The comparison table of 2 h postprandial blood glucose.

Number	Test group (mmol/L)	Control group (mmol/L)
1	6.17	6.55
2	6.52	6.72
3	6.43	7.59
4	6.87	6.32
5	5.96	6.35
6	5.92	6.65
7	6.29	6.38
8	6.61	6.92
9	6.19	7.35
10	5.89	6.21
11	6.57	5.99
12	6.54	5.93
13	5.49	6.93
14	6.55	6.46
15	5.58	6.35
16	5.56	6.38
17	5.98	6.93
18	6.48	6.84
19	6.19	6.35
20	5.90	6.38
21	5.30	6.34
22	6.85	6.94
23	6.54	6.48
24	6.35	6.86
25	5.47	6.32
26	6.25	6.58
27	6.34	6.45
28	5.37	6.67
29	5.96	6.38
30	6.41	7.91
31	5.99	10.28
32	5.91	6.92
33	5.52	6.32
34	5.92	11.07
35	6.21	7.41
36	6.10	6.35
37	6.21	6.84
38	5.79	6.35
39	5.56	6.38
40	5.40	6.67

statistically significant ($P < 0.05$). There is no significant difference in the incidence of placenta previa and premature rupture of membranes between the experimental group and the control group ($P < 0.05$). In conclusion, in addition to placenta previa and premature rupture of membranes, in the comparison of pregnancy outcome indicators such as gestational hypertension, premature birth, cesarean section, polyhydramnios, fetal distress, postpartum hemorrhage,

and urinary tract infection, the incidence rates of related pregnancy outcomes in the control group are higher than those in the experimental group, and the differences are statistically significant ($P < 0.05$).

With the increasing awareness of gestational diabetes, pregnant women generally attach great importance to the changes in their bodies during pregnancy, which lays a good foundation for strengthening nursing interventions during

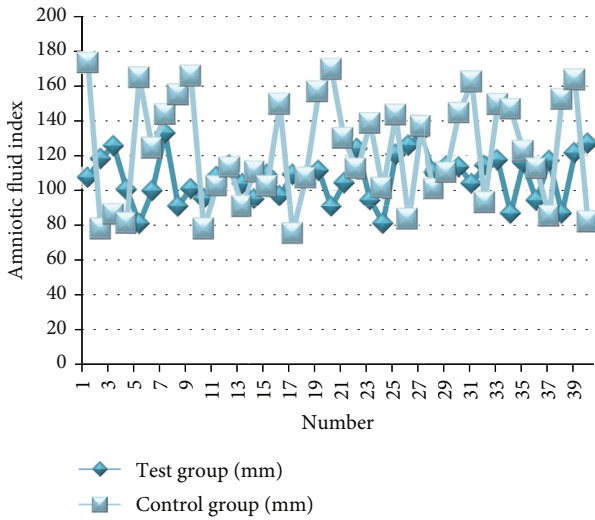


FIGURE 1: Statistical diagram of amniotic fluid index.

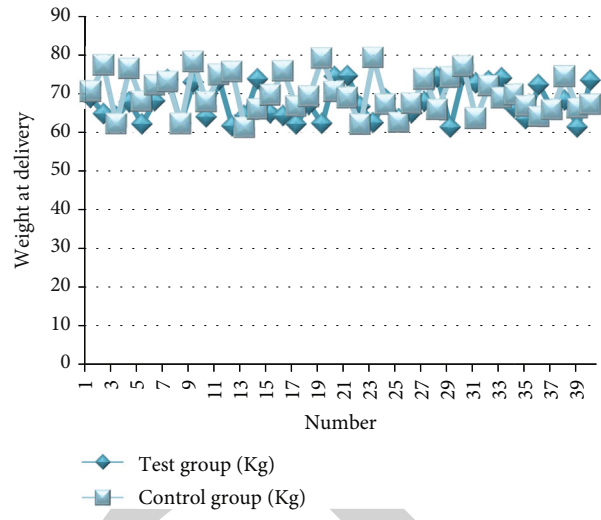


FIGURE 4: Statistical diagram of weight at delivery.

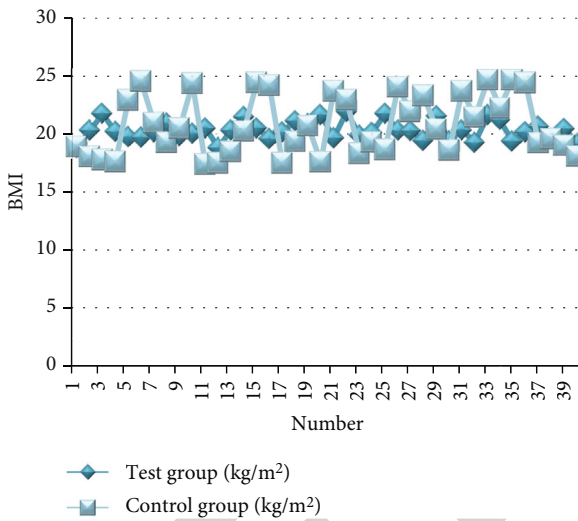


FIGURE 2: Statistical diagram of BMI.

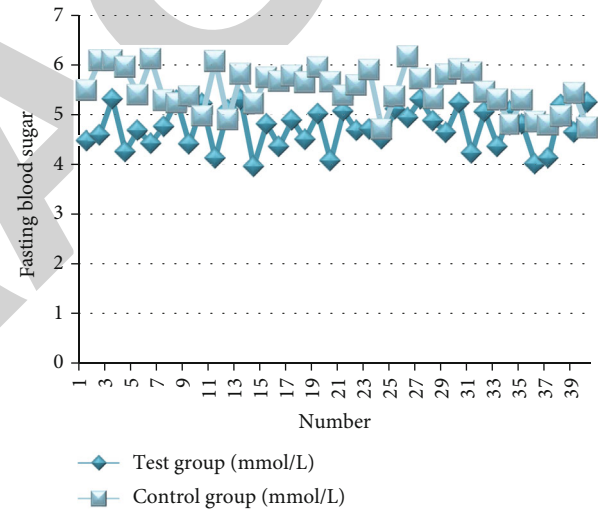


FIGURE 5: Statistical diagram of fasting blood glucose.

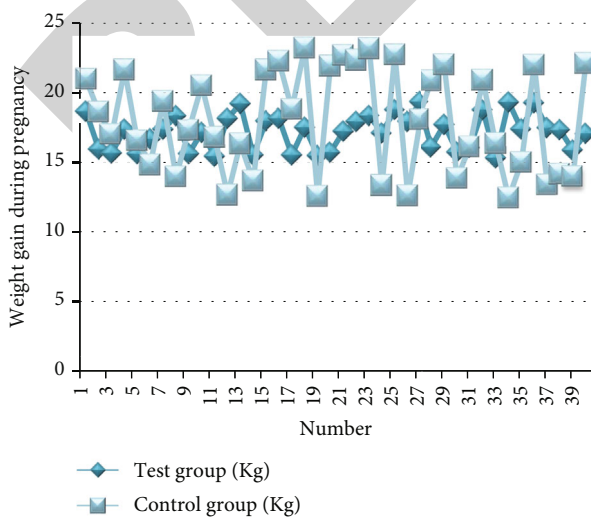


FIGURE 3: Statistical diagram of weight gain during pregnancy.

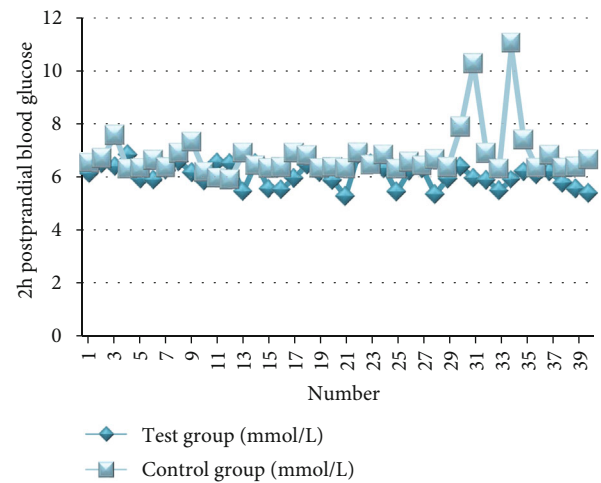


FIGURE 6: Statistical diagram of 2 h postprandial blood glucose.

pregnancy. Moreover, how to control and manage the amniotic fluid index, body weight, blood sugar, and other indicators during pregnancy is of great significance to ensure the health of mothers and babies. Health education intervention can effectively improve the diet, exercise, and personal hygiene habits of pregnant women with gestational diabetes mellitus, improve the compliance of pregnant women with gestational diabetes mellitus, and significantly improve pregnancy outcomes. In addition, dietary intervention is the basis and the most important factor in the treatment of gestational diabetes. Through dietary intervention, indicators such as weight gain during pregnancy and delivery weight can be effectively managed and controlled, thereby effectively improving pregnancy outcomes. At the same time, dietary intervention is greatly affected by factors such as the pregnant woman herself and her family's living habits, and there are many troublesome factors in the intervention process, making it more difficult to implement. Therefore, the simultaneous use of dietary interventions and interventions such as health education has a more significant effect on improving pregnancy outcomes. Moreover, dietary and nutritional care of patients with gestational diabetes mellitus is very important. Through reasonable dietary intervention, it is beneficial to maintain the blood sugar level in a reasonable range, and dietary intervention is very necessary and very important for pregnant women with gestational diabetes mellitus. However, when implementing dietary intervention for pregnant women with gestational diabetes mellitus, the daily calorie intake should be reasonably determined based on the specific conditions of each pregnant woman. While ensuring the effective supply of nutrients and heat energy for the healthy growth and development of pregnant women and their fetuses, avoid starvation ketone bodies and postprandial hyperglycemia. Therefore, dietary nursing intervention plays an important role in the comprehensive nursing intervention for pregnant women with gestational diabetes mellitus.

The effect of exercise therapy for gestational diabetes patients cannot be ignored. Pregnant women with gestational diabetes maintain proper exercise, which is not only beneficial to the health of mothers and babies, but also to better control of blood sugar levels. The reason is that the movement of skeletal muscle can not only consume energy but also help to increase the sensitivity of insulin binding to receptors. Improving glucose tolerance and reducing insulin requirements in patients with gestational diabetes can be achieved through appropriate exercise. Studies have shown that exercise has a positive effect on enhancing the sensitivity of peripheral tissues to insulin, improving the uptake and utilization of glucose by muscle cells, and eliminating insulin resistance. Moreover, upper extremity exercise intervention can help improve the pregnancy outcomes of pregnant women with high risk factors for diabetes, and safe and effective appropriate exercise can help to reasonably control the blood sugar level of pregnant women with gestational diabetes. However, the specific exercise method and the single exercise time need to be determined in combination with each pregnant woman's own conditions.

Data Availability

The labeled dataset used to support the findings of this study are available from the corresponding author upon request.

Conflicts of Interest

The authors declare no competing interests.

Acknowledgments

This study is sponsored by The Affiliated Hospital of Medical School of Ningbo University.

References

- [1] P. T. H. Nguyen, C. W. Binns, C. L. Nguyen et al., "Gestational diabetes mellitus reduces breastfeeding duration: a prospective cohort study," *Breastfeeding Medicine*, vol. 14, no. 1, pp. 39–45, 2019.
- [2] P. T. H. Nguyen, N. M. Pham, K. T. Chu, D. Van Duong, and D. Van Do, "Gestational diabetes and breastfeeding outcomes: a systematic review," *Asia Pacific Journal of Public Health*, vol. 31, no. 3, pp. 183–198, 2019.
- [3] L. Feng, Q. Xu, Z. Hu, and H. Pan, "Lactation and progression to type 2 diabetes in patients with gestational diabetes mellitus: a systematic review and meta-analysis of cohort studies," *Journal of diabetes investigation*, vol. 9, no. 6, pp. 1360–1369, 2018.
- [4] P. Kaul, S. L. Bowker, A. Savu, R. O. Yeung, L. E. Donovan, and E. A. Ryan, "Association between maternal diabetes, being large for gestational age and breast-feeding on being overweight or obese in childhood," *Diabetologia*, vol. 62, no. 2, pp. 249–258, 2019.
- [5] R. Tanda, I. R. Chertok, Z. T. Haile, and B. B. Chavan, "Factors that modify the association of maternal postpartum smoking and exclusive breastfeeding rates," *Breastfeeding Medicine*, vol. 13, no. 9, pp. 614–621, 2018.
- [6] R. Lamminpää, K. Vehviläinen-Julkunen, and U. Schwab, "A systematic review of dietary interventions for gestational weight gain and gestational diabetes in overweight and obese pregnant women," *European Journal of Nutrition*, vol. 57, no. 5, pp. 1721–1736, 2018.
- [7] Y. Huang, Y. Q. Ouyang, and S. R. Redding, "Maternal prepregnancy body mass index, gestational weight gain, and cessation of breastfeeding: a systematic review and meta-analysis," *Breastfeeding Medicine*, vol. 14, no. 6, pp. 366–374, 2019.
- [8] K. E. Hannan, A. L. Juhl, and S. S. Hwang, "Impact of NICU admission on Colorado-born late preterm infants: breastfeeding initiation, continuation and in-hospital breastfeeding practices," *Journal of Perinatology*, vol. 38, no. 5, pp. 557–566, 2018.
- [9] S. Rajaei, J. Rigdon, S. Crowe, J. Tremmel, S. Tsai, and T. L. Assimes, "Breastfeeding duration and the risk of coronary artery disease," *Journal of Women's Health*, vol. 28, no. 1, pp. 30–36, 2019.
- [10] S. K. Orr, N. Dachner, L. Frank, and V. Tarasuk, "Relation between household food insecurity and breastfeeding in Canada," *CMAJ*, vol. 190, no. 11, pp. E312–E319, 2018.
- [11] B. M. Casey, M. M. Rice, M. B. Landon et al., "Effect of treatment of mild gestational diabetes on long-term maternal outcomes," *American Journal of Perinatology*, vol. 37, no. 5, pp. 475–482, 2020.

Retraction

Retracted: Deep Image Watermarking to JPEG Compression Based on Mixed-Frequency Channel Attention

Computational and Mathematical Methods in Medicine

Received 27 June 2023; Accepted 27 June 2023; Published 28 June 2023

Copyright © 2023 Computational and Mathematical Methods in Medicine. This is an open access article distributed under the Creative Commons Attribution License, which permits unrestricted use, distribution, and reproduction in any medium, provided the original work is properly cited.

This article has been retracted by Hindawi following an investigation undertaken by the publisher [1]. This investigation has uncovered evidence of one or more of the following indicators of systematic manipulation of the publication process:

- (1) Discrepancies in scope
- (2) Discrepancies in the description of the research reported
- (3) Discrepancies between the availability of data and the research described
- (4) Inappropriate citations
- (5) Incoherent, meaningless and/or irrelevant content included in the article
- (6) Peer-review manipulation

The presence of these indicators undermines our confidence in the integrity of the article's content and we cannot, therefore, vouch for its reliability. Please note that this notice is intended solely to alert readers that the content of this article is unreliable. We have not investigated whether authors were aware of or involved in the systematic manipulation of the publication process.

Wiley and Hindawi regrets that the usual quality checks did not identify these issues before publication and have since put additional measures in place to safeguard research integrity.

We wish to credit our own Research Integrity and Research Publishing teams and anonymous and named external researchers and research integrity experts for contributing to this investigation.

The corresponding author, as the representative of all authors, has been given the opportunity to register their agreement or disagreement to this retraction. We have kept a record of any response received.

References

- [1] J. Tan, Y. Hu, Z. Shi, and B. Wang, "Deep Image Watermarking to JPEG Compression Based on Mixed-Frequency Channel Attention," *Computational and Mathematical Methods in Medicine*, vol. 2022, Article ID 9880038, 12 pages, 2022.

Research Article

Deep Image Watermarking to JPEG Compression Based on Mixed-Frequency Channel Attention

Jun Tan ¹, Yanan Hu,¹ Ziming Shi ², and Bin Wang ¹

¹The Key Laboratory of Advanced Design and Intelligent Computing, School of Software Engineering, Dalian University, Dalian 116622, China

²Dalian University Experimental Center, Dalian University, Dalian 116622, China

Correspondence should be addressed to Ziming Shi; szm_zz@163.com and Bin Wang; wangbin@dlu.edu.cn

Received 27 May 2022; Accepted 21 June 2022; Published 14 July 2022

Academic Editor: Pan Zheng

Copyright © 2022 Jun Tan et al. This is an open access article distributed under the Creative Commons Attribution License, which permits unrestricted use, distribution, and reproduction in any medium, provided the original work is properly cited.

Deep blind watermarking algorithms based on an end-to-end encoder-decoder architecture have recently been extensively studied as an important technology for protecting copyright. However, none of the existing algorithms can fully utilize the channel features of the image to improve the robustness against JPEG compression while obtaining high visual quality. Therefore, we propose firstly a mixed-frequency channel attention method in the encoder, which utilizes different frequency components of the 2D-DCT domain as weight coefficients during channel squeezing and excitation. Its essence is to suppress the useless feature maps and enhance the feature maps suitable for watermarking embedding by introducing frequency analysis in the channel dimension. The experimental results indicate that the PSNR of our method reaches over 38 and the BER is less than 0.01% under the JPEG compression with quality factor $Q=50$. Besides, the proposed framework also obtains excellent robustness for a variety of common distortions, including Gaussian filter, crop, crop out, and drop out.

1. Introduction

As the mobile Internet industry develops rapidly, people gain access to large amounts of multimedia information. However, the deluge of multimedia information has resulted in a series of issues, including copyright conflicts and malicious tampering. Image encryption [1, 2], steganography [3, 4], digital watermarking [5], and other technologies came into being to solve the problem caused by information leakage. Digital watermarking, an effective technology for protecting copyright, has been used in image, audio, video, and other fields [6–11]. Digital image watermarking is one of the most important research directions for digital watermarking. The principle of digital image watermarking is to embed secret messages into the cover image in a way that is imperceptible to the human visual system, and the secret messages can still be recovered even if the encoded image is modified.

Traditional digital image watermarking algorithms are mainly divided into spatial watermarking and frequency watermarking. The spatial watermarking algorithms embed

the watermark directly by modifying the image pixel, but this method is easily detected by a statistical method [12]. Therefore, researchers began to pay attention to the frequency domain, and they found that watermark embedding in DCT [13], DWT [14], and other frequency domains has better robustness and image visual quality. However, these traditional methods rely heavily on artificial shallow feature extraction, and they cannot make full use of the cover image, which greatly limits the robustness of the algorithm.

In recent years, with the success of deep neural networks in information hiding [15, 16] and other fields [17–21], some digital watermarking algorithms based on the deep neural network (DNN) have emerged [22, 23]. Kandi et al. [24] firstly applied a Convolutional Neural Network (CNN) to watermarking, which offers superior invisibility and robustness over traditional methods. However, the method is nonblind watermarking, which only applies in a narrow area. Ahmadi et al. [25] proposed a blind watermarking based on CNN, in which the circular convolution blocks are used to expand secret messages into the whole cover image to withstand geometric distortions. Zhu et al.

[26] proposed an end-to-end DNN-based model for watermarking and a method called JPEG-Mask, which simulates the nondifferential JPEG compression. However, the simulated JPEG compression added as a noise layer to the training cannot achieve the effect that real JPEG compression plays. Therefore, a two-stage separable deep watermarking framework [27] was proposed. In stage I, only the encoder and decoder were initially trained to perform powerfully in encoding and decoding, and the decoder is individually fine-tuned by nondifferential distortions in stage II. The two-stage method may find the locally optimal results but cannot find the globally optimal results. Jia et al. [28] proposed a Mini-Batch of Real and Simulated JPEG compression (MBRS) method. For each minibatch image, one of the simulated JPEG, real JPEG compression, and a noise-free layer (identity) is selected randomly as the noise layer, and the gradient direction is updated in real time to find the globally optimal result. However, the above-mentioned methods ignore the frequency analysis, which can be combined with channel feature selection to improve the visual quality and robustness.

In order to address the aforementioned problems, based on the previous work [29, 30] about frequency analysis being introduced into DNN, we proposed a new attention method in this paper, which consists of two branches. One branch utilizes several squeeze-and-excitation (SE) [31] blocks to extract the lowest-frequency components of the DCT domain [32] from the channel feature maps to obtain the basic information of the cover image. The other branch utilizes frequency channel attention (FCA) [29] blocks to extract the low-frequency components of channel feature maps to reserve some details. Intuitively, we think that multifrequency components can capture more details to improve visual quality and the combined components of channels can withstand JPEG compression. Besides, we add a diffusion block that is a fully connected layer used in [28] into the message processor to diffuse the secret message into the whole image. In our architecture, we use the strength factor to adjust the trade-off between robustness and imperceptibility. The results indicate that under JPEG compression, our method can achieve higher image quality and the decoding bit error rate (BER) is close to almost 0%. Moreover, we can train a model with a combined noise layer, making it robust for many common distortions.

In summary, the contributions of this paper are as follows:

- (i) To our knowledge, we are the first to introduce the frequency channel attention into digital watermarking, and we propose a mixed-frequency channel attention method for robust and blind image watermarking
- (ii) We choose 16 low-frequency channel components according to the zigzag form as the compression weight coefficients for the FCA channel attention block in our proposed scheme. Experimental results show that this selection scheme is superior to the midfrequency and high-frequency components when the noise layer is JPEG compression

- (iii) We propose a two-branch structure, which concentrates on the information from the lowest-frequency channel feature map and other low-frequency channel feature maps. The results of the experiments indicate that this structure can perform better than other mixed-frequency channel attention structures

The remainder of the paper is arranged as follows. Section 2 introduces the details of the proposed framework. Experiments and comparisons with relative schemes are presented in Section 3. The discussion and analyses are described in Section 4. Section 5 concludes the paper.

2. Proposed Framework and Method

2.1. Network Architecture. As shown in Figure 1, the whole model includes five components: message processor, encoder, noise layer, decoder, and adversary.

2.1.1. Message Processor MP. The message processor is mainly responsible for processing the message and inputting the processed feature maps into the encoder. MP receives the binary secret message M of length l that is composed of $\{0, 1\}$ and outputs the message feature maps M_{en} of shape $C' \times H \times W$, where C' is the channel number of the feature map. Specifically, the message M is generated randomly with a length of l and is reshaped to $\{0, 1\}^{1 \times l \times w}$. It is then amplified by a 3×3 ConvBNReLU layer, which consists of a convolutional layer, batch normalization, and ReLU activation function and is expanded to $C \times H \times W$ by several transposed convolution layers. Finally, to expand the message more appropriately, the features of the message are extracted by several SE blocks that maintain the shape.

2.1.2. Encoder E. An encoder with the parameter θ_E takes a RGB color image I_{co} of the shape $3 \times H \times W$ and the message maps M_{en} as input and outputs an encoded image I_{en} of the shape $3 \times H \times W$. For selecting channel features better, we utilize a mixed-frequency channel attention block that includes several SE blocks and an FCA block as shown in Figure 1. The whole encoder consists of several 3×3 ConvBNReLU layers, a mixed-frequency channel attention block, and a 1×1 convolutional layer. Firstly, we amplify the cover image through a 3×3 ConvBNReLU layer and then extract image features of the same shape with the proposed attention block. The feature maps obtained by the attention block are then concentrated through a 3×3 ConvBNReLU layer. We feed the cover image features and message feature maps obtained from the message processor into a 3×3 ConvBNReLU layer for simple fusion. Then, we concatenate the obtained tensor and the cover image into a new tensor and feed it into a 1×1 convolutional layer to obtain the encoded image I_{en} . Training the encoder is aimed at minimizing the L_2 distance between I_{co} and I_{en} by updating θ_E :

$$L_{E_1} = \text{MSE}(I_{co}, I_{en}) = \text{MSE}(I_{co}, E(\theta_E, I_{co}, M_{en})). \quad (1)$$

2.1.3. Noise Layer N. The robustness of the whole model is provided by the noise layer. We select different noises from

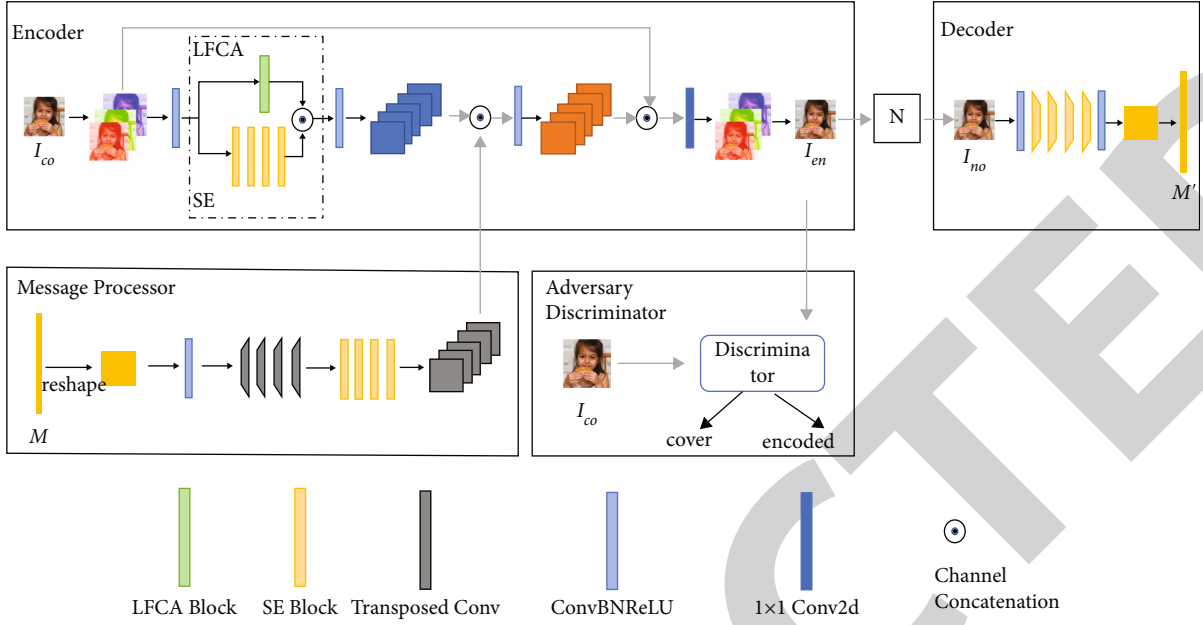


FIGURE 1: Overall model architecture. The message processor can learn the method for expanding message and realizing redundancy by the transposed convolutional layer; the encoder includes the mixed-frequency channel attention block which embeds the secret message into the whole cover image, the noise layer changes the kind of noise according to the MBRS method for offering the robustness, and the decoder extracts the secret message from the encoded image. An adversary discriminator is used to distinguish the cover image and the encoded image.

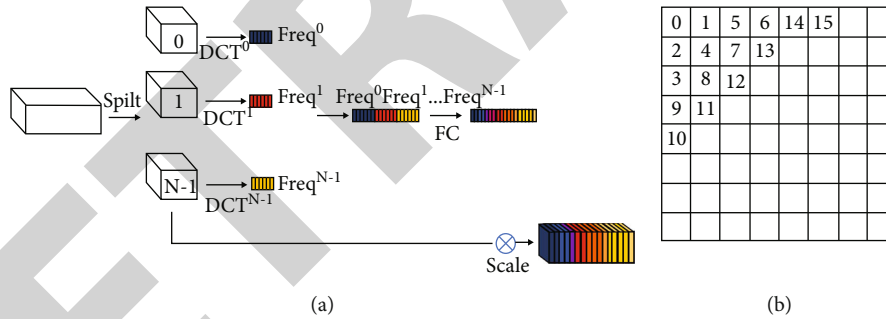


FIGURE 2: (a) The working theory of the FCA block. (b) The method of selecting frequency components in the DCT domain.

the appointed noise pool as the noise layer. It receives I_{en} and outputs the noised image I_{no} of the same shape. Besides, the end-to-end model requires all noises to join in the process of training. Therefore, we proposed the MBRS method [28] as the training method for the noise layer.

2.1.4. Decoder D. The task of the decoder with parameter θ_D is to recover the secret message M_D of length L from the noised image I_{no} . The component determines the ability of the whole model to extract watermarking. In the decoding stage, we feed the noised image I_{no} to a 3×3 ConvBNReLU layer and downsample the obtained feature maps by several SE blocks. Then, we convert the multichannel tensor into a single-channel tensor through a 3×3 convolutional layer and change the shape of the single-channel tensor to obtain

the decoded message M_D . The objective of decoder training is to minimize the distance between M and M_D by updating parameters θ_D to make them the same:

$$L_D = \text{MSE}(M, M_D) = \text{MSE}(M, D(\theta_D, I_{no})). \quad (2)$$

Since it plays an important role in the bit error rate indicator, the loss function accounts for the largest proportion of the total loss function.

2.1.5. Adversary Discriminator A. The adversary discriminator [33] consists of several 3×3 ConvBNReLU layers and a global average pooling layer. Under the influence of the adversarial network, the encoder will try to deceive the adversary as much as possible, so that the adversary cannot make a correct judgment on I_{co} and I_{en} . And update

TABLE 1: Comparison with the SOTA. We realized the model opening source in [28], while directly using the results included as reported in [26, 27] under quality factor 50. However, SSIM is not reported in [26, 27], for which we empty these items. PSNR is measured for RGB channels, except in [26]; they use the Y channel of the YUV color space.

Model	HiDDeN [26]	TSDL [27]	MBRS [28]	Ours
Image size	128×128	128×128	128×128	128×128
Message length	30	30	64	64
Noise layer	JPEG-Mask	JPEG	Mixed	Mixed
PSNR	30.09	33.51	36.49	38.13
SSIM	—	—	0.9173	0.9472
BER	15%	22.3%	0.0092%	0.0078%



FIGURE 3: Examples of showing the robustness of the model against JPEG compression ($Q = 50$) with experimental results. From top to bottom are the cover images, the encoded images, the noised images, the residual between cover images and encoded image, and the normalization of the residual signal.

parameters θ_E to minimize L_{E_2} to improve the encoding visual quality of the encoder:

$$L_{E_2} = \log(A(\theta_A, I_{\text{en}})) = \log(A(\theta_A, E(\theta_E, I_{\text{co}}, M_{\text{en}}))). \quad (3)$$

The discriminator with parameters θ_A needs to distinguish between I_{co} and I_{en} as a binary classifier. The goal of the adversary is to minimize the loss of classification L_A by updating θ_A :

$$L_A = \log(1 - A(\theta_A, E(\theta_E, I_{\text{co}}, M_{\text{en}}))) + \log(A(\theta_A, I_{\text{co}})). \quad (4)$$

The total loss function is $L = \lambda_E L_{E_1} + \lambda_D L_D + \lambda_A L_{E_2}$, and loss L_A is for the adversary discriminator.

2.2. Squeeze-and-Excitation Networks. An SE channel attention mechanism focuses on exploring the correlation of channel dimensions by modelling the relationships between channels and adaptively adjusting the feature values of each channel so that the attention network learns global information and reinforces the useful information while suppressing the useless information. The SE channel attention network is divided into two-step operations including squeeze and excitation. Squeeze is specifically a global average pooling operation that compresses the size of feature map from $C \times h \times w$ into $C \times 1 \times 1$, the result of which can represent global

TABLE 2: Results of robustness against other distortions. We add an additive diffusion block into the message processor for improving the shortcoming that our original structure is not robust enough against crop, crop out, and drop out and make a comparison with [26–28] trained by a combined noise layer. The strength factor is adjusted for comparison under PSNR = 33.5.

Noise	Identity	Crop out ($p=0.3$)	Drop out ($p=0.3$)	Crop ($p=0.035$)	GF ($\sigma=2$)	JPEG ($Q=50$)
HiDDeN [26]	0%	6%	7%	12%	4%	37%
TSDL [27]	0%	2.7%	2.6%	11%	1.4%	23.8%
MBRS [28]	0%	0.0027%	0.0087%	4.15%	0.011%	4.48%
Ours	0%	0.0013%	0.0080%	3.24%	0.293%	2.61%

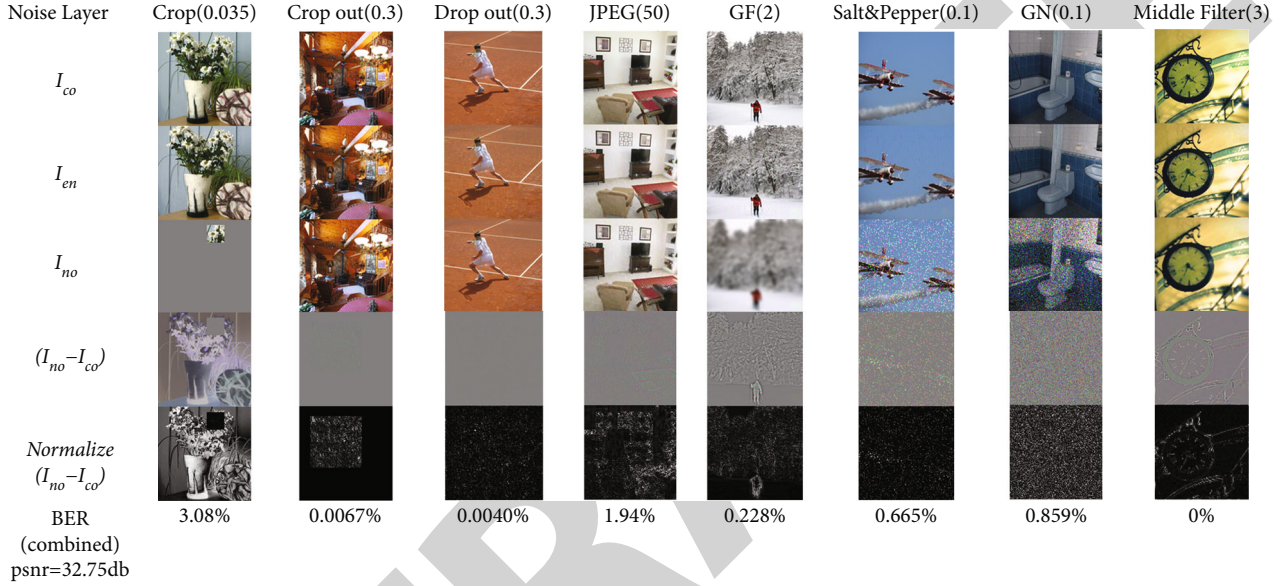


FIGURE 4: Robustness against different traditional noises. We tested different noises including those that were not included in the trained combined noise layer under strength factor $s=1$. The combined noise layer consists of JPEG-Mask ($Q=50$), real JPEG ($Q=50$), identity, and crop ($p=0.0225$). Top: cover image I_{co} ; second: encoded image I_{en} ; third: noised image I_{no} ; fourth: residual between I_{no} and I_{co} ; and bottom: the normalization of the residual signal.

information. The excitation operation can be considered a combination of two fully connected layers. The tensor obtained after the squeeze operation is first fully connected to compress the C dimensional tensor to C/r dimension and activated by the ReLU function and then fully connected again to transform the C/r dimension back to c dimension and activated by the sigmoid function to obtain the weight tensor. Finally, the weight tensor with 1×1 obtained by the excitation operation is scaled by the original tensor with $C \times h \times w$.

2.3. Frequency Channel Attention

2.3.1. The Basic Principle on FCA. Previous studies have tried to explain the relationship between the DCT and global average pooling (GAP) and hoped to mine the information of the DCT domain to better extract features from channels. In this section, we firstly review the formulas of 2D-DCT and GAP, and then, based on the aforementioned work, we elaborate on the principle of the FCA block and the selection of frequency components.

To express the basic functions of the two-dimensional (2D) DCT and the entire 2D-DCT more simply, we removed

some constant normalization coefficients, but they did not affect the results, just a principle explanation:

$$b_{u,v}^{i,j} = \cos\left(\frac{\pi u}{H}\left(i + \frac{1}{2}\right)\right) \cos\left(\frac{\pi v}{W}\left(j + \frac{1}{2}\right)\right), \quad (5)$$

$$F_{u,v}^{2d} = \sum_{i=0}^{H-1} \sum_{j=0}^{W-1} x_{i,j}^{2d} b_{u,v}^{i,j}. \quad (6)$$

F^{2d} is the computed 2D-DCT transform domain matrix, x^{2d} is the input, H is the height of x^{2d} , W is the width of x^{2d} , and $u \in \{0, 1, \dots, H-1\}$ and $v \in \{0, 1, \dots, W-1\}$. GAP is a special case of 2D-DCT when $u=0$ and $v=0$ in equation (6), and its result is proportional to the lowest-frequency component of 2D-DCT and is confirmed in [29]:

$$\begin{aligned} F_{0,0}^{2d} &= \sum_{i=0}^{H-1} \sum_{j=0}^{W-1} x_{i,j}^{2d} \cos\left(\frac{0}{H}\left(i + \frac{1}{2}\right)\right) \cos\left(\frac{0}{W}\left(j + \frac{1}{2}\right)\right) \\ &= \text{gap}\left(x^{2d}\right)HW. \end{aligned} \quad (7)$$

TABLE 3: Results of transparency against other distortions. For revealing the advantage of our proposed method, we make a comparison of PSNR and SSIM with [26, 28] by adjusting strength factor S to keep the BER at 0%. Because the experiment of [27] is not done, we do not list it.

Metric	Model	Crop ($p = 0.035$)	Crop out ($p = 0.3$)	Drop out ($p = 0.3$)	GF ($\sigma = 2$)	Identity
PSNR	HiDDeN [26]	35.20	47.24	42.52	40.55	44.63
	MBRS [28]	32.15	46.77	48.50	40.74	42.81
	Ours	33.01	47.26	49.43	42.30	45.71
SSIM	HiDDeN [26]	—	—	—	—	—
	MBRS [28]	0.7872	0.9910	0.9936	0.9670	0.9740
	Ours	0.8225	0.9924	0.9945	0.9760	0.9867
BER	HiDDeN [26]	0%	3%	0%	0%	0%
	MBRS [28]	0.72%	0%	0%	0%	0%
	Ours	0.29%	0%	0%	0%	0%

TABLE 4: BER, PSNR, and SSIM values under different strength factors S and quality factors of JPEG Q .

Strength factor	0.4	0.6	0.8	1.0	1.2	1.4	
BER	$Q = 10$	35.03%	27.91%	21.80%	16.86%	13.02%	10.06%
	$Q = 30$	15.65%	5.94%	1.63%	0.33%	0.047%	0.0053%
	$Q = 50$	7.74%	1.11%	0.0778%	0.0050%	0.0012%	0.00%
	$Q = 70$	3.87%	0.370%	0.0170%	0.0009%	0.00%	0.00%
	$Q = 90$	2.53%	0.202%	0.0078%	0.0006%	0.00%	0.00%
PSNR	45.92	42.40	39.89	37.95	36.37	35.03	
SSIM	0.9893	0.9773	0.9623	0.9455	0.9274	0.9086	

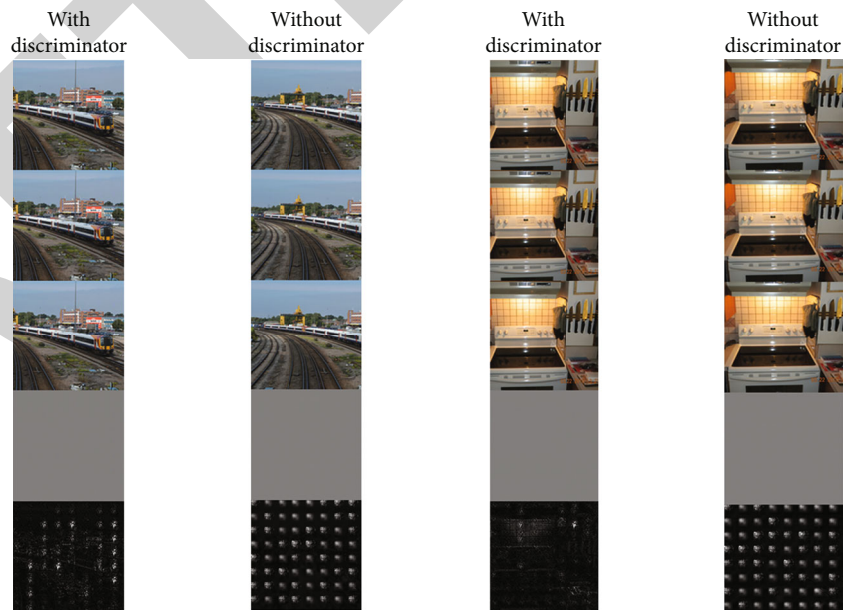


FIGURE 5: The results of encoding with and without a discriminator: top: cover image I_{co} ; second: encoded image I_{en} ; third: noised image I_{no} ; fourth: residual signal between I_{en} and I_{co} ; and bottom: the normalization of the residual signal.

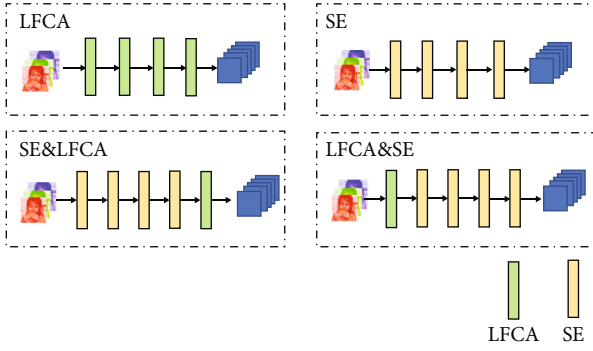


FIGURE 6: The other structures of mixed-frequency channel attention, which are proposed in the ablation experiment. The structure called LFCA is only composed of several frequency channel attention blocks with low-frequency components. The structure called SE consists of several SE channel attention blocks. The structure called SE&LFCA inserts an FCA block behind the SE blocks. The structure called LFCA&SE inserts FCA blocks in front of the SE blocks.

The input to the channel attention block is divided into many parts along the channel dimension. A corresponding 2D-DCT frequency component is assigned to each part, and the 2D-DCT-transformed results can be used as the compression results of channel attention. All transformed parts are concatenated to produce a complete compressed vector. Finally, the obtained compressed weight tensor with $1 \times 1 \times C$ and the original input tensor are multiplied to get the final result.

2.4. Criteria for Choosing Frequency Components. According to the above proof, the squeezing operation of the SE attention block is equivalent to the lowest-frequency component in the corresponding 2D-DCT coefficients. Usually, this component concentrates on most of the energy information of the image, and the conclusion is also valid for channel features. SENets are a very effective attention network used in most computer vision tasks, but most of the frequency domain components are discarded, some of which are beneficial to improve the performance of watermarking and should not be excluded. Therefore, in order to better compress the channel and introduce more information, we used the FCA block to expand the GAP to more 2D-DCT frequency components. Specific details of the implementation are shown in Figure 2(a). We divide 8×8 blocks according to the principle of JPEG compression and select the lowest-frequency component and 15 other low-frequency components according to the form of zigzag as the coefficients of the squeezing operation in the FCA block, as shown in Figure 2(b).

2.5. Noise Layer

2.5.1. JPEG Compression. In the real JPEG compression process, we need to quantize the DCT coefficients according to the quantization tables and round them up to the nearest whole number, but the process is nondifferential, which means that the gradient propagates back and the decoding

loss will be zero. To address the above-mentioned problem, we use the MBRS method, which can effectively solve the problem about nondifferential distortions.

2.5.2. Traditional Noise Attack. In the field of blind watermarking, some typical noises are often used to test the robustness of the model. In our work, we train five different models separately on the noises, which include crop ($p = 0.035$), crop out ($p = 0.3$), drop out ($p = 0.3$), Gaussian filter ($\sigma = 2$), and identity. Besides, we train a combined noise model with JPEG-Mask ($Q = 50$), JPEG ($Q = 50$), crop ($p = 0.0225$), and identity, which can resist most of the distortions.

2.6. Strength Factor. We use $I_{\text{diff}} = I_{\text{en}} - I_{\text{co}}$ to represent the residual signal between the encoded image and the cover image and adjust the trade-off between the visual quality and the bit error rate by the strength factor S : $I_{\text{en},s} = I_{\text{co}} + S \cdot I_{\text{diff}}$. The generated image $I_{\text{en},s}$ is fed into the noise layer to obtain the noised image I_{no} . We keep S on 1 in the training process and change the S in the testing process for different applications. Because our method is a blind watermarking, the trick is used only in the encoder.

3. Experiments and Results

3.1. Experimental Setup, Metrics, and Baselines. To evaluate the effectiveness of the proposed method, we use 10000 random images from the ImageNet dataset [34] for training and 5000 images from the COCO dataset [35] for testing, aiming at ensuring the generation of the trained model. We select the JPEG compression function in the PIL package as testing. The strength factor is set as 1 during training. For the weight factors of the loss function, we choose $\lambda_E = 1$, $\lambda_D = 10$, and $\lambda_A = 0.0001$. For the optimized function, Adam [36] is applied with a learning rate of 10^{-3} and default hyperparameters. Each model is trained for 100 epochs with a batchsize 16. PSNR and SSIM [37] measure the similarity between I_{en} and I_{co} . Robustness is measured by the the difference called BER between the decoded message and secret message. Our baselines for comparison are [26, 27] and [28]. In pursuit of the real results, we realize the MBRS [28] based on the open source of both codes and models. We also try to conduct experiments of [26, 27] but could not reproduce the best performance that they reported. In order to respect the results that they reported, we directly use their published results.

3.2. Comparison with SOTA Methods

3.2.1. Robustness. We train a model with JPEG-Mask ($Q = 50$), real JPEG ($Q = 50$), and identity to demonstrate the robustness of our model against JPEG compression. All the testing processes are performed under real JPEG ($Q = 50$). As shown in Table 1, compared to the other method, our model achieves the PSNR that is higher than 38 and the BER that is less than 0.01%, which indicates that our model not only maintains higher image quality for JPEG compression but also achieves lower BER. Figure 3 indicates that the messages are embedded in most areas of the cover images. In

TABLE 5: Comparison with the ablation experimental results, with the best results in bold and second bests in blue. We compared the performance with four mixed-frequency channel attention variants under JPEG compression ($Q = 50$).

Model	SE	LFCA	SE&LFCA	LFCA&SE	Ours
Image size	128×128	128×128	128×128	128×128	128×128
Message length	64	64	64	64	64
Noise layer	Mixed	Mixed	Mixed	Mixed	Mixed
PSNR	37.70	37.32	38.21	37.49	38.13
SSIM	0.9445	0.9428	0.9553	0.9487	0.9472
BER	0.0082%	0.0081%	0.0059%	0.0081%	0.0078%

TABLE 6: BER comparison between the proposed scheme and ablation schemes, with the best results in bold, second bests in blue, and the worst results in red. The strength factor is adjusted for comparison under PSNR = 33.5.

Noise	Identity	Crop out ($p = 0.3$)	Drop out ($p = 0.3$)	Crop ($p = 0.035$)	GF ($\sigma = 2$)	JPEG ($Q = 50$)
SE	0%	0.0027%	0.0093%	5.07%	0.011%	3.22%
LFCA	0%	0.0%	0.0027%	4.23%	0.031%	5.62%
SE&LFCA	0%	0.0040%	0.0179%	6.21%	0.185%	22.87%
LFCA&SE	0%	0.0047%	0.0053%	18.06%	0.006%	9.12%
Ours	0%	0.0013%	0.0080%	3.24%	0.293%	2.61%

TABLE 7: The ablation experiment of skip connection. Baseline: no attention model; +SE: add SE channel attention networks; +skip connection: based on SE nets, add a skip connection of LFCA.

(a)

Model	Metric	JPEG ($Q = 50$)	Crop ($p = 0.035$)	Crop out ($p = 0.3$)	Drop out ($p = 0.3$)	GF ($\sigma = 2$)
Baseline		32.60	32.60	32.59	32.57	32.59
+SE	PSNR	32.55	32.58	32.57	32.56	32.56
+skip connection (LFCA)		32.75	32.76	32.76	32.73	32.76
Baseline		0.8150	0.8157	0.8149	0.8146	0.8150
+SE	SSIM	0.8161	0.8165	0.8160	0.8157	0.8159
+skip connection (LFCA)		0.8263	0.8266	0.8263	0.8259	0.8265
Baseline		3.09%	6.96%	0%	0.0007%	0.168%
+SE	BER	2.19%	4.30%	0.0013%	0.0067%	0.0054%
+skip connection (LFCA)		1.94%	3.08%	0.0067%	0.0040%	0.228%

(b)

Salt&Pepper ($p = 0.1$)	GN ($p = 0.1$)	MF ($s = 3$)
32.59	32.59	32.58
32.55	32.56	32.55
32.75	32.76	32.75
0.8148	0.8153	0.8154
0.8156	0.8159	0.8160
0.8260	0.8271	0.8263
0.830%	1.23%	0%
0.813%	1.51%	0%
0.665%	0.859%	0%

TABLE 8: BER comparison between the proposed scheme and ablation schemes. We train three different ways of frequency domain component selection for the FCA attention block in the mixed-frequency channel attention block under JPEG compression. Low frequency: 16 coefficients of low-frequency components; middle frequency: 16 coefficients of middle-frequency components; and high frequency: 16 coefficients of high-frequency components.

Model	PSNR	SSIM	BER
High frequency	37.77	0.9407	0.6781%
Middle frequency	38.02	0.9472	0.5782%
Low frequency	38.13	0.9472	0.0078%

addition to JPEG compression distortion, our model is also robust to other image processing distortions, such as Gaussian filter (GF), crop, crop out, and drop out. We also train a combined noise model to embed a 30-bit message into 128×128 images with the noise layer consisting of JPEG-Mask ($Q=50$), real JPEG ($Q=50$), identity, and crop ($p=0.0225$) and add a diffusion and an inverse-diffusion block mentioned in [28] into the message processor for diffusing a secret message to the whole cover image to resist geometry attacks. As shown in Table 2, our trained model shows robustness against most noises. We also tested some noises not included in the noise layer for the combined noise model, and the experimental results are shown in Figure 4.

3.2.2. Transparency. In order to show that our method can learn more frequency features from cover images, we separately train five models with the noise layer. For GF ($\sigma=2$) and identity, we embed 64-bit messages into $3 \times 128 \times 128$ images without a diffusion block. For crop ($p=0.035$), crop out ($p=0.3$), and drop out ($p=0.3$), we embed 30-bit messages into $3 \times 128 \times 128$ images with the diffusion block. Besides, we compare the PSNR and SSIM between I_{co} and I_{en} by adjusting S under roughly the same BER. As shown in Table 3, the results of the proposed method perform better than those of other models under most distortions, but our specialized trained model performs worse for the crop attack. Since the information diffusion block we use has more information embedded on a single channel, it has some shortcomings compared to [26] of broadcasting single-bit information on a single channel.

3.3. Ablation Study

3.3.1. Strength Factor. The strength factor is a parameter used to balance robustness and imperceptibility. We set the value of the strength factor S , from 0.1 to 2.0, with an interval of 0.1, and test the model under different quality factors for JPEG compression. The results are shown in Table 4. With the increment of S , PSNR and SSIM values decrease, the quality of the encoded image becomes worse, and the extraction accuracy becomes higher. In the study, we adjust the value of S to obtain the similar visual quality of different models for fair comparison.

3.3.2. Discriminator. To demonstrate that the discriminator can help the encoder generate higher-quality images, we trained the noise-free model with and without the discriminator separately. As can be seen from the normalized watermarking residuals in Figure 5, the watermarking model without the discriminator does not produce a uniform distribution of watermarking and produces visual artifacts on the resulting watermarked image. However, the watermarking model with a discriminator generates an even distribution of watermarking, and no aggregation of watermarking occurs.

3.3.3. Different Mixed-Frequency Channel Attention. To demonstrate that our two-branch structure is superior to other combined mixed-frequency channel attention blocks, we conduct experiments for the encoder with different frequency channel attention structures. We proposed another four kinds of structures to be applied in the encoder. The first is called LFCA, which only consists of several FCA blocks with low-frequency components, the second is called SE&LFCA, in which we insert an FCA block behind the SE blocks, the third is composed of several SE blocks, and the last is called LFCA&SE, in which we insert an FCA block in front of the SE blocks. Their detailed structures are shown in Figure 6. We list the results of experiments separately under JPEG compression and combined noises for the above-mentioned four structures in Tables 5 and 6.

The channel attention mechanism assigns weights to the feature maps. SE only selects the lowest-frequency component coefficients of the 2D-DCT to enhance all channel feature maps through multiple SE blocks, while LFCA chooses to divide the feature maps on the channels and select multiple low-frequency component coefficients of the 2D-DCT to enhance through several LFCA blocks. We believe that when the noise layer only includes JPEG compression, the weights of LFCA enhancement are spread over multiple low-frequency components relative to SE, and thus, the performance will be worse than that of SE. However, combining SE blocks and LFCA blocks gives better performance. As can be seen from Table 5, the performance of SE&LFCA and LFCA&SE is better than that of SE and LFCA. SE&LFCA firstly allocates the lowest-frequency component coefficients through an SE block and then uses several LFCA blocks to enhance multifrequency component coefficients on the basis of the lowest-frequency component, which has a good effect. Although LFCA&SE is also composed of an SE block and several LFCA blocks, its effect is not as good as that of SE&LFCA. We believed that this is caused by LFCA assigning weights in the first place.

Our parallel structure is a better way of feature fusion when the noise layer includes multinoises. We believe that the reason why the experimental results of SE&LFCA and LFCA&SE perform worse is that they have no skip connection. Our proposed method achieves better performance with skip connection of FCA, which is confirmed by the experimental results in Table 7.

3.3.4. Selection Scheme of Frequency Components. To demonstrate that the FCA attention block in our method chooses

the low-frequency component coefficients of the DCT to improve the robustness to JPEG compression, we select 16 components of low frequency, 16 components of middle frequency, and 16 components of high frequency as the weight coefficients of FCA from the 8×8 coefficients, respectively, and train them under JPEG compression. It can be seen from Table 8 that the selection of frequency domain components has a certain impact on the robustness and imperceptibility of the model. When the low-frequency components are selected, the metrics such as PSNR, SSIM, and BER all reach the highest.

3.3.5. Skip Connection. To show the important role of introducing frequency analysis and skip connection, we trained three different watermarking models under a mixed-noise layer separately: baseline: without attention networks in the encoder; +SE: with the addition of the SE channel attention blocks in the encoder; and +skip connection: based on +SE, with the addition of the LFCA attention block via skip connection. Table 7 shows the results of experiments, where the performance of the model by adding SE attention block is improved compared to baseline under most of the noises. However, we find that the embedding of the watermark information by adding the SE attention block is more concentrated in the low-frequency region which is less affected by the Gaussian filter but will be more affected by the Gaussian noise. In order to further improve the robustness for noises such as JPEG compression, we added the LFCA attention block by skip connection on the basis of the SE attention blocks, and the experimental results show that the quality of the encoded image is improved by skip connection, the best robustness is achieved for most distortions, and our watermark embedding assignment is more reasonable.

4. Discussion and Analysis

According to Figures 2, 3, and 6 and Tables 5 and 6, some analyses are given as follows.

- (1) Our scheme significantly improved visual quality compared with relative schemes. We can find that the secret messages are embedded in most areas of the cover image including low-frequency and high-frequency components from Figure 3
- (2) To further reflect our scheme, we calculated the indicators SSIM and PSNR. SSIM can show the overall structure of images. PSNR is calculated based on the discrepancy between the corresponding two pixel values. PSNR and SSIM are utilized jointly to evaluate the visual quality of the encoded image
- (3) A frequency channel attention block with selected low-frequency channel components can effectively improve the robustness and imperceptibility of the proposed watermarking model under JPEG compression and combined noise layer, as shown in Tables 5 and 6. However, the performance of the variants suggests that the balance of robustness and

invisibility is very challenging. Our scheme chose the two-branch structure to concentrate on the features from the LFCA block and SE blocks. Experimental results demonstrate that skip connections provide better performance gains for the whole model

- (4) The performance of the watermarking algorithm depends largely on the selection of frequency channel components. We chose 16 low-frequency channel components according to the zigzag form. Compared to the lowest-frequency channel components extracted by the SE block and medium-high-frequency channel components, the multi-low-frequency channel components include the information that is beneficial to embedding messages and defence distortions
- (5) Although the method we proposed at the current stage has good performance in robustness and imperceptibility, we believe that it will also cause computational costs to a certain extent. Therefore, we hope to explore more concise and effective selection methods of channel feature components in the future

5. Conclusions

In the paper, we proposed a novel mixed-frequency channel attention block to improve the robustness and imperceptibility of existing deep robust image watermarking algorithms for JPEG compression. We divide the 2D-DCT frequency space into 8×8 parts according the principle of JPEG compression and utilize the SE block to obtain the lowest-frequency component in 2D-DCT domain, which is equal to GAP operation, as the weight coefficient for input. Then, we select the 16 low-frequency components in the 2D-DCT domain as the weight coefficients by the FCA block according to the zigzag form. Finally, we concentrate on the feature maps by skip connection in the channel dimension. Besides, we use an optional diffusion block in [28] for robustness against geometric attack. The comprehensive experiments have proven that the proposed method performs better in not only robustness but also image quality. Skip connection and the selection scheme of frequency components prove to be effective. In the future, we will also explore a more suitable channel selection method for watermarking embedding.

Data Availability

The dataset of this article was obtained from the dataset published on <http://images.cocodataset.org/zips/train2014.zip> and <http://image-net.org/download.php>.

Conflicts of Interest

The authors declare that there are no conflicts of interest regarding the publication of this article.

Acknowledgments

This work is supported by the National Key Technology R&D Program of China (No. 2018YFC0910500), the National Natural Science Foundation of China (Nos. 61425002, 61751203, 61772100, 61972266, and 61802040), the Liaoning Revitalization Talents Program (No. XLYC2008017), the Innovation and Entrepreneurship Team of Dalian University (No. XQN202008), the Natural Science Foundation of Liaoning Province (Nos. 2021-MS-344 and 2021-KF-11-03), the Scientific Research Fund of Department of Education of Liaoning Province (No. LJKZ1186), and the Dalian University Scientific Research Platform Program (No. 202101YB02).

References

- [1] Y. Shi, H. Yinan, and B. Wang, "Image encryption scheme based on multiscale block compressed sensing and Markov model," *Entropy*, vol. 23, no. 10, p. 1297, 2021.
- [2] S. Zhou, "A real-time one-time pad DNA-chaos image encryption algorithm based on multiple keys," *Optics & Laser Technology*, vol. 143, article 107359, 2021.
- [3] X. Liao, J. Yin, M. Chen, and Z. Qin, "Adaptive payload distribution in multiple images steganography based on image texture features," *IEEE Transactions on Dependable and Secure Computing*, vol. 19, no. 2, pp. 897–911, 2020.
- [4] W. Xiaotian and C.-N. Yang, "Partial reversible AMBTC-based secret image sharing with steganography," *Digital Signal Processing*, vol. 93, pp. 22–33, 2019.
- [5] L. Xiong, X. Han, C.-N. Yang, and Y.-Q. Shi, "Robust reversible watermarking in encrypted image with secure multi-party based on lightweight cryptography," *IEEE Transactions on Circuits and Systems for Video Technology*, vol. 32, no. 1, pp. 75–91, 2022.
- [6] A. Bamatraf, R. Ibrahim, B. Mohd Najib, and M. Salleh, "Digital watermarking algorithm using LSB," in *2010 International Conference on Computer Applications and Industrial Electronics*, pp. 155–159, Kuala Lumpur, Malaysia, 2010.
- [7] B. Tao and B. Dickinson, "Adaptive watermarking in the DCT domain," in *1997 IEEE International conference on acoustics, speech, and signal processing*, vol. 4, pp. 2985–2988, Munich, Germany, 1997.
- [8] M. Barni, F. Bartolini, V. Cappellini, and A. Piva, "A DCT-domain system for robust image watermarking," *Signal Processing*, vol. 66, no. 3, pp. 357–372, 1998.
- [9] M. D. Swanson, B. Zhu, and A. H. Tewfik, "Multiresolution scene-based video watermarking using perceptual models," *IEEE Journal on Selected Areas in Communications*, vol. 16, no. 4, pp. 540–550, 1998.
- [10] P. Bassia, I. Pitas, and N. Nikolaidis, "Robust audio watermarking in the time domain," *IEEE Transactions on Multimedia*, vol. 3, no. 2, pp. 232–241, 2001.
- [11] Y. Uchida, Y. Nagai, S. Sakazawa, and S. I. Satoh, "Embedding watermarks into deep neural networks," in *Proceedings of the 2017 ACM on international conference on multimedia retrieval*, pp. 269–277, Bucharest, Romania, 2017.
- [12] S. Dumitrescu, X. Wu, and Z. Wang, "Detection of LSB steganography via sample pair analysis," in *International Workshop on Information Hiding*, pp. 355–372, Springer, 2003.
- [13] M. Jiansheng, L. Sukang, and T. Xiaomei, "A digital watermarking algorithm based on DCT and DWT," *The 2009 International Symposium on Web Information Systems and Applications (WISA 2009)*, 2009, Citeseer, p. 104, 2009.
- [14] Y. Shen, C. Tang, X. Min, M. Chen, and Z. Lei, "A DWT-SVD based adaptive color multi-watermarking scheme for copyright protection using AMEF and PSO-GWO," *Expert Systems with Applications*, vol. 168, article 114414, 2021.
- [15] S. Baluja, "Hiding images within images," *IEEE Transactions on Pattern Analysis and Machine Intelligence*, vol. 42, no. 7, pp. 1685–1697, 2020.
- [16] J. Jing, X. Deng, X. Mai, J. Wang, and Z. Guan, Eds., "Hinet: deep image hiding by invertible network," in *Proceedings of the IEEE/CVF International Conference on Computer Vision*, pp. 4733–4742, 2021.
- [17] Y. Changqian, J. Wang, C. Peng, C. Gao, G. Yu, and N. Sang, "Bisenet: bilateral segmentation network for real-time semantic segmentation," in *Proceedings of the European conference on computer vision (ECCV)*, pp. 325–341, Munich, Germany, 2018.
- [18] P. Isola, J.-Y. Zhu, T. Zhou, and A. A. Efros, "Image-to-image translation with conditional adversarial networks," in *Proceedings of the IEEE conference on computer vision and pattern recognition*, pp. 1125–1134, Honolulu, Hawaii, 2017.
- [19] J.-Y. Zhu, T. Park, P. Isola, and A. A. Efros, "Unpaired image-to-image translation using cycle-consistent adversarial networks," in *Proceedings of the IEEE international conference on computer vision*, pp. 2223–2232, Venice, Italy, 2017.
- [20] T. Song, X. Zhang, M. Ding, A. Rodriguez-Paton, S. Wang, and G. Wang, "DeepFusion: a deep learning based multi-scale feature fusion method for predicting drug-target interactions," *Methods*, vol. 204, pp. 269–277, 2022.
- [21] X. Meng, X. Li, and X. Wang, "A computationally virtual histological staining method to ovarian cancer tissue by deep generative adversarial networks," *Computational and Mathematical Methods in Medicine*, vol. 2021, 12 pages, 2021.
- [22] M. Plata and P. Syga, "Robust spatial-spread deep neural image watermarking," in *2020 IEEE 19th International Conference on Trust, Security and Privacy in Computing and Communications (TrustCom)*, pp. 62–70, Guangzhou, China, 2020.
- [23] M. Jamali, N. Karim, P. Khadivi, S. Shirani, and S. Samavi, "Robust watermarking using diffusion of logo into autoencoder feature maps," 2021, <https://arxiv.org/abs/2105.11095>.
- [24] H. Kandi, D. Mishra, and S. R. Gorthi, "Exploring the learning capabilities of convolutional neural networks for robust image watermarking," *Computers & Security*, vol. 65, pp. 247–268, 2017.
- [25] M. Ahmadi, A. Norouzi, N. Karimi, S. Samavi, and A. Emami, "ReDMark: framework for residual diffusion watermarking based on deep networks," *Expert Systems with Applications*, vol. 146, article 113157, 2020.
- [26] J. Zhu, R. Kaplan, J. Johnson, and L. Fei-Fei, "HiDDeN: hiding data with deep networks," in *Proceedings of the European conference on computer vision (ECCV)*, pp. 657–672, Munich, Germany, 2018.
- [27] Y. Liu, M. Guo, J. Zhang, Y. Zhu, and X. Xie, "A novel two-stage separable deep learning framework for practical blind watermarking," in *Proceedings of the 27th ACM International Conference on Multimedia*, pp. 1509–1517, Nice, France, 2019.
- [28] Z. Jia, H. Fang, and W. Zhang, "MBRS: enhancing robustness of DNN-based watermarking by Mini-Batch of Real and

Research Article

Prognostic Evaluation of CT Imaging Big Data-Assisted Arterial Chemoembolization Combined with ^{125}I Seed Implantation for Non-Small-Cell Lung Cancer

Peng Xie ¹, Yan Zhang ², and Lidong He¹

¹Sixth Medical Center of PLA General Hospital, Beijing 100048, China

²China-Japan Friendship Hospital, Beijing 100048, China

Correspondence should be addressed to Peng Xie; xiepengsci112@163.com

Received 27 April 2022; Accepted 31 May 2022; Published 13 July 2022

Academic Editor: Pan Zheng

Copyright © 2022 Peng Xie et al. This is an open access article distributed under the Creative Commons Attribution License, which permits unrestricted use, distribution, and reproduction in any medium, provided the original work is properly cited.

Objective. To investigate the prognostic impact of computed tomography (CT) imaging big data-assisted arterial chemoembolization combined with iodine 125 (^{125}I) seed implantation on patients with non-small-cell lung cancer (NSCLC). **Methods.** A total of 116 patients with intermediate and advanced NSCLC hospitalized in our hospital from August 2019 to August 2020 were selected and divided into a control group and an experiment group (58 cases in each group) by random number table method for the study. The patients in the experiment group were treated with CT imaging big data-assisted arterial chemoembolization combined with ^{125}I seed implantation, while the patients in the control group were treated with arterial chemoembolization alone, with the use of gemcitabine combined with cisplatin (GP) in chemotherapy. The prognostic impact was determined by analyzing recent efficacy; the incidence of adverse effects; tumor size and CT perfusion parameters including blood volume (BV), blood flow (BF), and permeability surface (PS); frailty state and quality of life; and the levels of serum tumor markers including carcinoembryonic antigen (CEA), glycoconjugate antigen 125 (CA125), cytokeratin 19 fragment antigen 21-1 (CYFRA21-1), microRNA- (miRNA-) 137, and miR-379-5p. In addition, frailty status was evaluated using the Fried frailty phenotype (FP) scale, and quality of life was determined according to Karnofsky Performance Status (KPS) score. Kaplan-Meier (KM) method was used to analyze the survival rate of NSCLC patients after a 12-month follow-up. **Results.** The remission rate in the experiment group (77.59%) was higher than that in the control group (56.90%) ($P < 0.05$). Tumor size, BV, BF, PS, serum CEA and CA125 levels, and FP value in both groups were dramatically reduced after treatment compared with before treatment, especially in the experiment group after 1 and 3 months of treatment ($P < 0.05$). Meanwhile, the serum miR-137 and miR-379-5p levels and KPS scores in both groups were higher after treatment than before treatment, especially in the experiment group after 1 and 3 months of treatment ($P < 0.05$). However, there was no significant difference in the incidence of nausea and vomiting, alopecia, diarrhea, myelosuppression, and hemoptysis of NSCLC patients in both groups after treatment ($P > 0.05$). Further, the 12-month survival rate of NSCLC patients was higher in the experiment group (84.21%) than in the control group (64.29%) ($P < 0.05$). **Conclusion.** CT imaging big data-assisted arterial chemoembolization combined with ^{125}I seed implantation for NSCLC can improve recent efficacy and the prognosis of NSCLC patients by inhibiting tumor progression with a certain degree of safety.

1. Introduction

Lung cancer is a malignant cancer that ranks first in mortality for both sexes among various cancers, posing a heavy burden to human health [1]. According to cancer statistics in 2015, 733,000 people were diagnosed with lung cancer, and 610,000 patients with lung cancer died in China [2].

As investigated by the American Society for Cancer Investigation (ASCI) in 2019, lung cancer ranks second in morbidity among all cancers and first in mortality among the top ten malignant cancers [3]. Non-small-cell lung cancer (NSCLC), a subtype of lung cancers, accounts for more than 80% of lung cancers [4]. Most of patients are diagnosed with NSCLC at the intermediate and advanced stage, and the

opportunity for surgical treatment is missed, resulting in a poor prognosis [5].

The first-line treatment for NSCLC is chemotherapy [6]. Arterial chemoembolization has been widely used in clinical practice because of its good efficacy in treating NSCLC and advantages of less trauma and less toxic side effects compared with intravenous systemic chemotherapy [7]. In recent years, minimally invasive interventional therapy for solid tumors is developing rapidly. For example, iodine 125 (^{125}I) seed implantation can accurately and continuously inhibit tumor cell proliferation, achieving the purpose of eliminating tumors [8]. Accurate surgical operation is an important guarantee for good efficacy for arterial chemoembolization and ^{125}I seed implantation. A previous report indicated that computed tomography (CT) imaging data served key roles in guiding noninvasive decision support of NSCLC therapy [9]. Nevertheless, there is no data on the prognostic impact of CT imaging big data-assisted arterial chemoembolization combined with ^{125}I seed implantation on NSCLC patients, which would be assessed in the present study with the hope of providing new therapeutic tactics for NSCLC.

2. Materials and Methods

2.1. NSCLC Patients and Pathological Features. A total of 116 patients with intermediate and advanced NSCLC hospitalized in our hospital from August 2019 to August 2020 were selected and divided into a control group and an experiment group (58 cases in each group) by the random number table method after obtaining approval from the Ethics Committee of our hospital. The pathological features of NSCLC patients are shown in Table 1. Tumor-node-metastasis (TNM) classification for lung cancer patients was conducted according to the reported method [10].

2.2. Inclusion and Exclusion Criteria for NSCLC Patients. Inclusion criteria are listed as follows: (i) patients diagnosed with NSCLC according to the diagnostic procedures [11], (ii) patients with stage III-IV NSCLC, (iii) patients undergoing initial treatment, (iv) patients whose Karnofsky Performance Status (KPS) score ≥ 70 and survival rate > 6 months, (v) patients who had no contraindications for the drugs related to the study, and (vi) patients signing the written informed consent. Exclusion criteria are as follows: (i) patients with the mental disease(s); (ii) patients with metabolic disorders like diabetes, hyperglycemia, and hyperosmolar syndromes; (iii) patients with cardiovascular and cerebrovascular diseases, liver dysfunction, and kidney dysfunction; (iv) patients diagnosed with other cancers; and (v) patients with blood system diseases and autoimmune diseases.

2.3. Methods. The NSCLC patients in the experiment groups were treated with CT imaging big data-assisted arterial chemoembolization combined with ^{125}I seed implantation according to the following methods. Firstly, the NSCLC patients were subjected to chest CT plain scanning and enhanced chest CT scanning using an Aquilion One 320

slice CT scanner (Toshiba, Tokyo, Japan) to identify the location and scope of the lesion. Then, 5F catheter-sheath was inserted into the femoral artery by percutaneous puncture using Seldinger's technique, and 3~8 mL iohexol (320 mg/mL) was injected into the cubital vein at a rate of 1~2 mL/s to perform bronchial arteriography with puncture intubation using 5F Cobra catheter to identify the artery supplying the lesion. Afterward, the artery was administered with 1.0 g/m² gemcitabine (SFDA approval number: H20183448; Nanjing Pharmaceutical Factory, Nanjing, China) and 60~90 mg cisplatinum (CDDP; SFDA approval number: H20183341; Guangdong Lingnan Pharmaceutical Company, Guangdong, China) by puncture intubation. After 3~5 days of arterial chemoembolization, CT scanning was carried out using a radioactive particle treatment planning system (TPS) (HGGR-3000; Hokai, Zhuhai, China), and the images were transmitted to TPS to accurately delineate the tumor volume and calculate the number of ^{125}I radioactive seeds, the distribution of seeds, and the layout of the puncture needles. According to the formulated individualized treatment plan provided by TPS, the implantation of ^{125}I seed ($1.48 \times 10^7 \sim 2.96 \times 10^7$ MBp/seed; Tianjin Saide Biotechnology, Shanghai) into the edge of the central tumor was conducted using implant guns (Tianjin Saide Biotechnology). The patients in the control group were treated with arterial chemoembolization alone with the same treatment method and chemotherapy plan as the experiment group.

2.4. Measurement of Indexes

2.4.1. Recent Efficacy. Recent efficacy was evaluated by calculating the sum of the longest diameters of target lesions according to the Response Evaluation Criteria in Solid Tumors 1.1 (RECIST 1.1) [12] after 3 months of treatment. An increase by $\geq 20\%$ is considered as progression or the presence of new lesions; an increase of $< 20\%$ or a decrease of $< 30\%$ in the sum is considered as stability or no new appeared lesions. A reduction of $\geq 30\%$ in the sum is considered a partial remission. Complete remission is considered when the target lesion is largely gone and sustained for more than 4 weeks. Remission rate was calculated according to the formula that remission rate = (complete remission + partial remission)/total number of cases $\times 100\%$.

2.4.2. Tumor Size and CT Perfusion Parameters. The analysis of tumor size and CT perfusion parameters including blood volume (BV), blood flow (BF), and permeability surface (PS) was performed before treatment and after 1 and 3 months of treatment.

2.4.3. Serum Tumor Markers. Venous blood was collected from NSCLC patients before treatment or after 1 and 3 months of treatment, and the serum was collected by centrifuging at 350 r/min for 5 min. Then, we analyzed the levels of carcinoembryonic antigen (CEA) and carbohydrate antigen 125 (CA125) in serum by chemiluminescence immunoassay kits (ZECEN, Taizhou, China) as per the guidebook. Serum microRNA-137 (miRNA-137) and miR-379-5p expression were quantified by quantitative real-time polymerase chain reaction (qRT-PCR) with SYBR® Premix

TABLE 1: Comparison of general information between the two groups ($(\bar{x} \pm s)/n$ (%)).

Group	n	Gender (male/female)	Age (year)	Body mass index (kg/m ²)	TNM staging		Pathological typing		Cancer site		
					III period	IV period	Adenocarcinoma	Squamous carcinoma	Upper section	Middle section	Lower paragraph
Research group	58	38/20	41~76 (57.24 ± 7.52)	18.8 ~ 26.4 (23.15 ± 1.62)	37 (63.79)	21 (36.21)	42 (72.41)	16 (27.59)	12 (20.69)	27 (46.55)	19 (32.76)
Control group	58	33/25	38~75 (55.86 ± 8.10)	19.1 ~ 26.8 (23.46 ± 1.59)	40 (68.97)	18 (31.03)	45 (77.59)	13 (22.41)	10 (17.24)	31 (53.45)	17 (29.31)
χ^2/t		0.908	0.951	1.010		0.348		0.414			0.569
P		0.341	0.344	0.301		0.555		0.520			0.753

TABLE 2: Comparison of recent outcomes between the two groups (n (%)).

Group	n	Progress	Stable	Partial relief	Complete relief	Mitigation rate
Research group	58	3 (5.17)	10 (17.24)	31 (53.45)	14 (24.14)	45 (77.59)
Control group	58	7 (12.07)	18 (31.03)	25 (43.10)	8 (13.79)	33 (56.90)
χ^2						5.636
P						0.018

Ex Taq™ kit (TaKaRa, Dalian, China) and analyzed by the $2^{-\Delta\Delta Ct}$ method.

2.4.4. Frailty State and Quality of Life. Frailty state and quality of life of NSCLC patients were evaluated before treatment or after 1 and 3 months of treatment. Fried frailty phenotype (FP) scale [13] was used to evaluate frailty status, including fatigue, low physical activity, decreased grip strength, body mass, and walking speed.

2.5. Untoward Effects including the Incidence of Nausea and Vomiting, Alopecia, Diarrhea, Myelosuppression, and Hemoptysis

2.5.1. Survival Rate. The survival rate of NSCLC patients was analyzed by Kaplan-Meier (KM) method after a 12-month follow-up.

2.6. Statistical Analysis. Data were analyzed using the SPSS 22.0 software. Significant difference for attribute data was compared using χ^2 test. The results of variables data were shown as means \pm standard deviations. The comparisons between the two groups were performed using unpaired Student's t -tests or paired Student's t -tests. Log-rank test was used for comparing difference in Kaplan-Meier methods. $P < 0.05$ indicated statistical significance.

3. Results

3.1. Recent Efficacy. The remission rate was higher in the experiment group than in the control group after 3 months of treatment ($P < 0.05$), and the results are shown in Table 2.

3.2. Tumor Size and CT Perfusion Parameters. There was no difference in tumor size, BV, BF, and PS in the two groups before treatment ($P > 0.05$) (Table 3). But tumor size, BV, BF, and PS were dramatically reduced in both groups after treatment compared with before treatment, especially in the experiment group after 1 and 3 months of treatment ($P < 0.05$) (Table 3). CT images of typical cases are shown in Figures 1 and 2.

3.3. Serum Tumor Markers. There was no difference in serum CEA, CA125, miR-137, and miR-379-5p expression levels in the two groups before treatment (Table 4). But serum CEA and CA125 levels were dramatically reduced in both groups after treatment compared with before treatment, especially in the experiment group after 1 and 3 months of treatment ($P < 0.05$) (Table 4). Serum miR-137 and miR-379-5p expression had the opposite results (Table 4).

3.4. Frailty State and Quality of Life. There was no difference in FP and KPS in the two groups before treatment (Table 5). But FP was dramatically reduced in both groups after treatment compared with before treatment, especially in the experiment group after 1 and 3 months of treatment ($P < 0.05$) (Table 5). KPS had the opposite results (Table 5).

3.5. Untoward Effect. There was no significant difference in the incidence of nausea and vomiting, alopecia, diarrhea, myelosuppression, and hemoptysis of NSCLC patients in both groups ($P > 0.05$) (Table 6).

3.6. Survival Rate of NSCLC Patients. During the 12-month follow-up, one case in the experiment group was lost to follow-up (the 10th month after treatment), and 2 cases in the control group were lost to follow-up (the 7th and 9th months after treatments). The results showed that 48 patients survived and 9 cases died in the experiment group, with an 84.21% of survival rate (Figure 3(a)). In the control group, 36 patients survived and 20 cases died in the control group, with a 64.29% of survival rate (Figure 3(b)).

4. Discussion

CT has a high resolution for density and space and is not interfered by surrounding gas and adipose tissue, thus having great application value in NSCLC diagnosis, preoperative evaluation, and follow-up. A previous investigation has explained that valuable information about NSCLC tumor phenotypes can be acquired according to CT-based radiomic signature, thereby guiding NSCLC therapy [14].

Gemcitabine combined with cisplatin (GP chemotherapy) is required for the standard chemotherapy regimen for NSCLC [6]. Intravenous systemic chemotherapy has the disadvantage of greater systemic toxicity and side effects, leading to poor tolerance of NSCLC patients, thus causing poor chemotherapy efficacy. Compared with intravenous systemic chemotherapy, arterial chemoembolization can directly inject chemotherapy drugs into the tumor area, which can make the lesion keep high concentrations of chemotherapy drugs, thereby killing tumor cells more effectively, not affecting systemic blood concentration and liver metabolism, and helping to reduce adverse reactions [15]. The present study showed that CT imaging big data achieved good therapeutic effects in resisting arterial chemoembolization for NSCLC patients. It is because that CT scanning is helpful in puncture based on its accurate determination of the location and scope of the lesion and the artery supplying the lesion and thus ensures the accurate injection of chemotherapy drugs into the target lesion as well

TABLE 3: Comparison of tumor size and CT perfusion parameters before and after treatment between the two groups ($\bar{x} \pm s$).

Time	Group	<i>n</i>	Tumor size (cm ²)	BV (mL/100 g)	BF (mL/(min·100 g))	PS (mL/(min·100 g))
Before treatment	Research group	58	35.18 ± 5.74	9.16 ± 3.01	54.26 ± 16.85	23.50 ± 6.82
	Control group	58	33.46 ± 5.39	8.57 ± 2.82	52.07 ± 17.12	22.74 ± 6.49
	<i>t</i>		1.664	1.089	0.694	0.615
	<i>P</i>		0.099	0.278	0.489	0.540
1 month after treatment	Research group	58	25.71 ± 4.52 ^a	6.15 ± 1.97 ^a	28.15 ± 9.11 ^a	15.43 ± 3.78 ^a
	Control group	58	28.27 ± 4.86 ^a	7.22 ± 2.30 ^a	35.22 ± 10.35 ^a	17.76 ± 4.01 ^a
	<i>t</i>		2.938	2.691	3.905	3.220
	<i>P</i>		0.004	0.008	<0.001	0.002
3 months after treatment	Research group	58	19.05 ± 3.68 ^a	4.47 ± 1.48 ^a	19.49 ± 6.15 ^a	12.95 ± 3.29 ^a
	Control group	58	22.76 ± 4.07 ^a	6.23 ± 1.82 ^a	26.23 ± 8.17 ^a	15.52 ± 3.50 ^a
	<i>t</i>		5.149	5.714	5.020	4.075
	<i>P</i>		<0.001	<0.001	<0.001	<0.001

Note: compared with the same group before treatment, ^a*P* < 0.05.

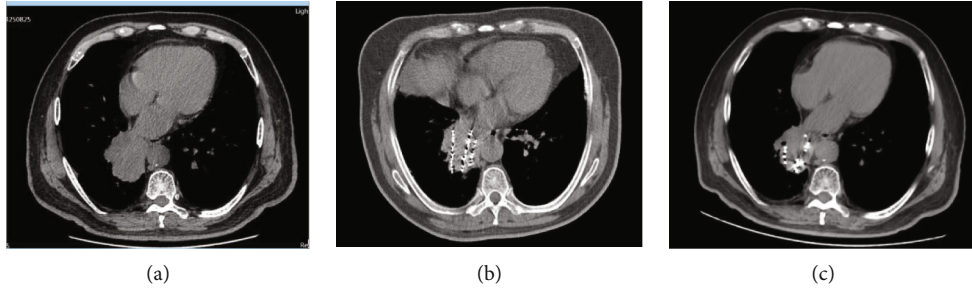


FIGURE 1: CT images of NSCLC patients in the control group before and after treatment. Patient Zhang XX, male, 70 years old, right lung squamous cell carcinoma, CT images before and after chemoembolization combined with ¹²⁵I seed implantation. (a) Before treatment; (b) 1 month after treatment; (c) 3 months after treatment. Overall evaluation: partial relief.

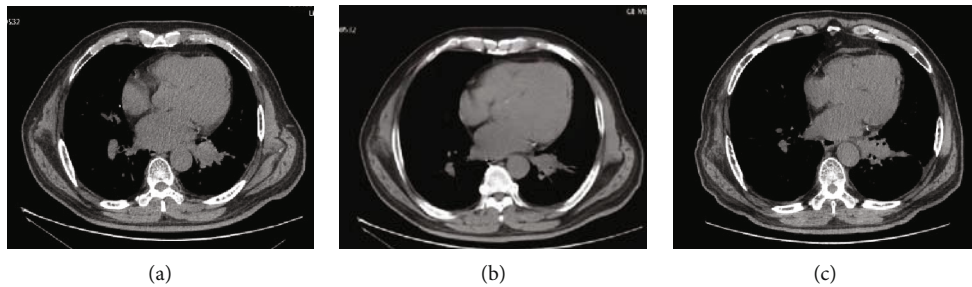


FIGURE 2: CT images of NSCLC patients in the experiment group before and after treatment. Patient Zhuang XX, male, 66 years old, left lung squamous cell carcinoma, CT images before and after bronchial arterial chemoembolization. (a) Before treatment; (b) 1 month after treatment; (c) 3 months after treatment. Overall evaluation: partial relief.

as the accurate killing of chemotherapy drugs to tumor cells, so as to achieve good chemotherapy effects [16]. Although arterial chemoembolization is an effective therapeutic method for NSCLC, the efficacy of chemotherapy alone is limited to a certain extent.

Radiotherapy includes external radiotherapy and internal radiotherapy, in which external radiotherapy is limited by the tolerance dose of lung tissues and its surrounding organs, resulting in a poor radiotherapy effect. Comparatively,

internally, internal radiotherapy can place radioactive substances into the lesions to achieve the purpose of precise radiotherapy and can greatly increase the dose of local radiotherapy to achieve a better radiotherapy effect. At present, the commonly used internal radiotherapy is ¹²⁵I seed implantation. ²⁵I seed implantation has been widely used to treat solid tumors, such as unresectable pancreatic cancer and NSCLC because it is almost not limited by the location and size of the lesions [17, 18]. Our data showed that the recent efficacy

TABLE 4: Comparison of serum indexes before and after treatment between the two groups ($\bar{x} \pm s$).

Time	Group	<i>n</i>	CEA (ng/mL)	CA125 (kU/L)	miR-137	miR-379-5p
Before treatment	Research group	58	90.12 ± 15.38	75.62 ± 8.39	0.44 ± 0.08	0.40 ± 0.07
	Control group	58	88.67 ± 14.76	74.13 ± 8.21	0.46 ± 0.07	0.42 ± 0.08
	<i>t</i>		0.518	0.967	1.433	1.433
	<i>P</i>		0.605	0.336	0.155	0.155
1 month after treatment	Research group	58	42.87 ± 8.62 ^a	53.16 ± 7.40 ^a	0.58 ± 0.10 ^a	0.55 ± 0.09 ^a
	Control group	58	51.06 ± 9.54 ^a	60.33 ± 8.05 ^a	0.53 ± 0.08 ^a	0.49 ± 0.08 ^a
	<i>t</i>		4.851	4.994	2.974	3.795
	<i>P</i>		<0.001	<0.001	0.004	<0.001
3 months after treatment	Research group	58	29.17 ± 5.78 ^a	44.38 ± 6.57 ^a	0.63 ± 0.11 ^a	0.61 ± 0.12 ^a
	Control group	58	36.42 ± 6.59 ^a	51.23 ± 7.18 ^a	0.55 ± 0.10 ^a	0.55 ± 0.10 ^a
	<i>t</i>		6.299	5.360	4.098	3.925
	<i>P</i>		<0.001	<0.001	<0.001	0.004

Note: compared with the same group before treatment, ^a*P* < 0.05.

TABLE 5: Comparison of debilitating status and quality of survival before and after treatment between the two groups ($\bar{x} \pm s$, points).

Time	Group	<i>n</i>	FP	KPS
Before treatment	Research group	58	4.05 ± 0.68	78.39 ± 4.56
	Control group	58	4.01 ± 0.65	79.12 ± 5.10
	<i>t</i>		0.234	0.813
	<i>P</i>		0.747	0.418
1 month after treatment	Research group	58	3.18 ± 0.50 ^a	85.21 ± 4.73 ^a
	Control group	58	3.49 ± 0.53 ^a	82.54 ± 4.60 ^a
	<i>t</i>		3.240	3.082
	<i>P</i>		0.002	0.003
3 months after treatment	Research group	58	2.09 ± 0.42 ^a	89.74 ± 5.12 ^a
	Control group	58	2.45 ± 0.47 ^a	86.31 ± 4.89 ^a
	<i>t</i>		4.350	3.690
	<i>P</i>		<0.001	<0.001

Note: compared with the same group before treatment, ^a*P* < 0.05.

of CT imaging big data-assisted arterial chemoembolization combined with ¹²⁵I seed implantation for NSCLC was higher than arterial chemoembolization alone, without significantly increasing the incidence of adverse reactions, suggesting that the combination treatment can effectively inhibit NSCLC progression. The reason for the results may be that ¹²⁵I radioactive seeds are a kind of long half-life particles and can emit continuously low energy gamma rays, which can enhance the self-sensitization of the tumor cells and improve the sensitivity and killability of cancer cells, thus greatly improving treatment effect [19, 20].

In addition, the accurate implantation of ¹²⁵I radioactive particles is important for therapy. CT image big data can guide the use of ¹²⁵I radioactive particles and puncture needles and can accurately show the distribution of ¹²⁵I radioactive seeds in the tumor after implantation, so as to ensure the therapeutic effect. Moreover, CT can measure tumor size and CT perfusion parameters [21], which can quantitatively

reflect the microvessel density and blood flow velocity inside the tumor and thus is important to lung cancer therapy. In the present work, we found that CT imaging big data-assisted arterial chemoembolization combined with ¹²⁵I seed implantation had advantages in repressing tumor growth and reducing CT perfusion parameters including BV, BF, and PS, further indicating that the combined treatment could enhance the recent efficacy of transarterial chemoembolization combined with ¹²⁵I seed implantation. Recent data have demonstrated that serum tumor markers play key parts in evaluating the efficacy of NSCLC treatment. As reported, CEA and CA125 levels were dramatically increased in the serum of NSCLC patients but presented decreasing trends after the tumors were effectively controlled [22]. In addition, the upregulation of miR-137, a cancer-related miRNA, can inhibit cancer cell proliferation and induce cell apoptosis [23]. miR-379-5p is reduced in NSCLC tissues and cells and induces NSCLC cell proliferation

TABLE 6: Comparison of the occurrence of adverse reactions between the two groups (n (%)).

Group	n	Nausea and vomiting	Hair loss	Diarrhea	Bone marrow suppression	Hemoptysis
Research group	58	26 (44.83)	15 (25.86)	9 (15.52)	22 (37.93)	17 (29.31)
Control group	58	21 (36.21)	11 (18.97)	6 (10.34)	19 (32.76)	10 (17.24)
χ^2		0.894	0.793	0.689	0.340	2.365
P		0.344	0.373	0.407	0.560	0.124

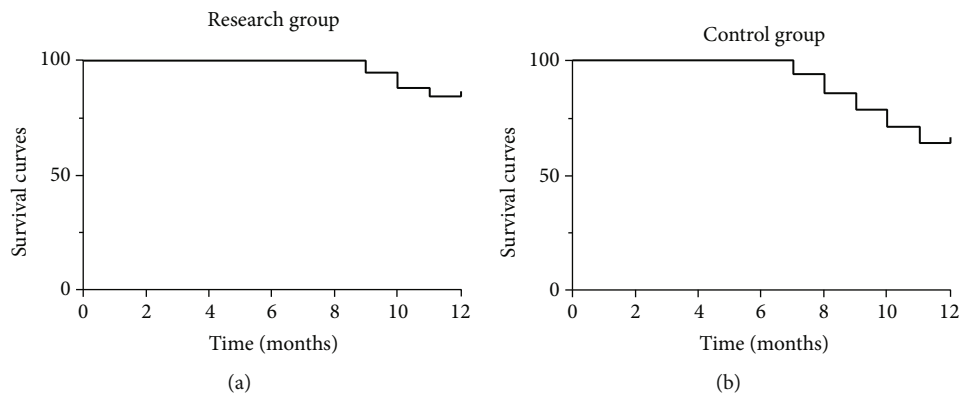


FIGURE 3: Survival rate analysis of NSCLC patients after 12-month follow-up.

inhibition and apoptosis promotion through interaction with β -arrestin-1, thus considered a therapeutic target for NSCLC [24]. In this work, CEA, CA125, miR-137, and miR-379-5p were employed to analyze the recent efficacy of CT imaging big data-assisted arterial chemoembolization combined with ^{125}I seed implantation for NSCLC patients. The results showed that the combination therapy could decrease CEA and CA125 levels and increase miR-137 and miR-379-5p levels in the serum of NSCLC patients. Further, the combination therapy can effectively inhibit tumor progression, improve the quality of life, reduce the frailty state, and improve the survival rate of NSCLC patients. Thus, the combination therapy is a reliable method to improve the recent efficacy and long-term prognosis of NSCLC patients.

Taken together, CT imaging big data-assisted arterial chemoembolization combined with ^{125}I seed implantation for NSCLC can reduce lesion blood perfusion, lesion volume, and serum CEA and CA125 levels and increase serum miR-137 and miR-379-5p levels to inhibit cancer progression, thereby improving short-term efficacy and long-term prognosis of NSCLC patients. However, a limitation should be considered when evaluating the present study. For example, the number of NSCLC patients (sample size) is small in the study, which may affect the results of the study to some extent. The limitation will be addressed in the following study.

Data Availability

The labeled dataset used to support the findings of this study are available from the corresponding author upon request.

Conflicts of Interest

The authors declare no competing interests.

Acknowledgments

This study is sponsored by the Sixth Medical Center of PLA General Hospital.

References

- [1] B. C. Bade and C. S. Dela Cruz, "Lung cancer 2020: epidemiology, etiology, and prevention," *Clinics in Chest Medicine*, vol. 41, no. 1, pp. 1–24, 2020.
- [2] W. Chen, R. Zheng, P. D. Baade et al., "Cancer statistics in China, 2015," *CA: a Cancer Journal for Clinicians*, vol. 66, no. 2, pp. 115–132, 2016.
- [3] R. L. Siegel, K. D. Miller, and A. Jemal, "Cancer statistics, 2019," *CA: a Cancer Journal for Clinicians*, vol. 69, no. 1, pp. 7–34, 2019.
- [4] Z. Chen, C. M. Fillmore, P. S. Hammerman, C. F. Kim, and K.-K. Wong, "Non-small-cell lung cancers: a heterogeneous set of diseases," *Nature Reviews. Cancer*, vol. 14, no. 8, pp. 535–546, 2014.
- [5] M. Alexander, S. Y. Kim, and H. Cheng, "Update 2020: management of non-small cell lung cancer," *Lung*, vol. 198, no. 6, pp. 897–907, 2020.
- [6] M. Reck, G. Shankar, A. Lee et al., "Atezolizumab in combination with bevacizumab, paclitaxel and carboplatin for the first-line treatment of patients with metastatic non-squamous non-small cell lung cancer, including patients with EGFR mutations," *Expert Review of Respiratory Medicine*, vol. 14, no. 2, pp. 125–136, 2020.

- [7] J. Liu, W. Zhang, J. Ren et al., "Efficacy and safety of drug-eluting bead bronchial arterial chemoembolization plus anlotinib in patients with advanced non-small-cell lung cancer," *Frontiers in Cell and Development Biology*, vol. 9, article 768943, 2021.
- [8] Y. Feng, B. Yang, and X. Li, "Clinical analysis of 125I seed implantation combined with apatinib in the treatment of locally advanced lung cancer: a case series," *The Journal of the Pakistan Medical Association*, vol. 71, no. 3, pp. 1025–1027, 2021.
- [9] W. Mu, L. Jiang, J. Zhang et al., "Non-invasive decision support for NSCLC treatment using PET/CT radiomics," *Nature Communications*, vol. 11, no. 1, p. 5228, 2020.
- [10] R. Rami-Porta, V. Bolejack, J. Crowley et al., "The IASLC lung cancer staging project: proposals for the revisions of the T descriptors in the forthcoming eighth edition of the TNM classification for lung cancer," *Journal of Thoracic Oncology*, vol. 10, no. 7, pp. 990–1003, 2015.
- [11] M. Dietel, L. Bubendorf, A. M. Dingemans et al., "Diagnostic procedures for non-small-cell lung cancer (NSCLC): recommendations of the European Expert Group," *Thorax*, vol. 71, no. 2, pp. 177–184, 2016.
- [12] L. H. Schwartz, S. Litière, E. De Vries et al., "RECIST 1.1—update and clarification: from the RECIST committee," *European journal of cancer*, vol. 62, no. 62, pp. 132–137, 2016.
- [13] J. B. Segal, H. Y. Chang, Y. Du, J. D. Walston, M. C. Carlson, and R. Varadhan, "Development of a claims-based frailty indicator anchored to a well-established frailty phenotype," *Medical Care*, vol. 55, no. 7, pp. 716–722, 2017.
- [14] H. Li, R. Zhang, S. Wang et al., "CT-based radiomic signature as a prognostic factor in stage IV ALK-positive non-small-cell lung cancer treated with TKI crizotinib: a proof-of-concept study," *Frontiers in Oncology*, vol. 10, p. 57, 2020.
- [15] Y. M. Li, R. Q. Guo, Z. X. Bie, B. Li, and X. G. Li, "Sintilimab plus bronchial arterial infusion chemotherapy/drug-eluting embolic chemoembolization for advanced non-small cell lung cancer: a preliminary study of 10 patients," *Journal of Vascular and Interventional Radiology*, vol. 32, no. 12, pp. 1679–1687, 2021.
- [16] C. Chen, W. Wang, Z. Yu, S. Tian, Y. Li, and Y. Wang, "Combination of computed tomography-guided iodine-125 brachytherapy and bronchial arterial chemoembolization for locally advanced stage III non-small cell lung cancer after failure of concurrent chemoradiotherapy," *Lung Cancer*, vol. 146, pp. 290–296, 2020.
- [17] M. Luo, J. Chen, Z. Zhong, and F. Zhang, "CT-guided 125I brachytherapy combined with chemotherapy for the treatment of unresectable or locally advanced pancreatic carcinoma," *Diagnostic and Interventional Radiology*, vol. 27, no. 1, pp. 50–58, 2021.
- [18] X. Wang and D. Wang, "Clinical analysis of 125I seed implantation combined with epidermal growth factor receptor-tyrosine kinase inhibitors in advanced non-small cell lung cancer," *Journal of BUON*, vol. 26, no. 5, pp. 1879–1886, 2021.
- [19] D. Y. Yang, Y. P. Lin, C. Xue et al., "CT-guided percutaneous implantation of (125) I particles in treatment of early lung cancer," *Journal of Thoracic Disease*, vol. 12, no. 10, pp. 5996–6009, 2020.
- [20] E. Chen, J. Wang, H. Zhang et al., "Analysis of the efficacy and safety of iodine-125 seeds implantation in the treatment of patients with inoperable early-stage non-small cell lung cancer," *Journal of Contemporary Brachytherapy*, vol. 13, no. 3, pp. 347–357, 2021.
- [21] S. Rajaian, A. S. Paulraj, and L. Murugesan, "Solitary neurofibroma of seminal vesicle," *Journal of Postgraduate Medicine*, vol. 65, no. 2, pp. 121–122, 2019.
- [22] Z. Li and J. Zhao, "Clinical efficacy and safety of crizotinib and alectinib in ALK-positive non-small cell lung cancer treatment and predictive value of CEA and CA125 for treatment efficacy," *American Journal of Translational Research*, vol. 13, no. 11, pp. 13108–13116, 2021.
- [23] S. Nuzzo, S. Catuogno, M. Capuozzo et al., "Axl-targeted delivery of the oncosuppressor miR-137 in non-small-cell lung cancer," *Molecular Therapy-Nucleic Acids*, vol. 17, pp. 256–263, 2019.
- [24] Y. Jiang, P. Zhu, Y. Gao, and A. Wang, "miR-379-5p inhibits cell proliferation and promotes cell apoptosis in non-small cell lung cancer by targeting β -arrestin-1," *Molecular Medicine Reports*, vol. 22, no. 6, pp. 4499–4508, 2020.

Retraction

Retracted: Risk Factors of Acute Radiation-Induced Lung Injury Induced by Radiotherapy for Esophageal Cancer

Computational and Mathematical Methods in Medicine

Received 26 September 2023; Accepted 26 September 2023; Published 27 September 2023

Copyright © 2023 Computational and Mathematical Methods in Medicine. This is an open access article distributed under the Creative Commons Attribution License, which permits unrestricted use, distribution, and reproduction in any medium, provided the original work is properly cited.

This article has been retracted by Hindawi following an investigation undertaken by the publisher [1]. This investigation has uncovered evidence of one or more of the following indicators of systematic manipulation of the publication process:

- (1) Discrepancies in scope
- (2) Discrepancies in the description of the research reported
- (3) Discrepancies between the availability of data and the research described
- (4) Inappropriate citations
- (5) Incoherent, meaningless and/or irrelevant content included in the article
- (6) Peer-review manipulation

The presence of these indicators undermines our confidence in the integrity of the article's content and we cannot, therefore, vouch for its reliability. Please note that this notice is intended solely to alert readers that the content of this article is unreliable. We have not investigated whether authors were aware of or involved in the systematic manipulation of the publication process.

In addition, our investigation has also shown that one or more of the following human-subject reporting requirements has not been met in this article: ethical approval by an Institutional Review Board (IRB) committee or equivalent, patient/participant consent to participate, and/or agreement to publish patient/participant details (where relevant).

Wiley and Hindawi regrets that the usual quality checks did not identify these issues before publication and have since put additional measures in place to safeguard research integrity.

We wish to credit our own Research Integrity and Research Publishing teams and anonymous and named external researchers and research integrity experts for contributing to this investigation.

The corresponding author, as the representative of all authors, has been given the opportunity to register their agreement or disagreement to this retraction. We have kept a record of any response received.

References

- [1] F. Zhang, L. Liao, S. Wei, and Y. Lu, "Risk Factors of Acute Radiation-Induced Lung Injury Induced by Radiotherapy for Esophageal Cancer," *Computational and Mathematical Methods in Medicine*, vol. 2022, Article ID 2416196, 6 pages, 2022.

Research Article

Risk Factors of Acute Radiation-Induced Lung Injury Induced by Radiotherapy for Esophageal Cancer

Faen Zhang , Lihua Liao, Song Wei, and Yuqing Lu

Department of Oncology, The People's Hospital of Hechi, Guangxi 547000, China

Correspondence should be addressed to Faen Zhang; zhanfae@163.com

Received 24 May 2022; Revised 28 June 2022; Accepted 4 July 2022; Published 13 July 2022

Academic Editor: Pan Zheng

Copyright © 2022 Faen Zhang et al. This is an open access article distributed under the Creative Commons Attribution License, which permits unrestricted use, distribution, and reproduction in any medium, provided the original work is properly cited.

Objective. To investigate the risk factors of acute radiation-induced lung injury (acute RILI) induced by radiotherapy for esophageal cancer. **Methods.** A total of 206 patients with esophageal cancer who received radiotherapy in our hospital from January 2017 to March 2020 were selected. The general data such as gender, age, and comorbidities of the patients were collected, as well as the levels of cytokines (TNF- α , TNF- β , and IL-6) in peripheral blood before radiotherapy; radiotherapy dose-related parameters were recorded during radiotherapy. Follow-up was 12 months after radiotherapy. The patients with induced acute RILI after radiotherapy were set as the observation group ($n=75$). Patients without acute RILI after radiotherapy were set as the control group ($n=131$). Univariate and multivariate logistic regression analysis was performed on the risk factors of acute RILI induced by radiotherapy for esophageal cancer. **Results.** Univariate analysis and multivariate logistic regression analysis showed that the combined diabetes, total radiation dose, combined lung disease, physical factors (V30, Dmean), and preradiotherapy cytokine (TNF- α , TNF- β , and IL-6) elevated level was an independent risk factor for radiotherapy-induced acute RILI in esophageal cancer ($P < 0.05$). **Conclusion.** Concomitant diabetes, total radiation dose, lung disease, physical factors (V30, Dmean), and levels of cytokines (TNF- α , TNF- β , and IL-6) before radiation therapy are risk factors for acute RILI induced by radiation therapy in esophageal cancer. The possibility of acute RILI should be comprehensively assessed according to the patient's condition, and the radiotherapy regimen should be adjusted to reduce and avoid the induction of acute radiation-induced lung injury.

1. Introduction

Esophageal cancer is a malignant tumor that occurs in the esophageal epithelium. Its typical manifestation is progressive aggravating dysphagia, which is one of the main malignant tumors that threaten the health of residents [1]. The incidence and mortality of esophageal cancer vary widely in different countries, and China is a country with a high incidence of esophageal cancer and one of the countries with a high mortality rate of esophageal cancer in the world [2]. There are gender, age, and regional differences in the incidence of esophageal cancer. The prevalence and mortality of esophageal cancer in men are higher than those in women, and the peak age of incidence is 45-80 years old. The incidence of esophageal cancer in rural areas is higher

than that in urban areas [3]. The preferred method of treatment for early-stage esophageal cancer is surgery. Once a patient with esophageal cancer is diagnosed, surgical treatment should be performed when physical conditions permit. Combined radiotherapy and surgery can increase surgical resection rate and improve long-term survival rate [4]. However, radiation therapy easily damages the normal lung tissue within the radiation field, which in turn causes an inflammatory response in the body, resulting in acute radiation lung injury (acute RILI) [5]. Acute RILI not only affects the efficacy of radiotherapy but also reduces the quality of life of patients and even leads to death of patients. At present, the risk factors of acute RILI induced by radiotherapy for esophageal cancer have not been fully clarified, and there may be regional differences. Therefore, this study explored

the risk factors of acute RILI induced by radiotherapy for esophageal cancer in Hechi City, Guangxi, and was aimed at finding an effective preventive method for acute RILI.

2. Materials and Methods

2.1. General Information. A total of 206 patients with esophageal cancer who received radiotherapy at the People's Hospital of Hechi from January 2017 to March 2020 were selected. Inclusion criteria were as follows: (1) patients with complete medical records and meeting the diagnostic criteria for esophageal cancer [6]; (2) patients who completed the first radiotherapy and subsequent radiotherapy in the People's Hospital of Hechi; (3) Karnofsky performance score (KPS) ≥ 70 points and no vocal cord paralysis; and (4) computed tomography (CT) examination showed that the tumor did not invade the aorta or tracheobronchi and other adjacent tissues and organs, and there was no obvious external invasion. Exclusion criteria were as follows: (1) patients with contraindications to radiotherapy; (2) patients with major dysfunction of the heart, liver, kidney, lung, and other organs; (3) patients with distant metastasis or esophageal fistula; and (4) patients with mental disorders and uncooperative patients.

2.2. Research Methods. All patients were treated with a Varian Clinac CX type 4994 linear accelerator. The radiotherapy was completed by the professional radiation therapist giving the corresponding target dose according to the patient's dose prescription. Percentage of lung volume to total lung volume when both lungs received 5 Gy, 10 Gy, 20 Gy, 30 Gy, and 40 Gy irradiation (V5, V10, V20, V30, V40), average dose of bilateral lung irradiation (Dmean), and total dose of radiotherapy wait until the data was collected.

The general data of the patients were collected, including age, gender, tumor location, tumor stage, smoking history, diabetes, lung disease, concurrent chemotherapy, and KPS score.

Cytokine detection: 2 mL of peripheral blood was collected from patients on an empty stomach before radiotherapy and centrifuged at 2500 r/min for 15 min. The upper serum was taken and stored at -80°C after aliquoting. The serum levels of TNF- α , TNF- β , and IL-6 were detected by enzyme-linked immunosorbent assay using a 680 automatic enzyme analyzer (BIO-RAD, USA). The testing personnel strictly follow the instructions of the kit (Shanghai Enzyme Link Biotechnology Co., Ltd.) and the instrument to perform the testing operation: TNF- α kit item number: ml-E12414, TNF- β kit item number: ml-063192, and IL-6 kit item number: ml-E12436.

The patients were followed up for 3 months after radiotherapy. The patients with acute RILI induced by radiotherapy were set as the observation group, and the patients without acute RILI after radiotherapy were set as the control group.

2.3. Observation Indicators. Clinical data: age, gender, tumor location, tumor stage, smoking history, diabetes, lung disease, concurrent chemotherapy, and KPS score

Physical parameters: the percentage of lung volume in the total lung volume when both lungs were irradiated with 5 Gy, 10 Gy, 20 Gy, 30 Gy, and 40 Gy (V5, V10, V20, V30, and V40), the average dose of bilateral lung irradiation (Dmean), and total radiation dose

Cytokines: TNF- α , TNF- β , and IL-6 levels in peripheral blood serum before radiotherapy

KPS scoring standard: according to the patient's health status score, 10 points are a grade, and the highest score was 100 points. A score of ≥ 80 was classified as a nondependent level; that is, patients can take care of themselves; 50-70 was classified as a semidependent level; that is, patient requires partial care; a score below 50 was a dependent level; that is, patient is in complete need of care

Acute RILI evaluation criteria: evaluation of acute RILI according to Common Terminology Criteria for Adverse Events 4.0 (CTCAE v4.0). Lung injury within 3 months from the first day of radiotherapy was defined as acute RILI, so all patients were followed up for 3 months after IMRT. Repeat chest CT at follow-up. According to the American Radiation Therapy Oncology Group (RTOG) acute lung injury grading scale, (1) there were occasional cough and dyspnea or there were no obvious respiratory symptoms during exertion, and only X-ray showed that pulmonary inflammatory reaction was grade 1. (2) There were persistent cough and chest tightness, and it was necessary to use narcotic cough medicine to relieve cough, which was grade 2. (3) There was severe cough and chest tightness, and the symptoms cannot be relieved by narcotic cough medicine, and intermittent oxygen inhalation or glucocorticoid treatment was required for grade 3. (4) Difficulty in breathing, insufficiency of ventilation and ventilation, and continuous oxygen inhalation or assisted ventilation were grade 4

2.4. Data Processing. SPSS 23.0 software was used for data statistics, categorical data were expressed by number (percentage), and chi-square test was used for comparison between two groups. Continuous data were expressed as mean \pm standard deviation, and *t*-test was used for comparison between two groups. The general data of the two groups were analyzed by univariate analysis, and then, the logistic regression analysis was performed to find out the risk factors of acute radiation-induced lung injury induced by radiation therapy for esophageal cancer. Statistical difference was indicated by $P < 0.05$.

3. Results and Discussion

3.1. The Occurrence of Acute RILI in Patients with Esophageal Cancer after Radiotherapy. The follow-up results showed that after radiotherapy of 206 patients with esophageal cancer in this study, a total of 75 patients developed acute RILI, of which 55 patients had grade 1, 20 had grade 2, and no grade 3 or 4 appeared. The incidence of was 36.41%. 75 patients with acute RILI were included in the observation group, and the remaining 131 patients were included in the control group.

3.2. Univariate Analysis of Acute RILI Induced by Radiotherapy for Esophageal Cancer. Univariate analysis

showed that there were no significant differences in age, gender, tumor location, tumor stage, smoking history, concurrent chemotherapy, KPS score, V5, V10, V20, and V40 between the two groups ($P > 0.05$). There were significant differences in the levels of diabetes, total radiotherapy dose, lung disease, physical factors (V30, Dmean), and peripheral blood cytokines (TNF- α , TNF- β , and IL-6) before radiotherapy between the two groups ($P < 0.05$), as shown in Table 1.

3.3. Multivariate Analysis of Acute RILI Induced by Radiotherapy for Esophageal Cancer. Multivariate logistic regression analysis showed that diabetes, total radiotherapy dose, lung disease, physical factors (V30, Dmean) increased, and cytokines (TNF- α , TNF- β , and IL-6) levels before radiotherapy increased. It was an independent risk factor for acute RILI induced by radiotherapy for esophageal cancer ($P < 0.05$), as shown in Table 2.

3.4. Discussion. Squamous cell carcinoma and adenocarcinoma are more common in esophageal cancer. According to the location of the tumor center, it can be divided into cervical esophagus cancer, upper thoracic esophageal cancer, middle thoracic esophageal cancer, and lower thoracic esophageal cancer. Middle esophageal cancer is the most common in China, followed by lower esophageal cancer [7, 8]. Symptoms of esophageal cancer are swallowing obstruction and progressive increase. From choking on swallowing and difficulty in eating hard food, it gradually developed into difficulty in eating soft food and drinking water. Its etiology is relatively complex, and it is generally believed to be related to nitrosamines, long-term smoking and drinking, and poor eating habits, and it has a certain genetic susceptibility [9, 10]. In the treatment of early esophageal cancer, surgical resection is the first consideration for resectable esophageal cancer. However, the recurrence and metastasis rate of esophageal cancer after surgery is relatively high. Combined radiotherapy and surgery can increase the surgical resection rate and improve the long-term survival rate. Therefore, radiation therapy is the main treatment for patients with advanced disease [11, 12]. The efficacy of radiation therapy depends on the radiosensitivity, and the degree of response of different tissues and organs and various tumor tissues after exposure to radiation varies [13]. The radiosensitivity of lung tissue is high, and radiotherapy of esophageal cancer is prone to cause acute RILI complications. The clinical manifestations of acute RILI are dry cough with little sputum, dysphagia, chest tightness, and chest pain and in severe cases are dyspnea, low-grade fever, pulmonary congestion, increased alveolar fibrin exudation or formation of hyaline membranes, and finally pulmonary interstitial fibrosis [14, 15]. Acute RILI greatly affects the treatment effect and long-term survival rate of esophageal cancer and reduces the quality of life of patients. Therefore, how to prevent or reduce the concurrent acute RILI during radiotherapy for esophageal cancer has become an increasingly concerned issue for oncology workers.

The results of this study showed that V30, Dmean, and total radiotherapy dose were independent risk factors for inducing acute RILI, which was consistent with the relevant

literature reports [16]. It shows that the risk of acute RILI increases significantly after radiotherapy in patients with esophageal cancer with a large area of lung tissue covered by the total dose of radiotherapy, the average dose of both lungs and the large area of lung tissue covered by the radiotherapy field. Therefore, the risk of acute RILI can be reduced by improving the radiotherapy regimen and controlling the dose of radiotherapy.

In terms of cytokines, the results of this study showed that increased levels of TNF- α , TNF- β , and IL-6 in peripheral blood before radiotherapy were independent risk factors for acute RILI. When the levels of TNF- α , TNF- β , and IL-6 were higher, the risk of acute RILI was also increased. TNF- α can initiate an inflammatory response to play an immunoregulatory role. When the level of TNF- α increases, the permeability of vascular endothelial cells can be enhanced, resulting in increased vascular exudation. Second, TNF- α has a chemotactic effect, and a variety of inflammatory cells enter the interstitial space under this effect, thereby producing an inflammatory response. In addition, TNF- α also has the effect of inducing the synthesis and secretion of prostaglandins, which can aggravate the inflammatory response. TNF- β plays an important role in cell growth, differentiation, and immune response. Studies have shown that elevated levels of TNF-beta can increase the risk of radiation-induced lung injury. IL-6 can promote lung fibroblasts to produce a large amount of acute phase proteins such as C-reactive protein, thereby exerting inflammation and immune regulation. The inflammatory state of the body can be reflected by the level of IL-6 in peripheral blood. Therefore, elevated levels of IL-6 may be closely related to radiation-induced lung injury [17].

Pulmonary disease and diabetes were the independent risk factors for radiotherapy-induced acute RILI in patients with esophageal cancer in this study ($P < 0.05$). Before radiotherapy, patients with pulmonary diseases (such as pneumonia, lung cancer, and bronchial asthma) have increased inflammatory cytokines, and the lung tissue has been damaged by chronic inflammation. At this time, the sensitivity of the lung tissue to radiation is increased, the resistance is low, and the self-repair ability is weakened. Therefore, such patients are more likely to induce radiation-induced lung injury after receiving radiation therapy [18, 19]. In order to prevent pulmonary inflammatory damage in patients, after surgical treatment, patients can be encouraged to improve lung function through abdominal breathing and other training, so as to reduce the risk of lung injury after radiotherapy. Oxygen radicals can kill cells and aggravate tissue damage by disrupting the structure and function of cell membranes. Therefore, after radiotherapy, medical staff can give patients appropriate aerosol treatment, appropriate application of antioxidants such as vitamin C, to reduce the generation of oxygen free radicals and damage to lung tissue cells. Patients with diabetes mellitus have higher blood glucose concentration and higher intravascular osmotic pressure, which may cause damage to the rupture of pulmonary microvessels, resulting in enhanced vascular permeability and increased exudation of inflammatory substances in the radiation field. This can increase the chance of lung damage. Therefore,

TABLE 1: Univariate analysis of acute RILI induced by radiotherapy for esophageal cancer.

Factors	Observation group (<i>n</i> = 75)	Control group (<i>n</i> = 131)	<i>t</i> / χ^2 *	<i>P</i>
Age, <i>n</i> (%)			1.272*	0.259
<60years	19 (25.33)	43 (32.82)		
≥60 years	56 (74.67)	88 (67.18)		
Gender, <i>n</i> (%)			1.037*	0.311
Male	41 (54.67)	62 (47.33)		
Female	34 (45.33)	69 (52.67)		
Tumor location, <i>n</i> (%)			1.345*	0.510
Upper chest	16 (21.33)	21 (16.03)		
Mid chest	39 (52.00)	67 (51.15)		
Lower chest	20 (26.67)	43 (32.82)		
TNM stage, <i>n</i> (%)			1.222*	0.543
I	37 (49.33)	69 (52.67)		
II-III	26 (34.67)	48 (36.64)		
IV	12 (16.00)	14 (10.69)		
Smoking history, <i>n</i> (%)			1.656*	0.198
Yes	47 (62.67)	70 (53.44)		
No	28 (37.33)	61 (46.56)		
Combined diabetes, <i>n</i> (%)			11.468*	0.001
Yes	51 (68.00)	57 (43.51)		
No	24 (32.00)	74 (56.49)		
Concurrent chemotherapy, <i>n</i> (%)			0.660*	0.417
Yes	55 (73.33)	89 (67.94)		
No	20 (26.67)	42 (32.06)		
Total radiation dose, <i>n</i> (%)			6.249*	0.012
≤60 Gy	39 (52.00)	91 (69.47)		
>60 Gy	36 (48.00)	40 (30.53)		
Combined lung disease, <i>n</i> (%)			10.013*	0.002
Yes	28 (37.33)	23 (17.56)		
No	47 (62.67)	108 (82.44)		
KPS score, <i>n</i> (%)			0.424*	0.515
>80 points	23 (30.67)	46 (35.11)		
≤80 points	52 (69.33)	85 (64.89)		
Physical factor				
V5 (Gy)	4421.3 ± 586.4	4586.4 ± 591.8	1.051 [#]	0.110
V10 (Gy)	4337.5 ± 536.8	4295.8 ± 574.1	0.514 [#]	0.608
V20 (Gy)	2513.7 ± 581.3	2431.6 ± 562.5	0.996 [#]	0.321
V30 (Gy)	1124.2 ± 359.7	843.1 ± 280.4	3.496 [#]	0.001
V40 (Gy)	364.6 ± 114.4	335.3 ± 110.1	0.990 [#]	0.110
Dmean (Gy)	1187.4 ± 343.6	913.4 ± 286.5	3.412 [#]	0.001
Cytokines				
TNF- α (pg/mL)	35.48 ± 11.12	21.36 ± 7.49	5.958 [#]	<0.001
TNF- β (pg/mL)	57.24 ± 15.92	45.67 ± 13.84	3.103 [#]	0.003
IL-6 (pg/mL)	11.59 ± 3.73	7.18 ± 2.01	5.888 [#]	<0.001

Note: #: *t*-test; *: chi-square test; KPS: Karnofsky performance score.

TABLE 2: Multivariate logistic regression analysis of acute RILI induced by radiotherapy for esophageal cancer.

Factors	B	SE	Wald	P	OR	95% CI
Combined diabetes	1.848	0.910	4.124	<0.001	6.345	2.026~19.877
Combined lung disease	1.281	0.632	4.112	0.004	3.600	1.178~11.000
Total radiation dose	1.399	0.752	3.464	0.012	4.050	1.306~12.557
V30 (Gy)	0.501	0.216	5.371	<0.001	1.650	1.272~4.750
Dmean (Gy)	0.453	0.196	5.362	<0.001	1.573	1.267~4.536
TNF- α (pg/mL)	1.564	0.931	2.822	0.003	4.778	2.159~10.782
TNF- β (pg/mL)	1.462	0.698	4.386	<0.001	4.315	1.134~9.641
IL-6 (pg/mL)	1.238	0.787	2.478	0.029	3.449	1.384~9.463

medical staff should pay attention to the changes of blood sugar in patients with esophageal cancer in the process of treatment. In patients with diabetes, glycemic control should be administered to reduce the risk of lung injury following radiation therapy [20]. Since this study is a single-center study, the sample size collected is small, which may have a certain impact on the results and conclusions. In the future, multicenter studies and larger sample sizes are needed to identify more significant risk factors and provide preventive guidance for radiotherapy-induced acute RILI in esophageal cancer.

4. Conclusion

Diabetes mellitus, pulmonary disease, total radiotherapy dose, elevated physical factors (V30, Dmean), and elevated levels of cytokines (TNF- α , TNF- β , and IL-6) before radiotherapy are the risks of esophageal cancer induced by radiotherapy for acute RILI factor. Before radiotherapy, the possibility of acute RILI can be comprehensively evaluated according to the patient's condition, and the radiotherapy plan can be adjusted and prepared before radiotherapy, so as to reduce and avoid the induction of acute RILI.

Data Availability

The labeled dataset used to support the findings of this study are available from the corresponding author upon request.

Conflicts of Interest

The authors declare no competing interests.

References

- [1] M. W. Short, K. G. Burgers, and V. T. Fry, "Esophageal cancer," *American Family Physician*, vol. 95, no. 1, pp. 22–28, 2017.
- [2] F. He, J. Wang, L. Liu et al., "Esophageal cancer: trends in incidence and mortality in China from 2005 to 2015," *Cancer Medicine*, vol. 10, no. 5, pp. 1839–1847, 2021.
- [3] M. Arnold, I. Soerjomataram, J. Ferlay, and D. Forman, "Global incidence of oesophageal cancer by histological subtype in 2012," *Gut*, vol. 64, no. 3, pp. 381–387, 2015.
- [4] S. Mönig, M. Chevally, N. Niclauss et al., "Early esophageal cancer: the significance of surgery, endoscopy, and chemoradiation," *Annals of the New York Academy of Sciences*, vol. 1434, no. 1, pp. 115–123, 2018.
- [5] C. Puttanawarut, N. Sirirutbunkajorn, S. Khachonkham, P. Pattaranutaporn, and Y. Wongsawat, "Biological dosiomic features for the prediction of radiation pneumonitis in esophageal cancer patients," *Radiation Oncology*, vol. 16, no. 1, p. 220, 2021.
- [6] M. Stahl, J. Oliveira, and On behalf of the ESMO Guidelines Working Group, "Esophageal cancer: ESMO clinical recommendations for diagnosis, treatment and follow-up," *Annals of Oncology*, vol. 20, no. Supplement 4, pp. iv32–iv33, 2009.
- [7] M. H. Versteegen, M. Harker, C. van de Water et al., "Metastatic pattern in esophageal and gastric cancer: influenced by site and histology," *World Journal of Gastroenterology*, vol. 26, no. 39, pp. 6037–6046, 2020.
- [8] B. Li, Y. Zhang, L. Miao et al., "Esophagectomy with three-field versus two-field lymphadenectomy for middle and lower thoracic esophageal cancer: long-term outcomes of a randomized clinical trial," *Journal of Thoracic Oncology*, vol. 16, no. 2, pp. 310–317, 2021.
- [9] F. L. Huang and S. J. Yu, "Esophageal cancer: risk factors, genetic association, and treatment," *Asian Journal of Surgery*, vol. 41, no. 3, pp. 210–215, 2018.
- [10] D. J. Uhlenhopp, E. O. Then, T. Sunkara, and V. Gaduputi, "Epidemiology of esophageal cancer: update in global trends, etiology and risk factors," *Clinical Journal of Gastroenterology*, vol. 13, no. 6, pp. 1010–1021, 2020.
- [11] F. Iriarte, S. Su, R. V. Petrov, C. T. Bakhos, and A. E. Abbas, "Surgical management of early esophageal cancer," *The Surgical Clinics of North America*, vol. 101, no. 3, pp. 427–441, 2021.
- [12] S. H. Lin, B. P. Hobbs, V. Verma et al., "Randomized phase IIB trial of proton beam therapy versus intensity-modulated radiation therapy for locally advanced esophageal cancer," *Journal of Clinical Oncology*, vol. 38, no. 14, pp. 1569–1579, 2020.
- [13] A. Gawish, A. A. Chughtai, and M. J. Eble, "Dosimetric and volumetric effects in clinical target volume and organs at risk during postprostatectomy radiotherapy," *Strahlentherapie und Onkologie*, vol. 195, no. 5, pp. 383–392, 2019.
- [14] A. N. Hanania, W. Mainwaring, Y. T. Ghebre, N. A. Hanania, and M. Ludwig, "Radiation-induced lung injury: assessment and management," *Chest*, vol. 156, no. 1, pp. 150–162, 2019.
- [15] Y. Huang, W. Zhang, F. Yu, and F. Gao, "The cellular and molecular mechanism of radiation-induced lung injury," *Medical Science Monitor*, vol. 23, pp. 3446–3450, 2017.
- [16] I. Madani, K. De Ruyck, H. Goeminne, W. De Neve, H. Thierens, and J. Van Meerbeeck, "Predicting risk of

Research Article

Diagnostic Value and High-Risk Factors of Two-Dimensional Ultrasonography Combined with Four-Dimensional Ultrasonography in Prenatal Ultrasound Screening of Fetal Congenital Malformations

Xinyou Yu,¹ Fang Liu,² Wei Gao,³ Xiangrong Shi,¹ Ruiping Lu,¹ and Lihua Pan ¹

¹Department of Prenatal Diagnosis Center, General Hospital of Ningxia Medical University, Yinchuan, 750004 Ningxia, China

²Department of Reproductive Medicine, Yinchuan Maternity and Child Health Care Hospital, Yinchuan, 750004 Ningxia, China

³Department of Ultrasound Examination, General Hospital of Ningxia Medical University, Yinchuan, 750004 Ningxia, China

Correspondence should be addressed to Lihua Pan; panlihuanxmu@163.com

Received 17 May 2022; Revised 19 June 2022; Accepted 23 June 2022; Published 12 July 2022

Academic Editor: Pan Zheng

Copyright © 2022 Xinyou Yu et al. This is an open access article distributed under the Creative Commons Attribution License, which permits unrestricted use, distribution, and reproduction in any medium, provided the original work is properly cited.

Objective. This study mainly analyzes the diagnostic value of two-dimensional ultrasonography (2D-US) combined with four-dimensional ultrasonography (4D-US) in prenatal ultrasound screening of fetal congenital malformations (CMs) and explores the high-risk factors affecting fetal malformations. **Methods.** The clinical and imaging data of 2247 pregnant women who underwent prenatal fetal malformation screening in the General Hospital of Ningxia Medical University between February 2020 and October 2021 were collected and analyzed, retrospectively. All pregnant women underwent 2D-US, and those with suspected fetal malformations were further inspected by 4D-US. The accuracy of ultrasound examination results relative to actual pregnancy outcomes was analyzed, taking the neonatal malformation after induced labor or actual delivery as the gold standard, and the risk factors influencing the occurrence of fetal malformations were discussed. **Results.** A total of 87 cases (3.87%) of fetal malformations were detected out of the 2247 parturients examined. The accuracy, sensitivity, and specificity of 2D-US diagnosis were 81.40%, 43.68%, and 82.92%, respectively, while the data were 83.67%, 51.72%, and 84.95% for 4D-US, respectively, and 93.59%, 90.80%, and 93.70%, respectively, for 2D-US +4D-US. The combined diagnosis of 2D-US +4D-US achieved statistically higher accuracy, sensitivity, and specificity than either of them alone. One-way analysis of variance and multivariate logistic regression analysis identified that the independent risk factors affecting fetal malformation were age ≥ 35 , history of adverse pregnancy and childbirth, medication during pregnancy, toxic exposure during pregnancy, and history of seropositive for TORCH-IgM. Folic acid supplementation was a protective factor. **Conclusions.** Prenatal US is an effective approach for screening fetal malformations. 2D-US +4D-US can effectively improve the diagnostic rate of fetal malformations. For pregnant women with high-risk factors, prevention should be given priority, and prenatal screening and prenatal diagnosis should be standardized to reduce the occurrence of fetal malformations.

1. Introduction

Birth defects (BDs) are an important cause of infant mortality and lifelong disability [1]. According to the 2010 Global Burden of Disease Study, BDs, which lead to 6.4% of neonatal deaths, rank fifth among all causes of death [2] and place an enormous burden on families and society. Notably, the impact of BDs is particularly severe in low- and middle-income countries, including China. Approximately 900,000

babies are born with BDs every year in China, accounting for 5.6 percent of all births, according to a 2012 Report on The Prevention of Birth Defects in China [3]. Fetal structural malformation refers to fetal structural or chromosomal abnormalities occurring in utero due to its own genetic factors or maternal or external environmental factors, which accounts for over 90% of BDs and is one of the prime reasons for perinatal death. Studies have shown that about 2-3% of pregnancies are complicated with fetal structural

abnormalities [4–6]. Generally speaking, it will lead to a series of deformities of different human systems in fetuses, such as nervous system, cardiovascular system, genitourinary system, and limb skeletal system, which has a great impact on the life and health quality of fetuses [7–9].

Ultrasound screening for fetal structural abnormalities is a routine component of prenatal care in resource-rich countries. Antenatal examination for structural abnormalities provides prospective parents with an opportunity to obtain early information about fetal structural abnormalities, including the nature, etiology, prognosis, and the feasibility of prenatal or postpartum treatment [10]. Prenatal screening can reduce the birth rate of malformed fetuses, which not only improves the quality of newborns but also promotes the development of every family and society at large [11]. Screening for chromosomal abnormalities is mainly based on the detection of serum in the second trimester of pregnancy. If abnormalities are indicated, further diagnosis can be made by amniocentesis or ultrasonography. Once the chromosome abnormalities is confirmed, the pregnancy will be terminated [12]. However, despite the high diagnostic accuracy of amniocentesis, puncturing or terminating a pregnancy in the second trimester can cause great harm to pregnant women, so finding a noninvasive and high-accuracy method for chromosomal abnormality screening is of utmost importance. As the most commonly used prenatal noninvasive examination method, ultrasound plays a critical role in fetal malformation and chromosome screening [13, 14]. At present, two-dimensional ultrasonography (2D-US) has become the main and routine method for prenatal screening because of its advantages of low cost, noninvasiveness and no X-ray exposure [15]. However, 2D-US is limited by the fact that its plane image can only show one side of the fetus, with limited detection metrics [16]. Studies have shown that the missed diagnosis or misdiagnosis of fetal craniocerebral abnormalities may be due to artifacts caused by umbilical cord interference [17]. Therefore, if fetal abnormalities are suspected on 2D-US and clearer images are needed for further evaluation, an examination modality with more advanced imaging capabilities is required. Four-dimensional ultrasonography (4D-US) is generated from continuous 3D images [18], which allows continuous monitoring of the fetal face and surface, including real-time movement and sharper images, giving a clear view of the fetus' overall appearance and fine structure [19]. 4D-US provides additional benefits in evaluating fetal prenatal condition [20]. However, the final performance of obstetric ultrasound images depends on various factors such as fetal recumbent position, uterine wall, abdominal wall fat, amniotic fluid, and number of gestational fetuses [21].

Therefore, if abnormalities are suspected on 2D ultrasound and clearer images and further evaluation are required, 4D ultrasound can be added to prenatal screening. This study retrospectively analyzed the ultrasonic features of 2247 pregnant women who were screened for prenatal fetal malformations. The main purpose was to explore the diagnostic effects of 2D-US and 4D-US on prenatal fetal malformations, and to compare the accuracy of their combined diagnosis and single diagnosis. Besides, we analyzed the risk

factors related to malformations of fetuses with abnormal development, which is of great significance to improve the quality of birth population. The report is as follows.

2. Data and Methods

2.1. Study Population. The clinical and imaging examination data of 2247 pregnant women who underwent prenatal fetal malformation screening in the General Hospital of Ningxia Medical University between February 2020 and October 2021 were retrospectively analyzed. The age of the enrolled pregnant women was 20–40 years old, with an average of 30.09 ± 4.44 years old, and the gestational weeks ranged from 18 to 32 weeks, with a mean of 26.54 ± 2.13 weeks. In terms of the types of parturients, there were 1157 primiparas and 1090 multiparas. Inclusion criteria: (1) normal intrauterine pregnancy; (2) single pregnancy; (3) those who underwent 2D-US and 4D-US examinations; (4) complete clinical, imaging, and follow-up data. Exclusion criteria: (1) twin or multiple pregnancies; (2) severe heart, liver, and kidney diseases; (3) severe mental illness; (4) blood diseases and autoimmune diseases; (5) incomplete clinical, imaging, and follow-up data. This study was reviewed and approved by the hospital ethics committee.

2.2. Inspection Methods. A total of 2247 pregnant women were examined by Voluson E8 color Doppler ultrasound scanner (GE Healthcare, USA) with a probe frequency of 5.0–7.0 MHz. During the 2D-US examination, all patients were placed in the supine position with the abdomen exposed, and all aspects of the fetus were comprehensively scanned according to a common operation standard to carefully observe the state, structure, and size of each part of the fetus. The biological indicators of the fetus, such as biparietal diameter, head circumference, femur length, humerus length, abdominal circumference, placental position, and amniotic fluid index and maximum depth, were measured. The integrity of fetal skull was observed, and the ossification degree of fetal brain structure was detected. In addition, the head circumference, biparietal diameter, and posterior fossa depth were measured, the fetal face was observed in multiple sections, and the spine was checked for continuity. The normal development of chest structures such as heart and lungs, as well as the growth and development of the fetus were strictly evaluated. For pregnant women with suspected fetal malformations, 4D-US examination was carried out using a special probe RAB4-8-D with a frequency of 2.5–7.0 MHz. The dynamic imaging of the fetus was presented to ensure the clarity of the image acquisition. The accuracy of inspection results relative to induced labor and fetal indicators after delivery was compared and analyzed. All prenatal ultrasound examiners have received unified provincial training on prenatal ultrasound diagnosis. To ensure the accuracy of diagnosis, all cases were diagnosed by sonographers with provincial prenatal screening and diagnosis qualifications.

2.3. Endpoints. Pregnant women with possible fetal malformations indicated by prenatal B-ultrasound screening were

followed up, and the accuracy, sensitivity, and specificity of 2D-/4D-US as well as their combined examinations in the diagnosis of fetal malformations were determined, with the neonatal malformation of pregnant women after induced labor or actual delivery as the gold standard. Accuracy = [(true positives + true negatives)/total cases] × 100%. Sensitivity = [true positives/(true positives + false negatives)] × 100%. Specificity = [true negatives/(true negatives + false positives)] × 100%.

The case data of pregnant women, including age, history of adverse pregnancy and childbirth, history of cold during pregnancy, history of medication during pregnancy, history of toxic exposure during pregnancy, and TORCH (toxoplasmosis, rubella, cytomegalovirus, and Herpes simplex virus) testing results of pregnant women, were investigated and analyzed by univariate and logistic regression analyses.

2.4. Statistical Analysis. The data of this study were tested by SPSS20.0 (IBM, NY, USA). Mean ± SD was used to represent measurement data; for count data recorded as n (%), the chi-square test was used for comparison. The threshold of significance was $P < 0.05$.

3. Results

3.1. Pregnancy Outcomes and Distribution of Fetal Malformations in Pregnant Women. A total of 87 cases (3.87%) of fetal malformations were detected in 2247 puerperae, including 21 neurological malformations, 15 cardiovascular malformations, 17 facial deformities, 5 digestive system malformations, 9 skeletal system deformity of extremities, 14 genitourinary system malformations, and 6 multiple malformations (Table 1). 2D-US imaging features of two malformed fetuses are shown in Figure 1.

3.2. Comparison of 2D- and 4D-US Diagnosis of Fetal Malformations. The comparison results between different inspection methods and the gold standard, namely, the occurrence of neonatal malformations after induced labor or actual delivery, were shown in Table 2. By calculation, it was found that the accuracy, sensitivity, and specificity of 2D-US diagnosis were 81.40%, 43.68%, and 82.92%, respectively, while the data for 4D-US were 83.67%, 51.72%, and 84.95%, respectively, and were 93.59%, 90.80%, and 93.70%, respectively, for 2D-US +4D-US. The combined diagnosis of 2D-US +4D-US achieved obviously higher accuracy, sensitivity, and specificity than either of them alone (Table 3).

3.3. Univariate Analysis of Risk Factors for Fetal Malformations. Univariate analysis showed that age ≥ 35 , adverse pregnancy and childbirth history, folic acid (FA) supplementation, medication history during pregnancy, toxic exposure history during pregnancy, and history of seropositive for TORCH-IgM in pregnant women were related to fetal malformations, and the differences were statistically significant ($P < 0.05$), as shown in Table 4.

3.4. Multivariate Logistic Regression Analysis of Risk Factors for Fetal Malformations. Variables with significant differ-

TABLE 1: Distribution of fetal malformations.

Classification of fetal malformations	Number of cases (n)	Constituent ratio (%)
Neurological malformation	21	24.14
Cardiovascular system malformation	15	17.24
Facial deformity	17	19.54
Digestive system malformation	5	5.75
Skeletal system deformity of extremities	9	10.34
Genitourinary system malformation	14	16.09
Multiple malformations	6	6.90
Total	87	100.00

ences in the univariate analysis were selected for further multivariate logistic regression analysis. It showed that age ≥ 35 , history of adverse pregnancy and childbirth, history of medication during pregnancy, history of toxic exposure during pregnancy, and history of seropositive for TORCH-IgM in pregnant women were independently associated with increased risks of fetal malformations, while FA supplementation was a protective factor ($P < 0.05$), as shown in Table 5.

4. Discussion

Prenatal invasive diagnosis such as amniocentesis remains the gold standard for diagnosing fetal chromosomal abnormalities. However, amniocentesis is a traumatic procedure that carries a high risk of infection and abortion, so most pregnant women are reluctant to undergo it [22]. At present, 2D-US is a routine approach to screen fetal malformations before delivery. However, it can only provide a cross-sectional image of a certain part of the fetus, which cannot show the subtle structural features of the fetus, nor can it provide clearer and more effective stereoscopic images [23]. With the advancement of modern medical technology and the trend of refinement of medical devices, 4D-US has become an important supplement to 2D-US [24].

In this paper, 87 fetal malformations were detected among the 2247 parturients examined, accounting for 3.87%. The accuracy, sensitivity, and specificity of 2D-US diagnosis were 81.40%, 43.68%, and 82.92%, respectively, while were 83.67%, 51.72%, and 84.95%, respectively, for 4D-US, and 93.59%, 90.80%, and 93.70%, respectively, for 2D-US +4D-US. It indicates that the combined diagnosis of 2D-US +4D-US has significantly superior higher accuracy, sensitivity, and specificity to either 2D-US or 4D-US. These findings are consistent with those of Wang et al., who found that 2D-US plus 4D-US can better identify various fetal brain abnormalities and provide early and more accurate information for clinicians and maternal patients to make decisions. In addition, 2D-US +4D-US has efficient application value in prenatal screening of fetuses at different gestational weeks. Deng et al. [25] found inferior diagnostic accuracy of 2D-US to 2D-US plus 4D-US for fetal anomaly at gestational week. Tudorache et al. [26] also reported that 2D-US and 4D-US are highly accurate tools for the early diagnosis of major congenital heart diseases by using high-quality systems and standard protocols.

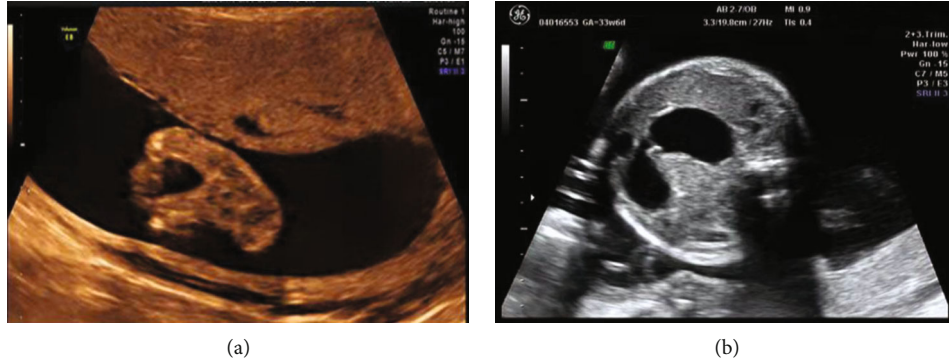


FIGURE 1: Two-dimensional ultrasonic imaging features of malformed fetuses ((a) two-dimensional ultrasonography shows a “crab pincer” splitting of one foot; (b) two-dimensional ultrasonography shows severe dilation to the stomach and duodenum near the obstruction, with fluid retention and double bubble signs).

TABLE 2: Comparison of 2D-US, 4D-US, and their combined detection results with pregnancy outcomes.

Examination method		Pregnancy outcomes		Total
		Positive	Negative	
2D-US	Positive	38 (1.69)	369 (16.42)	407 (18.11)
	Negative	49 (2.18)	1791 (79.71)	1840 (81.89)
4D-US	Positive	45 (2.00)	325 (14.46)	370 (16.47)
	Negative	42 (1.87)	1835 (81.66)	1877 (83.53)
Joint examination	Positive	79 (3.52)	136 (6.05)	215 (9.57)
	Negative	8 (0.36)	2024 (90.08)	2032 (90.43)

TABLE 3: Diagnostic efficacy analysis of different detection methods.

Examination method	Accuracy (%)	Sensitivity (%)	Specificity (%)
2D-US	81.40*	43.68*	82.92*
4D-US	83.67*	51.72*	84.95*
Joint examination	93.59	90.80	93.70

Note: * $P < 0.05$ vs. combination group.

This study also explored and analyzed the risk factors leading to fetal malformations. The results showed that age ≥ 35 , adverse pregnancy and childbirth history, medication history during pregnancy, toxic exposure history during pregnancy, and history of seropositive for TORCH-IgM in pregnant women were all independent risk factors for fetal malformations, while FA supplementation was a protective factor. According to the study of Ge et al. [27], advanced pregnancy is a high-risk pregnancy that is more prone to neonatal developmental malformations. In most cases, environmental factors such as exposure to certain drugs, infections, or radiation during pregnancy can cause fetal deformities, though sometimes genetic [28]. The history of medication during pregnancy is also critical to the development of fetal malformations. Misuse of progesterones, estrogens, and androgens early in pregnancy may potentially lead to fetal brain and skull malformations [29]. However, it is inevitable for pregnant women with underlying diseases to

take drugs to stabilize their condition. A study evaluating fetal malformations and seizure control in epileptic patients after discontinuation of sodium valproate (VPA) found that reducing the dose of VPA before pregnancy reduces the risk of fetal malformations, while discontinuation of VPA reduces harm to the general population, but at the cost of reduced seizure control during pregnancy [30]. This study also suggests that preventive measures should be taken when taking medicine during pregnancy, preferably by seeking medical advice. Multiple scientific evidence suggests that the environment may be associated with the occurrence of congenital malformations (CMs) such as limb deformities, orofacial clefts, and male genitourinary development, as well as with spontaneous abortion, which is more severe when parents are exposed to toxic pesticides [30, 31]. Parental exposure to toxic agrochemicals may increase the chances of children being born with CMs, particularly those related to the male reproductive system [32]. Maternal infections transmitted in utero by multiple pathogens at different stages of pregnancy are primarily responsible for newborn and infant deaths worldwide, with TORCH infections long associated with poor obstetric outcomes [33]. A prospective study on the relationship between TORCH infections and CMs in China demonstrated that TORCH infections are an important risk factor for severe fetal injury, especially CMs [34].

However, this study still has some limitations. First, we only studied patients during the second trimester of pregnancy and did not stratify the diagnostic value of 2D-US and 4D-US screening at different gestational weeks. Second,

TABLE 4: Univariate analysis of risk factors for fetal malformation.

Risk factors	Normal fetal group ($n = 2160$)	Malformed fetus group ($n = 87$)	χ^2	P
Age			22.7510	0.0069
<35	1651 (76.44)	47 (54.02)		
≥ 35	509 (23.56)	40 (45.98)		
Adverse pregnancy and childbirth history			29.3710	<0.0001
With	590 (27.31)	44 (50.57)		
None	1570 (72.69)	43 (49.43)		
Folic acid supplementation			7.9151	0.0049
Yes	705 (32.64)	41 (47.13)		
No	1455 (67.36)	46 (52.87)		
History of cold during pregnancy			1.9131	0.1666
Yes	882 (40.83)	42 (48.28)		
No	1278 (59.17)	45 (51.72)		
History of medication during pregnancy			54.9810	<0.0001
Yes	367 (16.99)	42 (48.28)		
No	1793 (83.01)	45 (51.72)		
History of toxic exposure during pregnancy			93.7010	<0.0001
Yes	77 (3.56)	22 (25.29)		
No	2083 (96.44)	65 (74.71)		
History			79.8510	<0.0001
Yes	74 (3.43)	20 (22.99)		
No	2086 (96.57)	67 (77.01)		

TABLE 5: Logistic regression analysis of risk factors for fetal malformations.

Risk factors	β	SE	P	OR	95% CI
Age (0: <35, 1: ≥ 35)	0.696	0.260	0.007	2.005	1.204-3.338
History of adverse pregnancy and childbirth (0: no, 1: yes)	2.076	0.637	0.001	7.974	2.288-27.793
Folic acid supplementation (0: no, 1: yes)	-3.232	0.790	0.000	0.039	0.008-0.186
Medication history during pregnancy (0: no, 1: yes)	2.117	0.530	0.000	8.306	2.941-23.461
Toxic exposure during pregnancy (0: no, 1: yes)	0.959	0.372	0.010	2.610	1.258-5.415
History of seropositive for TORCH-IgM (0: no, 1: yes)	0.831	0.348	0.017	2.296	1.160-4.542

there were other risk factors that were not considered, such as radiation, smoking or drinking history of the husband, and genetic diseases. Thus, more research should be conducted to comprehensively analyze the diagnostic value of 2D-US and 4D-US in the screening of fetal congenital malformations.

5. Conclusion

To sum up, the combination of 2D- and 4D-DS can effectively improve the diagnosis rate of fetal malformations. The popularization of prenatal screening and timely prenatal diagnosis contributes to the reduction of newborn BDs. At the same time, pregnant women should stay away from environmental teratogenic factors and avoid all kinds of high-risk factors leading to fetal malformations and strengthen the awareness of prenatal and postnatal care, to improve the quality of birth population.

Data Availability

The labeled dataset used to support the findings of this study are available from the corresponding author upon request.

Conflicts of Interest

The authors declare no competing interests.

Acknowledgments

This work was supported by the Key Research and Development Program of Ningxia (2021BEG03043).

References

- [1] C. T. Mai, J. L. Isenburg, M. A. Canfield et al., "National population-based estimates for major birth defects, 2010–2014," *Birth Defects Research*, vol. 111, no. 18, pp. 1420–1435, 2019.

- [2] R. Lozano, M. Naghavi, K. Foreman et al., “Global and regional mortality from 235 causes of death for 20 age groups in 1990 and 2010: a systematic analysis for the global burden of disease study 2010,” *The Lancet*, vol. 380, no. 9859, pp. 2095–2128, 2012.
- [3] W. Yue, E. Zhang, R. Liu et al., “The China birth cohort study (cbcs),” *European Journal of Epidemiology*, vol. 37, no. 3, pp. 295–304, 2022.
- [4] C. Rydberg and K. Tunón, “Detection of fetal abnormalities by second-trimester ultrasound screening in a non-selected population,” *Acta Obstetrica et Gynecologica Scandinavica*, vol. 96, no. 2, pp. 176–182, 2017.
- [5] W. F. Rayburn, J. A. Jolley, and L. L. Simpson, “Advances in ultrasound imaging for congenital malformations during early gestation,” *Birth Defects Research Part A: Clinical and Molecular Teratology*, vol. 103, no. 4, pp. 260–268, 2015.
- [6] M. Whitworth, L. Bricker, and C. Mullan, “Ultrasound for fetal assessment in early pregnancy,” *Cochrane Database of Systematic Reviews*, no. article CD007058, 2015.
- [7] S. W. Cater, B. K. Boyd, and S. V. Ghate, “Abnormalities of the fetal central nervous system: prenatal us diagnosis with postnatal correlation,” *Radiographics*, vol. 40, no. 5, pp. 1458–1472, 2020.
- [8] Y. Wang, J. Zhang, W. Feng et al., “Description of misdiagnosis and missed diagnosis of fetal complex heart malformations by prenatal echocardiography combined with postnatal cardiovascular casting,” *Prenatal Diagnosis*, vol. 40, no. 7, pp. 792–802, 2020.
- [9] Y. Liu and B. Mapow, “Coexistence of urogenital malformations in a female fetus with de novo 15q24 microdeletion and a literature review,” *Molecular Genetics & Genomic Medicine*, vol. 8, no. 7, article e1265, 2020.
- [10] L. Edwards and L. Hui, “First and second trimester screening for fetal structural anomalies,” *Seminars in Fetal and Neonatal Medicine*, vol. 23, no. 2, pp. 102–111, 2018.
- [11] M. Cloutier, L. Gallagher, C. Goldsmith, S. Akiki, N. Barrowman, and S. Morrison, “Group genetic counseling: an alternate service delivery model in a high risk prenatal screening population,” *Prenatal Diagnosis*, vol. 37, no. 11, pp. 1112–1119, 2017.
- [12] S. Zhang, M. Yin, J.-Z. Xu et al., “Cytogenetic analysis for fetal chromosomal abnormalities by amniocentesis: review of over 40,000 consecutive cases in a single center,” *Reproductive and Developmental Medicine*, vol. 1, no. 2, pp. 84–88, 2017.
- [13] L. Drukker, E. Bradburn, G. B. Rodriguez, N. W. Roberts, L. Impey, and A. T. Papageorghiou, “How often do we identify fetal abnormalities during routine third-trimester ultrasound? A systematic review and meta-analysis,” *BJOG: An International Journal of Obstetrics & Gynaecology*, vol. 128, no. 2, pp. 259–269, 2021.
- [14] N. Zhang, H. Dong, P. Wang, Z. Wang, Y. Wang, and Z. Guo, “The value of obstetric ultrasound in screening fetal nervous system malformation,” *World Neurosurgery*, vol. 138, pp. 645–653, 2020.
- [15] F. Vinals, P. Ruiz, G. Quiroz et al., “Two-dimensional ultrasound evaluation of the fetal cerebral aqueduct: improving the antenatal diagnosis and counseling of aqueductal stenosis,” *Fetal Diagnosis and Therapy*, vol. 42, no. 4, pp. 278–284, 2017.
- [16] C. Sklar, M. Yaskina, S. Ross, and K. Naud, “Accuracy of prenatal ultrasound in detecting growth abnormalities in triplets: a retrospective cohort study,” *Twin Research and Human Genetics*, vol. 20, no. 1, pp. 84–89, 2017.
- [17] P. Brandão, E. Soares, C. Estevinho, M. Freixo, A. S. Portela-Carvalho, and M. J. Ferreira, “Skeletal defect at mid-trimester ultrasound scan,” *Journal of Medical Ultrasound*, vol. 26, no. 3, p. 171, 2018.
- [18] D. Öcal, T. Nas, and İ. Güler, “The place of four-dimensional ultrasound in evaluating fetal anomalies,” *Irish Journal of Medical Science (1971-)*, vol. 184, no. 3, pp. 607–612, 2015.
- [19] A. C. Rossi and F. Prefumo, “Correlation between fetal autopsy and prenatal diagnosis by ultrasound: a systematic review,” *European Journal of Obstetrics & Gynecology and Reproductive Biology*, vol. 210, pp. 201–206, 2017.
- [20] N. Vora, S. Robinson, E. Hardisty, and D. Stamilio, “Utility of ultrasound examination at 10-14 weeks prior to cell-free DNA screening for fetal aneuploidy,” *Ultrasound in Obstetrics & Gynecology*, vol. 49, no. 4, pp. 465–469, 2017.
- [21] P. Bach-Ségura, “Facial clefts diagnosed before birth: routine ultrasound screening at the multi-disciplinary center for prenatal diagnosis (pcpd),” *Journal of Dentofacial Anomalies and Orthodontics*, vol. 15, no. 4, p. 402, 2012.
- [22] A. Rivas, M. Epelman, E. Danzer, N. S. Adzick, and T. Victoria, “Prenatal mr imaging features of caroli syndrome in association with autosomal recessive polycystic kidney disease,” *Radiology case reports*, vol. 14, no. 2, pp. 265–268, 2019.
- [23] J. Kurian, S. Sotardi, M. C. Liszewski, W. A. Gomes, T. Hoffman, and B. H. Taragin, “Three-dimensional ultrasound of the neonatal brain: technical approach and spectrum of disease,” *Pediatric Radiology*, vol. 47, no. 5, pp. 613–627, 2017.
- [24] L. S. Barišić, M. Stanojević, A. Kurjak, S. Porović, and G. Gaber, “Diagnosis of fetal syndromes by three-and four-dimensional ultrasound: is there any improvement?,” *Journal of Perinatal Medicine*, vol. 45, pp. 651–665, 2017.
- [25] B. Deng, D. Hu, J. Liu, H. Lin, Y. Zhang, and Z. Li, “Application of two-dimensional ultrasonography combined with four-dimensional ultrasonography in prenatal screening for fetal anomaly at different gestational weeks,” *Evaluation and Analysis of Drug-Use in Hospitals of China*, vol. 15, pp. 904–906, 2015.
- [26] Ş. Tudorache, M. Cara, F. Burada, C. Simionescu, A. Dragoescu, and D. Iliescu, “First trimester diagnostic accuracy of two-dimensional and four-dimensional ultrasound in major congenital heart diseases,” *Obstetrics & Gynecology*, vol. 64, pp. 221–232, 2016.
- [27] G. Ge, W. Chen, and N. Jiang, “The value of prenatal color ultrasonography in the diagnosis of fetal structural malformation and the causes of missed diagnosis,” *Acta Microscopica*, vol. 29, p. 3, 2020.
- [28] P. Tomà, A. Bartoloni, S. Salerno et al., “Protecting sensitive patient groups from imaging using ionizing radiation: effects during pregnancy, in fetal life and childhood,” *La Radiologia Medica*, vol. 124, no. 8, pp. 736–744, 2019.
- [29] W. Yingjin, C. Xiaoyuan, R. Z. S. Zhong, P. Yanyan, A. Peili, and G. Xinru, “Diagnostic value of two-dimensional plus four-dimensional ultrasonography in fetal craniocerebral anomalies,” *Iranian Journal of Public Health*, vol. 48, p. 323, 2019.
- [30] M. E. Ueker, V. M. Silva, G. P. Moi, W. A. Pignati, I. E. Mattos, and A. M. C. Silva, “Parenteral exposure to pesticides and

- occurrence of congenital malformations: hospital-based case-control study,” *BMC Pediatrics*, vol. 16, no. 1, pp. 1–7, 2016.
- [31] W. G. Foster, J. A. Evans, J. Little et al., “Human exposure to environmental contaminants and congenital anomalies: a critical review,” *Critical Reviews in Toxicology*, vol. 47, no. 1, pp. 59–84, 2017.
- [32] N. Z. Costa, C. R. D. Nora, L. H. D. Souto, F. D. Carlotto, R. . S. Afonso, and D. L. Riquinho, “Exposure to toxic agrochemicals and development of congenital malformations: a scoping review,” *Texto & Contexto-Enfermagem*, vol. 30, p. 3.s, 2021.
- [33] K. R. Prasoona, B. Srinadh, T. Sunitha et al., “Seroprevalence and influence of torch infections in high risk pregnant women: a large study from South India,” *The Journal of Obstetrics and Gynecology of India*, vol. 65, no. 5, pp. 301–309, 2015.
- [34] Y. Wang, S. Li, N. Ma et al., “The association of torch infection and congenital malformations: a prospective study in China,” *European Journal of Obstetrics & Gynecology and Reproductive Biology*, vol. 240, pp. 336–340, 2019.

Retraction

Retracted: Application of Mathematical Modeling in Cost Control of Medical Equipment Procurement in Public Hospitals

Computational and Mathematical Methods in Medicine

Received 27 June 2023; Accepted 27 June 2023; Published 28 June 2023

Copyright © 2023 Computational and Mathematical Methods in Medicine. This is an open access article distributed under the Creative Commons Attribution License, which permits unrestricted use, distribution, and reproduction in any medium, provided the original work is properly cited.

This article has been retracted by Hindawi following an investigation undertaken by the publisher [1]. This investigation has uncovered evidence of one or more of the following indicators of systematic manipulation of the publication process:

- (1) Discrepancies in scope
- (2) Discrepancies in the description of the research reported
- (3) Discrepancies between the availability of data and the research described
- (4) Inappropriate citations
- (5) Incoherent, meaningless and/or irrelevant content included in the article
- (6) Peer-review manipulation

The presence of these indicators undermines our confidence in the integrity of the article's content and we cannot, therefore, vouch for its reliability. Please note that this notice is intended solely to alert readers that the content of this article is unreliable. We have not investigated whether authors were aware of or involved in the systematic manipulation of the publication process.

Wiley and Hindawi regrets that the usual quality checks did not identify these issues before publication and have since put additional measures in place to safeguard research integrity.

We wish to credit our own Research Integrity and Research Publishing teams and anonymous and named external researchers and research integrity experts for contributing to this investigation.

The corresponding author, as the representative of all authors, has been given the opportunity to register their agreement or disagreement to this retraction. We have kept a record of any response received.

References

- [1] L. Chen, "Application of Mathematical Modeling in Cost Control of Medical Equipment Procurement in Public Hospitals," *Computational and Mathematical Methods in Medicine*, vol. 2022, Article ID 3425873, 12 pages, 2022.

Research Article

Application of Mathematical Modeling in Cost Control of Medical Equipment Procurement in Public Hospitals

Lihong Chen 

Department of Procurement Center, Shanghai Tenth People's Hospital, Shanghai 200072, China

Correspondence should be addressed to Lihong Chen; chenlihong225924@163.com

Received 26 April 2022; Accepted 16 May 2022; Published 7 July 2022

Academic Editor: Pan Zheng

Copyright © 2022 Lihong Chen. This is an open access article distributed under the Creative Commons Attribution License, which permits unrestricted use, distribution, and reproduction in any medium, provided the original work is properly cited.

The purpose of this study is to strengthen the procurement management of public hospitals and ensure the quality of medical equipment. In this paper, combined with the procurement process of medical equipment in public hospitals, on the basis of RFID technology, a JRP model of random demand for medical equipment procurement in public hospitals is established. At the same time, according to the type and quantity of decision variables, the DE solution algorithm is redesigned, and based on the support of the algorithm, a mathematical model for cost control of medical equipment procurement in public hospitals is established. It can be seen from the analysis results that the cost control system for medical equipment procurement in public hospitals based on the mathematical model proposed in this paper can play an important role in public hospital equipment procurement and promote the standardized operation of public hospital procurement management.

1. Introduction

Medical equipment investment is an important part of hospital construction planning. As the hospital now advocates the business model of “supporting doctors with skills,” the increase in various surgeries and inspection items will inevitably increase the investment in related medical equipment. How to effectively control the cost of medical equipment procurement, that is, how to balance the expenditure and recovery of funds in this area, has become a common concern. This paper discusses how to effectively control the procurement cost of medical equipment in a second-class A-level hospital, dynamically observes various constituent factors of the procurement cost of medical equipment, and puts forward many insights and methods to effectively control the procurement cost of medical equipment. Moreover, the effectiveness of the specific content of the comprehensive equipment procurement system to reduce the procurement cost is discussed. The results show that adopting appropriate bidding procurement methods and establishing a perfect and standardized procurement system are most conducive to scientifically controlling equipment procurement costs,

thereby reducing the overall cost of hospitals. Therefore, controlling the procurement cost of medical equipment and making it continue to decrease is one of the important and direct means to reduce the total cost of the hospital and increase the profit.

Budget management is the main method for the hospital to implement the refined management of large medical equipment. It is to control the activities of various kinds of medical equipment in the hospital and to demonstrate, purchase, manage, and coordinate the various resources of the hospital. Budgeting is also a comprehensive management model, which requires hospitals to forecast and arrange future hospital equipment procurement and distribution in light of business requirements and development, comprehensively consider the hospital's capital status and financial resources, demonstrate and analyze medical equipment, and make overall planning for equipment budgets. By strengthening budget management, it can provide support for the follow-up equipment management work. When carrying out equipment management, hospitals should carry out equipment management according to the requirements of budget management, strengthen equipment procurement,

maintenance, tracking, investigation, assessment, etc., to realize the overall arrangement of budget management, and combine with budget performance assessment to ensure the smooth completion of equipment management goals. The economic benefit analysis of large-scale medical equipment is the foundation of equipment budget management, and it is also the basis for equipment budget decision-making and review. By strengthening the application and benefit investigation and analysis of large-scale medical equipment, it can provide data reference for the deployment and management of hospital equipment and ensure the quality of equipment management.

According to the procurement process of public hospital medical equipment, this paper establishes a mathematical model of public hospital medical equipment procurement and controls the procurement cost of public hospital medical equipment through the intelligent model.

2. Related Work

No enterprise can operate independently from procurement activities. According to Porter's value chain profits, as long as the business remains in operation, then the purchasing activity is bound to happen. That is to say, enterprises must pay suppliers a certain amount of funds in exchange for goods and services, that is, to meet and maintain the operation of the organization through procurement activities [1]. In simple terms, procurement is the necessary economic activity for an enterprise to obtain the materials it needs, including a series of operations such as planning, decision-making, purchasing, tracking, acceptance, transportation, and storage [2]. Therefore, in a narrow sense, procurement is the purchase behavior of products or services according to their own needs for the purpose of operation and production [3]. From a broad perspective, procurement is an economic activity in which an enterprise obtains ownership of resources through multiple channels and methods, cyclically and continuously, and its purpose is to meet all of its own needs. With the blowout reform of science and technology and the in-depth development of regional economic integration, all enterprises today are faced with extremely fierce market competition and changing consumer market. Enterprises need to further shorten the reaction time to the market and continuously improve the quality of their own products, but also simultaneously reduce production and operation costs, so as to maintain a good capital flow and ensure the survival and competitiveness of enterprises [4]. Procurement activities are one of the important links in the operation of enterprises, and procurement costs account for about 60% of operating costs. If the procurement cost can be effectively controlled, it can directly reduce the operating cost of the enterprise and indirectly create value for the enterprise. Therefore, how to control procurement costs has become an extremely important factor for the survival and competitiveness of today's global enterprises [5].

With the continuous updating of procurement management theory, more and more enterprises use it for liter-

ature in the practice of procurement activities and gradually upgrade their procurement from traditional mode to strategic procurement. The core of transformation and upgrading is to comprehensively summarize and analyze the cost of product purchase, use, quality inspection, and maintenance in procurement activities through strategic procurement management and further strengthen cost control [6]. Literature [7] established a TCO model and analyzed the important material procurement activities of many companies through empirical research methods. Finally, by using the TCO model, it is confirmed that TCO can help enterprises select suitable suppliers, optimize supplier management, and strengthen cost management. The author further suggests that the TCO model can be promoted to leading enterprises in various industries, which will help these leading enterprises maintain their core competitiveness. Literature [8] proposed that TCO (full name total cost of ownership) is a concept of total cost integration. In the application of this theory in corporate procurement activities, it refers to all costs in the procurement process, including but not limited to ordering, acceptance, use, maintenance, and defect disposal. TCO can be used as a procurement tool for enterprises to better analyze all the costs incurred between enterprises and suppliers when the procurement relationship occurs. From the perspective of the time dimension of the procurement activities, the prepurchase cost is all the costs before the enterprise purchase order is determined, including the confirmation of procurement requirements, the development and selection of suppliers, and the internal communication between the enterprise demand department and the procurement department [9]. The interim cost of procurement is the relevant cost incurred when confirming the purchase order of the enterprise, including the cost of purchase price, transportation, delivery, tax payment, inspection, tracking, and after-sales. The postprocurement cost is the cost incurred at the end of the procurement activity cycle, including the cost of concession receipt, repair cost, maintenance, and upkeep [10].

Literature [11] starts from the TCO theory and studies multiple supplier selection models, focusing on the distinction between the hierarchical model and the mathematical programming model. At the same time, through the method of empirical research, it demonstrates the practicability of the multi-item model in procurement activities. The author stated in the article that the mathematical programming model is more suitable for the management of suppliers' selection in procurement activities, and this multi-item model can help companies obtain more accurate procurement costs. Literature [12] empirically analyzes the company's own procurement strategy and overall procurement cost based on historical procurement cost data and suppliers' procurement performance. The author uses a mathematical programming model to help companies select suitable suppliers and further reduce their overall procurement costs. Literature [13] studies the shortcomings of ABC in selecting and evaluating suppliers. The authors restate the total supplier cost of the

procurement process in the article, including the purchase price of the goods, the associated normal operating costs, and additional operating costs due to product defects. On this basis, empirical analysis is carried out through mathematical models, which improves the scientificity and objectivity of supplier selection and evaluation. Literature [14] takes the three dimensions of suppliers, enterprise purchase orders, and purchased products as the research objects and studies the selection cost of suppliers through quantitative analysis. The author makes full use of the TCO theory to construct a data model for cost structure analysis and uses a scientific method to solve the problem of supplier selection and purchase order allocation. Literature [15] quantifies the hidden procurement cost and establishes a comprehensive evaluation index system for the problem of more accurate selection of the best supplier. In this quantitative model, procurement-related factors such as procurement quality, procurement time, and delivery punctuality are fully considered, and the total procurement cost is calculated to improve the accuracy of supplier selection. Literature [16] believes that the best way to evaluate, analyze, and select suppliers is to use the TCO model. In the procurement practice of the enterprise, the TCO model can help the enterprise to better reduce the overall procurement cost, directly improve the profitability of the enterprise, and then ensure the comprehensive competitiveness of the enterprise from the perspective of operating benefits.

3. Mathematical Modeling of Procurement Cost Control

Under the periodic inspection strategy, the set inventory level is checked regularly, and the ordering process occurs when the inventory level is reduced to a certain level (minimum service level). The goal of inventory levels is to meet customer demand within the inspection cycle T and order lead time. The safety stock ST_i for different commodities is usually denoted $ST_i = z_i \sigma_i \sqrt{k_i T + L}$. Among them, z_i is the service level factor, σ_i is the standard deviation of the demand forecast error of commodity i , k_i is the joint procurement frequency of commodity i , and L is the order lead time. Multiplying the order lead time by the inventory cost of the classic JRP constitutes the inventory cost of the random demand, which is the basic random JRP and the basis for the construction of the random JRP in this paper.

The research on random demand JRP decision based on RFID technology has the following characteristics:

- (1) Based on the deterministic JRP, it is the first attempt to establish a JRP model based on the random demand of RFID technology. Using the link between RFID technology investment and RFID return on investment, it links the investment of RFID technology in the JRP process and the impact of RFID technology on JRP cost. Moreover, it takes the lowest total cost of JRP for RFID investment as the research goal and improves the procurement efficiency of

random JRP and the JIT efficiency in the process of inventory management

- (2) It reselects the parameters of the DE algorithm and designs the solution process. The DE algorithm is designed according to the type and number of decision variables of random JRP and the structure of the model, and the sensitivity analysis of the parameters of the algorithm is carried out
- (3) It solves the optimal investment level of RFID technology and improves the efficiency under the optimal investment level and analyzes the impact of its procurement cost and inventory cost, as well as the reasonable investment scale of RFID. Moreover, it examines the impact of parameter changes on RFID technology investment. Similar to the process of determining JRP, the schematic diagram of the JRP model under random demand conditions is shown in Figure 1

The JRP model of stochastic demand is also based on the JRP of deterministic demand, and the stochastic JRP still takes the total cost as the objective function, which is composed of inventory cost and joint procurement cost. The cost of joint procurement of deterministic JRP is the joint procurement cost of stochastic demand JRP model. It sets the warehouse's maximum inventory level and determines the inventory cost and out-of-stock cost of the JRP model of demand based on the distribution of random demand. These two costs are described in three sections below.

- (1) Joint procurement cost

According to the joint ordering cost of the determined demand, JRP is composed of the main ordering cost S and the secondary ordering cost s_i ; the corresponding random demand JRP annual ordering cost s_i is [17]:

$$C_o = \frac{S}{T} + \sum_{i=1}^n \left(\frac{s_i}{k_i T} \right) = \frac{1}{T} \left(S + \sum_{i=1}^n \left(\frac{s_i}{k_i} \right) \right). \quad (1)$$

- (2) Inventory cost

Referring to the inventory model of a single commodity, after the order for commodity i is placed, after the lead time L_i , the warehouse will receive the ordered commodity that has reached the maximum inventory level R_i of commodity i . In the mode of joint procurement, if the initial inventory level of commodity i is $R_i - D_i L_i$, and if the procurement frequency of commodity i is k_i , the order for this commodity will be issued at time $k_i T$, and the order will be received at time $k_i T + L_i$. Therefore, the inventory level of commodity i in the central warehouse before the arrival of the goods is $R_i - D_i(k_i T + L_i)$. Therefore, the average inventory level \bar{Q}_i

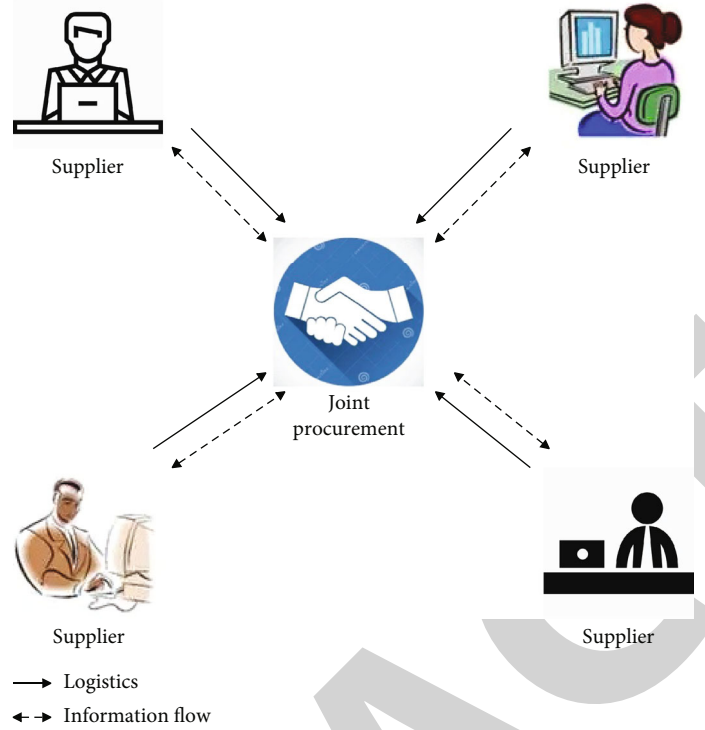


FIGURE 1: Schematic diagram of the JRP model under random demand conditions.

of commodity i in the central warehouse in time $k_i T + L_i$ is expressed as

$$\bar{Q}_i = \frac{1}{2} [(R_i - D_i L_i) + (R_i - D_i (k_i T + L_i))] = R_i - D_i \left(\frac{L_i + k_i T}{2} \right). \quad (2)$$

We assume that the demand for all purchased commodities is independent and identically distributed, and random demand follows a Brownian motion process. Moreover, under the premise that the decision variables k_i and T are determined, in the demand period of $k_i T$, the demand for commodity i follows a normal distribution, and its corresponding mean and standard deviation are expressed as $E(x_i, k_i T) = D_i k_i T$ and $\text{Var}(x_i, k_i T) = \delta_i k_i T$, respectively, and its probability density function is $f(x_i, k_i T + L_i)$.

Therefore, the maximum inventory level of a commodity is equal to the expected demand plus the amount of safety stock in the safety period. Considering that the lead time of commodity i is L_i , the maximum inventory level of commodity i in each purchasing cycle is expressed as [18]

$$R_i = D_i (k_i T + L_i) + z_i \sqrt{\delta_i (k_i T + L_i)}. \quad (3)$$

Among them, $f(z_i)$ and $F(z_i)$ are the probability density function (PDF) and cumulative distribution function CDF of the standard normal distribution corresponding to commodity i , respectively. Then, the inventory holding cost C_H

$$\begin{aligned} C_H &= \sum_{i=1}^n h_i \left[R_i - D_i \left(\frac{L_i + k_i T}{2} \right) \right] \\ &= \sum_{i=1}^n h_i \left[\frac{1}{2} D_i (k_i T) + z_i \sqrt{\delta_i (k_i T + L_i)} \right]. \end{aligned} \quad (4)$$

When the demand for commodity i is greater than the maximum inventory, the warehouse will be out of stock. In the out-of-stock mode under the regular inspection strategy, it will cause the corresponding out-of-stock cost to the central warehouse. The total out-of-stock cost C_s is expressed as [19]

$$\begin{aligned} C_s &= \sum_{i=1}^n \pi_i \int_{R_i}^{\infty} (x_i - R_i) f(x_i, k_i T + L_i) \frac{dx_i}{k_i T} \\ &= \sum_{i=1}^n \frac{\pi_i}{k_i T} \sqrt{\delta_i (k_i T + L_i)} \int_{z_i}^{\infty} (y - z_i) f(y) dy \\ &= \sum_{i=1}^n \frac{\pi_i}{k_i T} \sqrt{\delta_i (k_i T + L_i)} \left(\int_{z_i}^{\infty} y f(y) dy - \int_{z_i}^{\infty} z_i f(y) dy \right) \\ &= \sum_{i=1}^n \frac{\pi_i}{k_i T} \sqrt{\delta_i (k_i T + L_i)} (f(z_i) - z_i (1 - F(z_i))). \end{aligned} \quad (5)$$

(3) Total cost of joint procurement

By constructing purchasing cost, inventory cost, and out-of-stock cost, the stochastic JRP total cost TC with K , T , and z_i as decision variables is the sum of the above three costs:

$$\begin{aligned} TC(K, T, z_i) &= C_o + C_H + C_S = \frac{1}{T} \left(S + \sum_{i=1}^n \left(\frac{s_i}{k_i} \right) \right) \\ &+ \sum_{i=1}^n h_i \left[\frac{1}{2} D_i(k_i T) + z_i \sqrt{\delta_i(k_i T + L_i)} \right] \\ &+ \sum_{i=1}^n \frac{\pi_i}{k_i T} \sqrt{\delta_i(k_i T + L_i)} (f(z_i) - z_i(1 - F(z_i))). \end{aligned} \quad (6)$$

By derivation of TC with respect to z_i , the following formula can be obtained:

$$\begin{aligned} \frac{\partial TC(K, T, z_i)}{\partial z_i} &= h_i \sqrt{\delta_i(k_i T + L_i)} + \frac{\pi_i}{k_i T} \sqrt{\delta_i(k_i T + L_i)} \\ &\cdot \left(\frac{df(z_i)}{dz_i} - [1 - F(z_i)] + z_i f(z_i) \right). \end{aligned} \quad (7)$$

The standard normal distribution function satisfies $df(z_i)/dz_i = -z_i f(z_i)$. Therefore, we can get

$$\frac{\partial TC(K, T, z_i)}{\partial z_i} = \sqrt{\delta_i(k_i T + L_i)} \left(h_i - \frac{\pi_i}{k_i T} [1 - F(z_i)] \right). \quad (8)$$

At the same time, if $\partial TC(K, T, z_i)/\partial z_i = 0$, the optimal z_i^* must satisfy the following relation:

$$F(z_i^*(K, T)) = 1 - \frac{h_i}{\pi_i} k_i T. \quad (9)$$

Alternatively, it is written as an expression in the following inverse function form:

$$z_i^*(K, T) = F^{-1} \left(1 - \frac{h_i}{\pi_i} k_i T \right). \quad (10)$$

Because of $\partial^2 TC(K, T, z_i)/\partial z_i^2 = (\pi_i/k_i T) \sqrt{\delta_i(k_i T + L_i)} f(z_i) > 0$, once K and T are determined, z_i^* can be uniquely obtained by formula (10). By substituting formula (10) into formula (7), we obtain the expression of the objective function $TC(K, T, z_i)$ of the stochastic JRP, as shown in

$$\begin{aligned} \min TC(K, T, z_i) &= \sum_{i=1}^n \frac{1}{2} D_i h_i k_i T + \frac{1}{T} \left(S + \sum_{i=1}^n \left(\frac{s_i}{k_i} \right) \right) \\ &+ \sum_{i=1}^n \frac{\pi_i}{k_i T} \sqrt{\delta_i(k_i T + L_i)} f(z_i). \end{aligned} \quad (11)$$

We build a JRP model based on RFID investment stochastic demand. First, we need to clarify the relationship between RFID technology investment cost and return. Due

to the random uncertainty of demand, the capability of RFID technology is mainly reflected in the ability to improve the efficiency of joint procurement and reduce the cost of joint procurement. In order to distinguish the demand uncertainty JRP and the stochastic JRP after RFID investment in this section, we call the demand stochastic JRP as JRP1. Its corresponding total cost is $TC1$, and the random JRP of RFID investment demand is JRP2, and its corresponding total cost is $TC2$. The JRP decision model determined in this paper based on RFID technology is based on the JRP1 model. At the same time, referring to the RFID technology investment efficiency model, the JRP model of RFID investment is established. The model considers the impact of RFID on two costs of JRP, namely, the impact of ordering efficiency, and introduces the impact of efficiency factor R and inventory efficiency, which affects inventory cost and out-of-stock cost, and introduces JIT efficiency factor I .

After the ordering efficiency factor and the JIT efficiency factor are given, according to the equation, we get the total cost $TC2$ of the JRP model based on RFID technology to determine the demand:

$$\begin{aligned} TC2(T, K, z_i, I, R) &= I \cdot C_H + R \cdot C_O + I \cdot C_S + C_I + C_R \\ &= I \cdot \frac{T}{2} \sum_{i=1}^n k_i D_i h_i + R \cdot \frac{1}{T} \left(S + \sum_{i=1}^n \left(\frac{s_i}{k_i} \right) \right) \\ &+ I \cdot \sum_{i=1}^n \frac{\pi_i}{k_i T} \sqrt{\delta_i(k_i T + L_i)} f(z_i) + C_I + C_R. \end{aligned} \quad (12)$$

It can be seen from the equation that if $I = 1$, it means that there is no JIT efficiency improvement for the JRP process. If $I = 0$, it means that the commodity order is completed immediately, no inventory cost occurs, and no out-of-stock cost occurs, and the "Just in Time" for customer service is realized. Similarly, if $R = 1$, it means that there is no improvement in ordering efficiency for JRP process by RFID technology. When $R = 0$, it means that the supply capacity is infinite, and no order cost occurs. In order to find the best relationship between I and R , the relationship between I and C_I , and the relationship between R and C_R , we need to build a functional expression that relates these relationships. The order efficiency function and the JIT efficiency function are, respectively, expressed as

$$I = V + (U - V)e^{-\lambda C_I}, \quad (13)$$

$$R = N + (M - N)e^{-\beta C_R}. \quad (14)$$

Among them, $0 \leq V \leq U \leq 1$, U is the lowest JIT efficiency, that is, the efficiency without RFID investment, and V is the highest efficiency after the implementation of RFID technology. $0 \leq N \leq M \leq 1$, M is the lowest efficiency of ordering, that is, the efficiency without RFID investment, and N is the highest efficiency after the implementation of RFID technology. Here, the determination of U , V , M , and N values can refer to the experience of RFID project

Target vector:	2	5	4	3	0.23	3.1	2.5	3.8	1.5
X_{r1}^t :	1	3	2	5	0.65	2.9	2.0	1.1	3.9
X_{r2}^t :	2	2	3	4	0.53	3.1	1.4	1.2	3.6
X_{r3}^t :	5	1	4	1	0.12	3.6	1.9	3.9	1.9
Variant vector:	-0.2	2.4	1.6	6.2	0.81	2.7	1.8	0.02	4.6
Corrective vector:	2	2 (2.4)	2 (1.6)	3	0.81	1	1.8	3.8	1.5

$k_i \in (1, 5), T \in (0, 1), z_i \in (1, 4)$

FIGURE 2: Schematic diagram of mutation operation.

implementation and can be estimated by investigating the impact of the use of RFID technology in related industries on efficiency. Among them, λ, β is the RFID investment efficiency control coefficient, which is used to adjust the RFID technology investment effect according to the actual RFID implementation.

In order to analyze the efficiency improvement produced by the investment in RFID technology, we bring equations (13) and (14) into equation (11); if $TC2(T, K, z_i, I, R)$ is differentiated with respect to I and set to zero, we can obtain the following equation:

$$\begin{aligned} \frac{\partial TC2(T, K, z_i, I, R)}{\partial I} &= C_H + C_S + \frac{\partial C_I}{\partial I} \\ &= C_H + C_S + \frac{1}{\lambda} \frac{\partial [\ln(U - V) - \ln(I - V)]}{\partial I} \\ &= C_H + C_S - \frac{1}{\lambda} \frac{1}{I - V} = 0. \end{aligned} \quad (15)$$

From equation (15), if we can determine C_H and C_S , we can get the optimal I^* :

$$I^* = \frac{1}{\lambda \cdot (C_H + C_S)} + V. \quad (16)$$

Similarly, for equation (12), $TC2(T, K, z_i, I, R)$ takes the derivative of R and makes it zero, and if C_O can be determined, we can also obtain the optimal R^* :

$$R^* = \frac{1}{\beta \cdot C_O} + N. \quad (17)$$

By constructing the JRP model (JRD1) under the condition of random demand and the JRP model of random demand based on RFID technology, the optimal T, K, z_i, I, R is deduced. Next, we construct the DE solving algorithm based on the two stochastic demand JRP model structures, the number and type of decision variables.

The population length of the designed DE algorithm can be calculated in two ways. In the first way, all the decision variables can be randomly generated by the DE algorithm, but the range of each variable, especially z_i , needs to be determined. The population length of the DE algorithm is the length of the combined procurement cycle of commodi-

ties, the length of the basic procurement cycle, and the length of the safety stock factor. The decision variables of the second method are derived from formulas, which are calculated with reference to formula (10) given the joint procurement period K and the basic procurement period T of different commodities.

The base purchase period is a decimal value between 0 and 1. The safety stock factor needs to consider the properties of the population of the normal distribution function, when the confidence level is 0.6827, $z_i = 1.0$, and when the customer service level is 99.99%, $z_i \approx 3.08$. The level of customer service is determined according to the ability of the enterprise itself. Therefore, we can set the value range of 1 to 3, such as [1,3] or [1,2]. Under the second strategy, the search method of K and T can be completely referred to the content of Chapter 3, and then, the optimal combination of K and T is found and then the optimal z_i is calculated. For the sake of distinction, we call the JRP solution for the first strategy as JRP0 and the JRP solution for the second strategy as JRP1. Below, we set up the design process of the DE algorithm.

The solution process of the redesigned DE algorithm is also divided into the following three steps:

(1) Parameter setting and initialization process

The algorithm parameters are divided into two categories: problem-related parameters and DE algorithm-related parameters. The problem parameter setting can refer to relevant research examples, and the DE algorithm parameter setting is based on the actual solution experience. The specific setting process is as follows:

- (i) Problem parameter setting: we set the lower bound k_{Lower} and the upper bound k_{Upper} for each k_i , respectively, and we set $k_{Lower} = 1$ and $k_{Upper} = 5$, where $i = 1, 2, \dots, n$. At the same time, we design the initial value of T to be located at $[0, 1]$, and the value range of z_i to be $(1, 2)$.
- (ii) DE algorithm parameter setting: we set the DE algorithm population size pop , chromosome length l , mutation operator \tilde{F} , and crossover probability CR , respectively, and set t as the t -th generation population, and the objective function (total cost) as the fitness function fit. Since there are two initialization

Target vector:	3	4	1	1	0.18	2.2	2.3	1.8	1.2
Target vector:	0.16 < 0.4	0.78 > 0.4	0.42 > 0.4	0.32 < 0.4	0.95 > 4	0.63 > 0.4	0.51 > 0.4	0.35 < 0.4	0.94 > 0.4
Before crossing:	1	5	3	4	0.53	3.1	1.4	1.2	3.8
After crossing:	3	5	3	1	0.53	3.1	1.4	1.8	3.8

FIGURE 3: Schematic diagram of crossover operation.

methods, the pp -th chromosome e_{pp} of the t -th generation population is initialized:

$$\text{chromosome}_{pp}^t = (k_1, k_2, \dots, k_n, T, z_1, z_2, \dots, z_n) \quad (18a)$$

Alternatively, the pp -th chromosome e_{pp} of the t -th generation population is initialized as

$$\text{chromosome}_{pp}^t = (k_1, k_2, \dots, k_n, T). \quad (18b)$$

Among them, $pp = 1, 2, \dots, \text{pop}$, the chromosome length under two different strategies is $l = n + 1$ or $l = n + 1 + n$. After these parameters are set, the algorithm goes to the next step to initialize the population.

- (2) Initialize the population to calculate fitness and objective function values

Similar to the population initialization process of the DE algorithm in Chapter 3, if we define the algorithm population as P , the population is initialized as $P_{\text{pop}}^t = \{X_i^t | x_{i,j}^{\text{lower}} \leq x_{i,j}^t \leq x_{i,j}^{\text{upper}}, \tilde{i} = 1, 2, \dots, \text{pop}; \tilde{j} = 1, 2, \dots, l; x_{i,j}^t(t) \in X_i^t\}$. Among them, $x_{i,j}^{\text{lower}} = K^{\text{lower}}/T^{\text{lower}}$, $x_{i,j}^{\text{upper}} = K^{\text{upper}}/T^{\text{upper}}$, and when $\tilde{j} \leq n$, $x_{i,j}^t$ is usually calculated by

$$x_{i,j}^{t=0} = \text{round}\left(x_{i,j}^{\text{lower}} + \text{rand}(0, 1) \times (x_{i,j}^{\text{upper}} - x_{i,j}^{\text{lower}})\right). \quad (19)$$

Among them, "round" means rounding, and $\text{rand}(0,1)$ is used to generate random numbers between (0,1).

Here, we still take the objective function as the fitness function. The calculation process of TC and TC1 refers to formula (11), and the calculation process of TC2 refers to formula (12). The purpose of population initialization is to generate the current optimal solution, the best fitness, and the chromosomes under the best fitness. These parameters are used in the update process of the DE algorithm.

- (3) The main program of the DE algorithm runs

In order to better explain the flow of the DE algorithm, we take a four-commodity problem as an example to illustrate the three operations of the DE algorithm.

- (i) Mutation operation: here, the t -th generation chromosome of the DE algorithm population is selected

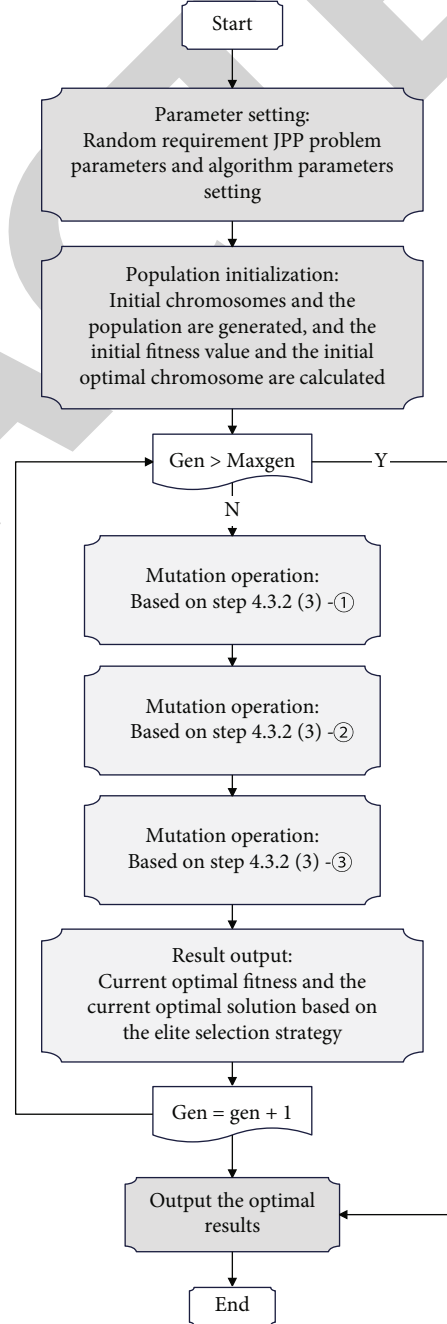


FIGURE 4: Flowchart of the DE algorithm.

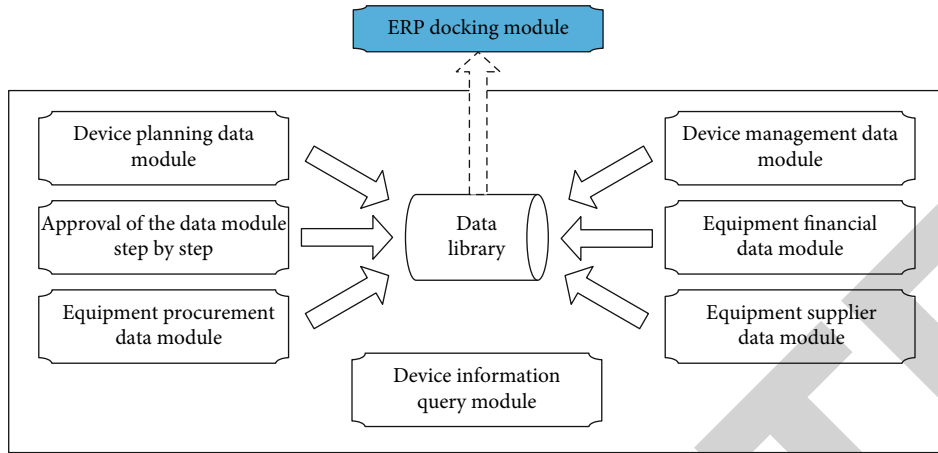


FIGURE 5: Equipment supply management system.

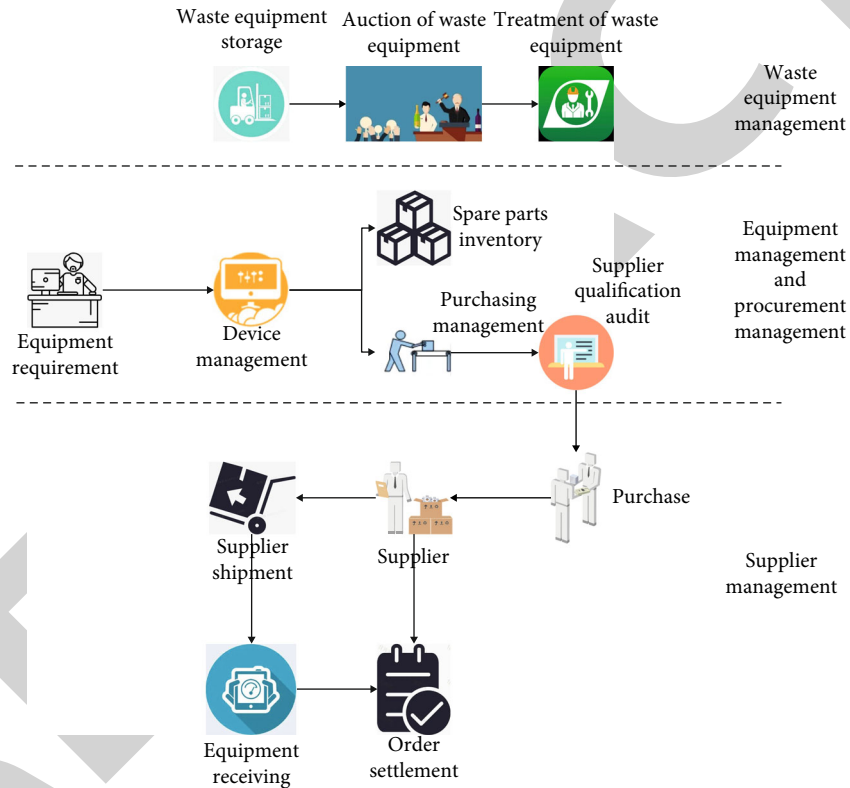


FIGURE 6: Schematic diagram of the procurement management information platform process.

as the target vector of mutation. Within the range of the t -th generation population, three different integer numbers r_1, r_2, r_3 that are different from the target vector are randomly generated, representing the r_1 -th, r_2 -th, and r_3 -th chromosomes of the population, respectively. If I presume mutation operator $F = 0.4$, then the whole mutation process according to the first strategy is shown in Figure 2. Figure 2 shows the schematic diagram of genes with multiple abnormal chromosomes after DE algorithm processing mutation. The basic processing idea is that if the mutated gene is abnormal, such as beyond the

defined range, it will be replaced by a randomly generated qualified number. If the generated gene falls within the defined domain, the algorithm rounds the locus of $\tilde{j} \leq n$. Similarly, for the gene processing at $\tilde{j} > n$, if it exceeds the defined range, it is replaced by a randomly generated qualified number; otherwise, the calculated value of the variation formula is taken

- (ii) Crossover operation: for each dimension, a vector with a length of 9 is randomly generated, which corresponds to the initial chromosome length of 9 (4 + 1 + 4), and a

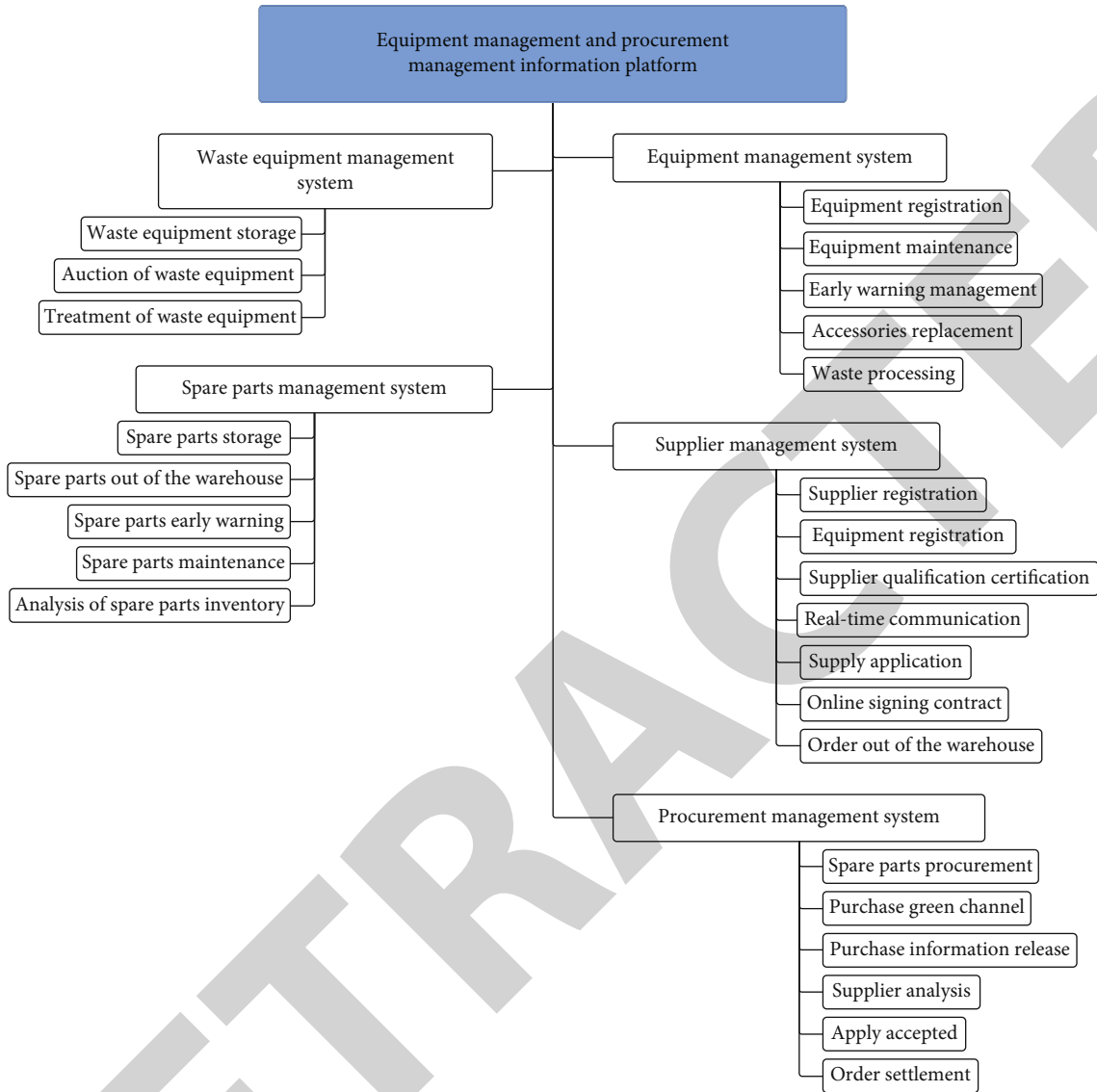


FIGURE 7: Architecture diagram of procurement management information platform.

new chromosome is constructed with reference to expression (4-18a). If $\text{randn}(t) = 4$, $\text{CR} = 0.4$, new chromosomes will be generated according to the quantum crossover rule, as shown in Figure 3

- (iii) Algorithm selection and update operations: according to the greedy selection rule, the selection operation of the DE algorithm is performed, the fitness of each chromosome is calculated, and the current optimal fitness and the current optimal chromosome are output
- (iv) The algorithm repeats algorithm steps (1)-(3) until the maximum number of iterations is reached or the algorithm converges
- (v) The algorithm outputs the optimal result
- (vi) When the maximum number of iterations is reached, the DE algorithm stops running and out-

puts the best fitness, the chromosome corresponding to the best fitness, and the optimal solution

The flow chart of DE algorithm to solve the random demand JRP is shown in Figure 4.

4. Cost Control System for Medical Equipment Procurement in Public Hospitals

Through the business demand analysis and data analysis of the medical equipment quota management system in the opposite hospital, various business flow charts have been used to clearly show the current equipment supply management business process. Therefore, the function that the system should achieve can be derived. Its functional modules include user login module, planning module, auditing module, equipment ordering module, storage and outgoing module, payment module, statistical query module, and equipment supplier data module. The specific functions that

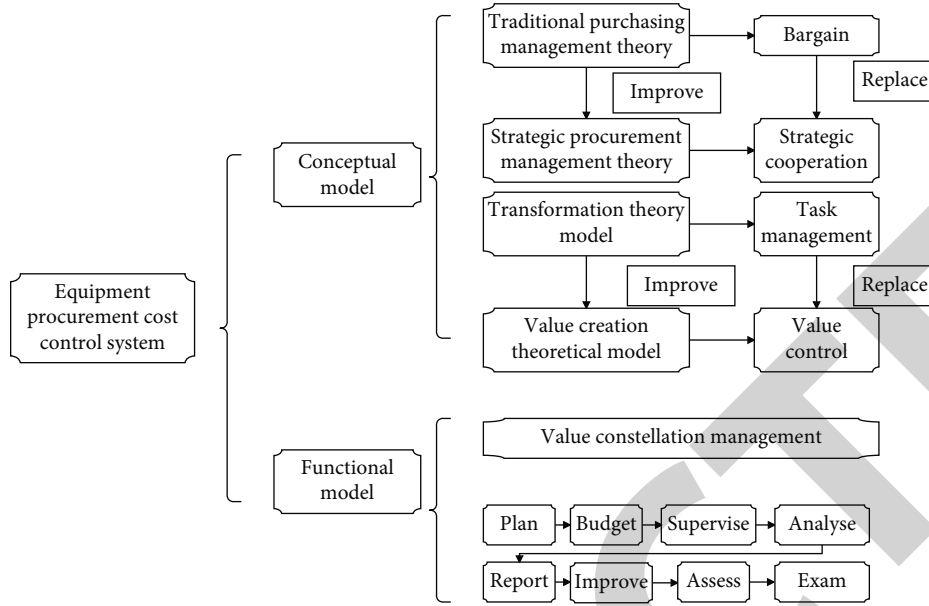


FIGURE 8: Overall framework of equipment procurement cost control system.

TABLE 1: Statistical table of the effect of the cost control system for medical equipment procurement in public hospitals based on mathematical modeling.

No.	Cost control	No.	Cost control	No.	Cost control
1	81.421	20	83.748	39	88.994
2	83.906	21	79.917	40	88.236
3	85.060	22	85.896	41	91.460
4	86.548	23	80.946	42	82.206
5	89.309	24	89.212	43	86.927
6	91.146	25	82.835	44	90.777
7	87.050	26	90.513	45	82.321
8	84.836	27	91.314	46	83.567
9	82.388	28	81.307	47	82.499
10	80.449	29	91.543	48	80.325
11	82.452	30	79.152	49	91.302
12	90.958	31	84.065	50	86.035
13	89.631	32	89.820	51	87.832
14	83.687	33	85.314	52	81.333
15	85.705	34	80.048	53	88.433
16	89.994	35	89.002	54	88.910
17	82.295	36	87.456	55	83.767
18	80.719	37	85.653	56	80.221
19	85.524	38	82.464		

can be realized are as follows: (1) user login: it is used to verify the user’s identity and access rights to determine their operation rights. (2) Plan input: it is used for the input of equipment plan. (3) Audit module: it is used to verify whether the equipment plan is reasonable. (4) Equipment order: it is used by the business department to input various information related to equipment into the system. (5)

Inbound and outbound: it is used for the management of equipment arrival, inbound, outbound, etc. by business departments and equipment users. (6) Payment: it supports input, statistics, and inquiry of expenses for equipment. (7) Statistical query: it is used for different needs of different users and can flexibly check and count data information related to the equipment. (8) Equipment supplier data: it is

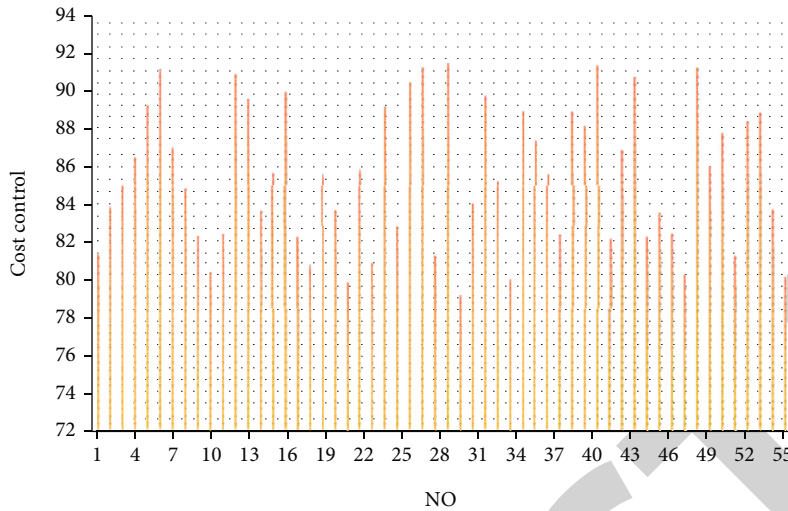


FIGURE 9: Statistical diagram of the effect of the cost control system for medical equipment procurement in public hospitals based on mathematical modeling.

used for the access, approval, and annual evaluation of suppliers. The connection between modules is shown in Figure 5.

As can be seen from Figure 6, the equipment management and procurement management platforms of public hospitals can be roughly divided into supplier management, equipment management and procurement management, and waste equipment management according to the order of equipment circulation.

After further refining the three-layer structure, the public hospital equipment management and procurement management information platform can be divided into five subsystems: equipment management system, supplier management system, procurement management system, spare parts management system, and waste equipment management system. The platform not only realizes the equipment safety management but also realizes the informatization of equipment procurement, so that the coal enterprises can greatly improve the continuous production capacity of the enterprises while producing safely. At the same time, purchasing equipment or accessories through online bidding not only ensures the quality of equipment or accessories but also greatly saves the procurement cost of enterprises. The architecture diagram of the equipment management and procurement management information platform is shown in Figure 7.

The conceptual model of the system is the theoretical basis of the equipment procurement cost control system and the most fundamental theoretical basis for the construction of the system. This construction is based on the optimization of the conceptual model of strategic procurement, changes the cooperation mode of the project, and replaces the bargaining based on the traditional procurement management theory by strategic cooperation. On the other hand, based on the theoretical model of value creation based on lean construction, the control method of the project is transformed, and the task management based on the transforma-

tion theoretical model is replaced by value management. The overall framework of the equipment procurement cost control system is shown in Figure 8.

On this basis, the effect of the model proposed in this paper is verified, and the procurement cost control effect of the model in this paper is counted. The results are shown in Table 1 and Figure 9.

From the analysis of the above chart data, we can see that the cost control system for medical equipment procurement in public hospitals based on mathematical modeling proposed in this paper can play an important role in equipment procurement in public hospitals.

5. Conclusion

Under the development situation of the new medical reform, my country has made major reforms in improving the procurement quality and efficiency standards of public hospitals, which has achieved the steady development of hospital business and promoted the transformation of hospitals from extensive management to refined management. In the management of large-scale medical equipment, by evaluating the benefits of large-scale medical equipment, the use efficiency of the equipment can be clarified, and it can also provide reference for the planning and project establishment of large-scale medical equipment. The benefit evaluation of the hospital's medical equipment before the purchase can judge the benefit of the capital investment, evaluate whether the investment is feasible, and prevent the waste of funds and idle equipment. Combined with the procurement process of medical equipment in public hospitals, this paper establishes a mathematical model of medical equipment procurement in public hospitals. Data analysis shows that the cost control system for medical equipment procurement in public hospitals based on the mathematical model proposed in this paper can play an important role in public hospital equipment procurement.

Research Article

Diagnosis of Brain Tumor Using Light Weight Deep Learning Model with Fine-Tuning Approach

Tejas Shelatkar,¹ Dr. Urvashi,¹ Mohammad Shorfuzzaman ,² Abdulmajeed Alsufyani ,² and Kuruva Lakshmanna ³

¹Department of Computer Science and Engineering, Dr. B. R. Ambedkar National Institute of Technology, Jalandhar 144011, India

²Department of Computer Science, College of Computers and Information Technology, Taif University, P.O. Box 11099, Taif 21944, Saudi Arabia

³School of Information Technology and Engineering, VIT-Vellore, India

Correspondence should be addressed to Kuruva Lakshmanna; lakshman.kuruva@vit.ac.in

Received 27 April 2022; Accepted 14 June 2022; Published 1 July 2022

Academic Editor: Pan Zheng

Copyright © 2022 Tejas Shelatkar et al. This is an open access article distributed under the Creative Commons Attribution License, which permits unrestricted use, distribution, and reproduction in any medium, provided the original work is properly cited.

Brain cancer is a rare and deadly disease with a slim chance of survival. One of the most important tasks for neurologists and radiologists is to detect brain tumors early. Recent claims have been made that computer-aided diagnosis-based systems can diagnose brain tumors by employing magnetic resonance imaging (MRI) as a supporting technology. We propose transfer learning approaches for a deep learning model to detect malignant tumors, such as glioblastoma, using MRI scans in this study. This paper presents a deep learning-based approach for brain tumor identification and classification using the state-of-the-art object detection framework YOLO (You Only Look Once). The YOLOv5 is a novel object detection deep learning technique that requires limited computational architecture than its competing models. The study used the Brats 2021 dataset from the RSNA-MICCAI brain tumor radio genomic classification. The dataset has images annotated from RSNA-MICCAI brain tumor radio genomic competition dataset using the make sense an AI online tool for labeling dataset. The preprocessed data is then divided into testing and training for the model. The YOLOv5 model provides a precision of 88 percent. Finally, our model is tested across the whole dataset, and it is concluded that it is able to detect brain tumors successfully.

1. Introduction

A brain tumor is a clump of uneven cells that forms a mass. Growth in this area might lead to cancerous consequences. As benign or malignant tumors develop, the pressure inside the skull will increase. Long-term brain damage and maybe death will happen as a result of this damage [1]. In India, this type of tumor affects 5 to 10 persons per 100,000 and is on the rise [2]. Considering children's brain and central nervous system, tumors are the second most common malignancy in children, accounting for around 26 percent of all malignancies.

Various advancements in the field of computer-aided diagnosis of brain tumors have been developed during the previous decade. These approaches are always available to assist radiologists who are unsure about the type of tumor

they are looking at or wish to investigate further. To identify tumors, doctors utilize MRI (magnetic resonance imaging) and CT-scan (computed tomography). MRI is the most preferred technique, and hence, researchers have concentrated their efforts on MRI. A critical stage in the diagnosis of a brain tumor is segmentation. To focus on this problem, researchers are using deep learning techniques [3, 4].

Machine learning is a branch of deep learning. It employs an artificial neural network to handle difficult problems containing large volumes of information. An artificial neural network is a network that functions similarly to the brain. The word "deep" in deep learning is defined as a network with several layers. Every neuron symbolizes a function, and each link does have a certain bit of weight. The backpropagation algorithm is employed by the network by adjusting the weights. With increasing precision on

complicated datasets, deep learning has changed the area of computer vision [4]. Image analysis uses a type of network called a convolutional network, which takes images as input and uses a kernel to convolve them into a picture map [5]. Deep learning models have a lot of benefits in medical imaging, including identifying critical components, pattern recognition in cell parts, feature extraction, and better outcomes for fewer datasets [6]. Transfer learning is a deep learning method in which the network's parameters (weights and biases) are taken from another network trained on a different dataset. The new network may now be trained using the transferred parameters as initialization (a process known as fine-tuning), or additional layers on top of the network can be formed and just those layers trained on the dataset of interest.

Using pretrained features on data is a common approach for neural network models [4, 7]. The network can now be developed using imported attributes as an initial process (a process known as fine-tuning), or additional layers can be placed on top of the network, with just the new layers being learned on the data of importance. Transfer learning has a number of benefits, including speeding up the data collecting process and improving generalization. It cuts down on the time it takes to train a huge dataset. In this study, we have applied YOLOv5's different variant algorithm on Brats 2020 annotated dataset to detect brain tumor location.

We used YOLO V5 to create our object detection model. The Darknet framework is utilized to maintain this model, and it provides a single network that can be used for both item categorization and prediction using bounding boxes. YOLO V5 is architecturally identical to YOLO V4, with the exception that it is built-in Python. Version 5 of YOLO is now significantly quicker and lighter. We utilized the YOLO V5 model, which was trained with the COCO dataset as a benchmark. Our unique annotated MRI pictures were used to train this model efficiently. YOLO is a single convolutional neural network, unlike other neural network-based frameworks for object identification [8, 9]. It has two fully connected layers for bounding box prediction and 24 convolutional layers for extracting information from pictures. The Darknet framework is used to build this network [10].

We have used all variations of the YOLOv5 model for brain tumor detection. The accuracy for YOLOv5s, YOLOv5n, YOLOv5m, YOLOv5l, and YOLOv5x models is 87%, 85.2%, 89%, 90.2%, and 91.2%, respectively. Lower training time, higher accuracy, and precision validate that the YOLOv5 detection model is suitable for brain tumor detection. As we have seen, there are a variety of approaches utilized in medical imaging, particularly MRI pictures of brain tumors. The algorithms for classification, segmentation, and detection were applied, but each has its own set of limitations [11, 12].

For this study, we have used a dataset from competition RSNA-MICCAI brain tumor radiogenic classification competition from Kaggle [13, 14]. The competition includes the Brats 21 dataset with a sample shown in Figure 1. The Center for Biomedical Image Computing and Analytics every year provides challenges for the researcher in terms of brain tumor analysis. The data evolves every year with

improvements. The challenge has been conducted since 2013. Brats 2014-17 had a similar type of data but was discarded since it had both pre- and postoperative scans. Since 2017, the current edition of the dataset has included glioma that has been annotated by experts in order to improve the training of our model. The dataset consists of MRI images with dimensions of 240×240. The dataset consisted of images of a brain tumor in 3 types of magnetic resonance imaging scans: T1 image, T2 image, and FLAIR image.

2. Related Work

For the diagnosis of brain tumors, many deep learning models have been used, although object detection methods have only been used in a limited number of studies, e.g., Pereira and co-authors employed the 3D Unet model, a new deep learning model that aids in the classification of tumors according to their severity. It has considered two areas of interest, the first of which is the whole brain, and the second of which is the malignancies zone of interest [1, 15].

Neelum et al. have had a lot of success with their problem analysis since they employ pretrained models such as DesNet and Inception-v3. Concatenation of features has greatly aided the model's improvement [16]. Mohammad et al. used a small dataset of 2D images to test several machine learning algorithms such as decision trees, support vector machines, convolutional neural networks, and deep learning models such as VGG 16, ResNet, and Inception. VGG19 was the most successful model, with an F1 score of 97.8 percent on top of the CNN framework. The author mentioned that there is a trade-off between model performance and temporal complexity. The ML approaches are simpler to use, whereas the DL methods are more efficient. The author also highlighted the need for a benchmark dataset. For tumor analysis automation, they used the algorithms FastAi and YOLOv5. However, YOLOv5 only achieves an accuracy of 85 percent. To compensate for the short dataset, they have not used any transfer learning techniques [17].

For minor health-care institutions [18], detailed research [19] on brain tumor analysis has been offered. The author conducted a poll that identified a number of issues with the methodology. They have also offered some suggestions for improving medical techniques. For bone identification, Al-masni et al. employed the YOLO model. As can be seen, the YOLO approach can produce significantly better results in medical imaging [20, 21].

Yale et al. [22] used the YOLO network to identify melanoma skin illness. Despite the fact that the test was run on a smaller dataset, the results were encouraging. The Darknet framework improves the speed of feature extraction. A better grasp of how YOLO works is still required. Kang et al. [23] suggested a hybrid model using deep features and machine learning classifiers along with the combination of several deep learning approaches with classifiers such as SVM, RBF, KNN, and others [24]. The ensemble feature has aided in the modeling of improved performance. However, the author claims that the proposed model is unsuitable for real-time medical diagnosis.

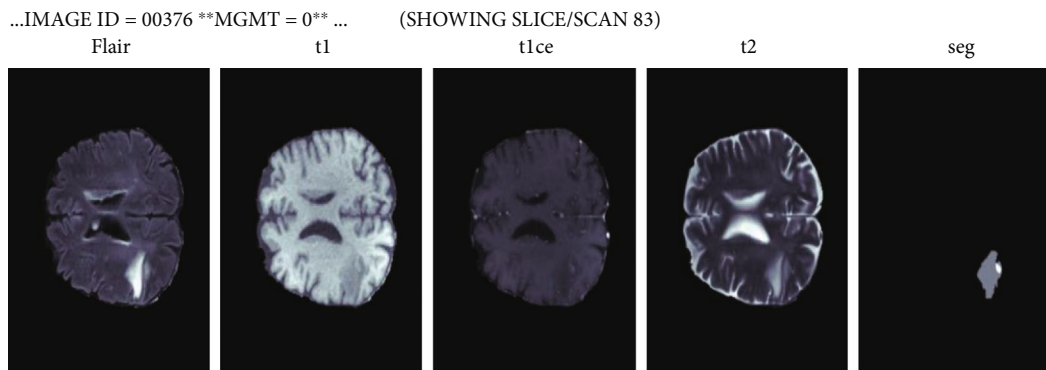


FIGURE 1: Brats21 dataset.

From 2015 to 2019, Muhammad et al. [17, 25] investigated several deep learning and transfer learning strategies. The author has outlined problems that must be overcome before any techniques to be used in the real world. While implementing models, researchers should pay attention to additional parameters in addition to accuracy. Some of the issues raised include the need for end-to-end deep learning models, improved run time, lower computing costs, and flexibility. The authors proposed contemporary technologies like edge computing, fog computing and cloud computing [26–28], federated learning, the GAN method, and IoT [7] as problem-solving technologies. As we have seen, there are a variety of approaches utilized in medical imaging, particularly on MRI pictures of brain tumors. The algorithms for classification, segmentation, and detection were applied, but each has its own set of limitations [11, 12].

3. Methodology

3.1. Dataset. For this study, we have used a dataset from competition RSNA-MICCAI brain tumor radiogenic classification competition from Kaggle [13, 14]. The competition includes the Brats 21 dataset with a sample as shown in Figure 1. The Center for Biomedical Image Computing and Analytics every year provides challenges for the researchers in terms of brain tumor analysis [29]. The data evolves every year with improvements. The challenge has been conducted since 2013. Brats 2014-17 had a similar type of data but was discarded since it had both pre- and postoperative scans. Since 2017, the current edition of the dataset has included glioma that has been annotated by experts in order to improve the training of our model. The dataset consists of MRI images with dimensions of 240×240. The dataset consisted of images of a brain tumor in 3 types of magnetic resonance imaging scans:

- (i) T1 image. In these MRI scans, the fat tissue is brighter. The subcutaneous fat is brighter which is present in the bone marrow of the vertebral bodies. The cerebrospinal fluid is not highlighted as it will appear black in the scans [30]
- (ii) T2 image. This scan is opposite to that of T1 as we can see cerebrospinal fluid brightly, and the bone cortex is black in the T1 scan

- (iii) FLAIR. It is known as fluid attenuated inversion recovery. Technically, FLAIR images help in reducing the vision of fluid content so we can directly analyze the tumor

The dataset is divided into dcm images based on scan types and axial positions, such as sagittal, which is the vertical plane perpendicular to the median plane; coronal, which is perpendicular to both sagittal and coronal planes; and axial, which is perpendicular to both sagittal and coronal planes.

Brats 21 dataset also contains the mgmt value which is an enzyme in a tumor known as methylguanine methyltransferase. The mgmt value is indirectly proportional to the chemotherapy effect on patients. So, Brats 21 also provides the data about the mgmt value [31]. For brain tumor detection, we need images with exact positions for that we need to define parameters [32]. For YOLOv5 training, we clone the YOLOv5 repository which contains the YOLOv5 model for training and trained weights from the cocoa model. The YOLOv5 repository also contains the hyperparameters setting for the training of the model [33].

3.2. YOLOv5. The YOLOv5 model requires image input. This image needs to be preprocessed before training the model. The images taken by the model are of dimension 512. The deep learning model requires more images to train and hence has bigger dataset, and we have taken 800 images dataset. Image scaling is done on the images for better magnification of the image and detection of the tumor. The data is labeled using the makesense.ai website, which saves the labels as well as the bounding box enclosing the tumor, as well as the annotation coordinates. The labels and images are divided into test and train with the coordinates of the four vertices of the rectangular box.

The YOLOv5 model has certain advantages in its model

- (i) The model's benefits include precise object recognition and tumor location, as well as high speed and detection accuracy
- (ii) The model is capable of detecting tiny tumor objects in photos that are noisy, hazy, or cloudy

The YOLOv5 is divided into three parts: backbone; neck; and prediction. The backbone of the YOLOv5 architecture is the Bottleneck Cross Stage Partial Darknet (BCSPD). The input images are fed to the backbone. For convolutional operations, the FOCUS module splits the input picture into four little ones and then concatenates them together. The $640 \times 640 \times 3$ pixel picture is reduced into four smaller $320 \times 320 \times 3$ pixel images, which are then concatenated into a $320 \times 320 \times 12$ pixel feature map. Once 32 convolutional kernels are used, the result is a $320 \times 320 \times 32$ feature map [34–36]. The model's CoBL module is a basic convolutional module that embodies the Conv2D+batch normalization (BN)+Leaky relu activation function. It eliminates the duplication of gradient information in CNN's optimization process and incorporates gradient changes into the feature map, decreasing input parameters and model size [37]. Two CoBL modules make up the BCSP: one residual unit and two 11 Conv2D kernels. The two CoBL modules and an adder are contained in a residual unit, and the adder adds the features of the previous CoBL module output and the features of two CoBL modules and then sends the local features to one 11 Conv2D layers. By modifying the width (w) and depth (d) of the BCSP module, the four models with varied input parameters, YOLOv5s, YOLOv5m, YOLOv5l, and YOLOv5x, may be obtained. In addition, the SPP module in the backbone interfaces with the BCSP module. The SPP module expands the network's receptive field and adds features of various scales. Second, YOLOv5 adds path aggregation network (PANet) in the neck area to improve information flow. The PANet is built on a feature pyramid network (FPN) topology, which transmits strong semantic characteristics from top to bottom. FPN layers also express significant positional characteristics from the bottom to the top. PANet also increases the transmission of low-level characteristics and the use of precise localization signals in the bottom layers. As a result, this improves the target object's position accuracy [38].

The prediction layer is also called the detection or YOLO layer, generating three different feature maps to attain multiscale prediction. However, the model can classify and detect small, medium, and large objects in the prediction layer.

The following is a synopsis of the YOLOv5 prediction process:

- (i) Phase 1. The backbone is fed with the photos at a resolution of 640 by 640 pixels at first. The FOCUS module slices the photos after that. The feature map is sent to the second concatenation layer after performing numerous convolutional operations and two BCSP1 operations. The feature map, on the other hand, is sent to the second concatenation layer after being run once by BCSP1, twice by BCSP2, twice by convolutions, and twice by upsampling. Both of them are combined in the second concatenation layer. The 80×80 sized feature map with scale 1 is created after the BCSP2 layers and 11 convolution operations are applied

- (ii) Phase 2. The 80×80 dimension feature map from phase 1 is filtered by one 33 percent convolutional kernel in the second step and sent to the third fusion layer. In addition, one 11 convolutional kernel executes the extracted features before the second upsampling and delivers it to the third concatenation layer. The final concatenation layer then joins the two together. The 40×40 scaled feature map as scale 2 is achieved after completing the BCSP2 layer and one 1×1 convolution operation
- (iii) Phase 3. In the third phase, the convolutional kernel processes the 40×40 sized feature map from phase 2 and sends it to the fourth concatenation layer. Furthermore, one 11 convolutional kernel executes the feature map before the first upsampling and sends it to the fourth concatenation layer. Both of them are concatenated at the fourth concatenation layer. The 20×20 sized feature map as scale 3 is then created using the BCSP2 layer and the 11 convolution procedure
- (iv) Phase 4. Finally, the feature maps of various sizes in scales 1 to 3 (i.e., 80×80 , 40×40 , and 20×20) are enhanced for recognizing tumor objects of various sizes using regression bounding boxes (BB). As a result, each feature map is predicted to have three regression bounding boxes at each position, resulting in three (80×80 , 40×40 , 20×20) = 25200 regression bounding boxes. Finally, as a final tumor detection outcome, the model's anticipated output with BB is displayed

The MSCOCO dataset has 80 preset object classes, and the YOLOv5 model was trained on it. The anticipated output tensor (POT) dimensions are $3(5 + 80) = 255$ where "3" signifies each grid cell prediction's three bounding boxes (BB), "5" specifies each prediction box's coordinates (x₀, y₀, w, and h) and confidence score (CS), and "80" denotes the predetermined item class (CL). As a result, we will need to tweak the YOLOv5 model's classifier. As a result of Equation (2), the projected output tensor (POT) dimension in our situation is $3(5 + 2) = 21$ [39].

For training our model, we have used the Google Colab environment. Once the dataset is preprocessed, we feed the training data to the pretrained model along with its hyperparameters provided by the YOLOv5 researchers for better results. In this research, we have used all the YOLOv5 variations which are available to get an in-depth analysis of the YOLOv5 model.

4. Evaluation Metrics

True positives (TP), false positives (FP), true negatives (TN), and false negatives (FN) are four important outcomes used to assess the efficacy of the proposed brain tumor classification and detection system. The performance of the proposed system is calculated using the following metrics: Accuracy determines the ability to correctly discriminate between different types of brain tumors [40]. The proportion of true

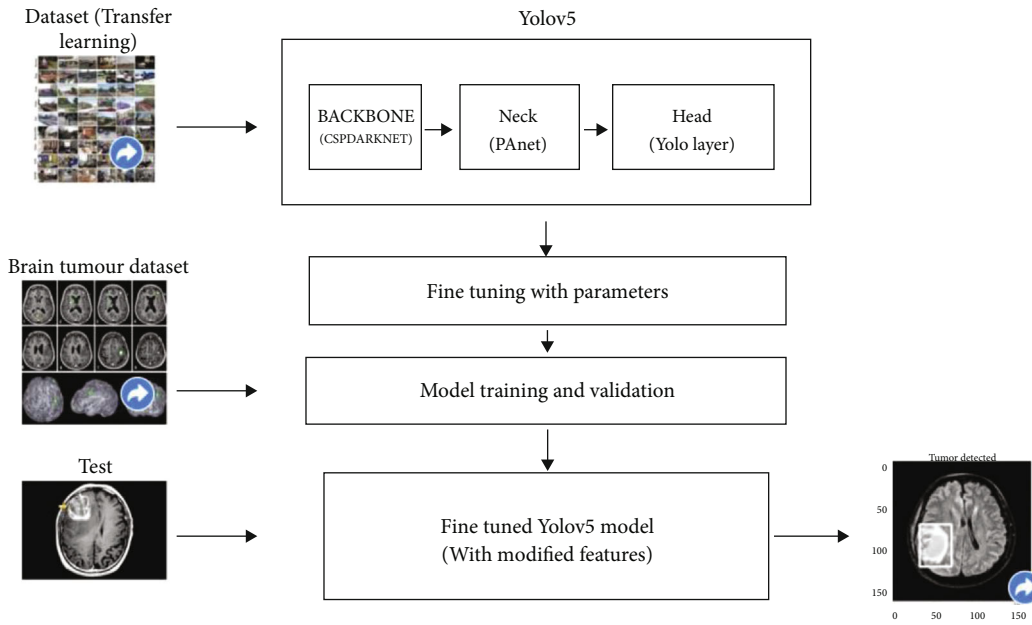


FIGURE 2: Fine-tuned YOLOv5 model.

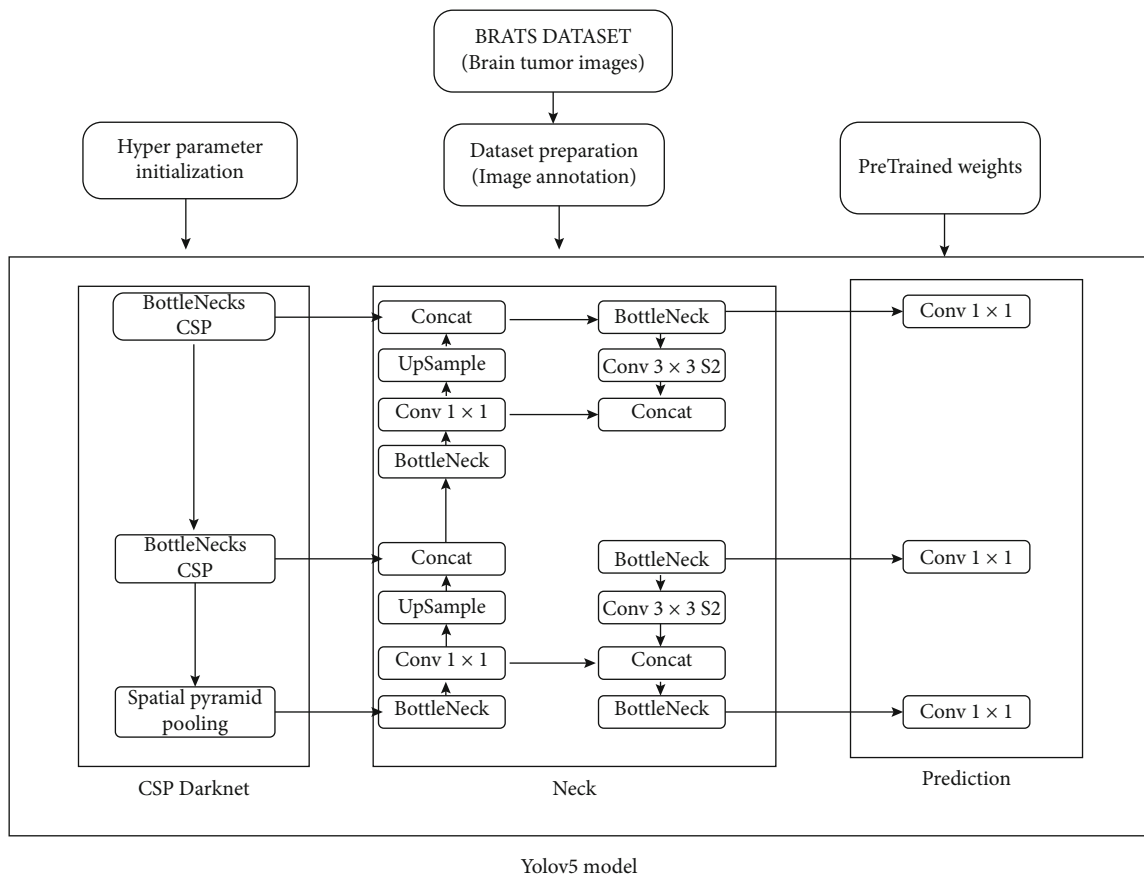


FIGURE 3: YOLOv5 model.

positive and true negative occurrences in all studied cases is computed using the formula below to establish a test's accuracy.

A true positive (TP) is when the model predicts the positive class properly. A true negative (TN), on the other hand, is a result in which the model properly predicts the negative

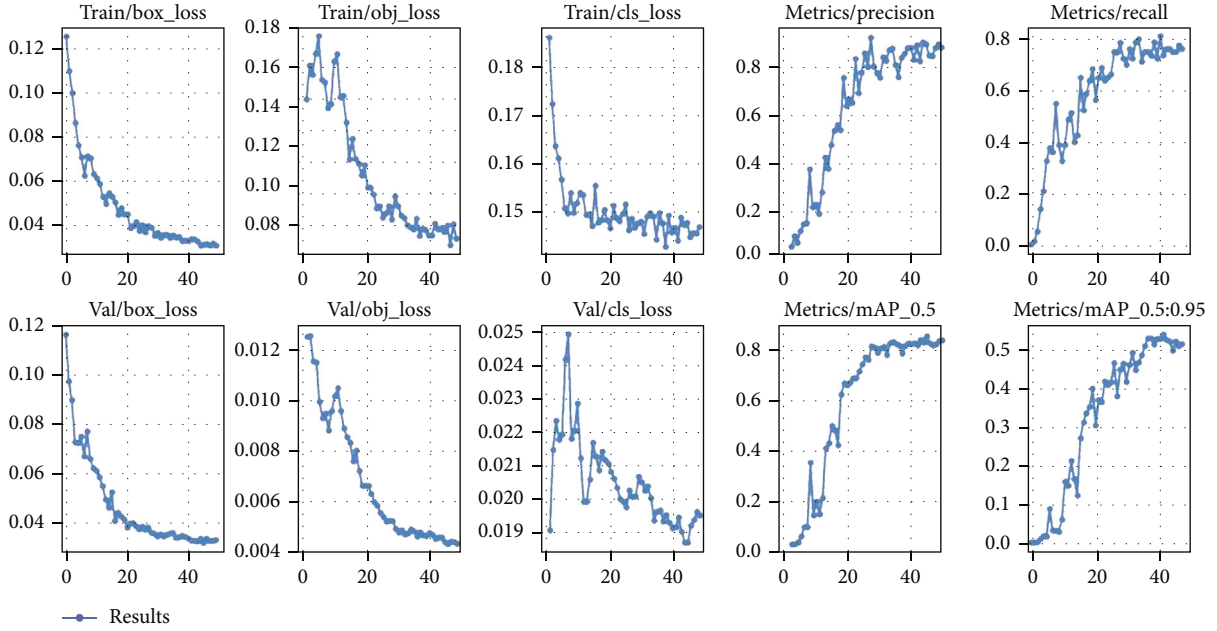


FIGURE 4: Accuracy curves for YOLOv5s, YOLOv5m, and YOLOv5l.

class. A false positive (FP) occurs when the model forecasts the positive class inaccurately. A false negative (FN) is an outcome in which the model forecasts the negative class inaccurately. Equation (1) has formula for accuracy, Equation (2) shows for precision, and Equation (3) represents recall. F1 formula as shown in Equation (4) is derived from precision and recall:

$$\text{Accuracy} = \frac{\text{TP} + \text{TN}}{\text{TP} + \text{TN} + \text{FP} + \text{FN}}, \quad (1)$$

$$\text{Precision} = \frac{\text{TP}}{\text{TP} + \text{FP}}, \quad (2)$$

$$\text{Recall} = \frac{\text{TP}}{\text{TP} + \text{FN}}, \quad (3)$$

$$\text{F1} = \frac{2 * \text{Precision} * \text{Recall}}{\text{Precision} + \text{Recall}} = \frac{2 * \text{TP}}{2 * \text{TP} + \text{FP} + \text{FN}}. \quad (4)$$

5. Proposed Model

We will be using the state-of-the-art model YOLOv5, as previously stated. COCO (Microsoft Common Objects in Context) dataset provided the pretrained weights. This parameter is used for fine tweaking. The BRat 2020 dataset is used to train the model. Patients' 3D scans are used to input the model. We use the test picture to obtain information about the tumor once the model has been trained. Using pretrained parameters on a dataset is a common approach in deep learning models [15]. The new network can now be trained using the transferred parameters as initialization (a process known as fine-tuning as shown in Figure 2), or additional layers can be built on top of the network, with only the new layers being trained on the dataset of interest. Transfer learning has a number of advantages, including speeding up

TABLE 1: YOLOv5 implementation analysis.

Model	Weight	mAP
Faster R-CNN [42]	200 mb	77.60
YOLOv4-tiny	33.2 mb	88.98
YOLOv5s	17 mb	87
YOLOv5n	12 mb	85.2
YOLOv5m	41 mb	89
YOLOv5l	90 mb	90.2
YOLOv5x	168 mb	91.2

TABLE 2: YOLOv5 comparison analysis.

Model	Weight	Precision	Times required (minutes)	Recall	mAP
YOLOv5s	17 mb	82.9	82.9	83	87
YOLOv5n	12 mb	81.5	81.5	82	85.2
YOLOv5m	41 mb	85.2	85.2	87.4	89
YOLOv5l	90 mb	88.2	88.2	86.2	90.2
YOLOv5x	168mb	89.1	190.1	9	91.2

the data collection process and improving generalization. In Figure 3, we can see we have input the preprocessed dataset along with pretrained weights and hyperparameter. The data is evaluated according to the model with various operations performed in the head, neck, and prediction phase of the YOLOv5 model. It cuts down on the time it takes to train a huge dataset.

Before we train the model with the YOLO model, we need to do some preprocessing. The tumor must be designated with a box region. This may be accomplished by utilizing a tool that produces a bounding box around the image's item of interest. We can utilize the NVIDIA transfer

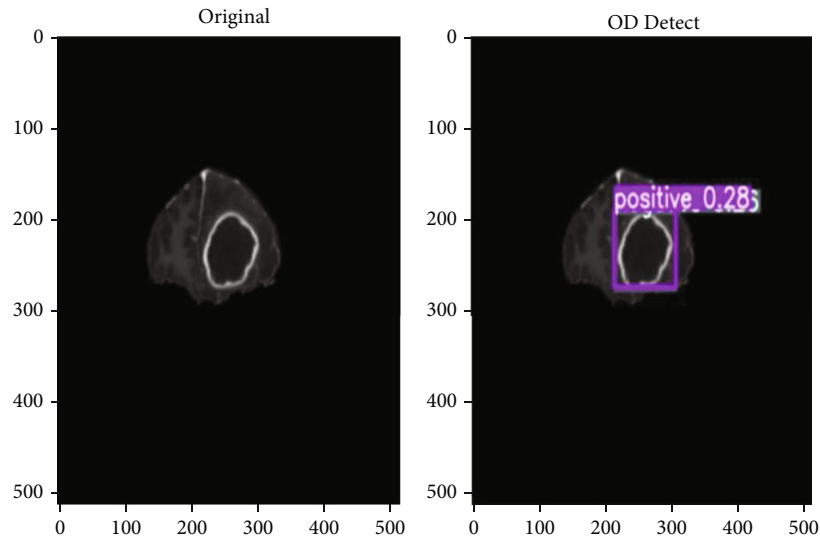


FIGURE 5: Brain tumor detection using proposed model.

learning toolbox for transfer learning, and we can feed the COCO dataset because it supports the YOLO architecture. This fine-tunes our model and compensates for missing or unlabeled data. Following that, we can use our model to train our Brats dataset. Google Colab, which provides 100 GB of storage, 12 GB of RAM, and GPU support, was used for development. The creators of YOLOv5 have made their training results accessible on the COCO dataset, which we may download and utilize for our own model. We need a labeled dataset for training to apply the YOLOv5 method to our model, which is available in the Brats dataset.

We will freeze several layers and put our own layer on top of the YOLO model for better results on the Brats dataset since we need to train it for better results on the Brats dataset. We will utilize the YOLOv5n model since we require a model that takes up less space. On the COCO dataset [13, 41], the YOLOv5 model gives us a mean average accuracy score of 72.4 and a speed of 3136 ms, as stated in the official repository. The key benefit of this model is that it is smaller and easier to produce than the prior YOLO model, and it is 88 percent smaller. At 140 frames per second, this model can process pictures. COCO (Microsoft Common Objects in Context) dataset provided the pretrained weights. This parameter is used for fine tweaking. The Brats 2020 dataset was used to train the model. We will use the YOLOv5 nano model in this case since it has a smaller architecture than the other models, and our major concern is model size. In comparison to the other models, the YOLO model has a significantly smaller 1.9M params. To be able to do brain scans, our model requires a specific setup. We do different treatments on the data, ranging from scaling to masking, because the scanned data of Brats is complicated.

Because the image data is saved in different formats with various types of scans such as FLAIR, T1, and T2, it is critical to handle the dataset according to our model's familiarity. Patients' scans are input into the model. We utilize the dice score, jaccard score, and map value to evaluate the outputs of our model, but our primary focus is on the model's

speed in order to improve its usefulness. The dataset has already been partitioned for training and testing purposes. There are around 360 patient scans for training and 122 patient scans for testing in our dataset. We may test the network using the YOLOv5 models' yml file for our specific setup. The classification has been set to three because we only have three classes. Our parameters in the backbone or head of our model must also be supplied to multiple convolution layers. The test picture dataset is fed to the models once the model has been trained. When compared to segmentation models, the predicted output of the proposed model must be close to a dice score of 0.85. In comparison to the previous models, this model uses less storage and processes the Brats dataset faster.

6. Experimental Results and Discussions

We have trained our model for different YOLOv5 variations. The YOLOv5 version includes YOLOv5s, YOLOv5n, and YOLOv5m. As we have trained from 0-50 epochs, this needs to be implemented according to lesser epoch data to check if our model is able to adapt according to lesser time requirement. Figure 4 shows the accuracy curves for YOLOv5s, YOLOv5m, and YOLOv5l, using the final picture dataset. The accuracy rate is initially quite low in all models, as shown in Figure 4, but it increases when the epochs are increased. Furthermore, the precision rate of the YOLOv5s model is from 75 to 85 percent, while the rates of the YOLOv5m and YOLOv5l models range from 78 to 89 percent and 83 to 95 percent, respectively. As a consequence, the YOLOv5l model outperforms the other two models in terms of benign and malignant tumor classification and prediction. Recall, on the other hand, refers to a model's capacity to recognize all relevant tumor classifications. It is also worth noting that as the number of epochs grows, so does the recall rate. Furthermore, the YOLOv5s model has a recall rate ranging from 80 percent to 90 percent, while the YOLOv5m model has a rate ranging from 85 to 95 percent,

and the YOLOv5l model has a rate ranging from 88 to 98 percent. As a result, the YOLOv5l model outperforms the other two models in terms of target tumor categorization and prediction. In addition, for all models, the mean average precision (mAP) is calculated. The mAP of the YOLOv5l model is higher than that of the YOLOv5m and YOLOv5s models, as can be shown in Table 1.

6.1. Performance. The impact of input dimensions on overall performance is shown in Table 1. The YOLOv5x variant generated the greatest mAP of 91.2% from the estimated findings from the test dataset. YOLOv5l came in second with 90.2%. Surprisingly, the YOLOv5n model did not improve on the YOLOv5s model. YOLOv5x had the greatest mAP, the accuracy of 89.1%, and RE of 90.4% in terms of total performance. With 85.2%, YOLOv5n had the lower mAP. However, as precision and complexity improve, the time required rises. The YOLOv5s model, which takes roughly 40 minutes to train for 50 epochs, requires the least amount of time. We examine different detection algorithms used for brain tumor analysis in Table 2. Faster R-CNN, as shown in Table 2, has worse accuracy than the other models, despite having greater weight and training time. YOLOv4 has a good accuracy score; however, it gives somewhat more weight to smaller models than YOLOv5. YOLOv5m produces the most consistent output with the best weight-to-accuracy ratio. After training our model, we are able to detect a tumor on any input image as shown in Figure 5.

7. Conclusion

In the proposed study, we have applied YOLOv5's different variant algorithm on Brats 2020 annotated dataset to detect brain tumor location. We were able to achieve 82-92 percent accuracy for the YOLO variant in which the YOLOv5l model provides us with the best accuracy than YOLOv5n and YOLOv5s. It was observed that the object detection model on brain tumor analysis gives slightly lesser accuracy than the classification and segmentation model. But we have also observed a substantial decrease in the training time and size of the model. We have also observed that while using the object detection model, there is a trade-off between the accuracy of our model with a combination of training time and model complexity. We have observed that in the YOLO model, the increase in complexity largely affects the training time, but there is an increase of about 5-6 percent in accuracy.

8. Future Scope

In the future, the accuracy of YOLOv5 smaller version models can be increased with further experimentation, and some additional research can be performed to decrease the trade-off between the accuracy and complexity of the model.

Data Availability

The data can be provided based on the request from the corresponding author.

Conflicts of Interest

The authors declare that they have no conflicts of interest.

Acknowledgments

We deeply acknowledge Taif University for supporting this study through Taif University Researchers Supporting Project number (TURSP-2020/115), Taif University, Taif, Saudi Arabia.

References

- [1] S. Pereira, R. Meier, V. Alves, M. Reyes, and C. A. Silva, "Automatic brain tumor grading from MRI data using convolutional neural networks and quality assessment," in *Understanding and interpreting machine learning in medical image computing applications*, pp. 106–114, Springer, Cham, 2018.
- [2] <https://www.ncbi.nlm.nih.gov/>.
- [3] A. Rehman, S. Naz, M. I. Razzak, F. Akram, and M. Imran, "A deep learning-based framework for automatic brain tumors classification using transfer learning," *Circuits, Systems, and Signal Processing*, vol. 39, no. 2, pp. 757–775, 2020.
- [4] P. Khan, M. F. Kader, S. M. R. Islam et al., "Machine learning and deep learning approaches for brain disease diagnosis: principles and recent advances," *IEEE Access*, vol. 9, pp. 37622–37655, 2021.
- [5] N. M. Dipu, S. A. Shohan, and K. M. A. Salam, "Deep learning based brain tumor detection and classification," in *2021 International Conference on Intelligent Technologies (CONIT)IEEE*.
- [6] K. Salçin, "Detection and classification of brain tumours from MRI images using faster R-CNN," *Tehnički glasnik*, vol. 13, no. 4, pp. 337–342, 2019.
- [7] R. Kaluri, D. S. Rajput, Q. Xin et al., "Roughsets-based approach for predicting battery life in IoT," 2021, <http://arxiv.org/abs/2102.06026>.
- [8] Z. Krawczyk and J. Starzyński, "YOLO and morphing-based method for 3D individualised bone model creation," in *2020 International Joint Conference on Neural Networks (IJCNN)IEEE*.
- [9] Z. Krawczyk and J. Starzyński, "Bones detection in the pelvic area on the basis of YOLO neural network," in *19th International Conference Computational Problems of Electrical EngineeringIEEE*.
- [10] M. Hammami, D. Friboulet, and R. Kechichian, "Cycle GAN-based data augmentation for multi-organ detection in CT images via YOLO," in *2020 IEEE International Conference on Image Process- ing (ICIP)IEEE*.
- [11] A. Bentajer, M. Hedabou, K. Abouelmehdi, and S. Elfezazi, "CS-IBE: a data confidentiality system in public cloud storage system," *Procedia Computer Science*, vol. 141, pp. 559–564, 2018.
- [12] A. Azougaghe, M. Hedabou, M. Belkasm, Z. Kartit, M. Belkasm, and M. El Marraki, "An efficient algorithm for data security in cloud storage," in *2015 15th International Conference on Intelligent Systems Design and Applications (ISDA)IEEE*.
- [13] <https://www.kaggle.com/c/rsna-miccai-brain-tumor-radiogenomic-classification>.
- [14] K. Lakshmana and N. Khare, "Mining dna sequence patterns with constraints using hybridization of firefly and group

- search optimization,” *Journal of Intelligent Systems*, vol. 27, no. 3, pp. 349–362, 2018.
- [15] K. Lakshmana, R. Kaluri, N. Gundluru et al., “A review on deep learning techniques for IoT data,” *Electronics*, vol. 11, no. 10, p. 1604, 2022.
- [16] N. Noreen, S. Palaniappan, A. Qayyum, I. Ahmad, M. Imran, and M. Shoaib, “A deep learning model based on concatenation approach for the diagnosis of brain tumor,” *IEEE Access*, vol. 8, pp. 55135–55144, 2020.
- [17] M. S. Majib, M. M. Rahman, T. M. S. Sazzad, N. I. Khan, and S. K. Dey, “VGG-SCNet: a VGG net-based deep learning framework for brain tumor detection on MRI images,” *IEEE Access*, vol. 9, pp. 116942–116952, 2021.
- [18] G. S. Gaba, M. Hedabou, P. Kumar, A. Braeken, M. Liyanage, and M. Alazab, “Zero knowledge proofs based authenticated key agreement protocol for sustainable healthcare,” *Sustainable Cities and Society Journal*, vol. 80, p. 103766, 2022.
- [19] M. Futrega, A. Milesi, M. Marcinkiewicz, and P. Ribalta, “Optimized U-net for brain tumor segmentation,” 2021, <http://arxiv.org/abs/2110.03352>.
- [20] M. A. Al-masni, M. A. Al-antari, J. M. Park et al., “Detection and classification of the breast abnormalities in digital mammograms via regional convolutional neural network,” in *2017 39th Annual International Conference of the IEEE Engineering in Medicine and Biology Society (EMBC)IEEE*.
- [21] A. P. Rodrigues, R. Fernandes, A. Shetty, K. Lakshmana, and R. M. Shafi, “Real-time twitter spam detection and sentiment analysis using machine learning and deep learning techniques,” *Computational Intelligence and Neuroscience*, vol. 2022, Article ID 5211949, 14 pages, 2022.
- [22] Y. Nie, P. Sommella, M. O’Nils, C. Liguori, and J. Lundgren, “Automatic detection of melanoma with YOLO deep convolutional neural networks,” in *2019 E-Health and Bioengineering Conference (EHB)IEEE*.
- [23] J. Kang, Z. Ullah, and J. Gwak, “MRI-based brain tumor classification using ensemble of deep features and machine learning classifiers,” *Sensors*, vol. 21, no. 6, p. 2222, 2021.
- [24] K. Zerhouni, E. M. Amhoud, and M. Chafii, “Filtered multicarrier waveforms classification: a deep learning-based approach,” *IEEE Access*, vol. 9, pp. 69426–69438, 2021.
- [25] T. R. Gadekallu, M. Alazab, R. Kaluri, P. K. R. Maddikunta, S. Bhattacharya, and K. Lakshmana, “Hand gesture classification using a novel CNN-crow search algorithm,” *Complex Intelligent Systems*, vol. 7, no. 4, pp. 1855–1868, 2021.
- [26] Y. Simpa Abdulsalam and M. Hedabou, “Security and privacy in cloud computing: technical review,” *MDPI Future Internet*, vol. 14, no. 1, 2022.
- [27] M. Hedabou, “Cloud key management based on verifiable secret sharing,” in *15th International Conference on Network and System Security. Lecture Notes in Computer Science*, pp. 289–303, Springer Verlag, 2021.
- [28] K. Lakshmana and N. Khare, “FDSMO: frequent DNA sequence mining using FBSB and optimization,” *International Journal of Intelligent Engineering Systems*, vol. 9, no. 4, pp. 157–166, 2016.
- [29] J. Amin, M. Sharif, A. Haldorai, M. Yasmin, and R. S. Nayak, “Brain tumor detection and classification using machine learning: a comprehensive survey,” *Complex Intelligent Systems*, vol. 8, pp. 1–23, 2021.
- [30] S.-Y. Lu, S.-H. Wang, and Y.-D. Zhang, “A classification method for brain MRI via MobileNet and feedforward network with random weights,” *Pattern Recognition Letters*, vol. 140, pp. 252–260, 2020.
- [31] B. H. Menze, A. Jakab, S. Bauer et al., “The multimodal brain tumor image segmentation benchmark (BRATS),” *IEEE Transactions on Medical Imaging*, vol. 34, no. 10, pp. 1993–2024, 2015.
- [32] T. Saba, A. S. Mohamed, M. El-Affendi, J. Amin, and M. Sharif, “Brain tumor detection using fusion of hand crafted and deep learning features,” *Cognitive Systems Research*, vol. 59, pp. 221–230, 2020.
- [33] <https://blog.roboflow.com/yolov5-v6-0-is-here/>.
- [34] N. Gundluru, D. S. Rajput, K. Lakshmana et al., “Enhancement of Detection of Diabetic Retinopathy Using Harris Hawks Optimization with Deep Learning Model,” *Computational Intelligence and Neuroscience*, vol. 2022, 2022.
- [35] E. M. Amhoud, E. Awwad, G. R. Ben-Othman, and Y. Jaouën, “Mode selection and larger set equalization for mode-multiplexed fiber transmission systems,” in *2015 Optical Fiber Communications Conference and Exhibition (OFC)*, pp. 1–3, IEEE, 2015.
- [36] E. M. Amhoud, G. R. B. Othman, and Y. Jaouën, “Concatenation of space-time coding and FEC for few-mode fiber systems,” *IEEE Photonics Technology Letters*, vol. 29, no. 7, pp. 603–606, 2017.
- [37] K. Lakshmana and N. Khare, “Constraint-based measures for DNA sequence mining using group search optimization algorithm,” *International Journal of Intelligent Engineering systems*, vol. 9, no. 3, pp. 91–100, 2016.
- [38] G. T. Reddy, M. Reddy, K. Lakshmana, D. S. Rajput, R. Kaluri, and G. Srivastava, “Hybrid genetic algorithm and a fuzzy logic classifier for heart disease diagnosis,” *Evolutionary Intelligence*, vol. 13, no. 2, pp. 185–196, 2020.
- [39] E. M. Amhoud, G. R. B. Othman, and Y. Jaouën, “Design criterion of space-time codes for SDM optical fiber systems,” in *2016 23rd International Conference on Telecommunications (ICT)*, pp. 1–5, IEEE, 2016.
- [40] K. Muhammad, S. Khan, J. Del Ser, and V. H. C. De Albuquerque, “Deep learning for multigrade brain tumor classification in smart healthcare systems: a prospective survey,” *IEEE Transactions on Neural Networks and Learning Systems*, vol. 32, no. 2, pp. 507–522, 2020.
- [41] U. Baid, S. Ghodasara, S. Mohan et al., “The rsna-asnr-miccai brats 2021 benchmark on brain tumor segmentation and radiogenomic classification,” 2021, <http://arxiv.org/abs/2107.02314>.
- [42] F. J. P. Montalbo, “A computer-aided diagnosis of brain tumors using a fine-tuned YOLO-based model with transfer learning,” *KSII Transactions on Internet and Information Systems (TIIS)*, vol. 14, no. 12, pp. 4816–4834, 2020.

Research Article

Observation of Visual Quality after Femtosecond Laser-Assisted Cataract Surgery Combined with Trifocal Intraocular Lens Implantation

Jianli Ma,¹ Xuequan Sun,¹ Yang Liu,¹ and Yumei Liu ²

¹Department of Ophthalmology, Zhengda Guangming Eye Group, Weifang Eye Hospital, Shandong 261000, China

²Department of Ophthalmology, Chongqing Wanzhou Aier Sunshine Eye Hospital, Wanzhou Chongqing 404100, China

Correspondence should be addressed to Yumei Liu; liuyumei2022@163.com

Received 13 May 2022; Revised 31 May 2022; Accepted 10 June 2022; Published 1 July 2022

Academic Editor: Pan Zheng

Copyright © 2022 Jianli Ma et al. This is an open access article distributed under the Creative Commons Attribution License, which permits unrestricted use, distribution, and reproduction in any medium, provided the original work is properly cited.

Objective. This study is the first observation of Alcon's PanOptix trifocal intraocular lens (IOL) implanted in 55 cataract patients with femtosecond laser-assisted cataract surgery. **Methods.** Fifty-five patients (63 eyes) with cataract were treated with femtosecond laser-assisted cataract surgery combined with trifocal IOL implantation. Visual acuity, defocus curve, higher order aberration (HOA), refractive stability, eyeglass removal rate, and satisfaction were evaluated and analyzed. **Results.** We found that the visual acuity of patients with near, intermediate, and distance vision was better than 0.1 LogMAR at 1, 3, and 6 months after the completion of surgery. The uncorrected near visual acuity (UCNVA), uncorrected intermediate visual acuity (UCIVA), and uncorrected distance visual acuity (UCDVA) of patients at 1, 3, and 6 months after surgery were compared with those before operation, showing statistical significance. Six months after the operation, all patients' surgical eyes had a smooth transition in the defocus range from +0D to -2.5D, and the visual acuity of the surgical eyes reached a level better than 0.1 LogMAR. The statistical results of 6-month follow-up showed that the eyeglass removal rate at near, intermediate, and far distances was 100%. At 6 months postoperatively, only 1 case had nocturnal glare, which affected life; 3 cases developed glare and halo but did not affect life. The patient satisfaction rate was 98.18%. **Conclusions.** Femtosecond laser-assisted cataract surgery with trifocal IOL implantation can remove the lens from the patient with satisfactory visual quality and significantly improve the postoperative satisfaction of the patient.

1. Introduction

Cataract, one of the most important blinding diseases in the world [1], is caused by various reasons, such as aging, genetic immunity, radiation injury, and other causes of lens metabolism disorders and protein denaturation, which makes the lens cloudy and the turbid lens block light from entering the retina, resulting in blurred vision [2]. At present, surgery is the main method to treat cataract [3]. In the earliest stage, the treatment is mainly to break the suspensory ligament around the lens, dislocate the lens, and sink into the vitreous cavity, so that light could enter the eye [4]. However, this method can only temporarily solve the problem, as the patient will be in a state equivalent to high myopia when refraction is lost after lens dislocation [5]. The sinking of the lens into the vitreous cavity

is more likely to cause inflammation and eventually loss of vision [6].

At present, phacoemulsification (PHACO) is the mainstay of treatment for cataract among various surgical treatments [7]. PHACO works by inserting a PHACO probe through a small incision made in the cornea or sclera, crushing the lens nucleus into a chylous shape using high-frequency vibration. The chylous is systematically sucked out, keeping the anterior chamber full, and then an intraocular lens (IOL) is implanted [8]. PHACO is an ideal cataract surgery with small incision, no pain, short operation time, and not obvious postoperative astigmatism [9]. However, the operation is costly and difficult to master, and it is still difficult to completely replace other methods [10]. Therefore, it is of great significance to find a more effective treatment that can facilitate recovery. Femtosecond

laser-assisted surgery, on the other hand, is a surgical procedure within the scope of PHACO technology, which is carried out by the computer according to the set program, with high stability and accurate cutting [11, 12]. However, there are still few reports investigating its therapeutic effect in cataracts.

The procedure involves removing the damaged lens, which is often replaced with a new artificial lens to restore vision [13]. An IOL is an artificial lens made from a synthetic material that can replace the lens and has been developed for six generations [14]. The original monofocal IOL cannot be adjusted by the ciliary muscle and the zonules as normal lenses do nor can it be adjusted to a certain range of focal length [15]. Bifocal IOL uses the refraction and diffraction principle of light to form the near and far focus, which relatively improves near vision, but has the problem of reduced contrast sensitivity [16]. Furthermore, the trifocal IOL also adopts the diffraction principle, but with optimized and improved structure to further improve the near and far vision [17]. However, there are few reports about femtosecond laser-assisted cataract surgery with trifocal IOL implantation in China. In this study, 53 cases (63 eyes) of cataract patients implanted with AcrySof® PanOptix® IOL were studied and analyzed for their clinical effects, so as to provide reference value for the extensive development of Focus IOL.

2. Materials and Methods

2.1. Research Participants. The study has been approved by the Ethics Committee of our hospital. Fifty-five patients (63 eyes) with cataract admitted to our hospital from November 2018 to November 2019 and met the surgical requirements were included. Inclusion criteria are as follows: (1) lens opacity; (2) patients with visual acuity <0.3 ; (3) regular corneal astigmatism $\leq 0.75D$; and (4) Alpha angle <0.5 mm and Kappa angle <0.3 mm. Exclusion criteria are as follows: (1) severe corneal opacity, obstructing the passage of laser; (2) unable to cooperate with this study; (3) severe systemic diseases (such as diabetes); and (4) other eye diseases, such as macular degeneration. All patients in this study signed an informed consent form and agreed to a 6-month follow-up visit. General information of subjects is shown in Table 1.

2.2. Preoperative Examination. Patients all underwent routine eye examinations before treatment, including eye B-ultrasound, slit lamp microscope, corneal endothelium, optical coherence tomography, best-corrected visual acuity (BCVA), and uncorrected visual acuity (UCVA). IOL was measured by an IOLMaster optical biometer. The power of IOL was calculated by SRK/T formula, and the target diopter was set close to 0° .

2.3. Surgical Methods. All operations were performed by the same experienced doctor. The pupils were fully dilated before the operation, and the surgical eye of the patient placed in the supine position was subjected to topical anesthesia. LenSx (Alcon, America, Figure 1(a)), a femtosecond laser-assisted cataract surgery system, was used to make a 2.2-mm main membrane incision at the 120° axial position of the cornea

and a 1.2-mm lateral corneal incision at the 20° axial position. The diameter of the femtosecond laser anterior capsule incision was 5.3 mm. After presplit nucleus treatment, the patient was transferred to the PHACO operating room. Following routine disinfection, the eyelid organs of the patient were opened, and viscoelastic agent was injected into the anterior chamber. After removing the free anterior capsule membrane with capsulorhexis forceps, the nucleus and cortex of lens were aspirated using an ophthalmic PHACO instrument (Shanghai Jumu Medical Instrument Co., Ltd., Figure 1(b)), the remaining cortex was fully injected and polished, and then the capsule was implanted into AcrySof® PanOptix® IOL (Alcon, Fort Worth, TX, USA), Figure 1(c)). The viscoelastic agent in the capsule was completely sucked out, and the anterior chamber was formed with the mouth closed. After the operation, we applied topical Bishu eye ointment and bandaged the operated eyes. AcrySof® PanOptix® IOL is a single aspheric IOL. The main body and support part were made of hydrophilic acrylic material with hydrophobic surface characteristics. The front surface was designed with a combination of refraction and diffraction, with an optical diameter of 6 mm, a maximum diameter of 11 mm, a short distance of 33d, a medium distance of 1.66d, a central 4.34 mm area with trifocal design, and a bifocal design for the surrounding area.

2.4. Postoperative Follow-Up and Observation Indexes. At 1, 3, and 6 months after surgery, the following postoperative detection indexes of patients were collected through medical records inquiries and telephone visits.

2.4.1. Vision Test. Uncorrected near visual acuity (UCNVA), uncorrected intermediate visual acuity (UCIVA), and uncorrected distance visual acuity (UCDVA) were measured before and 1, 3, and 6 months after operation. UCNVA was detected with standard near vision chart, and the detection distance was 40 cm. UCIVA was tested using the standard near vision chart, and the detection distance was 80 cm. And UCDVA was evaluated using the standard logarithmic visual acuity chart, with the detection distance of 40 m.

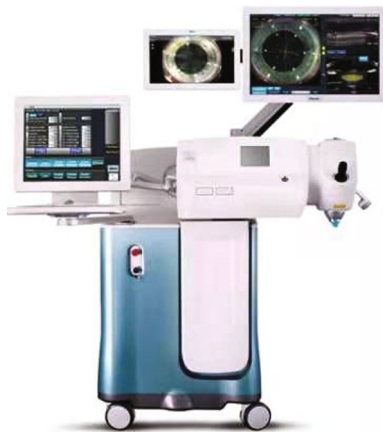
2.4.2. Defocus Curve Measurement. Six months postoperatively, the comprehensive refractometer was used to reduce the spherical degree from +2D to -4D with 0.5d as the first gear, and the corresponding spherical degree vision of the patient was detected. The defocus curve was drawn with visual acuity as Y-axis and spherical degree as X-axis.

2.4.3. Higher Order Aberration. The higher order aberration (HOA) was measured with an I-Trace visual function analyzer (Shanghai Hanfei Medical Instrument Co., Ltd.) with a pupil diameter of 3 mm. The total HOA, Trefoil, Coma, and Spherical aberration were recorded before operation and 1, 3, and 6 months after operation. All tests were completed by a doctor who is skilled in operating the system, instructing the patient to open both eyes and open the fixation target. The average was taken after three measurements.

2.4.4. Refractive Stability. Six months after the operation, the diopters (D) of the patients were observed and recorded, and the spherical equivalent (SE) of D was calculated. The

TABLE 1: General information of subjects.

Number of cases (n)	Operative eye (n)	Male (n)	Female (n)	Age ($\bar{x} \pm s$, years)	Astigmatism ($\bar{x} \pm s$, D)
55	63	21	34	57.94 \pm 8.41	0.34 \pm 0.17



(a)



(b)



(c)

FIGURE 1: (a) Femtosecond laser. (b) Phacoemulsifier for ophthalmology. (c) Alcon's PanOptix trifocal IOL.

histogram was drawn according to the interval distribution of $\pm 1.0D$, $\pm 0.75D$, $\pm 0.50D$, and $\pm 0.25D$.

2.4.5. Eyeglass Removal Rate and Satisfaction. Six months after surgery, the subjective visual quality of patients was investigated with the self-made questionnaire, including the rate of eyeglass removal and visual satisfaction. The postoperative eyeglass removal rate was assessed from UCNVA (watching mobile phone), UCIVA (reading), and UCDVA (watching TV). Visual satisfaction, evaluated according to halo, glare, and other visual interference phenomena, was divided into 4 grades ranging from dissatisfied to very satisfied.

2.5. Statistical Methods. SPSS 23.0 statistical software (IBM SPSS, Inc., Chicago, IL, USA) was used to statistically analyze the data. Qualitative data were expressed as n (%), and quantitative data were expressed as $(\bar{x} \pm s)$. Qualitative data, quantitative data, and repeated measurement data were analyzed by χ^2 , t -test, and analysis of variance (ANOVA), respectively. $P < 0.05$ means the difference is statistically significant.

3. Results and Discussion

3.1. Comparison of Preoperative and Postoperative Visual Acuity. At 1, 3, and 6 months after the operation, the near, intermediate, and distance vision of patients were found to be better than 0.1 LogMAR. UCNVA, UCIVA, and UCDVA at 1, 3, and 6 months after surgery were compared with those before surgery, and significant differences were determined ($P < 0.05$), while the comparison of UCNVA, UCIVA, and UCDVA at 1, 3, and 6 months after surgery revealed no statistical significance among different postoperative periods ($P > 0.05$, Figure 2).

3.2. Defocus Curve after Surgery. After the operation, we followed up all the patients for 6 months and found that all the operated eyes of patients had a smooth transition in the defocus range of $+0D$ to $-2.5D$, with a visual acuity level better than 0.1 LogMAR (Figure 3).

3.3. Comparison of HOA before and after Surgery. The HOA, trefoil aberration, coma aberration, and spherical aberration of patients 1, 3, and 6 months postoperatively were compared with those before the operation, and significant differences were determined ($P < 0.05$), while the HOA, trefoil aberration, coma aberration, and spherical aberration showed no statistical significance among different postoperative periods (1, 3, and 6 months after surgery) ($P > 0.05$, Figure 4).

3.4. Postoperative Refractive Stability Distribution of Patients. During the 6-month follow-up, we found that 63.49% of the affected eyes had SE within $\pm 0.25D$, 87.30% had SE within $\pm 0.50D$, 96.83% had SE within $\pm 0.75D$, and 100.00% had SE within $\pm 1.00D$ (Figure 5).

3.5. The Eyeglass Removal Rate and Satisfaction of Patients. We followed up the patients for 6 months after surgery and calculated to find that the eyeglass removal rate at the near, middle, and long distances was 100%. During the follow-up, only 1 patient was reported with night glare, which affected

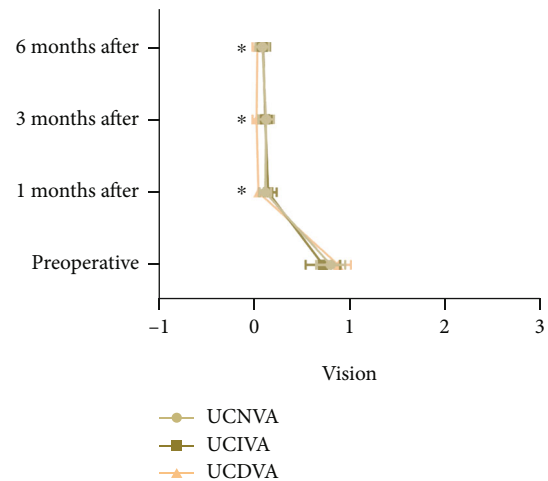


FIGURE 2: Comparison of patients' visual acuity before and after surgery. Note: * indicates $P < 0.05$ compared with before treatment.

life, and 3 cases experienced glare and halo that did not affect life. The patient's satisfaction rate was 98.18% (Figure 6).

4. Discussion

Cataracts can be divided into congenital cataracts and acquired cataracts. The former, also known as developmental cataracts, exists in the embryonic period and is mostly caused by genetic metabolic diseases, while the latter is attributed to the patient's own diseases, metabolic abnormalities, poisoning, trauma, etc. The pathogenesis of cataract is mainly crystal protein degeneration, oxidative stress, and lens epithelial cell (LEC) apoptosis [18]. The lens transmits light, which is projected onto the retina to produce vision. Lens proteins, which play an important role in maintaining lens transparency, come in two main types: water-soluble and insoluble. Water-soluble proteins are dominant, but when insoluble proteins begin to increase due to various reasons, the water-soluble ones will decrease accordingly, forming an uneven medium and light scattering that affects the light transmittance and light refraction ability of the lens, which is the basis for the onset of cataracts [19]. There are three main types of water-soluble proteins: α , β , and γ . The α -crystallin molecular chaperone active peptide can inhibit the production of insoluble proteins. Changes in the structure or quantity of β/γ -crystallin protein will alter the lens structure and produce insoluble proteins. Therefore, lens protein denaturation is to provide a material basis for the occurrence of cataracts [20]. The production of 8-hydroxyguanine, which is produced in deoxyribonucleic acid (DNA), disturbs the base pairing and causes changes in protein function. DNA single-strand breaks are also one of the factors in the formation of cataracts, and LEC apoptosis is the cytological basis [21].

LenSx is mainly based on the principle of photolysis and dielectric breakdown. It uses high irradiance, high-precision focusing, and short pulse laser spot to be highly localized in transparent tissues (such as cornea), so that the beam can be absorbed in a very short time. At $100^{\circ}C$ to $300^{\circ}C$, the energy

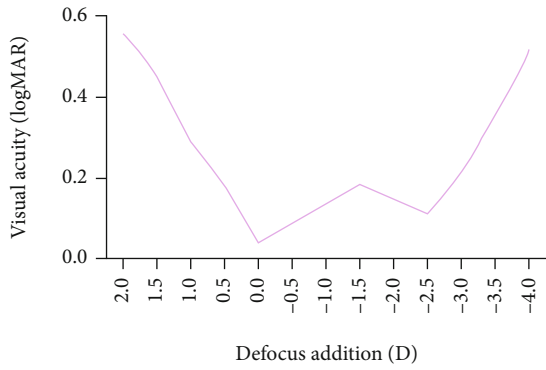


FIGURE 3: Defocus curve after trifocal IOL implantation.

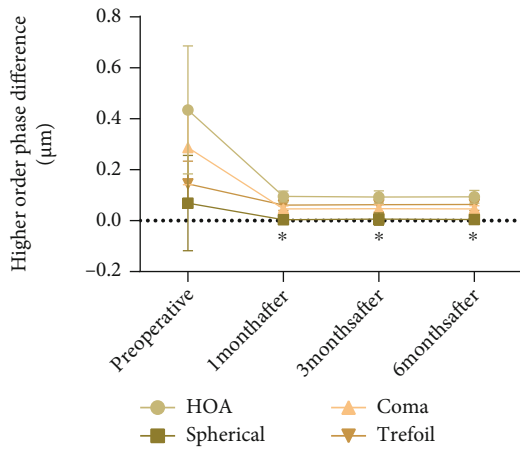


FIGURE 4: Comparison of HOA before and after surgery. Note: * indicates $P < 0.05$ compared with before treatment.

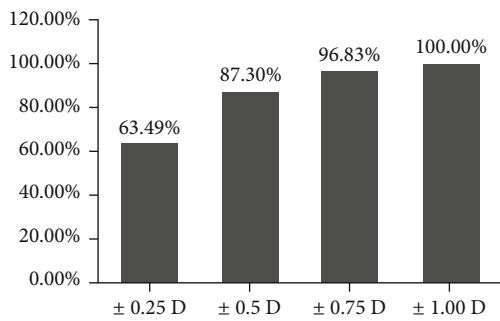


FIGURE 5: Postoperative refractive stability distribution of patients.

generates plasma, whose expansion and contraction generates shock waves. While the expansion and contraction of tissues leads to cavitation and formation of bubbles that fuse and burst to allow accurate cutting of adjacent tissues [22]. When this technology is applied to the cornea and lens, bubbles are generated only at the specified depth within the lens due to the wavelength (1053 nm) not being absorbed by corneal tissue and anterior lens capsule, which can evaporate the tissue in the micron-level plane.

In the development of IOL, monofocal IOL solves the problem of blindness that may occur after lens removal. However,

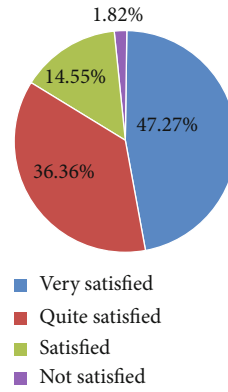


FIGURE 6: The eyeglass removal rate and satisfaction of patients.

because its lens can only be used as a lens to replace its refractive function, it is still necessary to wear glasses to adjust the vision after monofocal IOL implantation, so as to basically restore normal vision. The lens adjusts its thickness through the human body to adjust the focus, but the IOL can only obviously fix its size, and the implantation of it cannot use the principle of natural lens to adjust the focus. Therefore, bifocal IOLs were invented based on the principle of refraction and diffractive optics to adjust the focus. According to different principles, bifocal IOLs are divided into refractive, diffractive, and hybrid IOLs. The refractive IOL is a refracted light with aspherical concentric rings on its front surface to produce near and distance vision. The diffractive bifocal IOL uses the principle of light wave dynamics to construct diffraction steps and diffraction zones of the micro slope ring on the back surface to produce near and distance vision. The hybrid IOL is designed to achieve diffraction in the middle and refraction in the periphery. The width and height of the annulus are gradually changed from the center to the periphery to smooth out the light and thus achieve clear vision in the near and far. However, the disadvantage of these designs is that nonfocal imaging on the focal plane can also appear blurred, which will interfere with focus imaging, presenting as glare and halos, decreased contrast sensitivity, and loss of fine vision [23]. To solve these problems, a trifocal IOL was developed.

At present, trifocal IOLs include Fine Vision trifocal IOLs, Zeiss trifocal (AT LISA tri839MP) IOLs, and PanOptix trifocal IOLs. Fine Vision trifocal IOLs are developed based on the principle of diffraction, with the diffraction ring highly focused on myopia and intermediate vision, allowing for near vision increase by +3.5D and intermediate vision increase by +1.75D. The pupil size adjusts the light to enter to adjust distance vision, with 43% of the light used for distance vision, 28% for near vision, and 15% for intermediate vision [24]. AT LISA tri839MP IOLs are based on the design of aspheric refraction and diffraction. Optically, it is divided into two parts, namely, the trifocal area in the middle and the traditional bifocal area in the periphery, which can compensate +3.33D near vision and +1.66D intermediate vision [25]. The above two trifocal IOLs have achieved good results in clinical applications, but their astigmatism problems cannot be ignored.

PanOptix trifocal IOLs, which are the latest AcrySof series developed by Alcon Corporation of the United States in 2015, were used in this study. The optical diameter of such IOLs is 6.0 mm, and the total diameter is 13.00 mm, with 15 diffraction zones in the optical zone, which can distribute the light energy to 3 focal points. Among them, the energy of the first diffracted class is redistributed to the zero, second, and third classes. The zero class is used for distance vision to retain the original single focus lens vision, the second class is used for vision, increasing +2.17D, and the third class is used for near vision, increasing +3.25D [26]. The results of this study show that patients can obtain good vision better than 0.1 LogMAR in near, intermediate, and far vision at 1, 3, and 6 months after surgery, with well-recovered UCNVA, UCIVA, and UCDVA. Compared with the research results of the AT LISA tri 839MP IOL implantation by Kretz et al. [27], the application effect in this study is more ideal and stable.

The defocus curve is an important indicator evaluating the performance of multifocal IOLs, which mainly reflects the continuous visual range of patients [28]. The changes in vision are reflected by measuring the visual performance of patients at different distances. The change in distance is mainly due to the change of the lens to cause defocus, so it is called the defocus curve. The abscissa of the defocus curve is the power of the added lens, and the ordinate is the visual acuity. The 6-month postoperative defocus curve of this study showed two peaks at 0D and -2.5D, but the transition was smooth in the middle, and the visual acuity level of the surgical eye was better than 0.1 LogMAR. The two peaks indicate that the patient's distance and near vision are sufficiently clear after the operation, and the gentle change indicates that the far-near conversion is stable and clear. This is mainly because the PanOptix trifocal IOL increased +2.17D vision and increased +3.25D near vision, which is consistent with the findings of Poyales et al. [29].

Studies have pointed out that nonfocal imaging on the focal plane can also be blurred and interfere with focal imaging due to HOA. The glare and halo, decreased contrast sensitivity, and loss of fine vision after the above-mentioned bifocal IOL are due to HOA [30]. Measuring the total HOA of the trifocal IOL helps to reflect the objective changes in visual quality. This study found that the total HOA, coma aberration, spherical aberration, and clover aberration of the whole eye at each postoperative period were significantly lower than those before surgery, similar to the research results of Zein El-Dein et al. [31]. Therefore, the HOA in this study is not high, and the patients can obtain a more satisfactory visual quality.

Refractive stability reflects the performance of cataract surgery [32]. If the refractive stability is good, it means high-accuracy cutting during the operation will not damage the cornea and other tissues. In our study, 63.49% of the affected eyes had SE within $\pm 0.25D$, 87.30% had SE within $\pm 0.50D$, 96.83% had SE within $\pm 0.75D$, and 100.00% had SE within $\pm 1.00D$. It demonstrates the accuracy of LenSx and the advantages of small tissue damage, without damaging the cornea, iris, and other capsule tissues of the lens, which also provides an effective location for subsequent IOL implantation. Donmez et al. [33] reported that PanOp-

tix trifocal toric IOL has excellent refractive stability and can provide excellent visual quality for patients.

Patient satisfaction and eyeglass removal rate reflect the patient's overall surgery and postoperative recovery. In this study, the eyeglass removal rate of near, middle, and far distances was 100%. Six months after the operation, only 1 patient was reported with night glare, which affected life, and 3 cases experienced glare and halo that did not affect life. The patient's satisfaction rate reached 98.18%, which is relatively high. The results of the above complications and satisfaction rate were similar to those of Brozkova et al. [34]. Kretz et al. [27] also pointed out in their study that the surgical satisfaction rate of patients under trifocal IOL (AT LISA tri 839MP) intervention was 80%, which was significantly lower than that of 98.18% in this study.

The novelty of this study lies in the analysis of femtosecond laser-assisted cataract surgery combined with trifocal IOL implantation from the perspectives of visual acuity, defocus curve, HOA, refractive stability, eyeglass removal rate, and patient satisfaction. It is confirmed that femtosecond laser-assisted cataract surgery combined with trifocal IOL implantation has a positive effect on the visual quality of cataract patients and can provide comfortable visual perceptions for patients. However, this study still has several limitations. First, it is a small single-center study, which may have information collection bias. Second, the subjects included in this study were mainly middle-aged and elderly patients. If the study on young patients can be increased, it will be beneficial to further verify the effectiveness of femtosecond laser-assisted cataract surgery combined with trifocal IOL implantation in young patients. Third, the effect of this therapy on patients' contrast sensitivity and defocus curve has not been analyzed. In the future, the research project will be gradually improved around the above points.

This study, as far as we know, presents the first observation of Alcon's PanOptix trifocal IOL implanted in 55 cataract patients with femtosecond laser-assisted cataract surgery and studied and analyzed its clinical effects, providing valuable references for the wide development of trifocal IOLs. Femtosecond laser-assisted PHACO combined with trifocal IOL implantation has achieved good application effects in the treatment of cataract patients. It can provide natural full-course vision and quick recovery for patients, with small trauma, few side effects, high postoperative stability, and high patient satisfaction after surgery.

Data Availability

The labeled dataset used to support the findings of this study are available from the corresponding author upon request.

Conflicts of Interest

The authors declare no competing interests.

Acknowledgments

This study was funded by Weifang Soft Science Research Project (NO: 2021RKX157).

References

- [1] D. Laroche and P. Capellan, "The aging lens and glaucoma in persons over 50: why early cataract surgery/refractive lensectomy and microinvasive trabecular bypass can prevent blindness and cure elevated eye pressure," *Journal of the National Medical Association*, vol. 113, no. 4, pp. 471–473, 2021.
- [2] J. Eshagian, N. S. Rafferty, and W. Goossens, "Human cataracta complicata: clinicopathologic correlation," *Ophthalmology*, vol. 88, no. 2, pp. 155–163, 1981.
- [3] G. Garay-Aramburu, R. Bergado-Mijangos, R. Irizar-Amilleta et al., "Risk factors for predicted refractive error after cataract surgery in clinical practice. Retrospective observational study," *Archivos de la Sociedad Española de Oftalmología*, vol. 97, no. 3, pp. 140–148, 2022.
- [4] S. Lachovska, "Incidence of pseudoexfoliation syndrome and glaucoma in a set of more than 14,000 eyes of patients operated for a cataract," *Ceska a Slovenska Oftalmologie*, vol. 78, no. 2, pp. 56–62, 2022.
- [5] D. A. Kumar, A. Agarwal, D. Prakash, G. Prakash, S. Jacob, and A. Agarwal, "Glued intrascleral fixation of posterior chamber intraocular lens in children," *American Journal of Ophthalmology*, vol. 153, no. 4, pp. e1–e2, 2012.
- [6] A. Brini and J. Flament, "Cataracta glaucomatosa acuta," *Experimental Eye Research*, vol. 16, no. 1, pp. 19–28, 1973.
- [7] R. K. Jha and R. Kurumkattil, "Can lubrication of the eyelid speculum reduce overall pain perception associated with cataract surgery by phacoemulsification performed under topical anesthesia?," *Indian Journal of Ophthalmology*, vol. 70, no. 5, pp. 1606–1611, 2022.
- [8] N. Kamonporn and K. Pipat, "The visual outcomes and complications of manual small incision cataract surgery and phacoemulsification: Long term results," *Romanian Journal of Ophthalmology*, vol. 65, pp. 31–37, 2021.
- [9] A. Gupta and A. Ionides, "Does acute suprachoroidal haemorrhage during phacoemulsification cataract surgery need surgical treatment?," *Graefe's Archive for Clinical and Experimental Ophthalmology*, p. 10.1007/s00417-022-05689-4, 2022.
- [10] Z. Zhang, X. Jiang, Y. Wei, and S. Zhang, "Pars plana subcapsulotomy to remove condense subcapsular opacification in combined surgery of silicone oil removal and phacoemulsification," *International Ophthalmology*, vol. 42, no. 3, pp. 903–911, 2022.
- [11] V. V. Teplovodskaya, H. S. Husanbaev, N. A. Morina, and E. P. Sudakova, "Femtosecond laser-assisted cataract surgery," *Vestnik oftal'mologii*, vol. 135, no. 3, p. 128, 2019.
- [12] N. Homer and U. V. Jurkunas, "The use of femtosecond laser in refractive and cataract surgery," *International Ophthalmology Clinics*, vol. 57, no. 4, pp. 1–10, 2017.
- [13] A. El-Shehawy, A. El-Massry, M. S. El-Shorbagy, M. Atef, and M. Sabry, "Correction of pre-existing astigmatism with phacoemulsification using toric intraocular lens versus spherical intraocular lens and wave front guided surface ablation," *BMC Ophthalmology*, vol. 22, no. 1, p. 114, 2022.
- [14] R. Fernandez-Buenaga and J. L. Alio, "Intraocular lens explantation after cataract surgery: indications, results, and explantation techniques," *Asia-Pacific Journal of Ophthalmology*, vol. 6, pp. 372–380, 2017.
- [15] J. J. L. Britton, S. El-Defrawy, B. M. Wong et al., "Patient satisfaction and visual function following implantation of trifocal or extended range of vision intraocular lenses," *Clinical Ophthalmology*, vol. 16, pp. 669–676, 2022.
- [16] Y. Zeng, M. Liang, C. Fan et al., "Opacification of refractive bifocal intraocular lens in one month: three case reports," *Medicine*, vol. 101, no. 5, article e28757, 2022.
- [17] J. Lee, Y. Mori, K. Minami, and K. Miyata, "Influence of implantation of diffractive trifocal intraocular lenses on standard automated perimetry," *BMC Ophthalmology*, vol. 22, no. 1, p. 151, 2022.
- [18] M. Moshirfar, M. Mifflin, G. Wong, and J. C. Chang, "Cataract surgery following phakic intraocular lens implantation," *Current Opinion in Ophthalmology*, vol. 21, no. 1, pp. 39–44, 2010.
- [19] J. Li, X. Chen, Y. Yan, and K. Yao, "Molecular genetics of congenital cataracts," *Experimental Eye Research*, vol. 191, article 107872, 2020.
- [20] Y. Oie and K. Nishida, "Triple procedure: cataract extraction, intraocular lens implantation, and corneal graft," *Current Opinion in Ophthalmology*, vol. 28, no. 1, pp. 63–66, 2017.
- [21] A. Shiels and J. F. Hejtmancik, "Molecular genetics of cataract," *Progress in Molecular Biology and Translational Science*, vol. 134, pp. 203–218, 2015.
- [22] A. M. dos Santos, A. A. Torricelli, G. K. Marino et al., "Femtosecond laser-assisted LASIK flap complications," *Journal of Refractive Surgery*, vol. 32, no. 1, pp. 52–59, 2016.
- [23] C. Quigley, M. O. Ashraf, and S. Manning, "Reversible opacification of a hydrophobic acrylic intraocular lens," *Journal of Cataract and Refractive Surgery*, vol. 46, no. 2, p. 319, 2020.
- [24] M. S. Sachdev, "Commentary: indications and surgical techniques for intraocular lens explantation," *Indian Journal of Ophthalmology*, vol. 67, no. 8, pp. 1324–1325, 2019.
- [25] F. Vega, F. Alba-Bueno, M. S. Millan, C. Varon, M. A. Gil, and J. A. Buil, "Halo and through-focus performance of four diffractive multifocal intraocular lenses," *Investigative Ophthalmology & Visual Science*, vol. 56, no. 6, pp. 3967–3975, 2015.
- [26] A. B. Plaza-Puche and J. L. Alio, "Analysis of defocus curves of different modern multifocal intraocular lenses," *European Journal of Ophthalmology*, vol. 26, no. 5, pp. 412–417, 2016.
- [27] F. T. Kretz, C. Y. Choi, M. Muller, M. Gerl, R. H. Gerl, and G. U. Auffarth, "Visual outcomes, patient satisfaction and spectacle independence with a trifocal diffractive intraocular lens," *Korean Journal of Ophthalmology*, vol. 30, no. 3, pp. 180–191, 2016.
- [28] J. A. Davison and M. J. Simpson, "History and development of the apodized diffractive intraocular lens," *Journal of Cataract and Refractive Surgery*, vol. 32, no. 5, pp. 849–858, 2006.
- [29] F. Poyales, R. Perez, I. Lopez-Brea, Y. Zhou, and N. Garzon, "First results after implantation of hydrophilic and hydrophobic trifocal intraocular lenses: visual and optical performance," *Journal of Ophthalmology*, vol. 2021, Article ID 3514577, 8 pages, 2021.
- [30] R. Kosaki, J. Kozaki, and N. Maeda, "Higher-order aberrations in eye implanted with aspherical intraocular lenses," *Nippon Ganka Gakkai Zasshi*, vol. 117, no. 1, pp. 27–34, 2013.
- [31] A. A. Zein El-Dein, A. Elmassry, H. M. El-Hennawi, and E. F. Mossallam, "Objective and subjective evaluation of trifocal diffractive intraocular lens after cataract extraction with phacoemulsification: a prospective clinical study," *BMC Ophthalmology*, vol. 21, p. 179, 2021.

- [32] Z. Xu, D. Cao, X. Chen, S. Wu, X. Wang, and Q. Wu, "Comparison of clinical performance between trifocal and bifocal intraocular lenses: a meta-analysis," *PLoS One*, vol. 12, no. 10, article e0186522, 2017.
- [33] O. Donmez, B. S. Asena, and Y. Aydin Akova, "Subjective and objective clinical outcomes of a new trifocal toric intraocular lens and effect of femtosecond laser cataract surgery," *European Journal of Ophthalmology*, 2021.
- [34] M. Brozkova, M. Filipec, L. Filipova, A. Holubova, and Z. Hlinomazova, "Outcomes of trifocal toric lens implantation in cataract patients," *Ceska a Slovenska Oftalmologie*, vol. 72, pp. 58–64, 2016.

Retraction

Retracted: Induction of Resistance of Antagonistic Bacterium *Burkholderia contaminans* to Postharvest *Botrytis cinerea* in *Rosa vinifera*

Computational and Mathematical Methods in Medicine

Received 27 June 2023; Accepted 27 June 2023; Published 28 June 2023

Copyright © 2023 Computational and Mathematical Methods in Medicine. This is an open access article distributed under the Creative Commons Attribution License, which permits unrestricted use, distribution, and reproduction in any medium, provided the original work is properly cited.

This article has been retracted by Hindawi following an investigation undertaken by the publisher [1]. This investigation has uncovered evidence of one or more of the following indicators of systematic manipulation of the publication process:

- (1) Discrepancies in scope
- (2) Discrepancies in the description of the research reported
- (3) Discrepancies between the availability of data and the research described
- (4) Inappropriate citations
- (5) Incoherent, meaningless and/or irrelevant content included in the article
- (6) Peer-review manipulation

The presence of these indicators undermines our confidence in the integrity of the article's content and we cannot, therefore, vouch for its reliability. Please note that this notice is intended solely to alert readers that the content of this article is unreliable. We have not investigated whether authors were aware of or involved in the systematic manipulation of the publication process.

Wiley and Hindawi regrets that the usual quality checks did not identify these issues before publication and have since put additional measures in place to safeguard research integrity.

We wish to credit our own Research Integrity and Research Publishing teams and anonymous and named external researchers and research integrity experts for contributing to this investigation.

The corresponding author, as the representative of all authors, has been given the opportunity to register their agreement or disagreement to this retraction. We have kept a record of any response received.

References

- [1] F. Shen, Z. Liu, C. Du, J. Yuan, W. Wu, and D. Wei, "Induction of Resistance of Antagonistic Bacterium *Burkholderia contaminans* to Postharvest *Botrytis cinerea* in *Rosa vinifera*," *Computational and Mathematical Methods in Medicine*, vol. 2022, Article ID 7134161, 12 pages, 2022.

Research Article

Induction of Resistance of Antagonistic Bacterium *Burkholderia* contaminans to Postharvest *Botrytis cinerea* in *Rosa vinifera*

Fengying Shen,^{1,2} Zigang Liu,² Chenyang Du,² Junhai Yuan,² Weigang Wu ,² and Dong Wei^{1,2}

¹Hebei Key Laboratory of Quality & Safety Analysis-Testing for Agro-Products and Food, Hebei North University, Zhangjiakou City, Hebei Province, China 075000

²College of Agriculture and Forestry Science and Technology, North University of Hebei, Zhangjiakou City, Hebei Province, China 075000

Correspondence should be addressed to Weigang Wu; nlkxykyysk@163.com

Received 22 May 2022; Revised 7 June 2022; Accepted 16 June 2022; Published 29 June 2022

Academic Editor: Pan Zheng

Copyright © 2022 Fengying Shen et al. This is an open access article distributed under the Creative Commons Attribution License, which permits unrestricted use, distribution, and reproduction in any medium, provided the original work is properly cited.

In order to study the problem that grapes are vulnerable to microbial infection and decay during storage, a method based on antagonistic *Burkholderia* contaminans against postharvest *Botrytis cinerea* of *Rosa vinifera* was proposed in this paper. The method tested the resistance induction mechanism of *Botrytis cinerea* after harvest and determined the fruit decay rate treated by antagonistic *Burkholderia* contaminans. The results showed that the antagonistic bacterium B-1 had bacteriostatic effect on many common pathogens of fruits and vegetables to a certain extent, and the bacteriostatic range was wide. Among them, the inhibition rate of *Fusarium moniliforme* was 75.5% and that of *Botrytis cinerea* was 51.2%. After testing, it can be found that antagonistic bacteria have an inhibitory effect on pathogenic fungi and have an effect on phenylpropane metabolic pathway, reactive oxygen species metabolic pathway, and the activities of other resistance-related enzymes. Through comparison, it can be found that the antagonistic *Burkholderia* contaminans has a strong antibacterial mechanism against *Botrytis cinerea* of rose grape after harvest. The fruit treated with antagonistic B *Burkholderia* B-1 has significantly reduced the decay rate and increased the activity of antibacterial active protein.

1. Introduction

Rose grape is famous for its good taste, but it is not easy to keep fresh and easy to rot during storage. *Botrytis cinerea* is a common disease type after harvest. Due to the low-temperature resistance of the pathogen *Botrytis cinerea* in the Han Dynasty, it is easy to parasitize on grapes and affect the storage quality of grape (Figure 1). In order to better ensure the quality of grape products, there are anticorrosion technologies in biological control technology, which can improve the resistance to pathogens. The fruit postharvest resistance elicitor can effectively resist pathogens and reduce the degree of decay by stimulating plant disease resistance [1]. In this paper, the antagonistic *Burkholderia* contaminans was used as the biocontrol strain to study its induction mechanism of postharvest disease resistance of grapes, so as

to provide reference basis for the development of postharvest biological control technology of grapes [2].

2. Grape Industry and Preservation Technology

Fruits and vegetables account for an important proportion in the diet structure. In recent years, with the improvement of people's quality of life and health awareness, the demand for them has increased accordingly [3]. However, in the postharvest management of fresh fruits and vegetables, due to the lack of perfect preservation technology, the number of decay is huge, resulting in a situation of high yield but no harvest, which not only makes it difficult for fruits and vegetables to realize their due commodity and economic value, but also makes operators lose confidence in this industry. It is reported that the annual loss of fruits and

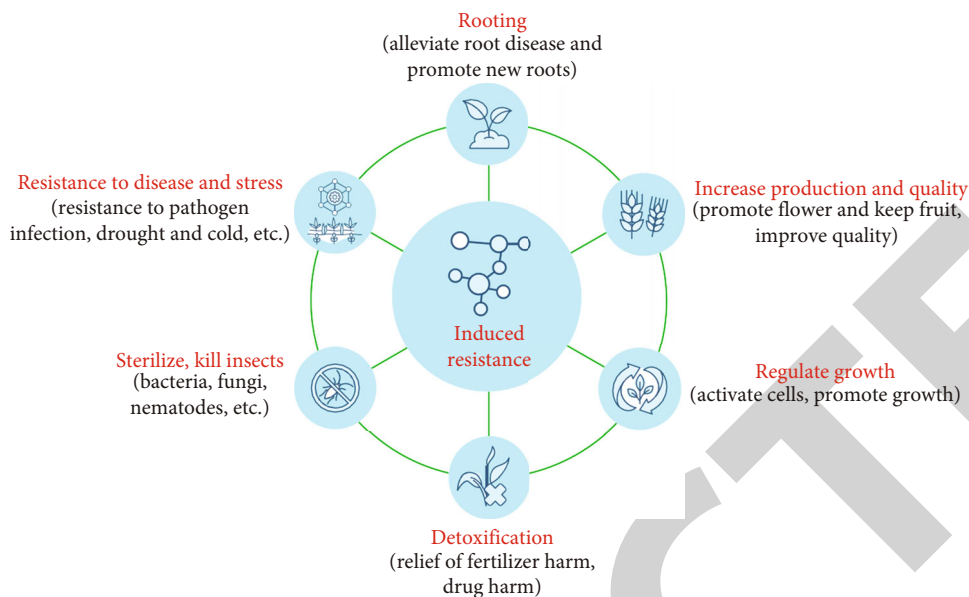


FIGURE 1: Antimicrobial guide.

vegetables in China due to improper postharvest management is more than 25% [4]. Because of its soft and juicy characteristics, grapes are more perishable and have greater economic losses in the process of postharvest transportation and storage. Among them, rose grape contains a large number of active substances, so it is very vulnerable to microbial infection in the process of postharvest preservation, which is difficult to maintain until sale, affecting the interests of fruit farmers [5].

At present, there are many kinds of grape storage and preservation technologies studied at home and abroad, mainly divided into physical and chemical methods. Although various technical principles focus on different aspects, they all achieve the purpose of preservation by controlling the process of fruit senescence, controlling the growth and reproduction of pathogenic microorganisms, and controlling internal water loss [6]. At present, the commonly used fresh-keeping methods include SO_2 and H_2O_2 fumigation storage, low-temperature storage, controlled atmosphere storage, and radiation storage. In addition, in recent years, the study of coating a layer of film on the surface of grapes to delay fruit shrinkage and maturity and aging also showed a good fresh-keeping effect. It was found that coating chitosan on the surface of grapes can improve the storage quality of grapes to a certain extent. However, the most common and effective preservation technology in practical production and application is low temperature combined with SO_2 fumigation [7].

2.1. Biological Control of Antagonistic Bacteria against Postharvest Diseases of Grapes. Biological control of pathogenic bacteria is a new research direction rising in recent years. It mainly refers to using the antagonism between microorganisms to select microorganisms that do not harm the host to inhibit the growth of pathogenic microorganisms and control the occurrence of host diseases [8]. The inhibi-

tion mechanism of antagonistic bacteria plays an important role in the application of fruits and vegetables. Due to the relatively complex mechanism of antagonistic bacteria, it will interact with pathogens and hosts under the influence of external environmental conditions [9]. The antagonistic effects are produced by the joint action of many factors. In the long-term coexistence of plants and their pathogens, pathogens produce different types of pathogenicity, and plants also form different forms of disease resistance. The production of plant disease resistance can hinder the infection of pathogens to a certain extent, so as to control the occurrence of diseases. There are many factors that can induce plant resistance. As a biological inducer, antagonistic bacteria can induce the resistance of fruits and vegetables to pathogens during postharvest storage, so as to reduce decay [10]. In general, antagonistic bacteria can change the resistance of fruits and vegetables by inducing the activity of resistance-related enzymes, regulating the metabolism of reactive oxygen species, promoting plants to produce defensins, and changing cell structure. It was found that the inoculation of *Candida albicans* on grape peel could induce the production of phytoalexin [11]. When antagonistic bacteria were used to treat fruits and vegetables, different treatment solutions had different inhibitory effects on pathogens. Fermentation of different antagonistic treatment solutions can have an excellent inhibitory effect on mycosis. When using this method to treat fruits, the control effect will also be improved with the increase of antagonistic concentration in a certain range.

At present, the sterilization technology of fresh-keeping vegetables and fruits abroad mainly adopts the chemical method of low temperature. However, it will increase the drug resistance of pathogenic microorganisms, lead to the accumulation of toxic substances in the human body, and cause environmental pollution. Therefore, it is necessary to develop more practical preservatives to ensure the freshness of fruits and vegetables [12]. In this paper, *Burkholderia contaminans*

of *Burkholderia* was used as the biocontrol strain to explore the antagonistic mechanism of antagonistic bacteria against postharvest gray mold of grape fruit, so as to lay a foundation for improving the economic value of food use.

2.2. In Vitro Inhibitory Effect of Burkholderia on Pathogenic Bacteria of Rosa rugosa. During the postharvest storage of grapes, the rot and deterioration of grapes were caused by fungal infection. The existing preservation technology is to inhibit the growth of pathogenic bacteria, in which *Botrytis cinerea* is a common pathogen type in postharvest storage of grapes [13]. Because of its low-temperature resistance, it is difficult to treat it by fresh-keeping technology. With the continuous development of microbial control technology, the antagonistic growth curve is explored according to the inhibition effect and principle of postharvest pathogenic bacteria of winter jujube, and the inhibition effect of culture medium on spore is tested based on its different state and time.

2.2.1. Materials, Equipment, and Methods

(1) *Antagonistic Bacteria and Pathogens.* The antagonistic bacteria selected in this experiment is *Burkholderia contaminans* B-1, which was isolated from the surface of fruits and vegetables through experiments. It was identified by comparing the nuclear dry acid sequences of ribosomal 26SD₁/D₂ region and its region and stored at 80°C.

The pathogen is *B. cinerea* on fresh grapes, which was isolated from naturally occurring fruits and identified by its region [14].

(2) *Reagents and Instruments.* The bacterial culture medium is LB medium: peptone 10.0 g, sodium chloride 5.0 g, yeast extract 10.0 g, and distilled water 1000 ml. The fungal culture medium is PDA medium: potato 200 g, glucose 20 g, agar 15 g, and distilled water 1000 ml.

Ls-b50l-i vertical pressure steam sterilizer; Dhp-9272 electric constant temperature incubator (Shanghai Yiheng Technology Co., Ltd.); Bsd-wf2200 oscillation incubator (Shanghai Boshun Industrial Co., Ltd.); Gl-20 (g-li centrifuge of Shanghai Anting Scientific Instrument Factory); Jeol-jem6490lv scanning electron microscope (Nippon Electronics Co., Ltd.) [15].

(3) *Method.* The antagonistic bacteria were activated on LB solid medium, and the activated antagonistic single bacteria were selected and cultured at 28°C and 200 R/min according to 1% of the inoculation amount. The concentration of bacterial solution was tested at different time points, and the regression equation of $Y = aX + b$ was obtained by SAS 9.0 according to the light absorption value and concentration to determine the growth curve of antagonistic bacteria [16]. This process was repeated for three times. The effect of antagonistic bacteria on the antibacterial ability of sporangium in different time periods needs to be inoculated into the culture medium, respectively, and the experimental results should be observed according to the time of 24 h,

48 h, 72 h, 96 h, and 120 h. The effect of antagonistic bacteria on the bacteriostasis of sporangium existed in different time periods. After the antagonistic bacteria were cultured for 24 hours, the antagonistic culture medium, the bacterial suspension, the filter solution, and the heat killing solution were used, respectively. Treatment method: Dip 20 μ L of treatment solution on the PDA plate. After drying, inoculate the spore mycelium block with a diameter of 5 mm in the center of the plate, and culture it at a constant temperature of 26°C for 5-7 d. Wait until the mycelium grows to the edge of the culture dish for inspection, and repeat the experiment three times. The antibacterial effect of antagonistic bacteria is different under different temperature conditions. It is necessary to take the antagonistic culture medium cultured in a shaking flask at 28°C for 24 hours under the conditions of 37°C, 45°C, 50°C, 80°C, and 100°C for 30 minutes, and then, use the Oxford cup method to measure the diameter of the antibacterial circle under different conditions (the method has the same effect as the antibacterial ability). Each treatment is repeated for 3 times, and the experiment is repeated for 3 times. The antagonistic culture medium cultured in shaking flask at 28°C for 24 hours was adjusted to pH 1, 4, 7, 9, and 14, respectively, and then stood for 24 hours [17]. The diameter of antagonistic circle under different conditions was measured by Oxford cup method, and the test was repeated three times. The hyphae of common pathogens of fruits and vegetables with a diameter of 5 mm were inoculated at 3.5 cm from the edge of the Petri dish on the PDA plate. Pick the activated single bacterial colony with the inoculation ring, and draw a line 3.5 cm away from the pathogen (the control is not drawn). All treatments were cultured in the dark in a 26°C incubator. After 6 days, the radius length of pathogenic bacteria colonies growing on the scribed side was measured, and the inhibition rate was calculated. Three repetitions were set for each treatment, and the experiment was repeated three times.

2.3. Results and Analysis. Use Excel 2007 and SAS 9.0 to statistically analyze the data, calculate the standard and draw the drawing, and analyze the significance of the data. $P < 0.05$ indicates that the difference is significant.

2.3.1. Determination of Antagonistic Growth Curve. According to the concentration measured by dilution plate method and its corresponding OD₆₀₀ value, the regression equation of 1G live bacteria number of antagonistic B-1 is determined as $Y = 2.6911X + 7.7307$, and R^2 value is 0.8978. The growth curve of antagonistic bacteria with inoculation time is shown in Figure 2. Within 8 h after inoculation, antagonistic bacteria grow slowly, and enter rapid growth after 8 h to 24 h: long state, logarithmic growth period, slow growth after 24 h, and enter stable period. At 48 h after inoculation, the concentration of the bacteria reaches the maximum value of 1.003×10^{13} cfu/mL, and enters decay period after 72 h. With the extension of culture time, the number of viable bacteria decreases gradually [18].

2.3.2. Effect of Antagonistic Culture Medium at Different Time on Antibacterial Ability of Spores. The results showed

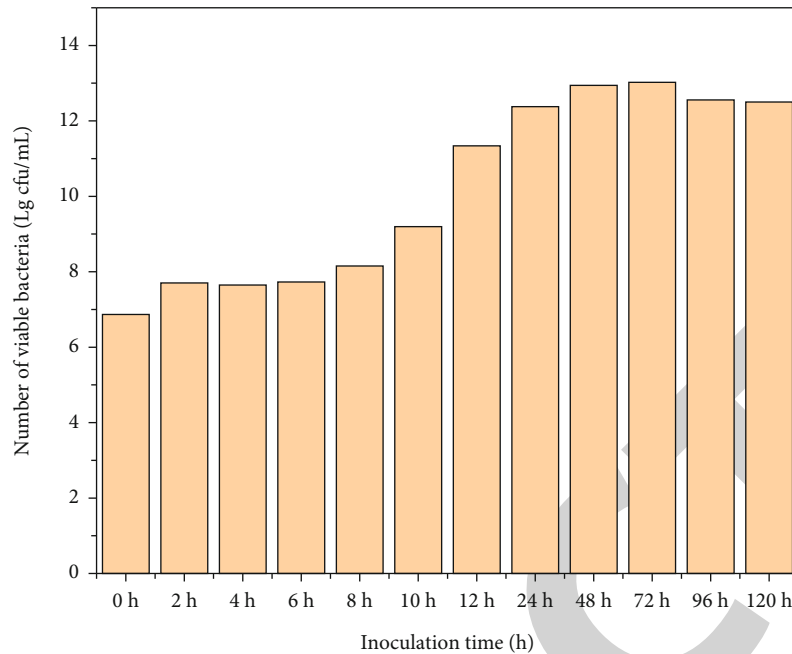


FIGURE 2: Growth dynamics of antagonists in LB medium.

that compared with the control, the culture medium with culture time of 24 h, 48 h, 72 h, and 96 h could inhibit the growth of *B. cinerea* in varying degrees. However, the size of the bacteriostatic circle produced by the culture medium at different times is different. The bacteriostatic circle of the culture medium is the clearest at 24 h, and its diameter is the largest (Table 1), which is 2.81 cm, followed by 48 h. With the extension of the culture time, the bacteriostatic circle gradually becomes blurred and narrowed. At 120 h, the bacteriostatic circle becomes very blurred, and the bacteriostatic effect is not obvious [19].

2.3.3. Antibacterial Ability of Different Antagonistic Treatment Solutions to *Botrytis cinerea*. It was found that the culture medium and bacterial suspension could completely inhibit the growth of *Botrytis cinerea* after 5 days of culture. *Botrytis cinerea* treated with filter solution, heat killing solution, and LB medium grew to the edge of the culture dish, which was no different from the control [20].

When the bacteriostatic circle diameter was slightly higher than that of the control when the bacteriostatic circle diameter was higher than that of the control when the bacteriostatic circle diameter was higher than 50°C (Figure 3), the bacteriostatic circle diameter was slightly lower than that of the control when the bacteriostatic circle diameter was higher than that of the control when the bacteriostatic circle diameter was higher than 50°C.

The bacteriostatic effect of antagonistic bacteria under different pH conditions is shown in Figure 4. It can be seen that the bacteriostatic circle diameter of antagonistic bacteria under neutral conditions (pH=7) is the largest, which is 2.9 cm, and the bacteriostatic effect under acidic conditions is reduced. When pH is 1, the diameter is 2.0 cm, and alkaline conditions have a significant impact on the bacterio-

TABLE 1: Effects of different culture time on bacteriostatic circle of spores.

Incubation time (h)	Bacteriostatic circle diameter (cm)
24	2.81 ± 0.34a
48	2.26 ± 0.33b
72	2.06 ± 0.28c
96	1.79 ± 0.37d
120	1.62 ± 0.21e

Note: the significance test is conducted at the level of 0.05, the same below.

static effect of antagonistic bacteria [21]. When pH is 9, the diameter is 1.7 cm, and when pH reaches 14, there is no bacteriostatic circle, and the bacteriostatic effect is lost.

As shown in Figure 5, antagonistic bacteria have a certain inhibitory effect on fruit and vegetable pathogens. The inhibition effect on *Fusarium moniliforme* was the best, and the inhibition rate was 75.5%. Compared with other pathogens, antagonistic bacteria have a medium to upper level in the inhibition effect of pathogen *B. cinerea* in this experiment, and the inhibition rate can reach 51.2%.

Botrytis cinerea is a common disease in grape postharvest storage. The pathogen parasitized on the fruit and led to grape decay. Through the study of antagonistic bacteria *B. contaminans* and *B. cinerea*, a series of experiments showed good antibacterial effect. During the experiment, both temperature and pH value had an impact on the antibacterial activity of antagonistic bacteria, and the antagonistic bacteria had a good antibacterial effect between the lethal temperature, indicating that the bacteria was acid resistant. The final experiment verified the effect of antagonistic bacteria on pathogenic bacteria, which can play a good

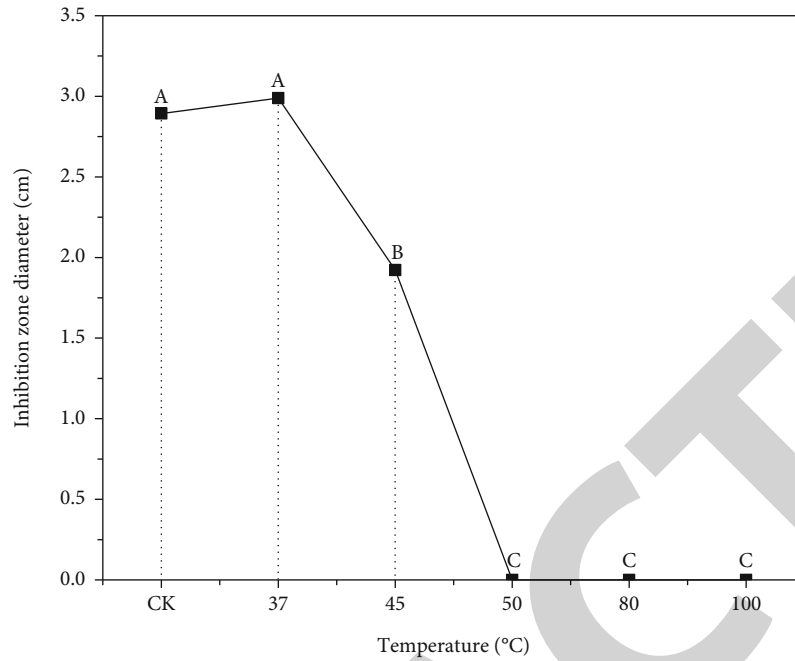


FIGURE 3: Effect of temperature on antagonistic inhibition zone.

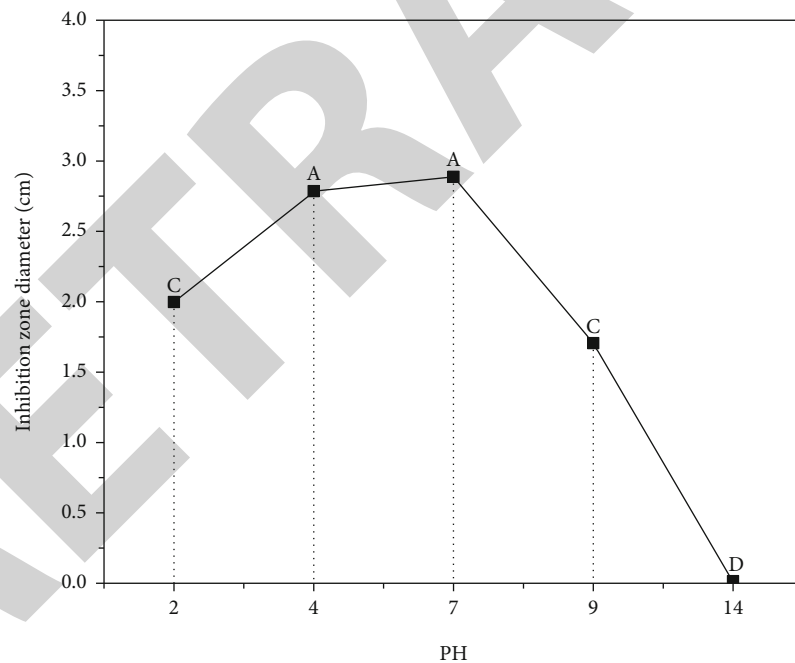


FIGURE 4: Effect of pH on antagonistic circle.

antibacterial effect, and the antibacterial rate reached 51.2%. It is speculated that the bacteria has a certain potential in the storage and preservation of fruits and vegetables [22].

3. Inhibitory Effect of Antagonistic Bacteria on Postharvest *B. cinerea* of *Rosa vinifera*

Due to the thin skin and high juice content of rose grape, it is difficult to store it. And the preservation technology is

closely related to pathogens. It is necessary to start with antagonistic bacteria to reduce the amount of bacteria before grape storage, so as to improve the preservation effect of fruits and vegetables after storage. The fixed value state of antagonists and pathogens in fruit wound was observed, and the related indexes were evaluated.

3.1. *Materials, Strains, and Reagents.* Rosemary grapes are collected from rosemary planting base in Taigu County,

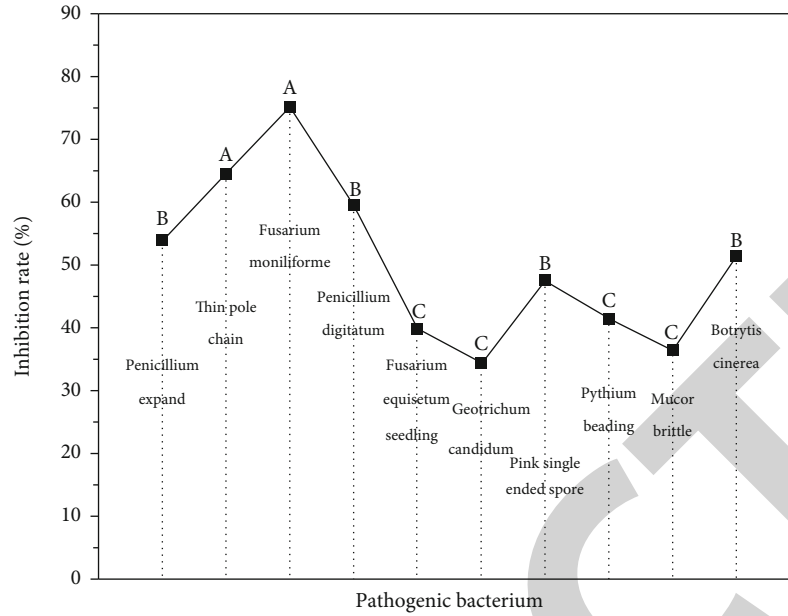


FIGURE 5: Antagonistic ability of *B. cinerea* against various pathogens.

Shanxi Province. They are picked when they reach the commercial maturity. On the day of picking, they are transported back to the laboratory for pre cooling and stored in 0°C cold storage. *Holderia* was isolated from the surface of apricot fruit by our laboratory and was identified according to the nucleotide sequence alignment and physiological and biochemical characteristics of ribosomal 26S D1/D2 region and its region; *Botrytis cinerea* was isolated from naturally occurring grape fruits and was identified by its region and morphological characteristics. The bacterial culture medium is LB medium: yeast extract 10.0 g/l, peptone 10.0 g/l, and sodium chloride 5.0 g/L. The fungal culture medium is PDA medium: potato 200 g/l, glucose 20 g/l, and agar 15 g/L. P-Aminobenzene Sulfonic Acid, 3,5-Dinitrosalicylic acid, potassium sodium tartrate, catechol (Tianjin Guangfu Fine Chemical Research Institute); Guaiacol α -Naphthylamine, kelp protein, chitin, riboflavin, snail enzyme (Beijing solabao Technology Co., Ltd.) [23].

3.2. Method

3.2.1. Preparation of Fermentation Stock Solution. After the antagonistic bacterium B-1 stored at -80°C was activated in LB solid medium, a single colony of antagonistic bacterium *B. contaminans* B-1 on the activated LB solid medium was selected and cultured in 300/1000 mL LB liquid medium at 200 r/min for 24 hours.

3.2.2. Preparation of Mold Spore Suspension. After *Botrytis cinerea* was cultured on PDA plate for 7 days, the conidia were scraped, and the spore suspension with the concentration of 1.0×10^5 spores/mL was prepared with sterile water by blood cell counting method.

The calculation formula is $N = \sum C / nn_1 + 0.1n_2nd$; during application, it is necessary to ensure that the diluent is

within the appropriate range, which is calculated according to the following formula: $N = \sum C / [n_1 + n_0.1 * n_2n] * ndn$.

Calculate the required solution dilution ratio according to the dilution:

$$N = \sum C / nn_1 + 0.1n_2nd = \frac{232 + 244 + 33 + 35}{[2 + n_0.1 * 2n] * 10^{-2}} = \frac{544}{2.2 * 10^{-2}} \quad (1)$$

3.2.3. Sample Treatment of Fruit Storage Effect. Select the *Rosa vinifera* with the same maturity and no mechanical damage in appearance, soak it in the culture solution of antagonistic LB with different concentrations ((a) fermentation stock solution; (b) diluted 5 times fermentation solution; and (c) diluted 10 times fermentation solution) for 2 min (the control is not treated), place it in the sterilized plastic basket (20 strings per basket, about 20 fruits per string), store it under the condition of 0°C for 70 days, and then check it. The experiment was repeated three times.

3.2.4. Determination of Indicators of Substances Related to Fruit Resistance and Sample Treatment. About 750 *Rosa vinifera* grapes without mechanical injury and with the same maturity were selected and randomly divided into control group and treatment group. The fruits of the two groups were soaked in 2% sodium hypochlorite solution for 2 minutes, dried with sterile air, and stabbed a wound with a diameter of 4 mm and a depth of 3 mm at the equator with a sterilization needle, one wound for each grape. In the treatment group, 30 μ L of 24-h fermentation broth of contaminants was added to the wound, and in the control group, 30 μ L of sterile water was added. After 2 hours, add 15 μ L mold spore suspension at each wound, dry it with sterile air, and then incubate it in a 25°C incubator for 6 days. 50 fruits of the treatment group and the control group were taken every day. The pulp at the junction of the wound

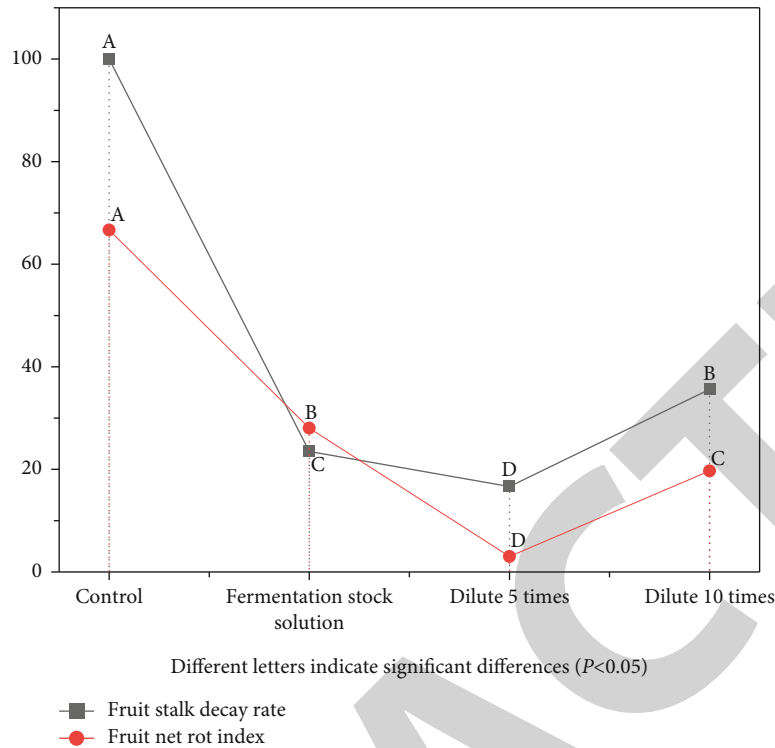


FIGURE 6: Inhibitory effect of antagonistic bacteria on postharvest storage decay of grapes.

lesion and the healthy tissue were used as the experimental material. After liquid nitrogen treatment, it was stored at -80°C for use. The experiment was repeated three times [24].

3.3. *Determination of Fruit Storage Effect.* The rotten degree of fruit and stem after 70 days storage was investigated. The fruit was graded according to the rotten degree and weighed. The rotten rate of stem and rotten index of fruit were calculated according to (1) and (2). The fruit stalk is mildewed to rot, and it is normal without mildewing.

$$\text{Fruit rot rate}/\% = \frac{\text{Rotten fruit count}}{\text{Total number of fruit stems}} * 100 \quad (2)$$

$$\text{Pulp rot index}/\% = \frac{\sum n \text{Proportion of rotten fruits at all levels} * \text{The representative value of this class}}{1 * \text{Representative value at all levels}} * 100 \quad (3)$$

4. Result Analysis

4.1. *Inhibitory Effect of Antagonistic Bacteria on Natural Decay of Rose Grape during Postharvest Storage.* Antagonistic bacteria could inhibit the natural decay of rose after harvest. It can be seen from Figure 6 that after *Rosa vinifera* was treated with antagonistic fermentation broth and stored at 0°C for 70 days, three different concentrations of fermenta-

tion broth can effectively inhibit grape decay ($P < 0.05$). Most of the stem and pulp of the control fruit were mildewed and rotted, while the degree of decay was significantly reduced after the treatment with antagonistic bacteria (*Burkholderia contaminans*). Among them, the storage effect of 5 times diluted fermentation broth is the best, followed by the effect of fermentation stock broth, and the effect of 10 times diluted fermentation broth is relatively poor. The decay rate

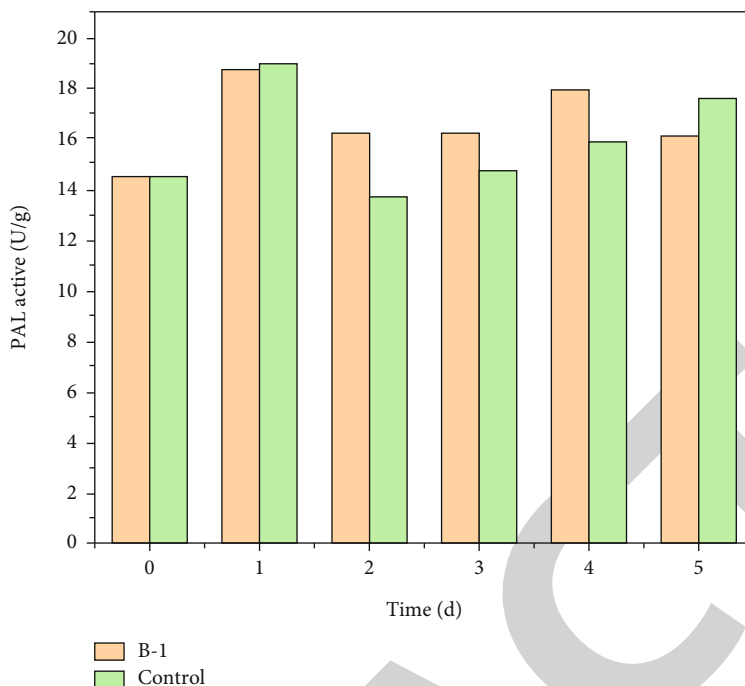


FIGURE 7: Effect of antagonistic treatment on pal activities of postharvest grapes.

of the control stem was 100%, and the decay index of the pulp was 67.14%. However, when the fermentation broth was diluted five times, the fruit stem decay rate was only 30.42%, the pulp decay index was only 3.21%, the fruit stem decay rate was reduced by 69.58%, and the pulp decay index was reduced by 63.93%.

4.2. Effects of Antagonistic Treatment on PAL, , and PPO Activities of Grape Fruit. As the key enzyme in the first step of phenylpropanoid metabolism, PAL is involved in the biosynthesis of disease resistance-related substances such as plant lignin, phytoalexin, and phenols. The highly toxic quinones produced by PPO oxidizing phenols can limit and kill invading pathogenic microorganisms. POD is closely related to the synthesis of lignin and phytoalexin in plants, and the removal of H_2O and $O_2\bullet$ is harmful to plant cells.

It can be seen from Figures 7, 8, and 9 that the PAL activity of the control and treatment reached the peak on the first day and there was a similar peak. In the following 1 ~ 5 days, the PAL activity of the fruits treated with antagonistic bacteria was stable higher than that of the control, and the difference between the two narrowed 5 days after treatment. The activity of the treatment group and the control group showed an upward trend as a whole. There was little difference in the enzyme activity in the first three days. From the third day, the POD activity of the treatment group increased rapidly, and the value was significantly higher than that of the control. By the fifth day, the difference between the two groups decreased. During the whole storage period, the PPO activity of the treated group was significantly higher than that of the control. Compared with the control, the PPO activity of the experimental group began to rise rapidly on the first day, reached the peak on the third day, and then began to decline.

4.3. Control Effect of Antagonistic Bacteria on Natural Decay of Grapes after Harvest. Grape fruits were treated and stored with different chemical treatment solutions. The results are shown in Table 2. Under different temperature conditions, different treatment solutions can inhibit grape fruit to a certain extent, and the nutrient solution diluted by 5 times has the best storage effect. And under different temperature conditions and storage for different days, compared with the control fruit stem, the decay rate decreased the antagonistic bacteria. The anticorrosion effect of suspension was only 5 times higher than that of culture.

4.4. Discussion. Some studies have found that some antibacterial strains can produce bacteriostatic circles in vitro, but they have no bacteriostatic effect when applied to fruits. The main reasons are as follows: some bacteria can only produce bacteriostatic substances in vitro, but not in vivo; the complex and changeable environment of living wound is not suitable for some bacteria to survive or weaken their vitality, including the antieffect. In the experiment, compared with the control group, the SOD activity of antagonistic grape fruit increased rapidly on the first day of storage, while the cat activity decreased significantly, which promoted the accumulation of H_2O_2 in grape fruit cells. The rapid accumulation of H_2O_2 plays an important role in the disease resistance response of plants. It not only has the direct function of antiviral microorganisms, but also its existence can cause damage to pathogens. In the later stage of storage, the cat activity of the treatment group was significantly higher than that of the control group, which eliminated the excessive H_2O_2 accumulated in the pulp, so as to avoid the body damage caused by excessive reactive oxygen species in the fruit. In conclusion, as a biological control technology, Burkholderia contaminans B-1 treatment can

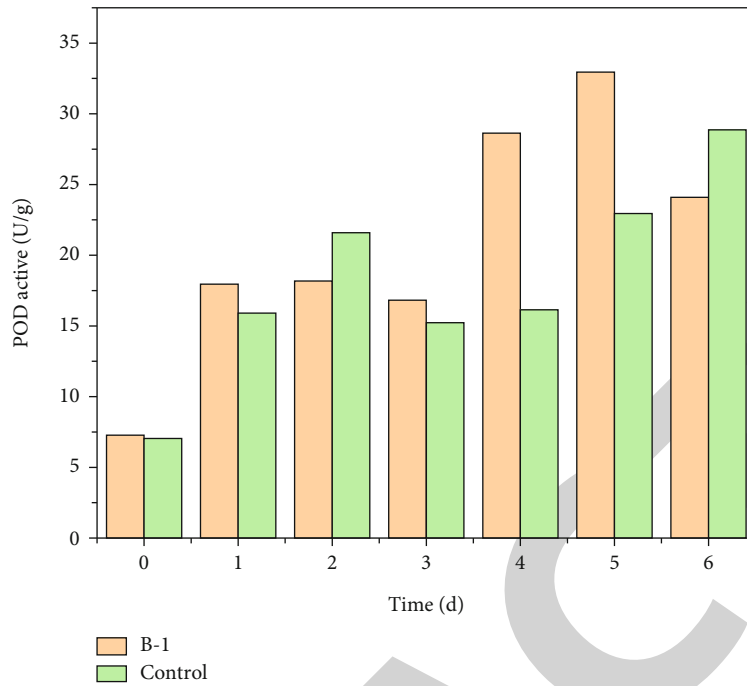


FIGURE 8: Effect of antagonistic treatment on POD activities of postharvest grapes.

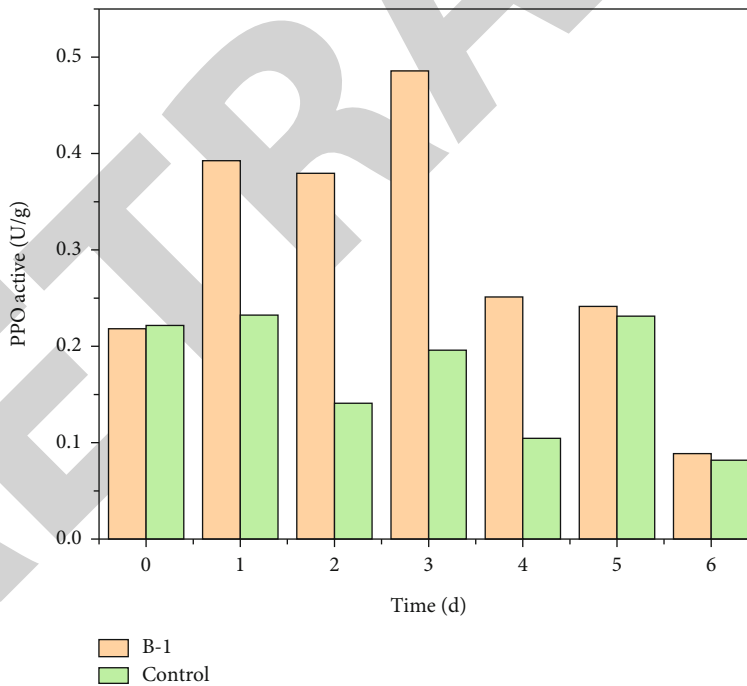


FIGURE 9: Effect of antagonistic treatment on PPO activities of postharvest grapes.

significantly improve the disease resistance of grapes in post-harvest storage and achieve the purpose of anticorrosion and fresh-keeping.

According to the above experiments, antagonistic bacteria, as a biological bactericide, have a good inhibitory effect on staphylococcal mycosis. However, because it is a living bacterial agent, it wants to promote the industrial-

ized production of the device. A large number of cultures are needed to screen the best medium formula for the basic nutrients needed by antagonists, so as to provide a more perfect theory for the preservation of fruits and vegetables.

The antagonistic bacteria were inoculated into 100/250 mL liquid medium after being activated in LB solid medium and

TABLE 2: Control effects of different treatment solutions of *B. contaminans* on grape stem and pulp.

Treatment	Fruit stalk(%)			Flesh(%)		
	26°C	16°C	0°C	26°C	16°C	0°C
Culture stock solution	28.96c	33.07d	76.47b	41.29c	26.97e	58.75c
Dilute 5 times	61.80a	57.37b	83.33a	59.60b	67.15b	5.22a
Dilute 10 times	25.00d	43.75c	64.29d	37.22d	48.21d	70.23b
Bacterial suspension	61.23a	71.56a	82.34a	70.02a	73.24a	89.31a
Supernatant	45.18b	58.49b	66.17c	37.19d	59.67c	69.48b

TABLE 3: Test factor level and coding table.

Code	Carbon source (%)	Nitrogen source (%)	Inorganic salt 1 (%)	Inorganic salt 2 (%)
-2	0.0	0.0	0.0	0.0
-1	1	0.75	0.0025	0.0025
0	2	1.5	0.05	0.05
1	3	2.2	0.0075	0.0075
2	4	3.0	0.10	0.1
△j	1	0.7	0.0025	0.0025

TABLE 4: Utilization capacity of antagonists to carbon and nitrogen sources.

Carbon source	OD ₆₀₀	Duncan's test ^a	Nitrogen source	OD ₆₀₀	Duncan's test ^a
Lactose	0.106	d	Fish peptone	0.278	h
Sucrose	0.522	bc	Soybean peptone	2.337	ab
Malt dust	0.447	d	Polypeptone	2.265	b
Glucose	0.429	bc	Yeast extract	2.385	a
Malt extract	1.454	a	Urea	0.568	g
Contrast	0.0417	d	Contrast	1.415	e

cultured in shaking flask at 28°C 200/min for 24 h to prepare seed solution. The addition amount of various carbon sources to be tested is 1%, and 11% YNB is the basic nitrogen source. Inoculate 1% of the inoculated amount into a 50/250 mL triangular flask, incubate for 24 hours under the condition of 200/min at 28°C, measure the value of OD₆₀₀ with a spectrophotometer, and repeat each treatment for 3 times.

4.4.1. Screening of the Best Nitrogen Source. Add 1% of all tested nitrogen sources, and take the selected best carbon source as the carbon source. Each treatment was repeated 3 times.

The composition of antagonistic medium was optimized by secondary general rotation combination. The test factors include carbon source, nitrogen source, and other components, and each factor contains five levels. The OD₆₀₀ value of antagonistic growth dilution 10 times was used as the response design (see Table 3 for the specific code), and each treatment was repeated three times.

The test data were counted by Design-Expert 8.0.6 statistical software and processed in group mode. The OD₆₀₀ value was measured after 10 times dilution.

As shown in Table 4, among the utilization capacity of antagonists to different carbon and nitrogen sources, it can

be seen that the utilization capacity of antagonists to malt leaching powder is the highest, which is significantly higher than that of other carbon sources. The utilization ability of yeast extract in nitrogen source was the strongest, which was significantly higher than that of other nitrogen sources.

According to Table 5, the concentration of carbon source sucrose is between 2.0 and 3.0%, and the antagonistic culture density is the largest. When the concentration of nitrogen source was 4.0%, the culture density was the highest.

The best level of each factor is determined by using Design-Expert 8.0.6 statistical software. According to the regression equation:

$$\begin{aligned}
 Y = & 1.35 + 0.099 X_1 + 0.12 X_2 - 0.013 X_3 - 0.002486 X_4 - 0.12 \\
 & X_1 X_2 + 0.013 X_1 X_3 + 0.004729 X_1 X_4 + 0.022 X_2 X_3 - 0.002687 \\
 & X_2 X_4 + 0.019 X_3 X_4 - 0.14 X_1^2 - 0.1 X_2^2 - 0.075 X_3^2 - 0.098 X_4^2
 \end{aligned}
 \quad (4)$$

Verify the regression coefficients. It is $X_1 = 0.115$, $X_2 = 0.538$, $X_3 = -0.002$, and $X_4 = -0.018$. The level before transformation into coding is as follows: malt extract powder is 2.11%, yeast extract is 1.9%, and the corresponding value is 1.38901. In order to verify the culture conditions, 2.11%

TABLE 5: Effects of different carbon and nitrogen sources on antagonistic culture density.

Concentration (%)	Nutrients			
	Malt extract		Yeast extract	
	OD ₆₀₀	Duncan's test ^a	OD ₆₀₀	Duncan's test ^a
0	2.185	ab	1.443	e
0.5	2.278	ab	2.187	d
1.0	2.276	ab	2.331	c
1.5	2.347	ab	2.519	b
2.0	2.355	ab	2.661	a
2.5	2.345	ab	2.694	a
3.0	2.470	a	2.689	a
3.5	2.002	b	2.707	a
4.0	1.175	c	2.716	a

malt powder and 1.9% yeast extract were used to dilute the obtained bacterial solution, and the OD₆₀₀ was 1.31. The error is 5.0%, indicating that the culture method is feasible.

5. Conclusion

In conclusion, when the antagonistic bacteria *Burkholderia contaminans* B-1 and *Botrytis cinerea* confront in vitro, the bacteriostatic circle diameter of 24-h culture medium and culture stock solution is the largest and clearest, and the inhibitory effect will be shown only when they are in certain contact with the pathogen; that is, on the one hand, the bacteriostatic mechanism of this bacterium is to produce bacteriostatic substances. UV irradiation, high-temperature treatment, and adjusting the pH of culture medium can all have a certain impact on the antibacterial activity of antagonistic bacteria, but it will lose its antibacterial effect only in extreme environment, that is, high temperature and high alkali, while the normal living environment has little impact on its antibacterial activity. When *Botrytis cinerea* spores were treated with antagonistic bacteria, the spore germination and the secondary length of bud tube were significantly inhibited, and the degree of inhibition increased with the increase of antagonistic concentration. Under scanning electron microscope, it was also found that *Botrytis cinerea* mycelium was seriously shrunk and deformed compared with the control. In addition, antagonistic B-1 has antibacterial effect on a variety of common pathogens in fruits and vegetables to a certain extent, with a wide range of inhibition, in which the inhibition rate of *Fusarium moniliforme* can reach 75.5%, and that of *Botrytis cinerea* is 51.2%. Antibacterial B-1 treatment increased the activities of resistance-related enzymes PPO, POD, PAL, CHI, GIU, and SOD in grape fruit to a certain extent, delayed the peak time of cat enzyme activity, and increased the accumulation of active H₂O₂. The changes of these resistance-related active substances enhanced the resistance of fruit to pathogens. The optimal formula of antagonistic growth was obtained by response surface test, namely, 2.11% malt extract and 1.9% yeast extract.

Although the effect of bile storage of postharvest rose grape with antagonistic bacteria is worse than that of commonly used chemical agents, and the strains used in this experiment are currently limited to laboratory research, they

have shown their unique advantages. Firstly, compared with chemical agents, biological agents have the advantages of no pollution to the environment, no resistance, and no damage to human health and have great application potential. Although the research on antagonistic bacteria *B. contaminans* in this experiment is in the early stage, all exploration and research will be devoted to its practical application in grape storage and preservation.

Data Availability

The labeled data set used to support the findings of this study is available from the corresponding author upon request.

Conflicts of Interest

The author declares that there are no conflicts of interest.

Acknowledgments

This work is supported by the Youth Foundation of Hebei North University, the establishment of multidrug resistance detection system for *Botrytis cinerea* (QN2018004); the Science and Technology Guidance of Education Department of Hebei Province, the study on multidrug resistance and bacteriostatic response mechanism of *Botrytis cinerea* group S (Z2019071); the Science and Technology Youth Fund Project of Hebei Education Department, the function of WRKY and its related genes in drought resistance and growth and development of potato (QN2019120); the Special Project of Special Commissioner for Science and Technology of Financial Support Project of Zhangjiakou in 2019, the study on the antibacterial mechanism of biocontrol *Streptomyces* against *Botrytis cinerea* group S (1911016C-7) and the study on the function of WRKY and other related genes in the growth and development of Duli under drought stress (1911016C-10); and the start-up fund for doctoral research of high-level talents of Hebei North University, the effect of combined application of biocontrol *Streptomyces* and fungicides on *Botrytis cinerea* (2022).

References

- [1] Y. Yurnaliza, D. I. Rambe, L. Sarimunggu, M. Purba, and A. Hartanto, "Screening of *Burkholderia* spp. from oil palm plantation with antagonistic properties against *ganoderma boninense*," *Biodiversitas Journal of Biological Diversity*, vol. 21, no. 8, pp. 3431–3437, 2020.
- [2] M. Santos, E. Albini, M. L. Corazza, N. Krieger, and F. Voll, "Kinetics of enzymatic cetyl palmitate production by esterification with fermented solid of *Burkholderia* contaminans in the presence of organic solvent," *Reaction Kinetics, Mechanisms and Catalysis*, vol. 132, no. 1, pp. 139–153, 2021.
- [3] M. Murugesan, J. Ranjan, N. K. Ragupathi et al., "Diagnostic methods and identification challenges experienced in a *Burkholderia* contaminans outbreak occurred in a tertiary care centre," *Indian Journal of Medical Microbiology*, vol. 39, no. 2, pp. 192–195, 2021.

Research Article

Effects of Body Posture and Different Exercise Intensity on Athletes' Limb Injury

Di Jin¹ and Qian Ma²

¹Anhui Normal University, Wuhu, Anhui 241000, China

²Wannan Medical College, Wuhu, Anhui 241000, China

Correspondence should be addressed to Di Jin; 1814011718@ecupl.edu.cn

Received 26 April 2022; Revised 25 May 2022; Accepted 2 June 2022; Published 28 June 2022

Academic Editor: Pan Zheng

Copyright © 2022 Di Jin and Qian Ma. This is an open access article distributed under the Creative Commons Attribution License, which permits unrestricted use, distribution, and reproduction in any medium, provided the original work is properly cited.

The purpose of this study was to solve the problem of the influence of body posture and different exercise intensity on athletes' limb injuries, to meet the needs of understanding athletes' injuries, and to make up for the lack of investigations on athletes' limb injuries; this also increases the chances of an athlete avoiding injury. Severe acute sports injuries of high-level gymnasts endanger the personal safety of athletes. Many movements in gymnastics are done in the air much higher than the ground, and there is no fulcrum when the athlete does the movements; this just can only maintain balance and change your body posture through your own feelings, a slight error can easily cause your head or upper body to fall down, and the fragile spine cannot withstand the strong impact of the ground, resulting in high vertebral fractures, high paraplegia, and even death. Therefore, through a survey of 126 rhythmic gymnasts who participated in the 2011 "China Art Sports Cup" China Rhythmic Gymnastics Championship, a total of 172 injuries were found in 136 gymnasts, and the injury risk analysis was carried out from the main characteristics of the injuries.

1. Introduction

With the continuous development of modern rhythmic gymnastics, the competition in international competitive sports is becoming increasingly fierce; in order to pursue higher, more difficult, new, and clever technical movements, special training with high intensity and large amount of exercise is carried out; the ensuing sports injuries are becoming more and more serious, which restricts the further improvement of the athletes' competitive level. How to solve the problem of prevention, treatment, and rehabilitation of athletes' injuries, so as to ensure the normal training and competition of athletes, is an important part of competitive work [1]. Competition is usually accompanied by risks. Under the traditional thinking concept of risk "entity" school, the general understanding of risk composition is as follows: risk is composed of a variety of elements; these elements mainly refer to risk factors, risk accidents, and risk losses. They work together to determine the existence,

occurrence, and development of risks [2]. Risk factors refer to conditions that are sufficient to cause or increase the possibility of a risk accident, the potential cause of a risk accident, and the inherent or indirect conditions or hidden dangers that cause losses; it promotes the occurrence of risk accidents or increases the frequency of accidents and losses. Risk events generally refer to accidental events that directly cause loss of life and property and are accidental events that directly lead to the consequences of loss, that is, the direct cause and external cause of the loss. Risk of loss is the result of unplanned, unintended, and unintentional conditions that cause economic loss or personal injury. Risk factors are the necessary conditions for the formation of risks and the premise for the occurrence and existence of risks. A risk event is a sufficient condition for the existence of a risk, central to the overall risk. Risk events are the bridge connecting risk factors and risk losses and the medium through which risks are transformed from possibility to reality. The relationship between risk factors, risk events, and risk losses

can be represented by the chain of action of risk; understanding the chain of action of risk is of great significance for dealing with risks [3], as shown in Figure 1.

Risk identification is the first step in risk management; it refers to the systematic understanding and analysis of a large number of reliable information from a large number of sources, to recognize the various risk factors existing in the project, then to determine the risks faced by the project and its nature, and to grasp its development trend.

2. Literature Review

Skinner and Isaacs said that by conducting a trauma epidemiological study of 88 rhythmic gymnasts, research shows that the top three incidence rates of common and frequently occurring diseases in rhythmic gymnasts are chronic sacrospinalis muscle injury at 15.9%; lumbar supraspinous ligament injury, lumbar interspinous ligament injury, psoas fasciitis, and anterior talofibular ligament injury accounting for 6.8% each; and lumbar three transverse process terminal disease, chronic traumatic synovitis of ankle joint, and bunion at 5.7% [4]. Chan et al. said that the occurrence of trauma is significantly related to excessive specific training, and the athletes' incorrect movement control and fatigue are the key to the occurrence of trauma [5]. Putra et al.'s research found that Chinese elite rhythmic gymnasts have an obvious trend of premature aging caused by sports injuries; especially the younger active athletes have obvious sports injuries [6]. Wilkinson and Mayhew found that the serious injuries of rhythmic gymnasts were in the waist and ankle with the highest incidence rate, moderate injuries have a high incidence of waist, instep, knee, and ankle, and the incidence of minor injuries to the instep, ankle, waist, and shoulder joints is high [7]. In general, the highest incidence of various parts is the waist, followed by the ankle, instep, knee, and shoulder. According to Constantinou et al.'s special survey results, they suggested to arrange training in the basic training stage according to the developmental characteristics of children and adolescents, strengthen the strength training of waist and ankle and other parts, and pay attention to the injury-prone period [8]. Halabchi and Hasabi conducted an injury investigation on 13 national athlete-level and 7 national-level rhythmic gymnasts and found that their injuries were mainly chronic strain injuries of the waist, knees, and feet [9]. The medical supervision of the team found that the main injury of rhythmic gymnasts was vertebral osteomyelitis, after strengthening the strength training of the lumbar and back muscles, and combining with massage, acupuncture, and sealing treatment, symptoms were basically relieved [10]. The results of research on the mechanism of sports injuries in rhythmic gymnasts show that 88.3% had a history of injury. The areas with a higher incidence of injury were the ankle, waist, and knee [11].

3. Research Method

3.1. Injury Investigation and Analysis of Gymnasts. A survey was conducted on 126 rhythmic gymnasts who participated

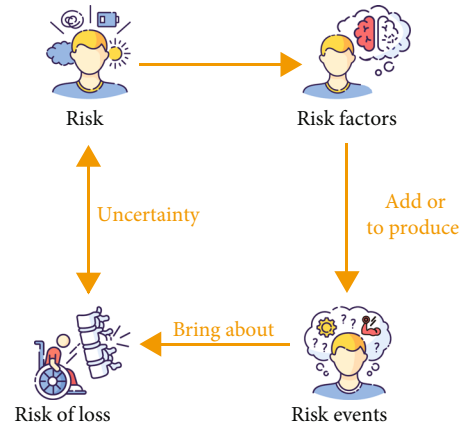


FIGURE 1: Relationship of risk, risk factor, risk event, and risk loss. Understanding the chain of action of risk is of great significance for dealing with risks.

in the 2011 “Zhongyi Sports Cup” China Rhythmic Gymnastics Championship. The basic situation is shown in Table 1.

A questionnaire survey was conducted on 126 rhythmic gymnastics players who participated in the 2011 “China Art Sports Cup” China Rhythmic Gymnastics Championship, and the results of the survey showed that 98 athletes had injuries of varying degrees, and 28 had no injuries, with a total injury rate of 77.78%, as shown in Table 2.

Through a survey of 126 athletes, the results showed that there were a total of 172 cases (/person) of sports injuries; among the 172 injuries, 30 were acute injuries, accounting for 17.44% of the total injuries. There were 142 chronic injuries, accounting for 82.56% of the total injuries, as shown in Table 3.

Through a survey of 126 athletes, 145 of the 172 injuries were mild injuries, accounting for 84.30% of the total injuries; 25 cases were moderate injury, accounting for 14.53% of the total injury; 2 cases were severe injury, accounting for 1.16% of the total injury, as shown in Table 4.

3.2. Overall Incidence of Sports Injuries. As shown in Figure 2, a questionnaire survey was conducted on 126 rhythmic gymnastics players who participated in the 2011 “China Art Sports Cup” China Rhythmic Gymnastics Championship, and 102 athletes had injuries of varying degrees; the survey results showed that there were 172 cases (/person-time) of sports injuries, and the total injury rate was 80.95%. The situation was very serious and posed a great threat to the development of Chinese rhythmic gymnastics. This shows that during the development of rhythmic gymnastics, more attention should be paid to athletes' injuries, and active and effective preventive measures should be taken; avoiding or reducing the occurrence of sports trauma as much as possible has become an important issue to be solved urgently [12].

Through a survey of 126 sports athletes, 32 of the 172 injuries were acute injuries, accounting for 18.60% of the total injuries. There were 140 chronic injuries, accounting

TABLE 1: Basic information of athletes.

$n = 126$	Age (y)	Height (cm)	Weight (kg)	Years of exercise (y)
Woman	15.24 ± 3.44	161.39 ± 7.58	42.84 ± 6.08	6.56 ± 2.95

TABLE 2: Incidence of sports injuries.

$n = 126$	Number of injuries	No injuries	Total
Woman ($n = 126$)	98	28	126
Percentage (%)	77.78	22.22	100

TABLE 3: The nature of sports injuries in rhythmic gymnastics athletes.

Damage nature	Acute injury	Chronic injury	Total
Visits	30	142	172
Percentage (%)	17.44	82.56	100

TABLE 4: Degree of sports injuries among athletes in rhythmic gymnastics.

Degree of damage	Mild	Moderate	Severe	Total
Visits	145	25	2	172
Percentage (%)	84.30	14.53	1.16	100

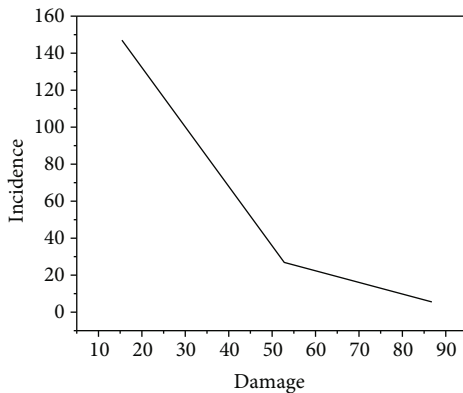


FIGURE 2: Incidence of rhythmic gymnastics injuries. This is during the development of rhythmic gymnastics.

for 81.40% of the total injuries. As in most competitive sports, chronic injuries are still common in rhythmic gymnastics, and the proportion is much higher than in other sports [13].

Due to the increased technical difficulty and the increase in exercise training time, load, and density, the incidence of chronic injuries has gradually increased. In addition, if systemic rehabilitation training is not carried out after acute injury, the acute injury will gradually turn into chronic injury [14]. It shows that there are still shortcomings in the current control of chronic injury and the solution of rehabilitation training after injury.

It can be seen from the survey that the sports injuries in rhythmic gymnastics are mainly mild injuries. Moderate and severe injuries force athletes to stop training and rest, which can have a greater impact on training and competition. This prompts us to prevent microduplication and actively take and improve the prevention and rehabilitation measures of injury, so as to reduce the probability of injury.

Among the 172 injuries in this investigation, 0 was skin injury, accounting for 0% of the total injury; 84 cases of skeletal muscle injury, accounting for 48.84% of the total injury; 35 cases of joint injury, accounting for 20.35% of the total injury; and 52 cases of bone injury, accounting for 30.23% of the total injury. There was 1 case of nerve injury, accounting for 0.58% of the total injury [15]. Obviously, skeletal muscle injuries and skeletal injuries account for the majority of sports injuries in rhythmic gymnastics [16]. Skeletal muscle injuries are mainly strains; it shows that the problem of muscle strength and posttraining recovery of rhythmic gymnasts should be highly valued.

3.3. Effects of Injury. The reason for the ankle injury is because rhythmic gymnastics is a ballet-based combined equipment (loop, ball, stick, belt, and rope) competitive events, so the movements are mostly done in the state of standing on the heels, and the weight of the human body must be on the ankles. In addition, when jumping, balancing, and rotating, the center of gravity of the human body shifts, and the gravity falls on the outer edge of the foot, causing uneven stress on the ankle and uneven stress between the muscles and ligaments of the ankle; it is easy to cause plantar flexion and varus sprain of the foot, which can damage the lateral synovium of the ankle joint and the anterior talofibular ligament.

Although the athlete had simple strength training, due to the lack of systematic rehabilitation training, it still feels pain; this may also be the main reason why all of his present injuries were to the right extremity. In order to avoid the pain during the movement of the right ankle joint, the movement pattern on the kinematic chain changes, which leads to an increase in the load on other parts, and the long-term accumulation results in the occurrence of injury [17]. Therefore, the pain in this part should be eliminated as soon as possible, and systematic rehabilitation training should be carried out to ensure that it can complete the training task and participate in the competition.

Rhythmic gymnastics requires the conversion of various difficult movements such as jumping, spinning, and rolling in a short period of time; especially in the process of jumping and spinning, due to the instability of the center of gravity, the knee joint often flashes sharply from side to side, and there are flexion, extension, and twisting movements. This can easily cause damage to the medial and lateral meniscus.

The player had obvious pain points in the anterior horn of the lateral meniscus of his right knee, and he had been closed twice because of the pain affecting training, but the effect was not obvious [18]. In the complete set of movements, there are many rotation movements that require the knee joint to be straightened and used as a support; due to the existence of this pain point, players are either unable to

complete or are very strenuous, and this can also cause functional compensation of other joints and muscles in the kinematic chain, thereby increasing the risk of injury by overloading these joints. Due to the approaching competition and heavy training tasks, the scientific research team negotiated with leaders, coaches, and players to choose conservative treatment. Therefore, a rehabilitation program was developed for them to ensure that they can train normally and participate in competitions [19].

Precompetition strain on the right waist is an important cause of low back pain, it is very common among athletes, the completion of many movements in rhythmic gymnastics involves flexion and extension of the waist, and the range is large. Therefore, the waist of rhythmic gymnastics athletes needs not only good flexibility but also good core strength.

Many athletes suffer from acute sprained waist without timely treatment and focus on future rehabilitation, resulting in gradual strain [20]. Lumbar muscle strain causes blood circulation disorders and fibrin adhesions can cause pain. Fascial adhesions cause pain, one is the traction of adhesions, and the other is that most of the adhesions have posterior cutaneous branches of spinal nerves, and the adhesion or adhesion of the nerves is involved during exercise, causing pain or numbness. Most patients can still adhere to the training of small and medium amount of exercise, often manifested as pain before and after training [21].

After the athlete suffered an acute back injury, the treatment and rehabilitation were incomplete, and he started training or was gradually strained. In addition, sweating and getting cold during training is also one of the important reasons. When the waist is cold at night, morning stiffness will appear, after warming up, the pain and stiffness disappear, and pain also occurs after a lot of exercise.

According to his symptoms, a set of individualized rehabilitation programs for his waist was formulated to eliminate pain as much as possible, strengthen core strength, and ensure his normal precompetition training and participation in competitions.

Assuming that the lengths of the big arm and the forearm are l_u and l_l , respectively, we can describe the position of each joint in the SCS coordinate system. Our SCS coordinate system is where the body plane (chest) represents the XZ plane and the body is oriented in the Y direction. The midpoint between the feet is the origin of the SCS coordinate system. Therefore, according to the Denavit-Hartenberg transformation rules, we can calculate the elbow and wrist joints accordingly. For example, when calculating the elbow joint position P_e , we can use the arm length l_u to calculate according to the following formula, as shown in

$$P_e = P_s + l_u \sin \psi_2, \quad (1)$$

$$P_e = P_s + l_u(\cos \psi_2 \times \sin \psi_1), \quad (2)$$

$$P_e = P_s + l_u(-\cos \psi_1 \times \cos \psi_2), \quad (3)$$

where P_s is the position of the shoulder joint, and $f(*)$ calculates the orientation vector from the shoulder joint

to the elbow joint. Similarly, the position P_w of the wrist joint can also be calculated accordingly, as shown in

$$P_w = P_e + g(\psi_1, \psi_2, \psi_3, \psi_4, l_l). \quad (4)$$

Therefore, according to Equation (1), the phase changes of labels b and r at these two positions (l_0 and l_s) can be expressed, as shown in

$$\Delta\theta(b, a) = \theta\beta(b, a) - \theta_0(b, a), \quad (5)$$

$$\Delta\theta(r, A) = \theta\beta(r, A) - \theta_0(r, A), \quad (6)$$

where $|\cdot|$ is used to calculate the Euclidean distance and $w(B)$ represents the phase change due to label angular rotation. The phase shift of the tag caused by the hardware can be completely eliminated here. Theoretically, if the distance AO is much larger than the distance $|Tb, oO|$, then the change of $|ATb, p| - |ATb, o|$ can be approximated as the projection of the distance difference Δx on the collinear direction, as shown in

$$\Delta x_b = |Tb, oO|(1 - \cos \beta). \quad (7)$$

Similarly, we can also calculate the distance difference Δx_r of the red label, as shown in

$$\Delta x_r = |Tr, oO|(1 - \cos \beta). \quad (8)$$

Therefore, given the distance between labels $|Tb, oTr, o|$, we can calculate the deflection angle β from it.

Through the investigation, it was found that the top three injured parts were the spine, ankles, and lower limbs, which was consistent with the characteristics of rhythmic gymnastics. Rhythmic gymnastics is a skill competition that requires a combination of various complex movements such as balance, jumping, turning, and similar skill movements. The spine is the hub of the trunk activity, and the muscles are the driving force of the spine movement [22]. Injuries to the spine include injuries to the five upper vertebral bodies, muscles, ligaments, and fascia of the cervical, thoracic, lumbar, sacral, and coccygeal vertebrae.

Rhythmic gymnastics requires athletes to have good spine flexibility and strong muscle strength and to establish stable dynamic stereotypes in order to complete difficult and complex movements. Rhythmic gymnastics spine movement range is large, speed is fast, and braking is too much; if the strength is insufficient and the movement is incorrect, it is easy to cause local cumulative damage; the muscles of the spine are rich, different in size, different levels, insufficient, or unbalanced muscle strength, which will cause deformation of the spine, such as cervical vertebral arch and thoracic scoliosis. The survey shows that the spinal curvature of athletes is very obvious, and the degree is different, and the deformation of the spine will in turn affect the center of the entire kinematic chain; then, a vicious circle occurs, which affects the training and competition of the players to a large extent. The injury to the spine greatly exceeds that of the knee and ankle joints in the past, accounting for

39.53% of the total injury; it is suggested here that the prevention and treatment of spinal injury is an urgent problem to be solved.

The spine is the central axis and pillar of the human trunk and has the function of supporting the load, and the spine is an arched structure with good elasticity, which plays the role of transmitting pressure and buffering vibrations [23, 24]. The spine performs various basic movements, acts as a lever for movement, and is the attachment point for many muscles. The characteristics of this project make the development of muscle strength on both sides of the spine unbalanced; as a result, the spine deforms, which in turn leads to a series of skeletal, muscle, and fascia injuries, without systematic rehabilitation training; these injuries lead to a vicious circle, which seriously affects the training and competition of athletes. The muscles on both sides of the spine are very rich, and the balanced development of muscle strength is the key to solving spinal injuries; therefore, attention should be paid to the development of muscle balance in the treatment and rehabilitation of spinal injuries, and strengthen core strength training, thereby reducing spinal deformation, thereby reducing damage to various structures on the spine. First, the weak chain is found through the muscle strength test. While the strength on both sides should be strengthened, the weak side should be developed, but the stretching of the strong side should not be ignored. Deep-level muscle strength should be trained to strengthen the stability of the spine, so that the spine is a normal physiological structure. In the recovery training, therapeutic manipulations, manipulation of spine, application of spinal guns, traction, etc. are added. Treatment and rehabilitation are combined with each other and penetrate each other, so as to achieve the purpose of spinal rehabilitation [25].

The reason for ankle injury is because rhythmic gymnastics is an athletic event based on ballet combined with equipment (rings, balls, sticks, belts, and ropes), so the movements are mostly completed in the state of standing on the heels, and the weight of the human body rests on the ankle [26]. In addition, when jumping, balancing, and rotating, the center of gravity of the human body is offset, and the gravity falls on the outer edge of the foot; uneven force on the ankle and uneven force between the muscles and ligaments of the ankle can easily cause plantar flexion and varus sprain of the foot and damage the lateral synovium of the ankle joint and the anterior talofibular ligament. If there is no systematic rehabilitation training, it is easy to cause repeated ankle injuries [27]. The inherent characteristic of rhythmic gymnastics is the feet walk in a "V" shape, so the outward opening training is an indispensable and important link for rhythmic gymnasts; in addition, the hip joint must be rotated to the maximum extent in the external opening training of the lower limbs, so that the centers of the hip, knee, and ankle joints are always in a straight line. However, if you start a "V" step, you must twist the ankle joint, so that the inner edge of the front foot touches the ground and "falls down"; in this state, the mother toe is in the pronation position, and the ankle joint does not fit in the groove, causing trauma such as ankle synovitis, bunion, and hallux valgus over time. The high incidence of ankle injuries should not be underes-

timated, as it often affects whether players can train and compete normally. Therefore, foot and ankle injuries should be given full attention, and it is very important to combine treatment with rehabilitation training, especially functional training after ankle injuries. A support belt or brace can be applied to the ankle before training, thereby reducing the occurrence of damage or preventing the recurrence of damage. Timely treatment after injury is the key; RICE, treatment, and rehabilitation after the acute phase cannot be ignored. After an injury, the muscle strength of the ankle joint, the range of motion of the joint, and the tissues around the joint need to be restored. For the complete rehabilitation of the foot and ankle in addition to normalization of its anatomy and tissue, it should also include the recovery of the complex functional capabilities of the site. For the balance function, this ability is extremely important for technologies such as landing buffers. The recovery of functional ability requires the muscles of the ankle to restore the ability to coordinate work and fine work [28].

4. Results and Analysis

The 172 cases of injury and illness in this investigation were treated by the following methods: massage, acupuncture, dressing, sealing, strength training, foot soaking, stretching, cupping, ice compress, scraping, repositioning, limbs, acupuncture, immobilization, nutritional medicine, and physiotherapy (mainly medium frequency, ultrashort wave, and roasting electricity). From the above statistics, it can be found that most of the injuries are treated by traditional methods, with acupuncture and massage therapy taking the initiative; the use of taping, ice compress, physiotherapy, rehabilitation training, and other methods still accounts for a small proportion. Most athletes in the survey reported that traditional treatment methods are effective in resolving pain from acute injuries, but injuries tend to recur frequently.

For the complete rehabilitation of the injured part, in addition to the normalization of its anatomical structure and tissue, it should also include the recovery of the complex functional capabilities of the part. The recovery of functional ability requires muscle groups to restore the ability to coordinate work and fine work, and the current injury treatment does not cover the content of rehabilitation training; thorough treatment of the injured area was neglected. In this case, repeated training will cause the injury to accumulate and gradually aggravate into a chronic injury.

The application of necessary support belt fixation technology and protective equipment is important, the application of joint support belt is an important means and effective method to control and protect knee and ankle joint injuries, and the application of knee pads can protect the impact of the carpet on the knee joint. The application of intramuscular effect has a good effect on the prevention of muscle and joint damage. Therefore, it is necessary for us to strengthen the application of taping in rhythmic gymnastics, so as to reduce the occurrence and aggravation of injury.

Strengthen strength training, especially specific muscle strength training, strength training for small muscle groups

and core strength training. Core strength training can significantly alter trunk stability in rhythmic gymnasts.

In order to achieve scientific training, on the one hand, we must do a good job of medical supervision: before training, the support belt fixation of vulnerable parts, wearing protective gear and other protective measures, paying attention to the warm-up activities before training, is conducive to reducing the occurrence of injury. After training, athletes can be fully relaxed by various means, especially the athlete's active stretching and relaxation; this can not only fully relax the athlete but also enhance the flexibility of the athlete's whole body, so that the body can more coordinately complete difficult movement techniques. Strengthen the standardization of technical movements during training and treat them differently. Athletes should take effective treatment in time after injury. Another aspect of scientific training is to do a good job of monitoring physiological and biochemical functions and to use scientific means to ensure a reasonable amount of training for athletes.

The best way to recover is to strengthen your core, especially your back. Specifically, training equipment such as elastic bands and Swiss balls is used to exercise, so as to improve the muscle strength of the core and reduce the risk of waist injury.

Increase asymmetrical movement exercises to strengthen stability and agility in asymmetrical states. Pay attention to stretch the tissues around the ankles, knees, and hips to maintain optimal joint mobility.

Strengthen core stability training and improve the stability of limbs and the ability to work together with muscles when supported on one or both sides. Stability exercises can be performed on Swiss balls and balance pads; for example, the single-leg support half squat, the supine, prone, and side-lying static support movements on the Swiss ball can reduce the chance of sports injuries.

5. Conclusion

Injury risk assessment provides a theoretical basis for the prevention and rehabilitation of rhythmic gymnasts' injuries; in each stage, an injury risk assessment test is conducted for athletes in the mode of assessment-rehabilitation-reassessment; this guides the implementation of rehabilitation measures at each stage. According to the results of the injury risk assessment, a personalized sports rehabilitation plan is scientifically formulated and implemented, so as to effectively control the injury problem of an athlete and ensure the normal training before the competition, and participated in the 2012 London Olympic Games in the best state, and achieved a historic breakthrough in the performance of China's rhythmic gymnastics individual events. It is proved that through the investigation of 126 rhythmic gymnasts participating in the 2011 "China Art Sports Cup" China Rhythmic Gymnastics Championship, the injury characteristics of gymnasts can be found, and the injury risk assessment can be carried out; it effectively solves the problem of the basis for the rehabilitation and prevention of athletes. It satisfies the needs of the athlete's injury risk assessment test, makes up for the deficiency that the gym-

nast cannot be assessed for injury, and can improve the recovery efficiency of the athlete after injury.

Data Availability

The data used to support the findings of this study are available from the corresponding author upon request.

Conflicts of Interest

The authors declare no conflicts of interest.

References

- [1] L. E. Osta, A. E. Helou, H. A. Hatem, and N. E. Osta, "Injury patterns among national-level athletes in Lebanon: a retrospective study," *Research in Sports Medicine*, vol. 1, pp. 1–18, 2021.
- [2] M. J. Best, B. A. Zikria, and J. H. Wilckens, "Anterior cruciate ligament injuries in the older athlete," *Sports Health*, vol. 13, no. 3, pp. 285–289, 2021.
- [3] A. Kap and B. Mjo, "Management of Achilles tendon injuries in the elite athlete," *Orthopedic Clinics of North America*, vol. 51, no. 4, pp. 533–539, 2020.
- [4] S. Skinner and J. Isaacs, "Extensor tendon injuries in the athlete," *Clinics in Sports Medicine*, vol. 39, no. 2, pp. 259–277, 2020.
- [5] J. J. Chan, K. K. Chen, S. Sarker, R. Hasija, and E. Vulcano, "Epidemiology of Achilles tendon injuries in collegiate level athletes in the United States," *International Orthopaedics*, vol. 44, no. 3, pp. 585–594, 2020.
- [6] Y. M. Putra, S. Purwanto, and E. Burhaein, "Effect of limb muscle power training with leaps on athlete's speed during the covid-19 pandemic," *International Journal of Human Movement Science*, vol. 9, no. 3, pp. 461–465, 2021.
- [7] J. Wilkinson and L. Mayhew, "The prevalence of musculoskeletal injuries, menstrual irregularity and disordered eating in junior elite athletics in the UK," *British Journal of Sports Medicine*, vol. 55, no. 16, p. 940.2–941, 2021.
- [8] D. Constantinou, N. P. Saragas, and P. N. Ferrao, "Bilateral navicular stress fractures with nonunion in an adolescent middle-distance athlete: a case report," *Current Sports Medicine Reports*, vol. 20, no. 5, pp. 236–241, 2021.
- [9] F. Halabchi and M. Hassabi, "Acute ankle sprain in athletes: clinical aspects and algorithmic approach," *World Journal of Orthopedics*, vol. 11, no. 12, pp. 4–28, 2020.
- [10] N. Elghoul, I. Elantri, A. Elghazoui, M. Benchakroun, and A. Jaafar, "Concomitant anterior shoulder dislocation and ipsilateral humeral pallet fracture in the athlete: case report and review of the literature," *Case Reports in Orthopedic Research*, vol. 3, no. 2, pp. 74–78, 2020.
- [11] M. Ehn, M. Teramoto, D. M. Cushman, K. Saad, and S. Willick, "The national interscholastic cycling association mountain biking injury surveillance system: 40,000 student-athlete-years of data," *Current Sports Medicine Reports*, vol. 20, no. 6, pp. 291–297, 2021.
- [12] T. L. Wong, C. F. Huang, and P. C. Chen, "Effects of lower extremity muscle fatigue on knee loading during a forward drop jump to a vertical jump in female athletes," *Journal of Human Kinetics*, vol. 72, no. 1, pp. 5–13, 2020.

- [13] A. Uzun and B. Demir, "Effect of pilates and reformer exercises on body composition," *International Journal of Applied Exercise Physiology*, vol. 9, no. 10, pp. 2322–3537, 2020.
- [14] S. Sharma, M. S. Dhillon, P. Kumar, and R. K. Rajnish, "Patterns and trends of foot and ankle injuries in Olympic athletes: a systematic review and meta-analysis," *Indian Journal of Orthopaedics*, vol. 54, no. 3, pp. 294–307, 2020.
- [15] H. S. Cho and C. H. Kim, "The effects of customized spinal corrective exercise program on the spinal curvature change and posture balance ability for flat back syndrome," *Journal of the Korean society for Wellness*, vol. 15, no. 1, pp. 409–417, 2020.
- [16] S. K. Jeripotula, A. Mangalpady, and G. R. Mandela, "Ergonomic assessment of musculoskeletal disorders among surface mine workers in India," *Mining, Metallurgy & Exploration*, vol. 38, no. 2, pp. 1041–1046, 2021.
- [17] S. S. Shin and W. G. Yoo, "The effects of differences on sagittal kinematics and muscle coordination during step up and step down in patients with spinal stenosis," *Journal of Back and Musculoskeletal Rehabilitation*, vol. 34, no. 3, pp. 453–459, 2021.
- [18] D. M. Knapik, C. D. Mack, R. Lee et al., "Epidemiology of tibial fractures in professional American football athletes from 2013 to 2019," *Orthopaedic Journal of Sports Medicine*, vol. 9, no. 11, 2021.
- [19] C. D. Park, J. M. Park, and J. Y. Cha, "Effects of neuromuscular training on posture stability and functional exercise performance abilities in wushu player," *Korean Journal of Sports Science*, vol. 29, no. 6, pp. 1169–1181, 2020.
- [20] S. W. Park and H. S. Lee, "Effects of posture correction exercise on muscle activity and onset time during arm elevation in subject with forward head and rounded shoulder posture," *Journal of the Korean Society of Physical Medicine*, vol. 15, no. 3, pp. 29–41, 2020.
- [21] H. Nitayarak and P. Charntaraviroj, "Effects of scapular stabilization exercises on posture and muscle imbalances in women with upper crossed syndrome: a randomized controlled trial," *Journal of Back and Musculoskeletal Rehabilitation*, vol. 34, no. 6, pp. 1031–1040, 2021.
- [22] Y. Endo and M. Miura, "Effects of posture and lower limb muscle strength on the results of the star excursion balance test," *Journal of Physical Therapy Science*, vol. 33, no. 9, pp. 641–645, 2021.
- [23] H. H. Son, "The effects of virtual reality games in posture correction exercise on the posture and balance of patients with forward head posture," *Journal of the Korean Society of Physical Medicine*, vol. 15, no. 2, pp. 10–21, 2020.
- [24] A. Golchini and N. Rahnama, "The effects of 12 weeks of systematic and functional corrective exercises on body posture of students suffering from pronation distortion syndrome," *Iranian Rehabilitation Journal*, vol. 18, no. 2, pp. 181–192, 2020.
- [25] R. S. Sabbagh, N. S. Shah, A. P. Kanhere, C. G. Hoge, C. G. Thomson, and B. M. Grawe, "Effect of the covid-19 pandemic on sports-related injuries evaluated in us emergency departments," *Orthopaedic Journal of Sports Medicine*, vol. 10, no. 2, 2022.
- [26] A. Dutta, S. P. Breloff, F. Dai, E. W. Sinsel, and J. Z. Wu, "Effects of working posture and roof slope on activation of lower limb muscles during shingle installation," *Ergonomics*, vol. 63, no. 9, pp. 1182–1193, 2020.
- [27] Z. Gong and H. Wiltshire, "Review on the effects of high heeled on body posture based on medical images," *Journal of Medical Imaging and Health Informatics*, vol. 10, no. 5, pp. 1165–1170, 2020.
- [28] C. D. Park and J. M. Park, "Effects of whole body vibration exercise on posture stability and lower segment movements in golf player," *Korean Journal of Sports Science*, vol. 30, no. 3, pp. 1205–1215, 2021.

Research Article

Early Diagnosis of Retinal Blood Vessel Damage via Deep Learning-Powered Collective Intelligence Models

Pranjal Bhardwaj,¹ Prajjwal Gupta ,¹ Thejineaswar Guhan ,²
and Kathiravan Srinivasan ¹

¹School of Computer Science and Engineering, Vellore Institute of Technology, Vellore 632 014, India

²School of Information Technology and Engineering, Vellore Institute of Technology, Vellore 632 014, India

Correspondence should be addressed to Kathiravan Srinivasan; kathiravan.srinivasan@vit.ac.in

Received 27 April 2022; Accepted 30 May 2022; Published 23 June 2022

Academic Editor: Pan Zheng

Copyright © 2022 Pranjal Bhardwaj et al. This is an open access article distributed under the Creative Commons Attribution License, which permits unrestricted use, distribution, and reproduction in any medium, provided the original work is properly cited.

Early diagnosis of retinal diseases such as diabetic retinopathy has had the attention of many researchers. Deep learning through the introduction of convolutional neural networks has become a prominent solution for image-related tasks such as classification and segmentation. Most tasks in image classification are handled by deep CNNs pretrained and evaluated on imagenet dataset. However, these models do not always translate to the best result on other datasets. Devising a neural network manually from scratch based on heuristics may not lead to an optimal model as there are numerous hyperparameters in play. In this paper, we use two nature-inspired swarm algorithms: particle swarm optimization (PSO) and ant colony optimization (ACO) to obtain TDCN models to perform classification of fundus images into severity classes. The power of swarm algorithms is used to search for various combinations of convolutional, pooling, and normalization layers to provide the best model for the task. It is observed that TDCN-PSO outperforms imagenet models and existing literature, while TDCN-ACO achieves faster architecture search. The best TDCN model achieves an accuracy of 90.3%, AUC ROC of 0.956, and a Cohen's kappa score of 0.967. The results were compared with the previous studies to show that the proposed TDCN models exhibit superior performance.

1. Introduction

Diabetic retinopathy (DR) is a medical condition caused due to complications caused by diabetes mellitus that influences the ocular perceivers and causes damage to the delicate tissues of the retina. This condition can occur in any adult who is suffering from either type 1 or type 2 diabetes. As diabetic retinopathy increases with time, it eventually causes a complete loss of vision. In this paper, we will be discussing the four different types of DR (nonproliferative DR, maculopathy, preproliferative, and proliferative). With the rise in cases for DR, there arises a need for automation for the detection of diabetic retinopathy in fundus images. Identification of individual characteristics and extraction of features are important for the assessment of eye disorders such as DR and other retinal diseases.

Manual inspection of fundus images can prove to be a tedious process to decipher subtle variations in microaneurysms, optic disks, hemorrhages, blood vessels, hard exudates, soft exudates, and macular edema. In such situations, CAD (computer-aided diagnostic) systems can significantly reduce the manual inspection load for professionals. These methods also reduce margins of error compared to ophthalmologists while examining the fundus images. With the introduction of convolutional neural networks, deep learning has become the de facto for computer vision-based problems. CNNs have the capability to extract features automatically and decipher patterns for better understanding of the data. Deep CNN models are large deep learning models which leverage the power of various CNNs and pooling layers. These models typically stack a bunch of CNNs together to form a feed-forward network and often produce state-of-the-art results. Most of the deep CNN

models are trained and tested on the imagenet classification dataset, and the versatility of deep learning enables it to transfer learning from one dataset to another. This aspect of transfer learning has made most computer vision problems efficient and solvable through training imagenet models on a dataset [1–5]. The imagenet models are usually employed with approaches like transfer learning.

Although transfer learning is a powerful concept, models trained on imagenet often do not obtain the best result when trained on an independent dataset. The reasons for the same could include the size of the dataset, the size of the model, and the type of the data, thus bringing the need for tailor-made models. Models can be proposed on the basis of the dataset, where a small dataset may require a lightweight model. With the help of lightweight models, better performance and high scalability can be achieved. In such a situation, tailor-made models could possibly be the most efficient model for the job. However, building tailored models can be computationally expensive. Moreover, in certain cases, the features extracted from the imagenet dataset would not be a great starting point, the reason for the same being the dissimilarity of the images in the imagenet dataset and the dataset on which the model is to be trained. For example, the imagenet dataset contains objects such as cars and animals which do not resemble fundus images.

Nature-inspired swarm algorithms have been heavily employed for feature selection on various tasks. These algorithms have performed efficiently in hyperparameter search/optimization. Hyperparameter optimization methods such as grid search have been computationally expensive methods and give the best result within a search space. Hence, swarm algorithms have been used for architectural proposals. Nature-inspired swarm algorithms are a subset of evolutionary algorithms. These algorithms in general have been known to shrink the search space whether it be feature selection or hyperparameter optimization. However, the usage of swarm-based algorithms has been limited to feature selection as demonstrated across in [6–8]. Most used cases of swarm-related algorithms in DR classification are restricted to either hyperparameter optimization or feature extraction. This methodology utilizes both methods by proposing new models with various hyperparameters based on the dataset. TDCNs are the outcomes of the swarm algorithms, and in this case, 2 algorithms are used. The objective of these models is to provide custom models which are efficient and accurate for a given dataset. The proposed models rely solely on architecture rather than fixed models with a set starting weight to achieve accuracy. Therefore, the significance of transfer learning diminishes which addresses the problems caused by imagenet models.

The major contributions of this paper include the following:

- (i) A formal definition of search space complexity for searching tailor-made models
- (ii) Utilizing two swarm intelligence algorithms, namely, ant colony optimization (ACO) and particle swarm optimization (PSO), to perform heuristic architecture search in multidimensional space

- (iii) Two tailored ConvNets (TDCN) called TDCN-ACO and TDCN-PSO were obtained from ACO and PSO-based searches. TDCN-PSO being significantly smaller (lightweight) achieves better performance over 3 metrics, accuracy, AUC ROC, and Cohen’s kappa, than the imagenet models. The model’s performance is solely defined on the basis of architecture search (a dynamic process) rather than designing a fixed model

- (iv) TDCN-PSO and TDCN-ACO produce competitive results with many proposed architectures in literature for fundus image classification

2. Related Works

Over the years, various deep learning approaches have been utilized to diagnose retinal vascular diseases, including usage of imagenet models, transfer learning, and image segmentation. Kanungo et al. [9] proposed an Inception-V3 architecture-based approach in which multiple convolution filter inputs are processed on the same input. This takes advantage of multilevel feature extraction from each input. The accuracy achieved is comparatively less than the other approaches based on similar architectures. Zeng et al. [10] proposed a deep Siamese CNN architecture for automatic diabetic retinopathy classification. The model takes two fundus images as input, i.e., the left and right eye image. Transfer learning approaches have shown great results in terms of DR classification. Lam et al. [11] proposed an approach using GoogleNet and AlexNet to demonstrate transfer learning. Sakaguchi et al. [12] used GNNs to construct the region of interest graphs which is helpful for further classification of DR using CNN. Although imagenet and transfer learning-based approaches perform well on benchmark datasets, they do not perform similarly on some niche datasets as they were designed keeping a general purpose in mind. In order to increase the performance of the model, the need for tailoring models arises.

Hyperparameter optimization (HO) plays a key role when designing tailor-made models for specific datasets. Over the years, automated hyperparameter search algorithms and libraries have become increasingly popular; the widely used ones include hyperopt [13], optuna [14], and Auto WEKA [15]. The total search space including all subsets is 2^n where n is the number of features, thus posing a high-dimensional problem. The early works focused on using Bayesian optimization for hyperparameter tuning [16–18], but these techniques suffer the drawback of being computationally complex. Li et al. address the problem of HO as an exploration-based nonstochastic infinite-armed bandit problem and proposed hyperband to solve the same [19]. Falkner et al. addressed the robustness and scalability of HO [20], and Hazan et al. addressed the high-dimensional problems [21], each work resulting in a manifold increase in performance over hyperband. Hintz et al. pointed out that a significant speedup can be achieved by carrying out the search on lower-dimensional data representation at the beginning and increasing the dimensions later in the optimization process [22]. Some of the recent works

revolve around using reinforcement learning for adaptive and dynamic HO in contrast to other approaches which require the user to set generic ranges in order to define the HO search space [23, 24].

Nature-inspired swarm-based techniques are a subset of swarm intelligence which in turn is a subset of metaheuristic algorithm. Nature-inspired swarm algorithms have been of great use when it comes to feature selection in the tabular dataset as it achieves optimal results with substantially lower computational resources [25]. This behavior of swarm-based techniques has been taken to advantage in hyperparameter selection which is a computationally expensive process as mentioned before. Bee colony optimization and dragonfly algorithm were used by Yasen and Al-Madi [26] to select the size of hidden nodes in the neural network. Crossover and mutation were also combined to devise new models. All in all, the models were trained on medical patients' data, and the comparative results were obtained. Similarly, Sun et al. [27] used PSO to determine the dimensionality of the autoencoder to be used, moving to the applications of swarm-based algorithms on the application of retinal fundus images.

Bajčeta et al. [7] proposed a segmentation model of blood vessels where they have applied ACO in fundus images, and ACO performs feature extraction. Hooshyar and Khayati [8] proposed a mathematical model in which they have used eigenvalues of the Hessian matrix. They used a Gabor filter bank to extract the features from retinal images. For classification purposes, fuzzy c-means and ACO models are produced. Asad et al. [28] proposed an approach to ensure improved ant clustering-based segmentation. The approach was developed with the help of a new heuristic function of the ACO algorithm. Kavitha and Ramakrishnan [29] employed an ACO algorithm using an OTSU method which is based on the inputs from optic disc and macula. Balakrishnan et al. [6] came up with a hybrid model for classification and feature extraction from retinal images. Channel extraction and median filter are used for preprocessing. After the preprocessing stage, the authors used a histogram of oriented gradient (HOG) with a complete local binary pattern (CLBP) to perform feature selection. Particle swarm optimization along with fuzzy membership functions is used by Bhimavarapu et al. [30] to cluster images, and then, probabilistic models were used to segment fundus images. Although nature-inspired swarm-based methods have been extensively studied on hyperparameter optimization, its application is restricted to feature selection alone in diabetic retinopathy. Furthermore, identifying intrinsic features in medical datasets has led researchers to build complex deep architectures which are computationally expensive. For faster convergence and inference, there is a requirement of lightweight models which can be achieved using the likes of nature-inspired swarm algorithms as discussed in further sections.

3. Methodology

The process of generation of a tailored model can be defined as a search on a set of models S_m formed by the combina-

tions of layers from a set of layers S_l using a selection metric f and a goal G . For a given S_m , the search is deemed successful if the set of resultant models S_r is a subset of the set of models S_r which satisfy G on f with an acceptable performance bound ϵ .

$$S_r = \{m : m \in S_m, f(m) + \epsilon - G\}. \quad (1)$$

The complexity of the search is determined by the cardinality of the set $S_m(t_s)$. For a given bound of the minimum number of layers B_l and a maximum number of layers B_u , t_s can be obtained by

$$t_s = \sum_{b=B_l}^{B_u} t_l^b, \quad (2)$$

where t_l is the cardinality of the set s_l .

This search space can be restricted by using various design parameters (order, count, blocks, etc.) on the occurrence of layers. This search space evidently becomes very large as t_l and B_l increase, and simple techniques like a brute force search become time and resource intensive. This problem can be solved using heuristic-based search algorithms, such as swarm intelligence algorithms as demonstrated further in this section.

For the two swarm-based techniques discussed in this paper (ACO and PSO), we obtain a single model (S_s) as the result of the search. We tested the results on three selection metrics as discussed in Section 4. The search goal G was set to the best result obtained in the case of imagenet models or better essentially resulting in a search which yields lightweight models of similar performance to imagenet models or high performance models or both. The value of ϵ was set such that the search resulted in a model which performed better than at least one of the imagenet models. The nature of results is characterized by the settings of B_l and B_u . The detailed success criterion is listed in Table 1.

The resultant architectures, TDCN-ACO, and TDCN-PSO have been described in the following sections using the abbreviations in Table 2.

3.1. TDCN-ACO Search Using Ant Colony Optimization.

Ants have inspired many methods and techniques, among which the most studied is the general purpose optimization technique known as ACO (ant colony optimization). ACO is inspired by the behavior of some ant species. These ants deposit pheromone on the ground to mark a favorable path for the rest of the members of the colony. Each ant moves randomly and more pheromone gets deposited on the path. The more the pheromone on the path, the higher is the probability of the path being followed. In this work, the implementation proposed by Byla and Pang [31] is used.

The search for models is based on the number of maximum ants and maximum search depth; the algorithm starts the process by creating an internal graph with just an input node. Sequentially, ants are created until the number of maximum ants allowed is created. These ants follow ant colony selection (ACS) rule, wherein the ants choose a

particular layer based on the algorithmic calculation in ACO. If the chosen layer has not been chosen by a previous ant, then the layer is added as a neighbor node to the node chosen by the previous ant. Based on the same rule, the parameters of the layer are also chosen from a specified list of parameters. Once the choice is made, ACS local pheromone update is done by the ant. The same is done until the maximum number of ants allowed, traverses through to the same depth. The paths are converted to neural networks, and based on the evaluation metric, the best ant is chosen, and now, an ACS global pheromone update is done. Note that the previous update is kept local to encourage the ants to pave new paths. Figure 1 conveys the same in a pictorial fashion.

For this dataset, 4 hyperparameters were mainly handled:

- (i) *Number of ants*: 8 and 16. Based on the experiments conducted by [31], it was found that the greatest decrease in error was identified when the number of ants was increased from 8 to 16. 32 may yield better results, but the duration of computation will increase
- (ii) *Search depth*: 32. Most of the available image models tend to be deep models; therefore, a search depth of 32 was used
- (iii) *Epochs*: it is kept at 10 epochs
- (iv) *Image size*: 32 and 64. When large image sizes are used, the accuracy more or less remains the same. This was surprising considering the performance output with respect to the image size

The permutations among the defined hyperparameters have generated 4 models. The trend across the models happens to look like this, C2D | BN till one max pooling, and lastly followed by a series of DE | BN layers. The choice of layers across models is almost comparable to the traditional model building approach, where usually every CN2D layer is succeeded by a pooling such as avg. pooling. However, the trend of using a pooling layer before flattening the outputs of CNN has generally shown success, and this process utilizes that.

As far as the search space is concerned, a total of 4 layers were permuted across C2D, MP or AP, BN, and DE. The search space for every layer varies as per requirements:

- (i) C2D: 9 permutations possible
- (ii) MP: 2 permutations possible
- (iii) BN: 1 permutation possible
- (iv) DE: 4 permutations possible

The number of permutations can be maintained within a permutation matrix which can be accessed simultaneously when a layer is accessed $L = [C2D, MP, BN, DE]$ and $= [9, 2, 1, 4]$. So if a layer L_i is chosen, then P_i is also chosen, where i is the index in the array L . So the search space when n is the

TABLE 1: Search goals and performance bounds used in this work.

Metric	G	ϵ
Accuracy	≥ 74.8	1.5%
AUC ROC	≥ 0.91	0.2
Cohen's kappa	≥ 0.776	0.02

number of layers is shown in

$$\text{Search space} = t_s = P_0^{\text{num C2D}} + P_1^{\text{num MP}} + P_2^{\text{num BN}} + P_3^{\text{num DE}}. \quad (3)$$

The search space is model independent and considering a model of 12 C2D | BN then MP and lastly 3 DE | BN layers gives a search space as shown in

$$t_s = 282, 429, 569, 261. \quad (4)$$

In total, there exist 16 ants at maximum denoted by *ant* for a total *depth* of 32. Equation (5) conveys the number of models which were trained in the tailor fitting process:

$$\text{Number of models trained} = \text{ants} * \text{depth} = 16 * 32 = 512. \quad (5)$$

3.2. TDCN-PSO Search Using Particle Swarm Optimization. Particle swarm optimization is a nature-inspired, population-based algorithm that has been found to optimize or converge better than standard optimization algorithms like conjugate descent, gradient descent, and Newton method in multidimensional space. Stochastic search is used to achieve the same by moving the particles (candidate solutions) in the search space using mathematical computations to calculate the velocity and direction of the particle swarm by considering the particle's current position and goal. A global best (in terms of position) is maintained as well as a local best for each particle is maintained which influences in making decisions for the particle's movement in consequent iterations. This results in the general behavior of the swarm moving towards the best solutions for the given search space.

The position and velocity after each generation or iteration of the algorithm can be obtained by

$$X^{t+1}ij = X^t ij + V^{t+1}ij, \quad (6)$$

$$V^{t+1}ij = w V^t ij + c_1 r^t 1 (pbestij - X^t ij) + c_1 r^t 2 (gbestj - X^t ij), \quad (7)$$

where X_i^t is the position vector of i^{th} particle at t^{th} and V_i^t is the position vector of i^{th} particle at t^{th} .

Many modifications to these equations have been proposed over time which offers specific benefits of their own, but the original algorithm is proceeded across for a general comparison of this algorithm with others.

TABLE 2: ConvNet layer abbreviations used in this work.

Abbreviation	Layer
C2D	Conv2D (convolutional layer with 2-dimensional filters)
BN	Batch normalization
DO	Dropout
MP	Max pooling
AP	Average pooling
DE	Dense or fully connected
F	Flatten

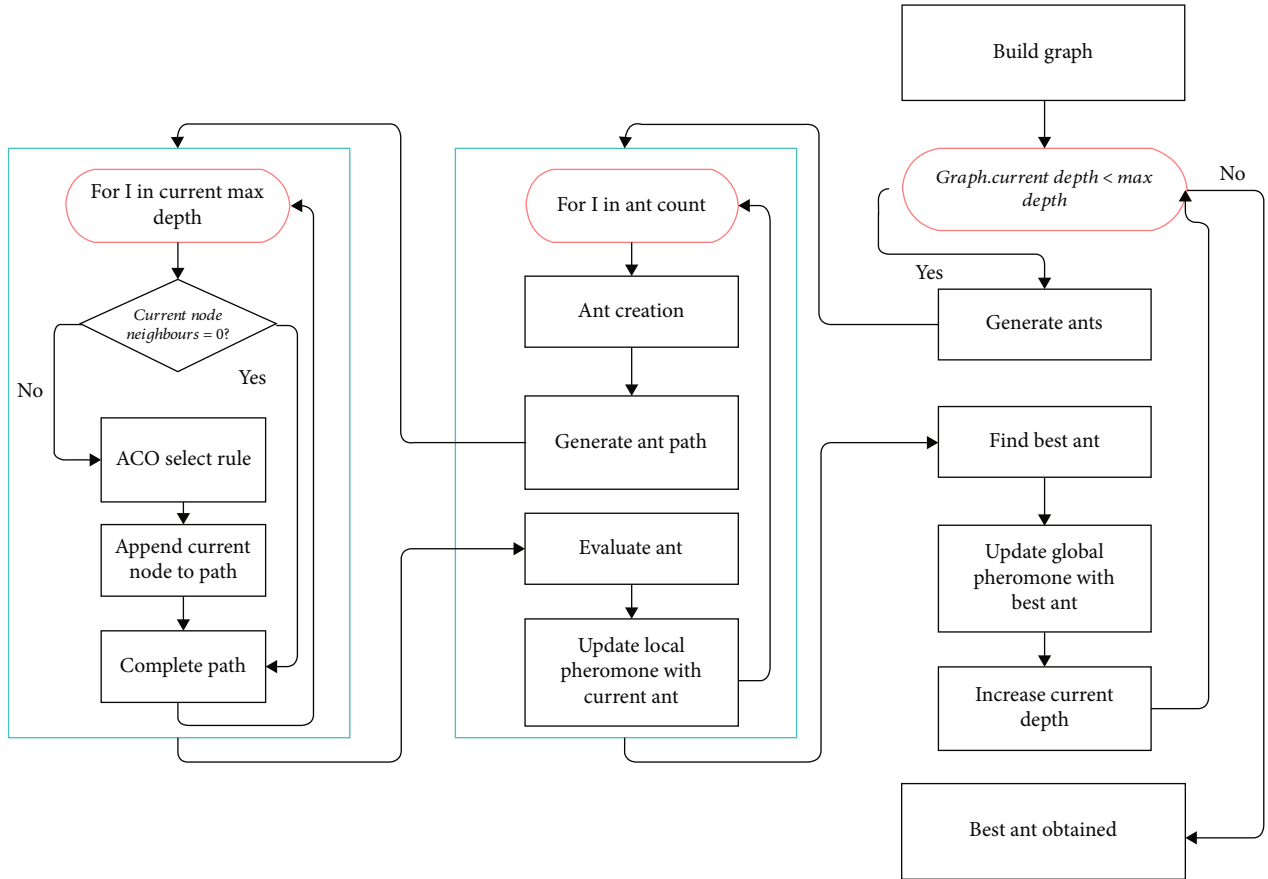


FIGURE 1: TDCN-ACO search using ant colony optimization.

The tailoring of models is carried out by taking several parameters into consideration such as population size, number of iterations and runs, the minimum and maximum number of layers, and probability of each type of layer. Using these parameters, the particles are initialized by assigning them random CNN architectures represented in an array form that satisfy the conditions and constraints defined by the parameters (number of layers, layer probabilities, kernel sizes, and so on). Then, each particle is fit and evaluated to find the local and global best based on the accuracy obtained on the validation data. The good blocks in the global best are passed onto further generations, and each particle is evaluated again in every iteration. An architecture search using PSO mainly involves six procedures, namely,

representation of particles in form of architectures (in our case deep ConvNets) of varying properties, initializing the particles, evaluating the fitness of individual particles, a measure of the difference between two particles, computation of velocity, and updating the particles as illustrated in Figure 2.

In this paper, the search on a set formed by the combination of 4 different kinds of layers is performed, namely, convolutional, max pooling, average pooling, and fully connected, making t_l as 4. We set the bounds $B_l = 3$ and $B_u = 20$, effectively giving us equation (8).

$$t_s = \sum_{b=3}^{20} 4^b \Rightarrow t_s = 1,466,015,503,680. \quad (8)$$

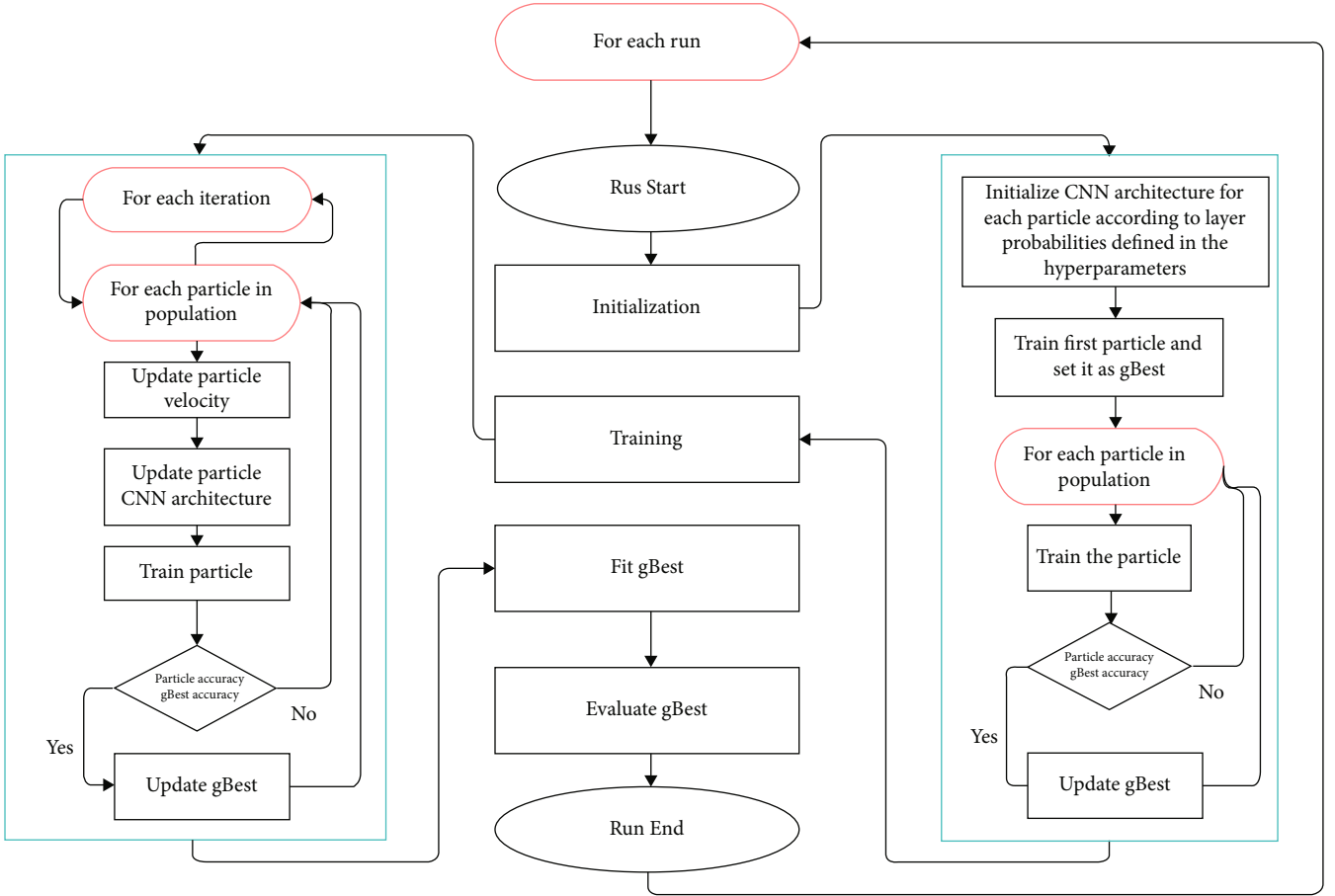


FIGURE 2: TDCN-PSO search using particle swarm optimization.

This means that the search space for the algorithm consists of more than 1466 billion models when no design constraints are applied. A simple design constraint was kept as follows:

- (i) At least 1 DE layer
- (ii) F has occurred before the first DE layer
- (iii) No C2D layer after F layer

This decreased the search space manifolds. The number of models searched by the PSO algorithm ($S_{m,ps0}$) is a function of the number of iterations i , number of runs, and swarm size p and is given by

$$S_{m,ps0} = r \times i \times p. \quad (9)$$

For this paper, the following hyperparameters are set $r = 5$, $i = 12$, and $p = 20$, which gives $S_{m,ps0} = 1200$. These values depend on the quality of TDCN required hardware availability and time constraints.

Note that each updated particle was considered as a new model. To carry out the architecture search, the implementation proposed by Junior et al. [32] was used.

TDCN-PSO is the model represented by the global best particle at the end of the architecture search. The hyperparameters used for the search can be found in Table 3. The resultant architecture has some peculiar features such as 4 consecutive pooling layers and irregular batch normalization and dropout layers, all of which are characteristics of a model unique to the dataset. The architecture of TDCN-PSO found for APTOS dataset is as follows: C2D | C2D | BN | DO | C2D | BN | MP | AP | MP | MP | DO | C2D | BN | F | DO | DE | BN.

4. Experimental Setup

The dataset that we used for this paper is ‘‘ATPOS 2019 Blindness Detection’’ from a Kaggle competition conducted in 2019. This dataset contains high-resolution images of the retina taken in different lighting conditions, with left and right fields for every test subject. The images have been captured through varying devices, offering different scenarios and generalizations of the developed model for adoption by a wide variety of hardware. The images present in the data are of different orientations too, some are shown anatomically (macula on left, optic nerve on right for right eye), and others are shown inverted. The training set consists of 3662 images, while the test set contains 1928 images.

TABLE 3: Hyperparameter setting for TDCN-PSO search.

Category	Hyperparameter	Value
Particle swarm optimization	Number of runs (r)	5
	Number of iterations (i)	12
	Swarm size (p)	20
	C_g	0.5
	Minimum number of outputs from a Conv layer	3
	Maximum number of outputs from a Conv layer	256
	Minimum number of neurons in a FC layer	1
CNN architecture initialization	Maximum number of neurons in a FC layer	300
	Minimum size of a Conv kernel	3×3
	Maximum size of a Conv kernel	7×7
	Minimum number of layers B_l	3
	Maximum number of layers B_u	20
	Dropout rate	0.5
	No. of epochs for the global best	100
Training	No. of epochs for particle evaluation	1
	Bath normalize layer outputs	Yes
	Probability of convolutional layer	0.7
Probability	Probability of pooling layer	0.15
	Probability of fully connected layer	0.15

TABLE 4: Classes in APTOS 2019 dataset.

Class ID	Class name	Number of samples
0	No DR	1805
1	Mild	370
2	Moderate	999
3	Severe	193
4	Proliferative DR	295

TABLE 5: Comparison of TDCN models with imagenet models and literature.

Model	Accuracy	AUC ROC	Cohen's kappa
Inception	73.2	0.91	0.738
Xception	74.8	0.87	0.772
Resnet50	73.8	0.89	0.776
Shaban.et al. [33]	88	0.930	0.910
S. Kassani et al. [34]	83.09	0.950	0.892
Taufiqurrahman et al. [35]	85	0.820	0.925
Bodapati et al. [36]	84.31	0.970	0.758
TDCN-ACO	78.4	0.907	0.795
TDCN-PSO	90.3	0.956	0.967

The images are categorized into 5 classes (Table 4). Thus, this dataset poses a classification problem. The preprocessing strategies applied involve resizing.

Resizing: resizing in the digital image is changing the horizontal and vertical resolution of an image. Since the input images are in different resolutions, coming from different hardware, we decided to resize the images to 256×256 for the imagenet models, 32×32 and 64×64 for ACO, and 128×128 for PSO-CNN. Smaller image size was used for the swarm algorithms because of the high computational complexity and the time required to train the models.

The dataset is split into 10-fold cross validation. The following method is used to preserve the class wise distribution while evaluating the model. Also, this gives considerate weightage to classes, such as severe and proliferate DR, with lower number of samples.

To compare the performance of the proposed model imagenet models along with existing models are used. Three deep CNN models with imagenet weights, namely, Xception, Resnet 50, and Inception-V3, are used. The choice was restricted to these models due to the lower number of layers and parameters present which would provide a fair comparison for models proposed by nature-inspired algorithms used through this study. All the models were trained till the validation metrics (AUC and accuracy) would converge which in this case was approximately 20 epochs. Hence, patience criteria was kept at 2.

The following metrics were used to evaluate the proposed models.

- (i) *Accuracy*: accuracy is a widely used metric for evaluating classification models. This metric is the ratio of predictions that the proposed model is correctly predicted and the total number of samples. Accuracy is defined in

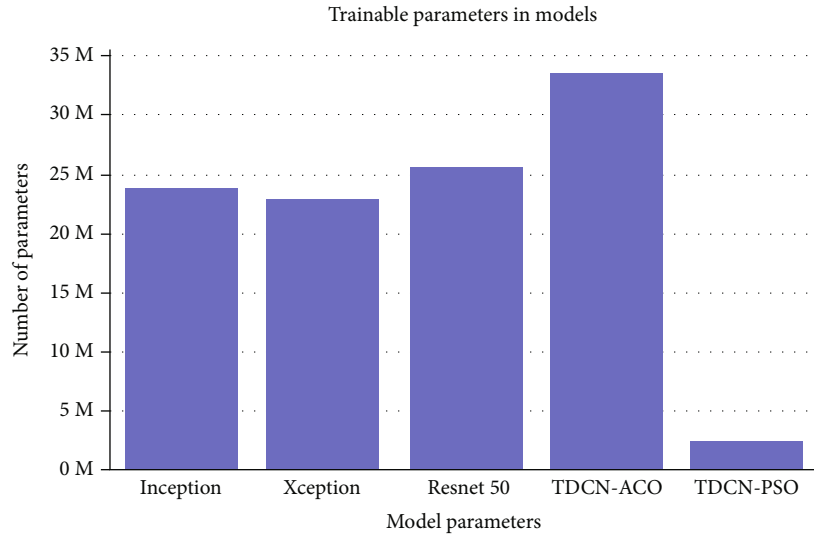


FIGURE 3: Size comparison of TDCN and imagenet models.

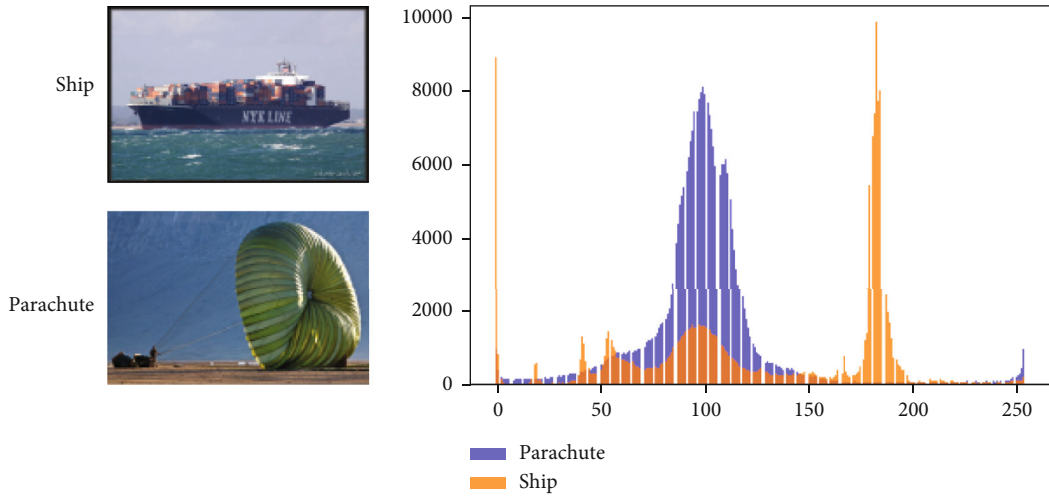


FIGURE 4: Pixel histogram for imagenet samples.

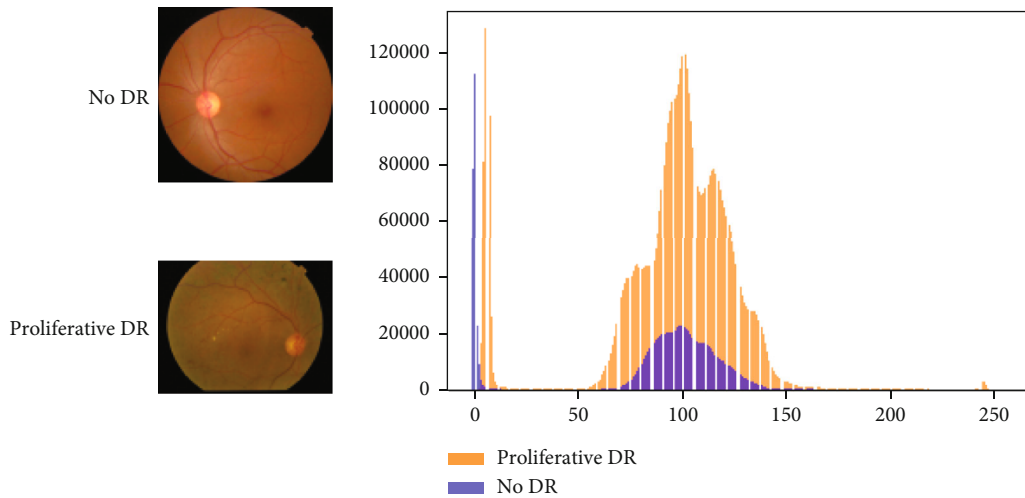


FIGURE 5: Pixel histogram for APTOS samples.

TABLE 6: TDCN-ACO results with respect to different hyperparameter settings.

Image	Ant	Accuracy	ROC AUC	Kappa
32	8	75.7	0.89	0.710
32	16	77	0.905	0.776
64	8	76.8	0.888	0.776
64	16	78.4	0.907	0.795

$$\text{Accuracy} = \frac{\text{True Positive} + \text{True Negative}}{\text{Total Number of Samples}} \quad (10)$$

- (ii) *AUC*: AUC means the area under the curve. It is a chart that visualizes the trade-off between true positive rate (TPR) and false positive rate (FPR) for every threshold. Expression for AUC is given in

$$\text{Recall/sensitivity} = \frac{\text{True positive}}{\text{True positive} + \text{false negatives}}, \quad (11)$$

$$\text{False positive rate} = \frac{\text{False positive}}{\text{True negative} + \text{false positive}} \quad (12)$$

- (iii) *Cohen's kappa score*: for the evaluation of the models, we have used a metric called Cohen's kappa coefficient which has been used for evaluating the submissions on the Kaggle competition for this dataset.

$$\text{Cohen's kappa score} = \frac{\text{pr}(o) - \text{pr}(e)}{1 - \text{pr}(e)} \quad (13)$$

Cohen's kappa is a quantitative measure of similarity between the ratings of two annotators on the same sample. It is calculated by taking into account the observed agreement and the hypothetical probability of chance agreement. Expression for Cohen's kappa is given in (13).

5. Results and Discussions

Table 5 represents the comparison of TDCN models with imagenet models and the other models in the literature. Figure 3 illustrates the size comparison of TDCN and imagenet models.

The results presented in Table 5 can be explained as follows:

- (i) In the case of imagenet models, Xception gave the best accuracy score of 74.8%, Inception gave the best AUC ROC score of 0.91, and Resnet50 gave the best Cohen's kappa score of 0.772

- (ii) TDCN-ACO provided a classification accuracy of 78.4% which is more than that observed in the case of imagenet models, AUC ROC score of 0.907, and Cohen's kappa score of 0.795. Only Inception gave better results than TDCN-ACO in terms of AUC ROC score
- (iii) TDCN-PSO outperformed all the imagenet models and TDCN-ACO in terms of all the three metrics recorded. It provided a classification accuracy of 90.3%, AUC ROC score of 0.956, and Cohen's kappa score of 0.967
- (iv) TDCN-PSO was significantly small in size with over 2.5 million parameters, which is about 9 times smaller than Xception and 13 times smaller than TDCN-ACO as shown in Figure 3
- (v) In terms of AUC ROC, only [31] provided better performance than TDCN-PSO, while [33, 34] gave comparable results
- (vi) Considering the performance over all the three metrics, TDCN-PSO gave one of the best results, while TDCN-ACO has a good place among the models and approaches compared

The imagenet dataset contains images distributed into 1000 different classes. The images from different classes differ significantly from each other in terms of features and entropy. Figure 4 shows two random images belonging to two classes, namely, ship and parachute. We plot the histogram of pixel value frequencies in order to study the distribution of features. Figure 5 shows the same histogram plot for two images from the APTOS dataset. From the two plots, it can be inferred that while the imagenet samples differ significantly in terms of distribution, the APTOS images are comparatively similar. This is one of the reasons why the tailor-fitted models TDCN-ACO and TDCN-PSO perform better than the imagenet models. Table 6 represents the TDCN-ACO results with respect to different hyperparameter settings.

Models proposed by TDCN-ACO with hyperparameters of image size 64 with 16 ants perform the best as shown in Table 6. By looking at the ROC AUC (Figure 6(a)) and confusion matrix (Figure 6(b)), it can be deduced that other than the class proliferate the model captures features that make for efficient detection. The number of parameters in the model is the highest compared to the other models but performs better than the imagenet models; therefore, one can conclude that difference in the number of parameters combats or performs better than the features captured by CIFAR training.

The AUC ROC curve and classification matrix for TDCN-PSO are shown in Figures 6(c) and 6(d). The mean training accuracy of all the runs was 89.48% with a standard deviation of 0.54%. Figure 7(a) shows that the lowest *gbest* accuracy was obtained in run 0 of 88.7% and the highest in run number 4 (the 5th run) of 90.31. An improvement of 0.83% accuracy over mean accuracy was obtained by

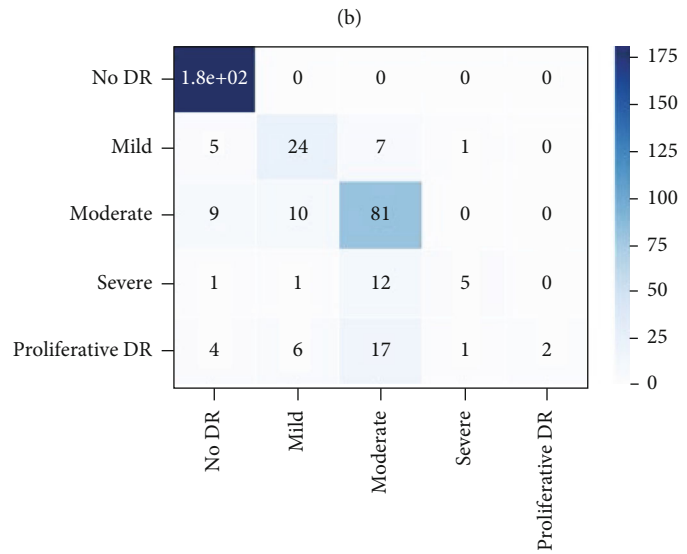
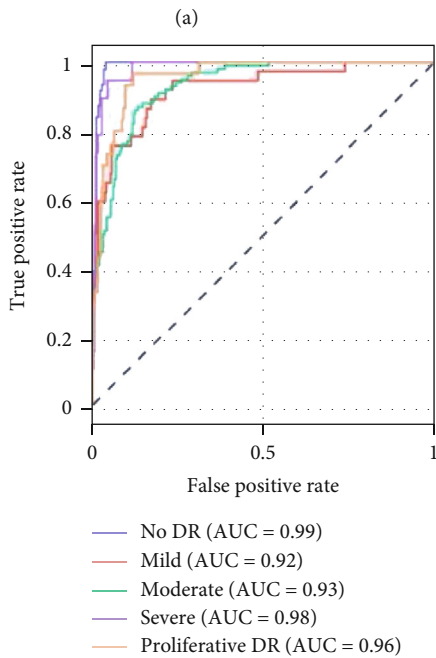
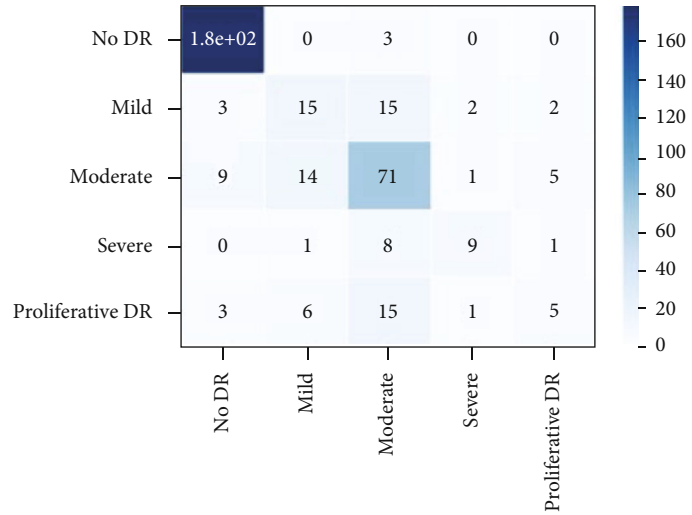
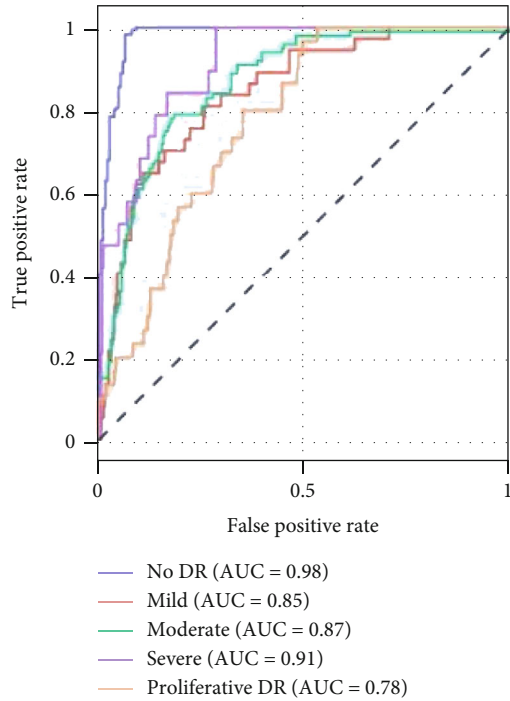


FIGURE 6: (a) TDCN-ACO AUC ROC curve, (b) TDCN-ACO confusion matrix, (c) TDCN-PSO AUC ROC curve, and (d) TDCN-PSO confusion matrix.

running the algorithm 5 times. Figures 7(b) and 7(c) show the trend of accuracy with respect to iterations for the 5th run which achieved the best results on the validation set. For this run, a new *gbest* was found in every iteration except from iterations 4 to 6 where the *gbest* remained the same and hence the flat nature of the curve. The steepness of the curve can be associated with the amount of information being passed from the *gbest* to the new particle in the subse-

quent evolutions (iterations). The best performing model (*gbest* model) out of the 5 runs provided an accuracy score of 90.3146%, AUC ROC score of 95.6, and a Cohen’s kappa score of 96.67 with 2,515,406 parameters which is a substantially better score than the state-of-the-art models with a significantly smaller model.

The results in Figure 6(c) show that the model found by TDCN-PSO performed really well in terms of AUC ROC

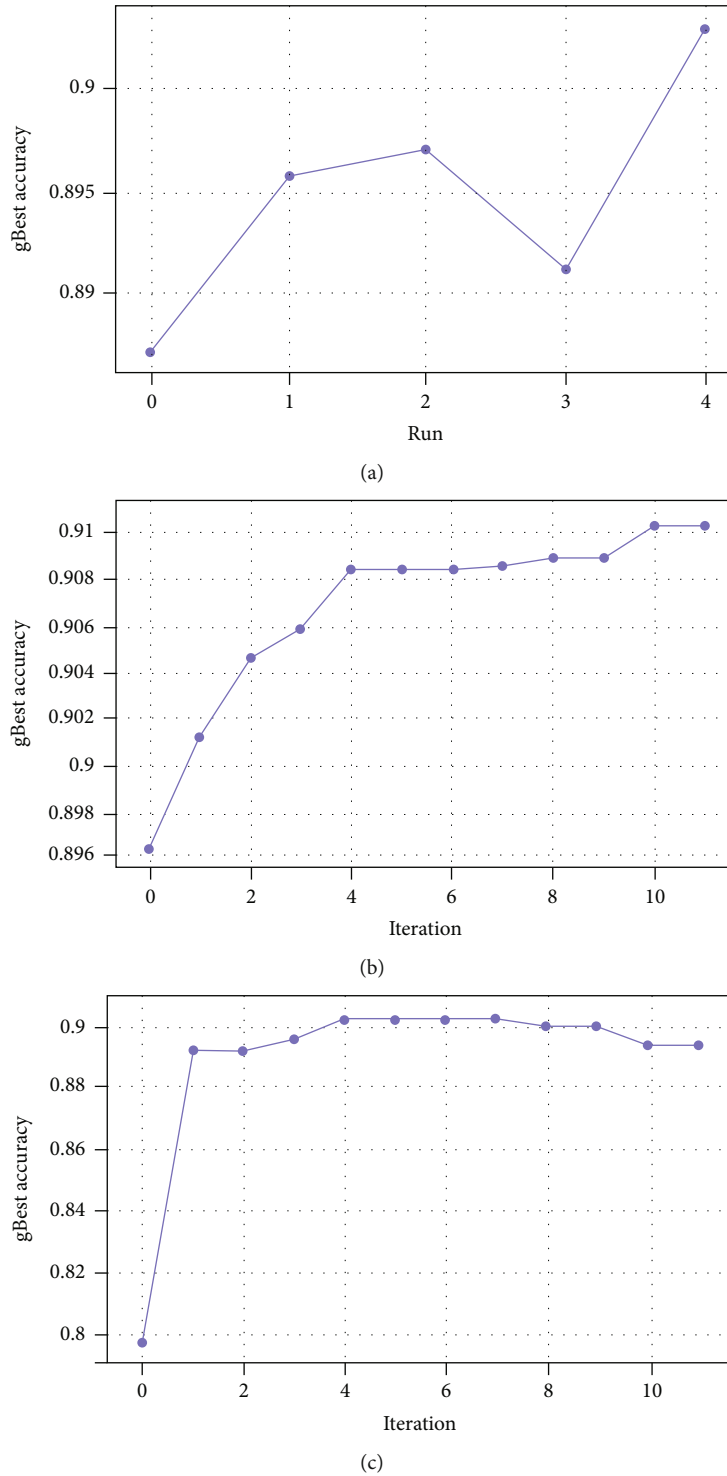


FIGURE 7: (a) Run vs. *gbest* accuracy, (b) run 5 *gbest* train accuracy, and (c) run 5 *gbest* validation accuracy.

scores. An AUC score of 0.99 for the “No DR” (no diabetic retinopathy) class conveys that the model is very accurate in classification when no diabetic retinopathy is present. In the confusion matrix obtained, it can be observed that the model was unable to produce highly accurate classifications for “severe” and “proliferative DR” classes. This was because of the skewed distribution of classes in the dataset, and the same was observed in TDCN-ACO.

6. Conclusions

In this paper, we have developed the lightweight deep learning-powered collective intelligence models for fundus image classification. The process of tailoring the model architecture is a problem that can be stated as a search in a multidimensional space. This paper highlights that for the chosen dataset, APTOS 2019, the models from architecture search

perform better than models trained using transfer learning from imagenet weights. We utilized two swarm intelligence algorithms, namely, ant colony optimization and particle swarm optimization, to efficiently search this large space. These algorithms take a heuristic-based approach which involves deriving information from the best performing entity in the swarm. The resultant tailored deep ConvNets (TDCN) called TDCN-ACO, and TDCN-PSO outperformed the imagenet models over the metrics accuracy, AUC ROC, and Cohen-Kappa scores. TDCN-PSO while being 9 times smaller achieved an improvement of 15.5% in terms of accuracy, 0.046 in terms of AUC ROC, and 0.191 in terms of Cohen-Kappa score when compared to the best performing imagenet models in each metric. The obtained results were compared with the previous studies to show that these tailored models perform similar if not better over some metrics. The future scope of this work includes leveraging the power of other swarms existing in nature. Furthermore, tailoring an ensemble of models for datasets can be the next step to further improve the results obtained in the paper.

Data Availability

The original contributions generated for this study are included in the article; further inquiries can be directed to the corresponding author.

Conflicts of Interest

The authors declare that there are no conflicts of interest regarding the publication of this paper.

Authors' Contributions

Prajwal Gupta and Thejineeswar Guhan contributed equally to this work.

References

- [1] G. T. Reddy, M. P. K. Reddy, K. Lakshmana et al., "Analysis of dimensionality reduction techniques on big data," *IEEE Access*, vol. 8, pp. 54776–54788, 2020.
- [2] T. R. Gadekallu, D. S. Rajput, M. P. K. Reddy et al., "A novel PCA-whale optimization-based deep neural network model for classification of tomato plant diseases using GPU," *Journal of Real-Time Image Processing*, vol. 18, no. 4, pp. 1383–1396, 2021.
- [3] T. R. Gadekallu, M. Alazab, R. Kaluri, P. K. R. Maddikunta, S. Bhattacharya, and K. Lakshmana, "Hand gesture classification using a novel CNN-crow search algorithm," *Complex & Intelligent Systems*, vol. 7, no. 4, pp. 1855–1868, 2021.
- [4] K. Srinivasan, L. Garg, D. Datta et al., "Performance comparison of deep cnn models for detecting driver's distraction," *CMC-Computers, Materials & Continua*, vol. 68, no. 3, pp. 4109–4124, 2021.
- [5] K. Srinivasan, A. Ankur, and A. Sharma, "Super-resolution of magnetic resonance images using deep convolutional neural networks," in *2017 IEEE International Conference on Consumer Electronics - Taiwan (ICCE-TW)*, pp. 41–42, Taipei, Taiwan, 2017.
- [6] U. Balakrishnan, K. Venkatachalapathy, and G. S. Marimuthu, "A hybrid PSO-DEFS based feature selection for the identification of diabetic retinopathy," *Current Diabetes Reviews*, vol. 11, no. 3, pp. 182–190, 2015.
- [7] M. Bajčeta, P. Sekulić, S. Djukanović, T. Popovic, and V. Popović-Bugarin, "Retinal blood vessels segmentation using ant colony optimization," in *2016 13th Symposium on Neural Networks and Applications (NEUREL)*, pp. 1–6, Belgrade, Serbia, 2016.
- [8] S. Hooshyar and R. Khayati, "Retina vessel detection using fuzzy ant colony algorithm," in *2010 Canadian Conference on Computer and Robot Vision*, pp. 239–244, Ontario, Canada, 2010.
- [9] Y. S. Kanungo, B. Srinivasan, and S. Choudhary, "Detecting diabetic retinopathy using deep learning," in *2017 2nd IEEE International Conference on Recent Trends in Electronics, Information & Communication Technology (RTEICT)*, pp. 801–804, Bangalore, India, 2017.
- [10] X. Zeng, H. Chen, Y. Luo, and W. Ye, "Automated diabetic retinopathy detection based on binocular Siamese-like convolutional neural network," *IEEE Access*, vol. 7, pp. 30744–30753, 2019.
- [11] C. Lam, D. Yi, M. Guo, and T. Lindsey, "Automated detection of diabetic retinopathy using deep learning," *AMIA Summits on Translational Science Proceedings*, vol. 2017, pp. 147–155, 2018.
- [12] A. Sakaguchi, R. Wu, and S. I. Kamata, "Fundus image classification for diabetic retinopathy using disease severity grading," in *Proceedings of the 2019 9th International Conference on Biomedical Engineering and Technology*, pp. 190–196, Tokyo, Japan, 2019.
- [13] J. Bergstra, B. Komer, C. Eliasmith, D. Yamins, and D. D. Cox, "Hyperopt: a python library for model selection and hyperparameter optimization," *Computational Science & Discovery*, vol. 8, no. 1, article 014008, 2015.
- [14] T. Akiba, S. Sano, T. Yanase, T. Ohta, and M. Koyama, "Optuna: a next-generation hyperparameter optimization framework," in *Proceedings of the 25th ACM SIGKDD International Conference on Knowledge Discovery & Data Mining*, pp. 2623–2631, Anchorage, AK, USA, 2019.
- [15] L. Kotthoff, C. Thornton, H. H. Hoos, F. Hutter, and K. Leyton-Brown, "Auto-WEKA: automatic model selection and hyperparameter optimization in WEKA," in *Automated Machine Learning*, pp. 81–95, Springer, Cham, 2019.
- [16] J. Snoek, H. Larochelle, and R. P. Adams, "Practical Bayesian optimization of machine learning algorithms," *Advances in Neural Information Processing Systems*, vol. 25, 2012.
- [17] J. Wu, X. Y. Chen, H. Zhang, L. D. Xiong, H. Lei, and S. H. Deng, "Hyperparameter optimization for machine learning models based on Bayesian optimization," *Journal of Electronic Science and Technology*, vol. 17, no. 1, pp. 26–40, 2019.
- [18] M. Feurer, J. Springenberg, and F. Hutter, "Initializing Bayesian hyperparameter optimization via meta-learning," *Proceedings of the AAAI Conference on Artificial Intelligence*, vol. 29, no. 1, 2015.
- [19] L. Li, K. Jamieson, G. DeSalvo, A. Rostamizadeh, and A. Talwalkar, "Hyperband: a novel bandit-based approach to hyperparameter optimization," *The Journal of Machine Learning Research*, vol. 18, no. 1, pp. 6765–6816, 2017.
- [20] S. Falkner, A. Klein, and F. Hutter, "BOHB: robust and efficient hyperparameter optimization at scale," *Proceedings of the 35th International Conference on Machine Learning*, vol. 80, pp. 1437–1446, 2018.
- [21] E. Hazan, A. Klivans, and Y. Yuan, "Hyperparameter optimization: A spectral approach," 2017, <https://arxiv.org/abs/1706.00764>.

- [22] T. Hinz, N. Navarro-Guerrero, S. Magg, and S. Wermter, "Speeding up the hyperparameter optimization of deep convolutional neural networks," *International Journal of Computational Intelligence and Applications*, vol. 17, no. 2, 2018.
- [23] X. Dong, J. Shen, W. Wang, L. Shao, H. Ling, and F. Porikli, "Dynamical hyperparameter optimization via deep reinforcement learning in tracking," *IEEE Transactions on Pattern Analysis and Machine Intelligence*, vol. 43, no. 5, pp. 1515–1529, 2021.
- [24] J. Wu, S. Chen, and X. Liu, "Efficient hyperparameter optimization through model-based reinforcement learning," *Neurocomputing*, vol. 409, pp. 381–393, 2020.
- [25] M. Rostami, K. Berahmand, E. Nasiri, and S. Forouzandeh, "Review of swarm intelligence-based feature selection methods," *Engineering Applications of Artificial Intelligence*, vol. 100, article 104210, 2020.
- [26] M. Yasen and N. Al-Madi, "Improved swarm intelligence optimization using crossover and mutation for medical classification," in *2019 2nd International Conference on new Trends in Computing Sciences (ICTCS)*, pp. 1–6, Amman, Jordan, 2019.
- [27] Y. Sun, B. Xue, M. Zhang, and G. G. Yen, "A particle swarm optimization-based flexible convolutional autoencoder for image classification," *IEEE Transactions on Neural Networks and Learning Systems*, vol. 30, no. 8, pp. 2295–2309, 2019.
- [28] A. H. Asad, E. El Amry, A. E. Hassanien, and M. F. Tolba, "New global update mechanism of ant colony system for retinal vessel segmentation," in *13th international conference on hybrid intelligent systems (HIS 2013)*, pp. 221–227, Gammarth, Tunisia, 2013.
- [29] G. Kavitha and S. Ramakrishnan, "Identification and analysis of macula in retinal images using ant colony optimization based hybrid method," in *2009 World Congress on Nature & Biologically Inspired Computing (NaBIC)*, pp. 1174–1177, Coimbatore, India, 2009.
- [30] U. Bhimavarapu and G. Battineni, "Automatic microaneurysms detection for early diagnosis of diabetic retinopathy using improved discrete particle swarm optimization," *Journal of Personalized Medicine*, vol. 12, no. 2, p. 317, 2022.
- [31] E. Byla and W. Pang, "Deepswarm: optimizing convolutional neural networks using swarm intelligence," in *UK Workshop on Computational Intelligence*, pp. 119–130, Springer, Cham, 2020.
- [32] F. Junior, F. Erivaldo, and G. Yen, "Particle swarm optimization of deep neural networks architectures for image classification," *Swarm and Evolutionary Computation*, vol. 49, no. 62–74, pp. 62–74, 2019.
- [33] M. Shaban, Z. Ogur, A. Mahmoud et al., "A convolutional neural network for the screening and staging of diabetic retinopathy," *PLoS One*, vol. 15, no. 6, article e0233514, 2020.
- [34] S. H. Kassani, P. H. Kassani, R. Khazaeinezhad, M. J. Wesolowski, K. A. Schneider, and R. Deters, "Diabetic retinopathy classification using a modified Xception architecture," in *2019 IEEE International Symposium on Signal Processing and Information Technology (ISSPIT)*, pp. 1–6, Ajman, United Arab Emirates, 2019.
- [35] S. Taufiqurrahman, A. Handayani, B. R. Hermanto, and T. L. E. R. Mengko, "Diabetic retinopathy classification using a hybrid and efficient MobileNetV2-SVM model," in *2020 IEEE Region 10 Conference (TENCON)*, pp. 235–240, Osaka, Japan, 2020.
- [36] J. Bodapati, N. Veeranjanyulu, S. Shareef et al., "Blended multi-modal deep ConvNet features for diabetic retinopathy severity prediction," *Electronics*, vol. 9, no. 6, p. 914, 2020.

Research Article

Boosted Sine Cosine Algorithm with Application to Medical Diagnosis

Xiaojia Ye ¹, Zhennao Cai ², Chenglang Lu ^{3,4}, Huiling Chen ^{2,4} and Zhifang Pan ^{3,4}

¹Shanghai Lixin University of Accounting and Finance, Shanghai 201209, China

²College of Computer Science and Artificial Intelligence, Wenzhou University, Wenzhou 325035, China

³College of Modern Information Technology, Zhejiang Institute of Mechanical and Electrical Engineering, Hangzhou, Zhejiang 310051, China

⁴The First Affiliated Hospital of Wenzhou Medical University, Wenzhou 325000, China

Correspondence should be addressed to Chenglang Lu; luchenglang@zime.edu.cn, Huiling Chen; chenhuiling.jlu@gmail.com, and Zhifang Pan; panzhifang@wmu.edu.cn

Received 24 April 2022; Revised 19 May 2022; Accepted 26 May 2022; Published 22 June 2022

Academic Editor: Pan Zheng

Copyright © 2022 Xiaojia Ye et al. This is an open access article distributed under the Creative Commons Attribution License, which permits unrestricted use, distribution, and reproduction in any medium, provided the original work is properly cited.

The sine cosine algorithm (SCA) was proposed for solving optimization tasks, of which the way to obtain the optimal solution is mainly through the continuous iteration of the sine and cosine update formulas. However, SCA also faces low population diversity and stagnation of locally optimal solutions. Hence, we try to eliminate these problems by proposing an enhanced version of SCA, named ESCA_PSO. ESCA_PSO is proposed based on hybrid SCA and particle swarm optimization (PSO) by incorporating multiple mutation strategies into the original SCA_PSO. To validate the effect of ESCA_PSO in handling global optimization problems, ESCA_PSO was compared with quality algorithms on various types of benchmark functions. In addition, the proposed ESCA_PSO was employed to tune the best parameters of support vector machines for dealing with medical diagnosis tasks. The results prove the efficiency of the proposed algorithms in solving optimization problems.

1. Introduction

1.1. Motivation. Many problems in real life can be summarized as global optimization problems. When it comes to increasingly complex optimization problems, traditional methods are generally unsatisfactory [1]. Therefore, many scholars began to explore new solutions. The metaheuristic algorithm (MA) is developed for obtaining and grasping information to effectively find approximately optimal solutions through learning strategies. MA has been applied to many scenarios owing to its effective optimization capability [2]. For example, MA has found the great potential in wind speed prediction [3], scheduling problem [4], parameter optimization [5], PID optimization control [6], gate resource allocation [7], fault diagnosis of rolling bearings [8], cloud workflow scheduling [9], energy vehicle dispatch [10], combination optimization problems [11], traveling salesman problem [12], object tracking [13], neural network training [14], and multiattribute decision making [15].

In 2016, a new swarm intelligence algorithm named sine cosine algorithm (SCA) [16] was proposed. SCA searches the solution based on the sine function and cosine function. It owns strong global searchability, which can significantly increase the global optimal solution through enough iterations. However, SCA also is faced with some problems, for instance, slow convergence speed, low convergence accuracy, and easily falling into local optimum. To overcome the problems existing in SCA, a hybrid SCA and PSO algorithm (SCA_PSO) was put forward by Nenavath et al. [17], which aims to solve optimization problems and target tracking. The search mechanism of the PSO algorithm is added to the traditional SCA to guide the search for potential candidate solutions. It should be noted that though the SCA_PSO has achieved promising results on object tracking when dealing with complex problems, it is still easy to skip the true optimal solution and lead to premature convergence.

According to “No Free Lunch” [18], we have introduced the differential evolution algorithm (DE) and combined

```

Input:  $MaxFEs, dim, ub, lb$ 
Output:  $best\_fitness$ 
While ( $t \leq MaxFEs$ )
  For each search agent
    Calculate fitness value
    If fitness value  $< SCA\_P_{best}$  in the iteration
      Move the current value to  $< SCA\_P_{best}$  matrix
    End if
    If Fitness value  $< SCA\_G_{best}$ 
      Set current value as  $< SCA\_G_{best}$ 
    End if
  End for
  For each search agent
    Update  $r_1, r_2, r_3, r_4$ 
    If  $r_4 < 0.5$ 
      Update X using Eq.(1)
    Else
      Update X using Eq.(2)
    End if
    Check and correct the new positions based on  $ub, lb$ 
  End for
  For each particle
    Initialize particle with  $PSO\_P_{best}$ 
    Set  $PSO\_G_{best}$  as  $SCA\_G_{best}$ 
  End for
  While ( $t \leq MaxFEs$ )
    For each particle
      Calculate fitness value
      If fitness value  $< PSO\_P_{best}$  in history
        Set current value as new  $PSO\_P_{best}$ 
      End if
    End for
    Choose the particle with the best fitness value of all the particle as the  $PSO\_G_{best}$ 
    For each particle
       $v_i^{t+1} = w^t + C_1 * rand * (SCA\_P_{best}^t - x_i^t) + C_2 * rand * (SCA\_G_{best}^t - x_i^t)$ 
       $x_i^{t+1} = x_i^t + v_i^{t+1}$ 
    End for
  End while
   $best\_fitness = PSO\_G_{best}$ 
  Return  $best\_fitness$ 

```

PSEUDOCODE 1: The pseudocode of the SCA_PSO.

mutation strategies into the original SCA_PSO to strengthen its capability of local search and reduce the occurrence of premature convergence. The proposed ESCA_PSO was validated on a benchmark test which includes various types of functions. Experimental results demonstrated that ESCA_PSO was significantly better than SCA_PSO and other competitive counterparts. In addition, the ESCA_PSO was also used to construct an optimal support vector machine model (SVM) to deal with the medical diagnosis problems in an effective manner. In general, ESCA_PSO has improved the performance of SCA_PSO in a significant manner.

1.2. Literature Review. SCA has been widely studied and applied in many fields because of its simple implementation and relatively excellent performance in realizing complex problems. For example, SCA was employed to tackle the

scheduling problem in [19]. A multiobjective SCA was proposed to solve engineering optimization problems in [20] and forecast the wind speed in [21]. SCA was employed to predict the time series by constructing an optimal support vector regression model in [22]. In [23], SCA was utilized to optimize the parameters of fuzzy k -nearest neighbor to build an optimized classifier for predicting the intention of students for a postgraduate entrance examination. In [24], SCA was applied to optimize the SVM's parameters and the boosted classifier was trained to predict students' entrepreneurial intentions.

In addition to applications, scholars have also proposed many improved SCA variants. Issa et al. [25] proposed a new idea of SCA, that is, the combination of SCA and PSO. This algorithm was used to solve the problem of pairwise local alignment to look for the longest continuous

```

Input: noP,MaxFEs, ub, lb, dim, fobj.
Output:  $SCA\_gbest$ ,  $cg\_curve$ .
While ( $t \leq \text{MaxFEs}$ )
  For each search agent
    Calculate fitness agent
    If fitness value <  $SCA\_P_{best}$  in this iteration
      Move the current value to  $SCA\_P_{best}$  matrix
    End if
    If Fitness value <  $SCA\_G_{best}$ 
      Set current value as  $SCA\_G_{best}$ 
    End if
  End for
  For each search agent
    Update  $r_1, r_2, r_3, r_4$ 
    If  $r_4 < 0.5$ 
      Update X using Eq.(1)
    Else
      Update X using Eq.(2)
    End if
    Check and correct the new positions based on  $ub, lb$ 
  End for
  For each particle
    Initialize particle with  $PSO\_P_{best}$ 
    Set  $PSO\_G_{best}$  as  $SCA\_G_{best}$ 
  End for
  Perform DE strategy
  While ( $t \leq \text{PSO\_MaxFEs}$ )
    For each particle
      Calculate fitness value
      If fitness value <  $PSO\_P_{best}$  in history
        Set current value as new  $PSO\_P_{best}$ 
      End if
    End for
    Choose the particle with the best fitness value of all the particle as the  $PSO\_G_{best}$ 
    For each particle
      Update  $v(k)$  with Eq. (9)
      Update  $v(k)$  with Eq. (10)
    End for
  End while
  Update  $X\_m\_Levy$  using Eq. (14)
  Update  $X\_m\_gaus$  using Eq. (12)
  Update  $X\_m\_cauchy$  using Eq. (13)
End while
Return  $SCA\_gbest$  and  $cg\_curve$ 

```

PSEUDOCODE 2: Pseudocode of the ESCA_PSO.

substring between two biological sequences, which has shown good performance in accuracy and calculation time. Nenavath and Jatoth [26] proposed to select the DE algorithm to merge into SCA and applied it to target tracking. Abd Elaziz et al. [27] mutated SCA (OBSCA) with opposition-based learning mechanisms, which has effectively boosted SCA's search efficiency and expanded its search scope. Qu et al. [28] improved the SCA by adding three strategies. Kumar et al. [29] tried to mix SCA with Cauchy and Gaussian distributions, which were named CGSCA. Simulations showed that the single-sensor tracking scheme based on CGSCA had better results in terms of

tracking time and tracking efficiency. Long et al. [30] combined SCA with inertia weight based on a position updating equation and a nonlinear conversion parameter strategy to ameliorate SCA's ability in solving high-dimensional problems. Tu et al. [24] proposed to adopt the chaotic local search enhanced SCA for training an optimal support vector machine to predict students' entrepreneurial intentions. Turgut [31] proposed that mixing SCA with a backtracking search algorithm (BSA) was an efficient way to realize the shell and tube evaporator's optimal design. With the proposed optimization method, the optimal values of the total design cost of the heat exchanger and the total heat transfer

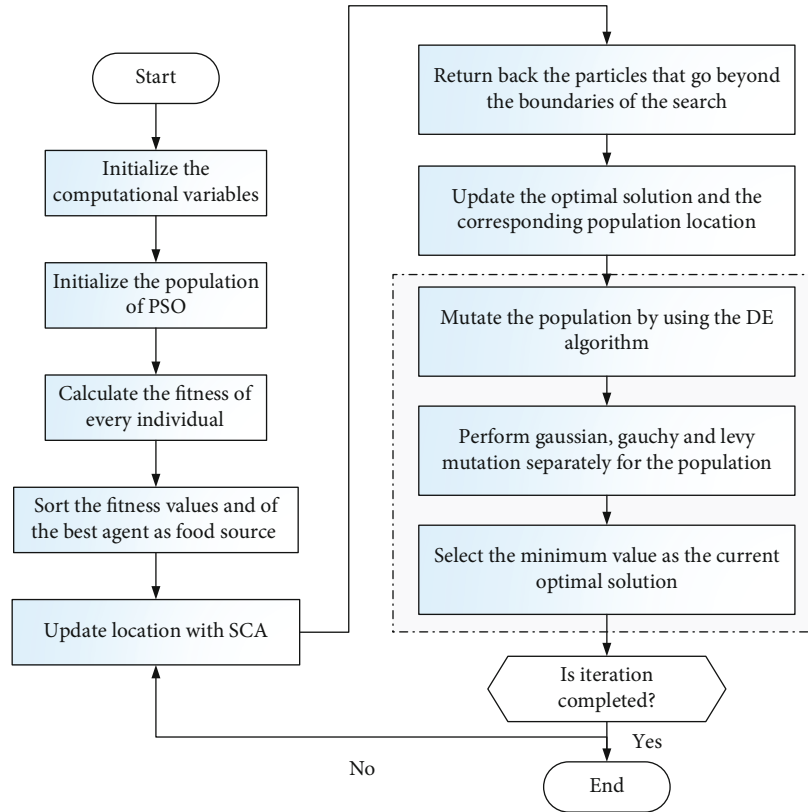


FIGURE 1: Flowchart of ESCA_PSO.

coefficient were better than the results of the other optimizers in the literature. Guo et al. [32] introduced the Riesz fractional derivative and the OBL strategy into SCA and applied the method to deal with the engineering problems. Gupta and Deep [33] proposed to add a leading guidance mechanism and simulated quenching algorithm together to SCA and applied it to train multilayer perceptron. Gupta and Deep [34] utilized the OBL strategy and the self-adaptive component to enhance the SCA. And this improved algorithm's efficacy was confirmed by lots of benchmark problems and engineering problems. Tawhid and Savsani [20] proposed a novel and effective multiobjective version of SCA (MO-SCA). The difference between MO-SCA and SCA is mainly reflected in two aspects, one is to improve the nondominated level by adding an elite nondominated sorting strategy, and the other is to maintain the diversity of optimal solutions by adding crowded distance method. At present, machine learning methods are still a research hotspot [35–42]. However, the hyperparameters of the model have a crucial impact on its performance. Therefore, combining the improved version of SCA with machine learning methods to obtain the best hyperparameter combination model is also a novel research angle.

1.3. Contribution and Paper Organization. The main contributions of this study are as follows:

(a) An improved SCA named ESCA_PSO is proposed

(b) The proposed ESCA_PSO has achieved superior performance to other peers on function optimization and machine learning tasks

(c) Successfully applied ESCA_PSO to SVM parameter optimization problem

(d) Successfully use ESCA_PSO-SVM in the field of medical diagnosis

The rest part of this paper is assigned as follows: The introduction of SCA and SCA-PSO is arranged in Section 2. Our proposed ESCA_PSO is presented in Section 3. The details information on experimental results and discussions are described in Section 4. Finally, in Section 5, conclusions and future works are summarized.

2. An Overview of SCA_PSO Algorithm

2.1. Standard SCA. In recent years, many new intelligent algorithms have been proposed to solve practical problems, such as hunger games search (HGS) [43], weighted mean of vectors (INFO) [44], Harris hawks optimization (HHO) [45], slime mould algorithm (SMA) [46], and Runge Kutta optimizer (RUN) [47]. These algorithms have shown great potential in various fields such as engineering, medicine, energy, finance, and education. In 2016, Mirjalili [16] put forward a novel swarm intelligence algorithm called SCA for global optimization tasks. Similar to other metaheuristics, it looks for the

TABLE 1: Description of 30 benchmark functions.

ID	Function equation	Range	Optimum value
Unimodal functions			
F1	Rotated high conditioned elliptic function	[-100, 100]	$f_1\{X_{\min}\} = 100$
F2	Rotated bent cigar function	[-100, 100]	$f_2\{X_{\min}\} = 200$
F3	Rotated discus function	[-100, 100]	$f_3\{X_{\min}\} = 300$
Simple multimodal functions			
F4	Shifted and rotated Rosenbrock's function	[-100, 100]	$f_4\{X_{\min}\} = 400$
F5	Shifted and rotated Ackley's function	[-100, 100]	$f_5\{X_{\min}\} = 500$
F6	Shifted and rotated Weierstrass function	[-100, 100]]	$f_6\{X_{\min}\} = 600$
F7	Shifted and rotated Griewank's function	[-100, 100]	$f_7\{X_{\min}\} = 700$
F8	Shifted Rastrigin's function	[-100, 100]	$f_8\{X_{\min}\} = 800$
F9	Shifted and rotated Rastrigin's function	[-100, 100]	$f_9\{X_{\min}\} = 900$
F10	Shifted Schwefel's function	[-100, 100]	$f_{10}\{X_{\min}\} = 1000$
F11	Shifted and rotated Schwefel's function	[-100, 100]	$f_{11}\{X_{\min}\} = 1100$
F12	Shifted and rotated Katsuura function	[-100, 100]	$f_{12}\{X_{\min}\} = 1200$
F13	Shifted and rotated HappyCat function	[-100, 100]	$f_{13}\{X_{\min}\} = 1300$
F14	Shifted and rotated HGBat function	[-100, 100]	$f_{14}\{X_{\min}\} = 1400$
F15	Shifted and rotated expanded Griewank's plus Rosenbrock's function	[-100, 100]	$f_{15}\{X_{\min}\} = 1500$
F16	Shifted and rotated expanded Scaffer's F6 function	[-100, 100]	$f_{16}\{X_{\min}\} = 1600$
Hybrid functions			
F17	Hybrid function 1 ($N = 3$)	[-100, 100]	$f_{15}\{X_{\min}\} = 1700$
F18	Hybrid function 2 ($N = 3$)	[-100, 100]	$f_{16}\{X_{\min}\} = 1800$
F19	Hybrid function 3 ($N = 4$)	[-100, 100]	$f_{17}\{X_{\min}\} = 1900$
F20	Hybrid function 4 ($N = 4$)	[-100, 100]	$f_{18}\{X_{\min}\} = 2000$
F21	Hybrid function 5 ($N = 5$)	[-100, 100]	$f_{19}\{X_{\min}\} = 2100$
F22	Hybrid function 6 ($N = 5$)	[-100, 100]	$f_{22}\{X_{\min}\} = 2200$
Composition functions			
F23	Composition function 1 ($N = 5$)	[-100, 100]	$f_{23}\{X_{\min}\} = 2300$
F24	Composition function 2 ($N = 3$)	[-100, 100]	$f_{24}\{X_{\min}\} = 2400$
F25	Composition function 3 ($N = 3$)	[-100, 100]	$f_{25}\{X_{\min}\} = 2500$
F26	Composition function 4 ($N = 5$)	[-100, 100]	$f_{26}\{X_{\min}\} = 2600$
F27	Composition function 5 ($N = 5$)	[-100, 100]	$f_{27}\{X_{\min}\} = 2700$
F28	Composition function 6 ($N = 5$)	[-100, 100]	$f_{28}\{X_{\min}\} = 2800$
F29	Composition function 7 ($N = 3$)	[-100, 100]	$f_{29}\{X_{\min}\} = 2900$
F30	Composition function 8 ($N = 3$)	[-100, 100]	$f_{30}\{X_{\min}\} = 3000$

solution in a random searching space. SCA obtains the optimal solution through triangle sine cosine functions [16].

The following location updating formulas are proposed for two phases:

$$X_i^{t+1} = X_i^t + r_1 \times \sin(r_2) \times |r_3 P_i^t - X_i^t|, \quad (1)$$

$$X_i^{t+1} = X_i^t + r_1 \times \cos(r_2) \times |r_3 P_i^t - X_i^t|, \quad (2)$$

where X_i^t is the position of the current solution in i -th

dimension at t -th iteration, r_1, r_2, r_3 are random numbers, P_i is the position of the target point in i -th dimension, and $||$ indicates absolute value.

Combining the above, the following equation can be obtained:

$$X_i^{t+1} = \begin{cases} X_i^t + r_1 \times \sin(r_2) \times |r_3 P_i^t - X_i^t|, & r_4 < 0.5, \\ X_i^t + r_1 \times \cos(r_2) \times |r_3 P_i^t - X_i^t|, & r_4 \geq 0.5, \end{cases} \quad (3)$$

where r_4 is a random number in the range $[0, 1]$.

TABLE 2: Parameters setting for involved algorithms.

Method	Parameter
ESCA_PSO	$a = 2; c_1 = 2; c_2 = 2; v_{\max} = 6$
SCADE	$\text{cmin} = 0.2; \text{cmax} = 0.8; \text{pCR} = 0.8$
SCA	$a = 2$
SCA-PSO	$M = 4; N = 9; v_{\max} = 6; w_{\max} = 0.9; w_{\min} = 0.2$
CGSCA	$\text{Delta} = 0.1$
GWO	$a = [0, 2]$
MFO	$b = 1; t = [-1, 1]; a = [-1, -2]$
BA	$a = 0.5; r = 0.5$
PSO	$c_1 = 2; c_2 = 2; v_{\max} = 6$
LSHADE	$\text{Pb} = 0.1; \text{Ar} = 1.4$

As the above formulae reveal, r_1, r_2, r_3 and r_4 are four important parameters with different meanings. The r_1 mainly decides whether the position of the next move is within the boundary range of solution and destination or outside the range. r_2 represents the distance required for the movement to reach the destination. The coefficient r_3 carries a random load for the destination to stochastically emphasize ($r_3 > 1$) or deemphasize ($r_3 < 1$) the effect of destination in describing the distance. r_4 switches from sine function to cosine function or vice versa in Eq. (3). The values of r_2 were set in $[0, 2\pi]$ in this study.

To achieve a steady global and local search, the range of sine and cosine functions in Eqs. (1)–(3) are altered adaptively according to the following formula:

$$r_1 = a - t \frac{a}{T}, \quad (4)$$

where t means the current iteration, T means the maximum number of iterations, and a is a constant with the value of 2.

2.2. SCA_PSO Algorithm. To eliminate the shortcoming of SCA, Nenavath et al. [17] came up with an improved hybrid SCA_PSO for dealing with optimization tasks. The SCA_PSO integrates PSO's strengths in exploitation and the SCA's strengths in exploration to approach the global optimal solution.

By adding internal storage to SCA, each individual is permitted to follow the coordinates associated with the adaptive values in the search space. And the personal historical best solution of each search agent in the present population is stored in the form of a matrix, $\text{SCA-}P_{\text{best}}$, which is the same as the concept of P_{best} in PSO each iteration. In addition, the solution also keeps track of the optimal value achieved so far by any nearby solution. As a new concept in SCA, P_{best} and G_{best} enhance the exploitation ability of SCA. The pseudocode of SCA_PSO is shown in Pseudocode 1.

3. Proposed ESCA_PSO

The improved ESCA_PSO is combined with two efficient strategies. Firstly, a DE with the "random variation" mode is

successfully combined with the SCA_PSO to strengthen the global search capability of the SCA_PSO. Then, a combined mutation with the mixed distributions of Gaussian, Cauchy, and Lévy was added to the combination mutation strategy, which can further improve the accuracy of the solution.

3.1. Combined Mutation of Gaussian, Cauchy, and Lévy. Gaussian distribution (GD) [48] is a significant probability distribution in many subjects such as engineering and mathematics. GD has many excellent features. Plenty of random variables and objects in nature can be presumably expressed as GD, and many probability distributions can be approximated or exported by this distribution. The probability density function of the GD can be expressed according to Eq. (5):

$$f(x) = \frac{1}{\sqrt{2\pi}\sigma} \exp\left(-\frac{(x-\mu)^2}{2\sigma^2}\right), \quad (5)$$

where μ and σ represent the mean and standard deviation, respectively.

Cauchy distribution [49] is also called Cauchy-Lorentz distribution. It is a continuous probability distribution named after Augustine-Louis-Cauchy and Hendrick-Lorentz. It is similar to normal distribution. Cauchy distribution is also widely used in statistics. It has the characteristics of the nonexistence of expectation and variance and additivity. The probability density function of the Cauchy distribution can be expressed according to Eq. (6):

$$f(x; x_0, \gamma) = \frac{1}{\pi} \left(\frac{\gamma}{(x-x_0)^2 + \gamma^2} \right), \quad (6)$$

where x_0 is the position parameter defining the location of the distribution peak; γ is the scale parameter defining half the width of the maximum half.

Lévy flights [50] based on Lévy distribution are consistent with the search behavior of many organisms in the nature and are widely used in optimization algorithms and optimal search processes. Moreover, the stochastic process can maximize the search efficiency of resources under uncertain conditions. In the search process, Lévy flights can make the whole search process more effective and stable, balancing the proportion of local search and global search. Due to the existence of the random process of the Lévy flight, the short-range exploratory local search and the occasional long-distance walk are in phase. Thus, the algorithm's local searching speed is faster, and the solutions are more easily searched near the current optimum. The decomposition can search far away from the current optimal value, thus ensuring that the algorithm does not fall into the local optimum (LO). The Lévy formula used is as follows:

$$\sigma = \left(\frac{\Gamma(1+\beta) \sin(\pi\beta/2)}{\Gamma[1+\beta/2]\beta 2^{\beta-1/2}} \right)^{(1/\beta)}, \quad (7)$$

where $\Gamma(x)$ is a continuation function of the factorial, that is, when the x is a positive integer $\Gamma(x+1) = x!$ The value

TABLE 3: Results of ESCA_PSO versus other algorithms on 30 benchmark functions.

	F1		F2		F3	
	Avg	Std	Avg	Std	Avg	Std
ESCA_PSO	8.77E+06	3.47E+06	7.49E+07	7.38E+06	9.44E+03	2.27E+03
SCADE	4.23E +08	9.19E+07	2.97E+10	4.56E+09	5.46E+04	6.21E+03
SCA	2.52E+08	7.02E+07	1.76E+10	2.68E+09	3.72E+04	5.71E+03
SCA_PSO	8.01E+06	2.83E+06	3.83E+07	8.40E+06	2.99E+03	1.04E+03
CGSCA	2.85E+08	8.98E+07	1.82E+10	4.06E+09	4.15E+04	5.63E+03
GWO	5.76E+07	4.69E+07	2.18E+09	2.05E+09	3.24E+04	8.29E+03
MFO	8.50E+07	1.06E+08	1.22E+10	7.01E+09	1.10E+05	6.34E+04
BA	7.40E+05	2.88E+05	5.24E+05	2.80E+05	4.11E+02	1.40E+02
PSO	9.30E+06	2.45E+06	1.46E+08	1.63E+07	9.60E+02	9.65E+01
LSHADE	4.41E+03	7.34E+03	2.00E+02	3.77E-14	3.00E+02	1.74E-11
	F4		F5		F6	
	Avg	Std	Avg	Std	Avg	Std
ESCA_PSO	4.73E+02	3.72E+01	5.21E+02	4.33E-02	6.29E+02	3.45E+00
SCADE	2.40E+03	5.90E+02	5.21E+02	3.58E-02	6.35E+02	1.86E+00
SCA	1.43E+03	2.20E+02	5.21E+02	4.98E-02	6.34E+02	2.32E+00
SCA_PSO	4.77E+02	4.19E+01	5.21E+02	6.37E-02	6.29E+02	3.03E+00
CGSCA	1.63E+03	2.92E+02	5.21E+02	5.14E-02	6.34E+02	2.33E+00
GWO	7.02E+02	2.37E+02	5.21E+02	5.08E-02	6.13E+02	2.06E+00
MFO	1.34E+03	8.51E+02	5.20E+02	1.59E-01	6.24E+02	3.73E+00
BA	4.40E+02	3.98E+01	5.21E+02	5.19E-02	6.34E+02	3.36E+00
PSO	4.68E+02	3.39E+01	5.21E+02	4.82E-02	6.23E+02	2.99E+00
LSHADE	4.04E+02	1.61E+01	5.20E+02	1.00E-03	6.11E+02	2.23E+00
	F7		F8		F9	
	Avg	Std	Avg	Std	Avg	Std
ESCA_PSO	7.02E+02	5.88E-02	9.83E+02	2.14E+01	1.13E+03	2.09E+01
SCADE	9.10E+02	3.53E+01	1.07E+03	1.63E+01	1.21E+03	1.63E+01
SCA	8.43E+02	2.36E+01	1.04E+03	2.05E+01	1.18E+03	1.64E+01
SCA_PSO	7.01E+02	7.70E-02	9.97E+02	3.65E+01	1.13E+03	3.53E+01
CGSCA	8.67E+02	2.74E+01	1.06E+03	1.61E+01	1.18E+03	1.59E+01
GWO	7.23E+02	1.75E+01	8.81E+02	1.77E+01	9.99E+02	2.43E+01
MFO	8.15E+02	7.39E+01	9.36E+02	2.91E+01	1.12E+03	5.57E+01
BA	7.01E+02	1.55E-01	1.03E+03	4.75E+01	1.20E+03	6.92E+01
PSO	7.02E+02	1.62E-01	9.71E+02	2.31E+01	1.12E+03	3.57E+01
LSHADE	7.00E+02	1.17E-02	8.00E+02	1.82E-01	9.36E+02	1.36E+01
	F10		F11		F12	
	Avg	Std	Avg	Std	Avg	Std
ESCA_PSO	4.71E+03	6.56E+02	5.69E+03	6.28E+02	1.20E+03	3.92E-01
SCADE	7.41E+03	3.71E+02	8.10E+03	3.58E+02	1.20E+03	2.15E-01
SCA	6.93E+03	4.80E+02	8.10E+03	3.38E+02	1.20E+03	2.81E-01
SCA_PSO	5.26E+03	7.19E+02	5.62E+03	7.81E+02	1.20E+03	3.01E-01
CGSCA	7.19E+03	3.88E+02	8.05E+03	3.20E+02	1.20E+03	2.86E-01
GWO	3.34E+03	4.08E+02	3.93E+03	4.80E+02	1.20E+03	8.77E-01
MFO	4.56E+03	9.40E+02	5.40E+03	8.30E+02	1.20E+03	2.55E-01
BA	5.16E+03	6.27E+02	5.43E+03	6.13E+02	1.20E+03	3.10E-01
PSO	4.97E+03	5.63E+02	5.70E+03	5.81E+02	1.20E+03	2.82E-01
LSHADE	1.00E+03	7.66E-01	2.91E+03	4.12E+02	1.20E +03	3.80E-02

TABLE 3: Continued.

	F13		F14		F15	
	Avg	Std	Avg	Std	Avg	Std
ESCA_PSO	1.30E+03	9.71E-02	1.40E+03	3.81E-02	1.52E+03	1.41E+00
SCADE	1.30E+03	3.33E-01	1.49E+03	1.18E+01	2.17E+04	7.85E+03
SCA	1.30E+03	3.27E-01	1.45E+03	8.31E+00	5.16E+03	3.72E+03
SCA_PSO	1.30E+03	6.25E-02	1.40E+03	4.86E-02	1.52E+03	1.49E+00
CGSCA	1.30E+03	3.16E-01	1.45E+03	1.06E+01	8.10E+03	5.63E+03
GWO	1.30E+03	3.97E-01	1.41E+03	7.06E+00	1.82E+03	8.98E+02
MFO	1.30E+03	1.45E+00	1.43E+03	2.16E+01	1.28E+05	3.08E+05
BA	1.30E+03	1.38E-01	1.40E+03	4.97E-02	1.53E+03	6.26E+00
PSO	1.30E+03	7.09E-02	1.40E+03	1.19E-01	1.52E+03	1.11E+00
LSHADE	1.30E+03	7.43E-02	1.40E+03	9.17E-02	1.51E+03	1.76E+00
	F16		F17		F18	
	Avg	Std	Avg	Std	Avg	Std
ESCA_PSO	1.61E+03	3.67E-01	4.35E+05	2.41E+05	1.93E+06	6.44E+05
SCADE	1.61E+03	2.26E-01	1.58E+07	5.49E+06	1.54E+08	9.16E+07
SCA	1.61E+03	2.37E-01	5.52E+06	2.43E+06	1.74E+08	7.49E+07
SCA_PSO	1.61E+03	4.47E-01	1.79E+05	1.09E+05	7.62E+05	4.43E+05
CGSCA	1.61E+03	2.29E-01	6.77E +06	3.75E+06	1.43E+08	7.47E+07
GWO	1.61E+03	7.29E-01	1.49E+06	1.54E+06	2.88E+06	1.02E+07
MFO	1.61E+03	4.74E-01	2.40E+06	3.10E+06	2.64E+07	9.98E+07
BA	1.61E+03	2.59E-01	1.09E+05	8.01E+04	9.42E+04	4.63E+04
PSO	1.61E+03	5.31E-01	2.76E+05	1.21E+05	2.19E+06	7.43E+05
LSHADE	1.61E+03	3.85E-01	1.49E+04	6.33E+04	1.95E+03	5.46E+01
	F19		F20		F21	
	Avg	Std	Avg	Std	Avg	Std
ESCA_PSO	1.92E+03	2.29E+00	3.81E+03	1.57E+03	1.29E+05	1.10E+05
SCADE	2.02E+03	1.98E+01	2.52E+04	1.06E+04	2.18E+06	1.12E+06
SCA	1.99E+03	2.80E+01	1.56E+04	3.39E+03	1.23E+06	6.00E+05
SCA_PSO	1.92E+03	2.72E+00	2.47E+03	2.22E+02	9.35E+04	4.63E+04
CGSCA	1.99E+03	1.65E+01	1.88E+04	5.54E+03	1.67E+06	7.22E+05
GWO	1.94E+03	2.47E+01	1.97E+04	1.35E+04	6.56E+05	1.16E+06
MFO	1.96E+03	4.95E+01	7.19E+04	8.18E+04	8.20E+05	1.10E+06
BA	1.92E+03	1.83E+01	2.36E+03	1.13E+02	5.26E +04	3.10E+04
PSO	1.92E+03	2.43E+00	2.32E+03	7.07E+01	1.17E+05	6.92E+04
LSHADE	1.91E+03	1.84E+00	3.11E+03	3.51E+03	2.78E+03	2.77E+02
	F22		F23		F24	
	Avg	Std	Avg	Std	Avg	Std
ESCA_PSO	2.97E+03	2.43E+02	2.50E+03	0.00E+00	2.60E+03	0.00E+00
SCADE	3.11E+03	1.85E+02	2.50E+03	0.00E+00	2.60E+03	5.15E-06
SCA	2.99E+03	1.42E+02	2.67E+03	1.07E+01	2.60E+03	1.00E-01
SCA_PSO	3.17E+03	2.89E+02	2.50E+03	0.00E+00	2.60E+03	0.00E+00
CGSCA	3.07E+03	1.26E+02	2.50E+03	0.00E+00	2.60E+03	3.55E-06
GWO	2.59E+03	1.83E+02	2.63E+03	9.77E+00	2.60E+03	9.56E-04
MFO	3.12E+03	2.90E+02	2.66E+03	2.48E+01	2.68E+03	2.64E+01
BA	3.33E+03	3.17E+02	2.62E+03	3.12E-03	2.67E+03	3.46E+01
PSO	2.90E+03	2.61E+02	2.62E+03	7.09E-01	2.63E+03	5.18E+00
LSHADE	2.43E+03	9.48E+01	2.62E+03	1.88E-12	2.64E+03	6.32E+00

TABLE 3: Continued.

	F25		F26		F27	
	Avg	Std	Avg	Std	Avg	Std
ESCA_PSO	2.70E+03	0.00E+00	2.70E+03	1.27E-01	2.90E+03	0.00E+00
SCADE	2.70E+03	0.00E+00	2.70E+03	4.66E-01	3.20E+03	2.10E+02
SCA	2.73E+03	8.20E+00	2.70E+03	5.56E-01	3.57E+03	3.51E+02
SCA_PSO	2.70E+03	0.00E+00	2.77E+03	4.48E+01	2.90E+03	0.00E+00
CGSCA	2.70E+03	0.00E+00	2.70E+03	3.72E-01	2.90E+03	0.00E+00
GWO	2.71E+03	3.94E+00	2.74E+03	6.01E+01	3.32E+03	1.24E+02
MFO	2.72E+03	8.77E+00	2.70E+03	1.42E+00	3.66E+03	1.76E+02
BA	2.73E+03	1.44E+01	2.70E+03	1.35E-01	3.91E+03	4.20E+02
PSO	2.71E+03	5.98E+00	2.78E+03	4.07E+01	3.39E+03	2.97E+02
LSHADE	2.71E+03	3.23E+00	2.71E+03	3.04E+01	3.25E+03	9.56E+01
	F28		F29		F30	
	Avg	Std	Avg	Std	Avg	Std
ESCA_PSO	3.00E+03	0.00E+00	3.19E+03	8.63E+01	3.88E+03	6.83E+02
SCADE	4.96E+03	9.21E+02	1.91E+07	1.01E+07	4.90E+05	1.70E+05
SCA	4.84E+03	2.97E+02	1.37E+07	7.32E+06	2.39E+05	7.38E+04
SCA_PSO	3.00E+03	0.00E+00	1.26E+04	3.99E+04	1.53E+04	1.08E+04
CGSCA	3.00E+03	0.00E+00	3.10E+03	0.00E+00	3.20E+03	0.00E+00
GWO	3.84E+03	2.03E+02	6.26E+05	2.36E+06	4.88E+04	4.04E+04
MFO	3.98E+03	2.29E+02	3.06E+06	3.58E+06	5.65E+04	4.66E+04
BA	5.29E+03	6.59E+02	3.13E+07	3.38E+07	1.30E+04	1.23E+04
PSO	7.32E+03	8.69E+02	9.61E+04	1.83E+05	1.44E+04	7.29E+03
LSHADE	3.73E+03	7.27E+01	3.68E+03	4.12E+01	5.47E+03	1.26E+03

of the variable β determines the shape of the Lévy probability density function, especially in the tail area.

$$\gamma = \frac{\mu}{|v|^{1/\beta}}, \quad (8)$$

where γ is the flight step, v , is the standard normal distribution, and μ is a normal distribution with the mean of 0 and the variance of σ^2 .

3.2. Combined Mutation Strategy. As mentioned in the foregoing, the DE algorithm can enhance the global search capability of SCA_PSO, while mutation of Gaussian, Cauchy, and Lévy is algorithms that can make the algorithm perform better in local search. A combined mutation strategy was proposed in this study, which combined the different characteristics of the three mutation strategies, making the SCA_PSO find a more balanced manner in performing explorative search and exploitative search. The whole algorithm steps are as shown below:

Step 1. Search using the mentioned SCA.

Step 2. Mutate the SCA_PSO by the DE algorithm and the new individual will be retained if its fitness value is better than the original one.

Step 3. Update using the formula of SCA_PSO. The update formula used is as follows:

$$v(k) = w \cdot v(k) + c1 \cdot r2 \cdot (pbest - x_i^k) + c2 \cdot r3 \cdot \left(SCA_{G_{best,i}^k} \right), \quad (9)$$

$$x_i^k = x_i^k + v(k), \quad (10)$$

where $c1$, $c2=2 \cdot r2$, and $r3$ are in the range of $[0, 1]$.

Step 4. Use combined mutation of Gaussian, Cauchy, and Lévy to mutate the current optimal individuals, find the individuals with the smallest of the three results, and update the fitness values and corresponding individuals.

$$X = \min \{X_{m_Levy}, X_{m_gaus}, X_{m_cauchy}\}, \quad (11)$$

$$X_{m_gaus} = X_i^t \cdot (1 + k \cdot \text{randn}), \quad (12)$$

$$X_{m_cauchy} = X_i^t \cdot (1 + k \cdot \text{cauchy}), \quad (13)$$

$$X_{m_Levy} = X_i^t \cdot (1 + k \cdot \text{Levy}(1)), \quad (14)$$

where $X_{m_Lévy}$, X_{m_gaus} , and X_{m_cauchy} are the values obtained by the Lévy, Gaussian, and Cauchy strategies, respectively.

TABLE 4: The p value of ESCA_PSO compared with other algorithms.

(a)

F	ESCA_PSO	SCADE		SCA		SCA_PSO		CGSCA		GWO	
F1	N/A	1.73E-06	+	1.73E-06	+	2.80E-01		1.73E-06	+	2.88E-06	+
F2	N/A	1.73E-06	+	1.73E-06	+	1.73E-06	—	1.73E-06	+	1.73E-06	+
F3	N/A	1.73E-06	+	1.73E-06	+	1.92E-06	—	1.73E-06	+	1.73E-06	+
F4	N/A	1.73E-06	+	1.73E-06	+	8.77E-01		1.73E-06	+	1.92E-06	+
F5	N/A	1.78E-01		1.25E-02	—	6.27E-02		1.48E-02	—	1.59E-01	
F6	N/A	3.52E-06	+	1.02E-05	+	4.53E-01		1.24E-05	+	1.73E-06	—
F7	N/A	1.73E-06	+	1.73E-06	+	1.73E-06	—	1.73E-06	+	1.73E-06	+
F8	N/A	1.73E-06	+	1.92E-06	+	1.53E-01		1.73E-06	+	1.73E-06	—
F9	N/A	1.73E-06	+	2.35E-06	+	5.30E-01		1.73E-06	+	1.73E-06	—
F10	N/A	1.73E-06	+	1.73E-06	+	9.84E-03	+	1.73E-06	+	1.73E-06	—
F11	N/A	1.73E-06	+	1.73E-06	+	6.88E-01		1.73E-06	+	1.73E-06	—
F12	N/A	2.37E-05	+	2.58E-03	+	8.94E-01		4.53E-04	+	3.18E-01	
F13	N/A	1.73E-06	+	1.73E-06	+	4.99E-03	—	1.73E-06	+	2.43E-02	—
F14	N/A	1.73E-06	+	1.73E-06	+	2.70E-02	—	1.73E-06	+	5.22E-06	+
F15	N/A	1.73E-06	+	1.73E-06	+	5.44E-01		1.73E-06	+	4.86E-05	+
F16	N/A	3.88E-06	+	1.73E-06	+	1.96E-03	+	1.92E-06	+	2.88E-06	—
F17	N/A	1.73E-06	+	1.73E-06	+	1.48E-04	—	1.73E-06	+	7.71E-04	+
F18	N/A	1.73E-06	+	1.73E-06	+	2.35E-06	—	1.73E-06	+	2.07E-02	+
F19	N/A	1.73E-06	+	1.73E-06	+	7.97E-01		1.73E-06	+	1.74E-04	+
F20	N/A	1.73E-06	+	1.73E-06	+	1.92E-06	—	1.73E-06	+	2.88E-06	+
F21	N/A	1.73E-06	+	1.73E-06	+	7.19E-02		1.73E-06	+	1.15E-04	+
F22	N/A	6.42E-03	+	3.18E-01		4.11E-03	+	1.36E-01		7.69E-06	—
F23	N/A	1.00E+00		1.73E-06	+	1.00E+00		1.00E+00		1.73E-06	+
F24	N/A	1.56E-02	+	1.73E-06	+	1.00E+00		2.44E-04	+	1.73E-06	+
F25	N/A	1.00E+00		1.73E-06	+	1.00E+00		1.00E+00		3.79E-06	+
F26	N/A	1.73E-06	+	1.73E-06	+	1.64E-05	+	1.73E-06	+	4.68E-03	+
F27	N/A	5.96E-05	+	1.73E-06	+	1.00E+00		1.00E+00		1.73E-06	+
F28	N/A	1.23E-05	+	1.73E-06	+	1.00E+00		1.00E+00		1.73E-06	+
F29	N/A	1.73E-06	+	1.73E-06	+	5.11E-03	+	5.61E-06	—	1.73E-06	+
F30	N/A	1.73E-06	+	1.73E-06	+	6.75E-05	+	1.32E-04	—	1.73E-06	+
+/-/=	/	27/0/3		28/1/1		6/8/10		22/3/5		20/8/2	
Avg	2	10		9		3		7		5	

(b)

F	MFO		BA		PSO		LSHADE	
F1	3.18E-06	+	1.73E-06	—	2.99E-01		1.73E-06	—
F2	1.73E-06	+	1.73E-06	—	1.73E-06	+	1.73E-06	—
F3	1.73E-06	+	1.73E-06	—	1.73E-06	—	1.73E-06	—
F4	1.73E-06	+	1.57E-02	—	9.75E-01		1.73E-06	—
F5	1.73E-06	—	8.45E-01		1.53E-01		1.73E-06	—
F6	1.15E-04	—	3.06E-04	+	7.69E-06	—	1.73E-06	—
F7	1.73E-06	+	1.73E-06	—	1.73E-06	+	1.73E-06	—
F8	1.64E-05	—	2.83E-04	+	5.45E-02		1.73E-06	—
F9	2.21E-01		7.51E-05	+	2.80E-01		1.73E-06	—
F10	4.53E-01		4.68E-03	+	1.85E-01		1.73E-06	—
F11	1.92E-01		1.11E-01		9.26E-01		1.73E-06	—

TABLE 4: Continued.

F	MFO		BA		PSO		LSHADE	
F12	1.73E-06	—	1.73E-06	—	4.20E-04	+	1.73E-06	—
F13	1.73E-06	+	6.56E-02		7.16E-04	—	1.80E-05	—
F14	1.73E-06	+	1.64E-05	+	1.48E-02	+	8.19E-05	+
F15	1.73E-06	+	1.92E-06	+	5.32E-03	—	1.73E-06	—
F16	4.29E-06	+	1.73E-06	+	5.30E-01		1.73E-06	—
F17	2.41E-03	+	2.88E-06	—	2.41E-03	—	2.13E-06	—
F18	3.59E-04	+	1.73E-06	—	1.85E-01		1.73E-06	—
F19	2.05E-04	+	6.87E-02		5.45E-02		1.73E-06	—
F20	1.73E-06	+	1.92E-06	—	1.92E-06	—	3.59E-04	—
F21	1.36E-04	+	2.84E-05	—	7.19E-01		1.73E-06	—
F22	4.72E-02	+	1.15E-04	+	2.21E-01		1.73E-06	—
F23	1.73E-06	+	1.73E-06	+	1.73E-06	+	4.32E-08	+
F24	1.73E-06	+	1.73E-06	+	1.73E-06	+	1.73E-06	+
F25	1.73E-06	+	1.73E-06	+	1.73E-06	+	1.73E-06	+
F26	1.73E-06	+	7.52E-02		1.24E-05	+	1.02E-01	
F27	1.73E-06	+	1.73E-06	+	1.73E-06	+	1.73E-06	+
F28	1.73E-06	+	1.73E-06	+	1.73E-06	+	1.73E-06	+
F29	1.73E-06	+	1.73E-06	+	8.73E-03	+	1.73E-06	+
F30	1.73E-06	+	1.73E-06	+	1.73E-06	+	4.29E-06	+
+/-/=	23/4/3		15/10/5		12/6/12		8/21/1	
Avg	8		6		4		1	

Pseudocode 2 and Figure 1 display the detailed steps and flowchart of ESCA_PSO, respectively.

First of all, the current optimal individual $SCA_{G_{best}}$ is obtained by SCA. Then, the particle swarm population is initialized with the help of $SCA_{G_{best}}$ and mutated with the help of DE strategy. Next, the population is updated using ESCA_PSO. Finally, it is updated by Gaussian, Cauchy, and Lévy flight strategies.

3.3. Complexity Analysis. The time complexity of the ESCA_PSO is mainly related to the number of four factors, which are algorithm iterations (T), PSO's iterations (P), population (N), and dimensions (D). And the whole time complexity is analyzed as follows: $O(\text{ESCA_PSO}) = O(\text{initialize}) + T \times (O(\text{calculate the fitness of population}) + O(\text{update location with SCA}) + P \times (O(\text{calculate the fitness of population}) + O(\text{update location with PSO})) + O(\text{perform combined mutation strategy}))$. The time complexity of initialization is $O(N \times D)$. Since there are N individuals, the fitness of the initial populations is $O(N)$. Updating location with SCA is $O(N)$. Updating location with PSO is $O(N \times D)$. Performing the combined mutation strategy is $O(N)$. All in all, it is not difficult to conclude that the total time complexity of ESCA_PSO is $O(\text{ESCA_PSO}) = O(N \times D) + T \times (O(N) + O(N) + P \times (O(N) + O(N \times D))) + O(N) = O(N \times D) + T \times (2O(N) + P \times (O(N) + O(N \times D))) + O(N)$.

4. Experimental Results

To confirm the effectiveness of ESCA_PSO, the proposed ESCA_PSO is compared with other competitive metaheuristic

algorithms on 30 functions of CEC2014 in this part. And then ESCA_PSO carries on the variation mechanism contrast experiment. Finally, ESCA_PSO is used for tuning SVM's parameters for medical diagnosis purposes.

4.1. Benchmark Functions. This experiment used 30 classical functions to substantiate the proposed method and other competitors. These functions include unimodal, multimodal, composition, and hybrid functions. F1-F3 are unimodal functions, F4-F16 are multimodal functions, and F17-F22 are hybrid functions. F23-F30 are composition functions, which are selected from CEC2014. These 30 different benchmark functions can comprehensively estimate the performance of the ESCA_PSO. The related descriptions are demonstrated in Table 1, where range means the boundary of the search space for the relevant functions. As we all know, a unimodal function corresponds to a globally optimal solution; so, it can be employed to benchmark development capability. Conversely, the multimodal function possesses a lot of LO solutions, which leads to the algorithm falling into LO. Such functions can test the capability of the method to refrain from stagnation and exploration ability. Moreover, both the hybrid function and multimodal function only have one global optimum but multiple LO solutions. The structures of composition functions are more complex.

All the algorithms in the following experiments are coded on MATLAB 2014b. And to be fair, the experimental verification is carried out under the unified condition, i.e., the population size is set to 30, the maximum evaluation

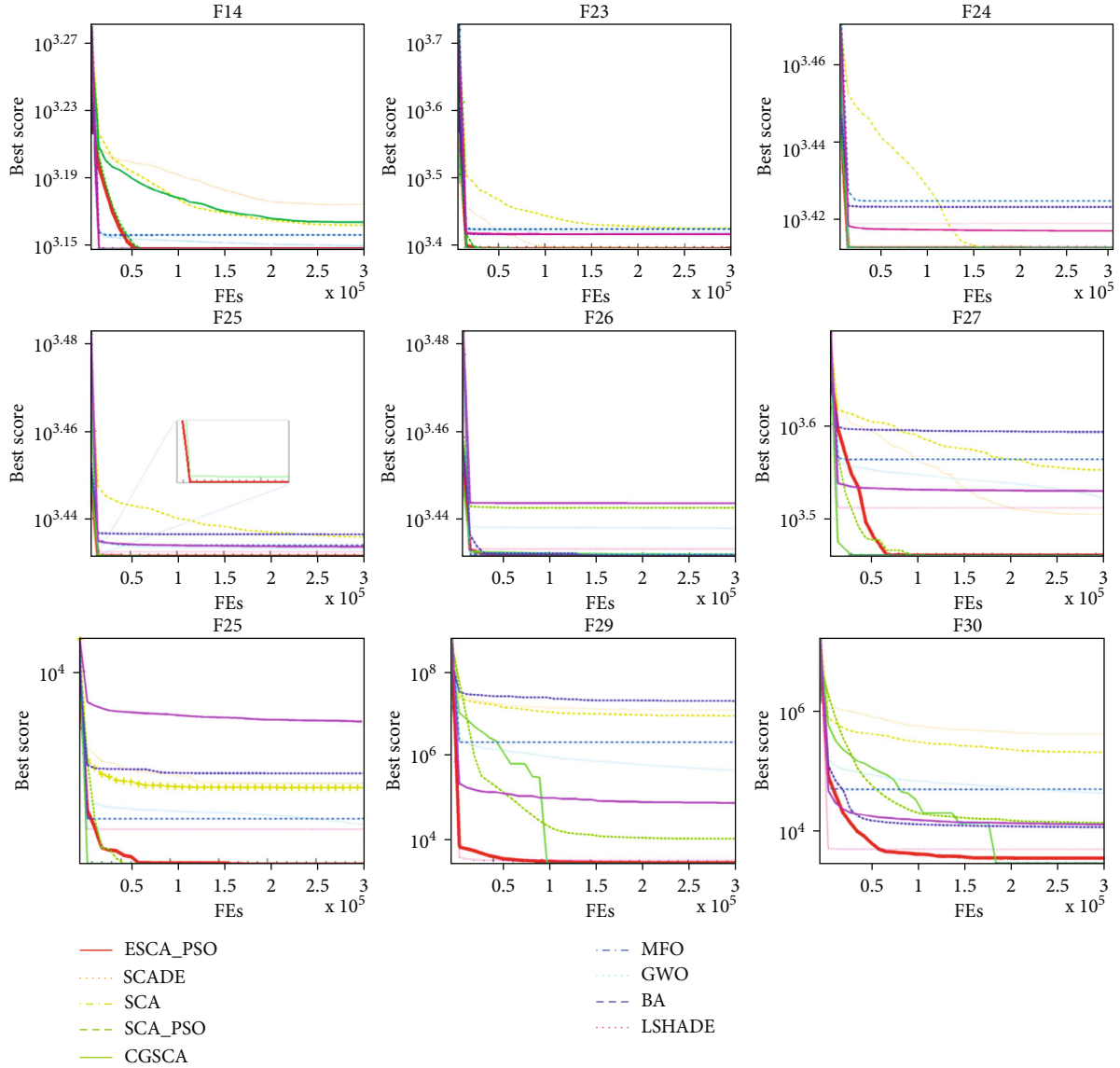


FIGURE 2: Convergence curves of ESCA_PSO and other algorithms on 9 selected benchmark functions.

time is set to 300000, the dimension is set to 30, and the number of runs is set to 30.

4.2. Comparison with Other Algorithms. In this experiment, the ESCA_PSO was contrasted to SCA, GWO [51], MFO [52], BA [53], and PSO [54] on the functions presented in Table 1. To further validate the effect of the proposed ESCA_PSO, two improved SCA variants including SCA_PSO and SCADE [26] were involved for comparison and compare with LSHADE [55] which is the champion algorithm of CEC2014. The parameter configuration of algorithms is shown in Table 2. The detailed comparison results including the average value (Avg) of the best solution and standard deviation (Std) of every approach in 30 independent runs are displayed in Table 3.

We can see that the advantages of ESCA_PSO are not very obvious in the unimodal functions and multimodal

functions. In these functions, ESCA_PSO is slightly better than the original algorithm SCA and its variants CGSCA and SCADE. But compared with high-quality algorithms such as LSHADE, there is still a certain gap. However, ESCA_PSO has a very good performance in the complex structure of the composition functions. Compared with other algorithms on F23-F30, it ranks first or second.

By the Friedman test, we can get the average ranking of test algorithms, which is usually used to get the difference between many test results. At the same time, to further analyze the experimental structure, Wilcoxon signed-rank test was adopted for statistical work.

In Table 4, all experimental results were taken from those two tests mentioned above. AVG in the table represents the average ranking of algorithms obtained by the Friedman test, and “+/-/=” represents the performance of the function compared with ESCA_PSO. Specifically, “+”

TABLE 5: Results of mutation mechanism comparison experiment.

	F1		F2		F3	
	Avg	Stdv	Avg	Stdv	Avg	Stdv
ESCA_PSO	1.0121E+07	4.1281E+06	7.2870E+07	6.7257E+06	9.0781E+03	1.6748E+03
ESCA_PSO1	1.0956E+07	6.3712E+06	7.5147E+07	7.5579E+06	9.4351E+03	2.5065E+03
ESCA_PSO2	8.8248E+06	4.3297E+06	7.5579E+07	6.4189E+06	8.9495E+03	2.0387E+03
ESCA_PSO3	8.9362E+06	3.2913E+06	7.6554E+07	5.5330E+06	8.2034E+03	2.8244E+03
	F4		F5		F6	
	Avg	Stdv	Avg	Stdv	Avg	Stdv
ESCA_PSO	4.7228E+02	4.7567E+01	5.2095E+02	7.3218E-02	6.2832E+02	3.6455E+00
ESCA_PSO1	4.8246E+02	4.3094E+01	5.2093E+02	5.9358E-02	6.2994E+02	3.6753E+00
ESCA_PSO2	4.8304E+02	3.1844E+01	5.2095E+02	4.0250E-02	6.2907E+02	2.8954E+00
ESCA_PSO3	4.6323E+02	3.5952E+01	5.2094E+02	6.0599E-02	6.2602E+02	3.6698E+00
	F7		F8		F9	
	Avg	Stdv	Avg	Stdv	Avg	Stdv
ESCA_PSO	7.0165E+02	6.6719E-02	9.7250E+02	1.7061E+01	1.1273E+03	2.1663E+01
ESCA_PSO1	7.0165E+02	5.8391E-02	9.7622E+02	2.0619E+01	1.1213E+03	2.3921E+01
ESCA_PSO2	7.0164E+02	4.8112E-02	9.7878E+02	1.5477E+01	1.1222E+03	2.4011E+01
ESCA_PSO3	7.0163E+02	6.2317E-02	9.5729E+02	1.6848E+01	1.1358E+03	3.5018E+01
	F10		F11		F12	
	Avg	Stdv	Avg	Stdv	Avg	Stdv
ESCA_PSO	4.9137E+03	7.2648E+02	5.6985E+03	5.0594E+02	1.2023E+03	3.2946E-01
ESCA_PSO1	4.9133E+03	6.5258E+02	5.6409E+03	7.1573E+02	1.2023E+03	2.7883E-01
ESCA_PSO2	4.9278E+03	6.4952E+02	5.6196E+03	5.2887E+02	1.2023E+03	2.8632E-01
ESCA_PSO3	3.9106E+03	7.0806E+02	5.7900E+03	6.4145E+02	1.2025E+03	1.9371E-01
	F13		F14		F15	
	Avg	Stdv	Avg	Stdv	Avg	Stdv
ESCA_PSO	1.3005E+03	8.0129E-02	1.4003E+03	5.5878E-02	1.5178E+03	1.8461E+00
ESCA_PSO1	1.3004E+03	6.5982E-02	1.4002E+03	3.9799E-02	1.5176E+03	1.4145E+00
ESCA_PSO2	1.3005E+03	1.3432E-01	1.4003E+03	5.0665E-02	1.5173E+03	1.5482E+00
ESCA_PSO3	1.3004E+03	9.2885E-02	1.4003E+03	1.0046E-01	1.5168E+03	1.2616E+00
	F16		F17		F18	
	Avg	Stdv	Avg	Stdv	Avg	Stdv
ESCA_PSO	1.6119E+03	3.7281E-01	3.5341E+05	1.5577E+05	1.9265E+06	5.4288E+05
ESCA_PSO1	1.6121E+03	2.7974E-01	4.7094E+05	5.3309E+05	1.9803E+06	5.1404E+05
ESCA_PSO2	1.6120E+03	3.9442E-01	4.2443E+05	3.0521E+05	2.1497E+06	4.0650E+05
ESCA_PSO3	1.6117E+03	3.5803E-01	4.4610E+05	3.0212E+05	1.7955E+06	4.8630E+05
	F19		F20		F21	
	Avg	Stdv	Avg	Stdv	Avg	Stdv
ESCA_PSO	1.9176E+03	2.6584E+00	4.6963E+03	2.1120E+03	1.5933E+05	1.2738E+05
ESCA_PSO1	1.9195E+03	1.1064E+01	4.8166E+03	2.4521E+03	1.6422E+05	1.1183E+05
ESCA_PSO2	1.9182E+03	2.6893E+00	4.2130E+03	1.8120E+03	1.7741E+05	1.5670E+05
ESCA_PSO3	1.9210E+03	1.6909E+01	2.5728E+03	3.9978E+02	1.2953E+05	9.6487E+04

TABLE 5: Continued.

	F22		F23		F24	
	Avg	Stdv	Avg	Stdv	Avg	Stdv
ESCA_PSO	3.0075E+03	2.5470E+02	2.5000E+03	0.0000E+00	2.6000E+03	0.0000E+00
ESCA_PSO1	3.0277E+03	1.8557E+02	2.5000E+03	0.0000E+00	2.6000E+03	0.0000E+00
ESCA_PSO2	2.9865E+03	2.5463E+02	2.5000E+03	0.0000E+00	2.6000E+03	0.0000E+00
ESCA_PSO3	2.8237E+03	2.0355E+02	2.5942E+03	4.7914E+01	2.6000E+03	3.1173E-04
	F25		F26		F27	
	Avg	Stdv	Avg	Stdv	Avg	Stdv
ESCA_PSO	2.7000E+03	0.0000E+00	2.7004E+03	7.7168E-02	2.9000E+03	0.0000E+00
ESCA_PSO1	2.7000E+03	0.0000E+00	2.7004E+03	9.2230E-02	2.9000E+03	0.0000E+00
ESCA_PSO2	2.7000E+03	0.0000E+00	2.7137E+03	3.4412E+01	2.9000E+03	0.0000E+00
ESCA_PSO3	2.7000E+03	0.0000E+00	2.7004E+03	7.1707E-02	3.4906E+03	3.4856E+02
	F28		F29		F30	
	Avg	Stdv	Avg	Stdv	Avg	Stdv
ESCA_PSO	3.0000E+03	0.0000E+00	3.1619E+03	5.6888E+01	3.7103E+03	6.0049E+02
ESCA_PSO1	3.0000E+03	0.0000E+00	3.4574E+03	4.0471E+02	5.0126E+03	1.8702E+03
ESCA_PSO2	3.0000E+03	0.0000E+00	7.4310E+04	2.6321E+05	1.1615E+04	8.8958E+03
ESCA_PSO3	3.9181E+03	8.8744E+02	3.1047E+03	4.4337E+00	3.2472E+03	4.9782E+01

means ESCA_PSO is better than this algorithm, “-” indicates that ESCA_PSO is inferior to this algorithm, and “=” means that the performance is similar to ESCA_PSO. In Wilcoxon signed-rank test, when the p value is less than 0.05, the performance between the two algorithms is significant. It was also used to evaluate the significance of ESCA_PSO versus other approaches. It can see from the table that ESCA ranks second on average, which is better than other algorithms overall. Compared with SCA, SCADE, CGSCA, GWO, and MFO, it is significantly better than 20 functions. However, it is indeed weaker than the champion algorithm LSHADE on multimodal functions and unimodal functions.

Figure 2 shows nine graphs of convergence we selected. As shown in Figure 2, it can be seen that ESCA_PSO does have a good convergence rate on these functions. It quickly converges to a lower point. And ESCA_PSO has a significant improvement over than original SCA. Of course, it is undeniable that some algorithms converge faster than ESCA_PSO, but ESCA_PSO has higher quality solutions.

Despite the great potential of the proposed ESCA_PSO, the approach of sacrificing a certain time complexity in exchange for an increase in terms of accuracy is insufficient side. Nevertheless, the algorithm is still competitive with LSHADE in unimodal and multimodal functions.

4.3. Comparison of Mutation Mechanism. As mentioned earlier, three mutation mechanisms were added to ESCA_PSO. To further analyze ESCA_PSO, we conducted comparative experiments on the mutation mechanism of ESCA in this section.

To compare the mutation mechanism, we construct three algorithms, namely, ESCA_PSO1, ESCA_PSO2, and

ESCA_PSO3. Compared with ESCA_PSO, ESCA_PSO1 only uses Gaussian mutation while others remain unchanged. By analogy, ESCA_PSO2 only uses the Cauchy mutation while ESCA_PSO3 only uses the Lévy mutation. The population dimension and the total number of iterations of this experiment are the same as those in the previous experiment settings.

The results obtained from the experiments are shown in Table 5, and there is not much difference between these four algorithms, which can be concluded by comparing the whole data. This is because most of the four algorithms are the same, and only the mutation mechanism has changed. From the numerical value obtained from the experiment, ESCA_PSO has not achieved the best results in functions many times. But relatively, ESCA_PSO is rarely ranked last. This is also because ESCA_PSO integrates three mutation mechanisms, which makes it applicable to more functions.

Figure 3 shows several convergence graphs in this experiment. From the figure, we can see that in F2, F17, and F19, the convergence curves of the four algorithms are relatively similar, and there is no big difference in general. In F27 and F28, the performance of ESCA_PSO3 is not as good as the other three algorithms. In F29 and F30, ESCA_PSO2 is quite different from the other three algorithms. However, ESCA_PSO can keep a good level in these functions. This shows that the combination of three different mutation mechanisms can help the algorithm adapt to more functions.

However, ESCA_PSO that we proposed is not perfect, and there are certain limitations. In the benchmark functions experiment, it can be seen that there is still a gap between the performance of this algorithm and champion algorithms in unimodal functions and multimodal functions.

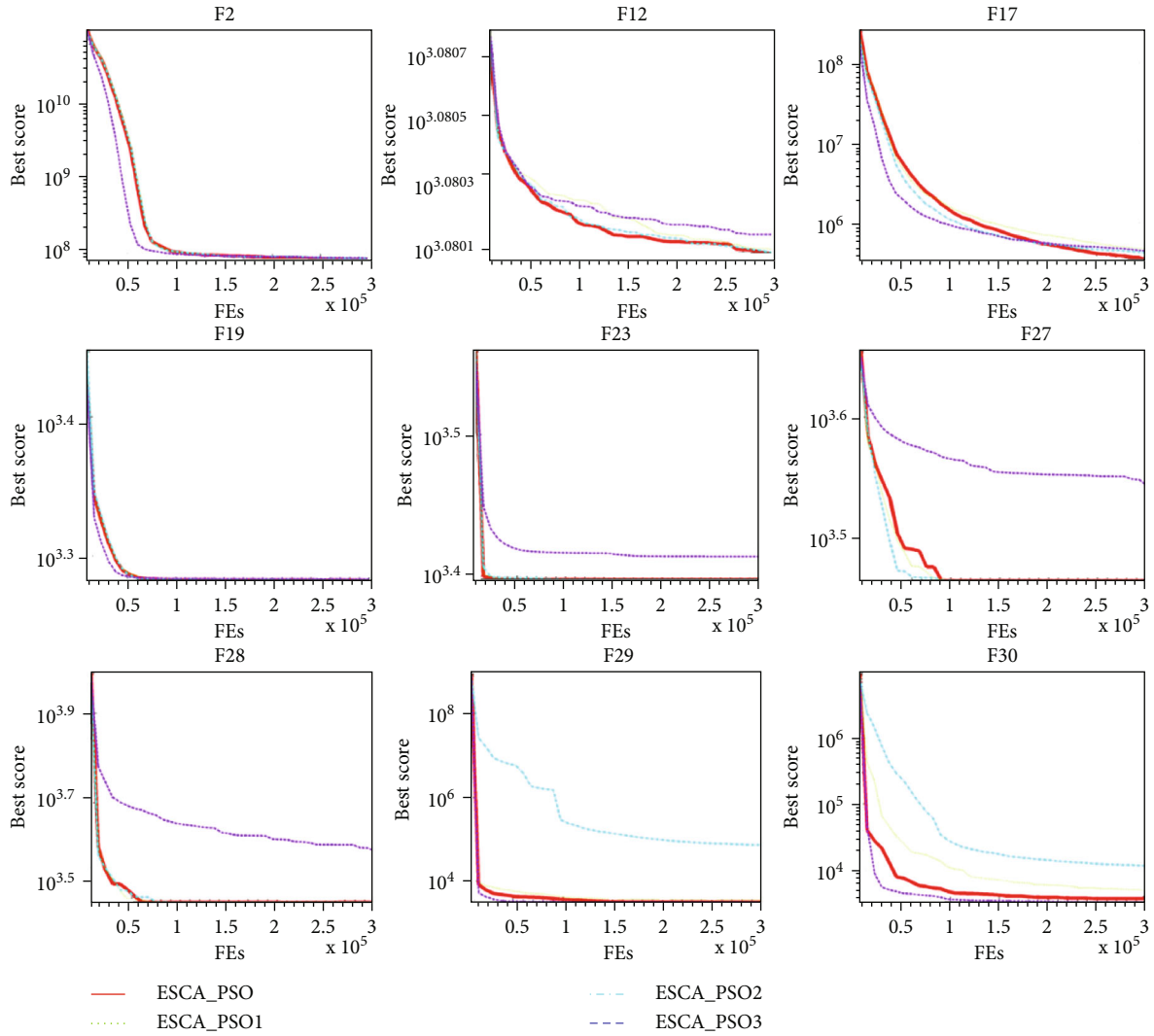


FIGURE 3: Convergence curves of ESCA_PSO and other algorithms on 9 selected benchmark functions.

4.4. *ESCA_PSO For Optimization of SVM.* Like many other machine learning methods [56], SVM has many advantages such as “simple structure,” “overcoming dimension disaster,” and “small sample,” which can overcome the weaknesses of conventional neural networks such as poor learning and generalization ability [57]. Since its introduction, SVM has found its application in many practical problems. Practice shows that the penalty factor C and kernel function variable g have the key influence on the recognition accuracy of the SVM model when solving the recognition problem based on the radial basis kernel function. When the penalty factor C is small, the recognition rate of training and test samples is low, and the SVM is under learning. When C is too large, the accuracy of the training sample is higher, the test sample recognition rate is lower, and the SVM is overlearning. The smaller the kernel function parameter g is, the higher the training sample recognition rate is and the lower the accuracy of the test sample is. When g is larger, the accuracy of training and test samples becomes lower, and SVM is under learning. Traditional methods such

as trial and error method and network search method cannot meet the requirements of accuracy in practical application. Currently, with the development and maturity of MAs, good results have been achieved in improving the performance of the SVM model. For example, Li et al. [58] proposed moth-flame optimization (MFO) to tune the best parameters of SVM and applied it to the diagnosis of tuberculous pleural effusion. Li et al. [59] proposed a chaotic enhanced gravitational search algorithm (GSA) for optimizing the parameters of SVM. Das et al. [60] proposed to use the teaching-learning-based optimization (TLBO) for parameter optimization of SVM, and the good performance was validated by a financial case. Tang et al. [61] proposed a Lévy flight-based shuffled frog-leaping algorithm for determining the best parameters of SVM. Ahmadi et al. [62] developed the imperialist competition algorithm (ICA) to determine the best parameters of SVM for stock market timing. Li et al. [22] proposed SCA to tune the best parameters of SVM, and the good results were verified on several benchmark datasets. Rojas-Dominguez et al. [63] proposed to use

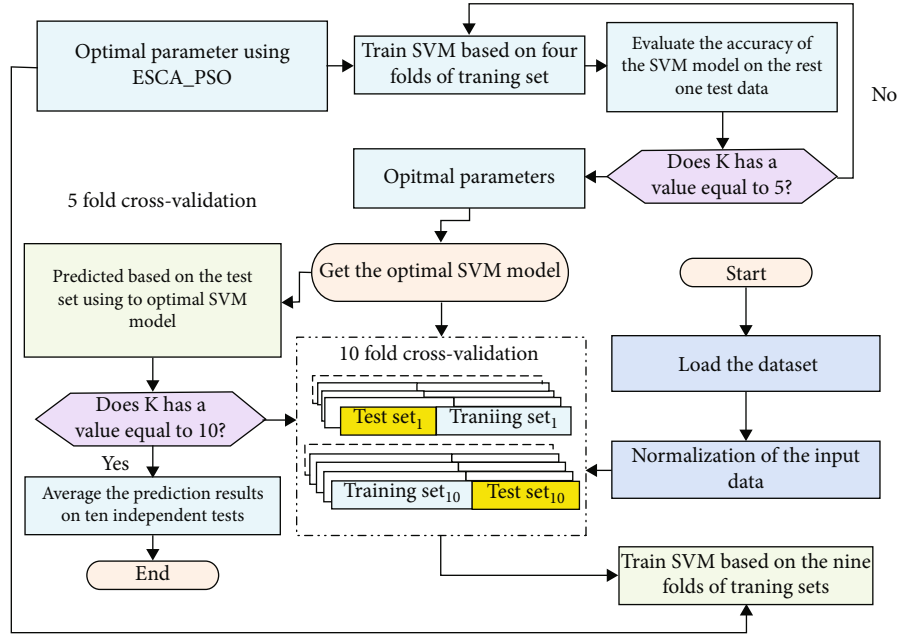


FIGURE 4: Flowchart of ESCA_PSO-SVM.

TABLE 6: Results obtained by ESCA_PSO-SVM on the Bupa liver problem.

Fold	ACC (%)	Sensitivity (%)	Specificity (%)	MCC
No. 1	74.29	61.54	81.82	0.4414
No. 2	67.65	36.36	82.61	0.2092
No. 3	80.00	71.43	85.71	0.5794
No. 4	82.35	90.91	78.26	0.6517
No. 5	82.35	64.29	95.00	0.6404
No. 6	71.43	54.55	79.17	0.3371
No. 7	64.71	55.56	75.00	0.3099
No. 8	62.86	38.89	88.24	0.3102
No. 9	77.14	65.00	93.33	0.5893
No. 10	67.65	53.33	78.95	0.3354
Avg.	73.04	59.18	83.81	0.4404
Max	82.35	90.91	95.00	0.6517
Min	62.86	36.36	75.00	0.2092

several metaheuristics to search for the best parameters of SVM, and the results showed that the estimation of distribution algorithms can achieve the best results. Tharwat et al. [64] proposed a chaotic antlion optimizer for tuning the best parameters, and the effectiveness was validated on an array of well-known datasets. Bablani et al. [65] proposed to use the bat algorithm (BA) to simultaneously determine the optimal parameters of SVM and the best subset of features and applied the model for dealing with the electroencephalography (EEG) data.

In this study, we applied ESCA_PSO to search for the best parameters of SVM, and the resultant model was called ESCA_PSO-SVM as shown in Figure 4. ESCA_PSO-SVM

was applied to predict two different medical problems including the Bupa liver and the Cleveland heart.

The Bupa liver diabetes dataset has a total of 345 samples and 7 features. Table 6 demonstrates the detailed results got by ESCA_PSO-SVM via 10-fold crossvalidation. As shown in Table 6, ESCA_PSO-SVM has got an average accuracy (ACC) of 73.04%, an average sensitivity of 59.18%, an average specificity of 83.81%, and an average Mathews correlation coefficient (MCC) of 0.4404.

From Figure 5, it is clear that ESCA_PSO-SVM has more excellent performance than SCA-SVM in such four indexes. Moreover, compared with the prediction accuracy, the ESCA_PSO-SVM has the best precision, while the KNN

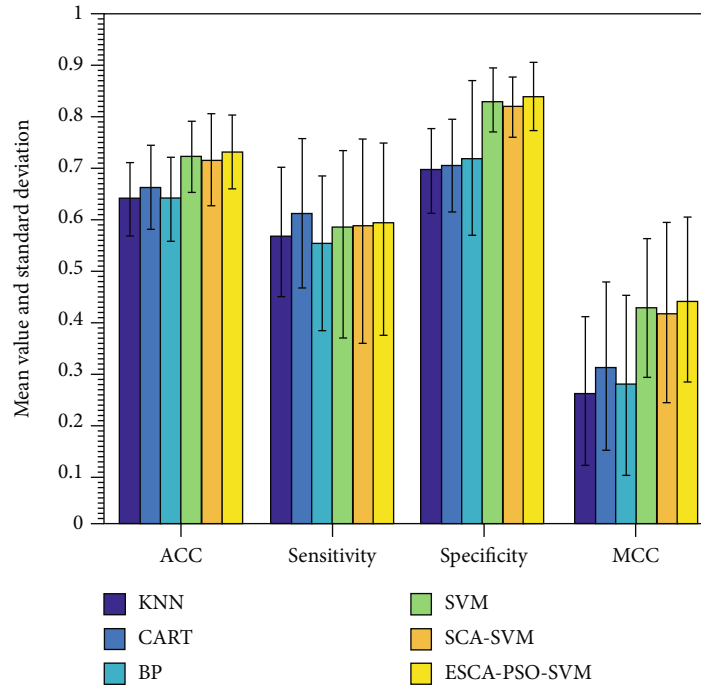


FIGURE 5: Comparison between the ESCA_PSO-SVM and other methods on the Bupa liver problem.

TABLE 7: Results obtained by ESCA_PSO-SVM on the Cleveland heart problem.

Fold	ACC (%)	Sensitivity (%)	Specificity (%)	MCC
No. 1	76.67	72.22	83.33	0.5443
No. 2	87.10	78.57	94.12	0.7427
No. 3	83.33	76.92	88.24	0.6591
No. 4	77.42	76.92	77.78	0.5424
No. 5	80.00	69.23	88.24	0.5909
No. 6	76.67	78.57	75.00	0.5345
No. 7	83.33	87.50	78.57	0.6652
No. 8	83.33	50.00	100.00	0.6325
No. 9	93.55	90.00	95.24	0.8524
No. 10	86.67	88.89	83.33	0.7222
Avg.	82.81	76.88	86.38	0.6486
Max	93.55	90.00	100.00	0.8524
Min	76.67	50.00	75.00	0.5345

model has the lowest precision. Based on the sensitivity metric, ESCA_PSO-SVM ranked second, while BP obtained the worst values. In terms of the obtained specificity, ESCA_PSO-SVM was the best, followed by SVM, SCA-SVM, BP, KNN, and CART. In terms of the MCC, ESCA_PSO-SVM provided the best value, followed by SVM, SCA-SVM, CART, BP, and KNN. It suggests that ESCA_PSO-SVM is more advantageous and stable in solving the Bupa liver problem.

The Cleveland heart data was got from the UCI repository, and it includes 303 samples and 76 features. Table 7 shows the detailed results of ESCA_PSO-SVM through 10-

fold crossvalidation on this dataset. From Table 7, ESCA_PSO-SVM has got an average ACC of 82.81%, a sensitivity of 76.88%, a specificity of 86.38%, and an MCC of 0.6486.

In Figure 6, ESCA_PSO-SVM is superior to SCA-SVM in terms of four evaluation indexes. Concerning the classification accuracy, it can be seen clearly that the ESCA_PSO-SVM has got the best ACC, whereas BP has the lowest precision. In terms of the sensitivity metric, the value of SVM is the same as that of ESCA_PSO-SVM which takes the first place. As for the specificity metric, although SCA-SVM ranked first place, it was only slightly superior to ESCA_

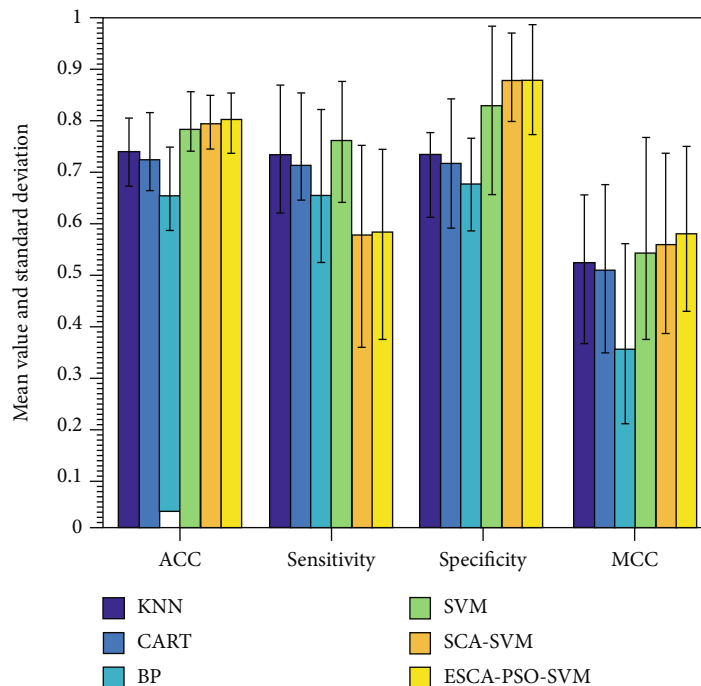


FIGURE 6: Comparison between the ESCA_PSO-SVM and other methods on the Cleveland heart problem.

PSO-SVM. According to the MCC metric, ESCA_PSO provided the best value, followed successively by SCA-SVM, SVM, KNN, CART, and BP. These all proved the robustness and stableness of the ESCA_PSO-SVM on the Cleveland heart problem. Shortly, many problems are waiting to be optimized for which ESCA_PSO can be applied, such as disease module identification [66], molecular signatures identification for cancer diagnosis [67], drug-disease associations prediction [68], drug discovery [69], and pharmacoinformatic data mining [70].

5. Conclusions and Future Directions

To make up for the deficiency of SCA_PSO, this paper proposed ESCA_PSO, an enhanced version of SCA_PSO. The chance of prematurely falling into convergence was effectively reduced by introducing DE and joint mutation mechanisms. To verify its performance, it was compared with seven advanced algorithms on 30 benchmark function sets. The experimental results showed that the performance of the proposed algorithm was better than that of the traditional optimization algorithms and had certain competitiveness with LSHADE. Inspired by the “No Free Lunch” theory, this paper further explored the application of ESCA_PSO in medical diagnosis and successfully applied it to hyperparameter optimization of support vector machine.

The results showed that the support vector machine model combined with the proposed algorithm outperformed the other five existing models and achieved an average accuracy of 82.81%. In conclusion, the proposed algorithm can be regarded as a reliable technique for solving practical problems.

For future work, there are still many problems worthy of study. First of all, we will continue to improve the algorithm, by means such as trying to introduce other metaheuristic algorithms or optimizing the time complexity while ensuring the effect. In addition, we will try to apply ESCA_PSO to other fields such as image segmentation, clustering optimization, and discrete optimization.

Data Availability

The data involved in this study are all public data, which can be downloaded through public channels.

Conflicts of Interest

The authors declare that they have no conflicts of interest.

Acknowledgments

This research was partially supported by Science and Technology Plan Project of Wenzhou, China (G20190020), Key Scientific Research Project of Wenzhou Polytechnic (WZY2019004), and Service and Technology Innovation Project of Wenzhou Science and Technology Association (2019KXCX-RH07).

References

- [1] C. A. Floudas and C. E. Gounaris, “A review of recent advances in global optimization,” *Journal of Global Optimization*, vol. 45, no. 1, pp. 3–38, 2009.
- [2] M. Wang, H. Chen, B. Yang et al., “Toward an optimal kernel extreme learning machine using a chaotic moth-flame

- optimization strategy with applications in medical diagnoses,” *Neurocomputing*, vol. 267, pp. 69–84, 2017.
- [3] M. Chen, G. Zeng, K. Lu, and J. Weng, “A two-layer nonlinear combination method for short-term wind speed prediction based on ELM, ENN, and LSTM,” *IEEE Internet of Things Journal*, vol. 6, no. 4, pp. 6997–7010, 2019.
- [4] H. Zhou, J. Pang, P.-K. Chen, and F.-D. Chou, “A modified particle swarm optimization algorithm for a batch-processing machine scheduling problem with arbitrary release times and non-identical job sizes,” *Computers & Industrial Engineering*, vol. 123, pp. 67–81, 2018.
- [5] L. Shen, H. Chen, Z. Yu et al., “Evolving support vector machines using fruit fly optimization for medical data classification,” *Knowledge-Based Systems*, vol. 96, pp. 61–75, 2016.
- [6] G.-Q. Zeng, X.-Q. Xie, M.-R. Chen, and J. Weng, “Adaptive population extremal optimization-based PID neural network for multivariable nonlinear control systems,” *Swarm and Evolutionary Computation*, vol. 44, pp. 320–334, 2019.
- [7] W. Deng, J. Xu, Y. Song, and H. Zhao, “An effective improved co-evolution ant colony optimisation algorithm with multi-strategies and its application,” *International Journal of Bio-Inspired Computation*, vol. 16, no. 3, pp. 158–170, 2020.
- [8] H. Zhao, H. Liu, J. Xu, and W. Deng, “Performance prediction using high-order differential mathematical morphology gradient spectrum entropy and extreme learning machine,” *IEEE transactions on instrumentation and measurement*, vol. 69, no. 7, pp. 4165–4172, 2020.
- [9] Z. J. Wang, Z. H. Zhan, W. J. Yu et al., “Dynamic group learning distributed particle swarm optimization for large-scale optimization and its application in cloud workflow scheduling,” *IEEE transactions on cybernetics*, vol. 50, pp. 2715–2729, 2019.
- [10] D. Liang, Z.-H. Zhan, Y. Zhang, and J. Zhang, “An efficient ant colony system approach for new energy vehicle dispatch problem,” *IEEE Transactions on Intelligent Transportation Systems*, vol. 21, pp. 4784–4797, 2019.
- [11] F. Zhao, S. Di, J. Cao, and J. Tang, “A novel cooperative multi-stage hyper-heuristic for combination optimization problems,” *Complex System Modeling and Simulation*, vol. 1, no. 2, pp. 91–108, 2021.
- [12] X. Lai and Y. Zhou, “Analysis of multiobjective evolutionary algorithms on the biobjective traveling salesman problem (1, 2),” *Multimedia Tools and Applications*, vol. 79, no. 41–42, pp. 30839–30860, 2020.
- [13] Z. Liang, J. Zhang, L. Feng, and Z. Zhu, “A hybrid of genetic transform and hyper-rectangle search strategies for evolutionary multi-tasking,” *Expert Systems with Applications*, vol. 138, p. 112798, 2019.
- [14] Z. Yang, K. Li, Y. Guo, H. Ma, and M. Zheng, “Compact real-valued teaching-learning based optimization with the applications to neural network training,” *Knowledge-Based Systems*, vol. 159, pp. 51–62, 2018.
- [15] J. Ye and W. Cui, “Modeling and stability analysis methods of neutrosophic transfer functions,” *Soft Computing*, vol. 24, no. 12, pp. 9039–9048, 2020.
- [16] S. Mirjalili, “SCA: a sine cosine algorithm for solving optimization problems,” *Knowledge-Based Systems*, vol. 96, pp. 120–133, 2016.
- [17] H. Nenavath, R. K. Jatoh, and S. Das, “A synergy of the sine-cosine algorithm and particle swarm optimizer for improved global optimization and object tracking,” *Swarm and Evolutionary Computation*, vol. 43, pp. 1–30, 2018.
- [18] D. H. Wolpert and W. G. Macready, “No free lunch theorems for optimization,” *IEEE transactions on evolutionary computation*, vol. 1, no. 1, pp. 67–82, 1997.
- [19] S. Das, A. Bhattacharya, and A. K. Chakraborty, “Solution of short-term hydrothermal scheduling using sine cosine algorithm,” *Soft Computing*, vol. 22, no. 19, pp. 6409–6427, 2018.
- [20] M. A. Tawhid and V. Savsani, “Multi-objective sine-cosine algorithm (MO-SCA) for multi-objective engineering design problems,” *Neural Computing and Applications*, vol. 31, no. S2, pp. 915–929, 2019.
- [21] J. Wang, W. Yang, P. Du, and T. Niu, “A novel hybrid forecasting system of wind speed based on a newly developed multi-objective sine cosine algorithm,” *Energy Conversion and Management*, vol. 163, pp. 134–150, 2018.
- [22] S. Li, H. Fang, and X. Liu, “Parameter optimization of support vector regression based on sine cosine algorithm,” *Expert Systems with Applications*, vol. 91, pp. 63–77, 2018.
- [23] A. Lin, Q. Wu, A. A. Heidari et al., “Predicting intentions of students for master programs using a chaos-induced sine cosine-based fuzzy K-nearest neighbor classifier,” *IEEE Access*, vol. 7, pp. 67235–67248, 2019.
- [24] J. Tu, A. Lin, H. Chen, Y. Li, and C. Li, “Predict the entrepreneurial intention of fresh graduate students based on an adaptive support vector machine framework,” *Mathematical Problems in Engineering*, vol. 2019, 16 pages, 2019.
- [25] M. Issa, A. E. Hassanien, D. Oliva, A. Helmi, I. Ziedan, and A. Alzohairy, “ASCA-PSO: adaptive sine cosine optimization algorithm integrated with particle swarm for pairwise local sequence alignment,” *Expert Systems with Applications*, vol. 99, pp. 56–70, 2018.
- [26] H. Nenavath and R. K. Jatoh, “Hybridizing sine cosine algorithm with differential evolution for global optimization and object tracking,” *Applied Soft Computing Journal*, vol. 62, pp. 1019–1043, 2018.
- [27] M. Abd Elaziz, D. Oliva, and S. Xiong, “An improved opposition-based sine cosine algorithm for global optimization,” *Expert Systems with Applications*, vol. 90, pp. 484–500, 2017.
- [28] C. Qu, Z. Zeng, J. Dai, Z. Yi, and W. He, “A modified sine-cosine algorithm based on neighborhood search and greedy levy mutation,” *Computational Intelligence and Neuroscience*, vol. 2018, Article ID 4231647, 2018.
- [29] N. Kumar, I. Hussain, B. Singh, and B. K. Panigrahi, “Single sensor-based MPPT of partially shaded PV system for battery charging by using cauchy and gaussian sine cosine optimization,” *IEEE Transactions on Energy Conversion*, vol. 32, no. 3, pp. 983–992, 2017.
- [30] W. Long, T. Wu, X. Liang, and S. Xu, “Solving high-dimensional global optimization problems using an improved sine cosine algorithm,” *Expert Systems with Applications*, vol. 123, pp. 108–126, 2019.
- [31] O. E. Turgut, “Thermal and economical optimization of a shell and tube evaporator using hybrid backtracking search-sine-cosine algorithm,” *Arabian Journal for Science and Engineering*, vol. 42, no. 5, pp. 2105–2123, 2017.
- [32] W. Guo, Y. Wang, F. Zhao, and F. Dai, “Riesz fractional derivative Elite-guided sine cosine algorithm,” *Applied Soft Computing*, vol. 81, p. 105481, 2019.

- [33] S. Gupta and K. Deep, "A novel hybrid sine cosine algorithm for global optimization and its application to train multilayer perceptrons," *Applied Intelligence*, vol. 50, no. 4, pp. 993–1026, 2020.
- [34] S. Gupta and K. Deep, "A hybrid self-adaptive sine cosine algorithm with opposition based learning," *Expert Systems with Applications*, vol. 119, pp. 210–230, 2019.
- [35] R. Wang, Z. Wu, J. Lou, and Y. Jiang, "Attention-based dynamic user modeling and deep collaborative filtering recommendation," *Expert Systems with Applications*, vol. 188, article 116036, 2022.
- [36] B. Bai, G. Li, S. Wang, Z. Wu, and W. Yan, "Time series classification based on multi-feature dictionary representation and ensemble learning," *Expert Systems with Applications*, vol. 169, article 114162, 2021.
- [37] W. Yan, G. Li, Z. Wu, S. Wang, and P. S. Yu, "Extracting diverse-shapelets for early classification on time series," *World Wide Web*, vol. 23, no. 6, pp. 3055–3081, 2020.
- [38] Z. Wu, R. Wang, Q. Li et al., "A location privacy-preserving system based on query range cover-up or location-based services," *IEEE Transactions on Vehicular Technology*, vol. 69, no. 5, pp. 5244–5254, 2020.
- [39] Z. Wu, S. Shen, X. Lian, X. Su, and E. Chen, "A dummy-based user privacy protection approach for text information retrieval," *Knowledge-Based Systems*, vol. 195, p. 105679, 2020.
- [40] Z. Mei, H. Zhu, Z. Cui et al., "Executing multi-dimensional range query efficiently and flexibly over outsourced ciphertexts in the cloud," *Information Sciences*, vol. 432, pp. 79–96, 2018.
- [41] Z. Wu, H. Zhu, G. Li et al., "An efficient Wikipedia semantic matching approach to text document classification," *Information Sciences*, vol. 393, pp. 15–28, 2017.
- [42] Z. Wu, L. Lei, G. Li et al., "A topic modeling based approach to novel document automatic summarization," *Expert Systems with Applications*, vol. 84, pp. 12–23, 2017.
- [43] Y. Yang, H. Chen, A. A. Heidari, and A. H. Gandomi, "Hunger games search: Visions, conception, implementation, deep analysis, perspectives, and towards performance shifts," *Expert Systems with Applications*, vol. 177, article 114864, 2021.
- [44] I. Ahmadianfar, A. Asghar Heidari, S. Noshadian, H. Chen, and A. H. Gandomi, "INFO: an efficient optimization algorithm based on weighted mean of vectors," *Expert Systems with Applications*, vol. 195, article 116516, 2022.
- [45] A. A. Heidari, S. Mirjalili, H. Faris, I. Aljarah, M. Mafarja, and H. Chen, "Harris hawks optimization: algorithm and applications," *Future Generation Computer Systems-the International Journal of Escience*, vol. 97, pp. 849–872, 2019.
- [46] S. Li, H. Chen, M. Wang, A. A. Heidari, and S. Mirjalili, "Slime mould algorithm: a new method for stochastic optimization," *Future Generation Computer Systems*, vol. 111, pp. 300–323, 2020.
- [47] I. Ahmadianfar, A. Asghar Heidari, A. H. Gandomi, X. Chu, and H. Chen, "RUN Beyond the Metaphor: An Efficient Optimization Algorithm Based on Runge Kutta Method," *Expert Systems with Applications*, vol. 181, article 115079, 2021.
- [48] K. Daoden and T. Thaiputhump, "A modified shuffled frog leaping algorithm using truncated Gaussian distribution in frog's Position updating process," in *Information Science and Applications (ICISA) 2016*, pp. 965–974, Singapore, 2016.
- [49] W. Hui, L. Hui, L. Yong, L. Changhe, and Z. Sanyou, "Opposition-based particle swarm algorithm with cauchy mutation," in *2007 IEEE Congress on Evolutionary Computation*, pp. 4750–4756, Singapore, 2007.
- [50] M. Jamil and H.-J. Zepernick, "3 - Lévy flights and global optimization," in *Swarm Intelligence and Bio-Inspired Computation*, X.-S. Yang, Z. Cui, R. Xiao, A. H. Gandomi, and M. Karamanoglu, Eds., pp. 49–72, Elsevier, Oxford, 2013.
- [51] S. Mirjalili, S. M. Mirjalili, and A. Lewis, "Grey wolf optimizer," *Advances in Engineering Software*, vol. 69, pp. 46–61, 2014.
- [52] S. Mirjalili, "Moth-flame optimization algorithm: a novel nature-inspired heuristic paradigm," *Knowledge-Based Systems*, vol. 89, pp. 228–249, 2015.
- [53] X.-S. Yang, "A new metaheuristic bat-inspired algorithm," in *Nature Inspired Cooperative Strategies for Optimization (NICSO 2010)*, vol. 284, pp. 65–74, Berlin Heidelberg, 2010.
- [54] J. Kennedy, "Particle swarm optimization," in *Encyclopedia of Machine Learning*, C. Sammut and G. I. Webb, Eds., pp. 760–766, Springer US, Boston, MA, 2010.
- [55] R. Tanabe and A. Fukunaga, "Improving the search performance of SHADE using linear population size reduction," in *2014 IEEE congress on evolutionary computation (CEC)*, Beijing, China, 2014.
- [56] Y. Li, W.-G. Cui, H. Huang, Y.-Z. Guo, K. Li, and T. Tan, "Epileptic seizure detection in EEG signals using sparse multiscale radial basis function networks and the fisher vector approach," *Knowledge-Based Systems*, vol. 164, pp. 96–106, 2019.
- [57] V. N. Vapnik, *The Nature of Statistical Learning Theory*, Springer, New York, 1995.
- [58] C. Li, L. Hou, B. Sharma et al., "Developing a new intelligent system for the diagnosis of tuberculous pleural effusion," *Computer Methods & Programs in Biomedicine*, vol. 153, pp. 211–225, 2018.
- [59] C. Li, X. An, and R. Li, "A chaos embedded GSA-SVM hybrid system for classification," *Neural Computing & Applications*, vol. 26, no. 3, pp. 713–721, 2015.
- [60] S. P. Das, N. S. Achary, and S. Padhy, "Novel hybrid SVM-TLBO forecasting model incorporating dimensionality reduction techniques," *Applied Intelligence*, vol. 45, no. 4, pp. 1148–1165, 2016.
- [61] D. Tang, J. Yang, S. Dong, and Z. Liu, "A lévy flight-based shuffled frog-leaping algorithm and its applications for continuous optimization problems," *Applied Soft Computing*, vol. 49, pp. 641–662, 2016.
- [62] E. Ahmadi, M. Jasemi, L. Monplaisir, M. A. Nabavi, A. Mahmoodi, and P. A. Jam, "New efficient hybrid candlestick technical analysis model for stock market timing on the basis of the support vector machine and heuristic algorithms of imperialist competition and genetic," *Expert Systems with Applications*, vol. 94, pp. 21–31, 2018.
- [63] A. Rojas-Dominguez, L. Carlos Padierna, J. M. Carpio Valadez, H. J. Puga-Soberanes, and H. J. Fraire, "Optimal hyperparameter tuning of SVM classifiers with application to medical diagnosis," *IEEE Access*, vol. 6, pp. 7164–7176, 2018.
- [64] A. Tharwat and A. E. Hassanien, "Chaotic antlion algorithm for parameter optimization of support vector machine," *Applied Intelligence*, vol. 48, no. 3, pp. 670–686, 2018.
- [65] A. Bablani, D. R. Edla, D. Tripathi, S. Dodia, and S. Chintala, "A synergistic concealed information test with novel approach for EEG channel selection and SVM parameter optimization," *IEEE Transactions on Information Forensics and Security*, vol. 14, no. 11, pp. 3057–3068, 2019.

- [66] Y. Su, C. Liu, Y. Niu, F. Cheng, and X. Zhang, "A community structure enhancement-based community detection algorithm for complex networks," *IEEE Transactions on Systems, Man, and Cybernetics: Systems*, vol. 51, pp. 2833–2846, 2019.
- [67] Y. Su, S. Li, C. Zheng, and X. Zhang, "A heuristic algorithm for identifying molecular signatures in cancer," *IEEE Transactions on Nanobioscience*, vol. 19, no. 1, pp. 132–141, 2020.
- [68] L. Cai, C. Lu, J. Xu et al., "Drug repositioning based on the heterogeneous information fusion graph convolutional network," *Briefings in Bioinformatics*, vol. 22, no. 6, article bbab319, 2021.
- [69] Y. Li, X. Li, J. Hong et al., "Clinical trials, progression-speed differentiating features and swiftness rule of the innovative targets of first-in-class drugs," *Briefings in Bioinformatics*, vol. 21, no. 2, pp. 649–662, 2020.
- [70] J. Yin, W. Sun, F. Li et al., "VARIDT 1.0: variability of drug transporter database," *Nucleic Acids Research*, vol. 48, no. D1, pp. D1042–D1050, 2020.

Retraction

Retracted: Analysis of Obstetric Clinical Nursing Integrating Situational Teaching Simulation

Computational and Mathematical Methods in Medicine

Received 27 June 2023; Accepted 27 June 2023; Published 28 June 2023

Copyright © 2023 Computational and Mathematical Methods in Medicine. This is an open access article distributed under the Creative Commons Attribution License, which permits unrestricted use, distribution, and reproduction in any medium, provided the original work is properly cited.

This article has been retracted by Hindawi following an investigation undertaken by the publisher [1]. This investigation has uncovered evidence of one or more of the following indicators of systematic manipulation of the publication process:

- (1) Discrepancies in scope
- (2) Discrepancies in the description of the research reported
- (3) Discrepancies between the availability of data and the research described
- (4) Inappropriate citations
- (5) Incoherent, meaningless and/or irrelevant content included in the article
- (6) Peer-review manipulation

The presence of these indicators undermines our confidence in the integrity of the article's content and we cannot, therefore, vouch for its reliability. Please note that this notice is intended solely to alert readers that the content of this article is unreliable. We have not investigated whether authors were aware of or involved in the systematic manipulation of the publication process.

In addition, our investigation has also shown that one or more of the following human-subject reporting requirements has not been met in this article: ethical approval by an Institutional Review Board (IRB) committee or equivalent, patient/participant consent to participate, and/or agreement to publish patient/participant details (where relevant).

Wiley and Hindawi regrets that the usual quality checks did not identify these issues before publication and have since put additional measures in place to safeguard research integrity.

We wish to credit our own Research Integrity and Research Publishing teams and anonymous and named external researchers and research integrity experts for contributing to this investigation.

The corresponding author, as the representative of all authors, has been given the opportunity to register their agreement or disagreement to this retraction. We have kept a record of any response received.

References

- [1] S. Xiao, J. Fang, X. Zhao, L. Yang, H. Tang, and Y. Wang, "Analysis of Obstetric Clinical Nursing Integrating Situational Teaching Simulation," *Computational and Mathematical Methods in Medicine*, vol. 2022, Article ID 6843196, 12 pages, 2022.

Research Article

Analysis of Obstetric Clinical Nursing Integrating Situational Teaching Simulation

Shanshan Xiao, Jing Fang, Xiaoxiao Zhao, Liqin Yang, Hongyan Tang, and Yuanping Wang 

The Affiliated Hospital of Medical School, Ningbo University, Ningbo 315020, China

Correspondence should be addressed to Yuanping Wang; wyp120724@163.com

Received 7 May 2022; Accepted 1 June 2022; Published 21 June 2022

Academic Editor: Pan Zheng

Copyright © 2022 Shanshan Xiao et al. This is an open access article distributed under the Creative Commons Attribution License, which permits unrestricted use, distribution, and reproduction in any medium, provided the original work is properly cited.

This paper applies the situational teaching mode to obstetric clinical nursing. When explaining the nursing operation skills, according to the pre written script, design some common clinical nurse-patient conflicts and carry out situational simulation performances, so as to inspire students to think about how to effectively communicate with patients and their families and establish a harmonious nurse-patient relationship. At the same time, this paper also urges students to improve their initiative of autonomous learning and actively participate in the whole process of learning, rather than passively accept knowledge. Finally, the teaching methods of combining obstetric clinical nursing teaching with experimental teaching were compared to explore the effectiveness of situational teaching simulation teaching mode. Through the experimental comparative analysis, it can be seen that the obstetric clinical nursing teaching model based on situational teaching simulation has a certain effect and has a good guiding significance for the practical teaching of obstetric clinical nursing.

1. Introduction

Scenario-based teaching refers to a teaching method in which teachers create a realistic teaching situation with the support of relevant technical conditions according to the requirements of teaching objectives, so that students can play roles in an environment close to the real situation, and learn relevant knowledge and skills from it. The nursing teaching of obstetrics and gynecology in secondary vocational education is a practical course. Students need to master proficient operating skills and be familiar with various practical problems during the study period, so that they can be handy in the future nursing work in obstetrics and gynecology, deal with various problems calmly, and improve patients' satisfaction with nursing. Therefore, the teaching of obstetrics and gynecology should actively introduce the situational teaching method to fully demonstrate the dominant position of students.

At present, with the wide application of information technology, the nursing teaching of secondary vocational

obstetrics and gynecology has made new progress. Teachers use the support of multimedia technology in the classroom, which can make the teaching content richer and more vivid, which is convenient for students to extensively study practical cases, and then guide their own professional skills training. However, the nursing work of obstetrics and gynecology contains many contents, even very trivial. In the treatment of gynecological diseases and maternal care, students need to have strong practical ability to provide effective nursing and help to patients. Therefore, the nursing course of obstetrics and gynecology has the characteristics of large amount of knowledge and abstract content, and the existing teaching work still has certain shortcomings.

The purpose of scenario teaching is to stimulate students' enthusiasm and initiative. Therefore, after selecting and creating scenarios, teachers should further set up specific tasks and problems to give students the opportunity to learn independently. Teachers can divide the students in the class into several groups and then introduce problems that need to be considered and dealt with in various situations and then

TABLE 1: Comparison of total test scores.

Number	Control group	Test group	Number	Control group	Test group
1	79.33	84.90	11	73.37	69.20
2	73.17	81.21	12	77.27	73.67
3	81.81	75.01	13	81.52	69.20
4	77.76	71.42	14	77.88	83.25
5	65.36	75.00	15	76.07	79.89
6	78.32	82.90	16	64.04	76.29
7	70.67	75.35	17	81.40	81.53
8	80.80	72.20	18	78.08	85.64
9	69.67	79.46	19	73.49	71.13
10	71.52	86.35	20	77.08	84.21

TABLE 2: Comparison of nurse-patient communication scores.

Number	Control group	Test group	Number	Control group	Test group
1	13.17	15.41	11	8.07	14.42
2	12.05	14.29	12	9.06	16.54
3	16.85	16.33	13	11.47	16.61
4	13.07	14.19	14	16.87	15.28
5	11.92	15.90	15	14.23	17.00
6	13.72	14.86	16	14.24	14.12
7	8.03	14.42	17	8.53	16.78
8	16.60	14.76	18	14.69	14.40
9	13.27	15.19	19	9.96	14.25
10	15.52	14.27	20	9.02	16.44

TABLE 3: Comparison of experimental operation skills scores.

Number	Control group	Test group	Number	Control group	Test group
1	68.26	63.05	11	65.91	58.88
2	56.17	65.46	12	69.77	58.03
3	61.25	57.62	13	62.21	66.85
4	65.03	57.33	14	68.19	63.16
5	60.71	61.03	15	65.98	67.05
6	65.19	70.88	16	62.60	70.44
7	65.67	56.60	17	56.37	65.35
8	64.40	60.60	18	67.33	62.93
9	56.89	57.54	19	60.27	68.56
10	58.24	60.45	20	64.72	69.45

discussed by the group members. The members of the group have both division of labor and cooperation, and they jointly apply the relevant knowledge points of obstetrics and gynecology nursing, break through difficulties, and propose solutions, so as to realize the integration of theory and practice. For example, after collecting and examining the medical history of obstetrics and gynecology patients, how to formulate nursing

measures according to different cases and the issues that should be paid attention to in the nursing work after natural childbirth, etc. can be used as topics for students to think about. Moreover, students draw and practice through simulation, and finally, the group representatives make a summary and share the results in the class. Through the analysis of different case scenarios, the team members communicated nursing plans, which not only realized mutual learning but also facilitated familiarity with more practical scenarios.

In order to improve the clinical nursing effect of obstetrics, this paper applies situational teaching to the clinical nursing research teaching of obstetrics, improves the teaching effect of obstetrics nursing, and promotes the nursing effect of hospital obstetrics.

2. Related Work

The situational teaching method dilutes the traditional teacher's "preaching" color, gives students more classroom practice, stimulates students' interest in learning, and creates a good classroom learning atmosphere. The situational teaching method changes students' passive acceptance state, encourages students to actively participate in teaching activities, and promotes abstraction. The specific theoretical knowledge can effectively make up for the shortcomings of traditional "cramming" teaching and optimize the teaching effect of obstetrics and gynecology nursing. In the simulation situation, students play a certain role in it, actively participate in practical activities, think and explain according to learning theory, and give students more opportunities to express and think [1]. Actively participating in classroom learning activities is conducive to improving the enthusiasm of classroom teaching, improving the openness of teaching, and enabling students to better grasp the knowledge of obstetrics and gynecology nursing [2].

In the process of situational teaching, the use of situational interaction can promote teachers and students to communicate on an equal footing. At the same time, teachers can also guide students to express their personal opinions, so that students can analyze and solve problems, put forward personal opinions, and improve students' innovative ability. The situational teaching mode breaks the traditional teaching mode, combines theory with practice, cultivates students' autonomous learning ability, urges students to deeply understand relevant theories, realizes entertaining, pays more attention to the cultivation of patients' true feelings, and improves the communication skills between nurses and patients [3]. Actual situational teaching can provide students with more opportunities for practical exercise and encourage students to combine the professional knowledge of obstetrics and gynecology nursing and related knowledge and use the simulation environment to encourage students to realize empathy and train their professional quality and thinking. Moral quality, psychological quality, and body speed, promote self-education and, at the same time, promote better development of students, realize division of labor and mutual learning through situational demonstrations, cultivate students' spirit of unity and cooperation, improve students' work ability, and lay a good

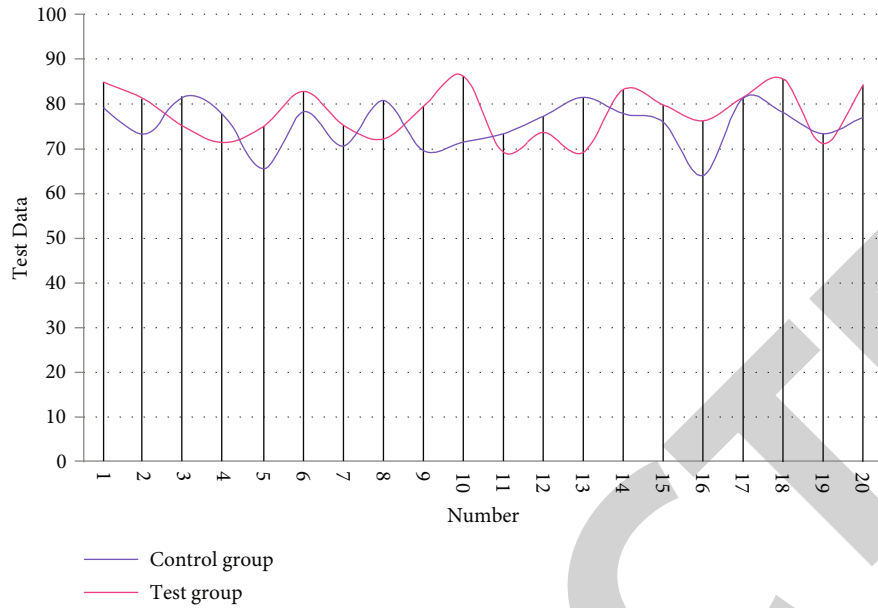


FIGURE 1: Comparison of total test scores.

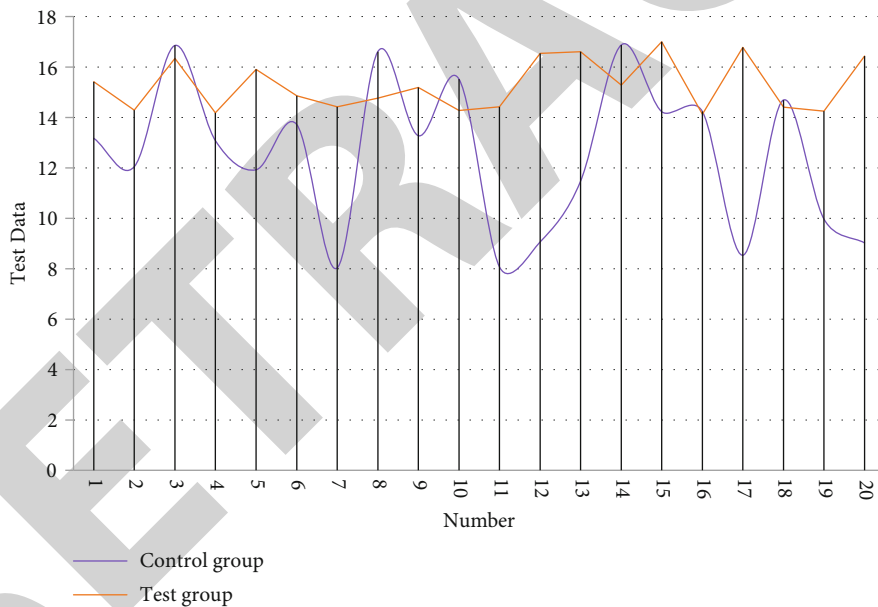


FIGURE 2: Comparison of nurse-patient communication scores.

foundation for students' future development. [4]. Therefore, the situational teaching mode is an open teaching mode, which is conducive to cultivating students' various abilities and meeting the requirements of cultivating high-quality applied talents [5].

During the situational teaching, students analyze and discuss nursing error cases, so that students can realize that once mistakes occur in the work, nursing errors may occur and then cultivate students to enrich medical theoretical knowledge and serious and responsible attitude, cultivate students' prudent and independent spirit, and avoid occurrences as much as possible. With the popularization and

development of hospital nursing systemization, the teaching focus has shifted to realize the integration of nursing teaching [6]. In the process of obstetrics and gynecology nursing training, doctors and nurses can be combined with clinical teaching, and theoretical learning and practice can be combined, which can promote strengths and avoid weaknesses, transform medical knowledge and nursing theory into practice, and promote students to better observe and analyze conditions, shorten the distance between theory and practice as much as possible, consolidate classroom knowledge, better understand and master nursing procedures and really apply them to practice, improve students' nursing level,

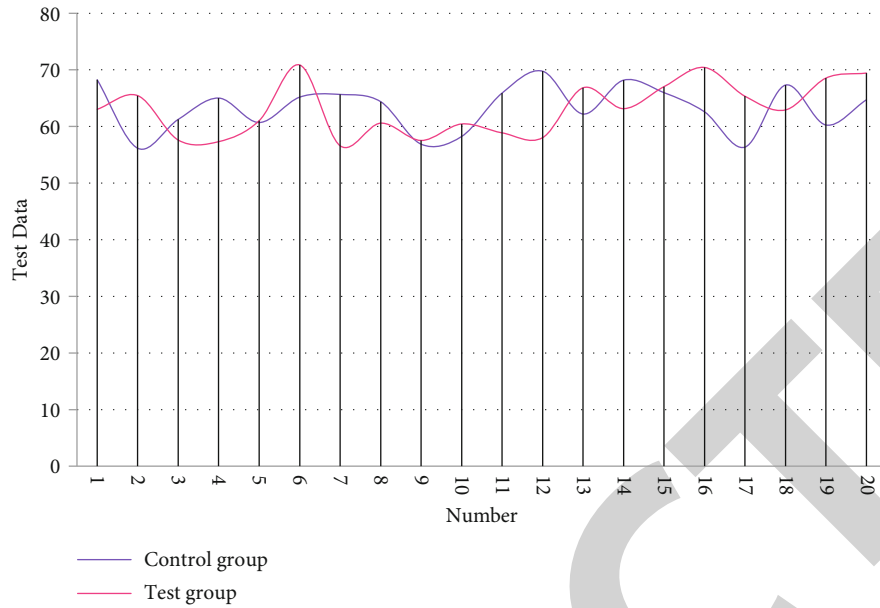


FIGURE 3: Comparison of experimental operation skills scores.

TABLE 4: Comparison of the theoretical test scores of the two groups of students.

Number	Control group	Test group	Number	Control group	Test group
1	59.13	76.91	11	70.80	63.78
2	69.79	79.32	12	61.92	72.48
3	66.05	73.87	13	62.23	69.18
4	74.85	64.78	14	75.34	67.72
5	60.12	72.40	15	62.59	75.78
6	79.77	60.59	16	59.45	69.25
7	72.42	78.84	17	76.71	69.30
8	75.97	69.51	18	61.08	73.04
9	70.78	59.59	19	64.39	76.68
10	73.48	76.79	20	61.98	66.96

and lay a good foundation for students' clinical practice and practical work [7].

During scenario teaching, teachers can guide students to analyze specific scenarios with the help of basic theories and then be able to identify problems, analyze problems, and choose the best solution. The combination of basic theory and specific practice can cultivate students' ability to integrate theory with practice, realize application of what they have learned, and cultivate students' clinical practice. It can change the current disconnection between knowledge and action and improve students' problem analysis ability and problem solving ability [8]. The situational teaching mode changes the traditional single teaching method, respects the dominant position of students in the classroom, realizes the bilateral interaction between teachers and students, and improves the teaching quality of obstetrics and gynecology nursing. It can optimize the effect of classroom teaching,

promote bilateral interaction between teachers and students, and gradually cultivate students' clinical thinking. The situational teaching mode is more vivid, intuitive, and vivid, which enables students to carry out practical exercises more concretely and deeply, gives students a better emotional experience, cultivates students' active learning attitude, and improves the teaching effect of obstetrics and gynecology nursing [9]. In the traditional teaching process, teachers pay more attention to the diagnosis and treatment of obstetrics and gynecology diseases of students, but they do not pay enough attention to cultivating students' comprehensive quality and overall nursing concept, which prevents students from effectively grasping the overall nursing effect [10]. From the current point of view, the overall nursing application in the teaching of obstetrics and gynecology nursing is not very ideal and thus cannot meet the requirements of clinical nursing and health care. Reforming teaching methods is conducive to cultivating more practical talents, improving students' business ability and professional ability, and improving the overall quality of nursing [11]. As a teaching practice and a feasible and effective teaching method, the situational teaching mode breaks through the traditional teaching mode, makes up for the shortcomings of pure knowledge imparting, promotes emotional resonance between teachers and students, and then stimulates students' interest in learning and improves the teaching of obstetrics and gynecology nursing. It can cultivate more practical and high-quality nursing talents [12].

3. Research Method

3.1. Test Preparation. We randomly select the students into groups and divided them into the experimental group and the control group. There is no significant difference in the medical education background of the two groups of students, and they were comparable. The theoretical and

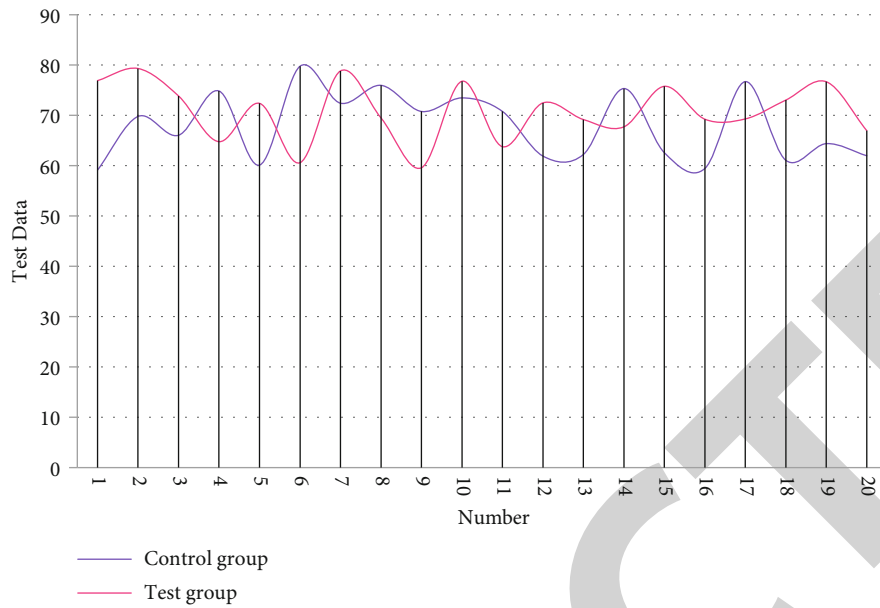


FIGURE 4: Comparison of the theoretical test scores of the two groups of students.

TABLE 5: Comparison of the ability to find the truth.

Number	Control group	Test group	Number	Control group	Test group
1	36.99	43.84	11	42.40	46.93
2	31.96	37.00	12	34.98	42.88
3	37.44	36.11	13	31.89	36.95
4	43.74	37.16	14	38.07	40.96
5	41.34	45.11	15	33.53	41.69
6	34.05	35.21	16	33.74	42.34
7	31.81	45.03	17	37.18	36.89
8	32.16	41.78	18	43.61	39.17
9	31.58	35.28	19	38.87	35.87
10	33.71	46.99	20	43.25	43.03

TABLE 6: Comparison of open minds.

Number	Control group	Test group	Number	Control group	Test group
1	41.13	45.29	11	37.33	35.57
2	32.85	43.05	12	44.60	38.16
3	37.22	43.83	13	44.11	37.73
4	40.36	45.92	14	37.20	41.02
5	33.35	41.87	15	43.37	43.14
6	35.50	35.46	16	35.31	46.75
7	43.42	41.11	17	36.71	38.02
8	39.49	36.81	18	34.42	44.55
9	40.20	45.48	19	34.47	42.71
10	39.88	39.62	20	36.77	36.57

experimental teaching of the two groups of students is all completed by the researchers themselves, and the teaching syllabus, teaching plan, number of hours, teaching objectives, and teaching progress are all the same. In the teaching of the experimental group, some experimental courses are selected to be taught by the PBL-scenario simulation teaching method, and the teaching of the control group is taught by the traditional teaching method.

The PBL teaching method adopts a problem-based teaching method, and the design and compilation of medical records is the core of the whole teaching. The design and compilation of medical records should be based on the undergraduate syllabus and teaching objectives, covering the teaching content of the taught courses, with prominent key points and difficulties, and students should be able to find enough relevant materials and reference books or learning websites for autonomous learning. The medical records are sufficiently representative, inspiring, and exploratory. The design of medical records should be clear in diagnosis and moderate in difficulty and in line with the cognitive characteristics and level of students in school and can be grasped and understood by students. When compiling PBL medical records, the teacher designs and compiles the cases according to the selected nursing operation techniques [13]. After forming the preliminary cases, the teachers of the teaching and research department will design and discuss in detail whether the various manifestations of the cases and the auxiliary examination conditions are true and complete when the teaching and research room meetings are held. Finally, in order to make the cases more standardized, systematic, and more in line with the actual clinical situation, after the preparation of the medical records, the cases are handed over to the teachers of the obstetrics and gynecology department of the internship hospital for discussion and revision in the department, and the final SC is formed. After the writing of SC is completed, it is rewritten according

TABLE 7: Comparison of analytical capabilities.

Number	Control group	Test group	Number	Control group	Test group
1	37.78	42.12	11	45.97	45.92
2	41.57	39.05	12	35.14	38.30
3	38.50	45.29	13	43.06	45.73
4	43.45	48.69	14	35.38	42.38
5	37.02	45.83	15	44.95	39.41
6	42.50	42.78	16	44.74	40.34
7	41.02	48.38	17	37.49	44.41
8	41.12	41.14	18	41.51	48.67
9	35.85	45.95	19	43.31	45.00
10	44.03	40.84	20	38.07	39.97

TABLE 8: Comparison of systematic capabilities.

Number	Control group	Test group	Number	Control group	Test group
1	34.06	45.40	11	36.82	34.65
2	44.16	45.00	12	44.92	44.11
3	40.88	37.04	13	33.56	38.00
4	34.24	40.72	14	43.96	34.46
5	39.00	35.07	15	37.48	34.51
6	41.12	38.05	16	41.40	36.71
7	40.78	36.41	17	34.11	35.15
8	45.12	35.26	18	43.44	44.28
9	41.66	37.40	19	36.23	44.17
10	45.11	36.13	20	38.35	36.18

TABLE 9: Comparison of self-confidence in critical thinking.

Number	Control group	Test group	Number	Control group	Test group
1	38.36	35.80	11	42.12	47.52
2	41.15	44.22	12	35.03	42.23
3	42.69	39.14	13	36.84	44.32
4	34.67	41.78	14	46.05	47.38
5	39.99	46.44	15	39.88	39.11
6	42.04	36.82	16	38.59	35.25
7	40.72	40.71	17	40.61	37.14
8	35.65	45.64	18	46.49	35.11
9	41.82	42.67	19	42.53	42.89
10	44.87	39.70	20	43.02	36.79

to the experimental content, and it is divided into student version and teacher version. In the case of the student version, there is a brief introduction of the medical history and a small number of physical examination results, which only serve to introduce the case and inspire students to think. The teacher's version of the case contains comprehensive medical history, physical examination, and laboratory

TABLE 10: Comparison of intellectual curiosity.

Number	Control group	Test group	Number	Control group	Test group
1	39.89	43.24	11	43.46	44.10
2	43.79	39.95	12	42.02	46.58
3	40.02	47.49	13	40.17	42.60
4	35.88	37.66	14	42.01	40.77
5	38.70	43.44	15	46.55	38.56
6	44.42	38.44	16	35.74	45.23
7	40.71	44.41	17	42.38	44.51
8	38.18	42.68	18	42.99	41.91
9	35.68	42.85	19	36.52	38.19
10	40.32	46.34	20	45.23	37.11

TABLE 11: Comparison of cognitive maturity.

Number	Control group	Test group	Number	Control group	Test group
1	36.50	43.10	11	34.27	40.39
2	38.49	36.38	12	39.16	34.93
3	44.63	44.79	13	37.23	44.98
4	45.28	41.93	14	36.03	40.54
5	44.68	35.52	15	42.34	40.28
6	38.87	35.49	16	41.75	40.58
7	43.69	39.13	17	40.33	44.14
8	45.13	39.19	18	33.77	45.71
9	39.51	44.41	19	41.74	43.18
10	45.56	40.51	20	39.58	34.63

test results, which are used for teachers to guide students' thinking.

For students, PBL situational simulation teaching is a brand-new teaching mode. Before this study, all students had never been exposed to this teaching method. Before teaching, students should give a brief introduction to the PBL scenario simulation teaching method. At the same time, it is necessary to do a good job of mobilizing students' thoughts, so that students have the necessary understanding of this teaching method and sufficient psychological preparation to accept a new teaching method. In addition, it is necessary to inform students that PBL teaching is a teaching method of "teacher-led, student-based, and case-based." The five-stage teaching process is applied in PBL teaching, namely, teachers raise questions, and students establish hypotheses, collect data, demonstrate hypotheses, and summarize [14]. In PBL teaching, only by thinking independently and independently can we acquire knowledge and solve problems. A situational teaching method means that in the process of teaching, teachers purposefully design or introduce realistic clinical scenarios, so that students can be immersed in the situation, arouse students' emotional experience, stimulate students to think actively, and finally inspire students to understand knowledge, analyze

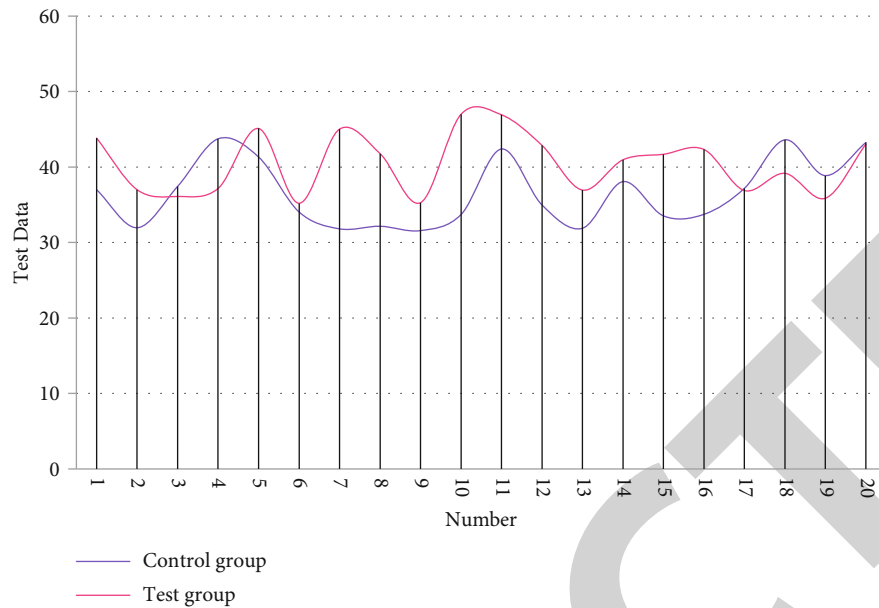


FIGURE 5: Comparison of the ability to find the truth.

problems, deal with emergencies, and communicate and coordinate. Moreover, situational teaching emphasizes placing learning in a real situation, so that students can have real experience and solve real problems.

After the SC preparation is completed, according to the characteristics of the case and the development process of the disease, a scenario simulation script is prepared. First of all, according to the needs of the development of the plot, the characters to appear are generally composed of 1 nurse, 1 patient, and 1.2 family members of the patient. Secondly, it is necessary to discuss the writing of the script with the nurse-patient communication teacher, set the nurse-patient conflict in the experiment, and write the script. For example, in scene 1, because of lack of medical knowledge, a woman with episiotomy who refused to perform genital scrubbing operation had some language conflicts with the nurse and refused to continue treatment. In scenario 2, there is a lack of breastfeeding knowledge, and there is difficulty in breastfeeding, and the mother and family members who are ready to choose supplementary feeding. In scene 3, the patient is faced with arrears and withdrawal of medication, the family members are waiting in the corridor for the patient to undergo vaginal lavage treatment, and the anxious family members speak rudely to the nursing staff and other common conflicts. Finally, after the playbook is finalized, teachers guide students to memorize and recite lines and guide and correct students' performances [15]. In order to avoid the students' performances being too exaggerated, false, and the traces of the performances too heavy, it is necessary to make all the students' attention focus on the performance itself, so as to avoid ignoring the solution of the problem and fail to achieve the purpose of promoting students' critical thinking. At the same time, the test site needs to be prepared according to the experimental requirements. The test site is set up in the classroom of the nursing department, and the simulated hospital bed is set up in the classroom.

As a new open teaching method, PBL-scenario simulation teaching method has higher requirements on teachers' own professional quality, classroom regulation ability, teaching skills, language communication ability, and so on. This teaching method not only requires teachers to be proficient and thorough in the content of this major and the course but also requires teachers to master a lot of knowledge of related disciplines and have the ability to ask and solve problems, the ability to use knowledge flexibly, more rigorous logical thinking, and good organizational skills and to be able to mobilize students' enthusiasm, achieve entertaining, and control the rhythm of the classroom [16]. Therefore, when teaching PBL-scenario simulation teaching method, teachers need to learn and read a large number of PBL and situational simulation teaching materials and be proficient in the PBL-scenario simulation teaching method. Before teaching, teachers should prepare lessons carefully, write medical records, and be familiar with the contents of cases and related knowledge of anatomy, physiology, and pathology. At the same time, it is also necessary to have rich clinical experience and communication skills and to be able to cope with the occurrence of emergencies, all of which put forward very high requirements for teachers.

3.2. Implementation of Scenario Simulation Teaching. In the first stage (20 minutes after the theory class), the problem is raised, and the division of labor is arranged. This stage is not completed in the experimental class, but in 20 minutes after the theoretical class, 3-5 days before the first experimental class, the teacher distributes the SC to the students, finds a student to read the SC aloud in the class, and guides the students to familiarize themselves with the case, so as to ensure that there are no questions that the students cannot understand in the case. After that, we need to select the leader of the group discussion and arrange for the leader to lead the

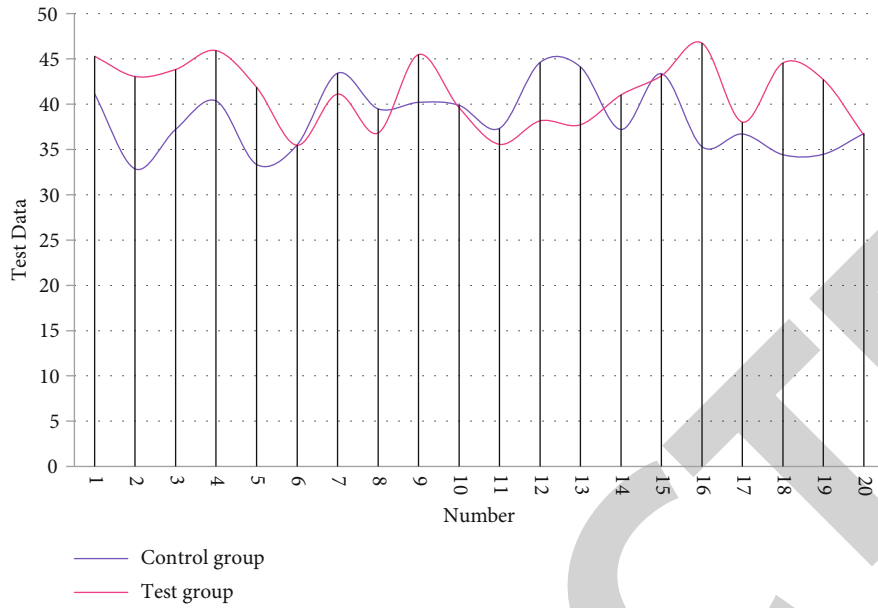


FIGURE 6: Comparison of open minds.

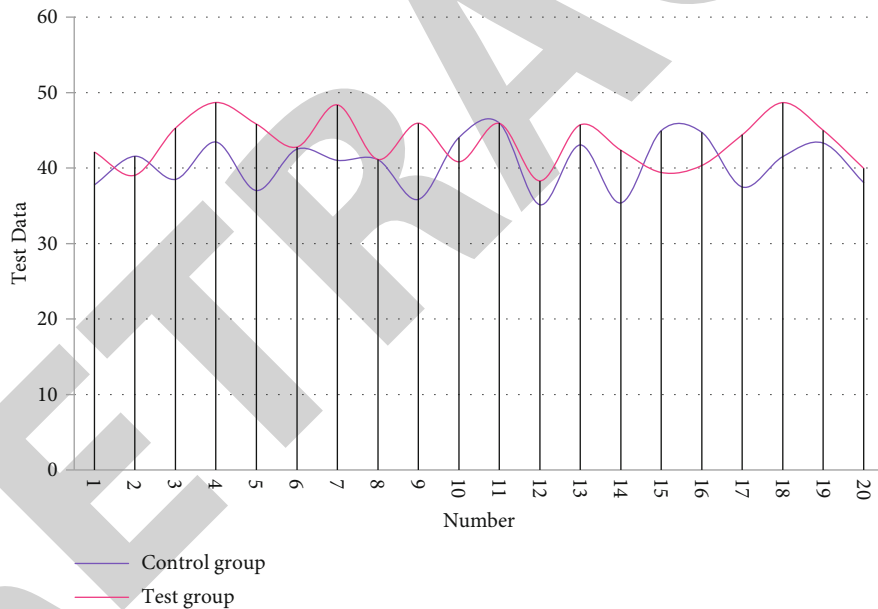


FIGURE 7: Comparison of analytical capabilities.

students to have an after-class discussion and ask interesting learning questions. At the same time, it is necessary to decompose, classify, and arrange the problems raised to ensure that each student in the group has a problem that needs to be solved. Finally, the reference books and websites that students use to solve problems are given to ensure that students can get enough help and expand their learning space and time. In the second stage (the first experimental class), there are class discussion and problem-solving stage. This stage is completed in the experimental classroom, and the patient and the patient's family will tell the medical history process according to the lines written in advance. After

listening to the narration of the medical history, the group members will discuss and share the materials they have collected with the group members and use the brainstorming method. After that, students need to be encouraged to put forward as many assumptions and questions as possible and then question these assumptions and questions one by one. At the same time, there needs to be an in-group discussion, the secretary records the feedback information, and then the students discuss further to solve the problem. After a large amount of data collection, information aggregation, and layer-by-layer analysis and after removing the false and keeping the truth, a summary is made, the most

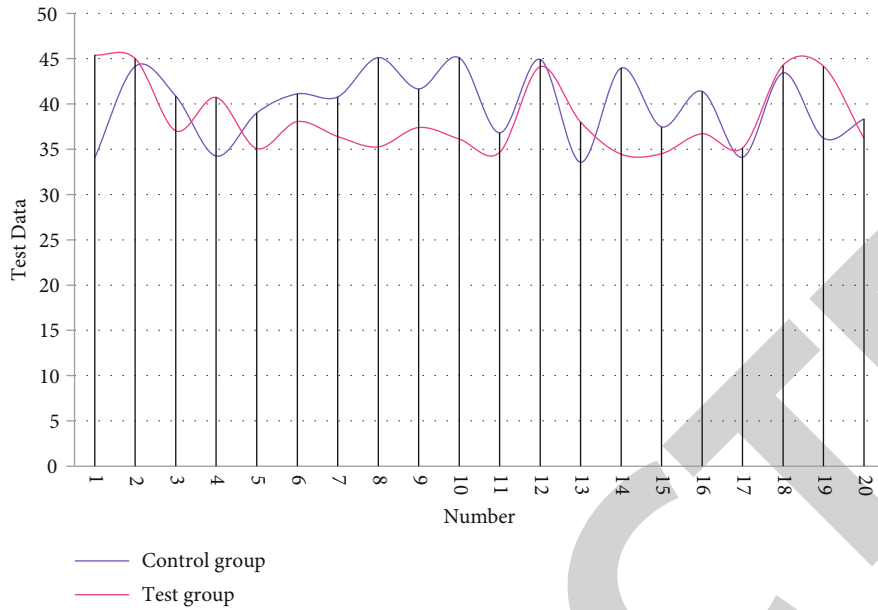


FIGURE 8: Comparison of systematic capabilities.

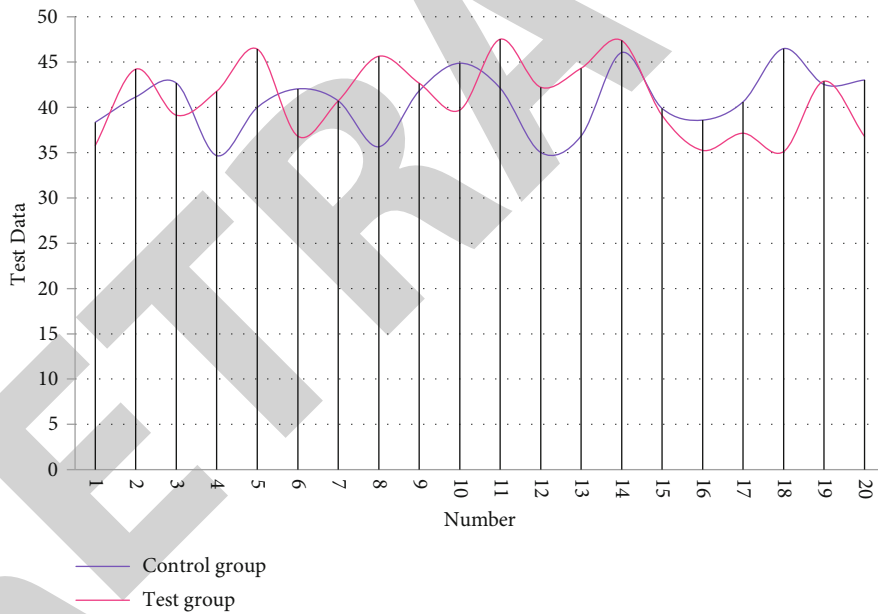


FIGURE 9: Comparison of self-confidence in critical thinking.

appropriate treatment method is found, and the students are guided to analyze the nursing operation skills most needed by the patients and lead to the experimental teaching content of the next class. At the same time, the teacher assigns the teaching tasks of the next experimental class to the students, shows the conflict script to the students, guides the students to discuss after class, and analyzes the method to resolve the conflict. In phase 3 (second lab session), questions left over from the previous session are discussed to ensure there are no more unresolved issues. After that, the teacher taught nursing operation techniques. During the process of the teacher's narration and teaching, the students

who played the patient and their family members performed according to the script written in advance, forming a conflict between nurses and patients. At this time, it is necessary to guide students to use the knowledge of nurse-patient communication that they have learned to analyze and resolve the conflict between nurses and patients and form a summary after class discussion. Finally, it is necessary to guide students to practice experimental operation techniques in groups and require students to master the experimental operation steps. Before getting out of class, the teacher assigns homework and asks each student to organize the knowledge gained from self-learning into documents,

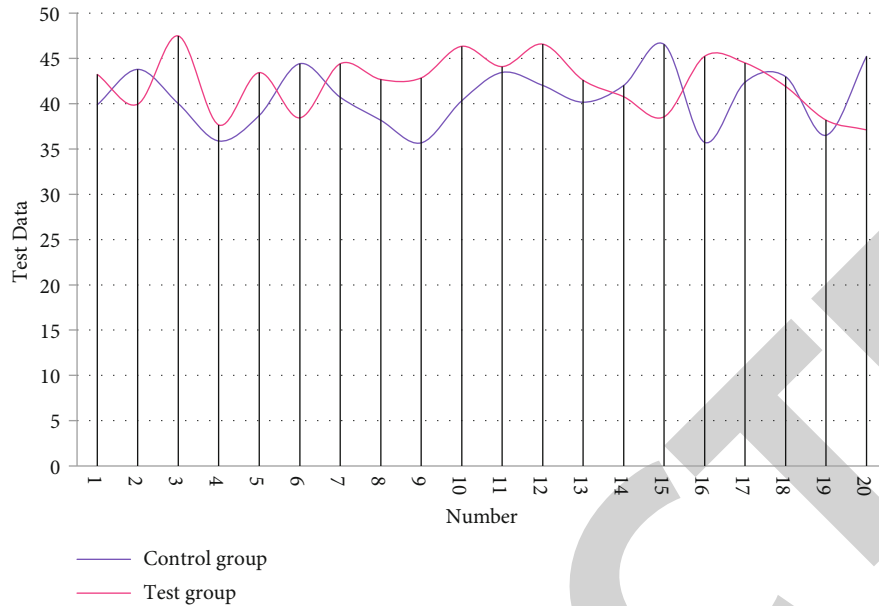


FIGURE 10: Comparison of intellectual curiosity.

send them to the public mailbox to report and exchange, and solve problems together through the sharing of information and experience. At the same time, the teacher summarizes the key points and difficulties of the teaching and gives feedback and evaluation of the teaching activities to give positive encouragement to students, affirm students' spirit of exploration and active learning performance, and give objective evaluations at the same time.

In the first experimental class, it is necessary to teach the experiment according to the requirements of the experimental outline, follow the experimental operation guidance steps, and tell the students about the experimental purpose, operation materials, experimental steps, and experimental precautions. At the same time, it is necessary to play the recorded experimental operation video and teach it and then guide the students to practice in groups and the teacher to patrol. In the second experimental class, it is necessary to point out the common mistakes and deficiencies of the students in the first experimental class and guide the students to practice in groups, and the teachers will inspect and help the students to correct the problems in time. Before the end of the experimental class, the teacher summarizes the steps that students are prone to make mistakes in operation and gives emphasis and guidance [17].

3.3. Data Collection. After the two experiments are completed, a questionnaire was distributed to investigate the teaching effect of the two experimental teaching methods. In order to ensure the effectiveness and fairness of the assessment, the distribution and recovery of the questionnaires are independently completed by the researchers themselves.

After the data was collected and sorted, SPSS13.0 software was used for statistical analysis and processing. In general, descriptive statistical analysis and chi-square test are used for

analysis. For students' theoretical test scores, experimental assessment scores, experimental teaching method teaching effect investigation, critical thinking ability measurement, and medical students' communication skills and attitude measurement, normality analysis of the data is carried out first. The data are normally distributed and are further tested by a *t*-test.

4. Result

The scores of nurse-patient communication and experimental operation skills all showed a normal distribution. The data are then subjected to descriptive statistics and independent samples *t*-test, and the results show that the students in the experimental group have higher test scores than the control group, and the difference is statistically significant. The test results are shown in Tables 1–3. The corresponding statistical chart is shown in Figures 1–3.

After the test results come out, the scores are input into SPSS13.0, and a single-sample normality analysis is carried out, which shows that the test scores are normally distributed. Then descriptive statistics and independent samples *t*-test are performed, and the analysis results show that there is no statistically significant difference in theoretical scores between the experimental group and the control group, as shown in Table 4 below. The corresponding statistical chart is shown in Figure 4.

The comparison of critical thinking is shown in Tables 5–11. The corresponding statistical chart is shown in Figures 5–11. Descriptive statistics and independent samples *t*-test are performed on the scores of the students in the two groups. The results show that the total score of the CTDI-CV scale of the students in the experimental group is higher than that in the control group, and the difference is statistically significant.

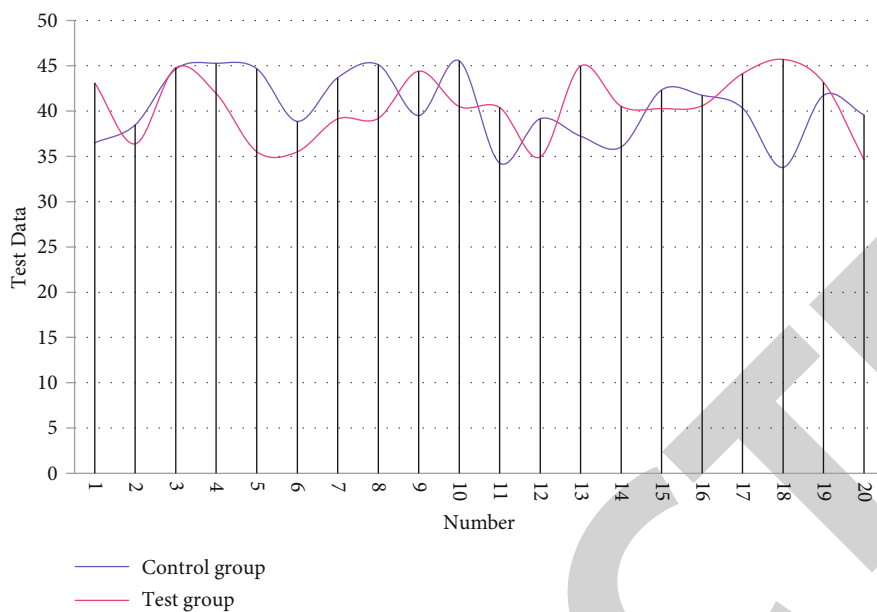


FIGURE 11: Comparison of cognitive maturity.

5. Analysis and Discussion

After reforming the traditional experimental course teaching, this research has preliminarily constructed the PBL-scenario simulation combined teaching method and applied it in the teaching of the experimental course of obstetrics and gynecology nursing. This teaching method combines PBL teaching with situational simulation teaching method. In the experiment, the teacher first gave the students SC and guides the students to study in groups, discuss, look up materials, analyze cases, and analyze layer by layer. In addition, teachers make students find the most appropriate treatment method and select patients who need nursing operation skills most. In the explanation of nursing operation techniques, according to the prewritten script, a situational simulation performance is performed, and some common clinical nurse-patient conflicts are designed to inspire students to think about how to communicate effectively with patients and their families and establish a harmonious nurse-patient relationship. Moreover, every link in the teaching process reflects the principle of “students as the main body, teachers as the main body, and cases as the main line.” It urges students to improve the initiative of self-learning and actively participate in the whole process of learning, instead of passively accepting knowledge.

Obstetrics and Gynecology Nursing, as the main clinical course of nursing, is offered in the sixth semester, which is the last semester for students to study at the school. At this point, students have learned all the basic medical courses and most of the clinical medical courses, laid a good medical foundation and self-learning ability, and formed a preliminary medical analysis ability. This enables PBL-scenario-simulation combined teaching to be opened and welcomed by students.

Data Availability

The labeled dataset used to support the findings of this study are available from the corresponding author upon request.

Conflicts of Interest

The authors declare no competing interests.

Acknowledgments

This work was supported by the Affiliated Hospital of Medical School, Ningbo University.

References

- [1] P. M. Hollenbach, “Simulation and its effect on anxiety in baccalaureate nursing students,” *Nursing Education Perspectives*, vol. 37, no. 1, pp. 45–47, 2016.
- [2] Y. Aksoy Derya and T. Pasinlioglu, “The effect of nursing care based on comfort theory on women's postpartum comfort levels after caesarean sections,” *International Journal of Nursing Knowledge*, vol. 28, no. 3, pp. 138–144, 2017.
- [3] M. Mert Karadas and F. Terzioglu, “The impact of the using high-fidelity simulation and standardized patients to management of postpartum hemorrhage in undergraduate nursing students: a randomized controlled study in Turkey,” *Health Care for Women International*, vol. 40, no. 5, pp. 597–612, 2019.
- [4] C. Linar, M. Badiran, and R. Hanum, “The study of nursing during the postpartum period from the perspective of Aceh culture in Gampong Asan Kareung, Lhokseumawe City,” *Journal La Medihealthico*, vol. 1, no. 5, pp. 30–39, 2020.
- [5] F. Ay, E. Tektaş, A. Mak, and N. Aktay, “Postpartum depression and the factors affecting it: 2000-2017 study results,” *Journal of Psychiatric Nursing*, vol. 9, no. 3, pp. 147–152, 2018.

Research Article

Body Weight Is a Valid Predictor of the Long-Term Prognosis of Cervical Cancer

Li Lu , Shuqi Ji, Jing Jiang, and Yu Yan

Department of Obstetrics and Gynecology, 2nd Affiliated Hospital of Harbin Medical University, China

Correspondence should be addressed to Li Lu; luli19721996@126.com

Received 3 May 2022; Revised 21 May 2022; Accepted 25 May 2022; Published 8 June 2022

Academic Editor: Pan Zheng

Copyright © 2022 Li Lu et al. This is an open access article distributed under the Creative Commons Attribution License, which permits unrestricted use, distribution, and reproduction in any medium, provided the original work is properly cited.

Objective. To identify and validate effective clinical predictors for the long-term prognosis of patients with cervical cancer. **Methods.** Cervical cancer patients were retrieved from the TCGA database, and patients' clinical data were collected and analyzed for the predictive value of long-term prognosis. In the other branch of the study, patients with cervical cancer and admitted to our hospital between January 1, 2016, and December 31, 2016, were retrieved and followed up for prognosis analysis. **Results.** In the database patient cohort of our study, 607 cases with cervical cancer were analyzed. Aneuploidy score ($p = 0.012$), Buffa hypoxia score ($p = 0.013$), histologic grade ($p = 0.01$), fraction genome altered >0.4 ($p < 0.001$), weight > 60 kg ($p < 0.001$), height > 160 cm ($p = 0.047$), BMI < 18.5 ($p = 0.023$), Winter hypoxia score ($p = 0.002$), and adjuvant postoperative radiotherapy were good predictors for disease-free survival (DFS), while aneuploidy score ($p = 0.001$), MSI sensor score > 0.5 ($p = 0.035$), person neoplasm status ($p < 0.001$), race ($p = 0.006$), Ragnum hypoxia score ($p = 0.012$), weight ($p < 0.001$), height ($p < 0.001$), and BMI < 18.5 ($p = 0.04$) were good predictors for overall survival (OS). In the admitted patient cohort, age over 60 years old at the time of diagnosis was the only clinical factor influencing the long-term DFS ($p = 0.004$). TNM stage above III ($p = 0.004$), body weight > 70 kg ($p < 0.001$), and complicated with other cancer ($p < 0.001$) were clinical factor influencing the long-term OS. **Conclusions.** Clinical factors, especially common to both cohorts, could be used to show the long-term prognosis of cervical cancer.

1. Introduction

The American Cancer Society predicts that in the year of 2022, there will be about 14,100 women who will be new cases of invasive cervical cancer, and about 4,280 women who will die from cervical cancer [1]. All over the world, women diagnosed with or died from cervical cancer in 2020 were estimated to be 604,127 or 341,831, respectively [2]. Thanks to the screening methods of Pap smear test and the recent detection of human papilloma virus (HPV) subtypes, both the incidence and the deaths caused by cervical cancer have been decreasing over the past 40 years in the United States [3].

Cervical cancer may present with different symptoms and signs at different clinical stages, from none at early

stages (about 44% of cervical cancer are diagnosed at this stage) to vaginal bleeding after intercourse between periods or after menopause, bloody vaginal discharge, or pain during intercourse at more advanced stages.

Serum or cancer tissue biomarkers for the prediction of prognosis of cervical cancer have been reported [4, 5]. The 5-year survival rate for overall cervical cancer is 66%, which is affected by race, ethnicity, age, and stage [2]. But the efficacy of those clinical factors in the prediction of prognosis of cervical cancer might be different due to the differences in race, genetic factors, living habits, and economic conditions across the world.

In this study, we investigated the efficacy of clinical factors in the prediction of the prognosis of patients with cervical cancer. We first analyzed data collected from a public

TABLE 1: Characteristics of analyzed patients from database (n = 607).

Variable	Mean \pm SD or subgroup	n
Age at diagnosis (years)	48.2 \pm 13.8	606
Weight (kg)	73.1 \pm 21.5	548
Height (cm)	161.0 \pm 7.3	265
DFS (months)	34.2 \pm 32.7	242
OS (months)	33.3 \pm 37.0	606
Clinical stage	IA	8
	IB	155
	IIA	26
	IIB	44
	IIIA	4
	IIIB	43
	IV	22
	I	36
Histologic grade	II	267
	III	237
	IV	2
	X	17
Race	White	415
	Black	59
	Asian	40
	American Indian Pacific islander	16 4
Fraction genome altered	0.27 \pm 0.18	293
Lymphovascular invasion indicator	Yes	82
	No	72
Neoplasm status	Tumor free	376
	With tumor	146
Mutation count	180.3 \pm 571.2	475

database and then analyzed and validated the findings in patients admitted to our hospital. We found that aneuploidy score, Buffa hypoxia score, histologic grades, fraction genome altered, weight, height, BMI, Winter hypoxia score, adjuvant postoperative radiotherapy, MSI sensor score, person neoplasm status, race, Ragnum hypoxia score were important clinical predictors for the 5-year prognosis of cervical cancer in patients from database, while age, TNM stages, and body weight, diagnosed with other cancer, were important clinical predictors for the 5-year prognosis of cervical cancer in patients admitted to our hospital.

2. Materials and Methods

2.1. Patients. We searched the TCGA database (<https://cancergenome.nih.gov>) and identified the cervical squamous cell carcinoma dataset ($n = 297$) and the cervical squamous cell carcinoma and endocervical adenocarcinoma dataset ($n = 310$). All cases with available information were included for analysis. Clinical data of patients diagnosed with primary cervical cancer and admitted to our hospital between

TABLE 2: Clinical factors for the prognosis of DFS of patients from database.

Clinical factors	p value (DFS)	n
Age at diagnosis (years)	0.773	242
Lymph node stage	0.959	206
Tumor stage	0.856	202
Squamous cancer	0.245	242
Aneuploidy score	0.012	170
Buffa hypoxia score	0.013	170
Histologic grade groups	0.01	239
Fraction genome altered (>0.4)	<0.001	242
Person neoplasm status	0.056	211
Race	0.322	211
Ragnum hypoxia score	0.3	123
Weight (<60 kg)	<0.001	222
Patient height (<160 cm)	0.047	107
BMI < 18.5	0.023	93
Corpus uteri involvement	0.641	56
Winter hypoxia score	0.002	118
Adjuvant postoperative radiotherapy	0.017	69
Total number pregnancies	0.829	103
Cigarette smoking pack year	0.055	35
Hysterectomy type	0.213	75

January 1, 2016, and December 31, 2016, were retrieved for analysis. Patients were followed up for prognosis information. This study was approved by the ethical committee of our hospital. Informed consents were obtained during follow up.

2.2. Data Extraction. Clinical characteristics, including age, disease-free survival (DFS), overall survival (OS), race, clinical stages, histologic grades, mutation count, weight, height, BMI, and postoperative radiotherapy, were extracted from the databases as well as patient records from our hospital.

2.3. Statistical Analyses. The measurement data were expressed as mean \pm standard deviation (SD). The Kaplan-Meier survival curve was employed to show the correlations between clinical characteristics and long-term prognosis, including DFS and OS. The receiver operating characteristic (ROC) curve was employed to show the effectiveness of clinical characteristics to predict 5-year survival. Statistical analyses were performed using SPSS 24.0 (SPSS Inc., Chicago, USA). A two-tailed p value of less than 0.05 was determined as statistically significant.

3. Results

3.1. Clinical Characteristics. There were 607 patients collected from the two TCGA database (Table 1). The mean age at diagnosis was 48.2 \pm 13.8 years old, with a mean DFS of 34.2 \pm 32.7 months, a mean OS of 33.3 \pm 37.0 months, and a mean body weight of 73.1 \pm 21.5 kg. Height, weight, TNM stage, histologic stage, fraction genome altered,

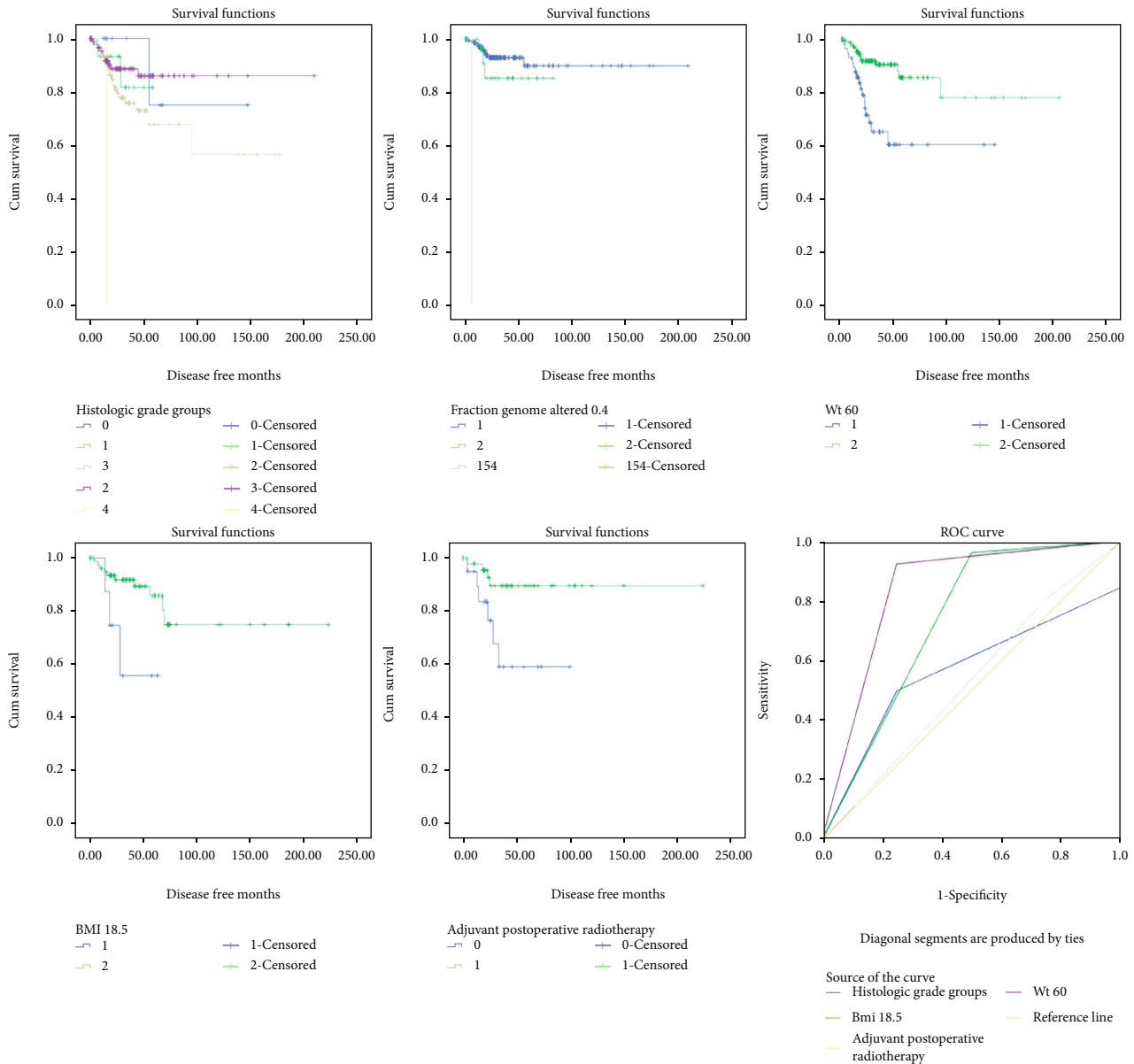


FIGURE 1: Kaplan-Meier survival curve and ROC curve of predictive value of clinical factors for DFS in database patients.

race, lymphovascular invasion indicator, neoplasm status, and mutation count were further analyzed (Table 1). On the other hand, ninety-four qualified patients were retrieved from the medical record at our hospital, and the complete data collected from 61 cases during our follow-up contact were collected and analyzed. The mean age of followed-up patients were 47.6 ± 9.1 years old, with a mean DFS of 59.2 ± 4.8 months, a mean OS of 58.0 ± 7.0 months, and a mean body weight of 61.0 ± 7.3 kg.

3.2. Determination of Predictive Factors for DFS in Database Patients. Aneuploidy score ($p = 0.012$), Buffa hypoxia score ($p = 0.013$), histologic grade ($p = 0.01$), fraction genome altered >0.4 ($p < 0.001$), weight >60 kg ($p < 0.001$), height >160 cm ($p = 0.047$), BMI <18.5 ($p = 0.023$), Winter hypoxia score ($p = 0.002$), and adjuvant postoperative radiotherapy

($p = 0.017$) were all significantly correlated with disease-free survival, whereas age at diagnosis, lymph node stage, tumor stage, squamous cancer, person neoplasm status, race, Ragnum hypoxia score, corpus uteri involvement, total number of pregnancies, cigarette smoking, and hysterectomy type were not (all $p > 0.05$, Table 2). Kaplan-Meier survival curves, as well as the corresponding ROC curves were shown in Figure 1. When judged by the area under the curve, weight <60 kg showed the best value (area = 0.837) in prediction of long-term DFS.

3.3. Determination of Predictive Factors for OS from Database Patients. Aneuploidy score ($p = 0.001$), MSI sensor score >0.5 ($p = 0.035$), person neoplasm status ($p < 0.001$), race ($p = 0.006$), Ragnum hypoxia score ($p = 0.012$), weight ($p < 0.001$), height ($p < 0.001$), and BMI <18.5 ($p = 0.04$)

were significantly associated with OS (Table 3). On the other hand, age at diagnosis, clinical stages, histologic grade, fraction genome altered, MSI MANTIS score, mutation count, corpus uteri involvement, Winter hypoxia score, adjuvant postoperative radiotherapy, total number pregnancies, cigarette smoking, and hysterectomy type were not correlated with OS (all $p > 0.05$, Table 3). Kaplan-Meier survival curves and ROC curves of corresponding factors were shown in Figure 2. Based on the area under the curve, Ragnum hypoxia score and MSI sensor score > 0.5 both showed the best value (area = 0.594) in prediction of long-term OS.

3.4. Predictive Factors for Admitted Patients. Age over 60 years old at the time of diagnosis was the only clinical factor influencing the long-term DFS ($p = 0.004$). TNM stage above III ($p = 0.004$), body weight > 70 kg ($p < 0.001$), and complicated with other cancer ($p < 0.001$) were clinical factors influencing the long-term OS (Table 4). In the corresponding ROC curves, age over 60 years had an area under the curve of 0.942 for the prediction of long-term DFS, whereas weight > 70 kg had an area under the curve of 0.722 for the prediction of long-term OS (Figure 3).

4. Discussion

In this study, due to the limited availability of many clinical exams, a lot of clinical factors determined to be predictors of the prognosis of cervical cancer in the database patient cohort could not be validated in our admitted patient cohort. Among clinical factors available in both database and admitted patients, there were still quite a lot of differences. Histologic grades, body weight, and adjuvant postoperative radiotherapy were predictive factors for database patients' DFS, whereas age > 60 years was the only predictive factors for admitted patients' DFS. On the other hand, body weight was the only predictive factors for database patients' OS, whereas TNM stage, body weight, and complicated with other cancer were the predictive factors for admitted patients' OS.

The finding of body weight as a predictor for the prognosis of cervical cancer patients coincided with a recent study, where patients received concurrent chemoradiotherapy [6]. However, only 159/547 (29%) of database patients and 34/61 (56%) of admitted patients in our study received adjuvant postoperative radiotherapy, suggesting the efficacy of weight or BMI as predictive factors for the prognosis of cervical cancer does not rely on chemoradiotherapy, but was really related to cervical cancer itself.

In the database cohort, 163/302 (54%) patients were diagnosed at clinical stage I, 70/302 (23%) at clinical stage II, 47/302 (16%) at clinical stage III, and 22/302 (7%) at clinical stage IV, whereas in the admitted cohort, 17/61 (28%) patients were diagnosed at clinical stage I, 34/61 (56%) patients were diagnosed at clinical stage II, 5/61 (8%) patients were diagnosed at clinical stage III, and 5/61 (8%) patients were diagnosed at clinical stage IV. The later stage at diagnosis in our admitted patients cohort suggests a late detection, which might reflect a lower rate of annual Pap smear and/or HPV screening, as well as the lower avail-

TABLE 3: Clinical factors for the prognosis of OS of patients from database.

Clinical factors	p value (OS)	n
Age at diagnosis (overall)	0.425	602
Lymph node stage	0.349	512
Tumor stage	0.998	484
Cancer type	0.849	604
Squamous	0.257	604
Aneuploidy score	0.001	293
Histologic grade	0.168	589
Fraction genome altered	> 0.05	297
MSIMANTIS score	> 0.05	297
MSI sensor score	> 0.05	297
MSI sensor score (> 0.1)	< 0.001	297
MSI sensor score (> 0.2)	< 0.001	297
MSI sensor score (> 0.5)	0.035	297
MSI sensor score (> 1)	0.572	297
Mutation count	> 0.05	533
Person neoplasm status	< 0.001	522
Race	0.006	534
Ragnum hypoxia score	0.012	293
Patient weight (overall)	< 0.001	547
Patient height (overall)	< 0.001	265
Patient height (< 170 cm)	0.01	265
BMI (overall)	0.032	218
BMI (< 18.5)	0.004	218
Corpus uteri involvement	0.289	118
Winter hypoxia score	> 0.05	293
Adjuvant postoperative radiotherapy	0.941	159
Total number pregnancies	0.174	269
Cigarette smoking pack year	> 0.05	95
Hysterectomy type	0.39	170

ability of HPV vaccination in China. Also, the finding that clinical stage showed a good predictive value as a predictive factor for the OS of cervical cancer in the admitted cohort, but not in the database cohort, might be due to the relatively higher percent (more weight) of clinical stage II patients.

The evolving development in big data techniques makes data mining from published database a feasible and affordable way for clinical studies [7, 8], although the inconsistency in study design and retrospectively collected data make a lot of parameters incomparable between different studies [9]. Ideally, comprehensive parameters in the field of psychology and social-economy need to be obtained for a better understanding of factors influencing the prognosis of cervical cancer. Interesting topics might include income, nutrient conditions, anxiety, depression [10], living habits, etc. In our admitted cohort, we included the parameter of "self-living," which, although did not show significant contribution to the long-term prognosis, was still near to statistical borderline ($p = 0.07$) and might be a promising factor if we include more cases in the future. Other clinical

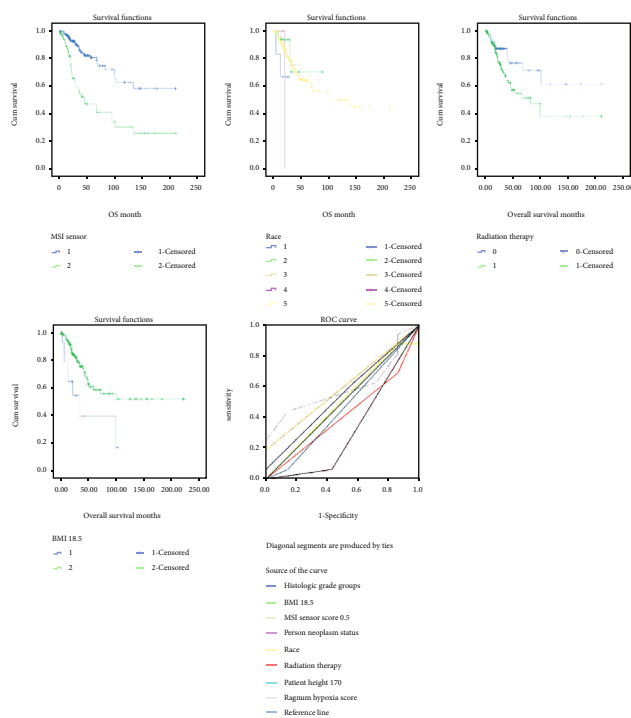


FIGURE 2: Kaplan-Meier survival curve and ROC curve of predictive value of clinical factors for OS in database patients.

TABLE 4: Predictive factors for survival of admitted patients.

Variable	Cutoff	<i>p</i> value of DFS	<i>p</i> value of OS
Age at diagnosis (years)	Overall	0.38	0.25
	>30	0.85	0.65
	>40	0.73	0.41
	>50	0.16	0.46
	>60	0.004	0.1
	Overall	0.87	0.004
TNM stage	II	0.53	0.49
	III	0.71	0.004
	IV	0.85	<0.001
	Overall	0.28	0.17
Histologic grade	II	0.57	0.61
	III	0.11	0.13
	Overall	0.98	0.005
Radiation and/or chemotherapy	>50	0.73	0.41
	>60	0.31	0.36
	>70	0.76	<0.001
Smoke	Yes	0.81	0.57
	Overall	1.00	0.65
	>1	0.70	0.88
Longest dimension of lesion (cm)	>2	0.34	0.12
	>3	0.18	0.98
	>4	0.72	0.39
	Overall	NA	<0.001
Self-living	Yes	0.89	0.07

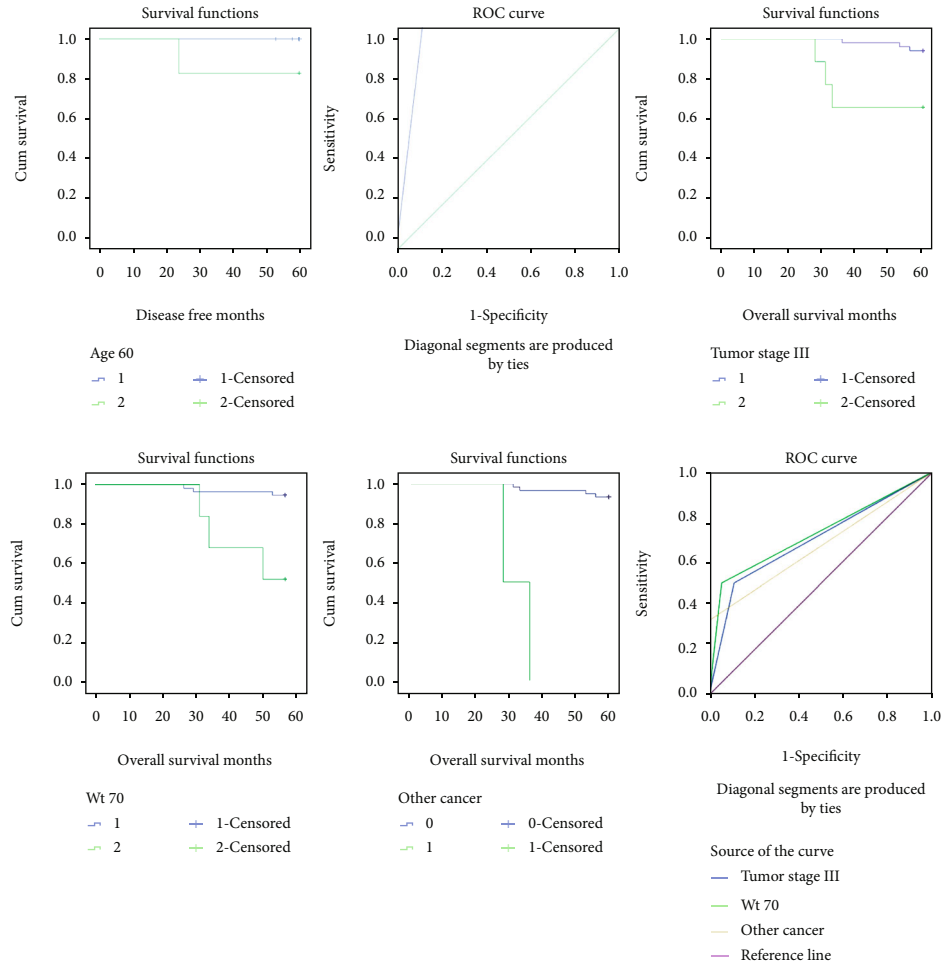


FIGURE 3: Kaplan-Meier survival curve and ROC curve of predictive factors for DFS and OS in admitted patients.

conditions, such as histories of labor induction [11], treatment of preterm labor [12], fulminant hepatitis [13–16], role of RNA interference [17], and HPV [18], might also contribute to the prognosis of cervical cancer.

To sum up, we found clinical factors, especially body weight, histologic grades, age, TNM stages, complicated with other cancers, and adjuvant postoperative radiotherapy, can be valid long-term predictors of prognosis of cervical cancer. A uniformed reporting system is needed for the benefit of future updates and analyses.

Data Availability

The datasets used in this study are available from the corresponding author on reasonable request.

Conflicts of Interest

The authors declare that they have no conflict of interest.

References

- [1] American Cancer Society, “Key statistics for cervical cancer,” April 2022, <https://www.cancer.org/cancer/cervical-cancer/about/key-statistics.html>.
- [2] American Society of Clinical Oncology (ASCO), “Cervical cancer: statistics,” May 2022, <https://www.cancer.net/cancer-types/cervical-cancer/statistics>.
- [3] Division of Cancer Prevention and Control and Centers for Disease Control and Prevention, “Cervical cancer statistics,” April 2022, <https://www.cdc.gov/cancer/cervical/statistics/index.htm>.
- [4] X. Ma, H. Xue, J. Zhong, B. Feng, and Y. Zuo, “Serum actinin-4 levels as a potential diagnostic and prognostic marker in cervical cancer,” *Disease Markers*, vol. 2020, Article ID 5327378, 6 pages, 2020.
- [5] X. Zhu, L. Long, H. Xiao, and X. He, “Cancer-derived exosomal miR-651 as a diagnostic marker restrains cisplatin resistance and directly targets ATG3 for cervical cancer,” *Disease Markers*, vol. 2021, Article ID 1544784, 16 pages, 2021.
- [6] A. Abe, M. Yuasa, Y. Imai et al., “Extreme leanness, lower skeletal muscle quality, and loss of muscle mass during treatment

- are predictors of poor prognosis in cervical cancer treated with concurrent chemoradiation therapy,” *International Journal of Clinical Oncology*, vol. 27, no. 5, pp. 983–991, 2022.
- [7] I. Kaur, M. N. Doja, T. Ahmad et al., “An integrated approach for cancer survival prediction using data mining techniques,” *Computational Intelligence and Neuroscience*, vol. 2021, Article ID 6342226, 14 pages, 2021.
- [8] Y. Li, F. Huo, Y. Wen, and M. Jiang, “Screening and identification of an immune-associated lncRNA prognostic signature in ovarian carcinoma: evidence from bioinformatic analysis,” *BioMed Research International*, vol. 2021, Article ID 6680036, 13 pages, 2021.
- [9] L. Lu, S. Ji, J. Jiang, and Y. Yan, “Clinical characteristics in the prediction of posttreatment survival of patients with ovarian cancer,” *Disease Markers*, vol. 2022, Article ID 3321014, 14 pages, 2022.
- [10] S. Li, L. Li, X. Shi, M. Wang, X. Song, and F. Cui, “Personalized prechemotherapy education reduces peri-chemotherapy anxiety in colorectal cancer patients,” *Disease Markers*, vol. 2021, Article ID 6662938, 5 pages, 2021.
- [11] X. M. Li, J. Wan, C. F. Xu et al., “Misoprostol in labour induction of term pregnancy: a meta-analysis,” *Chinese Medical Journal*, vol. 117, no. 3, pp. 449–452, 2004.
- [12] X. Li, Y. Zhang, and Z. Shi, “Ritodrine in the treatment of preterm labour: a meta-analysis,” *The Indian Journal of Medical Research*, vol. 121, no. 2, pp. 120–127, 2005.
- [13] X. M. Li, L. Ma, Y. B. Yang, Z. J. Shi, and S. S. Zhou, “Prognostic factors of fulminant hepatitis in pregnancy,” *Chinese Medical Journal*, vol. 118, no. 20, pp. 1754–1757, 2005.
- [14] Y. Yang, L. Deng, X. Li et al., “Analysis of prognosis-associated factors in fulminant viral hepatitis during pregnancy in China,” *International Journal of Gynaecology and Obstetrics*, vol. 114, no. 3, pp. 242–245, 2011.
- [15] Y. Yang, L. Deng, X. Li et al., “Evaluation of the prognosis of fulminant viral hepatitis in late pregnancy by the MELD scoring system,” *European Journal of Clinical Microbiology & Infectious Diseases*, vol. 31, no. 10, pp. 2673–2678, 2012.
- [16] L. Deng, X. Li, Z. Shi, P. Jiang, D. Chen, and L. Ma, “Maternal and perinatal outcome in cases of fulminant viral hepatitis in late pregnancy,” *International Journal of Gynecology & Obstetrics*, vol. 119, no. 2, pp. 145–148, 2012.
- [17] Z. Shi, R. Nicholson, A. Jaggi, and A. Nicholson, “Characterization of Aquifex aeolicus ribonuclease III and the reactivity epitopes of its pre-ribosomal RNA substrates,” *Nucleic Acids Research*, vol. 39, no. 7, pp. 2756–2768, 2011.
- [18] Y. Z. Bekmukhambetov, O. A. Mynbaev, A. Tinelli et al., “Human papillomavirus related issues in western Kazakhstan: protocol for a comprehensive study,” *Russian Open Medical Journal*, vol. 7, no. 4, article e0408, 2018.